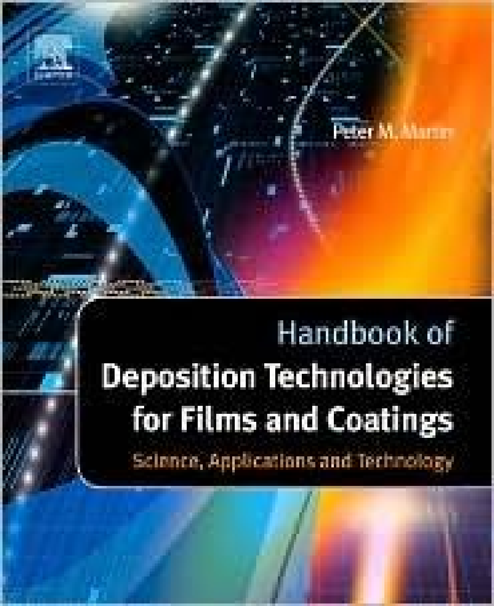

Peter M. Martin

Handbook of
Deposition Technologies for Films and Coatings

Science, Applications and Technology

Dedication

This volume is dedicated to Rointan Bunshah and my wife Ludmila. Rointan is the Editor of the first two handbooks and definitely one of the pioneers and leaders of thin film processes and technology. My wife Ludmila has been at my side through my entire career and Pacific Northwest National Laboratory and is an inspiration to me.

William Andrew is an imprint of Elsevier
The Boulevard, Langford Lane, Kidlington, Oxford OX5 1GB, UK
30 Corporate Drive, Suite 400, Burlington, MA 01803, USA

First edition 2002
Second edition 2005

Copyright © 2010 Peter M. Martin. Published by Elsevier Inc. All rights reserved

No part of this publication may be reproduced, stored in a retrieval system or transmitted in any form or by any means electronic, mechanical, photocopying, recording or otherwise without the prior written permission of the publisher

Permissions may be sought directly from Elsevier's Science & Technology Rights Department in Oxford, UK: phone (+44) (0) 1865 843830; fax (+44) (0) 1865 853333; email: permissions@elsevier.com. Alternatively you can submit your request online by visiting the Elsevier web site at http://elsevier.com/locate/permissions, and selecting *Obtaining permission to use Elsevier material*

Notice
No responsibility is assumed by the publisher for any injury and/or damage to persons or property as a matter of products liability, negligence or otherwise, or from any use or operation of any methods, products, instructions or ideas contained in the material herein. Because of rapid advances in the medical sciences, in particular, independent verification of diagnoses and drug dosages should be made

British Library Cataloguing in Publication Data
A catalogue record for this book is available from the British Library

Library of Congress Cataloging-in-Publication Data
A catalog record for this book is availabe from the Library of Congress

ISBN–13: 978-0-8155-2031-3

For information on all William Andrew publications
visit our web site at books.elsevier.com

Printed and bound in the United States

10 11 12 13 14 10 9 8 7 6 5 4 3 2 1

Working together to grow
libraries in developing countries

www.elsevier.com | www.bookaid.org | www.sabre.org

ELSEVIER BOOK AID International Sabre Foundation

Preface to the Third Edition

The first two editions of this Handbook, edited by Ron Bunshaw, were immensely popular, are still used extensively and have become classics. The second edition was published in 1994, over fourteen years ago, and there is now a critical need for updating every chapter. To that end, the Third Edition of this Handbook has been entirely modified and encompasses virtually every aspect of thin film deposition technology. It is being brought out primarily to update how deposition technologies are keeping pace with the vast new developments in thin film structures and materials and applications. Advances in thin film deposition technology and characterization, and emerging technologies are addressed. This book complements other handbooks by presenting a broad range of thin film deposition and plasma technologies and characterization techniques written by international experts in the field. All chapters have been updated when necessary, some deleted, and new chapters on atomic layer deposition (ALD), cathodic arc deposition, sculpted thin films (GLAD), polymer thin films and atmospheric plasmas have been added. The major role of plasmas has also been expanded.

Thin film coating technology is advancing rapidly to keep pace with new applications in semiconductor, optical, tribological, display, decorative, solar, and medical technologies. Performance demands on virtually all types of thin film materials are continuously increasing. To meet these demands, thin film coatings and structures are becoming more sophisticated with engineered properties. Superlattices, nanotubes, nanolaminates, composites, chiral structures and diffusion barriers, to name a few, are now used routinely. Because of this, process and technology handbooks published even ten years ago are already out of date. Deposition processes and technologies are also changing rapidly to keep pace with advanced thin film materials and applications. Conventional deposition processes are being adapted in novel coating geometries to produce thin film structures with improved performance and properties not achievable by conventional methods. Additionally new deposition processes, such as high power pulsed plasma magnetron sputtering, are being developed to achieve new materials and physical properties. Thin films are now being engineered with electrical, optical, and mechanical properties not possible a decade ago. Characterization techniques are also improving.

In addition to the new subject areas, the following core subjects from the second edition have been addressed by new authors, while retaining many of the exceptional contributors from the second edition: Evaporation, Physical Vapor Deposition (PVD), Ion Plating, Cathodic Arc Deposition (CAD), Plasma Enhanced Chemical Vapor Deposition (PECVD), Atmospheric Plasmas, Vacuum Polymer Deposition (VPD), Chemical Vapor Deposition (CVD), and Jet Vapor Deposition (JVD). The chapter on polymer coatings was added to include this very important family of materials, particularly in the area of gas and water barrier coatings for molecular electronic devices, thin film batteries and solar cells. Chapters on adhesion, structure of PVD deposits, tribological coatings, elemental and structural characterization, substrate cleaning, role of plasmas in deposition processes have all been completely revised. The chapter on Nucleation, Film Growth, and Microstructural Evolution has also been completely revised and is one of the most important subjects in this edition. The chapter on plasma assisted vapor deposition processes is eliminated since this material is redundant and covered in other chapters. Chapters on Deposition from Aqueous Solutions and Electrodeposition have also been eliminated because they are mature technologies with extensive publications and diminishing applications.

We hope that this edition will be just as or more useful to the multitude of disciplines represented by the technologists in this field and will remain germane for many years to come.

Peter M. Martin
Columbia Basin Thin Film Solutions LLC
Kennewick, Washington
September, 2009

List of Abbreviations

ABS	acrylonitrile butadiene styrene
ABS	arc bond sputtering
AEM	analytical electron microscopy
AES	Auger electron spectroscopy
AFM	atomic force microscopy
ALD	atomic layer deposition
APGD	atmospheric pressure glow discharge
APT	atom-probe tomography
AR	angle-resolved
AR	antireflective
ARE	activated reactive evaporation
ARXPS	angle resolved X-ray photoelectron spectroscopy
ASF	atomic sensitivity factor
ASH	atomic scale heating
ATR	attenuated total reflection
BARE	biased activated reactive evaporation
BE	binding energy
BF	bright field
CARS	coherent anti-Stokes Raman scattering
CCD	charge-coupled device
CCP	capacitively coupled plasma
CDC	carbide-derived carbon
Ch	chalcogen
CIGS	copper indium gallium diselenide
CIP	chemical ion plating
CIS	copper indium diselenide
CMA	coaxial cylindrical mirror analyzer
C:Me	metal-containing carbon
COF	coefficient of friction
CQ	collisional quenching
CSD	charge state distribution
CTEM	conventional transmission electron microscopy
CVD	chemical vapor deposition
DBD	dielectric barrier discharge
DC-MS	direct-current magnetron sputtering
DF	dark field

DFT	density functional theory
dHB	duMond–Hart–Bartels
DIET	desorption induced by electronic transitions
DLC	diamond-like carbon
DRAM	dynamic random access memory
DRS	direct recoiling spectroscopy
DRV	dimer row vacancy
DVD	directed vapor deposition
DVL	dimer vacancy line
EAG	Evans Analytical Group
EB	electron beam
EBSD	electron backscattering diffraction
EC	electrochromic
ECR	electron cyclotron resonance
ED	electron diffraction
EDTA	ethylene diamine tetraacetic acid
EDXS	energy-dispersive X-ray spectroscopy
EEDF	electron energy distribution function
EELS	electron energy-loss spectroscopy
EIS	electrochemical impedance spectroscopy
ELNES	energy loss near-edge structure
ELO	epitaxial lateral overgrowth
EM	effective medium
EMA	effective medium approximation
EMSL	Environmental Molecular Sciences Laboratory
ER	erosion resistance
ERDA	elastic recoil detection analysis
ERD-TOF	elastic recoil detection in the time-of-flight regime
ESCA	electron spectroscopy for chemical analysis
ESD	electron-stimulated desorption
ESZM	extended structure zone model
ETFE	ethylene-tetrafluoroethylene
EXAFS	X-ray absorption fine structure
EXELFS	extended electron energy loss fine structure
FCA	filtered cathodic arc
FCC	Federal Communications Commission
FHC	fused hollow cathode
FIB	focused ion beams
FTIR	Fourier transform infra-red spectroscopy
GB	grain boundary
GDMS	glow discharge mass spectrometry

GLAD	glancing angle (of incidence) deposition
GMR	giant magnetoresistance
GRIN	gradient-index
GRXRD	glancing-incidence X-ray diffraction
HA	hydroxyapatite
HAADF	high-angle annular dark field
HEIS	high-energy ion scattering
HEMT	high electron mobility transistor
H-HEAD	hybrid hollow electrode activated discharge
HIPIMS	high-power impulse magnetron sputtering
HMCTSZN	hexamethyl cyclotrisilazane
HMDSN	hexamethyl disilazane
HMDSO	hexamethyl disiloxane
HPPMS	high-power pulsed magnetron sputtering
HRPVD	high-rate physical vapor deposition
HRTEM	high-resolution transmission electron microscopy
HRXRD	high-resolution X-ray diffraction
IA	ion assist
IAD	ionization assisted deposition
IBAD	ion beam assisted deposition
IBED	ion beam enhanced deposition
IC	integrated circuit
IC	internal conversion
ICP	inductively coupled plasma
IEA	ion energy analyzer
IEDF	ion energy distribution function
IGC	inert gas condensation
IMFP	inelastic mean free path
IPA	isopropyl alcohol
IPVD	ionized physical vapor deposition
IR	infrared
ISC	intersystem crossing
ISE	ion-induced secondary electron
ISS	ion scattering spectroscopy
ITO	indium–tin oxide
ITU	International Telecommunications Union
IVD	ion vapor deposition
JVD	jet vapor deposition
KE	kinetic energy
KPZ	Kardar–Parisi–Zhang
LAFAD	large-area filtered arc deposition

LAIGC	laser-assisted inert gas condensation
LC	liquid crystal
LEED	low-energy electron diffraction
LEIS	low-energy ion scattering
LEL	lower explosive limit
LIF	laser induced fluorescence
LML	liquid multilayer
LPPD	low-pressure plasma deposition
LSCF	lanthanum strontium cobalt iron oxide
MBE	molecular beam epitaxy
MD	molecular dynamics
MDP	molecularly doped polymer
MEIS	medium-energy ion scattering
MEMS	microelectromechanical system
MF	mid-frequency
MF/DMS	mid-frequency/dual magnetron sputtering
MH	Mullins–Herring
MIM	metal–insulator–metal
ML	monolayer
MLD	molecular layer deposition
MNS	metal-nitride semiconductor
MOCVD	metal-organic chemical vapor deposition
MoDTC	molybdenum dialkyl dithiocarbamate
MS	magnetron sputtering
MS	mass spectrometry
MSRI	mass spectroscopy of recoiled ions
MW	microwave
nc	nanocomposite
NCD	nanocrystalline diamond
NIR	near infrared
NIST	National Institute of Standards and Technology
NPL	National Physical Laboratory
NRA	nuclear reaction analysis
NSOM	near-field scanning optical microscopy
OCP	open circuit potential
OES	optical emission spectroscopy
OIF	optical interference filter
OLED	organic light-emitting device
OTR	oxygen transmission rate
PACVD	plasma-assisted chemical vapor deposition
PC	polycarbonate
PC	photonic crystal

pc-D	polycrystalline diamond
PECVD	plasma-enhanced chemical vapor deposition
PET	polyethylene terephthalate
PICVD	plasma impulse chemical vapor deposition
PIIID	plasma immersion ion implantation deposition
PIXE	proton-induced X-ray emission
PLD	pulsed laser deposition
PLZT	lead lanthanum zirconate titanate
PML	polymer multilayer
PMMA	polymethyl methacrylate
PMS	plasma mass spectrometry
PPFC	plasma polymerized fluorocarbon
PPHC	plasma polymerized hydrocarbon
PPML	plasma polymer multilayer process
PPOS	plasma polymerized organosilicone
PTFE	polytetrafluoroethylene
PVD	physical vapor deposition
PZT	lead–zirconium–titanate
QA	QuinAcridone
QD	quantum dot
RBS	Rutherford backscattering spectrometry
RF	radio frequency
RHEED	reflection high-energy electron diffraction
RIE	reactive ion etching
RIP	reactive ion plating
RMS	Roughness Measurement System
RPE	reactive plasma etching
RS	Raman spectroscopy
RT	room temperature
RTSE	real-time spctroscopic ellipsometry
SAE	Society of Automotive Engineers
SAED	selected area electron diffraction
SBD	serial bideposition
SCF	supercritical fluid
SEG	selective epitaxial growth
SEM	scanning electron microscopy
SERS	surface-enhanced Raman spectroscopy
SIMS	secondary ion mass spectroscopy
S-K	Stranski–Krastanow
SPM	scanning probe microscopy
SS	stainless steel
SST	supersonic transport

STEM	scanning transmission electron microscopy
STF	sculptured thin film
STM	scanning tunneling microscopy
SZM	structure zone model
TACVD	thermally activated CVD
TCO	transparent conductive oxide
TCP	tricalcium phosphate
TE	transverse electric
TEG	triethyl gallium
TEM	transmission electron microscopy
TEOS	tetra ethoxysilane
TEOT	tetra ethoxy titanium
TFEL	thin film electroluminescent
TIPT	tetraisopropyltitanate
TLK	Terrace, Ledge, Kink
TM	transverse magnetic
TMA	trimethyl-aluminum
TMAA	trimethyl-amine alane
TMG	trimethyl gallium
TOF	time-of-flight
TPD	thermally programmed desorption
TPO	thermoplastic olefin
TRPL	time-resolved photoluminescence
UHV	ultrahigh vacuum
ULSI	ultra large scale integration
UV	ultraviolet
VASE	variable angle spectroscopic ellipsometry
VLSI	very large scale integration
VOC	volatile organic compound
VPD	vacuum polymer deposition
VPE	vapor phase epitaxy
VR	vibrational relaxation
VUV	vacuum ultraviolet
WVTR	water vapor transmission rate
XANES	X-ray absorption near-edge structure
XPS	X-ray photoelectron spectroscopy
XRD	X-ray diffraction
XRR	X-ray reflectivity
XTEM	cross-sectional transmission electron microscopy
YSZ	yttria-stabilized zirconia
ZDDP	zinc dialkyl dithiophosphate

CHAPTER 1

Deposition Technologies: An Overview

1.1 The Market

The second edition of this handbook lists market areas for surface engineered products, including thin film coatings as of the mid-1990s. Since then the market for several types of thin film products has exploded, including photovoltaics, energy conversion, energy efficiency, biomedical, pharmaceutical, and flat panel displays. The demand for advanced tribological and corrosion-resistant coatings has also increased. It is estimated that the global market for optical thin film coatings alone will exceed $7.5 billion by 2010. This includes optical components, telecommunications, window glazings, large area and decorative applications, laser mirrors, automotive coatings (electrochromic rear view mirrors, etc.), ophthalmic applications, and aircraft windows. The global market for solar cells will increase to $32 billion by 2012 and for thin film solar panels alone is estimated to be $8.3 billion by 2030. As of 2008, there are at least 50 companies marketing thin film photovoltaic devices and systems. And this will only grow with increased renewable energy demands, increased efficiency of organic and transparent solar cells, and low-cost solar concentrator systems. Additional energy applications include photocatalytic coatings, thin film fuel cells, thin film lithium batteries, hydrogen generation, electrochromic and thermochromic coatings, and solar control coatings. Molecular electronics, including organic light-emitting devices (OLEDs), has changed the entire manufacturing process for flat panel displays and will continue to do so for plastic windows. Advanced wear- and corrosion-resistant materials are being developed for medical implants, combustion and gas turbine engines, and aircraft engines and parts.

As stated in the second edition, surface engineering will remain a growth industry well into the next decade because surface engineered products increase and improve performance, add functionality, reduce costs, improve materials usage efficiency, and provide performance not possible with bulk materials. Thin films thus offer enormous potential due to the following:

- creation of entirely new and revolutionary products
- solution of previously unsolved engineering problems
- improved functionality of existing products; engineering, medical, and decorative
- production of nanostructured coatings and nanocomposites
- conservation of scarce materials
- ecological considerations – reduction of effluent output and power consumption.

Research and development (R&D) expenditures in surface engineering are very expensive. Industrial deposition systems can cost as much as $20 million. Even in the mid-1990s it was reported that Japan spent $100–150 million on R&D in diamond and diamond-like carbon (DLC) coatings, and this had certainly escalated by 2008 with the increased use of DLC. A number of companies in the USA and Europe are now marketing DLC coatings for a wide range of applications. Investments in photovoltaics worldwide have increased by a factor of 80 in the last decade. The United States Department of Energy spent approximately $24 billion on R&D in 2007. While government support for R&D in biomedical materials in the USA has plateaued, the market is steadily increasing, with European countries leading the way. The same is true for many energy efficiency markets (thermoelectric power generation, advanced glazings, etc.). R&D spending in China has reached $10 billion. The list continues to expand with the need for renewable energy sources, energy efficiency improvements, more sophisticated optical applications and telecommunication, advancing display technology, and advanced medical applications with an aging population.

1.2 Introduction

This is the third edition of this handbook. While many of the chapter headings are the same as those found in the second edition, thin film processes and technologies have advanced significantly in the past 14 years and descriptions in most cases are very different. New authors have been added who focus on different and advanced aspects of this technology. Some chapters found in the second edition present mature technologies with plateaued or diminishing applications, and have been eliminated. The reader is referred to the second edition of this handbook for a description of earlier technology.

Since the second edition was published in 1994, thin film deposition technology and the science have progressed rapidly in the direction of engineered thin film coatings and surface engineering. Plasmas are used more extensively. Accordingly, advanced thin film deposition processes have been developed and new technologies have been adapted to conventional deposition processes. The market and applications for thin film coatings have also increased astronomically, particularly in the biomedical, display, and energy fields. *Thin film* is the general term used for coatings that are used to modify and increase the functionality of a bulk surface or substrate. They are used to protect surfaces from wear, improve lubricity, improve corrosion and chemical resistance, and provide a barrier to gas penetration. In many cases thin films do not affect the bulk properties of the material. They can, however, totally change the optical, electrical transport, and thermal properties of a surface or substrate, in addition to providing an enhanced degree of surface protection.

Thin films have distinct advantages over bulk materials. Because most processes used to deposit thin films are non-equilibrium in nature, the composition of thin films is not constrained by metallurgical phase diagrams. Crystalline phase composition can also be varied to a certain extent by deposition conditions and plasma enhancement. Virtually every property of the thin film depends on and can be modified by the deposition process and not all processes produce materials with the same properties. Microstructure, surface morphology, tribological, electrical, and optical properties of the thin film are all controlled by the deposition process. A single material can be used in several different applications and technologies, and the optimum properties for each application may depend on the deposition process used. Since not all deposit technologies yield the same properties or microstructures, the deposition process must be chosen to fit the required properties and application (see Chapter 12). For example, DLC films are used to reduce the coefficient of friction (COF) of a surface and improve wear resistance, but they are also used in infrared optical and electronic devices. Titanium dioxide (TiO_2) is probably the most important and widely used thin film optical material and is also used in photocatalytic devices and self-cleaning windows, and may have important applications in hydrogen production. Zinc oxide (ZnO) has excellent piezoelectric properties but is also used as a transparent conductive coating and in spintronics applications. Silicon nitride (Si_3N_4) is a widely used hard optical material but also has excellent piezoelectric response. Aluminum oxide (Al_2O_3) is a widely used optical material and is also used in gas barriers and tribology applications. The list goes on.

Engineered materials are the future of thin film technology. Engineered structures such as superlattices, nanolaminates, nanotubes, nanocomposites, smart materials, photonic bandgap materials, molecularly doped polymers, and structured materials all have the capacity to expand and increase the functionality of thin films and coatings used in a variety of applications and provide new applications. New advanced deposition processes and hybrid processes are being used and developed to deposit advanced thin film materials and structures not possible with conventional techniques a decade ago. Properties can now be engineered into thin films that achieve performance not possible when the second edition of this handbook was published. For example, until recently it was important to deposit fully dense films for all applications, but now films with engineered porosity are finding a wide range of new applications [1]. Hybrid processes, combining unbalanced magnetron sputtering and filtered cathodic arc deposition for example, are achieving thin film materials with record hardness [2].

Organic materials are also playing a much more important role in many types of coating structures and applications, including organic electronics and OLEDs. These materials have several advantages over inorganic materials, including low cost, high deposition rates, large area coverage, and unique physical and optical properties. It is also possible to molecularly dope and form nanocomposites with organic materials [3]. Hybrid organic/inorganic deposition processes increase their versatility, and applications that combine organic and inorganic films are increasing [4].

In addition to traditional metallizing and glass coating, large area deposition, decorative coating and vacuum web coating have become important industrial processes. Vacuum web coating processes employ a number of deposition technologies and hybrid processes, most recently vacuum polymer deposition (VPD), and have new exciting applications in thin film photovoltaics, flexible displays, large area detectors, electrochromic windows, and energy efficiency.

Hybrid deposition processes are gaining new applications because a single deposition process may not be able to achieve the optimum coating performance for multilayer and nanocomposite thin films. Unbalanced magnetron sputtering and electron beam evaporation are combined with filtered cathodic arc deposition to deposit films with improved tribological properties. Plasma-enhanced chemical vapor deposition (PECVD) is combined with unbalanced magnetron sputtering, magnetron sputtering is combined with electron beam evaporation, and polymer flash evaporation is combined with physical vapor deposition (PVD) processes. In addition, thin films with new properties are deposited with new deposition processes such as atomic layer deposition (ALD) [5], high-power pulsed magnetron sputtering

(HPPMS) [6], mid-frequency/dual magnetron sputtering (MF/DMS) [7] and glancing angle of incidence deposition (GLAD) [8].

Deposition process technology must meet the demands of advanced thin film coating structures, such as superlattices, nanolaminates, and nanocomposites, with advanced processes, materials and microstructures, and control and reduce costs. Recent advanced deposition technologies presented in this third edition, such as ALD, GLAD, HPPMS, MF/DMS, VPD, and hybrid processes, provide materials with improved microstructure, compositional control, properties, adhesion, and tribological properties. Opposite ends of the spectrum are also represented; GLAD thin films have increased porosity and low density while HPPMS, ion beam sputtered and MF films have increased density, all of which lead to a new range of optical, electrical, and tribological properties. New compositions and nanocomposites are formed by DMS and hybrid deposition processes by cosputtering, advanced reactive sputtering techniques, cathodic arc deposition, and PECVD. Hybrid processes combine magnetron sputtering with cathodic arc deposition, electron beam evaporation, and PECVD. Control of plasmas and generation of highly dense plasmas has become very important in achieving new materials and improvements in conventional materials. High deposition rates and increased materials usage have helped industrial processes to become more productive and economical, and to deposit a wide range of new thin film materials.

Advanced deposition technologies are particularly successful in furthering medical and energy technologies, including thin film solar cells, thin film fuel cells (solid oxide fuel cells), biomedical products, and tribological applications. For example, tantalum (Ta) coatings deposited by cylindrical magnetron process have increased the lifetime and reduced the cost of medical stents [9]. Nanocomposites, superlattices, and nanolaminates form new coating structures with improved tribological properties.

1.3 Aim and Scope

Thin film coating technology is rapidly advancing. The performance demands on virtually all types of thin film materials are continuously increasing. To meet these demands, thin film coatings and structures are becoming more sophisticated with engineered microstructure and properties. Because of this, process and technology handbooks published even ten years ago are already out of date. Deposition processes and technologies are also changing rapidly to keep pace with advanced thin film materials and applications. Conventional deposition processes are also being adapted in novel coating geometries to produce thin film structures with improved performance and properties not achievable by conventional methods. In addition, new deposition processes are being developed to achieve new compositions and physical properties. Thin films are now being engineered with electrical, optical, and mechanical properties not possible a decade ago. Characterization techniques are also improving.

The aim of this handbook is to provide the reader with detailed and usable information on:

- deposition processes for thin film coatings
- new and advanced deposition processes
- advanced thin film applications and structures
- relationships between deposition process parameters and thin film microstructure
- nucleation and thin film growth processes
- characterization of composition, bonding, and microstructure
- the role of plasmas in thin film growth.

Because in many cases no single process can achieve films with the required properties, hybrid coating processes are also becoming important. Deposition processes such as ALD, high-power impulse magnetron sputtering, filtered cathodic arc, and VPD are now being used to deposit films with properties not possible with conventional processes. These processes are also being combined with each other and PVD processes to deposit novel thin film structures. Plasmas are also being used to enhance deposition processes. Another advantage of integrating process technologies is that manufacturing costs are being reduced.

This edition of the handbook encompasses virtually all aspects of thin film deposition technology with highlights on advances in thin film deposition technology and characterization, and emerging technologies. This book complements other handbooks by presenting a broad range of thin film deposition and plasma technologies and characterization techniques written by experts in the field. All chapters have been updated when necessary, and some deleted, and new chapters on ALD, cathodic arc deposition, sculpted thin films, polymer thin films, and emerging technologies have been added. The chapter on Plasma Assisted Vapor Deposition Processes in the second edition has been omitted in this edition because all information is now covered in chapters on Plasmas in Deposition Processes (Chapter 2), Evaporation Processes (Chapter 4), Sputter Deposition Processes (Chapter 5) and Plasma-Enhanced Chemical Vapor Deposition (Chapter 9).

1.4 Definitions and Concepts

1.4.1 Surface Engineering

The definitions of thin and thick films referenced in the second edition of this handbook have crossed over and are outdated. No attempt will be made to differentiate between these two types of films in this edition. The interested reader is therefore directed to the second edition for further details [10]. Thin films are now absorbed into the broad subject area of *Surface Engineering*. Surface engineering encompasses the modification of a surface by application of a thin film, plasma enhancement, ion bombardment, self-assembly, nanomachining, chemical treatment, or other processes. Surface engineering techniques are now being used in virtually every area of technology, including automotive, aerospace, missile, power, electronic, biomedical, textile, petroleum, petrochemical, chemical, steel, power, cement, machine tools, and construction industries. They are being used to develop a wide range of advanced functional properties, including physical, chemical, electrical, electronic, magnetic, mechanical, wear-resistant, and corrosion-resistant properties at the required substrate surfaces. Almost all types of materials, including metals, ceramics, polymers, and composites, can be deposited onto similar or dissimilar materials. It is also possible to form coatings of advanced materials (e.g. met glass, polymers, superlattices, photocatalysts), graded deposits, metamaterials, multicomponent deposits, etc.

Thin film coatings are used to modify the physical and chemical properties and morphology of a surface or substrate, which makes them a broad subset of surface engineering. A thin film can consist of one homogeneous composition, crystalline phase composition and microstructure, or have an inhomogeneous multilayer or composite structure. The structure of the multilayer can be periodic, have a set pattern or be entirely random. Examples of periodic structures are optical multilayer coatings, rugate filters, superlattices, and nanolaminates. Nanocomposites can be random or periodic in nature. Figure 1.1 shows the progression of the dimensionality of thin films to zero dimensions (quantum dots). The three-dimensional (3D) film is homogeneous in composition and crystalline structure, with thickness greater than ~ 20 nm. Superlattices, quantum wells and nanolaminates are 2D films consisting of hundreds to thousands of periodic compositions with the thickness of each layer in the range 1–10 nm. Total thickness of this structure can be as large as 20 μm. The quantum wire is a 1D structure with arbitrary length and thickness between 1 and 10 nm. Nanotubes fall into this category. The quantum dot is a 0D quantum well with width and thickness between 1 and 3 nm.

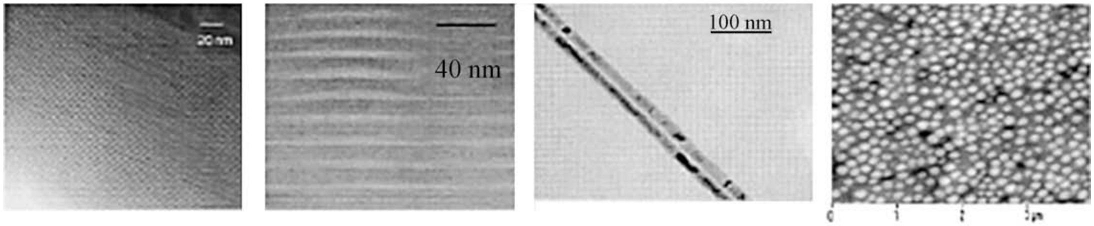

Bulk

Superlattice
2D

Nanowire
1D

Quantum Dots
0D

Figure 1.1: Progression of the dimensionality of thin film structures.

Substrate preparation is critical and the surface morphology and composition of a substrate can also be modified by diffusion, plasma treatment, self-assembly, chemical etch, and reactive heat treatment. The resulting surface will influence the properties, structure, adhesion, and surface texture of a thin film. For example, ion or gas nitriding hardens the surface of stainless steel and significantly improves the performance of tribological coatings deposited onto the surface.

It is informative to list the steps in the formation of a deposit. The three basic steps are [10]:

1. synthesis or creation of the depositing species
2. transport from source to substrate
3. deposition onto the substrate and subsequent film growth.

These steps can be completely separated from each other or can be superimposed on each other depending on the process under consideration. It is important to note that if, in a given process, these steps can be individually varied and controlled, a much greater degree of flexibility compared to one in which these steps are not independently variable will result. This is analogous to the degrees of freedom in Gibbs' phase rule. For example, consider the deposition of tungsten by a chemical vapor deposition (CVD) process from WF_6 and H_2. The reaction is defined as

$$\mathrm{WF_6(vapor)} + \mathrm{3H_2(gas)} \xrightarrow{(heated\ substrate)} \mathrm{W(deposit)} + \mathrm{6HF(gas)}$$

The rate of deposition is controlled by substrate temperature; at high substrate temperature, the deposition rate is high and the structure consists of large columnar grains. This may not be the desired structure. However, if tungsten is deposited by evaporation of pure tungsten, the deposition rate is essentially independent of substrate temperature so that the process can have a high deposition rate and a more desirable microstructure. Alternatively, a CVD process may be chosen over evaporation because of considerations of *throwing power* (ability to coat irregularly shaped objects) since high vacuum evaporation is basically a line-of-sight process.

1.5 Physical Vapor Deposition Process Terminology

PVD processes encompass a wide range of vapor-phase technologies, and is a general term used to describe any of a variety of methods to deposit thin solid films by the condensation of a vaporized form of the solid material onto various surfaces. PVD involves physical ejection of material as atoms or molecules and condensation and nucleation of these atoms onto a substrate. The vapor-phase material can consist of ions or plasma and is often chemically reacted with gases introduced into the vapor, called reactive deposition, to form new compounds. PVD processes include:

- thermal evaporation
- electron beam (e-beam) evaporation and reactive electron beam evaporation
- sputtering (planar magnetron, cylindrical magnetron, dual magnetron, high-power pulsed magnetron, unbalanced magnetron, closed field magnetron, ion beam sputtering, diode, triode) and reactive sputtering
- filtered and unfiltered cathodic arc deposition (non-reactive and reactive)
- ion plating
- pulsed laser deposition.

Variants on these processes are:

- bias sputtering
- ion-assisted deposition
- GLAD
- hybrid processes.

Hybrid processes combine the best attributes of each PVD and/or CVD process. Among the combinations are

- magnetron sputtering and e-beam evaporation
- magnetron sputtering and filtered cathodic arc deposition
- e-beam evaporation and filtered cathodic arc deposition
- VPD, polymer flash evaporation and magnetron sputtering/evaporation.

The basic PVD processes are evaporation, sputtering and ion plating. Materials are physically created in the vapor phase by energetic bombardment of a source (e.g. sputtering target) and subsequent ejection of material. A number of specialized PVD processes have been derived from these processes and extensively used, including reactive ion plating, reactive sputtering, unbalanced magnetron sputtering, HPPMS, and filtered cathodic arc deposition. There is also the possibility of confusion since many of these processes can be covered by more than one name. For example, if the *activated reactive evaporation* (ARE) process is used with a negative bias on the substrate, it is very often called *reactive ion plating*. Simple evaporation using a radio-frequency (RF) heated crucible is often called *gasless ion plating*. There is even more confusion over the ion plating process (Chapter 6), where the material is converted from a solid phase to the vapor phase using a number of processes involving thermal energy (evaporation), momentum transfer (sputtering), and electrical energy (cathodic arc), or supplied as vapor (similar to CVD processes). Logically, one could define all PVD processes as ion plating, but this ignores the most important aspect of ion plating: modification of the microstructure and composition of the deposit caused by ion bombardment of the deposit resulting from bias applied to the substrate.

To resolve this dilemma, it is proposed that we consider all of these basic processes and their variants as PVD processes and describe them in terms of three steps in the formation of a deposit as described in the previous section. Every PVD process can therefore be defined by three basic steps:

1. *Creation of vapor-phase species*. Material can be converted to a vapor phase by evaporation, sputtering, or chemical vapors and gases.
2. *Transport from source to substrate.* Transport of vapor species from the source to the substrate can occur under line-of-sight, thermal scattering, or molecular flow conditions (i.e. without collisions between atoms and molecules). Alternatively, if the partial pressure of the metal vapor and/or gas species in the vapor state is high enough for some of these species to be ionized (by creating a plasma), there will be a large number of collisions in the vapor phase during transport to the substrate.
3. *Film growth on the substrate*. Once the atoms or molecules are deposited, the film nucleates on the substrate and grows by a number of processes. Microstructure and composition of the film can be modified by bombardment of the growing film by ions from the vapor phase, resulting in sputtering and recondensation of the film atoms and enhanced surface mobility of the atoms in the near surface and surface of the film.

Every PVD process can be usefully described and understood in term of these three steps. The reader is referred to Chapter 11 for a more comprehensive treatment.

1.6 Classification of Coating Processes

Because of the overlap in process mechanisms and the formation of hybrid deposition processes, no one scheme can accurately define and classify all coating processes. While several attempts have been made to classify deposition process, including the second edition of this handbook, we take a much simpler and basic classification scheme. Refer to Appendix 1.1 for a full treatment of classification schemes described in the second edition. Four general categories of thin film deposition have emerged over the past few decades: atomistic growth, particulate deposition, bulk coating, and surface modification. The best summary to date is still given by Bunshaw and Mattox [11], with the addition of advanced techniques, shown in Table 1.1.

In atomistic processes, atoms form a film by condensing onto a substrate and migrating to nucleation and growth sites. Adatoms often do not occupy their lowest possible energy

Table 1.1: Vacuum deposition techniques [10]

Atomistic deposition	Particulate deposition	Bulk coatings	Surface modification
Electrolytic environment	Thermal spraying	Wet processes	Chemical conversion
Electroplating	Plasma spraying	Painting	Electrolytic
Electroless plating	D-gun	Dip coating	Anodization (oxide)
Fused salt electrolysis	Flame spraying	Electrostatic spraying	Fused salts
Chemical displacement	Fusion coatings	Printing	Chemical–liquid
Vacuum environment	Thick film ink	Spin coating	Chemical vapor
Vacuum evaporation	Screen printing	Cladding	Thermal
Ion beam deposition	Jet printing	Explosive	Plasma
Laser ablation	Enameling	Roll bonding	Leaching
Molecular beam epitaxy	Electrophoretic	Overlaying	Mechanical
Cathodic arc	Impact plating	Weld coating	Shot peaning
Vacuum polymer deposition			Thermal
Plasma environment			Surface enrichment
Sputter deposition			Diffusion from bulk
Activated reactive evaporation			Sputtering
Cathodic arc			Ion implantation
Plasma polymerization			Self-assembly
Ion plating			
Chemical vapor environment			
Plasma enhanced			
Atomic layer deposition			
Reduction			
Decomposition			
Spray pyrolysis			
Liquid phase epitaxy			

configurations and the resulting structure contains high concentrations of structural imperfections (dangling bonds, voids, lattice mismatch, etc.). The depositing atoms can also react with the substrate material to form a complex interfacial region.

The energy of the adatoms is a critical factor in determining the microstructure and morphology, and depends on the deposition process and source of atoms. Sources of atoms can be thermal evaporation, sputter deposition, vaporized chemical species (CVD), plasma species (ion plating, cathodic arc), or ionic species in an electrolyte (electrodeposition). Low-energy atomistic deposition is characterized by depositing species incident on a surface where they condense, are relatively immobile, and grow into a continuous coating. Mobility of adatoms to their lowest energy state increases with increased energy. Nucleation and growth mechanisms of the condensing species also determine the crystallography and microstructure of the thin film coating. These particles can react with or implant into the substrate in high-energy processes.

Particulate deposition processes involve molten or solid particles and the resulting microstructure of the deposit depends on the solidification or sintering of the particles. Bulk coating processes such as painting involve the application of large amounts of coating material onto the surface at one time. Surface modification involves ion, thermal, mechanical, or chemical treatments which alter the surface composition or properties.

1.7 New Deposition Technologies

Several new or advanced deposition technologies have emerged and become important since publication of the second edition of this handbook. Processes that are included in this edition are:

- vacuum polymer deposition (VPD)
- atomic layer deposition (ALD)
- high-power pulsed magnetron sputtering (HPPMS or HIPIMS)
- filtered cathodic arc deposition
- glancing angle deposition (GLAD).

Each will be discussed in detail in future chapters.

VPD and ALD have recently emerged as processes that can achieve molecular doping, polymer thin films and nanocomposites. Gas jet deposition can also form nanocomposites, as was presented in the second edition. Processes such as GLAD can achieve unique microstructures not possible with conventional substrate–source configurations and deposition processes. Films deposited by HPPMS have high density and excellent adhesion to the substrate, which makes them desirable for tribological, corrosion-resistant coatings, barrier coatings, and electronic applications. This should be kept in mind when reading the next section, Microstructure and Properties.

1.8 Microstructure and Properties

The microstructure of thin film materials deposited by vacuum processes depends on a number of factors, but primarily on the energy of the species (adatoms) incident upon the substrate. Energies range from a few tenths of eV for thermal evaporation to tens to hundreds of eV for sputtering, to higher energies used in ion implantation and ion milling. While much of the understanding of the relationship between adatom energy and microstructure is phenomenological, a number of models that simulate film growth have been developed. Growth of thin films is addressed in Chapters 12 and 13. Models include Monte Carlo simulations in two and three dimensions [12], percolation theory, and structure zone model [13]. Film growth mechanisms can be complicated by the fact that not only is the species from the source deposited, but additional processes such as resputtering, reflected neutrals, shadowing, and ion implantation can occur. Mobility of the deposited species on the substrate is also critical and depends on the energy of incident species, substrate temperature, ion bombardment, substrate morphology and cleanliness, interfacial reactions at the surface, deposition angle, and substrate rotation. Adhesion of the film to the substrate also depends on a number of these factors. If the coating and substrate materials are not chemically reactive and are insoluble, the interfacial region will be confined to an abrupt discontinuity in composition and possibly crystalline phase. Adhesion in this case can be poor. This type of interface can be modified by bombardment with high-energy particles to give high defect concentrations and implantation of ions, resulting in a ‘pseudodiffusion’ type interface. The type of interface formed will influence the properties of the deposited film. Because these interfaces can be very thin, compositional, phase, microstructural, and property analysis can be challenging.

The microstructure of the coating being deposited in atomic deposition processes depends on how adatoms are incorporated into the existing structure and can change with each atomic layer deposited. Surface roughness and geometric shadowing lead to preferential growth of elevated regions, resulting in a columnar type microstructure. Microstructure can be modified by substrate temperature, surface diffusion of the atoms, ion bombardment, impurity atom incorporation, and angle of incidence of the adatom flux. Several structure zone models have been developed [13–15] to explain the evolution of coating microstructure. An extreme example of this is GLAD coatings [8]. Adatom flux is incident on the substrate at very acute angles, resulting in a highly figured and porous chiral, whisker, or convoluted columnar microstructure. Defects in the substrate and growing film as well as particulates also affect microstructure.

In CVD, the chemical species being deposited is generally reduced or decomposed on the substrate surface, usually at high temperatures. Care must be taken to control the interfacial reactions between coating and substrate and between substrate and gaseous reaction products.

Coating microstructures are very similar to those achieved by vacuum deposition processes (small-grained columnar structures to large-grained equiaxed or oriented structures).

Because they are non-equilibrium processes, each atomistic deposition process has the potential to deposit materials that vary significantly from the source material in composition, microstructure, mechanical properties, tribological properties, and physical properties (conductivity, optical properties, etc.). The resulting films may have high intrinsic stress, high concentration of point defects, extremely fine grain size, highly oriented microstructures, metastable phases, incorporated impurities, and micro- to macroporosity. These properties have a significant influence on the physical, corrosion resistance, and mechanical and tribological properties of the deposited film. A unique microstructure of the deposited material may also lead to anomalously low annealing and recrystallization temperatures where internal stresses and high defect concentration aid in atomic rearrangement.

Incorporation of impurities or implantation of atoms during deposition can result in high intrinsic stresses or impurity stabilized phases not observed in bulk. Compounds such as nitrides, oxides, carbides, and borides can be deposited using reactive species in the vapor. Graded compositions can be formed by varying or changing the reactive species.

By being able to vary reactive species and source materials in vapor deposition, unique and/or non-equilibrium microstructures can be formed, including superlattices, nanolaminates, and nanocomposites. Films with properties superior to bulk or single layer films are readily deposited. Nanocomposites and nanolaminates have achieved hardness values not possible in bulk or single homogeneous layers.

1.9 Unique Features of Deposited Materials and Gaps in Understanding

Several features of materials can only be produced by vacuum deposition technologies, including:

- extreme versatility of range and variety of deposited materials
- applied coatings with properties independent of thermodynamic compositional constraints
- ability to vary defect concentration over wide ranges, thus resulting in a range of properties comparable to or far removed from conventional bulk materials
- high quench rate available to deposit amorphous materials
- controllable production of microstructures different from conventionally processed materials, e.g. a wide range of microstructures: ultrafine (superlattice, nanostructures) to single crystal films

- fabrication of thin free-standing shapes and foils, even from brittle materials
- ecological benefits with certain techniques.

Areas where more understanding and research are required are:

- relationships between plasma density, pulse length, coating density, and microstructure for high-power pulsed plasma deposition
- role of plasmas in large area deposition
- microstructure and properties in the thickness range 10–10,000 nm, particularly for low-dimensional structures, submicroelectronics, nanocomposites, tribological coatings, corrosion-resistant materials, reflective surfaces, and thermoelectrics
- ion energy and ion flux on properties of deposited material
- effect of energy of the depositing species on interfacial interaction, nucleation, and growth of the deposit
- effect of substrate surface condition and morphology on adhesion and mechanical properties of the deposit
- influence of process parameters on residual stress
- sculpted thin films and highly porous films.

1.10 Current Applications

Although there is significant overlap, current coating applications may be classified into the following generic areas:

- *optically functional* – laser optics (reflective, semi-transmitting and transmitting), phase separation, telecommunication filters (WDWM), architectural glazing, residential mirrors, automotive rear-view mirrors and headlamps, reflective and antireflection coatings, optically absorbing materials, low-e coatings, solar selective coatings, free-standing reflectors, transparent conductive films
- *energy related* – thin film battery, thin film fuel cell, thin film solar cell, thermoelectric thin films, superlattice, electrochromic coatings, low-e coatings, solar absorbers, barrier coatings (oxygen and water permeation barriers), transparent solar cells, organic solar cells, photocatalytic coatings
- *electrically functional* – electrical conductors, electrical contacts, semiconductor films, active solid state devices, electrical insulators, photovoltaics, transparent electrical contacts

- *mechanically functional* – tribological coatings, lubrication films, nanocomposites, diffusion barriers, hard coatings for dies and cutting tools, wear- and erosion-resistant coatings, biomedical coatings
- *chemically functional* – corrosion-resistant coatings, catalytic coatings, biomedical coatings, photocatalytic coatings, thin film electrolytes, organic materials.

1.10.1 Decorative/Functional Coating

Decorative coatings continue to be a large segment of the vacuum coating market. In addition to chromium coatings on plastic automotive parts such as grills, new color-shift automotive paints have flakes with Fabrey-Perot filters which change color with angle of incidence of the observer. Color shift paints are also used on high-end athletic shoes, eyeglass frames and jewelry. A wide variety of mirrors is produced using aluminum and silver films on glass and plastics. Electrochromic coatings are now used on automobile sun roofs, rear-view mirrors (interior and exterior) and glazings. It should be noted that because of environmental concerns, major efforts are underway to replace chromium with suitable thin film materials.

Refractory metal nitrides (TiN, ZrN, TaN, HfN) have wide ranges of decorative, as well as tribological, applications. Titanium nitride (TiN) has the reflective properties of gold and has decorative, tribological and optical applications. TiN coatings are used to give jewelry a gold color as well as protect it from corrosion and wear. Tantalum nitride (TiN) and zirconium nitride (ZrN) have reflective properties of silver and brass. Dichroic multilayer filters are applied to windows and mirrors to provide a range of colors in reflection and transmission.

Flexible polymers such as polyethylene terephthalate (PET) are metallized by vacuum web processes for heat insulation, food packaging, and decorative applications.

Black coatings, such as chromium carbon nitride (CrCN), titanium carbon nitride (TiCN), and titanium aluminum nitride (TiAlN), are becoming very fashionable, especially on small electronic devices such as mobile phones, personal digital assistants (PDAs), and cameras. Black coatings are deposited by reactive arc deposition or reactive sputter deposition.

1.10.2 Transparent Conductive Thin Films

Transparent conductive coatings and transparent conductive oxides (TCOs) in particular have a wide range of optical, device, photovoltaic, energy, and display applications. Cadmium oxide (CdO) was the first transparent conductive coating and was used in solar cells in the early 1900s. Tin oxide (SnO_2) was deposited on glass by pyrolysis and CVD in the 1940s for electroluminescent panels. Indium tin oxide (ITO) has the best combination of transparency and conductivity to date, but materials such as aluminum-, gallium-, and indium-doped zinc oxide (ZnO:Al, ZnO:Ga, and In_2O_3:ZnO) are also widely used. A number of ternary compounds have been developed in the past ten years, including Zn_2SnO_4, $ZnSnO_3$, $MgIn_2O_4$,

$(GaIn)_2O_3$, $Zn_2In_2O_5$, and $In_4Sn_3O_{12}$. They are critical for energy-efficiency applications such as low-e windows, solar cells, and electrochromic windows. Transparent conductive thin films are used as the transparent electrical contacts in flat panel displays, sensors, and optical limiters. While most TCOs are n-type semiconductors, p-type TCOs such as $CuFeO_2$, $CuAlO_2$, $AgCoO_2$, $NiCo_2O_4$, $ZnIr_2O_4$, Ga-doped SnO_2, Cu_2O-CoO:$CuAlO_2$, $CuGaO_2$, $CuInO_2$, $SrCu_2O_2$, and LaCuOCh (Ch = chalcogen) have also been developed, creating new applications such as transparent p-n diodes, transistors, and photovoltaics.

1.10.3 Thin Film Solar Cells and Batteries

Thin film solar cells and batteries have emerged as critical applications for many processes described in this handbook. While efficiencies of thin film solar cells are not as high as those of single crystal cells, they are significantly less expensive to fabricate and can be made in large areas on glass and polymer substrates. Amorphous silicon solar cells are now being deposited in large areas using primarily PECVD processes and have efficiencies near 11%. Copper indium diselenide ($CuInSe_2$, CIS) and copper indium gallium diselenide ($CuInGaSe_2$, CIGS) have efficiencies near 14%. Cadmium telluride (CdTe)-based cells also show promise and are amenable to large-scale production. Thin film lithium-polymer batteries promise to revolutionize energy storage technology with very high-energy current densities and the added advantage that they are rechargeable.

1.10.4 Friction and Wear: Nanolaminates and Superlattices

In addition to MoS_2, WSe_2, and lamellar low-friction thin film coatings used on bearings and other sliding parts, DLC and metal-containing carbon (C:Me) coatings such as W–C:H are extensively used in automotive engines. DLC coatings can have a COF as low as 0.01. DLC and other low-friction coatings, and nanocomposites are also being developed for medical implants, and artificial knees and hips. The majority of low-friction and low-wear coatings are deposited by magnetron sputtering, unbalanced magnetron sputtering, closed-field magnetron sputtering, and dual/mid-frequency magnetron sputtering. TiN, TiC, TiCN, TiYN, TiAlN, CrN, $CrMoC_xN_{1-x}$, and $Ti_{1-x}Cr_xN$ coatings have demonstrated good wear-resistance performance and low COF. Nanolaminates and superlattices have significantly increased wear resistance, often by a factor of 2.

1.10.5 Cutting Tools

Cutting tools are made of high-speed steel or cemented carbides, and are subject to degradation by abrasive wear as well as by adhesive wear. In adhesive wear, high temperatures and forces at the tool tip promote microwelding between the steel chip from the work piece and steel in the high-speed steel tool or cobalt binder phase in the cemented carbide. The resulting chip breaks the microweld and causes cratering and wear in the tool. Real improvement in tribological properties and corrosion resistance comes with deposition of multilayers, superlattices, nanolaminates, and nanocomposites [16–19]. A thin refractory metal coating such as TiC, TiN, CrC, or ZrN forms a diffusion barrier and prevents microwelding and can improve tool life by a factor of 300–800%. Cutting forces are also reduced. Tribological coatings are deposited by PVD and CVD processes.

Improvements in this area and superhard coatings have been achieved by new composition, composites and nanolaminate structures, such as:

- Ti alloy nitrides: (Ti,Al)N
- Ti alloy carbonitrides: Ti(C,N)
- nanocomposites: SiC/Si_3N_4
- nanolaminates: CrN/W_x, TiAlN/VN, AlN/Si_3N_4, NiAlN/TiBCN/Ti, C/Cr/CrN, NbN/CrN, nc-TiN/aSi_3N_4/nc-&TiSi_z, and nc-TiN/aSi_3N_4.

Several of these structures are deposited by a hybrid unbalanced magnetron/cathodic arc process.

1.10.6 Gas and Water Permeation Barriers on Plastic

Encapsulation of atmospherically sensitive organic electronic devices, thin film lithium batteries, and thin film solar cells is critical in achieving significant operating lifetimes. These structures are also now being deposited onto thin flexible plastic webs using vacuum web processes. Multilayer polymer/oxide coatings have demonstrated water and oxygen permeation values $< 10^{-6}$ gm/m^2/d, and are now being deposited onto these structures, on glass and plastic, by the VPD process.

1.10.7 Biomedical

Biomedical applications for thin film materials have mushroomed in the past decade, involving low-friction and wear-resistant coatings for medical implants and prostheses, Ta coatings on stents, photocatalytic coatings in an artificial lung, DLC coatings on hypodermic needles, ophthalmic coatings, and tribological coatings on surgical instruments. Many of these materials are Ta and Ti based because Ti and Ta have been shown to be biocompatible and do not cause thrombus. Alpha alumina, titanium carbide, ta-C, and DLC coatings also show promise. Most of these materials are deposited by some form of magnetron sputtering or CVD.

1.10.8 Thin Film Solid Oxide Fuel Cells

The operating temperature of a solid oxide fuel cell can be lowered and the efficiency increased by constructing it with thin films. The basic structure is a porous nickel or gallium-doped nickel, lanthanum strontium cobalt iron oxide (LSCF) cathode (for low operating temperatures, since it offers both electronic and ionic conductivity), and yttria stabilized zirconia (YSZ) electrolyte. The cell is operated at a temperature range between 370 and 550 °C, and maximum output power densities near 7 mW/cm^2 are obtained at 400 °C.

1.10.9 Flat Panel Displays and Molecular Electronics

Thin film polymers, light-emitting polymers, and small molecule organic materials are used extensively in OLEDs for flat panel displays, organic electronics, and organic solar cells. Organic materials have the advantage of a wide range of molecular doping combinations to achieve a wide range of electrical, optical, and electro-optical properties. Conductive polymers are also used extensively in organic circuitry and photovoltaics.

1.11 'Frontier Areas' for Applications of the Products of Deposition Technology

The following were listed in the first and second editions, published in 1982 and 1994, respectively:

First edition:

- reflective surfaces, e.g. for laser mirrors
- thermal barrier coatings for blades and vanes operating at high temperatures
- corrosion/erosion-resistant coatings at high temperatures, e.g. valves and other critical compounds in coal gasification plants
- advanced cutting tools
- wear-resistant surfaces without organic lubricants, particularly at high temperatures where lamellar solid state lubricants such as MoS_2 are ineffective
- first of all thermonuclear reactor vessels
- high-strength/high-toughness ceramics for structural applications
- ultrafine powders
- superconducting materials:
    - high transition temperatures > 23.2 K
    - manufacturability of these brittle materials into wire or ribbons
- catalytic materials
- thin film photovoltaic devices

- transparent conductive coatings in optoelectronic devices, photodetectors, liquid crystal displays, electrochromic windows and optical devices, solar photothermal absorption devices, heat mirrors
- biomedical devices, e.g. neurological electrodes, heart valves, artificial organs
- materials conservation
- submicrometer microelectronic devices; in this context, a good question is, ’How far can dimensions be reduced without running into some limit imposed by physical phenomena?’

Second Edition additions to the above list are:

- diamond and DLC for various applications:
    - tribology, particularly cutting tools
    - heat management – heat sinks of diamond sheet currently several square inches in area are on the market
    - hard protective coatings for infrared applications such as the protection of germanium and sodium chloride optics
- cubic boron nitride for various applications:
    - high-temperature use (up to 1200 °C) semiconductor devices; very perfect device quality single crystal films have been grown epitaxially on lattice matched TiC substrates
    - tribological uses for matching of hard steels
    - optical and optoelectronic devices
- films deposition using a high-velocity gas jet: Hayashi et al. [19] developed a process in which ultrafine powders ($\sim 10\,\text{nm}$ diameter) are carried on a high-velocity gas jet and impinge on a substrate to ‘write’ lines of deposited materials, e.g. YBCO superconductors. The usage of material is very high; almost 97% is collected as a deposit. Various applications are envisioned
- unbalanced magnetron sputter deposition – very useful new development where some of the electrons are allowed to escape from the magnetic trap at the sputtering target and form a plasma near the substrate from which ions can be extracted to bombard the growing film.

Third Edition additions are:

- ultra-low emissivity broadband high reflectors for advanced telescopes with ultra-high reflectance at near ultraviolet wavelengths

- photocatalytic coatings for biomedical, energy, hydrogen production, and self-cleaning windows
- thin film organic electronics, including solar cells; these devices are needed for low-cost renewable energy and display applications
- transparent photovoltaics applied to glazings, roofs, and buildings, using p- and n-type transparent conducting oxide thin films
- thin film lithium batteries for high-density energy storage
- superhard tribological coatings and transparent coatings with hardness >50 GPa for advanced wear applications, optical applications, aircraft windows, and windscreens
- HPPMS for high-density coatings with excellent adhesion
- GLAD coatings
- thin film thermoelectric structures for power generation and cooling
- atomic layer deposition in semiconductor processing
- thin film electrolytes for thin film solid oxide fuel cells and batteries
- free-standing nanolaminate satellite optics
- thin film coatings for microelectromechanical systems (MEMS) and nanotechnology applications
- nanocomposites and low-dimensional structures
- carbon nanotubes.

1.11.1 Selection Criteria

The selection of a particular deposition process depends on several factors:

- material to be deposited
- limitations imposed by the substrate, e.g. material, size, temperature stability
- specific application
- deposition rate
- adhesion of film to substrate
- throwing power
- purity of source material

Table 1.2: Criteria for deposition processes (taken partially from the Second Edition of this Handbook)

	Evaporation	Ion plating	Sputtering	Cathodic arc deposition	Chemical vapor deposition	Polymer deposition	Electrodeposition	Thermal spraying
Mechanism of production of depositing species	Thermal energy	Thermal energy	Momentum transfer	Thermal energy	Chemical reaction	Thermal energy	Solution	Flames or plasmas
Deposition rate	Can be very high (up to 750,000 A/min)	Can be very high (up to 250,000 A/min)	Low except for pure metals and dual magnetron	Can be very high	Moderate (200–2500 A/min)	Very high (up to 100,000 A/s)	Low to high	Very high
Deposition species	Atoms & ions	Atoms & ions	Atoms & ions	Ions	Atoms	Monomers/ polymers	Ions	Droplets
Throwing power for: Complex shaped objects	Poor, line of sight coverage except by gas scattering	Good, but nonuniforrm thickness distribution	Good, nonuniform, and uniform thickness distributions	Good, but nonuniform thickness distribution	Good	Good	Good	No
Into small blind holes	Poor	Poor	Poor	Poor	Limited	Poor	Limited	Very limited
Metal deposition	Yes	Yes	Yes	Yes	Yes	No	Yes, limited	Yes
Alloy deposition	Yes	Yes	Yes	Yes	Yes	No, but molecular doping possible	Quite limited	Yes
Refractory compound deposition	Yes	Yes	Yes	Yes	Yes	No	Limited	Yes
Energy of deposited species	Low (∼ 0.1–0.5 eV)	Can be high (1–100 eV)	Can be high (1–100 eV)	Can be high	Can be high with plasma assisted CVD	Low	Can be high	Can be high
Bombardment of substrate/deposit by inert gas ions	Generally no	Yes	Yes or no, depending on geometry	Yes	Possible with PECVD	No	No	Yes
Growth interface perturbation	Not normally	Yes	Yes	Yes	Yes (by rubbing)	No	No	No
Substrate heating (by external means)	Yes, normally	Yes or no	Yes or no	Yes or no	Yes	No, cooling generally required	No	Not normally

- apparatus required and availability of same
- cost
- safety considerations, e.g. toxicity
- process stability
- manufacturing considerations, e.g. batch size, throughput, process controls
- abundance of source materials.

To aid the reader in selecting a suitable deposition process, Table 1.2 lists criteria for each deposition process (taken partially from the second edition of this handbook). Usually one process cannot meet all of the above requirements and more than one technique can be used to deposit a given material. As a result, hybrid processes are now being used to deposit many thin film materials. Evaluation of each process for the specific application will help lead to a rational choice of deposition process or hybrid process.

1.12 Summary

In the previous discussion, we noted the following:

- There is a very large number and wide variation of deposition techniques.
- There is no unique method to classify these techniques. Depending on the viewpoint, the same process may fall into one or more classes.
- Each technique has its advantages and disadvantages.
- The choice of technique will depend on the various selection criteria, specific application, and available resources.
- More than one technique can be used to deposit a given thin film material, as shown in Figure 1.2 for microelectronics [20].
- Hybrid techniques are becoming more widely used and available.

Appendix 1.1 Deposition Process Definitions

Definitions of various deposition processes are given below. They are grouped in the same manner as in the second edition of this handbook.

Conduction and Diffusion Processes

- *Electrostatic Deposition* is the deposition of material in liquid form and the subsequent evaporation of the solvent to form a solid coating. The liquid is atomized and charged, and directed onto the substrate using an electrostatic field.

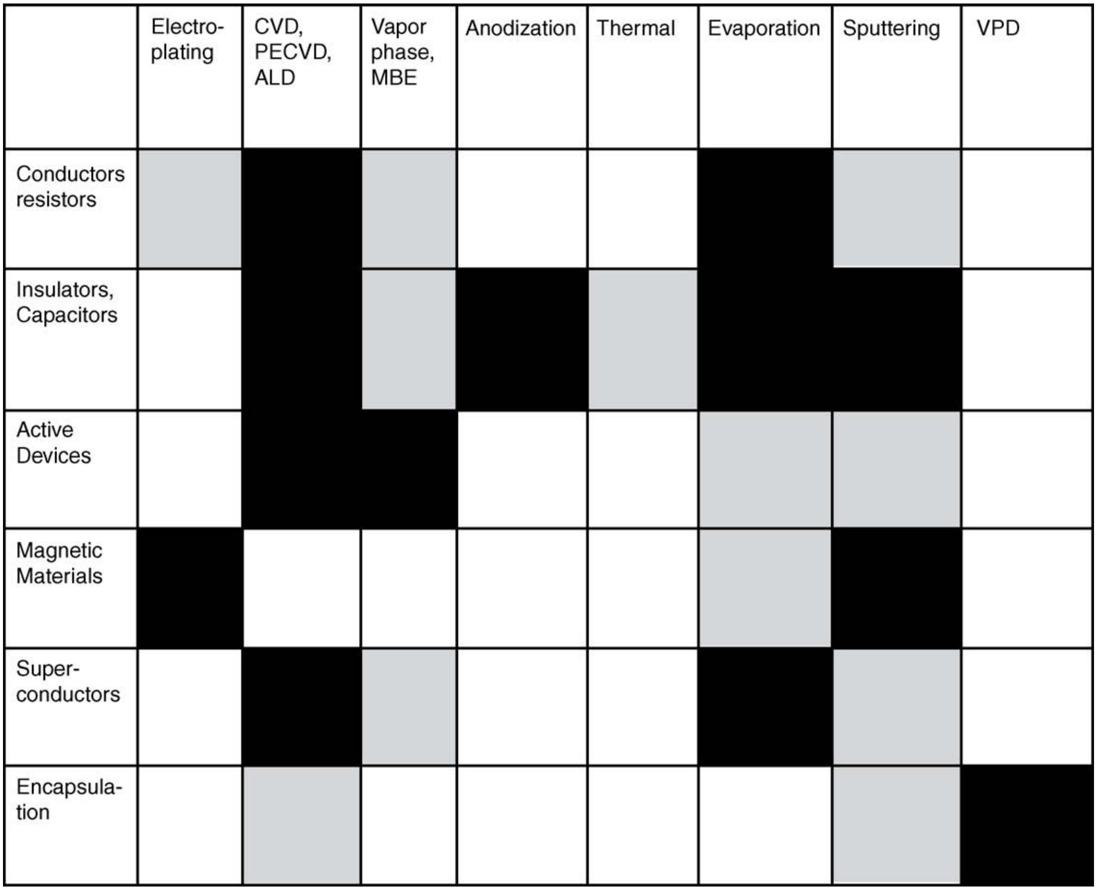

	Electro-plating	CVD, PECVD, ALD	Vapor phase, MBE	Anodization	Thermal	Evaporation	Sputtering	VPD
Conductors resistors	░	■	░			■	░	
Insulators, Capacitors		■	░	■	░	■	■	
Active Devices		■	■			░	░	
Magnetic Materials	■					░	■	
Super-conductors		■	░			■	░	
Encapsula-tion		░					░	■

Figure 1.2: Applicability of preparation methods to microelectronics. Light shading indicates that the component can be prepared by the method; dark shading indicates that the method is widely used [21].

- *Electrophoric Coating* produces a coating on a conducting substrate from a dispersion of colloidal particles. The piece to be coated is immersed in an aqueous dispersion which dissociates into negatively charged colloidal particles and cations. An electric field is applied with the source as anode; colloidal particles are transported to the anode, where they are discharged and form a film. Curing is required for a paint coating, which demonstrates that electrophoresis is not a very effective transport process. Consequently, electrodeposition may be a better term for this coating process.
- *Electrolytic Deposition* is primarily concerned with the deposition of ions rather than colloidal particles. Two electrodes are immersed in an electrolyte containing an ionic salt, which dissociates in aqueous solution into its constituent ions. Positive ions are deposited onto the cathode.

- *Anodization* is a process that occurs at the anode (hence its name) for a few specific metals. The anode reacts with negative ions from an electrolyte and becomes oxidized and forms a surface coating.
- *Gaseous Anodization* is a process in which the liquid electrolyte of the conventional wet process is replaced by a glow discharge in a low partial pressure reactive gas, producing oxides, carbides, and nitrides.
- *Ion Nitriding* is a gaseous anodization that produces a nitride diffusion coating on a metal surface, usually steel.
- *Ion Carburizing* is a gaseous anodization that produces a carbide diffusion coating on a metal surface, usually steel.
- *Plasma Oxidation* is gaseous anodization to produce an oxide film on the surface of metal (e.g. SiO_2 films on Si).
- *Diffusion Coating* is produced by diffusion of material from the surface into the bulk of the substrate.
- *Metalliding* is a method using electrodeposition in molten fluorides.
- *Spark-Hardening* is a technique in which an arc is periodically struck between a vibrating anode and the conducting substrate (cathode); material is transferred from the anode and diffuses into the substrate.

Chemical Processes

- *Conversion and Conversion/Diffusion Coating* is a process in which the substrate is reacted with other substances (which may be in the form of solids, liquids, or gases) so that its surface is chemically converted into different compounds having different properties (anodization could probably be described as an electrochemical conversion process). Elevated temperatures are often required for the reaction to occur and diffusion is often an essential feature.
- *Chemical Vapor Deposition (CVD)* is a process in which the substrate is exposed to one or more volatile precursors, which react and/or decompose on the substrate surface to produce the desired thin film deposit. The deposit can be a metal, semiconductor, alloy, nanocomposite, or refractory compound.
- *Plasma-Enhanced Chemical Vapor Deposition (PECVD)* is a form of CVD that involves creation of a plasma of the reacting gases and subsequent deposition onto a substrate. The plasma is generally created by an RF, DC or microwave discharge between two electrodes located in the space into which the reactive gases are introduced.

- *Atomic Layer Deposition (ALD)* is a self-limiting, sequential surface chemistry that deposits conformal thin films of materials onto substrates of varying compositions. ALD is similar in chemistry to CVD, except that the ALD reaction breaks the CVD reaction into two half-reactions, keeping the precursor materials separate during the reaction. ALD film growth is self-limited and based on surface reactions, which makes achieving atomic scale deposition control possible. By keeping the precursors separate throughout the coating process, atomic layer control of film grown can be obtained as fine as ~ 0.1 Å per monolayer. ALD has unique advantages over other thin film deposition techniques, as ALD grown films are conformal, pinhole free, and chemically bonded to the substrate. With ALD it is possible to deposit coatings perfectly uniform in thickness inside deep trenches, porous media and around particles. The film thickness range is usually 1–500 nm.
- *Plasma-Assisted Chemical Vapor Deposition (PACVD)* is a process similar to PECVD where the reaction between the precursors is stimulated or activated by creating a plasma in the vapor phase using techniques such as RF, microwave or cyclotron resonance excitation.
- *Pyrolysis* is a type of CVD which involves the thermal decomposition of volatile materials on the substrate.
- *Electroless Deposition* is often described as a form of electrolytic decomposition which does not require a power source or electrodes. It is actually a chemical process catalyzed by the growing film, so the electroless term is somewhat of a misnomer.
- *Disproportionation* is the decomposition of a film or crystal in a closed system by reacting the metal with a carrier gas in the hotter part of the system to form a compound, followed by dissociation of the compound in the colder section of the system to deposit the metal. Examples are epitaxial deposits of Si or Ge on single substrates and the Van-Arkel–deBoer process for metal purification and crystal growth.

Wetting Processes

Wetting processes are coating processes in which material is applied in liquid form and then becomes solid by solvent evaporation, spinning, curing, baking, or cooling.

- *Conventional Brush Painting and Dip Coating* are wetting processes in which the part to be coated is literally dipped into a liquid (e.g. paint) under controlled conditions, including withdrawal rate and temperature.
- *Spin coating* is a process used to apply uniform coatings to flat substrates, usually wafers. The process is initiated by applying an excess amount of a solution onto the substrate, which is then rotated at high speed in order to spread the fluid by centrifugal

force. Rotation is continued while the fluid spins off the edges of the substrate, until the desired thickness of the film is achieved. The applied solvent is usually volatile, and simultaneously evaporates. Thus, the higher the angular speed of spinning, the thinner the film. The thickness of the film also depends on the concentration of the solution and the solvent. Spin coating is widely used to create thin films with thicknesses below 10 nm, and is used intensively in photolithography, to deposit layers of photoresist about 1 μm thick.

- *Hydrophilic Method* is a surface chemical process known as the Langmeir Blodgett technique which is used to produce monolayers or multimonolayers of low-chain fatty acids. A film 2.5 nm thick can be deposited on a substrate immersed in water and pulled through a compressed layer of fatty acid residing on the surface of the water.
- *Welding Processes* are a range of coating techniques all of which rely on wetting.

Spraying Processes

- *Printing Processes* also rely on wetting and are processes in which ink, conventionally pigment in a solvent, is transferred to and deposited on a paper or other substrate, usually to form a pattern; the solvent evaporates to leave the required print.
- *Ink Jet Printing* is a process that operates by propelling variably sized (nanometer to micrometer size) droplets of liquid or molten material (ink) onto almost any medium.
- *Spraying Processes* can be divided into two categories:
  - Macroscopic, in which the sprayed particle consists of many molecules and is usually greater than 10 μm in diameter
  - Microscopic, in which the sprayed particles are predominantly single molecules or atoms (ink jet printing is a form of spraying).
- *Air and Airless Spraying* are the first of the macroscopic processes. When a liquid exceeds a certain critical velocity it breaks up into droplets, or atomizes. The atomized droplets, by virtue of their velocity (acquired from high-pressure air or airless source) can be sprayed onto a substrate.
- *Flame Spraying* is a process in which a fine powder (usually a metal) is carried in a gas stream and is passed through an intense combustion flame, where it becomes molten. The gas stream, expanding rapidly because of the heating, then sprays the molten powder onto the substrate where it solidifies.
- *Detonation Coating* is a process in which a measured amount of powder is injected into what is essentially a gun, along with a controlled mixture of oxygen and acetylene. The mixture is ignited and the powder particles are heated and accelerated

to high velocities with which they impinge on the substrate. The process is repeated several times a second.

- *Arc Plasma Spraying* is a process in which the powder is passed through an electrical plasma produced by a low-voltage, high-current electrical discharge. Even refractory metals can be deposited using this technique.
- *Electric-Arc Spraying* is a process in which an electric arc is struck between two converging wires close to their intersection point. The high-temperature arc melts the wire electrodes which are formed into high-velocity molten particles by an atomizing gas flow; the wires are continuously fed to balance the loss. The molten particles are then deposited onto a substrate similar to other spray processes.
- *Harmonic Electrical Spraying* is a process in which the material to be sprayed must be in liquid form, which will usually require heating. It is placed in a capillary tube and a large voltage is applied to the capillary tip. It is found that by adding an AC perturbation to the DC field, a collimated beam of uniformly sized and charged particles is emitted from the tip. As a result of being charged, these particles can be focused by an electric or a magnetic field to produce patterned deposits.
- *Vacuum Polymer Deposition* is a process in which a monomer is atomized in a vacuum and flash evaporated into a series of baffles. The resulting monomer vapor is homogeneous and is condensed onto a substrate or moving web substrate. The liquid monomer is then cross-linked to form a polymer by either ultraviolet radiation or electron beam heating. Polymer flash evaporation is generally combined with PVD processes to fabricate a wide range of functional coatings.

Physical Vapor Deposition Processes

- *Evaporation* is a process in which the boiling is carried out in a vacuum where there is almost no surrounding gas; the escaping vapor atom will travel in a straight line for a specified distance before it collides with structures in the vacuum chamber or residual gas atoms. Boiling is caused by thermal heating or electron beam heating of a source material.
- *Glow Discharge Evaporation and Sputtering* are processes performed in a soft vacuum (10^{-2}–10^{-1} torr) operating in the range $10^{-1} < pd < 10^{-2}$ torr cm, where p is the pressure and d is the source–substrate distance.
- *Molecular Beam Epitaxy* is an evaporation process performed in an ultra-high vacuum for the deposition of compounds of extreme regularity of layer thickness and composition from well-controlled deposition rates.

- *Reactive Evaporation* is a process in which small traces of a reactive gas are added to the vacuum chamber; the evaporating material reacts chemically with the gas so that the compound is deposited onto the substrate.
- *Activated Reactive Evaporation (ARE)* is the reactive evaporation process carried out in plasma which converts some of the neutral atoms into ions or energetic neutrals thus enhancing reaction probabilities and rates to deposit refractory compounds.
- *Biased Activated Reactive Evaporation (BARE)* is the same process as ARE with the substrate held at a negative bias voltage.
- *Sputter Deposition* is a vacuum process which uses a different physical phenomenon to produce the microscopic spray effect. When a fast ion strikes the surface of a material (target), atoms of that material are ejected by a momentum transfer process. As with evaporation, the ejected atoms or molecules can be condensed on a substrate to form a surface coating.
- *Reactive Sputter Deposition* is sputter deposition that involves a partial pressure of a reactive gas which reacts with the sputtered material to form a compound surface coating.
- *High-Power Pulsed Magnetron Sputtering (HPPMS)*, also known as high-power impulse magnetron sputtering (HIPIMS), utilizes extremely high-power densities of the order of kW/cm^2 in short pulses (impulses) of tens of microseconds at a low duty cycle (on/off time ratio) of $< 10\%$.
- *Dual Magnetron/Mid-Frequency Magnetron Sputtering* process achieves both high deposition rates and improved materials utilization. Dual magnetron sputtering uses a mid-frequency (~ 40–$300\,\text{kHz}$) pulsed power source and two magnetron cathodes. In its simplest form, the power source supplies a positive pulse to one magnetron cathode during the first half of the cycle while negatively biasing the other cathode and then supplying a positive pulse to the other magnetron cathode while negatively biasing the other cathode. In this manner, one cathode acts as an anode while the other is the sputtering cathode. Sputtering only occurs during negative bias. This process is very amenable to reactive sputtering.
- *Ion Plating* is an atomistic vacuum coating process in which the depositing film is continuously or periodically bombarded by energetic atomic-sized inert or reactive particles that can affect the growth and properties of the film. The source of depositing atoms can be from vacuum evaporation, sputtering, arc vaporization, or a chemical vapor precursor.

- *Reactive Ion Plating* is ion plating that involves a partial pressure of a reactive gas which reacts with the sputtered material to form a compound surface coating.
- *Chemical Ion Plating* is similar to reactive ion plating but uses stable gaseous reactants instead of a mixture of evaporated atoms and reactive gases. In most cases, the reactants are activated before they enter the plasma zone.
- *Ion Beam Deposition* is a process in which a beam of ions generated from an ion beam source, impinge and are deposited on the substrate.
- *Ion Beam Assisted Deposition (IAD*) – two versions are possible. In dual ion beam assisted deposition an ion beam is used to sputter a target and a second beam is used to bombard the growing film to change microstructure and properties. The other version uses an ion beam to bombard the growing film to change the structure and properties. In this case, conventional evaporation or sputtering techniques are used to generate a flux of the depositing species.
- *Cluster Ion Beam Deposition* is ion beam deposition in which atomic clusters are formed in the vapor phase and deposited on the substrate.
- *Filtered and Unfiltered Cathodic Arc Deposition (FCA)* processes can be considered a form of ion plating. Vacuum arc ion sources produce a plasma of the source material by microexplosions at the surface of the solid cathode, in contrast to production by gaseous ionization. The vacuum arc is a discharge between two metallic electrodes in a vacuum, which is characterized by a low burning voltage (about 20 V) and a high current (35–500 A). The current transfer is made possible by the production of plasma produced at micrometer-size cathode spots on the cathode surface. Vacuum arc is an efficient way of generating plasma. Plasmas of intense energetic ions can be used to carry out high-current ion plating for material surface modification applications.
- *Ion Implantation* is very similar to ion plating, except that now all of the depositing material is ionized, and accelerating energies are significantly higher. The depositing ions are thus able to penetrate the surface barrier of the substrate and become implanted in the substrate rather than on it.
- *Plasma Polymerization* is a process in which organic and inorganic polymers are deposited from a monomer vapor by the use of an electron beam, ultraviolet radiation, or glow discharge. Excellent insulating films can be prepared in this manner.

References

[1] K. Robbie et al., J. Vac. Sci. Technol. A13(3) (1995) 1032–1034.
[2] J. Hwan et al., J. Vac. Sci. Technol. A26(1) (2008) 146–150.

[3] J.D. Affinito, G.L. Graff, M.-K. Shi, M.E. Gross, P.A. Mounier, M.G. Hall, Proc. 42nd Annual Technical Conf. of the Society of Vacuum Coaters (1999) 102.
[4] S. Forrest, Proc. 44th Annual Technical Conf. of the Society of Vacuum Coaters (2001) 3.
[5] J.M. Grace, E.S. Brandt, Proc. 50th Annual Technical Conf. of the Society of Vacuum Coaters (2007) 77–83.
[6] V. Kouznetsov et al., Surf. Coat. Technol. 122 (1999) 290.
[7] D.H. Trinh et al., J. Vac. Sci. Technol. A 24(2) (2006) 309.
[8] M.M. Hawkeye, M.J. Brett, J. Vac. Sci. Technol. A 25(5) (2007) 1317–1335.
[9] D.L. Glocker, Proc. 51st Annual Technical Conf. of the Society of Vacuum Coaters (2008) in press.
[10] R.F. Bunshaw, Handbook of Deposition Technologies for Films and Coatings, 2nd ed., Noyes Publications (1994).
[11] R.F. Bunshaw, D.M. Mattox, Phys. Today (May 1970).
[12] K. Beardmore et al., Mol. Mater. 7 (1996) 155.
[13] J.A. Thornton, Annu. Rev. Mater. Sci. 7 (1977) 239.
[14] R. Messier et al., J. Vac. Sci. Technol. A 2 (1984) 500.
[15] H. Savaloni, M.G. Shahraki, Nanotechnology 15 (2004) 311–319.
[16] W.D. Sproul, in: D.M. Coaters, V. Mattox, Harwood Mattox (Eds.), 50 years of Vacuum Coating Technology and the Growth of the Society of Vacuum, Society of Vacuum Coaters (2007) 35.
[17] J. Li, S.R. Kirkpatrick, S.L. Rohde, Seattle, WA, October 14–19, Presentation SE-TuA1, AVS 2007 Fall Technical Conf. (2007).
[18] D.A. Glocker et al., 47th Annual Technical Conf. of the Society of Vacuum Coaters (2004) 183.
[19] C. Hayashi et al., Mater. Sci. Eng. (1993).
[20] A.P. Ehiasarian et al., Proc. 45th Technical Conf. of the Society of Vacuum Coaters (2002) 328.
[21] D.S. Campbell, in: L. Maissel, R. Glang (Eds.), Handbook of Thin Film Technology, McGraw-Hill (1970) Chap. 5.

CHAPTER 2

Plasmas in Deposition Processes

Scott G. Walton and J.E. Greene

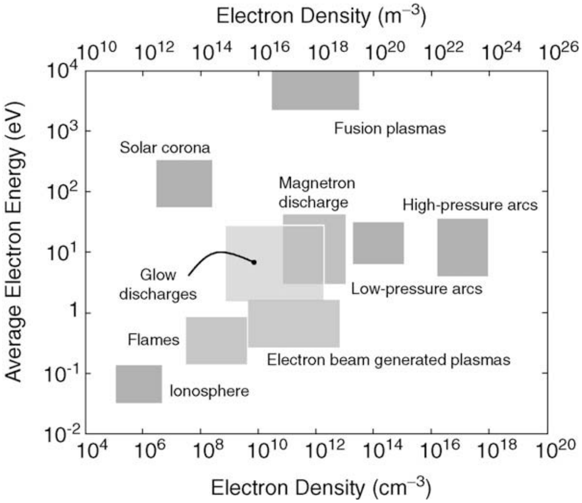

Figure 2.1: Ranges of average electron density and energy representative of various human-made and naturally occurring plasmas. (Adapted from [1].)

2.1 Introduction

Plasmas are partially ionized gases that contain approximately equal numbers of positively and negatively charged species. While plasmas are a common state of matter in the universe, they are rarely a natural occurrence on earth. Their unique properties, however, make them a powerful tool used in the modification of materials, ranging from material removal (etching) to the deposition of thin films and coatings. Plasmas are significantly different from non-ionized gases; a consequence of the mass difference between the positively charged ions and negatively charged electrons as well as the energy of these species. Figure 2.1 shows the various types of plasmas, characterized by their electron densities and energies. Although a number of plasmas have been used in materials processing including arcs, flames, and electron beam-generated plasmas, the most common types are discharge plasmas, generated by applying an electric field to a volume of gas.

When an electric field is applied to an ionized gas, energy is transferred more rapidly to the electrons than to the ions. The transfer of kinetic energy from an electron to a heavy particle (atom, molecule, or ion) in an elastic collision is proportional to the mass ratio of electrons and heavy particles and therefore very small ($\sim 10^{-5}$). Consequently, at low pressures, where electron collisions are not as common, the electrons can accumulate sufficient kinetic energy to have a high probability of exciting, dissociating, or ionizing the heavier gas atoms and molecules during inelastic collisions. The production of these species, and their interactions with surfaces and growing films, is one of the reasons that low-pressure discharge plasmas have assumed a dominant role in materials processing. More specifically, the kinetic and potential energy delivered by both inert and reactive particles provides a means to change the physical and chemical properties of a material's surface. While these changes are initiated at the atomic or molecular scale, plasmas are routinely used to modify surface areas up to tens of square centimeters. In some cases, treatment areas are of the order of square meters. Examples of processing application areas that utilize plasmas, some covered in this book, include: sputter deposition, reactive sputter deposition, activated reactive evaporation, ion plating, plasma-assisted chemical vapor deposition (PACVD), plasma-assisted physical vapor deposition (PAPVD), plasma-assisted etching, and plasma polymerization.

This chapter should not be considered a comprehensive discussion of the extensive physics and chemistry of plasmas, but rather an introduction to plasmas; and so, we review fundamental characteristics of plasmas and discharge plasmas in particular, which are of importance in understanding the role of plasma processes in materials modification applications. With that in mind, we cover topics related to particle interactions, discharge physics, and plasma-surface interactions.

2.2 Particle Collisions, Energy, and Motion

In any plasma-based materials processing application, the plasma parameters and resulting flux of species to the substrate determine the properties of the processed material or deposited film. Thus, it is important to understand the fundamental plasma properties and the gas-phase processes that influence these properties. The electron (or plasma) density, temperature, and energy distribution function are typically used to characterize the plasma. Collisions between electrons and heavy particles both sustain the plasma and determine the densities of reactive species while the collisions between the heavy particles further influence densities of reactive species, and particle fluxes at the substrate surfaces.

2.2.1 Collisions: Mean Free Path and Cross-Section

A plasma can be viewed as a medium in which energy is transported both in the gas and also to adjacent surfaces. In the case of a discharge plasma, electrical energy is transmitted, via an electric field, to a gas. The energetic gas particles are then used to promote chemical reactions in the gas or to interact with a surface to produce desirable effects such as surface reordering or sputtering. Thus, the process of energy exchange during collisions involving plasma-produced species is of fundamental importance.

Gas-phase collision probabilities are often expressed in terms of cross-sections. A related parameter is the mean free path or average distance traveled by particles between collisions. The mean free path λ and collision cross-section σ are generally defined by a simple relationship which treats the particles as hard or impenetrable spheres. The mean free path for

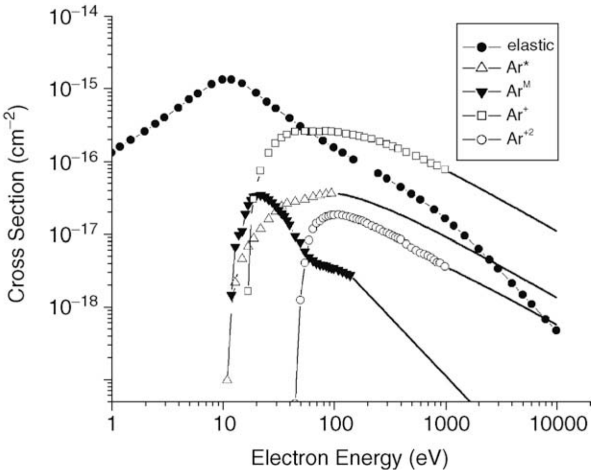

Figure 2.2: Collision cross-sections for electrons in argon. Products Ar^{+} and Ar^{+2} (from [2]), Ar^{m} (from [3, 4]), and Ar* (from [4, 5]). Momentum transfer from [6].

energetic particles passing through a gas of particle density N, where the gas particle is at rest is[1]

$$\lambda = 1/(N\sigma) \tag{2.1}$$

For electrons, the total collision cross-section can be written as

$$\sigma_{\text{tot}} = \sigma_{\text{elastic}} + \sigma_{\text{ex}} + \sigma_{\text{ion}} + \sigma_{\text{attach}} \tag{2.2}$$

where elastic, ex, ion, and attach subscripts indicate elastic, excitation, ionization, and attachment processes. In making plasma calculations it is useful to note the common units and values found in the appendix. In this work, distances are expressed in centimeters (cm), energy in electron volts (eV), and pressure in torr. Figure 2.2 shows the cross-sections for electrons interacting with argon gas. The cross-sections are typically a strong function of the energy of the colliding species. For the case of electrons colliding with room temperature gas particles (atoms or molecules), the kinetic energy of the gas particles is generally much less than that of the electrons and can be neglected (the energy of gas particles at 300 K is approximately 0.039 eV). Consequently, only the electron energy is used in Figure 2.2. The figure shows that at low electron energies (below the ionization energy of 15.75 eV), the

---

[1] When the projectile and the target molecule have the same velocity, the case of thermal ions drifting through a gas for example, the mean free path is properly defined as $\lambda = 1/(\sqrt{2}N\sigma)$.

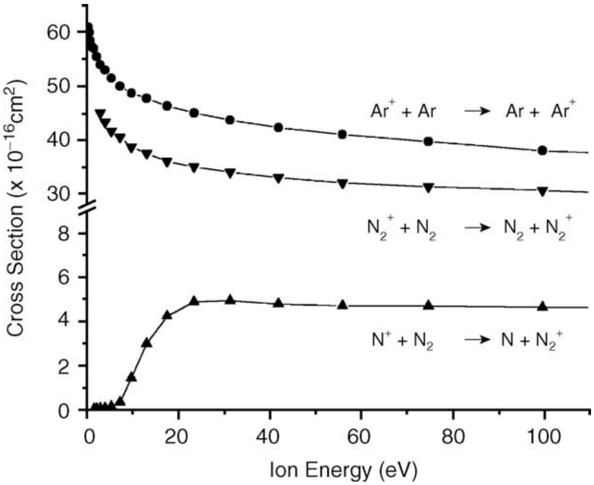

Figure 2.3: Cross-section for the charge exchange reaction of Ar^+ ions in argon and N^+ and N_2^+ ions in nitrogen. (From [10].)

primary collision processes are momentum exchange (σ_{elastic}) and, to a lesser degree, excitation (σ_{ex}). At energies considerably larger than the ionization potential, the primary process is ionization (σ_{ion}). Note that in electronegative gases like oxygen [7], the halogens, or compounds containing either (e.g. NO, CO, CO_2, CF_4, SiF_4, SF_6) [8, 9], electron attachment at lower energies is significant and should not be neglected.

Cross-sections are most easily measured for reactions involving a species such as an electron or ion, which can conveniently be formed as an energetic beam and passed through a stationary gas. Figure 2.3 shows the charge transfer cross-sections for energetic ions passing through their parent gas [10]. Note in comparing Figures 2.2 and 2.3 that the collision cross-sections are typically on the order of 10^{-16} to 10^{-15} cm^2 (i.e. a few to tens of angstroms in diameter) in magnitude. For collision types that cannot be investigated in beam experiments, typically those that occur at low projectile energies, the cross-sections are often deduced from measurements of macroscopic parameters such as viscosities, diffusion coefficients, drift velocities, and chemical reaction rates [11]. Thus, one finds reference to viscosity cross-sections, diffusion cross-sections, etc. Swarm experiments are a common approach to such measurements, where a swarm of particles is produced in a gas background that is subject to an electric field. These macroscopic parameters or transport coefficients are then measured as a function of the applied electric field. In general, the cross-sections can be calculated using the transport coefficients and vice versa [12, 13]. Depending on the type of analysis or calculation, either the cross-sections or transport coefficients are used. In plasma modeling using fluid approaches [14], one would use transport coefficients, while cross-sections would be better suited to kinetic treatments.

2.2.2 Electron Kinetic Energy

As noted, the electron energy can greatly exceed the energy of the gas background. The term 'non-equilibrium' is often used to describe such plasmas. To understand how this occurs, consider an electron elastically colliding with a heavy particle at rest. Using the conservation of energy and momentum, it can be shown that the maximum loss of electron energy in such a collision is [15]:

$$\Delta W = W_{\mathrm{ei}} - W_{\mathrm{ef}} = (4m_{\mathrm{e}}/M)W_{\mathrm{ei}} \tag{2.3}$$

where m_{e} and M are the electron and heavy-particle masses and W_{ei} and W_{ef} are the electron energies before and after the collision. Equation (2.3) indicates that only a small fraction of the electron kinetic energy is lost in such collisions. For a collision between an electron ($m = 1/1836$ amu) and an argon atom ($M = 40$ amu), the fraction is $\approx 5 \times 10^{-5}$.

Now consider a plasma electron in an electric field E. Between collisions with the gas particles, the electron will gain an energy W_{E} from the electric field that is equal to the force on the electron $F = qE$ (where q is the electronic charge) times the distance that it moves in the electric field. This distance can be approximated by the mean free path so that, on average, $W_{\mathrm{E}} = qE\lambda$. For a plasma at steady state, this electron energy gained must be balanced against the energy lost in collisions. Considering only elastic collisions, we equate ΔW in Eq. (2.3) to the energy W_{E} gained, and using Eq. (2.1) for λ, yields

$$W_{\mathrm{ei}} = (M/2m_{\mathrm{e}})(qE/N\sigma_{\mathrm{elastic}}) \tag{2.4}$$

Equation (2.4) shows that the electron energies can be very large. For the case of electrons in an Argon plasma at 1 torr and 300 K which is subjected to an electric field of 1 V/cm, $N = 3 \times 10^{16}\ \mathrm{cm}^{-3}$ and qE is 1 eV/cm. Using $\sigma_{\mathrm{elastic}} \approx 10^{-15}\ \mathrm{cm}^{-2}$ from Figure 2.1, Eq. (2.4) yields $W_{\mathrm{ei}} \sim 10^{3}$ eV. Thus, at steady state, the average electron energy will be much greater than that of the gas atoms, which is approximately 0.039 eV at 300 K. The actual average electron energy will not reach 10^{3} eV, however, because we have neglected other energy sinks. Nevertheless, the above analysis shows that even weak electric fields can cause electron kinetic energies in low-pressure glow discharge plasmas to be elevated well above gas particle energies.

On the other hand, if the plasma was generated in one atmosphere of argon (760 torr or $N = 3 \times 10^{19}\ \mathrm{cm}^{-3}$), we find $W_{\mathrm{ei}} \sim 1$ eV. In other words, collisions are so frequent in high-pressure plasmas that the electron energies are not as high. Moreover, electron/gas particle collisions are so frequent that the gas temperature increases. This behavior is illustrated in Figure 2.4 for the case of plasma arcs (the energies here are expressed as 'temperatures' in eV). When the electron and gas temperatures are the same, the term 'equilibrium plasmas' is often used. High-pressure plasmas, such as arcs or dielectric barrier

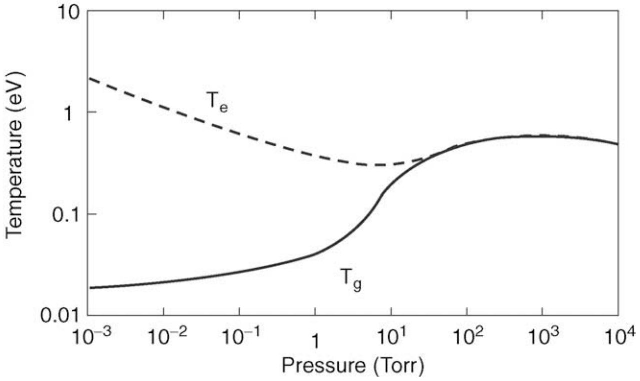

Figure 2.4: Electron (T_e) and gas temperatures (T_g) in an arc produced in an air background as a function of pressure. (Adapted from [17].)

discharges [16], are used for a variety of applications. However, the discussion in the following sections will be limited to the low-pressure case where $T_e > T_g$. In this situation, energetic electrons can produce high-temperature chemistry in low-temperatures gases [17, 18], which is an important factor when considering the use of plasmas to promote unique gas-phase chemistries. Indeed, an energy of 1 eV is equivalent to a temperature of about 11,600 K.

2.2.3 *Electron Energy Distribution*

For most purposes, the state of a glow discharge plasma can be characterized by the densities of heavy particles N_j, where j corresponds to the jth species, the electron density n_e, and the electron energy distribution function $F_e(E)$ [19]. Under conditions of local thermodynamic equilibrium [20], when the forward and reverse rates for all the electron energy exchange processes are equal (state of detailed balance) [21], the electrons will have a Maxwellian velocity distribution and their state can be defined by an electron temperature T_e. This is overly simplified since a state of equilibrium seldom exists in low-pressure discharge plasmas. It is, nonetheless, a common assumption.

Figure 2.5 schematically illustrates the electron energy distribution function. For a given Maxwellian energy distribution, the effect of an electric field is to increase the electron energies, thereby shifting the Maxwellian distribution toward higher energies. Elastic collisions, mainly electron–electron, tend to drive the distribution toward lower energies. In fact, electron–electron collisions tend to smooth the distribution and drive it toward the Maxwellian form. Inelastic collisions, on the other hand, will significantly alter the shape of the distribution, making it less Maxwellian. (The cross-section for a representative inelastic collision (ionization) is shown superimposed.) Electrons undergoing inelastic collisions will lose nearly all of their energy and are thus transferred out of the high-energy end of the

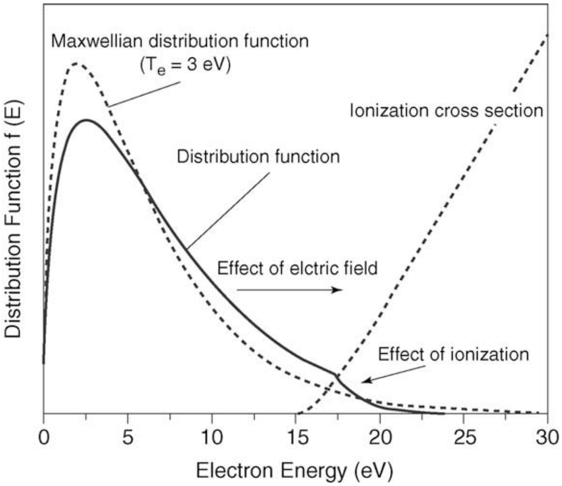

Figure 2.5: Schematic illustration of electron energy distribution function and inelastic (ionization) collision cross-section in argon. The applied electric fields tend to increase electron energies while inelastic collision will depopulate the higher energy electrons. Electron–electron collisions tend to drive the distribution toward a Maxwellian shape.

distribution. How these influence the shape of the distribution will depend on the type of inelastic collision. Excitations are dominant at low energies, particularly in molecular gases, while ionization dominates at high energies (see Figure 2.2 and Section 2.2.1). The shape of the distribution function has been shown to have a dependence on operating pressure and driving frequency [22] as well as power deposition [23] in low-pressure radio frequency (RF) power-driven plasmas. It is interesting to note that the electron temperature is established to balance the ionization and losses, thus for systems of comparable operating conditions (pressure, gas composition, size, and power), the electron temperature is not dependent on the source of electric power (i.e. RF, DC, microwave, etc.) [24].

Since, in practice, Maxwellian distributions are often assumed, it is common to use the electron temperature to describe the electrons. This assumption is best when the plasma electrons are collisional; that is, elastic electron collisions dominate and so the electric field perturbation is minimal. Such is the case for high-pressure discharges. The assumption is not as good in low-pressure discharges, where electron–electron collisions are not as significant as the electric field perturbation and the influence of inelastic collisions. In fact, it is not uncommon to find distributions that are bimodal (two peaks in the distribution). Bimodal distributions are often observed in low-pressure negative glow discharges of the type used in sputtering [25].

Electron energy distribution functions are usually measured by probe methods [26]. However, interpretation of the results is complicated, particularly in multicomponent plasmas [27] typically used in processing. There is a significant body of work concerning the use of probes in the literature and the interested reader should refer to this when performing such measurements. When great care is taken, the electron temperatures derived from probe measurements, although not strictly valid, are a reasonable approximation and can be used to describe the state of the plasma.

2.2.4 Collision Frequencies

The collision frequency is an important plasma parameter and is defined as the rate at which an average particle undergoes collisions of a specified type. The total electron–neutral collision frequency is the rate at which an average electron in a plasma undergoes collisions of all types with gas atoms and molecules. The general expression for the collision frequency ν is rather complex and involves the distribution functions of the colliding species [28]. For the electron–neutral case, the velocity of the heavy particles can be neglected and υ is given by

$$\upsilon_k = N \int_{E=0}^{E=\infty} (E/2m_\mathrm{e})^{1/2} \sigma_k(E) F_\mathrm{e}(E) dE \tag{2.5}$$

where k is the type of collision (e.g. elastic, excitation, ionization, etc). If the collision cross-section $\sigma_k(E)$ is assumed to be independent of energy and the electrons are assumed to have a Maxwellian distribution at an electron temperature T_e, then Eq. (2.5) reduces to

$$\upsilon_k = N \sigma_k \upsilon_\mathrm{e} \tag{2.6}$$

The average electron speed υ_e is

$$\upsilon_\mathrm{e} = (8\mathrm{k}T_\mathrm{e}/\pi\, m_\mathrm{e})^{1/2} \tag{2.7}$$

where k is Boltzmann's constant. It is customary to write kT_e in units of eV.[2] Thus, Eq. (2.7) becomes

$$\upsilon_\mathrm{e} = (6.7\times10^7)[\mathrm{k}T_\mathrm{e}(\mathrm{eV})]^{1/2}\ \mathrm{cm/s} \tag{2.8}$$

Because the velocity is determined using kT_e, σ_k in Eq. (2.6) is also approximated by its value at the electron energy kT_e. The electron–electron and electron–ion collision frequencies are of special interest. These are given by [29, 30]:

$$\upsilon_{\mathrm{ee}} = (3\times10^{-6}) n_\mathrm{e} \ln\Lambda / [\mathrm{k}T_\mathrm{e}(\mathrm{eV})]^{3/2}\ \mathrm{s}^{-1} \tag{2.9}$$

---

[2] From kinetic theory, the average particle energy in one dimension is 1/2 kT and the average energy in three dimensions is 3/2 kT. Since T and E are so closely related, it is customary in plasma physics to give temperature in units of eV. To avoid confusion with the number of dimensions involved, it is not the average energy but the energy corresponding to kT that is used to denote the temperature. By a 2 eV plasma, we mean that kT = 2eV, although the actual average energy in three dimensions is 3/2 kT or 3 eV.

and

$$\upsilon_{\mathrm{ei}} = (1.5\times10^{-6})n_{\mathrm{e}} \ln \Lambda/[\mathrm{k}T_{\mathrm{e}}(\mathrm{eV})]^{3/2}\ \mathrm{s}^{-1} \tag{2.10}$$

with

$$\lambda_{\mathrm{ee}} = (4.5\times10^{13})[\mathrm{k}T_{\mathrm{e}}(\mathrm{eV})]^2/(n_{\mathrm{e}} \ln\Lambda)\ \mathrm{cm} \tag{2.11}$$

where $\ln\Lambda$ is a weak function of $\mathrm{k}T_{\mathrm{e}}$ and n_{e}. The $\ln\Lambda$ term arises to correct for the infinite nature of collisions involving long-range coulomb forces. In a plasma, the presence of other charged species effectively shields charged particles from the influence of those outside a characteristic distance and so there can be no long-range coulomb forces. This characteristic distance is defined as the Debye length (see Section 2.3). The function $\ln\Lambda$ is tabulated in some books on plasma physics [31, 32], and has a value in the range of 10–15 for discharge plasmas of interest in this chapter.

It is useful to compare the electron collision frequencies of Eqs. (2.9) and (2.10) with other relevant collision frequencies. A plasma for which $\upsilon_{\mathrm{ee}} > \upsilon_{\mathrm{eA}}$, where υ_{eA} is the elastic electron–atom collision frequency, is said to be coulomb dominated. An approximate condition for coulomb domination is easily derived from Eqs. (2.6) and (2.9) [31]:

$$\frac{n_{\mathrm{e}}}{N} \gg \alpha_{\mathrm{c}} = (2.23\times10^{13})\frac{\sigma_{\mathrm{eA}}[\mathrm{k}T(\mathrm{eV})]^2}{\ln\Lambda} \tag{2.12}$$

The term α_{c} in Eq. (2.12) is known as the critical degree of ionization. Selecting $\mathrm{k}T_{\mathrm{e}} \approx 3\,\mathrm{eV}$ and $\sigma_{\mathrm{eA}} \sim 10^{-15}\,\mathrm{cm}^{-3}$ (Figure 2.2) yields $n_{\mathrm{e}}/N \approx 0.02$. Thus a moderate-temperature glow discharge plasma with 2% ionization can be dominated by coulomb collisions.

A consequence of coulomb domination can be seen by examining Eqs. (2.9) and (2.11). As the electron energy is increased, the electron collision frequency decreases and the mean free path will increase. Thus, electrons in an electric field will find that their energy gain is not clamped by collisions. Electron runaway is an important consideration in highly ionized plasmas [33] but seldom important in glow discharge plasmas because of inelastic collisions.

For heavy particle collisions, collision frequency can be approximated by an equation very similar to Eq. (2.6) [15, 34]. For the case of a heavy particle of mass M_k in a gas with density N_j of heavy particles of mass M_j, the collision frequency is given by

$$\upsilon_{kj} \approx (2.5\times10^5)\frac{(\sigma N)_{kj}}{(M^*)^{1/2}}\left[\frac{T}{300}\right]^{1/2} \tag{2.13}$$

where the cross-section is assumed to be independent of the velocity of impact and all the heavy particles are at the common temperature T. In Eq. (2.13) M^* is a reduced mass defined as

$$M^* = \frac{M_k M_j}{M_k + M_j} \tag{2.14}$$

where the masses are molecular weights expressed in grams.

2.2.5 Reaction Rates

The gas-phase reaction rate R is directly proportional to the collision frequency. For a process k involving electron collisions,

$$R_k = n_\mathrm{e} v_k \,\mathrm{cm}^{-3}\,\mathrm{s}^{-1} \tag{2.15}$$

If the electrons are assumed to have a Maxwellian velocity distribution at a temperature T_e, and if the cross-section for a given reaction is approximated by a step function of magnitude σ_o and threshold energy E_o as shown in Figure 2.6, then the reaction rate is given by

$$R_k = n_\mathrm{e} N \sigma_\mathrm{o} v_\mathrm{e} [1 + (E_\mathrm{o}/kT_\mathrm{e})] \exp(-E_\mathrm{o}/\mathrm{k}T_\mathrm{e}) \tag{2.16}$$

For reactions involving heavy particle collisions, reaction rate constants rather than actual collision frequencies are typically measured and used. For a reaction occurring via a two-body

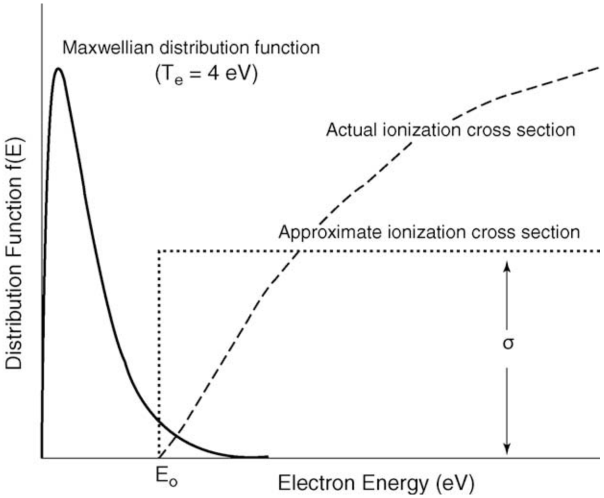

Figure 2.6: Ionization reaction rate approximation for a Maxwellian electron energy distribution.

Table 2.1: Charge exchange reactions and the associated reaction rate constants $\kappa(T)$ at 293 K

Reaction	Rate constant ($cm^3/mol\cdot s$)
$Ar^+ + Ar \rightarrow Ar + Ar^+$	4.6×10^{-10}
$Ar^+ + N_2 \rightarrow Ar + N_2{}^+$	1.3×10^{-11}
$Ar^+ + O_2 \rightarrow Ar + O_2{}^+$	4.9×10^{-11}
$Ar^+ + H_2 \rightarrow H + ArH^+$	8.9×10^{-10}
$N^+ + N_2 \rightarrow N_3{}^+$	1.3×10^{-13}
$N_2{}^+ + N_2 \rightarrow N + N_3{}^+$	2.8×10^{-12}
$N_2{}^+ + O_2 \rightarrow N_2 + O_2{}^+$	8.5×10^{-11}
$N_2{}^+ + Ar \rightarrow N_2 + Ar^+$	1.0×10^{-13}
$O^+ + O_2 \rightarrow O + O_2{}^+$	2.2×10^{-11}
$O_2{}^+ + N_2 \rightarrow NO + NO^+$	2.0×10^{-18}
$CH_4{}^+ + CH_4 \rightarrow CH_5{}^+ + CH_3$	1.2×10^{-9}

From [35].

collision between species i and j in a gas at temperature T, with rate constant $\kappa(T)$, the rate is

$$R = \kappa(T) N_i N_j \tag{2.17}$$

Table 2.1 gives the rate constants for various charge transfer processes.

2.2.6 Mobilities

Plasma transport properties are dependent on the frequency of elastic (momentum exchange) collisions. The mobility μ_j relates the electric-field driven drift velocity v_d of a given charged particle species j to the strength of the field E:

$$v_{dj} = \mu_j E \tag{2.18}$$

When the collision frequency is sufficiently large that the drift velocity is small compared to the thermal velocity,

$$\mu_j = \frac{1.6\times10^{-12}}{m_j v_{ji}} \tag{2.19}$$

where m_j is the particle mass in grams.

The mobility is generally used to describe the drift of ions through a plasma that is at a sufficiently high pressure to satisfy the collision frequency requirement ($v_{th} > v_d$). Reduced mobilities for several gases of interest are given in Table 2.2.

When a positive ion collides with a gas molecule or atom, two processes can occur. First, the ion and molecule can exchange momentum and energy in a collision. Second, an exchange of

Table 2.2: Reduced mobilities of ions in their own gas for a vanishing electric field

Ion–Gas	μ_{jo} (cm^2/V·s)
He^+–He	10.3
Ne^+–Ne	4.08
Ar^+–Ar	1.52
$O_2{}^+$–Ar	2.57
O^+–Ar	3.43
H^+–H_2	16.0
H^-–H_2	42.7
$N_2{}^+$–N_2	1.90
N^+–N_2	3.01
$O_2{}^+$–O_2	2.23
O^-–O_2	3.20

From [36].

Conditions are: $P = 760$ torr, $T = 300$ K, $E = 0$. Thus, $\mu_j = K\mu_{jo}$, where $K = (760/P)(T/300)$.

charge can occur. For example, fast ions colliding with slow neutrals can extract an electron from the slow neutral. After the exchange, the fast ion becomes a fast neutral while the slow neutral becomes a slow positive ion. For ions drifting through a gas at room temperature, repeated charge exchange collisions can effectively behave as though a single ion undergoes repeated collisions in which the ion loses all of its kinetic energy [37]. Resonant charge exchange, where the ion and neutral are identical (with the exception of charge), is an important consideration. For this process, the cross-section increases with decreasing ion energy (see Figure 2.3) and at low ion energies, is about one-half of the total cross-section [38]. Thus, resonant charge exchange contributes significantly to determining the mobility of ions drifting through their parent gas. Charge transfer is very important in high-pressure sputtering and ion-plating discharges where collision frequencies are high.

2.2.7 Conductivity and Diffusion

The electrical conductivity σ is just $qN\mu$, so that

$$\sigma_j = 1/\rho_j = 2.6\times10^{-31}(N_j/m_j\nu_{ji})\,(\mathrm{Wcm})^{-1} \tag{2.20}$$

where N_j is the particle density in cm^{-3} and m_j is the mass of the current carrier in grams. Since σ is the common symbol for both the electrical conductivity and the collision cross-section, the resistivity ρ is often used to avoid confusion.

The diffusion coefficient D relates the particle flux Γ to the density gradient. Thus, one has

$$\Gamma_j = N_j\upsilon_{dj} = D_j(dN_j/dx) \tag{2.21}$$

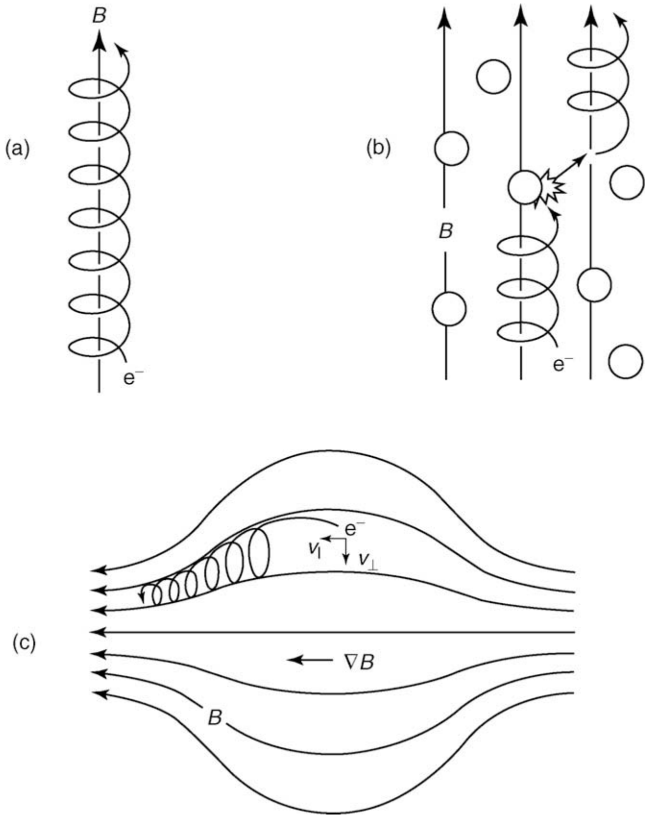

Figure 2.7: Electron paths in static magnetic fields.

where

$$D_j = \frac{\mathrm{k}T}{m_j \upsilon} = (1.6\times10^{-12})\frac{\mathrm{k}T(\mathrm{eV})}{m_j \upsilon}\ \ \mathrm{cm}^2/\mathrm{s} \tag{2.22}$$

This description of diffusion neglects the interaction of oppositely charged species and is thus often referred to as free diffusion. Ambipolar diffusion describes the diffusion of charged species and is covered in Section 2.3.2.

2.2.8 Particle Motion in Magnetic Fields

The force exerted on a charged particle in a magnetic field is given by $F_B = q(\nu \times B)$ and affects the motion of a particle in ways that are summarized in Figure 2.7. A charged particle in a uniform magnetic field B will orbit a field line as shown in Figure 2.7(a) while drifting along the field with parallel velocity $v_{||}$ that is unaffected by the field. The orbiting frequency is called the gyro or cyclotron frequency and is given by

$$\omega_c = eB/m \tag{2.23}$$

The orbiting radius is called the gyro, cyclotron, or Larmor radius and is given by

$$r_g = (m/3)(\upsilon_\perp/B) \tag{2.24}$$

There are a few points to consider when using magnetic fields in plasma processing systems. First, the use of magnetic fields to manipulate and confine plasmas requires that r_g be small compared to the critical apparatus size such as the chamber dimensions, electrode separations, or substrate locations. Note that r_g depends directly on the mass of the particle and so much larger magnetic fields are required to influence the motions of the plasma ions compared to the electrons. For particles of the same velocity subject to a given field, the ion gyro radius will be at least three orders of magnitude greater than the electron gyro radius. With this in mind, magnetic fields are generally chosen to be strong enough to influence the plasma electrons, not the ions. However, since electrostatic forces prevent the ions from escaping from the electrons, magnetically confined electrons in a discharge will provide considerable confinement for the plasma ions. Magnetic field strengths between 200 and 300 gauss are common in magnetrons.

For electrons, Eqs. (2.23) and (2.24) become

$$\omega_c = (1.76\times10^7)\,B\,\text{rad/s} \tag{2.25}$$

where B is in gauss, and

$$r_g = 3.37\,\frac{W_\perp}{B}\,\text{cm} \tag{2.26}$$

where $W_\perp$ is in eV. Thus, for electrons with an average energy $W_\perp$ of 10 eV and a magnetic field strength B of 100 G, the gyro radius is ≈ 0.1 cm. For Ar^+ ions of the same energy, the gyro radius is ≈ 270 cm. Recall, however, the energy of ions in the bulk plasma are typically in thermal equilibrium with the surrounding gas and so have a much lower energy than the electrons. In that case, the gyro radius is approximately 15 cm, still significantly larger than the electrons.

An electron that is trapped on a given magnetic field line can advance to an adjacent field line after colliding with a larger species, as indicated schematically in Figure 2.7(b). Collisional diffusion of electrons across magnetic field lines is an important consideration in many discharge devices.

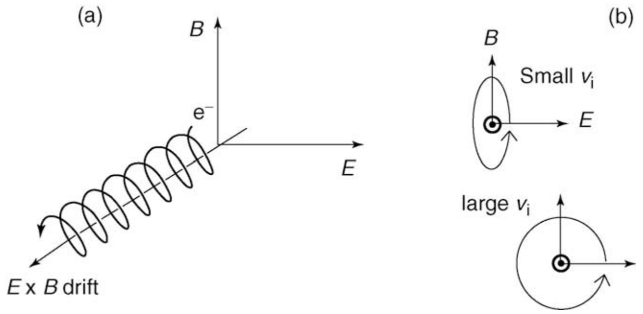

Figure 2.8: Electron paths in static magnetic and electric fields.

The drift of electrons along a magnetic field line can also be influenced by gradients in the magnetic field. An example of this behavior is shown in Figure 2.7(c), for a 'pinched-field' arrangement often used in discharge devices. In this configuration, the field strength increases as the field pinches (field lines get closer), and so ω_g increases while r_g remains fixed because electrons moving in such a field tend to conserve the magnetic moment, μ_M, defined by [29]

$$\mu_M = W_\perp / B \tag{2.27}$$

Thus, $W_\perp$ must increase as the electrons move in the direction of increasing field strength. Conservation of energy requires that $W_{||} + W_\perp$ be constant. Therefore $W_{||}$ must decrease, so that electrons will slow and will likely be reflected.

When both electric and magnetic fields are present, the electrons are subject to the forces of both, as shown in Figure 2.8. When the electric field E is directed parallel to the magnetic field B, the electrons are freely accelerated along the field lines. However, if the electric field has a component $E_\perp$ which is perpendicular to B, the electrons undergo a drift in a direction perpendicular to both $E_\perp$ and B, as shown in Figure 2.8(a). This motion is known as the $E \times B$. The motion is cycloidal if the initial electron energy is small compared to that gained from the electric field; it has the more circular form if the initial electron energy is large compared to the electric-field-induced variations that occur during the course of the orbit (Figure 2.8b). In both cases, the electron drift speed is given by

$$\upsilon_e = 108 \frac{E_\perp}{B} \text{ cm/s} \tag{2.28}$$

with $E_\perp$ in V/cm and B in gauss.

2.3 Plasma Parameters and Collective Behavior

Plasmas differ from non-ionized gases by their propensity for undergoing collective behavior associated with the interaction of charged species as well as the mass and energy difference between the charged particles. Three parameters: the Debye length λ_D, plasma frequency f_p, and critical degree of ionization α_c, provide a useful measure of the tendency toward collective behavior. These parameters are derived from basic plasma properties of gas density N, electron density n_e, and electron energy T_e.

The Debye length corresponds to the distance in which significant departures from charge neutrality occurs and is given by

$$\lambda_D = 743\left[\frac{kT_e}{n_e}\right]^{1/2}\text{cm} \tag{2.29}$$

with kT_e in eV and n_e in cm^{-3}. This characteristic length defines a plasma; one cannot exist in a space having dimensions less than λ_D.

The plasma frequency provides a measure of the tendency for electrostatic waves to develop and is expressed here as

$$f_p = \omega_p/2\pi = 9000[n_e]^{1/2}\,\text{Hz} \tag{2.30}$$

Waves can form if $\omega_p \gg \nu_{e,\text{elastic}}$ where $\nu_{e,\text{elastic}}$ is the electron collision frequency for momentum exchange. The inverse of f_p defines the characteristic time of the waves.

The critical degree of ionization α_c was defined by Eq. (2.12) and is listed again for completion:

$$\alpha_c = (2.23\times 10^{13})\frac{\sigma_{eA}[kT(\text{eV})]^2}{\ln\Lambda}$$

When the degree of ionization $\alpha = n_e/N$ is much greater than α_c, coulomb collisions dominate, and the charged particles behave as though they were in a fully ionized gas. This can occur at degrees of ionization of a few percent for plasmas with low average electron energies (≈1 eV).

2.3.1 Plasma Sheaths

Given a gas of particle density N and temperature T, the flux of particles passing to an adjacent wall is given by

$$\Gamma = n\upsilon/4 = (n/4)(8kT/\pi m)^{1/2} \tag{2.31}$$

For electrons, this becomes (see Eqs. 2.7 and 2.8)

$$\Gamma_e = (1.67\times 10^{7})n_e[kT_e(\text{eV})]^{1/2}\,\text{cm}^{-2}\,\text{s}^{-1} \tag{2.32}$$

which, in units of current density, is equal to

$$J_e = (2.7\times10^{-9})n_e[kT_e(\mathrm{eV})]^{1/2}\ \mathrm{mA/cm^2} \tag{2.33}$$

Thus, for a discharge with an electron density of $10^{10}\ \mathrm{cm}^{-3}$ and an average energy of 4 eV, $J_e \approx 60\ \mathrm{mA/cm^2}$.

For heavy particles such as ions, Eq. (2.31) can be written in the following useful form:

$$\Gamma_i = 10^4 n_i(40/M)^{1/2}(T/300)^{1/2} \tag{2.34}$$

where T is the gas temperature in Kelvin and M is the species molecular weight. In units of current density, Eq. (2.34) becomes

$$J_i = 1.6\times10^{-12}n_i(40/m)^{1/2}(T/300)^{1/2}\ \mathrm{mA/cm^2} \tag{2.35}$$

Thus, for a plasma produced in argon with an ion density of $10^{10}\ \mathrm{cm}^{-3}$ at 300 K, the ion current to the wall is $J_i \approx 1.6 \times 10^{-2}\ \mathrm{mA/cm^2}$.

The ratio of ion to electron fluxes (from Eq. 2.31) gives

$$\frac{\Gamma_i}{\Gamma_e} = \frac{n_e(kT_i/m_i)^{1/2}}{n_i(kT_e/m_e)^{1/2}}$$

For a plasma in quasi-equilibrium ($n_e \approx n_i$) and writing the masses in atomic mass units, Eq. (2.35) reduces to

$$\frac{\Gamma_i}{\Gamma_e} = \frac{1}{\sqrt{1836}}\sqrt{\frac{T_i}{T_e m_i(A)}}$$

It is clearly seen that the electrons tend to flow from a plasma to an adjacent wall at a faster rate than the ions. For an argon plasma where the electron temperature is 4 eV and the ions are at room temperature, $\Gamma_i/\Gamma_e \approx 3 \times 10^{-4}$. Because of this significant difference, a space charge region in which one species is largely excluded forms adjacent to such surfaces. These regions are called sheaths, and are typically several Debye lengths in thickness.

The nature of the sheath will depend on the current density passing across it. Except for cases involving very high current densities to anodes, the sheath will contain primarily the low-mobility ion species, and such sheaths are known as positive space charge sheaths or simply ion sheaths. This causes a potential to develop across the sheath, called the sheath potential or sheath drop, which forms a barrier capable of reflecting the more mobile electrons (except in the case of a strong magnetic field). The sheath potential adjusts itself so that the flux of electrons to the wall equals the electron current that is drawn from the wall by the external circuit. If the wall is electrically isolated, the electron flux is reduced to the point

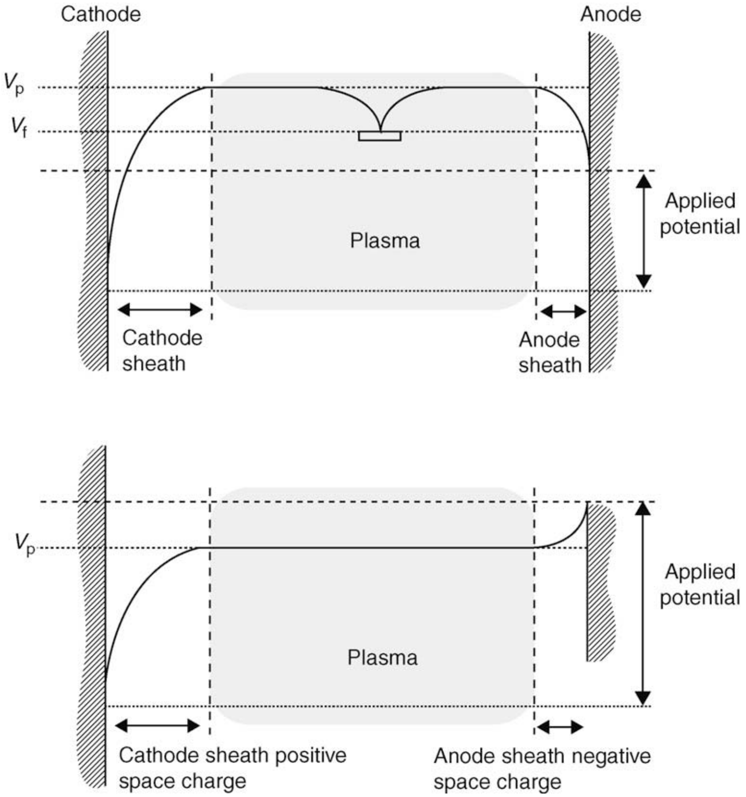

Figure 2.9: Schematic illustration of sheaths that form between a plasma discharge and the surrounding apparatus walls for systems having (top) a large anode and (bottom) a small anode. Also shown in (top) is a floating metal surface immersed in plasma.

which is equal to the ion flux. It is intuitive to note the importance of the sheath. Indeed, without it, the quasi-neutrality of the plasma is in jeopardy.

Figure 2.9 shows a schematic illustration of a typical discharge plasma which is in contact with surfaces that are either cathodes or anodes, or electrically isolated (floating). The plasma potential V_p forms with respect to the most positive surface (anode) [39]. The potential of a floating surface relative to the plasma potential is known as the floating potential V_f. For a Maxwellian energy distribution, the floating potential is given by [40]

$$V_f = \frac{kT_e(\text{eV})}{2e} \ln\left[\frac{\pi\, m_e}{2m}\right] \tag{2.36}$$

This is the potential with respect to the plasma potential and thus, when a floating surface is immersed in a plasma, the surface will be bombarded with ions having kinetic energies of up to $-e(V_p - V_f)$. The natural log term in Eq. (2.36) is typically on the order of 10 for most discharges used in processing and so V_f scales with electron temperature. Thus, values for V_f will be in the range 5–50 V.

In general, the anodes used in discharges are large enough that the current density is less than the current driven by T_e (Eq. 2.33). In this case, the plasma potential is above the anode potential (Figure 2.9(top)), there is a positive space charge sheath at the anode, and the sheath potential drop is between zero and $-(V_p - V_f)$. On the other hand, if the anode area is so small that the current density must exceed the T_e-driven current, then the anode potential will be above the plasma potential, as shown in Figure 2.9(bottom). The local electric field surrounding the anode will draw sufficient electrons to the anode to supply the external circuit.[3]

A large potential difference $V_{s,}$ approximately equal to the entire potential applied by the power supply, occurs in the cathode sheath as shown schematically in Figure 2.10. The sheath thickness d_s is taken to be the region over which the full potential drop V_s occurs. Over the sheath thickness, the electron density is negligible. For the low-pressure case, where the ion mean free path is larger than d_s, the ion current density J_i at the wall is related to d_s and V_s by the Child–Langmuir law [29]. It is useful to write this relationship as

$$J_i = 0.273(40/m_i)^{1/2}(V_s{}^{3/2}/d_s{}^2)\,\mathrm{mA/cm^2} \tag{2.37}$$

where V_s is in kV, d_s is in cm, and M_i is the ion mass in u. For an Ar sputtering plasma ($M_i = 40$) with $V_s = 1$ kV and $d_s = 1$ cm, $J_i = 0.27$ mA/cm^2. Here we find a higher current than that found earlier (see Eq. 2.35). Thus, the application of an applied bias will increase the current.

It is difficult to directly relate J_i to the density N_{io} of ions in the bulk plasma, because there is a quasi-neutral presheath region where a potential drop V_{ps} of about $1/2(\mathrm{k}T_e/e)$ occurs. However, the presheath density can be assumed to obey a Boltzmann distribution [41], such that $N_{is}/N_{io} = \exp(eV_{ps}/\mathrm{k}T_e)$, and the density can be estimated using

$$J_i \approx (9.12\times10^{-11})N_{io}(\mathrm{k}T_e/M_i)^{1/2}\,\mathrm{mA/cm^2} \tag{2.38}$$

where M_i is in u and $\mathrm{k}T_e$ is in eV.

Assuming quasi-neutrality in the bulk plasma ($N_{io} \approx n_e$), the sheath thickness d_s can be calculated by substituting Eq. (2.38) into Eq. (2.37) and introducing the Debye length from Eq. (2.29). This yields the expression

$$d_s = 185\lambda_D(V/\mathrm{k}T_e)^{3/4}\,\mathrm{cm} \tag{2.39}$$

---

[3] The potential increase at a small anode is largely limited by the ionization potential of the gas atoms. A potential increase of this amount causes the electrons to be accelerated to energies large enough to ionize the gas, which produces additional electrons that can then provide the required anode current. Thus, no additional rise in potential is needed to draw electrons form the plasma.

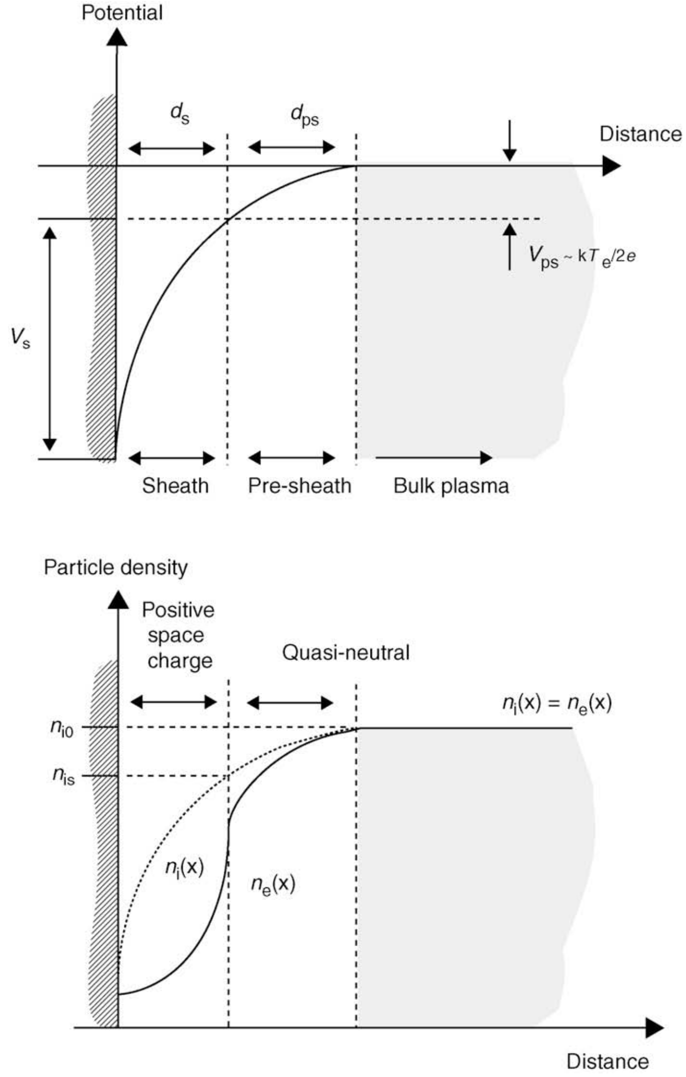

Figure 2.10: Schematic representation of the presheath and sheath that develop at a cathode. The top is the potential profile showing the presheath V_{ps} and sheath V_s potentials. The bottom shows the ion $n_i(x)$ and electron $n_e(x)$ density profiles along with the ion density at the plasma (n_{io}) and sheath (n_{is}) boundaries.

For the high-pressure case, where collisions are so frequent that the ion drift velocity is of the order of the thermal velocity, a mobility description is used for the ion motion [17]. Under this condition,

$$J_i = 9.95\times10^{-5}\mu_i(V_s^2/d_s^3)\ \mathrm{mA/cm^2} \tag{2.40}$$

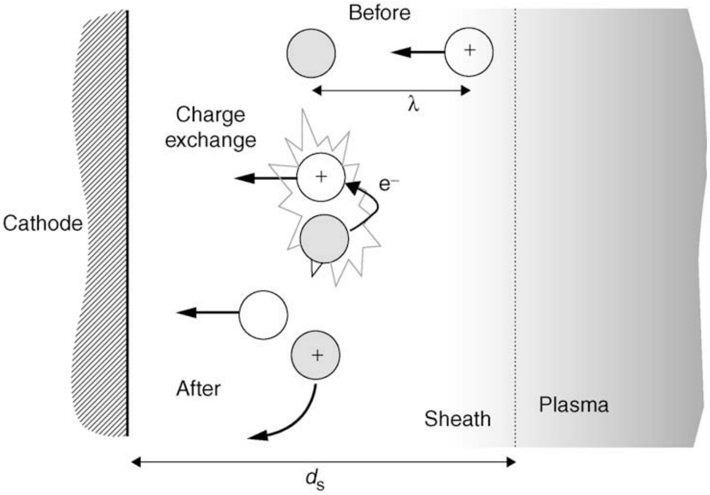

Figure 2.11: Schematic representation of a charge exchange reaction in the sheath, which produces a slow ion and fast neutral. After the collision, the slow ion is accelerated toward the cathode by the electric field in the sheath.

where μ_i is the ion mobility in cm^2/V-s, V_s is the sheath potential drop in kV, and d_s is the sheath thickness in cm. For an Ar plasma at 1 torr, $\mu_i = 1155\ cm^2/V$-s from Table 2.2. Taking $V = 1$ kV and $d_s = 1$ cm yields $J_i = 0.11\ mA/cm^2$.

In low-pressure plasmas, where the mean free path for charge exchange is greater than the sheath thickness, the ions will fall through the entire sheath potential and bombard the cathode with an energy about equal to eV_s. This is common in deposition processes using magnetrons. At higher pressures, where charge exchange is likely in the sheath, the bombarding flux will consist of both ions and fast neutrals having energies considerably less than eV_s as indicated schematically in Figure 2.11. The resulting ion energy distributions are discussed in Section 2.6.2. Charge exchange in the sheath is an important consideration in DC sputtering applications such as ion plating, high-pressure etching, or PACVD.

2.3.2 Ambipolar Diffusion

The previous discussion of sheath formation to ensure the equal flow of ions and electrons from a plasma can be extended to any region of space. That is, the flow of electrons and ions out of any volume must be equal or an electric field will develop to preserve charge neutrality over that volume. This coupled particle motion is called ambipolar diffusion. The diffusion flux Γ of electrons or ions is given by

$$\Gamma_e = D_a(dn_e/dx) = \Gamma_i = D_a(dn_i/dx) \tag{2.41}$$

The term D_a is called the ambipolar diffusion coefficient and can be written as

$$D_a = \frac{\mu_i D_e + \mu_e D_i}{\mu_i + \mu_e}$$

Noting that $\mu_e \gg \mu_i$ (see Eq. 2.19) permits D_a to be approximated as [42]

$$D_a \approx D_i(1 + T_e/T_i) \tag{2.42}$$

where D_i is given by Eq. (2.22). Thus, the effect of the ambipolar field is to enhance the diffusion of ions, but the diffusion rate of the two species together is primarily controlled by the slower species.

In the presence of a sufficiently strong magnetic field perpendicular to the direction of diffusion, the electron mobility can be reduced significantly and it, rather than the ion mobility can become rate limiting ($\mu_e \ll \mu_i$). Under this condition, a form similar to Eq. (2.41) is used,

$$D_{\perp a} \approx \{D_e/[1 + \omega_c^2/\nu_e)]\}(1 + T_i/T_e) \tag{2.43}$$

where D_e is the electron diffusion coefficient in the absence of a magnetic field. The effect of the magnetic field becomes strong when ω_e (given by Eq. 2.25) is much larger than the electron collision frequency ν_e, i.e. when the electrons are trapped on magnetic field lines as shown in Figure 2.7(a), and collisional hopping to adjacent field lines is infrequent. It should be noted that Eq. (2.42) is based on the assumption that electron losses along the lines can be neglected. Attention to these losses should be given when analyzing the performance of an actual device [29, 43].

2.3.3 Plasma Oscillations

The plasma state is rich in wave phenomena when the degree of ionization is large enough to make long-range forces important, particularly when a magnetic field is present [29]. Departures from charge neutrality in the bulk plasma capable of generating waves can occur in the form of charge bunching and separation over distances of the order of the Debye length (Eq. 2.29). A general discussion of such behavior is beyond the scope of this chapter. However, one case will be mentioned because of its potential importance in sputter deposition. Consider the case of a plasma in a uniform electric and magnetic field, as illustrated in the left side of Figure 2.12. There is an $E \times B$ drift perpendicular to both E and B, and in the absence of collisions, there should be no transport across the magnetic field in the direction of the applied electric field. If charge bunching occurs, as shown in the right side of Figure 2.12, the perturbation produces a local electric field E_p that can result in $E \times B$ drift across the magnetic field, in a direction parallel to the applied electric field. This anomalous collisionless transport

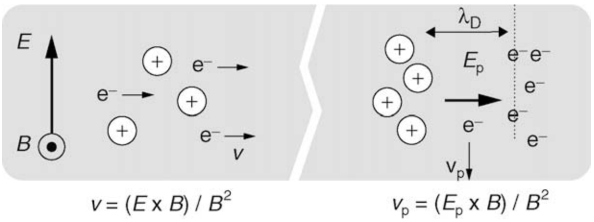

Figure 2.12: Schematic representation of charge neutrality breaking (charge bunching) resulting in electron transport across a magnetic field. The local electric field becomes dominant and causes a change in velocity.

across the magnetic field is believed to be an important mechanism in Penning discharges as well as in magnetron sputtering discharges [44].

2.4 Discharge Plasmas

2.4.1 Introduction

A discharge plasma is a low-temperature, relatively low-pressure gas in which a degree of ionization is sustained by energetic electrons. Discharge configurations used in materials processing differ in their general geometry, the type of applied field, and the orientation of the electric field that is used to provide energy to the electrons. Shown in Figure 2.13 are four general configurations for plasmas driven by AC power. Specific embodiments of these often used in materials processing are further illustrated in Figure 2.14. Discharges driven by DC power are shown in Figures 2.17–2.20.

In sputtering, simple planar diodes of the type shown schematically in Figure 2.13(a) can be used. They may be driven at radio frequencies (RF), as shown in the figure, or by a DC power supply. Bias sputtering is a common technique for controllably tuning, in real time, the chemistry, phase, microstructure, and, hence, physical properties of growing films. RF planar diode discharges are also used for plasma etching, and reactive ion etching. Systems with the configuration shown in Figure 2.13(d) are also used for PACVD.

In plasma etching, PACVD, and plasma polymerization, discharges are often sustained in glass or quartz reactor tubes by surrounding electrodes which are driven at high frequencies (from 300 kHz to microwave frequencies) [45]. Common electrode configurations are a pair of ring electrodes along the tube, a solenoidal coil electrode as shown in Figure 2.13(b), or clam-shell electrodes as shown in Figure 2.13(c). Alternatively, the coil could be flat as shown in Figure 2.13(d). It should be noted that all of these discharges are basically capacitive in nature. Although the coil electrode will introduce considerable inductance into the load seen by the matching network, the capacitive fields generated by the coil-to-coil potential drop dominate

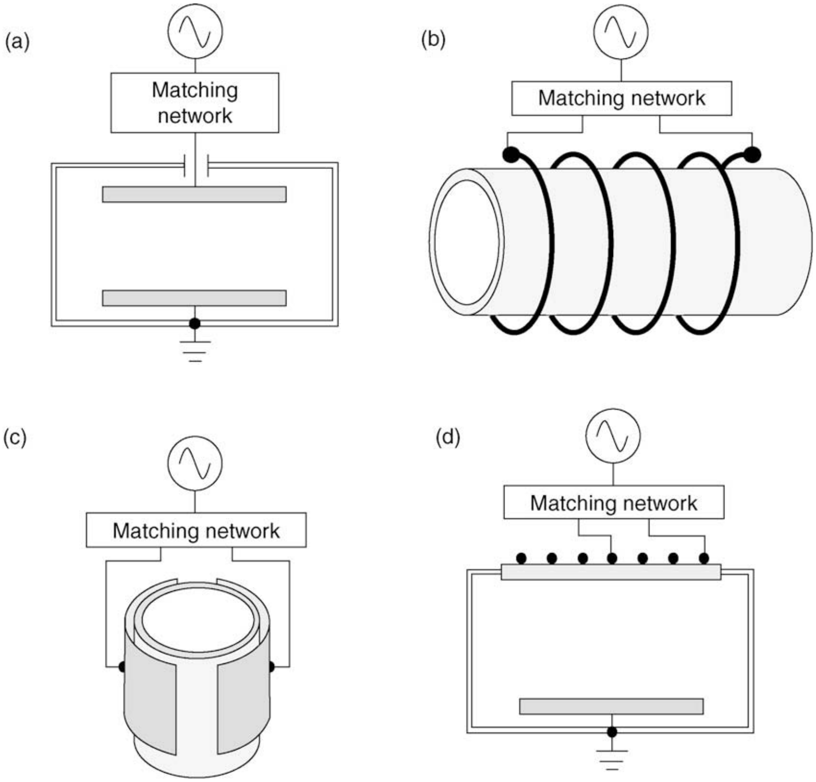

Figure 2.13: Schematic illustrations of generic RF-driven discharge devices: (a) parallel plate reactor, (b) barrel reactor ICP, (c) clam shell reactor, and (d) flat coil ICP.

over those generated by the time rate of change of magnetic flux and therefore act as the primary source of ionization unless special precautions are taken to shield them. Inductive sources will be discussed later. In the case of microwave discharges, the reactor tube is generally positioned within the waveguide at a location which places a strong electric field component within the tube [18, 45].

In ion plating, the discharge is generally sustained in a mixture of the evaporated flux and an inert working gas with the substrate holder biased negatively relative to the plasma potential. Usually this is done by simply making the substrate holder the cathode electrode for sustaining the plasma discharge, as shown in Figure 2.15(a). The ion bombardment of the growing coating has been shown to influence its microstructure [46]. Activated reactive evaporation is a similar approach where a plasma discharge, produced using a variety of electrode configurations driven either by DC or RF power, is sustained in a flux of evaporated material and reactive gas that is directed toward the substrates, as shown in Figure 2.15(b). The presence of the plasma has been shown to influence properties such as the chemical composition of the resultant films [47].

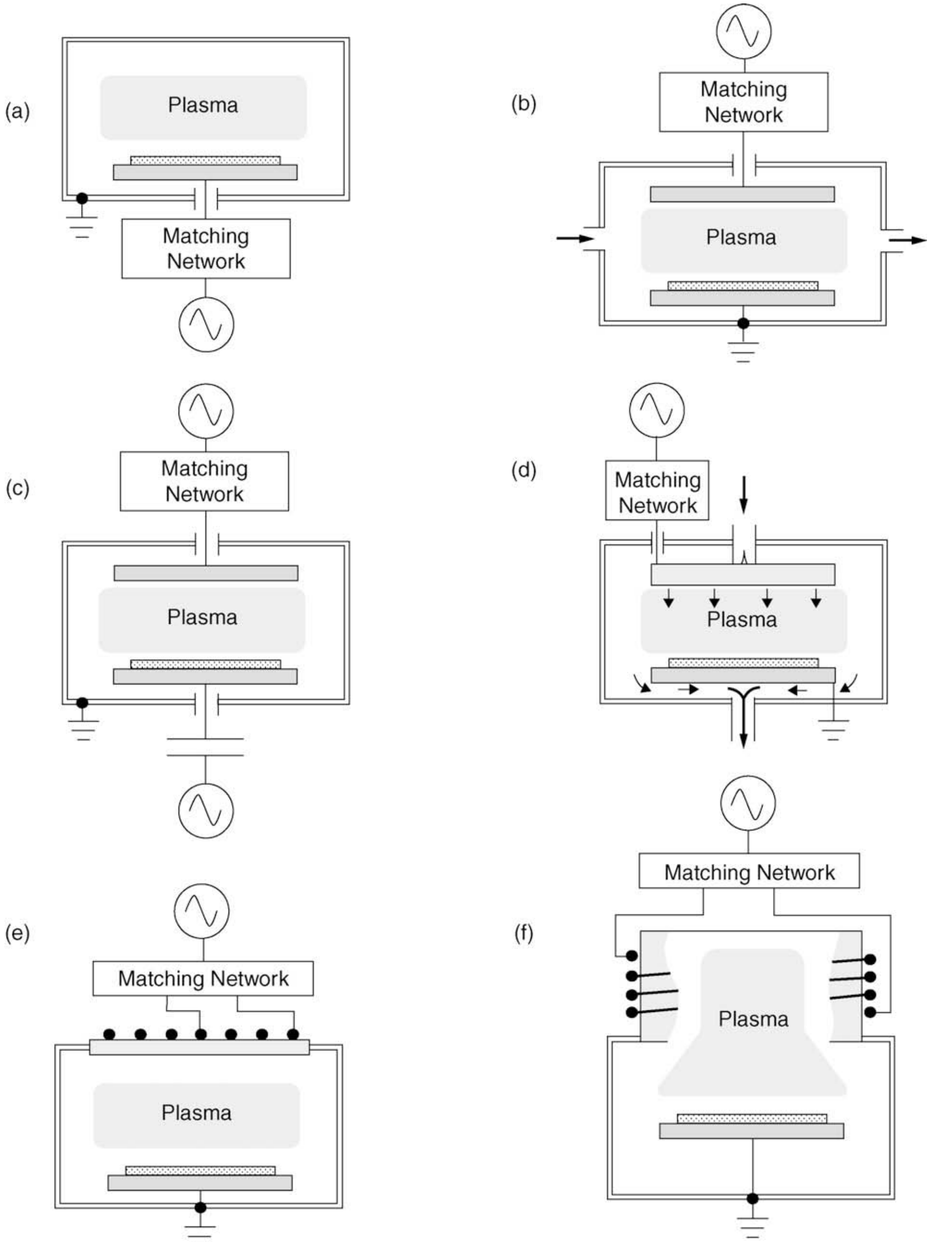

Figure 2.14: Schematic illustrations of RF-driven apparatus configurations used in materials processing. (a-d) Sources with power delivered through electrodes and (e-f) through dielectric barriers. (b) and (d) Show variations in gas flow. (c) Illustrates a multiple frequency source.

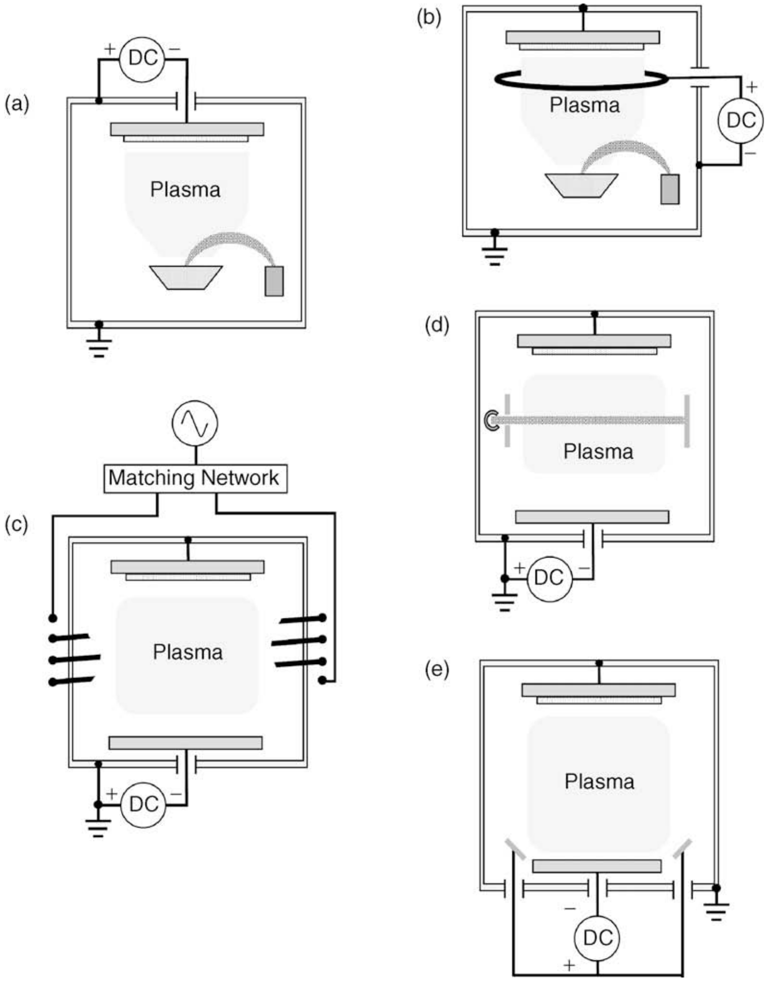

Figure 2.15: Schematic illustrations plasma-assisted PVD apparatus: (a) ion plating device, (b) activated reactive evaporation device, (c) ICP sputtering device, (d) electron beam generated plasma sputtering device, and (e) cathodic arc device.

2.4.2 Plasma Production and Breakdown

The degree of ionization in a glow discharge depends on a balance between the rate at which ionization proceeds via electron impact and the rate at which particles are lost by volume recombination and by passage to the walls of the apparatus. The rate of ionization depends on a relationship of the form (see Eqs. 2.6, 2.8, and 2.15)

$$R_\mathrm{i} \propto N n_\mathrm{e} \sqrt{\sigma_\mathrm{ion}(E)} \tag{2.44}$$

Thus, the rate of ionization depends on the type of gas (through the ionization cross-section σ_ion), the electric field strength (through the electron energy), and the gas pressure (through the

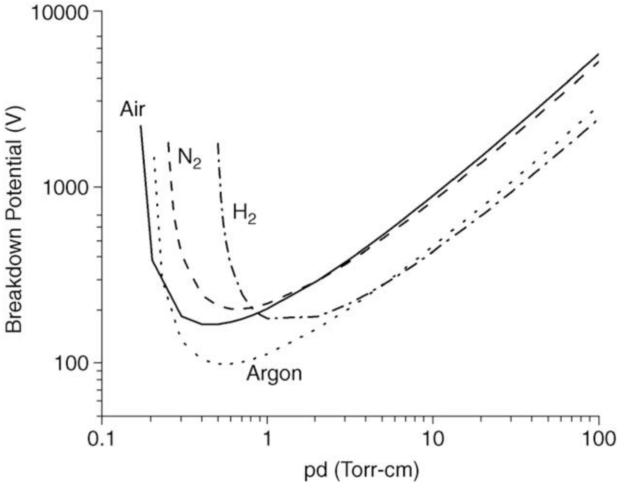

Figure 2.16: Paschen curves for breakdown between parallel, planar electrodes in air, nitrogen, hydrogen, and argon. (Adapted from [48], p. 209.)

particle density *N*). For most low-pressure configurations, wall losses generally dominate over volume recombination. Accordingly, the occurrence of a breakdown (i.e. the initiation of the plasma) and the resulting discharge depend on apparatus geometry, gas type and pressure, the electric field strength, and on the surface-to-volume ratio of the plasma. Figure 2.16 shows the interelectrode breakdown voltage as a function of the product of the gas pressure p and the electrode spacing d for plane parallel electrodes in various gases [48]. Such curves are determined experimentally and are known as Paschen curves. Relationships of the same general form apply to the conditions under which a steady-state discharge can be sustained. In such cases, the electrode separation d may be replaced by a characteristic diffusion length for the plasma reactor [18, 49].

The rise in voltage at the low pd side in Figure 2.16 occurs because the apparatus is small, or the gas density low, such that electrons are lost to the walls faster than they can be created through ionizing collisions. The rise in the required voltage on the right side happens because the electron energy is becoming too low to produce ionization. This can occur at high pressures, because electron collisions with gas atoms become so frequent that the electrons lose energy faster than they can accumulate it, and via field acceleration, in order to exceed the ionization potential. It can also occur at a given applied voltage in a very large chamber where local electric fields in the plasma are too weak to deliver sufficient energy to the electrons between collisions. That is, the electric fields are too weak to sustain the plasma over that volume of gas.

The curves in Figure 2.16 also provide a useful guide for adjusting the operating conditions within a given device in order to produce a plasma discharge. Conversely, the relation provides guidance for the prevention of breakdown on unwanted surfaces. In that case one simply

Table 2.3: Typical operating conditions and plasma parameters for low-pressure argon plasmas. The values of T_e and n_e are for the bulk plasma

Source	Driving frequency	Power (W)	Pressure (mtorr)	T_e (eV)	n_e (cm^{-3})	Ref.
Helicon	13.56 MHz	< 1300	4–35	3–5	10^{12}–10^{13}	[50]
ICP RF	13.56 MHz	1000	4–20	2–3	$2–6 \times 10^{11}$	[51]
CCP RF	13.56 MHz	25–50	7.6	5–2.5	$0.4–1 \times 10^{11}$	[52]
Magnetron	DC	100	3–15	1–3	$2–10 \times 10^{12}$	[53]
ECR	2.45 GHz	200–500	0.5–5	4–5	5×10^{11}	[54]
Electron beam	Pulsed	100	50	1.0	3×10^{11}	[55]

places a grounded shield over the surface to be protected, ensuring that the spacing d between the shield and the cathode is small enough that the required breakdown voltage is larger than the voltage used to form and sustain plasma discharge at the operating pressure of interest.

The above considerations are also important in apparatus scaling. A discharge sustained in a small apparatus must have a high average electron energy to counteract wall losses. Such a discharge, with the same electron density but in a larger apparatus size, will be sustained at a lower average electron energy. This can, in turn, change the active species that are produced. Thus, small-diameter discharge tubes are sometimes used in lasers to elevate the average electron energy to a desired value. Typical discharge electron densities are in the range of 10^8–10^{12} cm^{-3} with average electron energies of 1–30 eV (as shown in Figure 2.1). A sampling of densities and electron temperatures is shown in Table 2.3 for various plasma sources used in materials processing.

2.4.3 Cold Cathode Discharges

A low-pressure cold cathode discharge is one which is maintained primarily by secondary electrons emitted from the cathode due to bombardment by ions from the plasma. This is in contrast to hot cathodes, where electron emission is primarily thermionic. A classic example of a cold cathode glow discharge is illustrated in Figure 2.17. Ion-induced secondary electrons are accelerated in the cathode dark space and enter the negative glow, where they are known as primary electrons. Each primary electron must produce a sufficient number of ions to result in the ejection of another secondary electron from the cathode [36]. The secondary electron emission coefficient is typically about 0.1 for low-energy Ar^+ ions (a common ion in sputtering plasmas) incident on clean metal surfaces [56]. Thus, primary electrons must produce about ten ion–electron pairs. The coefficient is dependent on incident ion energy and surface conditions. For example, it is larger for some oxidized surfaces but still small enough that each primary electron must produce, or lead to the production of, a plurality of ions [36].

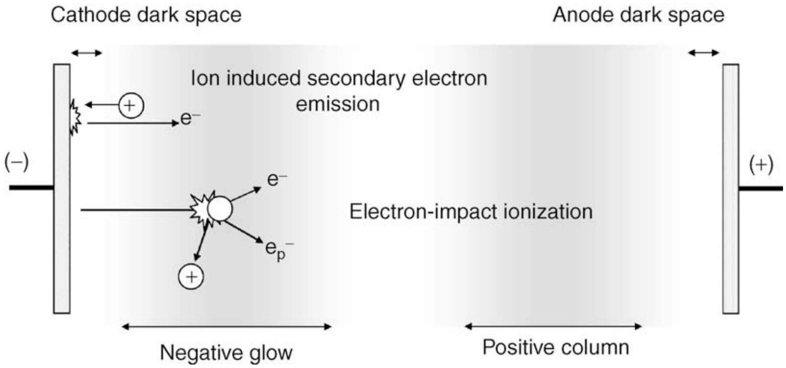

Figure 2.17: Schematic illustration of a simplified cold-cathode discharge. Ion-induced secondary electron emission at the cathode, which leads to ionization in the negative glow, is also shown.

The negative glow region of the plasma is where the primary electrons expend their energy, and its extent corresponds to the range of their travel from the cathode [17, 36], where the range depends on both electron energy and gas pressure. The electron energy distribution in the negative glow is multimodal. It consists of primary electrons, reduced-energy primary electrons (primaries that have lost some of their initial energy via collisions), and much larger numbers of low-energy electrons produced during ionization, which are considered part of the plasma electron population. In the classical glow discharge described in most textbooks, a positive column extends from the anode toward the negative glow [11, 21, 23]. In the positive column the electric field is just sufficient to transport the discharge current from the negative glow to the anode and to produce sufficient ionization to compensate for wall losses.

In planar-diode sources of the type shown in Figures 2.13 and 2.14, the substrate mounting table or anode generally intercepts the negative glow and there is no positive column. From the Paschen relationship discussion (Section 2.4.2), a consequence of this small interelectrode spacing is that the operating pressures are relatively high. For example, reasonable operating conditions for DC planar-diode Ar sputtering discharges are 75 mtorr pressure with a substrate-to-cathode spacing of 4.5 cm, a current density of 1 mA/cm^2, and a discharge voltage of 3 kV.

In order for a cold-cathode discharge to operate effectively at low pressures, it is necessary that the primary electrons be preserved and not lost from the system until they have had a chance to expend enough of their energy in ionization. The hollow cathode geometry shown in Figure 2.18 is effective in this respect because the electrons are trapped by the plasma. Electrons which are accelerated in the cathode dark space and enter the negative glow cannot escape once they have lost an amount of energy about equal to their initial ejection energy (which is only a few eV) [56] since they encounter a sheath with repulsive forces whenever they

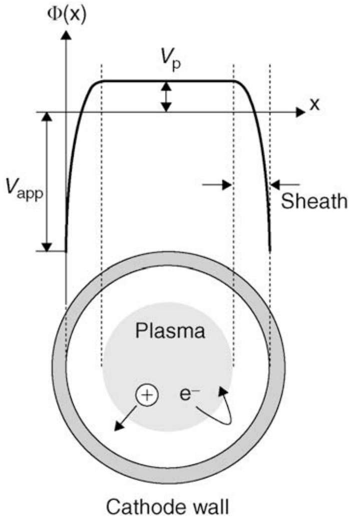

Figure 2.18: Schematic illustration of a hollow cathode discharge (cross-section) along with the potential profile.

approach the cathode wall. The only losses are out of the ends, and long hollow cathodes with minimized end losses can be operated effectively at low pressures and voltages. For this reason, hollow cathodes are often used as ionization [57] or electron [58] sources.

2.4.4 Magnetron Discharges

Magnetron discharge sources are quite prevalent in sputter deposition applications and will be discussed at the end of this chapter and in greater detail in later chapters. Magnetrons are cold cathode discharge devices in which magnetic fields are used in concert with cathode surfaces to form traps which are so configured that the $E \times B$ electron drift currents can close upon themselves [59]. The cylindrical-post configuration shown in Figure 2.19 provides one

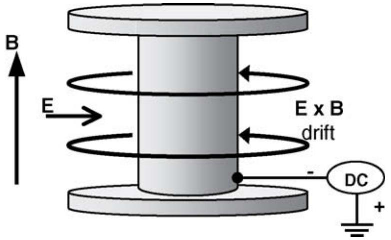

Figure 2.19: Cylindrical-post magnetron sputtering source.

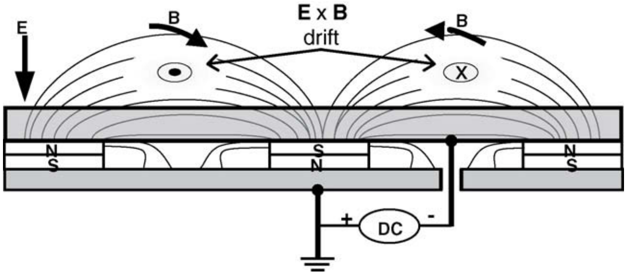

Figure 2.20: Planar magnetron sputtering source. (From [61].)

example of a magnetron. Primary electrons which leave the cathode rod and enter the plasma find themselves trapped in an annular cavity which is closed on three sides by the cathode surfaces (the hollow cathode effect) and on the fourth side by the magnetic field. The electrons can diffuse across the magnetic field and reach the anode only by making collisions (the process illustrated in Figure 2.7b) and by plasma oscillations (see Section 2.3.3) [44]. Like hollow cathodes, confinement leads to high ionization rates and so cylindrical-post magnetrons are extremely efficient and operate at pressures of less than 1 mtorr with high current densities (10–200 mA/cm^2) and low voltages (300–800 V). Planar magnetrons are perhaps the most important devices used in sputter-deposition technology [60]. An example of one is shown in cross-section in Figure 2.20. In this geometry, the magnetic fields confine the plasma above the cathode in annular rings, which produces the well-known erosion profile found in used cathode (target) materials.

Although the use of DC power is common in magnetrons, RF or pulsed power are also used. High-power impulse magnetron sputtering (HIPIMS) [62], a particular novel approach to the use of magnetrons, uses a short ($\sim 10\ \mu$s) high-voltage pulse delivered to the magnetron surface producing a transient plasma. During peak performance, current densities at the magnetron surface are on the order of ~ 1 A/cm^2 and plasma densities are as high as 10^{13} cm^{-3}. High ion fluxes, comprised of both metal and gas ions, at the substrate surface are useful for certain applications.

2.4.5 RF Discharges

RF-driven planar diode discharge devices of the type shown in Figures 2.13 and 2.14 are used for sputter deposition, plasma-assisted etching, and PACVD. Their application to sputtering is discussed in detail in later chapters.

The operating frequency is generally 13.56 MHz, since this is within the frequency range (10–20 MHz) allocated by the Federal Communications Commission (FCC) for industrial applications. At frequencies above about 1 MHz, only the electrons can follow the temporal variations in applied potential (see Section 2.3). Thus, the plasma can be pictured as an electron gas that moves back and forth at the applied frequency in a sea of relatively stationary ions. As the electron cloud approaches one electrode, it uncovers ions at the other electrode to form a positive ion sheath. This sheath takes up nearly the entire voltage as in the DC case. The ions are accelerated by this voltage and bombard the electrodes.

The RF discharge can be further understood by examining the electrode current flow. These discharges are often capacitive in nature, because of external capacitance which is placed in the electrical circuit and because one or both electrode surfaces are generally non-conducting, made of either semiconducting or insulating materials. Such plasma sources are thus called capacitively coupled plasmas (CCPs). Since the total ion and electron charge flow to a given electrode during an RF cycle must balance to zero, a DC self-bias (V_{sb}) that is negative with respect to the plasma potential develops on any surface that is capacitively coupled to an RF discharge [63]. The basis for this behavior is illustrated in Figure 2.21, where the current voltage characteristics are shown for an electrode immersed in a plasma. When an RF voltage signal is delivered to the electrodes, much larger currents are drawn when the electrode is positive relative to the floating potential than when it is negative, because of the mobility difference between the electrons and the ions (upper figure). In order to achieve zero net current flow, it is necessary for the DC self-bias to develop such that the average potential is negative relative to the floating potential, as shown in the lower figure. This offset means the electrodes only minimally exceed the floating potential (and become anodes), for short portions of each RF cycle. Most of the time they are cathodes. Because the ions largely respond to the DC self-bias they flow to both electrodes throughout the cycle in quantities that are equal to the time-averaged electron flow.

RF discharges in planar diodes can be operated at considerably lower pressures than DC discharges. Typical operating pressures are 5–15 mtorr. This is due to two reasons: a reduction in the loss of ionizing electrons and an increase in the volume ionization efficiency. In order to understand this, consider that a fraction of the ionizing electrons will be repelled from the electrode toward which they are accelerated as the cycle changes. Thus wall losses decrease, and electrons remain in the discharge longer to make additional ionizing collisions. In addition, electrons can gain energy from the RF field by making in-phase collisions with gas atoms. That is, if an electron, accelerated in one direction during a given half-cycle, makes an elastic collision in which its direction is reversed, it maintains most of its velocity (due to the large mass mismatch between electrons and ions). If this happens near the end of the cycle, it will again be accelerated during the next half-cycle and thus have gained energy during the complete cycle. As the pressure is increased, collision probability increases and the volume ionization due to electrons accelerated by the oscillating electric field becomes increasingly important. When the planar and cylindrical plasma discharge devices shown in Figure 2.14 are

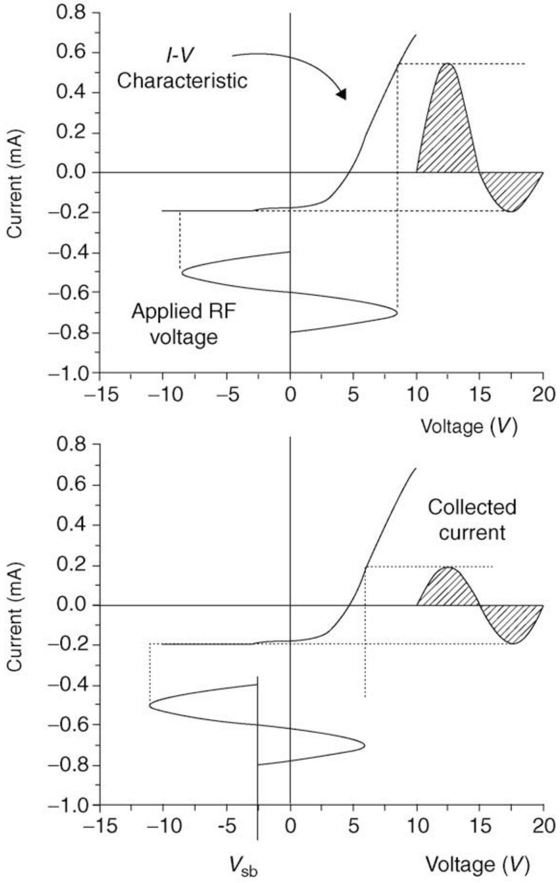

Figure 2.21: Illustration of the formation of a negative bias on a capacitively coupled surface in an RF glow discharge. (Adapted from [63].) The current–voltage (*I*–*V*) characteristic (similar to a Langmuir probe trace) defines the current collected at an electrode of a given voltage. With the RF voltage applied about zero, the time-averaged collected current will favor electrons. For the time-averaged current to equal zero, the surface to which the RF voltage is applied will adjust to a negative value (V_{sb}).

used for plasma-assisted etching, PACVD, and polymerization, the operating pressures are generally high enough that volume-accelerated electrons dominate in producing excitation and ionization. The same is true for high-frequency microwave-driven discharges, such as electron cyclotron resonance (ECR) sources.

The discussion of RF plasma generation has focused mainly on the electric field to excite the gas. That is, the changing applied electric field permeates the gas to directly accelerate (or decelerate) the plasma electrons. However, RF currents driven through coils will produce an alternating magnetic field, external to the coil, that can induce alternating currents in a gas. Plasma sources that rely on this type of energy transfer are called inductively coupled plasmas (ICPs) and are most common when the geometry is like that shown in Figure 2.13(b). This arrangement is similar to a transformer core, where the gas volume replaces the iron core and so the terms 'transformer coupling' and 'inductive coupling' are used interchangeably. An advantage of ICPs relates to the induced electron currents, which follow circular orbits in planes normal to the device axis. This motion limits the loss of electrons at the chamber walls. Thus, compared to CCPs, where the use of electrodes to deliver power further enhances wall losses, ICPs have plasma densities that are typically an order of magnitude (or more) greater than CCPs.

2.5 Gas-Phase Plasma Reactions

2.5.1 Introduction

The interaction of charged and neutral particles within the bulk plasma not only sustains the plasma but also defines the chemistry of the plasma, and the production of chemically active species is vital to the production and modification of materials. The complex nature of plasma generation, gas-phase chemistry, and delivery of species to the substrate are illustrated in Figure 2.22.

Electron bombardment of atoms and molecules can result in dissociation, excitation, and ionization. These inelastic collisional processes (kinetic energy is not conserved) are important

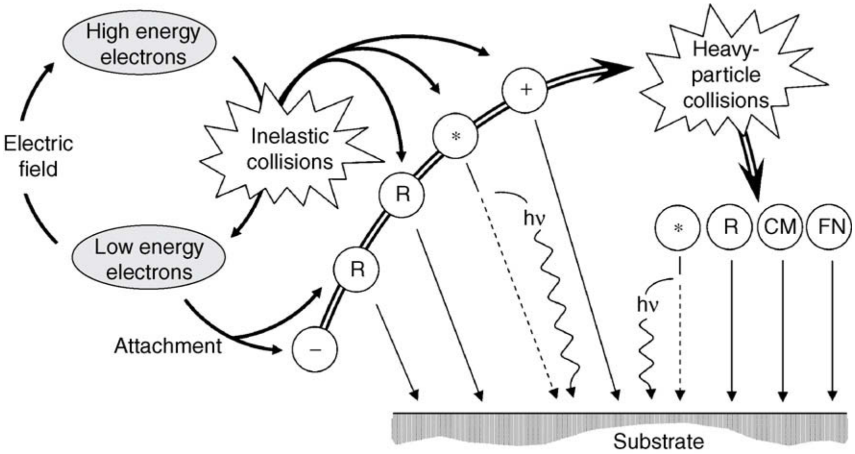

Figure 2.22: Schematic illustration of the generation of active species in a plasma produced in a molecular gas and their delivery to a negatively biased substrate. Included are: negative ions (−), radicals (R), excited species (*), photons (hν), compound molecules (CM), and fast neutrals (FN).

for a number of reasons. Electron ionization processes are obviously important in sustaining the plasma, while excitation and dissociation produce reactive species that are critically important in such processes as reactive sputter deposition, plasma-assisted etching, PACVD, and plasma polymerization. The variety of excited and ionized species, as well as radicals (reactive dissociation products), in a plasma has a much different chemical reactivity than those of the parent gas [64, 65]. For example, although He and Ar atoms are inert, He^+ ions with one valence electron are chemically similar to hydrogen, while Ar^+ ions can react with H_2 molecules to form ArH^+ ions [64]. Similarly, N_2 is largely inert, but N radicals formed from the dissociation of N_2 are reactive and important in the formation of metal-nitride thin films.

2.5.2 Electron–Atom Interactions

As noted, the interaction of energetic electrons with atoms can be either elastic or inelastic. The former is sufficiently understood classically; that is, a collision of two hard spheres in which kinetic energy and momentum is conserved. For inelastic collisions, where kinetic energy is not conserved, the interaction is not sufficiently understood classically. Instead, it is best understood by recognizing that the atom gains an amount of internal energy equal to the loss of electron kinetic energy. This internal energy results in the promotion of an electron to a higher energy level, thereby creating an excited atom. Of course, this transferred energy must be in discrete amounts since the energy levels are quantized. Excited states are limited in their lifetimes and will decay by emitting a photon as the electron falls back to its ground state level. Excited states called metastables, however, can last for very long times and can be significant in low-pressure discharges (see Section 2.5.4). If there is enough energy transferred, the electron can be liberated from the atom producing an ion [66]. For large impacting electron energies, the process could leave the ion in an excited state, the secondary (ejected) electron could have excess kinetic energy, or the impacting electron could retain a large amount of energy. All of these are best described by noting that an electron passing close by an atom does not simply knock an electron to a higher orbit or out of the atom, but produces a perturbation of the atom leading to either excitation or ionization.

In making plasma calculations, the average energy W_{ei} spent by an electron in creating an electron–ion pair in a given gas or gas mixture is often used. Values of W_{ei} for various atoms and molecules are shown in Table 2.4 along with values for the ionization potential I and first excited states. Typically, $W_{ei}/I \approx 2$–3. It should be noted that W_{ei} is determined using high-energy electrons and the values shown in Table 2.4 are valid for energies above several keV. At low impacting energies more energy is consumed in excitation and elastic collisions, thus more energy is required to produce an ion–electron pair. For plasmas with average electron energies in the range of a few eV, the values of W_{ei} will be larger than those given in Table 2.4 [67].

Table 2.4: W_{ei}, approximate energy spent to create electron–ion pairs [66], E_{ion}, the ionization energy, and E_m, the first metastable level

Atom or molecule	W_{ei} (eV)	E_{ion} (eV)	E_m (eV)
He	46	24.58	19.7
Ne	37	21.56	16.6
Ar	26	15.76	11.6
Kr	24	14.00	9.9
Xe	22	12.13	8.3
H_2	36	15.43	
N_2	36	15.59	
NO	29	9.250	
CO	35	14.04	
O_2	32	12.15	
CO_2	34	13.81	
C_2H_2	28	11.40	
CH_4	29	12.99	
C_2H_4	28	10.54	
C_2H_6	27	11.65	
C_3H_6	27	9.73	
C_3H_8	26	11.15	
C_6H_6	27	9.23	

2.5.3 Electron–Molecule Interactions

The interaction of energetic electrons with molecules differs from interactions with atoms because a molecule has many ways, or degrees of freedom, to absorb electron energy. The types of reactions to consider are listed roughly in terms of the energy threshold (although there is overlap) for a generic molecule:

Attachment: $e + AB \rightarrow AB^-$

Dissociative attachment: $e + AB \rightarrow A + B^-$

Excitation: $e + AB \rightarrow AB^* + e$

Dissociation: $e + AB \rightarrow A + B + e$

Ionization: $e + AB \rightarrow AB^+ + e + e$

Dissociative ionization: $e + AB \rightarrow A^+ + B + e + e$

Low-energy electrons can attach to electronegative molecules to form negative ions [68] and since there is an abundance of low-energy electrons in plasmas, negative ions are common in plasmas when the ambient contains electronegative gases such as CF_4, SF_6, and oxygen [69]. For oxygen, the reactions leading to negative ion formation are [70]:

$$e^- + O_2 \rightarrow O^- + O$$

$$e^- + O_2 + O_2 \rightarrow {O_2}^- + O_2$$

$$e^- + O_2 \rightarrow O^- + O^+ + e^-.$$

The production of O^- from the first reaction has a maximum cross-section of $1 \times 10^{-18}\,\mathrm{cm}^2$ at about 6.5 eV, while the three body reaction leading to the production of ${O_2}^-$ has an appreciable rate only when pressures approach 1 torr. Negative ion-positive ion pair production requires electron energies above about twice the ionization energy of O_2 and has a cross-section of about $0.3 \times 10^{-18}\,\mathrm{cm}^2$.

The processes of attachment and dissociative attachment convert a fraction, sometimes a significant fraction, of electrons to negative ions. This conversion can have a strong influence on the plasma characteristics given the large mass difference between the negative ions and electrons and can lead to lower conductivity compared to plasmas with little or no negative ion density. In rare cases, negative ions can be the primary negative charge carrier and significantly change the plasma characteristics [71, 72]. In most processing discharges, however, the attachment rate is too low to eliminate the dominance of electrons.

Electron interactions with molecules produce excitation and ionization via mechanisms essentially identical to those described above for atoms. The primary difference is in the fate of the excitation energy. In atoms, the excitation energy is lost by radiation unless the transitions are quantum-mechanically forbidden (see Section 2.5.4). In molecules, it may result in dissociation of the molecules. Consider the case of CF_4, a gas which is commonly used in plasma etching. The threshold for producing excitation is 12.5 eV [73]. The excitation reaction can be written as

$$e^- + CF_4 \rightarrow {CF_4}^* + e^-$$

where the symbol * refers to an excited species. There is evidence that all electronic excitation processes in CF_4 produce dissociation [73], wherein the excited states last for a short amount of time and the decay proceeds via dissociation of the molecule. In this two-step excitation–dissociation process, one bond is broken, and the reaction proceeds as

$${CF_4}^* \rightarrow CF_3 + F$$

The primary radicals produced favor F, rather than CF_2 and F_2 [74]. The active F atoms produced in this way play a very important role in many plasma etching processes.

Electron impact ionization can result in simple ionization. Such is the case for oxygen, where

$$e^- + O_2 \rightarrow O_2^+ + 2e^- \ (\Delta H = 12.15\,\text{eV})$$

Or the electron impact can result in dissociative ionization reactions of the form

$$e^- + O_2 \rightarrow O + O^+ + 2e^- \ (\Delta H \approx 18\,\text{eV})$$

The products of such reactions can be long lived in low-pressure plasmas. Gas-phase recombination of atomic constituents of small molecules such as F_2, H_2, or O_2 requires three body collisions to conserve both energy and momentum. At low pressures, the likelihood of such reactions is very small compared to high-pressure gases and so the lifetime for such atoms can be long. For the case of molecular radicals, however, the energy of dissociation can be distributed within a large number of internal degrees of freedom and so, recombination does not require a third body. Thus, the association efficiency is close to unity for simple molecular radicals [45]. One can have, for example,

$$CH_3 + CH_3 \rightarrow C_2H_6$$

The decay of initial reaction products in cascading reactions, with the development of high molecular weight species, is a well-known characteristic of the radiation chemistry of hydrocarbons and halocarbons in both the gas and solid phases [65].

2.5.4 Metastable Species and Processes

Metastable states are those excited states that are forbidden by quantum mechanical considerations from undergoing radiative transitions. Atoms or molecules can be excited directly into metastable states by electron impact or can arrive in these states by radiative decay after having been excited into states of higher energy. Atoms or molecules that are excited into electronic states which can decay radiatively have very short lifetimes ($\sim 10^{-9}$ s). However, metastable states can have sufficiently long lifetimes ($\sim 10^{-3}$ s) and, as such, they can carry their stored electronic energy far from their point of origin.

Metastable states are depopulated when the atoms undergo collisions with surfaces or other particles and may subsequently pass excitation energy to the substrate, target atom or molecule. Energy can be transferred during gas-phase collisions in Penning processes, causing the excitation or ionization of target atoms or molecules of lower ionization potential. Penning reactions are of the form [75]:

$$A^* + Y \rightarrow A + Y^*$$

$$A^* + XY \rightarrow A + XY^*$$

$$A^* + Y \rightarrow Y^+ + A + e^-$$

$$A^* + XY \rightarrow XY^+ + A + e^-$$

$$A^* + XY \rightarrow X^+ + Y + A + e^-$$

Large populations of metastable species can have important effects on the overall discharge characteristics. Gases with large metastable energies such as He, Ne, and Ar are often added to discharges to promote excitation and ionization rates. Also note that when large metastable populations exist in noble gas plasmas, excitation and ionization rates can also increase since excitation and ionization from metastable levels require less electron energy. However, the increase in ionization rates and thus ion current at substrates may not increase the sputtering rates. When lower mass species with large metastable energies (e.g. He) are used, the increased ion currents at substrates may be offset by the fact that lower mass ions will not remove material as effectively as heavy mass ions (e.g. Ar).

2.5.5 Applications of Volume Reactions

Plasma chemistry, the sum of all volume reactions, plays a significant role in applications like PAPVD, PACVD [76], plasma-assisted etching [77], and plasma polymerization [78]. In some cases, the plasma chemistry is unique in that the reactive species are only produced in plasmas. In most cases however, the advantage of using a plasma is that it can effectively deliver reactive species which promote surface reactions that would otherwise require high substrate temperatures. Examples include the plasma-assisted deposition of silicon nitride (Si_3N_4) using discharges produced in a gas mixture of silane (SiH_4) and ammonia (NH_3) or tetraethoxysilane [$(C_2H_5O)_4Si$] in an oxygen background to grow silicon dioxide (SiO_2) films. The plasma chemistry is complicated in both applications, but the important point is that the substrate temperature is typically 300 °C or lower. When the same reactions are carried out by conventional thermal CVD techniques, the substrate temperatures are typically between 800 and 1200 °C [79]. Lower substrate temperatures in PACVD are important in electronic applications where coatings are deposited onto device structures with low thermal budgets and particularly where substrates are sensitive to high surface temperatures, such as polymers.

A typical electron energy distribution (Figure 2.5) indicates that most electrons are below the ionization energy. Thus, most electron-impact reactions are non-ionizing and, as such, the number of radicals and excited species is quite high in most plasmas. The average electron energies in PACVD processes, for example, are typically between 1 and 10 eV, and the plasma chemistry is dominated by excited species and radicals rather than ions [80]. If the creation of radicals via dissociation of the precursor (donor) gases is critical to a given process, bond energies are an important consideration in the selection of precursors. Consider the example of nitride films, where one of the functions of the plasma during deposition is to provide atomic N in the gas phase since the partial pressure of atomic N required to obtain stoichiometric nitride films is much smaller than that of N_2. The dissociation of nitrogen via electron impact is given as

$$e^- + N_2 \rightarrow N + N + e^- \ (\Delta H = 9.83\,\text{eV})$$

Here, an electron energy of at least 9.83 eV is required to obtain N atoms by cleaving the N_2 molecule. Alternatively, N atoms can be obtained at lower impact energies through the following step cascade starting with NH_3:

$$e^- + NH_3 \rightarrow NH_2 + H + e^- \ (\Delta H = 4.76\,\text{eV})$$

$$e^- + NH_2 \rightarrow NH + H + e^- \ (\Delta H = 3.90\,\text{eV})$$

$$e^- + NH \rightarrow N + H + e^- \ (\Delta H = 3.42\,\text{eV})$$

in which no reaction step requires more than 4.76 eV. For this reason, NH_3 can be used in Si_3N_4 PACVD. Similarly, nitrous oxide (N_2O), rather than oxygen (O_2), can be used as a precursor molecule for atoms during PACVD deposition of oxides:

$$e^- + N_2O \rightarrow N_2 + O + e^- \ (\Delta H = 1.73\,\text{eV})$$

$$e^- + O_2 \rightarrow 2O + e^- \ (\Delta H = 4.13\,\text{eV})$$

Plasma-assisted etching is similar to PACVD, except that a volatile rather than a non-volatile compound is delivered to the substrate. Silicon etching is accomplished by using a discharge to generate reactive F atoms from an inert molecular gas such as CF_4. The F atoms cause etching of the Si by forming volatile compounds such as SiF_4 on the Si surface.

Plasma polymerization typically proceeds in a series of steps [81, 82]. For example, high molecular weight species can be formed in a discharge from low molecular weight starting material. These high molecular weight species then condense on substrates, where they are cross-linked by plasma radiation and particle bombardment to form a polymer film. Consider plasma polymerization in acetylene (C_2H_2) [83]. The process is initiated by the dissociation of acetylene

$$e^- + C_2H_2 \rightarrow C_2H + H + e^-$$

High molecular weight species can then be formed by the reaction of radicals and/or acetylene, such as

$$C_2H_2 + C_2H \rightarrow C_4H_3$$

$$C_2H_2 + C_4H_3 \rightarrow C_4H_4 + \text{products}$$

$$C_2H_2 + C_4H_3 \rightarrow C_6H_5$$

$$C_4H_4 + C_2H \rightarrow C_6H_5 + \text{products}$$

The gas-phase chemistry can be complex in polymerization processes, involving reactions of electrons and radicals as well as negative and positive ions. Reaction and deposition rates are also dependent on a number of process parameters, including pressure, gas flow, temperature, and delivered RF or DC power.

2.6 Plasma–Surface Interactions

2.6.1 Introduction

Surfaces in contact with plasmas are bombarded by slow and fast neutrals, electrons, ions, radicals, metastables, complex molecules, and photons, as illustrated in Figure 2.22. The relative importance of each species is largely dependent on the application of interest. Ion bombardment, for example, is of primary interest in sputtering. Electron, ion, and radical impacts are important in reactive ion etching and PAPVD. The interaction of all species is of importance in PACVD, polymer modification, and plasma polymerization. The relative number of ions and electrons which are incident on a surface depends on whether it is biased as a cathode or an anode, or is electrically isolated while the neutral and photon flux is independent of the surface potential. In this section, we briefly discuss some of these interactions and their effects.

2.6.2 Ion Bombardment

Ion bombardment of a surface can liberate neutral and charged species from a surface, as well as change the physical, electrical, and chemical properties of a surface. The momentum exchange associated with ion bombardment can cause surface rearrangement, which can have dramatic effects on the structure and properties of a growing film [46] and is of importance in the processes of ion plating and bias sputtering. Ion-impact can also lead to the ejection (sputtering) of surface atoms. Sputtering of this type is referred to as physical sputtering and will have a strong energy dependence [84]. In addition, ion bombardment can cause a chemical reaction that leads to desorption of volatile surface species in a process called chemical sputtering. Sputtering and desorption are important in the processes of reactive ion etching, sputter cleaning, and deposition. Accordingly, these mechanisms are discussed in later chapters.

Electrons, positive ions and negative ions can all be ejected as a result of ion impact. Ion-induced charged particle emission often involves more complicated mechanisms than simply momentum (and kinetic energy) exchange, but can lead to similar changes in the surface properties. In the simplest case, electrons can be ejected from a surface as a result of direct ion impact. In this case, ion energies must be high (> 1 keV) given the large mass difference between the ions and electrons [85]. At lower impact energies, however, potential electron emission [86] is an important mechanism and involves electron tunneling out of the metal when the ion is in close proximity to the surface. In a similar process, neutrals leaving the surface, as a result of physical sputtering, can become positive ions when the electron tunnels from the ejected neutral back to the metal [87]. Ion-induced emission of negative ions from a gas-covered surface has been described as an impact-driven surface excitation that can alternatively result in electron emission [88].

With the exception of ion implantation, the incident ion energies in plasma processing systems will not exceed a few keV and so it should be assumed that most types of emission mechanism discussed are worth considering, although the relative importance will vary. For the emission of either neutral or charged particles, there is an impact energy dependence to consider. Kinetic processes (i.e. momentum/energy transfer) require energies above some threshold which, generally, will be higher than the energy for the other emission processes mentioned above. The threshold of interest for ion-induced electron emission, for example, is about 1 keV. Above this, emission can be kinetic; below, emission is driven by potential energy differences.

The magnitude of the incident ion energy will depend on its transit through the sheath that forms adjacent to the surface. There are two general scenarios to consider: one in which ions transit the sheath without collisions and one in which ions collide with gas particles. For collisionless ion transport, the energy of ions bombarding a cathode surface will be about equal to the difference between the cathode potential and the plasma potential, approximately equal to the applied cathode-to-anode potential. This is typical for magnetron sputtering at low pressures (a few mtorr). The current density, bias voltage, sheath thickness, and plasma properties are related by Eqs. (2.38) and (2.39).

At higher pressures, where ion collisions become important, the bombarding flux consists of both ions and energetic neutrals because of charge exchange collisions (see Figure 2.11). In this case, the average bombardment energies can be considerably less than the potential drop across the sheath. This is illustrated in Figure 2.23 by incident ion energy distributions at a cathode for various pressure regimes (i.e. ratios of sheath length to mean free path). As the mean free path of ions is reduced with respect to the sheath length, an increasing amount of

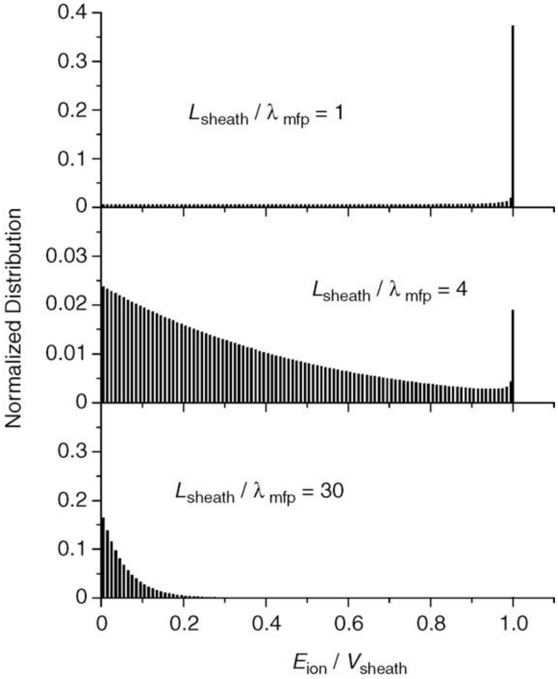

Figure 2.23: Calculated ion-energy distribution histograms showing the effect of charge exchange. (Adapted from [89, 90].) The variable between histograms is the ratio of sheath length L_{sheath} to change exchange mean free path λ_{ex}. Note scale changes on the vertical axis.

ions will undergo collision, and reach the cathode with less energy than is available from the sheath potential. Another example is shown in Figure 2.24 where different ion species in the same plasma can behave very differently [91]. Here, the cross-sections of interest for N_2^+ and N^+ differ by nearly an order of magnitude. That is, N_2^+ ions experience a more collisional sheath than N^+ ions. The sheath parameters for the high-pressure case are related to the ion current in Eq. (2.39).

Ion bombardment can greatly influence the processes involved in the adsorption of molecules onto surfaces and their subsequent reactions. The process of molecular adsorption [92], surface compound formation, and desorption is illustrated in Figure 2.25. The difference between etching and film growth is dependent on the nature of the compounds formed at the surface. When the products are volatile, etching occurs. Any of the steps shown in the figure can be rate limiting. Physical adsorption is due to polarization (van der Waals') bonding. It is a non-activated process and occurs with all gas–surface combinations under appropriate conditions of temperature and pressure. Adsorption energies are typically less than 0.5 eV. Chemisorption involves a rearrangement of the valence electrons of the adsorbed and surface atoms to form a chemical bond. The process has an activation energy and has a high degree of

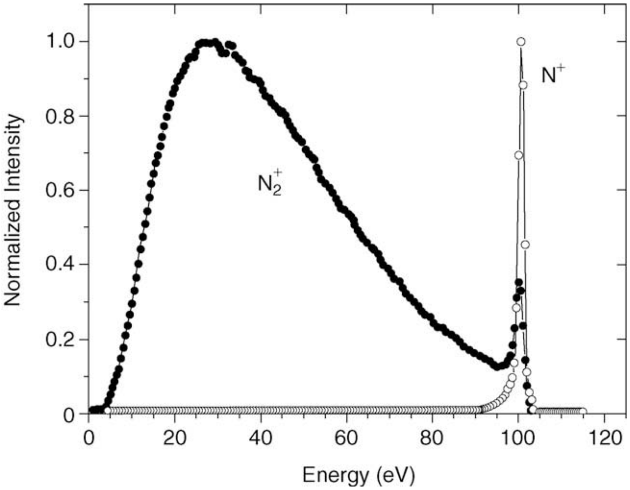

Figure 2.24: N_2^+ **and** N^+ **ion energy distributions at an electrode adjacent to a 100 V sheath. (From [91]. The plasma was produced in 160 mtorr of** N_2 **and Ar (12%).**

specificity between gas–surface combinations. Typical chemisorption energies are between 1 and 10 eV. Molecules may be chemisorbed in their molecular state or may dissociate into atoms. The latter case is known as dissociative chemisorption and is generally a precursor to compound formation, which is also an activated process. Various types of chemisorption bond sites can exist on a solid surface and so both molecular and dissociative chemisorption can occur simultaneously on the same surface. Ion bombardment can influence these processes in a number of ways. First, it can cause adsorbed molecules to dissociate, thereby overcoming the activation energy for this process. Ion bombardment can also create surface defect sites which have a reduced activation energy for chemisorption or for the formation of a solid compound.

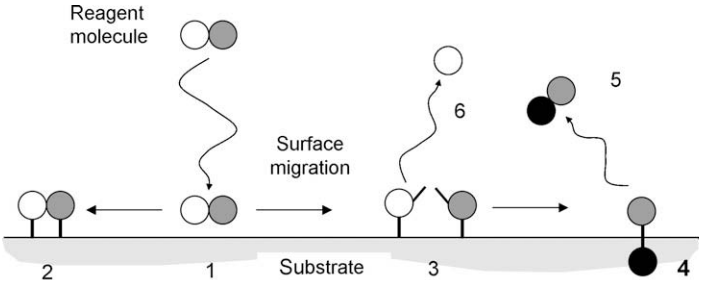

Figure 2.25: Schematic representation of surface adsorption, migration and compound formation during processing. Processes indicated are (1) physisorption, (2) chemisorption, (3) dissociative chemisorption, (4) volatile compound formation and (5) desorption, and (6) desorption of non-reactive species.

Lastly, ion bombardment can remove (by sputtering) foreign species which may inhibit chemisorption of preferred species.

Molecular ions can break apart upon impacting a surface and their fragments can participate in surface processes. For example, collisionally induced dissociative chemisorption of ions during reactive magnetron sputter deposition has been shown to play a major role in controlling the dynamics of film growth. During homoepitaxial growth of TiN(001) in mixtures of argon and nitrogen, for example, increasing the N_2 fraction from 10% to 100% increases the steady-state N coverage θ_N, which, in turn, increases the rate-limiting surface diffusion activation barrier E_s from 1.1 to 1.4 eV over the temperature range 500–865 °C [93, 94]. Corresponding *ab initio* density functional theory calculations [93–96] show that TiN_x ($x = 0, 1, 2, 3$) admolecules are the primary diffusing species. For pure nitrogen, TiN_2 and/or TiN_3 are the rate-limiting diffusing species, while reducing the nitrogen concentration to 10% increases the coverage of Ti and TiN adspecies at the expense of TiN_2 and TiN_3, leading to higher surface diffusivities (lower E_s) and the observed transition in nucleation kinetics. The reduction in N_2 not only reduces the neutral flux but also decreases the N_2^+ ion flux to the surface, thereby reducing the amount of N available for heavy nitride compound formation.

A similar mechanism can be used to control the evolution of preferred orientation in polycrystalline TiN [95, 97] and TaN [98] films deposited at low temperatures on amorphous substrates. Layers deposited in pure N_2, but under conditions of very little N_2^+ ion irradiation, exhibit approximately equal probabilities of (001) and (111) island nucleation. However, the layers grow with a columnar grain structure which evolves toward (111) preferred ordination in a kinetically limited process with increasing film thickness. The (111) columns gradually overgrow (001) columns owing to the higher chemical potential on high-diffusivity (001) surfaces (i.e. diffusing adspecies have a higher probability of becoming trapped on low-diffusivity (111) grains). However, dramatically increasing the N_2^+ ion flux to the growing films changes the preferred orientation in favor of (001) columns. Since there is no substantial change in θ_N, and (111) grains are always fully N terminated in a strongly reactive environment, collision-induced dissociation of N_2^+ ions preferentially increases the steady state N coverage on (001) grains, thereby decreasing the chemical potential, and thus the diffusivity on (001) surfaces.

Low-energy ion irradiation during film deposition can have dramatic effects on the microstructure and microchemistry, and hence physical properties, of as-deposited layers, as discussed in detail in [46]. Specifically, low-energy ion fluxes have been used to modify film microstructure in the following ways: densification and increased oxidation resistance of optical films; minimization or elimination of columnar microstructure in microelectronic metallization layers; altering the state of stress, average grain size, and preferred orientation; increased film/substrate adhesion; enhanced conformal coverage; controlled magnetic anisotropy in recording layers; and ‘low-temperature’ epitaxy.

Low-energy ion irradiation is often used during thin-film growth to controllably alter the composition of as-deposited layers. Examples include preferential sputtering from the growing film during deposition of alloys [99–102], enhanced reactive gas incorporation during deposition of compounds [103–106], and increased dopant incorporation probabilities combined with better control of dopant depth distributions [107, 108]. Here again, ion bombardment can result in potentially deleterious effects, depending on experimental design, such as rare-gas incorporation in sputter-deposited films [109–112]. Mechanisms associated with accelerated-particle–film interactions leading to changes in incorporation probabilities range from purely physical effects such as implantation and recoil processes to irradiation-assisted chemistry.

Most films in the above-mentioned application areas are deposited in the presence of a plasma, by either bias sputter deposition, PAPVD, or PACVD. Since the plasma–surface interface is complex, experiments to isolate ion irradiation effects are often carried out using ion beams. One example is illustrated in Figure 2.26, showing experimental and calculated (Monte Carlo simulations) densities of vapor-deposited CeO_2 films grown at ambient temperature while under O^+ ion beam irradiation. The experiments were carried out as a function of ion energy E, for an ion-to-vapor flux ratio of J_i/J_v of unity [113]. The film density initially increased with increasing ion energy; due primarily to ion implantation, recoil implantation (driving surface atoms into the bulk) and, to a lesser extent, sputtering of weakly bound species. However, at

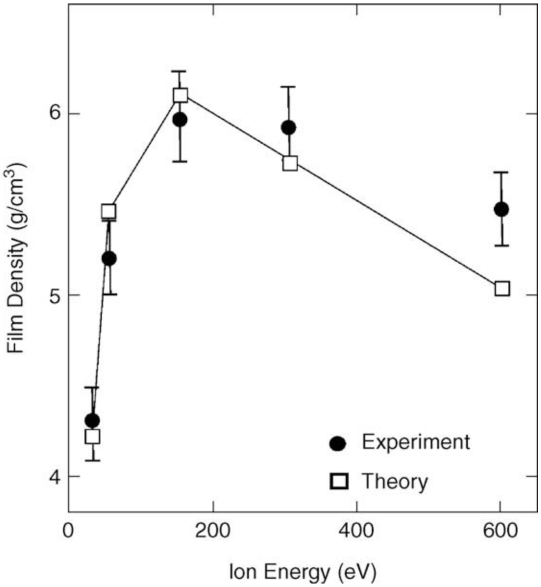

Figure 2.26: Experimental and theoretical values of the density of CeO_2 films deposited by simultaneous evaporation of Ce in O_2 and O^+ ion beam irradiation as a function of ion energy E. The bulk density of CeO_2 is 8.1 g/cm^3. (From [113].)

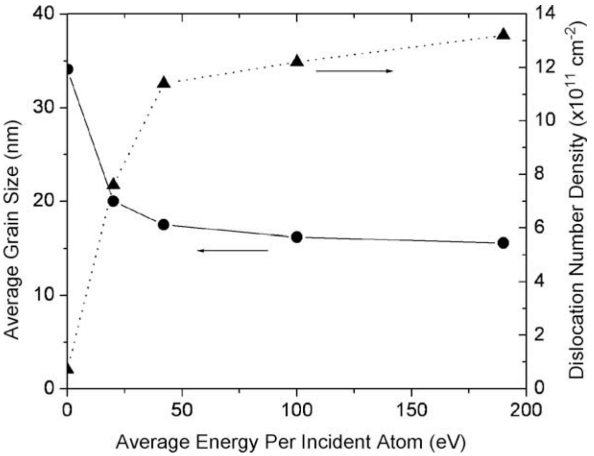

Figure 2.27: The average grain size and dislocation number density in Ag films deposited at room temperature as a function of the average energy per deposited atom. (From [114].)

high ion energies, an increasing fraction of the ion energy was lost deeper in the lattice leaving vacancies which could not be filled by the above processes The optimum ion energy for densification, which depends on the masses of the collision partners, was approximately 200 eV in this case.

In other ion beam experiments, it was found that while ion irradiation is useful for increasing the density and modifying the microstructure of films deposited at low temperatures, other irradiation-induced effects that are not beneficial, such as increased defect densities occurred simultaneously. This is shown in Figure 2.27 from the work of Huang et al. [114], who studied the effects of Ar^+ ion bombardment during the growth of Ag films at room temperature using a dual ion beam apparatus. They found that the grain size decreased while the dislocation number density increased with increasing average irradiation energy per deposited Ag atom. At elevated growth temperatures, however, low-energy ion irradiation can have the opposite effect and actually reduce residual defect densities in as-deposited films [115, 116]. Work on damage production and sputter cleaning of substrate surfaces prior to epitaxial growth [117–120] suggests that low-energy ion irradiation-induced damage can be continuously annealed out at elevated temperatures. Yu [120] used low-energy electron diffraction (LEED) to show that the temperature required to maintain a Si(111)7 × 7 surface reconstruction during Ne^+ ion irradiation decreased from ≈ 450 to 150 °C as the ion energy was decreased from 500 to 80 eV.

Low-pressure discharges and plasmas have been used to modify surface chemistry and promote adhesion with vacuum-deposited metal overlayers on polymers. X-ray photoelectron spectroscopy (XPS) studies of the effects of O_2 plasma treatments on acrylonitrile butadiene styrene (ABS), polypropylene [121], and polystyrene [122] surfaces showed the formation of

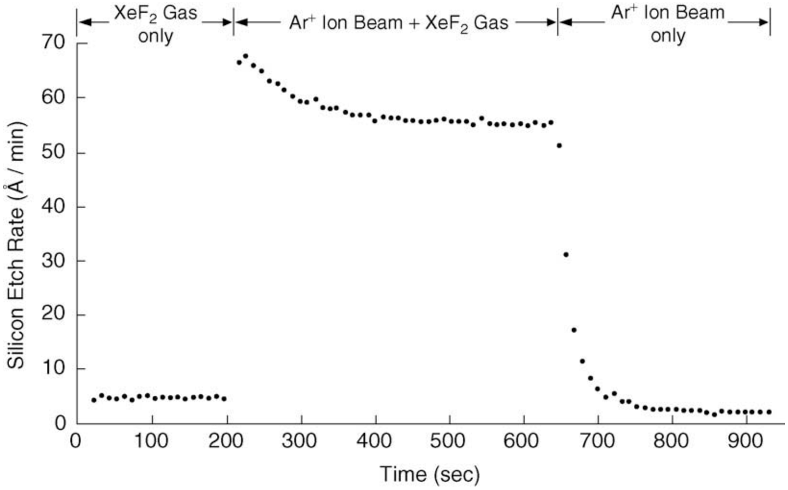

Figure 2.28: The results of ion beam experiments designed to investigate ion-stimulated etching of and Si in XeF_2. (From [126].)

both single and double C–O bonds. The incorporation of oxygen leads to stronger metal overlayer adhesion [123] through the formation of oxygen bridge bonds between C and metal atoms. Ion beam experiments [124] obtained similar increases in metal overlayer adhesion for Ti on polyethylene using an Ar^+ ion bombardment pretreatment to remove low molecular weight impurities, promote cross-linking, and allow the formation of a carbidic Ti–C interfacial layer as observed in XPS. Both Ar^+ ion irradiation and O_2 plasma pretreatments also increased the adhesion of Ti on polydimethylsiloxane (a silicone rubber) owing to the formation of Ti–C and Ti–O bonds [125].

Reactive ion etching technology also relies heavily on ion-irradiation induced effects for both stimulating chemical reaction channels and increasing the anisotropy of the etch profile. An example of the former is shown in Figure 2.28, illustrating results for Ar^+ ion-assisted F/Si chemistry. XeF_2 undergoes dissociative chemisorption on Si, forming the compound SiF_4 [74, 127], which is volatile at room temperature. The etch rate is limited by the XeF_2 flow. However, the Si etch rate increased by an order of magnitude when the Si surface was simultaneously bombarded by 450 eV Ar^+ ions. In this case, Ar^+ ion irradiation greatly increases the etch rate by promoting dissociative chemisorption. In the absence of XeF_2, the etch rate collapses to near zero.

2.6.3 Electron Bombardment

As previously noted, the time-averaged flux of positively and negatively charged species to surfaces exposed to a plasma is comparable. However, since the plasma potential is usually more positive than any surface it is in contact with, electrons are typically decelerated as they leave the plasma. Thus, electrons will impact adjacent surfaces at relatively low energies compared to the ions. Nonetheless, electron irradiation can cause surface heating and promote chemical changes.

Electron irradiation is a primary source of substrate heating during film deposition by DC and RF diode sputtering [128, 129]. Energetic electron, as well as photon, irradiation of ionically bonded substrates has also been shown to strongly affect film nucleation kinetics through the creation of charged surface vacancies which act as preferential adsorption sites [130–133]. Reduced epitaxial temperatures, for a given set of deposition conditions, have been reported for many film–substrate combinations, including Si and Ge on NaCl [134] and PbTe on CaF_2 [132].

Unlike the more massive ions, momentum exchange phenomena are not important until electron energies are very large. That is, physical sputtering of surface species is not possible at low electron energies, given the large mass difference between electrons and atoms and molecules. However, electron-stimulated desorption (ESD) [135] by low-energy electrons can cause the ejection of neutral or charged particles from the surface. In this process, low-energy electrons cause an excitation in surface species, allowing them to overcome the potential barrier (adsorption energy) such that the atom or molecule is ejected from the surface as a neutral, positive ion [136, 137], or negative ion [138]. Electron-induced surface excitations can give rise to changes in surface chemistry during film growth through, for example, excitation and ionization of adsorbed or surface molecules into states leading to dissociation, bond rearrangement, or desorption. In the treatment of polymers [139], electron radiation can create surface radicals, which leads to polymerization. It is important to recognize that this process is limited to the surface and will not influence the bulk properties directly, since electron penetration is limited owing to the low incident energies.

An example of electron-stimulated surface chemistry during plasma etching is shown in Figure 2.29. XeF_2 dissociatively chemisorbs on SiO_2, but etching does not occur because of a high activation barrier for the reaction channel leading to the formation of SiF_4. Electron bombardment alone has been observed to remove O from the surface of SiO_2 and produce elemental Si [140, 141], but it does not cause etching. However, when SiO_2 is subjected to electron bombardment in the presence of XeF_2, etching occurs at relatively high rates, $\approx$200 Å/min in the example given in Figure 2.29 [126].

2.6.4 Photon Interactions

Plasma emission will typically include the soft X-ray, ultraviolet, visible and near-infrared regions, which extend from about 50 nm up to 1000 nm, corresponding to energies ranging from about 25 eV to 1 eV. This range of energies is adequate to initiate excitation that leads to

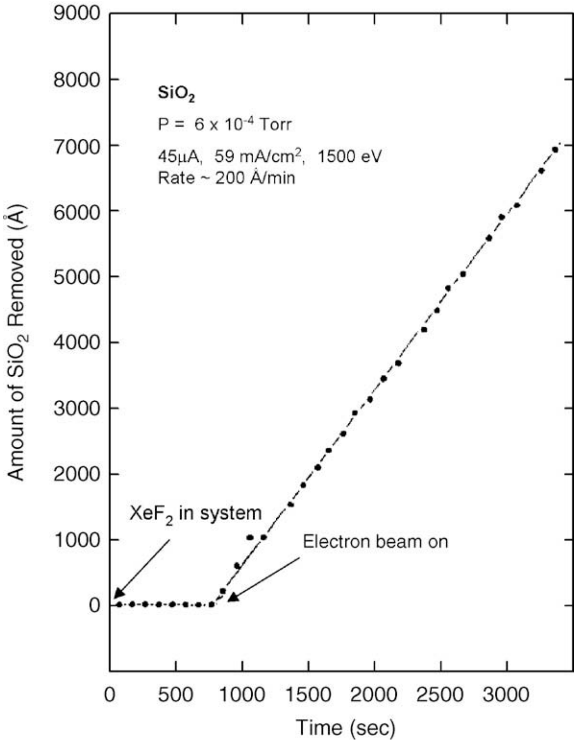

Figure 2.29: The results of beam experiments designed to investigate electron-stimulated etching of SiO_2 in XeF_2. (From [126].)

dissociation, bond rearrangement, or desorption as described above for electrons. In fact, the mechanisms for ESD are similar for photon-stimulated desorption [142, 143], and both fall into the more broadly described grouping, desorption induced by electronic transitions (DIET) [144]. The emission of neutral [145], positive ions [142], and negative ions [146] from gas-covered surfaces has been observed. Photon-induced radical formation in plasma-treated polymers has also been identified as a mechanism that can lead to polymerization [139]. It is important to recognize that unlike particle impact at low energies, photons can penetrate or even pass through certain materials. In the case of polymers, photons can promote chemical changes below the surface [147].

2.6.5 Summary of Surface Reactions

The plasma–surface interaction is a complex one. There are many different reactions to consider and each of these will depend on the operating parameters of a given plasma processing application. Particle and photon flux will vary strongly with background gas, operating pressure, and applied power. The secondary emission yield or chemical changes at the surface will, in turn, depend on the material, conditions of the surface, and surface bias.

Most of the mechanisms described above are studied in well-controlled experiments. Thus, the extrapolation of these reactions to plasma processing environments is, at best, an estimate. Moreover, the combined ion, electron, and photon flux can provide a certain synergy that may or may not be well understood. For these reasons, many plasma–surface reactions remain less than well understood even though the overall results are well known for a given plasma source and operating condition.

2.7 An Example: Magnetron Discharge for Deposition

The volumetric or gas-phase features of plasmas combined with plasma–surface interactions discussed in this chapter are important in understanding the operation of planar magnetrons for deposition applications. Many of these are exemplified by Figures 2.30 and 2.31, which show results from reactive magnetron sputter deposition of TiN_x $(0<x<1)$ as a function of Ar/N_2 gas composition (ranging from pure Ar to pure N_2) [148]. The total pressure prior to initiating

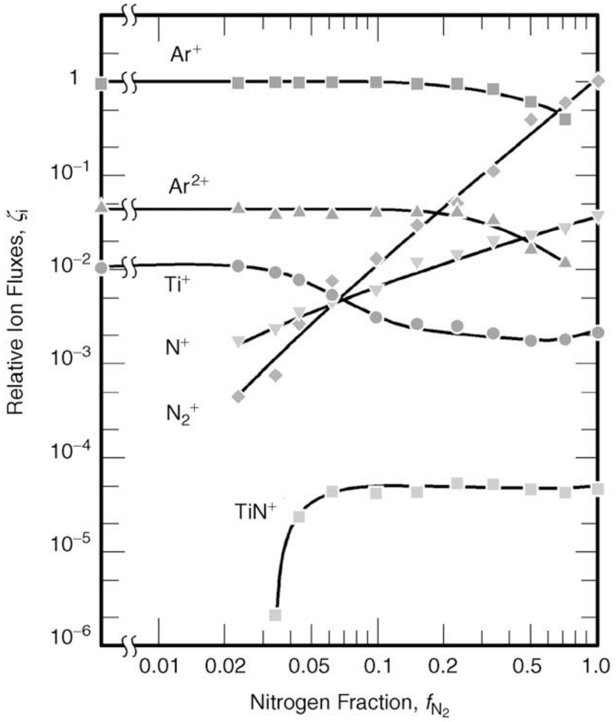

Figure 2.30: Relative ion fluxes measured during reactive magnetron sputter deposition of TiN_x in Ar/N_2 mixtures as a function of relative nitrogen concentration. (From [148].)

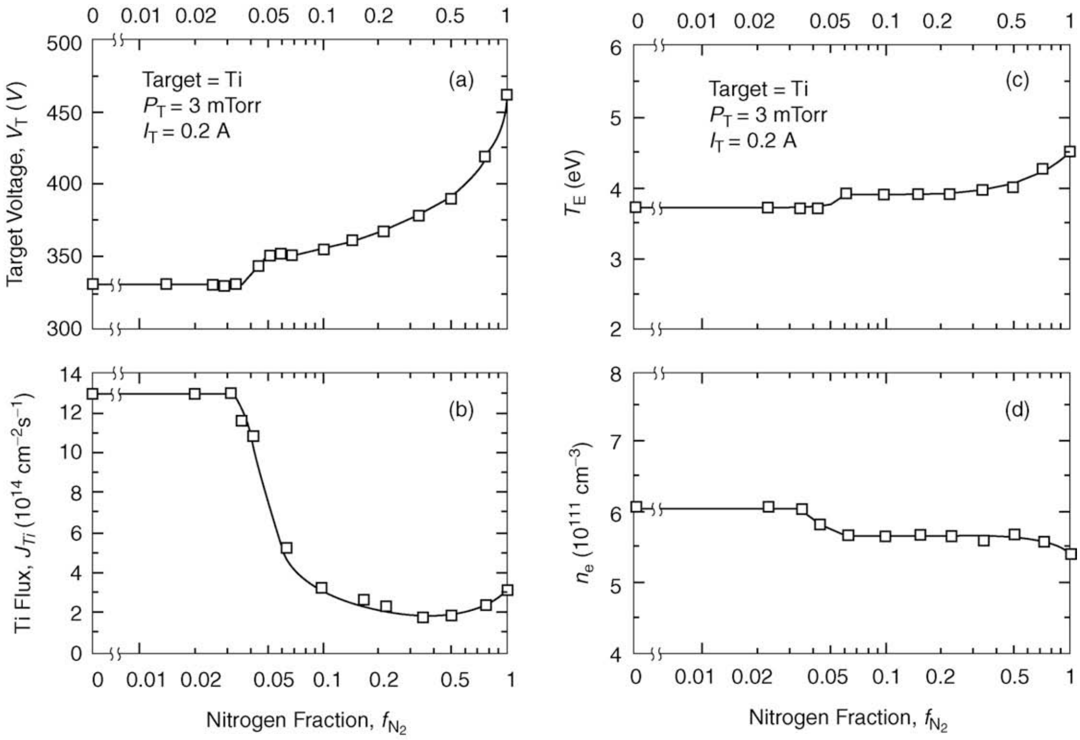

Figure 2.31: (a) Target voltage, (b) titanium flux, (c) electron temperature, and (d) plasma density measured as a function of relative nitrogen concentration during reactive magnetron sputter deposition of TiN_x in Ar/N_2 mixtures. (From [148].)

the discharge is maintained at 3 mtorr (0.4 Pa), for which the charge exchange mean free path is more than ten times the anode (substrate) sheath width. Figure 2.30 shows the relative fluxes of ions incident at the negatively biased substrate plane, determined using a combination of high-resolution mass and energy resolved spectrometry. The results of Figure 2.31 were determined using Langmuir probes, and measurements of film composition and deposition rate.

Comparing the incident-ion results from Figure 2.30, 'simple' plasmas composed of pure gases already yield some interesting results. In pure Ar, the dominant ion incident at the substrate is Ar^+, followed by Ar^{2+} at approximately 4%, and Ti^+ ions at less than 1%. The Ti^+ ions are sputtered atoms ionized in the plasma (the flux of Ti^+ ions sputter ejected from the target is more than an order of magnitude less) [148, 149]. For these three species, the ionization energies are as follows:

$$e^- + Ar \rightarrow Ar^+ + 2e^- \ (\Delta H = 15.76\,\text{eV})$$

$$e^- + Ar \rightarrow Ar^{2+} + 3e^- \ (\Delta H = 27.53\,\text{eV})$$

$$e^- + Ti \rightarrow Ti^+ + 2e^- \ (\Delta H = 6.83\,\text{eV})$$

As noted earlier in this chapter, only the electrons in the high-energy part of the distribution have sufficient energy to ionize gaseous species. It follows that Ar^{2+} ions, with a much higher ionization energy, are present at relatively low concentrations and that they are primarily formed in the narrow cathode sheath by inelastic collisions with fast electrons. The flux of Ti^+ ions is low (even though the Ti ionization potential is small) owing to the low partial pressure of Ti atoms compared to Ar.

In pure N_2 discharges, $N_2{}^+$ comprises approximately 96% of the total ion flux, while N^+ and Ti^+ account for only 3.5% and 0.2%, respectively. Even though the electron density and energy distribution has changed, the fact that $J(N_2^+) \gg J(N^+)$ is due primarily to the large difference in electron-impact ionization energies:

$$e^- + N_2 \rightarrow N_2{}^+ + 2e^- \ (\Delta H = 15.5\,\text{eV})$$

$$e^- + N_2 \rightarrow N^+ + N + 2e^- \ (\Delta H = 24.4\,\text{eV})$$

The Ti^+ ion flux is significantly reduced from its value in Ar and TiN^+ ions are also observed. In pure nitrogen, the target surface is fully nitrided (or 'poisoned') and the effect of this is to dramatically decrease the sputtered neutral Ti atom flux $J(Ti)$ (Figure 2.31b) since the sputtering yield of titanium nitride is much less than that of pure titanium. There is a small, but measurable, flux of TiN^+ ions arising from sputtered molecules ionized in the plasma. In addition, the secondary electron yield of titanium nitride is lower than that of Ti, resulting in an increase in the target voltage V_t (Figure 2.31a), since the magnetron is operated in constant current mode, which gives rise to an increase in the average electron temperature from 3.7 to 3.9 eV (Figure 2.31c).

For the discharges produced in Ar/N_2 mixtures, the addition of only ~3.5% N_2 ($f(N_2) = 0.035$) already leads to a small flux of molecular TiN^+ ions, indicating that even at this low N_2 gas-phase concentration, a steady-state coverage of chemisorbed N has accumulated on the target surface which is being sputtered at a relatively high rate. The decrease in the Ti^+ ion flux with increasing f_{N_2} is primarily reflecting the reduction in the Ti sputter rate, which occurs in concert with the appearance of TiN^+ ions, a decrease in $J(Ti)$, an increase in target voltage V_t, and a drop in the secondary electron yield and plasma density n_e (Figure 2.31d). A further small increase in $f(N_2)$ from 0.035 to ~0.060 results in $J(TiN^+)$, V_t, and $J(Ti)$ reaching saturation, a signature of complete nitridation of the target surface. Note that even at $f(N_2) = 0.3$, far past the point of saturation nitridation, Ar^+ remains the dominant ion, accounting for about 90% of the total ion flux at the substrate.

For Ar/N_2 mixtures with $f_{N_2} < 0.06$, Figure 2.30 shows that $J(N^+) > J(N_2{}^+)$, which is contrary to what might be expected from the above discussion. However, in Ar-rich plasmas, N^+ ions can be formed by a two-step process in which accelerated Ar^+ ions, fast neutrals, and long-lived Ar* metastables collisionally dissociate N_2 molecules to N atoms which can then be ionized by electron impact.

The ionized fraction of sputtered Ti remains relatively constant at $J(Ti^+)/J(Ti) \sim 7 \pm 2 \times 10^{-3}$, irrespective of Ar/$N_2$ gas composition. The small value of the ratio shows that Ti ions contribute little to film growth kinetics. Moreover, from the viewpoint of plasma chemistry, the fact that $J(Ti^+)/J(Ti)$ does not change significantly with $f(N_2)$ indicates that Penning ionization, via collisions with Ar* metastable species, does not play a dominant role in forming metal ions during reactive magnetron sputtering. In contrast to RF discharges, where Penning ionization provides a major contribution to target atom ionization in the gas phase [150], electron impact ionization dominates during DC magnetron sputtering owing to the lower operating pressures and the relatively high electron currents which characterize these devices.

Achieving high deposition rates (maximum when the target surface is pure metal) while depositing nearly stoichiometric compound films in a reactive gas can prove challenging. For example, it is extremely difficult to operate in the narrow $f(N_2)$ range 0.035–0.060, over which the target surface changes from essentially pure metal to pure nitride, when using a mass flow controller as a closed-loop feedback element. There are two issues here. First, a mass flow controller requires mechanical motion (change in orifice size), which is slow. Second, small perturbations can quickly drive the target to become fully poisoned. A slight increase in N concentration on the target leads to an additional decrease in sputtered Ti flux $J(Ti)$, which leads, in turn, to an increase in the extant N_2 partial pressure since the primary mechanism for nitrogen loss from the plasma is chemisorption by freshly deposited metal (sputter-deposited Ti acts as an internal sorption pump). The increased N_2 pressure further increases the N coverage on the target, and so on in an uncontrolled avalanche effect as the target rapidly becomes fully nitrided and the film deposition rate reaches a minimum. The solution is to use N_2 partial pressure, not the flow rate, as the feedback signal [151].

2.8 Summary

In this chapter, we surveyed fundamental aspects of plasmas as they relate to materials processing, particularly deposition and surface modification. This includes the basics of gas-phase interactions, discharge physics, and plasma–surface interactions. It should be clear that plasmas provide an environment not easily attained with other processing approaches. Within the plasma, electrons are able to produce reactive radicals and excited species from otherwise inert gases. At the surface, energetic charged particles bombard the growing film. For the electrons, their kinetic energies are a few electron volts; for the ions, incident energies can be tens of electron volts. In terms of temperature, 1 eV is equivalent to 11,604 K or roughly 40 times room temperature. This might not be a unique property if it were not for the fact that the background gas and adjacent surface are *not* in thermal equilibrium with the plasma species; both the gas and surfaces can be maintained at room temperature. This enables the modification of substrates and production of films at low gas and surface temperatures, which is advantageous for several substrate, gas, and film combinations.

The delivery of large fluxes of energetic ions to adjacent surfaces is beneficial in deposition applications. The ability to deliver a uniform flux over large areas is important in terms of material utilization and in industrial applications where throughput is of considerable importance. Moreover, most of the ion energy is deposited within a few monolayers of the surface, which is useful when sputtering high- or low-melting point and multicomponent material.

The production of plasma and plasma-based systems for materials processing is flexible. As outlined, there are many approaches to plasma production and each method has its advantages in terms of plasma and system characteristics. Over the years, several interesting developments have emerged in various processing communities, such as the development of hybrid systems that employ multiple plasma sources and an expansion of operating parameters. Examples include a number of interesting approaches to PAPVD, high-pressure plasma processing techniques in the hope of reducing capital and processing costs associated with maintaining a vacuum, and the use of microdischarges for processing on a very small scale.

Given the many unique characteristics of plasmas, it is not surprising that plasma-based systems are common to a wide range of applications. The development of new plasma-based processing systems has driven the evolution of materials and vice versa. It is reasonable to expect this close relationship to continue and so an understanding of the basic physics and chemistry of plasmas is vital.

Appendix 2.1

Système International (SI) units are not always the units used in plasma physics and we have adopted the more commonly used units throughout this chapter. The following constants, conversions, and formulae are useful:

- Unified atomic mass unit: $u = 1.66 \times 10^{-27}$ kg
- Atomic mass number: $A =$ (number of protons and neutrons) $\approx$ atomic weight (A_r)
- Electron mass: $m_e = 9.11 \times 10^{-31}\ \text{kg} = (1/1836)\ \text{u}$
- Heavy particle mass: $M = A \times 1.67 \times 10^{-27}$ kg
- Electron volt (eV): one electron volt is the energy gained by a particle with unit charge which is accelerated in an electric field produced by a potential difference of one volt ($1\ \text{eV} = 1.602 \times 10^{-19}\ \text{J} = 11{,}604\ \text{K}$)
- Electron plasma frequency: $f\,(\text{Hz}) = 9000\ (n_e\ (\text{cm}^{-3}))^{1/2}$

- Electron Debye length: λ_d (cm) = 740 (T_e (eV)/n_e (cm^{-3}))$^{1/2}$
- Average electron speed at electron temperature: v(cm/s) = 5.95×10^7 (T_e(eV))$^{1/2}$
- Average gas velocity at gas temperature: v(cm/s) = 1.58×10^4 (T(K)/M(u))$^{1/2}$
- Boltzmann constant (k): k = 1.38×10^{-23} J/K = 8.62×10^{-5} eV/K
- Ideal gas law: $PV = \mathrm{k}T$
- Room temperature: 20 °C = 293 K (for convenience 300 K is often used)
- Gas density (N): at 1 torr and 300 K (27 °C), $N = 3.2 \times 10^{16}$ particles/cm^3
- Atmospheric pressure at sea level: 760 torr
- 1 torr = 133.3 Pa = 1 mmHg = 1.316 mbar.

Acknowledgements

S.G. Walton gratefully acknowledges the support of the Office of Naval Research and his colleagues at the Naval Research Laboratory, Dr R.F. Fernsler and NRC/NRL postdoctoral research associates, Dr E.H. Lock and Dr M. Baraket for their helpful comments and discussions. J.E. Greene gratefully acknowledges the support of the Office of Naval Research and the Materials Science Division of the Department of Energy over the course of several years.

References

[1] J.A. Thornton, J.E. Greene, in: R.F. Bunshah (Ed.), Deposition Technologies for Films and Coatings, 2nd ed., Noyes Publications, Westwood, NJ (1994) 55.
[2] R. Rejoub, B.G. Lindsay, R.F. Stebbings, Phys. Rev. A 65 (2002) 042713.
[3] N.J. Mason, W.R. Newell, J. Phys. B 20 (1987) 1357.
[4] J. Bretagne, G. Callede, M. Legentil, V. Puech, J. Phys. D 19 (1986) 761.
[5] A. Chutjian, D.C. Cartwright, Phys. Rev. A 23 (1981) 2178.
[6] M. Hayashi, National Technical Information Document No. N82-18007. Copies may be obtained from the National Technical Information Service, Springfield, VA 22161.
[7] Y. Itikawa, J. Phys. Chem. Ref. Data 38(1) (2009) 1.
[8] D. Rapp, D.D. Briglia, J. Chem. Phys. 43(5) (1965) 1480.
[9] I. Iga, M.V.V.S. Rao, S.K. Srivastava, J.C. Nogueira, Z. Phys. D Atoms, Molecules and Clusters 24 (1992) 111.
[10] A.V. Phelps, J. Phys. Chem. Ref. Data 20(3) (1991) 557.
[11] J.O. Hirschfelder, C.F. Curtiss, R.B. Bird, Molecular Theory of Gases and Liquids, Wiley, New York (1954) 523.
[12] L.S. Frost, A.V. Phelps, Phys. Rev. 127 (1962) 1621.
[13] R.D. White, K.F. Ness, R.E. Robson, Appl. Surf. Sci. 192 (2002) 26.
[14] R.E. Robson, R.D. White, Z.Lj. Petrovic, Rev. Mod. Phys. 77 (2005) 1303.

[15] G.W. Sutton, A. Sherman, Engineering Magnetohydro-dynamics, McGraw-Hill, New York (1965).
[16] D.D. Pappas, A.A. Bujanda, J.A. Orlicki, R.E. Jensen, Surf. Coat. Technol. 203 (2008) 830.
[17] J.D. Cobine, Gaseous Conductors, Dover, New York (1958).
[18] R.F. Baddour, R.S. Timmins (Eds.), The Applications of Plasmas to Chemical Processing, MIT Press, Cambridge, MA (1967).
[19] J.A. Thornton, J. Vac. Sci. Technol. 15 (1978) 188.
[20] H.R. Griem, Plasma Spectroscopy, McGraw-Hill, New York (1964) 129.
[21] D. ter Haar, Elements of Statistical Mechanics, Holt, Rinehart and Winston, New York (1960) 381.
[22] H. Akashi, S. Samukawa, N. Takahashi, T. Sasaki, Jpn. J. Appl. Phys. 36 (1997) 877.
[23] B. Ramamurthi, D.J. Economu, I.D. Kaganovich, Plasma Source Sci. Tech. 12 (2003) 302.
[24] V. Godyak, Phys. of Plasma 12 (2005) 055501.
[25] S.-H. Seo, J.-H. In, H.-Y. Change, Plasma Source Sci. Tech. 13 (2004) 409.
[26] N. Herskowitz, in: D.A. Glocker, S. Ismath Shah (Eds.), Handbook of Thin Film Process Technology, Institute of Physics Publishing, Bristol (1995).
[27] R.F. Fernsler, Plasma Sources Sci. Technol. 18 (2009) 014012.
[28] D.J. Rose, M. Clar Jr, Plasmas and Controlled Fusion, MIT-Wiley, New York (1961) 80.
[29] F.F. Chen, Introduction to Plasma Physics, Plenum Press, New York (1974).
[30] J.D. Huba, NRL Plasma Formulary (Revised), Naval Research Laboratory, Washington, DC (1998).
[31] L. Spitzer Jr, Physics of Fully Ionized Gases, Interscience, New York (1956).
[32] S.M. Rossnagel, in: J.L. Vossen, W. Kern (Eds.), Thin Film Processes II, Academic Press, New York (1991) 42.
[33] J.L. Delcroix, Introduction to the Theory of Ionized Gases, Interscience, New York (1960) 128.
[34] S. Chapman, T.G. Cowling, The Mathematical Theory of Non Uniform Gases, Cambridge University Press, Cambridge (1960) 90.
[35] Y. Ikezoe, S. Matsuoka, M. Takebe, A. Viggiano, Gas Phase Ion–Molecule Reaction Rates Through 1986, Ion Reaction Research Group of the Mass Spectroscopy Society of Japan, Distributed by Maruzen Co., Tokyo, Japan (1989).
[36] H.W. Ellis, R.Y. Pai, E.W. McDaniel, E.A. Mason, L.A. Viehland, Atomic Data and Nuc. Data Tables 17 (1976) 177.
[37] S.C. Brown, Basic Data of Plasma Physics, MIT Press, Cambridge, MA (1959).
[38] E.W. McDaniel, The Mobility, Diffusion of Ions in Gases, Wiley, New York (1973) 132.
[39] M.H. Mittleman, in: F.H. Clauser (Ed.), Plasma Dynamics, Addison-Wesley, New York (1960) 54.
[40] F.F. Chen, in: R.H. Huddlestone, S.L. Leonard (Eds.), Plasma Diagnostic Techniques, Academic Press, New York (1965) 113.
[41] D. Bohm, E.H.S. Burhop, H.S.W. Massey, in: A. Guthrie, R.K. Wakerling (Eds.), The Characteristics of Electrical Discharges in Magnetic Fields, McGraw-Hili, New York (1949) 13.
[42] M.A. Lieberman, A.J. Lichtenberg, Principles of Plasma Discharges and Materials Processing, Wiley-Interscience, New York (1994).
[43] S. Glasstone, R.H. Louberg, Controlled Thermonuclear Reactions, Van Nostrand, New York (1960) 459.
[44] J.A. Thornton, J. Vac. Sci. Technol. 15 (1978) 171.
[45] F.K. McTaggart, Plasma Chemistry in Electrical Discharges, Elsevier, New York (1967).
[46] J.E. Greene, S.A. Barnett, J.E. Sundgren, A. Rockett, Ion Beam Assisted Film Growth, Elsevier, Amsterdam (1988) 101.
[47] R.F. Bunshah, A.C. Raghuram, J. Vac. Sci. Technol. 9 (1972) 1385.
[48] A. Fridman, L.A. Kennedy, Plasma Physics and Engineering, Taylor and Francis, New York (2004).
[49] S.C. Brown, A.D. MacDonald, Phys. Rev. 76 (1949) 1629.
[50] R.T.S. Chen, N. Hershkowitz, Phys. Rev. Lett. 80(21) (1998) 4677.
[51] K. Takenaka, Y. Setsuhara, K. Nishisaka, A. Ebe, S. Sugiura, K. Takahashi, K. Ono, Jpn. J. Appl. Phys. 45(10B) (2006) 8046.
[52] M. Nisha, K.J. Saji, R.S. Ajimsha, N.V. Joshy, M.K. Jayaraj, J. Appl. Phys. 99 (2006) 033304.

[53] P. Sigurjonsson, J.T. Gudmundsson, J. Phys.: Conference Series 100 (2008) 062018.
[54] D. Leonhardt, C.R. Eddy Jr, V.A. Shamamian, R.F. Fernsler, J.E. Butler, J. Appl. Phys. 83(6) (1998) 2971.
[55] S.G. Walton, D. Leonhardt, R.F. Fernsler, IEEE Trans. Plasma Sci. 33(2) (2005) 0093–3813.
[56] E.S. McDaniel, Collision Phenomena in Ionized Gases, Chap. 13, Wiley, New York (1964).
[57] D.G. Williams, J. Vac. Sci. Technol. 11 (1974) 374.
[58] S.G. Walton, C. Muratore, D. Leonhardt, R.F. Fernsler, D.D. Blackwell, R.A. Meger, Surf. Coat. Technol. 186(1–2) (2004) 40.
[59] J.A. Thornton, A.S. Penfold, in: J.L. Vossen, W. Kern (Eds.), Thin Film Processes, Academic Press, New York (1978).
[60] R. Parsons, in: J.L. Vossen, W. Kern (Eds.), Thin Film Processes II, Academic Press, New York (1991) 178.
[61] M. Baraket, Elaboration et caractérisation de revêtements nano-structurés à base de nitrure de chrome par pulvérisation cathodique magnétron en condition réactive – propriétés mécaniques et tribologiques, Thesis, Université de Technologie de Belfort-Montbéliard (2008).
[62] A.P. Ehiasarian, R. New, W.-D. Munz, L. Hultman, U. Helmersson, V. Kouznetsov, Vacuum 65 (2002) 147.
[63] H.S. Butler, G.S. Kino, Phys. Fluids 6 (1963) 1346.
[64] W.F. Libby, J. Vac. Sci. Technol. 16 (1979) 414.
[65] G.M. Burnett, A.M. North (Eds.), Transfer and Storage of Energy by Molecules, Wiley-Interscience, New York (1969).
[66] L.G. Christophourou, Atomic and Molecular Radiation Physics, Wiley-Interscience, New York (1971) 6.
[67] M.A. Lieberman, A.J. Lichtenberg, Principles of Plasma Discharges and Materials Processing, Wiley-Interscience, New York (1994) 81.
[68] L.G. Christophorou, D.L. McCorckle, A.A. Christodoulides, in: L.G. Christophorou (Ed.), Electron–Molecule Interactions and their Applications, Vol. 1, Academic Press, New York (1984).
[69] E. Stoffles, W.W. Stoffels, D. Vender, M. Haverlag, G.M.W. Krosen, F.J. DeHoog, Contrib. Plasma Phys. 35 (1995) 331.
[70] Y. Itikawa, A. Ichimura, K. Onda, K. Sakimoto, K. Takayanagi, Y. Hatano, M. Hayashi, H. Nishimura, S. Tsurubuchi, J. Phys. Chem. 18(1) (1989) 23.
[71] S.G. Walton, D. Leonhardt, R.F. Fernsler, R.A. Meger, Appl. Phys. Lett. 81(6) (2002) 987.
[72] S.G. Walton, R.F. Fernsler, Plasma Source Sci. Technol. 18 (2009) 022001.
[73] H.F. Winters, J.W. Coburn, E.J. Kay, Appl. Phys. 48 (1978) 4973.
[74] J.W. Coburn, H.F. Winters, J. Vac. Sci. Technol. 16 (1979) 392.
[75] E.E. Muschlitz Jr, Science 159 (1968) 599.
[76] J.R. Holiahan, R.S. Rosier, in: J.L. Vossen, W. Kern (Eds.), Thin Film Processes, Academic Press, New York (1978) 335.
[77] C.M. Melliar-Smith, C.J. Mogab, ibid., p. 497.
[78] H. Yasuda, ibid., p. 361.
[79] W. Kern, V.S. Ban, ibid., p. 257.
[80] T.B. Gorczyca, B. Gorowitz, in: N.G. Einspruch, D.M. Brown (Eds.), VLSI Electronics: Microstructure Science, Academic Press, New York (1984).
[81] H. Kobayashi, A.T. Bell, M. Shen, Macromolecules 7 (1974) 277.
[82] J.M. Tibbitt, R. Jensen, A.T. Bell, M. Shen, Macromolecules 10 (1977) 647.
[83] S. Stoykov, C. Eggs, U. Kortshagen, J. Phys. D 34 (2001) 2160–2173.
[84] H.H. Anderson, H.L. Bay, in: R. Behrisch (Ed.), Sputtering by Particle Bombardment I, Springer, Berlin (1981) 145.
[85] E.V. Alonso, M.A. Alurralde, R.A. Baragiola, Surf. Sci. 166 (1986) L155.
[86] H.D. Hagstrum, Phys. Rev. 96 (1954) 325 Phys. Rev. 96 (1954) 336.
[87] M.L. Yu, N.D. Lang, Nuc. Inst. Meth. B 14 (1986) 403.
[88] J.C. Tucek, S.G. Walton, R.L. Champion, Phys Rev B 53(21) (1996) 14127.
J.C. Tucek, S.G. Walton, R.L. Champion, in: Surf. Sci. 382 (1997) 137.

[89] W.D. Davis, T.A. Vanderslice, Phys. Rev. 131 (1963) 219.
[90] C.V. Budtz-Jørgensen, J. Bøttiger, P. Kringhøj, Vacuum 56 (2000) 9.
[91] C. Muratore, S.G. Walton, D. Leonhardt, R.F. Fernsler, D.D. Blackwell, R.A. Meger, J. Vac. Sci. Technol. A 22(4) (2004) 1530.
[92] J.R. Anderson (Ed.), Chemisorption and Reactions on Metallic Films, Academic Press, New York (1971).
[93] M.A. Wall, D.G. Cahill, I. Petrov, D. Gall, J.E. Greene, Phys. Rev. B 70 (2004) 035413.
[94] M.A. Wall, D.G. Cahill, I. Petrov, D. Gall, J.E. Greene, Surf. Sci. 581 (2005) L122.
[95] D. Gall, S. Kodambaka, M.A. Wall, I. Petrov, J.E. Greene, J. Appl. Phys. 93 (2003) 9086.
[96] S. Kodambaka, S.V. Khare, I. Petrov, J.E. Greene, Surf. Sci. Rep. 60 (2006) 55.
[97] I. Petrov, P.B. Barna, L. Hultman, J.E. Greene, J. Vac. Sci. Technol. 21 (2003) S117.
[98] C.-S. Shin, D. Gall, Y.-W. Kim, N. Hellgren, I. Petrov, J.E. Greene, J. Appl. Phys. 92 (2002) 5084.
[99] H.F. Winters, D.L. Ramondi, D.E. Horne, J. Appl. Phys. 40 (1969) 2996.
[100] M.L. Tarng, G.K. Wehner, J. Appl. Phys. 42 (1971) 2449.
[101] J.J. Cuomo, R.J. Gambino, J. Vac. Sci. Technol. 12 (1975) 79.
[102] J.L. Zilko, J.E. Greene, J. Appl. Phys. 51 (1980) 1549.
[103] M.J. Brett, R.R. Parsons, Can. J. Phys. 63 (1985) 819.
[104] S. Shimizu, T. Tsukakoshi, S. Komiya, Y. Makita, Y. GaAs, Y. Related Compounds, Inst. Phys. Conf. Series 79 (1985) 91.
[105] J.M.E. Harper, J.J. Cuomo, H.T.G. Hentzell, J. Appl. Phys. 58 (1985) 550.
[106] J.E. Sundgren, B.O. Johansson, A. Rockett, S.A. Barnett, J.E. Greene, Physics and Chemistry of Hard Coatings, American Inst. Phys. Series Conf. Proc. 149 (1986) 95.
[107] M.A. Hasan, J. Knall, S.A. Barnett, J.E. Sundgren, L.C. Markert, A. Rockett, J.E. Greene, J. Appl. Phys. 65 (1989) 172.
[108] P. Fons, N. Hirashita, L.C. Markert, Y.W. Kim, J.E. Greene, W.X. Ni, J. Knall, G.V. Hansson, J.E. Sundgren, Appl. Phys. Lett. 53 (1988) 1732.
[109] H.F. Winters, E. Kay, J. Appl. Phys. 38 (1967) 2928.
[110] A. Pan, J.E. Greene, Thin Solid Films 78 (1981) 25.
[111] D.W. Hoffman, J.A. Thornton, J. Vac. Sci. Technol. 20 (1982) 355.
[112] L. Hultman, L.C. Markert, J.E. Sundgren, J.E. Greene, Appl. Phys. Lett. 53 (1988) 1175.
[113] K.H. Muller, Appl. Phys. A 40 (1986) 209.
[114] T.C. Huang, G. Lim, F. Parmiagiani, E. Kay, J. Vac. Sci. Technol. A 3 (1985) 2161.
[115] L. Hultman, U. Helmersson, S.A. Barnett, J.E. Sundgren, J.E. Greene, J. Appl. Phys. 61 (1987) 552.
[116] L. Hultman, S.A. Barnett, J.E. Sundgren, J.E. Greene, J. Cryst. Growth 92 (1988) 639.
[117] R. Ronsille, R. Boch, G.L. Destefanis, J.L. Tissot, Appl. Phys. Lett. 44 (1984) 679.
[118] J.H. Comfort, L.M. Gaverick, R. Reif, J. Appl. Phys. 62 (1987) 3388.
[119] L.M. Gaverick, J.H. Comfort, T.R. Uyeh, R. Reif, F.A. Baiocchi, H.S.J. Luttman, J. Appl. Phys. 62 (1987) 3398.
[120] M.L. Yu, Appl. Phys. Lett. 40 (1982) 986.
[121] J.M. Burkstrand, J. Vac. Sci. Technol. 15 (1978) 223.
[122] J.M. Burkstrand, Appl. Phys. Lett. 33 (1978) 387.
[123] D. Leonhardt, C. Muratore, S.G. Walton, R.A. Meger, Surf. Coat. Technol. 188–189 (2004) 299.
[124] P. Bodo, J.E. Sundgren, J. Vac. Sci. Technol. A 2 (1984) 1498.
[125] P. Bodo, J.E. Sundgren, Thin Solid Films 136 (1986) 147.
[126] J.W. Coburn, H.F. Winters, J. Appl. Phys. 50 (1979) 3189.
[127] H.F. Winters, J.W. Coburn, Appl. Phys. Lett. 34(1) (1979) 70.
[128] D.J. Ball, J. Appl. Phys. 143 (1972) 3047.
[129] S.S. Lau, R.H. Mills, D.G. Muth, J. Vac. Sci. Technol. 9 (1972) 1196.
[130] D.J. Stirling, Appl. Phys. Lett. 9 (1966) 326.
[131] P.W. Palmberg, C.T. Todd, T.N. Rhodin, J. Appl. Phys. 39 (1968) 4650.
[132] M.R. Jordan, D.J. Stirland, Thin Solid Films 8 (1971) 221.

[133] D.G. Lord, M. Prutton, Thin Solid Films 21 (1974) 341.
[134] G. Shimaoka, J. Cryst. Growth 31 (1975) 92.
[135] R.D. Ramsier, J.T. Yates Jr, Surf. Sci. Rep. 12 (1991) 243.
[136] D. Menzel, R. Gomer, J. Chem. Phys. 41 (1964) 3311.
[137] P.A. Redhead, Can. J. Phys. 42 (1964) 886.
[138] M.L. Yu, Phys. Rev. B 19(12) (1979) 5995.
[139] N. Inagaki, Plasma Surface Modification and Plasma Polymerization, Technomic Publishing Co., Lancaster, PA (1996).
[140] S. Thomas, J. Appl. Phys. 45 (1974) 161.
[141] B. Carriere, B. Lang, Surf. Sci. 64 (1977) 209.
[142] M.L. Knotek, V.O. Jones, V. Rehn, Phys. Rev. Lett. 43(4) (1979) 300.
[143] D. Lichtman, Surf. Sci. 90 (1979) 579.
[144] A.R. Burns, E.B. Stechel, D.R. Jennison (Eds.), Desorption Induced by Electronic Transitions, DIET-V, Springer, Berlin (1992) and previous volumes.
[145] K. Fukutani, Y. Murata, Surf. Sci. 390 (1997) 164.
[146] S.G. Walton, B.L. Peko, R.L. Champion, Phys. Rev. B 58(23) (1998) 15430.
[147] A. Hollander, R. Wilken, J. Behnisch, Surf. Coat. Technol. 116-119 (1999) 788.
[148] I. Petrov, A. Myers, J.E. Greene, J.R. Abelson, J. Vac. Sci. Technol. A 12 (1994) 2846.
[149] A.W. Benninghoven, F.G. Rudenauer, H.W. Werner, Secondary Ion Mass Spectrometry: Basic Concepts, Instrumentation Aspects, Applications, and Trends, Wiley, New York (1987).
[150] J.W. Coburn, E. Kay, Appl. Phys. Lett. 43 (1971) 435.
[151] W.D. Sproul, D.J. Christie, D.C. Carter, Thin Solid Films 491 (2005) 1.

CHAPTER 3

Surface Preparation for Film and Coating Deposition Processes

3.1 Introduction

Surface preparation [1] includes surface treatments (surface modification) to change the properties of the surface in a desirable way [2] as well as cleaning, which is the reduction of surface contamination to an acceptable level. One objective of any surface preparation procedure is to produce as homogeneous a surface as possible. Reproducible surface preparation, as well as the associated handling and storage techniques, are obtained by having and following appropriate written specifications and procedures. In order to have reproducible surface preparation processes it is generally necessary to have a reproducible and homogeneous starting surface.

Surface modification can include surface treatments such as roughening or smoothing the surface, making a harder surface by plasma treatment, or by activating a polymer surface by plasma treatment. Care must be taken to ensure that the surface preparation processes do not change the surface in an undesirable or in an uncontrolled manner.

Cleaning is used so that desirable processing and film/coating properties can be obtained. As a practical matter a 'clean' surface is one that contains no significant amounts of undesirable material; thus what constitutes a clean surface depends on the requirements. The requirements range from those concerned with monolayer coverage and atomically clean surfaces, to gross cleaning such as used for fusion welding. General contamination such as a hydrocarbon surface layer can cause a low nucleation density of the depositing film on a surface, cause poor overall adhesion of a film to a surface, and prevent good electrical contact in the case of deposited electrical contacts. Local contamination (film or particle) can result in locally poor adhesion of a film to a surface giving pinholes in the film. Figure 3.1 shows how pinholes are formed in deposited thin films by particulate contamination on the surface, inclusions in the surface or by surface features. Cleaning should address local surface conditions such as porosity, embedded particles, steps, roughness, etc., that affect film properties, produce pinholes, and local loss of adhesion.

External cleaning takes place outside the deposition system as a separate process in a controlled environment. It includes gross cleaning to remove large amounts of contaminants often by removing some of the substrate surface, and specific cleaning, which is directed toward removing a specific contaminant such as particulates, or hydrocarbons. A clean processing environment, and proper handling and storage after the external cleaning are important to minimize recontamination of the cleaned surface before it is placed in the deposition chamber. For example, to control recontamination by particulates, a filtered air cleanroom can be used. Problems with recontamination are lessened if the cleaning procedure is integrated into the deposition line, the prepared surfaces are used immediately, and/or if there is a final in situ cleaning process in the deposition system.

The objective of cleaning processes is to facilitate the fabrication of an acceptable product in the most reproducible and economical way. Cleaning processes should be as simple and effective as possible in order to meet the processing requirements. Elaborate cleaning processes are often expensive and self-defeating. Often there is a tradeoff between the various stages of the cleaning process, handling/storage, and previous as well as subsequent processing. This can mean that simple changes in one stage make complex changes in another step unnecessary. The processing sequence as a whole should be considered when developing a cleaning process.

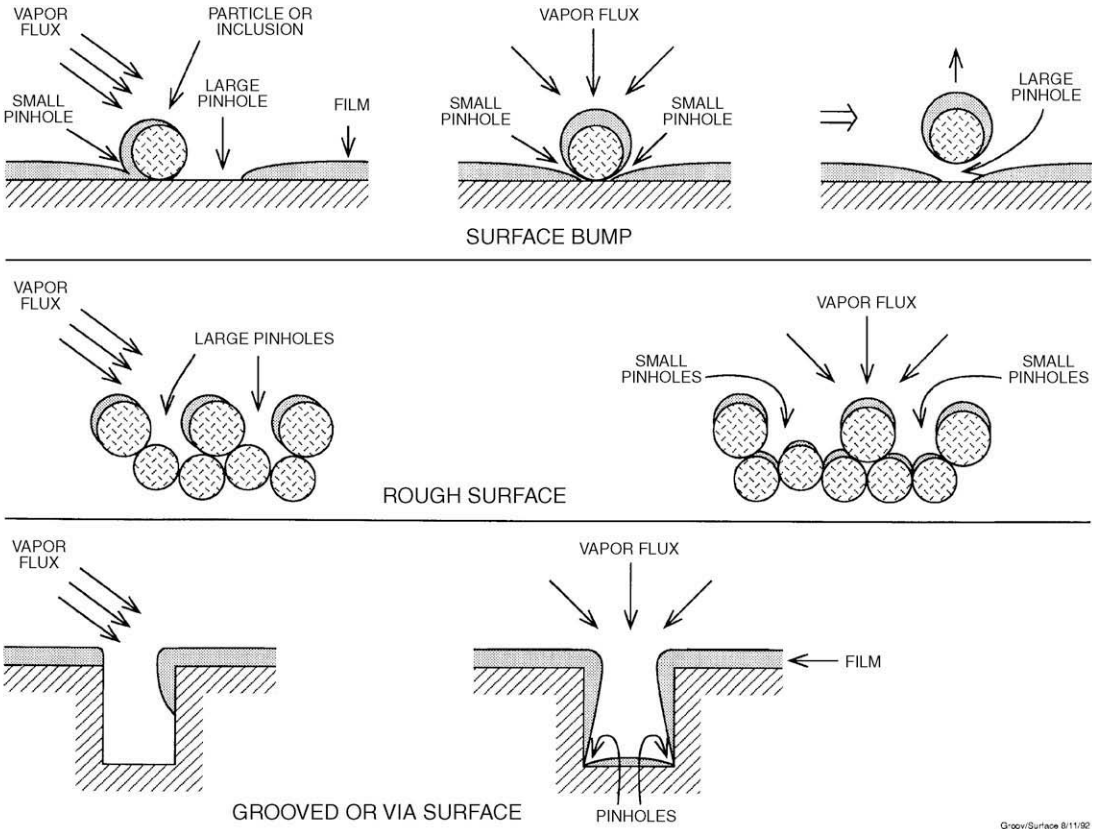

Figure 3.1: Pinhole formation. [From Society of Vacuum Coaters Education Guides to Vacuum Coating Processing (2009) – Atomistic Film Growth and Resulting Film Properties – Pinholes, with permission.]

3.2 External Cleaning

3.2.1 Gross Cleaning

In general, gross cleaning takes some of the substrate surface with it and can change the surface chemistry or morphology in an undesirable manner. After the gross contamination is removed, it is important to control the type and amount of contaminants to which the surface is exposed.

3.2.1.1 Stripping

In some cases, such as removing deposited film material from fixtures, or reprocessing parts with defective coatings, large amounts of undesirable material must be removed from a surface and the process is called stripping. Stripping is usually done by mechanical abrasion or by chemical etching.

3.2.1.2 Abrasive Cleaning

The removal of gross contamination by abrasive cleaning includes the use of:

- abrasive surfaces, e.g. sandpaper, emery paper, steel wool, Scotch-brite^{TM} and Soft-scour^{TM} scouring pads
- abrasive powders in a paste or fluid carrier, e.g. SiC, Al_2O_3, diamond, precipitated calcium carbonate ($CaCO_3$), CeO, and Snow-Floss^{TM} (diatomaceous earth with the calcium carbonate removed, leaving a friable silica network)
- impacting particles entrained in a high-velocity gas or liquid stream: vapor honing, glass bead blasting, liquid honing, grit blasting, sand blasting, etc.
- abrasives combined with an etchant to provide chemical–mechanical abrasion and polishing.

Abrasive particles can be used wet or dry. Commercially available abrasive particles include:

- aluminum oxide
- diamond
- cerium oxide
- glass beads
- crushed glass
- silicon carbide
- fractured cast iron grit
- sodium bicarbonate
- silica sand.

Dry glass bead blasting is a commonly used cleaning technique but, as with other grit abrasive techniques, can leave shards of glass embedded in soft surfaces. The amount of grit embedded depends on how long the glass beads have been used, i.e. how much they have been fractured. Water-soluble particles can be used for abrasive cleaning and allow easy removal of the water-soluble embedded particles. For example, the Prophy-jet^{TM} dental abrasive unit uses 5 μm sodium bicarbonate (baking soda) particles entrained in a high-velocity water stream.

Grit blasting uses grit such as fractured cast iron, alumina, or silica, of varying sizes and shapes accelerated in a gas stream to deform and gouge the surface. Particles can be entrained in a high-velocity gas steam by using a siphon system or a pressure system such as used in sand blasting equipment. In addition to removing gross contamination, grit blasting roughens the surface. The Society of Automotive Engineers (SAE) has specifications on grit size and type, e.g. SAE Specification J444 for cast iron grit in the range G10 (2820 μm maximum size) to G325 (120 μm maximum size), which gives the percentage by weight allowed on standard screens. Bombardment of a surface by grit is like shot peening and places the surface in compressive stress which may produce unacceptable distortion of the surface. Blasting can also be done with plastic media, which is less damaging than the harder grits; however, it can leave organic contamination on the surface.

Wet blasting uses an air-blasted slurry of fine abrasives in chemically treated water. It is sometimes called liquid honing since it is usually used when dimensional tolerances have to be maintained. Abrasion cleaning can be very mild, such as the use of CeO polishing slurry in a high-throughput wash system to preclean glass before the standard wash cycle [3].

3.2.1.3 Wet Chemical Etching

Chemical etching can be used to remove surface material along with the contaminants. This is a very useful technique for getting the surface into a known condition. Pickling is a term used to denote the removal of the large amounts of oxides (scale) that are formed on metals during the metal fabrication process. The process generally involves an alkaline clean before acid pickling in order to get uniform wetting and etching. For example, aluminum and aluminum alloys can be pickled by immersion in various combinations of sulfuric, nitric, hydrofluoric, and chromic acids; copper and copper alloys can be pickled in combinations of sulfuric and oxidizing acids, and iron and steel are pickled in sulfuric or hydrochloric acid solutions. Chemical etchants can be highly selective in their action. This can result in preferential etching of grain boundaries and when etching a two-phase system. Mild pickling is called a bright dip. Acid cleaning of metals can have the detrimental effect of introducing hydrogen into the surface and embrittling metals and ceramics [4]. If hydrogen embrittlement is a concern, either do not use an acid or the etched part should be high-temperature vacuum fired after etching.

Etching removes surface layers such as oxides, eliminates or blunts surface cracks in brittle materials, and removes difficult-to-remove contaminates. Common etchants for glass include sodium or ammonium bifluoride (100 g of ammonium bifluoride salt to 800 ml deionized water), trisodium phosphate, which is a mild etchant, and hydrofluoric acid, which is a very strong etchant. Hydrofluoric (HF) acid solution is a common etchant for silicon and can leave a silicon surface either hydrogen-terminated or hydroxyl-terminated. The silicon surface is hydrophobic if hydrogen-terminated and hydrophilic if hydroxyl-terminated.

When using etchants for cleaning, care must be taken to prevent selective removal of surface constituents that are important to further processing. For example, etching glass-bonded alumina ceramics in HF results in selective removal of the glass [Ca–Mg–Al–Si–O] phase which can weaken the ceramic surface and result in poor adhesion. Etchants can change the surface chemistry. For example, acid etching a soda lime glass surface, which is normally basic, leaches the sodium from the surface and makes the surface acidic, which changes its wetting properties [5].

Sometimes chemical etching does not remove some constituents from a surface and leaves a smut that must be removed by another etching step. For example, etching copper-containing aluminum alloys with NaOH leaves a copper smut and/or a silicon smut on the surface. The copper smut can be removed by an HNO_3 etch and a copper/silicon smut can be removed with a HNO_3/HF etch. In some cases an etchant can be devised that etches all the constituents uniformly. For example, in etching Al:Cu:Si alloys a concentrated nitric acid (100 ml) plus ammonium bifluoride (6.8 g) etch is used. The etching mechanism is solution of the copper, oxidation of the aluminum and the silicon, then etching of the resulting oxides. The etchant actually etches silicon more rapidly than the aluminum.

3.2.2 Specific Cleaning

3.2.2.1 Solvent Cleaning

Some contaminants can be removed from surfaces by solvents that dissolve (take into solution) the contaminant. Polar solvents such as water and water–alcohol mixtures are used to dissolve ionic materials that are polar contaminates. Non-polar solvents such as the chlorinated hydrocarbon (chlorofluorocarbon (CFC)) solvents are used to remove non-polar contaminates such as grease. Often there is a mixture of solvents used to dissolve both polar and non-polar contaminates. Solvents can vary greatly as to their ability to dissolve contaminants and their effectiveness needs to be determined by determining the solubility parameter for specific contaminants. The solubility parameter is the maximum (saturation) amount of a specific contaminant that can be dissolved in a specific amount of the solvent. Many non-chlorinated hydrocarbon-based or petroleum-based materials are used as solvents.

Chlorinated hydrocarbon non-polar solvents such as trichloroethylene are often preferred to hydrocarbon-based or petroleum-based solvents because of their lower flammability (i.e. higher flashpoint as determined by ASTM D-1310-63). However, there is concern with the toxicity, carcinogenic properties, and ozone-depleting action of some of the materials and they should be used in closed recirculating systems.

Chlorinated solvents can react with water to form HCl, which can react with metals, particularly aluminum, producing corrosion. For example, chlorinated solvents can react with Al, Mg, Be, and Zn (white metals) to form inorganic salts. Often stabilizers are added to the chlorinated solvents to reduce their tendency to react with water and form acids. If stabilizers are not used the pH of the cleaner should be monitored to keep a pH in the 6–7 range [6]. If there is a possibility of solvent trapping due to incomplete rinsing, particularly in stressed metal joints, chlorinated solvents should not be used since chloride residues enhance stress

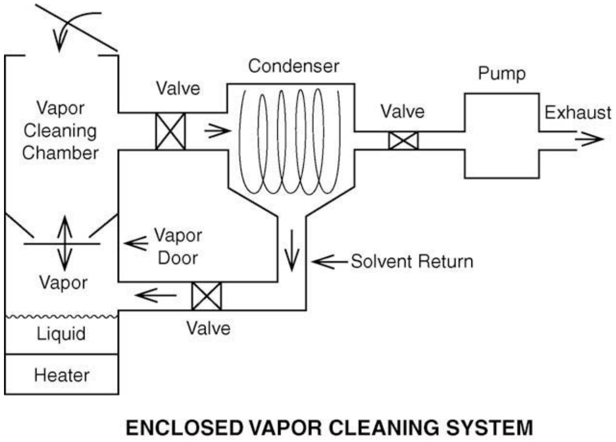

Figure 3.2: Recycling with VOCs. [From SVC Education Guides to Vacuum Coating Processing (2009) – Surface Preparation: Enclosed and Closed-Loop Cleaning Systems, with permission.]

corrosion. Cleaners containing chlorine-based oxidants can present the same stress corrosion problem.

Volatile organic compounds (VOCs) are those that have boiling points below 138 °C. The discharge of VOCs into the environment is regulated by local, state, and federal laws. In order to comply with these regulations it may be necessary to recycle the material by condensation of the vapors or to thermally destroy the vapors by burning before they are released into the atmosphere. Figure 3.2 is one such recycling system. Many clothes dry-cleaning establishments use VOCs with intensive recycling.

Some solvents for removal of greases are: *N*-methyl-2-pyrrolidone-based solvents such as GAF NMP^{TM} and GAF M-PYROL^{TM} (22–24), terpene-based solvents such as Bioact EC-7^{TM} and Genesolv 2000^{TM}, and *n*-propyl bromide (nPB), as well as the Fluoroinerts^{TM}, which do not contain chlorocarbon bonds. Reports indicate that the terpenes may be as effective as CFCs in many instances, although they have a greater tendency to leave residues. Terpenes suffer from the fact that they have low flash points (about 49 °C) and reduced lower explosive limits (LELs).

Supercritical fluids (SCF) can be used as solvents. There is a good correlation between the ability of a simple solvent to dissolve materials and its density. Solvents can be densified most easily when they are in the supercritical state, i.e. no distinction between the liquid and vapor state. Carbon dioxide (CO_2) has been shown to have a Hildebrand solubility parameter that can vary from 0 in the gas to 10 under high-pressure supercritical conditions. Values of 6–8 are typical, which is about the same as hexane and carbon tetrachloride. Supercritical CO_2 fluid (SCF-CO_2 – critical point 31 °C, 74 bar pressure) has the advantage that it is stable, has low toxicity and minimal cost, and is a solvent for many organic materials. Liquid CO_2 is used in some clothes dry-cleaning systems.

3.2.2.2 Alkaline Cleaners

Alkaline cleaners (generally silicate and phosphate based) are saponifiers which convert organic fats to water-soluble soaps. Alkaline cleaners have a pH of about 11 and are generally used hot. After using alkaline cleaners the surface should be neutralized by an acid dip before the water rinse since alkali salts adhere strongly to surfaces. Clean oxide surfaces strongly adsorb hydrocarbons, and detergents or solvents normally do not completely remove the hydrocarbons; alkaline or oxidative cleaners must be used to remove the remaining hydrocarbons. For example, carbonized hydrocarbon contaminants on glass can be removed by cleaning in a saturated water solution of KOH at 75 °C. Strong alkaline cleaners can etch aluminum and oxide surfaces, particularly glasses, so solution strength (pH), temperature, and exposure times should be carefully controlled.

Alkaline cleaners are used to clean the oil and oxide off steel drills. After rinsing in an acid rinse they are rinsed in a final rinse containing a flash rust inhibitor to protect the surfaces from oxidation as they dry.

3.2.2.3 Detergent (Soap) Cleaners

Detergent cleaning is a comparatively mild cleaning technique. In detergent cleaning, the detergent surrounds particles, taking them into suspension without actually dissolving the material. This action is assisted by wetting agents and surfactants that loosen the particles from the surface. Liquid dishwasher soap is an excellent detergent for many applications such as cleaning polymer surfaces. A major problem with soaps is that metal ions, such as the calcium and magnesium, which are found in hard water, make the soaps insoluble thus leaving a residue. Deionized (DI) water should always be used for residue-free detergent cleaning. Many detergents contain phosphates that can be environmentally harmful and subject to pollution regulations.

3.2.2.4 Solution Additives

When cleaning a surface with a fluid, the surface energies [7] of both the solid and the liquid, as well as the interfacial energy between the two, are important in the wetting and spreading of the fluid on the surface and the ability to displace particles and other contaminants from the surface. Wetting agents reduce the surface energy of fluids. Table 3.1 shows the effect of some additives on the surface tension of water.

Surfactants are the generic name for surface-active agents that reduce the interfacial energy of materials in contact. Surfactants used with water have both hydrophobic (water-hating) and hydrophilic (water-loving) groups. They dissolve in water by virtue of their hydrophilic groups and lower the surface energy of water to about 30 mJ/m^2. The surfactant collects at the

Table 3.1: Surface tension of fluids

Material	Temperature	Surface tension (in air)
Pure H_2O	18 °C	= 73.05 mJ/m^2 (dyne/cm)
	50 °C	= 67.91
	100 °C	= 58.9
n-Propanol	25 °C	= 23.32
H_2O + 30 vol% *n*-propanol	18 °C	= 26.9
Ethyl alcohol	30 °C	= 21.5
H_2O + 50 vol.% ethyl alcohol	30 °C	= 27.5
1000 g H_2O + 34 g NH_4OH	18 °C	= 57.05
1000 g H_2O + 17.7 g HCl	20 °C	= 65.75
1000 g H_2O + 14 g NaOH	18 °C	= 101.05
1000 g H_2O + 6 g NaCl	20 °C	= 82.55

interface between immiscible substances, such as oil and water, and lower the interfacial energy. Surfactants should only be used in deionized water.

In solutions pH adjusters are used to aid in the cleaning action. In general, it is found that basic solutions clean better than acidic solutions if chemical etching is not involved. The pH of the cleaning solution is often adjusted to the basic side using ammonia or ammonium hydroxide.

Chelating agents keep the normally insoluble phosphates, which are formed in hard water detergent cleaning, in solution. Glass cleaning solutions use chelating agents such as ethylene diamine tetraacetic acid (EDTA) and citric acid with salts containing hydroxyl and amine substitutes.

3.2.2.5 Wet Reaction Cleaning

Reactive cleaning uses liquids, gases and vapors or plasmas to react with a contaminant to form a volatile or soluble reaction product. Reactive cleaning liquids are often oxidizing solutions. Many acid-based systems can be used as oxidants. One system commonly used in the semiconductor industry is the 'piranha solution', i.e. hot (50 °C) concentrated sulfuric acid plus ammonium persulfate. The addition of the solid ammonium persulfate to the hot sulfuric acid produces peroxydisulfuric acid which reacts with water to form H_2SO_5 (Caro's acid), which further decomposes to form free atomic oxygen. The ammonium persulfate should be added just before the immersion of the substrate into the solution. The effectiveness of this oxidation technique can be shown by first placing a piece of paper in the hot sulfuric acid where it is carbonized, then adding the ammonium persulfate and watching the carbon disappear. This treatment is sometimes followed by a brief dip in a 10:1 solution of water and HF or immersion for 20 minutes in a hot solution of hydrogen peroxide and ammonium hydroxide in the ratio H_2O:H_2O_2 (30%):NH_4OH (29%) at 80 °C. Another similar oxidizing solution uses stabilized sulfuric acid–hydrogen peroxide.

A hot chromic–sulfuric acid cleaning solution prepared from potassium dichromate and sulfuric acid provides free oxygen for cleaning but has a tendency to leave residues and the surface must be rinsed very thoroughly.

$$K_2Cr_2O_7 + 4H_2SO_4 \rightarrow K_2SO_4 + Cr_2(SO_4)_3 + 4H_2O + 3O$$

Nitric acid can also be used as the oxidizing agent. Nitric acid together with an oxide etchant such as hydrofluoric acid or ammonium bifluoride can be used to simultaneously oxidize and etch oxidizable material such as the silicon in some aluminum alloys.

Hydrogen peroxide is a good oxidizing solution for cleaning glass. Often boiling 30% unstabilized H_2O_2 is used. The most common hydrogen peroxide has been stabilized, which reduces the release of free oxygen. Unstabilized H_2O_2 must be stored in a refrigerator to slow decomposition. Hydrogen peroxide is sometimes used with ammonium hydroxide, to increase the complexing of surface contaminants, and is used at a ratio of:

$$8\ (30\%\ H_2O_2):1\ (NH_4OH):1\ (H_2O)$$

However, the decomposition rate of the unstabilized H_2O_2 is greatly increased by combination with ammonium hydroxide.

In cleaning silicon, the ammonical hydrogen peroxide solution may be followed by an acid rinse and this procedure is called the RCA cleaning procedure. This solution has also been shown to be effective in removing particulate contamination from a surface. The wettability of silicon in an alkaline solution is very dependent on the prior surface preparation (such as etching) and shows a profound hysteresis with the number of wetting cycles. A technique called the modified RCA cleaning technique is performed using the following steps:

1. H_2SO_4:H_2O_2 at a ratio of 4:1
2. HF:DI water 1:100
3. NH_4OH:H_2O_2:DI water 1:1:5
4. HCl:H_2O_2:DI water 1:1:5
5. DI rinse.

Oxidative cleaning can be performed using chlorine-containing chemicals. For example, a water slurry of sodium dichloroisocyanurate (i.e. pool chlorine), which has 63% available chlorine, can be used to scrub an oxide surface to remove hydrocarbon contamination. This combines mechanical scrubbing with oxidation and improves the cleaning properties.

Anodic oxidation in an electrolysis cell can be used to clean surfaces. For example, carbon fibers, which are formed by the pyrolysis of polymer fibers, have a weak surface layer. This layer can be removed by anodically oxidizing the surface in an electrolytic cell, followed by hydrogen firing. This treatment increases the strength of the carbon fiber and improves the bond when the fiber is used as part of a composite material.

3.2.2.6 Reactive Gas Cleaning

Reactive gas cleaning relies on the formation of volatile reaction products of the contaminant. Oxidation cleaning is usually accomplished using oxygen, chlorine, fluorine, ozone, NO, etc. If non-volatile products result from oxidation (e.g. silicone oil to silica), then a residue is left on the surface. Oxidation cleaning can be used on surfaces where surface oxidation is not a problem.

Reactive gas cleaning uses a reaction with a gas at high temperature to form a volatile material. For example, air firing of an oxide surface oxidizes all of the hydrocarbons and they are volatilized. High-temperature air fire is an excellent way to clean surfaces that are not degraded by high temperature. For example, alumina can be cleaned of hydrocarbons by heating to 1000 °C in air. Some care must be taken in furnace firing in that particulate generation from the furnace liner may be a source of undesirable particulates and sodium from the insulating material may be an undesirable contaminant for semiconductor device fabrication. Self-cleaning kitchen ovens clean by oxidation at about 425 °C.

The use of oxidation at atmospheric pressure by ozone (O_3) created by ultraviolet (UV) radiation, which also causes bond scission of the hydrocarbon contaminants, has greatly simplified the production, storage, and maintenance of hydrocarbon-free surfaces [8, 9]. The UV is produced by a mercury vapor lamp in a quartz envelope so that both the 1849 Å and the 2537 Å radiation is transmitted. The mercury lamps can be custom made to a variety of shapes for specific applications. Ozone adsorbs UV so the substrates should be as close as possible to the UV source. UV radiation intensity should be maintained to about 1–10 mW/cm^2 at the substrate surface. In the UV/O_3 chamber the air may be stagnant or flowing. If flowing air is used, the air should be filtered.

Typical exposure times for cleaning are from a few minutes to remove a few monolayers of hydrocarbon contamination to hours or days or weeks for storage of cleaned surfaces. The UV/O_3 cleaning technique has the advantage that it can be used as an in situ cleaning technique. The UV/O_3 cleaning technique is also useful for cleaning holes (vias) in surfaces. In a correctly operating system, ozone can be detected by smell when the chamber is opened. The smell is similar to that of the air after a lightning storm and indicates that the ozone concentration is less than 10 ppm bv. Higher concentrations of ozone deaden the olfactory nerves and are harmful.

SAFETY: OSHA has set a limit of 100 ppb of ozone in the air over an 8-hour day, 6 days per week. At these levels some irritation and discomfort will be noted. A level of 10 ppb is more reasonable.

3.2.2.7 Reactive Plasma Cleaning

Reactive plasma cleaning is a variation of reactive plasma etching (RPE) that can be done in a plasma system separate from the deposition system. Reactive plasma cleaning uses a reactive species in the plasma to react with the surface to form a volatile species which leaves the surface at much lower temperatures than those necessary for reactive gas cleaning. The additional requirement on reactive plasma cleaning is that it does not leave a residue. Oxygen (from pure (‘medical’) air), hydrogen (pure or as ‘forming gas’), fluorine (from SF_6, CF_4, CHF_3, C_2F_6, C_3F_8, or SF_6), and chlorine (from HCl, CCl_4 or BCl_3) are the most widely used reactive gases. The reactive plasma cleaning/etching technique is typically specific and can be used to selectively remove the oxide from the surface and then have a low etch rate for the substrate material. Most metals are more easily cleaned using fluorine gas rather than with chlorine, since the fluorides are generally more volatile than the chlorides. An exception is aluminum, which is commonly etched using BCl_3.

Oxygen (or air) plasmas are very effective in removing hydrocarbons and absorbed water vapor from surfaces. The reaction of the oxygen with carbon on the surface can be monitored using a mass spectrometer to monitor the CO and CO_2 produced. Figure 3.3 shows a plasma cleaning system.

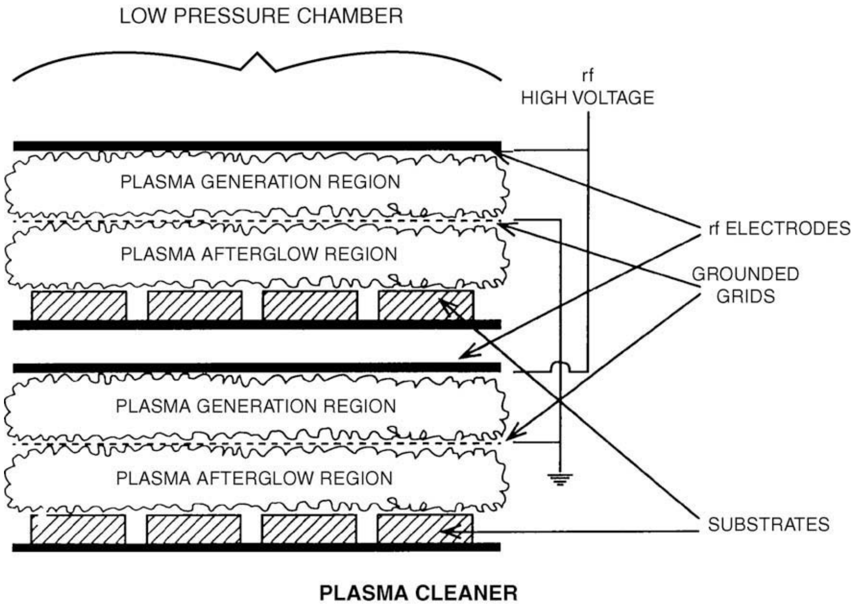

Figure 3.3: Plasma cleaning chamber. [From SVC Education Guides to Vacuum Coating Processing (2009) – Surface Preparation: Plasma Cleaning, with permission.]

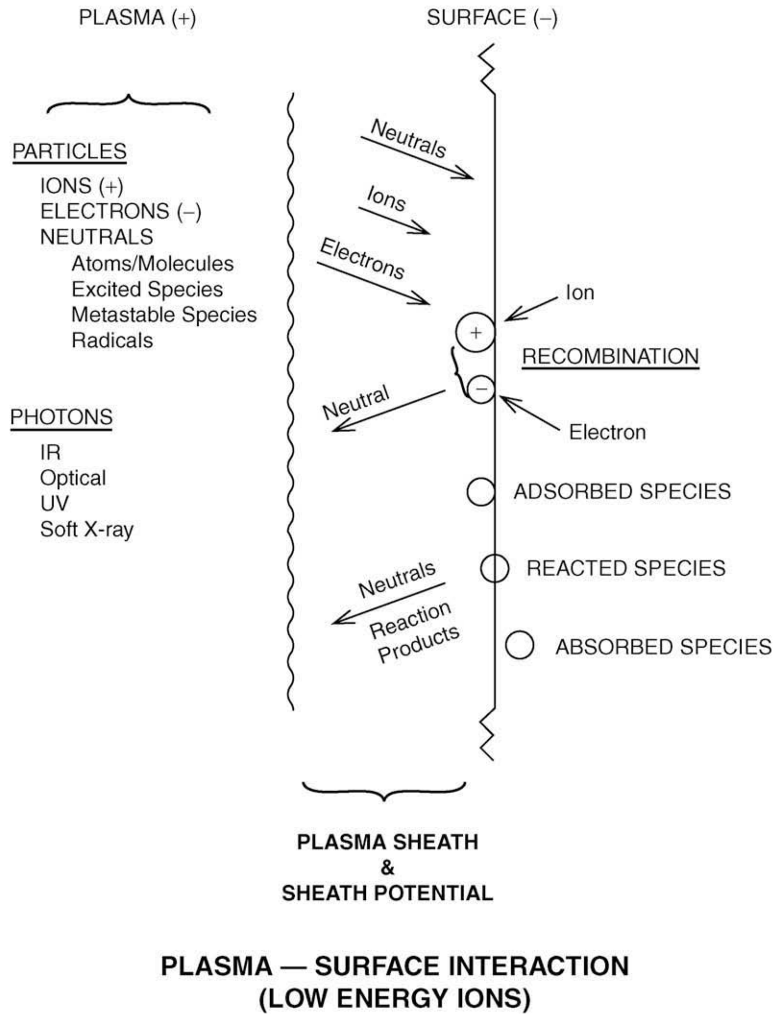

Figure 3.4: Plasma–surface interactions. [From SVC Education Guides to Vacuum Coating Processing (2009) – Surface Preparation: Plasma Cleaning, with permission.]

Figure 3.4 shows the processes that occur on a surface exposed to a plasma. The surface attains a potential (sheath potential) that is negative with respect to the plasma and ions are accelerated from the plasma to the surface. For the case of a cold plasma which has low-energy particles this sheath potential will only be a few volts. When the plasma particles are more energetic or the electrons are accelerated to the surface, the sheath potential can be tens of volts. In addition to being bombarded by ions the surface in contact with the plasma will be bombarded by activated species, excited species, and thermal species. Ions and excited species will release their energies of ionization or excitation when they impinge on the surface. For example, when a singly charged argon ion impinges on a surface it will give up its kinetic energy attained by acceleration through a potential and its ionization energy, which is 15.7 eV.[1] Locally this release of energy will generate a high local temperature. This process is sometimes called ion scrubbing.

Often mixtures of gases are used for etching and cleaning. Oxygen is often added to the fluorine system to promote the formation of atomic fluorine and thus increase the etch rate of silicon. One of the most common gas mixtures to etch silicon is 96% CF_4 with 4% O_2. A mixture of HF and H_2O can be used to removed SiO_x from silicon. Helium is often added as a diluent and to increase the thermal conductivity of the plasma, thus reducing the temperature rise of the surface during etching. Numerous gases and gas mixtures are available for RPE.

Etching and cleaning with compound gases should be used with caution since the decomposition products (B, C, Si) can react with or deposit on the surface, thereby changing the chemical composition or contaminating the surface. When using a carbon-containing chemical, e.g. CCl_4 or CF_3 in the plasma, a residual carbon contaminate often remains [10]. Using chlorine, HCl, or SF_6 avoids this problem. Exposure to reactive plasmas can leave a reacted/chemisorbed layer of halogen species. This layer can be very important to the sensitization of the surface to atomic nucleation or the wetability of organic species to a surface. RPE of silicon in CCF_4 plasmas has been reported to create a very thin fluoride layer that passivates the semiconductor surface to oxidation.

Reactive plasma cleaning is typically performed at gas pressures of 100–500 mtorr, usually using an RF-excited plasma as shown in Figure 3.3. The reactive gas can be oxygen or air (21% O_2) for cleaning surfaces that can withstand oxidation, or can be hydrogen or forming gas (90% N_2:10% H_2) for those that require a non-oxidizing environment. The surfaces to be cleaned are often placed in a region outside the plasma generation region (i.e. remote plasma region) as shown in Figure 3.3. As depicted in Figure 3.3 the plasma leaks from the plasma generation region through a grid electrode into the cleaning region.

Hydrogen plasmas can be used to remove hydrocarbon contamination when oxygen plasmas are unacceptable. This technique has been used to clean vacuum surfaces (stainless steel) in nuclear fusion reactors [11]. Hydrogen plasma cleaning using a remote plasma cleaning reactor can reduce the temperature necessary for hydrogen reduction of oxides. Such hydrogen plasmas have been shown to remove the oxide on silicon at 500 °C, rather than dry hydrogen

---

[1] An electron volt (eV) is the amount of energy attained by the acceleration of a singly charged particle (ion, ionized particle, or electron) through a potential of 1 volt. One eV is equivalent to a thermal temperature of about 11,000 °C.

firing at 900 °C. Hydrogen plasmas have been used to clean metals and semiconductor materials.

SAFETY: For reactive cleaning by oxidation, pure air (medical air) is generally used, although oxygen–gas mixtures such as O_2–Ar may be used. Be very careful if pure oxygen is used because compression of the oxygen in contact with hydrocarbon oil can cause an explosion (diesel effect) in a mechanical pump.

3.2.3 Application of Fluids

Fluids are often used in cleaning processes. There are a number of ways to apply the fluids to the surface to be cleaned. Fluid baths should be continuously filtered and monitored so as to replace or replenish the active ingredients as they are used or become contaminated. In cases of heavy oil contamination, the surface of the solution should be skimmed as contaminants such as oils rise to the surface. One method of doing this is to skim the surface with oil-absorbent (oleophilic) toweling.

3.2.3.1 Immersion

Probably one of the most widely used cleaning techniques for stubborn contaminants is soaking. Soaking involves extended times and therefore may not be a desirable technique for production. This may change in the future when less aggressive cleaning methods must be used because of environmental concerns. Immersion of a surface in a stagnant solution is generally a poor technique since the contaminants that are taken into solution are concentrated near the surface and must diffuse away. Mechanical disturbance uses agitation, wiping, brushing, or scrubbing in a fluid environment to break up the stagnant fluid layer near the surface, loosen particles, and aid in carrying contamination away from the surface. Care must be taken to ensure that any material that is used in a fluid does not produce particulates and is compatible with surfaces it contacts. When using any mechanical rubbing, care should be taken to prevent contamination by abrasive transfer from the rubbing media. Gentle pressure should be used.

A variety of brush materials is used in fluids, including: polypropylene, Teflon^{TM} and Nylon^{TM}. If wiping or scrubbing with a cloth is used, care should be taken that the cloth is lint free and desized by multiple washing before use. Special particulate-free sponge materials are available for wiping. In semiconductor technology mechanical scrubbing combined with high-pressure fluid jets (2000–3000 psi) and spinning are standard cleaning procedures.

3.2.3.2 Spraying

Liquid spray pressures can be low, at less than 100 psi, or high at several thousand psi. Spraying parameters include the type of fluid, pressure, angle of incidence, and volume of fluid. Liquid sprays should be directed at an oblique angle to the surface. Spray systems often use copious amounts of material so the fluid should be recycled. The fluid should be monitored by residue analysis, and when it is contaminated above a given level it should be replaced. With increasing concern about solvent vapors, many of the newer spray systems are self-contained with condensers to trap the solvent vapors as shown in Figure 3.2. Some systems allow the purification of the solvents by distillation. It should be noted that spraying can induce resonant vibrations that can cause component failure or deterioration.

3.2.3.3 Vapor Condensation

Vapor degreasers operate by putting a cold part in the hot vapor above a liquid solvent contained in a sump. The solvent condenses on the surface and flows off into the sump. Cleaning action only occurs during the condensation process. When the part reaches a temperature at which the solvent does not condense, cleaning stops and the part should be removed. Parts should never be immersed in the sump fluid. Fluid in the sump should be changed when it becomes contaminated. Vapor degreasers have, in the past, been open to the atmosphere so solvent vapors escape into the atmosphere. New designs use closed chambers and condensers to capture the vapors and return them to the solvent reservoir, as shown in Figure 3.2.

3.2.3.4 Ultrasonic Cleaners

Low-frequency ultrasonic cleaning relies on the jetting action of collapsing cavitation bubbles in contact with a surface to provide a high-pressure jet of fluid against the surface [12]. Ultrasonic cleaning is often a good way to remove loosely adhering particles after a grinding or abrasive procedure and can be used with solvents to remove adsorbed contaminants. The cavitation bubbles are formed by the tension wave portion of an ultrasonic wave in a fluid medium. The ultrasonic wave is produced by magnetostrictive or electrostrictive transducers(s), typically operating at 18–120 kHz, and at an energy density of about 100 W/gallon of fluid. The ultrasonic cleaner size can be from 5 gallons for a small cleaner up to very large systems using many transducers.

The size of cavitation bubbles in the fluid depends on the vapor pressure, surface energy, and temperature of the fluid. For example, water at 60 °C and 40 kHz has a cavitation bubble size of about 3 μm. The jet pressure from the collapsing bubble can be as high as 300 psi. The cavitation jetting is more energetic for cooler media and when there are no gases in the bubble to hinder its collapse. The ultrasonic energy density decreases with distance from the transducer; therefore the cavitation energy is greatest near the transducer surface. Acoustic streaming results in an overall movement of fluid away from the transducer surface (bottom of the tank). This brings contaminants that have settled to the bottom of the tank up into the cleaning region. Therefore the cavitating fluid should be continuously filtered.

When using a fixed-frequency transducer nodes and antinodes are formed (standing waves) in the fluid, which produce variations of cavitation energy with position. These standing wave patterns can be modified by reflection of the pressure waves from surfaces in the tank. This variation in cavitation with position can be overcome somewhat using swept-frequency generation. A typical system uses 40 ± 2 kHz. If frequency sweeping is not used or there are large variations of cavitation energy with position, the parts should be moved from one region to another in the tank during cleaning. The ultrasonic frequencies are above the hearing range of the human ear and the audible noise that is heard from an ultrasonic cleaner is due to vibration of surfaces in the cleaner.

Variables in ultrasonic cleaning include:

- amplitude and frequency of pressure wave (energy density, standing wave pattern)
- nature of the transducer fluid (density, viscosity, surface tension, vapor pressure)
- nature of the cleaning fluid if different from the transducer medium
- surfaces in the transducer medium that must transmit the pressure waves
- flow and filtering of the cleaner fluid
- temperature of fluid
- gas content of the fluid
- energy of cavitation implosion (temperature, pulse height of ultrasonic wave)
- cavitation density changes with position in tank
- cavitation density changes with time
- shape of the pressure pulse
- nature of ultrasonic cycle train (quiet time, degas time, cycles per train)
- geometry of the system and associated fixtures.

The temperature of the transducer/cleaning media is important, not only to degas the fluids but to enhance cleaning and maximize cavitation. For example, when using water with detergents and surfactants the optimal temperature for ultrasonic cleaning is in the range of ~ 55–$65\,^{\circ}$C.

The intensity with which cavitation takes place depends on the properties of the fluid. The energy required to form a cavitation bubble in a liquid is proportional to the surface tension and the vapor pressure. Thus the higher the surface tension of the fluid, the greater the energy required to form a bubble, and the greater the energy released on collapse of the bubble. Water, for instance, with its surface tension of about 70 dynes/cm, is difficult to cavitate. However, with a surfactant, the surface energy can be lowered to 30 dynes/cm and cavitation is easier.

Cavitation is enhanced with increasing temperature; however, the jetting energy is lessened at higher temperatures. Gases dissolved in the fluid enter the cavitation bubble and reduce the jetting energy. Solvents in particular are susceptible to dissolved gases.

Ultrasonic erosion or deformation of aluminum foil or an aluminum metallized glass surface can be used to determine the cavitation power that a surface is exposed to in the ultrasonic solution. A general rule is that ultrasonic cavitation should generate ten holes in a 1 × 2 inch area on aluminum foil of 1 mm thickness in 10 s. The cavitation intensity can be studied by observing the cavitation damage on a series of aluminum foils with increasing thickness. The damage changes from hole-generation to dimpling to pitting to no damage, with foil thickness. The cavitation intensity of an ultrasonic cleaner should be plotted as a function of position with fixtures and substrates in position since reflections from surfaces can change the cavitation energy distribution. The cavitation pattern should be checked periodically, particularly if the fixturing is changed. Some work has been done using sonoluminescence to visually monitor cavitation intensity [13].

Fixturing is very important in ultrasonic cleaning to insure that all surfaces are cleaned. In general, the total area of parts, in cm^2, should not exceed the volume of the tank, in cm^3. Parts should be separated and suspended with the surface to be cleaned parallel to the stress wave propagation direction. The parts must not trap gases which prevent wetting of the surface by the cavitating fluid. Metal or glass holding fixtures of small mass and an open structure should be used. Energy-adsorbing materials such as polyethylene or fluoropolymers should not be used in fixturing since they adsorb the ultrasonic energy.

Often the cleaning fluid is filtered in a flowing system that exchanges 25–50% of its volume per minute. This is particularly desirable when the system is used continuously. An overflow tank system can be used to continuously remove contaminants that accumulate on the fluid surface. A cascade ultrasonic system with perhaps three stations of increasing solvent or rinse water purity can be used in the cleaning process.

Ultrasonic cleaning must be used with care since the jetting action can produce high pressures that cause erosion and introduce fractures in the surface of brittle materials. For example, in high-power laser applications it has been shown that extended ultrasonic cleaning of glass surfaces increases the light scattering from the surfaces indicating surface damage. Ultrasonic agitation has been shown to create particles by erosion of the container surface. The erosion of stainless steel creates 500 times as many particles as the erosion of Pyrex^{TM} glass containers. In all cases studied, particles of the container material were produced on prolonged use. Resonance effects may also mechanically damage devices in an ultrasonic cleaner. Ultrasonic cavitation can also be a source of pitting and adhesion loss of thin films. Surface damage can be controlled by adjusting the energy density of the cavitation and/or controlling the time of application. Ultrasonic jetting is good for removal of large particles but less efficient as the particle size decreases into the submicrometer range.

High-frequency ultrasonic cleaning in the 400 kHz range does not cause cavitation. Instead, the action is a train of wave fronts that sweep across a smooth surface producing disruption of the viscous surface boundary layers on the substrate surface by viscous drag. The resulting pressure is less than 50 psi and does not hurt fragile surfaces. A high-frequency ultrasonic transducer can be focused to restrict the area of impact and allow lateral fluid flow from the area of concentration.

Megasonic cleaning uses high-frequency (>400 kHz) transducers to produce non-cavitating pressure waves. The megasonic agitation system is applicable to smooth surfaces, particularly for removing particles, but does not work on configured surfaces where the surface is shadowed from the pressure wave. The megasonic cleaning system is widely used in silicon wafer processing.

3.2.3.5 Removal of Particulate Contamination

Particulate contamination (including surface inclusions and irregularities) are a major source of pinholes in deposited films. The ability to remove particles from a surface depends on the size, shape, and composition of the particle, as well as the surface to which it adheres [14].

Removal: Mechanical

Removal of particulate contaminants from a surface is best done by mechanical disturbance in a flowing fluid environment. The mechanical disturbance should be done in a fluid environment containing detergents and wetting agents and the fluid should be continually filtered. There are a variety of brush materials. Camelhair and mohair are used for dry brushing. Polypropylene, Teflon, and Nylon are used for wet brushing. Mechanical scrubbing is often combined with high-pressure fluid jets (2000–3000 psi) as a standard cleaning procedure for particles in the semiconductor industry. Commercial particle cleaning solutions are available.

A mechanical particle removal technique is the use of high-purity CO_2 ‘snow’, formed and blown from a gaseous CO_2 cylinder. The snow mechanically scrubs the particles from the surface without leaving residuals, if the CO_2 gas is pure, or harming the surface. This technique is also reported to remove fingerprints and silicone from silicon wafers and to be as effective as solvent cleaning for the removal of hydrocarbons in many cases. The CO_2 snow technique is also used to clean the surface of aluminum coated astronomical mirrors. A major processing variable is the purity of the compressed CO_2 gas.

Removal: Blow-Off

Blow-off techniques have the advantage that they can be done after the substrates have been placed in fixtures and even in a deposition system. The best means of blow-off is to use filtered gas from a liquid nitrogen tank. The gas is filtered with a 0.2 μm or smaller filter in the nozzle and the nozzle should allow ionizing of the gas with a radioactive or electrostatic source.

Ionized gas should be used when blowing off insulator/organic surfaces to prevent electrostatic charge build-up on the insulator surface that attracts particles.

Blow-off of particulates is often done with dusters using canned pressurized gases. One environmentally friendly duster uses pressurized (and flammable) difluoroethane. Residuals from the blow-off gases should be checked, particularly with the spray can in the inverted position where liquid sprays out instead of vapor.

Removal: Spraying

The fluid sprays are generally effective for removing large particles but are not effective on submicrometer-sized particles. The jetting action by the collapsing cavitation bubble acts as a high-pressure fluid spray that displaces the particle. Ultrasonic jetting is good at removing large particles but as the particle size decreases to submicrometer the cleaning effectiveness decreases.

Removal: Megasonic

The fluid drag associated with a pressure wave moving over a smooth surface in megasonic cleaning creates turbulence that knocks particles loose from the surface. If the surface is not smooth, particles can accumulate in depressions on the surface.

Removal: Contact Cleaning

Particles can be removed from surfaces by covering the surface with a liquid polymer, allowing it to solidify then stripping the polymer from the surface. This technique is used by the optics industry to remove particles from mirror surfaces and protect surfaces from abrasion during assembly. There are many variations on strip coats, with various coatings leaving differing residues on stripping and having differing corrosion compatibility with surfaces.

Another technique for contact cleaning uses an elastomer material that picks up the particles. This technique has been used for continuously cleaning a polymer film in web coating [15].

3.2.4 Rinsing

After any wet cleaning process the surface should be thoroughly rinsed in an ultrapure liquid, usually water, before allowing to dry. This avoids leaving residues on the surface. The most common rinsing technique is to use successive rinses (cascading rinsing) in ultrapure water until the rinse water retains a high resistivity (> 12 megohm). This is called rinse to resistivity. After rinsing the surface should be dried as quickly as possible since the residual water film on the surface will cause particles to stick to the surface and on drying the particles will stick very tenaciously. Figure 3.5 shows a cascade rinse system and Figure 3.6 shows an in-line cleaning system.

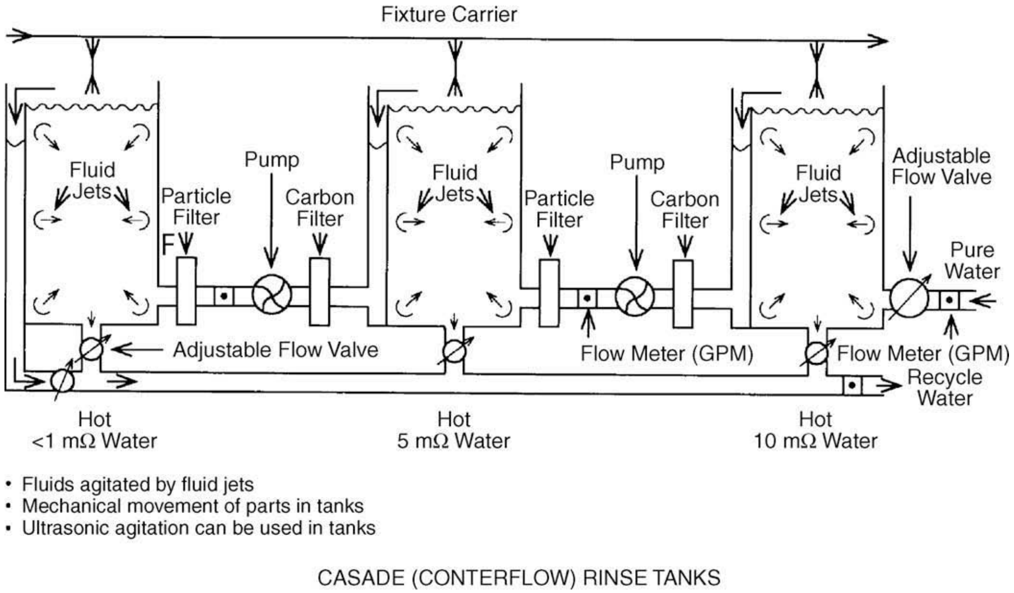

Figure 3.5: Cascade rinse system. [From SVC Education Guides to Vacuum Coating Processing (2009) – Surface Preparation: Cleaning Lines, with permission.]

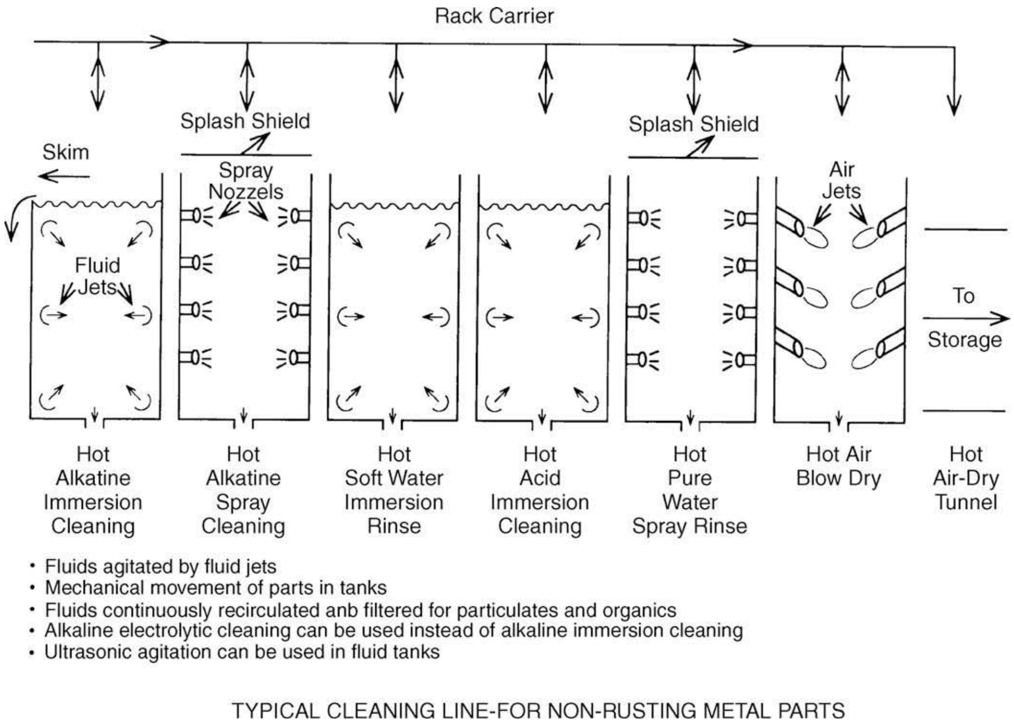

Figure 3.6: In-line cleaning system. [From SVC Education Guides to Vacuum Coating Processing (2009) – Surface Preparation: Cleaning Lines, with permission.]

3.2.4.1 Ultrapure Water

Ultrapure or deionized (DI) water (18 megohm-cm resistivity) is used for rinsing since it leaves a minimum of residues. Water purity is measured using a conductivity cell that measures the ionic concentration in the water. Spontaneous dissociation of the water molecule limits the resistivity of water to 18 megohms between electrodes spaced 1 cm apart. Conductivity measurements do not measure the organic or biological contamination and some type of residue analysis must be used to measure these impurities. There are a number of techniques for determining the nature of the contaminants.

Typical semiconductor specifications for ultrapure water for endpoint use are:

- resistivity – 18 megohm-cm continuous at 25 °C
- particle count – less than 500 particles (0.5 μm or larger) per liter
- bacteria count – less than one colony (cultured) per cm^3
- organics – less than one part per million
- total electrolytes – less than 5 parts per billion NaCl equivalent
- quantity requirements
- peak-level usage.

High volumes of ultrapure water are made by:

- pretreatment – pH adjustment, coagulation, filtration
- reverse osmosis – semipermeable membrane (pore size of 10^{-3} to 10^{-4} μm) which rejects salts, dissolved solids (90–98%), and organics (99%), and requires 150–600 psi feedwater
- degasification – removes dissolved CO_2
- ion exchange (anion and cation) – ion-exchange resins remove ions by exchanging H^+ for cations and OH^- for anions
- absorption materials (activated carbon) – remove organics
- filtration – removes particulates and biological matter – 0.2 μm for bacterial, 1.0 μm prefilter
- ultraviolet radiation or ozone bubbling – kills bacteria on filters
- endpoint filtration – 0.2 μm.

Smaller amounts of ultrapure water can be prepared by the same process using steps beginning with the ion-exchange process.

Ultrapure water should be stored or distributed in plumbing or containers using uPVC (unplasticized) or a fluoropolymer such as Teflon, or HALAR^{TM} with heat bonding or welding instead of glue bonding. In distribution systems the water should be continuously flowing or allowed to flow before use and the electrical conductivity measured at the point of use. Ozone may be injected into the water in the distribution system to continuously remove organics by oxidation.

3.2.5 Drying, Outgassing, and Outdiffusion

3.2.5.1 Drying

Drying is the vaporization of water or other fluid adsorbed on the surface or absorbed in the bulk. Porous and rough surfaces retain fluids more readily than do smooth surfaces and are more difficult to dry since the fluids are trapped in capillaries. Oxide layers on metals are often porous and retain fluid molecules readily. Drying by removal or displacing the water has the advantage that when the water is removed it takes the bulk of the potential residues with it, whereas vaporization of large amounts of fluid concentrates the potential residues giving a water spot of residue. After fluid cleaning and rinsing it is important to dry the surface quickly to prevent the water film from collecting particles. Drying can be done in the following ways.

Drying: fluid

Anhydrous alcohol, such as isopropyl alcohol (IPA), anhydrous ethyl alcohol denatured with acetone or methanol, or a commercial drying agent are good drying agents. They displace the water and when the surface is removed from the fluid the surface dries rapidly. Drying fluids should be residue free and should be discarded or recycled as they take up water, either from the drying process or from the ambient. The water content of the drying fluid can be monitored by its specific gravity or by monitoring the infrared adsorption peak for water.

One of the best drying techniques is an alcohol vapor dry where the cold surface is immersed in the vapor above a heated anhydrous alcohol sump. The cold surface condenses the alcohol vapor that flows off into the sump taking water and particulates with it. When the surface becomes hot, condensation ceases and the hot surface, when withdrawn, dries rapidly. This should be done in a closed recirculation system as is shown in Figure 3.2.

Drying: mechanical

Surfaces may be dried by spinning at a high velocity (> 2000 rpm). The equipment for high-velocity spinning is common in the semiconductor industry where spinners are used to coat surfaces with photoresist. Spin drying tends to leave liquid along the outside edges of the substrate which can produce contamination in this area unless copious amounts of pure fluids are used. This technique can leave a thin layer of water on the surface.

Drying: blow-off

Fluids can be blown from the surface using a low- or high-velocity gas stream. This technique has the advantage that the fluid takes most of the potential residues with it as it is blown from the surface. When using nitrogen as the blow-off gas, it is best to obtain the nitrogen from the vapor above liquid nitrogen in a Dewar flask next to the workstation and transport the nitrogen through fluorocarbon or stainless steel tubing. When blowing, a nozzle with a 0.2 μm or smaller particulate filter should be used in the nozzle. In addition, when drying insulator surfaces the gas should be ionized to prevent charge build-up on the surface. The gas can be ionized with an electrostatic (corona), laser or nuclear (Polonium-210) ionizer. Electrostatic ionizers can arc and produce particulates. Nuclear ionizers are not sold any more but can be leased.

A high-velocity jet of gas can be shaped to blow-off a moving surface. The jet is often shaped into a long, thin configuration and this ‘air knife’ is used to remove fluid from a moving surface such as a large glass plate. Exiting the air knife the gas velocity can be as high as 35,000 fpm (feet per minute). The jet should hit the oncoming wet surface at about a 30° angle. At the trailing edge a droplet will form and spread back over the surface when the jet has passed, so the water on the surface should be ultrapure. The size of the droplets can be reduced by reducing the surface tension of the water by the addition of alcohol. This technique leaves a thin layer of water on the surface so subsequent heat drying may be necessary.

Drying: thermal

Water can be removed from a surface by evaporation. The most common means is to use vacuum baking or gas drying in a hot oven. The vacuum environment aids in evaporation but a circulating gas dryer is most often used. This technique suffers from the fact that the residue is concentrated as the water dries, leaving a water spot unless the water is very pure.

SAFETY: See CRC Handbook of Laboratory Safety (2000) [16]; A Comprehensive Guide to the Hazardous Properties of Chemical Substances (2007) [17].

3.2.5.2 Outgassing

Volatile material from the bulk of the material is removed by outgassing. Outgassing involves the diffusion of the material to the surface and vaporization from the surface. Heating should be such as not to decompose the material. The material can be heated in a hot oven or by microwave absorption which heats the water directly. The outgassing rate is increased by heating in a vacuum. A common mistake is to not allow sufficient time for outgassing the material. The time–temperature environment for outgassing should be determined using weight-loss measurements or by analysis of the outgassing ambient. Often outgassing can take

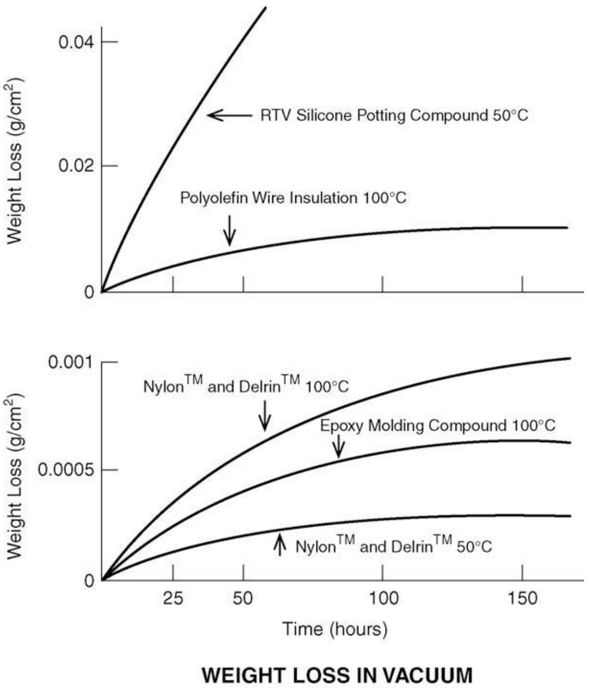

Figure 3.7: Typical ougassing curves. Note the long times needed for outgassing. [From SVC Educational Guides to Vacuum Coating – Surface Preparation: Cleaning Lines, with permission.]

hours or days, particularly if the material is thick and/or the temperature is low. Figure 3.7 shows some typical outgassing curves.

3.2.5.3 Outdiffusion

Outdiffusion is the diffusion of material to the surface that is not volatilized. This material must be removed by surface cleaning techniques. In some cases where there is a lot of such material in the bulk, the surface may have to be cleaned many times before an acceptable contaminant level is attained.

In some cases the diffusing material may be sealed in using a surface barrier layer (basecoat) such as a UV curing polymer.

3.3 Evaluating and Monitoring of Cleaning

In order to have a reproducible cleaning process it is necessary to have process documentation that is followed faithfully.

3.3.1 Cleaning Tests

The best monitoring technique for cleaning is the ability of the process to provide surfaces that can be processed in an acceptable manner. The testing of a surface invariably results in contamination of the surface, so tested surfaces generally cannot be used for subsequent processing. In some cases witness sample surfaces can be tested for certain properties to determine surface conditions. These tests include the following.

3.3.1.1 Test: Sheeting

The cleanliness of smooth surfaces can be determined during the rinse operation by observing the wetting and sheeting of water on the surface. Sheeting is the flow of the water over the surface as it drains, giving a smooth water surface. If there is hydrophobic contamination on the surface the water will avoid that area and the sheet of water will break up. This test is often called the water break test [18].

3.3.1.2 Test: Contact Angle

A common check on the cleaning of a glass surface uses the contact angle of a liquid drop on the surface of the cleaned glass. If the surface is clean it has a high surface energy, and the liquid wets and spreads over the surface. In the case of water on a clean glass surface the contact angle is less than 5° as measured with a contact angle goniometer [7]. This technique must be used with some care since, if a hydrophilic contaminant, such as a soap residue, is present, the contact angle may be low even though the surface is contaminated. For sensitive characterization of surface energies, liquids of various surface tensions can be used. Liquids of 30–70 dynes/cm (as per ASTM D-2578) are available. Advancing and receding contact angle behavior can be studied using systems that add or remove fluid or tilt the substrate.

The surface energy of a surface can be determined using liquids having various surface energies and determining the contact angle (ASTM D-2578-84). When using the dyne test make sure that the dyne solutions do not dissolve the surface layer or chemically react with the surface. The dyne test can also be performed using marking pencils having various dyne inks.

3.3.1.3 Test: Nucleation

A smooth clean surface will give uniform nucleation of a vapor on the surface. A common test is to breathe on the surface and look at the nucleation pattern. This is called the black-breath test [18]. For example, nucleation of water on the mirror in a shower room will show up the swipes where the mirror surface has not been cleaned very well.

3.3.1.4 Test: Adsorption and Desorption Behavior

Absorption of a tracer material such as a fluorescent dye or radiochemical (e.g. MESERAN$^{\text{TM}}$ technique) can be used to detect the presence of many contaminants. Evaporative rate analysis

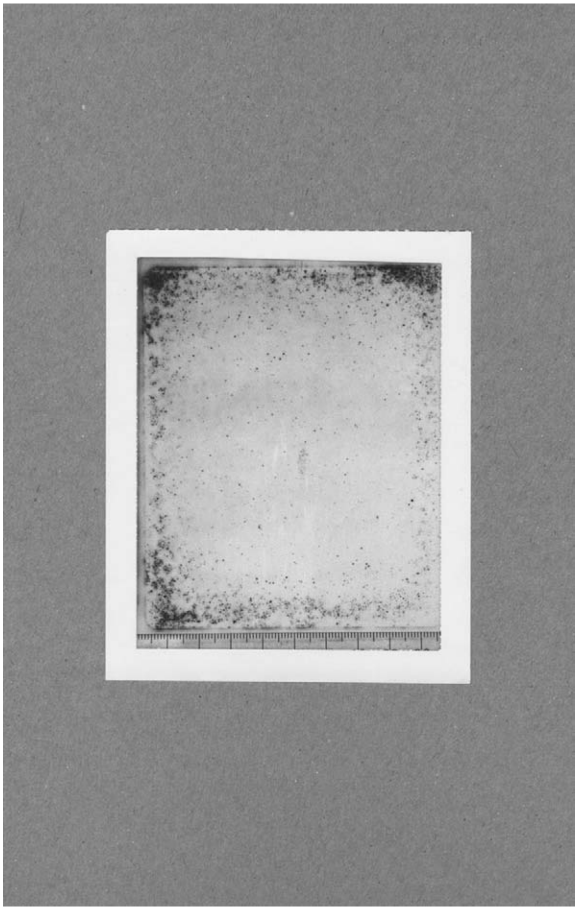

Figure 3.8: ^{85}Kr autoradiography of a cleaned 94% alumina surface. The black areas are where retained contamination has absorbed the ^{85}Kr. Centimeter scale.

may be used to characterize surfaces and contaminants. Figure 3.8 shows the adsorption of the radioisotope ^{85}Kr on a fused alumina surface as determined by autoradiography [19]. Residual contamination after cleaning adsorbs the ^{85}Kr, which then exposes the film use in autoradiography.

3.3.1.5 Test: Friction and Marking

A clean glass surface has a high coefficient of friction that can be detected by feel (squeaky clean). If the surface feels slick then it is probably contaminated. One type of friction test is the marking test where materials having various surface energies are rubbed on a surface. There is adhesion and abrasive transfer if the surface is of higher surface energy than the marking material. For example, indium writes on clean glass.

3.3.1.6 Test: Extraction and Analysis

Contaminant material may be extracted from a surface and analyzed. Ionic contamination changes the electrical conductivity of water and the conductivity can easily be monitored. Non-ionic materials can be determined by residue analysis.

3.3.1.7 Test: Surface Analytical Spectroscopies

Surface spectroscopies such as Auger electron spectroscopy (AES), ion scattering spectroscopy (ISS), secondary ion mass spectroscopy (SIMS), and X-ray photoelectron spectroscopy (XPS) can be used to characterize contamination levels on very small areas. Problems with the use of these techniques for cleaning evaluation include the small area analyzed and the potential for recontamination before the analysis can take place. When only a small area is analyzed the true contamination condition of the total surface can be misjudged. The surface spectroscopies are quite useful in detecting and identifying heavy elemental contaminants that cover a surface, particularly in the semiconductor industry.

3.3.2 Particle Detection on Smooth Surfaces

Particulate contamination on smooth surfaces such as polished silicon wafers can be detected by observing scattered light with an optical microscope or by using a scanning laser microscope which integrates all the scattered light. Laser scattering is a sensitive technique and is capable of detecting particles as small as 0.2–0.15 μm in diameter with a probability of 90–50% respectively. Using angle-resolved light scattering it is possible to obtain compositional and morphological data on the particle. Scanning interferometry can also be used to detect particles on smooth surfaces. Ultraviolet luminescence can be used to detect some types of particles.

Particles on surfaces can be observed using scanning electron microscopy (SEM) and in special cases transmission electron microscopy (TEM). Compositional analysis of inorganic particles can be done using the SEM in the EDAX mode (SEM/EDAX) and by small area electron diffraction in the TEM.

3.3.3 Particle Detection on Rough Surfaces

Particles on rough surfaces can only be detected by extraction techniques. For example, a strippable coating or tape can be applied and removed taking the particles with them. A particle count can then be made and the particles identified. The particles can be removed from the surface by ultrasonic cleaning, collected, and identified.

3.4 Recontamination in the Ambient Environment

An integral, and often neglected, aspect of cleaning, is that of handling and storage before the next processing step or usage. Handling and storage during processing and after cleaning are major sources of contamination and recontamination. It is not unusual to see a carefully cleaned substrate placed into a plastic bag where it is recontaminated by the polymer – either by the volatile constituents in the polymer or by abrasive transfer. The best procedure is to integrate the cleaning line with the deposition process so as to eliminate or minimize handling and storage. For example, in metallizing compact discs (CDs) the molded disc is taken directly from the molding machine into the deposition system, where it is individually metallized with a cycle time of less than 3 s. Another example is the metallizing of mirrors, where the glass is scrubbed, rinsed, and dried in-line with the metallizing system [3].

3.4.1 Ambient Environment

Clean surfaces are very reactive and easily recontaminated. Recontamination can occur from the adsorption of vapors, collection of particles, contact with other surfaces, or reaction with reactive gases. Important aspects of cleaning are the conditions existing in the processing area, the handling of the surfaces, and storage of the cleaned part. Dust is a particular concern in many instances since particulates on the substrate surface will result in pinholes in the deposited film. Figure 3.9 shows the recontamination of a clean gold surface in a very clean environment, a typical cleanroom environment, and a machine shop environment as determined

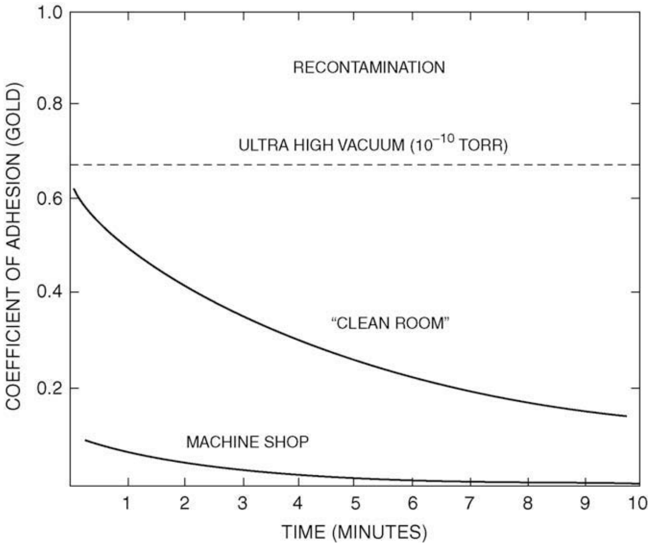

Figure 3.9: Recontamination of cleaned gold surfaces in several environments [20].

by coefficient of adhesion measurements between gold surfaces [20]. The recontamination is primarily by the adsorption of hydrocarbon vapors on the clean gold surfaces.

Avoidable contaminants in the processing area include large and small particulates, some vapors, and some reactive gases such as chlorine. The least expensive action that should be taken to reduce contaminants in the processing area is to remove as many sources of contaminants as possible. This can mean good housekeeping, separation of contaminant-producing processing from the cleaning area, elimination of particulate-producing materials, and elimination of vapor-producing materials such as many molded plastics and vinyl coverings. Personnel doing the cleaning should not use particulate-producing products such as mascara or body powders.

Vapor contamination is generally not controlled in the processing environment except by ventilation, construction, and segregation of vapor-producing processes such as soldering, etching, and electroplating from the clean area. Vapor-producing and aerosol-producing processes should be performed in ventilated work areas such as chemical hoods. Some filter systems use activated carbon to filter organic vapors. Activated carbon is an amorphous material with a high surface area (500–1500 m^2/g). For use in gases, it has a pore size of 12–200 Å. Activated carbon has a high affinity for the absorption of organic molecules. It is better for adsorbing non-polar molecules than polar molecules. Catalytic agents (Cu, Ag, Cr) in the activated carbon can be added to improve the absorption of complex organic molecules and are used in gas mask filters.

Another action that can be taken to reduce contamination is to contain contaminant-producing sources as much as feasible. Humans and their clothing shed large amounts of particulates that are pumped out through the loose weave of the clothing as the person moves about. The use of head coverings, facial hair coverings, and coats or coveralls (bunny suits) of tightly woven long-fiber cloth will contain the particulates somewhat. In particular, the hair and mouth should be covered since the head is often over the surface being processed.

Cleanrooms and clean areas are generated by using mechanical filtering of the air along with control of the air flow pattern [21, 22].

3.4.2 Handling

It is preferable to handle surfaces using fixtures or tools; however, in many cases the surfaces must be handled directly and gloves may be used. Gloves may be of a woven fabric or of a polymer film that is either molded to shape or heat welded from flat sheet. Polymer gloves for general use are often powdered to make donning the gloves easier, but for cleaning applications unpowdered gloves must be specified in order to avoid particulate contamination. Glove lengths can vary from wrist-length to elbow-length.

There are a number of choices for polymer glove material, including latex rubber, nitrile rubber, vinyl, polyethylene, and fluorocarbon materials such as Teflon, as well as polymer blends such as latex–nitrile–neoprene–natural rubber blends for use with acids. All glove material should have low extractables for the chemicals with which they may come into contact. Vinyl gloves are comfortable and are often used in handling surfaces. A problem with the vinyl is that when in contact with alcohol, a common wipe-down material and drying agent, the alcohol extracts phthalate plasticizers from the vinyl. Those extractables on the glove surface can then contaminate surfaces. It is generally best not to have vinyl gloves in the cleaning area.

Unplasticized polyethylene gloves are compatible with alcohol and most cleaning chemicals and are good gloves for clean handling. A disadvantage of polyethylene gloves is that they are rather awkward and uncomfortable and operators will readily discard them when they are not required. Latex or nitrile rubber gloves are often used in suiting-up for the cleanroom. A problem is that is they are then used all day long, thereby transferring contamination from one place to another. When handling clean surfaces an unplasticized polyethylene glove should be put on over the latex glove and then discarded when the handling is over. A disadvantage of the polymer gloves is that the soft polymer can be easily transferred to a clean surface by abrasive transfer. Abrasive transfer is dependent on the materials and the adhesion and friction between the surfaces. Another disadvantage of the polymer gloves is that they are slippery and it may be desirable to use fabric gloves such as Nylon when handling large or heavy parts.

Desized and lint-free Nylon or Dacron^{TM} woven fabric gloves are used when friction in handling is desirable or abrasive transfer from softer polymer gloves is a problem. Woven fabrics will wick oils from the skin to the glove surface, so polyethylene or latex gloves or finger cots should be used under the fabric gloves.

3.4.3 Storage

Cleaned surfaces should be stored in a non-recontaminating environment. Often surfaces to be stored are held in clean fixtures to reduce the necessity for handling the surfaces directly. The fixtures must be compatible with the storage environment. Non-contaminating storage environments can be passive or active.

3.4.3.1 Storage: Passive

Passive storage environments are those which have been carefully cleaned. A commonly used passive environment is a clean glass container such as a Petri dish. Clean surfaces can be stored by wrapping them in a clean material. Wrapping the surfaces in clean Nylon fabric or clean aluminum foil works well. Usually it is best to avoid wrapping in paper or polymer wrap because of contaminants in the material and abrasive transfer of contaminants. A simple method of passive storage is to place cleaned surfaces in contact with one another. This has been called wafer bonding in the semiconductor industry.

Cleaned parts may be stored under liquids to exclude reactive gaseous agents. Metals stored in anhydrous liquids such as anhydrous alcohol or anhydrous acetone do not reoxidize as rapidly as if they were exposed to the atmosphere. Storage of surfaces in degassed (boiled) water decreases the oxidation of the surface compared to water containing dissolved air (cold water).

In some cases the surface condition can be preserved by covering the surface with a liquid polymer, allowing it to solidify and then stripping the polymer from the surface when the surface is to be used. This technique is used by the optics industry to protect optical surfaces from abrasion and particulate contamination during assembly. Various strippable coatings leave differing residues on stripping and have differing corrosion compatibility with surfaces.

3.4.3.2 Storage: Active

Active storage environments are those where the contaminants are continually removed from the storage environment by adsorption or reaction. Hydrocarbon adsorption can be on freshly oxidized aluminum or activated carbon. Hydrocarbon contaminants can be continually removed by having an oxidizing atmosphere. A UV/O_3 cleaning cabinet provides such an environment [8, 9]. The UV/O_3 cleaning chamber is by far the best technique for storing surfaces where surface oxidation is not a problem.

For some storage applications moisture is the main contaminant to be considered and an actively desiccated environment is desired. Common desiccants include:

- silica gel
- phosphorous pentoxide (P_2O_5)
- magnesium perchlorate ($Mg[ClO_4]_2$).

Phosphorous pentoxide is probably the most effective desiccant material. It should be used to reduce particle formation. Desiccants must be used with care since they tend to be friable and produce particulates. It is best to isolate the desiccants from the storage chamber by means of a particle filter.

3.5 In Situ Cleaning

In situ cleaning is done in the deposition system and is intended to remove the small amount of contamination that has developed since the external or primary cleaning process was performed. The most common in situ cleaning techniques for PVD processing are as follows.

3.5.1 Sputter Cleaning

At low gas pressures of 1–10 mtorr the mean free path for particle collision is long and the ions from a plasma can be accelerated to high energies before they impinge on a surface. Figure 3.10 shows the effect of this energetic particle bombardment on the surface and near-surface region of a material [23]. The energy and momentum transferred from the bombarding particle to surface atoms creates a collision cascade in the near-surface region. Much of this energy becomes heat but some energy can be transferred to surface atoms causing them to be physically ejected. This non-thermal vaporization is called physical sputtering or just sputtering.

Sputter cleaning uses sputtering to remove the surface layer, which includes the contaminants. Sputtering has been called the universal etch since conceptually everything can be removed by the sputtering process. However, certain types of surface contamination, such as inorganic particles and inclusions, are difficult to remove by sputtering. Electrically conductive surfaces can be sputtered using an applied DC potential. The sputtering potential on electrically insulating surfaces must be applied with an RF field, a pulsed DC, or by generating a high self-bias on the surface.

Often a major problem with sputter cleaning is to have a uniform bombardment over the surface to be cleaned. In areas where the bombardment is low, contaminates may accumulate by redeposition from areas being cleaned. Sputter cleaning configurations can be tailored to

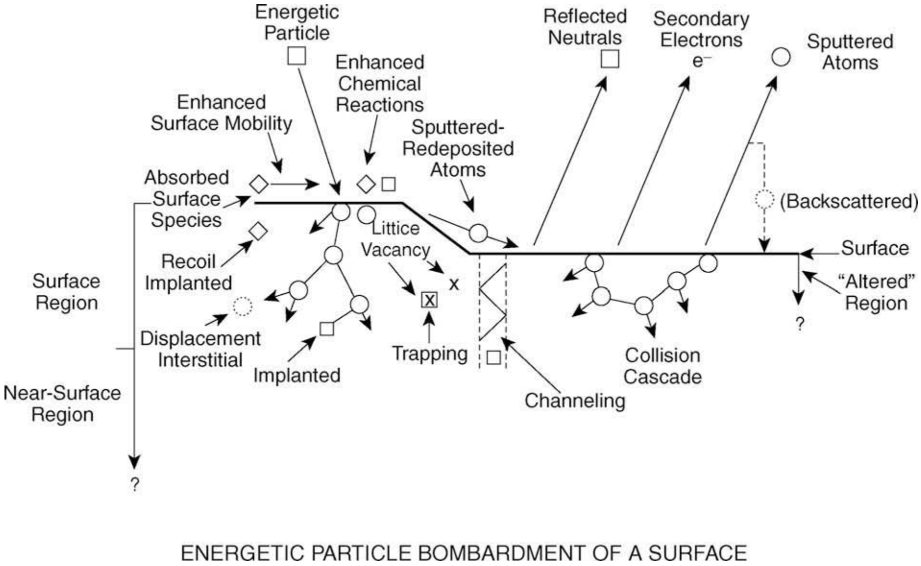

Figure 3.10: Processes that occur on a surface and in the near-surface region of a surface being bombarded by energetic atomic-sized particles [23].

the surface being cleaned in much the same way as are sputtering targets in the physical vapor deposition (PVD) process of sputter deposition (see Chapter 5).

During sputter cleaning the bombarding gas can become incorporated into the surface and subsequently released on heating. In thin film deposition technology this can cause loss of adhesion of films deposited on the bombarded surface. To avoid this problem, the substrate should be heated during bombardment or before film deposition to prevent or remove gases included in the substrate surface. Sputtering from a plasma environment has the disadvantage that contamination, such as oxygen, in the plasma becomes activated and can react with the surface being cleaned. One way to avoid this problem is to sputter clean the surface in a good vacuum using an ion source (ion gun) where the ions are formed in a plasma and then extracted and accelerated through a grid electrode system into the processing chamber. Both inert (e.g. argon) and reactive (e.g. oxygen) ions can be formed in ion guns.

This cleaning process can be easily integrated into the deposition process so as to have no time for recontamination between the cleaning and the deposition process, as in the ion plating process (Chapter 6).

Often a major problem with sputter cleaning is to have a uniform plasma over the surface to be cleaned. If the plasma is not uniform the surface will not be cleaned uniformly. In areas where the bombardment is low, contaminates may accumulate by redeposition from areas being cleaned.

3.5.2 Ion Scrubbing

Ion scrubbing of a surface occurs when a surface, which is in contact with an inert gas plasma, develops a wall sheath and is bombarded by inert gas ions accelerated across this wall sheath, where it gives up its kinetic energy as well as its energy of ionization. The plasma-surface effects are shown in Figure 3.4. The ion energy is generally too low to cause surface damage or physical sputtering but does aid in desorption of the adsorbed surface contaminants.

3.5.3 Reactive Plasma Cleaning

When there is a reactive gas such as oxygen or hydrogen in the plasma, ion scrubbing can cause chemical reactions that create a volatile compound of the contaminant. This plasma cleaning process using air or oxygen is widely used in the optical coating industry for substrate preparation in the vacuum deposition system using a DC air discharge. When generating a DC plasma in a system for cleaning purposes, the cathode should be hidden from the surface to be cleaned and the discharge pressure should be high enough to prevent high-energy reflected neutrals from bombarding the surface, i.e. 10 mtorr or higher.

A glow bar is a high-voltage cathode used for generating a plasma for plasma cleaning at a gas pressure of a few micrometers up to several torr. A glow bar often can be found in deposition

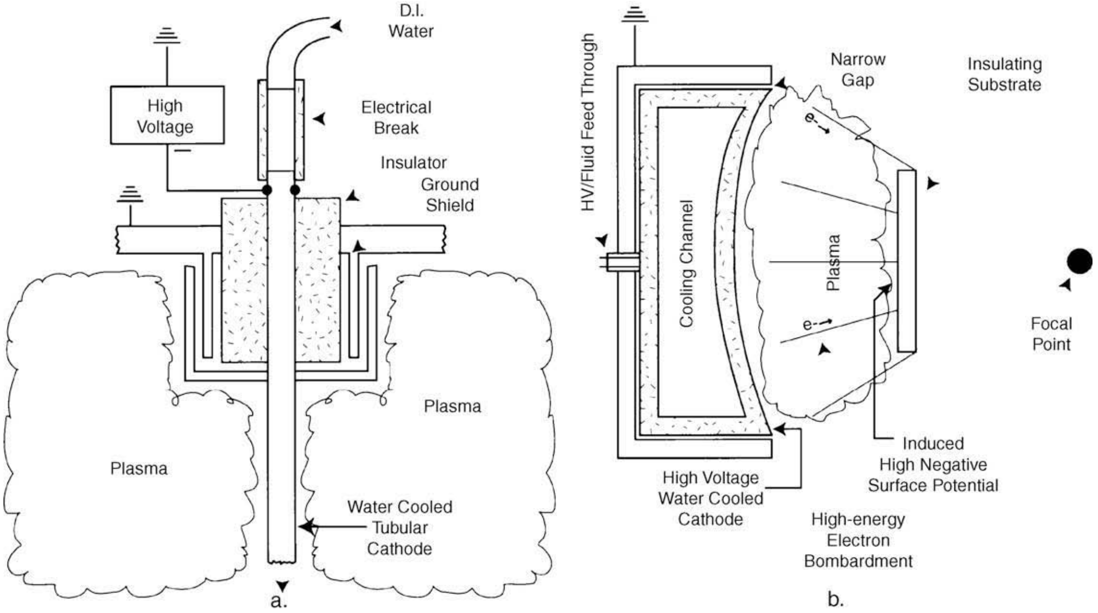

Figure 3.11: (a) Shielded high-voltage feedthrough for use with a glow bar. The gaps between the shields should be less than the cathode dark space distance. (b) Watercooled shaped glow discharge cathode where the active surface is defined by the conformal ground shield. The focused and accelerated electrons from the cathode increase the shield potential at the substrate surface. [From SVC Educational Guides to Vacuum Coating – Surface Preparation: Glow Bars for Plasma Cleaning, with permission.]

systems, such as in optical coating facilities using thermal evaporation, where the deposition takes place in a good vacuum. Figure 3.11 shows a feedthrough design for a glow bar and a shaped cathode design for plasma cleaning.

Low-energy ion bombardment can be used to clean surfaces without electronic damage of semiconductor materials. The ions may be accelerated to the surface under an applied potential or a self-bias. The low-energy ion bombardment can be obtained from high-pressure plasmas, in downstream processing with low biases, and with low-energy ion beams. In silicon technology low-energy (2 ev) bombardment is effective in removing adsorbed contaminants but is unable to remove the oxide.

In a simple DC diode (non-magnetically confined) discharge, electrons are accelerated away from the cathode. These establish the plasma, but also many of the electrons reach high energies and bombard any surface on which they impinge. Thus, the glow bar provides three possible cleaning mechanisms: (1) plasma cleaning, which occurs on all surfaces in contact with the plasma; (2) electron bombardment of surfaces facing the cathode; and (3) on an electrically floating or electrically insulating surface the electron bombardment can generate a self-bias that accelerates ions to the surface (see Chapter 6, Figure 6.9).

Figure 3.4 shows the cleaning processes that occur at the surface in contact with a plasma. Photon irradiation, hot gases and energy from de-excitation and deionization can cause volatile species to desorb from the surface, while the UV radiation can cause chemical bond scission and volatilization of some species. The sheath potential accelerates positive ions from the plasma and these energetic species can ion scrub the surface to remove contaminants. Reactive species from the plasma can react with the contaminants on the surface, forming volatile reaction products that leave the surface. For example, oxidized hydrocarbons will volatilize as CO, CO_2, and H_2O. Reaction with no volatilization will leave a residue on the surface. For example, if silicone oil is present on the surface, an oxygen plasma will oxidize the oil to SiO_2, which will remain on the surface as a residue.

If a hydrogen plasma is used for cleaning, the hydrocarbon contaminants are hydrogenated to more volatile hydrocarbon species such as acetylene (C_2H_6). The amount of volatile species formed by reactive plasma cleaning can be monitored using a differentially pumped mass spectrometer.

Other reactive gases, such as those containing fluorine or chlorine, can be used to remove oxide layers from materials. For example, a CF_4 plasma is used to preferentially remove silicon oxide from silicon. The addition of oxygen to the CF_4 plasma allows rapid etching of silicon since the oxygen plasma continuously reacts with the silicon surface to form the oxide. When using reactive gases for plasma cleaning, care should be taken that the vacuum pumping oils are compatible with the gases being used. For example, pure oxygen should never be pumped using hydrocarbon oils in an oil-sealed mechanical pump, as an explosion can occur.

Reactive plasma cleaning is typically done at gas pressures where the plasma particle density is high and the mean free path for collision is small. Under these conditions it is impossible to accelerate ions to high kinetic energies in an electric field.

Reactive plasma cleaning and sputter cleaning can often be integrated into the processing line. Reactive plasma cleaning using an oxygen plasma is more rapid than the ultraviolet/ozone cleaning (UV/O_3) cleaning process, although the processes are very similar.

SAFETY: When using an electrically isolated metal chamber, be sure to turn off the plasma power supply before venting the chamber. If you do not, the chamber may lose its ground as the chamber is vented, allowing the O-ring to expand. The plasma will attempt to take the now electrically floating surface to the cathode potential, giving a high voltage on the metal chamber. To prevent this, the chamber can be grounded at all times or the plasma supply turned off before the chamber is vented.

3.6 Recontamination in the Deposition System

Particulates in a deposition system are generated during use from a variety of sources, including:

- general and pinhole flaking of deposited film material on walls and fixtures
- wear debris from surfaces in contact, i.e. opening and closing valves
- debris from maintenance and installation, i.e. insertion of bolts, wear of handtools, motor tools, and from personnel and their clothing
- unfiltered gas lines
- particulates brought in with fixtures and substrates
- particulates brought in with processing gases and vapors
- particulates formed by gas-phase nucleation of vaporized material or decomposed chemical vapor precursors.

Film build-up on walls and fixtures may flake as it becomes thick, particularly if the film material has a high residual stress. For example, sputtering $TaSi_2$ produces a large number of particulates because the deposited material is brittle and is generally highly stressed. One way to alleviate the problem somewhat is to occasionally overcoat the brittle deposit with a softer material such as aluminum. Pinholes form in films on surfaces producing flakes and this source of particulates is called pinhole flaking. Liners which may be easily removed and cleaned or discarded to prevent deposit build-up should be used. Heating or mechanical vibration of surfaces contributes to flaking and wear.

The control of particulate contamination in a system is very dependent on the system design, fixturing, ability to clean the system, and the gas source/distribution system. The use of dry lubricants decreases wear and particle generation. In particular, bolts used in the vacuum chamber should be silver plated to prevent wear and galling. Some types of plasma etching processes generate large amounts of particulates.

Hydrocarbon vapors in the deposition chamber can originate from the vacuum pumping system. Pump oil and lubricant vapors can backstream into the system. Backfill gases can contain oil vapors from the ambient environment. This type of contamination can be detected by placing a clean glass slide in the system, going through the pumping (and heating) sequence, and then checking the wetting angle on the glass surface. If vapor contamination is suspected or detected the system can be cleaned using an air plasma discharge.

The most common vapor in a good vacuum system is water vapor. The water molecule is highly polar and is strongly adsorbed on clean metal and oxide surfaces. Water vapor often presents a major variable in many PVD processes. Water and water vapor in the vacuum system affect the pumpdown time and the contamination level during the deposition process. Water vapor is much more difficult to pump away than a gas because the water vapor molecule has a long residence time on a surface compared to the gas molecule. Thus, if many adsorption–desorption collisions are necessary for the water molecules to reach a pump, the time to reduce the chamber pressure to a given base pressure will be long compared to an open system.

The best procedure for eliminating water vapor in the vacuum chamber is to prevent its introduction in the first place. This can be done by: (1) backfilling with a dry gas; (2) reducing the time the system is open to the ambient; (3) maintaining a flow of dry gas through the system while it is open; (4) keeping the chamber walls and surfaces warm to prevent condensation; and (5) drying and warming the fixtures and substrates before they are introduced into the chamber. Large volumes of dry gas can be obtained from the vaporization of liquid nitrogen (LN_2) usually from above the LN_2 in a tank (1 liter of LN_2 produces 650 liters of dry gas at STP), by compression and expansion of air, or by using high-volume air dryers. Gas dryers dry gas by desiccants, refrigeration, or membrane filtering.

When introducing substrate materials that can absorb moisture, such as many polymers, the history of the material may be an important variable in the amount of water vapor released by outgassing in the deposition chamber, as shown in Figure 3.7. In this case the history of the material must be controlled and perhaps the materials outgassed before they are introduced into the deposition chamber. In some web coaters, the web material is unwound in a separately pumped vacuum chamber before it is introduced into the deposition chamber. This isolates the deposition chamber from most of the water vapor released during the unrolling operation.

Contamination from the processing gas can come from an impure gas source or contamination from the distribution line. Distribution lines for gases should be of stainless steel or a fluoropolymer to reduce contamination. Gases can be purified near the point of use using cold traps to remove water vapor or purifiers to remove reactive gases. Purifiers may be hot metal chips or cold catalytic nickel surfaces and should be sized to match flow requirements. Reactive gases can come from the ambient processing environment around the system.

Often the process itself introduces contamination into the deposition system. This contamination can be associated with removable surfaces such as fixtures, the source material, the substrate material, or with processes related to the deposition process itself such as ultrafine particles from vapor-phase nucleation of the vaporized source materials. Surfaces and materials that are to be introduced into the deposition system should be cleaned and handled commensurate with the contamination level that can be tolerated.

3.7 Some Surface Modification Processes

3.7.1 Ex Situ Surface Modification

3.7.1.1 Surface Morphology

Basecoats: polymer

Polymer basecoats such as the UV curing epoxies are used not only to flowcoat and smooth a surface but also to seal in materials that can outgas or outdiffuse from a polymer substrate.

Surface chemistry

There are several ways to treat polymer surfaces and increase their surface energy or modify the functional groups on the surface to make them more amenable to adhesive bonding to another polymer or to a metal. These treatments include flame treatments, corona (atmospheric) treatments, and plasma treatments. In vacuum coating technology, flame or corona treatments are the most common external treatments, while plasma treatments are the most common for in situ treatment in the deposition system [24].

Surface hardness

In addition to changing the surface morphology and chemistry, the hardness of the near-surface region can be changed by diffusion. Diffusion hardening can be done by high-temperature pack cementation or by plasma-enhanced gaseous diffusion (e.g. ionitriding) [25–27]. Table 3.2 gives some typical values of hardness and thicknesses (case depth) formed by high-temperature diffusion [2].

Surface barrier layers

Float glass is generally a soda lime glass and is a common substrate material. A problem with float glass in some cases is the diffusion of sodium out of the glass and into the film during

Table 3.2: Hardening of surfaces by diffusion [2]

Treatment	Substrate	Microhardness	Case thickness (kg/mm^2)
Carburizing	Steel: low C, medium C, C–Mn Cr–Mo, Ni–Mo, Ni–Cr–Mo	650–950	50–3000
Nitriding (ion)	Steel: Al, Cr, Mo, V, or W Austenitic stainless	90–1300	25–750
Carbonitride	Steel: low C, medium C, Cr Cr–Mo, Ni–Cr–Mo	550–950	25–750
Boriding	Steel: Mo, Cr, Ti, cast Fe Cobalt-based alloys Nickel-based alloys	1600–2000	25–500

processing. To avoid this problem a barrier layer of silica can be deposited by spray pyrolysis on the air side of the glass on the float glass line.

Basecoats: inorganic

An example of an inorganic basecoat to increase the functionality of a coating is the use of a diamond-like carbon (DLC) basecoat to increase the scratch resistance of a decorative coating on a soft substrate [28].

3.7.2 In Situ Surface Modification

There are several techniques to modify surface in the deposition system. They include:

- Plasma immersion ion implantation deposition (PIIID), where a metallic cathode is immersed in a plasma and pulsed momentarily to a high voltage (50–100 kV) [29, 30]. Ions are accelerated from the plasma and before there is an arc the pulse is terminated. When using nitrogen and a high part temperature this process is similar to ionitriding
- Plasma anodization is a method of growing a very coherent oxide layer on the surface of some metal compounds and silicon [31, 32]
- A plasma may be used to change the functional groups on the surface of a polymer to change the surface energy and make the surface more acidic or more basic. This can change the contact angle on the treated surface, as shown in Figure 3.12
- Polymer evaporation and flow coating. The deposition of a film of liquid polymer on the substrate surface is similar to flow coating and can be used to reduce the number of surface defects in vacuum web coating [33, 34].

Plasma treatment by nitrogen plasmas (N_2 or NH_3) can produce functional groups such as imine (C=N), amide (N–C=O) or amine C–N) groups [35, 36], which can aid in

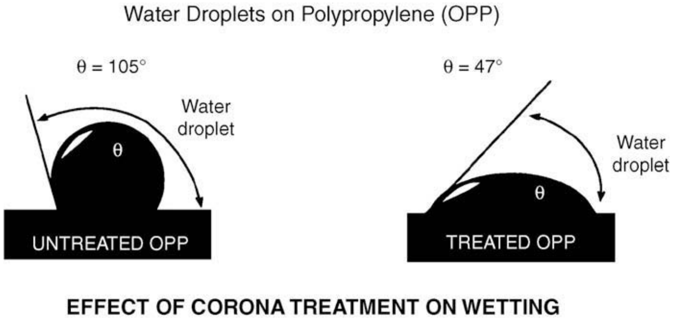

Figure 3.12: Contact angle. [From SVC Education Guides to Vacuum Coating Processing (2009) – Surface Preparation: Surface Energy, Wetting Agents, and Surfactants, with permission.]

metal–polymer adhesion. Oxygen-containing plasmas are used to produce covalent bonds (C–O–C), where the oxygen can bond to oxygen-active metals [37].

References

[1] D.M. Mattox, Surface preparation for vacuum surfaces and vacuum coating, Chap. 21, in: 50 Years of Vacuum Coating Technology and the Growth of the Society of Vacuum Coaters, SVC (2007) 151.

[2] D.M. Mattox, Surface effects on the growth, adhesion and properties of reactively deposited hard coatings, Surf. Coat. Technol. 81 (1996) 8.

[3] E.J. Wegener, Glass cleaning utilizing cerium oxide solution in a high volume production environment, in: 36th Annual Technical Conference Proceedings of the Society of Vacuum Coaters (1993) 495.

[4] R.E. Cuthrell, Influence of hydrogen on the deformation and fracture of the near surface region of solids: proposed origin of the Rebinder–Westwood effect, J. Mater. Sci. 14 (1979) 612.

[5] J.M. Fowkes, D.W. Wright, J.A. Manson, T.B. Lloyd, D.O. Tischer, B.A. Shaw, Enhanced mechanical properties of polymer composites by modification of the surface acidity or basicity of fillers, in: D.M. Mattox, J.E.E.E. Baglin, R.J. Gottschall, C.D. Battich (Eds.), Adhesion in Solids, MRS Symposium Proceedings, Vol. 119 (1988) 223.

[6] ASTM-D-2989 Acidity/Alkalinity of Hydrogenated Organic Solvents.

[7] K. Mittal (Ed.), Contact Angle, Wettability, and Adhesion, Vol. 5, Brill Academic Publishers (2008).

[8] R.R. Sowell, R.E. Cuthrell, R.D. Bland, D.M. Mattox, Surface cleaning by ultraviolet radiation, J. Vac. Sci. Technol. 11 (1974) 474.

[9] J.R. Vig, UV/ozone cleaning of surfaces, J. Vac. Sci. Technol. A 3(3) (1985) 1027.

[10] G.J. Kominiak, D.M. Mattox, Reactive plasma cleaning of metals, Thin Solid Films 40 (1977) 141.

[11] H.F. Dylla, A review of the wall problem and conditioning techniques for TOKAMACKS, J. Nucl. Mater. 93-94 (1980) 61.

[12] F.J. Fuchs, New ultrasonic technology improves cleaning and prevents surface damage due to cavitation erosion effects, in: 45th Annual Technical Conference Proceedings of the Society of Vacuum Coaters (2002) 64.

[13] R.R. Young, Sonoluminescence, CRC Press (2005).

[14] V.B. Menon, Particle adhesion to surfaces: theory of cleaning, in: R.P. Donovan (Ed.), Particle Control for Semiconductor Manufacturing, Marcel Dekker (1990) 359.

[15] S. Hamilton, Yield Improvement in Metallizing Lines by Using Contact Cleaning Technology, in: 51st Annual Technical Conference Proceedings of the Society of Vacuam Coaters (2008) 778.

[16] A.K. Furr, CRC Handbook of Laboratory Safety, 5th ed., CRC Press (2000).

[17] P. Patnaik, A Comprehensive Guide to the Hazardous Properties of Chemical Substances, 3rd ed., John Wiley and Sons (2007).

[18] L. Holland, The cleaning of glass, Chap. 5, in: The Properties of Glass Surfaces, Wiley (1964).

[19] D.M. Mattox, R.R. Sowell, Kr^{85} Autoradiography for nondestructive/noncontaminating surface porosity measurements, in: Proc. 7th International Vacuum Congress and 3rd International Conference on Solid Surfaces (1977) 2659.

[20] R.E. Cuthrell, D.W. Tipping, Rev. Sci. Instrum. 47 (1976) 595.

[21] W.J. Whitfield, Ultra-Clean Room USP 3158457 (Filed May 14, 1962, Issued Nov. 1964).

[22] W.J. Whitfield, A new approach to clean room design, Sandia Corp. Technical Report No. SC-4673 (RR), (1962).

[23] D.M. Mattox, Particle bombardment effects on thin film deposition: a review, J. Vac. Sci. Technol. A 7(3) (1989) 1105.

[24] R.A. Wolf, Which surface activation system should i use for optimizing adhesion to polymers? in: 50th Annual Technical Conference Proceedings, Society of Vacuum Coaters (2007) 704.

[25] S. Guruvenket, L. Duanjie, A. Revah, J. Szpunar, L. Martinu, J.E. Klemberg-Sapieha, Tribological properties of duplex treated 410 martensitic stainless steel, in: 51st Annual Technical Conference Proceedings of the Society of Vacuum Coaters (2008) 712.

[26] R.F. Bunshah (Ed.), Handbook of Hard Coatings, Noyes Publications (2001).

[27] A. Raveh, I. Zukerman, R.Z. Shneck, R. Avni, I. Fried, Thermal stability of TiAlBN and TiN/TiCN coatings, High Temp. Mater. Process. 10(3) (2006) 445.

[28] P. Peeters, J. Soldán, J. Landsbergen, R. Tietema, T. Krug, DLC base coat as part of decorative coating for scratch resistant support on soft substrates, in: 51st Annual Technical Conference Proceedings of the Society of Vacuum Coaters (2008) 735.

[29] J.R. Conrad, R.A. Dodd, S. Han, M. Madapura, J. Scheuer, K. Sridharan, F.J. Worzala, Ion beam assisted coating and surface modification with plasma source ion implantation, J. Vac. Sci. Technol. A 8(4) (1990) 3146.

[30] A. Anders (Ed.), Handbook of Plasma Immersion Ion Implantation and Deposition, John Wiley and Sons (2000).

[31] D.W. Hess, Plasma-assisted oxidation, anodization, and nitridation of silicon IBM, J. Res. Dev. 43(1/2) (1999) 127.

[32] A. Raveh, M. Gelbstein, G. Moshe, M. Weiss, J.E. Klemberg-Sapieha, L. Martinu, Wear-corrosion study of tantalum-oxide layers produced by plasma anodization using inductively coupled plasma, in: 51st Annual Technical Conference Proceedings of the Society of Vacuum Coaters (2008) 739.

[33] C.A. Bishop, Polymer web surface cleanliness, in: 45th Annual Technical Conference Proceedings, Society of Vacuum Coaters (2002) 476.

[34] P.M. Martin, J.D. Affinito, M.E. Gross, C.A. Coronado, W.D. Bennett, D.C. Stewart, Multilayer coatings on flexible substrates, in: 38th Annual Technical Conference Proceedings of the Society of Vacuum Coaters (1995) 163.

[35] L.J. Gerenser, Surface chemistry for treated polymers, in: D.A. Glocker, S.I. Shah (Eds.), Handbook of Thin Film Process Technology, Vol. 2, IoP Publishing (2002) Section E3.1.

[36] M.R. Wertheimer, L. Martinu, E.M. Liston, Plasma sources for polymer surface treatment, in: D.A. Glocker, S.I. Shah (Eds.), Handbook of Thin Film Process Technology, Vol. 2, IoP Publishing (2002) Section E3.0.

[37] J.M. Burkstrand, Electron spectroscopic study of oxygen-plasma-treated polymer surfaces, J. Vac. Sci. Technol. 15 (1978) 223.

CHAPTER 4

Evaporation: Processes, Bulk Microstructures, and Mechanical Properties

S. Ismat Shah, G. Hassnain Jaffari, Emre Yassitepe and Bakhtyar Ali
University of Delaware

4.1 Introduction

Physical vapor deposition (PVD) technology consists of the techniques of evaporation, ion plating and sputtering. It is used to deposit *films and coatings* or *self-supported shapes* such as sheet, foil, and tubing. The thickness of the deposits can vary from angstroms to millimeters. The wide variety of applications of these techniques ranges from decorative to utilitarian over significant segments of the engineering, chemical, nuclear, microelectronics and related industries. Their use has been increasing at a very rapid rate since modern technology demands multiple, and often conflicting, sets of properties from engineering materials, e.g. combinations of two or more of the following: high-temperature strength, impact strength, specific optical, electrical or magnetic properties, wear resistance, ability to be fabricated into complex shapes, biocompatibility, cost, etc. A single or monolithic material cannot meet such demands in high-technology applications. The solution is, therefore, a composite material, i.e. a core material and a coating each having the requisite properties to fulfill the specifications.

PVD technology is very versatile, enabling one to deposit virtually every type of inorganic material – metals, alloys, compounds and mixtures thereof, as well as some organic materials. The deposition rates can be varied from 10 to 750,000 Å (10^{-3} to 75 μm) per minute, the higher rates having come about in the past 20 years with the advent of electron beam (e-beam)-heated sources. For zinc and aluminum, deposition rates as high as 25 μm/s have been reported using e-beam evaporation sources.

The thickness limits for thin and thick films are somewhat arbitrary. A thickness of 10,000 Å (1 μm) is often accepted as the boundary between thin and thick films. A recent viewpoint is that a film can be considered thin or thick depending on whether it exhibits surface-like or bulk-like properties.

Historically, the first evaporated thin films were probably prepared by Faraday [1] in 1857 when he exploded metal wires in a vacuum. The deposition of thin metal films in vacuum by Joule heating was discovered in 1887 by Nahrwold [2] and was used by Kundt [3] in 1888 to measure refractive indices of such films. In the ensuing period, the work was primarily of academic interest concerned with optical phenomena associated with thin layers of metals, research into kinetics and diffusion of gases, and gas metal reactions [4, 5]. The application of these technologies on an industrial scale had to await the development of vacuum techniques and therefore dates to the post-World War II era, i.e. 1946 and onwards. This proceeded at an exponential pace in thin films and is covered in an excellent review by Glang [6] on evaporated films and in other chapters of the Handbook of Thin Film Technology [7], as well as in the classic text by Holland [8]. A more recent reference on the Science and Technology of Surface Coatings [9] includes material on PVD techniques as well as the other techniques for surface coatings. The work on mechanical properties of thin films has been reported in several review articles [10–15].

The work on the production of full-density coatings or self-supported shapes by high-deposition rate PVD processes started around 1961 independently at two places in the USA. Bunshah and Juntz at the Lawrence Livermore Laboratories of the University of California produced very high-purity beryllium foil [16–21] and titanium sheets [22], and studied the variation of impurity content, microstructure, and mechanical properties with deposition conditions, thus demonstrating that the microstructure and properties of PVD deposits can be varied and controlled. At about the same time, Smith and Hunt were working at Temescal Metallurgical Corporation in Berkeley on the deposition of a number of metals, alloys and compounds, and reported their findings in 1964 [23, 24].

In the years between 1962 and 1969, there was considerable effort on the part of various steel companies to produce Al and Zn coatings on steel using the high-rate physical vapor deposition (HRPVD) techniques on a production scale [25, 26]. In 1969, Airco Temescal Corporation decided to manufacture Ti–6Al–4V alloy foil in pilot production quantities for use in honeycomb structures on the supersonic transport (SST) aircraft. The project was eminently successful but the SST died. The results of this work were published in 1970 [27]. To give some idea of the production capability, 1200 feet/run of Ti–6Al–4V foil, 12 inches wide and 0.002 inches thick was produced at the rate of 2–3 feet/min. The stated cost at that time was about one-fifth of the cost for similar material produced by rolling (i.e. $60/lb for HRPVD vs $300/lb for rolled material). It is very difficult to roll this alloy because it work-hardens very rapidly and therefore needs many annealing cycles to be reduced to thin gauge [28]. The work on thick films and bulk deposits has matured later than the work on thin films and reviews on it have been given by Bunshah [29, 30] and by Paton et al. [31] who summarized the work done at the Paton Electric Welding Institute up to 1973. In addition, the Soviet literature in the 1960s has numerous references to the extensive work on thin and thick films by Palatnick and co-workers of the Kharkov Polytechnic Institute (see Appendix). Note should also be made of a recent book in German on e-beam technology by Schiller et al., in which many of the PVD aspects are treated [32].

4.2 Scope

The scope of this chapter will be to review the evaporation technologies, theory and mechanisms, processes, deposition of various types of materials, the evolution of the microstructure and its relationship to the properties of the deposits, preparation of high-purity metals, current and future applications, and finally cost analysis as far as possible.

4.3 PVD Processes

4.3.1 Preamble

In general, deposition processes may principally be divided into two types: (1) those involving droplet transfer such as plasma spraying, arc spraying, wire-explosion spraying, and detonation gun coating, and (2) those involving an atom-by-atom transfer mode such as the PVD processes of evaporation, ion plating and sputtering, chemical vapor deposition (CVD), and electrodeposition. The chief disadvantage of the droplet transfer process is the porosity in the final deposit, which affects the properties.

There are three steps in the formation of any deposit:

1. Synthesis of the material to be deposited:
    (a) transition from a condensed phase (solid or liquid) to the vapor phase
    (b) for deposition of compounds, a reaction between the components of the compound, some of which may be introduced into the chamber as a gas or vapor.
2. Transport of the vapors between the source and substrate.
3. Condensation of vapors (and gases) followed by film nucleation and growth.

There are significant differences between the various atom transfer processes. In CVD and electrodeposition processes, all of the three steps mentioned above take place simultaneously at the substrate and cannot be independently controlled. Thus, if a choice is made for a process parameter such as substrate temperature (which governs deposition rate in CVD), one is stuck with the resultant microstructure and properties. On the other hand, in the PVD processes, these steps (particularly steps 1 and 3) can be independently controlled and one can therefore have a much greater degree of flexibility in controlling the structure and properties, and deposition rate. This is a very important consideration.

4.3.2 PVD Processes

There are three PVD processes, namely evaporation, ion plating, and sputtering. Ion plating is a hybrid process. In the evaporation process, vapors are produced from a material located in a source which is heated by direct resistance, radiation, eddy currents, e-beam, laser beam, or an arc discharge. The process is usually carried out in vacuum (typically 10^{-5}–10^{-6} torr) so that the evaporated atoms undergo an essentially collisionless line-of-sight transport prior to condensation on the substrate. The substrate is usually at ground potential (i.e. not biased).

4.3.2.1 Electron Beam Evaporation

Figure 4.1 is a schematic of a vacuum evaporation system illustrating e-beam heating. It may be noticed that the deposit thickness is greatest directly above the center-line of the source and decreases away from it [33, 34]. This problem is overcome by imparting a complex motion to substrates (e.g. in a planetary or rotating substrate holder) so as to even out the vapor flux on all parts of the substrate; or by introducing a gas at a pressure of 5–200 μm into the chamber so that the vapor species undergo multiple collisions during transport from the source to substrate, thus producing a reasonably uniform (± 10%) thickness of coating on the substrate. The latter technique is called gas-scattering evaporation or pressure plating [35, 36].

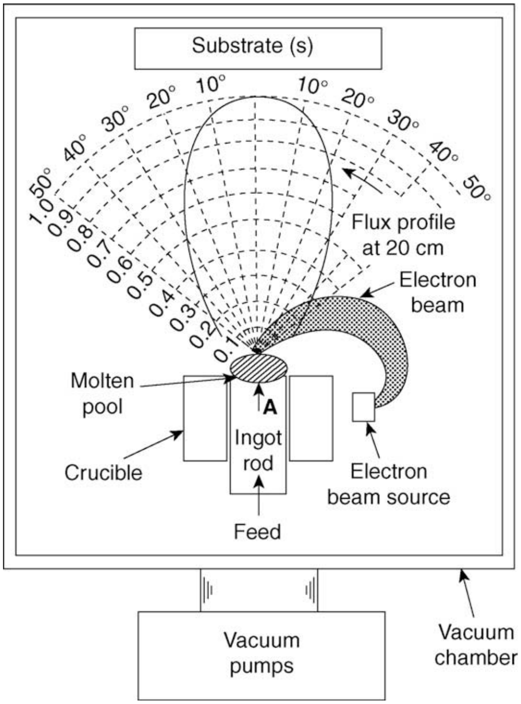

Figure 4.1: Vacuum-evaporation process using electron beam heating.

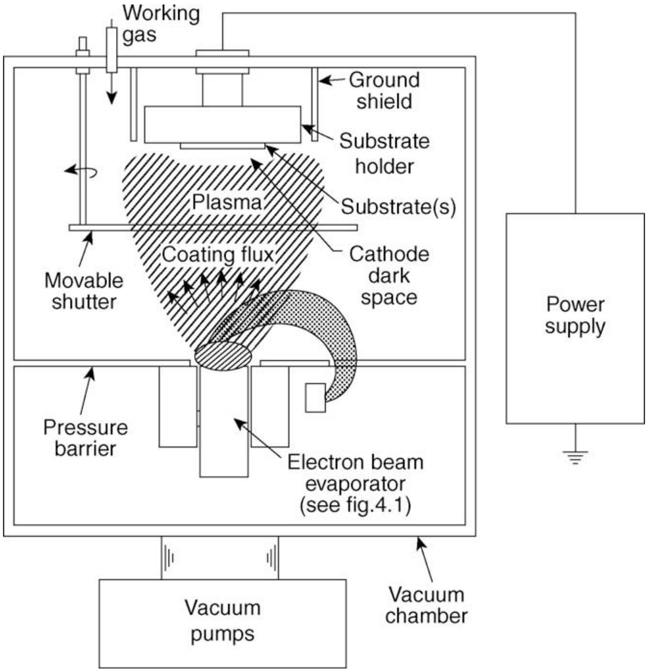

Figure 4.2: Ion-plating process.

4.3.2.2 Ion-Plating Process

In the ion-plating process, the material is vaporized in a manner similar to that in the evaporation process but passes through a gaseous glow discharge on its way to the substrate, thus ionizing some of the vaporized atoms (Figure 4.2). The glow discharge is produced by biasing the substrate to a high negative potential (−2 to −5 kV) and admitting a gas, usually argon, at a pressure of 5–200 mtorr into the chamber. In this simple mode, which is known as diode ion-plating, the substrate is bombarded by high-energy gas ions which sputter off the material present on the surface. This results in a constant cleaning of the substrate (i.e. a removal of surface impurities by sputtering), which is desirable for producing better adhesion and lower impurity content. This ion bombardment also causes a modification in the microstructure and residual stresses in the deposit. However, it produces the undesirable effects of decreasing the deposition rates since some of the deposit is sputtered off, as well as causing a considerable (and often undesired for microelectronic applications) heating of the substrate by the intense gas ion bombardment. The latter problem can be alleviated by using the supported discharge ion-plating process [37, 38] where the substrate is no longer at the high negative potential; the electrons necessary for supporting the discharge come from an auxiliary heating tungsten filament. The high gas pressure during deposition causes a reasonably uniform deposition of all surfaces owing to gas-scattering, as discussed above.

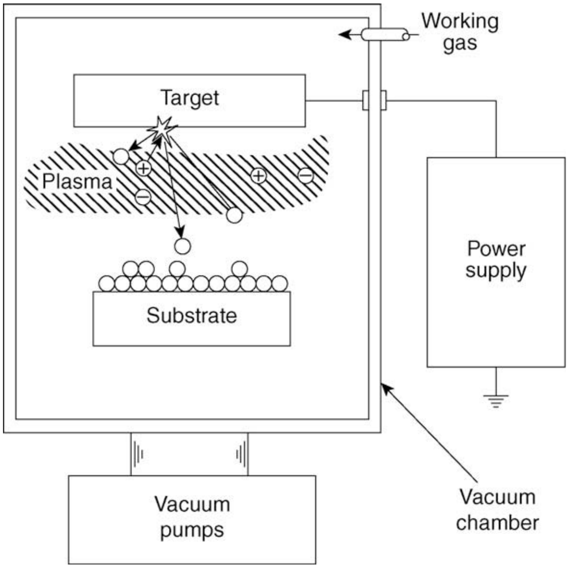

Figure 4.3: Basic sputtering process.

4.3.2.3 Sputtering

In the sputtering process, illustrated schematically in Figure 4.3, positive gas ions (usually argon ions) produced in a glow discharge (gas pressure 20–150 mtorr) bombard the target material (also called the cathode), dislodging groups of atoms which then pass into the vapor phase and deposit onto the substrate. Alternate geometries of importance in various processing applications are shown in Figure 4.4. For example, hollow cathode sputtering would be the ideal geometry for coating the outer surface of a wire. Sputtering is an inefficient way to induce a solid to vapor transition. Typical yields (atoms sputtered per incident ion) for a 50 eV argon ion incident on a metal surface are unity. Thus the phase change energy cost is from three to ten times larger than evaporation [39]. Thornton [39] has provided an excellent review on sputtering as applied to deposition technology. The reader is also referred to the proceedings of a special conference on 'Sputtering and Ion Plating' [40].

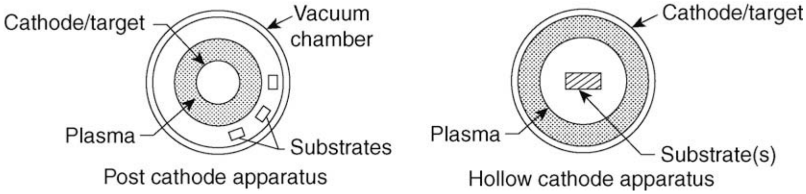

Figure 4.4: Cylindrically symmetric sputter-coating systems.

Table 4.1: Deposition rates for various PVD processes

Evaporation (Å/min)	100–250,000
Ion plating (Å/min)	100–250,000
Sputtering (Å/min)	25–10,000

In special cases to 500,000 Å/s.

The deposition rates for the various processes are indicated in Table 4.1. The deposition rates of the evaporation and ion-plating processes are much higher than those of the sputtering process. Recently, Schiller and Jasch [41] reported on large-scale industrial applications of deposition of Al on strip steel continuously at a deposition rate of 20 μm/min. It should be noted that sputter deposition rates at the high side (approximately 10,000 Å/min) with diode sputtering can only be obtained for target materials of high thermal conductivity like copper, since heat extraction from the target is the limiting parameter. For most materials, it is much lower, i.e. 50–1000 Å/min. With magnetron sputtering, much higher deposition rates are obtained (see Chapter 5).

4.3.2.4 Inert Gas Condensation

Inert gas condensation (IGC) is a process in which vaporized material is rapidly cooled into solid phase by interactions with a condenser gas. In 1930 Pfund synthesized bismuth nanoparticles by evaporating bismuth over tungsten wire [42]. However, a contemporary version of the IGC process was developed by Gleiter's group to synthesize Fe nanoparticles [43, 44]. In this process, the vaporized material is obtained by resistive heating of a refractory metal boat or crucible which acts as the evaporation source. The material to be evaporated is supplied to the source either by directly placing it on the source before the evaporation or by a variety of continuous loading mechanisms during evaporation, e.g. wire insertion. Interactions between the vaporized material with inert gas molecules and chamber walls provide the rapid cooling. Upon cooling, vaporized material supersaturates and nucleation starts. Nuclei are taken away from the growth region by either a convective or a forced flow. Finally, the particles are collected on a cold surface that is in the form of a solid cold finger or a filter with porous surface that can trap the particles.

Important parameters controlling particle size

Gas pressure, evaporation temperature, inert gas type, and cooling rate are the main parameters that control the particle size and shape in the IGC process. Studies show that pressure is the most important parameter that affects the particle size as compared to all other parameters. The total gas pressure in the chamber regulates the diffusion rate of the vaporized material from the growth region and, therefore, the particle size [45–47]. Increasing vapor pressure by increasing flux of the evaporated species in the growth region forces more coalescence which results in the formation of larger particles. Evaporation temperature also affects particle size, albeit in a smaller way. Since the kinetic energy of the particles gets larger with the increase of the evaporation temperature, the nuclei possess excess energy and coalesce after collisions. Evaporation temperature is also connected with the vapor pressure. Lower evaporation temperature corresponds to lower vapor pressure, yielding smaller particles [48]. Inert gas type also plays an important role on the particle size. It is the size of the inert gas molecules that changes the dynamics. Since massive gas particles can block the escape of the evaporated particles from the growth region more efficiently than the less massive ones, the resulting particle size is smaller for inert gas with lower molar (atomic) mass, for instance helium. Thermal conductivity of the inert gas also has a secondary effect. Helium is usually chosen owing to its highest thermal conductivity amongst all the noble gases and provides a higher cooling rate.

Particle growth processes

Particle growth in the IGC process can be classified into three stages: nucleation, coalescent coagulation, and agglomeration. These three stages are depicted in Figure 4.5. Initially, the temperature in the vicinity of the evaporation source is high to obtain a reasonable vapor pressure of the evaporant. As the evaporant moves away from the source, the temperature decreases, causing supersaturation of the vaporized material leading to the homogeneous nucleation in the gas phase. At high supersaturation, a large amount of small particles is formed upon rapid nucleation of the vapors. Nucleation usually starts very fast and continues at a very high rate. The nucleation process reduces the supersaturation and slows down further nucleation. Particles subsequently grow by Brownian coagulation as they are removed from the evaporation region to the particle collection region. Particles coalesce quickly after coagulation. Further decrease in temperature slows down the coalescence rate and agglomerate growth takes over.

Particles produced by the IGC technique can form agglomerates by either hard or soft agglomeration depending on the material properties, the atmosphere, and the temperature–time history. Hard agglomeration is a result of strong bonding of primary particles via neck formation, whereas soft agglomeration results from the weak bonding of

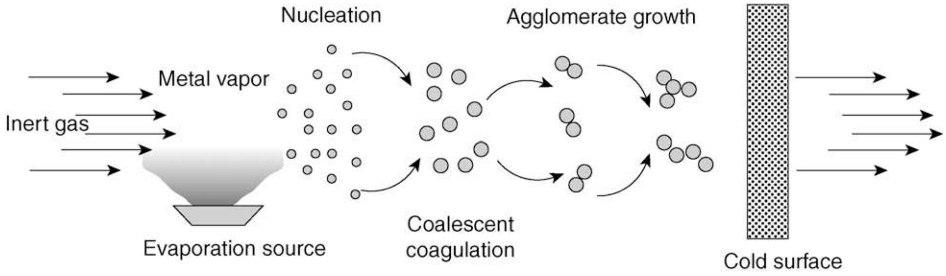

Figure 4.5: Schematic diagram of the processes that contribute to particle growth in IGC.

primary particles due to van der Waals' forces. Although soft agglomerates can be separated into their constituent primary particles, separation of hard agglomerates is extremely difficult. Details on particle growth mechanism in IGC are reported by Flagan and Lunden [47].

Experimental set-up of IGC system

A schematic diagram of the IGC system is shown in Figure 4.6. It is composed of two main sections. The left side, where there are two ports for two different evaporation sources, is for the production of vaporized material, and the right side is for the collection of the particles. Evacuation of the system can be maintained by mechanical and turbo pumps connected in series.

Pressure readings are taken by thermocouple and cold cathode gauges. Inert gas circulation is realized by a roots blower. A suitable power supply is used for the resistive evaporation. The maximum temperature that can be reached depends on the evaporation source and the power supply. In order to maintain continuous particle production, a wire feeding mechanism is used to provide material to the hot boat. Monometallic wires, like Fe [49] and Ag [50], or bimetallic wire in the desired ratio for alloys like CuAg [51] or NiFe [52], can be evaporated. Ward et al. reported the preparation of Mn nanoparticles from evaporation of Mn powder by IGC [53]. In the IGC technique the collection of the particles is done by condensing the agglomerates either on a liquid nitrogen cooled surface or on a cylindrical stainless steel filter that has micrometer-size pores on its surface, placed in the collection chamber. Circulating inert gas passes through the filter while leaving the agglomerates on the filter surface. Since the particles reaching the filter are agglomerates of micrometer size, they are easily captured by

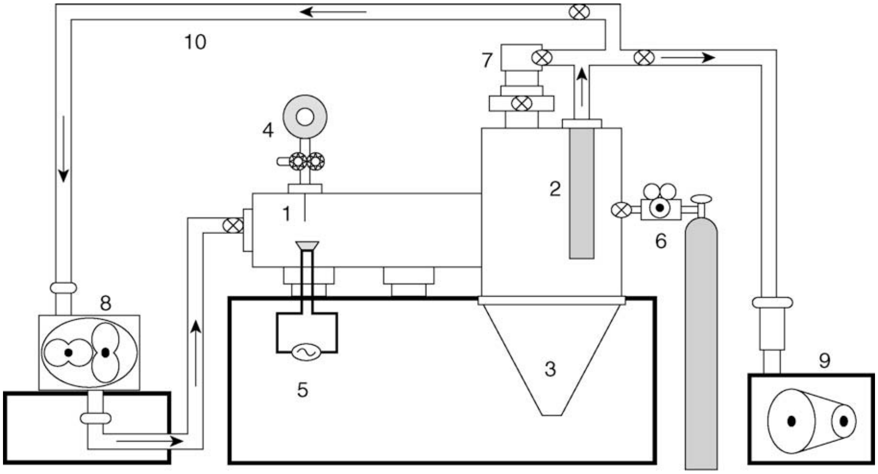

Figure 4.6: Schematic diagram of the IGC system. 1: Evaporation boat; 2: stainless steel filter; 3: hopper for the collection of particles; 4: wire feeding unit; 5: power supply; 6: inert gas cylinder; 7: turbo pump; 8: roots blower; 9: mechanical pump; 10: gas circulation line.

the pores. Particles accumulated on the filter surface are lifted off from the filter surface by occasionally reversing the inert gas flow direction. Reverse flow knocks the particles off the filter surface. The displaced particles fall down into the hopper underneath the collection chamber. There are minor variations in the IGC processes depending on what type of material is being evaporated. For example, powder evaporation requires a specific evaporator, whereas a wire evaporation can be done on a continuous basis, as shown in Figure 4.6. Selection of the evaporation source also depends on the materials being evaporated.

4.3.2.5 Pulsed Laser Deposition

Pulsed laser deposition (PLD) is a useful technique for thin film deposition [54] and was first used by Smith and Turner [55]. In PLD high-power laser pulses ablate a small amount of material from a solid target when a focused laser beam is absorbed by a small area of the target surface. The absorbed energy is utilized to ablate the target. During the ablation, chemical bonds of the molecules within the solid target are broken and the material is evaporated in a certain direction. The resultant evaporated material is comprised of ions, molecules, neutral atoms, and free radicals of the target material in their ground and excited states. This further absorbs a large amount of energy from the laser beam producing an expansion of hot plasma (plume). The plume is then expanded away from the target with a velocity distribution of different particles in the forward direction [56]. Finally, the ablated species condense on a substrate, placed at an angle opposite to the target, forming a thin film.

A typical set-up for laser ablation and thin-film deposition is shown in Figure 4.7, which is a Lambda Physik LPX 305 excimer laser with a wavelength of 248 nm and a maximum energy

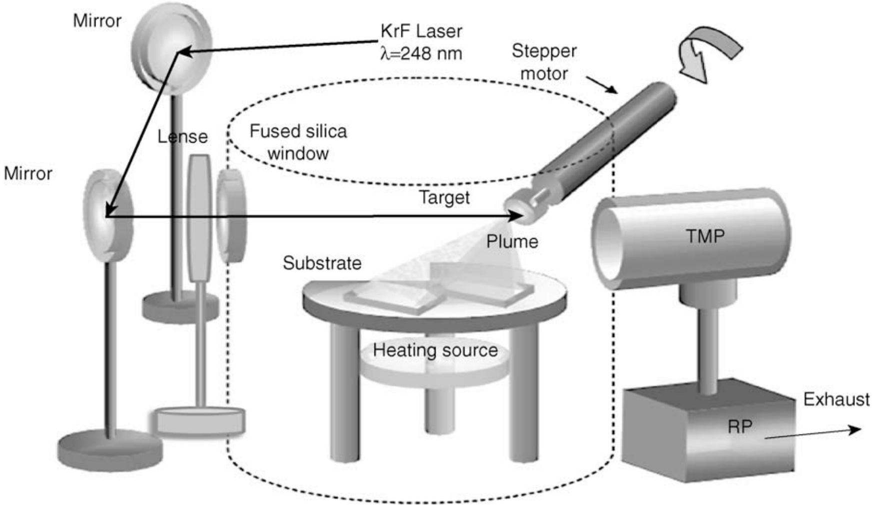

Figure 4.7: Schematic of a pulsed laser deposition process.

of 1.2 J per pulse [57]. The ablation process takes place in a vacuum chamber, either under base vacuum or in the presence of a gas. A laser beam is focused (via convex lenses) on the surface of a target through a transparent fused silica port on the chamber. The stoichiometry of the material is preserved in the ablation process owing to the simultaneous evaporation of all the components in the target, irrespective of their binding energies. This is mainly due to the fast and intense heating of the target surface by the laser beam. The accumulation of target material on the substrate from a large number of laser pulses leads to the gradual formation of a film. The micrograph of a typical thin film of Co–TiO_2, grown by the set-up described above, is shown in Figure 4.8. The cross-sectional view of the same film is shown in Figure 4.8(b). The uniformity of the film is obvious from these scanning electron micrograph (SEM) pictures, which reveal that PLD can be used to obtain good-quality films. Moreover, the PLD process is a non-equilibrium process which helps the deposition of the materials without segregation or spinodal decomposition, e.g. it is quite helpful in obtaining Co-doped TiO_2 having Co substituted for Ti.

Deposition by laser ablation is known worldwide to produce quality films of various kinds such as semiconductors, high T_c superconductors, ceramics, ferroelectrics, multilayer polymers, etc. [58–61]. In particular, PLD is useful for ablating materials in the combinatorial forms that cannot be easily produced by other methods [62, 63]. Recently, PLD has also been used to synthesize nanotubes [64], nanopowders [65], quantum dots [66], and some organic thin films that have applications in optoelectronics [67].

Parameters that can be controlled during PLD are fluence (energy per unit area), wavelength, pulse duration, pulse repetition, and preparation conditions, as well as system configurations including target to substrate distance, substrate temperature, background gas, and pressure [57]. All of these parameters and configurations influence the film growth, film quality and film properties. Usually the raw laser beam is of rectangular shape of size 2 × 3 cm^2 and is

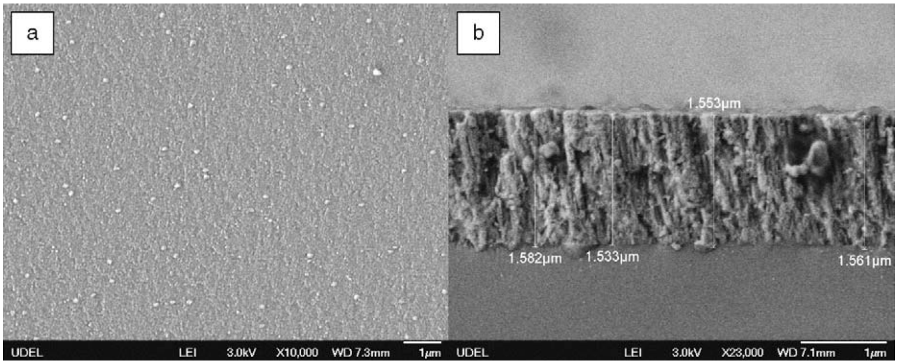

Figure 4.8: (a) SEM micrograph of the surface of the PLD grown Co–TiO_2 thin film; (b) cross-sectional view of the same film.

further shaped, collimated, and focused by converging lenses. The maximum fluence of the laser is determined by the focal length of the lens. For a given focal length f of a convex lens, the demagnification factor is:

$$M_\mathrm{d} = \frac{d_0}{f} - 1 \tag{4.1}$$

where d_0 is the distance of the mask from the lens. Thus, using the above expression we can calculate the appropriate demagnification and, therefore, get the right fluence at the target surface.

PLD can be used in combination with the IGC set-up (called laser-assisted inert gas condensation (LAIGC)). With this technique one can prepare different particles, for example with core/shell structure for environmental applications, etc. This method makes it possible to prepare nanoparticles that cannot be made with the conventional IGC method described above and is shown in the next subsection, on Co-evaporation. Furthermore, modification of the conventional PLD technique has made possible the deposition of complex materials in complex configurations such as multilayers. For example, the combination of PLD with molecular beam epitaxy (MBE) and/or sputtering systems and CVD techniques has been developed for the deposition of particulate-free and conformal thin films of several materials [68]. There are other modifications to conventional PLD. One such modification uses a combinatorial approach to explore novel material properties. Such an approach is best implemented in the form of a thin film combinatorial library, where on a substrate as small as 1 cm^2, different compositions can be integrated, synthesized, and screened, for the desired physical properties [69].

Although laser evaporation is an attractive approach for the synthesis of high-purity metal alloys and compound films, it suffers from the following limitations:

- complex transmitting and focusing systems need to be employed to direct the beam from the laser located outside the vacuum system onto the evaporant placed inside the system. This involves special optical path designs and increases the cost of the set-up. Also, a window material which efficiently transmits the wavelength band of the laser must be found and mounted in such a way that it is not rapidly covered up by the evaporated material
- it is not always possible to find a laser with a wavelength compatible with the absorption characteristics of the material to be evaporated because material properties, such as reflectivity and absorption coefficient of the solid target, depend on the wavelength of the laser used. Thus the wavelength of the laser has a significant effect on the yield of the ablated particles
- energy conversion efficiency is very low – usually around 1–2%

- the size of the deposited film is small (10–20 mm or 0.4–0.8 inches in diameter), resulting from the small size of the laser impact spot
- the ‘splashing effect’ [70], which involves the production of microparticles between 0.1 and 10 μm in size, diminishes film quality.

The main advantages of this technique are:

- the production of high-energy species, which enhances film quality
- reflectivity of most materials for lasers with short wavelengths (ultraviolet (UV)) is much lower than long infrared (IR) wavelengths [71]. When the reflectivity decreases, a larger part of a laser pulse is absorbed, increasing the number of ablated particles. Also, the absorption coefficient is larger in the UV region, such that the beam energy is absorbed in a thin surface layer and the ablation occurs more efficiently
- excellent transfer of stoichiometry between the target and the film, for example, the deposition of hydroxyl apatite thin films for biomedical applications such as implants. The macroparticle density can be decreased by lowering the power level at the expense of deposition rate. The latter may not be important for many thin film applications. The question of large area deposition has been recently addressed by Greer [72]. He constructed a vacuum deposition system in which the laser beam is scanned on a rotating YBCO target and the substrate is itself rotated. This rather complex apparatus is capable of depositing YBCO films onto 2- or 3-inch diameter substrates.

4.3.2.6 Co-evaporation Processes

Preparation of thin films by magnetron sputtering has been a very popular method for decades. There have been a few successful attempts to prepare a variety of nanoparticles with sputtering. Qiu and Wang reported that the $L1_0$ phase of FePt nanoparticles can be controlled by modifying magnetron sputtering [73]. Also, non-convention $(FeCo)_{core}Au_{shell}$ and $(FeCo)_{core}Ag_{shell}$ nanoparticles can be prepared by combined sputtering and evaporation techniques [74]. $(FeCo)_{core}Au_{shell}$ nanoparticles prepared by this technique showed a three-fold increase in saturation magnetization compared with that of iron oxide nanoparticles and a better oxidation resistance of the FeCo nanoparticles. Bai and Wang [75] used the same technique to prepare $(FeCo)_3Si–SiO_x$ core shell nanoparticles by natural oxidation after the preparation of the particles. The set-up, which combines sputtering and evaporation, is shown in Figure 4.9. This system combines two different PVD processes and has proven to be useful in enhancing different properties of materials, e.g. in the case of magnetic nanoparticles oxidation of the nanoparticles could be prevented. As reported by Bai and Wang [75], two kinds of in situ methods, namely sputtering and evaporation, were used to deposit the shell layers on the surface of FeCo nanoparticles during their flight in the shell-deposition chamber. The formation of the core/shell structure needs low velocity of FeCo nanoparticles, high

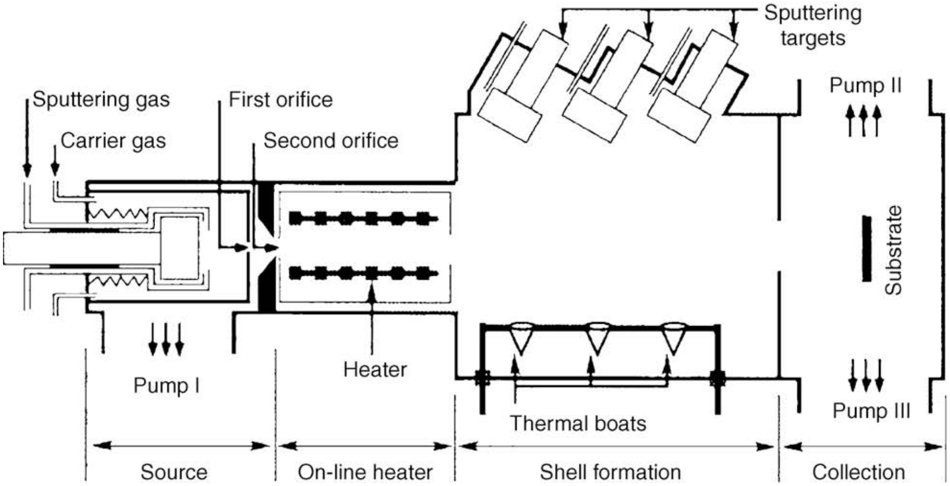

Figure 4.9: Schematic configuration of the integrated nanocluster deposition system for fabrication of the core-shell-type nanoparticles [75].

Au/Ag deposition rate, and a long deposition zone, which favors the shell formation, and vice versa.

Similarly, IGC and laser ablation techniques can be combined to synthesize core/shell structures [76]. The set-up of this system is the same as described above (Inert gas condensation subsection) with the addition of a laser target incorporated, as shown in Figure 4.10. The core/shell structured nanoparticles can be synthesized by simultaneously using resistive evaporation and laser ablation techniques in an IGC system. Usually metals can be evaporated by IGC and a subsequent oxygen passivation leads to a corresponding metal and its oxide core-shell structure. However, the need for the synthesis of one type of metal and another type of oxide shell requires a combination of IGC and laser ablation techniques. Laser ablation provides the deposition of a wide range of target materials at room temperature. The process often takes place as a sequence of steps, initiated by the laser beam interaction with the solid target, absorption of energy and localized heating of the surface, and subsequent material evaporation. The system shown in Figure 4.10 is composed of two parts. In the first part, resistive evaporation is used to synthesize core material which is carried to the next stage, where a shell of the particles is formed on the core as it passes through the laser-ablated material. The synthesis of Ni as core and CoO as shell has been reported [76].

4.3.3 Advantages and Limitations

There are several advantages of PVD processes over competitive processes such as electrodeposition, CVD, and plasma spraying. They are:

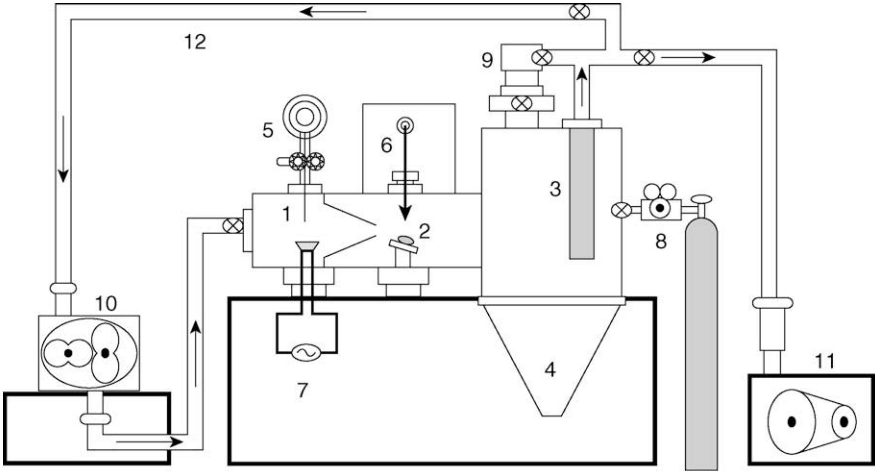

Figure 4.10: Schematic of the IGC system. 1: Evaporation boat; 2: laser ablation target; 3: stainless steel filter; 4: hopper for collection of particles; 5: wire feeding unit; 6: laser source; 7: power supply; 8: inert gas cylinder; 9: turbo pump; 10: roots blower; 11: mechanical pump; 12: gas circulation line.

- extreme versatility in composition of the deposit – virtually any metal, alloy, refractory or intermetallic compound, some polymeric type materials and their mixtures can be easily deposited. In this regard, they are superior to any other deposition process
- the ability to produce unusual microstructures and new crystallographic modifications, e.g. amorphous deposits
- the substrate temperature can be varied within very wide limits from subzero to high temperatures
- the ability to produce coatings or self-supported shapes at high deposition rates
- deposits can have very high purity
- excellent bonding to the substrate
- excellent surface finish, which can be equal to that of the substrate
- elimination of pollutants and effluents from the process, which is a very important ecological factor.

The present limitations of PVD processes are:

- inability to deposit polymeric materials, with certain exceptions, e.g. PLD
- a higher degree of sophistication of the processing equipment and hence a higher initial cost.

4.4 Theory and Mechanisms

4.4.1 Vacuum Evaporation

Reference to the various steps in the formation of a deposit enumerated in the previous section shows that the theory of vacuum evaporation involves thermodynamic considerations, i.e. phase transitions from which the equilibrium vapor phase pressure of materials can be derived, as well as the kinetic aspects of nucleation and growth. Both of these are of obvious importance in the evolution of the microstructure of the deposit.

The transition of solids or liquids into the gaseous state can be considered to be a macroscopic or an atomistic phenomenon. The former is based on thermodynamics and results in an understanding of evaporation rates, source-container reactions and the accompanying effect of impurity introduction into the vapor state, changes in composition during alloy evaporation, and stability of compounds. An excellent detailed treatment of the thermodynamic and kinetic bases of evaporation processes is given by Glang [6]. He points out that the application of kinetic gas theory to interpret evaporation phenomena resulted in a specialized evaporation theory. Such well-known scientists as Hertz, Knudsen, and Langnuir were the early workers in evaporation theory. They observed deviations from ideal behavior which led to refinements in the theory to include concepts of reaction kinetics, thermodynamics, and solid state theory. From the kinetic theory of gases, the relationship between the impingement rate of gas molecules and their partial pressure, p, is given by

$$\frac{dN_{\mathrm{i}}}{A_{\mathrm{e}}dt} = (2\pi mkT)^{-\frac{1}{2}}p \tag{4.2}$$

where N_{i} is the number of molecules striking a unit area of surface, and A_{e} is the area of the surface.

Hertz [77], in 1882, first measured the evaporation rate of mercury in high vacuum and found that the evaporation rate was proportional to the difference between the equilibrium vapor pressure of mercury, p^*, at the evaporant surface and the hydrostatic pressure, p, acting on the surface, resulting from the evaporant atoms or molecules in the gas phase. Thus, the evaporation rate based on the concept of the equilibrium vapor pressure (i.e. the number of atoms leaving the evaporant surface is equal to the number returning to the surface) is given by:

$$\frac{dN_{\mathrm{i}}}{A_{\mathrm{e}}dt}(2\pi mkT)^{-\frac{1}{2}}(p^* - p)\mathrm{cm}^2\ \mathrm{s}^{-1} \tag{4.3}$$

such that dN_{e}, the number of molecules evaporating from a surface area A_{e} in time dt, is equal to the impingement rate of gas molecules based on the kinetic theory of gases with the value of p^* inserted therein, minus the return flux corresponding to the hydrostatic pressure p of the evaporant in the gas phase. In the above equations, m is the molecular weight, k is

Boltzmann's constant, and T is the temperature in K. The maximum possible evaporation rate corresponds to the condition $p = 0$. Hertz measured evaporation rates only about one-tenth as high as the theoretical maximum rates. The latter were subsequently measured by Knudsen [78] in 1915. Knudsen postulated that some of the molecules impinging on the surface were reflecting back into the gas phase rather than becoming incorporated into the liquid. As a result, there is a certain fraction $(1 - \alpha_\mathrm{v})$ of vapor molecules which contribute to the evaporant pressure but not to the net molecular flux from the condensed phase into the vapor phase. To this end, he postulated the evaporation coefficient, α_v, which is defined as the ratio of the real evaporation rate in vacuum to the theoretically possible value defined by Eq. (4.3). This then results in the well-known Hertz–Knudsen equation:

$$\frac{dN_\mathrm{e}}{A_\mathrm{e}dt} = \alpha_\mathrm{v}(2\pi mkT)^{-\frac{1}{2}}(p^* - p) \tag{4.4}$$

The value of α_v is very dependent on the cleanliness of the evaporant surface and can range from very low values for dirty surfaces to unity for clean surfaces. In very high-rate evaporation with a clean evaporant surface, it has been found that the maximum evaporation given by Eq. (4.4) has been exceeded by a factor of 2–3 for the evaporation of a light metal such as beryllium [21] using e-beam heating. The reason for this is that the high power input results in considerable agitation of the liquid evaporant pool resulting in a real surface area much larger than the apparent surface area. The directionality of evaporating molecules from an evaporation source is given by the well-known cosine law. Figure 4.11 shows a small surface

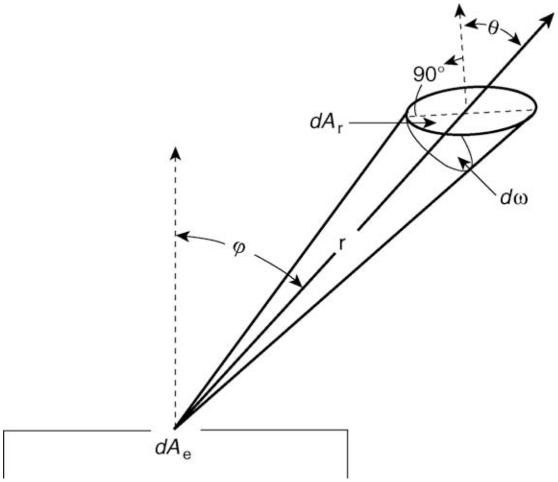

Figure 4.11: Surface element dA_r receiving deposit from a small area source dA_e. (From Handbook of Thin Film Technology [7]. © 1970, McGraw-Hill. Used with permission of McGraw-Hill Book Company.)

element dA_r receiving deposit from a small area source dA_e. The mass deposited per unit area

$$\frac{dM_\mathrm{r}(\sigma,\theta)}{dA_\mathrm{r}} = \frac{M_\mathrm{e}}{\pi r^2}\cos\varphi\cos\theta \tag{4.5}$$

where M_e is total mass evaporated.

For a point source, Eq. (4.5) reduces to:

$$\frac{dM_\mathrm{r}}{dA_\mathrm{r}} = \frac{M_\mathrm{e}}{\pi r^2}\cos\varphi \tag{4.6}$$

For a uniform deposit thickness, the point source must be located at the center of the spherical receiving surface such that r is a constant and $\cos\theta = 1$.

In high-rate evaporation conditions, e.g. using a high-power e-beam-heated source, the thickness distribution is steeper than with a point or small area source discussed above. This has been attributed by some authors [33, 34, 79] to the existence of a virtual source of vapor located above the molten pool. On the other hand, at high power, the e-beam impact area on the surface of the molten pool is not flat but pushed down into an approximate concave spherical segment which, as Riley shows [80], can equally well account for the steeper thickness distribution.

The above discussion points out one of the problems with evaporation technology, i.e. the variation in thickness of the deposit on a flat substrate. Numerous solutions are possible which involve either moving the substrate in a manner so as to randomly sample the vapor flux, the use of multiple sources, or sources of special shapes. These have been discussed in some detail by Holland [8] as well as by Bunshah and Juntz [81].

Models have also been presented for calculating the deposit temperature [82] and thickness distribution [83] during high-rate evaporation and verified against experimental data. In a more recent paper, Szekely and Poveromo [84] have given a more general formulation describing the net rate of vapor deposition from a molten source onto an initial cold surface, making allowance for both molecular transport and diffusion effects.

With PVD metal can be also be evaporated, vaporized, and then condensed in the form of nanoparticles. Okuyama et al. reported production of ultrafine metal oxide aerosol particles by thermal decomposition of metal alkoxide vapors [85]. A comprehensive study on the growth dynamics of the particles is presented by Flagan et al. [86]. The temperature required for vaporization can be achieved by Joule heating, although thermal plasmas [87], laser ablation [88], and spark ablation sources [89] operate in the same manner. In these processes vapors migrate from the hot source into a cooler gas by a combination of convective flows and diffusion. Although dilution resulting from the latter transport mechanism decreases the partial pressure of the vapor from the saturation condition at the source, the decreasing temperature leads to a far more rapid decrease in the equilibrium vapor pressure and correspondingly high supersaturation. Nanostructured materials can be synthesized by condensation from the vapor phase in the presence of inert carrier gas, most often in a buoyant plume above a hot vapor source. Particle growth in these condensation processes can be classified into three stages as nucleation, coalescent coagulation, and agglomerate growth. The growth characteristics are determined by both the probability for interparticle collisions due to Brownian motion and the velocity of interparticle coalescence. Furthermore, agglomeration is characterized by the equality of the characteristic collision and coalescence times, denoted by τ_{col} and τ_{coa}, respectively. The coalescence time is mainly determined by the diffusivity and, thus, depends strongly not only on the temperature, but also on the activation energy and the diffusion constant. If we consider surface diffusion the predominant sintering mechanism, the following equations for the coalescence and collision times can be obtained [86, 90, 92]:

$$\begin{aligned} \tau_{\mathrm{coa}} &\propto d \cdot T \exp\left(\frac{E_{\mathrm{a}}}{\mathrm{k_B} T}\right) \\ \tau_{\mathrm{col}} &\propto d^{\frac{5}{2}} T^{-\frac{1}{2}} \end{aligned} \tag{4.7}$$

where d, T, E_{a}, and $\mathrm{k_B}$ denote the particle diameter, the temperature, the activation energy for diffusion, and the Boltzman constant, respectively.

The metal atoms effused from the source will rapidly lose their energy by collision with carrier gas atoms. The nucleation process is performed homogeneously in the vapor phase and the collision mean free path is very short, i.e. in the order of 100 nm. If one further assumes a steady-state cluster formation and distribution is considered, the nucleation rate depends on the supersaturation of metal vapor in the gas phase, S [86]:

$$J \propto \exp\left(\frac{-\sigma^3}{\ln^2 S}\right) \tag{4.8}$$

where σ is the surface tension. The free energy barrier against nucleation is also a function of σ and S as follows [92, 93]:

$$\Delta G = \frac{16}{3}\pi \frac{\sigma^2}{(\rho \mathrm{R} T \ln S)^2} \tag{4.9}$$

where ρ is the particle density, R is the gas constant, and T is temperature. Since the supersaturation of metal vapor is caused by the collision of the metal atoms with the gas atoms, the amount of undercooling determines the supersaturation and thus the nucleation process. It is known that the value of vapor phase undercooling depends on the evaporation temperature. This model has been applied on Ag nanoparticles prepared by IGC [92, 93].

4.5 Evaporation Process and Apparatus

4.5.1 The System

A schematic of the evaporation apparatus has been illustrated in Figure 4.1. It consists of the following: chamber, vacuum pumps, vacuum gauges, including total and partial pressure gauges on sophisticated systems, evaporation sources, substrate holders, rate monitors, process controller, etc.

4.5.1.1 Vacuum Chamber

This ranges from a simple bell jar or rectangular box for experimental or batch type production to more complex gear for production applications. The latter may consist of a deposition chamber with loading and unloading chambers attached to the deposition chambers by manifolds with isolation high-vacuum valves. These are called fast cycle coaters. Alternate approaches are semi-continuous in-line systems where a strip substrate stored in the vacuum chamber can be fed continuously over the source (Figure 4.12) or a continuous system where the strip or sheet substrate is inserted and removed from the deposition chamber through air-to-air seals [4, 94] (Figures 4.13 and 4.14).

4.5.1.2 Vacuum Pumping System

The gas loads in evaporation processes are fairly high owing to outgassing from chamber walls promoted by the heat load from the evaporation source and substrate heaters, particularly for high deposition rate conditions. Therefore the pumping system is usually based on a diffusion pump with a liquid nitrogen cooled anticreep type baffle backed with a mechanical pump or a Roots blower/mechanical pump combination for large systems. For very high-purity,

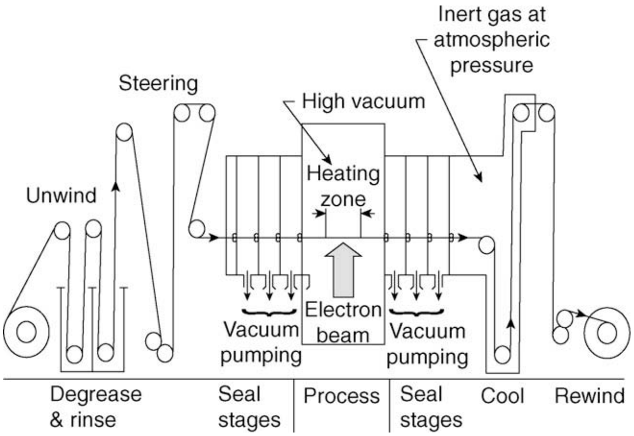

Figure 4.12: Schematic representation of a 24 inch continuous high vacuum strip processing line.

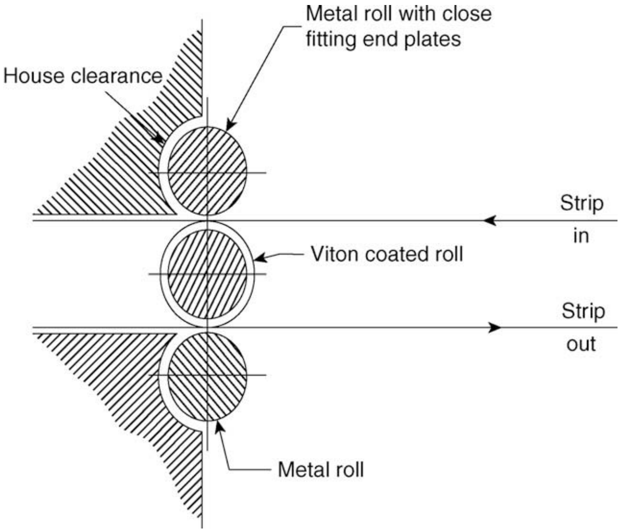

Figure 4.13: Three-high roll seal arrangement for stripline.

low-deposition rate, low-heat flux conditions, ion pumped systems backed with cryosorption rough pumping are used, since a base pressure of 10^{-9}–10^{-10} torr is needed. More recently, turbomolecular and cryogenic pumps have been used instead of diffusion pumps where desired (e.g. oil-free systems). This is particularly true for molecular beam epitaxy where extreme

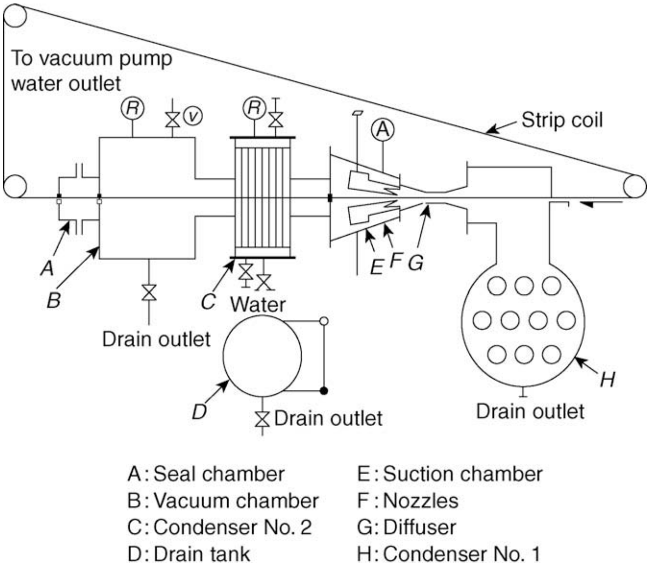

Figure 4.14: Vacuum seal using steam jet or curtain.

control over composition and layer thickness is essential and deposition rates can be quite low. In such cases, the chamber and pumps are to be baked as with any other ultrahigh vacuum operation.

4.5.1.3 Pressure Measurement

The vacuum gauges used depend again on specific applications, such as a combination of high-pressure gauges (such as the Pirani or Thermocouple Gauge) for monitoring the roughing of the system and high-vacuum gauges (such as the hot cathode ionization gauge and/or capacitance manometer). A partial pressure gauge is highly desirable, particularly for ultraclean applications, as well as for leak hunting.

4.5.1.4 Evaporation Sources

These are discussed separately in Section 4.6.

4.5.1.5 Substrate Holders and Heaters

Substrate holders may be very simple for stationary flat substrates or can incorporate quite complex motions as illustrated by planetary or rotating devices. The reason for this is to ensure deposition thickness uniformity and control over a large number of small parts such as lenses or silicon wafers. Substrate heating can be accomplished by radiant heaters with refractory wires or quartz lamps acting as the heat source. Occasionally, substrates are directly heated by a scanning or diffuse e-beam.

4.5.1.6 Deposition Rate Monitors

These are discussed in Section 4.7.

4.6 Evaporation Sources

4.6.1 General Considerations

Evaporation sources are classified by the mode of heating used to convert the solid or liquid evaporant to the vapor phase. Thus one talks of resistance, arc, induction, electron beam, arc imaging, lasers, and exploding wire types of sources. It is very important to note that we cannot evaporate every material from any of the types of sources listed above, for the following reasons:

- chemical interaction between the source material and the evaporant would lead to impurities in the deposit. For example, evaporation of titanium from a MgO source would cause oxygen and magnesium contamination of the deposit; the titanium would reduce the MgO. Therefore, for the evaporation of reactive metals such as titanium or zirconium, water-cooled copper crucibles are used

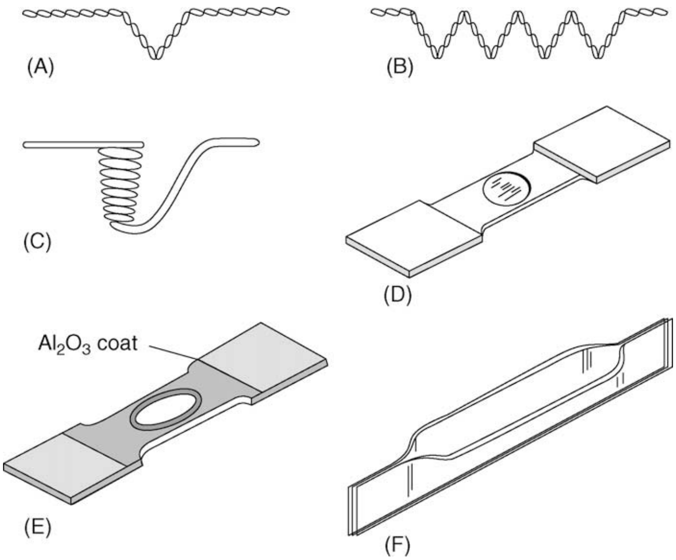

Figure 4.15: Wire and metal-foil sources: (A) hairpin source; (B) wire helix; (C) wire basket; (D) dimpled foil; (E) dimpled foil with alumina coating; (F) canoe type. (From Handbook of Thin Film Technology [7]. © 1970, McGraw-Hill. Used with permission of McGraw-Hill Book Co.)

- reaction between metallic source (such as a W or Ta boat) and evaporant (Ti) could occur. In many cases at high temperatures two metals can mutually dissolve in each other, leading to destruction of the source
- the power density (i.e. W/cm^2) varies greatly between the various heat sources.

Table 4.2, from the article by Glang [6], lists the temperature and support materials to be used in the evaporation of elements. Similar tables are found in the literature of many of the manufacturers.

Evaporation of alloys and compounds poses additional problems, and they are considered in Section 4.9.

4.6.2 Resistance-Heated Sources

The simplest vapor sources are resistance-heated wires and metal oils of various types shown in Figure 4.15.

They are available in a variety of sizes and shapes and at sufficiently low prices so that they can be discarded after one experiment if necessary. They are usually made from the refractory metals, tungsten, molybdenum, and tantalum, which have high melting points and low vapor pressure so as not to contaminate the deposit. Their properties are given in Table 4.3.

Table 4.2: Temperatures and support materials used in the evaporation of the elements

Element and predominant vapor species	Temp. (°C)		Support materials		Remarks
	mp	$p^* = 10^{-1}$ torr	Wire, foil	Crucible	
Aluminum (Al)	650	1220	W	C, BN, TiB_2-BN	Wets all materials readily and tends to creep out of containers. Alloys with W and reacts with carbon. Nitride crucibles preferred
Antimony (Sb_4, Sb_2)	630	530	Mo, Ta, Ni	Oxides, BN, metals, C	Polyatomic vapor, $\alpha_2 = 0.2$. Requires temperatures above mp. Toxic
Arcenic (As_4, As_2)	820	∼ 300	–	Oxides, C	Polyatomic vapor, $\alpha_2 = 5.10^{-6}$–5.10^{-2}. Sublimates but requires temperatures above 300 °C. Toxic
Barium (Ba)	710	610	W, Mo, Ta, Ni, Fe	Metals	Wets refractory metals without alloying. Reacts with most oxides at elevated temperatures
Beryllium (Be)	1283	1230	W, Mo, Ta	C, refractory oxides	Wets refractory metals. Toxic, particularly BeO dust
Bismuth (Bi, Bis)	271	870	W, Mo, Ta, Ni	Oxides, C, metals	Vapors are toxic
Boron (B)	2100 ± 100	2000	–	C	Deposits from carbon supports are probably not pure boron
Cadmium (Cd)	321	265	W, Mo, Ta, Fe, Ni	Oxides metals	Film condensation requires high supersaturation. Sublimates, Wall deposits of Cd spoil vacuum system
Calcium (Ca)	850	800	W	Al_2O_3	
Carbon (C_2, C, C_2)	∼ 3700	∼ 2600	–	–	Carbon-arc or electron-bombardment evaporation. $\alpha_2 < 1$

(*Continued*)

Table 4.2: (*Continued*)

Element and predominant vapor species	Temp. (°C)		Support materials		Remarks
	mp	$p^* = 10^{-1}$ Torr	Wire, foil	Crucible	
Chromium (Cr)	∼ 1900	1400	W, Ta	–	High evaporation rates without melting. Sublimation from radiation-heated Cr rods preferred. Cr electrodeposits are likely to release hydrogen
Cobalt (Co)	1495	1520	W	Al_2O_3, BeO	Alloys with W, charge should not weigh more than 30% of filament to limit destruction. Small sublimation rates possible
Copper (Cu)	1084	1260	W, Mo, Ta	Mo, C, Al_2O_3	Practically no interaction with refractory materials. Mo preferred for crucibles because it can be machined and conducts heat well
Gallium (Ga)	30	1130	–	Beo, Al_2O_3	Alloys with refractory metals. The oxides are attacked above 1000 °C
Germanium (Ge)	940	1400	W, Mo, Ta	W, C, Al_2O_3	Wets refractory metals but low solubility in W. Purest films by electron-gun evaporation
Gold (Au)	1063	1400	W, Mo	Mo, C	Reacts with Ta, wets W and Mo. Mo crucibles last for several evaporations
Indium (In)	156	950	W, Mo	Mo, C	Mo boats preferred
Iron (Fe)	1538	1480	W	Beo, Al_2O_3, ZrO_2	Alloys with all refractory metals. Charge should not weigh more than 30% of W filament to limit destruction. Small sublimation rates possible
Lead (Pb)	328	715	W, Mo, Ni, Fe	Metals	Does not wet refractory metals. Toxic
Magnesium (Mg)	650	440	W, Mo, Ta, Ni	Fe, C	Sublimates

Table 4.2: (*Continued*)

Element and predominant vapor species	Temp. (°C)		Support materials		Remarks
	mp	$p^* = 10^{-1}$ Torr	Wire, foil	Crucible	
Manganese (Mn)	1244	940	W, Mo, Ta	Al_2O_2	Wets refractory metals
Molybdenum (Mo)	2620	2530	–	–	Small rates by sublimation from Mo foils. Electron-gun evaporation preferred
Nickel (Ni)	1450	1530	W, W foil lined with Al_2O_3	Refractory oxides	Alloys with refractory metals; hence charge must be limited. Small rates by sublimation from Ni foil or wire. Electron-gun evaporation preferred
Palladium (Pd)	1550	1460	W, W foil lined with Al_2O_3	Al_2O_3	Alloys with refractory metals. Small sublimation rates possible
Platinum (Pt)	1770	2100	W	ThO_2, ZrO_5	Alloys with refractory metals. Multistrand W wire offers short evaporation times. Electron-gun evaporation preferred
Rhodium (Rh)	1966	2040	W	ThO_2, ZrO_5	Small rates by sublimation from Rh foils. Electron-gun evaporation preferred
Soleneum (Se_2, Se_n: n = 1–8)	217	240	Mo, Ta, stainless steel 304	Mo, Ta, C, Al_2O_3	Wets all support materials. Wall deposits spoil vacuum system. Toxic $\alpha_v = 1$
Silicon (Si)	1410	1350	–	Beo, ZrO_5, ThO_2, C	Refractory oxide crucibles are attacked by melten Si and films are contaminated by Sio. Small rates by sublimation from Si filaments. Electron-gun evaporation gives purest films
Silver (Ag)	961	1030	Mo, Ta	Mo, C	Does not wet W. Mo crucibles are very durable sources
Strontium (Sr)	770	540	W, Mo, Ta	Mo, Ta, C	Wets all refractory metals without alloying

Table 4.2: (*Continued*)

Element and predominant vapor species	Temp. (°C)		Support materials		Remarks
	mp	$p^* = 10^{-1}$ torr	Wire, foil	Crucible	
Tantalum (Ta)	3000	3060	–	–	Evaporation by resistance heating of touching Ta wires, or by drawing an arc between Ta rods. Electron-gun evaporation preferred
Tellurium (Te_2)	450	375	W, Mo, Ta	Mo, Ta, C, Al_2O_3	Wets all refractory metals without alloying. Contaminates vacuum system. Toxic. $\alpha_v = 0.4$
Tin (Sn)	232	1250	W, Ta	C, Al_2O_3	Wets and attacks Mo
Titanium (Ti)	1700	1750	W, Ta	C, ThO_2	Reacts with refractory metals. Small sublimation rates from resistance-heated rods or wires. Electron-gun evaporation preferred
Tungsten (W)	3380	3230	–	–	Evaporation by resistance heating of touching W wires, or by drawing an arc between W rods. Electron-gun evaporation preferred
Vanadium (V)	1920	1850	Mo, W	Mo	Wets Mo without alloying. Alloys slightly with W. Small sublimation rates possible
Zinc (Zn)	420	345	W, Ta, Ni	Fe, Al_2O_3, C, Mo	High sublimation rates. Wets refractory metals without alloying. Wall deposits spoil vacuum system
Zirconium (Zr)	1850	2400	W	–	Wets and slightly alloys with W. Electron-gun evaporation preferred

From Handbook of Thin Film Technology [6]. Copyright © 1970, McGraw-Hill. Used with permission of McGraw-Hill Book Company.

Table 4.3: Properties of refractory metals

Property	Tungsten	Molybdenum	Tantalum
Melting point (°C)	3380	2610	3000
T (°C) for $p^* = 10^{-6}$ torr	2410	1820	2240
Electrical resistivity, 10^{-4} ohm-cm			
At 20 °C	5.5	5.7	13.5
At 1000 °C	33	32	54
At 2000 °C	66	62	87
Thermal expansion (%)			
From 0 to 1000 °C	0.5	0.5	0.7
From 0 to 2000 °C	1.1	1.2	1.5

From Handbook of Thin Film Technology [7]. Copyright © 1970, McGraw-Hill. Used with permission of McGraw-Hill Book Company.

Platinum, iron, or nickel is sometimes used for materials which evaporate below 1000 °C. The capacity (total amount of evaporant) of such sources is small. The hairpin and wire helix sources are used by attaching the evaporant to the source in the form of small wire segments. Upon melting, the evaporant must wet the filament and be held there by surface tension. This is desirable to increase the evaporation surface area and thermal contact. Multistrand filament wire is preferred because it increases the surface area. The maximum amount that can be held is about 1 g. Dimpled sources and basket boats may hold up to a few grams.

Since the electrical resistance of the source is small, low-voltage power supplies, 1–3 kW, are recommended. The current in the source may range from 20 to 500 A. In some cases, the evaporant is electroplated onto the wire source.

The principal use of wire baskets is for the evaporation of pellets or chips of dielectric materials which either sublime or do not wet the wire on melting. In such cases, if wetting occurs, the turns of the baskets are shorted and the temperature of the source drops.

The rate of evaporation from such sources may vary considerably owing to localized conditions of temperature variation, wetting, hot spots, etc. Therefore, for a given thickness of film, the procedure is to load the source with a fixed weight of evaporant and evaporate to completion or use a rate monitor and/or thickness monitor to obtain the desired evaporation rate and thickness.

4.6.3 Sublimation Sources

For materials evaporating above 1000 °C, the problem of non-reactive supports may be circumvented for materials such as Cr, Mo, Pd, V, Fe, and Si which reach a vapor pressure of 10^{-2} torr before melting. Hence, they can *sublime* and produce a sufficiently high vapor density. The contact area between the evaporant and the source crucible is held to a minimum. Figure 4.16 shows such a source designed by Roberts and Via.

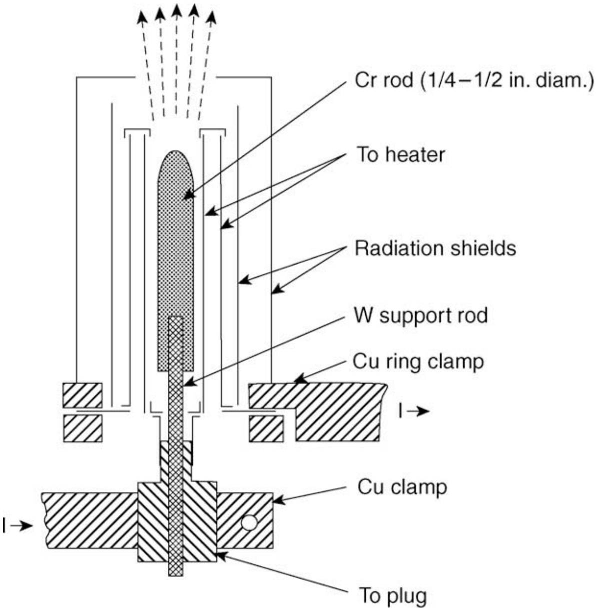

Figure 4.16: Chromium sublimation source (after Roberts and Via). The electric current flows through the tantalum cylinder (heavy lines). (From Handbook of Thin Film Technology [7]. © 1970, McGraw-Hill. Used with permission of McGraw-Hill Book Co.)

A different type of sublimation source is used for the vaporization of thermally stable compounds such as SiO which are commonly obtained as powders or loose chunks. Such source material would release large quantities of gases upon heating, thus causing ejection of particles of the evaporant which may get incorporated into the film. Figure 4.17 shows two sources which solve this problem by reflection of the vaporized material.

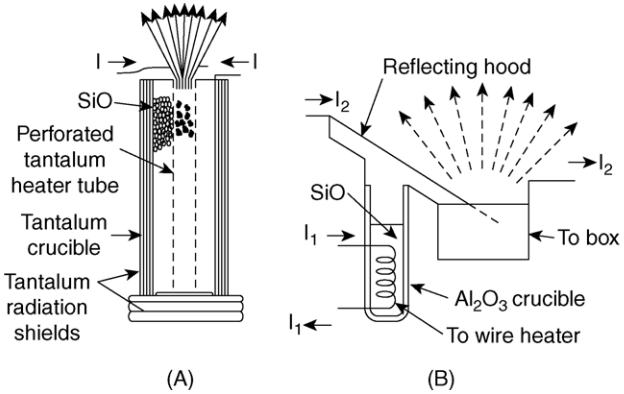

Figure 4.17: Optically dense SiO sources. (A) The Drumheller source; (B) compartmentalized source (after Vergara, Greenhouse and Nicholas). (From Handbook of Thin Film Technology [7]. © 1970, McGraw-Hill. Used with permission of McGraw-Hill Book Co.)

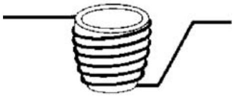

Figure 4.18: Oxide crucible with wire-coil heater. (From Handbook of Thin Film Technology [7]. © 1970, McGraw-Hill. Used with permission of McGraw-Hill Book Co.)

4.6.4 Evaporation Source Materials

We have already discussed the potential problems concerned with the reaction between metal sources and evaporants. Oxides and other compounds are more stable than metals. Table 4.4 gives the thermal stability of refractory oxides in contact with metals. There are many metals not listed in Table 4.4 which can be evaporated from refractory oxide sources. Note that there is no such thing as an absolutely stable oxide, nitride, or other compound. Reaction is controlled by kinetics, i.e. temperature and time.

Oxide crucibles have to be heated by radiation from metal filaments or their contents can be heated by induction heating. This is illustrated in Figures 4.18 and 4.19 for resistance-heated sources.

Other source materials are nitrides such as boron nitride. A well-established crucible material is 50% BN–50% TiB_2. This material (HAD composite, Union Carbide) is a fairly good electrical conductor and hence can be directly heated to evaporate materials. It can be readily machined to shape.

Pyrolytic BN and carbon are also used.

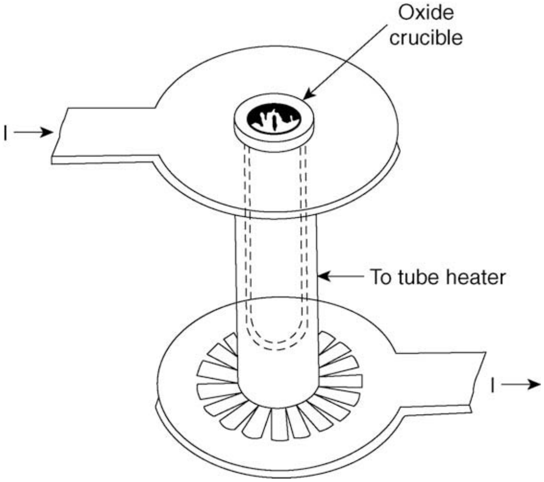

Figure 4.19: DaSilva crucible source. (From Handbook of Thin Film Technology [7]. © 1970, McGraw-Hill. Used with permission of McGraw-Hill Book Co.)

Table 4.4: Thermal stability of refractory oxides in contact with metals

Metal	Temp. for 10^{-2} torr (°C)	Refractory oxides				
		ThO_2	BeO	ZrO_2	Al_2O_3	MgO
W	3230	Slight reduction at 2200 °C	Stable at 1700 °C; reaction > 1800 °C	Stable 1800 °C; little reaction up to 2000 °C	Limited by the onset of Al_2O_3 sublimation at 1800 °C	Limited by the onset of MgO sublimation at 1600–1900 °C
Mo	2530	Little reaction up to 2300 °C	Stable at 1900 °C but not active	Stable at 2000 °C: ZrO_5 decomposes at 2300 °C		
Ta	3060	Stable up to 1900 °C	Stable up to 1600 °C	Stable up to 1600 °C		
Zr	2400	Interaction begins at 1800 °C	Interaction begins at 1600 °C	Slight interaction at 1800 °C	Oxide attacked at 1600 °C	
Be	1230	Only slight interaction at **1600** °C			Oxide discolored at **1400** °C	Stable at **1400** °C but not at **1600** °C
Si	1350	Little or no attack at **1400** °C; noticeable reaction at 1600 °C			Slight reaction at 1400 °C	Slight reaction at 1400 °C, strong at 1600 °C
Ti	1750	Slight interaction at **1800** °C	Little reaction at 1600 °C but considerable at 1800 °C		Little reaction at 1400 °C but considerable at 1800 °C	
Ni	1530	Ni (l) is stable in contact with all oxides at **1800** °C				

Boldface type indicates metal–oxide pairs which can be used for thin film deposition.
After Johnson, Economos and Kingery, and Kohl.
From Handbook of Thin Film Technology [7]. Copyright © 1970, McGraw-Hill. Used with permission of McGraw-Hill Book Company.

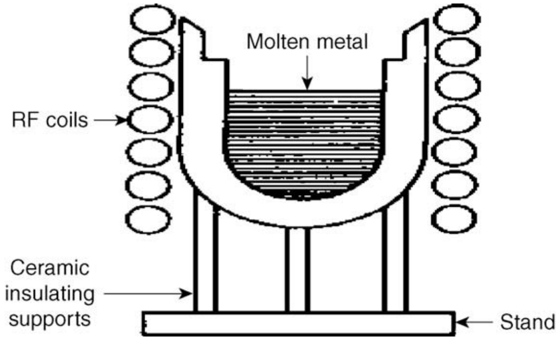

Figure 4.20: RF-heated aluminum source with boron-nitride/titanium-diboride crucible (after Ames, Kaplan and Roland). (From Handbook of Thin Film Technology [7]. © 1970, McGraw-Hill. Used with permission of McGraw-Hill Book Co.)

4.6.5 Induction-Heated Sources

Figure 4.20 shows the induction-heated sources using a BN–TiB_2 crucible. Figure 4.21 shows an induction-heated evaporation sublimation source using a water-cooled copper crucible [19]. This is suited to the evaporation of reactive metals such as Ti, Be, etc., which will react with all the refractory oxides, nitrides, etc.

4.6.6 Electron Beam-Heated Sources

Electron beam-heated sources have two major benefits. One is a very high power density and hence a wide range of control over evaporation rates from very low to very high. The other is that the evaporant is contained in a water-cooled copper hearth, thus eliminating the problem of crucible contamination.

The evaporation rate for pure metals like Al, Au, and Ag, which are good thermal conductors, from water-cooled copper crucibles decreases owing to heat loss to the crucible walls. In such cases, crucible liners of carbon and other refractory materials are used.

Any gun system must consist of at least two elements: a cathode and an anode. In addition, it is necessary to contain these in a vacuum chamber in order to produce and control the flow of electrons, since they are easily scattered by gas molecules. A potential difference is maintained between the cathode and the anode. This varies from as little as a few kilovolts to hundreds of kilovolts. In melting systems, a normal operational range is of the order of 10–40 kV. In the simple diode system, the cathode emits electrons, which are then accelerated to the anode across the potential drop. Where the anode is the workpiece to be heated, this is termed a work-accelerated gun. It is shown schematically in Figure 4.22(a). In a self-accelerated gun structure, an anode is located fairly close to the cathode, and electrons leave the cathode

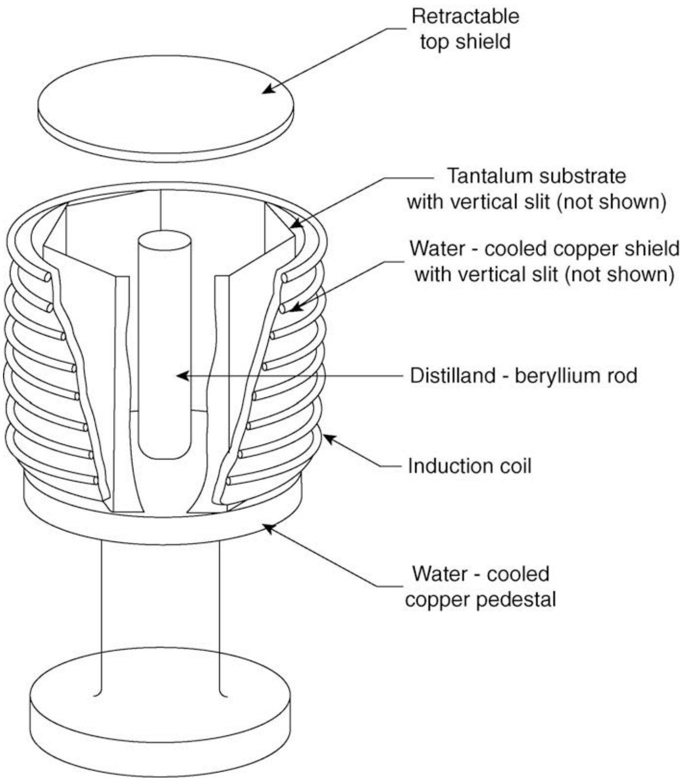

Figure 4.21: Schematic representation of the distillation set-up.

surface, are accelerated by the potential difference between the cathode and anode, pass through the hole in the anode, and continue onward to strike the workpiece. Self-accelerated guns have become the more common type in use and offer more flexibility than work-accelerated guns.

Electron beam guns may be further subdivided into two types depending on the source of electrons: thermionic guns and plasma guns.

4.6.6.1 Thermionic Guns

In thermionic guns, the source of electrons is a heated wire or disk of a high-temperature metal or alloy, usually tungsten or tantalum. Such guns have the limitation of a minimum operating gas pressure of about 1×10^{-3} torr. Higher pressures cause scattering of the e-beam as well as a pronounced shortening of the cathode life (if it is a wire or filament) owing to erosion by ion bombardment. Figure 4.23 shows examples of thermionic e-beam-heated work-accelerated sources. The close cathode gun shown in Figure 4.23(A) is not a desirable configuration since molten droplet ejection from the pool impinging on the cathode will terminate the life of the

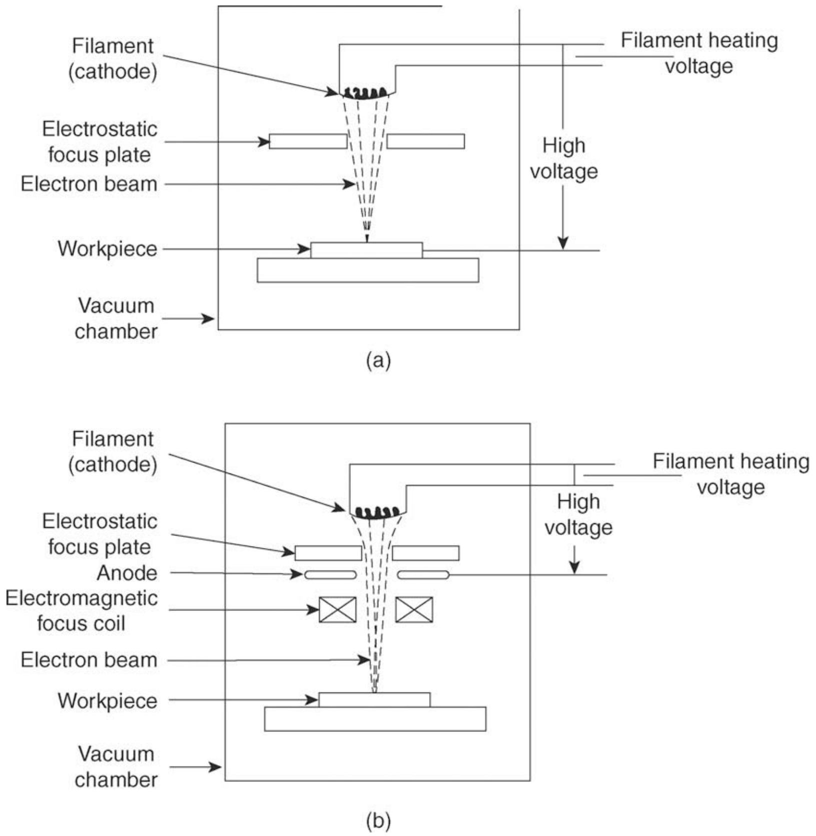

Figure 4.22: Simple electron beam guns. (a) Work-accelerated gun; (b) self-accelerated gun.

cathode owing to low melting alloy formation. Thus cathodes are hidden from direct line of sight of the molten pool and the e-beam is bent by electrostatic fields (Figure 4.23B, C) or a magnetic field (Figures 4.24 and 4.25) generated by electromagnets. The latter is a preferred arrangement since variation of the X and Y components of the magnetic field can be used to scan the position of the beam on the molten pool surface.

Figures 4.23–4.25 show linear cathodes (i.e. wires or rods) and are referred to as transverse linear cathode guns. Figure 4.26 shows a disk cathode which is characteristic of a high-power Pierce-type electron beam gun. Low-power Pierce type guns may have a hairpin filament or a wire loop as the cathode. In either case the beam geometry of the Pierce gun is different from that of the transverse linear cathode guns. In some instances, the electron emitter assembly is located at a distance from the crucible in a separately pumped chamber to keep the pressure below 1×10^{-3} torr, with a small orifice between the emitter chamber and the crucible chamber for the passage of electrons.

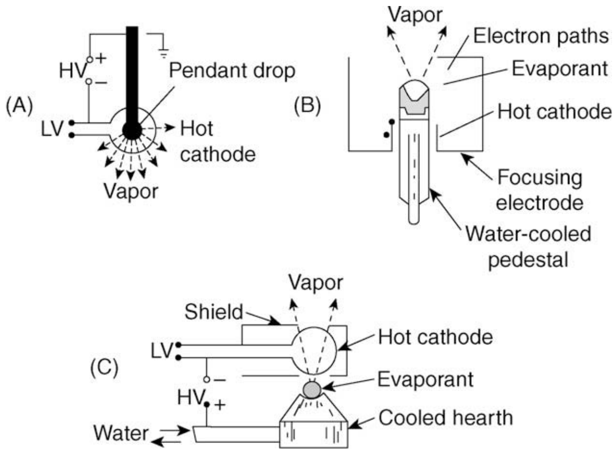

Figure 4.23: Work-accelerated electron-bombardment sources: (A) pendant-drop method; (B) shielded filament (Unvala); (C) shielded filament (Chopra and Randlett). (From Handbook of Thin Film Technology [7]. © 1970, McGraw-Hill. Used with permission of McGraw-Hill Book Co.)

4.6.6.2 Plasma Electron Beam Guns

A plasma is defined as a region of high-temperature gas containing large numbers of free electrons and ions. By a proper application of electrical potential, electrons can be extracted from the plasma to provide a useful energy beam similar to that obtained from thermionic guns. There are two types of plasma e-beam gun:

- *Cold cathode plasma electron beam* – the plasma e-beam gun has a cylindrical cathode cavity made from a metal mesh or sheet (Figure 4.27) containing the ionized plasma

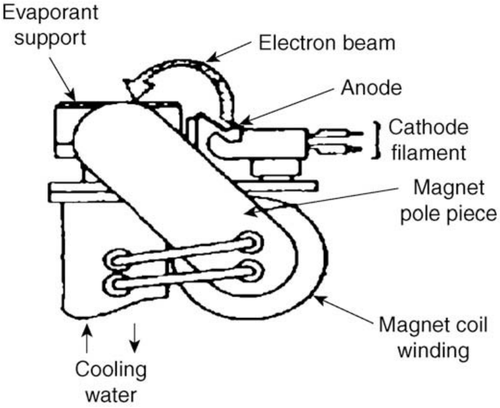

Figure 4.24: Bent-beam electron gun with water-cooled evaporant support (with permission of Temescal Metallurgical Co., Berkeley, CA). (From Handbook of Thin Film Technology [7]. © 1970, McGraw-Hill. Used with permission of McGraw-Hill Book Co.)

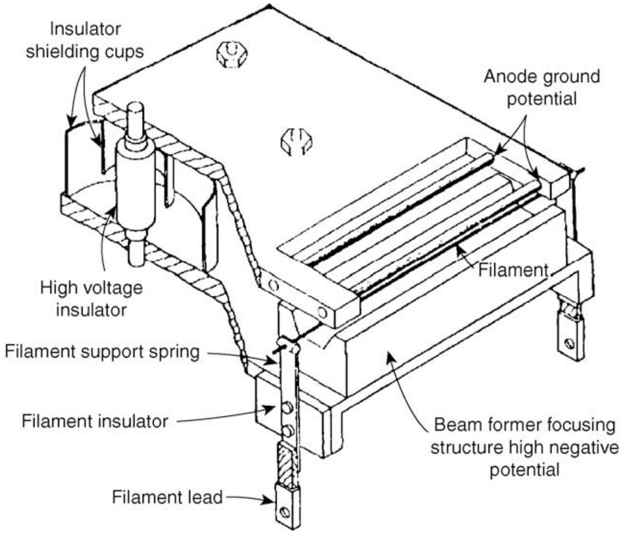

Figure 4.25: Transverse electron beam gun.

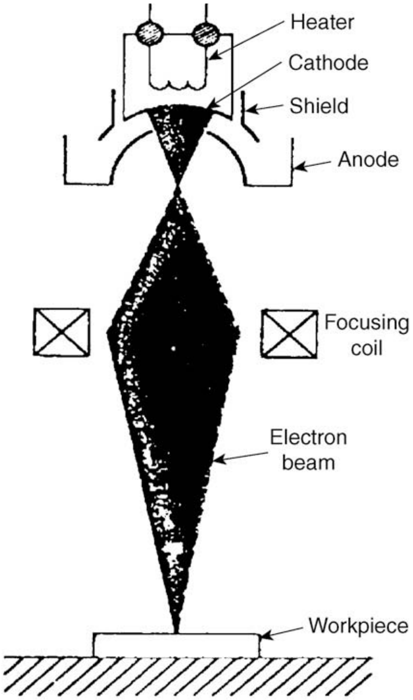

Figure 4.26: Schematic representation of a Pierce gun.

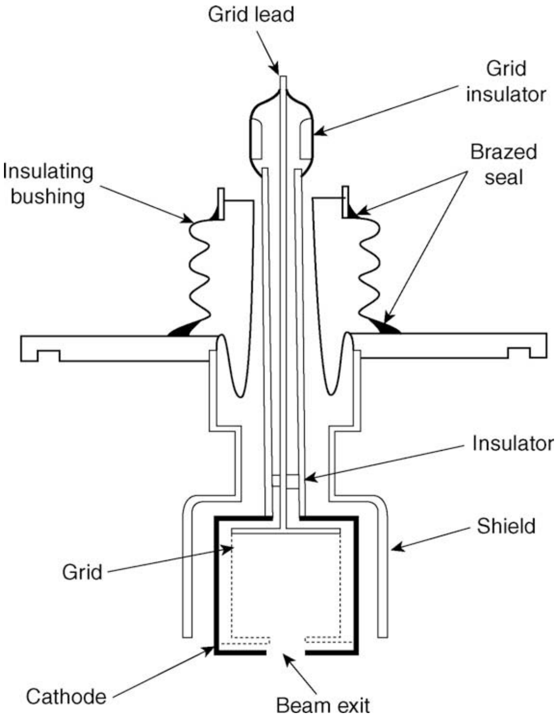

Figure 4.27: Cold cathode plasma electron beam gun.

from which electrons are extracted through a small aperture in one end. The cathode is maintained at a negative potential, e.g. -5 to -20 kV, relative to the workpiece and remainder of the system, which are at ground potential. After evacuation of the system, a low pressure of ionizable gas in the range of 10^{-3}–10^{-1} torr is introduced. Depending on the high-voltage level, a long path discharge between the cathode and other parts of the system will occur in the gas at a particular pressure. Ionizing collisions in the gas then produce positive ions which are accelerated to the cathode, causing electrons to be released from the cathode surface. Although the cathode may heat up slightly owing to ion bombardment, no heating is required for electron emission. Upon proper adjustment of cathode voltage and gas pressure, a beam mode of operation is established, since interaction between the plasma inside and outside of the cathode and the electric fields between cathode surface and plasma boundary will largely confine electron emission to the end of the cathode and its interior. In argon, a beam mode is supported at about 10^{-2} torr with 5–10 kV. Beam currents range up to 3 A for a 3 inch diameter cathode in argon at 20 kV. With lighter gases, e.g. helium, higher pressure to about 10^{-1} torr will yield a beam mode in this same voltage range. Beam current will vary with voltage and pressure control. More specific information is

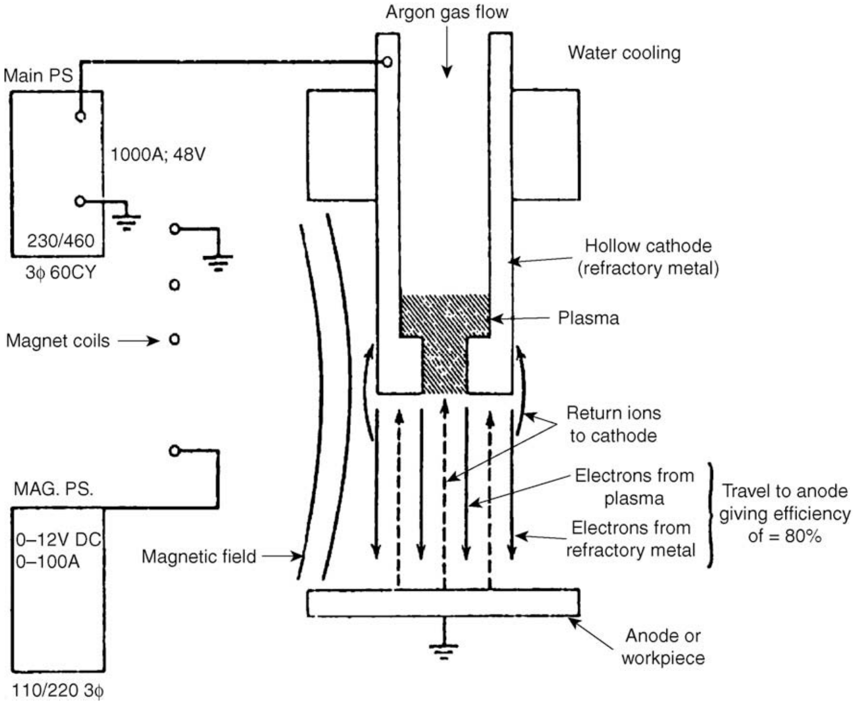

Figure 4.28: Schematic of the hot hollow cathode electron beam gun.

given by Cocca and Stauffer [95]. The beam is self-collimating because of the focusing effect of positive ions in the beam path and the electrostatic lensing action of the aperture since it separates regions of different potential gradient. The beam is well collimated, having a cross-section equal to that of the cathode aperture. Adjustment of focus can be achieved to some extent by varying pressure and voltage, but external focusing may also be used if desired, with magnetic or electrostatic lenses, as with conventional election beams.

- *Hot hollow cathode discharge beam* – the hollow cathode discharge beam applied to vacuum processing has been reported by Morley [96] and differs in a number of respects from the plasma beam. A schematic of the hollow cathode discharge beam is shown in Figure 4.28. Here the cathode must be constructed of a refractory metal since it operates at elevated temperatures. An ionizable gas, usually argon, is introduced into the system through the tubular-shaped cathode. A pressure drop across the orifice in the cathode provides a sufficient amount of gas inside the cathode to sustain the plasma, which generates the beam.

A low-voltage, high-amperage direct current (DC) power source is utilized. When radio-frequency (RF) power from a commercial welding starter is coupled to the gas, it becomes ionized and the plasma is formed. Continued ion bombardment of the cathode results in heating of the cathode and increased electron emission. Ultimately, a high-current 'glow discharge' will occur, analogous to that experienced in vacuum arc melting at higher pressures. At this point, the discharge appears as a low power density beam 'flowing' from the cathode aperture and fanning out in conical shape into the chamber. However, a parallel axial magnetic field is imposed on the beam (as seen in Figure 4.28) which then forms a high power density, well-collimated beam. The hollow cathode discharge beam is operationally stable and efficient over the pressure range from 10^{-4} to 10^{-1} torr. A more detailed description of physical aspects, operational characteristics, and cathode design has been given by Morley [96].

4.6.6.3 Comparisons

Thermionic and plasma e-beam guns can be used equally well for evaporation. Focusing of the beam spot is easier for the thermionic guns. The plasma guns have the advantage of being able to operate at higher pressures, which can be important for gas scattering evaporation, reactive evaporation, and ion plating.

4.6.7 Arc Evaporation

Definitions of arcs include: 'A discharge in a gas or vapor that has a voltage drop at the cathode of the order of the minimum ionizing or exciting potential of the gas or vapor' (Karl T. Compton, Princeton University).

Berghaus [97] describes the use of arcs to form refractory compounds by reactive evaporation. Since 1940, consumable and non-consumable vacuum arc melting processes have been developed to melt and refine various reactive metals such as Ti, Hf, Zr, etc. More recently, arc techniques have been used to deposit metals [98, 99] and refractory compounds, and even for extraction of ions from the vacuum arc plasma for the deposition of metal films [100].

Wroe [101] in 1958 and Gilmour and Lockwood [102] suggested vacuum arcs as a source for metallic coatings. The US patents to Snaper [103, 104] in 1971 and the Russian patents to Sablev [105, 106] in 1974 set the stage for the commercial production of arc coatings, which were achieved in the USSR around 1977–1978. The first commercial use of the arc evaporation-deposition method was for TiN coatings deposited at low temperatures, particularly for high-speed steel cutting tools by arc evaporation of titanium in a nitrogen plasma. This follows on the heels of the activated reactive evaporation (ARE) process, developed in 1971 for deposition of refractory compounds such as TiN using e-beam evaporation techniques and discussed in Section 4.8.6. There is very extensive Russian literature on vacuum arc coating technology and the reader can find a convenient source in recent reviews by Sanders [107] and by Martin [108].

There are two types of cathodic arc systems: pulsed and continuous. In the pulsed devices, the arc is repeatedly ignited and extinguished using a capacitor blank to supply the arc power [102]. Pulsed arcs have the advantage of letting the target cool between the pulses. The disadvantage is the decrease in steady-state coating rates.

The continuous cathodic arc can be random in nature or controlled. By the use of an insulating ring, a random arc source can be constrained at the edge of the target, but allowed random motion within that constraint. Random arc sources have the advantage of simplicity and excellent target utilization because the entire target (except near the very edge) is utilized in the arc of very large parts. The main disadvantage of random arcs is the formation of macroparticles which may cause the resulting coating to be unsuitable in some applications. Figure 4.29 shows that macroparticles are ejected at small angles with respect to the target surface, and can therefore be minimized using appropriate shielding. Such a strategy has made possible arc-produced decorative coatings where surface finish and optical peculiarity are of concern.

Magnetic fields can be used to control the trajectories of the arcs. These fields can be used to discourage the arc from leaving the desired portion of the target surface or can be used to define a well-controlled path for the arc to follow, in the ‘steered arc’ devices. While the mechanism is still the subject of some debate, it is clear, at least in the case of ceramic coatings based on refractory metals, that steered arcs can produce coatings having extremely low or no measurable macroparticle component.

Macroparticles can also be removed by the use of suitable filters, as discussed by Sanders [107] and by Martin [109]. This is known as the filtered arc evaporation process. Other

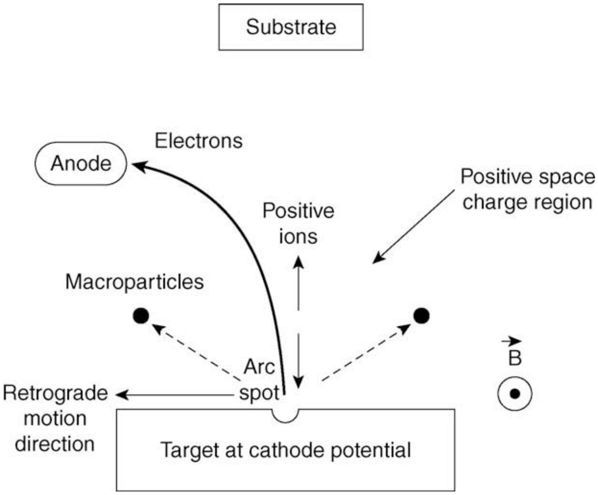

Figure 4.29: Phenomena occurring at a discrete cathodic arc spot.

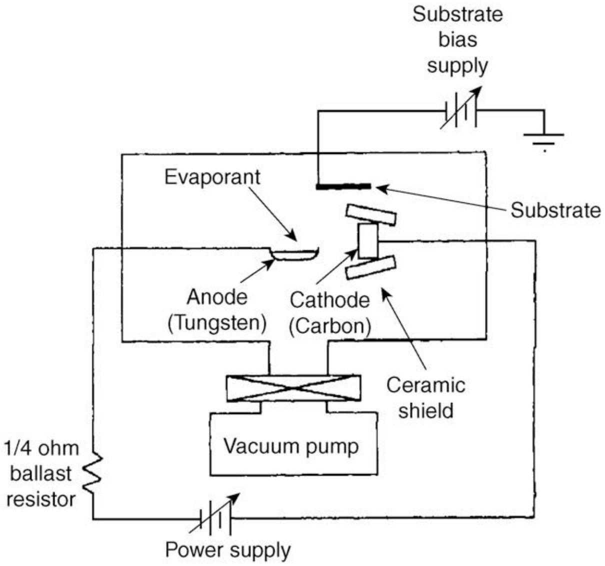

Figure 4.30: Schematic of the anodic arc evaporation process.

strategies for macroparticles involve the production of diffuse arcs. In one case, the cathode is contained in a crucible which is allowed to heat up to a temperature where the target material has a substantial vapor pressure [110]. This causes a decrease in the arc voltage and current density, the discharge becomes diffuse and macroparticles no longer form. The other approach is the 'anodic arc' [111–113] (Figure 4.30). In this process the cathode initially supplies electrons as well as ions until the anode heats up. At this point, with sufficient electron emission, a diffuse arc forms on the hot anode target material which supplies the ions necessary to sustain the discharge. The cathode material is not evaporated and the coating material now emanates from the anode. There are no macroparticles formed. High deposition rates (several micrometers per minute) are obtained for a variety of metals including Al, Ti, V, Ca, Mn, Fe, Ni, Cu, Pd, Ag, Au, and Pt [111]. Since the substrate is left relatively cool, the process makes it possible to produce adherent coatings on plastics at temperatures less than 70 °C, which makes this relatively new process a competitor for sputter deposition. Alloy coatings such as stainless steel can be readily deposited with good stoichiometric transfer. For example, Ni, Al, and stainless steel coatings less than 1 μm thickness impart excellent corrosion protection to iron [114].

One of the main advantages of arc deposition processes is the relatively high level of ionizing atoms in the plasma. This makes it convenient to extract ion beams from the plasma and deposit macroparticle free coatings entirely from the ion beam [107, 109].

4.7 Deposition Rate Monitors and Process Control

The properties of deposits are dependent on the control exercised during the process. The thinner the deposit, the more critical the control of the operation.

4.7.1 Monitoring of the Vapor Stream

4.7.1.1 Ionization Gauge Rate Monitor

This device is very similar to a hot cathode ionization gauge and monitors the atom density in the vapor phase by ionizing the vapors, collecting and measuring the ion current. Several arrangements are shown in Figure 4.31.

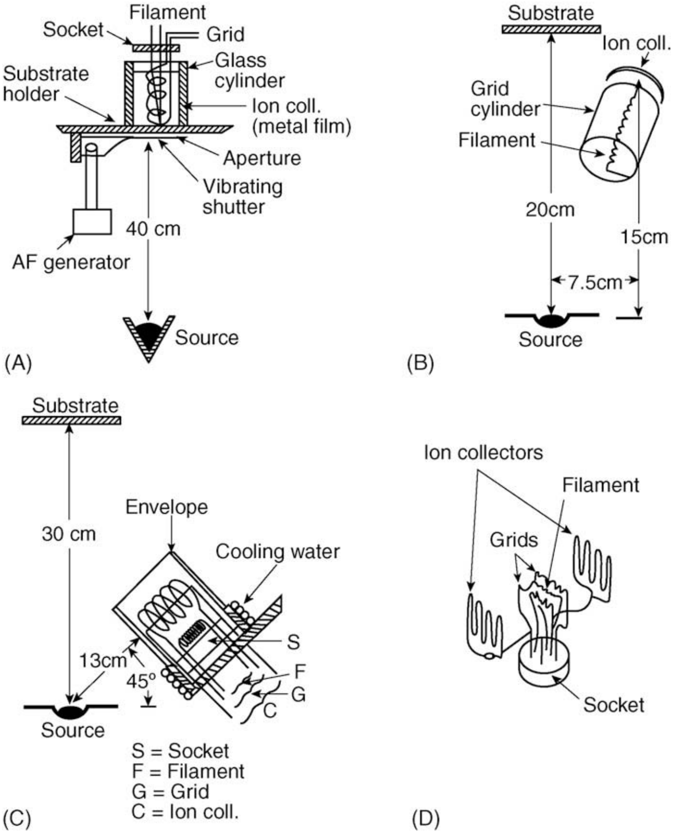

Figure 4.31: Ionization rate monitor designs and arrangements: (A) after Schwarz; (B) after Giedd and Perkins; (C) after Perkins; (D) after Dufour and Zega. (From Handbook of Thin Film Technology [7]. © 1970, McGraw-Hill, Used with permission of McGraw-Hill Book Co.)

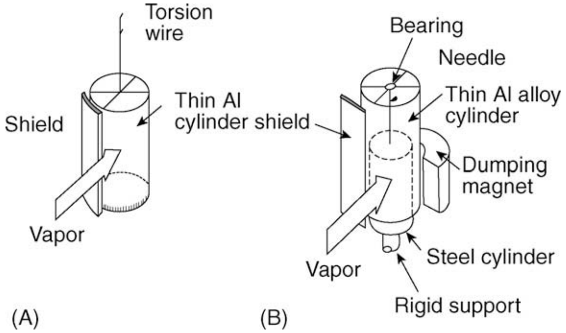

Figure 4.32: Particle-impingement-rate monitors: (A) torsion-wire device (after Neugebaur); (B) pivot-supported device (after Beavitt). (From Handbook of Thin Film Technology [7]. © 1970, McGraw-Hill. Used with permission of McGraw-Hill Book Co.)

4.7.1.2 Particle Impingement Rate Monitors

The gauge, which is a cylinder suspended by a wire or riding on a bearing, is imparted a momentum by the impinging particles which can be measured by the torsional forces. They are illustrated in Figure 4.32.

4.7.1.3 Ion Current Monitor for Electron Beam-Heated Source

An e-beam-heated molten pool has a plasma sheath above it. Positive ions from the plasma follow a very similar trajectory as the electrons with a slightly larger radius of curvature, owing to their higher mass, and are beamed away from the molten pool by the same magnetic field which bends the electrons towards the pool. Therefore an ion collector can be placed so as to intercept this ion beam and the resultant ion current can be used in a feedback loop to control the evaporation rate. Two manufacturers of e-beam guns have offered this option.

4.7.1.4 Spectroscopic Methods

Monitoring and control of the deposition rate can be done on the basis of mass spectrometry, atomic absorption spectrometry, and electron emission impact spectrometry. Each of them involves the choice of an appropriate materials-selective sensor. The principles, advantages, and limitations of each of these are presented in a good review paper by Lu. The reader is referred to this paper and the references cited therein [115].

4.7.2 Monitoring of Deposited Mass

4.7.2.1 Microbalances

There are various types of devices which measure a change in mass due to condensed atoms based on elongation of a thin quartz-fiber helix, the tension of a wire, or the deflection of a pivot-mounted beam. Examples are shown in Figures 4.33 and 4.34.

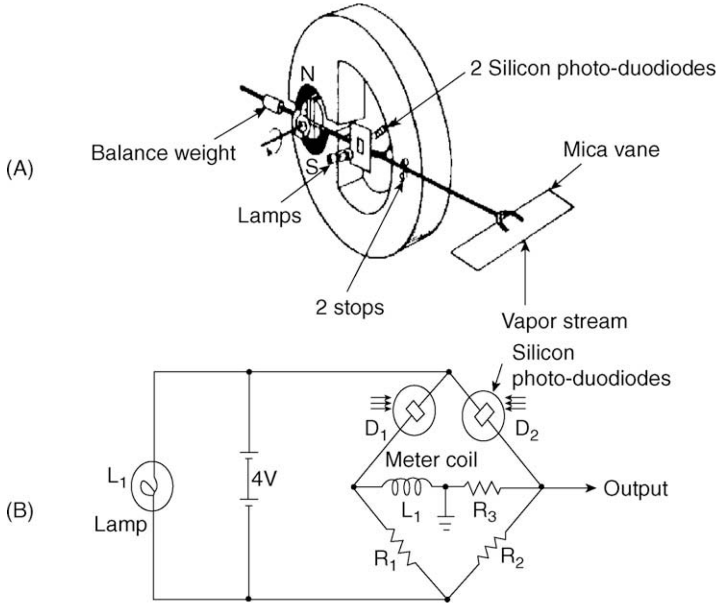

Figure 4.33: (A) Schematic drawing and (B) circuit diagram of a microbalance constructed from a microammeter movement (Hayes and Roberts). (From Handbook of Thin Film Technology [7]. © 1970, McGraw-Hill. Used with permission of McGraw-Hill Book Co.)

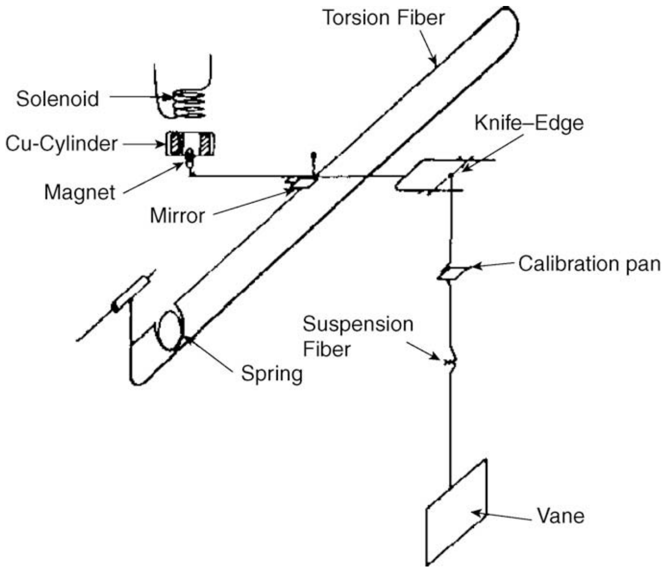

Figure 4.34: Microbalance with torsion-fiber suspension and electromagnetic force compensation at beam end (Mayer et al.). (From Handbook of Thin Film Technology [7]. © 1970, McGraw-Hill. Used with permission of McGraw-Hill Book Co.)

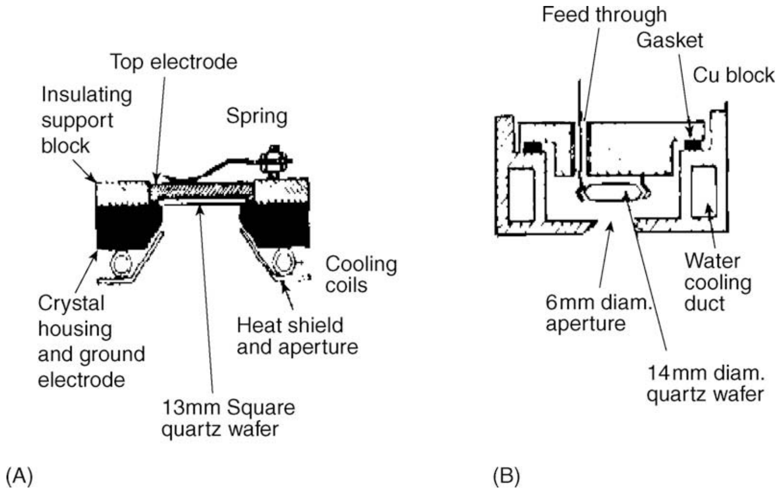

Figure 4.35: Oscillator crystal holders for deposition monitoring: (A) after Behrndt and Love; (B) after Pulker. (From Handbook of Thin Film Technology [7]. © 1970, McGraw-Hill. Used with permission of McGraw-Hill Book Co.)

4.7.2.2 *Crystal Oscillators*

The crystal oscillator monitor utilizes the piezoelectric properties of quartz. The resonance frequency induced by an alternating current (AC) field is inversely proportional to crystal thickness. In practice, the change in frequency of a crystal exposed to the vapor beam is compared to that of a reference crystal. An example is shown in Figure 4.35.

4.7.3 Monitoring of Specific Film Properties

In preparing thin films, often only one property is of interest, e.g. optical or electrical.

Optical monitors measure phenomena such as light absorbance, transmittance, reflectance or related interference effects during film deposition. An example is shown in Figure 4.36.

Using *resistance monitors*, the film thickness can be continuously monitored using in situ resistance measurements as shown in Figure 4.37.

4.7.4 Evaporation Process Control

4.7.4.1 Thickness Control

Usually monitoring of an evaporation process is combined with the means to control film deposition. Frequently, the only requirement is to terminate the process when the thickness or a thickness-related property has reached a certain value. The simplest way is to evaporate a

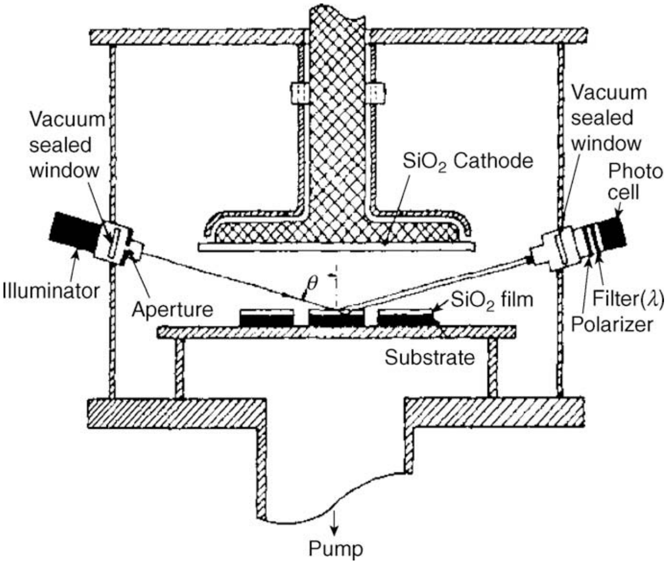

Figure 4.36: Schematic of an RF sputtering system (after Davidse and Maissel) with optical-thickness monitor. (From Handbook of Thin Film Technology [7]. © 1970, McGraw-Hill. Used with permission of McGraw-Hill Book Co.)

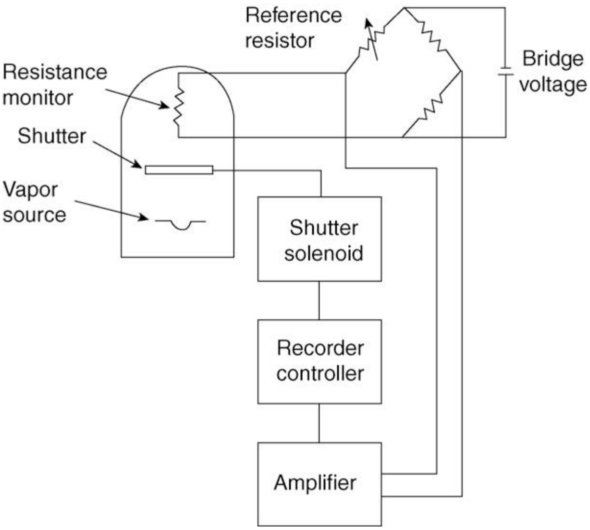

Figure 4.37: Wheatstone-bridge circuit for resistance monitoring. (From Handbook of Thin Film Technology [7]. © 1970, McGraw-Hill. Used with permission of McGraw-Hill Book Co.)

weighed amount of source material to completion. Knowing the emission characteristics of the source will allow the film thickness to be calculated. Alternately, monitoring devices discussed earlier can be calibrated to measure thickness directly.

4.7.4.2 Rate Control

Rate control is a more complex task and involves measuring the signal from a rate monitor and using it in a feedback loop to control the power to the source and hence its temperature and evaporation rate. Table 4.5 illustrates the pros and cons of various evaporation process control methods.

4.8 Deposition of Various Materials

4.8.1 Deposition of Metals and Elemental Semiconductors

Evaporation of single elements can be carried out from a variety of evaporation sources subject to the restrictions discussed above dealing with melting point, reactions with container, deposition rate, etc. A typical arrangement is shown in Figure 4.1 for e-beam heating.

4.8.2 Deposition of Alloys

Alloys consist of two or more components, which have different vapor pressure and hence different evaporation rates. As a result, the composition of the vapor phase, and therefore the deposit, has a constantly varying composition. There are two solutions to this problem: multiple sources and single rod-fed or wire-fed e-beam sources.

4.8.2.1 Multiple Sources

This is the more versatile system. The number of sources evaporating simultaneously is equal to or less than the number of constituents in the alloy. The material evaporated from each source can be a metal, an alloy, or a compound. Thus, it is possible to synthesize a dispersion strengthened alloy, e.g. Ni–ThO_2. On the other hand, the process is complex because the evaporation rate from each source has to be monitored and controlled separately. The source to substrate distance has to be sufficiently large (15 inches for 2 inch diameter sources) to have complete blending of the vapor streams prior to deposition, which decreases the deposition rate (Figure 4.38). Moreover, with gross differences in density of two vapors, it may be difficult to obtain a uniform composition across the width of the substrate owing to scattering of the lighter vapor atoms. In another example, Nicholls et al. reported hot corrosion-resistant Ni–Cr–Al coatings by magnetron sputtering or multiple target e-beam evaporation [116].

Table 4.5: Evaporation process control

Control method	Electrical signal		Prerequisites for	
	Available	Related to	Thickness control	Rate control
Evaporation to completion	No	–	Weighed evaporant change	Not applicable
Control of source temperature, power, or current	Yes	Evaporation rate	Rates must be integrated	Error-signal feedback
Ionization rate monitor	Yes	Evaporation rate	Rates must be integrated	Error-signal feedback
Particle impingement devices	No	–	Direct observation on pivoted models, manual stop	Direct observation on torsion-wire models, manual power adjustment
Microbalances	Electromagnetic or electrostatic models: yes	Deposit thickness	Strip-chart recorder, preset microswitch for automatic termination	Programmed weight increase or second signal by electronic differentiation
Crystal oscillator	Yes	Deposit thickness	Counter, meter, or recorder; preset microswitch for automatic termination	Second signal by differentiation; servoloop
Optical monitors	With photocell: yes	Deposit thickness	Strip-chart recorder; fairly complex circuitry for automatic termination	Has not been implemented yet
Resistance monitors	Yes	Deposit thickness	Strip-chart recorder and preset microswitch, or digital techniques	Second signal by electronic differentiation; servoloop
Capacitance monitors	No	Deposit thickness or rate	Planar capacitor substrate; oscillator circuit with reference capacity and comparator	Direct rate indication from Riddle's vapor capacitor

From Handbook of Thin Film Technology [7]. Copyright © 1970, McGraw-Hill. Used with permission of McGraw-Hill Book Company.

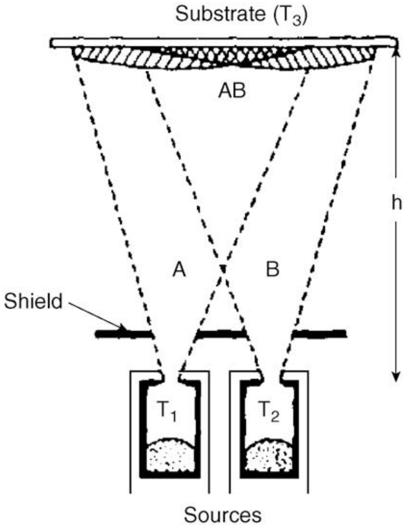

Figure 4.38: Two-source evaporation arrangement yielding variable film composition. (From Handbook of Thin Film Technology [7]. © 1970, McGraw-Hill. Used with permission of McGraw-Hill Book Co.)

Some examples are given in Table 4.6. It is possible to evaporate each component sequentially, thus producing a multilayered deposit which is then homogenized by annealing after deposition. This procedure makes it even more difficult to achieve high deposition rates. A multiple source arrangement for production of alloy deposits at high rates is not known.

4.8.2.2 Single Rod-Fed Electron Beam Source

The disadvantages of multiple sources for alloy deposition can be avoided by using a single source [117, 118]. It can be a wire-fed or rod-fed source; the latter is shown in Figure 4.39. There is a molten pool of limited depth above the solid rod. If the components of an alloy, A1B10, have different equilibrium vapor pressures, then the steady-state composition of the molten pool will differ from the feed rod, e.g. A1B10. Under steady-state conditions, the composition of the vapor is the same as that of the solid being fed into the molten pool. One has the choice of starting with a button of appropriate composition A1B10 on top of a rod A1B1 to form the molten pool initially, or starting with a rod of alloy A1B1 and evaporating until the molten pool reaches composition A1B10. Precautions to be observed are that the temperature and volume of the molten pool have to be constant to obtain a constant vapor composition. A theoretical model has been developed and confirmed by experiment. Ni–20Cr, Ti–6Al, Ag–5Cu, Ag–10Cu, Ag–20Cu, Ag–30Cu, Ni–xCr–yAl–xY alloy deposits have been successfully prepared. To date, experimental results indicate that this method can be used with vapor pressure differences of a factor of 5000 between the components. This method cannot be used where one of the alloy constituents is a compound, e.g. Ni–ThO_2.

Table 4.6: Two-source evaporation, experimental conditions, and types of films obtained

Evaporated constituents	Evaporation conditions and method of control	Substrate temp. (°C)	Films obtained
Alloy and multiphase films			
Cu + Ni	Sequential evaporation	Low	Stratified films annealing at 200 °C yields two-phase alloy films
Cu, Ag, Au, Mg, Sn, Fe, Co	Simultaneous evaporation from two sources Isolation-rate monitor control, ±1%	-193	Binary alloy films of metastable structures
Cu, Ag, Au, Al, Ni, and others	Simultaneous evaporation from two sources. Rates adjusted by varying source temperature	25–600	Binary alloy films of varying composition and structure
Ni + Fe	Two wire-ring sources, evaporation rates controlled by quartz-crystal oscillator	300	Permalloy films. $d' \approx 10\,\text{Å}\,\text{s}^{-1}$
Nb + Sn	Two sources, rates monitored by particle impingement-rate monitor. Impingement ratio $N_{Nb}{:}N_{Sn} = 3$	25–700	Superconducting Nb_2Sn films, $d' \approx 10\,\text{Å}\,\text{s}^{-1}$. $\alpha_c \approx 1$
V, Nb + Si, Sn	Two electron-gun sources, rates monitored by measuring ionization current	–	Superconducting films of approx composition Nb_2Sn and V_2Si
ZnS + LiF	Two sources, rates monitored by a micro-balance. Variable impingment ratios	30–40	Mixed dielectric films of different composition. $d' \approx 10\text{–}30\,\text{Å}\,\text{s}^{-1}$
Au, Cr + SiO, MgF_2	Two-source evaporation with ionization-rate monitor content (±1–2%)	25–300	Au–SiO, Au–MgF_2, Cr–SiO, and Cr–MgF_2; resistor films of different compositions
Cr + SiO	SiO source at 1100 °C, Cr source at 1500 °C. Impingement ratio varied with location on substrate	400	High-resistivity Cr–SiO films of variable composition
Cd + S	Two effusion overs, Cd at 400–450 °C, S at 120–150 °C. Cd excess	400–650	Stoichiometric CdS crystals
Cd + Se	Impingement films controlled by source temperature. $N_{Cd} \approx 2 \times 10^{15}$, $N_{Se} \approx 10^{12}\text{–}10^{15}\ \text{cm}^{-1}\ \text{s}^{-1}$	200	Stoichiometric CdS films

(*Continued*)

Table 4.6: (*Continued*)

Evaporated constituents	Evaporation conditions and method of control	Substrate temp. (°C)	Films obtained
PbSn + PbTe	Source temperature varied around 750 °C	300	Epitaxial films of $PbSe_{1\sim s}Te_2$ on NaCl crystals
Bi + Te	Bi source at 750 °C, Te source temperature variable. $N_{Te}:N_{Bi} = 10–40$	400–500	Stoichiometric films of $BiTe_2$. *n*-type, 2×10^{15} electrons cm^{-3}
Bi + Se	Rate control by quartz-crystal oscillator. Se source at 250 °C; Bi source temperature variable	52	Vitreous, semiconducting films of non-stoichiometric composition
Al + Sb	Source temperature adjusted by quartz-crystal oscillator to yield $N_{Sb}:N_{Al}$ ratios of 1.6–16	550	Stoichiometric AlSb films $d' \approx 10$ Å s^{-1}
Ga + As	Ga source at 940–970 °C, As source at 300 °C $N_{As}:N_{Ga} = 10$; Ga implingement flux: 10^{15} cm^{-2} s^{-1}	550	Stoichiometric GaAs films. Epitaxial on (100); NaCl, polycrystalline on quartz
Ga + Aa	Ga source at 910 °C, As source at 295 °C. Deposition rate: <2 Å s^{-1}	375–450	Stoichiometric GaAs films on GaAs. Ga, and Al_2O_3 single-crystal substrates. Filter featured to single-crystalline
In + As	Incident fluxes: $N_{In} = 5 \times 10^{15}$ cm^{-2} s^{-1}, $N_{As} = 5 \times 10^{15}$ cm^{-2} s^{-1}	230–680	Stoichiometric InAs films: *n*-type
In + Sb	Incident fluxes: $N_{In} = 5 \times 10^{14}$ cm^{-2} s^{-1}, $N_{Sb} = 5 \times 10^{15}–5 \times 10^{17}$ cm^{-2} s^{-1}	400–520	Stoichiometric InSb films: *n*-type
	Source temperature adjusted by microbalance to yield $N_{Sb}:N_{In} = 1.1$	250	Stoichiometric InSb films: α_c of Sb ≈ 0.6

From Handbook of Thin Film Technology [7]. Copyright © 1970, McGraw-Hill. Used with permission of McGraw-Hill Book Company.

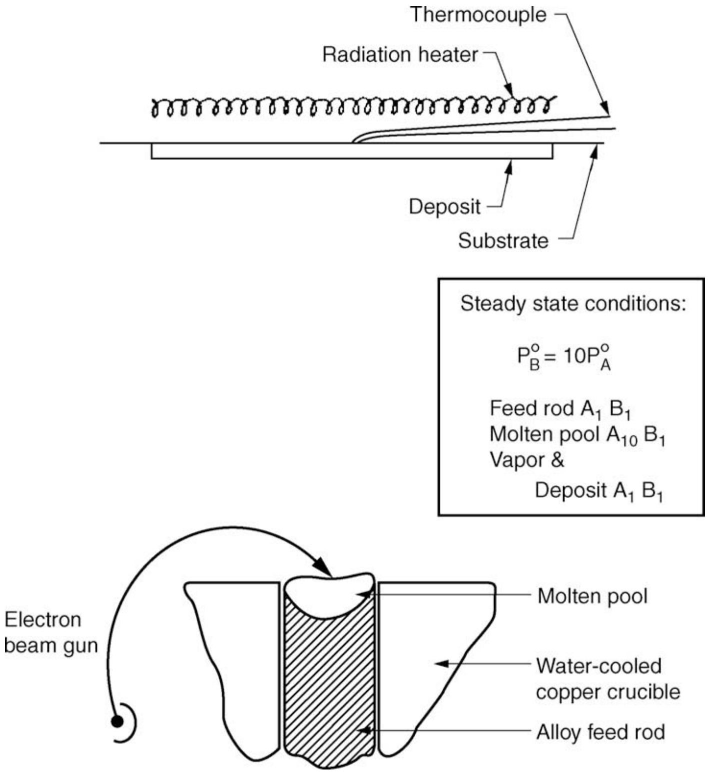

Figure 4.39: Schematic of direct evaporation of an alloy from a single rod-fed source.

Suzuki et al. deposited TiAl alloy by intense pulsed ion beam evaporation [119]. When pure Ti and Al targets were used they were unable to produce intermetallic compound. However, sintered Ti/Al target successfully produced the Ti_3Al thin film. The schematics of the apparatus is shown in Figure 4.40.

Shevakin et al. [120] investigated the relationship between the composition of the evaporant material and the condensates for alloy evaporation using e-beam evaporation techniques. They used this method to determine thermodynamic activities of the components of binary alloys at temperatures above the melting point of the alloy.

4.8.3 Deposition of Intermetallic Compounds

Intermetallic compounds which are generally deposited, such as GaAs, PbTe, InSb, and TiAl, have as their constituents elements with low melting points and high vapor pressures. These compound semiconductors need to have a carefully controlled stoichiometry, i.e. cation:anion ratio. Therefore, they can best be prepared by flash evaporation or sputtering.

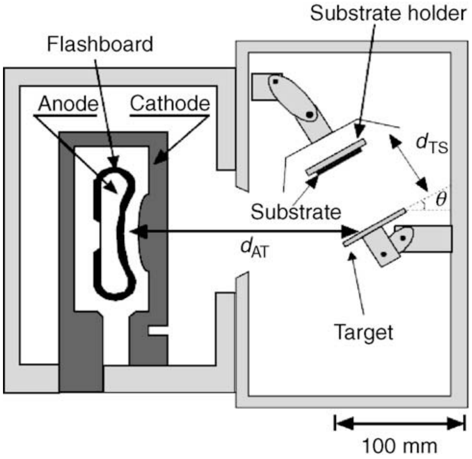

Figure 4.40: Intense pulsed ion beam evaporation system.

A_3B_5 compounds are harder to deposit because of their stoichiometry and the fact that the elements of 5A group are volatile. Lida deposited InSb films by flash evaporation to investigate the effects of dislocation levels on electrical resistivity. He found that the texture depends on the evaporation source temperature [121]. Flash evaporation techniques have advantages on depositing A_3B_5 compounds for texture studies [122]. First, any excess antimony above the stoichiometric composition is not effectively re-evaporated from the substrate if the substrate is kept at temperatures lower than 350 °C. Therefore, deposition methods, like MBE, cannot be used effectively in that low-temperature deposition region. Second, while the sublimation of antimony leads to a vapor composed mainly of Sb_4 molecules, the evaporation of InSb leads to a vapor containing more antimony in the form of Sb and Sb_2 molecules. This facilitates the crystallization process, especially at low temperatures, and shifts down the transition temperature between the amorphous and crystalline state.

In flash evaporation, powder or chips of the two components are sprinkled onto a superheated sheet to produce complete evaporation of both components. Various possible arrangements are shown in Figure 4.41. Table 4.7 gives examples of the use of this technique.

4.8.4 Deposition of Refractory Compounds

Refractory compounds are substances like oxides, carbides, nitrides, borides, and sulfides which characteristically have a very high melting point (with some exceptions). In some cases, they form extensive defect structure, i.e. exist over a wide stoichiometric range. For example, in TiC, the C:Ti ratio can vary from 0.5 to 1.0, demonstrating vacant carbon lattice sites. In other compounds, the stoichiometric range is not so wide.

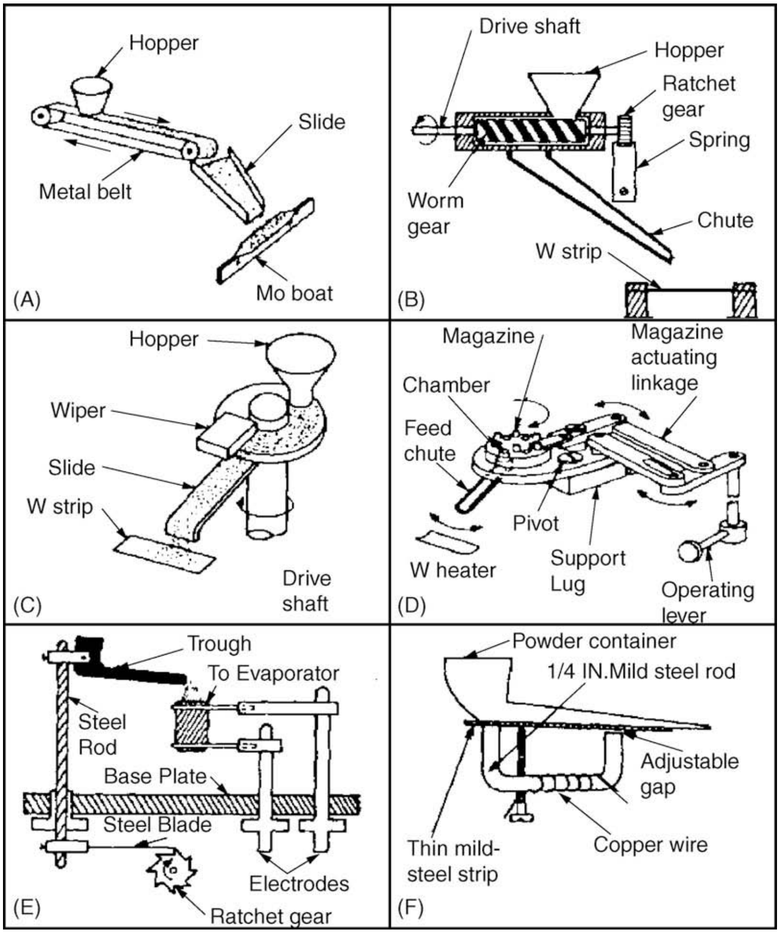

Figure 4.41: Flash-evaporation mechanisms: (A) belt feeder (Harris and Siegel); (B) worm-drive feeder with mechanical vibrator (Himes, Stout, and Thun, Braun and Lood); (C) disk feeder (Beam and Takahashi); (D) disk magazine feeder (Marshall, Atlas, and Putner); (E) mechanically vibrated trough and cylinder source (Richards); (F) electromagnetically vibrated powder dispenser (Campbell and Hendry). (From Handbook of Thin Film Technology [7]. © 1970, McGraw-Hill. Used with permission of McGraw-Hill Book Co.)

Evaporation processes for the deposition of refractory compounds are further subdivided into two types: (1) direction evaporation [123], where the evaporant is the refractory compound itself; and (2) reactive evaporation [124] or ARE [125], where the evaporant is a metal or a low-valence compound, e.g. where Ti is evaporated in the presence of N_2 to form TiN or where Si or SiO is evaporated in the presence of O_2 to form SiO_2.

Recently, Alberdi et al. [126] deposited Cr–TiAl–N films by simultaneous arc evaporation of Cr and Ti–Al targets under a mixture of Ar and N_2 gas atmosphere. The nanocomposite film

Table 4.7: Flash evaporation of materials

Materials	Form of evaporant	Feeder mechanism	Filament temp. °C	Substrate temp. °C	Comments on films
Metals and alloys					
Aa(64)–Cd(36), Cu(52)–Zn(48)	Powdered alloys, 80/100 mesh	Moving bell	–	–	Au–Cd and β brass films have combination of source
Ni + Fe	Mixed powders	Disk and wiper	1930	–	Ni–Fe films with ±1% control of composition
Ni(86)–Fe(14)	Alloy wire	Spool and guide tube	2000	300	Ni–Fe film composition equal to that of source ±0.2%
Ni; Fe; Cu constants; chromel; alumel	Pellets	Disk magazine	2000	200–250	Thin film thermocouples. Rates: 5–300 $\text{Å}\,\text{s}^{-1}$ across 12 cm distance
Ni(80)–Cr(20)	Alloy wire	Spool and guide tube	1620	–	Nichrome film, Cr content varies with filament temperature
Ni + Cr(20, 55, 70% Cr)	Mixed powders, 100/300 mesh	Vibrating chute	1800	300	Alloy films within 1% of source composition. Rates: 1–10 $\text{Å}\,\text{s}^{-1}$
Sn; nylon	Wire; strands	Two spools and cutting knives	200 (nylon)	~0	Alternate layers of metal and insulator
Metal-dielectric mixtures					
Cu + SiO (1: 5)	Mixed powders	Rotating tube	–	−269	Highly disordered films of high resistivity
Cr + 30 mol% SiO	Mixed powders, 325/500 mesh	Worm drive	~2000	200	250 Ohm-sq resistor films with +20 to 50% deviations
Cr + SiO (82 and 74 mol% Cr)	Mixed powders, 125/325 mesh	Worm drive	2000	400	Resistor films; SiO content less than source. Rates: 4 $\text{Å}\,\text{s}^{-1}$ across 23 cm distance

(*Continued*)

Table 4.7: (*Continued*)

Materials	Form of evaporant	Feeder mechanism	Filament temp. °C	Substrate temp. °C	Comments on films
Cr–SiO (60–100 mol % Cr)	Sintered pellets, ~0.7 mm size	Disk and wiper	2050 ± 60	200	Resistor films, SiO content equals that of source ±1–3%. Rates: 20–30 Å s^{-1} across 70 cm distance
Cr(15)–Si(85)	Powdered alloy	Vibrating chute	2000	200–500	Resistor films
$Cr_2Si + TaSi_2 + Al_2O_3$	Mixed powders	Worm drive	2500	200–400	Resistor films with ±10% control
Compounds					
AlSb	Powder, 100/150 mesh	Vibrating trough	1400–1600	700	Imperfect epitaxial films on Ge
GaP	Powder, 100/150 mesh	Vibrating trough	1500	540	Epitaxial films on Ge crystals
GaAs	Powder, 100/200 mesh	Vibrating trough	1450	300–670	Epitaxial films on Ge crystals above 600 °C. Rates: 2–30 Å s^{-1}
	Powder, 100/200 mesh	Worm drive	1400–1800	530 ± 10	Epitaxial films on GaAs crystals. Rates: 2–5 Å s^{-1} across 21 cm distance
	Powder, 100/150 mesh	Vibrating trough	1300–1800	475–525	Epitaxial films on Ge crystals
	Powder, 40/60 mesh	Micrometer screw and piston	1325	525–575	Highly oriented films on Ge and GaAs crystals. Rates: 10–25 Å s^{-1} across 10 cm distance
GaSb	Powder, 100/150 mesh	Vibrating trough	1650	500	Epitaxial films on Ge crystals
InP	Powder, 100/150 mesh	Vibrating trough	1400–1650	300	Epitaxial films on Ge crystals
InAs	Powder, 100/150 mesh	Vibrating trough	1500	500	Epitaxial films on Ge crystals
InSb	Granules	Vibrating trough	1600	450–460	Epitaxial films on InSb crystals. *n*-type, 10^{15}–10^{17} donors per cm^2

Table 4.7: (*Continued*)

Materials	Form of evaporant	Feeder mechanism	Filament temp. °C	Substrate temp. °C	Comments on films
	Powder, 100/150 mesh	Vibrating trough	1650	300–400	Epitaxial films on Ge crystals
Cu_2S, Cu_2Se	Powders of 250–300 μm	Vibrating trough	1400	25	Semitransparent, conductive films of $Cu_{1,8}S$ and $Cu_{18}Se$
$BaTiO_2$	Sintered powder, 100/200 mesh	Vibrating chute	2300	500–700	Crystalline films, dielectric constants of 400–700. Rate: 3 Å s^{-1} across 8 cm distance
Various perovskites	Sintered powder, 100/200 mesh	Vibrating trough	2050–2300	500–700	Perovskite films, epitaxial on LiF crystal. Rates: 1–3 Å s^{-1} across 8 cm distance

From Handbook of Thin Film Technology [7]. Copyright © 1970, McGraw-Hill. Used with permission of McGraw-Hill Book Company.

was deposited on WC–Co insets and high-speed steel samples. In order to improve the adhesion of the nanocomposite film, they applied −900 V bias voltages at the beginning of the deposition. CrN is more malleable than TiN; however, it has better oxidation resistivity. By adding another improved oxidation-resistant material such as CrN to TiAlN, the wear resistance of the nanocomposite thin film has been improved [126]. Chang et al. studied the wear resistance and hardness with TiSiN alloys by cathodic arc plasma evaporation [127]. According to their results the wear mechanism is controlled by counter-materials; however, no clear relation between bias voltage and wear resistance has been found.

4.8.4.1 Direct Evaporation

Table 4.8 gives the experimental conditions for the direct evaporation of refractory compounds. Evaporation can occur with or without dissociation of the compound into fragments. As seen from Table 4.8, the observed vapor species show that very few compounds evaporate without dissociation. Examples are SiO, MgF_2, B_2O_3, CaF_2, and other group IV divalent oxides (SiO homologs like GeO and SnO).

In the more general case, when a compound is evaporated or sputtered, the material is transformed to the vapor state not as compound molecules but as fragments thereof. Subsequently, the fragments have to recombine, most probably on the substrate, to reconstitute the compound. Therefore, the stoichiometry (anion:cation ratio) of the deposit depends on several factors including the deposition rate and the ratios of the various molecular fragments, the impingement of other gases present in the environment, the surface mobility of the fragments (which in turn depends on their kinetic energy and substrate temperature), the mean residence time of the fragments of the substrate, the reaction rate of the fragments on the substrate to reconstitute the compound, and the impurities present on the substrate. For example, it was found that direct evaporation of Al_2O_3 resulted in a deposit which was deficient in oxygen, i.e. which had the composition Al_2O_{3-x} [128]. This O_2 deficiency could be made up by introducing O_2 at a low partial pressure into the environment. In other cases, for example the direct evaporation of TiB_2 and ZrB_2, the deposit contains both the monoboride and diboride phases [129].

4.8.4.2 Reactive Evaporation

The difficulties involved in direct evaporation processes due to fragmentation of the vaporized compounds are overcome in reactive evaporation where a metal is evaporated in the presence of the reactive gas; the compound is formed by reaction of the evaporated metal species with the molecules of the reactive gas. Though this technique has been extensively used to deposit a variety of oxide films for optical applications, it is generally observed that the films are deficient in oxygen. It is also observed in some cases, especially in the synthesis of carbide films, that the deposition rate becomes a limiting factor governing the growth of the films. In such cases, stoichiometric TiC films could only be deposited at very low rates (∼ 1.5 Å/s max.)

Table 4.8: Direct evaporation of inorganic compounds

Compound	Vapor species observed (in order of decreasing frequency)	mp, °C	T, °C, at which $p^* = 10^{-7}$ Torr	Comments on actual evaporation temperatures, support materials used, and related experience
Oxides				
Al_2O_3	Al, O, AlO, Al_2O, O_2, $(AlO)_2$	2030	~1800	From W and Mo supports at 1850–2250 °C. With telefocus gun at 2200 °C, no decomposition From W support: Al_2O_3 films have small oxygen deficits. O_2-dissociation pressure at 1780 °C: 1.5×10^{-15} torr
B_2O_3	B_2O_3	450	~1700	From Pt and Mo supports at 940–1370 °C
BaO	Ba, BaO, Ba_2O, $(BaO)_2$, Ba_2O_3, O_2	1925	1540	From Al_2O_3 crucible at 1200–1500 °C. From Pt crucible with only slight decomposition, pO_2 (1540 °C) = 3.5×10^{-15} torr
BeO	Be, O, $(BeO)_n$, $n = 1$–6, Be_2O	2530	2230	From W support at 2070–2230 °C. With telefocus gun at 2400–2700 °C, no decomposition
Bi_2O_3	–	817	1840	From Pt support
CaO	Ca, CaO, O, O_2	~2600	~2050	Support materials: ZrO_2, Mo, W. The latter two form volatile oxides, molybdates, and wolframates at 1900–2150 °C
CeO_2	CeO, CeO_2	1950	–	From W support without decomposition
In_2O_2	In, In_2O, O_2	–	–	From Pt support with only little decomposition. Vapor species observed at 1100–1450 °C. At 1000–1450 °C from Al_2O_3 crucible, more In_2O than In
MgO	Mg, MgO, O, C_2	2800	~1560	Mo or W supports at 1840–2000° form volatile oxides, molybdates, and wolframates. With telefocus gun at 1925 °C, no decomposition. From Al_2O_3 at 1670 °C

(*Continued*)

Table 4.8: (*Continued*)

Compound	Vapor species observed (in order of decreasing frequency)	mp, °C	T, °C, at which $p^* = 10^{-7}$ Torr	Comments on actual evaporation temperatures, support materials used, and related experience
MoO_2	$(MoO_3)_3$, $(MoO_3)_n$, $n = 4.5$	795	610	From Mo oven at 500–700 °C, the trimer is the main species. Above 1000 °C, there is some decomposition into $MoO_2(s) + O_2(g)$. At 730 °C, the oxygen-decomposition pressure is 1.1×10^{-14} torr. From Pt at 530–730 °C
NiO	Ni, O_2, NiO, O	2090	1586	From Al_2O_3 crucible at 1300–1440 °C. Heavy decomposition with $p_{O_2} = 4 \times 10^{-1}$ torr at 1586 °C
Sb_2O_3	–	656	∼450	Lower oxides result if evaporated from W supports. Pt heaters do not produce decomposition
SiO	SiO	–	1025	Usually evaporated from Ta or Mo heaters at residual gas pressure below 10^{-6} torr and at temperatures between 1150 and 1250 °C. Dissociation into Si and O_2 begins above 1250 °C and may lead to oxygen-deficient films
SiO_2	SiO, O_2	1730	∼1250	With telefocus gun at 1500–1600 °C, no decomposition. Ta, Mo, W supports are attacked by SiO_2 and contribute volatile oxides. From Al_2O_3 at 1630 °C, SiO: vapor species is present
SnO_2	SnO, O_2	–	–	From SiO_2 crucible at 975–1250 °C. Films directly evaporated from W support are slightly oxygen deficient

Table 4.8: (*Continued*)

Compound	Vapor species observed (in order of decreasing frequency)	mp, °C	T, °C, at which $p^* = 10^{-7}$ Torr	Comments on actual evaporation temperatures, support materials used, and related experience
SrO	Sr, O_2, SrO	2460	~1760	From Al_2O_3 at 1830 °C. Evaporation from Mo or W at 1700–2000 °C produces volatile Mo and W oxides, molybdates, and wolframates
TiO_2	TiO, Ti, TiO_2, O_2	1840	–	TiO_2 source material decomposes into lower oxides upon heating. p_O, at 2000 °C is 10^{-10} torr. Nearly stoichiometric films by pulsed electron-beam heating
WO_2	$(WO_2)_3$, WO_2	1473	1140	From Pt oven at 1040–1300 °C. From Pt support at 1220 °C. From W heater with only slight decomposition; p_{O_3} at 1120 °C is 3×10^{-10} torr
ZrO_2	ZrO, O_2	2700	–	From Ta support at 1730 °C, volatile TaO. From W support, oxygen-deficient films. ZrO_2 source material loses oxygen when heated by electron beams
Sulfides, Selenides, Tellurides				
ZnS	–	1830 ($p \approx 150$ atm)	1000	From Mo support. Minute deviations from stoichiometry if allowed to react with residual gases. From Ta at 1050 °C
ZnSe	–	1520 ($p \approx 2$ atm)	820	
CdS	S, Cd, S, Si, Su	1750 ($p \approx 100$ atm)	670	From Pt oven at 740 °C. Films tend to deviate from stoichiometry. Suitable support materials: graphite, Ta, Mo, W, SiO_2, Al_2O_3–coated W: evaporation at 600–700 °C
CdSe	Se_2, Cd	1250	660	From Al_2O_3 crucible

Table 4.8: (*Continued*)

Compound	Vapor species observed (in order of decreasing frequency)	mp, °C	T, °C, at which $p^* = 10^{-7}$ Torr	Comments on actual evaporation temperatures, support materials used, and related experience
CdTe	Te_2, Cd	1100	570	From Ta boat at 750–850 °C: film stoichiometry depends on condensation temperature
PbS	PbS, Pb, S_2, $(PbS)_2$	1112	675	From quartz crucible at 625–925 °C. From Mo support. Purest films from quartz furnace at 700 °C; Fe or Mo boats reacts and form volatile sulfides
Sb_2S_3	–	546	550	From Mo support
Sb_2Se_3	Sb_2, $(SbSe)_2$, (Sb_2), (SbSe)	611		From graphite at 725 °C. From Ta oven at 500–600 °C, fractionation and films of variable stoichiometry
Halides				
NaCl	NaCl, $(NaCl)_2$, $(NaCl)_3$	801	670	From Ta, Mo, or Cu ovens at 550–800 °C
KCl	KCl, $(KCl)_2$	772	635	From Ni or Cu oven at 500–740 °C
AgCl	AgCl, $(AgCl)_3$	455	690	At 710–770 °C. From Mo support, $p^* = 10^{-2}$ torr at 790 °C
MgF_2	MgF_2, $(MgF_2)_2$, $(MgF_2)_3$	1263	1130	From Pt oven at 950–1230 °C. From Mo support. Very little dissociation into the elements
CaF_2	CaF_2, (CaF)	1418	∼1300	From Ta oven at 980–1400 °C. From Mo support
$PbCl_2$	–	678	∼430	Direct evaporation possible

From Handbook of Thin Film Technology [7]. Copyright © 1970, McGraw-Hill. Used with permission of McGraw-Hill Book Company.

[130]. This limitation of deposition rate in the case of the reactive evaporation process is due to the reaction kinetics of the compound formation by this process. The presence of a 'plasma' in the ARE process influences the reaction kinetics by providing activation energy to the reactive species, thereby making it possible to synthesize compound films at considerably higher rates [131–133] and lower temperatures.

Hass et al. studied the single and multiple source effect on metal oxide coatings (CeO_2, ZrO_2, Y_2O_3) by e-beam directed vapor deposition (DVD) [134]. In this approach, in order to make the deposition uniform, transonic helium carrier gas was used with the e-beam to transport metal vapor to a substrate. Metal oxide coatings were then produced by adding oxygen to the carrier gas. Their model is based on the vapor pressures of each individual evaporation source. According to their result the phase morphology is similar between a single metal source of zirconia and reactive deposition of yttria and zirconia source samples.

4.8.4.3 Activated Reactive Evaporation

The ARE process generally involves evaporation of a metal or an alloy in the presence of the plasma of a reactive gas [131, 135]. For example, TiC and TiN coatings are deposited by this process by evaporating Ti in the presence of C_2H_2 and N_2 plasma, respectively. The two basic variants of the ARE process are shown in Figures 4.42 and 4.43. For more information on the ARE process, refer to a review by Bunshah and Deshpandey [132]. The role of the plasma in

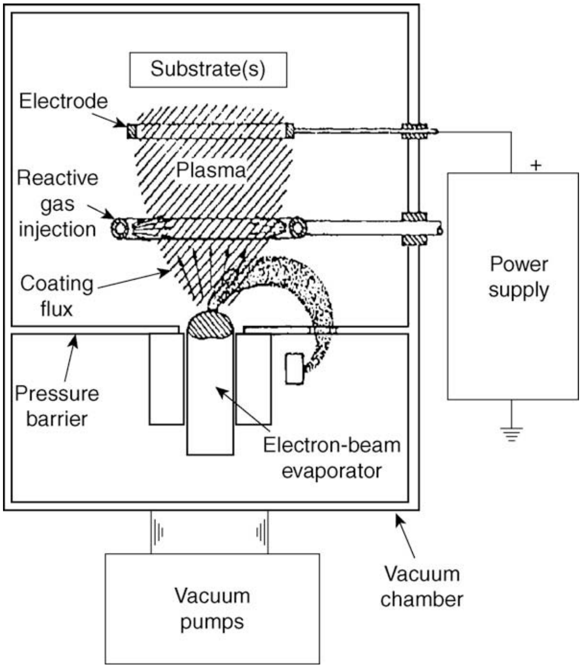

Figure 4.42: Schematic of the activated reactive evaporation (ARE) process.

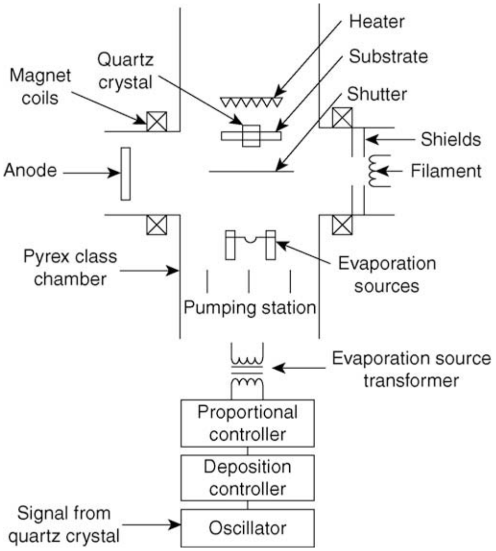

Figure 4.43: Activated reactive evaporation (ARE) Process [136] using a resistance-heated evaporation source.

this process is two-fold:

- to enhance the reactions that are necessary for deposition of compound films
- to modify the growth kinetics and hence the structure/morphology of the deposits.

In the following section we discuss the above two aspects.

Thermodynamic and kinetic considerations in plasma-assisted deposition processes

For the formation of a compound by any chemical reaction, the corresponding thermodynamic and kinetic constraints must be satisfied which also apply to the deposition of refractory compound films by reactive evaporation. In order to understand the role of plasma in enhancing the chemical reactions essential for the formation of a particular compound, one has therefore to consider the kinetics of these reactions.

Let us consider the reactions involved in the synthesis of some oxides, carbides, and nitrides by reactive evaporation. Given below are the reactions for forming Al_2O_3, TiC, and TiN.

$$\begin{array}{ll} 2Al + \frac{3}{2}O_2 \rightarrow Al_2O_3 & \Delta G^\circ = -250\,\text{kcal}\ \ (\text{mol}\,O_2)^2\ \ \text{at}\ \ 298\,\text{K} \\ 2Ti + C_2H_2 \rightarrow 2TiC + H_2 & \Delta G^\circ = -7.65\,\text{kcal}\ \ (\text{mol}\,O_2)^{-1}\ \ \text{at}\ \ 298\,\text{K} \\ 2Ti + N_2 \rightarrow 2TiN & \Delta G^\circ = -73.5\,\text{kcal}\ \ (\text{mol}\,N_2)^{-1}\ \ \text{at}\ \ 298\,\text{K} \end{array}$$

As can be seen from the above reactions, the thermodynamic criterion of free energy of formation is satisfied for the respective compounds.

The reaction kinetics in reactive evaporation process can be treated in exactly the same manner as for reactions occurring in heterogeneous systems of condensed phases. The model for heterogeneous metallurgical kinetics involves: (1) transport of reactant to the reaction interface; (2) transport of reaction products away from the reaction interface; (3) the chemical reaction at the chemical interface; (4) the nucleation of new phase; and (5) heat transfer to or away from the reaction interface.

For reactive evaporation, this model may be depicted as follows (e.g. for TiC formation):

Reactants	Products
Ti (metal atoms)	TiC (deposit)
C_2H_2 (gas)	H_2(gas)

Reaction interface

On the basis of the above model, the rate-controlling steps in the reactive evaporation process are: (1) adequate supply of reactants; (2) adequate collision frequency; (3) the rate of chemical reactions at the interface; and (4) the rate of removal of the reaction products from the interface.

It is easy to satisfy (1), (2), and (4) above for a reactive evaporation process. However, condition (3), i.e. the rate of reaction, becomes the rate governing step. The ‘plasma’ in the ARE process influences this step, i.e. the rate of reaction, by providing the necessary activation energy to the reactive species. The effect of plasma on rate of reaction can be clearly demonstrated by considering the results of Abe et al. [130] and Bunshah and Raghuram [133] on deposition of TiC coatings. Abe et al. found that titanium carbide with a carbon to titanium ratio of 1 could be formed by a reaction between Ti and C_2H_2 or C_2H_4 molecules on a substrate at 300–500 °C only if the deposition rate is 1–1.5 Å/s. At higher deposition rates, no TiC was formed. Clearly, the activation barrier could not be overcome at the higher deposition rates. Bunshah and Raghuram [133, 137] have similarly reported that the deposition of TiC by reactive evaporation at higher deposition rates (150–200 Å/s) required a very high substrate temperature, exceeding 1000 °C. However, in the presence of plasma, these authors reported that it was possible to deposit TiC at a high rate at a relatively low substrate temperature. The plasma imparts sufficient energy to the reacting species to overcome the activation energy barrier, and hence condition (3), i.e. the rate of reaction, no longer remains the rate-governing step.

Basic variants of the ARE process

The two basic variants of the ARE process are ARE with an e-beam evaporation source [131] and ARE processes with a resistance-heated source [138].

ARE processes with an *electron-beam-heated evaporation source* are illustrated in Figure 4.42. In this process, the metal is heated and melted by a high-acceleration-voltage e-beam that produces a thin plasma sheath on top of the melt. The low-energy secondary electrons from the plasma sheath are pulled upward into the reaction zone by an electrode placed above the pool biased to a low positive DC or AC potential (20–100 V), thus creating a plasma-filled region between the electrode and the electron beam gun. The low-energy electrons have a high ionization cross-section, thus ionizing or activating the metal and gas atoms and increasing the reaction probability on collision. Charge-exchange processes between positive ions and neutral atoms take place in the plasma. In addition, as suggested by Yee [139], transient highly excited compound species are formed. The formation of the compound is completed most probably on the substrate from these energetic and excited transient species. The synthesis of TiC by reaction of Ti metal vapor and C_2H_2 gas atoms with a carbon to metal ratio approaching unity was achieved with this process [131, 133]. Moreover, by varying the partial pressure of either reactant, the carbon to metal ratio of carbides could be varied [133, 140] at will. The ARE process has also been applied to the synthesis of all five different Ti–O oxides [141]. These authors noted that in the ARE process (i.e. with a plasma) as compared to the RE process (i.e. without a plasma), a higher oxide is formed for the same partial pressure of O_2, thus demonstrating a better utilization of the gas in the presence of a plasma. The same observation was noted by Bunshah and Raghuram [137] as well as by Granier and Besson [142] for the deposition of nitrides.

A variation of the ARE process uses a *resistance-heated evaporation source*. The basic ARE process uses e-beam-heated sources, which are expensive and inconvenient for the evaporation of low melting point, high vapor pressure materials. Nath and Bunshah [138] modified the ARE process for resistance-heated sources, as shown in Figure 4.43. The metal vapors are generated from the chamber; the reaction is enhanced by a plasma generated by injecting low-energy electrons from a heated thoriated tungsten emitter towards a low-voltage anode assembly. A transverse magnetic field is applied to cause the electrons to go into a spiral path, thus increasing the probability of electron/atom collision and subsequent ionization.

Modifications of the basic ARE process

The ARE process has substantial versatility since the substrate can be grounded, positively or negatively biased, or it can be allowed to float electrically. There are several modifications of the basic ARE process, as illustrated in Figure 4.44.

1. Enhanced ARE process [143, 144]. This is the conventional ARE process using e-beam heating with the addition of a thermionic electron emitter (e.g. a tungsten filament) for the deposition of refractory compounds at lower deposition rates as compared to the basic ARE process. The low-energy electrons from the emitter sustain the discharge, which would otherwise be extinguished since the primary e-beam (used to melt the metal) is so weak that it does not generate an adequate plasma sheath above the molten pool from which low-energy electrons can be extracted by positively biased interspace electrode. The substrate may be biased, grounded, or floating.

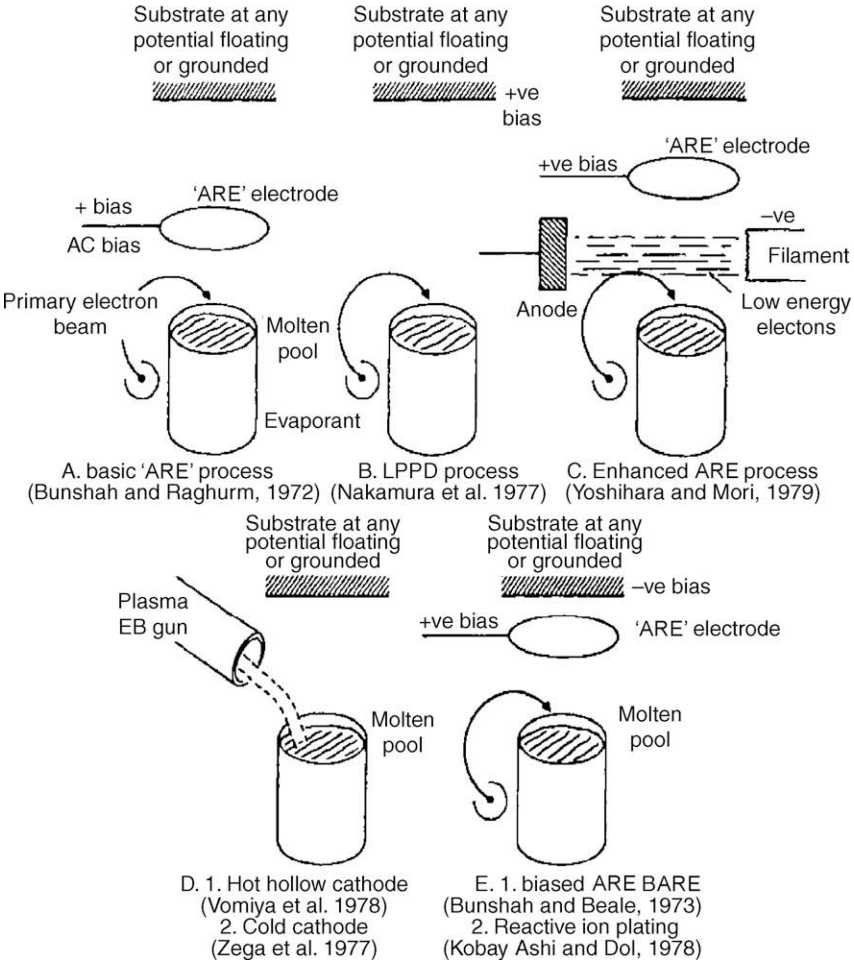

Figure 4.44: Basic 'ARE' process and later variations.

2. Low-pressure plasma deposition process. Using e-beam evaporation sources, the electric field may be generated by biasing the substrate positively instead of using a positively biased interspace electrode. In this case, it is called low-pressure plasma deposition (LPPD) [145, 146]. However, this version has a disadvantage over the basic ARE process since one does not have the freedom of choice to ground the substrate, let it float, or bias it negatively (the BARE process; see no. 4 below).

3. ARE using plasma electron-beam guns. The plasma e-beam gun, instead of the thermionic e-beam gun, can be used to carry out the ARE process. The hot hollow cathode gun has been used by Komiya et al. [147] to deposit TiC films, whereas Zega et al. [148] used a cold cathode discharge e-beam gun to deposit titanium nitride films. The plasma e-beam sources produce an abundant supply of low-energy electrons for the ARE-type process.

4. Reactive ion-plating processes. If the substrate is biased in the ARE process, it is called biased activated reactive evaporation (BARE). This bias is usually negative to attract the positive ions in the plasma. The BARE process has been reinvented and called reactive ion plating by Kobayashi and Doi [149]. Ishida et al. deposited Ni–TiC films by ion plating with cation ratios varying between Ti:Ni 0.35 and 3 [150]. Reactive ion plating (RIP) is very similar to the reactive evaporation process in that metal atoms and reactive gases react to form a compound aided by the presence of a plasma. Since the partial pressures of the gases in reactive ion plating are much higher ($> 10^{-2}$ torr) than in the ARE process ($> 10^{-4}$ torr), the deposits can become porous or sooty. The plasma cannot be supported by lower pressure in the simple diode ion plating process; therefore, Kobayashi and Doi [149] introduced an auxiliary electrode biased to a positive low voltage (as originally conceived for the ARE process) to initiate and sustain the plasma at low pressure ($\sim 10^{-3}$ torr). This is no different than the ARE process with a negative bias on the substrate reported much earlier by Bunshah [135], which was designated by him as the biased ARE (or BARE) process.
5. Another variation of reactive ion plating using a triode configuration [151] involves injection of electrons into the reaction zone between the e-beam-heated evaporation source and the negatively biased substrate from a heated tungsten filament transversely to the metal vapor path. These low-energy electrons are pulled across the reaction zone by a positively biased anode located opposite to the cathode. The arrangement is very similar to that shown in Figure 4.33 except for the use of an e-beam-heated evaporation source, and is also very similar to triode sputtering. This adds versatility as well as complexity to the process through the addition of another process variable.
6. Murayama [152] uses an e-beam-heated source with a negatively biased substrate and RF activation of the reactants by means of a coil electrode of aluminum wire in the reaction zone to deposit oxide and nitride films.
7. ARE process using an arc evaporation source. Evaporation of metals using a low-voltage arc in the presence of a plasma and a negatively biased substrate is used by Snaper [103, 104] and Dorodnov [153] to deposit nitride and carbide films, with N_2 and hydrocarbon reactive gases, respectively.
8. Reactive arc filtered evaporation. The system consists of conventional bell jar vacuum system and uses a magnetic field steering arc and a plasma duct formed from a free-standing and isolated high-current solenoid [154]. The advantage of this system is that it preserves the target material and achieves higher ionization rates with respect to the ion-plating process.

Recent developments in the ARE process

New techniques based on ARE are being developed for synthesis of novel and unique materials. The emphasis of such developments is generally on two aspects: (1) new approaches to produce the vapor species; and (2) new plasma excitation and confinement techniques and development of modified plasma excitation geometries.

Westerwaal et al. studied the nucleation of MgH_2 films by the ARE system [155]. Their results showed that they had 10% unreacted Mg remaining in the structure, but by heat treating the films and subsequent rehydrogenation procedures they were able to obtain 100% MgH_2 films.

New approaches to produce the various species The basic process involves evaporation of the constituent metal alloy or compound using e-beam or resistance/induction-heated sources. However, it is difficult to use this approach with certain materials such as boron and carbon. Two possible solutions can be used to overcome these difficulties: (1) use a low melting point compound of the respective element, and (2) use a pulsed laser beam where the pulse rate and pulse width can be appropriately adjusted to control the rate of material generation and fragmentation. Moreover, in many cases, the energy of the laser beam can also be used as a source for plasma excitation.

Both of these approaches have been explored. A process developed by Bunshah et al. [156] for the synthesis of cubic boron nitride involves boric acid as an reactant, which can be easily evaporated from a resistance-heated tungsten boat. In addition to the ease of evaporation, this process excludes the toxicity problems associated with fine boron particles which can be produced during e-beam evaporation of boron. A similar approach can be extended to evaporation of carbon using a low melting point carbon compound such as adamantine. It is likely that many new materials hitherto difficult to synthesize may possibly be deposited using this routine. Moreover, this novel approach may contribute to further development in reactive MBE processes and other vapor deposition processes involving organometallic compound reactants.

The use of pulsed laser beams in an ARE type of process has been demonstrated in recent literature on high T_c superconducting films. Films with high T_c (90 K) and high critical current density (0.7×10^6 A·cm^{-2} at 77 K) have been produced [157]. It is claimed that pulsing of the laser beam avoids fractionation of the compound and hence good control of film stoichiometry is achieved. It is also suggested that the photon energy is sufficient to activate the reactive gas/metal species thereby increasing their reactivity, leading to an increased oxygen concentration in the deposited films.

New plasma excitation modes and geometries As discussed earlier, the attributes of the ARE processes are due to the possibility of controlling the plasma parameters independently of the deposition process.

However, improvement in excitation and confinement of the plasma, as well as control and optimization of plasma parameters in the ARE processes, are likely to enhance the process capabilities. Recent developments include (1) the use of inductively coupled RF with parallel plate RF geometries, and (2) the use of multiple filaments and anodes with magnetic confinement. These enhancements have led to substantial improvements in film properties as well as process control. Examples are high-rate deposition of a-Si–H films [158], transparent conducting films on polymeric substrates [159], and TiS_x and MoS_x [160, 161] films with variable x values.

Two additional modes of ionization are being explored. Currently, an auxiliary RF excitation source similar to that reported by Oeschner [162] is being developed for use in ARE. It is believed that the high electron density and energy selectivity offered by this source is likely to enhance advantages of the ARE processes for compound synthesis. Also, work is underway to integrate electron cyclotron resonance (ECR) excitation at microwave frequencies with the ARE process. ECR plasmas are characterized by a very high level of ionization and excitation, and may greatly enhance the use of ARE for the deposition and synthesis of films.

Sakai et al. studied plasma-enhanced reactive evaporation of TiO_2 thin films for photocatalytic applications [163]. The system consists of a Ti e-beam evaporation source and an ECR oxygen plasma source, and a sample holder as shown in Figure 4.45. In conventional plasma-enhanced systems the sputtering rate is low because the target gets oxidized and reduces the deposition rate. In Sakai's system the modification is such that the Ti atoms and O_2 gas flow to the

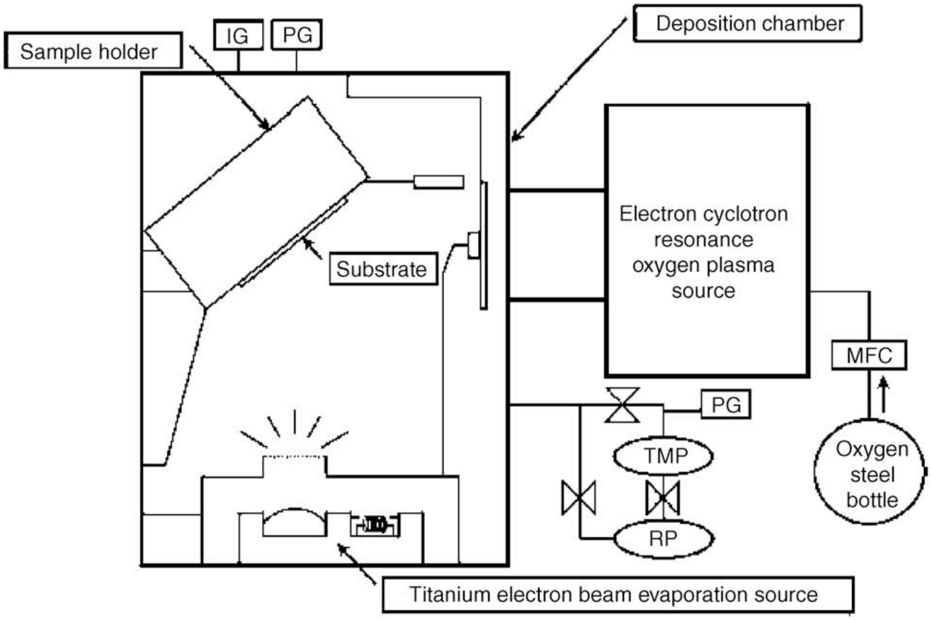

Figure 4.45: Reactive evaporation system [163].

substrate independently so that the target does not get poisoned [163]. According to their results the crystal structure of the TiO_2 thin film changes as they increase the deposition rate from 18 nm/min to 145 nm/min. The crystalline phase shifts from anatase to rutile as the deposition rate increases.

Mechanism of the ARE process

A reactive evaporation process can be simply written as a reaction between the reactants giving rise to the products. Illustrating this for the deposition of TiC films, one may write:

$$x\text{Ti(vapor)} + \text{C}_x\text{H}_y\text{(gas)} \rightarrow x\text{TiC(solid)} + y\text{H(gas)}$$

In a plasma-assisted deposition process, the reactants dissociate into fractions/radicals and ionic species are produced. Therefore a multiplicity of reaction paths are possible and the overall reaction becomes more complex. Deshpandey et al. [164] studied the synthesis of TiC and TiN films, evaporating Ti in a plasma of C_xH_y gases for the synthesis of TiC films and N_2 or NH_3 with Ti for the synthesis of TiN films. Several spectroscopies were used to carry out diagnostics on the plasma in the source-substrate volume to determine the species present and the potential reaction paths leading to film formation. Neutral mass spectrometry (MS), plasma mass spectrometry (PMS), and optical emission spectroscopy (OES) were used to examine the nature and relative concentrations of neutral, excited, and ionized species present in the process.

The main results of these investigations are as follows:

- Polymerizing reactions producing higher molecular weight hydrocarbon species are dominant in the case of methane. Polymerization increases with increasing flow rate of CH_4 for a given e-beam current. The above reactions lead to the formation of relatively soft films containing TiC and graphitic phases.
- Hard, single-phase TiC films are formed at flow rates of about 50 standard $\text{cm}^3\,\text{min}^{-1}$ C_2H_2 for beam currents in the range of 0.2–0.3 A. Polymerization reactions do not take place when C_2H_2 is used as a reactive gas. Species such as carbon, CH, and CH_2 formed in the plasma from the dissociation of C_2H_2 react with titanium to form TiC. The PMS and MS data indicate the following possible routes for formation of TiC:
  (a) formation of TiC in the plasma volume through reactions such as:

$$\text{Ti} + \text{C} \rightarrow \text{TiC}$$
$$\text{Ti} + \text{CH} \rightarrow \text{TiC} + \text{H}$$
$$\text{Ti} + \text{CH}_2 \rightarrow \text{TiC} + 2\text{H}$$
$$\text{Ti} + \text{CH}_3 \rightarrow \text{TiC} + 3\text{H}$$

followed by condensation of TiC molecules on the substrate; or

(b) formation of Ti_xC_y or Ti_2C_y or $Ti_2C_yH_z$ complexes in the plasma volume followed by condensation on the substrate to form TiC according to:

$$Ti_xC_y \rightarrow TiC + C$$
$$Ti_xC_yH_z + CH_2 \rightarrow TiC + C_yH_z$$

Present data are not sufficient to determine which of these two schemes is dominant in the formation of TiC. PMS and MS sampling of the arriving flux on the substrate as well as studies with a biased substrate are necessary to resolve this issue.

Similar studies on the deposition of TiN films revealed the following:

- Evaporation of Ti in a N_2 plasma showed that the predominant species leading to hard stoichiometric TiN films is $2Ti^+ + N_2^+ \rightarrow 2TiN$. The ratio of Ti^+/N_2^+ in the plasma was 1.05, i.e. close to unity. When this ratio was increased to 1.5, soft films with excess Ti in the deposit were produced. Yee [139] also proposed the same reaction path based on his optical emission spectrographic studies.
- Evaporation of Ti in an NH_3 plasma showed similar results. Under conditions where the Ti^+/N_2^+ ratio was high, the films were soft and titanium rich. With a higher flow rate of NH_3, the N_2^+ concentration in the plasma was higher and the films were hard.

4.8.5 Materials Synthesized by Evaporation-Based Processes

A variety of metals, alloys, and compounds (oxides, nitrides, arbides, sulfides) have been deposited using evaporation and related processes. In particular, the plasma-assisted variant of the evaporation process, such as ARE, has been successfully used for deposition of a variety of compounds for tribological as well as optoelectronic applications. Recently, a modified process based on the ARE technique has also proved to be successful in synthesizing c-BN [156, 165]. A representative list of the compounds synthesized by the ARE process is given below. In a very recent development, the ARE process has been able to deposit Al_2O_3 films at very high deposition rates (8 to 12 μm/h); these rates are 10–30 times higher than those by sputter deposition [166].

The compounds synthesized by the ARE process include:

- Carbides: TiC, HfC, ZrC, VC, W_2C, TaC
- Carbonitride: Ti (C, N)
- Nitrides: TiN, HfN, ZrN, CrAlTiN, TiSiN
- Oxides: TiO_2, ZrO_2, Al_2O_3, SiO_2

- Sulfides: TiS_2, MoS_2, MoS_3
- Superconductors: low T_c: Nb_3Ge, $CuMo_6S_8$; high T_c: $YBa_2CU_3O_{7-8}$
- Photovoltaic materials: a-SiH, $CuInS_2$
- Optoelectric materials: $In(Sn)O_2$, ZnO
- Novel materials: c-BN, Diamond, i-C, a-C.

4.8.6 Deposition of Nanocomposite Materials

Nanocomposite thin films containing embedding metals in polymer matrices can be prepared by various techniques. Nanocomposites provide the flexibility of tuning electrical, magnetic, and other physical properties of the deposited film independently by controlling the chemistry of the constituents. Biswas et al. deposited Ni nanoparticles with Teflon layers by vapor-phase tandem evaporation [167]. This technique allows metals and polymers to be evaporated at the same time. They controlled the Ni nanoparticle size while generating low to relatively high cluster-volume filling in the polymer. In evaporation of metals Takele et al. tuned the electrical and structural properties by the simultaneously evaporation of metal (Ag, Au) and polymer [168]. One of the most crucial factors in this deposition is the sticking coefficient of metal nanoparticles on polymers. The electrical properties mainly depend on the metal filling factor, particle size, size distribution, and metal particle/insulator interface properties. Zaporojtchenko et al. described the effects of metal interaction with various polymer matrices by evaporating Cu, Ag, and Au on fully cured polymer films [169].

4.9 Microstructure of PVD Condensates

4.9.1 Microstructure Evolution

PVD condensates deposit as single crystal films on certain crystal planes of single crystal substrates, i.e. by epitaxial growth [170], or in the more general case, the deposits are polycrystalline. In the case of films deposited by evaporation techniques, the main variables are: (1) the nature of the substrate; (2) the temperature of the substrate during deposition; (3) the rate of deposition; (4) the deposit thickness; (5) the angle of incidence of the vapor stream; and (6) the pressure and nature of the ambient gas phase. Contrary to what might be intuitively expected, the deposit does not start out as a continuous film one monolayer thick and grow. Instead, three-dimensional (3D) nuclei are formed on favored sites on the substrates, e.g. cleavage steps on a single crystal substrate; these nuclei grow laterally and in thickness (the so-called island growth stage), ultimately impinging on each other to form a continuous film. The average thickness at which a continuous film forms depends on the deposition temperature and the deposition rate (both of which influence the surface mobility of the adatom) and varies from 10 Å for Ni condensed at 15 K to 1000 Å for Au condensed at 600 K. This familiar model of island growth of a polycrystalline film during the initial stages of deposition illustrates the case where there is limited interaction between depositing atoms and the substrate. This is not always the case.

Petrov et al. [171] reviewed film growth processes which include nucleation, coalescence, competitive grain growth, and recrystallization. They also discussed evolution as a function of deposition variables including temperature, the presence of reactive species, and the use of low-energy ion irradiation during growth [171]. Types of substrates, such as amorphous and polycrystalline, used in PVD processes play an important role in the microstructural evolution in thin films synthesized by low-temperature PVD. The use of amorphous substrates allows the isolation of the effects of individual deposition variables on texture development. However, polycrystalline substrates bias texture through local pseudomorphic epitaxy, with the same overall microstructure evolution toward the final state driven by the deposition conditions. On both types of substrates, film growth proceeds via a 3D or Volmer–Weber model [171].

The growth processes controlling microstructure evolution, nucleation, island growth, impingement and coalescence of islands, grain coarsening, formation of polycrystalline islands and channels, development of a continuous structure, and film growth, are presented schematically in Figure 4.46. In the formation of film, grain coarsening, i.e. recrystallization through grain boundary (GB) migration, can occur both during and after island coalescence. The nucleation barrier is generally expected to be small, leading to randomly oriented islands, for low-temperature deposition on amorphous substrates [173, 174]. In situ transmission electron microscopy (TEM) investigations confirm this for studies of Au/SiO_2 [175, 176] and In/C [177, 178]. Nucleation kinetics depend on the adatom binding energy, crystal structure of the substrate material, lattice defects, surface steps, and contamination.

Polop et al. studied the initial stages of polycrystalline Ag film formation deposited by thermal evaporation on the amorphous Si layer [179]. The deposition temperature was 300 K and the deposition rate 8×10^{-3} nm/s. After the deposition the films were analyzed by in situ scanning tunneling microscopy (STM). Figure 4.47 displays STM topographs of the evolution of Ag film morphology as a function of the film thickness. Polop's results show that the film morphology is distinguished by three regimes: (1) film thicknesses smaller than 0.8 nm – the nucleation and island formation (Figure 4.47a), (2) film thicknesses between 0.8 and 10 nm – island growth regime (Figure 4.47b–d) and (3) film thicknesses higher than 10 nm – continuous film regime (Figure 4.47e–f).

Akkari et al. deposited $CuInS_2$ films by thermal evaporation with a flux angle Θ with rotation of the substrate [180]. In Figure 4.48, when the flux angle Θ increases, the tilting of the columns also increases. When the substrate is not rotated the film structure consists of

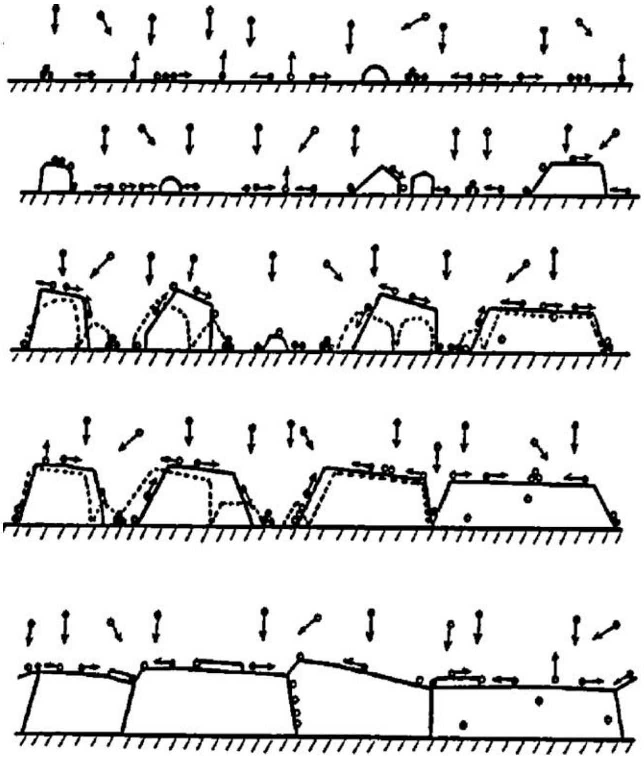

Figure 4.46: Schematic diagram illustrating fundamental growth processes controlling microstructural evolution [171, 172].

nanocolumns that are inclined towards the evaporation source. When the substrate is rotated and the angle is at 80°, the structure takes straight wire forms [180].

Important differences have been observed. Namba and Mori [181] found that by converting a significant fraction ($\sim 10\%$) of the vapor flux of Ag to positive ions, epitaxial growth of a single crystal Ag film on a single crystal NaCl substrate biased to -3000 V was observed, whereas with vacuum evaporation, the Ag film was polycrystalline. No clear explanation is possible except to note that the mobility of the deposited species is much greater when partially ionized than for neutral vapor species. The effective surface temperature of the growing film is much higher owing to ion bombardment, thus permitting greater surface mobility and resulting in epitaxial growth. Taylor [182] used low-energy electron diffraction (LEED) techniques to study the epitaxial deposition of Cu onto a single crystal [183] face of tungsten under ultrahigh vacuum conditions. This represents the case where there is appreciable bonding between depositing atoms and the substrate. The deposit on a clean tungsten surface was a uniformly thin [184] Cu film, i.e. no island growth prior to the formation of a continuous film even at

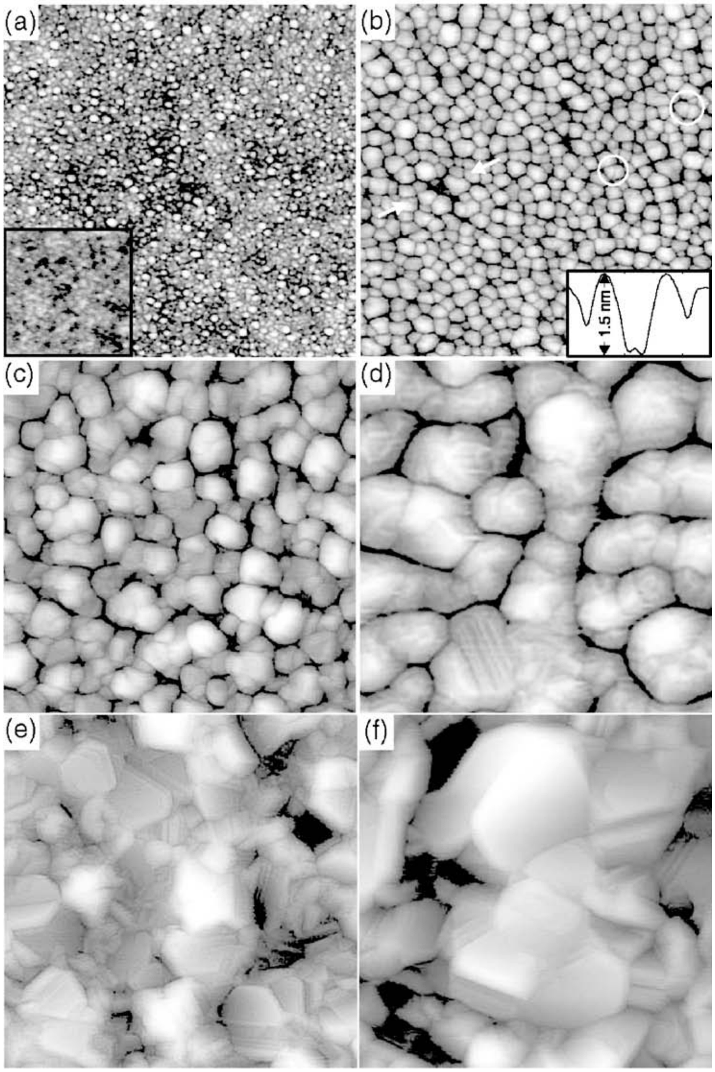

Figure 4.47: STM topographs of Ag films deposited at 300 K with thicknesses of (a) 0.3 nm, (b) 1.0 nm, (c) 2.7 nm, (d) 8.5 nm, (e) 15.9 nm, and (f) 30.0 nm. Image size = 160 × 160 nm. The inset in (a) shows an STM image (60 × 60 nm) of the amorphous substrate, and in (b), a line scan between the arrows in the topograph, which reaches down to the substrate. The circles in (b) enclose islands with GBs.

thicknesses of 1{1/2} atomic layers. He further observed that chemisorption of even a half monolayer of oxygen severely inhibited epitaxial growth.

Sherman et al. [185] studied the deposition of thick Mo films onto a rolled Mo sheet substrate as a function of deposition temperature. They observed polycrystalline deposits at all

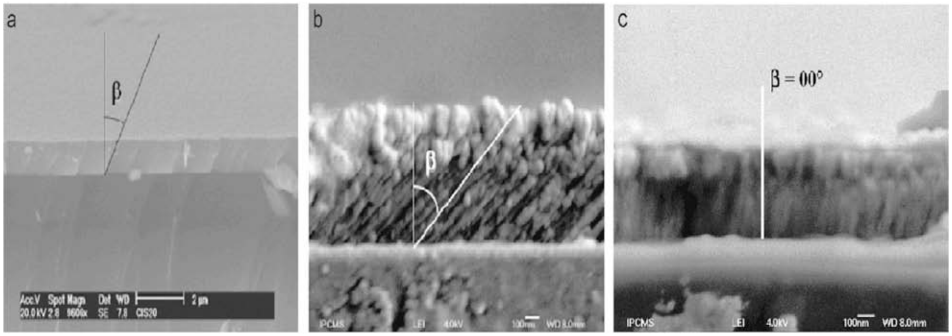

Figure 4.48: Cross-sectional SEM images of the $CuInS_2$ thin films deposited at different flux angles: (a) $\Theta = 40°$; (b) $\Theta = 80°$ without substrate rotation; and (c) $\Theta = 80°$ with substrate rotation $\omega = 0.033$ rev/s.

temperatures except in the range of 973–1188 K, where the surface oxide MoO_3 is unstable and evaporates rapidly, thereby leaving behind a ‘clean’ Mo surface on which epitaxial growth can readily occur aided by the high surface mobility at the elevated deposition temperature.

Once a continuous film has formed, the subsequent evolution to the final structure of the thin film is poorly understood at present. It undoubtedly depends on the factors mentioned above, which in turn influence the primary variables of nucleation rate, growth rate, and surface mobility of the adatom. The problem has been tackled by Van der Drift [186] and is also the subject of a paper by Thornton [187].

The microstructure and morphology of thick single-phase films have been extensively studied for a wide variety of metals, alloys, and refractory compounds. The structural model was first proposed by Movchan and Demchishin [123] (Figure 4.49), and was subsequently modified by

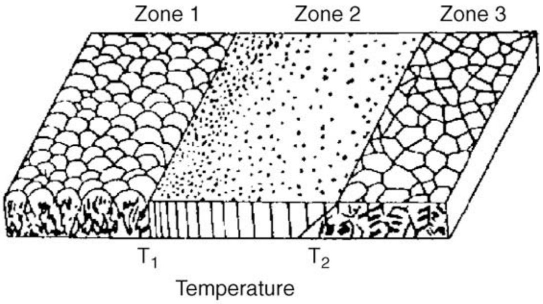

	Zone 1	Zone 2	Zone 3
Metals	< 0.3 T’m	0.3 - 0.45 T’m	> 0.45 T’m
Oxides	< 0.26 T’m	0.26 - 0.45 T’m	> 0.45 T’m

Figure 4.49: Structural zones in condensates [123].

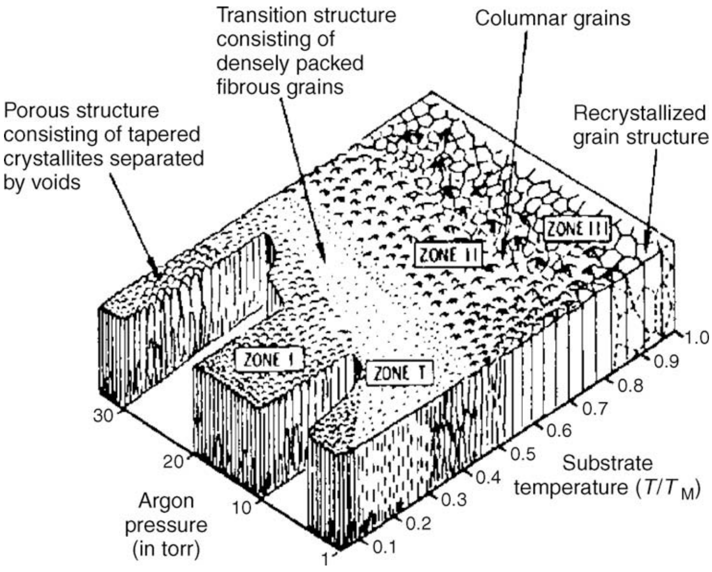

Figure 4.50: Structural zones in condensates [187].

Thornton as shown in Figure 4.50. Movchan and Demchishin's diagram was arrived at from their studies on deposits of pure metals and did not include the transition zone of Thornton's model, zone T, which is not prominent in pure metals or single-phase alloy deposits, but becomes quite pronounced in deposits of refractory compounds or complex alloys produced by evaporation, and in all types of deposits produced in the presence of a partial pressure of inert or reactive gas, as in sputtering or ion-plating processes.

The evolution of the structural morphology is as follows.

At low temperatures, the surface mobility of the adatoms is reduced and the structure grows as tapered crystallites from a limited number of nuclei. It is not a full-density structure but contains longitudinal porosity of the order of a few hundred angstroms' width between the tapered crystallites. It also contains a high dislocation density and has a high level of residual stress. Such a structure has also been called 'Botryoidal' and corresponds to zone 1 in Figures 4.49 and 4.50.

As the substrate temperature increases, the surface mobility increases and the structural morphology first transforms to that of zone T, i.e. tightly packed fibrous grains with weak grain boundaries, and then to a full-density columnar morphology corresponding to zone 2 (Figure 4.50).

The size of the columnar grains increases as the condensation temperature increases. Finally, at still higher temperatures, the structure shows an equiaxed grain morphology (zone 3). For pure metals and single phase alloys, T1 is the transition temperature between zone 1 and zone 2 and T2 is the transition temperature between zones 2 and 3. According to Movchan and Demchishin's original model [123], T_1 is 0.3 T_m for metals, and 0.22–0.26 T_m for oxides, whereas T_2 is 0.45–0.4 (T_m is the melting point in K).

Thornton's modification shows that the transition temperatures may vary significantly from those stated above and, in general, shift to higher temperatures as the gas pressure in the synthesis process increases. It should be emphasized that:

- The transition from one zone to the next is not abrupt but smooth. Hence the transition temperatures should not be considered as absolute, but as guidelines.
- All zones are not found in all deposits. For example, zone T is not prominent in pure metals, but becomes more pronounced in complex alloys, compounds, or in deposits produced at higher gas pressures. Zone 3 is not seen very often in materials with high melting points.

The reader is referred to a more extensive description given by Greene in Chapter 12, which includes a discussion of the effects of substrate surface roughness and pressures.

Most thick deposits exhibit a strong preferred orientation (fiber texture) at low deposition temperatures and tend toward a more random orientation with increasing deposition temperature. Figure 4.51 shows the evolution of a large-grained columnar morphology in a Be deposit from a much larger number of fine grains which were originally nucleated on the substrate. As growth proceeds, only those grains with a preferred growth direction survive, presumably owing to considerations of the minimization of surface energy.

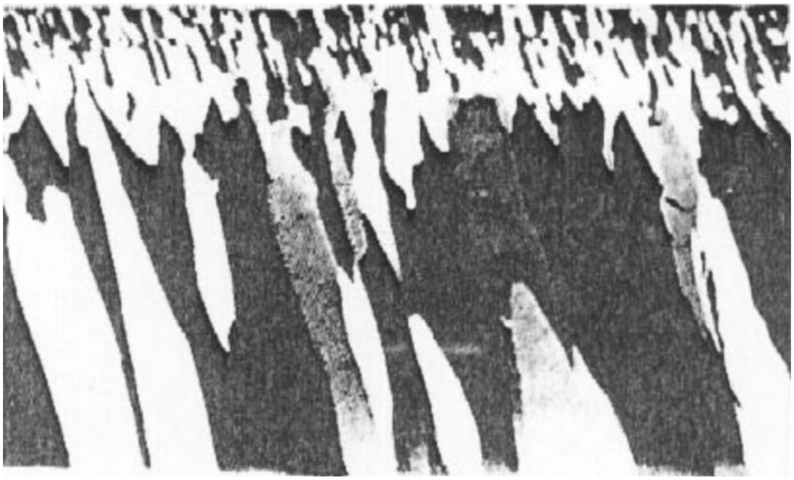

Figure 4.51: Photomicrograph of a Be deposit showing the evolution of large columnar grains.

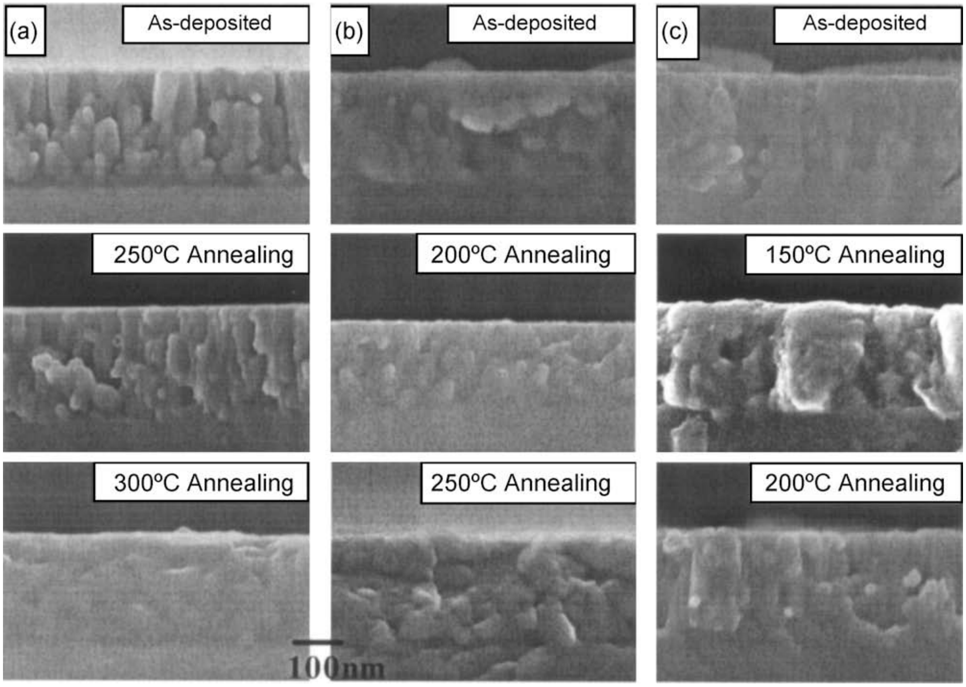

Figure 4.52: SEM micrographs of TiO_2 films annealed at various temperatures. Substrate temperatures: (a) 150 °C, (b) 200 °C, (c) 250 °C.

Chen et al. studied the effects of deposition temperature on the microstructure of TiO_2 films. Films were deposited by ion assisted deposition in which e-beam evaporation was used to evaporate Ti_3O_5 and a Kaufman-type ion-beam source was used to modify the morphology of the films [188]. Figure 4.52 shows the microstructure of the as-deposited 150 °C film which has a columnar structure. The microstructure persisted up to the annealing temperature of 300 °C. The increase in deposition temperature affected the columnar growth of the film. As the deposition temperature increased columns became denser. The as-deposited samples show different recrystallization temperatures. The crystallization temperature was determined from SEM images, X-ray diffraction (XRD) data and refractive indices of the films. For films deposited at 150, 200 and 250 °C, the crystallization temperature was found to be 300, 250 and 200 °C, respectively.

Elegant proof of the importance of surface mobility was also provided by Movchan and Demchishin [123]. Plots of the log of the grain diameter versus the inverse of deposition temperature in zones 2 and 3 yield straight lines from which activation energies can be computed. It was found that the activation energy for zone 2 growth corresponded to that for surface self-diffusion and for zone 3 growth to volume self-diffusion. The morphological results reported by Movchan and Demchishin for nickel, titanium, tungsten, Al_2O_3, and ZrO_2

Table 4.9: Transition temperatures between various structural zones

Material	Melting temp., T_m (K)	T_1 (K)	T_1 (K)/T_m (K)	T_2 (K)	T_2 (K)/T_m (K)	Ref.
Ti	1945	653 ± 10	0.3	923	0.5	[98]
Ti	1945	673 ± 20	0.31	Phase transformation overlaps	–	[113]
Ni	1726	543 ± 10	0.3	723 ± 10	0.45–0.5	[98]
Ni	1726	–	–	777 ± 20	0.45	[114]
W	3683	1133 ± 50	0.3	1723 ± 50	0.45–0.5	[98]
Mo	2883	923 ± 20	0.3–0.34	1200	0.44	[189]
Fe	1810	–	–	Phase transformation overlaps	–	[190]
Be	1573	473 ± 20	0.29	1023 ± 50	0.63	[191]
Ni-20Cr	1673	500 ± 50	0.3	870	0.52	[192]
ZrO_2	2973	648 ± 10	0.22	1273	0.45–0.5	[98]
Al_2O_3	2323	623 ± 10	0.26	1173	0.5	[98]
TiC	3340	1070 ± 30	0.31	Not observed up to 1723 K or 0.51 T_m	–	[113]
NbC	Obeys the Movchan–Demchishin model					[193]
ZrO_2	Obeys the Movchan–Demchishin model					[193]

From structures observed at a specific deposition temperature, Au–Cr[58] *and V*[37] *appear to obey the Movchan–Demchishin model.*

have been confirmed for several metals and compounds. The data are given in Table 4.9 [29, 30, 194, 195].

Bunshah and Juntz [196] studied the influence of condensation temperature on the deposition of titanium. Their microstructures, shown in Figure 4.53, agree substantially with those of Movchan and Demchishin for zones 1 and 2 and T_1, the transition temperature between zones 1 and 2. However, they failed to observe zone 3 at the temperatures above 700 °C found by Movchan and Demchishin [123]. The structure was columnar up to 833 °C, which is the $\alpha{:}\beta$ phase transformation temperature for titanium. At deposition temperatures above 833 °C, the deposit crystallizes as the β phase and on cooling to room temperature, should transform to the α phase, resulting in the typical 'transformed-beta' microstructure shown in Figure 4.53 (900 °C deposit), which could be mistaken for an equiaxed microstructure. Hence, the claim of such a transition in structure from zone 2 to 3 by Movchan and Demchishin for titanium deposits is confusing.

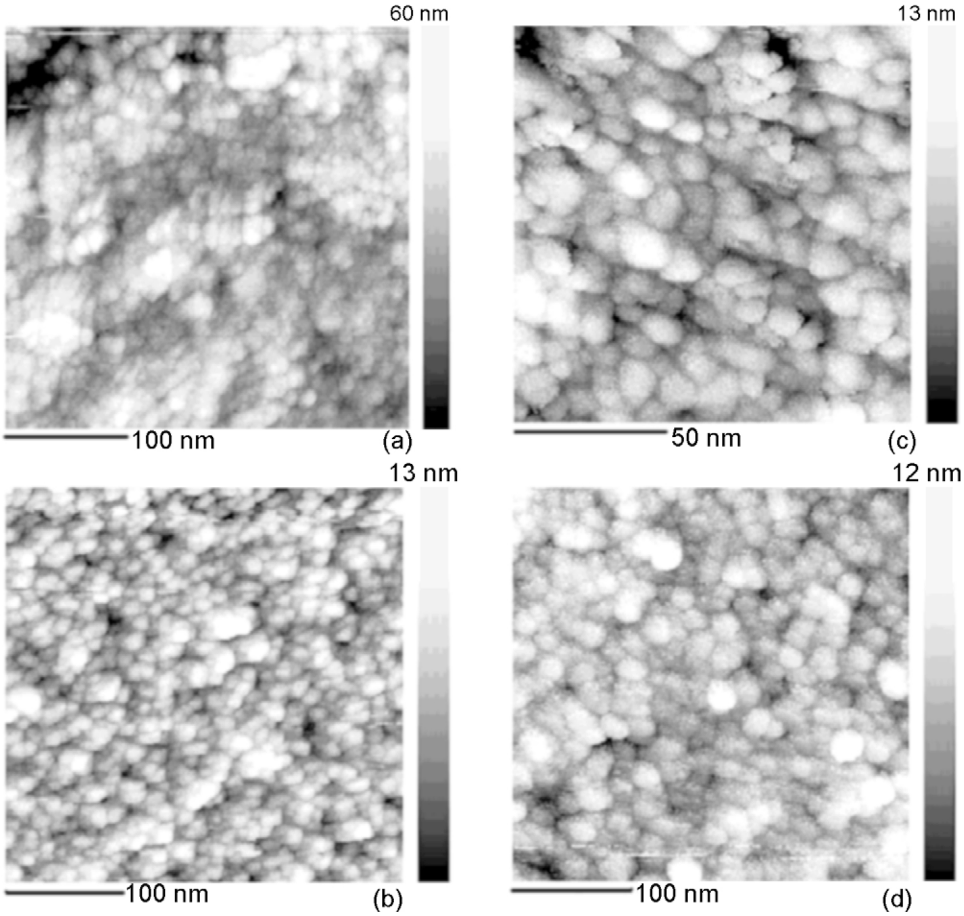

Figure 4.53: Structure of titanium deposits at various substrate temperatures [200].

Semaltianos and Wilson [197] investigated the surface morphology of thermally evaporated gold thin films on mica, glass, silicon, and calcium fluoride substrates, and at different temperatures. According to Figure 4.54, the average particle size of gold films is 15, 20, and 25 nm for mica, CaF_2, and Si substrates. However, for glass substrates large accumulations of gold are formed consisting of many smaller particles. The increase in particle size for Si and CaF_2 can be due to ionic interaction between the substrate and the film.

Kane and Bunshah [198] observed the change in morphology in deposited nickel sheet. At 425 °C deposition temperature, the deposit showed a zone 2 morphology, whereas at 554 °C, the deposit showed a zone 3 morphology.

Chambers and Bower [199] studied the deposition of magnesium, copper, gold, iridium, tungsten, and stainless steel. Of the photomicrographs presented, gold and magnesium showed zone 2 columnar morphology at the appropriate substrate temperatures.

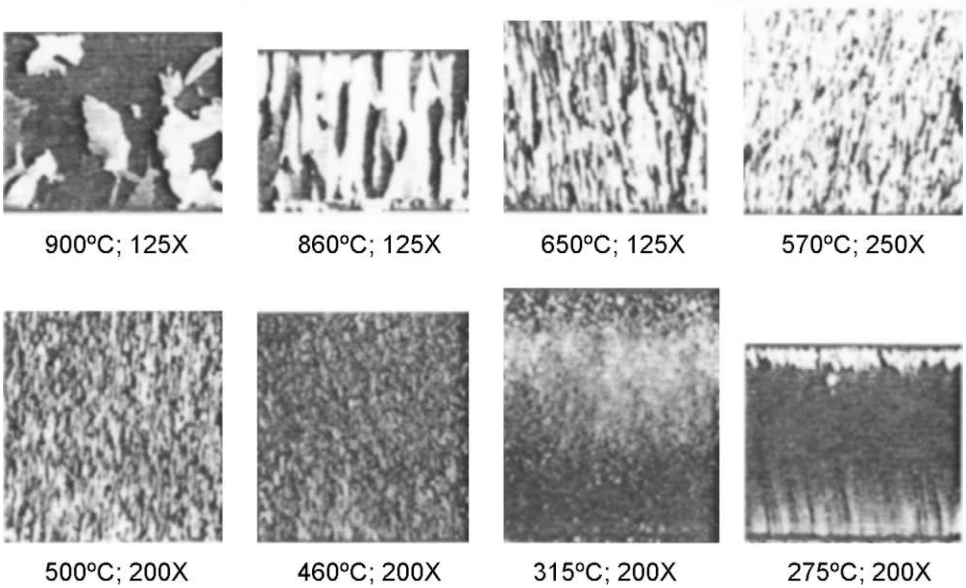

Figure 4.54: STM images of gold films grown on (a) glass, (b) mica, (c) CaF_2, and (d) Si with the substrates held at room temperature.

Figure 4.55 shows surface and cross-section photomicrographs of a Ni–20Cr sheet deposited by Agarwal et al. [194]. At 950 °C, 760 °C, 650 °C, and 427 °C deposition temperatures, the surface and cross-section showed an equiaxed zone 3 morphology.

Mah and Nordin [201] found that the Movchan–Demchishin model was obeyed by beryllium. They observed structures corresponding to all three zones with transition temperatures as predicted by the model.

Neirynck et al. [202] studied the influence of deposition rate and substrate temperature on the microstructure, adhesion, texture, and condensation mechanism of aluminum and zirconium coatings on steel substrates and wires in batch and continuous-coating methods.

Kennedy [203] showed a change in morphology from columnar to equiaxed in Fe and Fe–10Ni alloy with higher deposition temperature. Deposits of Fe–1%Y, which is a two-phase alloy, showed columnar morphology only, the structure becoming coarser at higher deposition temperature. The second phase appears to nucleate new grains so that the grain size in Fe–1%Y alloys is much finer than that of iron.

The microstructure of copper–nickel alloys [31] produced by co-deposition from two sources showed a single phase, as might be expected for this system, which shows a complete solid solubility. On the other hand, sequential deposition of Cu and Ni from two sources shielded from each other onto a rotating substrate produced a microlaminate structure in the deposit

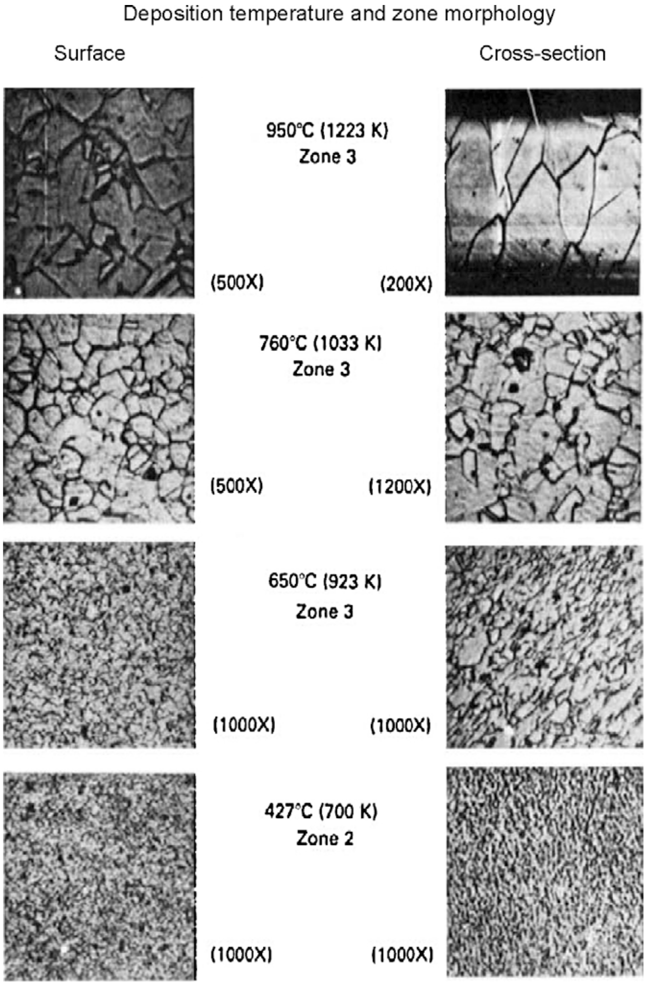

Figure 4.55: Photomicrographs of typical Ni–20Cr deposits at various substrate temperatures [194].

where the laminate size could be varied from 0.01 to 40 μm by adjusting the deposition parameters [204]. Similar structures were also developed in the Fe–Cu [204] and Ti–B_4C systems [204].

In alloy systems showing the presence of several phases, e.g. Ni–B and Cr–Si, the deposits showed that the phases present corresponded to those expected from the diagram [31].

Smith et al. [27] studied the deposition of the two-phase ($\alpha + \beta$) type Ti–6Al–4V alloy deposited from a single rod-fed source. The microstructure was very similar to wrought material with the same characteristic $\alpha + \beta$ morphology present on a finer scale in the deposited material.

Dispersion-strengthened alloys produced by co-deposition from multiple sources have also been produced. Paton et al. [31] produced Ni–TiC, Ni–NbC and Ni–ZrO_2 alloys. The particle size increased from 100 to 1000 Å by changing the deposition temperature from 350 to 1000 °C. The size of the dispersed carbide phase particles increased on annealing at 1000–1100 °C owing to their slight solubility in nickel. On the other hand, the size and distribution of ZrO_2 dispersion remained constant even after exposure at 1300 °C for 5 h, as shown in Figure 4.56.

Movchan et al. [205] produced Fe–NbC and Fe–Ni–NbC dispersion strengthened alloys by co-evaporation. The microstructure exhibited columnar morphology, with the inclusion of a fine dispersion of NbC particles.

Raghuram and Bunshah [206] studied the microstructure of TiC deposits from 500 to 1450 °C (Figure 4.57). They observed the transition from the tapered crystallite (zone 1) to columnar structure at 973 K, or 700 °C (0.3 T_m). The highest deposition temperature (1450 °C) used by these investigators was not sufficient to produce an equiaxed structure, although this temperature corresponds to 0.51 T_m.

Xu et al. investigated the growth texture of MgO films deposited by e-beam deposition at different inclination angles [207] using SEM. The results are shown in Figure 4.58. Their study showed that the deposition rate increases with the increasing inclination angle. However, the surface loses its smoothness and shows more voids at higher angles, especially after 50°.

The energy of the depositing beam of atoms can be increased if some of them are ionized. It has been shown [23] that a small fraction of the vaporized species from an e-beam-heated source is ionized owing to collisions with electrons in the plasma sheath above the molten pool. Bunshah and Juntz [200] biased the substrate to -5000 V during the deposition of beryllium at 570 °C and found that the columnar grain size was markedly refined by the ion bombardment as compared to the grain size produced without biasing the substrate at the same deposition temperature. It may be postulated that the ion bombardment causes a localized increase in temperature at the surface where deposition is occurring, thus causing a higher nucleation rate and a finer grain size. Similar results have been reported for tantalum [208]. The use of a hollow cathode gun intensifies the degree of ionization of the vapor species, resulting in a marked increase in kinetic energy of the vaporized atoms [209]. The effects of substrate bias are, therefore, easier to observe. Increasing the substrate bias results in a change in morphology from columnar to fine, equiaxed grains for silver deposited on beryllium and stainless steel [210], and silver and copper deposited on stainless steel [211].

The presence of a gas at high pressures (5–20 μm) results in a net decrease in kinetic energy of the vaporized atoms due to multiple collisions during the transverse from source to substrate. This degrades the microstructure to lose columnar grains [211] and eventually to an agglomerate of particles. (This is a way to produce fine powders by evaporation and

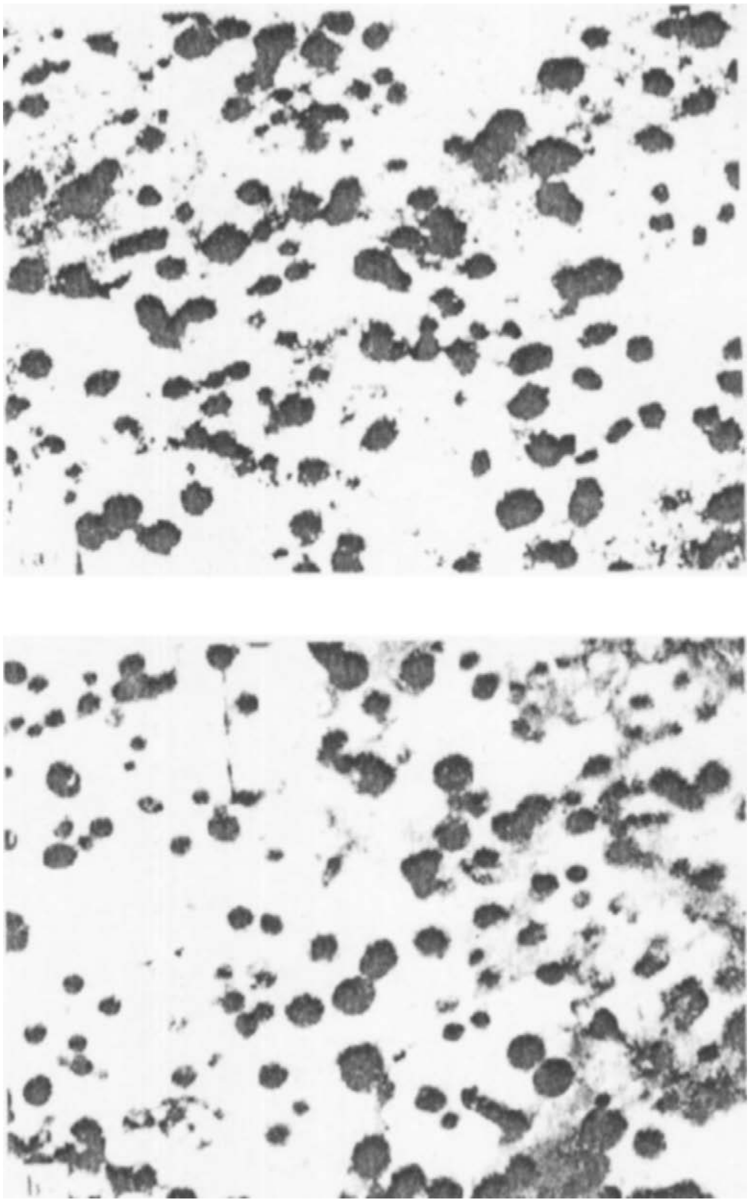

Figure 4.56: Microstructure of dispersion strengthened Ni–ZrO_2 alloy before and after exposure at 1300 °C for 5 h [31].

subsequent gas-phase nucleation and condensation.) The negative effects of the presence of a high gas density on the kinetic energy and the mobility of adatoms on the deposit surface can be overcome by biasing the substrate [211, 212] and/or heating the substrate to a higher temperature [213].

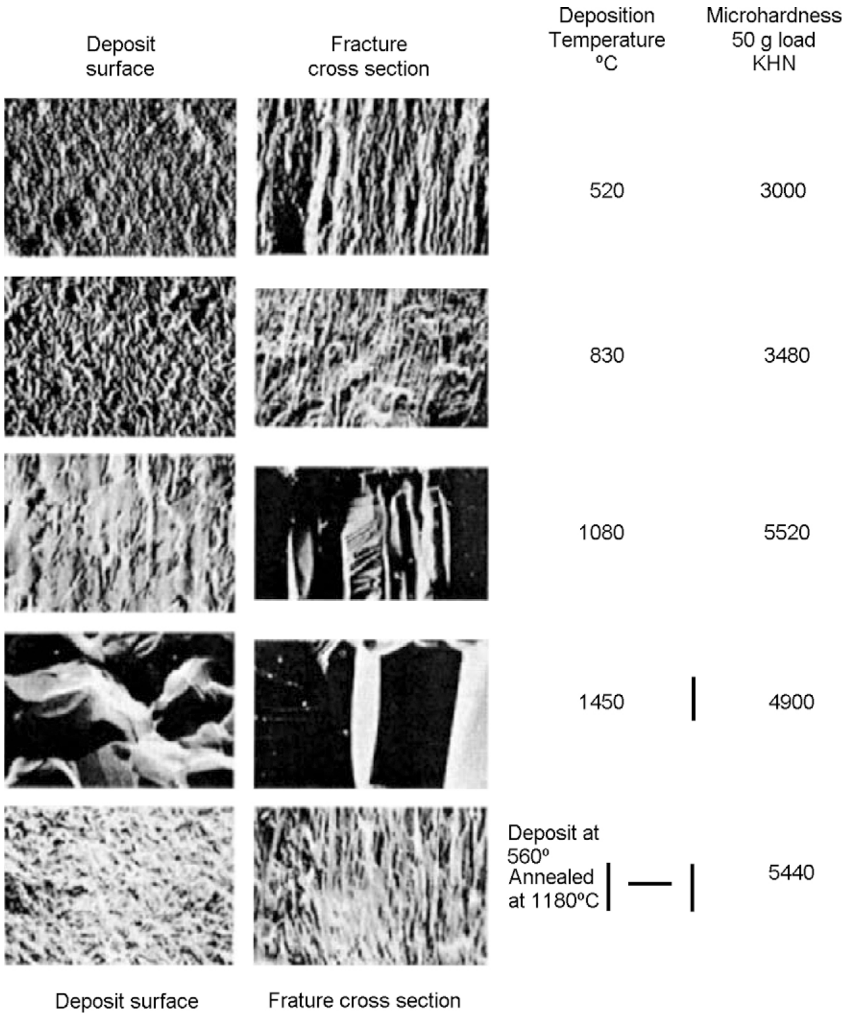

Figure 4.57: Structure of TiC deposits at various substrate temperatures [206].

4.9.2 Texture

The texture of evaporated deposits is, in general, dependent on deposition temperature. At low deposition temperatures, a strong preferred orientation is generally observed: {211} in iron [203], {220} in TiC [206], and {0002} in Ti [214]. As deposition temperature increases, the texture tends to become more random. In the case of beryllium [29], the texture changed to a {110} orientation at high deposition temperatures. The presence of a gas tends to shift the preferred orientation to higher index planes [215]. For silver, increasing the substrate bias changes the preferred orientation from {111} to {200} and back to {111} [201]. The inclination angle affects the texture of the film. According to Xu et al., when inclination angle

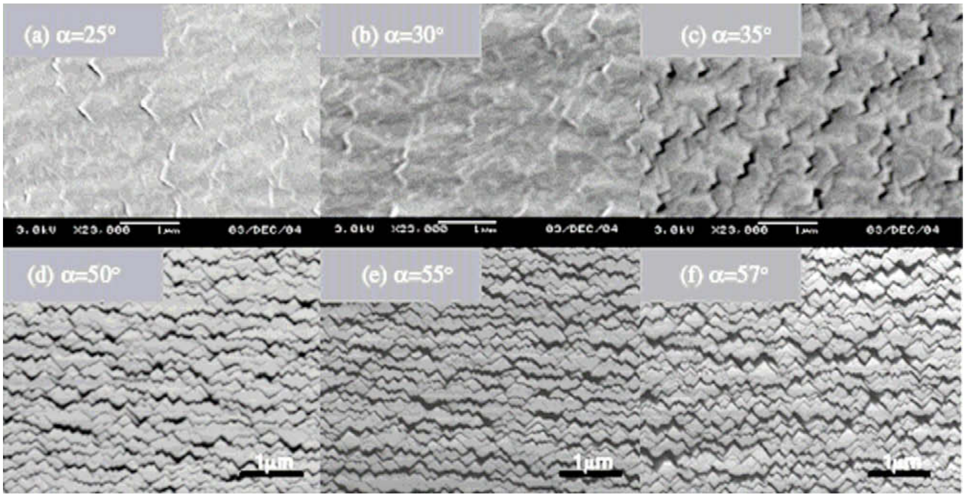

Figure 4.58: Surface morphology of the MgO e-beam evaporated films, with different inclination angles between source and the substrate [207].

increases, out-of-plane texture grows more quickly. However, when the angle is decreased, in-plane texture shows limited grain alignment, whereas better alignment was observed at higher angles [207].

4.9.3 Residual Stresses

Residual stresses in deposits are of two types. The first kind arises from the imperfections built in during growth (the so-called growth stresses). An increase in deposition temperature produces a marked decrease in the magnitude of this stress [206, 216, 217]. The other source of residual stress is due to the mismatch in the coefficient of thermal expansion between the substrate and the deposit. Its magnitude and size depend on the values of the thermal expansion coefficients as well as the thickness and size of the substrate and deposit. In order to compare residual stresses, the thermal stress component should be subtracted from the measured values [216]:

$$\sigma_{\text{thermal}} = \Delta\alpha \cdot \Delta T \cdot \frac{E_{\text{c}}}{1 - \upsilon_{\text{c}}} \tag{4.10}$$

where $E_{\text{c}}/(1 - V_{\text{c}})$ is the biaxial modulus for the film, $\Delta\alpha$ is the difference in the coefficient of thermal expansion between the substrate and film material, and ΔT is the difference in temperature between deposition temperature and room temperature.

The influence of a negative bias on the substrate produces a compressive stress in the deposit, which reaches a maximum value at −200 to −300 V DC bias and then decreases [212].

High residual stresses can cause plastic deformation (buckling or bending), cracking in the deposit or the substrate, or cracking at the substrate–deposit interface. The latter can be minimized by grading the interface, i.e. producing the change in material over a finite distance instead of producing it abruptly at a sharp interface. A graded interface can be produced by gradually changing the deposition conditions or by interdiffusion, which is enhanced by higher substrate temperature or increased kinetic energy of the vapor species.

4.9.4 Defects

Let us next consider the 'defects' found in vapor-deposited materials. The first one is classified as a *spit*, or small droplet ejected from the molten pool, which lands on the substrate and is incorporated into the coating [218]. An example is shown in Figure 4.59. The composition of the droplet is different from that of the coating in the case of an alloy and can therefore be the site of corrosion initiation. The bond between the droplet and the surrounding material is usually poor. Hence, corrosion attack can proceed down the boundary to the substrate or undermine the coating. The spit may also fall out, leaving a pinhole behind which can act as a stress concentrator and limit the ductility or the uniform elongation of a sheet material. Spits or pinholes do not affect the yield strength or reduction of area in a ductile material, but they can be stress raisers and sites for fatigue-crack initiation. Both spits and foreign particles on the substrate surface induce preferential growth of the deposit in that area because of higher exposure to the vapor flux than the general growing interface. This region of preferential growth is termed a *flake*; typical flakes are shown in Figure 4.60. There is marginal bonding

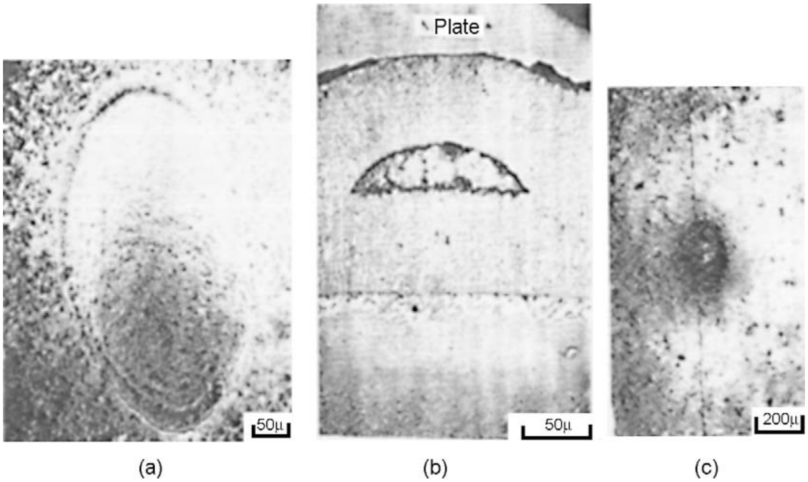

Figure 4.59: Vapor source droplet (spit) defect in M–Cr–Al–Y coatings. (a, b) Defects overcoated with additional material; (c) fatigue crack initiated at spit [218]. (Courtesy of American Institute of Physics.)

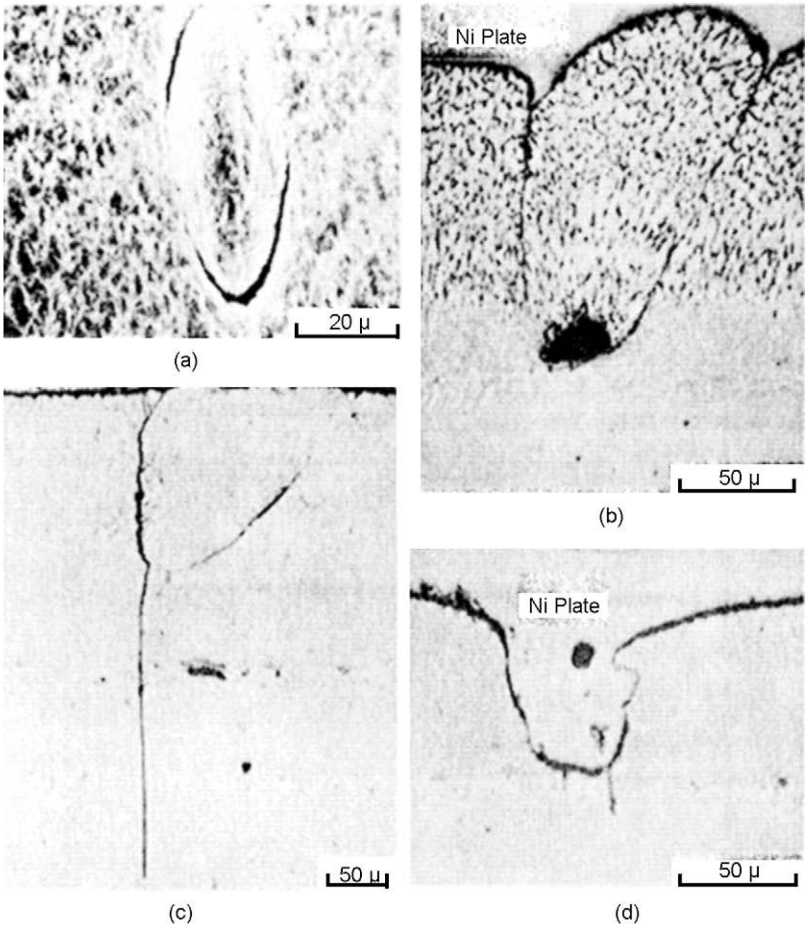

Figure 4.60: Flake defects in (a) and (b) produced by accelerated coating deposition on foreign particles. Glass bead peening incorporates flake into the coating (c) or knocks it out and forms a pit (d) [218]. (Courtesy of American Institute of Physics.)

between the flake and the deposit, which can lead to formation of a pit or crack, or to nucleation of corrosive attack.

Spits can be suppressed by eliminating porosity, oxide inclusions, and compositional inhomogeneities in the evaporant source material, since spitting can be caused by included-gas release or by the release of bound gas through thermal decomposition. In e-beam evaporation, the beam of electrons dissipates energy over a path extending as much as a mil (25 μm) or more into the melt. If this energy is delivered at a rate faster than the coating material can accommodate by evaporation, conduction, or radiation, a pocket of vapor forms and spitting occurs. Spits are also caused by gas pockets included in the evaporant rod that suddenly expand when rapidly heated by the beam. Non-metallic inclusions can trap pockets of superheated vapor below them, which can erupt in a shower of molten droplets. Spits can be avoided by using a high-purity vacuum melted rod as the evaporant. Flake formation can be avoided by avoiding the presence or impingement of foreign particles on the substrate (primarily by substrate surface cleaning and good housekeeping of the deposition apparatus). Deep grooves or ridges on the substrate can also produce flake-type defects by shadowing adjacent regions of the specimen surface.

Another type of defect occurs in complex alloys [218] such as M–Cr–Al–Y (where M can be nickel, cobalt, or iron), where even at deposition temperatures of 955 °C, the deposit morphology corresponds to the fibrous transition zone between zones 1 and 2. The grain boundaries in this morphology are weak, causing intergranular corrosive attack (Figure 4.61). The problem can be obviated by increasing the adatom mobility through the use of a higher substrate temperature or specimen bias of about −200 V, or by using a postcoating process that consists of a room temperature high-intensity glass bead peening followed by a high-temperature anneal in hydrogen. Compound rotation of the specimen, which exposes higher surface irregularities to varying angles of impingement of incoming vapor atoms, produces a significant decrease in the number and size of open, columnar defects.

Another problem in deposits of complex alloys is due to the variation in deposit chemistry attributable to segregation in the ingot and large pool temperature variations caused by the finite size of the e-beam [218, 219]. Improved ingot quality, development of improved e-beam sources, and decrease in the temperature gradient at the crucible walls by using crucible liners or coolant of lower heat capacity, such as NaK, instead of water would minimize this problem.

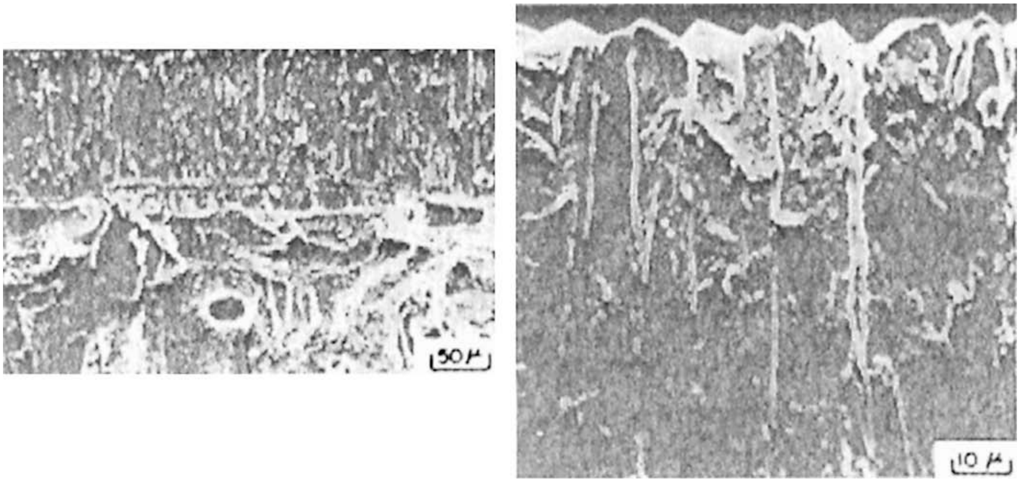

Figure 4.61: SEM photomicrograph of impact fracture surface of as-deposited overlay coating. Fracture is intercolumnar indicating weak boundaries [218]. (Courtesy of American Institute of Physics.)

In a more recent investigation on the origin of defects and continuing on the above [220], it was found that spits in M–Cr–Al–Y type alloys consist of ejected pool material exhibiting enrichment in impurity elements of low vapor pressure as a result of superheating of non-metallic particles (carbides or oxides) in the melt initiating the ejection of pool material. Flakes, generally cone shaped, were found to originate at non-metallic particles loosely attached to the surface. Leader formation was found to be weakly dependent on the angle of incidence of the arriving vapor flux. Both flakes and leaders seem to be enhanced by preferential growth and shadowing phenomena.

Wolfe et al. deposited titanium carbide/chromium carbide layers by co-evaporation of the transition metal and carbon simultaneously using e-beam PVD [221]. Figure 4.62 shows the spit defect on the surface of the $TiC/Cr_{23}C_6$ multilayer coating. According to Figure 4.62, the obtained microstructure is columnar but the surface of the film is not faceted. Porosity has been observed between the columnar grains. This suggests that the columnar grains are dense multilayers of chromium and titanium carbides.

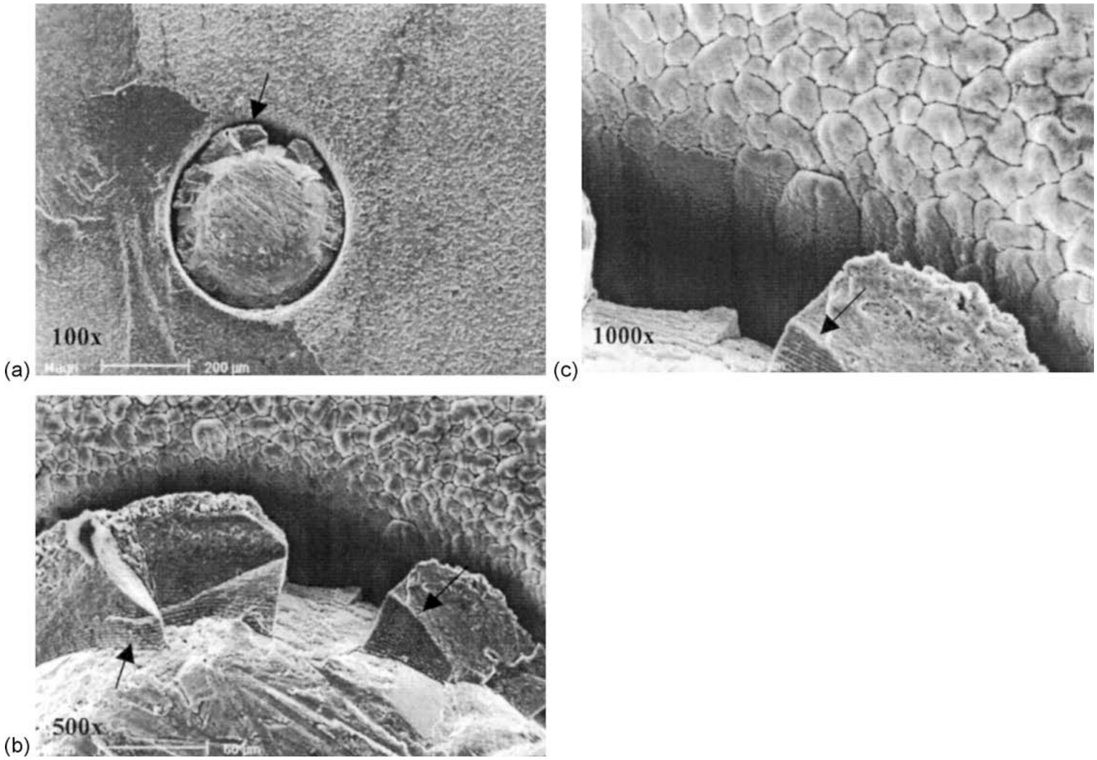

Figure 4.62: Surface morphology of titanium carbide/chromium carbide layer showing the spit defect [221].

4.10 Physical Properties of Thin Films

The Handbook of Thin Film Technology [7] contains an extensive section on the electrical and electronic conduction, piezoelectric and piezoresistive, dielectric and ferromagnetic properties of thin films. The reader is referred to it.

4.11 Mechanical and Related Properties

4.11.1 Mechanical Properties

4.11.1.1 Mechanical Property Determination

A number of testing techniques have been used to determine the strength properties of thin films. They include the high-speed rotor test [222], the bulge test [223–227], microtensile testing machines of the soft [228–231] and the hard categories [223–227], and even fixtures which can be operated in the electron microscope [232, 233]. Hoffman [234, 235] reviewed the test techniques and the reader could do no better than to read Hoffman's articles or the original references. The basic handling problem encountered with the preparation and mechanical property testing of thin film specimens is much less severe with thick films for which many of the standard test specimens, machines, and techniques can be readily used. Therefore, the spectrum of mechanical properties measured on thick films is much broader than with thin films.

4.11.1.2 Tensile Properties Of Thin Films

The tensile properties of thin films have been reviewed [234–237]. As Hoffman concludes [234], the data reported are not very consistent even on the same material. The reader is advised to consult the references for details. In general, the observed strength of vapor-deposited metal films consists of three parts:

$$\sigma_{\mathrm{OBS}} = \sigma_{\mathrm{Bulk}} + \sigma_{\mathrm{Imperfections}} + \sigma_{\mathrm{Thickness}} \tag{4.11}$$

where σ_{OBS} is the inherent strength level of bulk polycrystalline material in the annealed state, $\sigma_{\mathrm{Imperfections}}$ is the contribution due to point defects in excess of those normally found in the bulk annealed state, and $\sigma_{\mathrm{Thickness}}$ is the contribution arising from the smallest dimension of the film and its limiting effect on grain size such that dislocation multiplication and migration are impeded [230].

Table 4.10 gives the strength properties of thin films of some metals and compares them to bulk values [235]. In many cases, the strengths are about 200 times those of annealed bulk samples and three to ten times those of hard drawn samples. The tensile strength values are given numerically as well as by fractions of the shear modulus. The ductility of the high-strength films is very limited, which is similar to the behavior of high-strength fibers or

Table 4.10: Strength of properties of thin films

Material	Structure	Maximum tensile strength (kg/mm^2)	Shear modulus[a]	Strain at fracture (%)	Thickness dependent	Ref.
Au	Bulk hard-drawn	28[b]	G/114	[c]	–	–
	(111) crystal film	81	G/36	1.2	No	[79]
	(100) crystal film	27	G/110	0.5	Yes	[141]
	(110) (111) Polycrystalline film	49	G/59	1	No	[148]
	Polycrystalline film	55	G/54	0.7	Yes	[139]
	(100) crystal film	26	G/115	3.5	No	[151]
	Polycrystalline film	32	G/92	2.3	No	[151]
Ag	Bulk hard-drawn	37[b]	G/75	–	–	–
	Polycrystalline film	59	G/47	0.7	Yes	[128]
	Polycrystalline film	42	G/68	0.3–0.4	–	[30]
Cu	Bulk hard-drawn	49[b]	G/98	–	–	–
	Polycrystalline film	93	G/51	1.8	Yes	[196]
	Polycrystalline film	88	G/54	–	No	[145]
	Rolled foil	19	G/256	10–15	No	[198]
Ni	Bulk cold-rolled	125[b]	G/67	–	–	–
	Polycrystalline film	210	G/40	1.8	Yes	[149]
Al	Bulk cold-rolled	16[b]	G/171	–	–	–
	Polycrystalline film	42	G/66	0.5–0.8	–	[30]

[a] *Shear moduli from AIP Handbook, 1957 [237].*

[b] *Bulk tensile strength from Handbook of Chemistry and Physics, 1961 [238].*

[c] *Fracture strain not quoted for bulk material.*

whiskers. A principal point of contention is whether the ultimate tensile strength is a function of the film thickness or not. The discrepancy also appears to be dependent on the test method used, i.e. between the bulge test and tensile test. In many cases, it appears that the strength decreases as the film thickness increases from approximately the 200–300 Å range to about the 2000–4000 Å range. At the greater thickness, the strength is about the same as that of heavily worked bulk material. There are several papers relating the strength properties of thin films to the ‘crystallite size’ and ‘block structure’ as influenced by the deposition temperature, stress, recovery, and recrystallization process [184, 240–248]. One manifestation of this is the phenomenon of creep or plasticity in room temperature tensile tests as exhibited by an irreversible initial loading curve but almost reversible unloading and reloading curves as long as the previous stress level is not exceeded. An example of this is shown in Figure 4.63 from Neugebauer [229] as the change in slope of the stress–strain curve. The possibility that this change in slope is related to an elastically soft measurement or to creep in the cementation of the grips cannot altogether be discarded.

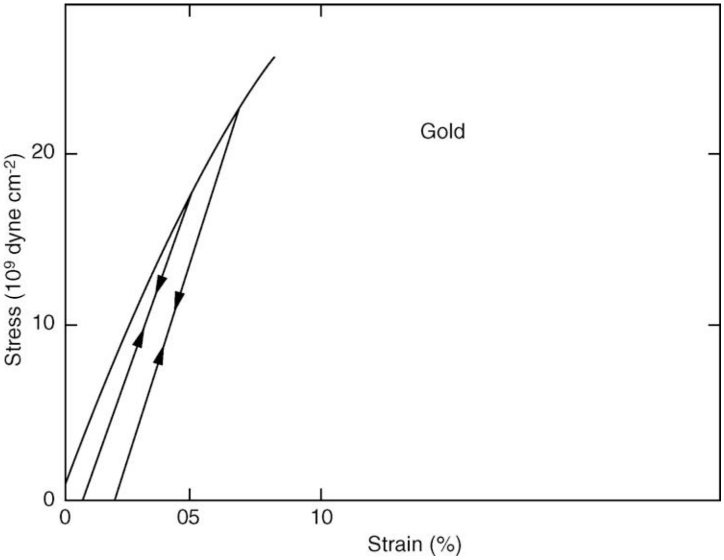

Figure 4.63: Typical stress–strain curve for thin film.

Long-term creep rates have been measured and for gold they vary from 10^{-7} to 10^{-4} min^{-1} depending on load, dimensions and the amount of prestrain [229]. The estimates of the relative elastic and plastic extension at fracture vary from completely elastic to an almost even mixture of elastic and plastic deformation.

Fracture in ductile gold single crystal films [236] results from a localized plastic deformation with resultant thinning of the film and a rise in stress level. Eventually the smaller cracks formed in this manner join to cause fracture. The dislocations – necessary for the deformation – are not the grown-in dislocations but those which nucleate and multiply in discontinuous regions. Most observations show no necking prior to fracture. The maximum stress appears to correspond to that needed to propagate cracks from flaws existing in the specimen. In polycrystalline nickel, the fracture is the ‘clean cleavage’ type [230].

4.11.1.3 Mechanical Properties of Thick Condensates and Bulk Deposits

Table 4.11 lists the mechanical properties of thick deposits of metals, alloys, refractory compounds, and laminated structures. In many cases, the mechanical test data are quite extensive showing yield strength, ultimate tensile strength, hardness, and ductility as a function of grain size, deposition temperature, and test temperature. One of the features of the data is that the properties of thick deposits of metals and alloys are very similar to those of wrought materials which are produced by the conventional processes of melting, casting, mechanical working, and heat treatment.

Table 4.11: Mechanical properties of thick films or bulk condensates

Material	0.2% yield stress (kg/mm^2)	Ultimate tensile strength	% Elong. (or % RA)	Microhardness (kg/mm^2)	Deposition temp. (°C)	Grain size (μm)	Thickness (μm)	Test temp. (°C)	Ref.
Al	–	–	–	200	200	–	40	25	[192]
	–	–	–	160	300	–	–	–	–
	–	–	–	80	400	–	–	–	–
	–	–	–	8 Knoop at 0.5 g load	250–350	–	1–2	25	[182]
Cu	15	–	–	–	–	1	4–10	25	[169]
	28	–	–	–	–	0.7	–	–	–
	40	–	–	–	–	0.1	–	–	–
	45	–	–	–	–	0.07	–	–	–
	–	18–22	35	–	400–800	–	1000	25	[190]
	–	–	–	240	120	–	>15	25	[200]
	–	–	–	170	180	–	–	–	–
	–	50	2.38	–	–	–	3–20	25	[198]
	–	16 (annealed 500 °C)	0.27	–	–	–	–	–	–
	–	60	–	–	–	0.1	0.5	25	[31]
	–	40	–	–	–	0.6	3–5	–	–
Ag	10	–	–	–	–	1	5–20	25	[169]
	35	–	–	–	–	0.1	–	–	–
Fe	–	66–72	–	250	–	–	20	25	[196]
	45	46	4	120	400	–	1000	25	[191]
	20	35	20	90	550	–	–	–	–
	15	25	18	75	700	–	–	–	–
Be	–	140	0.1	240 (Knoop)	350–425	–	75–100	25	[188]
	–	281	0.3	215	480–550	–	–	–	–

(*Continued*)

Table 4.11: (*Continued*)

Material	0.2% yield stress (kg/mm^2)	Ultimate tensile strength	% Elong. (or % RA)	Microhardness (kg/mm^2)	Deposition temp. (°C)	Grain size (μm)	Thickness (μm)	Test temp. (°C)	Ref.
	–	316	0.45	168	625–685	–	–	–	–
	–	295	1.0	170	760–790	–	–	–	–
	62 (bend test)	–	> 4 (bend test)	–	–	100	1000	25	[18]
	47 (bend test)	–	> 5.2 (bend test)	–	–	–	–	–	–
Ni	–	115	0.3	–	–	0.2	0.2–2	25	[191]
	–	66–74	–	250	400–420	–	20	25	[199]
	–	–	–	450	260	–	–	–	–
	–	–	–	600	220	–	–	–	–
	129	338	39 (20)	96.6	554	26	275	25	[113]
	135	336	32 (20)	109	245	19	375	–	–
	155	366	35 (21)	104	329	12.7	375	–	–
	247	403	21 (21)	125	260	3.7	375	–	–
	140 (melted and wrought)	407	44 (30)	91	–	18	357	–	–
	–	138	0.6	–	–	–	2.6	25	[142]
	–	–	–	–	250	620	1000	25	[97]
	–	–	–	–	400	420	–	–	–
	–	–	–	–	600	380	–	–	–
	–	28	20	–	400	–	1000	25	[190]
	–	38	12	–	800	–	–	–	–
Ti	189	295	25 (66)	–	800	32	250	25	[112]
	225	302	20 (38)	–	600	8	250	25	–

Table 4.11: (*Continued*)

Material	0.2% yield stress (kg/mm^2)	Ultimate tensile strength	% Elong. (or % RA)	Microhardness (kg/mm^2)	Deposition temp. (°C)	Grain size (μm)	Thickness (μm)	Test temp. (°C)	Ref.
	436	471	3 (25)	–	450	1	250	25	–
	189 (melted and wrought)	302	40 (61)	–	–	50	250	25	–
	–	–	–	560	200	–	1000	25	[97]
	–	–	–	200	400	–	–	–	–
	–	–	–	130	500	–	–	–	–
	280–420	–	20	–	–	–	100–250	25	[134]
	140–280	–	35	–	–	–	–	200	–
Mo	14	19	(5.3)	191	990	530	300	–	[186]
	24	28	(0.8)	169	704	85	–	–	–
	38	44	(1.0)	186	804	19	–	–	–
Nb	19	–	7.3	112	745	10	300	–	[186]
V	37	–	22	115	540	0.7	300	–	[186]
W	–	–	–	720	600	–	1000	25	[97]
	–	–	–	460	1000	–	1000	25	–
	–	–	–	300	1000	–	1000	25	–
Ni–20Cr	337	540	26 (27)	80	950	13	375	25	[189]
	577	780	21 (26)	112	780	2.6	375	25	–
	752	871	18 (19)	131	680	1.8	375	25	–
	1195	1223	6 (8)	180	427	0.5	375	25	–
	393 (melted and wrought)	569	37 (31)	78	–	10.4	325	25	–
	25	49	25 (21)	–	950	13	375	1000	–

Table 4.11: (*Continued*)

Material	0.2% yield stress (kg/mm^2)	Ultimate tensile strength	% Elong. (or % RA)	Microhardness (kg/mm^2)	Deposition temp. (°C)	Grain size (μm)	Thickness (μm)	Test temp. (°C)	Ref.
	40.9	60	53 (41)	–	680	1.8	375	1000	–
Ti–6Al–4V	970–1195	1068–1195	1–12	–	–	–	79	25	[32]
80Ni–20Cu	–	35–45	8–25	–	400–800	–	375	1000	[190]
50Ni–50Cu	–	40–55	5–20	–	400–800	–	375	1000	–
20Ni–80Cu	–	27–42	10–30	–	400–800	–	375	1000	–
80Ni–16Fe	–	180	–	650	200	–	–	25	[200]
(permalloy)		150	–	250	400	–	–	25	–
Al_2O_3	–	–	–	380	400	–	300	25	[97]
	–	–	–	80	600	–	300	25	–
	–	–	–	200	1000	–	300	25	–
	–	–	–	1000	1400	–	300	25	–
	–	–	–	500–800	1100	–	300	25	[202]
ZrO_2	–	–	–	450	400	–	300	25	[97]
	–	–	–	350	600	–	300	25	–
	–	–	–	400	1000	–	300	25	–
	–	–	–	1000	1400	–	300	–	–
Y_2O_3	–	248	–	384	120	3.2	100	25	[203]
	–	226	–	256	210	5	100	25	–
	–	215	–	331	304	8	100	25	–
	–	208	–	320	416	14	100	25	–
	–	205	–	360	538	21	100	25	–
	–	198	–	502	721	58	100	25	–
Ti_2O	–	–	–	960–1960	750	–	–	25	[102]
TiO	–	–	–	700–2015	1100	–	–	25	–
SiO_2	–	–	–	300	–	–	10	25	[203]
Ta_2C	–	–	–	1907–2440	500	–	–	25	[197]

Table 4.11: (*Continued*)

Material	0.2% yield stress (kg/mm^2)	Ultimate tensile strength	% Elong. (or % RA)	Microhardness (kg/mm^2)	Deposition temp. (°C)	Grain size (μm)	Thickness (μm)	Test temp. (°C)	Ref.
TaC	–	–	–	1800–2400	500	–	–	25	–
SiC (RF sputter)	–	–	–	3500–4000	–	–	2.6	25	[205]
TiC (ARE process)	–	–	–	2710	520	–	50	25	[116]
	–	–	–	2955	730	–	50	25	–
	–	–	–	2955	830	–	50	25	–
	–	–	–	4110	1080	–	50	25	–
	–	–	–	4160	1120	–	50	25	–
	–	–	–	2400	–	–	5	25	[206]
ZrC	–	–	–	2500–2800	550	–	50–75	–	[101]
(Hf–3Zr)C	–	–	–	2700–3030	550	–	50–75	–	–
VC	–	–	–	2350	550	–	50–75	–	[101]
NbC	–	–	–	2300	550	–	50–75	–	–
Laminates									
Cu–Ni laminate	–	35–55	13	–	–	–	2	25	[207]
Cu–Fe laminate	35–70	110	–	400–800	240–360	–	15–25	25	[208]
Cu–Ni laminate	–	80	1.8	–	300	–	0.1	25	[209]
Cu–Fe laminate	–	125	0.88	–	150	–	0.04	25	–

Table 4.11: (*Continued*)

Material	0.2% yield stress (kg/mm^2)	Ultimate tensile strength	% Elong. (or % RA)	Microhardness (kg/mm^2)	Deposition temp. (°C)	Grain size (μm)	Thickness (μm)	Test temp. (°C)	Ref.
Ni–Fe laminate	–	150	0.45	–	150	–	0.04	25	–
Ni–SiO	–	150	–	300	–	–	20	25	[217]
	–	105	–	300	–	–	20	200	–
	–	95	–	300	–	–	20	400	–
	–	80	–	200	–	–	20	600	–
Ti–TiC	–	251	1.8	–	500	–	250	–	[211]

We consider each type of material separately since the behavior of metals and alloys is vastly different from that of refractory compounds.

The early work in this area was that of Bunshah [17, 18], Bunshah and Juntz [22], and Smith [23], who deposited thick films of Be, Ti, and Cu, respectively, and measured mechanical properties. In 1965, Palatnik et al. published a paper on mechanical properties of Al condensates [240]. It is impossible to review in detail all the papers. The pertinent data are shown in Table 4.11 and the discussion below concentrates on the highlights.

4.11.1.4 Tensile Properties and Hardness of Metal and Alloy Deposits

Movchan and Demchishin [123] studied the tensile properties and microhardness of Ni, Ti, and W condensates produced at various deposition temperatures. No tensile tests were performed on specimens deposited in zone 1 (Figure 4.62). Tests on specimens deposited in zone 2 showed high strength and low ductility at low deposition temperature. The strength decreased and the ductility increased with deposition temperature. The strength and ductility values of specimens deposited in zone 3 showed approximately the same values as for recrystallized specimens produced from wrought material. The microhardness variation with deposition temperature for Ni, Ti, and W is shown in Figure 4.64. The tapered crystallite morphology in zone 1 showed a high hardness much greater than that of annealed metal. The hardness decreased rapidly with increasing deposition temperature to a fairly constant value for zone 3 morphology, which corresponds to the hardness of recrystallized metals.

Bunshah and co-workers studied the effect of deposition temperature on the grain size, tensile properties, and hardness of Ti [22, 196], Ni [198], Nb, V, Mo [185], and Ni–20Cr [194] alloys for deposits made in zones 2 and 3. They found that increasing deposition temperature produced larger grain size, lower strength, higher ductility, and lower hardness. Even at the

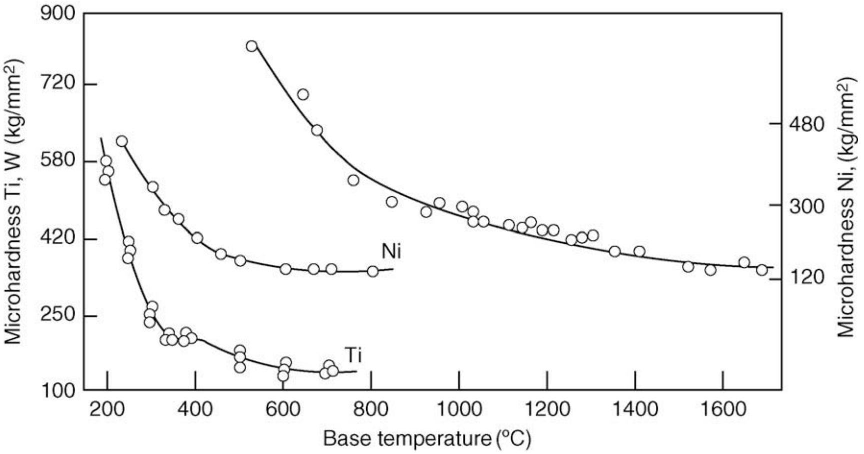

Figure 4.64: Variation of microhardness with deposition temperature of metals.

lowest deposition temperature in zone 2, the ductility was good (> 20% RA for 1 μm grain diameter Ti at a yield strength of 56,000 psi). Moreover, they found that both the yield strength and hardness varied as the inverse square root of grain diameter, i.e. followed the Hall–Petch relationship [249, 250], which is

$$\sigma_{ys} = \sigma_o + kd^{-\frac{1}{2}} \tag{4.12}$$

where σ_{xy} is the yield strength, d is the grain diameter, and σ_o and k are constants. Figure 4.65 shows an example of this relationship for Ni–20Cr alloy.

For all these metals and alloys, the yield strength, ductility and hardness values correspond to those of the same materials produced by casting, mechanical working, and recrystallization. The variation of yield strength and hardness with grain size, i.e. Hall–Petch type relationships, were also very similar between the deposited and wrought materials, small variations being

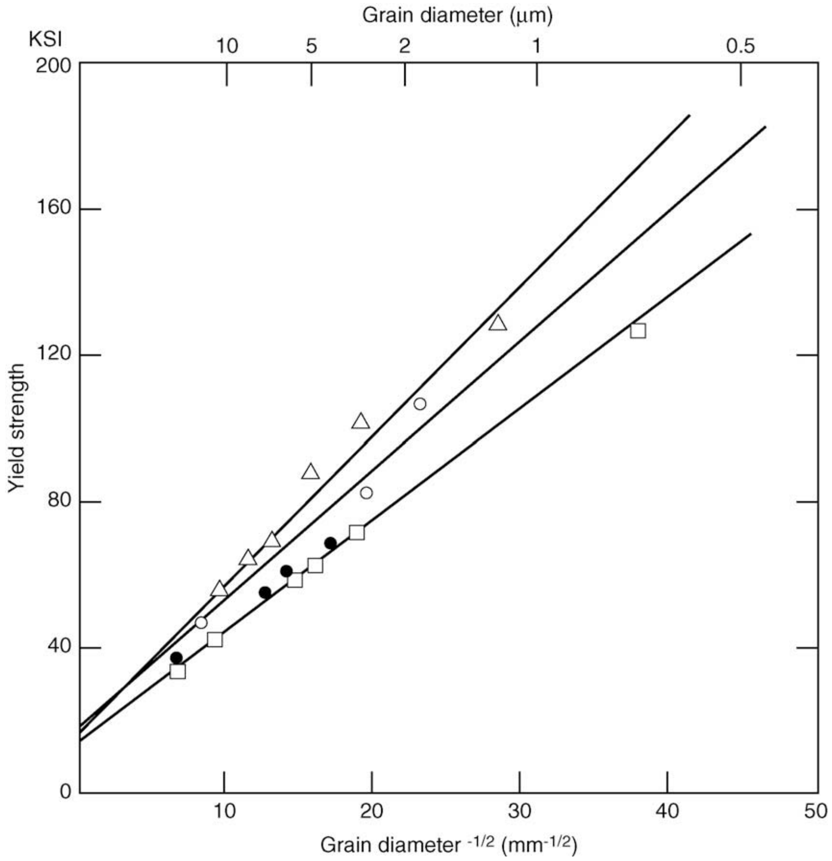

Figure 4.65: Yield stress vs inverse square root of average diameter for Ni–20Cr alloy at 25 °C. △: wrought; O: deposited; □: Wilcox et al.; •: Webster ([251], Refs 12 and 13).

ascribable to differences in grain morphology and preferred orientations. The Ni–20Cr alloy showed good strength at 1000 °C and also obeyed the Hall–Petch relationship.

The Hall–Petch relationship is also obeyed by thick films of Cu and Ag to grain sizes as small as 0.05 μm, as shown by Nenioto et al. [252]. Thus, these thick deposits behave as true engineering materials.

Chambers and Bower [253] studied the mechanical properties of 18-8 stainless steel, gold, and magnesium, and showed that their tensile properties were very similar to their wrought counterparts.

Smith et al. [27] studied the $(\alpha + \beta)$ type Ti–6Al–4V alloy. They showed that the tensile properties are very similar to the wrought material except for a much smaller value in percentage elongation due to premature onset of plastic instability in a tensile test at pinholes in the deposited samples. The bend ductility was, however, superior to the wrought material.

Shevakin et al. [120] studied the strength and hardness of aluminum and copper condensates as a function of the deposition parameters. They found that the mechanical properties varied widely with changes in process parameters. The deposited materials also showed higher strength and plasticity than the same materials conventionally fabricated, i.e. casting followed by the neomechanical treatments. They also found that the hardness values obeyed the Hall–Petch relationships.

Paton et al. [31] showed that it is possible to produce thick deposits of all the alloys across the Cu–Ni system and that the mechanical properties vary systematically with composition, as would be expected.

Dispersion-strengthened alloy deposits

The first data on dispersion-strengthened alloys produced by evaporation methods were reported by Paton et al. [31], who showed that Ni–ZrO_2 alloys produced by co-evaporation from two sources contained ZrO_2 particles in the size range of 150–3000 Å by changing the deposition temperature from 650 to 1100 °C. They also showed that the creep strength at 1000 °C increased with volume fraction of zirconia. These alloys showed remarkable stability in the microstructure and mechanical properties even after creep exposures of 5 h at 1300 °C. Subsequently, Movchan et al. studied the structure and properties of Ni–ZrO_2 alloys [183], and Fe with Al_2O_3, ZrO_2, ZrB_2, TiB_2, NbC, or TiC second phases [254]. The alloys were produced by co-evaporation of the constituents from e-beam-heated evaporation sources.

One of the very striking effects of the incorporation of a dispersed phase in an evaporated metallic coating is a very pronounced refinement in grain size, often by a factor of 10–100, or more, and the inhibition of grain growth at elevated temperatures. This was first reported by Kennedy [203] for the incorporation of Y_2O_3 dispersions in Fe condensates. It was also observed by Majumder [207] for Cu–Al_2O_3 deposits and by Jacobson et al. [256] in Ni–Al_2O_3

deposits. In a very recent paper, Movchan and Demchishin [123] show the grain size reduction in the Ni–Al_2O_3, Fe–ZrO_2, Fe–ZrB_2, and Fe–NbC deposits. The most intense grain refining effect is observed at low volume fractions (0.5 vol.%) of the second phase.

Of particular interest to this topic is a subsequent paper by Majumder [257] showing the strong effect of alumina content in increasing creep strength, which confirms the model proposed by Mott [258], who suggested that the ideal creep-resistant material is one with a fine grain size in which the grain boundaries are filled with some substance, say a refractory oxide, to inhibit the motion of grain boundaries.

Perhaps the most interesting result from Movchan's work [181, 254, 259] is that the dispersed phase alloys show a maximum in room temperature ductility in the W–ZrO_2 system at 1 vol.% ZrO_2, in the Fe–Al_2O_3 system at 0.3 vol.% Al_2O_3, and in the Fe–NbC system at 0.1 vol.% NbC. The yield strength and tensile strength do not show such a maximum but monotonically increase with volume fraction of the oxide phase. The significance of this observation lies in the possibility of increasing the ductility of MCrAlY coatings which, in turn, would result in increased resistance to spalling, thermal shock, and fracture, thus improving the performance of the coating. One might speculate on reasons for this effect, including strain–relaxation sites at particle matrix interface, or at grain boundaries owing to the greatly increased grain boundary area, favorable changes in residual stress distribution in the coating possibly due to changes in elastic modulus or strength, increased toughness or crack propagation resistance conferred by the dispersed phase particles, change in crystallographic texture, etc.

Movchan et al. [260] recently presented a very detailed treatment on the regulation of microstructure and mechanical properties of thick vacuum condensates with the help of dispersed phases. They give a detailed theoretical model of (1) the influence of dispersed phases on grain size; (2) the size and shape of dispersed particles as affected by deposition parameters; (3) strength and ductility of two-phase condensates as influenced by the grain size, particle size, mean free path, nature of the particle (deformable vs non-deformable) and particle-matrix adhesion energies; and (4) steady-state creep behavior. The model is then confirmed by the experimental results. As a good illustration of one of these points, Movchan [206] studied the difference in strength and ductility versus volume fraction of second phase when the latter is deformable or non-deformable. For both types of particles, there is a ductility maximum at a particular D_g/L ratio, but the strength behavior is diametrically opposite, showing a monotonic increase for a non-deformable particle and a minimum for the deformable particle. D_g is the grain size in the plane perpendicular to the vapor flux direction and L is the interparticle spacing. This model forms an excellent basis for design of experiments to study the effect of dispersed phases on the structure and properties of MCrAlY alloys.

Another fascinating observation by Movchan et al. [260] applies to two-phase alloys with deformable particles having a high adhesion to the matrix. The ductility of the alloys exceeds that of the pure matrix material at room temperature by a factor of 1.5–2 at a strain rate of $1.67 \times 10^{-3}\ s^{-1}$ ($0.1\ min^{-1}$). At high temperatures, the elongation at fracture exceeds 100%, i.e. superplasticity is developed.

Laminate composites

Laminate composites are attractive and preferable to fibrous composites because of their uniform properties in the plane of the sheet. In comparison to mechanical methods of producing laminate composites, e.g. bonding of sheets or foil, PVD techniques are very suited to the production of such composites, particularly if each lamella is to be very thin (0.01–1 μm thickness) in order to improve the strength and toughness of the composite.

From theoretical considerations, it may be expected that the mechanical properties of microlaminate composites would follow an adaptation of the well-known Hall–Petch relationship [249, 250] (yield strength or hardness $= \alpha d^{-\{1/2\}}$, where d is a characteristic microstructural parameter such as grain diameter, subgrain diameter, or lamina thickness). This correlation will be explored later.

In another approach, Koehler [261] proposed that a laminate structure which is formed of thin layers of two metals, A and B, where one metal, A, as a high dislocation-line energy and the other metal, B, has a low dislocation line energy, should exhibit a resistance to plastic deformation and brittle fracture well in excess of that for homogeneous alloys. If the dislocation-line energies are so mismatched, the termination of the motion of dislocations in metal B is energetically favored over dislocation propagation across the layer interface into metal A. In the case of thick layers, the dislocations generated in either of the layers will pile up in B at the A–B interface and thereby provide the stress concentrations needed for premature yield. Therefore, to suppress the generation of new dislocations in the layers, the thicknesses of A and B must be small. Thus, there is a critical minimum layer thickness required for the generation of dislocations.

This model does not take into account a high imperfection content in the laminate layers but assumes that their mechanical properties are similar to bulk annealed materials.

Most of the prior work on microlayer condensates was investigated in condensates produced at low deposition temperatures [262–270] ($T < 0.3\ T_m$) thus resulting in a high imperfection content. Moreover, the deposits were very thin (< 25 μm in thickness), which makes it very difficult to measure the mechanical properties (particularly ductility) and draw good correlations with theory. The systems investigated were Ge/GaAg, Al/Mg, Be/Al, Al/Cu, Al/Ag, Ni/Cu, Mg/Cu, and Al/Al_2O_3.

Recently, Lehoczky [270] studied the layer thickness dependence of the yield strength of Al–Cu and Al–Ag laminates of thin specimens prepared by alternate vapor deposition. Below the critical layer thicknesses required for dislocation generation in the layers, the experimental results are in good agreement with Koehler's predictions. For layer thicknesses greater than those required for dislocation generation, he has extended the theoretical model to include dislocation pile-up groups.

A very recent investigation by Bunshah et al. [204] used high deposition temperatures ($T \cong 0.4–0.45\ T_m$) where equilibrium structures are formed, and thick specimens (200–1000 μm thickness) containing a very large number of microlayers were produced such that mechanical properties could be easily measured on standard test specimens. Fe–Cu and Ni–Cu microlaminate composites were prepared by sequential deposition from two evaporation sources. Very marked increases in strength were observed, by as much as a factor of 10 as compared to the pure metals and a factor of 5 as compared to the solid solution Cu–Ni alloy of the same composition. The ductility decreased somewhat but was still appreciable (5% elongation) for the highest strength alloys. The strength and hardness values followed the Hall–Petch relationship. Superplastic behavior was observed in Fe–Cu microlaminates when the average grain size of the metal equals the interlammellar spacing (approximately 0.45–0.50 μm) at a test temperature of 600 °C and a strain rate of $0.005\ \text{min}^{-1}$.

High-temperature creep properties of thick Fe/Cu and Ni/Cu microlaminate condensates were studied at 600 °C as a function of layer thickness. Steady-state creep rate has been found to increase with a decrease in microlayer thickness. Microstructural study of the specimens after creep tests revealed the disintegration of iron and nickel layers in Fe/Cu and Ni/Cu condensates, respectively, with the formation of separate inclusions of an oval shape. The creep rate variation in the microlayer condensates is explained with the help of a structural model of high-temperature creep.

Refractory compounds

Deposits of refractory compounds, oxides, nitrides, and carbides are very important for wear-resistant applications in industry. Their structure and properties are strongly dependent on the deposition process. Their behavior is very different from metals and alloys. It is also very hard to measure the mechanical properties of ceramics by tensile tests similar to those used for metals and alloys because of their brittle nature. A very good test to measure the fracture stress of such brittle coatings is the Hertzian fracture test, which measures the fracture stress and the surface energy at the fracture surface [271]. Colen and Bunshah [136] used this test to measure the fracture behavior of Y_2O_3 deposits of various grain sizes.

Figure 4.66 shows the variation in microhardness with deposition temperature for Al_2O_3 and ZrO_2, from the work of Movchan and Demchishin [123], showing that the behavior of these oxide deposits is quite different in one respect from that of metals (Figure 4.59). The hardness falls when the structure changes from tapered crystallites (zone 1) to columnar grains (zone 2), as with metals. However, unlike metals, the hardness increases markedly as the deposition temperature rises from 0.3 to 0.5 T_m. The authors attribute this to a more 'perfect' material

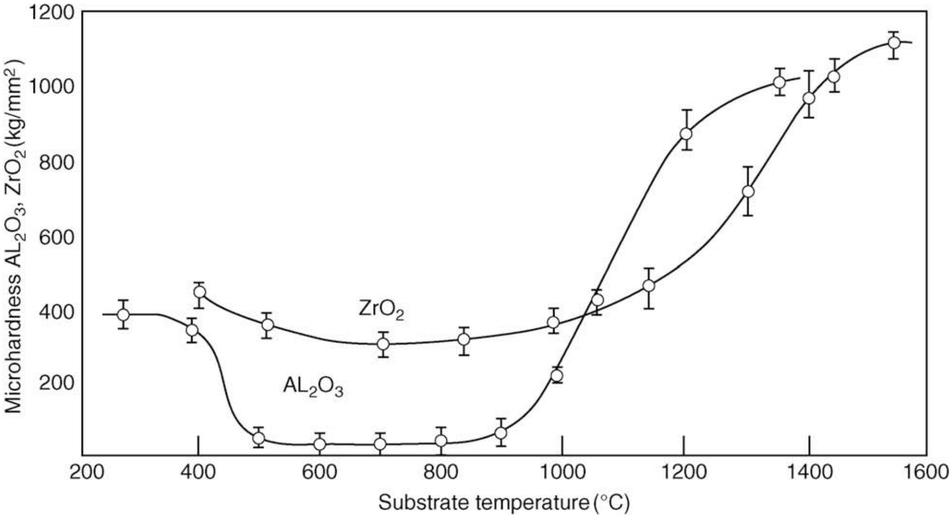

Figure 4.66: Variation of microhardness with deposition temperature for Al_2O_3 and ZrO_2.

produced at the higher deposition temperature due to volume processes of sintering. A similar hardness curve was obtained for Y_2O_3 deposits [136].

Figure 4.67, from the work of Raghuram and Bunshah [206], also shows a very marked increase in microhardness of TiC deposits on going from 0.15 T_m (500 °C) to 0.3 T_m

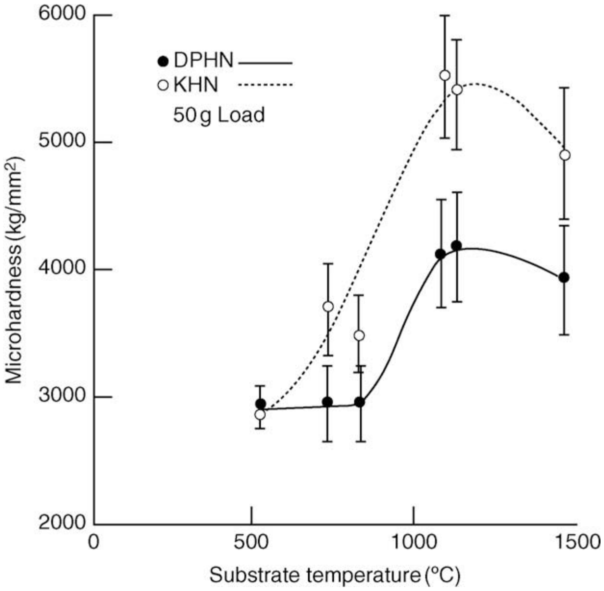

Figure 4.67: Variation of microhardness with deposition temperature for TiC.

(1000 °C). The hardness increases for the oxides and TiC with increasing deposition temperature. Both sets of results may be explained by the following concept. Since the strength of ceramics is very adversely effected by growth defects and at the higher deposition temperature the occurrence of these defects is markedly reduced, the hardness (or strength) increased very significantly. However, it should be noted that the absolute value of the hardness of the oxides is much lower than that of the carbides. Thus the possibility of a different explanation for the 'similar' behavior of these materials, i.e. the hardness increase with the deposition temperature, needs to be investigated.

The hardness data on sputtered TiC and TiN coatings are quite similar to those produced by evaporation techniques [272].

4.11.2 Magnetic Properties

Magnetic nanoparticles prepared by IGC have attracted a lot of attention because it is a relatively simple preparation method compared to other synthesis techniques. Various metals, e.g. Fe and Mn, are reportedly evaporated by IGC [49, 273]. The particle size effect on the exchange bias field for Fe/Fe oxide core/shell structure nanoparticles prepared by IGC was investigated by Ceylan et al. [49]. The hysteresis curves for particles with different sizes recorded at 5 K after cooling in 2 T field are shown in Figure 4.68. The effect on the magnetic properties such as exchange bias and vertical shift is reported to correlate strongly with structural disorder at the surface of the nanoparticles.

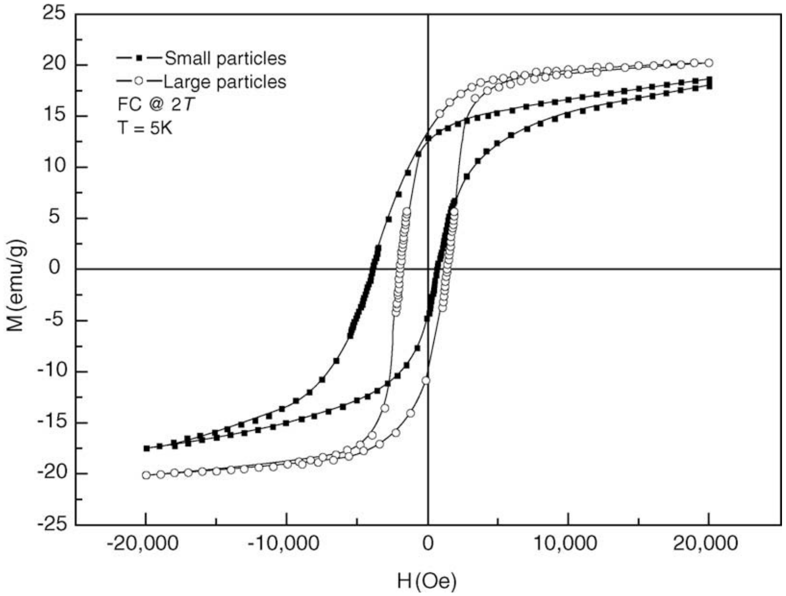

Figure 4.68: Field cooled hysteresis loops for small and large particles at 5 K.

Ceylan et al. further reported that two techniques, namely IGC and laser ablation, can be combined to prepare core–shell structure by evaporating Ni using IGC particles and in situ coating of Co using laser ablation [76]. The structural and magnetic analyses of the Ni/NiO/Co_3O_4 structure showed that these particles had layered core–shell structure and had improved magnetic properties, such as increased exchange bias due to increased anisotropy of NiO via interlayer coupling between the NiO and Co_3O_4 layers.

Ding et al. reported deposition of Co films on the GaAs(001) surface by using an e-beam evaporation method. The magnetization of the films was found to decrease with increasing film thickness. They found that slight degradation of magnetic properties could be attributed to increasing roughness on the Co surface or the Co/GaAs interface during the Co deposition [274]. Furthermore, multilayer Co/Au was prepared by e-beam evaporation, with Au layer thickness ranging 5 to 30 Å and Co layer thickness of 10–40 Å, with a total thickness of 800 Å [275]. Magnetic properties showed strong dependence of remanent magnetization, saturation magnetization, and coercivity on Au layer thickness related to the effect of interlayer magnetic coupling.

Kim et al. reported structural and magnetic properties of bcc $Co_{1-x}Fe_x$ ($0.1 < x < 0.4$) alloy films prepared on MgO (001) substrates using e-beam evaporation and pulsed laser ablation deposition (PLD) methods [276]. They found that for $x \geq 0.3$ at high substrate temperature T_s (500 °C), alloy films deposited by e-beam evaporation exhibit a bcc (001) growth, showing the magnetic anisotropy with easy axis parallel to the MgO (100) crystal axis. In the PLD technique, the excellent bcc (001) film growth is observed at $T_s = 300\,°C$ for $x = 0.25$, which is close to the concentration limit of the bcc regime in the equilibrium bulk phase diagram, whereas the same compound films deposited at high T_s reveal the mixed phase of fcc (001) and bcc (001) structures. Also, magnetic hysteresis measurements of the film grown by the PLD technique exhibit similar results to those of the films deposited by e-beam evaporation [276].

Preparation of thin films by magnetron sputtering is a popular method. However, it has also been shown that it is possible to prepare magnetic nanoparticles with sputtering, as discussed earlier in this chapter (PVD Processes). Qiu et al. reported that the $L1_0$ phase of FePt nanoparticles can be controlled by modifying magnetron sputtering [277]. Also, non-conventional $(FeCo)_{core}Au_{shell}$ and $(FeCo)_{core}Ag_{shell}$ nanoparticles can be prepared by combined sputtering and evaporation technique [278]. $(FeCo)_{core}Au_{shell}$ nanoparticles prepared by this technique showed a three-fold increase in saturation magnetization compared to that of iron oxide and better oxidation resistance than FeCo nanoparticles. Bai et al. used the same technique to prepare $(FeCo)_3Si$–SiO_x core–shell nanoparticles by natural oxidation after preparation of particles [279].

References

[1] M. Faraday, Phil. Trans. 147 (1857) 145.
[2] R. Nahrwold, Ann. Physik. 31 (1887) 467.
[3] A. Kundt, Ann. Physik. 34 (1888) 473.
[4] F. Soddy, Proc. R. Soc. Lond. 78 (1967) 429.
[5] I. Langmeir, J. Am. Chem. Soc. 35 (1913) 931.
[6] R. Glang, in: L.I. Maissel, R. Glang (Eds.), Handbook of Thin Film Technology, McGraw-Hill (1970) 1–7.
[7] L.I. Maissel, R. Glang (Eds.), Handbook of Thin Film Technology, McGraw-Hill (1970).
[8] L. Holland, Vacuum Deposition of Thin Films, Chapman & Hall (1956).
[9] B.N. Chapman, J.C. Anderson (Eds.), Science and Technology of Surface Coatings, Academic Press (1974).
[10] J.A. Allen, Rev. Pure Appl. Chem. 4 (1954) 133.
[11] G.A. Bassett, D.W. Pashley, J. Inst. Metals 87 (1958) 449.
[12] R.W. Hoffman, Thin Films, American Society for Metals (1964) 99.
[13] R.W. Hoffman, Physics of Thin Films, Vol. 3, Academic Press, New York (1966) 246.
[14] W. Buckel, J. Vac. Sci. Technol. 6 (1969) 606.
[15] W. Kinosita, Thin Solid Films 12 (1972) 17.
[16] R.F. Bunshah, Conf. No. 170, Oak Ridge National Laboratory, Physical Metallurgy of Beryllium, April (1963).
[17] R.F. Bunshah, Materials Science and Technology for Advanced Applications, Vol. 2, American Society for Metals (1964) 31.
[18] R.F. Bunshah, Metals Eng. Q. (November 1964) 8.
[19] R.F. Bunshah, R.S. Juntz, Beryllium Technology, Vol. 1, Gordon and Breach (1966).
[20] R.F. Bunshah, Press Universitaires de France, Grenoble, Proc. Int. Conf. on Beryllium (1965) 63.
[21] R.F. Bunshah, R.S. Juntz, Trans. Vacuum Metallurgy Conf., American Vacuum Society (1966) 209.
[22] R.F. Bunshah, R.S. Juntz, Trans. Vacuum Metallurgy Conf., American Vacuum Society (1965) 200.
[23] H.R. Smith, Materials Science and Technology for Advanced Applications, Vol. 2, American Society for Metals (1964) 569.
[24] H.F. Smith Jr., C.D'A. Hunt, Trans Vacuum Metallurgy Conf., American Vacuum Society (1964) 227.
[25] R.F. Meyers, R.P. Morgan, Trans. Vacuum Metallurgy Conf., American Vacuum Society (1966) 271.
[26] J.F. Butler, J. Vac. Sci. Technol. 7 (1970) S–52.
[27] H.R. Smith Jr., K. Kennedy, F.S. Boericke, J. Vac. Sci. Technol. 7 (1970) S48.
[28] A.B. Sauvegot, TMCA Tech. Report AFML-TR-67 (1967) 386.
[29] R.F. Bunshah, J. Vac. Sci. Technol. 11 (1974) 633.
[30] R.F. Bunshah, New Trends in Materials Processing, American Society for Metals (1976) 200.
[31] B.A. Paton, B.A. Movchan, A.V. Demchishin, Iron and Steel Institute of Japan, Proc. 4th Int. Conf. on Vacuum Metallurgy (1973) 251.
[32] J. Schiller, U. Heisig, Evaporation Techniques, Veb Verlag Technik, Berlin (1975) (in German).
[33] E.P. Graper, J. Vac. Sci. Technol. 8 (1971) 333.
[34] J. Vac. Sci. Technol. 10 (1973) 100.
[35] K.D. Kennedy, G.R. Schevermann, H.R. Smith Jr., Res. Dev. Mag. 22 (1971) 40.
[36] H.A. Beale, R.F. Bunshah, Iron and Steel Institute of Japan, Tokyo, Proc. 4th Int. Conf. on Vacuum Metallurgy (June 1973) 238.
[37] C.T. Wan, D.L. Chambers, D.C. Carmichael, Iron and Steel Institute of Japan, Tokyo, Proc. 4th Int. Conf. on Vacuum Metallurgy (June 1973) 231.
[38] G.A. Baum, Report No. RFP-686, Dow Chemical Co., Golden, CO. (February 6, 1967).
[39] J.A. Thornton, SAE Transactions (1973).
[40] Sputtering and Ion Plating, NASA SP-511 (1972).
[41] S. Schiller, G. Jasch, Thin Solid Films 54 (1978) 9.
[42] A.H. Pfund, Phys. Rev. 35 (1930) 1434.

[43] R. Birringer, H. Gleiter, Phys. Lett. 102A (1984) 365.
[44] H. Gleiter, Progress in Mater. Sci. 33 (1989) 223.
[45] C.G. Granqvist, R.A. Buhrman, J. Appl. Phys. 47 (1976) 2200.
[46] A.R. Tholen, Acta Metal. 27 (1979) 1765.
[47] M.M. Flagan, R.C. Lunden, Mater. Sci. Eng. A 204 (1995) 113.
[48] S. Yatsuya, S. Kasukabe, R. Uyeda, Jpn. J. Appl. Phys. 12 (1973) 1675.
[49] A. Ceylan, C.C. Baker, S.K. Hasanain, S.I. Shah, J. Appl. Phys. 100 (2006) 034301.
[50] M. Raffi, A.K. Rumaiz, M.M. Hasan, S.I. Shah, J. Mater. Res. 22 (2007) 12.
[51] A. Ceylan, K. Jastrzembski, S.I. Shah, Metal. Mater. Trans. A 37 (2006) 2033.
[52] A. Ceylan, S. Ozcan, C. Ni, S.I. Shah, J. Mag. Mag. Mater. 320 (2008) 857.
[53] M.B. Ward, R. Brydson, R.F. Cochrane, J. Phys. Conf. Ser. 26 (2006) 296.
[54] D.B. Chrisey, G.K. Hubler, Pulsed Laser Deposition of Thin Films, John Wiley & Sons, New York (1994).
[55] H.M. Smith, A.F. Turner, Appl. Opt. 4 (1965) 147.
[56] D. Bauerle, Laser Processing and Chemistry, 3rd ed., Springer, Berlin (2000).
[57] A.K. Rumaiz, B. Ali, A. Ceylan, M. Boggs, T. Beebe, S.I. Shah, Solid State Commun. 144 (2007) 334.
[58] S. Otsubo, T. Maeda, T. Minamikawa, Y. Yonezawa, A. Morimoto, T. Shimizu, Jpn. J. Appl. Phys. 29 (1990) L133.
[59] H. Kidoh, A. Morimoto, T. Shimizu, Appl. Phys. Lett. 59 (1991) 237.
[60] Y. Tsuboi, M. Goto, A. Itaya, J. Appl. Phys. 85 (1999) 4189.
[61] Y. Tsuboi, A. Itaya, Chem. Lett. 27 (1998) 521.
[62] D.H. Lowndes, in: J.C. Miller, R.F. Haglund (Eds.), Experimental Methods in the Physical Sciences, Vol. 30, Academic Press, New York (1998) 475.
[63] E. Agostinelli, S. Kaciulis, M. Vittori-Antisari, Appl. Surf. Sci. 156 (2000) 143.
[64] Y. Zhang, H. Gu, S. Iijima, Appl. Phys. Lett. 73 (1998) 3827.
[65] D.B. Geohegan, A.A. Puretzky, D.J. Rader, Appl. Phys. Lett. 74 (1999) 3788.
[66] T.J. Goodwin, V.J. Leppert, S.H. Risbud, I.M. Kennedy, H.W.H. Lee, Appl. Phys. Lett. 70 (1997) 3122.
[67] L.D. Wang, H.S. Kwok, Thin Solid Films 363 (2000) 58.
[68] B. Holzapfel, B. Roas, L. Schultz, P. Bauer, G. Saemannischenko, Appl. Phys. Lett. 61 (1992) 3178.
[69] G. Bricen, H. Chang, X. Sun, P.G. Schultz, X.D. Xiang, Science 270 (1995) 273.
[70] X.D. Wu, D. Dijkkamp, S.B. Olgale, A. Ina, E.W. Chase, P.F. Miceli et al., Appl. Phys. Lett. 51 (1987) 861.
[71] M.V. Allmen, A. Blatter, Laser-Beam Interactions with Materials, Springer, Berlin (1995).
[72] J.A. Greer, J. Vac. Sci. Technol. 10 (1992) 1821.
[73] J.M. Qiu, J.-P. Wang, Appl. Phys. Lett. 88 (2006) 192505.
[74] J. Bai, Y.-H. Xu, J. Thomas, J.-P. Wang, Nanotechnology 18 (2007) 065701.
[75] J. Bai, J.-P. Wang, Appl. Phys. Lett. 87 (2005) 152502.
[76] A. Ceylan, A.K. Rumaiz, S.I. Shah, J. Appl. Phys. 101 (2007) 094302.
[77] H. Hertz, Ann. Physik. 17 (1882) 177.
[78] M. Knudsen, Ann. Physik. 47 (1915) 697.
[79] H.R. Smith, Society of Vacuum Coaters, Detroit, MI, Proc. 12th Ann. Tech. Conf. (1969) 50–54.
[80] T.C. Riley, The Structure and Mechanical Properties of Physical Vapor Deposited Chromium, PhD Thesis, Stanford University (November 1974).
[81] R.F. Bunshah, R.S. Juntz, Trans. Vacuum Metallurgy Conf., American Vacuum Society (1967) 799.
[82] R. Chow, R.F. Bunshah, J. Vac. Sci. Technol. 8 (1971) VM 73.
[83] R. Nimmagadda, R.F. Bunshah, J. Vac. Sci. Technol. 8 (1971) VM 85.
[84] J. Szekely, J.J. Poveromo, Met. Trans. 5 (1974) 289.
[85] K. Okuyama, Y. Kousaka, N. Tohge, S. Yamamoto, J.J. Wu, R.C. Flagan, J.H. Seinfeld, AIChE J. 32 (1986) 2010.
[86] R.C. Flagan, M.M. Lunden, Mater. Sci. Eng. A 204 (1995) ll3.
[87] S.L. Girshick, C.P. Chiu, P.H. McMurry, Plasma Chem. Plasma Process 8 (1989) 145.
[88] E. Werwa, A.A. Seraphin, L.A. Chiu, C.X. Chou, K.D. Kohlebrander, Appl. Phys. Lett. 64 (1994) 1821.

[89] W.A. Saunders, P.C. Sercel, R.B. Lee, H.A. Atwater, K.J. Vahala, R.C. Flagan, Appl. Phys. Lett. 63 (1993) 1549.
[90] D.L. Olynick, J.M. Gibson, R.S. Averback, Phil. R. Soc. Mag. A 77 (1998) 1205.
[91] S. Stappert, B. Rellinghausa, M. Acet, F. Wassermann, Eur. Phys. J. D 24 (2003) 351.
[92] A. Simchi, R. Ahmadi, S.M.S. Reihani, A. Mahdavi, Mater. Des. 28 (2007) 850.
[93] M. Raffi, A.K. Rumaiz, M.M. Hasan, S.I. Shah, J. Mater. Res 22 (2007) 3378.
[94] H.R. Smith, C.D'A. Hunt, Trans. Vacuum Metallurgy. Conf., American Vacuum Society (1965) 227.
[95] M.A. Cocca, L.H. Stauffer, Trans. Vacuum Metallurgy Conf., American Vacuum Society (1963) 203.
[96] J.R. Morley, Trans. Vacuum Metallurgy Conf., American Vacuum Society (1963) 186.
[97] B. Berghaus, German Patent 683,414 (1939).
[98] L.P. Sabalev, et al., US Patents 3,783,231 (January 1, 1974); 3,793,179 (February 19, 1974).
[99] A.M. Dorodnov, Soviet Phys. Tech. Phys. 23 (1978) 1058.
[100] V.A. Osipov et al., Soviet Rev. Sci. Inst. 21 (1978) 1651.
[101] H. Wroe, Br. J. Appl. Phys. 9 (1958) 488–491.
[102] A.S. Gilmour Jr., D.L. Lockwood, Proc. IEEE 60(8) (1972) 977–991.
[103] A.A. Snaper, Arc Deposition and Apparatus, US Patent 3,625,848 (1971).
[104] A.A Snaper, Arc Deposition and Apparatus, US Patent 3,836,451 (1974).
[105] L.P. Sablev, Apparatus for Vacuum Evaporation of Metals under the Action of an Electric Arc, US Patent 3,783,231 (1974).
[106] L.P. Sablev, Apparatus for Metal Evaporation Coating, US Patent 3,793,179 (1974).
[107] D.M. Sanders, in: S. Rosnagel, J.J. Cuomo, W.D. Westwood (Eds.), Handbook of Plasma Processing Technology, Noyes Publications (1990) 419.
[108] P.J. Martin et al., Thin Solid Films 153 (1987) 91.
[109] P.J. Martin, R.P. Netterfield, T.J. Kinder, Thin Solid Films 193/194 (1990) 77.
[110] A.I. Vasin, A.M. Dorodnov et al., Sov. Tech. Phys, Lett. (Engl. Trans. of Pis'ma Zh. T Fiz.) 5(23–24) (1979).
[111] H. Ehrich, B. Hasse et al., Essen University, Proc. 8th Int. Conf. Discharge Appl. (1985) 591–592, 596.
[112] A.M. Dorodnov, A.N. Kunetsov et al., Sov. Tech. Phys. Lett. (Engl. Trans. of Pis'ma Zh. T Fiz.) 5(418–419) (1979).
[113] H. Ehrich, J. Vac. Sci. Technol. A6 (1988) 134–138.
[114] S. Meassick, C. Chan, R. Allen, Thin Film Deposition Techniques using the Anodic Arc, Surface & Coating Technology 54(1–3) (1992) 343–348.
[115] Lu, Thin Solid Films 45 (1977) 487.
[116] J.R. Nicholls, K.J. Lawson, L.H. Al Yasiri, P. Hancock, Corrosion Sci. 35(5–8) (1993) 1209–1223.
[117] R. Nimmagadda, A.C. Raghuram, R.F. Bunshah, J. Vac. Sci. Technol. 9 (1972) 1406.
[118] T. Santala, M. Adams, J. Vac. Sci. Technol. 7 (1970) s22.
[119] T. Suzuki, M. Kishima, W. Jiang, K. Yatsui, Jpn. J. Appl. Phys. 40 (2001) 1042.
[120] Y.F. Shevakin, L.D. Kharitonova, L.M. Ostrovskaya, Thin Solid Films 62 (1979) 337.
[121] S.J. Lida, Appl. Phys. 65 (1989) 2.
[122] M. Oszwaldowskia, T. Berus, A. Borowska, M. Nowicki, A. Richter, K. Sangwal, J. Crystal Growth 265 (2004) 83.
[123] B.A. Movchan, A.V. Demchishin, Fizika Metall. 28 (1969) 653.
[124] M. Auwarter, US Patent 2,920,002 (1960).
[125] R.F. Bunshah, A.C. Raghuram, J. Vac. Sci. Technol. 9 (1972) 1385.
[126] A. Alberdi, M. Marin, B. Diaz, O. Sanchez, R.E. Galindo, Vacuum 81 (2007) 1453.
[127] C.-L. Chang, C.-T. Lin, P.-C. Tsai, W.-Y. Ho, D.-Y. Wang, Thin Solid Films 516 (2008) 5324.
[128] D. Hoffman, D. Liebowitz, J. Vac. Sci. Technol. 9 (1972) 326.
[129] R.F. Bunshah, R. Nimmagadda, W. Dunford, B.A. Movchan, A.V. Demchishin, N.A. Chursanov, Thin Solid Films 54 (1978) 85.
[130] T. Abe, K. Inngawa, R. Obusa, Y. Murakami, Julich, Proc. 12th Symp. on Fusion Technology (1982).
[131] R.F. Bunshah, US Patent 3,791,852 (1972).

[132] R.F. Bunshah, C. Deshpandey, in: J.L. Vossen, M.H. Francombe (Eds.), Physics of Thin Films, Academic Press, New York (1987) 60.
[133] R.F. Bunshah, A.C. Raghuram, J. Vac. Sci. Technol. 9 (1972) 1385.
[134] D.D. Hass, J.F. Groves, H.N.G. Wadley, Surf. Coat. Technol. 146–147 (2001) 85.
[135] R.F. Bunshah, Thin Solid Films 107 (1983) 21.
[136] M. Colen, R.F. Bunshah, J. Vac. Sci. Technol. 13 (1976) 536.
[137] R.F. Bunshah, A.C. Raghuram, J. Vac. Sci. Technol. 9 (1972) 1389.
[138] P. Nath, R.F. Bunshah, Thin Solid Films 69 (1980) 63.
[139] K.K. Yee, Proc. 5th Int. Conf. Chemical Vapor Deposition (1975) 238.
[140] Y.H.C. Cha, P.G. Kim, H.J. Doerr, R.F. Bunshah, Surf. Coat. Technol. 90 (1997) 35.
[141] W. Grossklaus, R.F. Bunshah, J. Vac. Technol. 12 (1975) 593.
[142] J. Granier, J. Besson, Proc. Plansee. Semin. 9 (1977).
[143] H. Yoshihara, M. Mori, J. Vac. Sci. Technol. 16 (1979) 1007.
[144] T. Fujii, N. Sakata, J. Takada, Y. Miura, Y. Daitoh, M. Takano, J. Mater. Res. 9 (1994) 6.
[145] K. Nakamura, K. Inagawa, K. Tsuroka, T. Narasawa, Thin Solid Films 40 (1977) 155.
[146] S. Prakash, K. Chou, G. Potwln, C.V. Deshpandey, H.J. Doerr, R.F. Bunshah, Supercond. Sci. Technol. 3 (1990) 543.
[147] S. Komiya, N. Unezu, T. Narasawa, Thin Solid Films 54 (1978) 51.
[148] B. Zega, M. Korrmann, J. Amiquet, Thin Solid Films 54 (1977) 57.
[149] M. Kobayashi, Y. Doi, Thin Solid Films 54 (1978) 57.
[150] A. Ishida, K. Ogawa, T. Kimura, A. Takei, Metall. Protect. Layers 191 (2000) 69.
[151] A. Matthews, D.G. Teer, Thin Solid Films 80 (1981) 41.
[152] Y. Murayama, J. Vac. Sci. Technol. 12 (1975) 818.
[153] A.M. Dorodnov, Sov. Phys. Tech. Phys. 40 (1977) 211.
[154] N.M. Mustaph, R.P. Howson, Vacuum 60 (2001) 361.
[155] R.J. Westerwaal, C.P. Broedersz, R. Gremaud, M. Slaman, A. Borgschulte, W. Lohstroh et al., Thin Solid Films 516 (2008) 4351.
[156] R.F. Bunshah, K.L. Chopra, C. Deshpandey, V.D. Vankar, US Patent 4,714,625 (1987).
[157] A. Inam, M.S. Hegde, X.C. Wu, T. Venkatesan, D. England, P.F. Miceli et al., Appl. Phys. Lett. 53(10) (1988) 908.
[158] C.Y. Chen, MS Thesis, Department of Materials Science and Engineering, University of California, Los Angeles (1987).
[159] B.P. O'Brien, MS Thesis, Department of Materials Science and Engineering, University of California, Los Angeles (1987).
[160] D. Zender, C. Deshpandey, B. Dunn, R.F. Bunshah, in: J.B. Boyle, L.C. DeJognhe, R.A. Huggins (Eds.), Proc. of the Fifth Int. Conf. on Solid Ionics, Part 1, North Holland, Amsterdam (1986) 813.
[161] H. Shin, H.J. Doerr, C. Deshpandey, R.F. Bunshah, B. Dunn, Surf. Coat. Technol. 39/40 (1989) 683.
[162] H. Oeschner, personal communication.
[163] T. Sakai, Y. Kuniyoshi, W. Aoki, S. Ezoe, T. Endo, Y. Hoshi, Thin Solid Films 516 (2008) 5860.
[164] C. Deshpandey, B.P. O'Brien, H.J. Doerr, R.F. Bunshah, Surf. Coat. Technol. 33 (1987) 1.
[165] P. Lin, C. Deshpandey, H.J. Doerr, R.F. Bunshah, K.L. Chopra, V.D. Vankar, Thin Solid Films 153 (1987) 487.
[166] J.S. Yoon, C. Deshpandey, H.J. Doerr, R.F. Bunshah, Surf. Coat. Technol. 43/44 (1990) 213.
[167] A. Biswas, Z. Marton, J. Kanzow, J. Kruse, V. Zaporojtchenko, F. Faupel, Nano Lett. 3 (2003) 69.
[168] H. Takele, S. Jebril, T. Strunskus, V. Zaporojchenko, R. Adelung, F. Faupel, Appl. Phys. A 92 (2008) 345.
[169] V. Zaporojtchenko, T. Strunskus, K. Behnke, C.V. Bechtolsheim, A. Thran, F. Faupel, Microelectron. Eng. 50 (2000) 465.
[170] D.W. Pashley, Adv. Phys. 5 (1956) 1973.
[171] I. Petrov, P.B. Barana, L. Hultman, J.E. Greene, J. Vac. Sci. Technol. A 21 (2003) s117.
[172] P.B. Barana, M. Adamik, Thin Solid Films 317 (1998) 27.

[173] D.A. Smith, in: D. Wolf, S. Yip (Eds.), Materials Interfaces, Atomic Level Structure and Properties, Chapman and Hall, London (1992) Chap. 6.
[174] C.V. Thompson, R. Carel, Mater. Sci. Eng. B 32 (1995) 211.
[175] D.W. Paschley, Philos. Mag. 15 (1966) 173.
[176] H. Lewis, Thin Solid Films 7 (1971) 179.
[177] J.F. Pocza, A. Barna, P.B. Barna, J. Vac. Sci. Technol. 6 (1969) 172.
[178] J.F. Pocza, A. Barna, P.B. Barna, I. Pozsgai, G. Radnoczi, Jpn. J. Appl. Phys. 2 (1974) 525.
[179] C. Polop, C. Rosiepen, S. Bleikamp, R. Drese, J. Mayer, A. Dimyati, T. Michely, N. J. Phys. 9 (2007) 74.
[180] F.C. Akkari, M. Kanzari, B. Rezig, Physica E 40 (2008) 2577.
[181] Y. Namba, J. Mori, J. Vac. Sci. Technol. 13 (1976) 693.
[182] N.J. Taylor, Surf. Sci. 4 (1966) 161.
[183] B.A. Movchan, A.V. Demchishin, G.F. Badilienko, Thin Solid Films 40 (1977) 237.
[184] M. Ya Fuks, L.S. Palatnik, V.V. Belozerov, Y.V. Zolotnitsky, S.T. Roschchenko, Fizika Metall. 36 (1973) 316.
[185] M. Sherman, R.F. Bunshah, H.A. Beale, J. Vac. Sci. Technol. 11 (1974) 1128.
[186] A. Van der Drift, Phillips Res. Rep. 22 (1967) 267.
[187] J.A. Thornton, Annu. Rev. Mater. Sci. (1977) 239.
[188] H.-C. Chen, C.-C. Lee, C.-C. Jaing, M.-H. Shiao, C.-J. Lu, F.-S. Shieu, Appl. Opt. 45 (2006) 9.
[189] H.M. Smith, A.F. Turner, Appl. Opt. 4 (1965) 147.
[190] H. Sankur, J. DeNatale, W. Gunning, J.G. Nelson, J. Vac. Sci. Technol. A5 (1987) 2869.
[191] J.T. Cheung, J. Madden, J. Vac. Sci. Technol. B5 (1987) 705.
[192] X.D. Wu, D. Dijkkamp, S.B. Olgale, A. Ina, E.W. Chase, P.F. Miceli et al., Appl. Phys. Lett. 51 (1987) 861.
[193] J.T. Cheung, J.S. Chen, N. Otsuka, Proc. IRIS IR Detector Specialty Meeting, Seattle, WA (August 1987). (This work was followed by several other similar investigations presented at the 34th National Symposium of the American Vacuum Society, Anaheim, CA, November 1987.).
[194] N. Agarwal, N. Kane, R.F. Bunshah, New York, National Vacuum Symposium (1973).
[195] R.F. Bunshah, J. Vac. Sci. Technol. 11 (1974) 814.
[196] R.F. Bunshah, R.S. Juntz, Met. Trans. 4 (1973) 21.
[197] N.G. Semaltianos, E.G. Wilson, Thin Solid Films 366 (2000) 111.
[198] N. Kane, R.F. Bunshah, Iron and Steel Institute of Japan, Tokyo, Proc. of the 4th Int. Conf. on Vacuum Metallurgy (June 1973) 242.
[199] D.L. Chambers, W.K. Bower, J. Vac. Sci. Technol. 7 (1970) S63.
[200] R.F. Bunshah, R.S. Juntz, J. Vac. Sci. Technol. 9 (1972) 404.
[201] G. Mah, C.W. Nordin, Proc. of the 16th Ann. Conf., in: Society of Vacuum Coaters, Chicago, IL (1973) 103.
[202] M. Neirynck, W. Samaey, L. Van Poucke, J. Vac. Sci. Technol. 11 (1974) 647.
[203] K. Kennedy, Trans. of the Vacuum Metallurgy Conf., American Vacuum Society (1968) 195.
[204] R.F. Bunshah, R. Nimmagadda, H.J. Doerr, B.A. Movchan, N.I. Grechanuk, E.V. Dabizha, Thin Solid Films 72 (1980) 261.
[205] B.A. Movchan, A.V. Demchishin, L.V. Kooluck, J. Vac. Sci. Technol. 11 (1974) 640.
[206] A.C. Raghuram, R.F. Bunshah, J. Vac. Sci. Technol. 9 (1972) 1389.
[207] Y. Xu, C.H. Lei, B. Ma, H. Evans, H. Efstathiadis, M. Rane et al., Supercond. Sci. Technol. 19 (2006) 835.
[208] D.M. Mattox, G.J. Kominiak, J. Vac. Sci. Technol. 9 (1972) 528.
[209] J. Morley, H.R. Smith, J. Vac. Sci. Technol. 9 (1972) 1377.
[210] G. Mah, P.S. McLeod, D.G. Williams, J. Vac. Sci. Technol. 11 (1974) 663.
[211] W.R. Stowell, D. Chambers, J. Vac. Sci. Technol. 11 (1974) 653.
[212] R.D. Bland, G.J. Kominiak, D.M. Mattox, J. Vac. Sci. Technol. 11 (1974) 671.
[213] R.F. Bunshah, unpublished research.
[214] C.F. Turk, H.L. Marcus, Trans. AIME 242 (1968) 2251.
[215] H.A. Beale, R.F. Bunshah, unpublished research.
[216] L. Karlsson, L. Hultman, J.-E. Sundgren, Thin Solid Films 371 (2000) 167–177.

[217] J.A. Thornton, New Industries and Applications for Advanced Materials Technology, Vol. 19, SAMPE (1974) 443.
[218] D.H. Boone, T.E. Strangman, L.W. Wilson, J. Vac. Sci. Technol. 11 (1974) 641.
[219] R.C. Krutenat, J. Vac. Sci. Technol. 11 (1974) 1123.
[220] W. Grossklaus, N.E. Ulion, H.A. Beale, Thin Solid Films 40 (1977) 271.
[221] D.E. Wolfe, J. Singh, K. Narasimhan, Surf. Coat. Technol. 160 (2002) 206.
[222] J.W. Beams, J.B. Breazeale, W.L. Bart, Phys. Rev. 100 (1955) 1657.
[223] J.W. Beams, Structure and Properties of Thin Films, Wiley, New York (1959) 183.
[224] A. Catlin, W.P. Walker, J. Appl. Phys. 31 (1960) 2135.
[225] S. Jovanovic, C.S. Smith, J. Appl. Phys. 32 (1961) 121.
[226] P.I. Krukover, V.A. Buravikhin, Fizika Metall. 22 (1966) 144.
[227] D.G. Brandon, Z. Bauer, Israel J. Technol. 8 (1970) 247.
[228] D.M. Marsh, J. Sci. Instrum. 38 (1961) 229.
[229] C.A. Neugebauer, J. Appl. Phys. 31 (1960) 1096.
[230] C. D'Antonio, J. Hirschorn, L. Tarshis, Trans. AIME 227 (1964) 1346.
[231] J.M. Blakely, J. Appl. Phys. 36 (1964) 1756.
[232] H.G.F. Wilsdorf, Rev. Sci. Instrum. 29 (1958) 323.
[233] D.W. Pashley, Proc. R. Soc. Lond. A225 (1960) 218.
[234] R.W. Hoffman, Thin Films, American Society for Metals (1964) 99.
[235] R.W. Hoffman, Physics of Thin Films, Vol. 3, Academic Press, New York (1966) 246.
[236] J.W. Menter, D.W. Pashley, Structures and Properties of Thin Films, Wiley, New York (1959) 111.
[237] F.V. Hunt, in: D.E. Gray (ed.), AIP Handbook, McGraw-Hill Book Company, Inc., New York (1957) 3–33.
[238] D.R. Lide (ed.), CRC Handbook of Chemistry and Physics, 89th edition, CRC Press/Taylor and Francis (2009).
[239] C.A. Neugebauer, in: G. Hass, E. Thun (Eds.), Physics of Thin Films, Vol. 2, Academic Press, New York (1964).
[240] L.S. Palatnik, A.I. Ill'inski, G.V. Federov, V.S. D'yachenko, VUZ Izvestra, Fizika (Soviet Physica Journal) 1 (1966) 122.
[241] R.L. Grunes, C. D'Antonio, F.K. Kies, J. Appl. Phys. 36 (1965) 2735.
[242] M. Ya Fuks, V.V. Belozerov, Y.F. Boyko, Fizika Metall. 33 (1972) 571.
[243] K. Kinosita, K. Maki, K. Nakamizo, K. Takenchi, Jpn. J. Appl. Phys. 6 (1967) 42.
[244] M. Ya Fuks, V.V. Velozero, Y.F. Boyko, Fizika Metall. 33 (1972) 571.
[245] F.A. Doljack, R.W. Hoffman, Thin Solid Films 12 (1972) 71.
[246] B.Y. Pines, N.S. Tan, Fizika Metall. 19 (1965) 899.
[247] I.T. Aleksanyan, Fizika Metall. 25 (1968) 947.
[248] R.W. Hoffman, Thin Solid Films 34 (1976) 185.
[249] E.O. Hall, Proc. Phys. Soc. Lond. B 64 (1951) 747.
[250] N.J. Petch, J. Iron Steel Inst. 174 (1951) 25.
[251] J. Vac. Sci. Technol. 12(2) (1975) 662.
[252] M. Nenioto, R. Jumbou, H. Suto, Trans. Jpn. Inst. Met. 12 (1971) 113.
[253] D.L. Chambers, W.K. Bower, J. Vac. Sci. Technol. 7 (1970) S62.
[254] B.A. Movchan, A.V. Demchishin, L.D. Kooluck, Thin Solid Films 44 (1977) 285.
[255] K.S. Majumder, Thin Solid Films 42 (1977) 327.
[256] B.E. Jacobson, J.R. Springarn, W.D. Nux, Thin Solid Films 45 (1977) 517.
[257] K.S. Majumder, Thin Solid Films 42 (1977) 343.
[258] N.F. Mott, Phil. Mag. 44 (1953) 742.
[259] B.A. Movchan, Soviet Phys. Dokl. 20(7) (1975) 575.
[260] B.A. Movchan, G.F. Badilenko, A.V. Demchishin, Thin Solid Films 63 (1979) 67.
[261] J.S. Koehler, Phys. Rev. B 2 (1970) 547.

[262] M.J. Hordon, in: R.I. Jaffee, H.M. Burte (Eds.), Titanium Science and Technology, Vol. 4, Plenum Press (1973) 2347–2357.
[263] C.A.O. Henning, F.W. Boswell, J.M. Corbett, Acta. Met. 23 (1975) 193.
[264] L.S. Palatnik, A.I. Ill'inski, Soviet Phys. Dokl. 9(1) (1961) 93.
[265] L.S. Palatnik, A.I. Ill'inski, N.P. Sapelin, Soviet Phys. Solid State 8(8) (1967) 2016.
[266] L.S. Palatnik, A.I. Ill'inski, N.M. Biletchenko, R.I. Sinel'nikova, Fizika Met. Metalloved. 32(6) (1971) 1312.
[267] I.I. Solonovich, V.I. Startsev, Problemy Prochnosti 1 (1973) 28–30.
[268] M.J. Hordon, M.A. Wright, in: Metal-Matrix Composites, Symposium of the Metallurgical Society, AIME, DMIC Memorandum 243 (1969) 10–12.
[269] R.W. Springer, D.S. Catlett, Thin Solid Films 54 (1978) 197.
[270] S.L. Lehoczky, J. Appl. Phys. 49 (1978) 5479.
[271] F.C. Frank, B.R. Lawn, Proc. R. Soc. Lond. A 229 (1967) 291.
[272] G. Mah, C.W. Norden, J.F. Fuller, J. Vac. Sci. Technol. 11 (1974) 371.
[273] M.B. Ward, R. Brydson, R.F. Cochrane, J. Phys. Conf. Ser. 26 (2006) 296.
[274] Z. Ding, P.M. Thibado, C. Awo-Affouda, V.P. LaBella, J. Vac. Sci. Technol. B 22(4) (2004) 2068.
[275] P. Chubing, D. Daosheng, F. Ruiyi, PRB 46 (1992) 18.
[276] T.H. Kim, Y.H. Jeong, J.-S. Kang, J. Appl. Phys. 81(8) (1997) 4764.
[277] J.M. Qiu, J.P. Wang, APL 88 (2006) 192505.
[278] J. Bai, J.P. Wang, APL 87 (2005) 152502.
[279] J. Bai, Y.H. Xu, J. Thomas, J.P. Wang, Nanotechnology 18 (2007) 065701.

Further Reading

Books

J.C. Andrews (Ed.), The Use of Thin Films in Physical Investigation, Academic Press (1966).
R.W. Berry, P.M. Hall, M.T. Harris, Thin Film Technology, D. Van Nostrand Co. (1968).
R.F. Bunshah (Ed.), Techniques of Metals Research, Vol. 1, John Wiley & Sons (1968) Part 3.
B. Bhushan, B.K. Gupta, Handbook of Tribology, McGraw-Hill (1992).
B.N. Chapman, J.C. Anderson (Eds.), Science and Technology of Surface Coatings, Academic Press (1974).
K.L. Chopra, Thin Film Phenomena, McGraw-Hill Book Co. (1969).
D.A. Glocker, S.I. Shah (eds.), Handbook of Thin Film Process Technology (1998).
L. Holland, Vacuum Deposition of Thin Films, Chapman and Hall (1968).
L.I. Maissel, R. Glang (Eds.), Handbook of Thin Film Technology, McGraw-Hill Book Co. (1970).
D.M. Mattox, Handbook of Physical Vapor Deposition (PVD), (Materials Science and Process Technology Series), Society of Vacuum Coaters (1998).
M. Ohring, Materials Science of Thin Films, Academic Press (1992).
Physics of Thin Films, Vols 1-6, Academic Press (1963–1971).
D.L. Smith, Thin-Film Deposition: Principles and Practice, Noyes Publications (1995).
R. Glover (ed.), Thin Films, American Society for Metals (1964).

CHAPTER 5

Sputter Deposition Processes

D. Depla[1], **S. Mahieu**[1] **and J.E. Greene**[2]
[1] *Department of Solid State Sciences, Ghent University, Belgium*
[2] *Materials Science and Physics Departments and the Frederick Seitz Materials Research Laboratory, University of Illinois, Urbana, Illinois, USA*

Summary

Sputter deposition is a widely used technique to deposit thin films on substrates. The technique is based on ion bombardment of a source material, the target. Ion bombardment results in a vapor due to a purely physical process, i.e. the sputtering of the target material. Hence, this technique is part of the class of physical vapor deposition techniques, which includes thermal

evaporation and pulsed laser deposition. The most common approach for growing thin films by sputter deposition is the use of a magnetron source in which positive ions present in the plasma of a magnetically enhanced glow discharge bombard the target. This popular technique forms the focus of this chapter. The target can be powered in different ways, ranging from direct current (DC) for conductive targets to radio frequency (RF) for non-conductive targets, to a variety of different ways of applying current and/or voltage pulses to the target. Since sputtering is a purely physical process, adding chemistry to, for example, deposit a compound layer must be done ad hoc through the addition of a reactive gas to the plasma, i.e. reactive sputtering. The undesirable reaction of the reactive gas with the target material results in a non-linear behavior of the deposition parameters as a function of the reactive gas flow. To model this behavior, the fluxes of the various species toward the target must be determined. However, equally important are the fluxes of species incident at the substrate because they not only influence the reactive sputter deposition process, but also control the growth of the desired film. Indeed, the microstructure of magnetron sputter-deposited films is defined by the identity of the particles arriving at the substrate, their fluxes, and the energy per particle.

5.1 Introduction: How Popular is Sputter Deposition?

One way to compare sputter deposition with other deposition techniques is to count the relative number of scientific publications and patents published each year for each deposition technique. In order to provide a baseline for the rate of increase in publications in general, we first determine the number of publications per year that refer to the combination of keywords *'gold' OR 'silver' OR 'copper'* on the Web of Sciences [1]. Similarly, a baseline for published patents is easily found by counting the number of patents published annually by entering the search term '*the*' in the Delphion Database [2]. Figure 5.1(a) is plot of the relative number of scientific papers per year per deposition technique. Figure 5.1(b) provides the same information for patents. For the different physical vapor deposition (PVD) techniques, magnetron sputtering is clearly used extensively in the scientific community, and competes with pulsed laser deposition (PLD) as the most important deposition technique. From the search in the patent database, it can be concluded that sputter deposition is still the most popular technique.

Hence, a chapter on sputter deposition in a book about thin films is quite relevant since this technique is applied in both research laboratories and industrial plants to deposit a wide variety of materials. In this chapter, we focus on key aspects of sputter deposition. Describing the physics behind the sputter process, i.e. the interaction between the ion and the target, is a first priority. However, since many review articles are available [3–9], only the essential points are discussed here. Then, a basic system design is described. It should be noted that in this chapter we exclude ion beam sources, which have been well reviewed in the literature [10], owing to

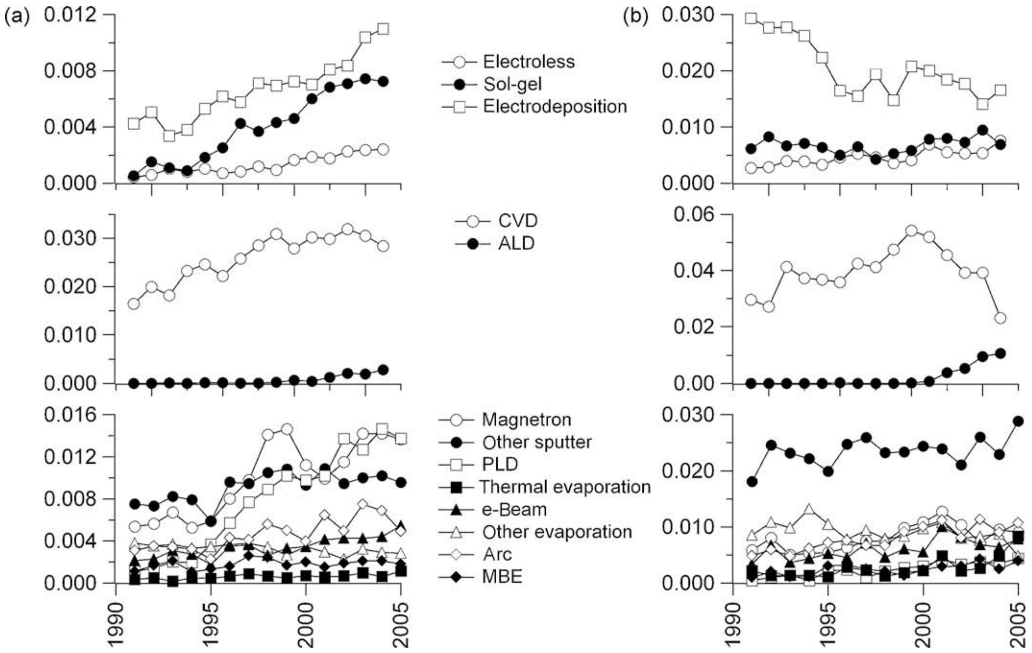

Figure 5.1: (a) (left): Normalized number of publications per year per deposition technique based on data from the Web of Science. (b) (right) Normalized number of publications per year per deposition technique based on data from Delphion.

limitations associated with scalability and power supply options. In the following sections several discharge sputter deposition configurations are discussed.

Sputter deposition is also used to deposit compound films by adding a reactive gas to the discharge. This, however, greatly increases the complexity of the deposition process, and explains the ongoing interest in academia to investigate this technique of which several aspects are not completely understood.

Sputtered target atoms are ejected with substantial kinetic energy, of the order of or larger than bond energies, and hence can significantly affect film growth kinetics and microstructure. Thus, energy loss mechanisms during transport in the gas phase are important. The chapter ends with a discussion of the typical microstructure of sputter-deposited coatings.

5.2 What is Sputtering?

Sputtering is the ejection of atoms by the bombardment of a solid or liquid target by energetic particles, mostly ions. It results from collisions between the incident energetic particles, and/or resultant recoil atoms, with surface atoms. A measure of the removal rate of surface atoms is

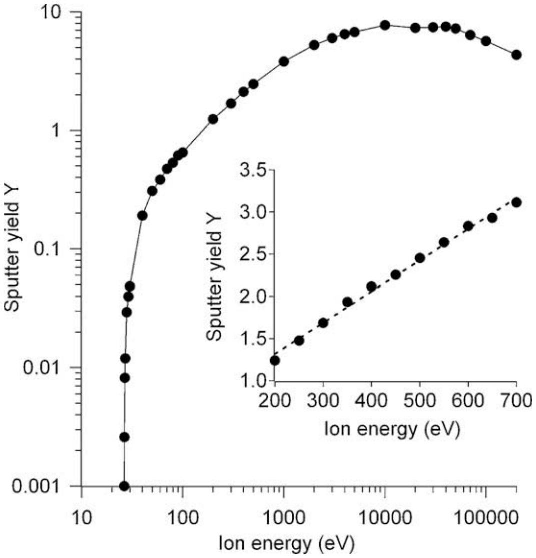

Figure 5.2: Sputtering yield *Y* of Cu as a function of the energy of Ar^+ at normal incidence as calculated using the SRIM code. Note that $Y(E_{Ar^+})$ is linear over the typical range of operation during magnetron sputtering (E_{Ar^+} = 250–750 eV).

the sputter yield *Y*, defined as the ratio between the number of sputter-ejected atoms and the number of incident projectiles. Excellent review articles on sputtering are available in the literature [3–9], and only the essential features are discussed here.

Based on the large amount of experimental (e.g. [11]) and calculated data as a function of ion and target material, several trends are apparent. For a given ion mass and target, *Y* exhibits a maximum as a function of ion energy as well as a minimum (threshold) energy. An example is shown in Figure 5.2 for Ar^+ bombardment of Cu.

When comparing the sputter yield of target materials bombarded by a given ion at constant energy, one notices a trend related to the position of the element in the periodic table (see Figure 5.3 and the following discussion).

Several authors have derived equations describing the sputter yield as a function of energy and projectile–target combinations. P. Sigmund is the father of these theories. His work ‘Theory of sputtering I. Sputter yield of amorphous and polycrystalline targets’, published in Physical Review [12], is a benchmark in this field. According to the theory of Sigmund, the sputter yield near threshold, i.e. at low ion energy, is given by

$$Y = \frac{3}{4\pi^2}\alpha\frac{4M_1M_2}{(M_1+M_2)^2}\frac{E}{U_s} \tag{5.1}$$

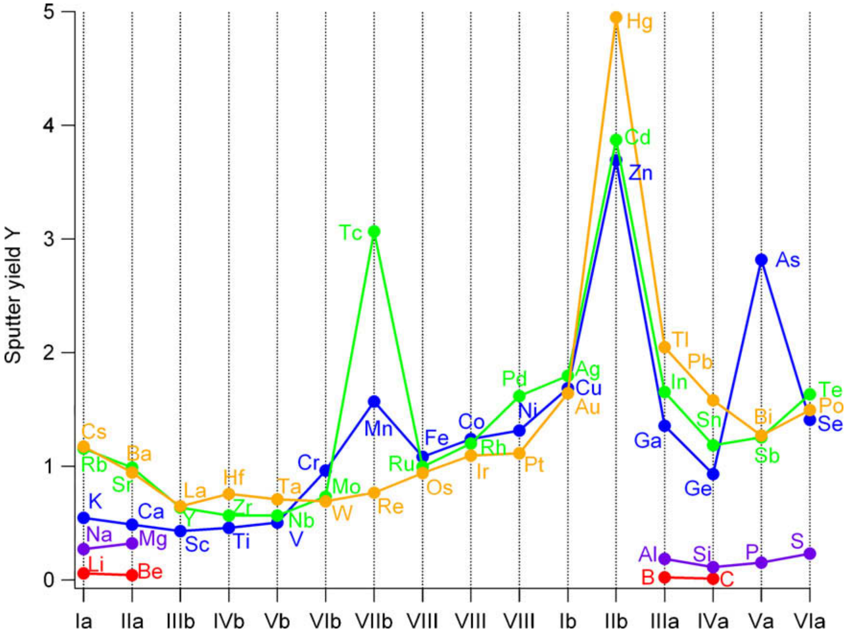

Figure 5.3: Dependence of the sputter yield of several elements (ordered according their position in the periodic table) calculated using SRIM (initial conditions: 300 eV Ar, other input parameters where set at the standard values given by SRIM: lattice binding energy, surface binding energy displacement energy, and normal incidence).

with E the energy of the projectile, and M_1 and M_2 the masses of the projectile and the target atom (in amu). U_s is the surface binding energy and α a dimensionless parameter depending on the mass ratio and the ion energy. At low energy, and mass ratios M_2/M_1 lower than 1, α is of the order of 0.2. This equation can be understood as follows. An incoming ion transfers its momentum to the target atoms which explains the term $4M_1M_2/(M_1+M_2)^2$ with a maximum when $M_1=M_2$. To sputter an atom from the target, momentum transfer from the ion-induced collision must overcome the surface barrier, given by the surface binding energy U_s. Therefore, we can expect an inversely proportional relationship between the yield and the surface binding energy. Based on Eq. (5.1), we can expect that for the energy range of interest for sputter deposition, the sputter yield will vary linearly with the ion energy (see Figure 5.2). The behavior of the sputter yield over the periodic table can also be understood from Eq. (5.1), because the sputter yield is defined by momentum transfer and surface binding energy. However, differences in atomic density among different materials also affect Y through variations in the range (depth) of momentum transfer.

In addition to the theory of Sigmund, heuristic approaches based on semi-empirical equations, and simulations (for an overview on sputter yield simulations, see [13]) are also available.

Table 5.1: Overview of the terms in Yamamura formulae

Symbol	Definition
$Q(Z_2)$	Tabulated dimensionless parameter
α	$0.249(M_2/M_1)^{0.56}+0.0035(M_2/M_1)^{1.5},\ \ M_1\leq M_2$ $0.0875(M_2/M_1)^{-0.15}+0.165(M_2/M_1),\ \ M_1\geq M_2$
E_{th}	$\frac{6.7}{\gamma}U_{\mathrm{s}},\ \ M_1\geq M_2$ $\frac{1+5.7(M_1/M_2)}{\gamma}U_{\mathrm{s}},\ \ M_1\leq M_2$
γ	$\frac{4M_1M_2}{(M_1+M_2)^2}$
Γ	$\frac{W(Z_2)}{1+(M_1/7)^3}$
$W(Z_2)$	Tabulated dimensionless parameter
s	Tabulated dimensionless parameter
k	Linhard electronic stopping coefficient
$S_{\mathrm{n}}(E)$	$\frac{84.78Z_1Z_2}{(Z_1^{2/3}+Z_2^{2/3})^{1/2}}\frac{M_1}{M_1+M_2}s_{\mathrm{n}}^{\mathrm{TF}}(\varepsilon)$
ε	Lindhard–Scharff–Schiott reduced energy
$s_{\mathrm{n}}^{\mathrm{TF}}(\varepsilon)$	Reduced nuclear stopping cross-section

For more details, see [14].

Commonly used semi-empirical formulae for the calculation of the sputter yield were developed by Yamamura et al. [14]. The equations are valid for the bombardment of monoatomic solids by projectiles at normal incident, and the sputter yield $Y(E)$ is given by

$$Y(E)=0.042\frac{Q(Z_2)\alpha(M_1/M_2)}{U_s}\frac{S_n(E)}{1+\Gamma k\varepsilon^{0.3}}\left[1-\sqrt{\frac{E_{th}}{E}}\right]^s \tag{5.2}$$

with E, M_1, M_2, and U_{s} as defined for Eq. (5.1). U_{s}, the surface binding energy, is intimately connected with, and explains the presence of the threshold energy (E_{th}) for sputtering (Table 5.1). The other symbols are defined in Table 5.1.

Although these equations provide a value for the sputter yield Y as a function of ion energy and material choice, they are not instructive in explaining the sputtering process in detail.

Hence, some authors have developed simpler, and more transparent, models of the sputtering process. An excellent example is the work of Mahan et al. [15], in which the sputter yield $Y(E)$ is derived based on the following assumptions. The effective number of recoiling target atoms created per incident ion is multiplied by the probability that the recoil is close enough to the surface to escape and by the probability that the recoils are traveling toward the surface, or

$$Y=\frac{E}{E_{\mathrm{avg}}}\frac{R_{\mathrm{pr}}}{R_{\mathrm{pp}}}\frac{1}{4} \tag{5.3}$$

with E the projectile energy and E_{avg} the average energy of the recoils. The ratio E/E_{avg} gives the average number of recoils. The ratio between the projected range of the recoils R_{pr} and the projected range of the projectile R_{pp} gives the probability that the recoils are close enough to the surface to escape. Finally, the term {1/4} is the average probability that the recoils are moving toward the surface. Using approximations, the average recoil energy and the projected range can be calculated straightforwardly giving insight into the sputtering process. A good example of this is the calculation of the threshold energy. The physics behind the threshold energy is that the recoil atom has insufficient energy to overcome the surface energy barrier U_{s} when its average energy E_{avg} is equal to or lower than the surface barrier energy. The average recoil energy in this simplified model is calculated as

$$E_{\mathrm{avg}} = U_{\mathrm{s}} \ln(\gamma E / U_{\mathrm{s}}) \tag{5.4}$$

and the threshold energy $E = E_{\mathrm{th}}$ is therefore found by substituting U_{s} for E_{avg}, and obtaining $E_{\mathrm{th}} = 2.72\, U_{\mathrm{s}}/\gamma$, which is similar to the formulae proposed by Yamamura et al. (see Table 5.1).

Another approach to obtain a value for the sputter yield is to simulate the overall sputtering process (see [13] for an overview). The most commonly used simulation package is the well-known SRIM code [16] developed by Ziegler et al. and completely described in their book [17]. Figures 5.2 and 5.3 were simulated using this code. All features discussed in the previous paragraphs are present in both figures. SRIM is a static simulation code. That is, it does not account for target changes due to the ion bombardment itself. To account for these changes, Möller et al. developed a dynamic version of SRIM, i.e. TRIDYN [18].

All approaches also provide the angular and energy distribution of the sputtered particles. Thompson [19] showed that within a certain (low) ion energy range, the energy distribution follows the expression

$$\frac{dY}{dE} \propto \frac{E}{(E + U_{\mathrm{s}})^3} \tag{5.5}$$

which is based on the assumption of a planar surface barrier for sputtered particles. This expression gives a peak at $U_{\mathrm{s}}/2$. Falcone [20] estimated the average energy of sputtered particles $\bar{E}$ as

$$\bar{E} = 2U_{\mathrm{s}} \left(\ln \frac{E}{E_{\mathrm{th}}} - \frac{3}{2} \right) \tag{5.6}$$

Substituting reasonable values into Eq. (5.6) shows that the energy of the sputtered particles is at least one order of magnitude higher than the corresponding thermal evaporation energy for

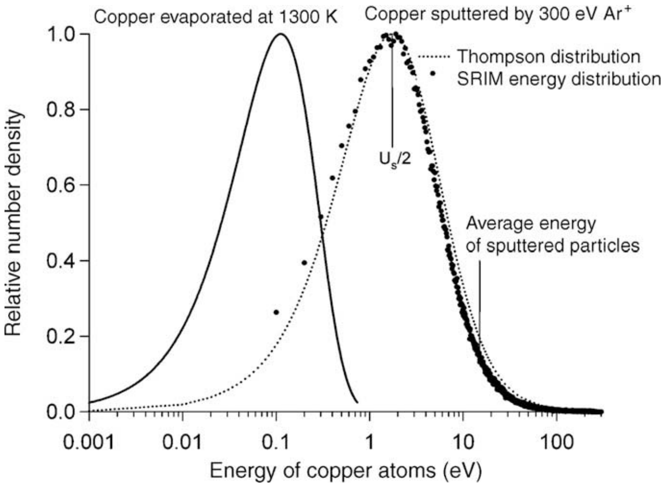

Figure 5.4: Comparison between the thermal energy distribution for copper evaporated at 1300 K and the energy distribution of sputtered copper atoms.

the same particle flux (Figure 5.4). Indeed, at 1000 K the thermal energy is only of the order of 0.1 eV. With a surface binding energy of a few eV (for Cu it is 3.5 eV [17]), the maximum in the energy distribution occurs at 1.8 eV, and using the SRIM calculated threshold energy, the average energy is 15.1 eV. If the pressure during deposition is low enough, the sputtered particles in the gas phase are ballistic and can reach the substrate with few or no collisions in the gas phase.

In all of this work, one important concept is not addressed at all, i.e. the sputter yield of compound materials. The Yamamura formulae can be applied to multicomponent materials such as compounds and alloys using weighted average values for Z_2, M_2, and U_s [13]. Surface binding energies, in particular, are difficult to obtain for oxides and nitrides. For metals, the surface binding energy is generally set equal to the vaporization enthalpy, but this approach is not applicable to oxides, nitrides, sulfides, etc. In the context of the preferential sputtering of oxygen from oxides during depth profiling of oxide thin films for analytical approaches, models have been proposed to estimate a value of the surface binding energy of the metal and the oxygen atoms. Using these values, the modification of the surface composition by ion bombardment is calculated and compared with experimental values. Results typical for this kind of study, including a model for the surface binding energy, are published by Malherbe et al. [21]. Some simulation codes, e.g. TRIDYN, use a different approach [18], where the effective surface binding energies of O and M are chosen to be dependent on the actual surface composition by use of a matrix method. The matrix elements of surface binding energies are $SBV_{O\text{–}O}$, $SBV_{O\text{–}M}$, $SBV_{M\text{–}O}$, and $SBV_{M\text{–}M}$. These elements are evaluated by the formulae

$$\begin{aligned}
&\mathrm{SBV}_{\mathrm{O-O}} = 0 \\
&\mathrm{SBV}_{\mathrm{M-M}} = U_{\mathrm{s,M}} \\
&\mathrm{SBV}_{\mathrm{O-M}} = \frac{1}{2}U_{\mathrm{s,M}} + \frac{n+m}{2nm}\Delta H^{\mathrm{f}} + \frac{n+m}{4n}\Delta H^{\mathrm{diss}}
\end{aligned} \tag{5.7}$$

where n and m depend on the stoichiometry of the oxide $\mathrm{M_nO_m}$. $U_{\mathrm{s,M}}$ is the metal surface binding energy, ΔH^{f} denotes the formation enthalpy per molecule of the compound, and ΔH^{diss} denotes the dissociation energy of the oxygen molecule. If the concentrations of O and M at the surface are C_{O} and C_{M}, respectively, we obtain the surface binding energy of M and O in the following way:

$$\begin{aligned}
&\mathrm{SBE(M)} = \mathrm{C_O} \cdot \mathrm{SBV}_{\mathrm{O-M}} + \mathrm{C_M} \cdot \mathrm{SBV}_{\mathrm{M-M}} \\
&\mathrm{SBE(O)} = \mathrm{C_M} \cdot \mathrm{SBV}_{\mathrm{O-M}} + \mathrm{C_O} \cdot \mathrm{SBV}_{\mathrm{O-O}}
\end{aligned} \tag{5.8}$$

5.3 How are the Energetic Particles Generated?

Sputtering is initiated by the bombardment of energetic particles at the target. These energetic particles are generally ions. Two approaches can be followed to produce ions and sputter the target materials. The first is quite straightforward by using an ion source which is aimed toward the target. Collecting the sputtered particles on a substrate enables the deposition of a thin film. However, ion beam sputtering is not widely used for industrial large-scale applications. Ions guns are more often utilized in surface analytical techniques such as secondary ion mass spectrometry (SIMS) or to bombard the substrate during thin film deposition [22]. As such, these external sources of ions will not be covered in this chapter. A good overview can be found in [10].

Another source of ions is a plasma. By applying a high negative voltage to the cathode, i.e. the target, positively charged ions are attracted from the plasma toward the target. The ions gain energy in the electric field and bombard the target with sufficient energy to initiate sputtering. Sputtering was first discussed in the literature by W.R. Grove in 1852, who used this kind of set-up [23].

A good starting point to discuss plasma-based sputter deposition is using the simplest experimental arrangement. That is, a cathode and an anode are positioned opposed to each other in a vacuum chamber. Typically, the vacuum chamber is pumped by a combination of turbomolecular and rotary pumps, although a diffusion pump is still often used. After pumping

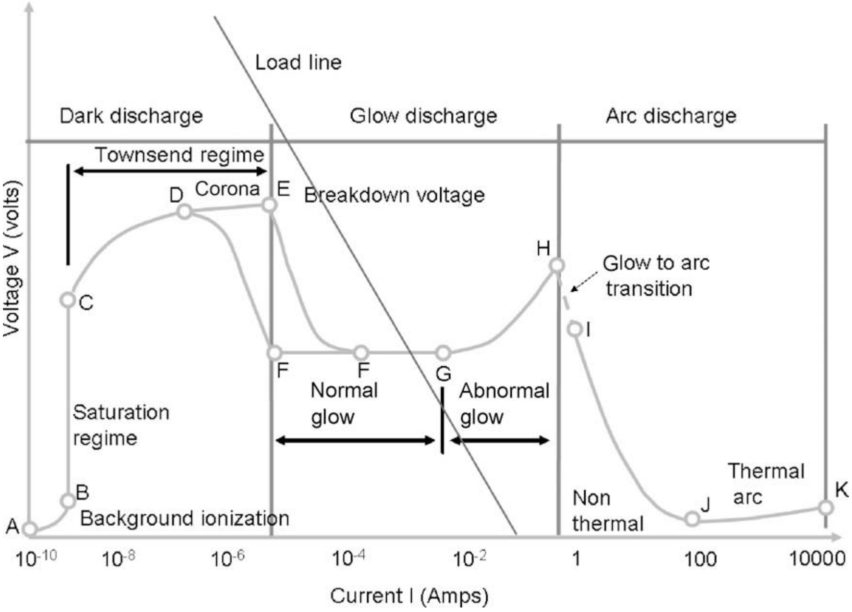

Figure 5.5: The three primary regions of a gas discharge. The straight line is a typical load line.

to a base pressure of the order of 1×10^{-4} Pa [1] or lower, a noble gas (usually argon) is introduced into the vacuum chamber, reaching a pressure between 1 and 10 Pa. When a high voltage difference in the range of 2000 V is applied between cathode and anode, a glow discharge is ignited. It is not in the scope of this chapter on sputter deposition to describe all details related to a glow discharge, but discussing a few can be instructive. To define a glow discharge, one can follow the current–voltage (*I*–*V*) characteristics. It is important to realize that these characteristics depend also on the pressure and the separation between cathode and anode. The main characteristics of the discharge, such as breakdown voltage, *I*–*V* characteristics, and structure of the discharge, depend on the geometry of the electrodes (cathode and anode) and vacuum vessel, the gas(es) used, and the electrode material. The *I*–*V* characteristics of such a discharge are illustrated in Figure 5.5 for a wide range of currents. Three general regions can be identified in the figure, the dark discharge region, the glow discharge, and the arc discharge. The electric circuit of the discharge gap also includes an external ohmic resistance *R*. In this case, Ohm's law for the circuit can be written as

$$\mathrm{EMF} = V + RI \tag{5.9}$$

---

[1] Other commonly used pressure units are mtorr and mbar: 1 mtorr corresponds to 0.133 Pa; 1 mbar corresponds to 100 Pa.

where EMF is the electromotive force and V is the voltage of the gas discharge. Equation (5.9) is usually referred to as the load line, and is also shown in Figure 5.5. Intersection of the I–V characteristic and the load line gives the actual value of current and voltage in a discharge. By adjusting the ballast resistor in the circuit diagram, we can sweep out an I–V characteristic that is highly non-linear and shows the three general regions. Each of these regions encompasses many interesting phenomena.

Let us first focus on the dark discharge regime, between A and E in Figure 5.5. The name refers to the fact that the discharge remains invisible to the eye, i.e. there is no visible light emitted except for the corona discharge and the breakdown itself. The change in the I–V characteristic can be understood from a description of the responsible physical processes. Between A and B, the ions and electrons formed by the background ionization move toward the electrodes due to the applied electrical field, producing a weak electrical current. Increasing the applied voltage results in a better collection efficiency, i.e. a larger fraction of the produced ions and electrons will reach the electrodes. At a sufficient high voltage, the current will saturate because all produced electrons and ions reach the electrodes. Hence, in the region between B and C, the current remains constant with increasing voltage. Some radiation counters, e.g. a Geiger–Müller counter, make use of the fact that the measured current will depend linearly on the strength of the radiation source. When the voltage across the low-pressure discharge tube is increased further, one notices a strong increase in current (see regions C–E). Hence, more electrons and ions must be produced. The origin of the current increase is found in the impact ionization of atoms by the original electrons accelerated across the electric field. Hence, an avalanche of electron and ion production will follow, leading to a strong increase in current. This region is called the Townsend discharge.

Corona discharges (D–E) occur in Townsend dark discharges, prior to electrical breakdown, in regions of high electric field near sharp points, edges, or wires. If the corona currents are high enough, corona discharges are technically ‘glow discharges’ and visible to the eye. For low currents, the entire corona is dark. Corona discharges are often applied to treat the surface of polymers and to render the surface more ‘active’ by breaking atomic bonds. Finally, at sufficiently high electrical fields, breakdown will occur due to addition of secondary electrons emitted from the cathode as a result of ion and photon impact (see below). At the breakdown potential (point E), the current may increase significantly, and is usually limited by the internal resistance of the power supply connected between the plates. If the internal resistance of the power supply is very high, the discharge tube cannot draw enough current to break down the gas, and the tube will remain in the corona regime with small corona points (brush discharges) present on the electrodes. If the internal resistance is lower, then the gas will break down at the indicated voltage and move into the normal discharge regime (region F–G). The breakdown voltage for a particular gas and electrode material depends on the product of the pressure P

and the distance d between the electrodes, as expressed in Paschen's law:

$$V_{\text{breakdown}} = \frac{BPd}{\ln(APd) + \ln\left(\ln\left[\frac{1}{\gamma} + 1\right]\right)} \tag{5.10}$$

with A and B constants, and γ the electron emission yield induced by photon and ion bombardment. The constants A and B depend on the chosen gas and define the Townsend ionization coefficient. This latter coefficient gives the electron production per unit length, or the multiplication of the electrons per unit length along the electric field.

In contrast to the dark discharge regime, the plasma in the region F–G is luminous in the visible, and hence it is called a glow discharge. The excitation of the gas atoms by electron impact forms the origin of the gas glow. The plasma density is now sufficiently high that the electric field between the electrodes becomes distorted from its original configuration in the Townsend discharge. Along the discharge, one can notice, especially at low pressure, a sequence of dark and bright layers. These layers have special names. Close to the cathode is a dark layer known as the Aston dark space, followed by a thin layer of the cathode glow. This bright layer is then followed by the cathode dark space. Sharply separated from this latter region is the negative glow. The luminosity of the negative glow decreases toward the anode, becoming the Faraday dark space. After the Faraday dark space is the positive column. At the anode side, the positive column goes over into the anode dark space followed by a narrow anode glow. A schematic overview is shown in Figure 5.6.

Most of the voltage drop between cathode and anode occurs between the cathode and the negative glow. The length of the cathode fall region or 'the dark space' from the cathode to the boundary of the negative glow is typically a few centimeters. So, within this region most power is dissipated and one notices a strong voltage drop. The voltage drops over a distance

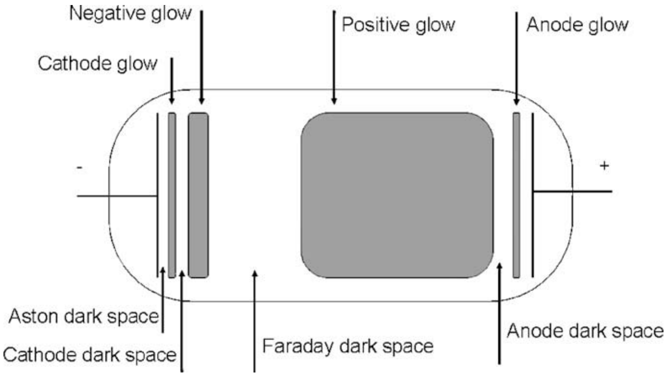

Figure 5.6: Schematic representation of the structure of a glow discharge.

which is generally not exactly equal to the width of the dark space. To distinguish between the two regions, one refers to the first region as the cathode sheath. When the glow discharge covers only a part of the cathode, the discharge is in the normal glow discharge mode. In this regime, the current density at the electrodes is independent of the discharge voltage and hence by increasing the current, the part covered by the plasma increases at constant discharge voltage (see region F–G). From point G on, the plasma completely covers the cathode surface and with increasing discharge current, the discharge voltage increases. In this regime, the abnormal discharge region, sputter deposition is typically performed. At point H, the electrodes become sufficiently hot that the cathode now emits electrons thermionically. If the DC power supply has a sufficiently low internal resistance, the discharge will undergo a transition from glow to arc. As the energy of the arriving fast neutrals and ions defines the sputter yield, it is interesting to study the typical ion energy distribution in a glow discharge. Indeed, the erosion speed of the target will be defined by the flux of ions and fast neutrals bombarding the cathode and the sputter yield which depends on the energy and mass of these species. At the typical pressures of a DC argon glow discharge, the Ar^+ ions have a small mean free path. This means that the distance the ion travels before it makes a collision, or it ceases to be an ion, is short. The short mean free path is due primarily to the following effect. When an Ar^+ ion passes close enough (a few Å) to an Ar atom, quantum mechanical tunneling occurs. So, the ion becomes again an atom, while the atom from which the electron is removed now becomes an ion. This process is called a symmetric charge exchange collision because the result is still an ion and an atom. However, the ion which has already gained energy by acceleration in the electric field within the cathode region becomes a neutral Ar atom with the same energy, while the atom becomes an ion with the low energy of the atom. This newly created ion is now accelerated by the voltage gradient in the cathode region. The fast neutral Ar atom cannot gain energy anymore, and owing to the high pressure will lose energy by collision with other atoms. So, even with the strong electric field, defined by the high discharge voltage and the cathode sheath thickness, the number of high energy ions arriving at the cathode will be quite small. Davis and Vanderslice [24] fit the measured the energy distributions of the ions reaching the target based on the following equation:

$$\frac{V_c}{N_0}\frac{dN}{dV} = \left(\frac{L}{\lambda}\right)\left[\frac{1}{2\,(1 - V_x/V_c)}\right] e^{-(L/\lambda)\left[1-(1-V_x/V_c)^{1/2}\right]} \tag{5.11}$$

with N_o the number of ions starting from the negative glow, L the sheath thickness, and λ the mean free path for charge transfer.

This distribution is plotted for various values of L/λ in Figure 5.7. It will be noted that equation (5.11) does not account for the ions that do not suffer any collisions, and arrive at the cathode with the full cathode fall energy. Their relative number, given by $e^{-L/\lambda}$, is indicated at the right end of the curves. So, with an experimental value of L/λ of 25 (see [24]), we can conclude that

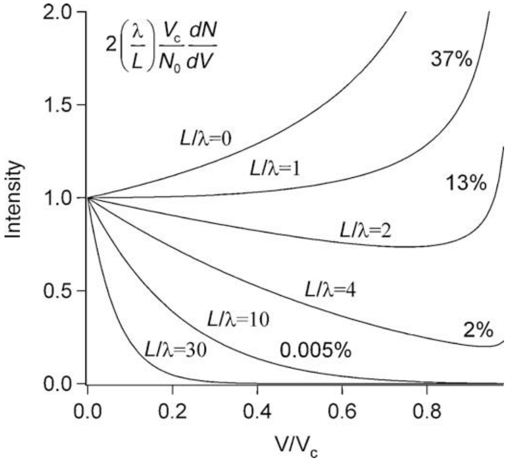

Figure 5.7: Ion energy distributions calculated according to the model of Davis and Vanderslice [24].

essentially no ions arrive at the target with energy equal to the applied target voltage. Experiments and simulation on this topic are also described by Bogaerts et al. [25, 26].

While the sputter yield is determined by the energy and mass of the ions at the target, the sputtering rate of the target depends on the total power. For a simple DC diode system, the ion current density is uniform over nearly the entire target during the abnormal glow discharge mode. Experimentally, one finds that the current density is proportional to $(V - V_0)^{3/2}$, where V_0 is the voltage required to maintain the discharge, and to $(p - p_0)$, where p_0 is the gas pressure needed to maintain the discharge. So, to obtain higher current densities it is necessary to increase either V or p, or both. A high pressure is not interesting as the energy of the sputtered particles arriving at the substrate is low and many sputtered atoms are scattered back to the target. Increasing the discharge voltage is also not an option. Many electrons that are ejected from the target will reach the anode without losing much energy in collisions because the ionization cross-section decreases strongly with increasing electron energy. Hence, when the electron has obtained its full energy by acceleration in the electrical field in the cathode region, it is less likely to ionize gas atoms far from the cathode. Increasing the discharge voltage results in a higher electron current density at the anode. These energetic electrons can deliver significant power to the anode, thus resulting in substrate heating which may limit the substrate choice for this deposition process.

In conclusion, DC glow discharge sputtering has some drawbacks as a deposition process. Hence, several other sputtering techniques have been developed to overcome these drawbacks. The most important technique is magnetron sputter deposition, which is the subject of the next section.

5.4 Efficient Trapping of Electrons Leads to Magnetron Sputter Deposition

In a diode glow discharge arrangement, electron trajectories are only defined by the electrical field between the cathode and the anode. Hence, the electrons are accelerated over the cathode sheath, and move with high velocity toward the anode. To ensure that the electrons produce sufficient ions to sustain the discharge, the pressure must be quite high, i.e. of the order of a few Pa. The classical approach to avoid the rapid loss of electrons from the discharge is to apply a magnetic field. By applying a magnetic field during glow discharge sputter deposition, one can trap the electrons in the discharge longer and, hence, produce more ions for the same electron density. As the electron trajectory is elongated, the probability of ionizing a gas atom during their travel from cathode to anode increases, which enables a reduction in the discharge pressure and the cathode sheath. In this way, the ions can reach the cathode with almost the full discharge voltage and the sputtered atoms can reach the substrate with only a few collisions. Also, the deposition rate, a technically meaningful criterion, will dramatically increase compared to simple diode glow discharge systems.

5.4.1 Post Magnetrons

In post magnetrons (Figure 5.8) a uniform magnetic field, $\vec{B}$, is applied parallel to the surface of a cylindrical target. It has approximately the same strength at all points on the target surface.

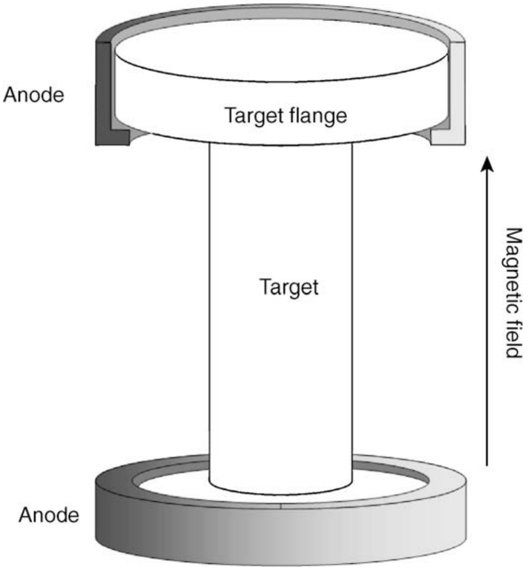

Figure 5.8: Schematic drawing of a post magnetron.

Electrons emitted from the target by ion impact are accelerated by the potential over the sheath (see Section 5.3). The presence of the magnetic field influences the trajectory of the electrons, and forces them in cycloidal orbits, bringing them back to the cathode, unless they make a collision. The electron trajectory can be described by the Lorenz equation:

$$\vec{F} = q(\vec{E} + \vec{v}\times\vec{B}) \tag{5.12}$$

with q the negative charge of the electron, $\vec{E}$ the electric field over the dark space, $\vec{B}$ the magnetic field, and $\vec{v}$ the velocity of the electron. Once the electron has left the cathode sheath, its trajectory is defined primarily by the magnetic field. The Lorenz force on the electron depends on its velocity and the magnetic field strength, and is orthogonal to both their directions. The first component of the electron motion is the movement along the magnetic field lines. A second component is the gyration of the electrons around the magnetic field lines with the Larmor radius:

$$r_{\mathrm{L}} = \frac{mv_{\perp}}{qB} \tag{5.13}$$

in which $v_{\perp}$ is the velocity of the electron perpendicular to the target. Finally, the third component of the electron trajectory is the $\vec{E}\times\vec{B}$ Hall drift. This drifting 'around' the post in a helical motion occurs perpendicular to the electric and magnetic fields. Summarizing, the electrons move continuously in one direction around the target and are accelerated and decelerated close to the target surface.

The average electron energy loss per ionization, W, is of the order of 30 eV for Ar magnetron discharges [27]. This number can be retrieved based on Monte Carlo simulations (e.g. [28]). If we assume that the voltage drop across the sheath is approximately equal to the discharge voltage V_{d}, eV_{d}/W ion–electron pairs will be produced on average by one electron. This implicitly assumes, as a first approximation, that there is no ionization in the sheath. This approximation is reasonable as the sheath width is of the order of a few millimeters (and varies as $1/P$), and much smaller than the electron path length. If all eV_{d}/W ions reach the cathode, and γ_{e} is the ion-induced electron emission yield, then $(eV_{\mathrm{d}}/W)\gamma_{\mathrm{e}}$ electrons will be emitted from the target. To sustain the discharge, we can write

$$\frac{eV_d}{W}\gamma_e = 1 \tag{5.14}$$

from which we can derive an equation for the minimum required voltage:

$$V_{\mathrm{d}} = \frac{W}{e\gamma_{\mathrm{e}}} \tag{5.15}$$

Using a typical value for W of 30 eV, and γ_{e} of the order of 0.1 for metal targets (e.g. [29]), a value of -300 V is obtained. Of course, electrons can be lost to ground before they have created the maximum number of electron–ion pairs. A possible loss mechanism occurs when the magnetic field line which the electron follows crosses the anode or the chamber walls. Also, ions produced far from the cathode sheath will not reach the target. Both loss mechanisms can be included in Eq. (5.15) by introducing the coefficients ε_i and ε_e for ion and electron collection efficiency, respectively. The values of these coefficients are close to one for magnetrons. Thus,

$$V_\mathrm{T} = \frac{W}{e\gamma_\mathrm{e}\varepsilon_\mathrm{i}\varepsilon_\mathrm{e}} \tag{5.16}$$

In the derivation of Eq. (5.16), we assumed that no ionization occurs in the sheath. However, when the magnetic field is strong, the electron paths are close to the target, and therefore substantial ionization can occur in the sheath. The electrons produced in the sheath will also gain energy and can contribute to the production of electron–ion pairs. This process can be seen as a multiplicative process for the original electron. We include this effect in Eq. (5.16) by introducing the multiplication parameter m. We notice, as expected, that more sheath ionization results in a lower discharge voltage to sustain the discharge, i.e.

$$V_\mathrm{T} = \frac{W}{e\gamma_\mathrm{e}\varepsilon_\mathrm{i}\varepsilon_\mathrm{e}m} \tag{5.17}$$

We can further improve Eq. (5.17) by realizing that an electron which does not interact with the gas will return to the target with its initial energy (typical a few eV [30]). Hence, an electron which has not collided with a gas atom can be reflected at the target surface and continue its path, or it can be absorbed (or recaptured) by the target. In the latter case, the electron is lost for further ionization. Increased recapture will therefore result in a higher discharge voltage. To account for this effect we introduce the effective ionization probability f into Eq. (5.17), which is a number between 0 (all electrons are recaptured) and 1 (no electrons are recaptured):

$$V_\mathrm{T} = \frac{W}{e\gamma_\mathrm{e}\varepsilon_\mathrm{i}\varepsilon_\mathrm{e}mf} \tag{5.18}$$

The pressure dependence of a magnetron discharge can be understood from this latter process. When the pressure in a DC diode glow discharge is reduced, the electrons emitted from the target will reach the anode without ionizing gas atoms, and hence the electron is lost for the ionization process. Therefore, at too low of a pressure, the DC diode glow discharge will extinguish. However, for a magnetron discharge, the high-energy electron cannot reach the anode very easily owing to the presence of the magnetic field. Nevertheless, when the pressure is decreased, the magnetron discharge will ultimately extinguish. The loss process for the electrons is now electron recapture at the target. At high pressure, the effective ionization probability will be close to one because the emitted electrons can easily interact with the gas atoms. Inelastic collisions (such as ionization and excitation of the gas atoms) result in energy loss. As a result of this energy loss, the electrons cannot return to the target. At lower pressure the ionization probability is smaller and hence electrons can be recaptured. Therefore, we expect a higher discharge voltage (when keeping the other parameters such as magnetic field, magnetron type, and discharge current constant) at lower pressure.

In a post magnetron, flanges are placed at the end of the target. The flanges are at the same negative potential as the target, and prevent the electrons which drift over the target from escaping axially.

5.4.2 Planar Magnetrons

Although cylindrical and planar magnetrons have different geometries, the basic principles of operation are the same, but are generally easier to understand from the symmetry of the cylindrical case. However, planar magnetrons are more widely used because of their convenience. One example is the easy ability to design air-to-air systems for flat substrates. In a planar magnetron design, permanent magnets are generally placed behind the target. For a circular target, there is a central disk magnetic pole and an annular pole so that the magnetic field lines between the poles have a circular symmetry. This way of generating a magnetic field has its consequences. First, the magnetic field strength varies over the target surface. Also, the direction changes over the target surface as the direction of $\vec{B}$ is tangent to the field line. Thus, the magnetic field is only parallel to the target surface at unique points, but at most points the magnetic field has a component parallel to the target. The effect of this parallel component is similar to the one described in the previous section. It results in cycloid orbits above the target surface. The vertical component of the magnetic field is also important, preventing electrons from escaping the target by generating an electromagnetic 'bottle'. Indeed, as an electron moves along the target, it has its velocity vector parallel to the target surface. Hence, the presence of the vertical component of the magnetic field will force the electron (see Eq. 5.11) toward the central area between the magnets. For a circular planar magnetron the $\vec{E} \times \vec{B}$ drift will be parallel to the target and the electron will follow a circular path around the target and will not escape the magnetic 'bottle' (Figure 5.9) unless it collides with gas atoms.

In the case of a rectangular planar magnetron (Figure 5.10), the magnet configuration is designed to assist the electrons to move around corners of the target. For both circular and rectangular magnetrons, the magnet configuration results in maximum ionization in the region between the magnets. Hence, most ions will be formed at this position, and as the ions move in a perpendicular trajectory toward the target, the ion current density will be the highest at this position. For a circular magnetron, a torus-shaped plasma will be formed (see Figure 5.9), leading to a circular 'racetrack' erosion pattern. The sputtering process must be interrupted to prevent cooling water entering the vacuum system when the erosion groove becomes too deep such that it may break through the target. Moreover, the formation of the erosion pattern

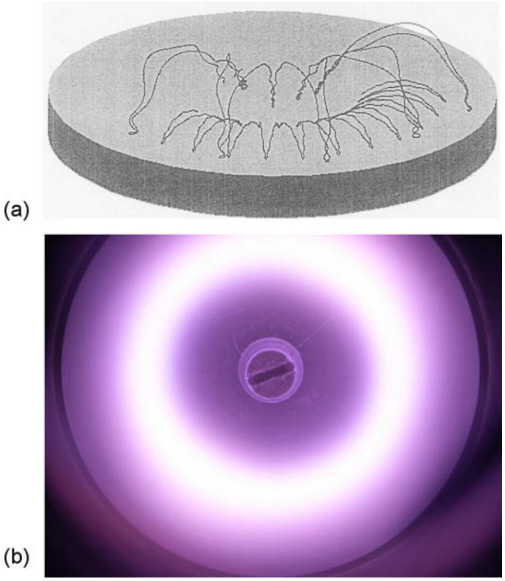

Figure 5.9: Simulated part of a trajectory of an electron on a circular planar magnetron (a) and the resulting torus-shaped argon plasma (b).

results in a continuously stronger magnetic field strength above the surface because the target surface recedes toward the magnets as material is sputtered. Hence, the erosion rate increases (and the voltage usually decreases) as a function of sputtering time. Several companies offer solutions to increase the target utilization. Optimization of the magnetic field design is a common solution, but even with an optimized magnet design target utilization remains less than 50% for stationary magnets. By moving the magnets in a complex geometry under the target, higher target utilization can be achieved.

Figure 5.10: Two types of planar magnetrons: (left) a circular 5 cm diameter magnetron; (right) a rectangular magnetron (notice the clear erosion groove or racetrack in both cases).

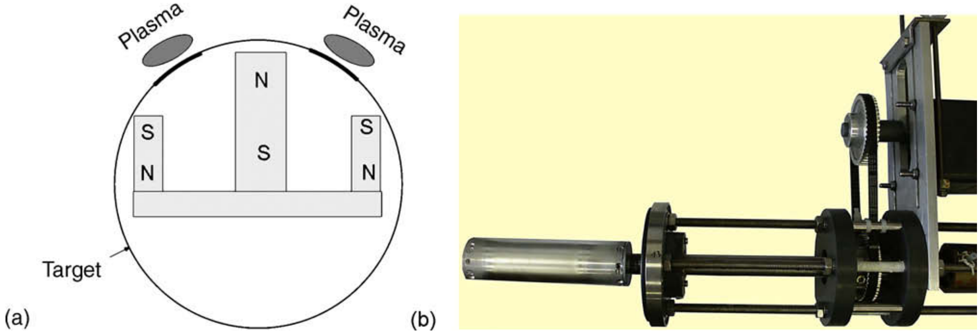

Figure 5.11: Magnet configuration for a rotating cylindrical magnetron (left) and a laboratory-scale magnetron of this type.

5.4.3 Rotating Cylindrical Magnetrons

To improve target utilization, rotating cylindrical magnetrons have been developed. Their magnetic field design is quite similar to that of planar magnetrons. However, the target is a cylindrical tube and is rotated around a stationary magnet configuration (Figure 5.11). The disadvantage of these magnetrons is the same as for post magnetrons, i.e. a complex target design and fabrication. For some metals, a tube can be used, but for many materials the target material must be flame or plasma sprayed onto a cylinder or backing tube, which is water cooled and holds the magnet configuration. The bearing design is crucial with this magnetron type as the water flow is inside the vacuum system. The much higher target utilization, up to 85%, is the main advantage. A major problem with planar targets is the build-up of compound material on the target during reactive magnetron sputtering. The compound layer on non-sputtered target parts forms the origin of arcing in insulating reactive systems such as Al/O_2. With a rotating cylindrical magnetron, this compound layer is sputtered again after each target rotation, resulting in better process stability during reactive magnetron sputter deposition.

5.4.4 Some General Features of Magnetrons and Magnetron Discharges

5.4.4.1 The Discharge Voltage

The discharge voltage is an easily measurable quantity and Eq. (5.18) helps to explain its behavior as a function of experimental parameters. We discuss the most important of these, and refer to [31] for more details.

When using a planar magnetron, the discharge voltage will decrease as a function of time. This behavior can be readily explained by the increase in magnetic field strength adjacent to the target (see Section 5.4.2) due to the erosion groove formation. As such, electrons will move

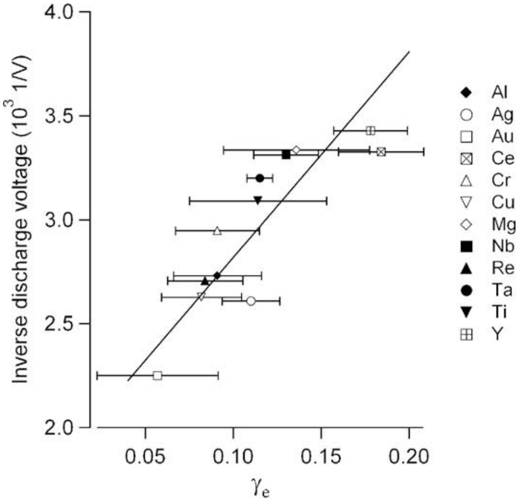

Figure 5.12: The inverse of the discharge voltage measured in pure argon discharges as a function of the ion-induced secondary electron yield. Measurements are performed with a conventional 5 cm diameter circular magnetron (argon pressure 0.3 Pa, discharge current 0.3 A).

closer to the target, and more sheath ionization will occur, and according to Eq. (5.18) the discharge voltage should decrease as m becomes larger.

The discharge voltage also depends strongly on the target material and the condition of the target (see Section 5.5). The material dependence of the discharge voltage can be related to the value of the ion-induced electron emission yield γ_e. Changing the target material and/or the target condition will result in a change in γ_e, and consequently the discharge voltage will change. As can be understood from Eq. (5.18), the discharge voltage is, to a first approximation, inversely proportional to the electron yield, as shown in Figure 5.12.

5.4.4.2 I–V Characteristics

One typical measurement when studying magnetron discharges is the *I–V* characteristic. The behavior of the discharge voltage as a function of experimental parameters has been investigated in detail [32]. Another important parameter is the discharge current, as it is combined with the discharge voltage to provide power delivered to the target. At constant pressure, the discharge current increases rapidly with discharge voltage. To express this relationship, or the *I–V* characteristics, several empirical scaling laws have been proposed. The one used most often is

$$I = kV^n \tag{5.19}$$

The exponent n is a measure of the magnetron efficiency, and can have values of the order of 10 or higher. The behavior of the *I–V* characteristics as a function of the operating pressure is

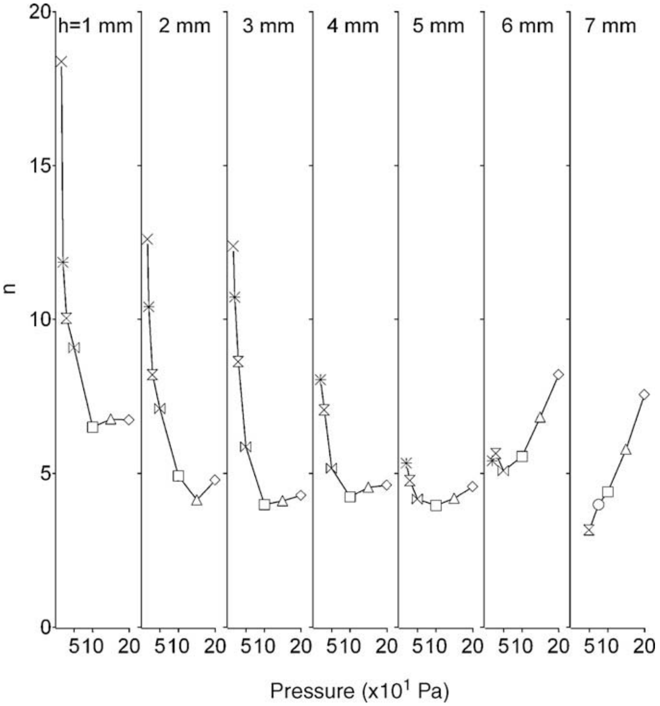

Figure 5.13: The exponent *n* (see Eq. 5.19) for *I–V* characteristics measured under different conditions of target thickness and pressure. A conventional 5 cm diameter circular magnetron was used with a copper target. At low magnetic field or for thick targets (see *h* = 7 mm) the slope increases with pressure. However, the opposite behavior is observed for a high magnetic field or thin targets (see *h* = 1 or *h* = 2 mm).

not fully understood. At low magnetic field strengths, the value of *n* increases with increasing pressure, but the reverse behavior is apparent at high magnetic field strengths [32], as shown in Figure 5.13.

The origin of this steep behavior is a current topic of discussion and research as it is related to the diffusion of electrons perpendicular to magnetic field lines. Based on the description given above, one could conclude that electrons can only escape from the magnetic trap by losing nearly all their energy in collisions. This is not completely true; as a result of frequent collisions with Ar atoms, electrons can be scattered and ‘hop’ between field lines. This description is the classical diffusion of electrons based on collisions between electrons and gas atoms. However, experimental work shows that diffusion perpendicular to the magnetic field is greater than expected from the classical diffusion model [33]. Although several authors have proposed mechanisms to explain this enhanced diffusion, there are still doubts and unanswered questions.

5.4.4.3 Magnet Balance

The magnet configuration in planar and rotating cylindrical magnetrons is used to trap electrons, thereby producing a high ion density near the target for a given pressure. With an optimum design of system geometry and operating pressure, the electrons are lost from the target area when their energy becomes less than the ionization threshold. Therefore, one can expect that only low-energy electrons are present in the bulk plasma region and in the vicinity of the substrate. This can be a distinct advantage to the glow discharge process, but in some cases (see further) it can also be advantageous to deliver more energy to the substrate. A possible solution is 'unbalancing' the magnetron configuration, or changing the magnetic field strength of the inner versus outer magnets. In this way, the configuration of the magnetic trap is changed (Figure 5.14) to allow electrons to escape the magnetic trap follow the magnetic

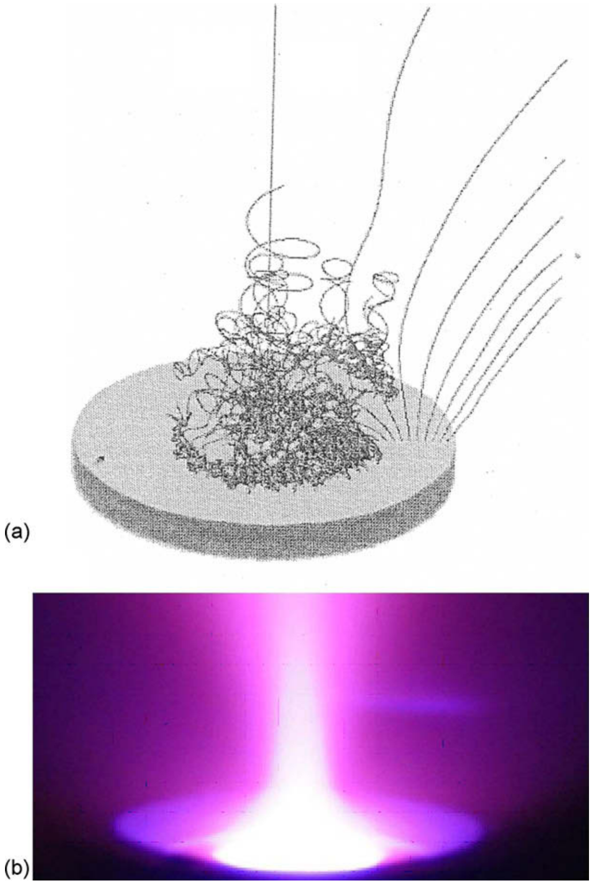

Figure 5.14: Some simulated electron trajectories for an unbalanced magnetron (a) together with the cone-shaped argon plasma (b). Note that unbalancing the magnetic circuit opens a 'leak' in the plasma trap and allows independent control of substrate ion bombardment.

field lines toward the substrate. This results in a strong electron flux in the region of the substrate. By modifying the magnetic field strength balance between the outer and inner magnets, one can tune the electron flux, and hence the ion flux, incident at the substrate. One way to characterize the magnet balance is the ratio K between the magnetic flux through the outer and the inner magnets:

$$\mathrm{K} = \frac{\Phi_{\text{out}}}{\Phi_{\text{in}}} = \frac{\int_{S_{\text{out}}} B_{\perp\text{out}} d S_{\text{out}}}{\int_{S_{\text{in}}} B_{\perp in} d S_{\text{in}}} \tag{5.20}$$

where $B_{\perp}$ represents the magnetic field strength perpendicular to the magnet, and S is the area of the magnet [34].

One way of changing the magnet balance is shifting the position of the inner and outer magnets relative to the target surface (Figure 5.15). This results in a different n value for the I–V characteristic (see Eq. 5.19). Shifting the magnets also changes the discharge voltage, which modifies the sputter rate of the target at constant current. The combination of both

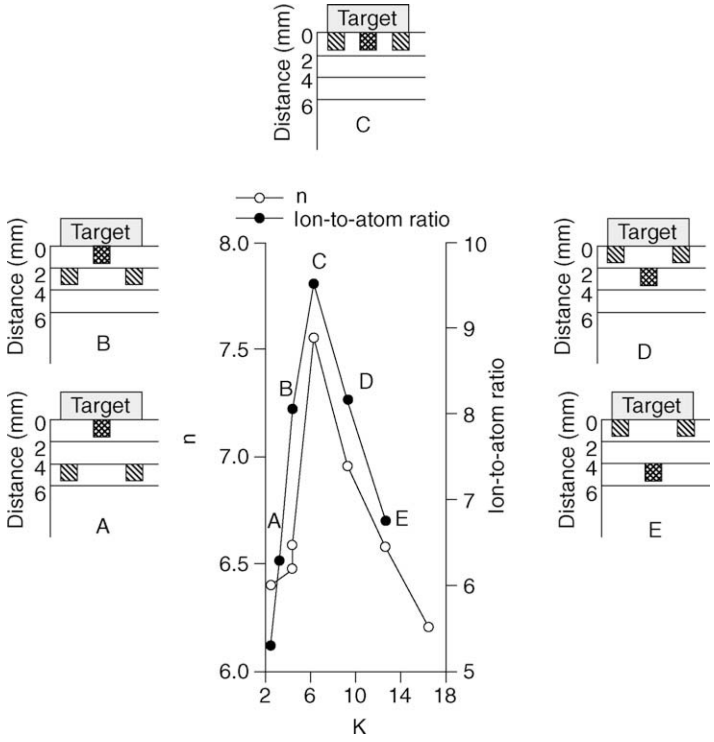

Figure 5.15: Influence of the magnet balance on the *n* value (see Eq. 5.19) and the ion-to-atom ratio. The magnet balance, expressed by the value *K* (see Eq. 5.20), is changed by shifting the inner or the outer magnet relative to target surface. Several situations are depicted schematically.

changes enables one to modify the ion-to-atom ratio at the substrate. The ion-to-atom ratio is a significant parameter during thin film growth (see Section 5.7).

A more straightforward and completely tunable approach to unbalance the magnetic circuitry of the magnetron is to incorporate a Helmholtz coil external to the permanent magnets in order to increase the field strength of the outer magnet [35]. This opens a leak in the plasma trap and dramatically increases the incident ion/atom ratio at the substrate from typically 0.1–0.5 (depending on the gas, substrate bias, and system geometry) to > 50 with no significant change in film deposition rates. Moreover, these high ion/atom ratios can be achieved using very low ion energies (< 10–20 eV) which, in most cases, are below the film damage threshold. Just as significantly, the ion energy and ion flux incident at the substrate are now controlled independently by the substrate bias and the external magnetic field, respectively. That is, the advantages of an ion beam deposition system are now obtainable using high-rate magnetron sputtering.

5.4.5 Powering the Magnetron

Magnetrons can be powered by a variety of methods. One can choose among radio frequency (RF), direct current (DC), pulsed DC and, recently, high-power impulse magnetron sputtering (HIPIMS).

5.4.5.1 Radio-Frequency Magnetron Sputtering

When using thick electrically non-conducting targets, RF power is the only option to sputter deposit thin films. An important point must be emphasized. The discussion of the magnetron sustaining mechanisms in Sections 5.4.1 and 5.4.2 is not completely valid for RF powered magnetrons. Indeed, owing to the rapidly changing electric field, the entire electron distribution shifts up in energy through ‘in-phase’ collisions, allowing either increased ionization (and, hence, discharge current) at constant pressure or operation at decreased pressure. The term ‘in-phase’ collisions refers to the fact that there is a fraction of the electron population in the discharge that, while being accelerated by the instantaneous electric field, will make a collision before the field direction switches and will then have a velocity component in the direction of the switched field. Through this mechanism, the overall distribution of electrons increases in energy and, therefore, the concentration of electrons that have energies above the gas ionization potential increases, thus decreasing the overall discharge impedance.

When applying a high-frequency (typically 13.56 MHz) power source between two electrodes, the light (low-mass) electrons respond instantaneously to the rapidly varying field, while the heavier ions are inertially confined. That is, the ion transit time to either electrode is very much less than the RF period, forcing both electrodes to charge negatively. In order to maintain charge neutrality per cycle, the entire RF waveform must then shift down in voltage such that each electrode is positive (attracting electrons) for less than 1% of an RF period and the ions, to first order, respond to an average applied voltage which is approximately one-half the RF peak-to-peak potential. As in DC sputtering discussed above (Section 5.4), the average ion impact energy is only a small fraction of the applied field owing primarily to charge exchange collisions. In order to define the target and substrate in RF powered systems, one electrode (the substrate table) is made to be very much larger than the other electrode (the target) by electrically connecting the substrate table to the entire system. The electrodes now act as a leaky capacitively coupled voltage divider for which the applied voltage is distributed as $V_t/V_s=(A_s/A_t)^m$, where the subscripts t and s refer to target and substrate, A is the electrode area, and $m=4$ in the ideal case, but is typically 1.5–2 for real systems.

An important lesson here is that when using RF power, one is always doing bias sputtering. It is intrinsic in the nature of how these systems function that there is an average negative voltage (and, hence ion bombardment) at the substrate. V_s depends on the pressure, the gas, and system geometry (i.e. a smaller system confines the plasma and increases V_s). The substrate voltage can range from 15–20 V negative to a few hundred volts negative. It is also important to remember that since RF power supplies are designed to look into circuits with a purely resistive 50 Ω load, a tunable matching network is required to damp out the complex reactance (both capacitance and inductance) of the discharge.

The primary disadvantage of the use of RF power supplies, in addition to expense and reliability, for magnetron sputtering is the inherently low deposition rate. That is, n decreases significantly in the power-law I–V relationship of Eq. (5.18). This is because magnetron sputtering, which relies on a closed electromagnetic trap at the target, is fundamentally a DC concept. The RF field alternately opens and closes the trap, allowing electrons to escape when the trap is open and forcing electrons to cross magnetic field lines, and hence drop power in the discharge, which decreases the available power at the target, when it is closed. The deposition rate for a given applied target power decreases with both increasing frequency [36] and increasing magnetic field [37].

5.4.5.2 Direct Current Magnetron Sputtering

The simplest and least expensive way to operate the magnetron is using a DC power supply. Today, special power supplies for sputter deposition have been developed which include an arc suppression unit. Arcs often occur during reactive sputter deposition of, for example, non-conductive oxides from a metal target in pure O_2 or mixed Ar/O_2 discharges, due to a build-up of oxide on the edges of the erosion groove where the sputter rate is low. Arcs (see Figure 5.5) can be characterized as a low voltage and high current discharge. When the electric circuit ‘detects’ a strong decrease in the discharge voltage and/or a strong increase in the discharge current, it switches the power off for a small period (typically a few microseconds) to draw electrons, decrease charging, and prevent the arc from fully developing. Arcing can seriously damage a target by local melting, but it also degrades quality of the deposited film owing to the presence of particulates and/or pinholes while eventually destroying the power supply.

5.4.5.3 Pulsed DC Magnetron Sputtering

An effective way to prevent arcing during reactive magnetron sputtering (discussed below) is pulsing the applied voltage. In contrast to RF magnetron sputtering, the frequency is much lower and, is typically 50–250 kHz depending on the application [38]. The discharge voltage generally cycles between a high negative voltage and a low positive voltage. The negative voltage part of the cycle is used to perform the sputtering, as the ions bombard the cathode. The low positive voltage part of the cycle is used to attract electrons to prevent charge build-up. Because of the higher mobility of the electrons, this part of the cycle can be relatively short compared to the total cycle time.

An alternative approach is the use of two magnetron sources, i.e. dual magnetron sputtering, and switching the negative and positive voltage between both targets. In this way, each magnetron alternately has the function of a sputtering target and an anode. Thus, both targets can be neutralized during each cycle. This not only prevents charge build-up but also solves problems related with anodes being covered with insulating thin films (the 'disappearing anode'). The disadvantages here are the higher cost and the fact that power to each target must be turned off before igniting the other target when using mid-frequency AC power supplies. Thus, transients are more severe in this approach. For pulsed DC dual magnetron sputtering, plasma ignition may be required after each half-cycle depending on operation conditions. Dual magnetron power supplies also require electromagnetic and RF interference shielding.

5.4.5.4 High-Power Impulse Magnetron Sputtering

HIPIMS uses a large energy impulse supplied to the cathode over a very short period, typically $\sim 100\ \mu\text{s}$. This requires a very different type of power supply, the heart of which is a large bank of capacitors. The HIPIMS process delivers a large low-energy flux of ions to the substrate. Peak powers up to several MW/pulse with pulse widths between 100 and 150 μs must be generated by the power supply. Average powers are ~ 20 kW with frequencies up to 500 Hz. In addition to supplying pulsed power, arc suppression is necessary. This process takes advantage of enhanced ionization resulting from the high-energy pulse. Power densities applied to the target are in the neighborhood of 1–3 kW/cm^2, compared to traditional magnetron sputtering with power densities $\sim$ 1–10 W/cm^2.

The high-power pulse is the core of this process. Typical operating conditions are as follows. The voltage pulse is between 1.3 and 1.5 kV and total pulse duration is $\sim 120\ \mu\text{s}$. The target current increases and peaks at ~ 200 A as the voltage pulse decays. The power density at that point is ~ 600 W/cm^2. This method of powering the target results in a high-density plasma with a high ionization degree of the sputtered target material. During each sputtering pulse, the discharge begins as gas supported, but owing to the huge powers quickly becomes metal supported (self-sputtering) due to gas rarefaction. HIPIMS has recently been reviewed in detail [39].

5.5 Reactive Magnetron Sputter Deposition

Using an electrically conducting, and generally, a metallic target makes powering the magnetron much easier as several alternatives are now possible. However, it limits the choice in the materials that can be deposited with this technique. To mitigate this problem, a reactive gas can be added to the discharge. The reactive gas, e.g. nitrogen, oxygen, or hydrogen sulfide, can react with the sputtered material to form a compound on the substrate. However, the addition of the reactive gas to the discharge influences the deposition process in several ways while increasing the complexity of the overall process. Some aspects of the reactive sputter deposition processes are discussed in this section.

5.5.1 Hysteresis of Reactive Gas Pressure and Discharge Voltage

To add or remove a reactive gas from the discharge, one generally uses a flow controller. A typical experiment is to stepwise increase the reactive gas flow over a given interval, and wait between the steps until the process is stable, at which time the process parameters (pressure, voltage, current, deposition rate) are recorded. After reaching a maximum flow, the reactive gas flow is stepwise decreased, and again one gives the system sufficient time to stabilize after each step. At sufficiently low pumping speed and high discharge current one notices that at a given reactive gas flow, for many reactive gas/target material combinations, there is an abrupt change in the total pressure and discharge voltage, as shown in Figure 5.16. One also notices that the reactive gas flow must be decreased to a much lower value than the critical value detected during reactive gas addition. Or stated differently, there is a hysteresis in both reactive gas pressure and discharge voltage. The low oxygen flow region is defined as ‘metal mode’, and is characterized by a low reactive gas partial pressure and a high deposition rate. The deposited layer is not a pure compound, but rather a doped metal. The high oxygen flow region is defined as the ‘compound mode’ or ‘poisoned mode’, with a high partial pressure and a low deposition rate. The film is essentially a pure compound.

5.5.2 Understanding the Hysteresis Behavior: Modeling the Reactive Sputter Process

To understand the hysteresis behavior, several authors have modeled the process. The most well known, the ‘Berg’ model, is named after S. Berg from Uppsala University [40]. The model has value because of its simplicity and the fact that it captures much of the physics of the process. As stated by Berg et al., the results should be considered as a first order approximation. Nevertheless, some authors state that the model fits their experimental results. This statement is dangerous, because the fitted parameters are often not experimentally verified, or have no physical meaning. Some experimental results can be better explained by changing the description of the processes occurring at the target, i.e. by including reactive ion implantation. This was first proposed by Depla et al. [41, 42], and the combined model will be

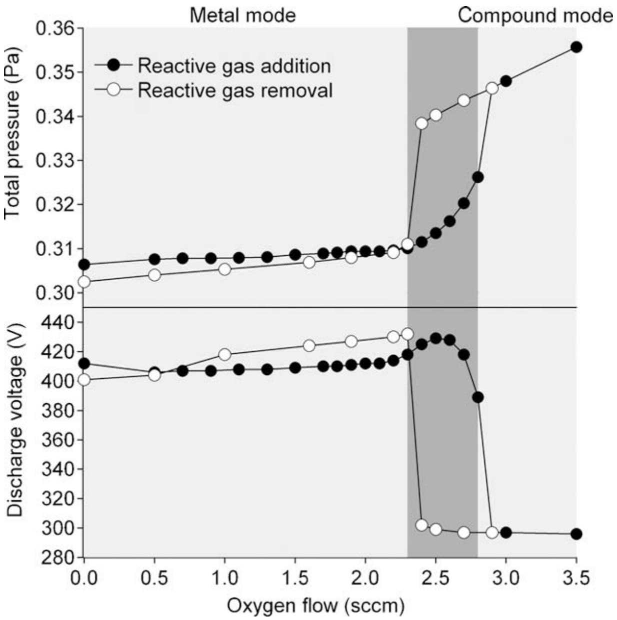

Figure 5.16: Discharge voltage and total pressure behavior during reactive magnetron sputtering of Al in an Ar/O$_2$ mixture. The argon pressure and the total current were kept constant at 0.3 Pa and 0.3 A.

briefly reviewed in this chapter. A user-friendly, shareware code, entitled RSD2009 [43], is available.

The model is based on balance equations, an approach followed by many authors, and originally proposed by Berg et al. The first balance equation is related to the flow:

$$q_0 = q_P + q_R + q_S \tag{5.21}$$

and states that the reactive gas flow introduced into the vacuum system (q_o) must equal the sum of the reactive gas flows to the pump (q_p), and the number of reactive gas molecules consumed per unit time in reactions at the target (q_T), and at the substrate (q_S). The reactive gas flow toward the pump depends solely on the partial pressure of the reactive gas P and the pumping speed S, and can be expressed as

$$q_P = PS \tag{5.22}$$

The reaction on the substrate between the reactive gas molecules and the deposited target material is described as by Berg et al. as a chemisorption process. Hence, the flow toward the substrate will depend on the reactive gas coverage at the substrate, θ_s. It will also depend on the sticking coefficient of the reactive gas α_s and the substrate area A_s. The latter expresses the area of all surfaces on which deposition occurs. Hence, the term ‘substrate’ refers to the entire system except the target. Summarizing,

$$q_{\mathrm{S}} = \alpha_{\mathrm{s}} F \left(1 - \theta_{\mathrm{s}}\right) A_{\mathrm{s}} \tag{5.23}$$

with F the flux of reactive gas molecules toward the substrate. This latter term is defined as

$$F = \frac{P}{\sqrt{2\pi m \mathrm{k} T}} \tag{5.24}$$

with m the mass of the reactive gas molecule, k the Boltzmann constant, and T the gas temperature.

The reaction at the target cannot be described solely by reactive gas chemisorption. One must include other reaction paths. In the model proposed by Depla et al., two mechanisms are included, i.e. direct reactive ion implantation and knock-on of chemisorbed atoms into the target. Including these extra reaction paths makes the model more complex but strongly enhances the understanding of reactive magnetron sputtering. In the model, one distinguishes between the surface layer and the subsurface region. Using this description of the target, the steady-state flow toward the target can be written as

$$q_{\mathrm{t}} = \left(F\alpha\theta_{\mathrm{sm}} - \frac{I\beta\theta_{\mathrm{sc}}}{2} + \frac{z}{2} Y_{\mathrm{s}} \theta_{\mathrm{rb}}\right) A_{\mathrm{t}} \tag{5.25}$$

with A_{t} the target surface area and z defined by the stoichiometry of the compound MR_{z} with M the metal and R the reactive gas. Equation (5.25) takes into account chemisorption of the reactive gas on the metal fraction of the target, θ_{sm}. Knock-on of chemisorbed atoms into the target will depend on the ion current density I, the knock-on yield β, and the fraction of the target covered with chemisorbed oxygen atoms θ_{sc}. Finally, direct reactive ion implantation is also included. In this mechanism, the compound is formed in the subsurface region of the target and, owing to target erosion, it reaches the surface. The fraction of the compound in the subsurface region, i.e. just beneath the surface layer, is expressed as θ_{rb}. The target erosion is defined by the ion current density and the total sputter yield of the target Y_{s}, which depends on the surface composition:

$$Y_{\mathrm{s}} = \theta_{\mathrm{sm}} Y_{\mathrm{m}} + \theta_{\mathrm{sc}} Y_{\mathrm{c}} + \theta_{\mathrm{sr}} Y_{\mathrm{r}} \tag{5.26}$$

with θ_{sr} the compound surface fraction and Y_{r}, the compound yield. Clearly,

$$\theta_{\mathrm{sm}} + \theta_{\mathrm{sc}} + \theta_{\mathrm{sr}} = 1 \tag{5.27}$$

The next step in the model is to calculate the different surface and bulk fractions of compound and unreacted target material. We need also to calculate the reactive gas substrate coverage, θ_{s}.

This latter term is perhaps the easiest to start with. Essentially three processes occur at the substrate:

- chemisorption of reactive gas on the metal fraction of the substrate
- sputter deposition of compound onto the substrate
- sputter deposition of metal onto the substrate.

These three processes lead to the following steady-state equation:

$$\frac{2F}{z}\alpha_{\mathrm{c}}\left(1-\theta_{\mathrm{s}}\right)+\frac{\left(Y_{\mathrm{c}}\theta_{\mathrm{sc}}+Y_{\mathrm{r}}\theta_{\mathrm{sr}}\right)IA_{\mathrm{t}}}{A_{\mathrm{c}}}\left(1-\theta_{\mathrm{s}}\right)-\frac{Y_{\mathrm{sm}}\theta_{\mathrm{sm}}IA_{\mathrm{t}}}{A_{\mathrm{c}}}\theta_{\mathrm{s}}=0 \tag{5.28}$$

For simplicity, compound sputtering is described as molecular, but in reality the compound will leave the target primarily as atoms.

Implicitly, this equation assumes a uniform deposition profile, which is of course too simple. By subdividing the substrate in different areal cells, with areas $A_{\mathrm{c,i}}$ and calculating the metal and compound flux arriving at each substrate cell using a transport code (see next section), one can describe the condition of the substrate locally by solving Eq. (5.22) for $\theta_{\mathrm{s,i}}$, the condition of each substrate cell. This gives a much better description of the substrate composition as a function of the oxygen flow.

Similarly, we describe the surface and bulk condition of the target. At the surface, three processes are described by the model: chemisorption, knock-on, and sputtering, which leads to the following relations:

$$\begin{aligned}
&\frac{2F}{z}\alpha\theta_{\mathrm{ms}}=Y_{\mathrm{c}}\theta_{\mathrm{cs}}I+\frac{I}{z}\beta\theta_{\mathrm{cs}}\\
&\frac{I}{z}\beta\theta_{\mathrm{cs}}+IY_{\mathrm{c}}\theta_{\mathrm{mb}}=Y_{\mathrm{m}}\theta_{\mathrm{ms}}I+\frac{2F}{z}\alpha\theta_{\mathrm{ms}}\\
&v_{\mathrm{s}}(t)\theta_{\mathrm{rb}}n_{\mathrm{o}}=I\theta_{\mathrm{rs}}Y_{\mathrm{r}}
\end{aligned} \tag{5.29}$$

The first equation describes the balance between chemisorption (left side) and sputtering of the chemisorbed atoms and knock-on events (right side). The second equation describes the metal surface balance. Knock-on processes of chemisorbed atoms result in an increase in the metal surface fraction. We must also take into account that metal from the bulk is transported toward the surface owing to target erosion. At the right side, two mechanisms leading to a decrease of the metal fraction are described, i.e. sputter removal and chemisorption. The third equation describes the balance between sputter removal of compound material and the transport of compound from the subsurface region to the surface region, defined by the target erosion speed v_{s}.

To include the reaction of the implanted and knock-on implanted reactive gas atoms with the target material, one needs to account for target erosion, implantation, and chemical reaction. This leads to the following equations:

$$\begin{aligned}
\frac{\partial n_{\mathrm{r}}(x,t)}{\partial t} &= 2fIp(x) - kzn_{\mathrm{r}}(x,t)n_{\mathrm{m}}(x,t) + I\theta_{\mathrm{cs}}\beta p_{\mathrm{c}}(x) - v_{\mathrm{s}}(t)\frac{\partial n_{\mathrm{r}}(x,t)}{\partial x} \\
\frac{\partial n_{\mathrm{m}}(x,t)}{\partial t} &= -kn_{\mathrm{r}}(x,t)n_{\mathrm{m}}(x,t) - v_{\mathrm{s}}(t)\frac{\partial n_{\mathrm{m}}(x,t)}{\partial x}
\end{aligned} \tag{5.30}$$

The first describes the time evolution of the concentration n_{r} of non-reacted implanted reactive gas atoms, while the second does the same for the concentration n_{m} of non-reacted target atoms. The amount of reactive gas atoms which becomes implanted depends on the mole fraction f of reactive gas molecules in the discharge. The directly implanted reactive atoms are distributed over the subsurface region according to the implantation profile $p(x)$. A similar approach can be used to describe the distribution of knock-on implanted atoms, i.e. $p_{\mathrm{c}}(x)$. As a result of target erosion, there is material transport toward the target surface (last term in both equations). The chemical reaction between both the reactive gas atoms and the target atoms is defined by their concentrations and the reaction rate constant k. In steady state, these equations simplify to

$$\begin{aligned}
v_s\frac{\partial n_r(x,t)}{\partial x} &= 2fIp(x) - kzn_r(x)n_m(x) + I\theta_{cs}\beta p_c(x) \\
v_s\frac{\partial n_m(x,t)}{\partial x} &= -kn_r(x)n_m(x)
\end{aligned} \tag{5.31}$$

The cascade of equations in the model can be solved quite easily by iteration. One assumes a given target subsurface reaction, i.e. θ_{rb}. For a given partial pressure of reactive gas, one can calculate, using Eqs (5.29), the target surface condition and the erosion rate. This enables the solution of Eqs (5.31), which describe the target subsurface condition. At steady state, the calculated reaction state should equal the initial value. If the value obtained is too high, the partial pressure (or the mole fraction), is altered, and the calculation is repeated. With the calculated surface and subsurface conditions, it is possible then to calculate the flow toward target, substrate, and pump. By summing these three flows, the target condition, the substrate condition, and the partial pressure as a function of the reactive gas flow can be calculated. Or stated differently, a hysteresis experiment can be simulated. To facilitate the use of this model, a downloadable program was written, which predicts the influence of different parameters on the hysteresis curves [43]. Essentially the program provides an output as shown in Figure 5.17. Comparing simulation with experimental results (see Figure 5.16) enables the understanding of the origin of the hysteresis effect. At low reactive gas flow, the partial pressure of the reactive gas, oxygen in this example, is negligible because most of it is consumed by the metal deposited on the substrate. Indeed, as Figure 5.17 shows, the target composition remains

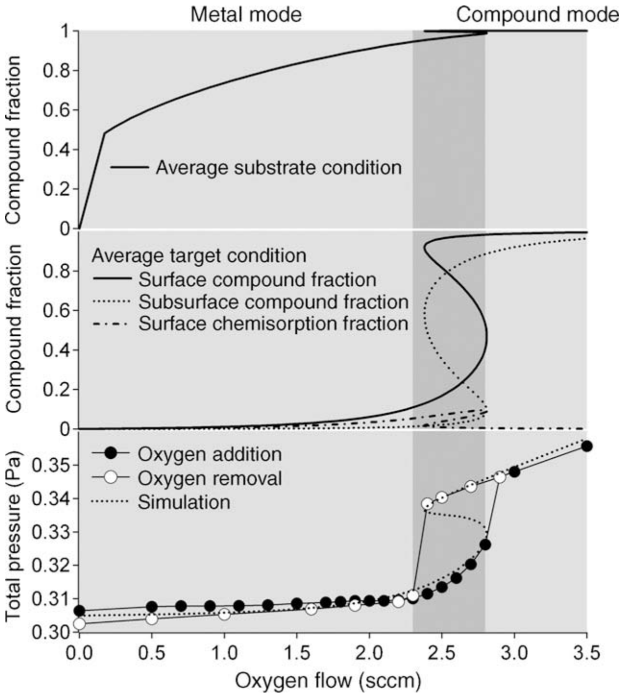

Figure 5.17: Simulation of the reactive sputter deposition process using RSD2009 [43]. The experimental results are shown in Figure 5.16.

almost unaffected (middle panel), especially in the subsurface region. Preferential sputtering enriches the surface region with the compound and, together with the chemisorption of oxygen, results in substantial surface oxidation. The difference between unaffected subsurface and oxidized surface regions can explain the small initial increase in discharge voltage noticed in the experiment during oxygen addition in the metal mode (see Figure 5.16). The oxidation of the surface region results in a decrease in the total sputter yield, as the compound material sputters less efficiently than the metal owing to a higher surface binding energy. Hence, less metal is deposited, and more reactive gas becomes available for target oxidation. An avalanche situation develops which results in complete and rapid oxidation of the substrate and the target. This also causes an abrupt change in the partial pressure and other deposition parameters such as discharge voltage. The simulation shows that within the hysteresis region (dark shaded area), the slope of the partial pressure vs flow curve is negative. Hence, this region is not stable under flow control. To return to metal mode from the compound mode, one needs to lower the oxygen flow to a value smaller than the critical flow measured during the flow increase. This behavior is due to the large difference in sputter yield between the metal and the compound.

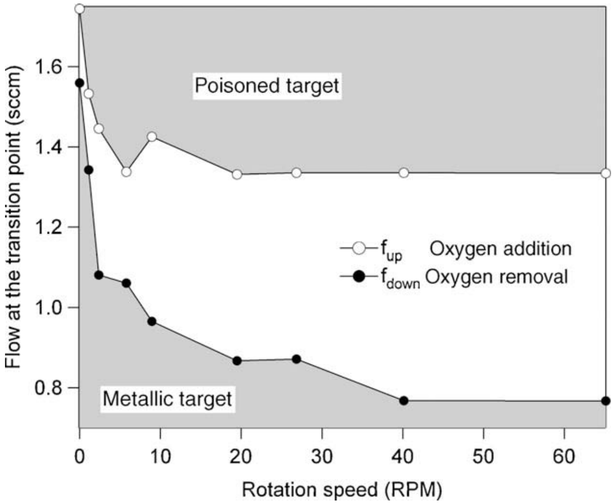

Figure 5.18: Flow at the transition points as a function of the rotation speed.

For rotating cylindrical magnetron, the hysteresis is also a function of the rotation speed. Figure 5.18 shows the behavior of the critical point as function of the rotation speed for the laboratory scale rotating magnetron depicted in Figure 5.11.

Understanding this behavior requires a time-dependent, rather than a steady-state, description of the reactive sputter process, because, owing to target rotation, processes which occur outside the racetrack influence the process as that region rotates into the discharge. Moreover, an additional process must be taken into account, i.e. redeposition of sputtered material onto the cathode [44].

5.5.3 Circumventing the Hysteresis Problem

Hysteresis behavior hinders the application of reactive magnetron sputter deposition. Indeed, when controlling the process by regulating the flow, one notices that the smallest change in the reactive gas flow and/or other deposition conditions can result in a runaway situation from metal mode to compound mode. Optimal use of reactive magnetron sputter deposition appears to require using a reactive gas flow close to the edge of the metal mode region, as this combines nearly stoichiometric compound layers with a high deposition rate. The problem with this is that minor perturbations in the discharge, which always occur, are amplified and move the system beyond its metastable operation point. However, several solutions are available. A first solution, as described by Berg et al. [40], requires a dramatic increase in pumping speed. In this situation, hysteresis will be avoided, as the reactive gas partial pressure in the vacuum chamber is to a large extent controlled by the pump, and not by the deposition process. However, this is not a cost-effective solution. An alternative approach was proposed by Sproul et al. [38]. The reactive gas flow is controlled by a feedback system which measures the partial pressure of the reactive gas, the optical emission spectrum of the metal, or the discharge voltage. So, one switches from flow control to partial pressure control. Indeed, as simulation results show (see Figure 5.17), if one interchanges pressure and flow axes, full control is possible and one can combine complete compound formation with a relatively high deposition rate. The disadvantage of this approach is the complexity and the cost of the equipment. Another solution is using conductive substoichiometric targets (e.g. TiO_{2-x} with x of the order of 0.2 [45]), for which only a low reactive gas flow is required, and generally the deposition process does not show a hysteresis behavior. However, substoichiometric target processing is more expensive and complicated as these targets are mostly ceramics. In conclusion, circumventing the hysteresis problem is possible, but it always comes with an additional cost and/or increased system complexity.

5.6 Moving Toward the Substrate

5.6.1 Sputtered Particles

All sputtered particles leaving the target can collide with the gas atoms present in the vacuum chamber during transit to the substrate. The same is true for ions which are neutralized and reflected at the target, and for negative ions formed at the target [46]. Collisions will alter particle energy, direction, and momentum, and therefore also the morphology and microstructure of the growing film (see next section). The most important parameter influencing gas phase transport is pressure.

Several models have been proposed [47] to simulate the transport of sputtered particles. Recently, Van Aeken et al. [48] have developed a user-friendly shareware model, SiMTRA (Simulation of Metal TRAnsport). This flexible model enables calculation of the energy, direction, and flux of sputtered particles incident on every defined surface in the vacuum chamber. The output is not only the deposition profile, but also the energy of the arriving particles on the substrate. The output of the code can be combined with the reactive sputter deposition model RSD2008, described in the previous chapter, enabling a more detailed description of the reactive sputtering process. Figure 5.19 shows the result of such a calculation. Oxidation of the substrate, here a tube with the magnetron source located at the top center of the tube, is tracked as a function of the oxygen flow. At low oxygen flows, only the material deposited at the bottom of the tube is fully oxidized (black). As the oxygen flow increases, all deposited material becomes oxidized. The transition from metal mode to compound mode occurs when the deposited material is nearly fully oxidized.

The SiMTRA model provides insight into the mechanisms controlling the transport of sputtered particles toward the substrate (Figure 5.20). The ejection positions of the sputtered

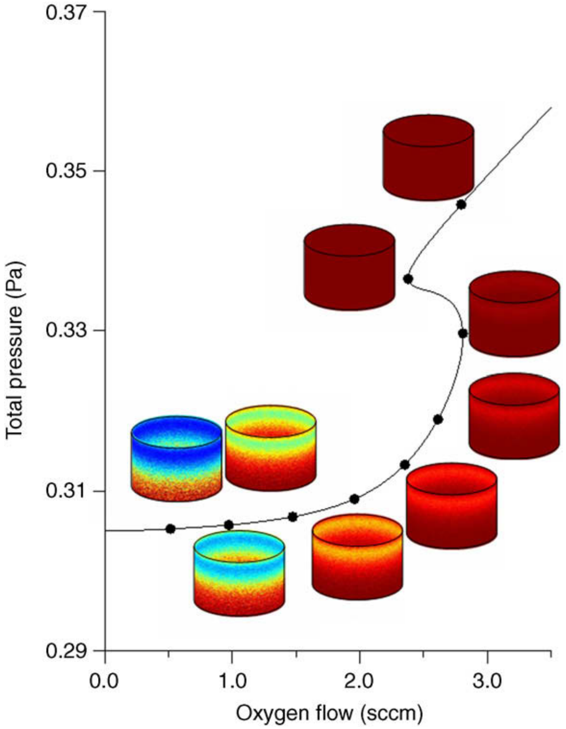

Figure 5.19: By placing a 5 cm diameter magnetron source in the upper part of a tube, the surface on which material is deposited is well defined, and the influence of the area of this surface and the deposition profile on the hysteresis behavior during reactive magnetron sputtering can be studied. The illustrations shows the result of a simulation in which the deposition profile is included. The oxidation of the deposited target material is shown on the cylinder. Black represents a fully oxidized surface, while white represents a pure metal surface. Experimental conditions: constant argon pressure 0.3 Pa, constant discharge current 0.43 A, pumping speed, 100 l/s. The tube had a diameter of 26 cm and a height of 53 cm. The oxygen was introduced at the bottom of the tube. The target material was Al.

particles are based on the (simulated) racetrack of the magnetron. One can use the Thompson equation (see Eq. 5.5) to describe the energy distribution of the sputtered particles, and the nascent angular distribution can be calculated using SRIM or can be based on experimental input. The model assumes that the sputtered particles are neutral atoms in the ground state, and these atoms only undergo elastic collisions with neutral gas atoms. For DC magnetron sputtering, this is a reasonable approach for two reasons. First, the ionization degree is generally very low. Most authors report an ionization degree of the order 0.1% and lower (e.g. [33, 49, 50]). Second, the sputtered particle density is much less than the gas density. The ratio between the sputtered particle density and the gas density depends on the pressure and the

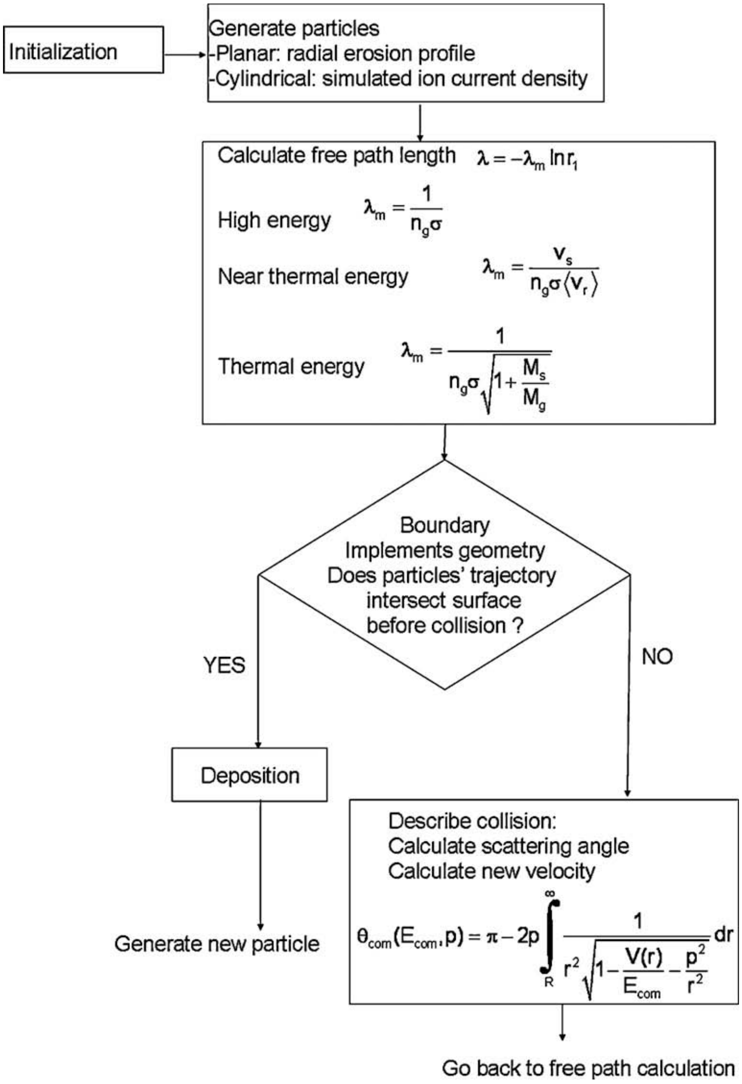

Figure 5.20: Flowchart for SiMTRA describing all steps during the transport of a sputtered particle toward the substrate. n_g: sputter gas density; σ: collision cross-section; v: velocity (subscripts s: sputtered atom; g: gas atom; r: relative); θ_{com} and E_{com}: polar scattering angle and kinetic energy in the center-of-mass system; p: impact parameter; $V(r)$: interaction potential; R: distance of closest approach.

power, but is of the order of 10^{-4} (e.g. [50, 51]). Based on these assumptions, the path of the sputtered atom can be described as a sequence of straight trajectories each terminated by a binary elastic collision with a gas atom, until deposition on a surface occurs. Classical scattering theory follows [27]. The free path length λ until the next collision is derived from a mean free path length λ_m as

$$\lambda = -\lambda_m \ln r_1 \tag{5.32}$$

with r_1 a random number uniformly chosen over the range]0,1]. The description of the mean free path length depends on the velocity of the sputtered particles v_s compared to the velocity of the gas atoms v_p. At high velocity ($v_s > 5v_p$), the gas atoms are considered stationary. When v_s drops below $5v_p$ the thermal motion of the gas atoms is taken into account. Finally, when the energy of the sputtered particles falls below $3/2\,kT$ the sputtered particle is considered thermalized.

5.6.2 *Other Particles Arriving at the Substrate*

Besides the arrival of sputtered particles (see Section 5.6.1), the flux of other particles arriving at the substrate is important as these particles determine the total energy and momentum flux toward the substrate and hence they play a crucial role in the thin film growth (see Section 5.7). The total energy flux per incoming metallic particle E_{tot} can be described as a linear summation of different contributions [52–56]:

$$E_{tot} = E_{cond} + E_{pl} + E_t + E_{sp} + E_{refl} + E_{gas} + E_{el} + E_{ion} \tag{5.33}$$

as summarized in Table 5.2.

Based on a combination of modeling, and measurements with a Langmuir probe, retarding field analyzer, quartz microbalance, and energy-resolved mass spectrometer, Mahieu et al. quantified the total energy flux and showed the relationship with the crystallographic orientation and microstructure of deposited TiN films [59, 60]. This connects the energy (and momentum) flux to properties of the films (such as hardness), and to deposition conditions. In the next section, we focus on the relationship between deposition conditions and microstructure.

5.7 Sputter-Deposited Thin Films: Morphology and Microstructure

Several authors have attempted to summarize the influence of deposition parameters on film morphology and microstructure in a single diagram. These diagrams are known as structure zone models (SZMs). The SZM best known in the sputter deposition community is the one published by Thornton [61], which shows microstructure and morphology as a function of deposition pressure and substrate temperature. This historically important model forms the basis of several studies (e.g. [62]). Recently, Mahieu et al. [63] published an extended structure zone model (ESZM) which has the advantage that it not only summarizes the influence of deposition parameters on film microstructure, but also provides insight into sputter-deposited thin film growth. Hence, film structure (microstructure and crystallographic orientation) is

Table 5.2: Different contributions to the energy flux toward the substrate

Particle	Energy contribution	Description and comments
Photons	E_{pl}	The energy flux due to plasma radiation. As discussed in Section 5.4.1, the average energy per ionization W is approximately 30 eV in an Ar discharge. However, the actual ionization energy of Ar is only 15.76 eV. Hence, approximately 14 eV will be transferred to the plasma per ionized Ar
	E_t	The energy flux due to thermal radiation from hot bodies in the vacuum deposition system
Atoms, molecules	E_{sp}	The energy flux due to the kinetic energy of the sputtered particles which, as shown in Section 5.2, is substantially larger then the thermal energy (see Figure 5.4)
	E_{cond}	The energy flux due the formation of a compound by a chemical reaction on the substrate and/or the condensation of a metallic species on the substrate
	E_{refl}	The energy flux due to neutralized and reflected working gas atoms. Just before impact at the target, a high energy ion will be neutralized and it can be reflected towards the substrate
	E_{gas}	The energy flux due to working gas atoms. Normally this contribution can be neglected, but the interaction of the sputtered particles with the gas (see Section 5.6.1) can result in gas heating, also known as gas rarefaction [57, 58]
Electrons	E_{el}	Energy flux due to incident electrons
Ions	E_{ion}	Energy flux due to the ion flux toward the substrate

plotted as a function of adatom mobility which depends on the energy flux per sputtered particle (see previous section); which in turn depends on the deposition parameters. To quantify the ESZM, it is necessary to calculate all energy flux contributions toward the substrate. In this section, we will discuss the ESZM.

5.7.1 Zone I Films

At low energy per incident particle, adatom mobility is low, and each particle will stick to the growing film at more or less the position at which it arrives. Stated differently, the adatoms have a low probability of overcoming the existing diffusion barriers. Hence, one refers to this part of the ESZM as the ‘hit and stick’ region. Formation of large, compact, crystalline islands is therefore not possible and only small crystallites can develop. Film structure has an amorphous appearance, and its crystallographic orientation is not preferential. The films are rough due to statistical, or kinetic, roughening and self-shadowing. Even for normal adatom incidence, overhang structures can be formed, shadowing the underlying layers and preventing further local growth. Such films typically have reduced density and high porosity and are classified as zone Ia films.

Film density can be improved by bombardment of energetic species (ions, fast neutrals, sputtered particles, and neutralized reflected ions). Bombardment results in knock-on events that destroy the overhang structures of zone Ia films. Voids between the columns of a zone Ia film begin to be filled, and a more dense columnar structure evolves. As the energetic bombardment only results in 'reorganization', the structure still has an amorphous appearance. This type of film can also be grown by using an ion beam incident at the substrate during thermal evaporation. The change in microstructure from zone Ia to zone Ib is not possible by just increasing the substrate temperature alone.

When the energy flux toward the substrate is increased, the adatoms will become more mobile, resulting in compact crystalline islands. So, in contrast to zone Ia and Ib, the grains in zone Ic will be faceted. Crystallographic diffraction scans in combination with electron microscopy show that only the crystal planes with lowest crystallographic normal growth rate will survive, and therefore the grains in zone Ic are terminated by these planes. The normal growth rate is strongly influenced by many parameters, but under common deposition conditions and low energetic bombardment, two parameters are important: the sticking coefficient of the adatoms versus crystallographic orientation and adatom mobility. A higher sticking coefficient results in a higher normal growth rate. The influence of the mobility is more complex. If the mobility is high, the adatom can reach the edge of the crystal or grain, where it can descend the step (depending on the Ehrlich barrier height). Hence, a high mobility is conducive to lateral growth, while low mobility results in a higher normal growth rate of the crystal plane. In the case of a rather low energy flux, what is characteristic for zone Ic, the probability that adatoms diffuse from one grain to another is low, owing to the small diffusion length. Hence, neighboring grains will not interchange adatoms and thus will not interact with each other. This results in a microstructure consisting of straight, clearly faceted columns as each grain grows independently in a direction perpendicular to the substrate. There is no competition among the growing columns. However, the tallest columns will capture more sputtered atoms and can shadow the adjacent columns. Nevertheless, little preferential out-of-plane orientation is observed.

5.7.2 Zone T Films

Further increasing the adatom mobility results in a microstructure arising from adatoms diffusing between adjacent grains. This results, in turn, in an overgrowth mechanism, different

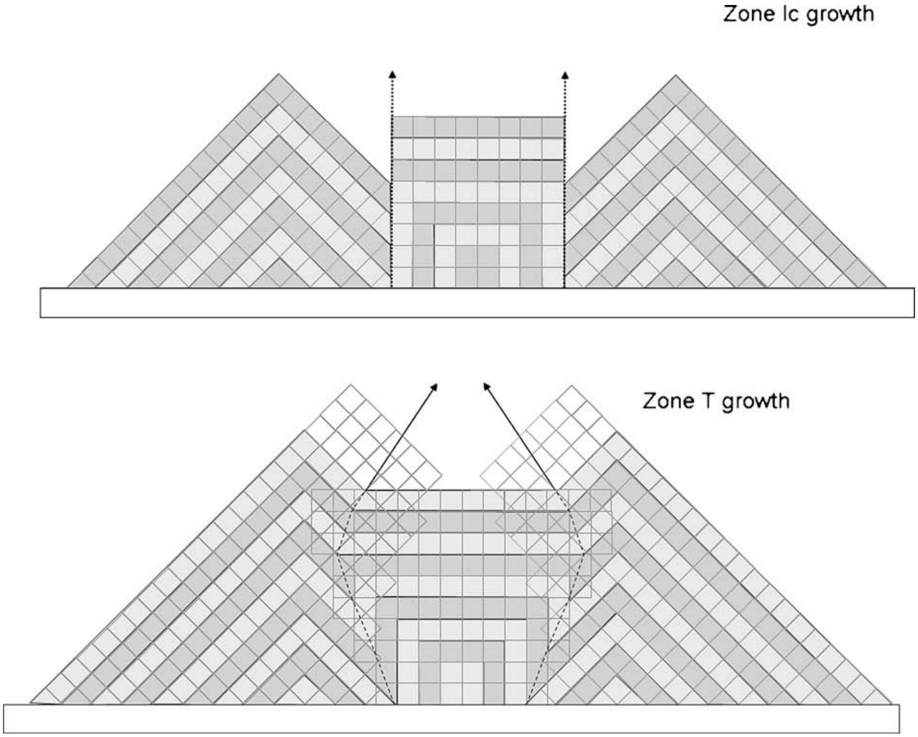

Figure 5.21: Schematic comparison between zone Ic and zone T growth. To indicate the identical normal growth rate of the planes of both grains, alternating coloring is used. In zone T, an overgrowth of one grain by an adjacent grain is observed.

from the shadowing mechanism discussed in the previous section. Initially, well-faceted grains will form on the substrate. The facets are defined by the planes with lowest normal growth rate. The out-of-plane orientation of these grains will be different if nucleation occurs randomly. Let us focus on two differently oriented grains. In zone T, the arriving adatoms have a high surface mobility, and can therefore diffuse from one grain to the other. Upon impingement of the two grains, a grain boundary is created. The position at the substrate of the grain boundary is fixed because restructuring grain growth (see zone II for a definition) is not possible under zone T conditions.

However, the direction of this grain boundary can change during the film growth owing to evolutionary growth. As depicted in Figure 5.21, the grains with the most tilted facets with respect to the substrate plane will overgrow other grains because they have the fastest geometric growth rate in the direction perpendicular to the substrate. This has an important consequence. At a given layer thickness, all grains merge toward the same crystallographic orientation. Thus, zone T films have properties which vary with thickness. So, summarizing this mechanism: owing to an evolutionary overgrowth, a film structure is obtained with a clearly faceted surface, V-shaped columns, and a preferential crystallographic orientation, corresponding to the orientation with the fastest geometric growth rate.

5.7.3 Zone II Films

The specific microstructure of zone T films is kinetically determined. At higher energy flux, additional processes can occur which one can summarize as restructuring grain growth. This includes processes such as ripening, cluster diffusion or grain boundary migration. The final result of these processes is actually the same, i.e. from the nucleation stage on, film growth evolves along a path which minimizes the total system energy. These restructuring grain growth processes are driven not only by the minimization of the island or grain surface area, but also by the minimization of the surface and interface energy and anisotropy in elastic constants (hence in strain energy density versus orientation). The first result is that the film consists of straight columns with a curved surface. As a result, column tops will, depending on the column diameter, not be perfectly flat but be slightly curved. A second important consequence of restructuring grain growth is the development of a preferential out-of-plane crystal orientation. Surface energy depends on the specific crystallographic plane. Hence, if restructuring grain growth drives the film to minimize the total surface energy, grains with a high-energy plane parallel to the substrate will be consumed by grains with a low-energy plane parallel to the substrate. Therefore, the resulting preferred out-of-plane orientation is the crystallographic orientation perpendicular to the plane of lowest surface energy. Owing to high surface diffusion and restructuring grain growth, shadowing will have a minor influence on growth. Hence, tilting the substrate to the incoming material flux will not cause significant inclination of the columns. Further increasing the energy flux increases the effects of restructuring grain growth. Thus, the columns forming the film will increase their diameter.

5.8 Conclusions

Several aspects of the sputter deposition process are still not completely understood. Fundamental points relating to the sputter process and the discharge include the quantification of the sputter yield of compounds, the emission of negative species from oxide and oxidized targets, the description of high-energy electron diffusion perpendicular to the magnetic field, and the understanding of the discharge voltage behavior during reactive magnetron sputtering. New trends, such as HIPIMS, bring new questions and problems. Hence, there is ongoing research toward a better description of this technique. However, many of the fundamental issues which are not yet understood do not hinder the application of this interesting technique. This explains the wide field of applications for sputter deposition.

References

[1] The Web of Science is part of the ISI Web of Knowledge Platform produced by Thompson Scientific. Available from: <http://apps.isiknowledge.com/>.

[2] The patent database Delphion is part of the Thomson Corporation. Available from: <http://www.delphion.com>.

[3] G. Carter, J.S. Colligan, Ion Bombardment of Solids, American Elsevier, New York (1968).

[4] L.I. Maissel, Applications of sputtering to the deposition of films, in: L.I. Maissel, R. Glang (Eds.), Handbook of Thin Film Technology, McGraw-Hill, New York (1970).

[5] G.K. Wehner, G.S. Anderson, The nature of physical sputtering, in: L.I. Maissel, R. Glang (Eds.), Handbook of Thin Film Technology, McGraw-Hill, New York (1970).

[6] M. Nastasi, J. Mayer, J.K. Hirvonen, Ion–Solid Interactions: Fundamentals and Applications, in: Cambridge Solid State Science Series, Cambridge University Press, Cambridge (2004).

[7] R. Behrish, W. Eckstein (Eds.), Sputtering by Particle Bombardment: Experiments and Computer Calculations from Threshold to MeV Energies, Springer, Berlin (2007).

[8] R.A. Baragiola, Phil. Trans. R. Soc. Lond. A 362 (2004) 29–53.

[9] V.S. Smentkowski, Prog. Surf. Sci. 64 (2000) 1–58.

[10] W.D. Westwood, Sputter deposition, AVS Education Committee Book Series, Vol. 2, AVS, New York (2003).

[11] H.H. Andersen, H.L. Bay, Sputter yield measurements, in: R. Behrish (Ed.), Topics in Applied Physics, Vol. 47, Sputtering by Particle Bombardment I, Springer, Berlin (1983).

[12] Sigmund, Phys. Rev. 184 (1969) 383–416.

[13] T. Ono, T. Kenmotsu, T. Muramoto, Simulation of the sputtering process, in: D. Depla, S. Mahieu (Eds.), Reactive Sputter Deposition, Springer, Berlin (2008).

[14] Y. Yamamura, H. Tawara, At. Data Nucl. Data Tables 62 (1996) 149.

[15] J.E. Mahan, A. Vantomme, J. Vac. Sci. Technol. A 15 (1997) 1976–1989.

[16] Stopping and Range of Ions in Matter, available from www.srim.org.

[17] J.F. Ziegler, J.P. Biersack, M.D. Ziegler, Stopping and Range of Ions in Matter, SRIM Co (2008).

[18] W. Möller, W. Eckstein, Nucl. Instr. Methods Phys. Res. B 2 (1984) 814–818.

[19] M.W. Thompson, Vacuum 66 (2002) 99–114.

[20] G. Falcone, Phys. Rev. B 28 (1988) 6398–6401.

[21] J.B. Malherbe, S. Hoffmann, J.M. Sanz, Appl. Surf. Sci. 27 (1986) 355–365.

[22] A. Anders, Surf. Coatings Technol. 200 (2005) 1893–1906.

[23] W.R. Grove, Phil. Trans. R. Soc. Lond. 142 (1852) 87–101.

[24] W.D. Davis, T.A. Vanderslice, Phys. Rev. 131 (1963) 219.

[25] M. Van Straaten, A. Bogaerts, R. Gijbels, Spectrochim. Acta B 50 (1995) 583–605.

[26] A. Bogaerts, M. Van Straaten, R. Gijbels, Spectrochim. Acta B 50 (1995) 179–196.

[27] M.A. Lieberman, A.J. Lichtenberg, Principles of Plasma Discharges and Materials Processing, John Wiley & Sons, New York (1994) 81.

[28] G. Buyle, Simplified model for the d.c. planar magnetron discharge, PhD thesis, Ghent University (2005) (available from www.draft.ugent.be).

[29] A.V. Phelps, Z. Lj Petrovic, Plasma Sources Sci Technol. 8 (1999) R21.

[30] H. Hagstrum, Phys. Rev. 96 (1954) 336.

[31] D. Depla, S. Mahieu, R. De Gryse, invited review, Thin Solid Films 517 (2009) 2825–2839.

[32] D. Depla, G. Buyle, J. Haemers, R. De Gryse, Surf. Coatings Technol. 200 (2006) 4329–4338.

[33] J.W. Bradley, S. Thompson, Y. Aranda Gonzalvo, Plasma Sources Sci, Technol. 10 (2001) 490–501.

[34] I.V. Svadkovski, D.A. Golosov, S.M. Zavatskly, Vacuum 68 (2003) 283–290.

[35] I. Petrov, F. Adibi, J.E. Greene, W.D. Sproul, W.-D. Munz, J. Vac. Sci. Technol. A 10 (1992) 3283.

[36] G. Estes, W.D. Westwood, J. Vac. Sci. Technol. A 6 (1988) 1845.

[37] A. Furuya, S. Hirono, J. Appl. Phys. 68 (1990) 304.

[38] W.D. Sproul, D.J. Christie, D.C. Carter, Thin Solid Films 491 (2005) 1–17.

[39] U. Helmersson, M. Lattemann, J. Bohlmark, A.P. Ehiasarian, J.T. Gudmundsson, Thin Solid Films 513 (2006) 1–24.

[40] S. Berg, T. Nyberg, Thin Solid Films 476 (2005) 215–230.

[41] D. Depla, S. Heirwegh, S. Mahieu, R. De Gryse, J. Phys. Appl. Phys. D 40 (2007) 1957–1965.

[42] D. Depla, S. Mahieu, R. De Gryse, Depositing aluminium oxide: a case study of reactive magnetron sputtering, in: D. Depla, S. Mahieu (Eds.), Reactive Sputter Deposition, Springer, Berlin (2008).

[43] RSD2008 and SIMTRA are available from www.draft.ugent.be.

[44] X.Y. Li, D. Depla, W.P. Leroy, J. Haemers, R. De Gryse, J. Phys. D Appl. Phys. 41 (2008) 035203(6 pp.).

[45] H. Poelman, H. Tomaszewski, D. Poelman, D. Depla, R. De Gryse, Surf. Interface Anal. 36 (2004) 1167–1170.

[46] S. Mahieu, D. Depla, Appl. Phys. Lett. 90 (2007) 121117/1–1121117/2.

[47] S. Mahieu, K. Van Aeken, D. Depla, Transport of sputtered particles through the gas phase, in: D. Depla, S. Mahieu (Eds.), Reactive Sputter Deposition, Springer, Berlin (2008).

[48] K. Van Aeken, S. Mahieu, D. Depla, J. Phys. D.: Appl. Phys. 41 (2008) 205–307.

[49] E. Martines, R. Cavazzana, G. Serianni, M. Spolaore, L. Tramontin, M. Zuin, V. Antoni, Phys. Plasmas 8 (2001) 3042–3050.

[50] I. Petrov, A. Meyers, J.E. Greene, J.R. Abelson, J. Vac. Sci. Technol. A 12 (1994) 2846.

[51] O. Leroy, L. de Poucques, C. Boisse-Laporte, M. Ganciu, L. Teulé-Gay, M. Touzeau, J. Vac. Sci. Technol. A 22 (2004) 192–200.

[52] S.D. Ekpe, S.K. Dew, J. Vac. Sci. Technol. A 21 (2003) 476.

[53] T.P. Drüsedau, T. Bock, T.M. John, F. Klabunde, W.J. Eckstein, Vac. Sci. Technol. A 17 (1999) 2896.

[54] R. Wendt, K. Ellmer, K. Wiesemann, J. Appl. Phys. 82 (1997) 2115.

[55] H. Kersten, G.M.W. Kroesen, R. Hippler, Thin Solid Films 332 (1998) 282.

[56] H. Kersten, E. Stoffels, W.W. Stoffels, M. Otte, C. Csambal, H. Deutsch, R.J. Hippler, Appl. Phys. 87 (2000) 3637.

[57] D.W.J. Hoffman, Vac. Sci. Technol. A 3 (1985) 561.

[58] S.M.J. Rossnagel, Vac. Sci. Technol. A 6 (1988) 19.

[59] S. Mahieu, D. Depla, R. De Gryse, Surf. Coatings Technol. 202 (2008) 2314–2318.

[60] S. Mahieu, D. Depla, topical review paper, J. Phys. D: Appl. Phys. 41 (2009).

[61] J.A. Thornton, J. Vac. Sci. Technol. 11 (1974) 666–670.

[62] I. Petrov, P.B. Barna, L. Hultman, J.E. Greene, J. Vac. Sci. Technol. A21 (2003) S117.

[63] S. Mahieu, P. Ghekiere, D. Depla, R. De Gryse, Thin Solid Films 515 (2006) 1229–1249.

CHAPTER 6

Ion Plating

6.1 Introduction

Most deposition processes are concerned with the source of the depositing material. Ion plating [1, 2] is a physical vapor deposition (PVD) process that utilizes concurrent or periodic bombardment of the substrate and depositing atoms of film material by atomic-sized energetic particles. The bombardment prior to deposition, sputter cleans the surface. Bombardment during deposition is to obtain good adhesion, densify the depositing material, aid in chemical reactions, modify residual stress, and otherwise modify the structure, morphology, and properties of the depositing film or coating. Ion plating is also called ion assist (IA) deposition, ionization assisted deposition (IAD) [3, 4] or ion vapor deposition (IVD) [5]. Bombardment prior to deposition is used to sputter clean the substrate surface. Bombardment during the initial deposition phase can modify the nucleation behavior of the depositing material such as the nucleation density and interface formation. During deposition the bombardment is used to modify and control the morphology and properties of the depositing film such as film stress and density. It is important, for best results, that the bombardment be continuous between the cleaning and the deposition portions of the process in order to maintain an atomically clean interface.

In ion plating the energy, flux and mass of the bombarding species along with the ratio of bombarding particles to depositing particles, are important processing variables. The depositing material may be vaporized by evaporation, sputtering, or arc vaporization, or by decomposition of a chemical vapor precursor (chemical ion plating (CIP)). The energetic particles used for bombardment are usually ions of an inert or reactive gas (reactive ion plating) or, in some cases, ions of the condensing film material (‘film ions’, IPVD) [6]. Ion plating can also be done using periodic bombardment if the deposit build-up between bombardment cycles is small (1–5 atomic layers) such as with a rotating drum type substrate holder. If there is too much deposit build-up between bombardment cycles a layered structure will be generated.

Ion plating can be done in a plasma environment where ions for bombardment are extracted from the plasma or it may be done in a vacuum environment where ions for bombardment are formed in a separate ‘ion gun’ as shown in Figure 6.1b. The configuration shown in

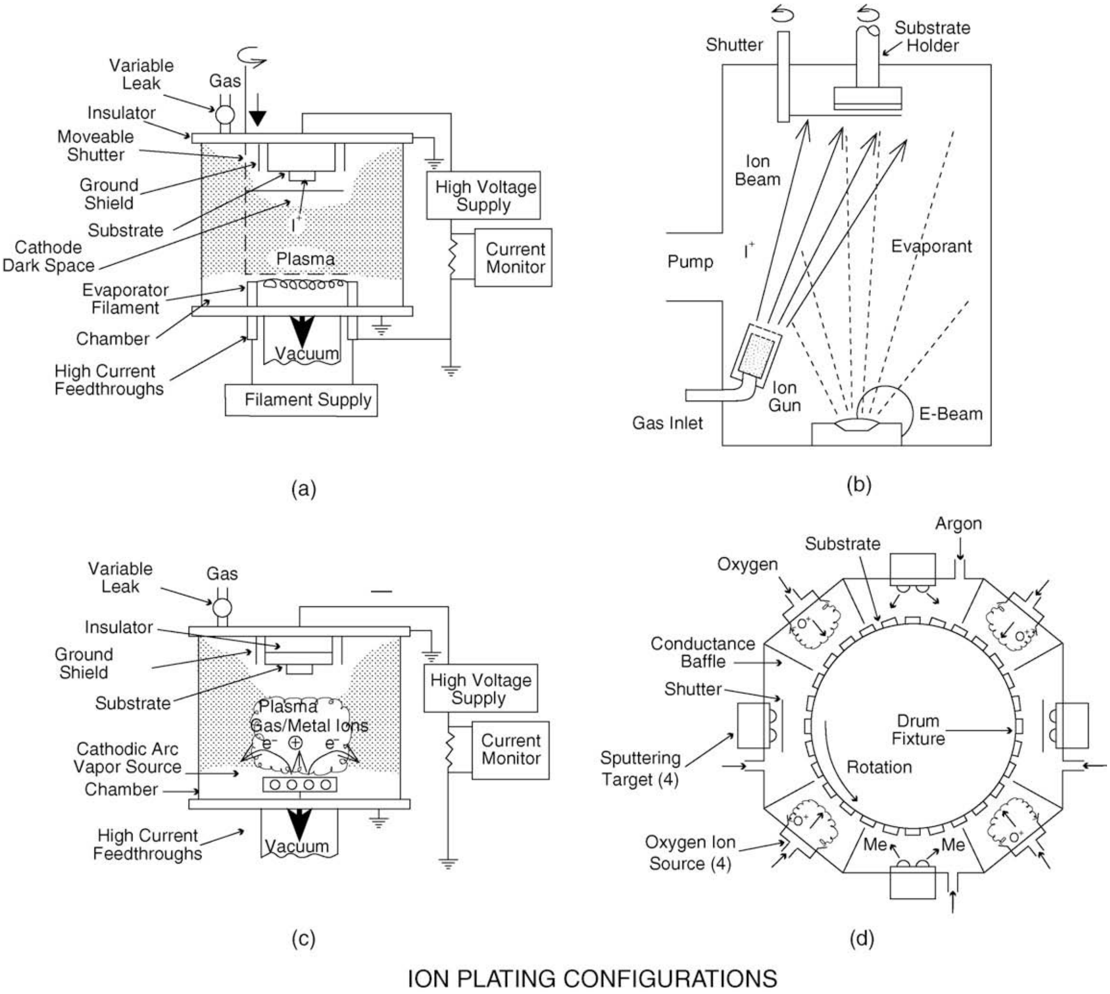

Figure 6.1: Ion plating configurations: (a) thermal evaporation source with bombardment from a plasma; (b) electron beam evaporation source in vacuum with bombardment from an ion source; (c) arc vapor source with bombardment from a plasma; and (d) alternately, deposition from a deposition source and bombardment from an ion source (alternating ion plating). (Adapted from SVC Education Guides to Vacuum Coating Processing – Fundamentals of Ion Plating (2009), with permission.)

Figure 6.1(b) is often called ion beam assisted deposition (IBAD) or ion beam enhanced deposition (IBED) [7]. The configuration shown in Figure 6.1(d) has been called alternating ion plating [8] and uses broad beam ion sources [9]. By using a reactive gas or vapor in the plasma, films of compound materials can be deposited (reactive ion plating). Bombardment by atomic sized particles may be intentional or unintentional depending on the deposition conditions or configuration. Densification by bombardment with atomic sized particles is often called atomic peening.

6.2 Bombardment: Surface and Near-Surface Effects

When an atomic-sized particle hits a surface it gives up energy by momentum transfer. If the particle is ionized it also gives up its energy of ionization (a few eV to several tens of eV). This energy release is confined to a small area on the surface. As the particle energy is increased the total energy transferred is increased. Most of the energy from the bombardment goes into heating. Figure 6.2 shows the surface and near-surface effects of bombarding particle energies in the few tens of eV to few thousand eV range [10].

The energy from the momentum of the bombarding particle is transferred to atoms in the surface and causes a collision cascade into the near-surface region. The collision cascade can cause a surface atom to be ejected (sputtered; see Chapter 5). The bombarding particle may be reflected from the surface as a neutral with appreciable residual energy. If the gas pressure is higher than about 5 mtorr the reflected and sputtered atoms will collide with gas atoms and become ‘thermalized’ and scattered before they reach the substrate. Some may return to the

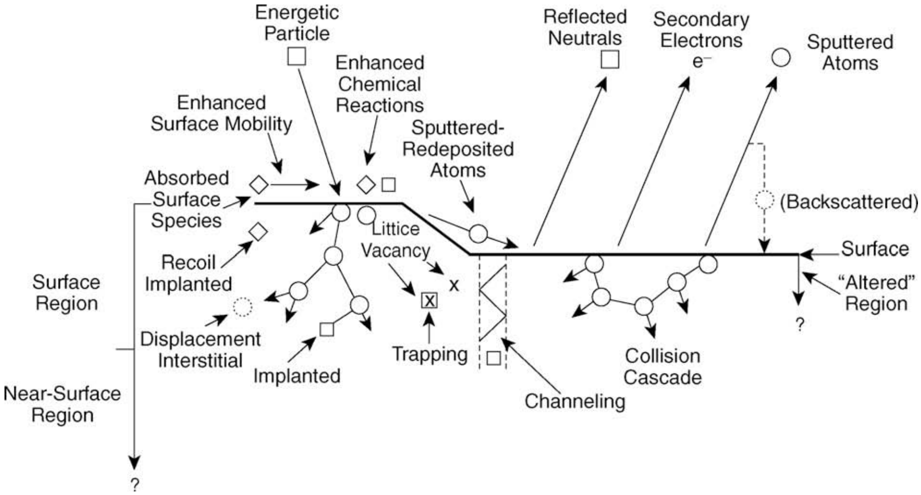

Figure 6.2: Schematic depiction of the effect of energetic particle bombardment on the surface and near-surface region of a solid [10].

surface. Particle bombardment also causes ejection of electrons that will be accelerated away from a surface that is at a negative potential.

The energy of bombardment can cause a variety of changes in the near-surface region. The collision cascade may cause atomic displacement, creating lattice defects and lattice stress. The energetic particle may be trapped (subplanted) into the near-surface region. As a rule of thumb when bombarding with argon ions with less than 200–300 eV of energy, argon atoms will not be retained in the bombarded surface.

In order for a film or coating to form by ion plating it is necessary for the flux of depositing atoms to be greater than the number of atoms being sputtered. This means that the surface shown in Figure 6.2 is continually being buried by new material. In the case of reactive deposition with nitrogen or oxygen the exposed surface material must react with the reactive species before it is buried since, in general, there will be little diffusion during deposition.

6.3 Bombardment: Effects on Adhesion, Film Growth, and Properties of the Deposited Material

The structure zone models for vacuum evaporation (Movchan and Demchiskin model) and sputter deposition (Thornton model) [11, 12] both show a low-density, high surface area morphology when the deposit is made on a substrate with a temperature below half of the melting point (in degree, Kelvin) of the material. This columnar (‘matchstick’) morphology develops for both crystalline and amorphous materials.

Figure 6.3 shows sputtered deposited chromium without and with concurrent argon ion bombardment [13]. The columnar growth morphology and the effect of ion bombardment on the growing film have been modeled [14, 15]. The models indicate sputtering and redeposition as well as knock-on atoms filling the open spaces and voids in the growing film. Sputtering and redeposition also help in macroscopic surface coverage. The flux, mass, and energy of the bombarding species, as well as the deposition rate and angle of incidence of the depositing flux, determine to what degree the deposit is densified.

Energy from the bombarding particle will be deposited in a very small area/volume but will represent a very high local temperature. The amount of energy available locally can determine how an adatom nucleates and condenses. If the amount of energy is small – as in the case of thermally evaporated atoms (condensation energy) or sputtered atoms that have been thermalized (condensation energy plus a small amount of thermal energy) – the adatom will be quenched in position before it reaches its lowest energy configuration, and the deposit will be less than fully dense, have a tensile stress, and develop a columnar structure.

If bombardment adds a small amount of energy (a few eV), the adatom will have a higher surface mobility and in some cases may develop an epitaxial structure [16]. At higher

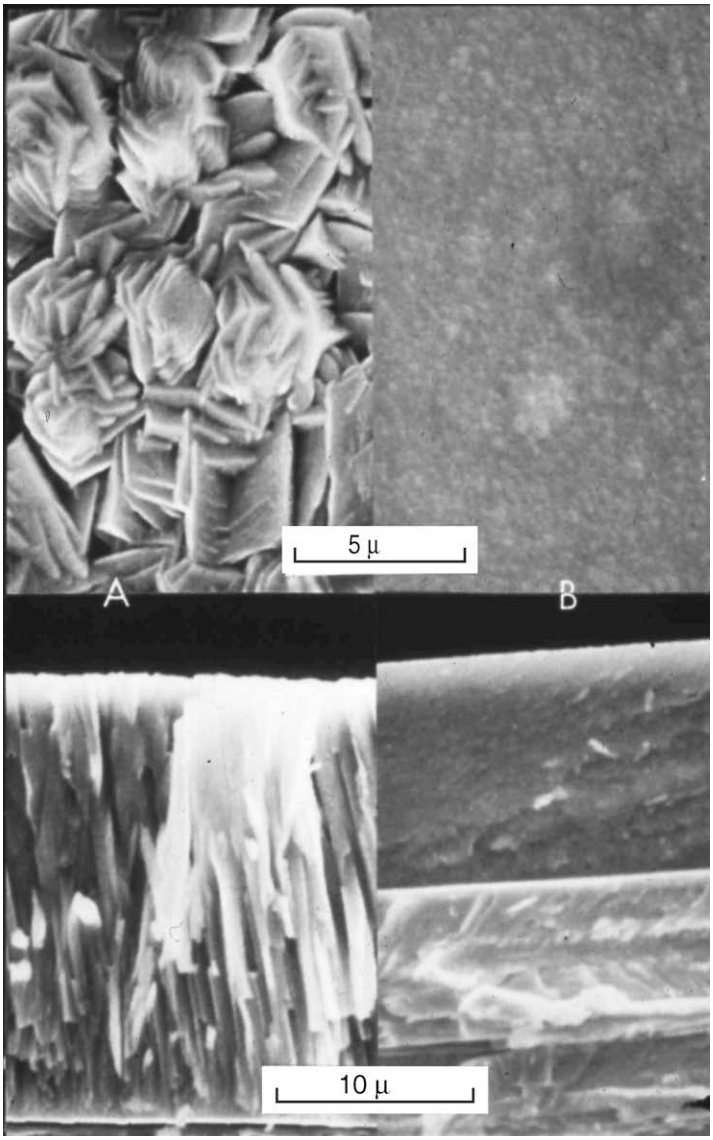

Figure 6.3: Fracture cross-section (bottom) and surface morphology (top) of a thick RF sputter deposited chromium deposit: (A) without a bias (no bombardment) and (B) with concurrent bombardment (−500 V bias on the substrate) [13].

bombarding energies, the adatoms and surface atoms are knocked about, thus densifying the deposited material. However, if the atoms are stuffed into the atomic structure by too much bombardment, they will develop a high compressive stress and in some cases an unusual atomic arrangement such as diamond-like carbon (DLC). If the bombarding particle is an ion, it will also release its energy of ionization as it bombards the surface.

Reactive deposition processes present additional considerations. In reactive deposition, the reacting species may release energy (exothermic) to form the compound. This requires a three-body collision in the gas phase or a two-body collision on a surface. This is why chemical reaction generally does not occur in the gas phase. This local energy release on the surface has to be added to the energies already discussed. In reactive deposition, the depositing surface atoms must react with the reactive species before they are buried and become unavailable for reaction. In many cases the reactive species have been 'activated' (ionized or excited) in the plasma, which makes them more reactive. When performing reactive sputter deposition, it is common to have both a heavy gaseous species (argon) mixed with the lighter reactive species (nitrogen, oxygen). A key component of reactive sputter deposition is to have good control of the partial pressure of the reactive gas(es) in the chamber.

In addition to reactive deposition by continuous bombardment, reactive deposition can be performed by using a rotating drum type substrate fixture and periodically depositing a few monolayers of one material, then bombarding it with a reactive material, usually from a broad beam (gridless) ion source [17, 18] as shown in Figure 6.1(d). By repeating the process a thick deposit can be built up [19]. Figure 6.4 shows a gridless end Hall ion source.

Obtaining the desired properties by bombardment with massive energetic particles often requires control of the flux and energy of the bombarding particles and the flux of depositing

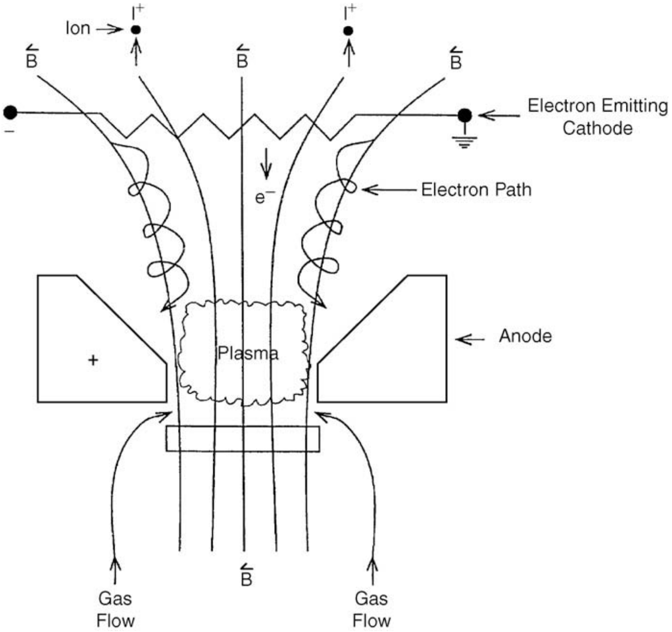

Figure 6.4: Gridless end Hall ion source. (From SVC Education Guides to Vacuum Coating Processing (2009) – Broad beam reactive plasma sources – 1: DC sources, with permission.)

atoms. Unless film ions are primarily being used (as is the case in arc vapor deposition or High Power Impulse Magnetron Sputtering – HPIMS), the incorporation of gaseous atoms in the deposit is undesirable, and so the bombarding energy should be less than 300 eV. The flux of the bombarding species can be difficult to determine. Measuring the energy of massive neutral particles is complicated and requires a technique such as a time-of-flight mass spectrometry.

6.4 Sources of Depositing Material

The properties of films and coatings deposited by the ion plating process depend primarily on the deposition conditions on the growing surface and minimally on the source of the depositing atoms/molecules.

Vacuum evaporation is generally performed either with a resistively heated evaporation source or using high-voltage electron beam heating. When using resistive heating a plasma can be established using an electrically isolated substrate holder such as a cathode or radio frequency (RF) electrode or by having an auxillary plasma source such as an RF induction coil or a hot filament–cathode plasma source between the evaporation source and the substrate. In order to establish a plasma the pressure in the chamber must be raised to about 0.5–15 mtorr, depending on the power source. This pressure does not affect the evaporation of the source material.

Higher pressures increase the probability of gas scattering and three-body collisions that give rise to vapor phase nucleation (‘sooting’) of the evaporated material. In a plasma these particles will become negatively charged and will be suspended in the plasma. If the substrate holder is electrically isolated and biased negatively the particles will not deposit on the substrates. Scattering of evaporated particles in the plasma will tend to increase the surface coverage to out-of-line-of-sight to the evaporation source.

High-current, low-voltage electron beams from hot hollow cathode electron emitting sources can be used to thermally evaporate material [20, 21]. The electrons will also form a plasma if a gas (e.g. Ar) is present. Depending on the electron flux, high ion density plasmas can be formed between the substrate and the evaporating material as shown in Figure 6.5.

Establishing a plasma in a high-voltage, focused electron beam evaporation system is not generally a good idea since the positive ions rapidly sputter away the electron emitting filament, which is at a high negative potential. High-voltage electron beam evaporators can be used with a plasma by having the electron emitter in a separate differentially pumped chamber where the pressure is low. The electron beam is extracted into the plasma chamber through a small, low-conductance hole [22].

Hollow cathode arc activated electron beam evaporation is performed by using one or more electron emitting hollow cathodes to inject electrons into the gas and vapor near the substrate

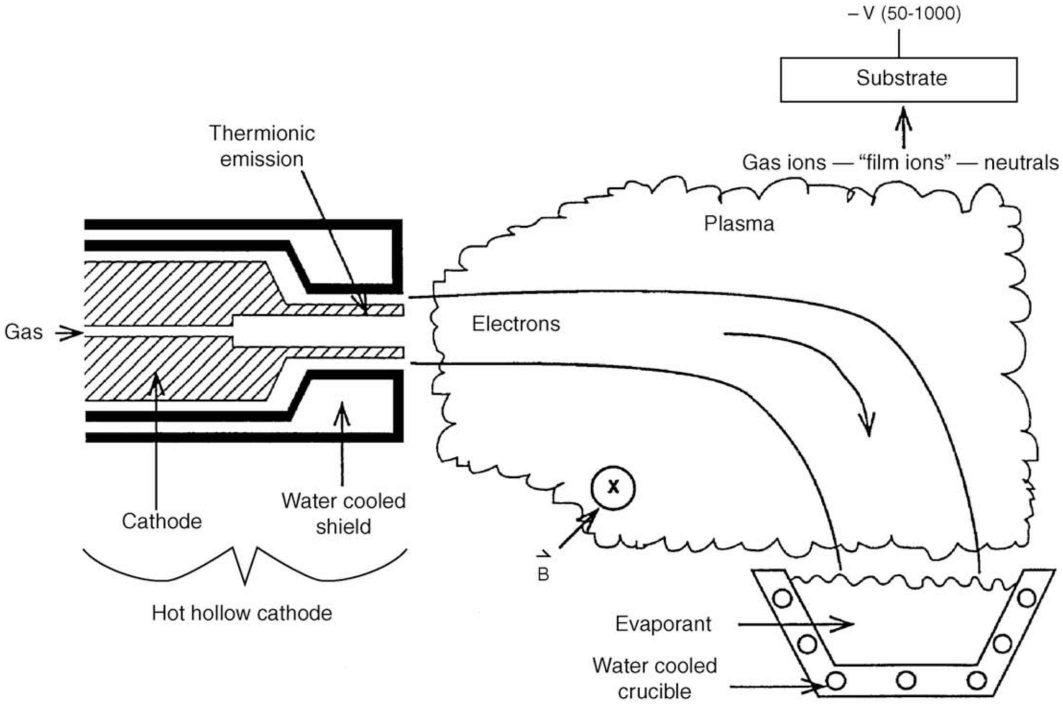

Figure 6.5: Hollow cathode electron source for electron beam melting/evaporation [38].

[23, 24]. The electrons ionize gases (Ar, O, N, C_2H_2) and a small portion of the depositing vapor. The electrons from the hollow cathode can be distributed in defined ways using a magnetic field between the cathode and the anode. This technique is particularly useful in depositing insulating films since charge build-up on the depositing surface (self-bias) will be negative and controlled by the electron temperature in the plasma.

Plasma-based sputter deposition is ideal for ion plating since the plasma is present to allow bombardment of the depositing material. When using a non-magnetron DC configuration for sputtering the substrate will be bombarded with electrons accelerated away from the cathodic target. In a magnetron sputtering configuration the magnetic field should be configured so as to let some electrons escape from the magnetic confinement and form a plasma between the source and the substrate (unbalanced magnetron sputtering, linked field magnetron sputtering) [25].

The term ionized physical vapor deposition (IPVD) refers to using a plasma generated between the vapor source (evaporation, sputtering) to enhance the ionization of the vapor species [26, 27]. The plasma may be formed by an RF coil, a hollow cathode electron emitter, or a hot filament electron emitter. Some authors place high-power pulsed magnetron sputtering (HIPPMS) in this category because of the high ionization fraction of the vaporized material.

In 1999 a technique for HIPPMS, also called high-power impulse magnetron sputtering (HPIMS or HIPIMS), which uses short pulses of very high power to sputter a target was published [28–31]. Peak powers may be as high as 3 MW at greater than 1 A/cm^2 when using a low duty cycle (0.1 5%) and pulsing frequencies up to a few kHz. This technique generates pulses of highly ionized pulses of the depositing material [32]. Low-power sputtering with a superimposed high-power pulse may be used to increase the overall deposition rate [33].

Ion plating using ion beam ('ion gun') sputtering in a good vacuum may be done by using a second ion gun in the system to bombard the growing deposit. If the substrate or depositing material is not electrically conductive the ion beam may be neutralized by adding electrons to the ion beam, making it a plasma beam to prevent surface charge build-up [34, 35].

Cathodic arc vaporization results when a cathodic arc 'runs' over the surface of the source of material as shown in Figure 6.1(c). A large fraction of the vaporized material is ionized and may be accelerated to the substrate as 'film ions' [36, 37].

Arc vaporization, where a large fraction of the vaporized material is ionized, can be formed in an arc with a consumable anode (anodic arc). A hollow cathode can be used to evaporate material through a dense electron cloud so as to increase ionization of the evaporated material, as shown in Figure 6.5 [38–40].

6.5 Sources of Bombarding Particles

The most common energetic particles for bombardment are energetic gaseous ions. When a plasma is present, ions may be accelerated to the surface by having a negative bias on the surface. The same types of waveforms used for sputtering [24] can be used for biasing. These include continuous DC, mid-frequency (MF) pulsed DC, bipolar pulsed power, and RF.

Energetic ions can be formed in ion sources and used to bombard the deposit. Ion sources can be from a grid extraction ion source (gun) where the ions are relatively monoenergetic or from a broad-beam ion source where there is a spectrum of ion energies.

High-energy neutral atom bombardment can have the same effects as high-energy ion bombardment. At low pressure, high-energy neutrals are formed by reflection of bombarding ions from the sputtering cathode [41, 42]. The sputtered atoms also leave the target surface with a high energy. These high-energy neutrals reach the substrates with high energies because of the long mean free path for collision at low pressures [43]. High-energy neutrals can also be formed by charge exchange between a high-energy ion and a low-energy neutral [44]. Figure 6.6 shows the film stress generated by sputter deposition as a function of gas pressure in

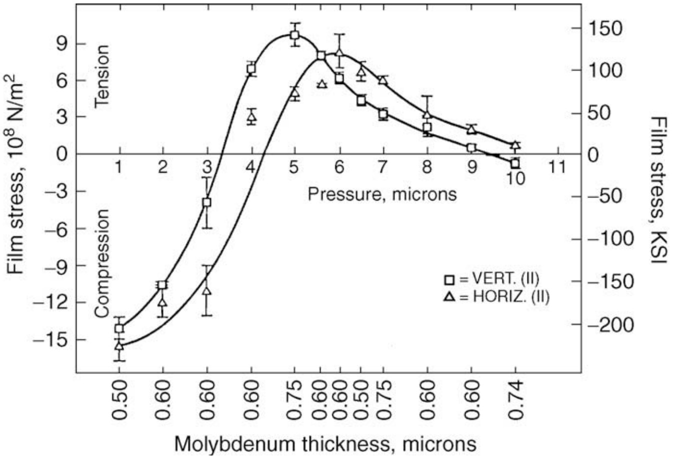

Figure 6.6: Stress as a function of processing pressure due to high-energy neutral bombardment during deposition [44].

a post cathode magnetron sputtering system [45, 46]. This source of energetic bombardment is often an uncontrolled variable of sputter deposition. From Figure 6.6 it can be seen that small changes in pressure can give big changes in the stress in the deposit.

In arc vaporization, IPVD, HIPPMS [47], pulsed laser deposition (PLD) [48, 49], and hollow-cathode gas-flow sputtering [50, 51], ions of both the gaseous species and the film material (film ions) may be accelerated to the depositing material. It has been shown that the thermal load on the substrate is less with HIPIMS than with a DC discharge [52].

In some cases, where the vapor originates from a sputtering source having two components of different electronegativities, negative ions may be formed and accelerated away from the negative source. If the substrate is at ground potential and in-line-of-sight, it will be bombarded by high-energy negative ions [53–55]. This is a particular problem with depositing superconducting compounds containing oxygen (e.g. $YBa_2Cu_3O_7$).

6.6 Substrate Potential

Figure 6.7 shows some of the types of fixtures used in vacuum deposition technologies. In some cases the substrate holder is fixed and may be easily electrically isolated and a bias potential applied. In other cases the substrate holder is moving and biasing the substrates becomes more difficult. If water cooling is used on the substrate holder there should be an electrical break in the tubing and deionized (DI) water should be used.

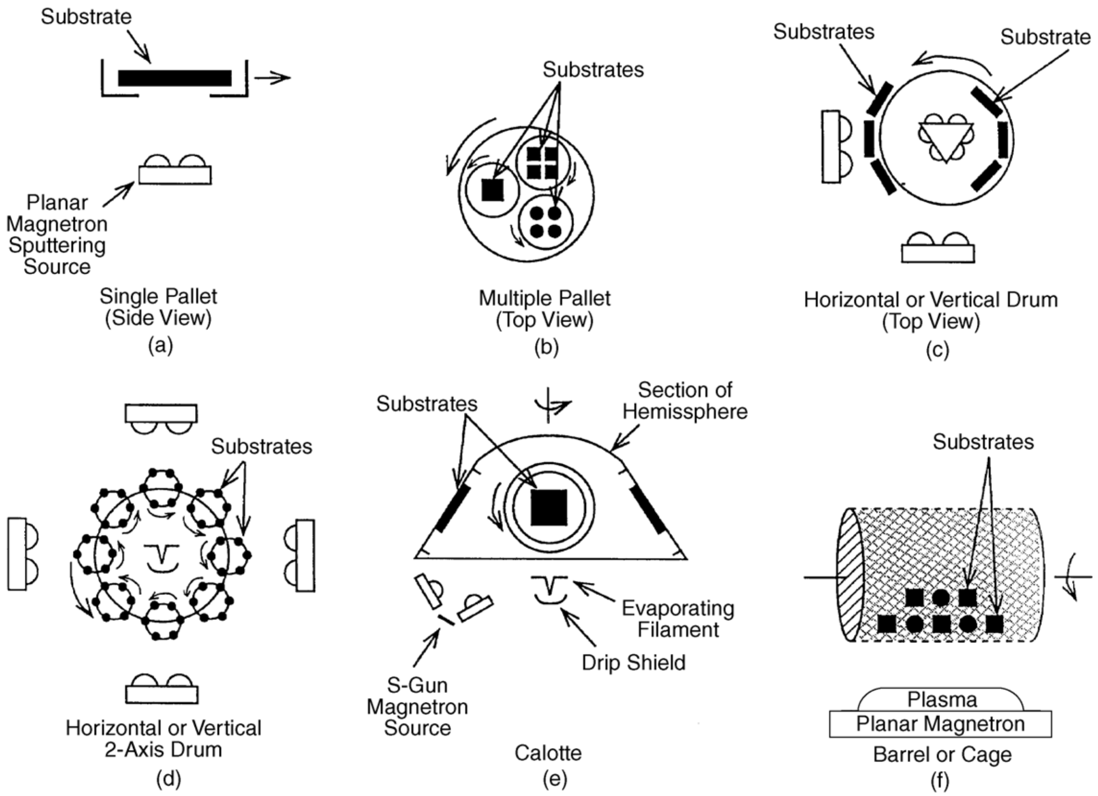

Figure 6.7: Fixtures for holding substrates. (From SVC Education Guides to Vacuum Coating Processing (2009) – Fixtures and Tooling, with permission.)

Figure 6.8 shows a ‘barrel ion plating’ fixture that allows coating of small parts being ‘tumbled’ inside a barrel/cage at high voltage [56]. This technique is used for aluminum coating fasteners for the aerospace industry to prevent galvanic corrosion [5].

As with sputtering there are a number of types of voltage waveforms that can be used to bias substrates. These include continuous DC, low-frequency (50 Hz) AC, pulsed DC, bipolar pulsed power,[1] mid-frequency (20–250 kHz) AC, RF, high-impulse power, etc.

As with reactive sputter deposition of insulating compounds a pulsed DC, mid-frequency AC, and bipolar pulsed AC,[1] or RF bias on the depositing insulating material is used to prevent arcing. The pulse bias may be at the same or different frequency [57] as the sputtering frequency.

---

[1] Some authors use the term bipolar pulsed DC for this waveform. The author prefers the term bipolar pulsed power since if you sent the waveform through a full wave rectifier it would not come out bipolar.

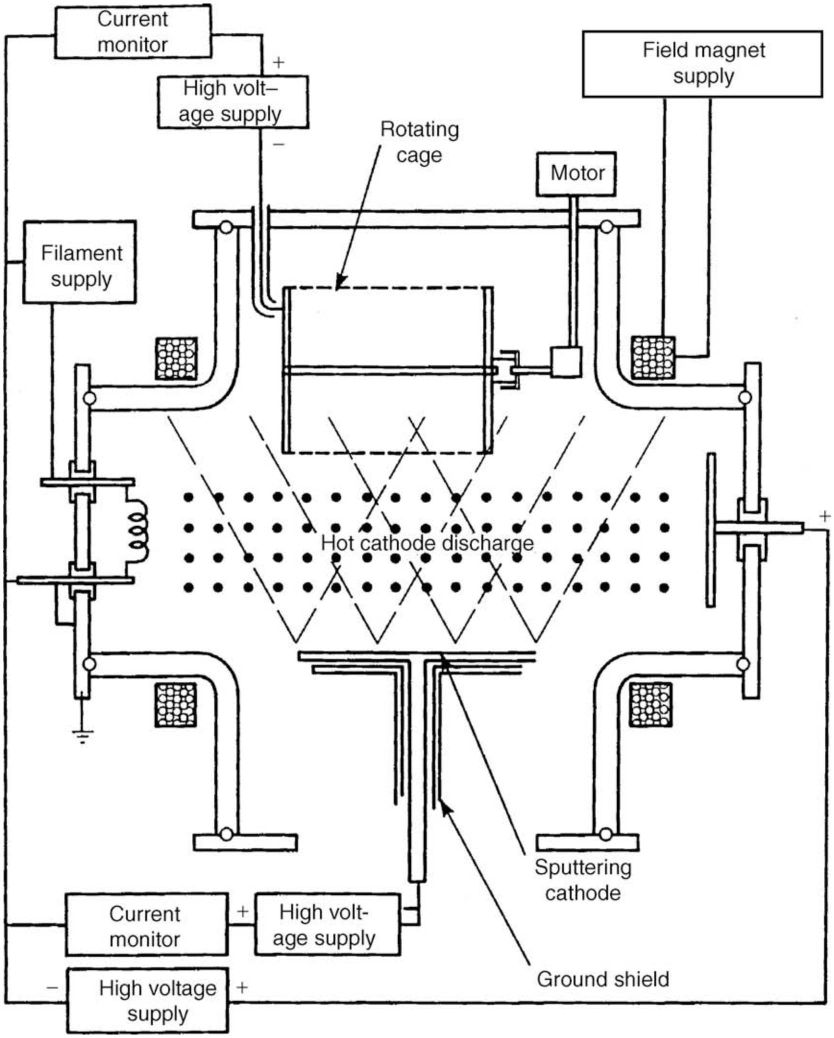

Figure 6.8: Barrel ion plating configuration [63].

In pulsed DC sputtering there is a significant large positive overshoot as the pulse is turned off owing to the inductance in the circuit. This raises the plasma potential and causes energetic ions to bombard the substrate [58].

The electron temperature in a plasma determines the self-bias on an insulating surface or a surface with a floating potential (ungrounded) in contact with the plasma. The self-bias may be from a few volts to several hundred volts. Figure 6.9 shows a technique to bias an insulating film or floating substrate holder using an electron emitting source and magnetic confinement to form a plasma and induce a high negative potential on the electrically floating or insulating surface [59].

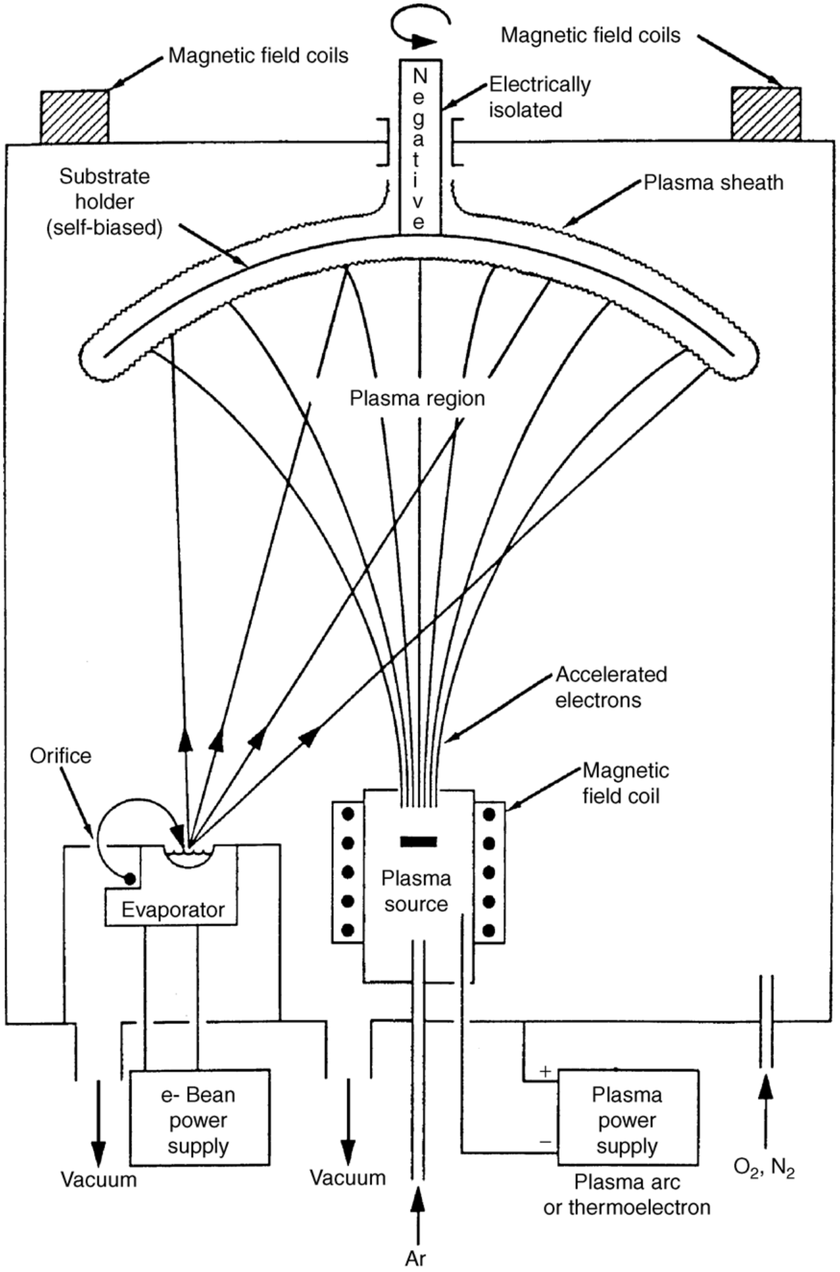

Figure 6.9: Self-bias generated by accelerating electrons away from a source and magnetically confining them so they strike an electrically floating substrate or substrate holder [59].

6.7 Some Applications of Ion Plating

Ion plating is used to deposit adherent coatings, dense coatings, and conformal coatings on complex surfaces, and to tailor coating properties such as stress, density, grain size, and crystallography. Some specific examples are:

- adhesion of low shear metal lubricants on metal surfaces, e.g. bearings for X-ray tubes
- aluminum coating of aircraft fasteners to prevent galvanic corrosion (IVD)
- corrosion protective coatings on materials with coherent oxides without removing too much material [60, 61]
- coatings on strip steel [62]
- coating on aero engine parts [51]
- densification of high and low index of refraction films on optical components [59, 63]
- hard coatings of compound materials (Ti, Al, Zr, Cr – O, N, C, B) on tools, injection molds, etc. [64]
- adhesion layer ('strike') for subsequent electroplating of materials such as Zr, U, and Ti [65].

References

[1] D.M. Mattox, Film deposition using accelerated ions, Electrochem. Technol. 2 (1964) 295.
[2] H.K. Pulker, Ion plating as an industrial manufacturing method, J. Vac. Sci. Technol. A10(4) (1992) 1669.
[3] A. Matthews, Developments in ionization assisted processes, J. Vac. Sci. Technol. A3(6) (1985) 2354.
[4] S.M. Rossnagel, J.J. Cuomo, W.D. Westwood, Handbook of Plasma Processing Technology: Fundamentals, Etching, Deposition, and Surface Interactions, Noyes Publications (1990).
[5] IVD (Ion Vapor Deposition) – Military Specification MIL-C-83488.
[6] U. Helmersson, M. Lattemann, J. Bohlmak, A.P. Ehiasarian, J.T. Gudmundsson, Ionized physical vapor deposition (IPVD): a review of technology and applications, Thin Solid Films 513 (2006) 1–24.
[7] C. Weissmantel, G. Reisse, H.J. Erler, F. Henny, K. Beuvilogue, U. Eberbach, C. Schurer, Thin Solid Films 63 (1979) 315.
[8] S. Schiller, U. Heisig, K. Goedicke, Alternating ion plating – a method of high-rate ion vapor deposition, J. Vac. Sci. Technol. 12 (1975) 858.
[9] H.R. Kaufman, J.M.E. Harper, J.J. Cuomo, Developments in broad-beam, ion-source technology and applications, J. Vac. Sci. Technol. 21(3) (1982) 762.
[10] D.M. Mattox, Particle bombardment effects on thin film deposition: a review, J. Vac. Sci. Technol. A7(3) (1989) 1105.
[11] J.A. Thornton, High rate thick film growth, Annu. Rev. Mat. Sci. 7 (1977) 239.
[12] J.A. Thornton, Influence of apparatus geometry and deposition conditions on the structure and topography of thick sputtered coatings, J. Vac. Sci. Technol. 11 (1974) 666.
[13] R.D. Bland, G.J. Kominiak, D.M. Mattox, Effects of ion bombardment during deposition on thick metal and ceramic deposits, J. Vac. Sci. Technol. 11 (1974) 671.

[14] K.-H. Müller, J. Appl. Phys. 58 (1985) 2573.

[15] P.J. Martin, R.P. Netterfield, D.R. McKenzie, I.S. Falconer, C.G. Pacey, P. Tomas, W.G. Sainty, Characterization of a Ti vacuum arc and the structure of deposited Ti and TiN films, J. Vac. Sci. Technol. A5 (1987) 22.

[16] T. Ohmi, T. Shibata, Advanced scientific semiconductor processing based on precision controlled low-energy ion bombardment, Thin Solid Films 241 (1993) 159.

[17] H.R. Kaufman, J.M.E. Harper, Ion assist applications of broad-beam ion sources, SPIE Proceedings (2004) 5527.

[18] D.M. Gardner, W.G. Sainty, Characterization of a high output gridless ion source, in: 48th Annual Technical Conference Proceedings of the Society of Vacuum Coaters (2005) 95.

[19] P.M. Lebvre, J.W. Seeser, R.I. Seddon, M.A. Scobey, B.W. Manley, Process for depositing optical thin films on both planar and non-planar substrates, U.S. Patent 5,798,027 (August 25, 1998).

[20] P.S. McLeod, G. Mah, The effect of substrate bias voltage on the bonding of evaporated silver films, J. Vac. Sci. Technol. 11 (1974) 119.

[21] Y.S. Kao, R.F. Bunshah, D. Okkrent, Hot hollow cathode and its application in vacuum coating: a concise review, J. Vac. Sci. Technol. A4(3) (1983) 397.

[22] D.L. Chamber, D.C. Carmichael, Developing of processing parameters and electron-beam techniques for ion plating, in: 14th Annual Technical Conference Proceedings of the Society of Vacuum Coaters (1971) 13.

[23] S. Schiller, M. Neumann, H. Morgner, N. Schiller, Plasma-activated high-rate deposition of oxides on plastic films, in: 37th Annual Technical Conference Proceedings of the Society of Vacuum Coaters (1994) 203.

[24] C. Metzner, H. Morgner, J.-P. Heinss, B. Scheffel, New developments for plasma activated high-rate electron beam evaporation for large surfaces, in: 51st Annual Technical Conference Proceedings of the Society of Vacuum Coaters (2008) 370.

[25] D. Ochs, P. Ozimek, A. Klimczak, T. Rettich, Comparison of mid-frequency and bipolar dc power supplies for dual magnetron sputtering, in: 51st Annual Technical Conference Proceedings of the Society of Vacuum Coaters (2008) 366.

[26] J.A. Hopwood (Ed.), Ionized Physical Vapor Deposition, Academic Press (2000).

[27] U. Helmersson, M. Lattemann, J. Bohlmak, A.P. Ehiasarian, J.T. Gudmundsson, Ionized physical vapor deposition (IPVD): a review of technology and applications, Thin Solid Films 513 (2006) 1.

[28] V. Kouznetsov, K. Macak, J.M. Schneider, U. Helmersson, I. Petrov, A novel pulsed magnetron sputter technique utilizing very high target power densities, Surf. Coat. Technol. 122 (1999) 290.

[29] V. Kouznetsov, Method and apparatus for magnetically enhanced sputtering, U.S. Patent 6,296,742 (October 2, 2001).

[30] D. Ochs, P. Ozimek, A. Ehiasarian, R. Spenser, Historical development of HIPIMS power supplies: from laboratory to production, in: 51st Annual Technical Conference Proceedings of the Society of Vacuum Coaters (2008) 288.

[31] G. Greczynski, J. Bohlmark, High power impulse magnetron sputtering for industrial applications: deposition of chromium films on inclined surfaces, in: 51st Annual Technical Conference Proceedings of the Society of Vacuum Coaters (2008) 282.

[32] R. Bandorf, S. Falkenau, K. Schiffmann, H. Gerdes, U. Heckmann, Properties of nichrome sputtered by HIPIMS in unipolar and DC-superimposed modes, in: 51st Annual Technical Conference Proceedings of the Society of Vacuum Coaters (2008) 317.

[33] M. Vergohl, O. Werner, S. Bruns, T. Wallendorf, G. Mark, Superimposed MF-HiPIMS processes for the deposition of ZrO2 thin films, in: 51st Annual Technical Conference Proceedings of the Society of Vacuum Coaters (2008) 307.

[34] H.R. Kaufman, J.M.E. Harper, J.J. Cuomo, Focused ion beam designs for sputter deposition, J. Vac. Sci. Technol. 16 (1979) 899.

[35] S.M. Rossnagel, J.J. Cuomo, W.D. Westwood, Handbook of Plasma Processing Technology: Fundamentals, Etching, Deposition, and Surface Interactions, Noyes Publications (1990).

[36] A. Anders, Cathodic Arcs: From Fractal Spots to Energetic Condensation, Springer, New York (2008).

[37] P.J. Martin, Coatings from the vacuum arc – vacuum arc deposition, Chap. 6, in: R.L. Boxman, P.J. Martin, D.M. Sanders (Eds.), Handbook of Vacuum Arc Science and Technology: Fundamentals and Applications, Noyes Publications (1995).

[38] P.S. McLeod, G. Mah, The effect of substrate bias voltage on the bonding of evaporated silver films, J. Vac. Sci. Technol. 11 (1974) 119.

[39] S. Schiller, M. Neumann, H. Morgner, N. Schiller, Plasma-activated high-rate deposition of oxides on plastic films, in: 37th Annual Technical Conference Proceedings of the Society of Vacuum Coaters (1994) 203.

[40] G. Mah, P.S. Mcleod, D.G. Williams, Characterization of silver coatings deposited from a hollow cathode source, J. Vac. Sci. Technol. 11 (1974) 663.

[41] H.F. Winters, H.J. Coufal, W. Eckstein, Influence of energy reflected from the target on thin film characteristics, J. Vac. Sci. Technol. A 11 (1993) 657.

[42] T.P. Drusedau, T. Bock, T.-M. John, F. Klabunde, W. Eckstein, Energy transfer into the growing film during sputter deposition: an investigation by calorimetric measurements and Monte Carlo simulations, J. Vac. Sci. Technol. A17 (1999) 2896.

[43] R.F. Somekh, The thermalization of energetic atoms during the sputtering process, J. Vac. Sci. Technol. A2(3) (1984) 1285.

[44] W.D. Davis, T.A. Vanderslice, Phys. Rev. 131 (1963) 219.

[45] R.E. Cuthrell, D.M. Mattox, C.R. Peeples, P.L. Dreike, K.P. Lamppa, Residual stress anisotropy, stress control, resistivity in post cathode magnetron sputter deposited molybdenum films, J. Vac. Sci. Technol. A6(5) (1988) 2914.

[46] D.M. Mattox, R.E. Cuthrell, C.R. Peeples, P.L. Dreike, Preparation of Thick stress-free Mo films for a resistively heated ion source, Surf. Coat. Technol. 36 (1988) 117–124.

[47] V. Sittinger, B. Szyszka, R. Bandorf, M. Vergohl, A. Pflug, D. Christie, F. Ruske, Research on promising applications for high power pulse magnetron sputtering, in: 51st Annual Technical Conference Proceedings of the Society of Vacuum Coaters (2008) 293.

[48] H. Ohta, M. Orita, M. Hirano, H. Tanji, H. Kawazoe, H. Hosono, Appl. Phys. Lett. 76(19) (2000) 2740.

[49] H. Agura, A. Suzuki, T. Matsushita, T. Aoki, A. Mori, M. Okuda, Thin Solid Films 445 (2003) 263.

[50] K. Ishi, High-rate kinetic gas-flow-sputtering system, J. Vac. Sci. Technol. A7 (1989).

[51] C. Leyens, A. Kohns, T. Haubold, R. Braun, Coatings for aero engines applications, in: 51st Annual Technical Conference Proceedings of the Society of Vacuum Coaters (2008) 695.

[52] G.T. West, P. Barker, A. Mishra, G.C.B. Clarke, P.J. Kelly, J.W. Bradley, Substrate heating and deposition rate measurement in a HIPIMS discharge, in: 51st Annual Technical Conference Proceedings of the Society of Vacuum Coaters (2008) 277.

[53] L.A. Capuano, N. Newnan, Off-axis sputter deposition of thin films, Supercond. Ind. 3(1) (1986) 34.

[54] D.J. Kester, R. Messier, Predicting negative ion sputtering in thin films, J. Vac. Sci. Technol. A4 (1968) 496.

[55] M.H. Sohn, D. Kim, S.J. Kim, N.W. Paik, S. Gupta, Super-smooth indium–tin oxide thin films by negative sputter ion beam technology, J. Vac. Sci. Technol. A 21 (2003) 1347.

[56] D.M. Mattox, F.N. Rebarchik, Sputter cleaning and plating small parts, Electrochem. Technol. 6 (1968) 374.

[57] A. Audronis, A. Matthews, A. Leyland, Pulse-bias sputter deposition of chromia and alumina films at low substrate temperature, in: 51st Annual Technical Conference Proceedings of the Society of Vacuum Coaters (2008) 134.

[58] P.J. Kelly, G. West, Q. Badey, J.W. Bradley, I. Swindells, G.C.B. Clarke, Comparisons of planar and cylindrical magnetrons operating in pulsed DC and AC modes, in: 51st Annual Technical Conference Proceedings of the Society of Vacuum Coaters (2008) 332.

[59] S. Bißwenger, A.S. Alimonda, K. Matl, A. Zoller, Low temperature optical coating with high packing density produced with plasma ion-assisted deposition, in: 37th Annual Technical Conference Proceedings of the Society of Vacuum Coaters (1994) 21.

[60] D.M. Mattox, R.D. Bland, Aluminum coating of uranium reactor parts for corrosion protection, J. Nucl. Mater. 21 (1967) 349.

[61] L. Li, W.B. Nowak, Biased magnetron sputter deposition of corrosion resistant Al–Zn alloy thin films, J. Vac. Sci. Technol. A 12 (1994) 1587.

[62] S. Schiller, G. Hoetzsch, K. Goedicke, O. Zywitzki, Plasma-activated high rate EB deposition of metals and oxides onto strip steel, in: 38th Annual Technical Conference Proceedings of the Society of Vacuum Coaters (1995) 401.

[63] P.J. Martin, R.P. Netterfield, W.G. Sainty, C.G. Pacey, The preparation and characterization of optical thin films produced by ion-assisted deposition, J. Vac. Sci. Technol. A 2 (1984) 341.

[64] W.D. Sproul, PVD processes for depositing hard tribological coatings, Chap. 6, in: D.M. Mattox, V. Harwood Mattox (Eds.), 50 Years of Vacuum Coating Technology and the Growth of the Society of Vacuum Coaters, SVC (2007) 35.

[65] J.W. Dini, Ion plating can improve coating adhesion, Metal Finish. 80(9) (1993) 15.

CHAPTER 7

Chemical Vapor Deposition

Jan-Otto Carlsson and Peter M. Martin

7.1 Introduction

Chemical vapor deposition (CVD) is parent to a family of processes whereby a solid material is deposited from a vapor by a chemical reaction occurring on or in the vicinity of a normally heated substrate surface. The resulting solid material is in the form of a thin film, powder, or single crystal. By varying experimental conditions, including substrate material, substrate temperature, and composition of the reaction gas mixture, total pressure gas flows, etc., materials with a wide range of physical, tribological, and chemical properties can be grown. A characteristic feature of the CVD technique is its excellent throwing power, enabling the production of coatings of uniform thickness and properties with a low porosity even on

Table 7.1: Summary of chemical vapor deposition (CVD) process family

Type	Pressure range	Description
Atmospheric pressure CVD (APCVD)	High–atmospheric	Processes at atmospheric pressure
Low-pressure CVD (LPCVD)	Low	Processes at subatmospheric pressures
Ultrahigh vacuum CVD (UHVCVD)	Typically below 10^{-6} Pa ($\sim 10^{-8}$ torr)	Processes at a very low pressure
Aerosol-assisted CVD (AACVD)		Precursors are transported to the substrate by means of a liquid/gas aerosol, which can be generated ultrasonically
Direct liquid injection CVD (DLICVD)		Precursors are in liquid form (liquid or solid dissolved in a convenient solvent). Liquid solutions are injected in a vaporization chamber towards injectors (typically car injectors). Then the precursor's vapors are transported to the substrate as in classical CVD process
Microwave plasma-assisted CVD (MPCVD)		
Remote plasma-enhanced CVD (RPECVD)		Utilizes a plasma to enhance chemical reaction rates of the precursors, and allows deposition at lower temperatures
Atomic layer CVD (ALCVD) or ALD		Deposits successive layers of different substances to produce layered, crystalline films
Hot wire CVD (HWCVD)		Also known as catalytic CVD (Cat-CVD) or hot filament CVD (HFCVD). Uses a hot filament to chemically decompose the source gases
Metal-organic chemical vapor deposition (MOCVD)		Based on metal-organic precursors
Hybrid physical–chemical vapor deposition (HPCVD)		Vapor deposition processes that involve both chemical decomposition of precursor gas and vaporization of a solid source
Rapid thermal CVD (RTCVD)		Uses heating lamps or other methods to rapidly heat the wafer substrate
Vapor-phase epitaxy (VPE)		

substrates of complicated shape. Another important feature is the capability of localized, or *selective* deposition, on patterned substrates.

CVD and related processes are employed in many thin film applications, including dielectrics, conductors, passivation layers, oxidation barriers, conductive oxides, tribological and corrosion-resistant coatings, heat-resistant coatings, and epitaxial layers for microelectronics. Other CVD applications are the preparation of high-temperature materials (tungsten, ceramics, etc.) and the production of solar cells, high-temperature fiber composites and particles of well-defined sizes. Recently, high T_c superconductors, and more recently carbon nanotubes, have also been made by this technique [1]. Since oxygen activity in the vapor can be precisely controlled during the deposition, no annealing in oxygen is needed to achieve superconductivity.

There exists a multitude of CVD processes, listed in Table 7.1. In thermally activated CVD (TACVD), the deposition is initiated and maintained by heat. However, photons, electrons, and ions, as well as a combination of these (plasma activated CVD), may induce and maintain CVD reactions. In this chapter, the underlying principles of TACVD are introduced. In addition, large-area deposition and selective CVD on patterned substrates are discussed.

7.2 Important Reaction Zones in CVD

In every CVD process, gaseous reactants are admitted into a reactor (Figure 7.1). Near or on a heated substrate surface the following chemical reaction occurs:

$$\text{Gaseous reactants (g)} \rightarrow \text{Solid material (s)} + \text{Gaseous products (g)}$$

Five important reaction zones related to gas flows and temperature are developed during the CVD process, as shown in Figure 7.2. The properties of CVD materials are affected by the interacting processes occurring in these reaction zones. In a CVD process, a main gas flow (the reaction gas mixture) passes over the substrate/coating surface. Fluid dynamics of the process results in a more or less stagnant boundary layer occurring in the vapor adjacent to the

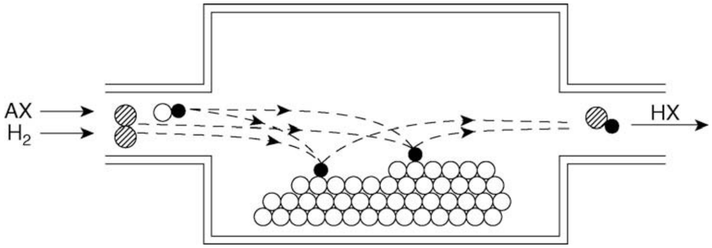

Figure 7.1: The principle of CVD.

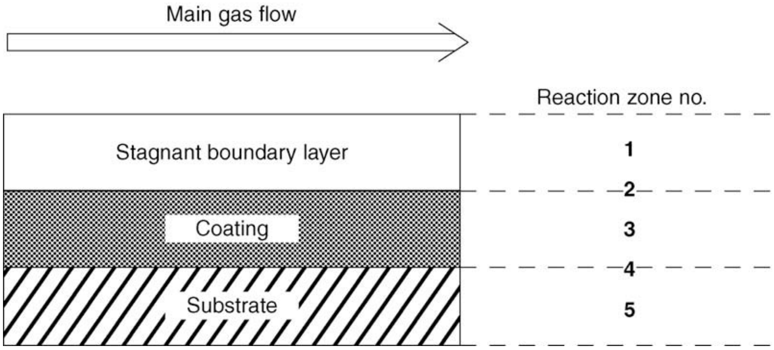

Figure 7.2: Important reaction zones in CVD.

substrate/coating. During the deposition process, the gaseous reactants and the gaseous reaction products are transported across this boundary layer. In reaction zone 1 (Figure 7.2) as well as in the main gas stream, homogeneous reactions may occur in the vapor, which may lead to an undesirable homogeneous nucleation characterized by a flaky and non-adherent coating. In some cases, however, these reactions, when not accompanied by homogeneous nucleation, are favorable to the CVD process (e.g. CVD of Al_2O_3 [2], of $B_{13}C_2$ [3], and of Si [4]). Heterogeneous reactions occur in the phase boundary vapor/coating (zone 2). These reactions typically determine the deposition rate and properties of the coating. Relatively high temperatures can be used during CVD, leading to various solid state reactions (e.g. phase transformations, precipitation, recrystallization, grain growth) that can occur in zones 3–5. In zone 4, which is a diffusion zone, it is possible to form various intermediate phases. The reactions in this zone are important for the adhesion of the coating to the substrate.

7.3 Design of CVD Experiments

Because not all reactors are exactly alike, every CVD experiment is unique. However, some general aspects in the design of CVD experiments can be given. Design is usually an iterative procedure. For instance, the choice of the reaction gas mixture affects the design of the CVD system, the cleaning procedure, the adhesion of the coating, etc.

7.3.1 Classification of CVD Reactions

CVD processes frequently proceed by complex chemical reaction schemes. However, a general classification of use of CVD reactions can be made.

Thermal decomposition reactions or pyrolytic reactions are characterized by thermal dissociation of a gaseous compound AX into A (solid material) and X (gaseous reaction product):

$$\mathrm{AX(g) \rightarrow A(s) + X(g)}$$

Thermal decomposition reactions normally result in relatively pure coatings. Examples of thermal decomposition reactions are given below:

$$\mathrm{SiH_4(g) \rightarrow Si(s) + 2\ H_2(g)}$$

$$\mathrm{B_2H_6(g) \rightarrow B(s) + 3\ H_2(g)}$$

$$\mathrm{Ni(CO)_4(g) \rightarrow Ni(s) + 4\ CO(g)}$$

$$\mathrm{Si(CH_3)Cl_3(g) \rightarrow SiC(s) + 3\ HCl(g)}$$

Processes like carburizing and nitriding are also classified in this reaction category. In carburizing, for instance, a carbon-carrying vapor species, e.g. methane, is allowed to react at/on a heated surface. Methane then decomposes in principle according to

$$\mathrm{CH_4 \rightarrow C(s) + 2\ H_2(g)}$$

Deposited carbon reacts immediately with the substrate, yielding a solid solution of carbon in the substrate and/or, if they exist, carbides of the substrate material.

Reduction reactions, where hydrogen acts a reducing agent, are frequently used (see also *Coupled reactions* below):

$$\mathrm{2\ AX(g) + H_2(g) \rightarrow 2\ A(s) + 2\ HX(g)}$$

Straightforward reduction reactions are almost used exclusively in the CVD of elements.

$$\mathrm{WF_6(g) + 3\ H_2(g) \rightarrow W(s) + 6\ HF(g)}$$

$$\mathrm{2\ BCI_3(g) + 3\ H_2(g) \rightarrow 2\ B(s) + 6\ HCI(g)}$$

$$\mathrm{SiCI_4(g) + 2\ H_2(g) \rightarrow Si(s) + 4\ HCl(g)}$$

Exchange reactions are characterized by an element E replacing another element, for instance X, in the molecule AX according to

$$\mathrm{AX(g) + E(g) \rightarrow AE(s) + X(g)}$$

Examples of exchange reactions are:

$$Zn(g) + H_2S(g) \rightarrow ZnS(s) + H_2(g)$$

$$SiCl_4(g) + CH_4(g) \rightarrow SiC(s) + 4\ HCl(g)$$

$$SnCl_4(g) + O_2(g) \rightarrow SnO_2(g) + 2\ Cl_2(g)$$

Disproportionation reactions are rarely used in CVD, and occur when the oxidation number of an element both increases and decreases through the formation of two new species. CVD of A from AX can be obtained in disproportionations such as

$$2\ AX(g) \rightarrow A(s) + AX_2(g)$$

$$3\ AX(g) \rightarrow 2\ A(s) + AX_3(g)$$

$$4\ AX(g) \rightarrow 3\ A(s) + AX_4(g)$$

Examples of disproportionation reactions are

$$2\ GeI_2(g) \rightarrow Ge(s) + GeI_4$$

$$2\ TiCl_2(g) \rightarrow Ti(s) + TiCl_4(g)$$

$$2\ SiI_2(g) \rightarrow Si(s) + SiI_4(g)$$

Coupled reactions are often used in CVD. The coupled CVD reaction of Al_2O_3 from $AlCl_3$, CO_2 and H_2 can be described in an overall reaction:

$$2\ AlCl_3(g) + 3\ CO_2(g) + 3\ H_2(g) \rightarrow Al_2O_3(s) + 3\ CO(g) + 6\ HCl(g)$$

where the reaction in which water is formed

$$CO_2(g) + H_2(g) \rightarrow CO(g) + H_2O(g)$$

is coupled to the hydrolysis reaction

$$AlCl_3(g) + 3\ H_2O(g) \rightarrow Al_2O_3(s) + 6\ HCl(g)$$

i.e. a reduction reaction is coupled to an exchange reaction [2]. Other examples of overall coupled CVD reactions are

$$TiCl_4(g) + NH_3(g) + 1/2\ H_2(g) \rightarrow TiN(s) + 4\ HCl(g)$$

$$Ga(CH_3)_3(g) + xPH_3(g) + (1 - x)AsH_3(g) \rightarrow GaAs_{1-x}P_x(s) + 3\ CH_4(g)$$

In general, several options for preparing a thin film material by CVD exist. For practical reasons however, relatively few alternatives will remain after a critical evaluation of the requirements of the process (temperature, total pressure, compatibility with the substrate and the reactor, the reaction's gas mixture, costs, toxicity of the substances, etc.).

7.3.2 Thermodynamics

Thermodynamic calculations are a useful tool when selecting experimental conditions (temperature, total pressure, reaction gas composition) for deposition of a certain material, and also serve as a guide when changing the experimental conditions in a CVD process. A number of computer programs are in use for these calculations and there are now practically no limitations on the number of materials that can be included in the calculations. For reviews of computational methods, the reader is referred to [5–8].

Computer programs are typically based on the so-called *free energy minimization* technique. The free energy G is given by the following equation:

$$G = \sum_i n_i \mu_i$$

where n_i is the number of moles of a substance i and μ_i is the chemical potential. The chemical potential is defined as

$$\mu_i = \mu_i^{\mathrm{o}} + \mathrm{R}T \ln a_i$$

where μ_i^{o} is the reference chemical potential, and a_i is the activity. Assuming ideal gas conditions, the activity of the gaseous species may be expressed as its partial pressure

$$a_i = p_i = (n_i/n)P$$

where n is the number of moles in the gas phase, and P the total pressure. For pure condensed substances, activities are equal to unity.

Eriksson [9] developed a computer program (SOLGAS) based on the minimization of the free energy. This program became a prototype for many other equilibrium calculation programs. From the basic equations given above, the dimensionless quantity $G/\mathrm{R}T$ was defined (see equation below) and used in the calculations.

$$\frac{G}{\mathrm{R}T} = \sum_{i=1}^{m} n_i^g \left[\frac{\mu^{\mathrm{o}}}{\mathrm{R}T}\right]_i^g + \ln P + \ln\frac{n_i^g}{n} + \sum_{i=1}^{n} n_i^s \left[\frac{\mu^{\mathrm{o}}}{\mathrm{R}T}\right]_i^s$$

Superscripts g and s refer to the gas phase and the solid phase, respectively. The value of μ_o/RT for a specific substance is calculated from

$$\frac{\mu^o}{RT} = \frac{(G^o - H^o_{298})}{RT} + \frac{\Delta H^o_{f,298}}{RT}$$

where $(G_o - H_o)/RT$ = free energy function, and $H^o_{f,298}$ = heat of formation at 298.1 K.

By minimizing G/RT (or G) and using mass balance equations as subsidiary conditions, the equilibrium composition of a system can be calculated.

Input data for the calculations are the number of moles of the different reactants, total pressure, substrate temperature, different substances, and their thermochemical data. From the calculations, various quantities like the partial pressures of the vapor species, amounts of the different substances available for CVD, i.e. the yield, and thermodynamic functions (supersaturation, reaction enthalpies, driving force of different processes, etc.) are obtained.

Figures 7.3–7.5 illustrate results from equilibrium calculations. Figure 7.3 shows the change in equilibrium composition when SiH_4 is added to a H_2/WF_6 gas mixture. *CVD phase diagrams*

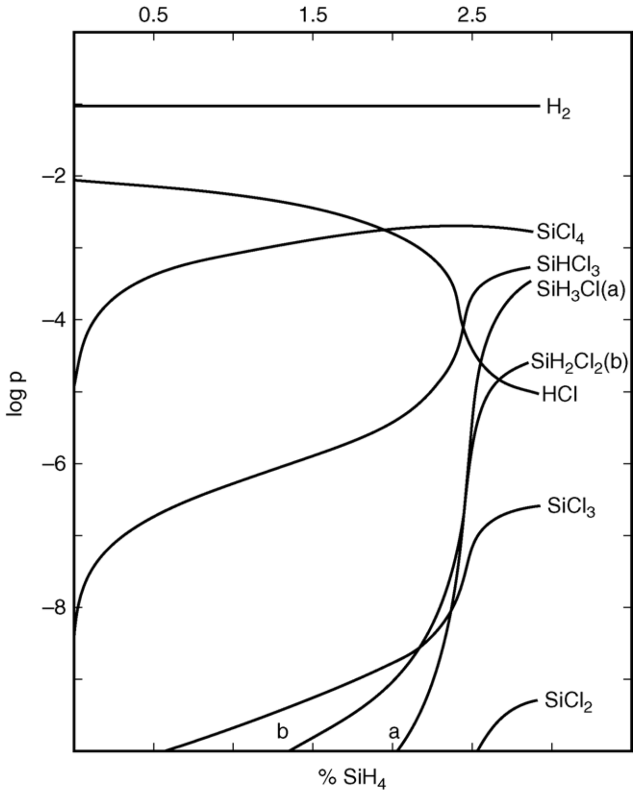

Figure 7.3: Partial pressures of vapor species in the homogeneous reaction between H_2, WF_6 and SiH_4. Total pressure = 0.1 torr, temperature = 300 °C, H_2/WF_6 = 30 [10].

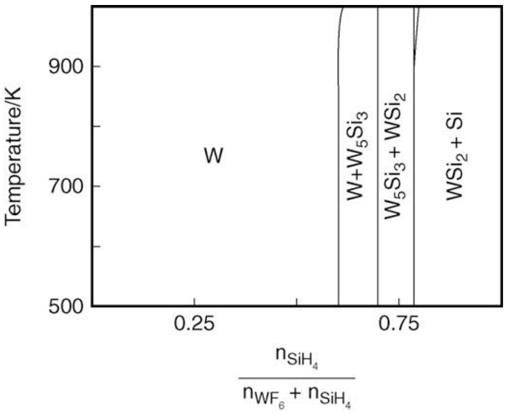

Figure 7.4: Calculated CVD phase diagram for the W– Si system. Reactants WF_6, SiH_4 and H_2, total pressure = 0.1 torr, $H_2/WF_6 = 39$ [10].

are constructed to provide an overview of experimental conditions used in depositing a certain thin film material [11]. Figures 7.4 and 7.5 are examples of calculated CVD phase diagrams. The number of variables required to construct a complete CVD phase diagram is given by the phase rule. Normally various sections (constant temperature, constant total pressure, constant molar ratio between two of the reactants, while varying the number of moles of a third reactant) are used. Finally, for more theoretical work, *predominance diagrams* with element chemical potentials as variables are employed. In these diagrams, the phase stability ranges are limited by straight lines.

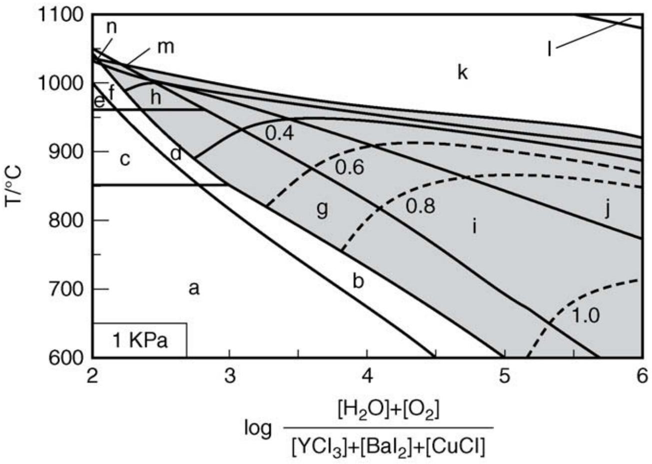

Figure 7.5: Calculated CVD phase diagram for deposition of high-temperature superconductor $YBa_2Cu_3O_{7-x}$. Gray-shaded stability regions contain the superconducting phase. Contour lines represent the yield of $YBa_2Cu_3O_{7-x}$. Precursors YCl_3, BaI_2 and CuCl, O_2, and H_2O, molar ratios YCl_3:BaI_2:CuCl = 1:2:3, O_2:H_2O = 1:1, total pressure 1 kPa [13].

The reliability of the equilibrium computations described above is dependent on the availability and accuracy of thermochemical data as well as the identification of all substances – vapor species and condensed phases – that are of importance in the system. Examples of sources of thermochemical data are given in [12–14]. In cases where data do not exist or the data are unsatisfactory or unreliable, estimation procedures can be used [e.g. 13]. Finally, a few references illustrating the use of thermodynamic computations in CVD have been selected [15–24].

7.3.3 Adhesion

Production of adherent coatings with desired properties is the ultimate goal of all CVD work. There are, however, several factors which degrade adhesion between the coating and the substrate.

Stress can be introduced as intrinsic stress (due to deposition conditions) or resulting from a mismatch in thermal expansion coefficients between the substrate and the coating when cooling down after deposition. Stress can be reduced to a certain extent by depositing a ductile buffer layer prior to the final CVD process. Total stress can also be reduced by decreasing the thickness of the coating as well as by changing the grain size and morphology of the coating.

Homogeneous nucleation in the vapor produces a flaky/powdery deposit. By reducing the degree of supersaturation or the driving force of the process, homogeneous nucleation can be eliminated.

Intermetallic compounds formed at the coating/substrate interface may be brittle, leading to the formation of cracks. The likelihood of crack formation increases with increasing thickness of the layer containing the intermetallic compounds. Deposition of a buffer layer may also improve adhesion in this case.

Hydriding of the substrate may cause poor adhesion. Hydrogen is frequently used in the cleaning procedure prior to deposition. Some metals/alloys can absorb a considerable amount of hydrogen. If the deposition process is run at a temperature at which hydrogen is liberated, the coating will crack and lose adhesion. Hydriding can be eliminated by using other cleaning procedures or by heating the substrate in vacuum or an inert gas after cleaning in hydrogen.

Pores at the coating/substrate interface reduce the adhesion not only because of the fewer bonds at the interface but also because they act as crack initiators. Pores can originate from the coalescence step at the beginning of the CVD process as well as from Kirkendal diffusion (differences in diffusion fluxes of the atoms over the coating/substrate interface).

Oxide films or other surface contaminants can reduce adhesion. A proper cleaning procedure will usually solve this problem.

Chemical attack on the substrate by the reaction products formed during the CVD process (HCl for example) can cause poor adhesion. Chemical attack of the substrate can occur as long as the substrate is exposed to the vapor and is described in the following reactions:

$$2\ \mathrm{AX(g)} + \mathrm{H_2(g)} \rightarrow 2\ \mathrm{A(s)} + 2\ \mathrm{HX(g)}$$

Volatile reaction product HX reacts with the substrate S according to the reaction

$$2\ \mathrm{S(s)} + 2\ \mathrm{HX(g)} \rightarrow 2\ \mathrm{SX(s)} + \mathrm{H_2(g)}$$

Solid substance SX formed may cause poor adhesion. The above reaction can be predicted from thermodyamics.

7.3.4 Substrate Cleaning Procedures

A clean substrate surface free from oxides and other contaminants is critical for good adhesion. The cleaning procedure depends on the substrate used, the material to be deposited, the CVD process, etc. Examples of cleaning techniques are given below. Refer to Chapter 3 for detailed substrate cleaning procedures. Before substrates are placed in the reactor, pickling, grit blasting, etching, degreasing, etc., are carried out. In the CVD reactor surfaces containing hydrogen-reducible oxides, e.g. tungsten oxides, are heated in a hydrogen gas flow at temperatures above the deposition temperature. Metals forming volatile oxides are cleaned by heating in an inert atmosphere. Finally, the heating operations in the cleaning step remove dust particles from the surface, in some cases by the formation of carbides at the surface. After the cleaning procedure the reactor is purged with an inert gas/hydrogen before the deposition process (interlayers or final coating).

7.3.5 The CVD System

Choice of the CVD system is determined by a number of factors:

- reactants used in the process
- maximum acceptable leak rate for air into the system
- purity of the deposit
- size and shape of the substrate
- process economy.

In the following sections, general comments on the design of CVD systems are given.

A CVD system is constructed in three modules:

- reaction gas dispensing system
- reactor, including components for defining gas flows
- exhaust system containing a total pressure controller, vacuum pump, scrubber/or reactant recycling system.

7.3.5.1 Gas Dispensing System

Reactants, which are gases at room temperature, are stored in gas bottles. After pressure regulation, their flows are measured with, for instance, mass flow meters. Use of mass flow meters yields high accuracy and allows microprocessor control of gas flows.

Liquids or solid reactants at room temperature must be fed to the system in other ways (Figure 7.6). They can be admitted into the system by simply heating them above the boiling or sublimation point. The evaporation rate can be varied by varying the source temperature and/or the dimensions of the capillary from the sources. Another way of introducing these substances is to use an evaporator or sublimator and a carrier gas. When an evaporator is used, the carrier gas is bubbled through the liquid to be evaporated or flowed over its surface. The carrier gas picks up the liquid material and transports it into the reactor. Evaporation rate depends on temperature of the liquid, liquid level in the container, and flow rate of the carrier gas. For best possible reproducibility it is important to have a constant level of the liquid in the container. However, some alternatives to these evaporators exist which use carrier gases and are independent of the liquid level. In one alternative, the liquid is evaporated from a vessel, cooled and condensed in a chiller, leaving the carrier gas saturated at the temperature of the chiller. If two or more reactant liquids are used in the process, it is seldom possible to vaporize them in the same evaporator while maintaining the predetermined molar ratio since they normally have different vapor pressures.

The principle of the sublimator is similar to that of the evaporator, in which the material is transferred to the vapor by sublimation (solid $\sim$ gas) and then transported to the reactor by carrier gas.

Non-gaseous reactants at room temperature can also be introduced into the reactor by generating them in situ in the gas dispensing system. If, for instance, the halide $AlCl_3$ is used in a process, the generator is filled with aluminum sponge. Aluminum chloride is then obtained by passing hydrogen chloride through the generator. Generator variables are temperature, flow rate, and concentration of the hydrogen chloride (varied by dilution with an inert gas).

Direct metering of liquids/solids followed by immediate vaporization in a vessel can also be used. Flow meters and various dispensing pumps are available for metering liquids. The final

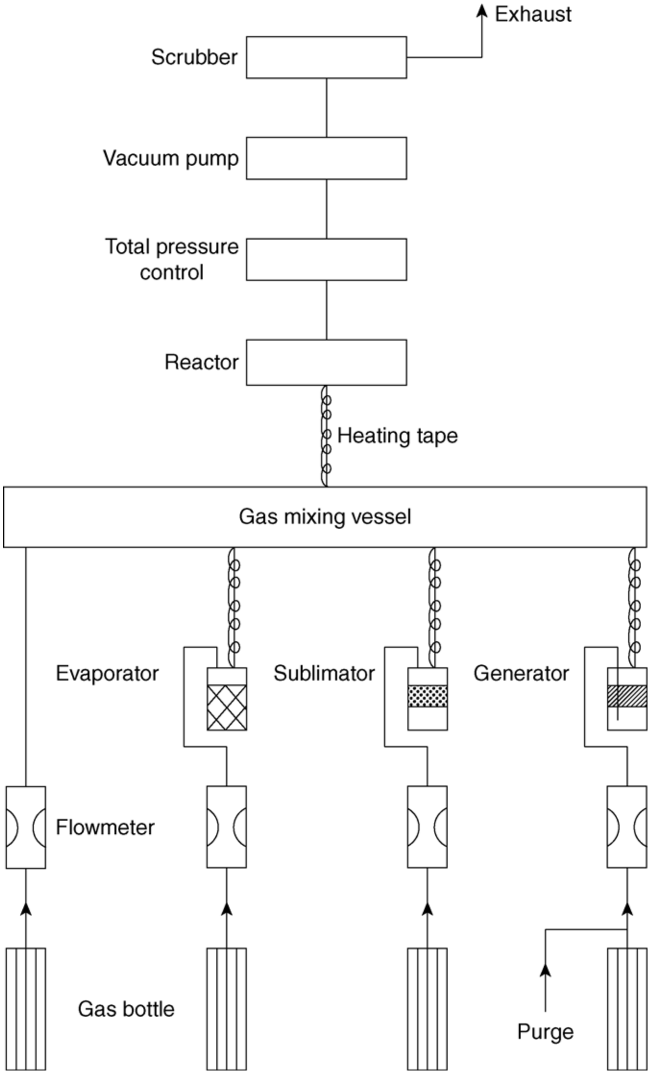

Figure 7.6: Sketch of a CVD system.

vaporization takes place in, for instance, a flash vaporizer [25], a vessel containing pieces of high-temperature porcelain.

Many CVD processes are strongly degraded by contaminants in the vapor. Contaminants originate from the reactants themselves and from various chemical reactions between the gases and the materials in the gas dispensing system (in the tubes, evaporators, sublimators) and from air leakage. The contamination level can be reduced by:

- purifying the reactants: hydrogen and argon can be purified to a level of 1 ppm in commercially available purifiers
- a low leak rate
- using carrier gases which are non-reactive with the materials to be vaporized (in evaporators and sublimators)
- using materials in tubes, vaporizers, reactors, etc., which are compatible with the gases used
- using degassed O-rings that are used as vacuum seals
- installing purge lines, which is important when reactive gases, e.g. halides, are used.

Finally, explosive, flammable and toxic gases (hydrogen, silane, phosphine, arsine) are frequently used in CVD processes. Correct handling of the gases is critical for safety, and every precaution should be taken. Effective ventilation systems and gas detectors (commercially available) should also be used.

7.3.5.2 Reactor

The process selected and the size, shape, and number of substrates define the type of reactor and its geometry. Two main reactor types can be distinguished:

- In a *hot wall reactor* (Figure 7.7), the reactor tube is surrounded by a tube furnace. As a result, the substrates and walls of the reactor all have the same temperature. In addition to the film growth occurring on the substrates, film growth is likely to occur on the inside of the reactor walls. With thicker films on reactor walls, there is a risk that particles will break loose and fall down on the surface of the growing film; thus introducing pinholes. A reaction between the material in the reactor wall and the vapor may also be a source of contamination in this reactor type. Homogeneous reactions affecting the deposition reactions and hence the structure of the films may also take place in the vapor. There is a successive depletion of the reactants as they are

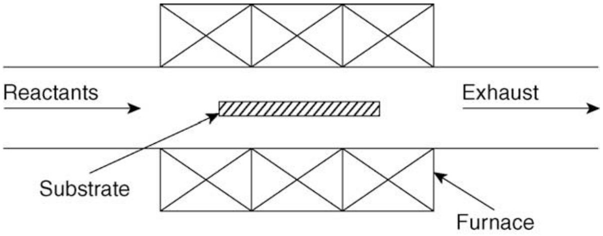

Figure 7.7: Hot wall CVD reactor.

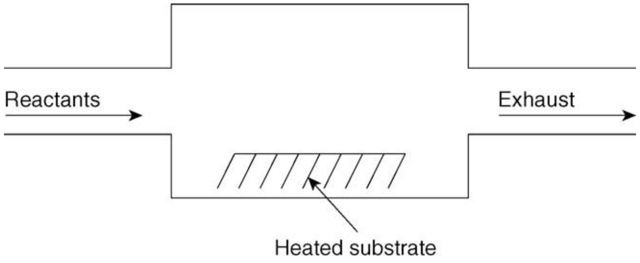

Figure 7.8: Cold wall CVD reactor.

transported through the reactor. Such a depletion may yield different deposition conditions and compositions within the reactor. Finally, many compositions can be deposited simultaneously.

- The walls of a *cold wall reactor* (Figure 7.8) are unheated and, as a result, no deposition occurs on the walls, eliminating the risk of particles breaking loose from the walls. Furthermore, a low wall temperature reduces the risk of contaminating vapor/wall reactions. In this type of reactor, homogenous reactions in the vapor are suppressed and the importance of the surface reactions is increased. Steep temperature gradients near the substrate surface can potentially introduce severe natural convections resulting in a non-uniform film thickness and microstructure. However, there is a tendency to use cold wall reactors frequently in microelectronics owing to their higher flexibility, high cleanliness, high deposition rates (resulting in high wafer throughput), high cooling rates combined with the needs of thickness uniformity, automatic wafer handling, and use of increasing wafer diameter.

Various techniques exist for heating the substrates [27]. Conductive substrates can be heated resistively or by radiofrequency induction. Non-conductive substrates are normally heated by optical techniques (tungsten filament lamps, lasers), thermal radiation techniques, or by susceptors and radiofrequency induction heating. Examples of reactors are shown in Figure 7.9. Fluidized bed techniques can be used for coating a large number of small pieces [26].

To illustrate how the choice of reactor depends on the substrate to be coated, an example of applying a coating inside a tube is given. In this case the tube itself is the reactor. The reactants are introduced in the tube and transported to the heated zone where the deposition occurs. Induction heating as well as tubular furnace heating can be employed. By moving the tube or the heating sources continuously, a coating with uniform thickness can be produced [e.g. 28].

Arrangement of gas flows as well as gas flow rate are of highest importance for obtaining good coatings. Gas flow dynamics are discussed in Section 7.4.

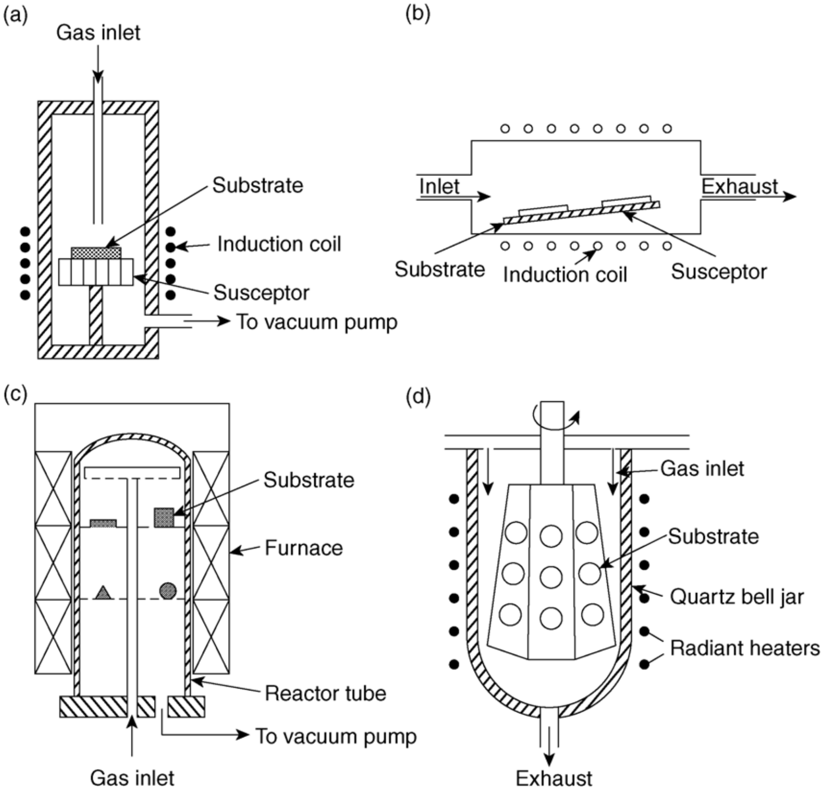

Figure 7.9: Examples of some CVD reactors: (a, b) RF heated cold wall reactors; (c) vertical hot wall reactor; (d) barrel reactor.

7.3.5.3 Exhaust System

The exhaust system contains a vacuum pump, total pressure control, scrubbers, and a recycling system (if used). Processes working at atmospheric pressure do not require vacuum pumps and total pressure control. At reduced pressures, however, pumps as well as some kind of total pressure control must be used.

The choice of the vacuum pump depends on the process (pumping capacity required, pressure range to be used, gases to be pumped). At higher process pressures (> 30 torr), water ring pumps and various mechanical *chemical pumps* are used. Chemical pumps are also employed at lower pressures (1 torr), and at the lowest pressures in combination with, for example, mechanical boosters. When mechanical pumps are used in CVD processes, the pump oil can polymerize or be damaged/contaminated in other ways by certain gaseous species. Pump oil should be chosen with respect to its compatibility with the specific gaseous species. Polymerization of oil can readily be tracked by measuring its viscosity at different times.

Mechanical pumps also produce back-diffusion of oil molecules into the system. Back-diffusion can be held in a trap (zeolite trap, liquid nitrogen cold trap) placed above the pump. With the current trend for using lower pressures to create abrupt interfaces and superlattices, diffusion (to pump hydrogen) and turbo pumps are also utilized. Finally, external oil filtering systems reduce wear in mechanical pumps in processes where solid particles are formed and transported in the vapor to the pump.

In a CVD process, toxic, explosive, and corrosive gases are generally used and formed. Scrubbers are used to remove them before exhaust. Scrubber type must be appropriate to the CVD process used. Halides can easily be neutralized in a water scrubber. Carbon monoxide and hydrogen can be burned in a flame, and arsine can be removed by simply heating the reactor gas in a furnace especially designed for this purpose (i.e. with a high efficiency for stripping arsenic from the gas stream).

Recycling is frequently used to reduce process costs, and becomes necessary in large-scale processes in which expensive reactants are utilized and conversion efficiency of the reactants is low. Techniques for recycling are process dependent. Simple recycling can be achieved in some processes by selective condensation, which can be easily applied in systems where the component to be recycled has the highest boiling point. In the production of boron fibers for example, where hydrogen and boron trichloride are used, unconverted boron trichloride is condensed in the exit stream from the reactor, while the hydrogen and the hydrogen chloride (formed in the process) are not condensed.

7.3.5.4 Analysis of the Vapor in a CVD Reactor

Various spectroscopic techniques can be used to analyze the vapor in a CVD reactor. The purpose of these analyses is to achieve a better understanding of the chemical species in the process. Spectroscopic techniques are also used for process control. Mass, Raman, and infrared spectroscopy are used most extensively [29–33].

7.4 Gas Flow Dynamics

The rate and arrangement of gas flows in a CVD reactor influence deposition conditions considerably. Some fundamentals of gas flow dynamics are given in this section. For further details the reader is referred to textbooks in chemical engineering or other books treating transport processes.

A variety of different states can be present in a gas. In the molecular state, the mean free path of the molecules is much longer than the dimensions of the vessel. In the viscous state, the mean free path is much shorter than the vessel dimensions. The viscous state can be divided into two flow regimes: (1) laminar flow regime where gas velocity is low and the flowing gas layers are parallel, and (2) turbulent flow which occurs at higher velocities. The demarcation

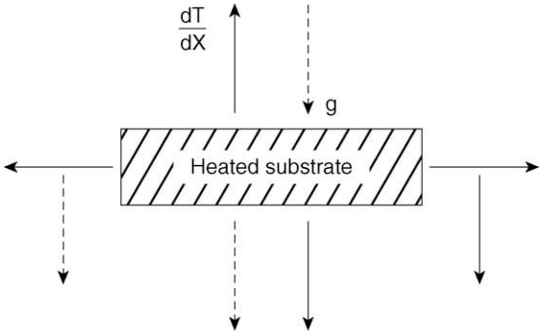

Figure 7.10: Forces near a heated substrate surface. *g*: gravitational force; *dT*/*dx*: temperature gradient.

between laminar and turbulent flow is defined as the value of Reynold's number, R_e:

$$R_e = \frac{\rho V D}{\eta}$$

where $\rho =$ density of the gas, $V =$ velocity, $\eta =$ viscosity, and $D =$ diameter of the tube.

Flow is laminar for $R_e < 1100$, while for $R_e > 2100$ flow is turbulent. The range 1100–2100 is a mixed flow regime.

The Reynold's number characterizes flow in an isothermal environment. In a non-isothermal environment that exists in a cold wall reactor, natural convection produces turbulence even at low flow rates. Consider the region above a heated surface shown in Figure 7.10. For small temperature gradients *dT*/*dx*, the density variation of the gas along the coordinate *x* is compensated by the gravitational field and no movement of the gas occurs. For larger *dT*/*dx*, the gas starts to move and laminar flow can no longer be sustained. From Figure 7.10 it can be understood that turbulence above a heated substrate surface can occur at different regions. For example, when the *dT*/*dx* is perpendicular to the gravitational field, turbulence occurs at smaller temperature gradients than in the antiparallel case.

Different dimensionless quantities are used to identify conditions of laminar and turbulent flow at different geometries. The Rayleigh number, R_a, and the Grashof number, G_r, define these flow regimes [32]. R_a is simply the product of G_r and the Prandtl number (nearly equal to one for gases).

Diagrams like those shown in Figure 7.11, depicting flow stability regions, are constructed for different geometries and reaction gas mixtures in order to summarize flow. In an isothermal environment, G_r is equal to zero and R_e describes the situation completely. In a non-isothermal environment G_r is greater than zero (increases with increasing DT). Turbulence occurs at a specific value of G_r, depending on flow rate of the specific gas mixture and temperature difference between the hot and cold parts of the reactor.

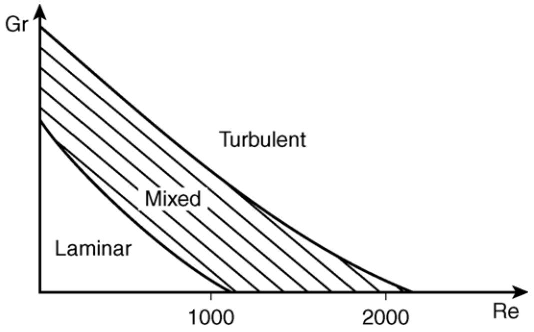

Figure 7.11: Diagram showing flow stability regions.

The laminar flow region is typically used in most CVD processes. High flow rates (turbulence) usually decrease conversion efficiency of the reactants to deposit the coating and very large gas volumes have to be handled. The flow environment around the object to be coated can be visualized as a smoke experiment where smoke is generated inside the reactor from, for example, titanium tetrachloride and water.

7.4.1 Gas Flow Patterns

Gas flow patterns are of greatest importance for growth of films with uniform thickness and composition, particularly at 'high' pressures (about 1 atm). The diffusivity of the vapor species increases at reduced pressures, which results in better mixing of the process gases, and hence the flow fields become less important.

Gas flow patterns are very complicated in many CVD reactors with complex geometries because flow is driven by both pressure differences (forced convection) and gravity (free convection). Free convection contributes to the gas flow pattern not only in cold wall reactors with their steep temperature gradients but also in hot wall reactors with small axial temperature gradients. Free convection is employed for correction of the successive depletion of the reactants in the vapor as they flow through the reactor. Fluid flow phenomena characteristic of various CVD reactors have been reviewed by Westphal [33] and Jensen [34].

In gas flow calculations the continuity equation for the total mass for single components, energy and momentum must be solved. For a suitable choice of experimental conditions (flow regimes and reactor geometries) simplifying equations and boundary conditions, resulting in reasonable computer times, are obtained. As an introduction, results from detailed flow calculations for two main reactor types are summarized. Wahl [35] calculated flow fields in several cold wall reactors for the laminar flow region (atmospheric pressure) for CVD of silicon nitride from SiH_4 and N_2. The reactor geometry is shown in Figure 7.12. Flow patterns calculated for this geometry and the inverted geometry (difference in the buoyance-driven

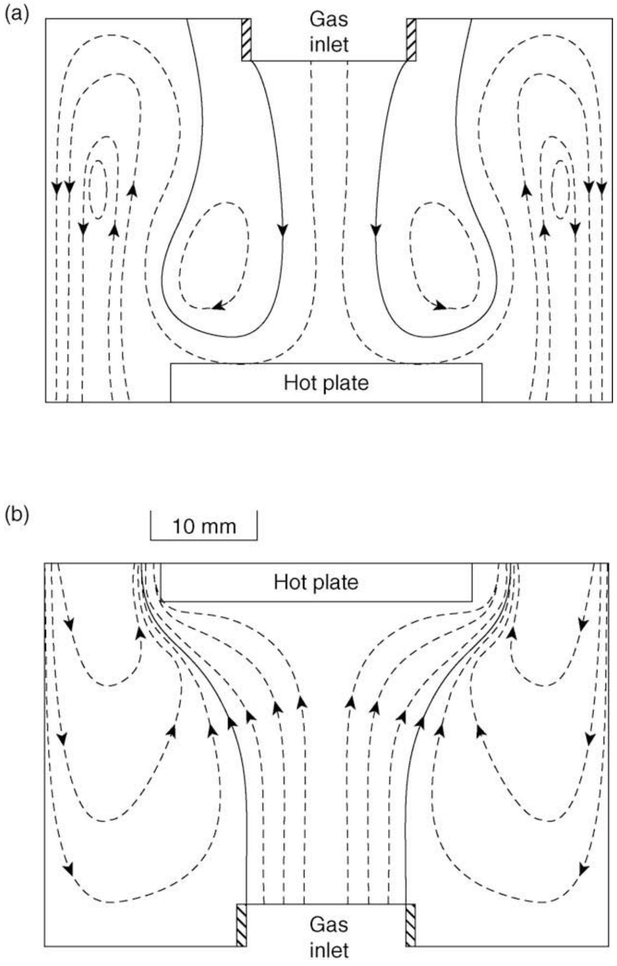

Figure 7.12: Gas flow pattern in a cold wall reactor, where the forced and buoyance-driven convection (a) interact, and (b) counteract, substrate temperature 900 K, Re = 50 [35].

convection) are shown in Figure 7.12. The flow pattern becomes more complicated for the inverted geometry, i.e. when forced convection and gravity interact. The flow pattern, including generation of loops and rolls, is strongly dependent on the ratio of the free convection and forced convection.

To demonstrate the influence of the reactor geometry on the flow pattern, a calculation of Wahl and Hoffman [36] will be used as an example. The reactor geometry considered as well as the results from the calculations are shown in Figure 7.13. The flow pattern in this geometry is not as complicated as that obtained in the previous geometry (Figure 7.12), where the diameter of the inlet gas tube was half the diameter of the hot plate.

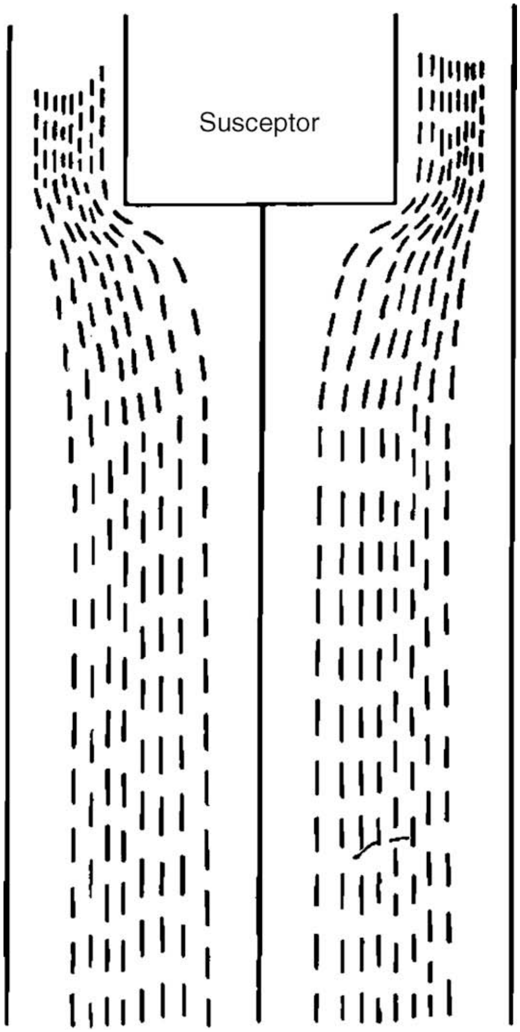

Figure 7.13: Gas flow pattern in a cold wall reactor with geometry different than that shown in Figure 12 [36].

A technique frequently used for correction of the successive depletion of the reactants as they are transported through a hot wall reactor is the application of a temperature gradient in the axial (flow) direction of the reactor. Even small temperature gradients, however, can induce buoyancy-driven convection. The flow pattern in a hot wall reactor with a temperature gradient for the atmospheric CVD of GaAs in the Ga–$AsCl_3$–H_2 system was calculated for different temperature gradients, gas flow velocities, and reactor heights by Westphal [33]. A typical result from their calculations is shown in Figure 7.14. It can be seen that a convection roll, induced by free convection, is generated. The effect of free convection on the gas flow pattern

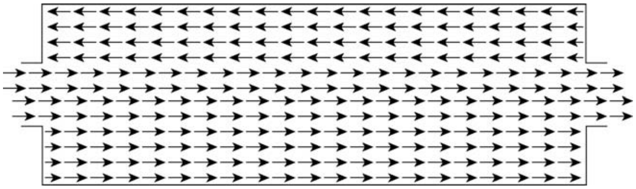

Figure 7.14: Gas flow pattern in a hot wall reactor with a temperature gradient of 6 K/cm, linear gas flow velocity of 2 cm/s, and channel height 5 cm, for deposition system Ga–$AsCl_3$–H_2 [33].

decreased with decreasing temperature gradients, increasing gas flow velocities and decreasing reactor heights. No extreme conditions were required to generate the convection rolls shown. They were obtained at a temperature gradient of 6 K/cm, gas flow velocity of 2 cm/s and reactor height of 5 cm.

Convection rolls are frequently generated in CVD, and can cause dilution of the reaction gas with reaction products, resulting in an alteration of the deposition conditions. Resultant rolls may cause problems for multilayer growth with well-defined phase boundaries and for the creation of sharp doping profiles. These problems can be solved by using extreme low total pressures (in the 10^{-3} torr range).

7.4.2 Boundary Layers

In CVD the substrates are immersed in a gas stream. From fluid mechanics it is known [37] that boundary layers are developed near the substrate surface. Boundary layers are defined as the region near the substrate surface where gas stream velocity, concentration of the vapor species and temperature are not equal to the same parameters in the main gas stream. Thus, a velocity boundary layer, concentration boundary layer and thermal boundary layer develop. The development of a velocity boundary layer in a laminar flow region is sketched in Figure 7.15. Gas velocity is zero at the substrate surface and increases to a constant value (the bulk gas flow velocity). The boundary layer is the layer over which the gas flow velocity changes.

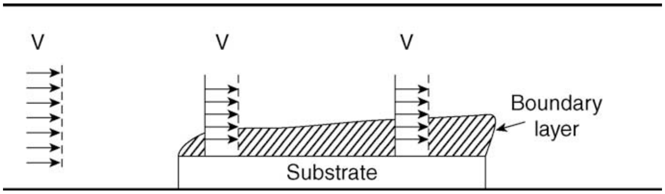

Figure 7.15: Definition of the velocity boundary layer.

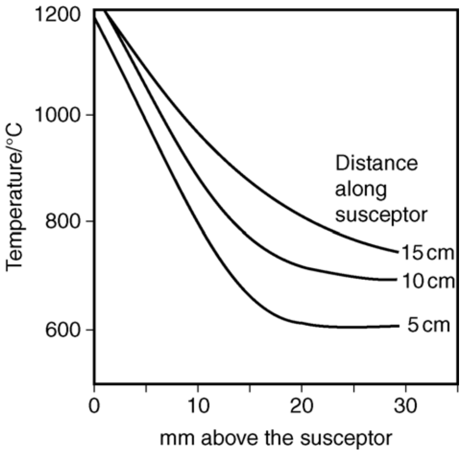

Figure 7.16: Temperature profile in He. Linear gas flow velocity: 24.9 cm/s [29].

The thickness δ of the boundary layer (laminar flow) at a position X on the substrate or susceptor [37] is given by

$$\delta = a(\eta X/\rho V)^{1/2}$$

where a is a proportionality constant, η is the viscosity of the gas, v is the velocity of the gas, and ρ is the density of the gas. From knowledge of the temperature and pressure dependence of η, v, and ρ [32, 37] it is deduced that the thickness of the boundary layer increases with increasing temperature and decreasing total pressure. Moreover, thickness also increases with increasing transport distance of the gases along the substrate surface.

Development of boundary layers in CVD processes has been investigated both experimentally and theoretically. Eversteijn et al. [38] used smoke experiments to visualize the flow pattern in a horizontal epitaxial reactor. Smoke was generated from $TiCl_4$ and H_2O. They observed an immobile layer of gas, called the stagnant boundary layer, above the susceptor. It was shown later, however, that in steep temperature gradients (near the susceptor) fine particles are driven away from the susceptor by thermophoretic forces [39]. This demonstrated that smoke experiments can only be used to map flow at large distances from a heated susceptor.

Ban and Gilbert [29] investigated heat transport in a cold wall reactor by heating a susceptor in helium and measuring the temperature at different locations above it with a small diameter thermocouple. The very steep temperature gradient is apparent in Figure 7.16.

Ban and Gilbert also investigated concentration profiles of various vapor species in silicon CVD from $H_2/SiCl_4$ gas mixtures. They introduced a fine capillary probe attached to a mass spectrometer at different locations above the susceptor. The concentration profile of $SiCl_4$ and reaction product HCl can be seen in Figure 7.17. The thickness of the concentration boundary

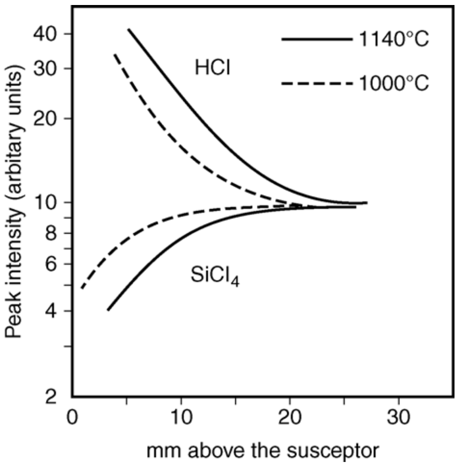

Figure 7.17: Concentration profiles of $SiCl_4$ and HCl in the CVD of silicon from $SiCl_4$ and H_2. Transport distance along the susceptor: 12.5 cm; linear gas flow velocity: 24.9 cm s^{-1}, - - - 1000 °C, – 1140 °C [29].

layer in this case is greater than 2 cm. Successive depletion with respect to the reactants as they were transported through the reactor is shown in Figure 7.18. At a height of 7 mm above the susceptor and 15 cm downstream of the susceptor, partial pressure of $SiCl_4$ was reduced to $\sim$50% of the initial value. Sedgwick et al. [30] measured temperature and concentration

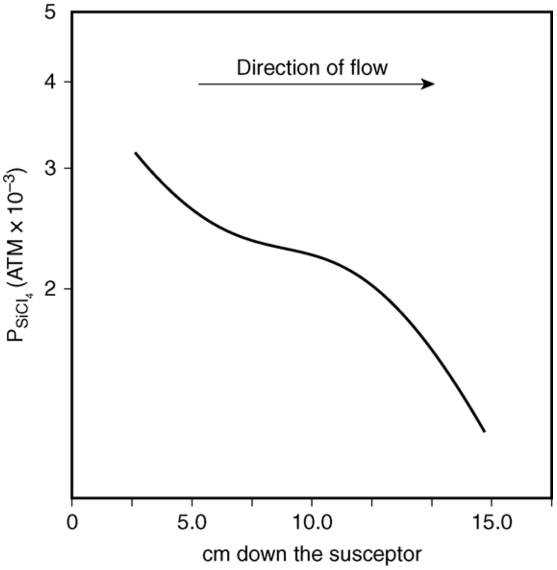

Figure 7.18: Partial pressure profile of $SiCl_4$ as a function of the transport distance along the susceptor at a height of 7 mm above the susceptor [29].

profiles in an air-cooled horizontal cold wall reactor using Raman scattering. They observed a steep temperature gradient near the susceptor. The temperature profile developed was dependent on the position along the susceptor.

Giling [40] investigated gas flow patterns and temperature profiles at atmospheric pressure in air-cooled and water-cooled horizontal epitaxial reactors using interference holography. H_2, He, N_2, and Ar gases were used. H_2 and He yielded stable laminar flows through both the water-cooled and the air-cooled reactors. At flow velocities higher than 40 cm s^{-1} a cold gas finger, indicating incompletely developed flow and temperature profiles, was observed in the air-cooled reactor. N_2 and Ar behaved quite differently from H_2 and He, and as a result, different convective effects were observed. At flow velocities greater than 4 cm s^{-1}, a laminar layer about 8 mm thick developed near the susceptor, while the gas above this layer appeared to be in turbulence.

Giling also pointed out the importance of entrance effects, i.e. that it takes a specific distance (the entrance length) from the susceptor edge for full velocity and temperature profiles to develop. According to Schlichting [37], the entrance length for development of a full velocity profile is given by the equation

$$X = 0.04h\mathrm{R_e}$$

where h is the height of the channel. Hwang and Cheng [41] predicted that the thermal entrance length was seven times larger than the flow entrance length. Giling's measurements confirmed this for H_2.

Coltrin et al. [42] developed a mathematical model for silicon CVD from silane in a cold wall reactor. The model includes gas-phase chemistry as well as fluid mechanics and predicts temperature, velocity, and concentration profiles for many vapor species. Figure 7.19 depicts the temperature contour for a typical calculation. The thickness of the boundary layer is in the centimeter range and increases with increasing gas transport distance along the susceptor.

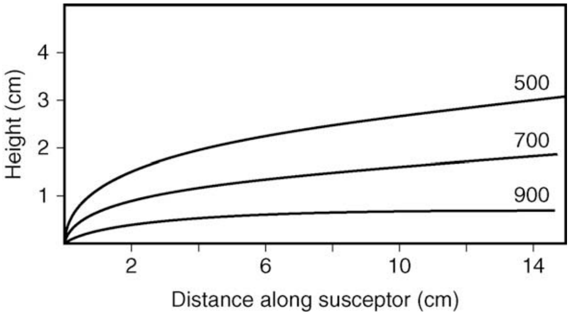

Figure 7.19: Calculated temperature contours for silicon CVD from silane (0.6 torr) and helium as a carrier gas (600 torr). Temperature: 1018 K; gas flow velocity: 15.3 cm s^{-1} [42].

7.4.3 Mass Transport Processes Across a Boundary Layer

Four mass transport processes across a boundary layer can be distinguished:

- Fickian diffusion occurs from a concentration gradient across the boundary layer.
- Thermal diffusion or Soret diffusion is induced by a temperature gradient in, for example, a cold wall reactor [32]. This type of diffusion is most important in systems having large differences in molecular weights and molecular size between vapor species.
- A concentration gradient leads to a density gradient, resulting in a buoyancy-driven *advective flux* [42].
- In the overall CVD reaction, the number of moles of gas may be changed. This creates flux (Stefan flux) towards or away from the substrate surface. In, for example, the CVD of boron from BCl_3 and H_2 according to the reaction

  $$2\ BCl_3(g) + 3\ H_2(g) \rightarrow 2\ B(s) + 6\ HCl(g)$$

  the number of moles in the vapor is changed from 5 to 6, causing a flux from the substrate [43].

7.5 Rate-Limiting Steps During CVD

Various sequential process steps occur in CVD. Each of these steps can be rate limiting in the absence of thermodynamic limitations. Plausible rate-limiting steps are as follows (see also Figure 7.20): (a) transport of gaseous reactants to the boundary layer surrounding the substrate (free and forced convection); (b) transport of gaseous reactants across the boundary layer to the surface of the substrate (diffusion and convections flows); (c) adsorption of reactants on the surface of the substrate; (d) chemical reactions (surface reactions between adsorbed species, between adsorbed species and reactants in the vapor and or between reactants in the vapor), (e) nucleation (at least at the initial stage); (f) desorption of some of the reaction products from the

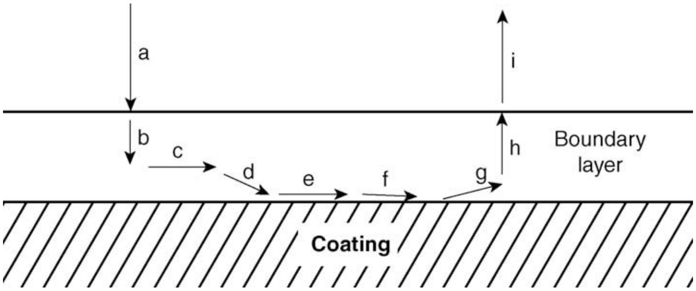

Figure 7.20: The various steps in a CVD process.

surface of the substrate; (g) transport of reaction products across the boundary layer to the bulk gas mixture; (h) transport of reaction products away from the boundary layer. In each of these steps several processes may proceed simultaneously.

Even though several rate-limiting steps can be identified in a CVD process, only five main categories of control are normally discussed:

- *Thermodynamic control* implies that the deposition rate is equal to the mass input rate into the reactor (corrected for the yield of the process). This occurs at extreme deposition conditions (very low flow rates, high temperatures, etc.). Temperature dependence of the deposition rate is obtained from thermodynamic calculations.
- *Surface kinetics control* or nucleation control exist if the deposition rate is lower than the mass input rate into the reactor and the mass transport rate in the vapor to or from the substrate. Surface kinetics control is favorable for obtaining coatings of uniform thicknesses on substrates with complex shapes. Mechanisms of surface reactions are discussed in Section 7.6.
- *Mass transport control* is used to control a process in the vapor in the reactor or from the substrate surface. This occurs frequently at high pressures and high temperatures.
- *Nucleation control.* At low supersaturation the deposition rate may be controlled by the nucleation.
- *Homogeneous reaction control.* In some processes the formation rate of key species in the vapor may control the deposition rate.

Since mass transport in the vapor or surface kinetics usually controls the deposition rate, the following discussion is limited to only these two cases. Surface kinetics control is normally desirable and results in a maximum throwing power or optimum step coverage. Figure 7.21 shows conditions of complete mass transport control, complete surface kinetics control and mixed control. In the surface kinetics control regime, fast diffusion in the vapor is combined with slow surface reaction. For mass transport control, surface kinetics is fast while mass transport in the vapor is slow.

Reaction resistances are often used to predict rate-limiting steps or control in CVD. To illustrate their principle use, reaction resistances are employed to define the surface reaction control and the mass transport control, respectively.

Diffusion flux J_D across the boundary layer is given by

$$J_D = \frac{D}{\mathrm{R}T}\frac{P_b - P_s}{\delta}$$

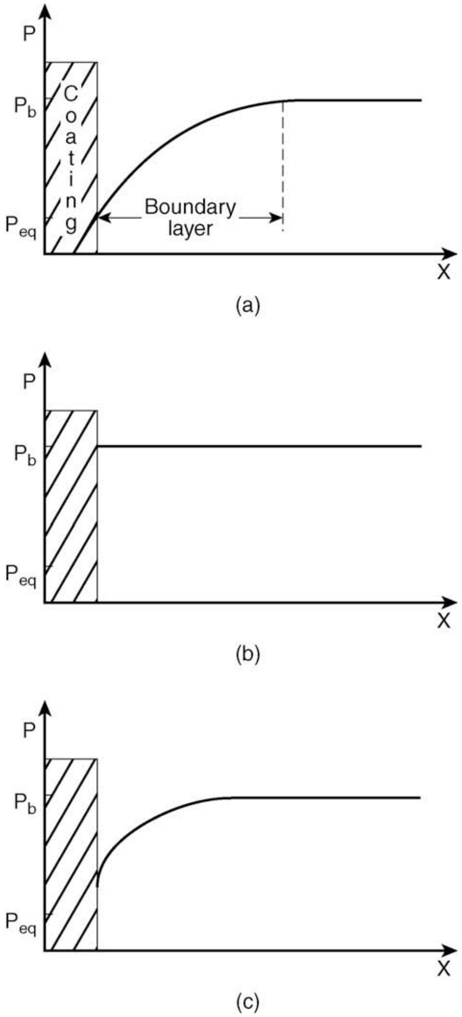

Figure 7.21: Diagrams illustrating examples of complete mass transport control in the vapor (a) and surface kinetics control (b), respectively; (c) shows conditions of mixed control.

where D = diffusion coefficient, R = gas constant, T = absolute temperature (K), b = boundary layer thickness; P_b and P_s: see Figure 7.21.

Mass flux J_M towards the surface is expressed as

$$J_M = \frac{k_m}{RT}\left(P_s - P_{eq}\right)$$

where k_m is the mass transfer coefficient.

P_b and P_{eq} are derived from the reaction gas composition and from thermodynamic calculations, respectively. P_s can be eliminated by assuming steady-state conditions ($J_M = J_o$)

$$P_s = \frac{P_b + \frac{k_m \cdot \delta}{D} \cdot P_{eq}}{\frac{k_m \cdot \delta}{D} + 1}$$

J_m is thus given by

$$J_M = \frac{1}{RT} \frac{P_b - P_{eq}}{\frac{\delta}{D} + \frac{1}{k_m}}$$

$P_b - P_{eq}$ is the driving force for the process and δ/D and $1/k_m$ are reaction resistances. If $\delta/D \gg 1/k_m$ the process is controlled by the mass transport in the vapor, while surface reaction control is achieved when $1/k_m \ll b$.

As stated previously, surface kinetics control is a condition prerequisite to obtaining coatings with uniform thickness on complex shaped substrates. Temperature and pressure dependence of the reaction resistances must be analyzed to achieve surface reaction control.

Thickness δ of the boundary layer (laminar flow) at a position x on the substrate is

$$\delta = a\{\eta x/\rho v\}^{1/2}$$

where a = proportionality constant, η = viscosity of the gas, v = velocity of the gas, and ρ = density of the gas.

The value of ρ depends on both temperature and pressure, while η and v depend only on temperature.

$$\rho = Mp/RT$$

where M = molecular weight and p = total pressure;

$$\eta = \eta_o(T/T_o)^m$$

where T_o = reference temperature, η_o = reference value, m = constant ($0.6 < m < 1.0$), and

$$v = v_o T/T_o$$

where v_o = reference velocity.

From the equations for ρ, η, and v, the pressure and temperature dependence of δ is expressed as

$$\delta = \mathrm{const}(T^{m/2}/p^{1/2})$$

The pressure and temperature dependence of the diffusion coefficient D is

$$D = D_{i,\mathrm{o}}\,(p_i/p)(T/T_\mathrm{o})^{1.75}$$

where $D_{i,\mathrm{o}}$ is the reference value of the diffusion coefficient and p_i is the partial pressure of species i. The reaction resistance is then

$$\delta/D = \mathrm{const}\ p^{1/2}/T^{(1.75-m/2)}$$

Hence δ/D increases with increasing pressure and decreasing temperature.

The value of k_m follows the Arrhenius equation

$$k_\mathrm{m} = A\exp^{E_\mathrm{a}/\mathrm{R}T}$$

where E_a is an activation energy. Thus surface reaction resistance increases with decreasing temperature. This increase is more rapid than the δ/D increase with decreasing temperature. Hence surface reaction control can be achieved at lower temperatures.

The surface reaction control regime should be chosen because it generally possesses the most attractive process conditions (highest throwing power). Conditions for surface kinetics control can be identified from Arrhenius plots (logarithm of the deposition rate versus the reciprocal temperature). In this case, the slope of the Arrhenius plot has a high negative value, often in the range 100–300 kJ/mol. For mass transport control, the slope of the Arrhenius plot can be either positive (exothermic processes) or negative (endothermic processes) (Figure 7.22). When total pressure decreases, the diffusion rate of the species in the vapor increases, indicating that surface kinetics control is readily achieved at low pressures. Figure 7.23 illustrates that the temperature region of surface kinetics control expands at lower pressures.

Surface kinetics can also be attained by increasing the gas flow velocity (Figure 7.24). At low gas flow velocities, the thermodynamics control the deposition. Increasing the gas flow means entering the mass transport controlled regime. The surface kinetics control is reached at even higher gas flow velocities.

The fourth possibility to achieve the surface kinetically controlled region is to use another precursor with a higher thermochemical stability. As shown in Figure 7.25, use of $SiCl_4$ instead of SiH_4 results in surface kinetics control at higher temperatures.

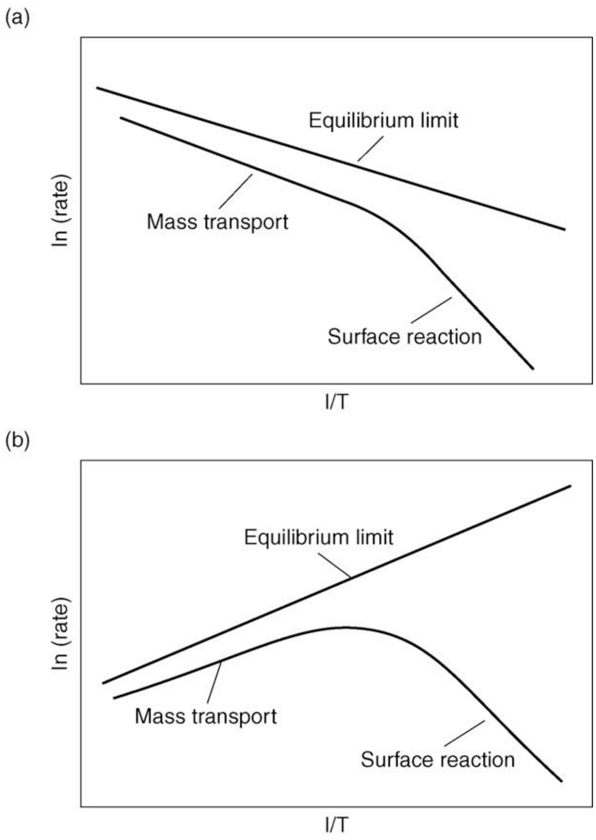

Figure 7.22: Schematic Arrhenius plots for (a) endothermic and (b) exothermic processes.

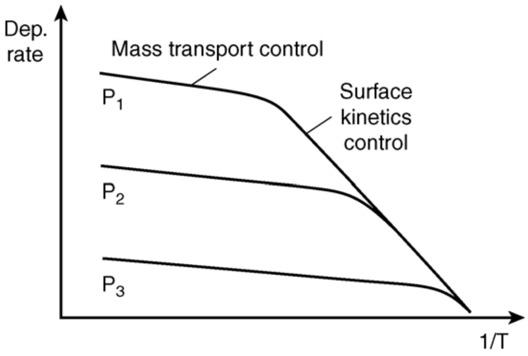

Figure 7.23: Regions of mass transport and surface kinetics control at different total pressures ($P_1 < P_2 < P_3$).

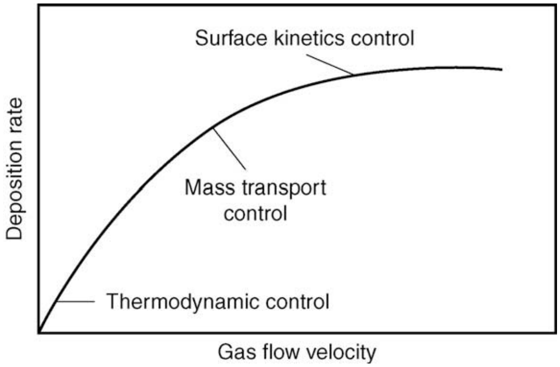

Figure 7.24: Influence of gas flow velocity on the control of a CVD process.

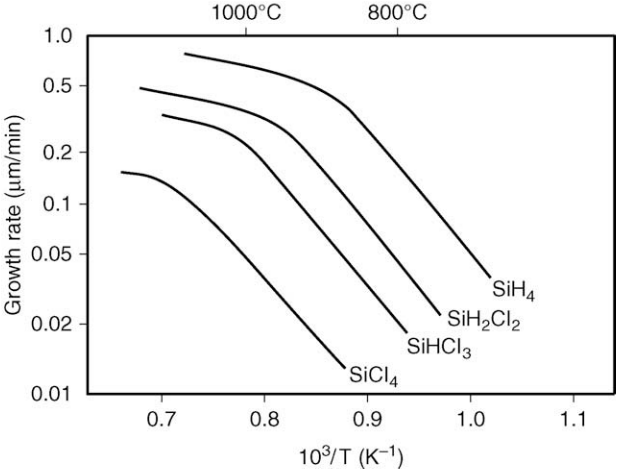

Figure 7.25: Influence of the thermochemical stability of the precursor on the process control at silicon CVD.

7.6 Reaction Mechanisms

Reaction mechanisms in CVD processes are very complicated and only a few are well known. Reactants are transported to the substrate surface in the deposition process. Molecules and/or atoms are adsorbed on specific surface sites. After surface diffusion, the molecules/atoms are incorporated in a step and finally, after diffusion along the step, incorporation in a stable crystallographic site takes place. The investigation by Bloem and Claassen [45] of CVD rate-determining reactions of silicon from SiH_2Cl_2 in the temperature range 800–1000 °C illustrates the various steps of a CVD process. A list of the reactions considered is given below.

1. Transport of SiH_2Cl_2 across the boundary layer:

$$SiH_2Cl_2(g) \rightarrow SiH_2Cl_2(g)$$

2. Homogeneous reactions in the vapor:

$$SiH_2Cl_2(g) \rightarrow SiCl_2(g) + H_2(g)$$

$$SiCl_2(g) + HCI(g) \rightarrow SiHCl_3(g)$$

3. Adsorption at free surface sites *:

$$SiH_2Cl_2(g) + * \rightarrow SiH_2Cl_2*$$

$$SiCl_2(g) + * \rightarrow SiCl_2*$$

$$HCl(g) + * \rightarrow Cl* + 1/2\ H_2(g)$$

$$1/2\ H_2(g) + * \rightarrow H*$$

4. Surface reactions:

$$SiH_2Cl_2* \rightarrow Si* + 2\ HCl(g)$$

$$SiH_2Cl_2* \rightarrow SiCl_2* + H_2(g)$$

$$SiCl_2* + H_2(g) \rightarrow Si* + 2\ HCl(g)$$

$$SiCl_2* + HCI(g) \rightarrow SiHCl_3(g)$$

$$SiCl_2* + SiCl_2(g) \rightarrow SiCl_4(g) + Si(cryst)$$

Si(cryst) = stable crystallographic site in the crystal grown.

5. Growth reactions; surface step sites are denoted (st):

$$Si* \rightarrow Si(st)$$

$$Si(st) \rightarrow Si(cryst)$$

$$SiCl_2* \rightarrow SiCl_2\ (st)$$

$$SiCl_2\ (st) + H_2(g) \rightarrow Si(cryst) + 2\ HCI(g)$$

In CVD of silicon from SiH_2Cl_2, the last reaction given was rate determining.

7.7 Nucleation

Since the properties of a material are influenced by grain size, defects, inclusions, etc., nucleation is the most important process in the deposition of materials. At the initial stages of growth, nucleation on a foreign substrate determines the grain size in the ‘first layer’, defects in it and, to a large extent, adhesion. In the subsequent growth secondary nucleation may occur with a generation of new grains, defects, inclusion of vapor species in pores, etc.

The various steps during the heterogeneous nucleation of an element A on a foreign substrate is schematically shown in Figure 7.26, in which hydrogen and AX react. A atoms deposited are adsorbed on the surface of the substrate. Subsequently the adsorbed atoms may desorb from the substrate, diffuse into the substrate, possibly with the formation of intermediate phases, or react with HX with the formation of AX. Unstable aggregates of A atoms, embryos, are formed after surface diffusion and direct impingement of A atoms from the vapor. Some of these embryos will grow at the expense of others and attain the status of stable A nuclei (supercritical A nuclei). A continuous layer is formed after lateral growth and coalescence. The growth rate of the nuclei is determined by the concentration of adatoms. Finally, the coalescence generates, in general, defects, i.e. grain boundaries.

Three-dimensional nucleation typically occurs on foreign substrates. However, when nucleation takes place on native substrates (nucleus and substrate of the same material)

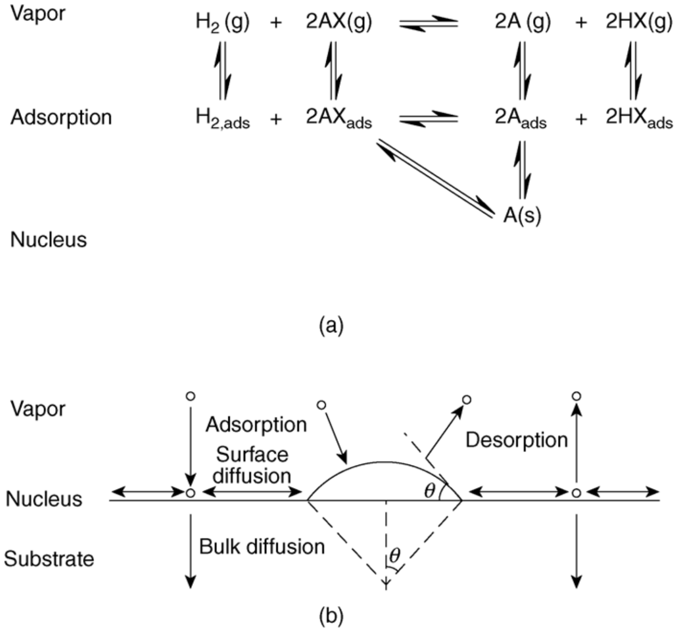

Figure 7.26: Schematic representation of nucleation of A on a substrate during hydrogen reduction of AX (a), and various ‘mechanistic pathways’ that can be followed by A (b).

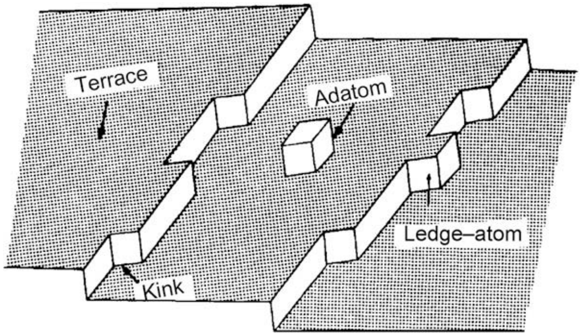

Figure 7.27: The Terrace, Ledge and Kink (TLK) model of a surface.

two-dimensional (2D) nucleation is possible. The TLK model (Terrace, Ledge, Kink) of a surface is used to describe 2D nucleation (Figure 7.27). Besides terraces, ledges, and kinks, atoms adsorbed on the surface (adatoms) exist. Deviation from the equilibrium concentration of the adatoms is a measure on the driving force of the growth process (positive deviation) or of the etching process (negative deviation). Surfaces grow by incorporating surface-diffusing atoms into the steps. This corresponds to a lateral movement of the steps.

The probability of generating new nuclei between the surface steps depends on surface diffusion and deposition rate (the impingement flux of atoms). At a high temperature and a low deposition rate, adatoms have time enough to diffuse and reach the surface steps and be captured by them. A lower temperature and/or higher deposition rate results in shorter diffusion distances, facilitating clustering of adatoms between the steps (2D nucleation). At even lower temperatures and/or higher deposition rates (shorter diffusion distance) amorphous growth occurs [46]. Finally, defects are introduced into the layers when advancing steps meet each other or nuclei.

Surface diffusion is strongly affected by the accessibility of free surface sites. In a CVD process, it is likely that most of the surface sites are occupied by strongly adsorbed molecules. During CVD of silicon from Si–H–Cl gas mixtures, for example, 99% of surface sites are occupied by hydrogen and chlorine atoms [47]. Moreover, impurity adsorption on surface steps can effectively prevent capture of diffusing adatoms. The result is that supersaturation sufficient for nucleation can be built up between surface steps [48]. In summary, layer growth (no nucleation) can only be expected at high temperatures, low deposition rates, and low adsorption. This requires long diffusion distances and the free incorporation of diffusing adatoms at the steps.

The nucleation rate is frequently high ($\sim 10^{10}\ \text{cm}^{-2}\ \text{s}^{-1}$) after a suitable incubation time. A saturation value of the nucleus density, which remains constant during a relatively long period, is thus achieved (Figure 7.28) [49]. The saturation value is obtained at a stage when the nuclei are so dense that a saturation high enough for nucleation cannot be built up between the nuclei,

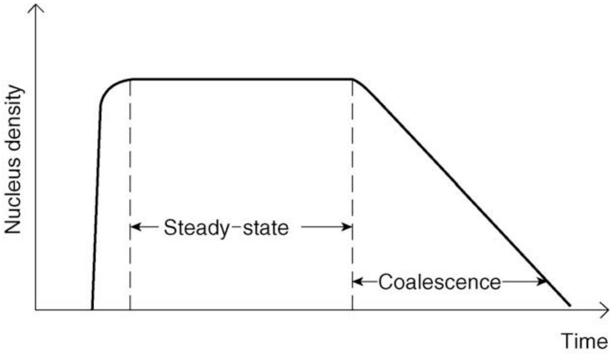

Figure 7.28: Nucleus density as a function of process time.

i.e. when the mean diffusion distance is longer than half the mean nucleus distance. Subsequently, nuclei grow laterally and nucleus density is constant until coalescence occurs. The saturation nucleus density, N_s, is strongly dependent on process conditions. Figure 7.29 shows the influence of temperature on N_s for different silanes for silicon CVD.

Because of high supersaturation possible in CVD, nuclei of critical size consist of only a few atoms. This means that the thermodynamic treatment of nucleation on the basis of microscopic aggregates [51] is not justified. Instead, statistical mechanical methods must be applied [52].

The highest nucleation rate is attained at locations where supersaturation required for nucleation is most rapidly built up. This is assumed to occur at sites having long adatom

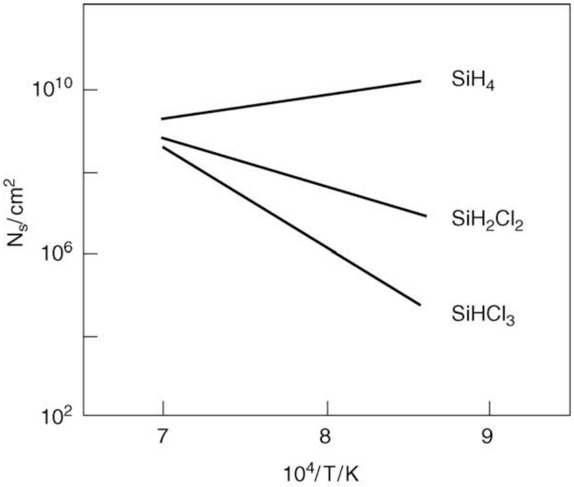

Figure 7.29: Influence of temperature on the saturation nucleus density at silicon CVD from various silanes [50].

residence times and/or at sites of high deposition rate of adatoms. Owing to the long residence time, nucleation on surface steps is highly probable at low deposition rates. Grain boundaries can be favorable diffusion paths, resulting in a high deposition rate of adatoms and hence nucleation of grain boundaries.

Nucleation is strongly affected by surface roughness. An example based on an investigation of preferential nucleation of boron on tungsten filaments illustrates this process. The tungsten filaments used had a rough surface (Figure 7.30a), which originated from the filament drawing process. The ridges on the filament served as nucleation sites (Figure 7.30b). Preferential nucleation on the ridges of the filament is explained as follows [53]. At the onset of the

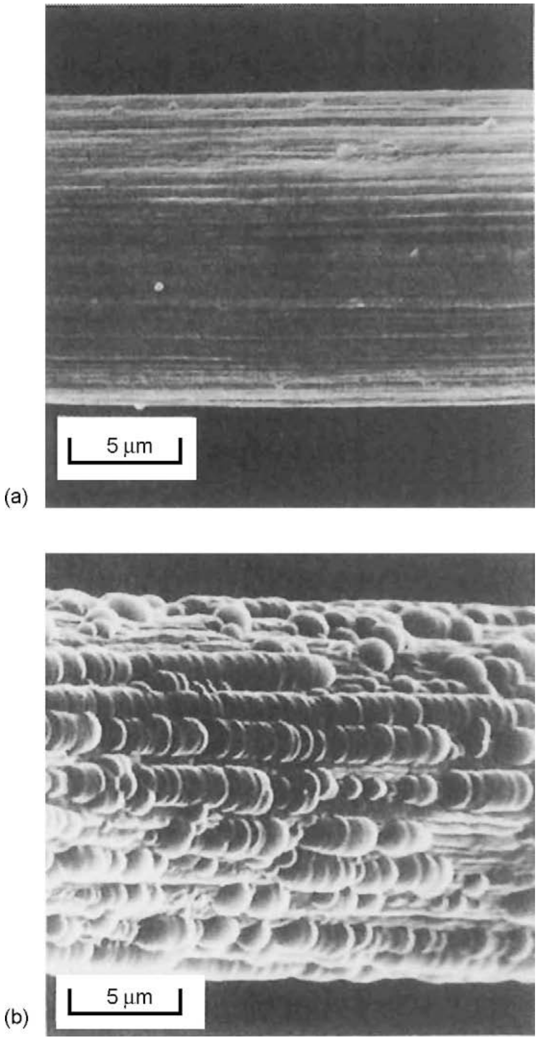

Figure 7.30: (a) Surface of a tungsten filament, and (b) preferentially nucleated boron on ridges of the filament [53].

deposition reaction, boron atoms are added to the substrate surface. Simultaneously, boron is lost from the surface by diffusion into the substrate with the formation of tungsten borides. The diffusion flux, which initially is equal to the deposition rate, later decreases with increasing boride layer thickness (increased diffusion resistance). For geometric reasons it is obvious that the thickness of the boride layer increases at a higher rate under a ridge than under a groove. Consequently, the critical surface concentration for nucleation of boron is reached earlier on a ridge than in a groove.

7.8 Surface Morphology and Microstructure of CVD Materials

Surface morphology and microstructure of CVD materials are controlled by many factors that are often interrelated, such as substrate, temperature, supersaturation, deposition rate, impurities, temperature gradients, and gas flows. In this section a number of theories and classifications of CVD morphologies and microstructures are introduced.

Van den Brekel and Jansen developed and applied a stability theory for single-phase vapor growth [54]. If an arbitrary perturbation at the vapor/solid interface decreases with increased time, the interface is considered stable. However, the interface during CVD in an isothermal condition is unstable. On the other hand, because of the fact that relaxation times in films are much longer than deposition times (a few minutes) smooth layers can be grown even in unstable processes.

The instability of the interface in a vapor growth process can also be described in the same terms as those used to explain dendritic growth from a melt in a negative temperature gradient. Random surface irregularities are frequently formed in growth processes. Surface irregularities have a higher rate of growth if they extend into regions of higher supersaturation. In a CVD process, surface irregularities have better access to fresh reaction gas, which results in a higher supersaturation and hence a higher deposition rate. Also, a negative temperature gradient, as in the cold wall reactor, may result in a higher supersaturation for outgrowths.

Blocher related the various microstructures formed in CVD to temperature and supersaturation process conditions [55]. Epitaxial growth occurs at high temperature/low supersaturation (Figure 7.31). Decreasing temperature/increasing the supersaturation results in the formation of platelets, whiskers, etc. At high supersaturation, a powder resulting from the homogeneous nucleation in the vapor is obtained. Only comments on the growth of selected microstructures are given below.

Epitaxial growth, which is frequently used in the microelectronics industry, occurs at relatively low growth rates. It is affected by the deposit–substrate crystallographic misfit, substrate surface quality, thermal stresses over the substrate, and polycrystalline regions in the substrate. High surface mobility of adsorbed species is required for epitaxial growth, i.e. usually enhanced by a high temperature.

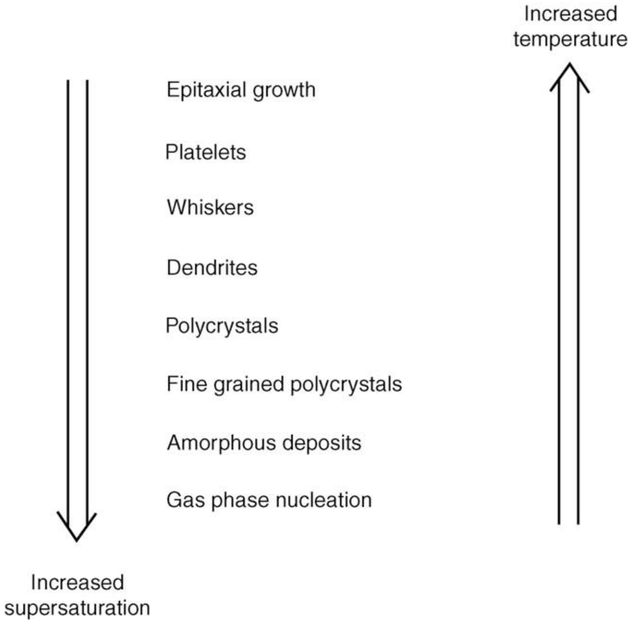

Figure 7.31: Microstructure sequence of CVD materials [55].

Columnar grains are common in CVD films, which can exhibit a high degree of texture. During initial nucleation, nuclei of different crystallographic orientations are formed. Depending on the anisotropy in the growth rate of various crystal surfaces, nuclei will grow at different rates. This preferential growth results in a characteristic columnar growth. Numerous examples of columnar growth in CVD can be found in Proceedings of the International CVD Conference series published by the Electrochemical Society.

Surfaces grow by incorporating surface-diffusing adatoms into surface steps. However, preferential adsorption of molecules at surface steps prevents surface-diffusing adatoms from being captured. Thus a new growth mechanism is required. Throughout the years, the structure of CVD materials has been modified by adding small amounts of foreign substances (growth modifiers) to the reaction gas mixture.

7.9 Selective Deposition

CVD can readily be scaled up to a large-area deposition technique. However, CVD is also well adapted for local deposition or *selective deposition*, where deposition occurs only on specific regions of the substrate surface. Selectivity is achieved by using various focused beams (photons [56], electrons [57–59], or ions [60, 61]). Energetic beams induce local CVD reactions on those areas which are incident. It is also possible to irradiate the substrate surface through a mask with, for example, a laser [62]. Openings in the mask define the substrate areas where the deposition takes place.

Selective CVD can also be achieved on patterned substrates. Selectivity in this case is based on differences in the initial interfacial reactions between the different substrate materials and vapor. Interfacial reactions on one substrate material should be inhibited completely to avoid nucleation, while deposition reactions should be stimulated on those substrate areas where deposition is required.

Several major categories of selective deposition systems exist. In the system described above, deposition takes place on one substrate material while no deposition takes place on the other. However, different phases can also be deposited simultaneously and selectively on different materials, resulting in phase-selective deposition. Analogous to phase-selective deposition, films of different microstructures or different chemical compositions can be deposited on different substrate materials, and hence selectivity in microstructure or chemical composition is attained.

Selective deposition is an emerging field and the demand is great for these processes in many application areas. With the continuous miniaturization of integrated circuit feature sizes there is a need for self-aligned processes. Examples are selective tungsten metallization in very large scale integration (VLSI) and selective gallium arsenide (GaAs) epitaxy for monolithic integration of optoelectronic devices. Other applications include micronics, heterogeneous catalysis, engineering of film/substrate interfaces, and growth of artificial 2D and 3D materials (e.g. photonic crystals). Since selective deposition on patterned substrates is based on interfacial chemistry, there are practically no restrictions on the dimensions of the deposited material islands. This opens up a fascinating perspective of constructing materials with microstructures without thermodynamic or kinetics limitations. The underlying principles of selective deposition are briefly discussed below.

7.9.1 Area-Selective Growth

7.9.1.1 Epitaxial Growth Conditions

There is considerable technological interest today in area-selective epitaxy of both silicon and GaAs. A brief discussion of area-selective growth with reference to silicon and GaAs, respectively, is given below.

Epitaxial films can be grown at relatively high rates near equilibrium conditions, i.e. at a low driving force (low supersaturation) in the deposition process. For heterogeneous nucleation, a higher supersaturation is generally required. This means that conditions of selective growth prevail at supersaturations lower than that required for heterogeneous nucleation. This fact was used by Joyce and Baldrey for growth of silicon from $SiCl_4$ at 1200 °C and atmospheric pressure in openings etched in a SiO_2 mask [63]. A historical review of selective epitaxial growth (SEG) was published by Borland [64]. In SEG, growth is stopped when the surface of the growing film reaches the mask surface. Continued growth results in an overgrowth over the mask. The process is then called epitaxial lateral overgrowth (ELO). For a review of the ELO process, the reader is referred to [65].

A key point in SEG is the suppression of nucleation on the mask (usually silicon oxide or silicon nitride). As mentioned in Section 7.7, the incubation time for nucleation varies with substrate material and deposition conditions. In an ideal case, the incubation time is longer than the deposition time required to prepare the desired structures. However, by using an alternating growth and etching process, SEG can be achieved even for conditions of short incubation times for nucleation [66]. Growth conditions then prevail for about the incubation time. After the growth cycle, the process is switched over to etching with, for example, HCl. A small amount of etching of single crystal silicon also occurs in the SiO_2 openings.

The GaAs SEG/ELO is nearly as old as the silicon SEG/ELO. Tausch and Lapierre reported in 1965 on a GaAs ELO process based on a chloride vapor transport system [67]. With the development of purification techniques for metal-organic compounds such as trimethyl gallium (TMG) and triethyl gallium (TEG), CVD as well as molecular beam epitaxy (MBE), based on the use of these compounds together with AsH_3, are highly attractive for GaAs SEG. MBE and elemental sources yield single crystal growth in etched openings as well as polycrystalline GaAs on the mask (microstructure-selective deposition) [70]. GaAs SEG has received much attention during recent years as a technique for achieving monolithic integration of electronic and optoelectronic devices.

Growth of GaAs from AsH_3 and TMG by MBE or CVD is usually considered to be a non-equilibrium process. The perfection of the crystals grown, their morphology, and the correlation between growth rate and thermodynamic parameters indicates that near-equilibrium conditions exist at the interface between the vapor and the solid. Hence thermodynamics can be utilized to analyze selective growth as well heterogeneous nucleation conditions in GaAs CVD.

According to nucleation theory, a minimum supersaturation is needed for heterogeneous nucleation on the mask. From experimental selectivity data, the maximum supersaturation for maintaining selectivity can be calculated. The supersaturation is generally expressed in terms of chemical potentials. The influence of temperature on chemical potential of GaAs (expressed in elemental chemical potentials of Ga and As_2) at equilibrium with solid GaAs is shown in Figure 7.32. Growth will occur if the chemical potential of GaAs for homogeneous equilibrium in the vapor is higher than that for heterogeneous equilibrium.

The experimental technique used to determine the temperature required to achieve SEG is to raise the temperature successively until no nucleation on the mask can be observed. Since the

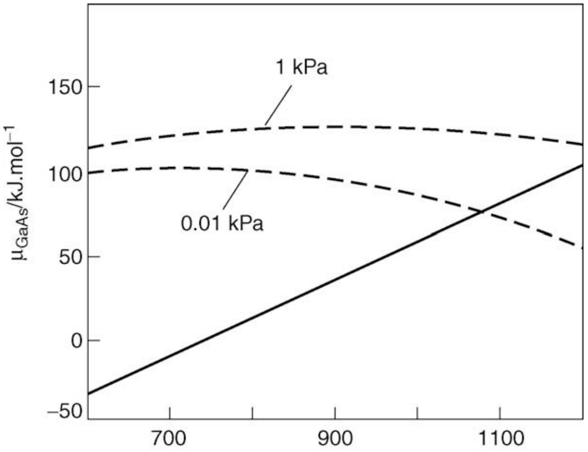

Figure 7.32: Chemical potential of GaAs for heterogeneous equilibrium (solid line), and for two homogeneous equilibria at different total pressures (dashed lines). $H_2/AsH_3/TMG = 500/10/1$[68].

chemical potential of GaAs for the homogeneous equilibrium in the vapor has only a slight temperature dependence (Figure 7.2), the driving force for the deposition (or supersaturation) will decrease upon a temperature increase and a driving force value, yielding no heterogeneous nucleation, will be reached.

Thermodynamics and MBE and CVD experimental SEG data were used in an effort to put experimental selectivity observations on a common basis [69, 70]. A much lower pressure is used in MBE than in CVD. However, irrespective of the growth technique used, experimental SEG data fall in the supersaturation region indicated in Figure 7.33. By using thermodynamics, selectivity data from CVD can be converted to MBE and vice versa.

7.9.1.2 Substrate-Activated Selective Growth

When a substrate of a material other than that being deposited is exposed to the vapor in a CVD process, regions of different activities or reactivities are thus exposed. One material may, for example, act as an effective reducing agent or as a catalyst of dissociative adsorption of gaseous reactants, which may favor deposition. The other material may be relatively inert towards the vapor and growth will be inhibited. Inertness can be selectively increased by using gas additives which are preferentially adsorbed by one of the substrate materials. Strongly adsorbed molecules will strongly passivate a substrate surface and completely suppress the deposition process. A tendency toward substrate-activated area-selective growth is frequently seen during the initial growth stage in CVD on polycrystalline, multiphase substrates. Different phases and different crystallographic orientations of the grains exposed to the vapor represent surface regions of different activities/reactivities and initial growth conditions. Taken

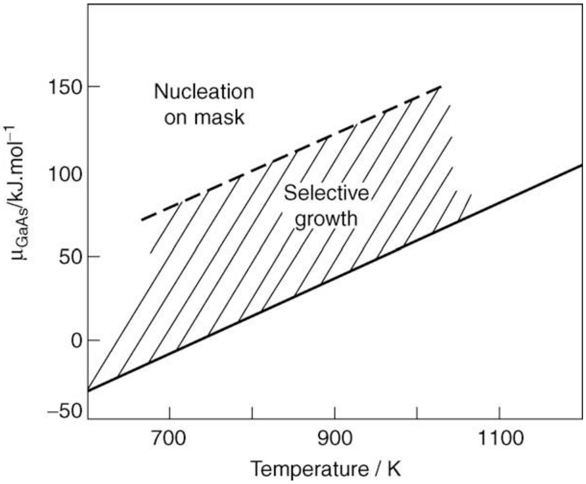

Figure 7.33: Selective growth regime for GaAs. Precursors: $Ga(CH_3)_3$, AsH_3 [70].

to its extreme, the end result is that deposition is inhibited on some substrate areas, while other areas are open for deposition.

Area-selective deposition of refractory metals is of highest interest for metallization in VLSI and ultra large scale integration (ULSI) processes. Selective deposition of refractory metals for metallization has been reviewed by several authors [71–74]. Substrate-activated area-selective growth is well illustrated by the selective tungsten deposition from WF_6 and H_2 on Si/SiO_2 substrates. This process is described below.

Tungsten can be deposited by CVD at low temperatures (300 °C) from H_2 and WF_6 according to the reaction

$$3\ H_2(g) + WF_6(g) \rightarrow W(s) + 6\ HF(g)$$

Deposition occurs on all substrate surfaces exposed to the vapor, since both the source material (WF_6) and reducing agent (H_2) are gases. However, if the reducing agent is replaced by a solid reducing agent (like elemental Si), deposition would occur only on those substrate regions having a reducing agent. Thus, tungsten is deposited only on the Si regions and not on adjacent SiO_2 regions. Si in SiO_2 cannot act as a reducing agent since this silicon has its maximum oxidation number. This is the basis of the initial stage of selective tungsten CVD.

Selective tungsten deposition may proceed according to the process described above as long as elemental Si is exposed to vapor. After a certain time, however, tungsten deposited onto elemental Si will separate Si from the vapor: hence a self-limiting growth process is obtained. The mechanism of self-limitation is still under discussion and may also be due to a polymerization reaction involving lower tungsten fluorides [75]. The polymer formed can also

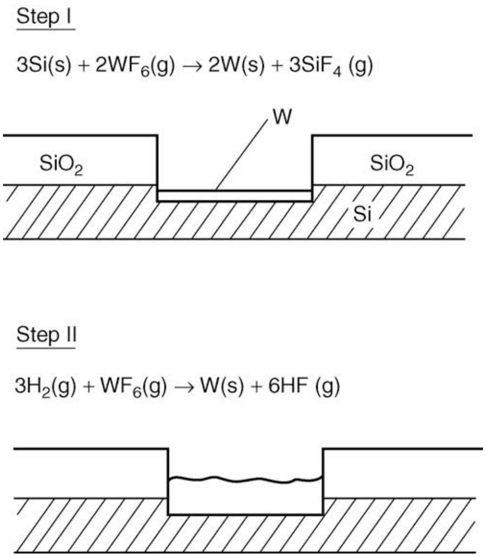

Figure 7.34: The two reaction steps in selective tungsten CVD.

separate Si from the vapor, hence inhibiting the growth process. For growth of thicker tungsten layers, a reducing agent, H_2, must be added to the reaction gas. If the WF_6 concentration is low and H_2 concentration is high enough, i.e. conditions for low supersaturation, tungsten will be deposited on previously deposited W (on elemental Si) and not on SiO_2. For deposition onto SiO_2, resulting in a loss of selectivity, tungsten nucleation must take place. This nucleation step requires a much higher supersaturation than growth. Hence there exists a deposition window, ranging from supersaturation corresponding to equilibrium conditions up to the value needed for heterogeneous tungsten nucleation on SiO_2. Finally, selective deposition of tungsten to substrate regions where tungsten has already been deposited is favored by the dissociation of hydrogen molecules on these areas [76].

In summary, two main reaction steps can be distinguished in tungsten CVD (Figure 7.34):

1. Elemental Si will act as the predominant reducing agent even if a large amount of hydrogen is used in the reaction gas. This results in tungsten deposition on those substrate regions where elemental Si is exposed to the vapor. The reaction step includes an etching of elemental silicon, i.e. Si is consumed.

$$2\ WF_6(g) + 3\ Si(s) \rightarrow 2\ W(s) + 3\ SiF_4(g)$$

   Considering the stoichiometry of this reaction, about 200 Å Si is consumed for 10 Å tungsten deposited. The topography of the Si/W interface is affected by this reaction. Etching and hence the topography can be reduced by, for example, addition of SiF_4 to the reaction gas mixture [77].

2. Another reducing agent, H_2, must take over, since the tungsten film, and probably the resultant tungsten fluoropolymer, prevent reactions between the vapor and Si.

Chemical reactions in the first step are usually extremely fast and a thermodynamically controlled CVD process results. In the second process step, the deposition process is operated at low supersaturation to avoid nucleation on the mask material (SiO_2). Growth conditions in the second step are close to those existing in the area-selective epitaxy discussed above and can be described by thermodynamics. Thermodynamics is used as a guide for prediction of trends in selectivity and substrate etching when deposition conditions are changed. It has also been used for identification of plausible (and often undesired) side reactions as well as gaseous selectivity modifiers, improving selectivity [10].

7.9.1.3 Adsorption-Induced Selective Growth

As discussed above, heterogeneous nucleation on one of the substrate materials must be suppressed for a relatively long time in an ideal selective growth system. The incubation time for nucleation is influenced by many factors: temperature, substrate reactivity, adsorption, etc. Adsorbed molecules can reduce the rate of surface reactions and, in extreme, inhibit nucleation completely. The concept of strongly adsorbed molecules onto one of the substrate materials was used to achieve area-selective growth of boron carbide on a patterned substrate exposing areas of titanium (Ti) and molybdenum (Mo) to the vapor [78]. Boron trichloride, ethylene, and hydrogen were used as reactants and the deposition temperature was 1400 K. Ethylene molecules (or fragments of them) were preferentially and strongly adsorbed on molybdenum and no nucleation of boron carbide was observed. On titanium, however, fast nucleation kinetics was achieved. Deposition was located only on those substrate areas having titanium. Boron carbide was amorphous and contained about 21 at.% carbon. This illustrates that adsorbed molecules can act as masks and can be used to inhibit deposition on prescribed substrate regions.

7.9.2 Phase-Selective Deposition

A new dimension in the field of selective growth is realized in phase-selective growth. Phase-selective growth results when several phases are selectively and simultaneously deposited on prescribed substrate materials/regions. This can result in growth of, for example, a semiconductor together with an insulator, i.e. selectivity in properties is also achieved. Phase-selective deposition can be achieved in different ways. In this chapter, two principles of phase-selective growth are discussed: phase-selective deposition attained by differential nucleation behavior and by secondary processes in or on the growing film, respectively.

7.9.2.1 Phase-Selective Deposition by Differential Nucleation Behavior

Initial substrate/vapor reactions and nucleation kinetics are usually dependent on substrate material. This can result in nucleation of different phases on different substrate materials.

Provided that no secondary processes like phase transformation in the solid state occur in the film or that no new phase is nucleated on top of the growing film, the originally nucleated phases will continue to grow and a phase-selective deposition is obtained.

This principle is used for phase-selective growth of two boron carbides: Ti–BC_x and $B_{13}C_2$. The substrate used is that obtained after area-selective growth of boron carbide described above, i.e. the substrate exposes molybdenum and amorphous boron carbide to the vapor. The vapor contained boron trichloride, methane, and hydrogen, and the growth temperature was 1400 K. Ti–BC_x was obtained on the amorphous boron carbide while $B_{13}C_2$ was grown on molybdenum. This phase-selective growth is attributed to differential nucleation kinetics since no secondary processes were observed in or on the films [79].

7.9.2.2 Phase-Selective Deposition Achieved Using Secondary Processes

Elemental boron (B) has several crystalline polymorphs and amorphous boron also exists. Phase-selective growth was studied in this system by using the Ti/Mo patterned substrates described above. Fast nucleation was observed on both Ti and Mo. Amorphous boron was obtained on Ti, while a-rhombohedral boron was grown on Mo. Boron grown on Ti contained a small amount of Ti (about 500 ppm) throughout the layers, while no traces of Mo was detected in a-B (detection limit 1 ppm). Titanium stabilizes the originally nucleated amorphous boron [80]. To obtain crystalline boron, a phase transformation in the solid state is needed and such a transformation can be assumed to have a high energy barrier to overcome. Amorphous boron can also be obtained initially on Mo. However, an immediate phase transformation is expected because of the deposition temperature used. Moreover, the film did not contain any substrate contaminants contributing to a stabilization of amorphous boron. The morphology of the phase-selectively deposited boron is shown in Figure 7.35. Amorphous boron is characterized by the rounded nodules.

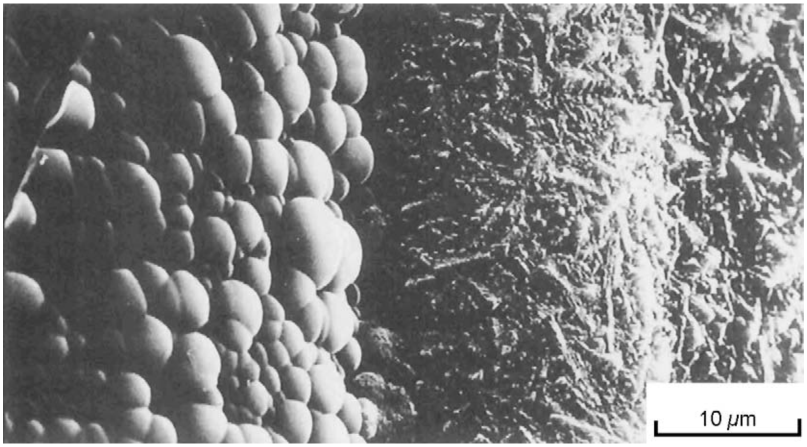

Figure 7.35: Phase-selective growth of amorphous boron (rounded nodules) and a-rhombohedral boron on a substrate exposing titanium and molybdenum [80].

7.10 Selected Applications of the CVD Technique

The CVD technique is known for its versatility in producing materials of greatly varying properties. This is illustrated by the examples given in the applications list below.

- *Microelectronics* industries use CVD for growth of epitaxial layers (vapor-phase epitaxy (VPE)) and for making films serving as dielectrics (low and high *k*), conductors, passivation layers, diffusion barriers, oxidation barriers, etc. An emerging field is selective deposition of refractory metals and silicides for metallization in VLSI.
- *Semiconductor lasers* of GaAs/(Ga,AI)As and InP/(In,Ga)As. These materials are also used in microwave devices and solar cells.
- *Optical fibers* for telecommunication. Optical fibers are produced by coating the inside of a fused silica tube with oxides of silicon, germanium, boron, etc., for obtaining the correct refractive index profile. After the deposition, a fused silica tube is collapsed to a rod and the rod is then drawn into a fiber.
- *Solar energy* conversion by the utilization of selective absorbers and of thin film solar cells of silicon and gallium arsenide, and dye sensitized solar cells.
- *Carbon nanotubes* for advance electronic, biological and chemical devices and detectors.
- *Wear-resistant* coatings have wide industrial applications. Coatings of TiC, TiN and Al_2O_3 on cemented carbide cutting-tool inserts and of TiC on steels (punches, nozzles, free wheels, etc.) are used extensively.
- *Friction-reducing* coatings for use in sliding and rolling contacts, for example.
- *Corrosion-resistant* coatings (Ta, Nb, Cr, etc.).
- *Erosion-resistant* coatings (TiC, Cr_7C_3, B_4C, etc.).
- *Heat-resistant* coatings ($A1_2O_3$, SiC, Si_3N_4, etc.).
- *High temperature superconductors* for use in medical, power grid, high-energy physics applications. Examples are $Bi_2Sr_2Ca_nCu_{n+1}O_{2n+6}$ (BSCCO) and $YBa_2Cu_3O_7$ (YBCO).
- *Fibers* for use in fiber-reinforced materials (fibers of boron, silicon carbide, boron carbide, etc.).
- *Structural shapes* (tubes, crucibles, heating elements, etc.) of, for example, tungsten and silicon carbide.
- *Decorative* coatings of, for example, TiN (gold color) on watches.
- *Conductive coatings* for integrated circuit interconnects, display applications, solar control, electrochromic windows, automotive windows.

7.11 Outlook

CVD offers many advantages in thin film deposition and has given birth to a wide variety of related technologies. With the use of new precursors and plasma enhancement deposition temperature can be lowered considerably. By lowering total pressure, extremely sharp interfaces with respect to chemical composition and topography can be obtained. Atmospheric pressure CVD is attractive for many applications with its high deposition rates and resulting short process times. Since CVD processes are based on interfacial chemistry, they are sensitive to contamination and loadlock systems must be used to keep the contamination level low. Selective deposition opens fascinating prospects for the future, not only for microelectronic applications but also for materials science in general, and for engineering of interfaces and artificial materials.

References

[1] A. Eftekhari et al., Carbon 44 (2005) 1343.
[2] J.N. Lindstrom, H. Schachner, in: H.E. Hintermann (Ed.), Proc. 3rd European Conf. on CVD (1980) 208.
[3] U. Jansson, J.O. Carlsson, B. Stridh, S. Soderberg, M. Olsson, Thin Solid Films 172 (1989) 81.
[4] W.A.P. Claassen, J. Bloem, J. Cryst. Growth 51 (1981) 443.
[5] F.J. Zeleznik, F.J. Goedon, S., Ind. Eng. Chem. 60 (1968) 27.
[6] F. van Zeggeren, S.H. Storey, The Computation of Chemical Equilibria, Cambridge University Press, Cambridge (1970).
[7] W.R. Smith, Ind. Eng. Chem. Fundam. 19 (1980) 1.
[8] W.R. Smith, R.W. Missen, Chemical Reaction Analysis, Wiley Interscience, New York (1982).
[9] G. Eriksson, Acta Chem. Scand. 25 (1971) 2651.
[10] J.O. Carlsson, A. Harsta, Thin Solid Films 158 (1988) 107.
[11] K.E. Spear, in: T.O. Sedgwick, H. Lydtin (Eds.), Proc. 7th Int. Conf. on CVD, The Electrochemical Society, Pennington, NJ (1979) 6.
[12] M. Ottoson, A. Harsta, J.O. Carlsson, J. Electrochem. Soc. 138 (1991) 778.
[13] D.R. Stull et al., JANAF Thermochemical Tables, Nat. Stand. Ref. Data Ser., NBS 37 (1971).
[14] I. Barin, O. Knacke, Thermochemical Properties of Inorganic Substances, Springer, Berlin (1973).
[15] O. Kubaschewski, E.L. Evans, C.B. Alcock, Metallurgical Thermochemistry, Pergamon, Oxford (1967).
[16] M. Ducarroir, C. Bernard, J. Electrochem. Soc. 123 (1976) 136.
[17] T.M. Bessman, K.E. Spear, J. Electrochem. Soc. 124 (1977) 786.
[18] C. Bernard, in: J.M. Blocher Jr., G.E. Vuillard, G. Wahl (Eds.), Proc. 8th Int. Conf. on CVD, Electrochemical Society, Pennington, NJ (1981) 3.
[19] R. Colmet, R. Naslain, P. Hagenmuller, C. Bernard, ibid. (1981) 17.
[20] L. Vandenbulcke, ibid. (1981) 32.
[21] C.F. Wang, K.E. Spear, ibid. (1981) 54.
[22] M. Boman, J.O. Carlsson, Surf. Technol. 24 (1985) 173 Chemical Vapor Deposition 431.
[23] M. Boman, J.O. Carlsson, in: M. Robinsson, C.H.J. van den Brekel, G.W. Cullen, J.M. Blocher Jr., P. Rai-Choudhury (Eds.), Proc. 9th Int. Conf. on CVD, Electrochemical Society, Pennington, NJ (1984) 150.
[24] K.E. Spear, ibid. (1984) 81.
[25] J.O. Carlsson, J. Vac. Sci. Technol. A6 (1988) 1656.
[26] C.F. Powell, J.H. Oxley, J.M. Blocher Jr., Vapor Deposition, John Wiley & Sons, New York (1966).
[27] K.K. Yee, Int. Met. Reviews 1 (1978) 19.

[28] A.J. Perry, C. Beguin, H.E. Hintermann, in: H.E. Hintermann (Ed.), Proc. 3rd European Conf. on CVD (1980) 131.

[29] V.S. Ban, S.L. Gilbert, J. Cryst. Growth 31 (1975) 284.

[30] T.O. Sedgwick, J.E. Smith, Rh. Ghez, M.E. Cowher, J. Cryst. Growth 31 (1975) 264.

[31] J. Nishizawa, M. Saito, in: J.M. Blocher Jr., G.E. Vuillard, G. Wahl (Eds.), Proc. 8th Int. Conf. on CVD, Electrochemical Society, Pennington, NJ (1981) 113.

[32] R.B. Bird, W.E. Stewart, E.N. Lightfoot, Transport Phenomena, John Wiley & Sons, New York (1960).

[33] G. Westphal, J. Cryst. Growth 65 (1983) 105.

[34] K.F. Jensen, in: M. Robinsson, C.H.J. van den Brekel, G.W. Cullen, J.M. Blocher Jr., P. Rai Choudhury (Eds.), Proc. 9th Int. Conf. on CVD, Electrochemical Society, Pennington, NJ (1984) 3.

[35] G. Wahl, Thin Solid Films 40 (1977) 13.

[36] G. Wahl, R. Hoffman, Rev. Int. Hautes Temp. Refract. 17 (1980) 7.

[37] H. Schlichting, Boundary Layer Theory, 6th ed., McGraw-Hill, NewYork (1968).

[38] F.C. Eversteijn, P.J.W. Severin, C.H.J. vanden Brekel, H.L. Peek, J. Electrochem. Soc. 117 (1970) 925.

[39] L. Talbot, R.K. Cheng, R.W. Schefer, D.R. Willis, J. Fluid Mech. 101 (1980) 737.

[40] L.J. Giling, J. Electrochem. Soc. 129 (1982) 634.

[41] G.J. Hwang, K.C. Cheng, J. Heat Transfer, Trans. ASME 95 (1973) 72.

[42] M.E. Coltrin, R.J. Kee, J.A. Miller, in: M. Robinsson, C.H.J. van den Brekel, G.W. Cullen, J.M. Blocher Jr., P. Rai Choudhury (Eds.), Proc. 9th Int. Conf. on CVD, Electrochemical Society, Pennington, NJ (1984) 31.

[43] F. Rosenberger, Fundamentals of Crystal Growth, Springer, New York (1979).

[44] J.O. Carlsson, J. Less-Common Metals 97 (1980) 70.

[45] W.A.P. Claassen, J. Bloem, J. Electrochem. Soc. 50 (1980) 807.

[46] J.A. Venables, C.R. Price, in: J.W. Matthews (Ed.), Epitaxial Growth, Academic Press, New York (1975) 381.

[47] A.A. Chernov, J. Cryst Growth 42 (1977) 55.

[48] J.O. Carlsson, in: H.E. Hintermann (Ed.), Proc. 3rd European CVO Conference (1980) 10.

[49] J.A. Venables, Phil. Mag. 27 (1973) 698.

[50] W.A.P. Claassen, J. Bloem, J. Electrochem. Soc. 127 (1980) 1836.

[51] J.P. Hirth, G.H. Pound, Condensation and Evaporation, MacMillan, New York (1963).

[52] D. Walton, J. Chem. Phys. 37 (1962) 2182.

[53] J. Vega-Boggio, O. Vingsbo, J.D. Carlsson, J. Mater. Sci. 12 (1977) 1750.

[54] C.H.J. van den Brekel, A.K. Jansen, J. Cryst. Growth 43 (1978) 364.

[55] J.M. Blocher Jr., J. Vac. Sci. Technol. 11 (1974) 680.

[56] D.J. Eherlich, J.Y. Tsao, J. Vac. Sci. Technol. B1 (1983) 969.

[57] B.H. Chin, G. Ehrlich, Appl. Phys. Lett. 15 (1981) 253.

[58] S. Matsui, K. Mori, J. Vac. Sci. Technol. B4 (1986) 299.

[59] R.R. Kunz, T.E. Allen, T.M. Mayer, J. Vac. Sci. Technol. B5 (1987) 1427.

[60] J. Melngailis, J. Vac. Sci. Technol. B5 (1987) 469.

[61] T. Kato, H. Morimoto, K. Saitoh, H. Nakata, J. Vac. Sci. Technol. B3 (1985) 50.

[62] G.S. Higashi, G.E. Blonder, C.G. Fleming, in: V.M. Donelly, I.P. Herman, M. Hirose (Eds.), Photon, beam, and plasma stimulated chemical processes at surfaces, 75, Materials Research Society, Pittsburgh, PA (1987) 117.

[63] B.D. Joyce, J.A. Baldrey, Nature 195 (1962) 485 Chemical Vapor Deposition 433.

[64] J.O. Borland, in: G.W. Cullen, J.M. Blocher Jr. (Eds.), Proc. 10th Int. Conf. on CVD, Electrochemical Society, Pennington, NJ (1987) 307.

[65] L. Jastrzebski, J. Cryst. Growth 63 (1983) 493.

[66] L. Jastrzebski, J. Corboy, J. McGinn, R. Pagliaro Jr., J. Electrochem. Soc. 130 (1983) 1571.

[67] F.W. Tausch Jr., A.G. Lapierre III, J. Electrochem. Soc. 112 (1965) 706.

[68] Y. Furumura, F. Mieno, T. Nishizawa, M. Maeda, J. Electrochem. Soc. 133 (1986) 379.

[69] J.O. Carlsson, in: M. Ostling (Ed.), Proc. 13th Nordic Semiconductor Meeting, Royal Institute of Technology, Stockholm (1988) 298.

[70] J.O. Carlsson, Unpublished.

[71] M.L. Green, J.O. Borland, in: G.W. Cullen, J.M. Blocher Jr. (Eds.), Proc. 10th Int. Conf. on CVD, Electrochemical Society, Pennington, NJ (1987) 603.

[72] P. Lami, Y. Pauleau, J. Electrochem. Soc. 135 (1988) 980.

[73] Y. Pauleau, P. Lami, A. Tissier, R. Panyel, J.C. Oberlin, Thin Solid Films 143 (1986) 259.

[74] M.L. Green, Y.S. Ali, T. Boone, B.A. Davidsson, L.C. Feldman, S. Nakahara, J. Electrochem. Soc. 134 (1987) 2285.

[75] N. Lifshitz, Appl. Phys. Lett. 51 (1987) 967.

[76] C.M. McConica, K. Krisnamani, J. Electrochem. Soc. 133 (1986) 2542.

[77] R.A. Levy, M.L. Greene, P.K. Gallagher, Y.S. Ali, J. Electrochem. Soc. 133 (1986) 1905.

[78] U. Jansson, J.O. Carlsson, J. Vac. Sci. Technol. A6 (1988) 1733.

[79] U. Jansson, J.O. Carlsson, L.M. Markert, J.E. Greene, J. Vac. Sci. Technol. A7(6) (1989) 3172.

[80] U. Jansson, J.O. Carlsson, L.M. Markert, J.E. Greene, J. Vac. Sci. Technol. A9(2) (1991) 266.

CHAPTER 8

Atomic Layer Deposition

Arto Pakkala and Matti Putkonen
Beneq Oy, Vantaa, Finland

8.1 Introduction and Background

Atomic layer deposition (ALD) is a chemical gas phase thin film deposition method based on sequential, self-saturating surface reactions [1–5]. Two or more precursor chemicals, each containing different elements of the materials being deposited, are introduced to the substrate surface separately, one at a time. Each precursor saturates the surface forming a monolayer of material. Most of the commercial ALD deposition systems are based on using inert carrier gas, e.g. nitrogen, at about 1 mbar. Short precursor chemical pulses are injected into the flowing carrier gas, separated by short purge or evacuation periods. A defined amount, typically a monolayer of about 1 Å, of the thin film material is grown during each ALD cycle (pulse of precursor 1 – purge – pulse of precursor 2 – purge). Typical cycle times are from one second to several seconds. Process temperatures range from room temperature to over 500 °C. Most ALD processes operate between 200 °C and 400 °C. ALD processes have been developed for oxides, nitrides, carbides, fluorides, certain metals, II–VI and III–V compounds, and recently also for the first organic materials.

The ALD method was developed for commercial use in Finland in the mid-1970s by Dr Tuomo Suntola and co-workers [1–3]. ALD was initially developed to enable production of thin film electroluminescent (TFEL) flat panel displays, and is currently also used for multiple other industrial applications, including semiconductor device manufacturing. In addition, ALD-related research is conducted in a large number of universities, research centers, and companies.

8.2 Principle of Atomic Layer Deposition

ALD thin film deposition method utilizes highly reactive precursor chemicals, each containing different elements of the material being deposited, by introducing each precursor chemical separately into the reaction zone. In this way uncontrolled gas-phase reactions are prevented, and film growth takes place through controlled and self-saturating surface reactions. This film growth mechanism leads to extremely conformal and uniform material layers. In addition, film growth is quite insensitive to process parameters other than choice of the precursor chemicals and process temperature.

One ALD cycle is illustrated in Figure 8.1. In this example Al_2O_3 is grown from $AlCl_3$ and H_2O. First, a short pulse of $AlCl_3$ is introduced into the flowing carrier gas and an Al-containing monolayer is formed on the surface through a self-terminating reaction. Excess $AlCl_3$ is purged away during a short purge period, when only the inert carrier gas is flowing. H_2O is introduced next and it reacts with the Al-containing monolayer on the surface forming a monolayer of Al_2O_3. Finally, the ALD cycle is completed with a second purge period to remove the excess H_2O and the reaction by-products. The typical film growth rate is about 1 Å

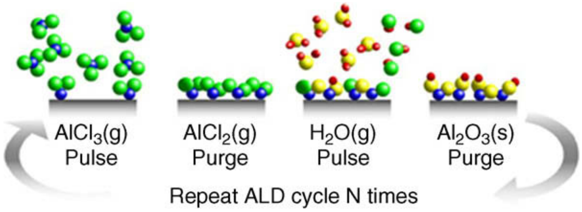

Figure 8.1: Schematic illustration of one ALD cycle.

Table 8.1: Advantages of ALD

Extreme surface conformality	Unique conformality; for nanotubes, nanowires, particles, diffractive optics, DRAM, 3D parts
Pinhole-free films	'Bottom up' growth of ALD is naturally pinhole free; excellent for passivation, barriers, and insulators
Repeatability	Robust in production; without in situ feedback
Scalability	Processes based on robust ALD precursor chemistries straightforward to scale up for production
Ultrathin, dense, smooth films	One atomic layer at a time; gate oxides, tunneling insulators, e.g. for hard disc drives
Artificial materials	Digital control of ALD provides a way to create artificial materials; enables R&D innovations

per cycle, somewhat less than a full monolayer, primarily owing to 'shadowing' of the ligands of the precursor chemicals. The desired film thickness is achieved by repeating the ALD cycle digitally. Typical cycle times range from less than one second to several seconds, depending on the ALD system and process design. Film thicknesses range typically from nanometers to several micrometers.

8.3 Advantages of Atomic Layer Deposition

The advantages of ALD, listed in Table 8.1, are based on the surface-controlled and self-saturating film growth principle. This list provides guidance when coating method options are selected for a specific application. When one or more of these advantages are important for the application, ALD is a viable candidate to provide the coating solution, from research to industrial-scale implementation.

8.3.1 Conformality

Extreme surface conformality is a unique benefit of ALD technology. The conformality of various thin film coating methods is illustrated in Figure 8.2. The surface-controlled film

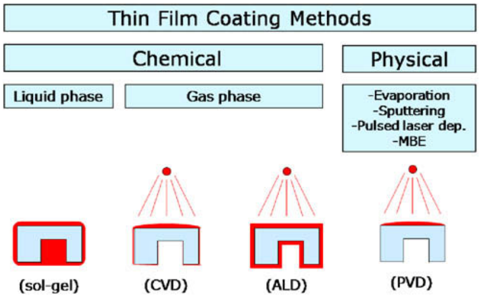

Figure 8.2: Comparison of thin film coating methods.

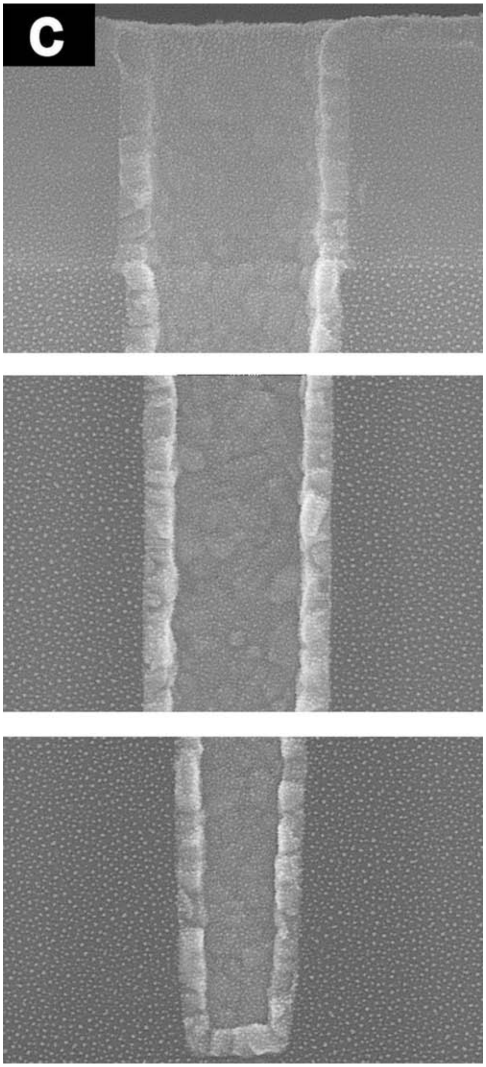

Figure 8.3: High-resolution SEM images of a cross-section of a deep trench with 20 nm HfO_2 deposited by a $(CpMe)_2HfMe_2/O_3$ process at 450 °C. Trench aspect ratio is 50:1 with 6.2 μm depth and 120 nm opening. The upper images show the top part of the trenches, those below show the middle and the bottom at a depth of 6.2 μm [6].

growth of ALD provides highly uniform coatings over surfaces of three-dimensional (3D) parts, vias, deep trenches, porous materials, and particles. The use of ALD to coat the trenches of semiconductor memory devices is one example (Figure 8.3) [6]. ALD is also ideally suited for trench filling planarization coatings, for example on diffractive optics parts (Figure 8.4) [7].

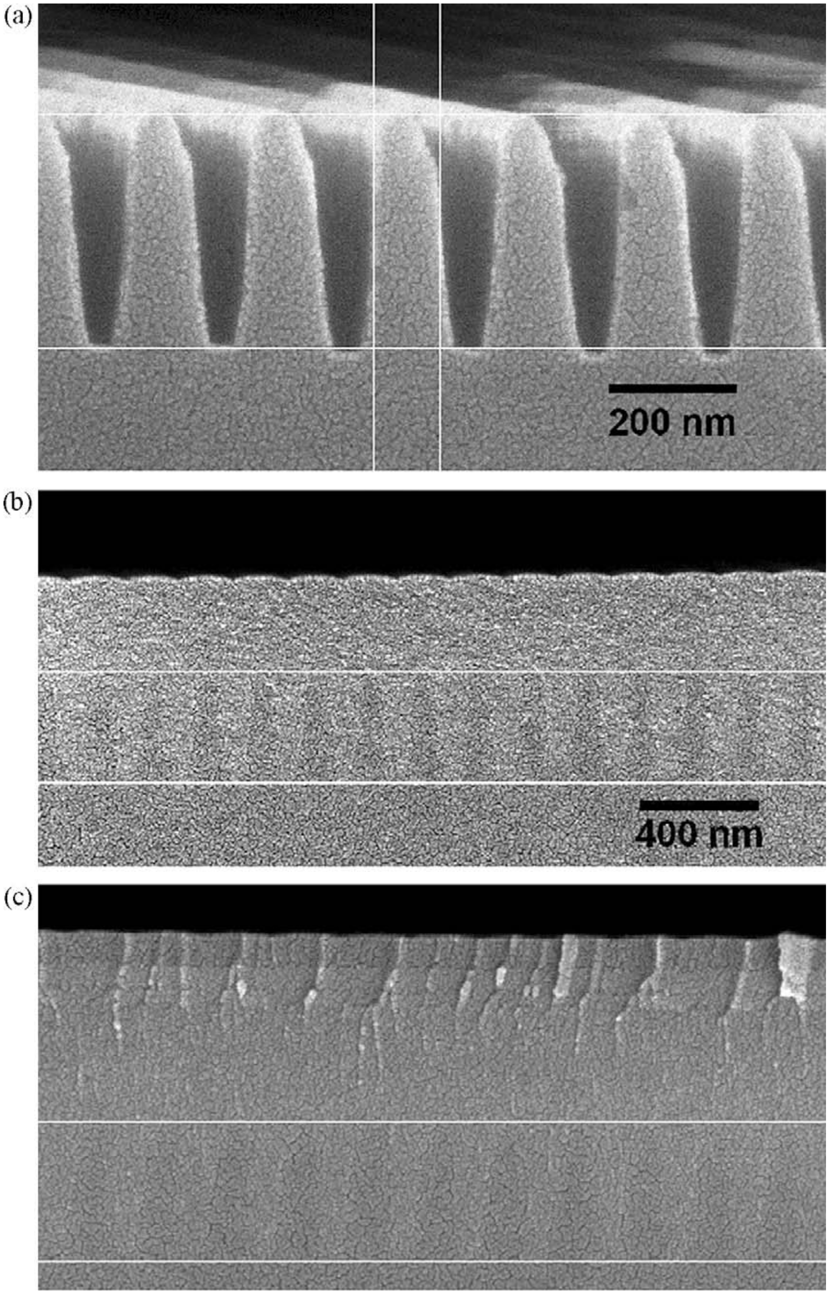

Figure 8.4: Trench filling of optical parts with conformal ALD coating [7].

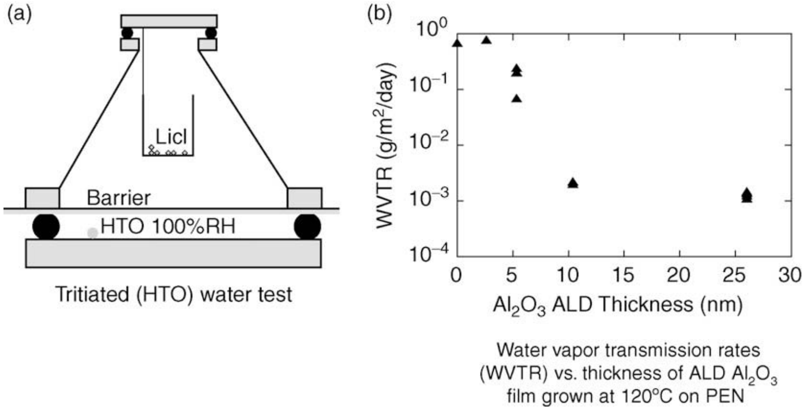

Figure 8.5: Water vapor transmission rate of ALD Al_2O_3 vs film thickness [9].

8.3.2 Pinhole-free Coatings

As a result of the 'bottom–up' film growth mechanism most ALD coatings are naturally pinhole free. This feature is valuable in barrier and passivation applications. ALD also enables high-quality, high-yield insulators over large areas. The TFEL displays are high electrical field devices and ALD-based insulators have been a key factor in the high reliability of the products and for the high production yield [2, 8]. In addition, ALD technology is widely investigated as an option for oxygen and humidity barriers for organic and flexible electronics devices (Figure 8.5). Major improvements in the barrier properties are already achieved in the 10 nm film thickness range [9].

8.3.3 Repeatability of Coatings

High repeatability of ALD processes is based on the surface-controlled and self-saturating film growth mechanism. Selection of robust and proven ALD precursor chemistries is also a key factor for production repeatability and precision. Most of the ALD processes are operated in production without in situ control or tuning, and the processes run automatically, without the need for continuous operator attendance.

ALD technology enables a powerful platform to evaluate and optimize materials and material combinations to provide industrial coating solutions. Development of a challenging, new coating solution usually takes some time, and the end result is often a tailored and optimized stack of materials. After verification of the solution, it is, however, quite straightforward to scale up and implement the development result in production, owing to the high repeatability of ALD.

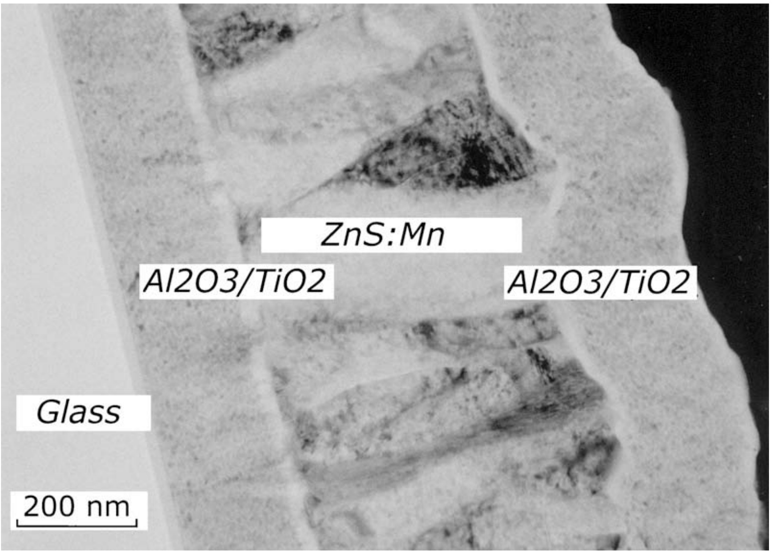

Figure 8.6: Cross-section of TFEL display structure. (Courtesy of Planar Systems and Beneq Oy.)

As an example, the TFEL display structure (Figure 8.6) is a stack of two nanolaminate insulators (Al_2O_3/TiO_2) and the phosphor layer (ZnS:Mn). Precision of individual layers is in the nanometer range, and the total thickness of the stack is over 1 μm. The stack is processed in batch mode and in single pump-down, using six precursor chemicals ($AlCl_3$, $TiCl_4$, H_2O, $ZnCl_2$, $MnCl_2$, and H_2S), and the processes are operated automatically without operator attendance (see Figure 8.13). Production of these TFEL displays began in the mid-1980s and is currently operated in Finland by Planar Systems Inc.

Modified TiO_2 is another example of the high precision and repeatability of ALD technology. The high index of TiO_2 with very low absorption is achieved by modifying crystalline TiO_2 with subnanometer-scale intermediate layers [10] (Figure 8.7). The high repeatability of ALD enables reliable processing of this new material on an industrial scale, without in situ control.

8.3.4 Scalability

The surface-controlled and self-saturating film growth mechanism, and selection of robust and proven ALD precursor chemistries, enable efficient scalability of the ALD processes. The first flow type ALD system was based on a 100 mm main vacuum tube [3, 4]. The first production ALD systems were based on a 250 mm main vacuum tube, followed by a 400 mm tube batch version, and an 800 mm tube version, P800, for large batches and large parts (Figure 8.8). The 400 mm tube P400 series batch ALD systems have been the workhorses of the TFEL display

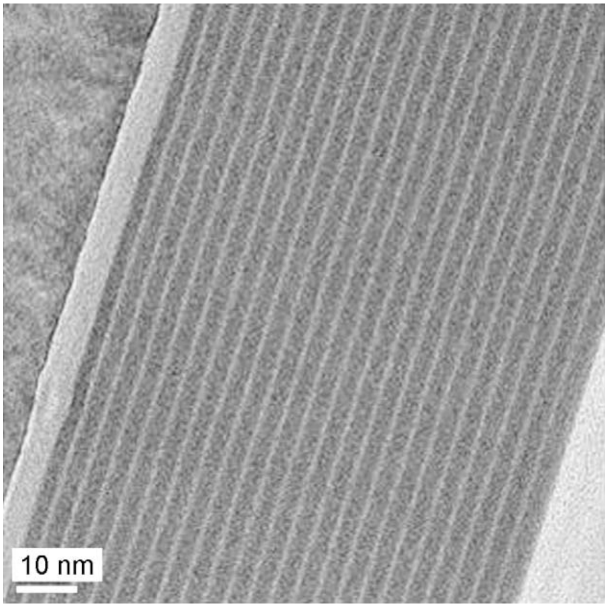

Figure 8.7: High index optical material, modified TiO_2 [10]. (HR TEM picture courtesy of E. Kauppinen and H. Jiang, HUT, Finland.)

production in Finland since the mid-1980s. Similarly, the first single-wafer ALD systems were for 100 mm wafers, and current state-of-the-art production systems are for 300 mm wafers (see Figure 8.15). More recently, photovoltaic and display industries have been driving the development of high-throughput, large-area, single-substrate ALD systems, in both cluster and in-line formats (Figure 8.9). Roll-to-roll ALD systems are also under development [11], to meet the demand for flexible electronics and packaging applications. This development and progress demonstrate the scalability of ALD processes and equipment, to meet new business and market demands.

8.3.5 Ultrathin Films

Most ALD films grow in about 1 Å sequences (growth per cycle), enabling precise deposition of highly conformal films in the nanometer and subnanometer thickness range (Figure 8.10). These features attracted the semiconductor industry's interest in ALD technology, starting during the late 1990s [12, 13]. After extensive research and development work, ALD was first adapted in the semiconductor memory industry in 2005 [14], and at the end of 2007 in the microprocessor industry, by Intel, for gate oxides [15, 16].

Another industry that has widely adapted ALD technology and is utilizing ultrathin films is hard disk drive application, for the insulator in the thin film magnetic head. ALD enabled the

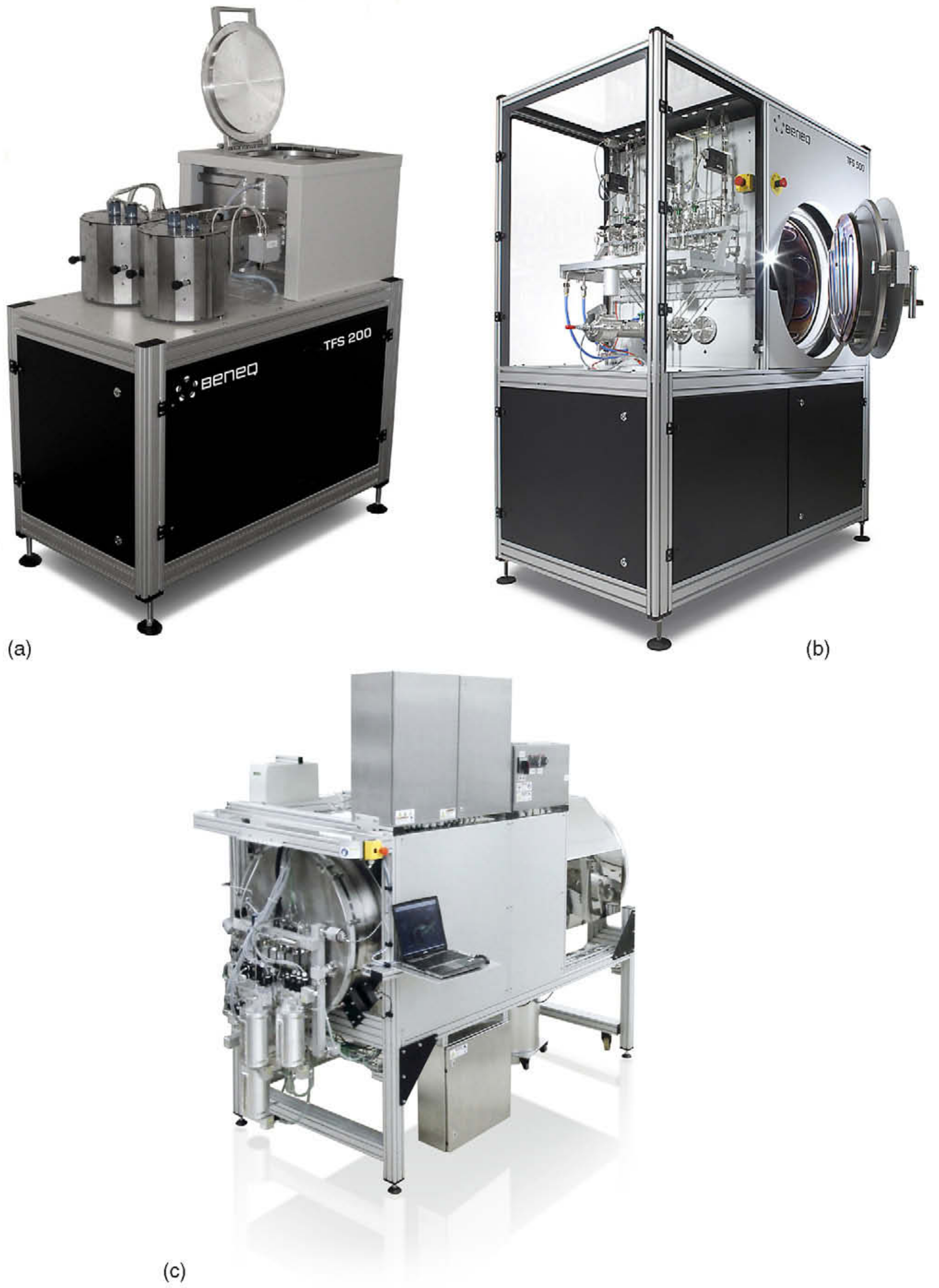

Figure 8.8: ALD systems, from research to industrial production (courtesy of Beneq Oy): TFS 200, TFS 500 and P800.

Figure 8.9: Scalability of ALD, 1.2 × 1.2 m^2 glass substrate coated with in-line TFS 1200 ALD system. (Courtesy of Pekka Soininen and Jarmo Skarp, Beneq Oy.)

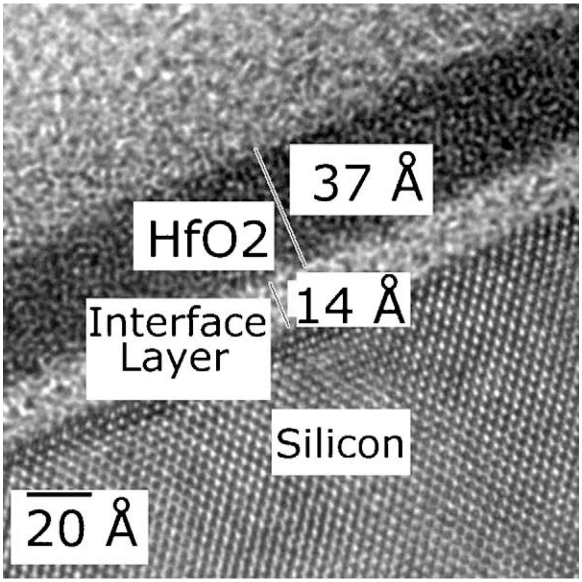

Figure 8.10: HfO_2 gate oxide on a 200 mm wafer. (Courtesy of Beneq Oy.)

industry to continue to scale down dimensions and performance to meet the packaging density requirements [17]. The pinhole-free feature of ultrathin ALD insulators has been a key enabler in this application.

ALD technology is also being used actively in nanotechnology research. For example, high-speed single-wall carbon nanotube field-effect transistor memory elements have been developed recently, based on ultrathin HfO_2 gate insulator, made with ALD [18]. This type of nanotechnology research, enabled with ALD, paves the way beyond silicon-based microtechnology.

8.3.6 Artificial Materials

Probably the most powerful benefit of ALD is the ability to combine two or more different materials in nanoscale, making possible the creation of new ‘artificial’ materials, with unique features. This makes ALD a uniquely powerful enabling technology for state-of-the-art nanotechnology research and for innovation to functionalize surfaces. These new functional materials, combined with precision, high repeatability and scalability of ALD, make ALD technology one of key enablers of new nanotechnology products.

The TFEL display structure (Figure 8.6) was developed in the early 1980s and the ATO insulators are ALD nanolaminates of Al_2O_3 and TiO_2 [19]. The insulator was originally tailored to match optical properties by combining the high and low index materials. During that work it turned out that by fine tuning the nanolaminate ratios, it was possible to optimize the new material for electrical breakdown strength (Figure 8.11). This invention solved the early reliability and electrical breakdown yield issues and enabled production of the TFEL displays. ALD enabled the nanomaterial breakthrough and production scale-up.

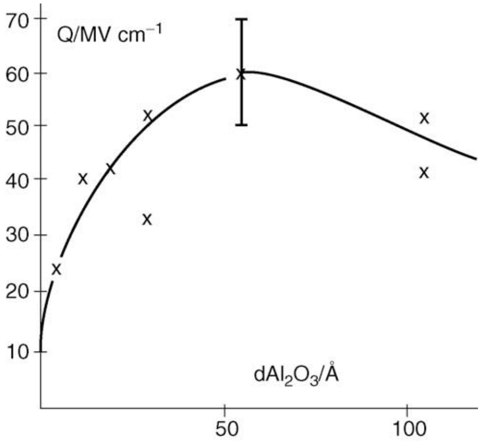

Figure 8.11: Electrical breakdown field strength of ATO insulator vs Al_2O_3/TiO_2 ratio [19].

Another example of nanoscale modifications of material properties is modified TiO_2 (Figure 8.7) [10]. An optical refractive index of 2.3–2.4 at 550 nm is achieved by using a rather high processing temperature of over 250 °C. The high processing temperature, however, leads to polycrystalline TiO_2 and the grain boundaries cause unnecessary optical absorption. Crystal growth is limited by using nanometer-thin intermediate layers of amorphous Al_2O_3. The ALD method enables reliable processing of this modified material, with subnanometer precision.

8.4 Atomic Layer Deposition Precursors, Processes, and Materials

New ALD processes and materials are being actively developed at several Universities. ALD was demonstrated for the TFEL application for the first time by ZnS deposition using elemental zinc and sulfur in the mid-1970s, followed by the use of $ZnCl_2$ and H_2S [20]. After the initial period, several other inorganic precursor types have emerged. During the second half of the 1980s metal organic precursor chemicals were adapted for ALD material research [21, 22]. This opened up plenty of possibilities for new ALD chemistries and processes. A large number of ALD processes have been demonstrated and published to date, and the list keeps growing (Table 8.2).

Table 8.2: Examples of materials deposited by ALD [20]

Materials	Examples
Oxides	
Dielectric	Al_2O_3, TiO_2, ZrO_2, HfO_2, Ta_2O_5, Nb_2O_5, Sc_2O_3, Y_2O_3, MgO, B_2O_3, SiO_2, GeO_2, La_2O_3, CeO_2, PrO_x, Nd_2O_3, Sm_2O_3, EuO_x, GdO_3, Dy_2O_3, Ho_2O_3, Er_2O_3, Tm_2O_3, Yb_2O_3, Lu_2O_3, $SrTiO_3$, $BaTiO_3$, $PbTiO_3$, $PbZrO_3$, Bi_xTi_yO, Bi_xSi_yO, $SrTa_2O_6$, $SrBi_2Ta_2O_9$, $YScO_3$, $LaAlO_3$, $NdAlO_3$, $GdScO_3$, $LaScO_3$, $LaLuO_3$, $Er_3Ga_5O_{13}$
Conductors/semiconductors	In_2O_3, In_2O_3:Sn, In_2O_3:F, In_2O_3:Zr, SnO_2, SnO_2:Sb, ZnO, ZnO:Al, ZnO:B, ZnO:Ga, RuO_2, RhO_2, IrO_2, Ga_2O_3, V_2O_5, WO_3, W_2O_3, NiO, FeO_x, CrO_x, CoO_x, MnOx
Other ternaries	$LaCoO_3$, $LaNiO_3$, $LaMnO_3$, $La_{1-x}Ca_xMnO_3$
Nitrides	
Semiconductors/dielectric	BN, AlN, GaN, InN, SiN_x, Ta_3N_5, Cu_3N, Zr_3N_4, Hf_3N_4
Metallic	TiN, Ti-Si-N, Ti-Al-N, TaN, NbN, MoN, WN_x, WN_xC_y
II–VI compounds	ZnS, ZnSe, ZnTe, CaS, SrS, BaS, CdS, CdTe, MnTe, HgTe
II–VI-based TFEL phosphors	ZnS:M (M = Mn, Tb, Tm), CaS:M (M = Eu, Ce, Tb, Pb), SrS:M (M = Ce, Tb, Pb)
III–IV compounds	GaAs, AlAs, AlP, InP, GaP, InAs
Fluorides	CaF_2, SrF_2, MgF_2, LaF_3, ZnF_2
Elements	Ru, Pt, Ir, Pd, Rh, Ag, W, Cu, Co, Fe, Ni, Mo, Ta, Ti, Al, Si, Ge
Others	La_2S_3, PbS, In_2S_3, Cu_xS, $CuGaS_2$, Y_2O_2S, WS_2, TiS_2, SiC, TiC_x, TaC_x, WC_x, $Ca_x(PO_4)_y$, $CaCo_3$, $Ge_2Sb_2Te_5$

8.4.1 ALD Precursors in General

General ALD precursor requirements differ from other chemical gas-phase methods since all gas-phase reactions should be excluded and reactions take place only at the surface. Although chemical vapor deposition (CVD) precursors can sometimes be used for ALD, nowadays specific precursors have been synthesized for ALD because this deposition technique allows the use of significantly more reactive precursors than CVD. In the ALD method, in order to avoid uncontrolled reactions, sufficient thermal stability of the precursors is needed in the gas phase as well as on the substrate surface within the deposition temperature range, which is typically 150–500 °C. Since ALD relies on self-limiting reactions, a sufficient amount of the precursor is only required during one pulse to cover the adsorption sites on the surface and the excess will be purged by the inert gas between the reactive precursors. Because ALD is a gas-phase process, solid and liquid precursors must be volatile under the operating temperature and pressure, and if heating is required to obtain sufficient vapor pressure, thermal stability of the precursor over a prolonged period is necessary. Stability is key issue, especially when stable industrial processes are designed.

In summary, there are some general requirements for ALD precursors, which include:

- sufficient volatility at the deposition temperature
- no self-decomposition allowed at the deposition temperature
- precursors must adsorb or react with the surface sites
- sufficient reactivity towards the other precursor, e.g. H_2O
- no etching of the substrate or the growing film
- availability at a reasonable price
- safe handling and preferably non-toxicity.

8.4.2 Non-Metal Precursors

Because of the sequential nature of ALD, metal and non-metal precursors are typically separated from each other. The ability to select an oxidizing or reducing precursor in conventional ALD processes makes it possible to control reactivity and reactions of the metal precursor.

In a non-oxidizing regime, reducing the precursor is also necessary for depositing elemental metal films. Hydrogen is perhaps the most widely used reducing agent [23], but metallic zinc vapor [24, 25], silanes [26, 27], and B_2H_6 [28] have also been successfully applied. Molecular hydrogen is quite inert towards typical metal precursors and therefore quite high deposition temperatures are needed to maintain ALD reactions.

Deposition of nitride thin films by ALD requires both a nitrogen source and a reducing agent in order to obtain clean surface reactions. In many cases one compound, e.g. NH_3, serves as both nitrogen source and reducing agent. Ammonia has been used for depositing, for example, TiN, Ta_3N_5, W_2N, NbN, and WCN thin films by ALD, although its reactivity at low temperatures is limited. Other nitrogen-containing compounds, such as $(CH_3)NNH_2$, $^tBuNH_2$, and CH_2CHCH_2NH, have also been studied.

For chalcogenide thin films it is possible to use elemental S, Se, and Te as precursors provided that the other source is a volatile and reactive metal. The first ALD process to be developed was ZnS deposition using elemental zinc and sulfur. For other precursor types, including halides, β-diketonates, and organometallics, simple hydrides, such as H_2S, H_2Se, and H_2Te, have typically been used as a second precursor, although their toxicity must be carefully addressed. Recently, novel Se and Te precursors have been utilized for ALD, enabling the deposition of selenides and tellurides [29].

Typically in the case of ALD-processed oxide films, precursors attached to the surface can be oxidized with H_2O, H_2O_2, N_2O_4 [30], N_2O [31], O_2, or O_3, the choice dependent on the metal precursor selected. Water has frequently been used as an oxygen source and indeed it readily reacts with many metal halides, alkyls, and alkoxides. For metal β-diketonate-type compounds, only ozone or oxygen plasma can be used owing to the higher thermal stability of the precursor. The use of a strong oxidizer guarantees that only a small amount of carbon is left in the film, as well as ensuring better interface quality.

8.4.3 Metal Precursors

The most used volatile metal-containing ALD precursors can be classified into five different main categories, namely halides, β-diketonate complexes, N-coordinated compounds (amides, amidinates), alkoxides, and true organometallics, i.e. metal alkyls and cyclopentadienyl-type compounds. Other compounds have occasionally been used as ALD precursors for thin films, for example metal nitrates, carboxylates, and isocyanates [32, 33].

Several metal halide precursors have been applied in ALD processes, usually with water as an oxygen source. They have enough high deposition rates and the price for industrial use is reasonable. However, for delicate applications halide contamination of the film may cause problems at low deposition temperatures. In addition, HX ($X = F$, Cl, Br, or I) evolution during the deposition process may cause problems such as corrosion and etching of the film.

β-diketonate-type metal chelates are known for their volatility and therefore they were originally synthesized for the separation of metals by fractional sublimation [34], but they can be also be used for CVD [35, 36]. The good thermal stability and reasonable volatility of the β-diketonate-type metal chelates make them suitable for ALD if a strong oxidizer can be used. Coordinatively unsaturated β-diketonate-type compounds may oligomerize or react with the environment and become less volatile [37, 38]. This causes instability, especially with larger and basic central ions such as strontium and barium.

Organometallic precursors, i.e. compounds with metal to carbon bond, usually offer high reactivity in ALD. They were first used for GaAs depositions by using either $(CH_3)_3Ga$ [39, 40] or $(CH_3CH_2)_3Ga$ [41] as a gallium source, with AsH_3 as a second reactant. However, their true capabilities were realized when their usefulness for the deposition of oxide materials was discovered. Al_2O_3 is maybe the most frequently studied ALD-processed material since. For example, $(CH_3)_3Al$ has been used with H_2O, H_2O_2, NO_2, N_2O, O_2- plasma [42, 43] or O_3 [44] as oxygen sources [45]. Other metal alkyls such as $(CH_3)_2AlCl$, [46] $(CH_3)_2AlH$ [47] or $(CH_3CH_2)_3Al$ have also been used as aluminum sources. The $(CH_3)_3Al/H_2O$ process works in a wide temperature range of 100–500 °C with a reasonably high deposition rate of up to 1.2 Å/cycle. At very low deposition temperatures OH-type impurities remain in the film. Different oxygen sources including plasma have been studied either to minimize the impurity content or to optimize the electrical properties.

As a second example of metal alkyl precursors, zinc alkyls, especially diethyl zinc, have also been used for the deposition of ZnO thin films. ZnO thin films have been deposited using H_2O as a second reactant and doped with boron [48, 49], gallium [50], or aluminum [51, 52] with B_2H_6, $(CH_3)_3Ga$ or $(CH_3)_3Al$, respectively, to increase the conductivity of the films.

Cyclopentadienyl compounds (i.e. metallocenes) have at least one direct metal-carbon bond to the C_5H_5 ligand. As many metallocene compounds are volatile and thermally stable and they are also suitable for use as ALD precursors, where high reactivity can be controlled by sequential pulsing of the precursors. Although there exists a large family of different ligands based on the C_5H_5, only a few of the simplest alkylated cyclopentadiene compounds have been used as ALD precursors.

Simple metallocenes have been used for the deposition of metal oxides, such as for MgO [53], Sc_2O_3 [54], and In_2O_3 [55]. For example, compared to the traditional β-diketonate/ozone process [56], $(C_5H_5)_2Mg/H_2O$ gives almost a ten times higher film deposition rate and a wider temperature window for MgO film growth. However, because the larger size of the heavier alkaline earth metals, simple $(C_5H_5)_2Sr$ and $(C_5H_5)_2Ba$ compounds do not possess sufficient thermal stability for controlled ALD growth. Therefore deposition of strontium- and barium-containing films has been studied using bulkier ligands. For example, $SrTiO_3$ [57, 58] and $BaTiO_3$ [58] thin films have been deposited from $(C_5{}^iPr_3H_2)Sr$, $(C_5Me_5)Ba$ and $(C_5{}^tBu_3H_2)Ba$ as alkaline earth metal precursors and $Ti(OCH(CH_3)_2)_4$ and H_2O as titanium and oxygen sources, respectively.

For integrated circuit (IC) applications ZrO_2 and HfO_2 thin films can be processed by ALD. In addition to the conventional halide [59–61], nitrate [62], and amide [63, 64] precursors, organometallic cyclopentadiene compounds have been used to produce insulating HfO_2 thin

Table 8.3: Published ALD processes for HfO_2 thin films [66]

Metal precursor/ oxygen source	Range of T_{growth} (°C)	Preferred or most frequently used T_{growth} (°C)
$HfCl_4/H_2O$	160–940	300
$HfCl_4/O_3$	300	300
$HfCl_4/Hf(NO_3)_4$	150–190	150–190
$HfCl_4/H_2O$ or H_2O_2	225–500	300
$HfCl_4/O_2$	400–755	570–755
$Hf(NEtMe)_4/H_2O$	200–350	250
$Hf(NEtMe)_4/O_3$	100–400	250–300
$Hf(NMe_2)_4/H_2O$	50–500	< 350
$Hf(NMe_2)_4/O_3$	160–420	200–320
$Hf(NEt_2)_4/H_2O$	50–500	< 450
$Hf(O'Bu)_4/O_2$	350–480	350–480
$Hf(O'Bu)_4/O_3$	250	250
$Hf(O'Bu)_2(mmp)_2/H_2O$[a]	275–400	360
$Hf(mmp)_4/H_2O$	275–425	360
$Hf(ONEt_2)_4/H_2O$	250–350	300
$Hf(NO_3)_4/H_2O$	160–190	180
Cp_2HfMe_2/H_2O	300–500	350–400
$Cp_2Hf(CH_3)_2/H_2O$		350

[a] *a = mmp 51-methoxy-2-methyl-2-propanolate ($OCMe_2CH_2OMe$).*

films [65] (Table 8.3). Controlled growth has been obtained by using cyclopentadienyl-type $(C_5H_5)_2HfCl_2$ and $(C_5H_5)_2Hf(CH_3)_2$ as a hafnium source. Because of the similar ionic radius and analogous chemistry between zirconium and hafnium, organometallic hafnium compounds behave almost identically to the corresponding zirconium precursors [66].

The selection of the best possible precursor for a desired material and application is not straightforward. The film quality, including optical, electrical, and mechanical properties, is often the most critical quality factor. The selected precursor and deposition temperature will affect the deposition temperature and impurity content.

8.4.4 Novel ALD Processes

Constant precursor development has been carried out for different types of materials. Typically, the ALD growth of metal oxides and nitrides proceeds through two surface-limited half-reactions. Recently, novel processes have been reported where a different type of self-limiting growth has been obtained; for example, rapid deposition of SiO_2 using TMA as a catalyst [67].

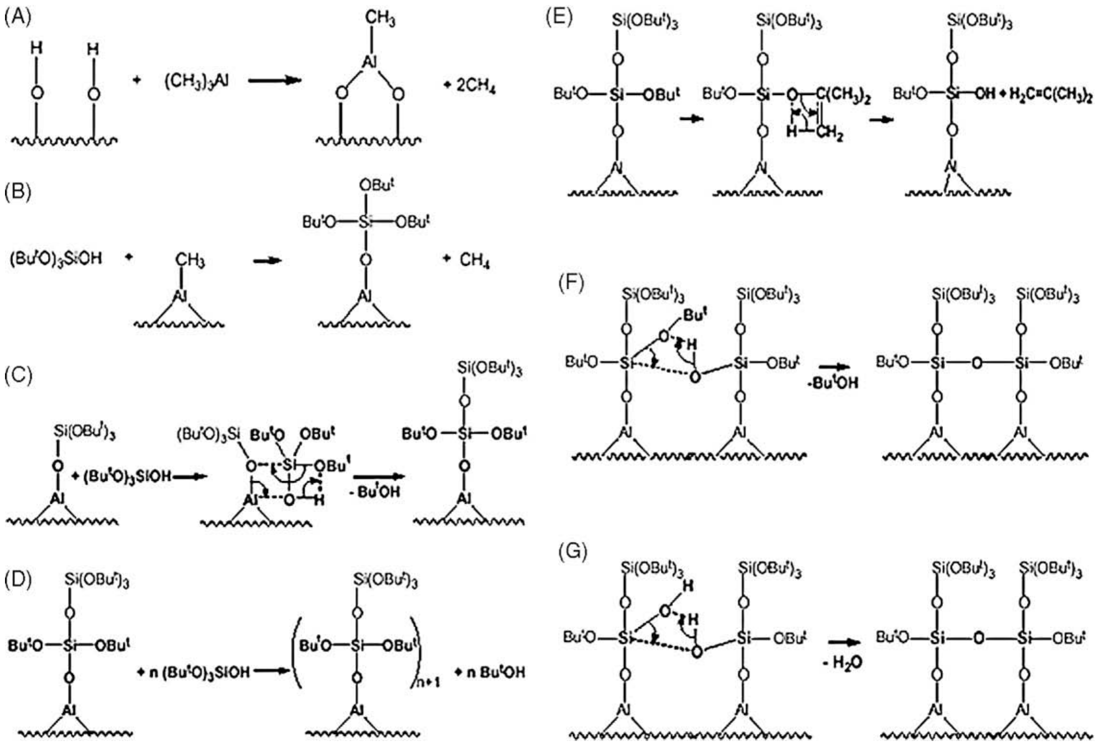

Scheme 8.1: Catalytic SiO_2 deposition by ALD [67].

The low reactivity or high toxicity of the non-metal precursors often limit the use of novel processes. For example, for metal fluorides and phosphates the selection of reactive fluorine or phosphorous compounds is quite limited. In principle, it is possible to use HF, PH_3 derivatives, and alkyl selenides as precursors, but owing to their corrosive nature and toxicity they are not widely used.

The deposition mechanism of Ca–P–O has been studied by using $Ca(thd)_2/O_3$ and $(CH_3O)_3PO/H_2O$ as precursors. The first $Ca(thd)_2/O_3$ cycle produces first a monolayer of $CaCO_3$ on the surface. During the second stage, the $(CH_3O)_3PO/H_2O$ cycle, the phosphate groups replace the carbonate species without changing the deposition rate.

Pilvi et al. [68] reported the deposition of metal fluorides (MgF_2, CaF_2, LaF_3) by using metal β-diketonates as a metal precursors and solid TiF_4 or TaF_5 as a second precursor. This reaction proceeds through ligand exchange reaction between metal β-diketonate and volatile metal fluoride. It is interesting to note that although there are oxygen coordinated β-diketonate ligands present, no significant amount of oxygen is left on the films. However, some titanium or tantalum is left on the films as an impurity.

Recently, different alkylsilyl compounds have been studied for tellurium and selenium precursors. It has been demonstrated that metal chlorides react with $(Et_3Si)_2Te$ and $(Et_3Si)_2Se$, producing metal tellurides and selenides, respectively. For example, the Sb_2Te_3 and GeTe processes using $SbCl_3$, $GeCl_2{\cdot}C_4H_8O_2$ and $(Et_3Si)_2Te$ as precursors were combined to produce GST films [29].

Surface-limiting growth can also be applied to the deposition of polymer thin films. This polymer ALD is usually referred to as molecular layer deposition (MLD) [70]. For example, the surface-limiting growth of polymer thin films has been demonstrated for poly(*p*-phenylene terephthalamide) [71], polyimides [72], and Nylon 66 [73]. Since these depositions can be carried out using similar coating tools to those used in conventional ALD, the preparation of inorganic–organic hybrid materials and nanolaminates is straightforward [74].

8.5 Applications

The main industrial application of ALD is in the manufacture of semiconductor devices, both memory devices and microprocessors. TFEL displays (Figure 8.12) have been manufactured for over 20 years using ALD technology. The read heads of hard disk drives are enabled by ALD. The silver jewelry industry has selected ALD coatings as a way of preventing tarnishing of silver products. In addition to its established industrial uses, ALD is being investigated for a large number of other production applications.

8.5.1 Displays

ALD technology was developed initially to enable TFEL display production. Production started in Finland in the mid-1980s and several million TFEL displays have been produced to

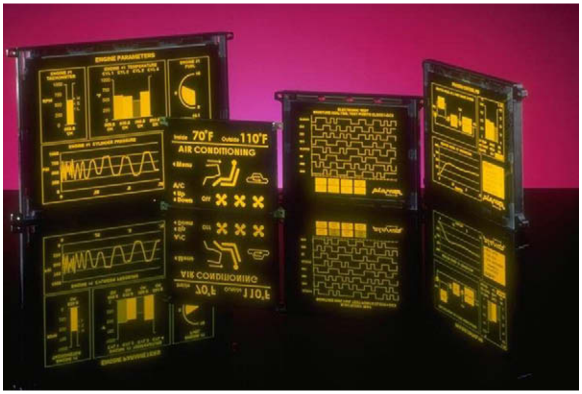

Figure 8.12: Thin film electroluminescent (TFEL) displays. (Courtesy of Planar Systems.)

Figure 8.13: P400 series batch mode (TFEL) manufacturing ALD systems. (Courtesy of Planar Systems.)

date. In addition to the active dielectric–phosphor–dielectric stack (Figure 8.6), ALD technology is used to deposit a pinhole-free ion barrier layer on a soda lime glass substrate and as a passivation layer on top of the device structure [8]. Production is based on efficient batch-mode ALD systems (Figure 8.13). Since the end of 1990s, ALD technology has been used in Japan by Denso Corporation to produce transparent TFEL displays for automotive and other applications (Figure 8.14).

The high quality and yield of ALD oxide materials over large areas, as well as high conformality, are key advantages when considering and investigating ALD technology for TFT (Thin Film Electroluminescent) liquid crystal display (LCD) applications [75], as well as for microelectromechanical (MEMS)-based display applications [76].

Several research centers are investigating the use of an ALD barrier and passivation layers in the development of flexible organic light-emitting device (OLED) displays. ALD films enhance the barrier properties of plastic substrates at thickness levels of only tens of nanometers [9, 77]. ALD coatings can also be used to enhance the properties of barriers made with other coating methods, such as plasma-enhanced chemical vapor deposition (PECVD) [78].

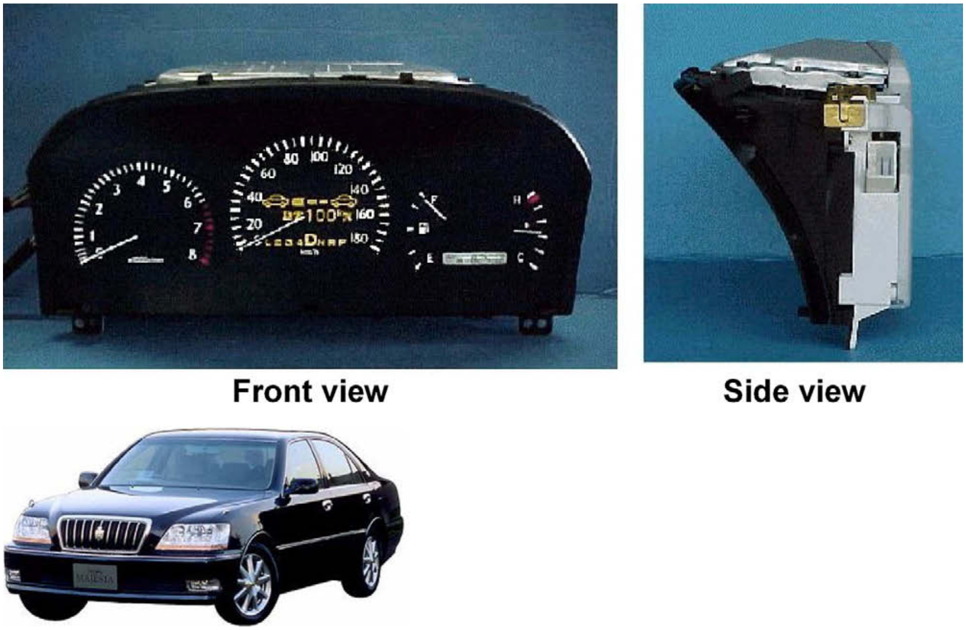

Front view

Side view

Figure 8.14: Transparent car dashboard TFEL displays for automotive applications. (Courtesy of Denso Corporation.)

8.5.2 Integrated Circuits

Because of the high precision of ultrathin films, and the low defect density and extreme conformality of ALD films, ALD has been adapted by semiconductor companies in the manufacture of IC products. Development work on semiconductor memory and microprocessor applications started in the 1990s, and ALD is now an established thin film coating technology in the semiconductor industry. The development of new material solutions for semiconductor applications is a demanding task. In addition to the materials themselves, surface pretreatments, interfaces, impurities, and postprocessing conditions all have roles. ALD is a powerful technology for this development work, as surface chemistry has an important role in the selection and optimization of materials, processes, and process conditions for electronic devices [79].

The high conformality of ALD films has been one of the main drivers to investigate and adapt ALD for semiconductor memory applications. Cylinder/stack architecture or deep trenches, with aspect ratios of 50:1 or more, are easily coated with ALD dielectrics [6, 80]. ALD has now been used for dynamic random access memory (DRAM) production since 2005, and is enabling further scaling down to smaller feature size and trenches with a 100:1 aspect ratio [14].

Scaling down of the thickness of SiO_2-based gate oxides and feature sizes has enabled the semiconductor industry to follow Moore's law, that the number of transistors on a chip will double about every two years. Semiconductor industry has kept this pace for nearly 40 years. In the 1990s semiconductor companies started the search for new materials and processes to replace the SiO_2-based gate oxide with a high-k material [12, 13]. ALD technology was also introduced in the Sematech roadmap for the first time in 1999 [81]. After extensive work and evaluation of several different materials and material combinations, Hf-oxide-based gate oxides made with ALD were introduced into production for the first time, and products at 45 nm node were produced by Intel at the end of 2007 [15, 16].

Production ALD systems for front-end semiconductor manufacture are typically either 300 mm single-wafer systems (Figure 8.15) or 300 mm wafer semi-batch systems.

In addition to the mainstream use of ALD for memory cell and transistor manufacturing, ALD is being widely investigated for back-end processes. Examples are ALD-based barrier, e.g. TaN, and copper seed layer, e.g. Ru, materials to meet the requirements of shrinking

Figure 8.15: Pulsar 3000, a 300 mm single-wafer ALD production tool for manufacturing of semiconductor devices. (Courtesy of ASM International.)

interconnection dimensions [82]. An additional challenge is matching of the barrier and seed layer processes with the low-*k* processes and materials.

The semiconductor industry recognized the importance of ALD technology for semiconductor applications at Semicon Europe 2004, when the European SEMI Award 2004 was awarded to Dr Tuomo Suntola for the development of ALD technology for semiconductor applications.

8.5.3 Hard Disk Drives

Smaller critical dimensions and more challenging topographies of magnetic recording heads have led to a need to replace conventional physical vapor deposition (PVD) coating technology with a more conformal coating method. ALD was selected as a new method to enable further scaling down. An additional benefit of ALD was the high quality of ultrathin insulating layers with low pinhole density [17, 83]. ALD AlOx has been used in read heads for several years, and ALD thin films and nanolaminates are being investigated for other applications in the read/write head process flow, such as trench filling, tunneling barriers, and encapsulation.

8.5.4 Functional and Protective Coatings on Parts

The use of ALD technology for functional and protective coatings on parts is still for the most part in an early phase of investigations. Possible applications range from chemical- and corrosion-resistant coatings to the enhancement of the mechanical properties of parts. Examples of enhancements of mechanical properties investigated for MEMS applications are solid lubricants [84] and tribological coatings [85]. The high surface conformality of ALD enables reliable coating of complex parts as well, including the inside of tubes and cavities.

One of the production uses of protective ALD coatings on parts is the nSILVER® ALD barrier layer, which prevents tarnishing of silver objects, such as jewelry, collectible coins, and special mirrors. Tarnishing of silver is mostly caused by airborne sulfur, which reacts with the surface of a silver object and generates black silver sulfide. A thin, transparent, and pinhole-free nSILVER ALD coating provides sufficient protection against tarnishing. The high surface conformality of ALD coatings enables cost-efficient coating of a large number of parts using simple processing chamber and rack configurations (Figure 8.16).

8.5.5 Photovoltaics

ALD technology and coatings provide potential for conversion and cost-efficiency improvements in multiple photovoltaic applications. The use of ALD coatings has been investigated for several photovoltaic technologies, including crystalline silicon solar cells, thin film solar cells, and organic solar cells.

Figure 8.16: Loading of silver jewelry into ALD processing chamber for nSILVER® coating. (Courtesy of Lapponia Jewelry.)

ALD coatings for back-surface passivation of thin silicon solar cell wafers have been investigated and the initial results have been encouraging [86, 87]. ALD Al_2O_3 appears to be an ideal candidate for high-quality surface passivation of p-type silicon and solar cells application, owing to the negative fixed charge at the interface with silicon. This leads to low surface recombination velocities, with a potential for conversion efficiency improvement.

Thin film solar cells are another field of active development work using ALD technology as an option for efficiency improvements. ALD-based In_2S_3 [88], Zn(O,S), and (Zn,Mg)O [89] have been investigated as a buffer layer in $Cu(In,Ga)Se_2$ thin film solar cells.

ALD has been used to deposit blocking layers by atmospheric pressure systems to reduce recombination reactions in flexible dye-sensitized solar cells (DSSCs) [90]. The encapsulation of flexible organic solar cells presents similar challenges to the encapsulation of flexible

OLED displays. Pinhole-free ALD coatings have been considered and investigated as one potential solution [91].

8.5.6 Optical Components

The benefits of ALD – high conformality, precision, and repeatability – are valuable in optical applications [92, 93]. The optical quality of several ALD films is high, and ALD enables new artificial optical materials to be developed by combining two or more different materials in nanoscale (Figure 8.7), for new product opportunities. Examples of ALD materials for optical coatings are SiO_2, Al_2O_3, TiO_2, ZnO, ZnO:Al, ZrO_2, HfO_2, Ta_2O_5, ZnS, and Al_2O_3:Er.

ALD can be used to make high-quality interference filters, e.g. infrared cut-off filters, and dielectric mirrors, e.g. heat reflectors, on highly curved and structured surfaces. ALD also provides a pinhole-free protective layer for the part to be coated. In situ double-sided coating of flat substrates is also straightforward with ALD.

One ideal ALD application is trench filling and planarization of diffractive optical parts with conformal ALD coating [7]. The mechanical durability of an optical element with trenches could be enhanced considerably, while maintaining the optical and functional quality. The conformality and precision of ALD coatings can also be utilized for making optical micro- and nano-sized lens arrays with a high fill factor, through conformal growth of dielectric monolayers on to prepatterned templates using ALD [94]. In addition, it is possible to coat the surfaces of tubular objects with highly uniform films using ALD. Owing to the high surface conformality, ALD is a powerful technology for the development of photonic crystals [95]. Doped waveguides have also been investigated using ALD technology [96, 97].

8.5.7 Other Applications

MEMS devices are a natural application for highly conformal, functional ALD coatings [84, 85]. ALD can also be used to make or modify yttria-stabilized zirconia (YSZ) and other layers for solid oxide fuel cells [98, 99] and to make fuel cell catalysts [100]. ALD has been used to develop catalyst supports for producing new families of catalytic materials by coating porous silica and alumina structures with ALD [101]. Novel sunblocking materials can be fabricated by coating ultraviolet-absorbing films, e.g. ZnO, using ALD technology on primary particles used by the cosmetics industry [102]. ALD coatings have also been used to form homogeneously dispersed nano-sized titanium dioxide (TiO_2) particles within a polymer matrix, to replace traditionally melt-compounded nanofillers [103]. The ALD technique has also been introduced for improving the crack resistance of glass. Suppressing the crack resistance is most likely to be based on the filling of Griffith-like flaws by 10–20 nm thick Al_2O_3 or SiO_2 [104].

Since ALD produces highly conformal thin films it can also be utilized quite straightforwardly for tailoring surface properties in biotechnology applications. Interactions between biological and inorganic interfaces are surface-related phenomena, so ALD is well suited for making these thin surface modifications. Typically tens of nanometers are enough to alter the surface properties. Deposition of photocatalytic TiO_2 films has been studied by ALD. Typically, activation of TiO_2 is carried out by ultraviolet light [105–107] but careful doping by H_2S activation can also be carried out by visible light [108]. Recently, ALD-deposited Al_2O_3 [109], TiNOx [110], and hydroxyapatite-like films [111] have been studied for biomedical interactions on different surfaces.

8.6 Summary

ALD technology was developed over 30 years ago, and it has been used for the industrial production of TFEL displays for more than 20 years. Since the semiconductor industry adapted ALD as a mainstream technology during the past few years, ALD has become clearly visible and now ALD technology is being developed and adapted for a large number of other industrial applications, ranging from nanotechnology coatings on particles to large-area coatings for photovoltaic applications. At the same time ALD material and process research continues actively throughout the world, providing new capabilities for the industry.

Acknowledgments

The authors thank Mr Jarmo Maula and Mr Jarmo Skarp for their discussions and contributions.

References

[1] T. Suntola, J. Antson, US Patent No. 4,058,430 (1977).
[2] T. Suntola, A. Pakkala, S. Lindfors, SID 80 Digest 11 (1980) 108.
[3] T.S. Suntola, A.P. Pakkala, S.G. Lindfors, US Patent No. 4,389,973 (1983).
[4] T.S. Suntola, A.P. Pakkala, S.G. Lindfors, US Patent No. 4,413,022 (1983).
[5] M. Ritala, M. Leskelä, in: H.S. Nalwa (Ed.), Handbook of Thin Film Materials, Vol. 1, Academic Press, San Diego (2002) 103–159.
[6] Niinisto et al., Chem. Mater 19(13) (2007) 3319.
[7] Wang et al., Optics Lett. 30(14) (2005).
[8] Planar Systems Inc. <http://www.planarembedded.com/technology/el/>.
[9] M.D. Groner et al., Appl. Phys. Lett. 88 (2006) 051907.
[10] Patent EP1674890.
[11] E. Dickey et al., SVC Conference, W-18 (May 9–14, 2009) in press.
[12] E.P. Gusev et al., IBM J. Res. Dev. 43 (1999) 265.
[13] E.P. Gusev et al., Appl. Phys. Lett. 76 (2000) 176.
[14] T.E. Seidel, 14-1, in: R. Doering, Y. Nishi (Eds.), Handbook of Semiconductor Manufacturing Technology, 2nd ed. CRC Press, Boca Raton (2008).

[15] Mark Bohr et al., IEEE Spectrum Online (October 2007).
[16] K. Mistry et al., IEDM Tech. Dig. (2007) 247.
[17] A. Devasahayam, Solid State Technol. (September 2005).
[18] M. Rinkiö et al., Nano Lett. 9(2) (2009) 643–647.
[19] J. Skarp, US Patent 4,486,487 (1984).
[20] M. Ritala, J. Niinistö, Atomic layer deposition, in: A.C. Jones, M.L. Hitchman (Eds.), Chemical Vapour Deposition: Precursors, Processes and Applications, Royal Society of Chemistry (2009) 158–206.
[21] G.S. Higashi et al., J. Vac. Sci. Tech. B3 (1985) 1460.
[22] G.S. Higashi et al., Appl. Phys. Lett. 55 (1989) 1963.
[23] H. Kim, J. Vac. Sci. Technol. A 21 (2003) 2231.
[24] M. Juppo, M. Vehkamäki, M. Ritala, M. Leskelä, J. Vac. Sci. Technol. A 16 (1998) 2845.
[25] M. Juppo, M. Ritala, M. Leskelä, J. Vac. Sci. Technol. A 15 (1997) 2330.
[26] J.W. Elam, C.E. Nelson, R.K. Grubbs, S.M. George, Surf. Sci. 479 (2001) 121.
[27] J.W. Klaus, S.J. Ferro, S.M. George, Appl. Surf. Sci. 162–163 (2000) 479.
[28] M. Yang, H. Chung, A. Yoon, H. Fang, A. Zhang, C. Knepfler et al., Proceedings of the Advanced Metallization Conference (2001) 655.
[29] V. Pore, T. Hatanpää, M. Ritala, M. Leskelä, J. Am. Chem. Soc. (2009), doi: 10.1021/ja8090388.
[30] V.E. Drozd, V.B. Aleskovski, Appl. Surf. Sci. 82/83 (1994) 591.
[31] V.E. Drozd, A.P. Baraban, I.O. Nikiforova, Appl. Surf. Sci. 82/83 (1994) 583.
[32] J.C. Badot, S. Ribes, E.B. Yousfi, V. Vivier, J.P. Pereira-Ramos, N. Baffier, D. Lincot, Electrochem. Solid State Lett. 3 (2000) 485.
[33] K. Kobayashi, S. Okudaira, Chem. Lett. (1997) 511.
[34] E.W. Berg, J.J.C. Acosta, Anal. Chim. Acta 40 (1968) 101.
[35] L. Ben-Dor, R. Druilhe, P. Gibart, J. Cryst. Growth 24–25 (1974) 172.
[36] L. Ben-Dor, E. Fischbein, I. Felner, Z. Kalman, J. Electrochem. Soc. 124 (1977) 451.
[37] J.M. Buriak, L.K. Cheatham, R.G. Gordon, J.J. Graham, A.R. Barron, Eur. J. Solid State Inorg. Chem. 29(Suppl) (1992) 43.
[38] M.L. Hitchman, S.H. Shamlian, D.D. Gilliland, D.J. Cole-Hamilton, S.C. Thompson, S.L. Cook, B.C. Richards, Mater. Res. Soc. Symp. Proc. 33 (1994) 249.
[39] H. Yokoyama, M. Tanimoto, M. Shinohara, N. Inoue, Appl. Surf. Sci. 82/83 (1994) 158.
[40] J.G. Reitl, H.M. Uridianyk, S.M. Bedair, Appl. Phys. Lett. 59 (1991) 2397.
[41] J.P. Simko, T. Meguro, S. Iwai, K. Ozasa, Y. Aoyagi, T. Sugano, Thin Solid Films 225 (1993) 40.
[42] S.-W. Choi, C.-M. Jang, D.-Y. Kim, J.-S. Ha, H.-S. Park, W. Koh, C.-S. Lee, J. Korean Phys. Soc. 2 (2003) S975.
[43] C.-W. Jeong, J.-S. Lee, S.-K. Joo, Jpn. J. Appl. Phys. 40 (2001) 285.
[44] J. Kim, K. Chakrabarti, J. Lee, K.-Y. Oh, C. Lee, Mater. Chem. Phys. 78 (2003) 733.
[45] R.L. Puurunen et al., ECS Trans. 11(7) (2007) 3.
[46] K. Kukli, M. Ritala, M. Leskelä, J. Jokinen, J. Vac. Sci. Technol. A 15 (1997) 2214.
[47] R. Huang, A.H. Kitai, J. Electron. Mat. 22 (1993) 215.
[48] B. Sang, A. Yamada, M. Konagai, Sol. Energy Mater. Sol. Cells 49 (1997) 19.
[49] Y. Yamamoto, K. Saito, K. Takahashi, M. Konagai, Sol. Energy Mater. Sol. Cells 65 (2001) 125.
[50] A.W. Ott, R.P.H. Chang, Mater. Chem. Phys. 58 (1999) 132.
[51] V. Lujala, J. Skarp, M. Tammenmaa, T. Suntola, Appl. Surf. Sci. 82/83 (1994) 34.
[52] L. Stolt, J. Hedström, J. Skarp, Conf Rec Photovoltaic Spec Conf (1994) 250.
[53] M. Putkonen, L.-S. Johansson, E. Rauhala, L. Niinistö, J. Mater. Chem. 9 (1999) 2449.
[54] M. Putkonen, M. Nieminen, J. Niinistö, T. Sajavaara, L. Niinistö, Chem. Mater. 13 (2001) 4701.
[55] J.W. Elam, A.B.F. Martinson, M.J. Pellin, J.T. Hupp, Chem. Mater. 18(15) (2006) 3571–3578.
[56] M. Putkonen, L.-S. Johansson, E. Rauhala, L. Niinistö, J. Mater. Chem. 9 (1999) 2449.
[57] M. Vehkamäki, T. Hänninen, M. Ritala, M. Leskelä, T. Sajavaara, E. Rauhala, J. Keinonen, Chem. Vap. Depos. 7 (2001) 75.

[58] M. Vehkamäki, T. Hatanpää, T. Hänninen, M. Ritala, M. Leskelä, Electrochem. Solid State Lett. 2 (1999) 504.
[59] M. Ritala, M. Leskelä, L. Niinistö, T. Prohaska, G. Friedbacher, M. Grasserbauer, Thin Solid Films 250 (1994) 72.
[60] K. Forsgren, A. Hårsta, J. Aarik, A. Aidla, J. Westlinder, J. Olsson, J. Electrochem. Soc. 149 (2002) F139.
[61] H.B. Park, M. Cho, J. Park, S.W. Lee, C.S. Hwang, J.-P. Kim et al., J. Appl. Phys. 94 (2003) 3641.
[62] J.F. Conley Jr., Y. Ono, R. Solanki, G. Stecker, W. Zhuang, Appl. Phys. Lett. 82 (2003) 3508.
[63] D.M. Hausmann, E. Kim, J. Becker, R. Gordon, Chem. Mater. 14 (2002) 4350.
[64] K. Kukli, M. Ritala, T. Sajavaara, J. Keinonen, M. Leskelä, Chem. Vapor Depos. 8 (2002) 199.
[65] J. Niinistö, M. Putkonen, L. Niinistö, in: American Vacuum Society Topical Conference on Atomic Layer Deposition, San Jose, CA, USA (August 4–6, 2003).
[66] J. Niinistö, M. Putkonen, L. Niinistö, S.L. Stoll, K. Kukli, T. Sajavaara, M. Ritala, M. Leskelä, J. Mater. Chem. 15 (2005) 2271–2275.
[67] D. Hausmann et al., Science 298 (2002) 402.
[68] T. Pilvi, E. Puukilainen, U. Kreissig, M. Leskelä, M. Ritala, Chem. Mater. 20 (2008) 5023–5028.
[69] T. Pilvi, M. Ritala, M. Leskelä, M. Bischoff, U. Kaiser, N. Kaiser, Appl. Opt. 47 (2008) C271–C274.
[70] S.M. George, B. Yoon, A.A. Dameron, Surface Chemistry for Molecular Layer Deposition of Organic and Hybrid Organic–Inorganic Polymers, Acc. Chem. Res. 42(4) (2009) 498–508.
[71] N.M. Adamczyk, A.A. Dameron, S.M. George, Langmuir 24(5) (2008) 2081–2089.
[72] M. Putkonen, J. Harjuoja, S. Timo, L. Niinistö, J. Mater. Chem. 17 (2007) 664.
[73] Y. Du, S.M. George, J. Phys. Chem. C 111(24) (2007) 8509–8517.
[74] A.A. Dameron, D. Seghete, B.B. Burton, S.D. Davidson, A.S. Cavanagh, J.A. Bertrand, S.M. George, Chem. Mater. 20(10) (2008) 3315–3326.
[75] K. Murata et al., ECS Trans. 11(7) (2007) 31.
[76] A. Londergaan et al., Proceedings of the Asia Display Conf. SID, Vol. 1 (2007) 107–112.
[77] P.F. Carcia et al., ECS Trans. 11(7) (2008) 15.
[78] S.-H. Ko Park et al., ETRI J. 27(5) (2005) 545–550.
[79] F. Zaera, The surface chemistry of thin film atomic layer deposition (ALD) processes for electronic device manufacturing, J. Mater. Chem. 18 (2008) 3521–3526.
[80] S.J. Choi et al., Oyo Butsurigaku Kankei Rengo Koenkai Koen Yokoshu 46(2) (1999) 643.
[81] International Technology Roadmap for Semiconductors (ITRS), Semiconductor Industry Association, 1999 ed., SEMATCH, Austin, TX (1999) 76.
[82] S. Kumar et al., Interconnect Technology Conference, 2008. IITC 2008 (June 1–4, 2008) 96–98.
[83] M. Mao, R. Bubber, T. Schneider, ESC Transaction 1 (2006) 37–47.
[84] T.W. Scharf et al., Acta Mater. 54 (2006) 4731–4743.
[85] C. Nistorica et al., J. Vac. Sci. Technol. A 23(4) (2005) 836.
[86] G. Agostinelli et al., Solar Energy Mater. Solar Cells 90 (2006) 3438–3443.
[87] B. Hoex et al., ALD 2008 Conference, Tue A2-4.
[88] D. Hariskos et al., Thin Solid Films 480/481 (2005) 195–198.
[89] A. Hultqvist et al., Thin Solid Films 517(7) (2009) 2305–2308.
[90] W.J. Potscavage, Appl. Phys. Lett. 90 (2007) 253511.
[91] J. Baker, ALD 2008 Conference, Tue A2-5.
[92] M. Ritala et al., Optical Interference Coatings, OSA Technical Digest Series, Optical Society of America (2004) Paper MB1.
[93] J.J. Wand, ALD 2008 Conference, Tue A2-1.
[94] J.J. Wang et al., IEEE Photonics Technol. Lett. 18(24) (2006) 2650–2652.
[95] E. Graugnard et al., Appl. Phys. Lett. 89 (2006) 181108.
[96] K. Solehmainen et al., IEEE Photonics Technol. Lett. 16(1) (2004).
[97] L. Norin, E. Vanin, P. Soininen, M. Putkonen, CLEO (2007).
[98] J.H. Shim et al., ALD 2008 Conference, Wed A2b-5.

[99] C. Brahim, F. Chauveau, A. Ringuede, M. Cassir, M. Putkonen, L. Niinistö, J. Mater. Chem. 19 (2009) 760–766.

[100] H.C.M. Knoops et al., ALD 2008 Conference, Wed A2b-6.

[101] R.L. Puurunen, Doctoral dissertation, Department of Chemical Technology, Helsinki University of Technology (October 2002).

[102] D.M. King et al., Advanced Functional Materials 18 (2008) 607–615.

[103] N.A. Isomäki et al., AVS 55th International Symposium & Exhibition Paper TF-TuM11 (October 21, 2008).

[104] M. Putkonen et al., AVS 55th International Symposium and Exhibition Tue A-10 (October 21, 2008).

[105] V. Pore, A. Rahtu, M. Leskelä, M. Ritala, T. Sajavaara, J. Keinonen, Chem. Vap. Depos. 10(3) (2007) 143–148.

[106] H. Kawakami, R. Ilola, L. Straka, S. Papula, J. Romu, H. Hänninen et al., J. Electrochem. Soc. 155(2) (2008) C62–C68.

[107] M. Raulio, V. Pore, S. Areva, M. Ritala, M. Leskelä, M. Lindén et al., Destruction of *Deinococcus geothermalis* biofilm by photocatalytic ALD and sol-gel TiO_2 surfaces, J. Ind. Microbiol. Biotechnol. 33(4) (2006) 261–268.

[108] V. Pore, M. Ritala, M. Leskelä, S. Areva, M. Järn, J. Järnström, J. Mater. Chem. 17 (2007) 1361–1371.

[109] D.S. Finch, T. Oreskovic, K. Ramadurai, C.F. Herrmann, S.M. George, R.L. Mahajan, J. Biomed. Mater. Res. Part A 87A(1) (2008) 100–106.

[110] G.K. Hyde, S.D. McCullen, S. Jeon, S.M. Stewart, H. Jeon, E.G. Loboa, G.N. Parsons, Biomed. Mater. 4 (2009) 025001.

[111] M. Putkonen, T. Sajavaara, P. Rahkila, L. Xu, S. Cheng, L. Niinisto, H.J. Whitlow, Thin Solid Films 517 (2009) 5819–5824.

CHAPTER 9

Plasma-Enhanced Chemical Vapor Deposition of Functional Coatings

L. Martinu, O. Zabeida and J.E. Klemberg-Sapieha
Department of Engineering Physics, École Polytechnique de Montréal, CP 6079, Station Centre-Ville, Montréal, Québec H3C 3A7, Canada

---

Summary

Plasma-based technologies are increasingly used for the fabrication of thin films and coatings for numerous applications ranging from optics and optoelectronics to aerospace, automotive, biomedical, microelectronics, and others. The present chapter reviews the advances in plasma-enhanced chemical vapor deposition (PECVD). Based on knowledge of fundamental physical and chemical processes in the active plasma environments, we describe present understanding of plasma–surface interactions that are the cornerstone for tailoring the materials' functional characteristics, in particular their optical, mechanical, electrical, tribological, protective, and other properties. We illustrate the state of the art in PECVD by the description of the performance of different coating systems and thin film architectures suitable for industrial-scale applications. This chapter represents a source of information for those who wish to familiarize themselves with the status of knowledge in the area of materials science of functional coatings, in particular in PECVD, as well as for those who seek inspiration for practical surface engineering solutions.

9.1 Introduction

9.1.1 Functional Coating Considerations

Recent advances in science and technology have stimulated the development of new coating materials, surface and interface engineering processes, and thin film systems, that provide ever-improving performance in numerous areas, ranging from optics and optoelectronics to aerospace, automotive, biomedical, microelectronics, and other applications. Many successful solutions in these fields have been identified which are generally based on a layered functional coating architecture, schematically illustrated in Figure 9.1. In each case, one individual layer or the whole thin film system may simultaneously fulfill several functions (e.g. selective optical absorption and mechanical protection; optical transparency and gas barrier; antistatic

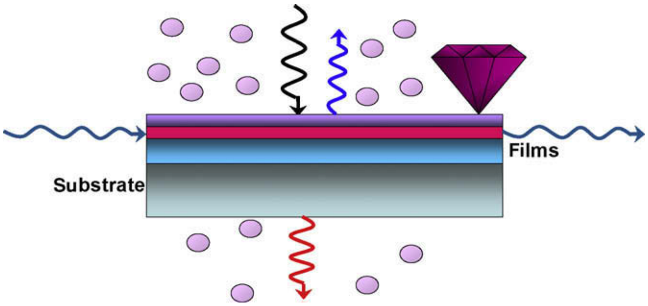

Figure 9.1: Schematic illustration of a functional coating system.

Table 9.1: Main functional characteristics of PECVD coatings and thin film systems

Functional properties	Controlled characteristics
Optical	Refractive index, n Extinction coefficient, k Optical loss, absorption coefficient, α Color: La^*b^* or Xyz coordinates
Mechanical	Adhesion: work of adhesion, W_a; critical load, L_C Stress, σ Hardness, H Young's modulus, E Toughness, K_T
Tribological	Coefficient of friction, μ Scratch resistance: critical load, L_C Wear coefficient, K Erosion rate, E_R Corrosion resistance: open circuit potential, OCP; corrosion current, I_{corr}
Electrical	Resistivity, ρ Dielectric loss, tan δ Charge carrier density, N_C Charge mobility, μ_C
Thermal	Coefficient of thermal expansion, CTE Thermal conductivity, γ_T
Barrier	Gas permeability, OTR Water vapor permeability, WVTR

properties and scratch resistance; erosion and corrosion resistance; fatigue resistance and high thermal conductivity; wear resistance and biocompatibility; photocatalytic effect and hydrophobicity; and numerous other combinations of properties summarized in Table 9.1). Therefore, it is increasingly important to assess and optimize the film characteristics not only individually, but in their complexity, with respect to their compatibility with other layers, and with respect to their designed applications. This imposes particular requirements on the fabrication methods and characterization.

Functional coating systems can be fabricated by different deposition techniques reviewed in detail in the present book; these include physical vapor deposition (PVD) from a solid primary source (e.g. thermal or electron beam evaporation, magnetron or ion beam sputtering, cathodic arc deposition), chemical vapor deposition (CVD) from a gas-phase primary source, plasma-enhanced chemical vapor deposition (PECVD) from a gas-phase source with activation in a glow discharge environment, and other vacuum and non-vacuum techniques (sol-gel, flame hydrolysis, electrochemical and electroless deposition, thermal-, plasma-, and cold-spraying, and others).

Among the above processes, PECVD has received particular attention, as documented by earlier reviews [1–8]; it has been employed industrially in microelectronics for several decades, and it has now penetrated into a large number of other sectors as illustrated in Table 9.2. In certain areas (e.g. in optics), its industrial acceptance was originally slow, mainly owing to the complexity of the plasma–chemical reactions, plasma–surface interactions, and process control. However, thanks to fundamental and applied research and the development of new instrumentation tools, recent advances in plasma processing, and in PECVD in particular, have greatly increased the interest in PECVD for the fabrication of different coating systems. Its industrial use has been significantly broadened, as also illustrated throughout this chapter and in the relevant references. Not only can PECVD provide materials with functional characteristics similar to those obtained by their PVD and non-vacuum counterparts, but the PECVD processes can frequently address numerous novel aspects of functional coating fabrication. The main driving forces and stimulation for such interest reside with the following attributes, addressed in detail throughout this chapter:

- The broad range of control of plasma–chemical reactions and plasma–surface interactions allows one to optimize the film composition and microstructure: the films generally possess a high packing density ($\sim 98\%$), and are therefore hard and environmentally stable. This can be achieved by tailoring the energetic interaction between the plasma and the surface, frequently by using bias-controlled or pulsed plasma techniques. In one deposition reactor, one can fabricate a multifunctional system (such as the one schematically illustrated in Figure 9.1), while providing a combination of the desired optical, mechanical, thermal, and other properties.
- PECVD is suitable for the fabrication of films with different compositions and microstructures, allowing one to continuously vary film characteristics as a function of depth (graded or inhomogeneous films). This can be used for the fabrication of a very attractive category of optical devices such optical rugate filters, as well as hard and tough protective coatings and biomedical materials. The absence of abrupt interfaces (in addition to specific optical and other effects) leads to a uniform distribution (or compensation) of internal stresses, generally giving rise to enhanced adhesion and mechanical integrity.
- PECVD provides high deposition rates ($r_D \sim 1$–10 nm/s, or more), substantially higher than other, more traditional vacuum-based techniques (e.g. PVD). This is the basis for a reliable low-cost fabrication technology.
- Different substrate shapes (including 3D) can be uniformly coated (flat, hemispherical, cylindrical shapes, interior of tubes, etc.).

Table 9.2: Applications of PECVD functional coatings

Application	Examples of devices and film systems
Microelectronics and microsystems	Transistors Microelectromechanical systems (MEMS)
Optics, photonics, telecommunication and information technologies	Optical interference filters (including antireflective (AR) coatings) Ophthalmic lenses Optical waveguides Displays (including barrier coatings) Decorative (protective) coatings Optical coatings on plastics Protective coatings for storage media
Aerospace and outer space	Protective coatings against solid particle erosion and corrosion Protection against space environment (atomic oxygen, radiation, thermal cycling, charge accumulation)
Automotive	Protective coatings for engine components (low friction and wear) Protective coatings for light assemblies (corrosion resistance) Protective coatings for fuel distribution (permeation barriers)
Energy generation and saving	Photovoltaics (amorphous and polycrystalline silicon, AR coatings) Protective coatings for fuel cells Corrosion-resistant coatings Self-cleaning (photocatalytic) surfaces Smart windows
Biomedical and pharmaceutical	Protective coatings for implants Protective coatings for surgical tools Biocompatible coatings
Sensors	Miniaturized microphone (mechanoacoustic effects) Gas and vapor sensors (electrical, optical, and structure-related effects)
Manufacturing	Protective coatings on cutting tools (high-speed machining, dry machining, machining of non-ferrous metals, of non-metals and composites) Antisticking coatings (e.g. molds)
Textiles	Hydrophobic coatings Antiseptic textiles
Packaging	Barriers against gas and vapor permeation coatings on flexible substrates

- The PECVD process is compatible with different types of film fabrication equipment – this appears very attractive when retrofitting existing hardware to accommodate this deposition technology. In addition, the deposition process occurs at low temperatures (typically ranging from near room temperature (RT) with no intentional heating, to about 350 °C, when additional heating is applied).
- In recent years, we have witnessed an increasing interest in materials processing using atmospheric pressure glow discharge (APGD) [9, 10]. This has also stimulated much progress in PECVD at elevated pressures pointing toward possible low-cost, high-throughput, coating fabrication approaches.

9.1.2 Plasma Processing of Materials

Historically, the real onset of the plasma processing of materials (specifically using glow discharges) came in the late 1960s with the advent of integrated circuit technology. Electronics, in mid-1990 a $1.5 trillion industry worldwide, has enabled most other products to evolve (see Table 9.2). The electronics industry, in turn, is fed by the $100–200 billion annual semiconductor market, which is based on $40–50 billion equipment and materials sectors, of which plasma reactors constitute annual sales exceeding $2 billion [11]. These numbers are continuously increasing, given the acceptance of plasma-based technologies in other areas.

Based on the variability and the role of the initial gas-phase processes and plasma–surface interactions (involving atoms and molecular fragments – radicals, ions, and energetic photons), materials processing using 'cold' (thermodynamically non-equilibrium) plasma can be divided into the following categories, based on the choice of the working gases or vapors and the discharge conditions:

- PECVD of inorganic thin films (such as oxides, nitrides and carbides of metals or semiconductors) or organic thin films (such as soft materials, also called 'plasma polymers', hard carbon films, crystalline diamond and others) – the main subject of this chapter
- plasma etching or sputter-etching (dry removal of materials), forming volatile products resulting from the chemical reactions of the plasma-generated free radicals and surface atoms, which are frequently ablated with additional ion bombardment assistance (for an overview, see [4, 12])
- surface modification, during which material is neither added nor removed in significant amounts, but the composition and structure of the surface and/or of the near-surface layers are controllably modified by plasma exposure; this process allows one to tailor the surface and interface properties (for example, to improve adhesion

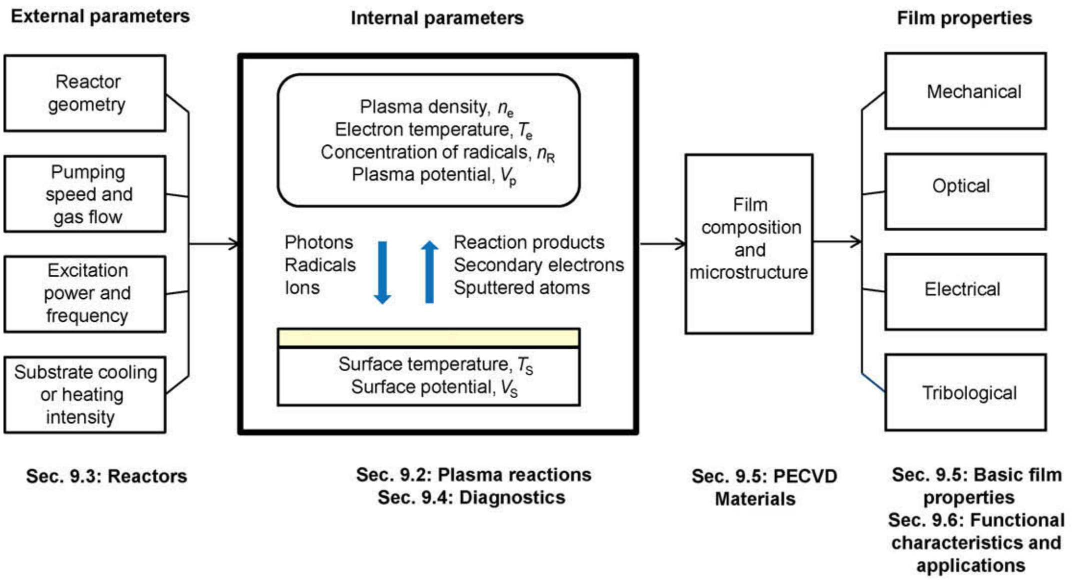

Figure 9.2: Schematic illustration of the structure of this chapter and of the relation between the deposition system, the internal and external process parameters, and the film characteristics.

before film deposition, surface hardness and control roughness, and/or to add specific surface functions providing wettability, biocompatibility, sterility, dye uptake, etc.) (for an overview, see [4, 11, 13, 14]).

Often, these three processes are in competition, and the prevalence of one of them can be controllably adjusted by the choice of the external plasma parameters (Figure 9.2).

The main objective of the present chapter is to review advances in PECVD of functional coatings for different applications (the first item in the above list). We start with a succinct overview of basic phenomena involved in the gas-phase reactions and plasma–surface interactions (Section 9.2) that are at the core of different reactor concepts (Section 9.3), while relying on the use and capabilities of different plasma diagnostic and process monitoring tools (Section 9.4). This is followed by the description of the properties of various PECVD materials, governed by their composition and microstructural characteristics, frequently tailored by an appropriate choice of the energy (E_{i}) and flux (Φ_{ι}) of the impinging ions (Section 9.5). Finally, we review PECVD film architectures suitable for specific applications illustrated by industrial-scale PECVD systems (Section 9.6). We wish to emphasize here that, considering the very extensive literature which now exists in this field, we have not attempted to list all of the relevant publications, but rather use a selection of examples which we feel represents the particular physical, chemical, materials science, surface engineering, and technological viewpoints advanced in this work.

9.2 Processes in PECVD

9.2.1 Process Parameters

In spite of the proliferation of low-pressure plasma processes already in use, or having potential for near-term or longer term industrial applications, there is still much ongoing research regarding the most efficient use of plasma. The reasons for this are the relative novelty of plasma, on the one hand, and its inherent complexity, on the other. To ensure high quality and reproducibility of a given plasma process, numerous parameters must be controlled (Figure 9.2); these include so-called 'external' parameters such as pressure, p, gas flow, discharge excitation frequency, f, power, P, and the resulting 'internal' plasma characteristics, particularly the electron (plasma) density, n_e, the electron energy distribution function, $f_e(E)$ or EEDF, electrical potentials, and fluxes of different species toward the surfaces exposed to plasma.

Gas-phase chemical processes are largely responsible for the chemical composition of the films deposited, along with plasma–surface interactions and substrate surface conditions, which dictate film microstructure and surface morphology.

9.2.2 Plasma Gas-Phase Reactions

During deposition, the bulk plasma parameters generally control the rate at which chemically active precursor species (molecular fragments – free radicals) and energetic species (electrons, ions, photons) are created. Even for relatively simple gas mixtures involving two or three gases, several dozens of plasma reactions are taking place and many new species are created. For many of these processes the reaction rates are not readily available. This complicates the detailed modeling of PECVD (e.g. [15]); instead, the experimental approach that takes into account the very general pathway combined with the process optimization is frequently used.

The EEDF is an essential parameter for plasma processing. It represents how many electrons are available for the ionization and other plasma reactions, for example, electron-impact dissociation, that produces free radicals. The radicals created in the plasma bulk interact further in the gas phase and at the surface, thus ultimately leading to film formation (Table 9.3).

EEDF is affected by all external parameters in a complex way. As an example, Figure 9.3 shows experimentally determined EEDFs in an active CH_4/H_2 radio frequency (RF) inductively coupled plasma (ICP), in which variation of p is seen to affect the mean electron energy and the energetic tail.

One of the important factors influencing the EEDF and processing plasma is the discharge field frequency, $f = \omega/2\pi$. Most often, high-frequency plasmas ($f > 1$ MHz) are used for PECVD of dielectric films, in order to avoid surface charging and plasma instabilities. These

Table 9.3: Basic reactions in active plasma environments

Reaction	General equation	Example
Reactions with electrons		
Ionization	$e + A \rightarrow A^+ + 2e$	$e + N_2 \rightarrow N_2^+ + 2e$
Excitation	$e + A \rightarrow A^* + e$	$e + O_2 \rightarrow O_2^* + e$
Dissociation	$e + AB \rightarrow e + A + B$	$e + SiH_4 \rightarrow e + SiH_3 + H$
Dissociative ionization	$e + AB \rightarrow 2e + A^+ + B$	$e + TiCl_4 \rightarrow 2e + TiCl_3^+ + Cl$
Dissociative attachment	$e + AB \rightarrow A^- + B$	$e + SiCl_4 \rightarrow Cl^- + SiCl_3$
Three-body recombination	$e + A^+ + B \rightarrow A + B$	$e + H^+ + CH_4 \rightarrow H + CH_4$
Radiative recombination	$e + A^+ \rightarrow A + h\nu$	$e + Ar^+ \rightarrow Ar + h\nu$
Reactions between heavy species		
Charge exchange	$A^+ + B \rightarrow A + B^+$	$N_2^+(\text{fast}) + N_2(\text{slow}) \rightarrow N_2(\text{fast}) + N_2^+(\text{slow})$
Penning ionization	$A^* + B \rightarrow A + B^+ + e$	$He^* + O_2 \rightarrow He + O_2^+ + e$
Ionization by interchange	$A^+ + BC \rightarrow AB^+ + C$	$N^+ + O_2 \rightarrow NO^+ + O$
Combination	$A + B \rightarrow AB$	$2SiH_3 \rightarrow Si_2H_6$
	$AB + CD \rightarrow AC + BD$	$SiH_2 + O_2 \rightarrow SiO + H_2O$
Heterogeneous interactions (with surfaces)		
Adsorption	$R_g + S \rightarrow R_S$	$CH_2 + S \rightarrow (CH_2)_S$
Metastable deexcitation	$A^* + S \rightarrow A + S$	$N_2^* + S \rightarrow N_2 + S$
Sputtering	$A^+ + B_S \rightarrow A + B$	$Ar^+ + H_S \rightarrow Ar + H$
Secondary electron emission	$A^+ + S \rightarrow S + e$	$O^+ + S \rightarrow S + e$

R: radical; S: surface; g: gas.

are, generally, the International Telecommunications Union (ITU)-approved industrial, scientific, and medical frequencies (13.56 MHz – radio frequency, RF; or 2.45 GHz – microwave, MW) [16]. Higher frequency leads to higher power efficiency, i.e. less power is needed (on average) to create one ion–electron pair [17]. As a consequence, the ionization and dissociation rates are higher in the MW plasma than in RF plasma, generally leading to a higher r_{D} and a higher ion flux, Φ_{i}, toward the exposed surface [18].

Optimization of the PECVD processes involves identification of discharge characteristics giving rise to the formation of large densities of free radicals (n_{R}) that diffuse toward the surface (flux of the film forming species, Φ_ν), as well as to high concentrations of ions (due to high n_{e}) favoring high Φ_{i}, as will be discussed in the subsequent sections.

9.2.3 Plasma–Surface Interactions

We have pointed out above that the choice of f defines the deposition reactor, and it influences the fundamental plasma properties such as the EEDF; however, it also has an important effect

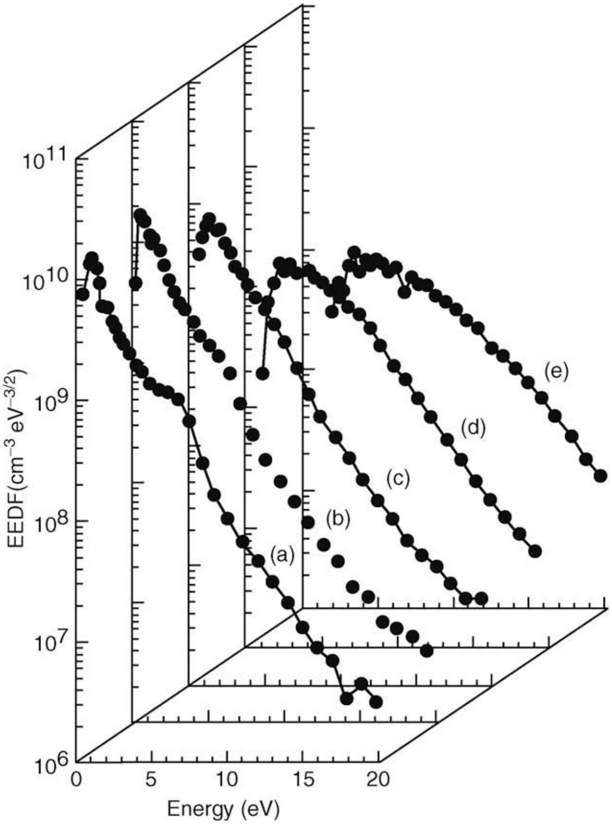

Figure 9.3: Electron energy distribution functions in a CH_4/H_2 (5:75 mixture) plasma as a function of pressure: (a) 50 mtorr, (b) 40 mtorr, (c) 30 mtorr, (d) 20 mtorr, and (e) 10 mtorr. This example pertains to an RF inductively coupled (ICP, 13.56 MHz) plasma reactor, 1 kW power, plasma volume of ~ 1.5 liters. (After [19].)

on how the plasma interacts with the exposed surface. At a surface in contact with plasma, there is an interface, the plasma sheath, which is electrically non-neutral, in contrast to plasma itself. An electrically isolated surface is at a floating potential, V_f, with respect to the plasma potential, V_p. Since $V_f < V_p$, positive ions are accelerated from the plasma to the surface, while some of the electrons are repelled. However, under steady-state conditions, no net current flows, since ion and electron fluxes are then equal. In this case, the thickness of the sheath, d_s, is a few times the Debye length, λ_D, and grows with increasing average electron energy and decreasing n_e.

Assuming, for simplicity, that the EEDF is Maxwellian, and that the surface immersed in the plasma is a plane, the potential difference across the sheath can be approximated by [20]:

$$V_p - V_f = (k_B T_e/2e)\ln(m_i/2\pi m_e) \tag{9.1}$$

where k_B is the Boltzmann constant, T_e the electron temperature, e the electron charge, and m_i and m_e the masses of ions and of electrons. We note that on floating potential surfaces, the ion energy $E_i = e(V_p - V_f)$ is typically a few times the electron temperature expressed in electron volts. The ions always acquire some additional energy as they pass through the sheath on their way to the surface.

The energy of the charged particles impinging on a substrate can be adjusted by biasing it at a potential V_B with respect to V_p. For the case of an insulating material, it can only be biased by applying a periodic voltage. The substrate surface exposed to the plasma is then capacitively charged, that is, electrically polarized, providing a mean DC voltage component, V_B. When a positive ion diffuses from the plasma bulk into the sheath region, it will then be accelerated toward the substrate, which it strikes with a maximum kinetic energy $E_{i,max}$ [21–23]:

$$E_{i,max} = e|V_p - V_B| + \Delta E/2 \tag{9.2}$$

The last term is due to the periodic modulation of the sheath voltage. At low excitation frequency $\Delta E \approx 2\ V_{AC}$, while for the high f values this term is inversely proportional to the number of RF cycles needed for the ion to pass through the sheath. This leads to the fact that for the ions originated from the same plasma, the maximum energy they gain in the sheath can be almost two times higher for the light ions (e.g. H^+) than for the heavy ones (e.g. $TiCl_4^+$). In the pressure range generally used for plasma processing, the ions lose part of their energy owing to elastic and inelastic (e.g. charge transfer) collisions in the sheath, and exhibit an ion energy distribution function (IEDF), discussed in more detail in Section 9.4.

In conclusion, the processes leading to the deposition of thin films in the plasma environment include reactions in the gas phase, transport toward the surface involving specific energetic considerations, and reactions at the surface, giving rise to film formation and microstructural evolution, providing specific film functional properties (as indicated in Figure 9.2). Energetic aspects of plasma–surface interactions and the importance and ranges of ion and photon energies, particularly of the ultraviolet (UV) and vacuum ultraviolet (VUV) radiation, are discussed in Section 9.4.

9.3 PECVD Reactors and Deposition Concepts

9.3.1 General Considerations

Plasma deposition equipment usually consists of six modules or functions: its main part is the reactor chamber, completed by the pumping system, power supply and monitor, electrical

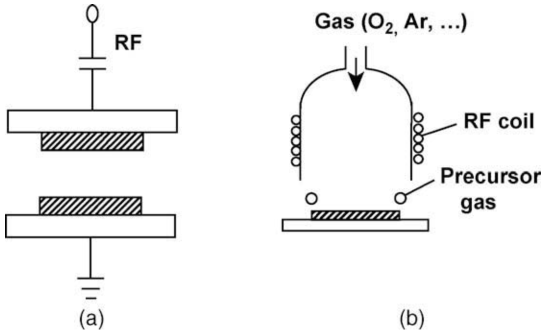

Figure 9.4: Schematic illustration of the reactor configurations of low-, mid- and radio-frequency PECVD systems: (a) parallel plate plasma reactor; (b) downstream (remote) RF inductively coupled plasma reactor.

matching network, process control and instrumentation, and process diagnostics. While most of the modules are similar for all PECVD and in many cases for PVD processes, they differ principally by the reactor configuration and the power supply modules, depending on the range of plasma excitation frequency, the nature of the substrates, and film quality requirements. In the following, we describe systems that have been successfully applied for the fabrication of PECVD functional coatings, some of which form the basis for industrial plasma equipment.

9.3.2 Low-, Medium- and Radio-Frequency Plasma Reactors

Low-, medium- and radio-frequency (LF, MF, RF) deposition systems can all possess internal electrodes, while the RF reactors can also use external plasma excitation using a coil or rings, as illustrated in Figure 9.4. This allows one to distinguish them based on the level of control of the bulk plasma characteristics and ion bombardment effects. The RF systems depicted in Figure 9.4 are similar to those frequently used in microelectronics for PECVD and reactive ion etching (RIE) [2, 3]. The r_D values on the grounded electrode are substantially lower than on the RF-powered electrode (usually 5–10 times) depending on the gas nature and composition. Typically, $E_{i,max} = 25\,eV$ on the grounded electrode (Eq. 9.2), while on the RF-powered electrode, E_i values may reach several hundred electron volts owing to high V_B.

9.3.3 Microwave and Dual-Mode MW/RF Plasma Systems

Many successful deposition systems for functional (mostly dielectric) coatings are based on the use of MW discharges that generally provide high n_e and hence high Φ_i values (Figure 9.5). In a single-mode MW reactor (Figure 9.5a–e), the substrate is placed on a grounded or electrically floating substrate holder, facing a MW (low water-content fused silica or alumina) window through which the MW power is supplied using different MW applicators [11, 24].

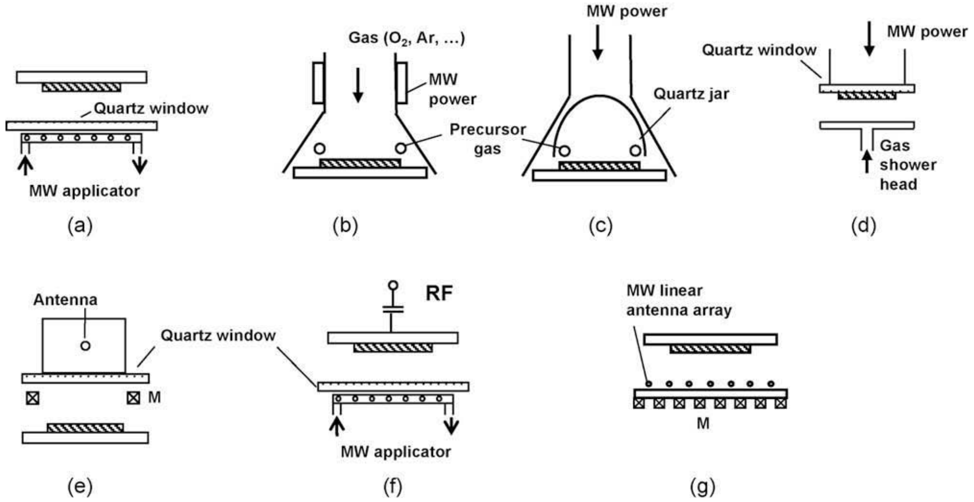

Figure 9.5: Schematic illustration of the reactor configurations of microwave frequency PECVD systems with different modes of excitation: (a) linear applicator; (b) remote MW excitation; (c) horn antenna; (d) plasma impulse CVD (PICVD); (e) electron cyclotron resonance (ECR); (f) dual-mode MW/RF; (g) distributed antenna array combined with ECR (DECR) (M indicates magnets).

Pulsed MW plasma with low pulsing frequency (f_p of about 100 Hz) and a low duty cycle ($D \leq 0.1$) have become prominent for optical and other functional coatings. This process has achieved a high level of sophistication at Schott Glaswerke GmbH (Mainz, Germany; see Figure 9.5d) [25, 26]. In their 'plasma impulse' chemical vapor deposition (PICVD) process, the dielectric substrates are placed directly on the MW window; in such a case, at a relatively high pressure on the order of 1 torr, very dense plasma is formed near the substrate during a very short pulse (typically 1–100 ms in duration).

A dual-mode MW/RF plasma approach has been developed at École Polytechnique in Montreal [18, 27, 28] (see Figure 9.5f) and also used by others [29, 30]. The substrates are placed on the RF-powered substrate holder facing the MW window, through which the MW power is applied with different types of linear applicators: slow wave structure, slotted waveguide, or surface wave launchers have been considered and tested [11, 24].

Other concepts include remote MW/RF reactors [29, 30] and electron cyclotron resonance (ECR) configurations (e.g. distributed ECR (DECR) [31] or integrated distributed ECR [32]), in which magnetic field is applied in conjunction with the MW discharge in order to further increase n_e and hence the dissociation rate (Figure 9.5e, g).

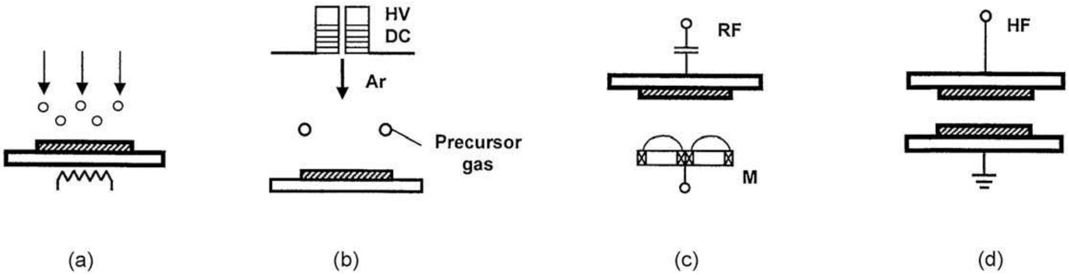

Figure 9.6: Schematic illustration of the reactor configurations using different modes of operation: (a) atomic layer deposition (ALD) or CVD; (b) cascade arc; (c) hybrid PECVD/PVD system combining a parallel plate RF electrode and magnetron sputtering; (d) atmospheric pressure plasma.

9.3.4 Complementary Plasma Systems

In addition to the basic configuration employing the thermal CVD technique (typically 300–800 °C) and the RF- and MW-based systems, there has been significant interest in novel complementary deposition approaches for functional coatings from a precursor gas or vapor using plasma enhancement alternatives; these include:

- The plasma-assisted atomic layer deposition (ALD) (Figure 9.6a) process in which the coatings are grown by sequentially introducing ‘pulses’ of a precursor; the final film then grows layer by layer, generally providing high surface conformity, very smooth surfaces, and other beneficial characteristics [33, 34].
- Cascade arc PECVD (Figure 9.6b), in which plasma of a carrier gas is excited in a series (cascade) of high-voltage arc electrodes. In such a system, developed at the Eindhoven University of Technology [35, 36], the activated gas expands at ultrasonic speed into a vacuum. On its way toward the substrate it dissociates, and activates precursor molecules that contribute to the film growth.
- Hybrid deposition systems benefit from the possibility of combining, in one reactor, both the PECVD and PVD approaches, such as illustrated in Figure 9.6c for the particular case of RF-PECVD and magnetron sputtering (or evaporation) [37]. This allows one to fabricate different coating architectures including multilayers or graded layers, or doped or nanostructured (nanocomposite) coatings with specific optical, mechanical, and other characteristics [38, 39].
- Much progress has recently been made in the development of APGD suitable for surface treatment [40] and explored for PECVD [9, 10] (Figure 9.6d). The system can be thought of as a capacitor, where one of the electrodes is covered with a layer of dielectric material (e.g. ceramic or glass). The high-voltage power supply, which

causes breakdown in the interelectrode gap, typically operates in the frequency range from 10 to 30 kHz. The pulseless (glow) discharge then has to be operated under specific conditions related to the choice of gases, power levels and frequency, in order to avoid corona (dielectric barrier discharge or silent discharge), which consists of a multitude of filamentary microdischarges [41, 42].

9.4 Process Diagnostics and Monitoring

9.4.1 Diagnostic and Monitoring Techniques

As indicated above, the relations between the external PECVD parameters available to the operator and the resulting film properties are rather complex. If we are to understand, control, and optimize the processes taking place inside the reactor, knowledge of internal parameters (such as particle generation, their flow and energies) is essential. The diverse plasma diagnostic techniques provide the possibility of accessing this information and developing understanding of the general process rules and interrelationships between input parameters and plasma characteristics, as well as the particularities of each PECVD system (Table 9.4).

The plasma bulk diagnostic techniques can be classified in many ways; for example; (1) by the particles they measure (electrons, ions, radicals, photons, etc.); (2) by being active (introducing additional signal into the system like a laser beam in laser-induced fluorescence (LIF) or external voltage in Langmuir probes); (3) by being passive (sampling neutrals in mass spectrometry or emitted light in optical emission spectroscopy (OES)); or (4) by the parameters they can help to assess (n_e, $n_{R,}$ etc.). An extensive literature describing principles and applications of different techniques is now available [43–46]. In addition, the list of available tools is completed by numerous techniques available for monitoring the film growth process directly on the substrate surface, and they are related to the films' mass/density, optical, electrical, and other properties [47–49].

The most popular techniques, the parameters detected, and other characteristics are summarized in Table 9.4. One of the most persistent problems in using diagnostics in any PECVD system is contamination of the electrical or optical components by the deposited films; this can substantially reduce precision, lead to artifacts, or even render the measurements impossible. The ways of dealing with such problems depend on both the technique and the process. There exist numerous possible solutions to such difficulties; including the use of shutters (opened only during the short period of the measurement itself); long inert gas purges; use of collimators with diaphragms to minimize deposition on windows and lenses; application of high positive or negative voltages to the electric (Langmuir) probes to heat-evaporate or to sputter-remove the accumulated film, and other approaches [43–45, 50–52].

Table 9.4: Diagnostic methods and their capabilities suitable for advanced analysis and control of PECVD processes

Diagnostics method	Measured parameters	Derived characteristics	Perturb the plasma	Time resolution	Space resolution	Cost	Contamination a problem	Advantages	Shortcomings/ comments
(a) Plasma bulk									
Langmuir probes	*I–V* characteristics; ion and electron currents	n_e, T_e, V_p, λ_D, EEDF	Slightly	10^{-5} s	5 mm	\$–\$\$	+++	Simple instrumentation	Complex interpretation
Mass spectrometry	Mass-selective intensity	Concentrations of atoms, molecules, and fragments	Slightly	10^{-3} s	1 cm	\$\$–\$\$\$	++	Many species, straightforward	Differential pumping, short-lived species
Ion energy analysis	Ion current	IEDF	Slightly	10^{-4} s	1 cm (0.1 mm)	\$	+++	Direct ion flux	No mass resolution
Optical emission spectroscopy	Spectrally resolved emission intensity	Concentrations of atoms, molecules, and fragments; vibrational and rotational temp., partial info. on EEDF	No	10^{-9} s	1 mm × 10 cm	\$-\$\$\$	+	Easy to set up	Indirect, convoluted interpretation
Absorption spectroscopy	Spectrally resolved absorption	Concentrations of atoms, molecules, and fragments	No	10^{-9} s	1 mm × 10 cm	\$\$\$	+	Access to radical densities	Bulky, limited set of species
Laser-induced fluorescence	Induced light intensity	Concentrations of atoms, molecules, and fragments	No	10^{-9} s	1 mm × 10 cm	\$\$\$	+	Access to radical densities	Bulky, limited set of species
Plasma impedance	Current, voltage, phase shift	Resistance, capacitance, n_e	No	10^{-3} s	None	\$	–	Simple	Indirect, convoluted interpretation
(b) In situ real-time film growth monitoring									
Quartz crystal microbalance	Vibration frequency	Mass, d, r_D, density (indirect)	Slightly	1 s	1–5 nm	\$	–	Simple	Sensitive to heating and to electric fields
Interferometry	Light intensity in transmission or reflection	d, n, r_D	No	10^{-3} s	1–5 nm	\$–\$\$	+	Simple	Single wavelength or multiwavelength; transparent films
Spectroscopic reflection/transmission	Spectrally resolved light intensity	d, n, r_D	No	10^{-3} s	1–5 nm	\$\$	+	Wide range of λ	Partially transparent films
Spectroscopic ellipsometry	Ellipsometric angles $\Psi(\lambda)$ and $\Delta(\lambda)$	d, n, k, r_D	No	10^{-1} s	0.2 nm	\$\$\$	+	Precise assessment of n and k in a wide range of λ	Costly, only for at least partially transparent films
Resistivity	Current, resistance	d	No	10^{-3} s	Depends on knowledge of the resistivity	\$	–	Simple	Only for conductors, affected by electric fields

9.4.2 Plasma Characteristics of PECVD Processes and Energetic Aspects of Thin Film Growth

Key parameters that influence the film microstructure in low-pressure, low-temperature deposition processes are E_i and Φ_i. In the PECVD process these are most frequently controlled by the choice of excitation frequency (RF vs MW), or by applying pulsed direct current (DC) or RF-induced negative substrate bias, V_B (see Section 9.3). The IEDF can be evaluated in the process chamber using a multigrid electrostatic ion energy analyzer (IEA) [53] or a quadrupole mass spectrometer integrated with an IEA [54, 55].

Examples of IEDFs in different PECVD systems in nitrogen are shown in Figure 9.7. In a parallel plate RF (13.56 MHz) system, with a discharge in N_2 at 40 mtorr, the E_i value at the grounded substrate holder is around 15 eV (Figure 9.7a) owing to the fact that typically $V_p = 20–25$ V, while E_i can reach many hundreds of eV on the capacitively coupled RF-powered electrode (Figure 9.7d). In the latter case, the IEDF is structured due to sheath modulation [21]. In fact, the IEDFs, n_e, V_B, and V_p values in PECVD are very similar to those encountered in magnetron sputtering and RIE.

MW plasmas usually yield high r_D, Φ_i, and n_e values, and high dissociation rates. In a simple MW reactor, a typical value of V_p is 10 V, generally yielding E_i of approximately 5–10 eV such as in the continuous wave (cw) mode in N_2 (Figure 9.7b). In such MW plasmas, two approaches can be used to control E_i and Φ_i, pulsed-mode discharges and RF-induced surface biasing (dual-mode or dual-frequency MW/RF plasma deposition). In pulsed MW plasma which is frequently used, two plasma regimes can be distinguished during each pulse cycle: high-density plasma during the T_{on} period, and decaying plasma during the T_{off} period. As a consequence, the IEDF adopts a bimodal shape (Figure 9.7c), with the high-energy peak corresponding to ions generated during the T_{on} period, and the low-energy peak being due to ions arising from the T_{off} period [53]. The ratio of the peak intensities depends on the duty cycle $D = T_{on}/(T_{on} + T_{off})$. This permits tuning of the plasma–surface interactions in deposition, as well as in etching or surface modification processes.

The possibility of selectively controlling E_i and Φ_i values over a large range is illustrated by the IEDFs in the dual-mode MW/RF discharge (Figure 9.7e, f). The effects of such control on adjusting film microstructure and, hence, specific properties and functional and device characteristics is discussed in more detail in Section 9.5.

Appropriate control of ion bombardment energy ($E_i < 1$ keV) is particularly important in the context of the deposition of thin films at low substrate temperature, T_S. Film growth, while under ion bombardment, leads to growth-related effects such as interfacial atom mixing, high surface mobility (diffusion) of deposited species, resputtering of loosely bound species, and deep penetration of ions below the surface, leading to the displacement of atoms (forward sputtering or knock-in effects) [3, 58]. Such phenomena give rise to the disruption of growth

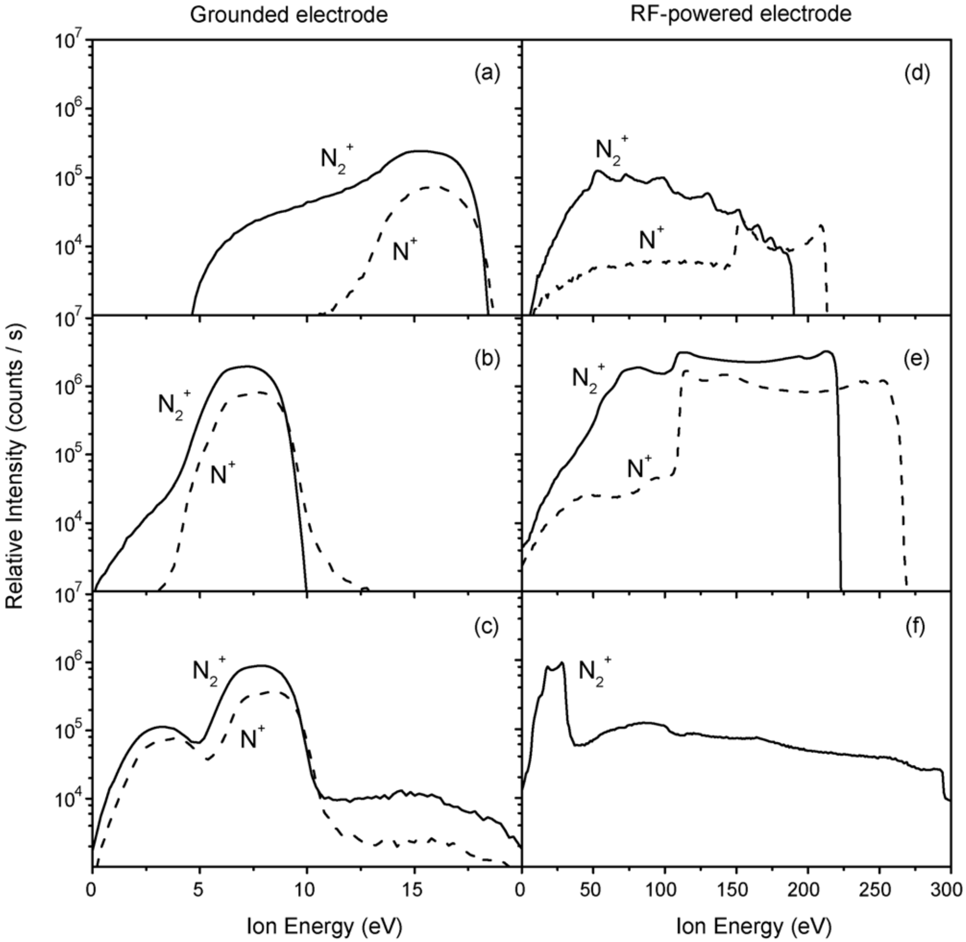

Figure 9.7: Examples of the IEDFs of N_2^+ and N^+ ions in high-frequency plasmas in nitrogen at 40 mtorr measured in the following configurations and detection positions: (a) grounded electrode in (continuous wave) cw-RF discharge such as in the reactor from Figure 9.4(a) ($V_B = -150$ V); (b) grounded electrode in cw-MW discharge such as in the reactor from Figure 9.5(a) ($P_{MW} = 300$ W); (c) grounded electrode in a pulsed MW discharge in the reactor from Figure 9.5(a) ($P_{MW} = 300$ W, pulse frequency = 1 kHz, duty cycle = 0.5); (d) RF-powered electrode in a cw-RF discharge such as in the reactor from Figure 9.4(a) ($V_B = -150$ V); (e) RF-powered electrode in the dual-mode cw-RF/cw-MW discharge in the reactor from Figure 9.5(f) ($V_B = -150$ V, $P_{MW} = 300$ W); (f) RF-powered electrode in the dual-mode cw-RF/pulsed-MW discharge in the reactor from Figure 9.5(f) ($V_B = -150$ V, $P_{MW} = 300$ W, pulse frequency = 1 kHz, duty cycle = 0.5). (Adapted after [55–57].)

nuclei, to the suppression of columnar structure, and hence to material densification. This is in agreement with the so-called structure zone model (SZM) first proposed by Movchan and Demchichin [59], improved by Thornton [60] and Messier et al. [61, 62], and finally refined by Kelly and Arnell [63].

Various approaches to quantitative description of ion bombardment have been taken. It appears that a key parameter for representing these effects is the energy E_P delivered to the growing film per deposited particle [64]:

$$E_{P(Ts=const)} = (E_i\,\Phi_i + E_m\Phi_m)/(\Phi_n + \Phi_r) \sim E_i\,(\Phi_i/\Phi_n), \tag{9.3}$$

where E denotes energy; Φ the particle flux; and the indices i, m, n, and r refer to ions, neutrals, condensing precursor species, and trapped inert gas, respectively. As a first approximation, one can neglect Φ_r compared to Φ_n and $E_m\Phi_m$ compared to $E_i\Phi_i$, and obtain the simplified relation in Eq. (9.3). Such an approximation is clearly possible in ion beam experiments; however, the energy flux of neutral particles may become significant in PECVD because a certain fraction of the initially accelerated ions become neutral due to charge transfer collisions in the sheath region. Detection of neutral species and determination of their energy is difficult, requiring careful measurements, using mass spectrometry combined with ion energy analysis [54, 55].

It has been proposed that there exist critical ion energies, and critical ion flux ratios ($E_{i,c}$ and $(\Phi_i/\Phi_n)_c$), which can be associated with transitions in the evolution of film microstructure and properties [18, 65]. Clearly, E_P in Eq. (9.3) can be adjusted to the same level by combining low and high E_i and Φ_i/Φ_n values. However, experience suggests that good-quality (dense, hard, chemically stable, low-stress) films are obtained under conditions of low (10–50 eV) or intermediate (about 100 eV) ion energies, sufficient for densification ($E_i \sim E_{i,c}$), but using high Φ_i. This reduces microstructural damage and gas entrapment, generally yielding low values of stress. High fluxes are highly advantageous, especially when one aims at achieving high r_D (>10 nm/s).

In Figure 9.8 the $E_{i,c}$ and $(\Phi_i/\Phi_n)_c$ values for PECVD SiO_2, Si_3N_4, TiO_2, and *a*-C:H films have been compared with the compilation of literature data by Harper et al. [65], who summarized examples of $E_{i,c}$ and $(\Phi_i/\Phi_n)_c$ values reported to be necessary for property modification in numerous materials deposited by different (non-PECVD) ion-assisted techniques. It was concluded that the $E_{i,c}$ values are lower, and $(\Phi_i/\Phi_n)_c$ values are higher for MW and MW/RF PECVD processes than for most other techniques. The energetic conditions leading to good-quality films obtained by the PICVD process also fall within the same energy limits, that is low E_i ($E_i < 10$ eV) but high Φ_i/Φ_n ($\sim$ 1–10) values, due to a high plasma density and ionization rate [25]. In this context, to derive appropriate relations between E_i and Φ_i/Φ_n, and to benefit from the availability of experimental data, one can apply the conversions for the experimentally measured ion current, where 1 mA/cm^2 corresponds to 6.25×10^{15} ions/cm^{2}s,

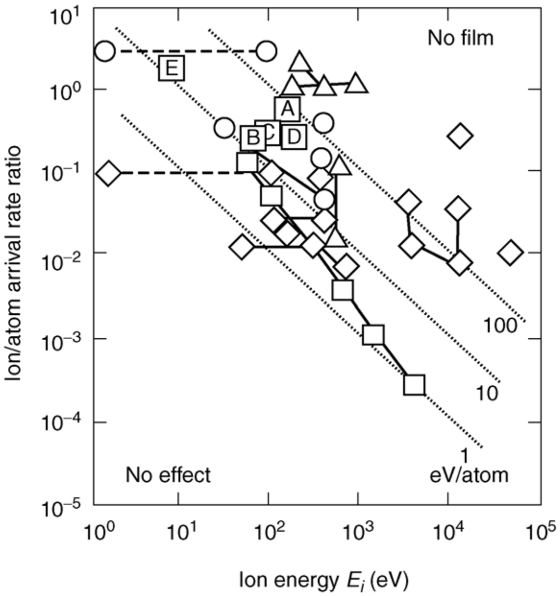

Figure 9.8: Plot of critical ion/condensing particle arrival rate ratios $(\Phi_i/\Phi_n)_c$ vs critical ion energy $(E_i)_c$, required for film structural modification, particularly densification: (A) $SiN_{1.3}$:H; (B) SiO_2:H; (C) *a*-C:H; (D) TiO_2 obtained from MW/RF plasma; (E) estimated for TiO_2 obtained in a PICVD discharge based on the data in [25]. Other data points are from [65] for different materials obtained by PVD techniques: (○) SiO_2, (△) other dielectrics, (□) metals, (◊) semiconductors. (After [7].)

and a useful relation [66]:

$$\Phi_n = r_D \rho N_A / m \tag{9.4}$$

where N_A is Avogadro's constant and ρ and m are the density and the molecular mass, respectively, of the material.

We conclude from Figure 9.8 that for most materials, energy may range from several to several hundreds of electron volts per particle [58]. These relatively high E_P values were obtained as a result of process and materials optimization, and point to the trend in recent deposition techniques, favoring lower E_i and high Φ_i [7, 66]. In addition, E_P appears to be higher for materials with a higher melting point, in agreement with the SZM. This rather simplified approach does not take into account the fact that, at a relatively high pressure, considerable energy is also delivered to the growing surface by energetic neutrals, as indicated in the full Eq. (9.3) [67].

The role of ion bombardment and the possibility of predicting its effect on the characteristics of individual films, of the interfaces, and on the performance of the thin film systems and

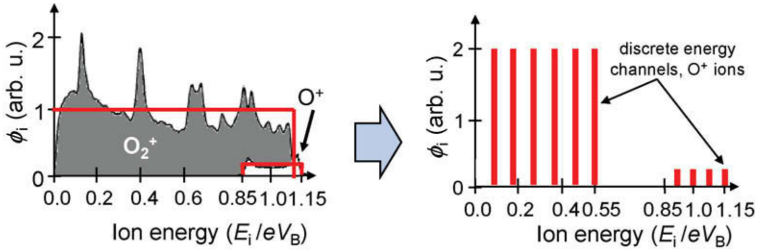

Figure 9.9: IEDF on the RF-powered electrode in a discharge in oxygen and its conversion into energy channels suitable for dynamic Monte Carlo simulations. (After [68].)

related coating architectures can also be assessed by complementary approaches, such as by dynamic TRIDYN Monte Carlo simulations combined with in situ real-time spectroscopic ellipsometry (RTSE) [68, 69]. These have shown that ion- and plasma-assisted deposition processes in the range of tens to a few hundreds of electron volts lead to thin film growth dominated by subsurface deposition, as a result of subplantation (shallow implantation).

As an example for the particular case of PECVD in an O_2-rich plasma at the RF-biased electrode, the experimentally determined IEDF has been modeled as shown in Figure 9.9. This distribution was divided into multiple channels (ten in this particular case), and the effect of ions on the structural changes has been simulated up to an experimentally relevant fluence (e.g. 10^{18} ions/cm^2, corresponding to a typical deposition duration). Such interactions were shown to predict very accurately the thickness of interfacial layers, depending on the Φ_i/Φ_n value (see Section 9.5.5).

RTSE measurements can be used for the study and monitoring of ion bombardment and thin film growth effects without perturbing film growth [47, 48]. As an example, evolution of the real ε_1 and imaginary ε_2 parts of the permittivity of superhard nanocomposite nc-TiN/SiN and nc-TiCN/SiCN coatings is illustrated in Figure 9.10. One can distinguish various regions corresponding to different surface phenomena during film deposition, including pumping (surface desorption) and substrate heating (actual surface temperature can be determined from the shift of the temperature-sensitive substrate parameters – region) beginning of actual film growth (region II), (until the film becomes opaque for the RTSE system wavelength range (region III)), and, finally, system cool-down and possible post-deposition surface interactions (region IV). Analyzing the behavior of the ε_1 and ε_2 values, one can make conclusions with respect to the film's optical, electrical, compositional, and microstructural characteristics (for more detail, see Section 9.5.4) [70].

As a complement to ion bombardment during the film growth, one should also consider another source of energetic plasma–surface interactions, namely photons in the entire range from infrared (IR) and visible to UV, VUV and soft X-ray regions (for a review, see [71]). In

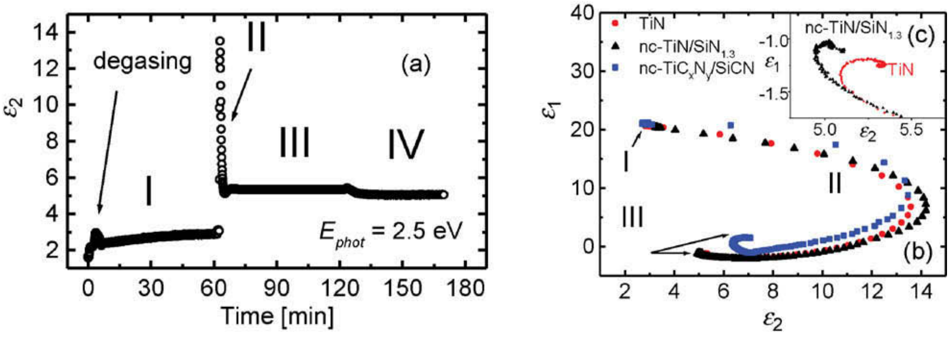

Figure 9.10: Evolution of the ellipsometric parameters during the growth of superhard nc-TiN/SiN$_{1.3}$ and nc-TiCN/SiCN films. The curves pertain to a wavelength of 500 nm (photon energy: 2.5 eV): (a) imaginary part of the permittivity as a function of time during the fabrication process; (b) ε_1 vs $_2$ plot of the real and imaginary parts of the permittivities during the film growth; (c) detail of the ε_1 vs ε_2 plot at a moment when the films become thick. (Modified after [70].) See text for more details.

particular, VUV photons play an important role in the interaction with organic (polymer) surfaces, since their energy, of more than 10 eV, can break any chemical bond. Of considerable importance in active plasmas is the radiation in discharges containing hydrogen with its strong Lyman line at 121 nm and intense molecular bands, oxygen with its strong resonant line at 130 nm and helium (intense lines at 57 nm and above), which are particularly effective (Figure 9.11) [11, 13]. In this context, intense VUV features due to the excitation of different

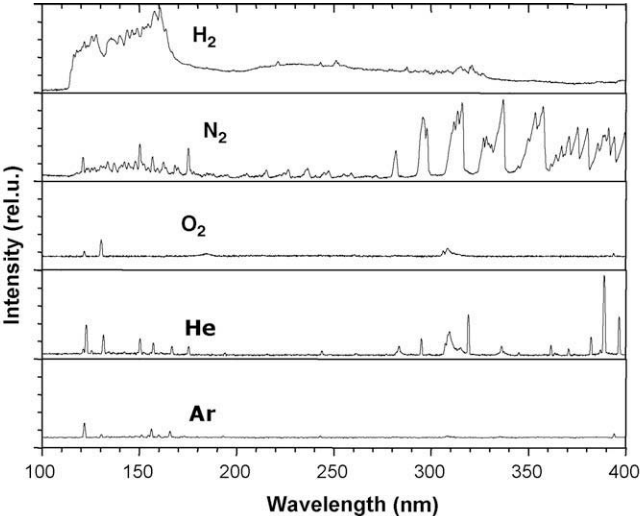

Figure 9.11: Vacuum ultraviolet (VUV) spectra emitted from glow discharges in different gases. (After [72].)

discharge components including impurities (fragments of H_2, SiH_4, CH_4, H_2O, hydrocarbons, and others) desorbed from chamber walls and from polymer substrates may be very important, and can play a significant role in controlling the characteristics of polymer surfaces and of coating–polymer interfaces (see Section 9.5.6).

9.5 PECVD Materials: Effect of Surface Processes on the Microstructure and Properties

Numerous PECVD functional coating materials have been investigated and considered for a large number of applications, and some of them are now applied on an industrial scale. Since there already exists a vast literature on this subject, we specifically focus in this section on coatings studied for their functional (or multifunctional) character, for various applications outside electronics. We particularly show examples of films for which there exist complete sets of microstructural, compositional, and functional characteristics, in close relationship with the energetic aspects of film growth, outlined in the preceding section. First, we introduce the most frequently used characterization methods (Section 9.5.1), and then provide examples of effects of deposition conditions on film characteristics.

For simplicity, we divide the materials described into four categories:

- silicon-based (inorganic) coatings (Section 9.5.2)
- carbon-based coatings and related covalently bonded materials (Section 9.5.3), including organic PECVD films such as plasma polymers
- metal-based PECVD coatings, including nanocomposites which exhibit superhardness and non-linear optical properties (Section 9.5.4)
- interface engineering aspects of film deposition onto various technologically important substrates (Section 9.5.5).

9.5.1 *Characterization Methodology Specific to PECVD Coatings*

Throughout this chapter, we frequently refer to film characteristics obtained by different, complementary, techniques which provide detailed information about the microstructure, composition, and properties of PECVD films. We comment on certain methodological issues that should be considered in the interpretation of results.

The microstructure of PECVD coatings is most often assessed by scanning electron microscopy (SEM), transmission electron microscopy (TEM), and X-ray diffraction (XRD), which are used to identify crystalline phases, lattice parameters, average crystal size, and surface roughness, the latter also frequently determined by atomic force microscopy (AFM). Chemical composition of the films, particularly the compositional depth profiles, is studied by elastic recoil detection in the time-of-flight regime (ERD-TOF) [73]. This technique allows one to establish quantitative data without standards. Moreover, ERD can quantify H concentration, [H], which is of primary importance for PECVD coatings, which are most often fabricated in hydrogen-containing environments. Complementary techniques include Auger electron spectroscopy (AES), X-ray photoelectron spectroscopy (XPS), and IR and Raman spectroscopies, used to evaluate chemical composition, chemical bonding, and short- and medium-range microstructure (for a review, see e.g. [74–76]).

Optical properties are determined either from spectrophotometric (reflectance, R, and/or transmittance, T) or ellipsometric measurements, among which variable angle spectroscopic ellipsometry (SE or VASE) combined with R and T data appears to be most powerful (for a review, see [7]). Ellipsometry deals with determination of the relative phase change of a reflected polarized light beam, as opposed to absolute intensity measurements in spectrophotometry, making it more sensitive to very small changes in the optical properties at the surface of the sampled material. Spectrophotometry is more appropriate when evaluating the performance of a coating system, such as an optical filter. For postprocess characterization (sometimes called reverse engineering), the two methods share the same difficulties, related to the optimization algorithms and models used for reproducing the measured data.

The most frequently used dispersion models for dielectric films are the semi-classical Sellmeier and Cauchy relations for the refractive index $n(\lambda)$ [77], and the Urbach tail relation for the extinction coefficient $k(\lambda)$ [78]. Recently, new dispersion relations, such as the Forouhi–Bloomer [79] and Tauc–Lorentz formulae [80], based on a simplified expression for $k(\lambda)$ due to allowed electronic transitions in solids, have been shown to work well for PECVD materials.

Effective medium approximation (EMA) models are frequently applied to account for index inhomogeneities, and to estimate porosity, surface roughness, or other microstructural features [81, 82]. The use of EMA is justified only when the scale of the inhomogeneities is much smaller than the wavelength of the probing light ($< \lambda/10$). The scale of the Bruggeman EMA is used for a heterogeneous medium with components of small size, randomly distributed, while the Maxwell–Garnett model is more appropriate when one of the components surrounds the others, and acts as a host material [83].

Components of the EMA models must be chosen with care to reflect the real composition of the material (sometimes including voids, or an optically absorbing phase, such as *a*-Si). However, one may question the utility of both the Maxwell–Garnett and Bruggeman EMA when the inhomogeneity is on the atomic scale; this applies to solid solutions such as SiO_xN_y films, or when dopants and impurities are present (H, F, Cl, C, etc.), in which cases no particular phases with bulk dielectric response can be identified [84].

Reliable determination of the optical properties is generally based on the (mostly non-global) fit optimization. In such situations, it is very important to have a good starting ‘guess’ for n, k, and the thickness, d. In the case of single-layer films for which one has no a priori knowledge of n and k, the optical characteristics can also be obtained from envelope methods which provide analytical expressions for n, k, and d as a function of T or R. For more detail, see the discussion in [7].

Mechanical characterization, to determine hardness, H, reduced Young's modulus, E, and other elastoplastic properties, is frequently performed by depth-sensing indentation, and analyzed by the method of Oliver and Pharr [85]. The intrinsic stress given by the internal structure of the material (in particular, structural defects like macroscopic voids, gas entrapment, or phase transformation) is measured by the curvature of the substrate, before and after film deposition, and calculated from the Stoney formula [76, 86]. The curvature is assessed by mechanical or optical profilometry, or by interference measurements. The wear coefficient, K, and friction coefficient, μ, characterizing the tribological behavior of the coatings, are usually determined by pin-on-disk tribometry. Different tests exist for determining adhesion: these include qualitative (peel test) and semi-quantitative (scratch test) approaches [87, 88].

Corrosion resistance is usually determined qualitatively by evaluating the surface morphology after exposure to a corrosive medium, or quantitatively by measuring the corrosion current or open circuit potential (OCP) [89]. Recently, tribocorrosion properties have been assessed in real time by simultaneously performed OCP and wear measurements [90]. The corrosion mechanism, and especially its relationship with microstructure, can be determined by electrochemical impedance spectroscopy (EIS), in combination with appropriate equivalent electrical models [89].

Complementary to the optical and tribomechanical characterization above, basic electrical testing of PECVD functional (usually dielectric) films is performed in a sandwich metal–insulator–metal (MIM) structure to determine DC resistance, ρ_E, dielectric loss tangent (tan δ) or permittivity, ε, breakdown voltage, leakage current and other electrical properties. For conductive films, ρ_E and carrier mobility are assessed by the four-point method and by Hall effect measurements [76, 91].

The basic optical and mechanical properties of the most frequently studied PECVD films are summarized in Figure 9.12, where they are compared with those of their PVD counterparts and of the most often used substrates. Each of the characteristics exhibits a certain range of values, related to the fabrication conditions and, hence, to the microstructure and composition, a subject of the following sections.

9.5.2 Silicon-Based (Inorganic) Coatings

Silicon compound films have been studied for many decades, because of their use in microelectronics, microelectromechanical systems (MEMS), optics and photonics, photovoltaics, and other areas. PECVD Si-based films are generally amorphous, and contain

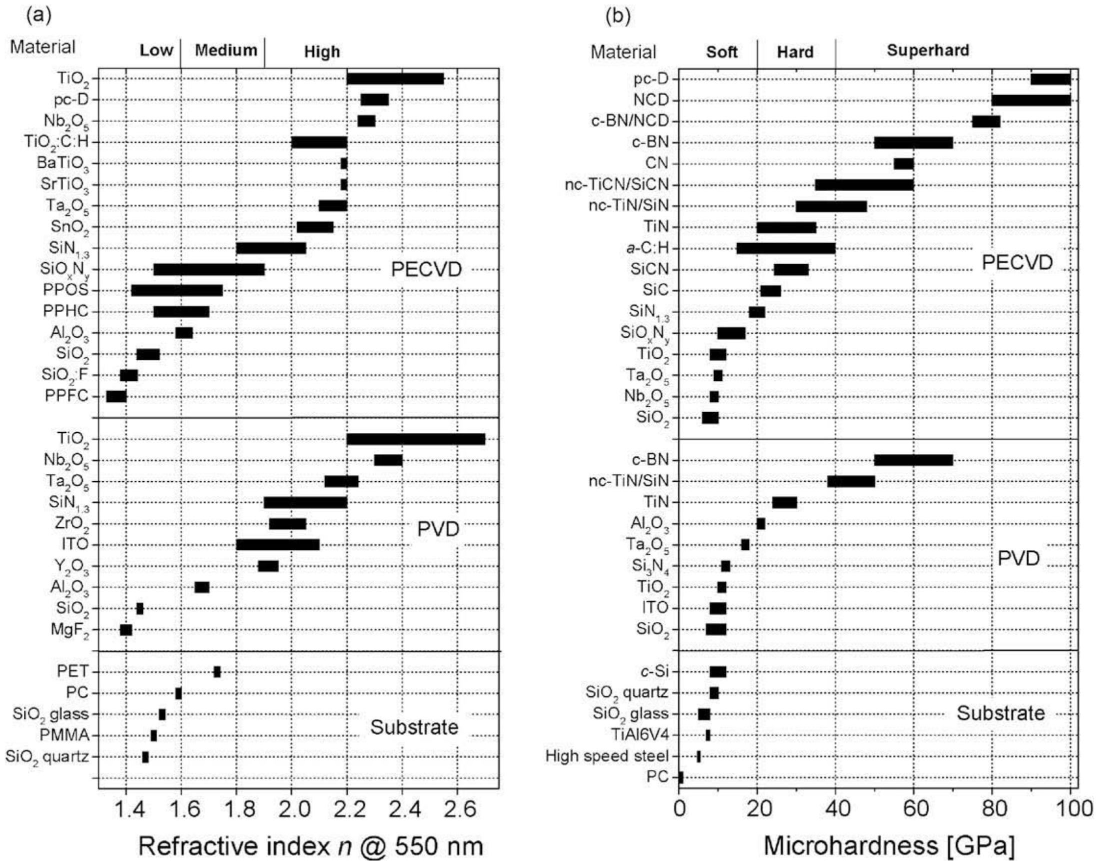

Figure 9.12: Physical properties for the most frequently studied PECVD films: (a) refractive index of transparent films; (b) microhardness. PVD films and often used substrates are shown for comparison.

considerable amounts of hydrogen, owing to the use of precursor gases such as silane (SiH_4) and different organosilicones (OS). The most frequently applied systems include hydrogenated amorphous silicon (a-Si:H), silicon oxide (a-SiO_2:H), silicon nitride (a-Si_3N_4:H), silicon oxynitride (a-SiO_xN_y:H), and silicon carbide (a-SiC:H). In the following, we focus particularly on functional silicon compound films. For simplicity, we apply an abbreviated nomenclature, namely SiO_2, $SiN_{1.3}$, SiON, SiC, and SiCN. The reader may consult other reviews dealing with amorphous, polycrystalline, crystalline and porous silicon, and related materials and their fabrication, properties and applications [2, 92].

9.5.2.1 Silicon Dioxide

Among all dielectric and silicon-compound coatings, SiO_2 is probably the most studied PECVD material. It is typically deposited from a mixture of SiH_4 and O_2 or N_2O. Both theoretical and experimental studies of the various phases of SiO_2 underline the link of the film characteristics, such as n, optical gap, E_g, and others, to microstructure, in particular the Si–O–Si mean bond angle, θ, density, and H incorporation [2, 93]. In amorphous SiO_2, changes in θ values can be estimated experimentally from IR spectra of the Si–O–Si stretching mode at 2260 cm^{-1}. A small θ value is related to a stressed network in a dense structure.

Small-angle Si–O–Si bonds are very unstable. They can be broken by an accumulation of stress in the film and force the network to relax, leading to a more flexible structure, accompanied by the formation of defect centers, or by reaction with water [94]. In the latter process, water absorption in pores may not necessarily be associated with aging, since not all types of pores give rise to water sorption, but the concept of 'open' and 'closed' pores and their size should be considered [95].

In SiO_2 deposition from SiH_4/O_2 mixtures, the O_2 flow rate is typically twice that of silane, or more, depending on the plasma conditions. Nitrous oxide (N_2O) is frequently used to replace O_2, since the chemical bonds in N_2O break more easily, leading to higher r_D (activation energy, $E_a = 2.5$ eV/molecule in N_2O [96] compared to $E_a = 6.5$ eV/molecule for O_2 [97]). The use of N_2O can introduce some N impurities; however, [N] is usually less than 3 at.% owing to the high affinity of Si with O, and even smaller if the film is produced using ion bombardment or is heated. The use of He has been shown to reduce the number of Si–H, Si–N, Si–OH, and N–H bonds in SiO_2 made from SiH_4/N_2O mixtures [98].

SiO_2 usually contains 5–15 at.% of hydrogen, mostly in the form of –OH, which has an effect on the optical and other properties, and on the stability of the material. It has been shown that during deposition from a SiH_4/O_2 mixture, the surface of the growing oxide is initially covered with silanol (SiOH) [99], owing to instant oxidation of SiH_x by atomic oxygen. The SiH_x groups react further with SiOH and Si–O–Si to yield H_2O and Si–O–SiH_x, which is oxidized by neutral O, leading to superficial–SiOH terminations.

O_2^+ bombardment seems to be particularly efficient for reducing [H] in the film [99]. When the dissociation of SiH_4 is high, Si exists on the surface, and it is easily oxidized, compared with SiH_2 and SiH_3 groups, for which several reactions with oxygen are needed to release all the H atoms. This means that high n_e (high discharge power) can reduce H concentration, such as in ECR [100], MW, or MW/RF [18] plasmas.

An important problem with silane as a precursor is the formation of particles. It can react with traces of humidity in the gas line and form powder that can reach the chamber, and clog valves and mass flow controllers; thus, it is essential to purge the lines periodically and keep them clean. In the plasma, silane produces radicals that can react rapidly in the gas phase, forming particles. This results in nodules and large voids in the films. Several steps can help to solve such problems, namely: (1) reduced operating pressure (e.g. ECR plasma); (2) dilution of SiH_4 in Ar or He; (3) heating the electrode; and (4) use of a pulsed discharge [101].

The use of OS precursors to replace SiH_4 is motivated by its hazards (it is strongly pyrophoric), and by the fact that SiH_4 leads to low surface coverage as a result of its low surface mobility. Therefore, deposition of SiO_2 from hexamethyl disiloxane (HMDSO) and tetra ethoxysilane (TEOS) is widely used; such organic precursors are liquid and require the use of a bubbler (see theoretical study in [102]) or a liquid injection system.

9.5.2.2 Fluorinated Silicon Oxide

Work on fluorinated SiO_2 (SiO_2:F or SiOF) has been stimulated by the search for low-refractive index and low-permittivity (dielectric constant: low-ε or low-κ) materials for optics, photonics, and intermetallic dielectric layers, to reduce the parasitic capacitance in multilevel interconnects in microelectronic devices [103]. In such case, n could be reduced to 1.41–1.43 (at 550 nm), compared to 1.45–1.48 for non-fluorinated SiO_2 (Figure 9.12).

Fluorine was chosen for this purpose, owing to the low-ε properties of fluoropolymers and the properties of fluorine-doped amorphous silicon (a-Si:F), in which fluorine plays a stabilizing role, while passivating dangling bonds and reducing [H]. Many methods involving plasma have been applied to fabricate SiOF, using different organic and inorganic precursors, such as TEOS, SiH_4, CF_4, and C_2F_6 mixed with oxygen (for a review, see [7]).

The low-ε properties of SiOF are usually attributed to ionic bonding, such as the change in Si–O bond strength in the neighboring Si(O–)F sites, or replacement of –OH bonds in its structure. Reduction of n and k has also been observed in the visible frequency range, associated with a relaxation of θ, lower density, shorter Si/Si interatomic distance at low [F], and void formation, especially for high [F] [104].

The conclusions of studies of SiOF deposition may be summarized as follows. Optimized conditions should lead to θ of about 148° without the formation of $Si(O–)_2F_2$ and voids. The use of high O_2 (or N_2O) concentrations was found to lead to dense films and to the incorporation of more F. These effects are attributed to higher O_2^+ bombardment. SiOF represents an attractive low-n and low-κ material; dense, stable films with $n = 1.41$ and [F] = 12 at.% can be used in numerous applications, while porous, unstable films with $n = 1.38$ and [F] = 20 at.% need to be combined with a dense barrier layer (e.g. $SiN_{1.3}$ or TiO_2) in multilayer systems.

9.5.2.3 Silicon Nitride

Among possible nitride materials, $SiN_{1.3}$ has been widely used because of its transparency, hardness, impermeability, and other advantageous functional properties. It can be deposited using SiH_4 mixed with nitrogen (N_2) or ammonia (NH_3). The use of OS precursors is limited by the presence of carbon in the final product.

When deposited at low temperature and low energy conditions, $SiN_{1.3}$ exhibits a columnar structure; therefore, more energy must be brought to the surface by ion bombardment or substrate heating in order to achieve high packing density. The residual gas concentration in the PECVD reactor must also be kept very low, as $SiN_{1.3}$ can react rapidly with traces of O_2 or H_2O [105].

The main 'impurity' in $SiN_{1.3}$ is hydrogen, which has a significant effect on the electronic and optical properties. Owing to the dense structure of the films and the valence of nitrogen versus oxygen, the amount of H (passivating broken bonds) is substantially higher in the nitride than in the oxide [18]; H mainly appears in Si–H and N–H bonds. Replacing Si–N by Si–H has little effect on the gap ($E_g = 5.3$ eV for H-free $SiN_{1.3}$) [106], but N–H bonds considerably reduce the value of n. For silicon-rich nitride, Si–H replaces Si–Si bonds, an approach to tailor the valence edge, and to increase E_g.

One way to avoid H incorporation is to use silicon halide precursors, such as $SiCl_4$ or SiF_4. The chemical affinity between Cl atoms and H atoms promotes the formation of HCl, which can further reduce the H concentration. In addition, the presence of halogen atoms gives rise to a competitive etching process during deposition, which can reduce the film roughness. For $SiN_{1.3}$ films grown in MW/RF plasma at $T_S = 25\,°C$, controlled ion bombardment gives rise to n values between 1.65 and 1.90 for V_B of 0 and 800 V, respectively [107]. The resulting hydrogen concentration is found to vary between 12 and 16 at.%, systematically less than in pure RF discharge [18]. It has been proposed that some of the hydrogen is not chemically bonded, but is trapped or chemisorbed on inner surfaces [18]. Attempts have been reported to deposit 'nitride-like' $SiN_{1.3}$ films from OS precursors, using for example hexamethyl disilazane (HMDSN) and hexamethyl cyclotrisilazane (HMCTSZN) [108], mixed with N_2 or NH_3.

9.5.2.4 Intermediate Oxide Materials

Several materials are particularly suitable for the fabrication of films with intermediate compositions, achieved by adjusting the gas mixtures [48, 107] or by controlling the film density [107, 109]. The most extensively used material for this purpose is SiON obtained from gas mixtures with SiH_4 using varying nitriding versus oxidizing gas ratio (e.g. NH_3/N_2O or N_2/O_2). Since O has more affinity to Si than N, one can choose to control only the O_2 flow.

According to detailed SE and electron spin resonance measurements, SiON films exhibit homogeneous and amorphous microstructures, close to those of a solid solution [110], and no crystal formation has been observed up to a temperature of 900 °C. These measurements lead to certain limitations in the use of EMA to model structural characteristics of such films; the main concerns are as follows: (1) H incorporated in the films reduces n. This is difficult to account for in the EMA model [110]; (2) films deposited at high E_i or T_S values represent solid solutions at the atomic level, containing O–Si–N bonds, hence no SiO_2 and $SiN_{1.3}$ domains can be distinguished; and (3) the optical and electrical characteristics may be dominated by the presence of pores (possibly filled with water vapor).

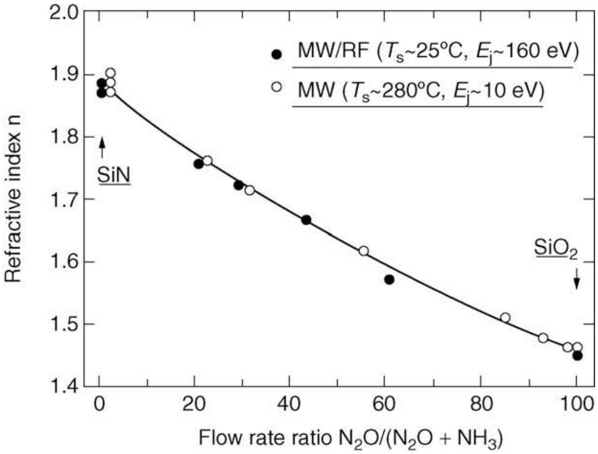

Figure 9.13: Refractive index of SiO_xN_y films as a function of the $N_2O/(N_2O + NH_3)$ concentration ratio in the gas mixture with SiH_4 in the MW and the dual-mode MW/RF plasmas. (After [111].)

The use of SiON films allows one to benefit from the advantages of the specific characteristics of individual SiO_2 and $SiN_{1.3}$ layers. In addition, as also discussed above, one can sensitively control evolution of the film microstructure by an appropriate choice of the ion bombardment conditions. Such choices are illustrated by the following examples.

By adjusting the NH_3/N_2O ratio in the mixture with SiH_4 in a dual-mode MW/RF discharge, one can vary n from high (corresponding to 1.9 for $SiN_{1.3}$) to low (corresponding to 1.45 for SiO_2) (Figure 9.13). This illustrates the possibility of obtaining films with any intermediate value of n, a useful property for the fabrication of discrete multilayer or graded (inhomogeneous) optical filters (discussed in detail in Section 9.6.1) or for other applications. In addition, one can distinguish, in Figure 9.13, two sets of data points, those pertaining to films prepared in pure MW plasma at $E_i = 10\,\text{eV}$ and $T_S = 250\,°\text{C}$, while essentially the same n values were obtained in a MW/RF plasma at $E_i = 160\,\text{eV}$ and $T_S = 25\,°\text{C}$ [107, 111]. A V_B was applied in excess of the $E_{i,c}$ necessary for ion-induced densification in agreement with the SZM.

The effect of V_B on the evolution of stress, σ, is illustrated in Figure 9.14 for films prepared in a MW/RF discharge from mixtures with SiH_4 at RT. The films develop a tensile stress at low ion bombarding energies (in pure MW discharge or at low V_B); when V_B is increased, the σ values pass through the zero-stress region, followed by a higher compressive stress, attributed to film densification and gas entrapment [112].

Silicon compound films have been shown to provide attractive electret properties. They can retain electric charge for extensive periods, suitable for such applications as electret microphones and electret-enhanced solar cells [112]. In such a case, when the film is exposed

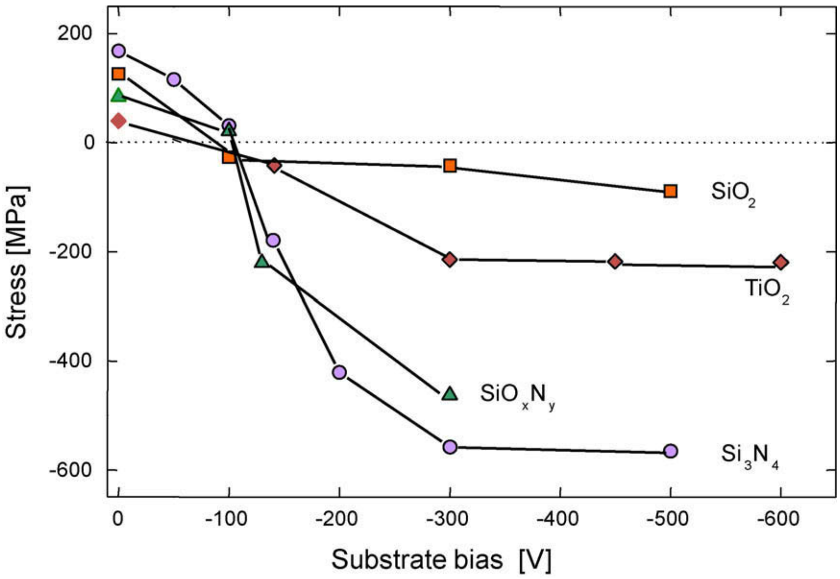

Figure 9.14: Evolution of stress in PECVD films as a function of substrate bias in the dual-mode MW/RF discharge. (Modified after [112].)

to corona-excited air, electric charges (electrons) are incorporated in traps in a range of energetic depth. Deep traps then release the electric charges when sufficient activation energy is supplied. Measured thermally stimulated currents from such electret structures (Figure 9.15) point to the fact that dense SiON films impregnated with OS vapors possess the deepest traps, thus providing very attractive electret properties.

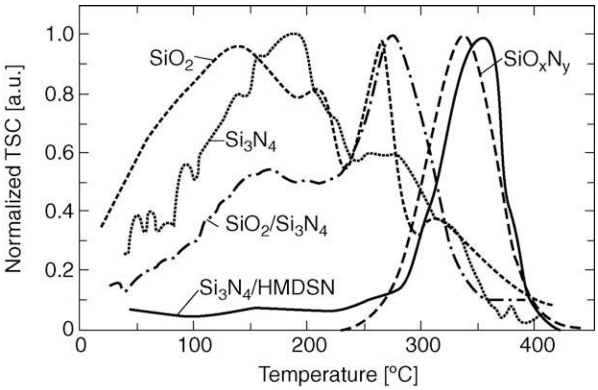

Figure 9.15: Thermally stimulated discharge currents in SiON electret films fabricated and treated under different conditions. (After [112].)

Other Si-based graded materials have also been studied. These include GeO_2/SiO_2 films obtained from a TEOS/O_2 mixture doped with TMGe [113], Si-rich SiN_x (absorbing) films considered for near-infrared (NIR) applications, and F-doped SiO_2 which have been studied for graded n optical filters [114].

9.5.2.5 Silicon Carbide and Silicon Carbon Nitride Coatings

Amorphous hydrogenated silicon carbide (*a*-SiC:H or SiC) coatings are attractive because of their optical, electronic, and mechanical properties [2, 115, 116]. Using PECVD, SiC is usually obtained from varying mixtures of SiH_4 and CH_4 or OS at relatively low substrates temperatures ($T_S = 200–400\,°C$) [115, 117]. Microstructural characteristics, composition, and mechanical properties of SiC can be controlled by an appropriate selection of process parameters.

Ternary Si compound coatings, such as SiCN, have become increasingly attractive since they can combine advantages of the individual binary materials and of their intrinsic properties, specifically of $SiN_{1.3}$, SiC, and CN. In this context, the important characteristics are: (1) high optical transparency and wide E_g ($\sim 5\,eV$) of $SiN_{1.3}$; (2) lower E_g ($\sim 2.8\,eV$) and interesting mechanical performance of SiC; and (3) high hardness, partial electrical conductivity, and high elastic rebound due to a fullerene-like microstructure of CN. These three materials are miscible; therefore, by changing the phase content and by controlling the short range order, it is possible to tune the properties of SiCN films for specific electronic, tribomechanical, and other applications. Many interesting results have been reported on such ternary SiCN films, including analysis of its complex chemical structure using infrared SE, and of its tribological properties [118].

9.5.3 Carbon-Based and Related Coatings

The study of various carbon-based materials has been stimulated by a combination of their very advantageous functional properties, ranging from high hardness and low friction to optical transparency in IR, high corrosion resistance, high heat conductivity and biocompatibility. They can be categorized, depending on the sp^2 and sp^3 hybridization, level of structural order, as well as by hydrogen concentration (Figure 9.16). The subject of carbonaceous coatings has been covered in other reviews [119, 120]. Here, we briefly introduce different categories of carbon, specify the nomenclature, and give several examples where the performance of different carbonaceous systems has been controlled by the growth parameters, in particular E_i and T_S.

We distinguish among the most frequent forms of carbon-based films, namely (1) PECVD diamond-like carbon (DLC) or amorphous hydrogenated carbon (*a*-C:H); (2) polycrystalline diamond (pc-D) or nanocrystalline diamond (NCD); and (3) soft organic carbonaceous coatings (plasma polymers) obtained under ‘mild’ plasma conditions. In this context, several

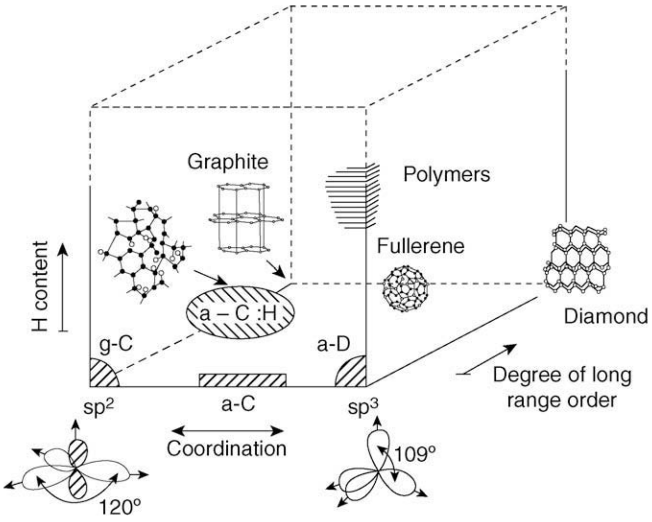

Figure 9.16: Schematic representation of different phases of carbon distinguished by the carbon coordination, degree of range order, and hydrogen content. (After [87].)

categories of organic amorphous PECVD films prepared from hydrocarbon precursors under controlled ion bombardment can be distinguished based on E_i: [7] (a) plasma polymers, $E_i < 30\,\mathrm{eV}$ ([H] = 35 at.%, and $n = 1.6$); (b) soft ('polymer-like') DLC, $E_i = 30$–$60\,\mathrm{eV}$ ([H] = 30 at.%, and $n = 1.6$–1.8); and hard DLC, $60\,\mathrm{eV} < E_i < 1\,\mathrm{keV}$ ([H] = 20 at.%, $n = 1.8$–2.2, and $E_g = 1.3$–$2.0\,\mathrm{eV}$).

Diamond-like carbon films obtained by PECVD from hydrocarbon gases or vapors have been studied for their possible use in functional coatings. They are particularly attractive in combination with their advantageous mechanical and tribological characteristics, such as high hardness ($H = 15$–$40\,\mathrm{GPa}$, see Figure 9.12), low friction coefficient ($\mu = 0.05$–0.15), high scratch resistance and biocompatibility. These properties strongly depend on the microstructure (sp^2/sp^3 hybridization ratio) and the hydrogen content [H] (for reviews, see e.g. [120–122]).

The presence of hydrogen contributes to the formation of C–H σ bonds at the expense of π bonds (sp^2 hybridization). The latter affect the density of states and E_g values [120]. Using ERD and IR analyses of DLC films deposited under controlled E_i and Φ_i values in RF and MW/RF discharges, it has been concluded that a significant amount of hydrogen is not chemically bonded, but is trapped inside the material [123]. In addition to its effect on H and thermal stability, the amount of unbonded hydrogen has also been related to density and stress. As illustrated in Figure 9.17, σ in DLC films obtained from CH_4/Ar mixtures is systematically higher for the RF mode of operation (high E_i, low Φ_i, low n_e and hence less gas-phase dissociation), compared to the MW/RF mode (low E_i, high Φ_i, high n_e). Recently, these experimental observations have been supported by molecular dynamics simulations which

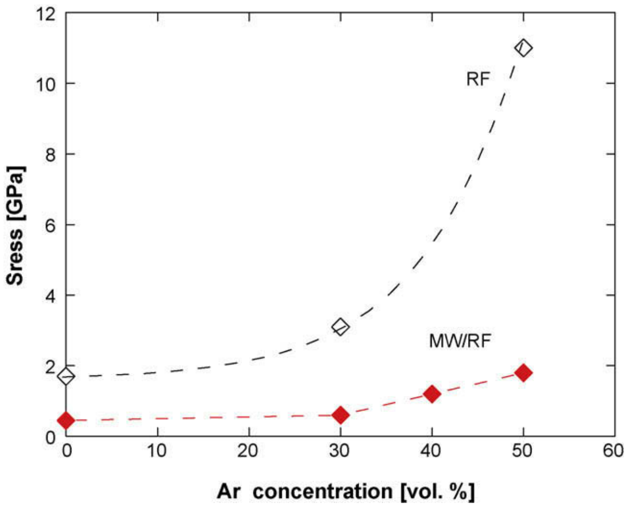

Figure 9.17: Effect of argon concentration in CH_4 on the evolution of compressive stress in hard DLC (*a*-C:H films) obtained in RF ($V_B = -500$ V) and in MW/RF ($V_B = -200$ V) plasmas. (After [123].)

predict that up to several tens of % of molecular hydrogen can be trapped in the internal volume of a DLC film [124].

The microstructure can also be influenced by doping *a*-C layers with nitrogen [125]. This can lead to higher optical absorption, higher electrical conductivity (N acting as a dopant near the edge of the density-of-states in the sp^3 matrix), and a higher Young's modulus (N acting to promote three-dimensional (3D) curvature and attachment in the sp^2 clusters). The addition of fluorine has been studied in an attempt to obtain higher transparency [126]. Incorporation of Si reduces stress and increases thermal and corrosion stability [127].

Polycrystalline diamond films have high refractive index ($n = 2.35$) and transparency over a large wavelength range (0.2–20 μm), and have attracted much attention owing to their extreme hardness ($H = 90$–100 GPa, see Figure 9.12), heat conductivity, and chemical inertness. Their unique properties have stimulated considerable interest for numerous applications, ranging from infrared optics to electronics, biomedical engineering, manufacturing, and numerous other sectors (for reviews, see [119, 128, 129]).

Diamond films are typically prepared from highly diluted mixtures of hydrocarbons (such as CH_4) in hydrogen (< 1% CH_4) in dense MW plasma, complementary to the thermal CVD technique. In plasma, atomic hydrogen acts as an etchant for the sp^2 (graphitic) phase, leaving behind the desired sp^3 (diamond) phase, resulting in polycrystalline structure formed at high T_S, in excess of 600 °C. In certain applications (e.g. optics), the use of diamond may be limited by the presence of relatively large crystals (~ 1 μm in size) leading to light scattering. However, very smooth, NCD films [130] or laser-polished films [129] have been reported.

Cubic boron nitride (c-BN) is the second hardest (70 GPa) material, and it possesses the second highest thermal conductivity (13 W cm^{-1} K^{-1}) compared to diamond (100 GPa, 20 W cm^{-1} K^{-1}). In fact, c-BN is superior to diamond in several respects: this includes high oxidation (1200 °C) and graphitization (1500 °C) temperatures (compared to 600 and 1400 °C for diamond), and it is a very promising wide bandgap semiconductor since it can be both n- and p-type doped. This material has attracted considerable interest stimulated by the development of coated cutting tools, and of thermal, optical, high-temperature, and high-frequency electronic devices (for review, see [131]).

Owing to the lack of an effective chemical reactant similar to hydrogen in CVD deposition of diamond films (selective etching of non-diamond phases and stabilization of the sp^3 hybridization [120, 230, 131]), it is necessary to apply a high negative bias voltage during c-BN growth in the PECVD reactor. c-BN film deposition using a mixture of different gases such as B_2H_6, BH_3NH_3, BF_3 and trimethyl borazol mixed with H_2, N_2, or NH_3 has been performed using DC jet, RF, ICP or ECR reactors [131]. Recently, films possessing very high hardness (70 GPa) have been obtained [132]. This value has even been significantly increased ($H = 82$ GPa) when fabricating c-BN/NCD mulilayer systems [133].

Research on o*rganic PECVD films (plasma polymers)*, especially on plasma polymerized fluorocarbons (PPFC), has been stimulated by the prospect of obtaining low n and low ε values similar to those of bulk polytetrafluoroethylene (PTFE, e.g. Dupont Teflon, with $n = 1.35$) or, more recently, for amorphous fluorocarbons, such as Dupont Teflon AF2400 ($n = 1.29$) or Teflon AF1600 ($n = 1.31$) [4, 134–136]. There is an abundant literature on the use of fluorocarbon plasmas for film deposition, and for anisotropic etching of silicon and silicon dioxide [12, 137]. By suitably adjusting the experimental parameters, one can shift the plasma conditions from etching to deposition modes [138]. Various precursors have been explored for deposition. These include C_2F_4, C_2F_6, C_4F_8, C_3F_6, $C_2H_2F_4$, CH_2F_4 and others [4, 134, 139]. The frequently observed low n is generally attributed to a high concentration of CF_2 groups in the films. Plasma-deposited layers usually contain a significant concentration of dangling bonds (estimated at 10^{18}–10^{20} spin/cm^3) [140], which can react with atmospheric oxygen or water vapor leading to the formation of C=O groups [140, 141] and to aging effects [142]. The use of pulsed PECVD has been shown to produce PPFC with lower concentrations of dangling bonds [139]. In general, PPFC films are very hydrophobic and not easily compatible with other layers in multilayer systems, owing to adhesion problems. They are, however, good candidates for water-repellent and smudge-resistant top coats [143].

Other plasma polymer materials include plasma polymerized organosilicones (PPOS), plasma polymerized hydrocarbons (PPHC), and hybrid (mixed organic–inorganic) coatings. In addition to their interesting tribological and optical properties, they are frequently considered for biomedical applications, because of their excellent biocompatibility. The reader is referred to numerous exhaustive reviews on the subject [4, 134].

9.5.4 Metal-Based Compound and Nanocomposite Films

Fabrication of metal oxide, nitride, and carbide films has been inspired by the prospect of obtaining high n, high hardness, advantageous tribological properties, and numerous other functional characteristics. The films are generally prepared from halocarbons or from metal-organic compounds which exhibit specific requirements on handling low vapor pressure sources and/or corrosive products [76]. In this section, we first focus on metal oxide layers, particularly on their optical and mechanical characteristics. In the second part, we describe metal nitrides and carbides, and review the microstructural features and the unique properties of superhard nanocomposite films.

9.5.4.1 Metal Oxides and Optically Passive and Active Films

Titanium dioxide (TiO_2) attracts much attention because of its large bandgap, high n (exceeding 2.4 at 550 nm), and photocatalytic properties. Its high n is due to high ionic character of the TiO_6 octahedral structure, the building block of rutile and of anatase.

The deposition of oxides of transition metals such as Ti (including Ta, Nb and others) is complicated by the fact that they can take different forms and stoichiometries (e.g. TiO or Ti_2O_3) [144]. In addition, in the case of TiO_2, three stable crystalline phases are possible: rutile, anatase, and brookite. Rutile, with the highest density, is the most desired phase in terms of transparency and index, but also has the highest birefringence, with $n_{\mathrm{ord}} = 2.9$ and $n_{ext} = 2.6$, and is often unwelcome because of light scattering. Anatase, which differs from rutile in the coordination number of its TiO_6 octahedra (10 in the case of rutile, 8 for anatase), is less birefringent, and has $n = 2.5$. Brookite, an unstable rhombohedral structure, is rarely observed in thin films.

The most frequently used precursors for plasma deposition of Ti-compounds are $TiCl_4$, tetraisopropyltitanate (TIPT), tetra ethoxy titanium (TEOT), $Ti(O–i–C_3H_7)_4$, and $Ti[OCH(CH_3)_2]_4$ (mixed with O_2 or N_2) (for review, see [7]). The use of metal-organic precursors has been stimulated by two considerations: (1) $TiCl_4$ is hazardous, highly corrosive, and requires special installations; and (2) Cl can be a major contaminant in TiO_2 and decreases long-term stability, increasing its absorption coefficient.

Both rutile and anatase are tetragonal and often coexist in films. High temperatures and ion bombardment energy may be needed during growth to control the rutile/anatase concentration ratio. At temperatures below 200 °C, anatase is frequently observed. Using a $TiCl_4/He/O_2$ mixture in an ECR/RF PECVD system [145], it was found that rutile is formed above 600 °C, and that it is the only phase observed above 900 °C. For higher E_{i}, lower r_{D} has been observed, resulting from RIE due to Cl, and competing with film densification. However, anatase is favored at high V_{B} values.

For most applications, crystallization of the films and the size of crystallites must be carefully controlled (e.g. to avoid light scattering). T_S is often kept below 200 °C to prevent crystal formation. The crystallization and phase change temperatures can vary with film thickness and impurities, and crystallization can also be suppressed by mixing TiO_2 with other materials such as SiO_2 [146]. RT-deposited films generally possess a low concentration of Cl (~ 6 at.%), which further decreases with increasing T_S and V_B, accompanied by an increase of n. The films often exhibit excess oxygen ($O/Ti > 2$), related to hydroxyl groups and to film density, an effect also found for sputtered TiO_2 layers.

Tantalum oxide and *niobium oxide* have been deposited by PECVD using a mixture of metal iso-propoxide (($Ta(OC_2H_5)_5$ or $Nb(OC_2H_5)_5$)) and O_2 with Ar and an RF plasma under intense ion bombardment. They exhibit good optical quality, suitable for various applications including interference filters and protective layers. Their n values were found to be between 2.12 and 2.16, and 2.26, for Ta_2O_5 and Nb_2O, respectively, and the H values between 8 and 10 GPa for both materials [147], comparable with those of the PVD coatings (see Figure 9.12).

Despite the use of O_2-rich deposition atmosphere, both Ta and Nb oxides exhibited about 6 at.% of carbon, uniformly distributed throughout the thickness. However, detailed optical measurements did not reveal any negative effect of the presence of C on the optical performance such as absorption. Both materials showed high temperature stability, with the onset of crystallization observed at 550 °C and 650 °C, respectively [148], making them very attractive high-index alternatives for optical, photonics, and other applications.

Studies of optically active PECVD materials have been stimulated by interesting linear and non-linear optical properties, and by their electrical and protective characteristics. These include:

- Transparent conductors such as *tin–oxide* (SnO_2) [149] and *indium–tin–oxide* [150], the latter obtained from indium nitrate pentahydrate and tin–chloride pentahydrate in water, using an ultrasonic nebulizer in combination with an RF ‘mist’ Ar/O_2 plasma.
- *Yttria-stabilized zirconia* (YSZ), *barium titanate* ($BaTiO_3$), and *strontium titanate* ($SrTiO_3$) were fabricated from metal β-diketonates [151]. The latter two were obtained by combining melted dipivaloylmethanato barium ($Ba(dpm)_2$) and strontium ($Sr(dpm)_2$) compounds with TIPT in an O_2 plasma. The n values of $BaTiO_3$ and $SrTiO_3$ were both found to be 2.19. The permittivity was estimated from capacitance–voltage curves to be 1×10^3 for $BaTiO_3$, and 1×10^2 for $SrTiO_3$, primarily due to a high ionic polarizability.
- *Aluminum oxide* (Al_2O_3) is most often prepared from $AlBr_3$, $AlCl_3$, trimethyl-aluminum (TMA), or trimethyl-amine alane (TMAA) precursors mixed with O_2 or N_2O [7, 76, 152, 153]. *Er^{3+}-doped Al_2O_3*, using

tris(2,2,6,6-tetramethyl-3,5-heptanedionato)erbium ($Er(thd)_3$) as the erbium precursor, has also been fabricated by PECVD [154].

- *Tungsten oxide* (WO_3) films obtained in RF plasma from WF_6 mixed with H_2 and O_2 [155, 156] were studied for their potential use in electrochromic devices including smart windows and sensors [157]. Growth rates (up to 10 nm/s) were maximized when the atomic F density was suppressed and the atomic O density enhanced. Optimal film density was obtained for medium E_i values $\sim$ (50–100 eV). The value of n was shown to be a sensitive indicator of the electrochromic performance. The absorption coefficients were similar for both Li^+ and H^+ ions, scaling with the degree of intercalation in the opaque state [158].
- Work on *nanocomposite (nc) optical materials*, formed by nanometer size (1–100 nm, mostly metal) particles embedded in dielectric matrices, has been stimulated by new film properties, such as optical selectivity (absorption filters; colored, decorative coatings; photothermal energy conversion) and optical non-linearity, phenomena linked with the surface plasmon resonance [159]. Depending on the choice of materials and particle concentration, size, and shape, different colors can be obtained. The presence of nanoparticles leads to a substantial local field enhancement [160], giving rise to third order susceptibility, $\chi^{(3)}$, up to 10^{-6} esu [161, 162].
  The nc structures are usually fabricated by hybrid processes, combining PECVD of organic (PPFC, PPHC) or inorganic (SiO_2, Al_2O_3, $SiN_{1.3}$, TiO_2) matrices with simultaneous sputtering or evaporation of metals, such as Au, Ag, Cu, and others (for more details, see [37–39]).

The effect of microstructure on the properties of such nc materials has been modeled using EMA to interpret experimental data obtained by SE and spectrophotometry. Using the generalized Maxwell–Garnett model, considering the permittivities of the host and particle materials, the depolarization factor and the interband and intraband electron transitions, particle concentration, size, and shape can be obtained from non-invasive optical measurements [38]. This particularly also applies to the study of Au/SiO_2 nc films exposed to heavy ion bombardment (tens of MeV) [39]. Energetic ion ‘hammering’ introduces locally significant internal stress, converting initially spherical particles into nanorods with high aspect ratio. Polarization-dependent non-linear optical absorption has recently been detected and modeled using a modified EMA approach [163].

9.5.4.2 Metal Nitrides, Carbides, and Nanocomposite Superhard Coatings

Metal nitrides and carbides (MeN, MeC) are widely used as protective coatings, owing to excellent mechanical properties [164–166] such as high hardness, adhesion, and corrosion resistance, which makes them attractive for tribological applications. In addition, such materials provide interesting colors [167] related to the bonding structure [168].

MeN and MeC are obtained by PECVD, when organometallic or chelate precursors are decomposed in mixtures containing N_2 or CH_4, Ar and H_2. The film microstructure can be selectively controlled by adjusting chemical reactions in the gas phase and at the growing surface, and by appropriate choice of E_i, Φ_i and Φ_n values, which affect the development of crystals, their size, shape, and orientation [164–166, 169–172]. One of the frequent concerns in this activity is handling hazardous and corrosive precursors, including metal chlorides.

Nanocomposite superhard coatings formed by nanometer size particles (usually MeN, MeC) embedded in amorphous or crystalline matrices are of considerable interest. These 3D architectures, also called 'third generation ceramic coatings', represent a new class of materials that exhibit exceptional mechanical, electronic, magnetic, and optical properties due to microstructural features which are reduced to approximately 5–10 nm [164–166, 168–173].

Such hard nc-MeN/hard matrix (usually amorphous such as $SiN_{1.3}$) materials have been fabricated by PECVD [164, 167, 169, 171, 172], complementary to the nc-MeN/soft matrix (usually metal, Me = Ti, Cr, W, V, Zr) films prepared by PVD [166]. Formation of nc structures is based on the thermodynamically driven segregation in binary, ternary, or quaternary systems, which leads to spontaneous self-organization of a stable nanoscale structure [164]. The microstructure of nc gives rise to high H with relatively low E providing high toughness, enhanced wear resistance, high elastic recovery, resistance against crack formation and crack propagation, high thermal stability (up to 1100 °C), and reduced thermal conductivity. These properties are explained by the difficulty of creating dislocations in grains of tens of nanometers in size, and by the reduction of intergranular sliding due to the thinness of the grain boundary region. In general, such properties are controlled by crystal size, orientation, and shape, and by grain boundary thickness, and they depend on the selection of materials, process parameters such as E_i and Φ_i, and deposition methods [166, 169–172].

Of all nc superhard ($H > 40$ GPa) films, TiN-based coatings with $SiN_{1.3}$ matrix have been the most frequently investigated. As an example, the effect of silicon concentration [Si] on H and E for nc-TiN/$SiN_{1.3}$ films, fabricated at $T_s = 500\,^{\circ}C$ is shown in Figure 9.18(a). Both clearly exhibit a maximum at an optimum [Si] situated between 5 and 10 at.% that corresponds to an amount of $SiN_{1.3}$ that forms a matrix which surrounds the TiN particles (5–10 nm in diameter). It has been proposed that the boundary between grains is about one monolayer thick [164, 169, 170, 173, 174].

In order to obtain insight into the microstructural characteristics on the nanoscale, and to determine complementary functional properties, electrical resistivity, ρ_E, of such nc films has been studied by in situ RTSE and ex situ four-point measurements [70, 167]. As an example, the effect of [Si] on ρ_E is presented in Figure 9.18(b). The metallic character of pure TiN and of the nc-TiN/$SiN_{1.3}$ was confirmed by low values of ρ_E until about [Si] ~ 40 at.%, above which the loss of metallic character was marked by the onset of a rapid increase in ρ_E due to

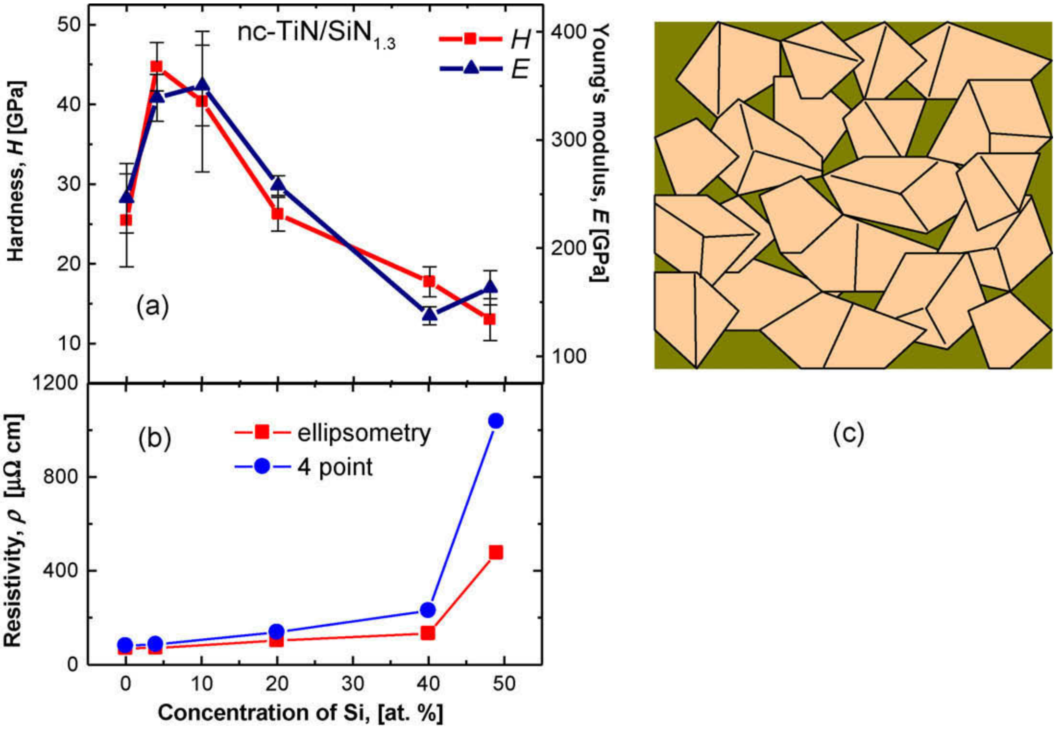

Figure 9.18: Characteristics of nanocomposite nc-TiN/SiN$_{1.3}$ films: (a) effect of Si concentration on the microhardness, *H*, and Young's modulus, *E* [171]; (b) effect of Si concentration on the resistivity measured by spectroscopic ellipsometry and by the four-point method [167]; (c) microstructural model of a superhard nanocomposite coating corresponding to the highest hardness [70].

percolation. Since ρ_E remains low at [Si] corresponding to the highest H value, the TiN particles appear to still be interconnected, as illustrated in the structural model schematically shown in Figure 9.18(c).

This model incorporates the main structural characteristics of the nc films, namely the presence of nanoparticles, the introduction of interface layers, and the possible presence of defects, indicated by charge carrier mean free path much smaller than the particle size [70]. The model suggests that the amorphous matrix fills the space between individual nanoparticles rather than forming a uniform layer around them. Consistent with the electrical properties [70, 167], it can explain the mechanical characteristics of nc films by the presence of inner interfaces, which hamper crack propagation.

Recently, molecular dynamics (MD) calculations have been used to support the experimental data regarding Ti(Si)N materials by fitting two-body empirical potentials using energies from

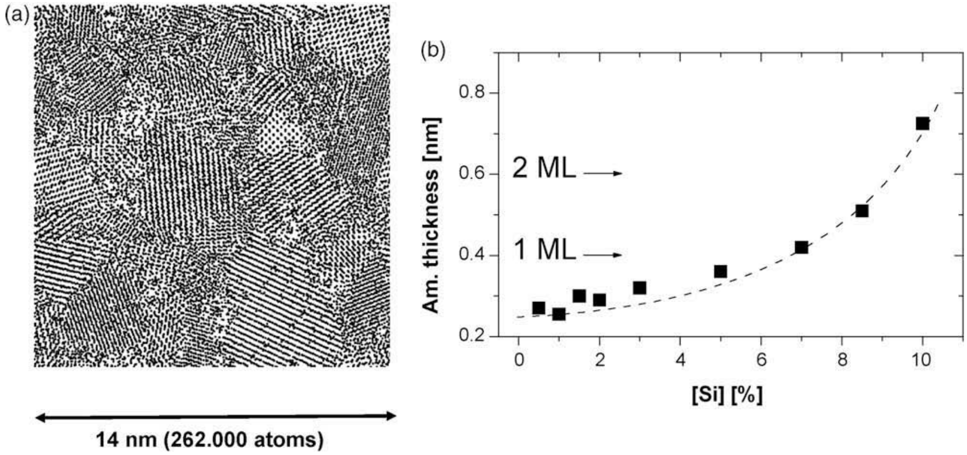

Figure 9.19: Molecular dynamics simulations of the characteristics of nanocomposite nc-TiN/SiN$_{1.3}$ films: (a) slice of the final structure corresponding to [Si] = 7 at.%; (b) thickness of the amorphous SiN$_{1.3}$ phase between the TiN particles. (After [174].)

ab initio calculations [174]. Thermodynamically preferred structures of various compositions were found by slow cooling from a melt: for TiN, it was confirmed that the preferred structure is a cubic (fcc) monocrystal, while for TiSiN, the heterogeneous structure consists of small (< 10 nm) crystals of TiN in a Si-rich amorphous matrix. In addition, the MD simulations predict other structural characteristics of this nc material: (1) a solubility limit of Si in TiN (close to 2%), above which the material becomes heterogeneous; (2) a distribution of sizes of TiN nanocrystals for various compositions (e.g. up to 6000 atoms corresponding to ≈5–9 nm particle size for [Si] = 7%) as illustrated in Figure 9.19(a); (3) the quality of the nanocrystals in terms of defects or angles between the crystalline planes; (4) the thickness of the amorphous phase between the nanocrystals – about 1–2 monolayers at [Si] = 7% (Figure 9.19b); and (5) a probability that the individual nanoparticles touch each other.

9.5.5 Interface Engineering

Interfaces in coating technology are of particular importance for several reasons: (1) to ensure compatibility and adhesion between the coating and the substrate and between the individual coatings; (2) to ensure the thickness (or abruptness) of the interfacial region, or to consider possible compositional and structural gradients inherent to the fabrication process; and (3) to control the characteristics of the interfacial region, ‘interphase’, in order to enhance the performance of the thin film system. In the following, we provide examples of several coating/substrate combinations for which the understanding of the role of plasma surface interactions is crucial.

9.5.5.1 Coatings on Inorganic Substrates

The role of ion bombardment and the possibility of predicting its effect in multilayer systems and related film architectures have recently been studied by RTSE combined with dynamic TRIDYN Monte Carlo simulations [68, 69] (see Section 9.4). It has been shown that ion- and plasma-assisted deposition processes in the range of tens to a few hundreds of electron volts lead to thin film growth dominated by subsurface deposition, as a result of subplantation (shallow implantation). Subplantation is shown to be responsible for significant subsurface modifications and interface broadening during the initial stages of film deposition, as a result of ion mixing.

Control of the thickness of the interfacial layer is very important for ensuring appropriate performance of interference filters and electronic devices, as well as tribological coatings; in specific cases the interphase can be comparable with the film thickness and it must be included in the coating system design.

For the particular case of TiO_2 grown on SiO_2 by PECVD (e.g. in the context of optical interference filters, using high and low values of n) in an O_2-rich plasma, at the RF-biased electrode, the experimentally determined IEDF has been modeled as shown in Figure 9.9. Given by the range of E_i, the formation of 2–4 nm-thick interfacial layers was predicted. The value predicted depended on the Φ_i/Φ_n ratio, which was controlled by varying r_D (Figure 9.20). Such behavior has been found in excellent agreement with RTSE, and has been directly confirmed by HRTEM for PECVD, and for PVD layers [68, 69].

Controlled modification of the interphase has been the subject of extensive work in the field of hard protective coatings on metal substrates and it is known as a duplex process [175]. Here, the metal piece to be coated (e.g. steel) is first exposed to a nitriding or carburizing plasma in order to sputter-clean the surface, and to harden the near-surface region by implementing a hardness gradient up to several μm in thickness due to the diffusion of nitrogen or carbon [176, 177]. In addition, specific interface engineering steps may include formation of a diffusion barrier at the interface, for example, to hamper diffusion of cobalt from a WC-Co substrate, when pc-D is deposited at elevated temperatures [178]. This would otherwise lead to the formation of a weak CoC interlayer. In contrast, routine plasma surface nitriding of steel can also have a negative effect on the corrosion resistance: when stainless steel is exposed to N_2-rich plasma, N preferentially reacts with chromium, leaving behind iron which becomes more prone to subsequent corrosion [179].

9.5.5.2 Coatings on Plastics

The role and control of interfaces between plastic substrates and inorganic coatings is of particular importance for the performance of the final devices. Energetic interactions of plasma with the exposed polymer surface lead to substantial modification of the physical and chemical

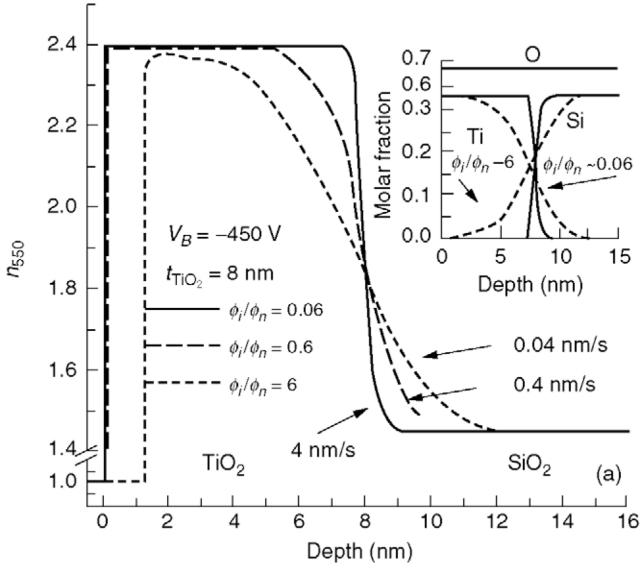

Figure 9.20: Ion bombardment effects in PECVD on the TiO_2/SiO_2 interface considering an IEDF according to Figure 9.9. The curves correspond to different ion/neutral flux ratios and their effect on the width of the TiO_2/SiO_2 interface represented by the "abruptness" of the refractive index at 550 nm. (After [68].)

properties of the surface and the near-surface region, and they affect the initial stage of the film growth.

Surface modification of polymers is particularly important to improve adhesion. In comparison with other methods of modifying polymer surfaces [14], including wet-chemical or mechanical treatments, exposure to flames, UV radiation, corona discharges, ion beams, and intermediate adhesive layers, low-pressure plasma modification appears very powerful, since it can address all of the adhesion mechanisms [11, 13, 180]. In this context, there are four major effects of plasma on polymer surfaces: (1) surface cleaning; (2) ablation (or etching); (3) cross-linking, and (4) surface chemical functionalization. All of them are always present to a certain degree, but one may dominate, depending on the polymer, gas, and operating conditions.

Adhesion enhancement by plasma pretreatment is illustrated in Figure 9.21(a), where PECVD $SiN_{1.3}$ was applied as a first layer in multilayer antireflective (AR) coatings or as a gas permeation barrier on polycarbonate (PC) and polyethylene terephthalate (PET) [143, 181, 182]. After pretreatment of PC in MW plasma, the highest adhesion was found when using N_2 (highest critical load, L_C, in the scratch test). Based on complementary surface analyses, adhesion improvement has been related to the formation of new N- and O-containing groups, which react with Si to form Si–N–C and Si–O–C bonds at the interface [181]. In addition,

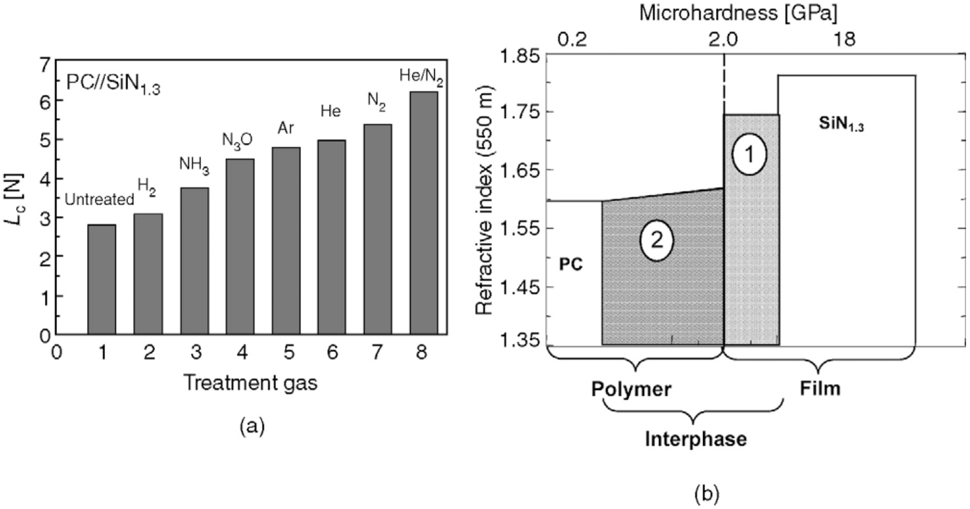

Figure 9.21: Effect of plasma treatment of polymer surface (example of polycarbonate) on the characteristics of the polymer/coating interface: (a) effect of different gases on the adhesion of $SiN_{1.3}$ films (critical load, L_c, film thickness 0.5 μm); (b) structured interfacial region (interphase) represented by the refractive index depth profile. (After [143].)

adhesion was further improved by exposing PC to He plasma, confirming a favorable effect of the VUV radiation.

Owing to the phenomena involving energetic photons, ions, and reactive species (see Section 9.4), the interphase is structured (Figure 9.21b). Similar depth profiles have been observed for other combinations of materials, including SiO_2, PET, polymethyl methacrylate (PMMA), and other polymers [183]. Using both non-invasive optical (in situ and ex situ SE, photometry, IR spectroscopy) and invasive methods, the interphase has been found to be several tens of nanometers thick [181–185]. It consists of a cross-linked layer (region 2 in Figure 9.21b), followed by a transition layer (region 1) formed by intermixing the growing film with the substrate materials [185] and possibly by voids [186]. In the case of $SiN_{1.3}$ considered in the context of optical or barrier applications, n increases from 1.59 for PC to 1.80, while H increases by two orders of magnitude from 0.2 GPa for bulk PC to ~2 GPa for the cross-linked surface layer, and up to 18 GPa for $SiN_{1.3}$ [143, 187]. This inhomogeneity generally leads to better adhesion, tribological properties, flexibility, stretchability, and other functional characteristics suitable for coated plastics.

Formation of the interphase has also been observed for situations when no specific plasma pretreatment has been performed. Indeed, the energetic conditions are still present when the film starts growing (nucleation), while the plasma is always a rich source of energetic photons, particularly owing to the presence of hydrogen originating from the precursor, from the

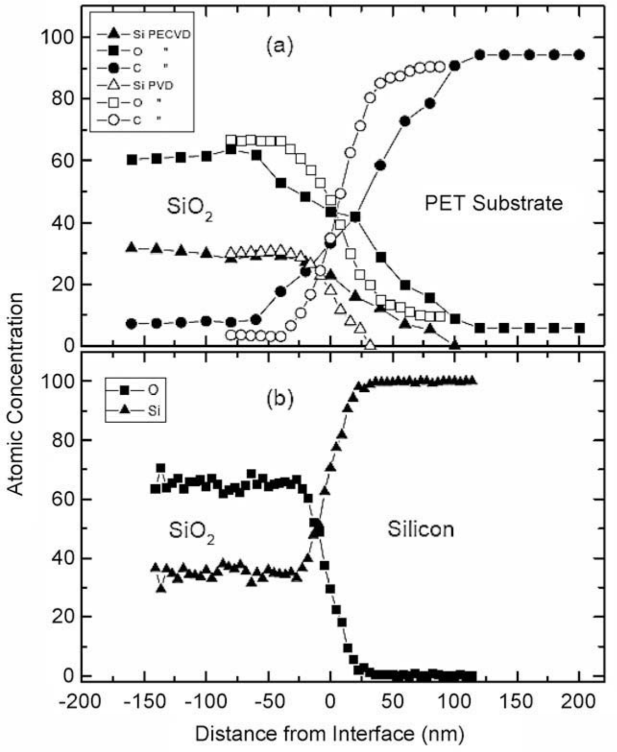

Figure 9.22: Comparison of compositional depth profiles of the SiO_2/substrate interfacial region obtained by ERD: (a) PECVD (320 nm, full symbols) and PVD (120 nm, open symbols) SiO_2 layers on PET; (b) thermal CVD (200 nm) SiO_2 on c-Si. (After [185].)

polymer material itself, or from residual water vapor. This situation is quite different from PVD processes in which hydrogen concentrations in the gas phase and energetic VUV radiation are less intense. In fact, no interphase (below detection) has been observed for inorganic films, such as SiO_2 on PET, fabricated by PVD compared to the PECVD layer [185] (Figure 9.22). This may explain the generally observed better mechanical performance of PECVD coatings on plastics, compared to their PVD counterparts.

9.6 Functional Characteristics and Applications of PECVD Coatings

In the previous sections, we have introduced basic phenomena governing the plasma processing of materials, the evolution of their microstructure and a number of concepts of structure–property relationships. Given the recent progress in this field, numerous attractive applications of PECVD have been proposed and investigated, based on the functional characteristics of the coating, which are related to basic properties. Examples are given in

Figure 9.12 and Table 9.1. Many of the applications have already left the laboratory and pilot scales and entered large-scale production.

Given the large number of applications, both under investigation and exploited commercially, we do not attempt to list them all. Rather, we focus on selected examples of specific functional properties of films illustrating advances in this field, while demonstrating the importance of plasma–surface interactions in their preparation. In particular, we describe two broad areas: optical and related coatings (Section 9.6.1), and protective tribological coatings (Section 9.6.2). The reader is referred to numerous publications covering other areas in which plasma processing has advanced significantly. These include electronics [1, 188], biomedical engineering [189, 190], and surface treatment of plastics [4, 11, 14].

9.6.1 Optical and Related Functional Coating Systems

The microstructure and composition of optical films depend on the choice of source precursor and of other gases, and on surface reactions during film fabrication, including the energetic conditions in film growth. These govern their optical, mechanical, and other functional characteristics which need to be taken into account when the films are applied to the fabrication of optical coating systems. In most cases, optical thin films are amorphous, since they are deposited at low substrate temperatures, typically below 250 °C. However, they can crystallize at higher temperatures or under energetic ion bombardment conditions [65, 66].

The principal characteristics of optical coatings, namely the refractive index and hardness of the most frequently studied PECVD materials, are summarized in Figure 9.12, where they are compared with those of the widely used PVD films. The values presented refer to published data, and clearly demonstrate film quality suitable for optical system fabrication. For comparison, we also include data pertaining to the most common substrate materials: silicon, fused silica, and float glass, as well as PC, PMMA, and PET, which are increasingly used in the optics industry, since they benefit from low optical absorption ($k < 10^{-4}$ at $\lambda = 550\,\text{nm}$) and enhanced mechanical characteristics (e.g. low weight and high impact resistance) [143].

Several deposition techniques aim at optimizing the energetics of the film growth, including ion bombardment effects, to obtain dense optical thin films. However, recent trends focus also on new opportunities for porous materials with well-defined porosity and pore sizes [191, 192]. These advances have been stimulated, especially, by the possibility of fabricating materials with very low n, low ε, and different levels of doping leading to birefringence, controlled pore-filling for specific optical and sensor applications, optical activity, etc. Optical design can also be simplified by taking advantage of a large difference between high and low refractive indices, $n_\mathrm{H} - n_\mathrm{L}$, possible in such structures.

Control of the film deposition process and microstructure, and adjustment of the films' passive and active optical properties, opens interesting opportunities for applications in optics, photonics, photovoltaics, energy saving, sensors, and other related areas (see Table 9.2). In the following section, we describe examples of film performance and of industrial applications in which PECVD has been explored for the fabrication of optical interference filters (OIFs, both discrete and graded), optical waveguides, and energy transformation (solar cells, displays, and smart windows).

9.6.1.1 Optical Interference Filters

PECVD can provide n_H, n_L, and n_M materials for any simple or complex optical coating system. The design strategies can be based on three types of approach: (1) multilayer (step index) design, using two or more materials with different indices; (2) inhomogeneous (graded index depth profile, $n(z)$) design; and (3) quasi-inhomogeneous design, when very thin layers with varied composition are consecutively applied, giving properties close to that of an inhomogeneous design. Traditionally, approach (1) is most frequently used both in industry and in the laboratory, but PECVD offers new possibilities, particularly in design strategy (2), which can also provide the added value of enhanced mechanical and tribological performance. In the following, we document this situation by selected examples.

Ophthalmic lenses and light assemblies (e.g. indoor reflectors, car light bezels) are probably the most well-known applications of optical coatings, specifically in situations in which plastic substrates are used, and for which PECVD has also been extensively explored. This application has a long history, but remains very active, owing to numerous challenges. These are related not only to the optical properties, but particularly, to the mechanical and tribological performance, which includes adhesion (affected by a two orders of magnitude difference between the coefficients of thermal expansion of the inorganic coatings and the plastic), scratch and wear resistance, and other functionalities [143 and references therein]. It is estimated that in the USA alone, 160 million people wear glasses, 80 million pairs of glasses are purchased every year, and more than 90% of the lenses are plastic. Low index PMMA ($n = 1.49$) has been considered for such applications since the 1930s, but it was dialyl diglycol dicarbonate, known as CR39 (trademark of the PPG company) that became popular after World War II, while high-index PC ($n = 1.59$) has increased in importance since the 1980s, owing to its toughness, impact resistance, and thermal stability [193].

Plastics are soft, requiring hard coats to protect them. This is most frequently achieved by dipping, spinning or spraying 3–5 μm thick silica-type materials. The original, brittle, films have been replaced either by thermally cured polysiloxanes, which contain organosilane modifiers, leading to less brittleness due to the cross-linking of the organic component, or by UV-cured urethane/acrylate hard coats, which provide better adhesion but lower hardness [193]. Promising hard coats have also been fabricated by PECVD, using organosilicone precursors [194, 195]. In this case, control of film growth allows one to enhance adhesion to the soft substrate by adjusting the gradient from organic to inorganic character by, for example, changing the oxygen content [195]. In addition, optical interference between the substrate and the hard coat can be reduced by depositing an optical matching layer ($n_{PC} = 1.59 > 1.52 > 1.46 = n_{SiO_2}$). Evaluation of mechanical properties of hard coat materials, using the scratch test method, pointed out the importance of controlling the interface properties [87, 196].

In many cases ophthalmic lenses are provided with AR coatings whose major role is to reduce double (ghost) images and back-side reflections. In this context, AR coatings are the most frequently used OIF systems, typically consisting of three to five layers, for the visible region [197]. However, they have also made their way into applications in the NIR (optoelectronics and solar cells), particularly using SiN_x and *a*-C:H, or deep UV (for 248 and 193 nm lithography), in order to reduce interference effects (using TiO_2 and Si-rich SiN_x) (for review, see [7]). In the context of ophthalmic lenses, PECVD AR films have also been investigated [198, 199], as an alternative to the more commonly used ion-beam and plasma ion-assisted deposition techniques [143].

When AR coatings are deposited directly onto a polymeric substrate, special care needs to be taken in relation to adhesion [143, 181] and to the presence of an interphase, as described in Section 9.5. For example, in the case of a four-layer AR system on PC [200], an optimized 'W-shape' design between 450 and 650 nm, using $SiN_{1.3}$ and SiO_2 as n_H and n_L materials, brought the original single-side reflection of 5.0% down to about 0.8%. However, corrections had to be introduced into the design to account for the presence of the interphase adjacent to the first n_H layer (see Figure 9.21). Benefiting from the knowledge of the existence of such an interphase, a reoptimized design was then capable of further reducing the overall reflectance.

In many instances the lenses are provided with top coats which are highly repellent to water and dust. These may be either hydrophobic or hydrophilic, but must be very thin (5–10 nm), so as not to contribute an additional optical effect. Hydrophobic top coatings are frequently obtained from wet solutions (by dipping) or by evaporation, but PEVCD films of PPFC ($n = 1.38$) have also shown promising results [201]: surface water contact angles for PECVD and non-PECVD coatings appear comparable, but the former exhibit better long-term stability, possibly due to their higher cross-linking. Good smudge resistance has also been reported for organosilicones with well-controlled O_2 concentrations and discharge power levels [194].

PECVD is well suited to the fabrication of inhomogeneous (graded-index) OIFs such as broadband AR quintic layers or rugate filters. In such cases, the n value is continuously varied between n_H and n_L, mostly by changing the gas composition [107, 146, 202], although variation of film density (or porosity) by changing the bias potential is also possible [192]. In such an approach, at each instant of the deposition process, the $n(\lambda)$ dispersion and r_D value must be known. A material well suited for such coatings is SiON (Figure 9.13), but TiO_2/SiO_2 [146], porous/dense $SiN_{1.3}$ [192], and Si-rich SiN_x [203, 204] systems have also been tested with success; specific examples illustrating the level of materials and process control that has been achieved are described below (see Figures 9.23 and 9.24).

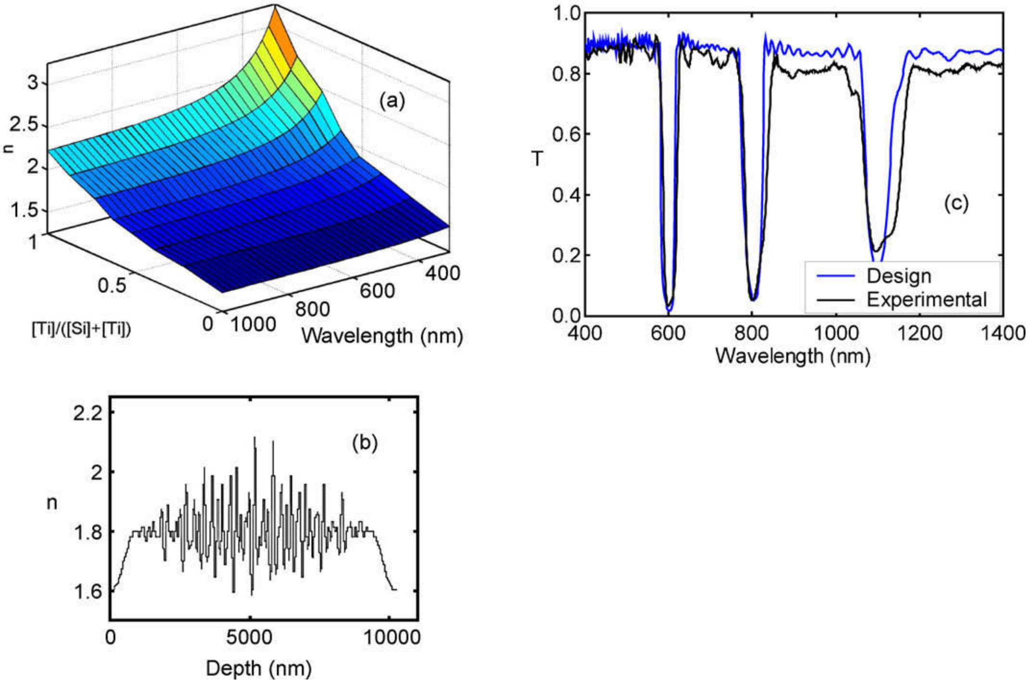

Figure 9.23: PECVD optical coatings based on TiO_2 and SiO_2: (a) refractive index dispersion curves for different TiO_2/SiO_2 compositional ratios; (b) refractive index depth profile for a sample three-band rugate filter; (c) measured and designed optical transmission of a three-band rugate filter with a refractive index depth profile from (b). (After [146, 205].)

Fabrication of a rugate filter starts with the establishment of $n(\lambda)$ dispersion curves corresponding to the materials of choice; an example is shown here for a mixture of TiO_2 and SiO_2 controlled by the flow-rate ratio of precursors, such as $TiCl_4$ and $SiCl_4$ (Figure 9.23a). Following the filter design (using a software specifically developed for graded coatings [206]) of a three-band inhomogeneous (rugate) filter as an example (Figure 9.23c), the desired $n(z)$ profile is rather complex owing to the existence of three peaks, continuous variation of n, apodization and incorporation of quintic layers at the filter–substrate and filter–air interfaces (Figure 9.23b) [205]. Such a filter, with a total thickness of about 10 μm, has been successfully reproduced, as documented by the comparison of the measured transmission spectrum with the design target (Figure 9.23c). Similar filters have also been fabricated using SiON, including on substrates such as glass and plastic [7].

In addition to their optical characteristics, such filters offer additional advantages due to their improved mechanical behavior, related to the absence of abrupt interfaces and to the uniform distribution of stress, particularly enhanced adhesion and scratch resistance [207, 208].

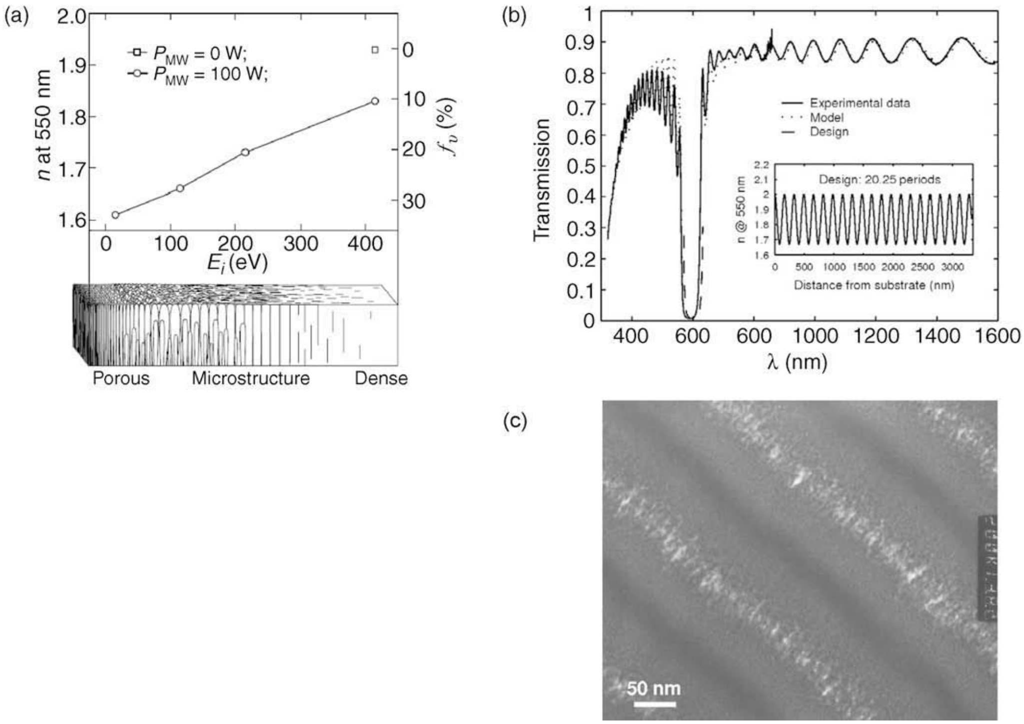

Figure 9.24: Single-material optical coatings based on the control of porosity in $SiN_{1.3}$ films: (a) variation of the refractive index and of the void volume fraction as a function of E_i in a MW/RF discharge; (b) optical transmission of a dense/porous graded (rugate) filter based on the continuous variation of *n* (see insert); (c) TEM micrograph of the filter in (b). (After [192, 209].)

The following example illustrates a possibility of tuning plasma–surface interactions in order to obtain a controlled $n(z)$ profile by changing the film microstructure (Figure 9.24). Controlling ion bombardment in the growth of $SiN_{1.3}$ films (by adjusting the surface bias or the duty cycle in a pulsed plasma as illustrated by the IEDF in Figure 9.7) allows one to vary n from 1.50 to 1.90, owing to the control of the film porosity (Figure 9.24a). This makes it possible to prepare (discrete) multilayer and inhomogeneous (rugate) filters (with a continuous sinusoidal variation of $n(z)$) using one single material. Such filters have been designed and fabricated, and examples of the corresponding $n(z)$ profile, optical transmission spectrum, and TEM micrograph are shown in Figure 9.24(b) and (c) [192, 209].

9.6.1.2 Optical Waveguides

Research on plasma-deposited optical waveguides for integrated optics began in the early 1970s, and has continued until now, with the aim of further improving their performance (low optical loss), increasing the deposition rate, and making them part of sophisticated integrated optical systems. In most cases the goal has been to fabricate waveguides on silicon substrates, where the cladding layer is a thermal- or a plasma-deposited film of silicon dioxide, followed by a patterned waveguiding core layer [7, 111, 210, 211]. Direct comparison of the reported optical loss values is rather difficult because of different measuring techniques and device concepts: for example, the difference, Δn, between n values of the core and the cladding layers determines the number of inner reflections in the waveguide and the depth of field penetration into the cladding. For smaller Δn, the effect of light scattering by surface (or interface) roughness becomes more important while, in turn, the cladding layer may be thinner, and the evanescent wave is not attenuated by the Si substrate.

In this context, SiON offers a good tradeoff between compactness, fiber match, fabrication complexity, and the possibility of combining optical and electronic components on one chip. As the most frequently used core-layer material, SiON is obtained from SiH_4 mixed with N_2O or O_2, but depositions using $SiH_4/N_2O/NH_3$ or $SiH_4/N_2O/N_2$ mixtures, or with $SiN_{1.3}$ from SiH_4/NH_3 have also been studied [212, 213]. Although n in SiON can vary between 1.45 and 1.90, a lower n range ($n < 1.7$) is more suitable owing to a smaller Δn (typically $\Delta n < 0.005$), and to a reduced dependence of n on the gas flow rate ratio. Non-uniformity and run-to-run reproducibility of such optical waveguides is 1–3%, associated with inhomogeneity and reproducibility of n of 0.7–1.7% [211].

Most of the waveguiding characteristics of Si-compound films have been evaluated in the visible region, where optical losses below 0.2 dB/cm in slab waveguides and between 0.1 and 1.5 dB/cm in channel waveguides have been reported [111, 211]. In the NIR region, however, H- and N-containing films absorb, owing to the presence of O–H (at 1400 nm) and Si–H, and therefore optical losses may increase considerably (< 10 dB/cm). The concentrations of these groups can be reduced by postannealing: the O–H absorption has been found to disappear at 800 °C, while the N–H and Si–H contributions vanished only at 1100 °C, both accompanied by a substantial drop of loss. When the waveguides are fabricated on low-loss buffer layers (such as thermal SiO_2), one can change the dimensions and index of the core SiON layer and avoid the problem of IR absorption, since the light propagates mostly in the cladding [214].

In addition to SiON, other waveguiding materials and chemistries have been employed. These include SiO_2:F or SiO_2:Ge (losses typically 0.1–1.5 dB/cm, 0.027 dB/cm at 1.55 μm), but also organosilicones, organometallics (Al_2O_3, ~ 20 dB/cm), and Er-doped epitaxial Si (for review, see [7]). PPFC ($n = 1.38$) core layers on Teflon AF cladding on Si have been considered, in view of the possibility of obtaining low optical loss in the NIR region, owing to the absence of O–H, Si–H, and N–H groups [215].

Plasma-deposited Si-compound waveguides were tested on chips of integrated optical devices, such as an interferometer pressure sensor [216], splitters [217], and in conjunction with light-emitting diodes, micromirrors, and photodetectors [218]. It should be mentioned that

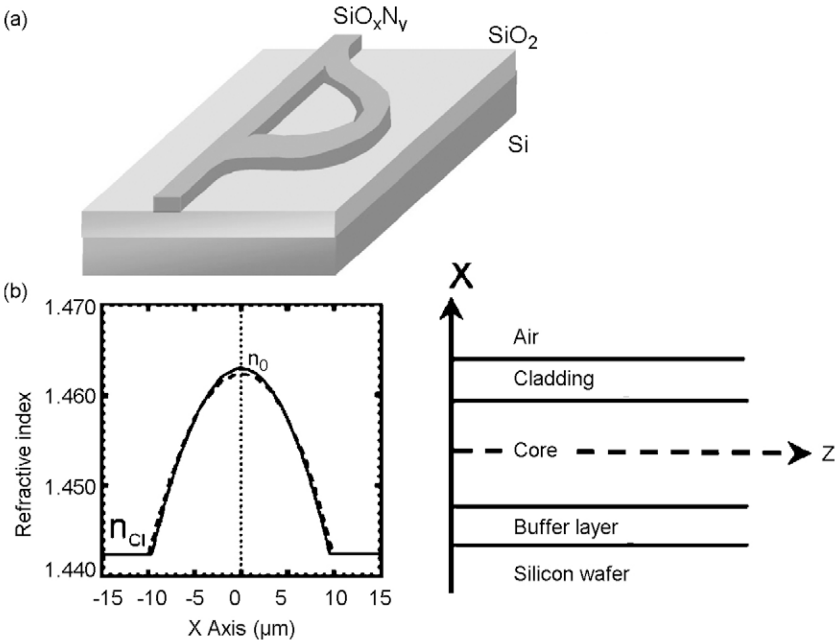

Figure 9.25: Examples of optical waveguide systems: (a) non-symmetric Mach-Zehnder interferometer sensor (after [219]); (b) structure of GRIN slab lens showing the refractive index profile and the layered structure (after [220]).

fabrication of such devices frequently combines several techniques, used in different steps; in addition to PECVD and RIE, these can include low-pressure CVD, sputtering, and implantation.

As an example, a non-symmetric Mach–Zehnder interferometer chemical sensor has been studied. In this configuration [219] the light propagating along the longer branch is affected more by the surrounding medium, whose refractive index is determined by its composition (e.g. gas or liquid solutions) than in the shorter counterpart (Figure 9.25a). This requires fewer fabrication steps than the symmetric interferometer sensor, which has to be equipped with a sensitizing window, but generally provides reduced sensitivity. Another interesting example, illustrating device fabrication, is the gradient-index (GRIN) planar slab lens on Si for use in a 1 × 7 coupler, or for coupling between a laser diode and a waveguide [220] (Figure 9.25b). In this case, inhomogeneously F-doped SiO_2 (using SiH_4, O_2, and CF_4; $n = 1.437–1.462$), with an approximately parabolic n profile, surrounded by a low-index buffer layer and cladding, was used, for a total thickness of about 24 μm. The layers were deposited at low temperature (< 250 °C), under ion bombardment (300 eV), resulting in a propagation loss of about 0.1 dB/cm. The advantage of PECVD in that case, compared to ion exchange, for example, is that only one fabrication step is required for fabrication of the entire GRIN lens.

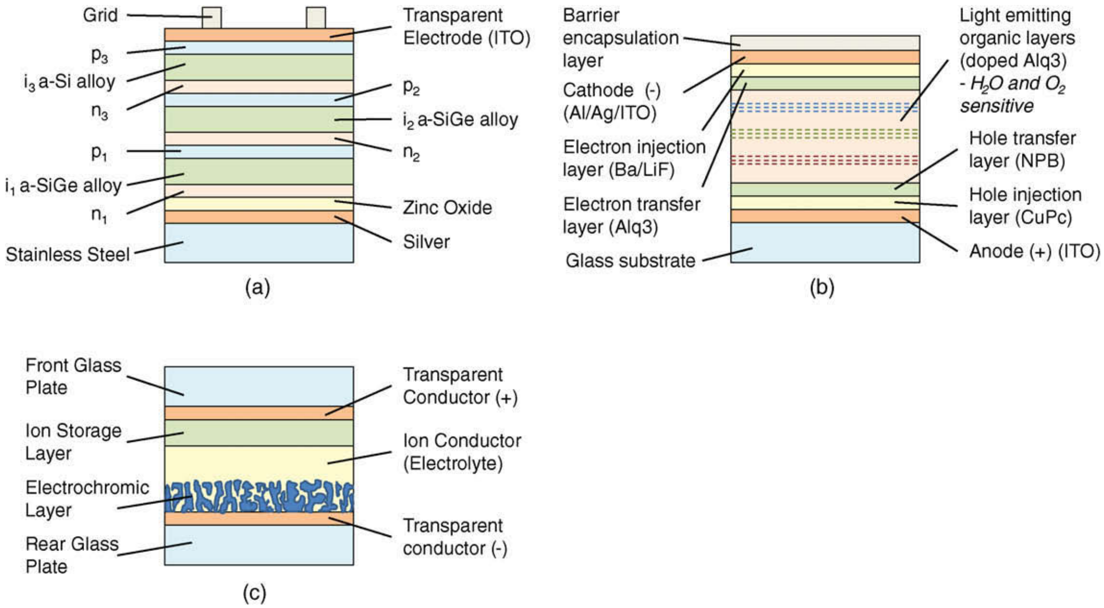

Figure 9.26: Schematic structure of active thin film devices: (a) triple-junction solar cell (after [222]); (b) thin film display (after [227]); (c) electrochromic device – smart window (after [234]).

In parallel with the integrated optics field, plasma has also been used for the deposition of Fe- or Ge-doped SiO_2 core layers on the inner surface of silica tubes for fiber optic preforms [26]. This is the first industrial use of PECVD for optical applications.

9.6.1.3 Thin Films for Solar Cells, Gas Permeation Barriers, and Smart Windows

Application of thin film technology in the fabrication of devices for energy generation, transformation, and reduced consumption has advanced rapidly with the implementation and demonstration of thin film solar cells, displays, smart windows, and numerous other devices. For all of these, the individual layers can be prepared by PECVD as indicated in the schematics in Figure 9.26, though other methods have also been successfully applied [157, 221]. The PECVD films, depending on their nature, composition, and microstructure, can fulfill different functions, such as the semiconductor layer, transparent conductive layer, barrier layer, electrochromic layer, AR coating, and possibly others.

Thin films for solar cells

Of the various thin film materials, PECVD hydrogenated amorphous semiconductors, especially silicon (*a*-Si:H), have received much attention for their use in low-cost solar cells [222]. Because of its broad wavelength range absorption characteristics (due to the inherent disorder), *a*-Si:H absorbs sunlight very efficiently, and very thin films (< 500 nm) are sufficient to form the solar cell structure. The main focus has been on single- and multijunction cells using *a*-Si:H, but *a*-SiGe:H, and more recently hydrogenated nanocrystalline silicon (NC-Si:H), have been explored [223], the latter reaching a higher conversion efficiency, η.

a-Si:H is usually prepared in glow-discharge from silane, but strong dilution in hydrogen has been found to favor formation of its NC phase. In fact, the best performing Si is grown at a dilution just below the edge of amorphous to NC transition [224], and the highest η values of NC solar cells are obtained when the hydrogen dilution pushes the material just above the edge [225]. Figure 9.26(a) shows a spectrum-splitting triple-junction structure that leads to good stability, and 13% stable AM1.5 efficiency.

The top cell using *a*-Si:H has a bandgap of about 1.8 eV and absorbs the blue photons. The middle and bottom cells, using *a*-SiGe:H alloys of different Si to Ge ratios, possess bandgaps of around 1.6 and 1.4 eV and absorb green and red photons. The nine-layer, triple-junction stack is deposited onto a thin, flexible stainless steel (SS) substrate coated with a textured silver-doped zinc oxide (Ag/ZnO) back-reflector, to facilitate light trapping. Transparent-conductive indium-tin oxide (ITO) is deposited on top of the top cell, serving as the contact as well as an AR coating. Thin and highly conductive *p*-type and *n*-type layers used in individual cells also form tunnel junctions between adjacent cells [226].

Gas permeation barriers

Permeation of gases (e.g. O_2) and vapors (e.g. H_2O) through polymers, which represents an important problem in device technology and in the packaging of various high added value consumer products, is particularly important in the context of encapsulation of organic electronic devices. These include organic light-emitting devices (OLEDs) (Figure 9.26b), organic solar cells, integrated circuits, and food and pharmaceutical products. Application of high-performance barriers can substantially extend the lifetime and performance of all of these.

PECVD SiO_2 and $SiN_{1.3}$ have received particular attention as barrier materials for polymeric substrates, mainly owing to their hardness, optical transparency [7, 184], good adhesion, and barrier properties [182, 228–230]. Films deposited by PECVD are found to be superior compared to other techniques such as PVD. Specifically, the main reason is considered to be formation of the interphase (about 50 nm thick) which is distinct in structure, composition, and mechanical properties from the coating and the substrate [185] (see Section 9.5.4).

It has been shown that oxygen transmission rate (OTR) and water vapor transmission rate (WVTR) decrease as much as 1000-fold with increasing coating thickness, to a certain asymptotic minimum value, when the thickness exceeds a ‘critical’ value, d_c, that has been estimated at ~15 nm for SiO_2 and ~8 nm for $SiN_{1.3}$, for which useful barrier characteristics can be achieved [182, 229, 230]. Typically found OTR values are about 0.5 scc/m^2day and WVTR about 0.3 g/m^2day, for barrier thicknesses exceeding such d_c, but the minimum permeation values depend on the concentration of defect sites in the coating and on the substrate surface roughness.

In order to mitigate the effect of defects, multilayer systems are applied (ultrabarrier coatings) to benefit from best performance of individual layers, and to minimize defects and pinhole concentration [230]. They typically combine two or more layers deposited by one process (e.g. PECVD), or by a hybrid process including fabrication of a smoothening layer (e.g. by evaporation) followed by a dense PECVD coating [231–233].

Electrochromic devices

An example of an electrochromic (EC) device is illustrated in Figure 9.26(c). It typically contains five layers between two substrates formed by glass or plastic. It features two transparent electrodes, an EC layer, such as WO_3, an electrolyte, and an ion-containing layer. The latter coating can eventually be also replaced by another EC layer that possesses properties inverse with respect to the former one [234]. For appropriate function of such a device, an EC film with controlled porosity is generally required. This can be achieved by appropriate control of film growth conditions, including medium-energy ion bombardment [156, 158] in conjunction with the structural evolution described by the SZM (see Section 9.5).

9.6.1.4 Industrial Scale-Up and Economic Considerations

It has become apparent that PECVD techniques can provide optical properties comparable to other techniques such as PVD, and the final choice of the deposition approach for each specific application depends on both technical and manufacturing factors. These include: (1) mechanical properties (e.g. adhesion and stress); (2) deposition rate; (3) process scale-up (uniformity, reproducibility, etc.); (4) process integration in the optical device fabrication; (5) manufacturing yield; and (6) cost of manufacturing (capital investment and operation). From this point of view, novel plasma-based processes, offering the possibility of selectively controlling E_i and Φ_i/Φ_n and frequently providing high r_D values, are advantageous. Furthermore, PECVD offers good mechanical performance and the possibility of pretreating or ‘engineering’ interfaces (e.g. in the case of plastic substrates).

Different plasma system concepts have been proposed for the fabrication of optical coatings. In general, the characteristics of a suitable plasma reactor are dictated by the requirements of the desired optical coating, in which the decisive factors are the choice of the n_H and n_L materials, control and reproducibility of $n(z)$, the component size and required film uniformity, and the total film thickness. In addition, the deposition rate is a tradeoff between factors such as film microstructure, film stress, and precision of the thickness control. Uniformity better than 1% over more than 50 cm can be achieved, while a deposition rate of 1–5 nm/s is a good practical value for high-quality (dense) optical coatings. It should be noted, however, that such considerations are very general, and specific aspects depend on the device to be fabricated. For example, the total thickness of AR coatings in the visible region is about 0.4 μm, while a narrowband filter in the NIR composed of more than 100 layers may be 50 μm thick or more, as compared to about 10 μm thickness for a homogeneous monomode optical waveguide.

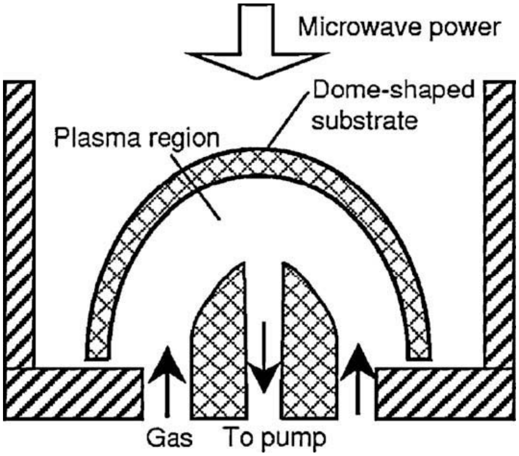

Figure 9.27: MW PICVD deposition system: schematic of the commercial reactor for coating individual lamps. (After [25, 26].)

Careful optimization is required in order to accommodate specific substrate materials (glass, polymers, etc.), sizes, and shapes (flat, curved, rough).

Despite considerable efforts to develop novel optical film materials using PECVD, there are relatively few publications documenting its use in industry. Significant among them appears to be the PICVD process of Schott Glaswerke GmbH (see Section 9.3.3), illustrated in Figure 9.27. This approach, in which the substrate forms part of the reactor walls, was originally developed to coat the inner surface of glass tube for fiber preforms, and is used to fabricate cold light reflectors for projection lamps and IR reflectors for energy-efficient lamps, as well as waveguides, and transparent barrier coatings [26]. Large production (several million lamps per year) is achieved by increasing the total number of small deposition chambers. Another example concerns a microwave PECVD used for the medium- and large-scale roll-to-roll deposition of AR coatings onto webs [235].

Commercialization and adoption of PECVD have been often hampered by high manufacturing cost. In order to avoid risks and unforeseen surprises, it is desirable to explore economic models allowing one to compare the PECVD process with other alternative technologies. An interesting example of such a study [236] has been performed for the particular case of tungsten oxide, which attracts much attention owing to its applications, such as smart windows, gas sensors, and displays [157].

The study compares the costs of manufacturing of WO_3 films deposited either by PECVD using an RF discharge or by DC reactive magnetron sputtering from metal targets, and it considers both inline systems for large area (2 m wide) glass substrates and roll-to-roll systems for flexible webs [236]. Assuming $r_D = 10\,\mathrm{nm/s}$ (confirmed experimentally in a static mode), the model PECVD process was predicted to give the best performance with the roll-to-roll system at a cost of \$5.26/m^2 and an annual capacity of 1.4 million m^2, while the cost was dominated by raw materials (primarily WF_6). On the other hand, the model DC sputtering process at $r_D = 0.6$ nm/s was predicted to give the best performance with the roll-to-roll system at a cost of \$15.00/m^2 and an annual capacity of 0.12 million m^2, and the cost was found to be dominated by labor and depreciation.

The study concludes that PECVD can produce WO_3 for as little as one-third the cost, and have more than ten times the annual production capacity of sputtering. However, in such situations, one has also to consider other (hidden) expenses related to handling potentially toxic and corrosive products, safety, and long-term projections of the cost of raw materials. Such approaches are well illustrated by examples from the area of microelectronics [188].

Examples of commercial processes using PECVD include both vendors and end users who apply high-frequency plasmas for the fabrication of coatings with specific optical, electrical, and barrier characteristics. By way of illustration, one type of commercial plasma machine using both MW (an array of linear plasma sources) and RF discharges is available in Germany (Roth & Rau AG) (Figure 9.28). The system allows one to coat areas up to $0.5 \times 0.5\,\text{m}^2$ with transparent multilayer barriers, AR coatings, and other related systems, and it also provides a possibility for uniform etching in microfabrication.

United Solar Ovonic has developed a roll-to-roll automated process for manufacturing solar cells on stainless steel (SS). Rolls of SS substrates, 2500 m long, 36 cm wide, and 125 μm thick continuously move through four compartments to perform (1) washing, (2) back-reflector

Figure 9.28: Large-area PECVD coating system for the fabrication of barrier and antireflective coatings over an area of up to 55 cm × 55 cm. (Courtesy of Roth & Rau.)

Figure 9.29: Large-area roll-to-roll deposition system for the fabrication of amorphous silicon triple-junction photovoltaic cells. (Courtesy of United Solar Ovonic.)

deposition (sputtered Al and ZnO), (3) PECVD of the triple junction alloy consisting of nine layers of *a*-Si and *a*-SiGe, and (4) AR coating deposition (ITO). The complete thin film solar cell device is illustrated in Figure 9.26(a), and the production machine is shown in Figure 9.29. The system is approximately 90 m long and 3 m tall; it contains a vertical central cathode, and three webs are transported on each side of the cathode parallel to it at a speed of 30 cm/minute. Deposition of 14.5 km of solar cells can be completed in about 72 hours.

9.6.2 Protective Tribological Coatings

In recent years we have witnessed an increasing need for protective coatings with improved durability and performance, preventing wear in dry and wet (tribocorrosion) conditions, erosion and corrosion, and providing environmental protection and thermal insulation. There have been considerable advances in the understanding of the mechanisms of wear and corrosion of coatings particularly related to the characteristics of film microstructure, interface properties, and wear and corrosion mechanisms.

The need to ensure good adhesion to numerous technological substrates has stimulated much research, exploring different interface engineering approaches, in order to improve the tribomechanical and tribocorrosion characteristics of coating–substrate systems. Specifically, numerous applications call for so-called duplex or triplex treatments (usually performed in the same reactor) to stabilize the interface by affecting its composition and microhardness, and frequently introducing property gradients such as hardness [176]. The commonly used methods consist of two or three of the following independent steps: (1) surface treatment in an active (non-deposition) plasma containing nitrogen, carbon, boron, or other gases, leading to surface nitriding, boriding, or carburizing, and generally giving to surface hardening; (2) deposition of an intermediate layer, usually metal or metal compound; and (3) deposition of the final, hard, protective tribological coating [175, 237].

In many respects, the protective coatings are categorized according to their hardness as described in Section 9.5 and illustrated for PECVD materials in Figure 9.12. However, tribological behavior of functional coatings is rather complex, and other material properties, such as Young's modulus, toughness, thermal conductivity, stress, friction coefficient, and density, have to be taken into account in order to optimize the coatings' desired performance in terms of wear, erosion and corrosion resistance, and other functional characteristics. In addition, since the material behavior under stress conditions is generally governed by a specific failure mechanism, the coating performance frequently depends on the test conditions for each particular application.

In general, for tribological coatings, H and μ have usually been considered primary properties affecting the wear resistance. However, it has recently been recognized that energy dissipation when two bodies are in relative motion is of primary importance [238, 239]. This allows one to link the tribological properties with the materials' elastoplastic characteristics in two ways: (1) the H/E ratio representing the 'plasticity index' or elastic strain to failure; this appears to be a suitable parameter for predicting wear resistance (K) and for explaining the deformation properties of surfaces in contact [240], by considering the elastic rebound; and (2) the H^3/E^2 ratio – known as resistance to plastic deformation or resilience – that appears to be a key parameter for predicting the tribological behavior [241] as well as the toughness of the coatings [239, 240, 242].

In this section, we describe selected examples of the performance of different tribological coatings, in the context of their applications in aerospace, automobile industry, manufacturing, and biomedical instrumentation (see Table 9.2). We focus particularly on metal-based polycrystalline, nanocrystalline and nanocomposite coatings, and then on covalently bonded amorphous carbonaceous coatings which, in numerous cases, have reached industrial scale.

9.6.2.1 Metal-Based Tribological Coatings

Binary metal nitrides, carbides, borides, and oxides are frequently used in different tribological applications including cutting tools, protection of different components of automobiles, aircrafts, and consumer products. Their most attractive characteristic is a combination of hardness with high wear, erosion and corrosion resistance, while some of them provide attractive colors and other advantageous functional characteristics. Such coatings are traditionally fabricated by CVD and PVD methods, but PECVD is increasingly taking its place because of the possibility of benefiting from the plasma chemical reactions, plasma–surface interactions, and interface engineering at low temperature.

In order to broaden the range of the film properties suitable for different applications, and especially to benefit from synergistic effects, ternary metal compounds (mostly including metal carbon nitrides), nanocomposites, and nanolaminate structures (multilayers formed by several to several tens of nanometer thick individual layers) appear to satisfy the ever increasing requirements.

In the context of aerospace and avionics applications, commercial, military, rescue or humanitarian aid aircraft or helicopters frequently operate in a hostile environment, in high humidity and marine salt concentrations. They may operate in the presence of aggressive chemicals, in heavily polluted regions, where the air can carry dust, sand particles, volcanic ash, and other compounds. Such conditions contribute to increased erosion and corrosion of aircraft engine components. This generally leads to decreased efficiency and increased fuel consumption, and can eventually result in catastrophic failure. Therefore, frequent inspections and parts replacements are necessary. These contribute to downtime and increased machine operation costs. Application of high-performance erosion-, wear-, and corrosion-resistant protective coatings can significantly extend the lifetime and performance of aircraft engine components and helicopter parts and thus lead to major reductions in maintenance costs, and to improved safety.

Examples of the wear properties of TiN-based coatings deposited onto martensitic 410 stainless steel are shown in Figure 9.30(a). In order to enhance adhesion, the hardness of the steel ($H = 5$ GPa) has been gradually increased at the interface by nitriding the near-surface region (to a depth of several μm, $H = 15$ GPa), followed by the deposition of 1 μm thick TiN ($H = 24$ GPa), on which 4 μm thick nc-TiN/SiN, nc-TiCN/SiCN coatings have been prepared ($H = 35$–42 GPa; triplex process) [237].

The figure shows that nc-TiCN/SiCN exhibits superior tribological properties compared to TiN and to nc-TiN/SiN coatings, such as low friction ($\mu = 0.17$ compared to 0.5 for the former two coatings) and low wear rate ($K = 1.6 \times 10^{-7}$ mm^3/Nm compared to 9.5×10^{-6} mm^3/Nm for the former coatings). The nc-TiCN/SiCN thus allows one to reduce wear by a factor of ~600 compared to bare SS410. It has been proposed that this performance is due to higher hardness, higher elastic rebound, and lower friction due to the presence of carbon-containing, flexible, Si–C and C–N bonds in the tribolayer [237]. In addition, the presence of carbon leads to attractive color changes compared to nc-TiN/SiN and to the traditional gold color of TiN [167].

The significant effect of applying nc coatings onto aerospace components has also been found by evaluating the erosion resistance (ER), following the ASTM G76 standard. As illustrated in

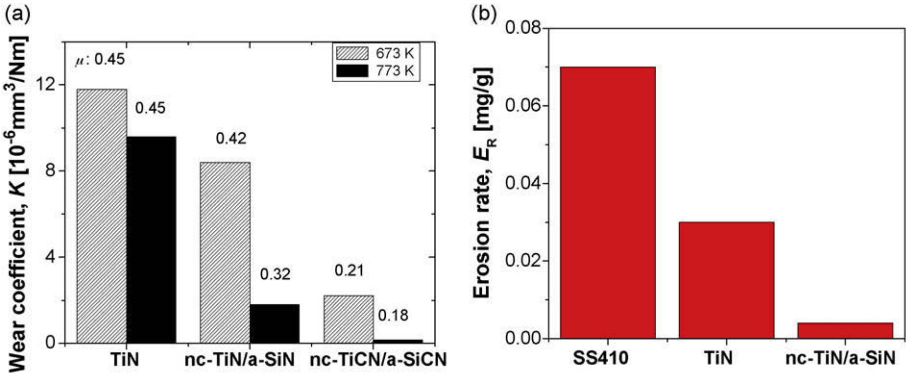

Figure 9.30: Tribological properties of TiN and nanocomposite nc-TiN/SiN$_{1.3}$ and nc-TiCN/SiCN films deposited at T_s of 673 K and 773 K, compared to: (a) the wear coefficient, K, and the coefficient of friction, μ (after [237]); (b) solid particle erosion rate of the coatings deposited on 410 stainless steel (Al$_2$O$_3$ particles, diameter 50 μm, speed 80 m/s) (after [243]).

Figure 9.30(b), application of PECVD TiN, nc-TiN/SiN, and nc-TiCN/SiCN films resulted in an increase of ER by a factor of 20, compared to uncoated SS410 substrates.

As discussed above, assessment of the tribological properties of coatings with respect to their elastoplastic characteristics opens the possibility of better prediction and optimization of their performance. In this context, the K and ER values of the TiN-containing coatings from Figure 9.30 are related to the H^3/E^2 ratio in Figure 9.31. It has been concluded that a substantial improvement in the film's tribological behavior (e.g. erosion and wear) occurs for $H^3/E^2 > 0.5$ GPa (or $H/E > 0.15$–0.20) [237, 243].

Recently, the $H^3/E^2 > 0.5$ GPa condition has also been predicted for such a tribological situation (Al$_2$O$_3$ erodent particles, 50 μm size, 85 m/s velocity) based on finite element calculations using a model considering tensile and shear stress, and yielding criteria for failure upon particle impact [244]. In other words, there is now growing evidence that a critical H^3/E^2 ratio (or H/E ratio) has to be satisfied for the coating to provide appropriate tribological protection. It also means that for successful tribological applications the H^3/E^2 and H/E ratios of the used materials should be maximized. In reality, it is generally important to ensure that the coating hardness is sufficiently higher than that of the eroding or wearing medium, but the E value should be minimized. Therefore, film microstructure should be adjusted to satisfy such conditions: in this respect, PECVD metal-based nc coatings are very suitable candidates for many surface engineering and tribological solutions.

9.6.2.2 Covalently Bonded Protective Carbonaceous Coatings

Carbonaceous tribological coatings have become very attractive because of their very low friction, chemical inertness, and biocompatibility. They have already established their

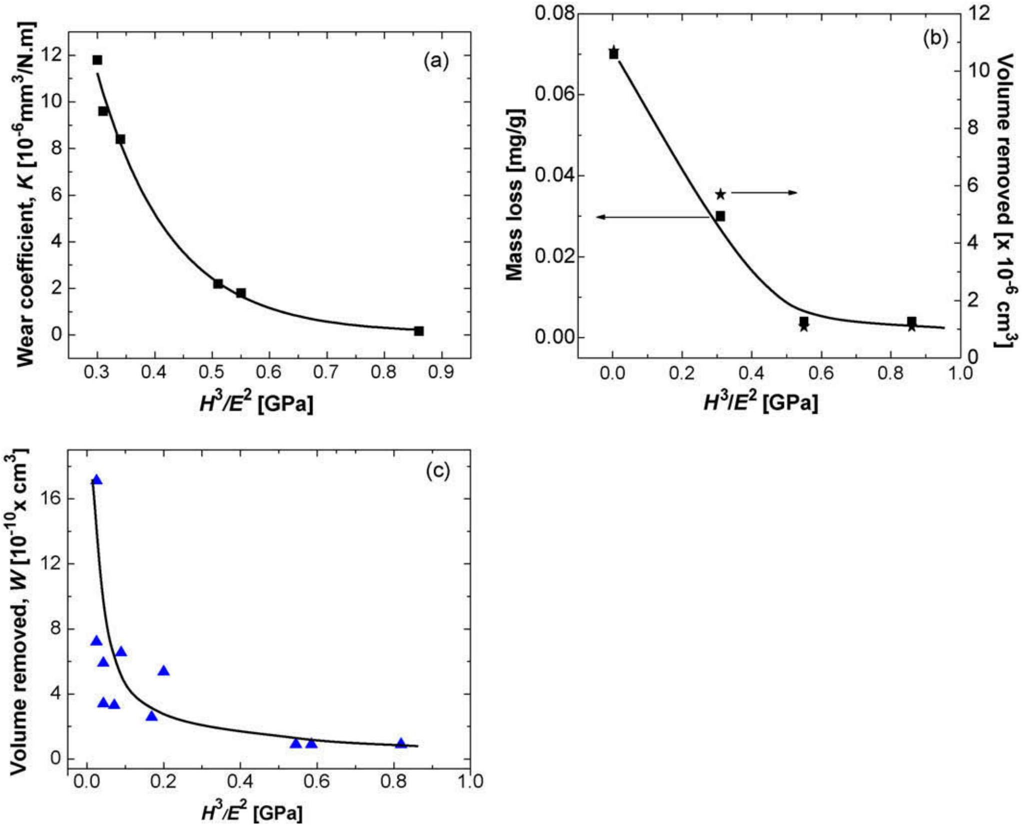

Figure 9.31: Tribological characteristics of TiN and nanocomposite nc-TiN/SiN$_{1.3}$ films as a function of the H^3/E^2 ratio: (a) wear coefficient (after [237]); (b) erosion rate (after [243]); (c) volume removed under single particle erosion (finite element modeling) (after [242]).

importance to the automobile sector, for reduced friction in engines, as sliding, hard, and optically transparent coatings in optics (e.g. barcode readers), and show much promise for biomedical applications (for review, see [245]).

In many cases, before a particular application is tested, frequent problems related to adhesion have to be solved, especially when dealing with metallic, non-carbide forming, substrates. In this respect, adhesion enhancement can be achieved by surface treatments using nitriding and carburizing, as in the case of metal compounds presented above [175–178]. Alternatively, intermediate layers may be applied (duplex or triplex processes). Among the latter, amorphous Si or metal-carbides [246] appear to be the most successful adhesive layers, for steel or non-ferrous metal substrates (e.g. Ti-6Al-4V, WC-Co), under dry sliding conditions.

When corrosion and wear are simultaneously involved, their synergistic action significantly degrades the performance of the materials in contact. Such situations occur, for example, in orthopaedic applications, such as artificial joints (e.g. hip and knee prosthesis), where the bearing surfaces subjected to sliding wear are immersed in the body fluid, so that corrosion is also a significant concern. For such applications, the coated metals and alloys must possess high tribocorrosion resistance. Otherwise, in the case of adhesion failure of prosthetic implants, particles generated by wear may induce reactions that provoke the release of inflammatory mediators from macrophages [247]. It is well established that the cellular response to wear debris depends, among other factors, on the number, shape, size, surface area, and materials chemistry of the particles, thus contributing to complex tribocorrosion reactions [248, 249].

It has been shown that applying a nitrided interface to DLC-coated medical-grade 316L stainless steel provides a significant improvement of the dry wear resistance [177]. However, this bond layer is insufficient when sliding wear takes place in body fluid conditions, even at low contact pressure. This was found to be mainly due to the infiltration of liquid through pores and the weakening of the interface owing to corrosion processes. In such case, the use of PECVD $SiN_{1.3}$ as an interface layer has been found to significantly improve wear resistance of DLC films in Ringer's solution [179]. By acting simultaneously as an adhesive and corrosion barrier layer, the $SiN_{1.3}$ film largely reduced the infiltration of liquid through the film and, hence, the possibility of interface weakening.

As an example of tribocorrosion behavior, OCP measurements were used to follow, in situ, the degradation of DLC-coated 316L stainless steel exposed to Ringer's solution, and the results are shown in Figure 9.32(a). A drop in the OCP indicates removal of the DLC layer and exposure of the active metal to the environment. Moreover, the OCP measured during the

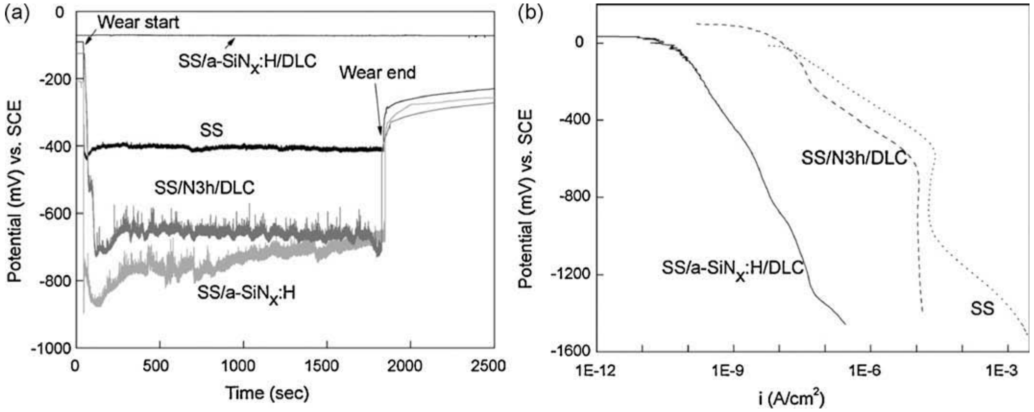

Figure 9.32: Tribocorrosion behavior of DLC-coated biomedical substrates exposed to Ringer's solution: (a) open circuit potential measurements during and after the reciprocal sliding test of SS, SS/N3h/DLC, SS/a-SiN_x:H, and SS/a-SiN_x:H/DLC; alumina ball, normal load: 9 N; frequency: 1 Hz; (b) cathodic polarization curves of bare SS and SS/N3h/DLC and SS/SiN/DLC coating systems. (After [179].)

tribocorrosion experiments was shown to strongly depend on the cathodic reaction rate on the unworn area; a slower rate of cathodic reaction resulted in lower potential during wear. Without an $SiN_{1.3}$ interlayer, OCP drops rapidly within the first tens of cycles of sliding, indicating complete removal of the coatings. When $SiN_{1.3}$ is present, the OCP remains constant during and after the wear test, while μ remains almost constant (0.08) throughout the entire sliding test.

As shown by the cathodic polarization curves in Figure 9.32(b), the presence of DLC and of the DLC/$SiN_{1.3}$ double layer decreases the current density. In addition, the curves show that the $SiN_{1.3}$ film significantly reduces the rate of the cathodic reaction, and therefore explains the low value of OCP measured for $SiN_{1.3}$ and DLC/$SiN_{1.3}$ during the sliding test.

In certain situations, lubricious coatings are needed to be applied on soft substrates, in the case of specific medical, pharmaceutical, or healthcare products. As an example, organic PECVD coatings obtained from MW discharge have been applied for enhanced tribological performance of hearing devices, which need to be inserted into the ear many times without long-term deterioration and skin irritation. In such a case, plasma-deposited organosilicone coatings were applied to silicone rubber components, and their surface friction has been assessed as a function of thickness (deposition time) (Figure 9.33). It has been shown that an equivalent of several hundreds of nanometer thickness is sufficient to ensure suitable long-term lubricity (the μ dropped by a factor between 5 and 10 compared to uncovered rubber), while providing a conformal coating on the substrate surface as confirmed by SEM (Figure 9.33b, c).

9.6.2.3 Industrial Scale-Up

Among possible PECVD processes, acceptance of hard carbon protective coatings by industry is probably most advanced, compared to other film systems. The main reasons appear to be the relative ease of fabrication from hydrocarbon gases and precursors, most frequently using methane, acetylene, or benzene, relative tolerance regarding the film thickness, stability of the process itself, and the fact that most of the deposition equipment is used to batch coat individual sets of differently shaped components. The use of DLC is very advanced in the automotive sector, where DLC coatings were already introduced by 1994, for diesel engine injection systems, followed by piston rings and tappets. Its use in racing cars, gears, and other components has been considered, and applied, since the 1990s (for detailed description, see [245, 251]).

An example of an industrial system, developed by Hauzer Techno Coating (the Netherlands), for DLC coatings onto automobile and other components is shown in Figure 9.34. The turbomolecularly pumped reactor contains six electrodes, up to 1.6 m long, for pulsed discharge excitation, and allows both PECVD and PVD processes to be combined in one chamber.

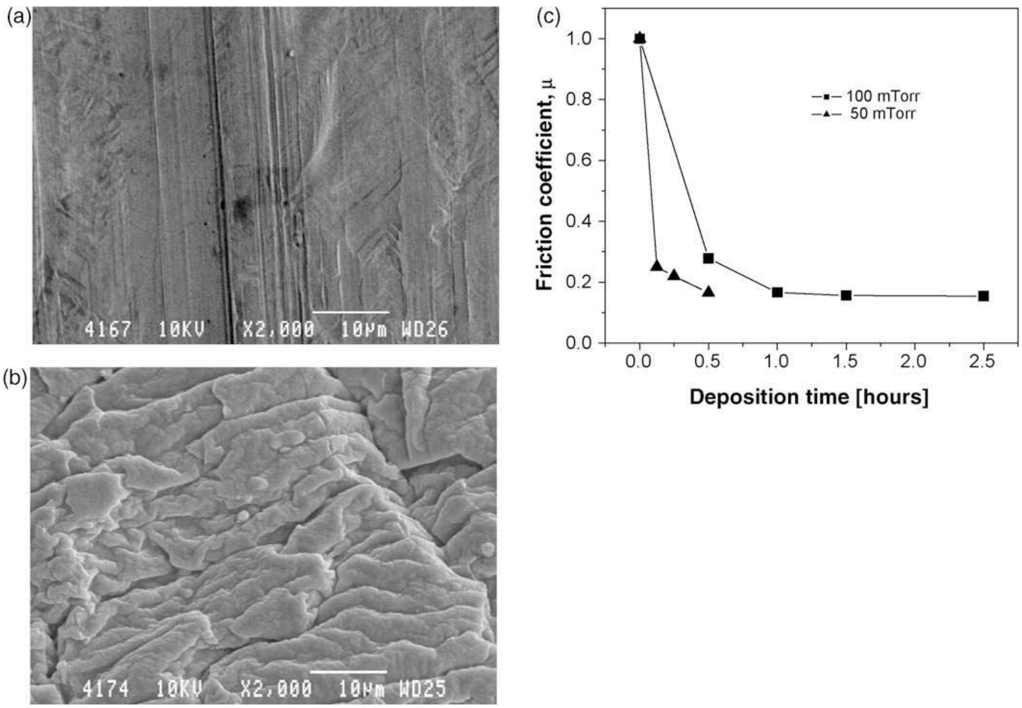

Figure 9.33: Effect of lubricious organosilicone protective coatings on the reduction of friction coefficient of multiusage hearing devices: SEM micrographs (a) before and (b) after coating; (c) coefficient of friction as a function of coating time. (After [250].)

Figure 9.34: Industrial multizone deposition system for the fabrication of DLC coatings for automotive parts and other applications. Each chamber contains six 1.6 m long electrodes. (Courtesy of Hauzer Techno Coatings.)

Figure 9.35: Example of a commercial system for the deposition of hard protective coatings. (Courtesy of PATT Technologies Inc.)

An interesting approach to the fabrication of metal nitrides, carbides, and borides as single layers, multilayers and nanolaminates has been developed and explored by PATT Technologies Inc. (Canada) (Figure 9.35). This producer fabricates such Ti-based and other metal-based coatings from metal halide precursors, specifically prepared in a furnace adjacent to the deposition chamber, using a reaction of solid metal with the halogen, such as Cl_2. Each chamber, of 1.6 m^3 volume, allows about 1600 kg of parts to be coated in one run, using high-power, medium-frequency pulsed plasmas.

Other concepts of deposition systems exist, each of which must be examined using an economic model related to the capital and operation costs, deposition rate at the given film quality, and potentially ‘hidden’ costs related to safety, precursor, and exhaust handling.

9.7 Future and Perspectives

During the past several decades, vacuum-based technologies for functional coatings have evolved significantly. Numerous PECVD concepts are industrially applied for optical, tribomechanical, protective, biomedical, and other applications. In each instance, recent advances in understanding the deposition processes and improved process control led to better film performance. This clearly gave rise to continuously increased acceptance of PECVD technologies in industry.

Physical and chemical understanding of the basic science underlying various deposition processes is now quite advanced. In this chapter we have underlined the key factors affecting the control of film microstructure: plasma density, and ion energy and ion flux. It has also been clearly shown that, when appropriately optimized, all of the deposition processes described here produce functional thin films possessing characteristics comparable with, or even better than PVD counterparts. Therefore, the final choice of the appropriate process will depend on other factors, such as those related to different scale-up issues and economic aspects.

Current trends point toward the invention of new and improved deposition approaches, in particular those focusing on creating nanostructured coatings for various new products. By tailoring the nanostructure and controlling the interfaces between layers and substrates the engineer can create new film systems for a variety of specific applications, including active optical filters (tunable filters, smart windows, etc.), displays, sensors, security devices, energy-conversion and energy-saving devices, optical MEMS, nanophotonic devices, active optical waveguides, protective coatings for aerospace, automobiles, and biomedical components, as well as numerous consumer products. Among the emerging technologies for PECVD of functional coatings, we are already witnessing considerable progress in high-energy-content plasma processes or in those requiring a precise control of the surface growth mechanisms; these include pulsed PECVD, plasma-assisted atomic layer deposition, atmospheric pressure plasma deposition, and hybrid systems. We also are entering an exciting period that is being marked by the development of new active materials. Examples are doped transparent conductive oxides and electrochromic, photochromic, and magneto-optic materials; porous and nanocomposite materials with well-controlled nanostructural characteristics (concentration, size, and shape of nanoparticles); new organic materials; and new challenges in the area of process control and in situ real-time monitoring, smart self-healing protective coatings, and numerous others.

References

[1] T. Sugano (Ed.), Applications of Plasma Processes to VLSI Technology, Wiley, New York (1985).
[2] J. Mort, F. Jansen, Plasma Deposited Thin Films, CRC Press, Boca Raton (1986).
[3] S.M. Rossnagel, J.J. Cuomo, W.D. Westwood (Eds.), Handbook of Plasma Processing Technology, Noyes, Park Ridge, NJ (1990).
[4] R. d'Agostino (Ed.), Plasma Deposition, Treatment and Etching of Polymers, Academic Press, Boston (1990).
[5] R.F. Bunshah (Ed.), Handbook of Deposition Technologies for Films and Coatings, Noyes, Park Ridge, NJ (1994).
[6] D. Glocker, I. Shah (Eds.), Handbook of Thin Film Process Technology, IOP, Bristol (1996).
[7] L. Martinu, D. Poitras, J. Vac. Sci. Technol. A 18 (2000) 2619.
[8] Chemical Vapor Deposition, 13 (2007), special issue on low pressure PECVD.

[9] Chemical Vapor Deposition, 11 (2005), special issue on atmospheric pressure PECVD.

[10] H. Caquineau, I. Enache, N. Gherardi, N. Naude, F. Massines, J. Phys. D: Appl. Phys. 42 (2009) 125201.

[11] M.R. Wertheimer, L. Martinu, E.M. Liston, Chap. E3.0, in: D. Glocker, I. Shah (Eds.), Handbook of Thin Film Process Technology, IOP, Bristol (1996).

[12] D.M. Manos, D.L. Flamm (Eds.), Plasma Etching – An Introduction, Academic Press, Boston (1990).

[13] E.M. Liston, L. Martinu, M.R. Wertheimer, J. Adhes. Sci. Technol. 7 (1993) 1091.

[14] K.L. Mittal, L. Pizzi (Eds.), Adhesion Promotion Techniques, Marcel Dekker, New York (1999).

[15] M.J. Kushner, J. Appl. Phys. 63 (1988) 2532.

[16] M. Moisan, J. Pelletier (Eds.), Microwave Excited Plasmas, Elsevier, Amsterdam (1992).

[17] M. Moisan, C. Barbeau, R. Claude, C.M. Ferreira, J. Margot, J. Paraszczak, J. Vac. Sci. Technol. B 9 (1991) 8.

[18] L. Martinu, J.E. Klemberg-Sapieha, O.M. Kuettel, A. Raveh, M.R. Wertheimer, J. Vac. Sci. Technol. A 12 (1994) 1360.

[19] K. Okada, S. Komatsu, S. Matsumoto, J. Vac. Sci. Technol. A 17 (1999) 721.

[20] C. Pomot, J. Pelletier, Chap. 13, in: M. Moisan, J. Pelletier (Eds.), Microwave Excited Plasmas, Elsevier, Amsterdam (1992).

[21] M.A. Lieberman, A.J. Lichtenberg, Principles of Plasma Discharges and Materials Processing, Wiley, New York (1994).

[22] P. Benoit-Cattin, L.-C. Bernard, J. Appl. Phys. 39 (1968) 5723.

[23] J.W. Coburn, E. Kay, J. Appl. Phys. 43 (1972) 4965.

[24] Z. Zakrzewski, M. Moisan, Plasma Sources Sci. Technol. 4 (1995) 379.

[25] J. Segner, Chap. 7, in: F.R. Flory (Ed.), Thin Films for Optical Systems, Marcel Dekker, New York (1995) 209.

[26] H. Bach, D. Krause (Eds.), Thin Films on Glass, Schott Series on Glass and Glass Ceramics, Springer, Berlin (1997).

[27] L. Martinu, J.E. Klemberg-Sapieha, M.R. Wertheimer, Appl. Phys. Lett. 54 (1989) 2645.

[28] J.E. Klemberg-Sapieha, O.M. Kuttel, L. Martinu, M.R. Wertheimer, Thin Solid Films 193/194 (1990) 965.

[29] C. Rostaing, F. Coeuret, B. Drevillon, R. Etemadi, C. Godet, J. Huc, Thin Solid Films 236 (1993) 58.

[30] R. Etemadi, C. Godet, M. Kildemo, J.E. Bouree, R. Brenot, B. Drevillon, J. Non-Cryst. Solids 187 (1995) 70.

[31] R.R. Burke, J. Pelletier, C. Pomot, L. Vallier, J. Vac. Sci. Technol. A 8 (1991) 2931.

[32] P. Bulkin, N. Bertrand, B. Drevillon, Thin Solid Films 296 (1997) 66.

[33] M. Leskela, M. Ritala, Thin Solid Films 409 (2002) 138.

[34] S.M. Rossnagel, A. Sherman, F. Turne, J. Vac. Sci. Technol. B 18 (2000) 2016.

[35] M. Creatore, J.-C. Cigal, G.M.W. Kroesen, M.C.M. van de Sanden, Thin Solid Films 484 (2005) 104.

[36] J.W.A.M. Gielen, M.C.M. van de Sanden, D.C. Schram, Appl. Phys. Lett. 69 (1996) 152.

[37] H. Biederman, L. Martinu, Chap. 4, in: R. d'Agostino (Ed.), Plasma Deposition, Treatment and Etching of Polymers, Academic Press, Boston (1990) 269.

[38] D. Dalacu, L. Martinu, J. Vac. Sci. Technol. A 17 (1999) 877.

[39] J.-M. Lamarre, Z. Yu, C. Harkati, S. Roorda, L. Martinu, Thin Solid Films 479 (2005) 232.

[40] S. Kanazawa, M. Kogoma, T. Moriwaki, S. Okazaki, J. Phys. D: Appl. Phys. 21 (1988) 838.

[41] B. Eliasson, U. Kogelschatz, IEEE Trans. Plasma Sci. 19 (1991) 309.

[42] U. Kogelschatz, Plasma Chem. Plasma Process. 23 (2003) 1.

[43] I.H. Hutchinson, Principles of Plasma Diagnostics, Cambridge University Press, Cambridge (2002).

[44] R. Hippler, S. Pfau, M. Schmidt, K.H. Shoenbach (Eds.), Low Temperature Plasma Physics: Fundamental Aspects and Applications, Wiley-VCH, Berlin (2001).

[45] F. Chen, Lecture Notes on Principles of Plasma Processing, Kluwer Academic/Plenum Publishers, New York (2003).

[46] V.M. Donnelly, J. Phys. D: Appl. Phys. 37 (2004) R217.

[47] M. Kildemo, Appl. Opt. 37 (1998) 113.

[48] M. Kildemo, P. Bulkin, B. Drevillon, O. Hunderi, Appl. Opt. 36 (1997) 6352.

[49] C. Lu, A.W. Czanderna (Eds.), Applications of Piezoelectric Quartz Crystal Microbalances, Elsevier, Amsterdam (1984).
[50] A. Grill, Cold Plasma in Materials Fabrication: From Fundamentals to Applications, IEEE Press, New York (1994).
[51] H. Aguas, R. Martins, E. Fortunato, Vacuum 56 (2000) 31.
[52] P. Spatenka, H. Suhr, Plasma Chem. Plasma Process. 13 (1993) 555.
[53] O. Zabeida, L. Martinu, J. Appl. Phys. 85 (1999) 6366.
[54] M. Zeuner, H. Neumann, J. Meichsner, Vacuum 48 (1997) 443.
[55] O. Zabeida, A. Hallil, M.R. Wertheimer, L. Martinu, J. Appl. Phys. 88 (2000) 635.
[56] A. Hallil, O. Zabeida, M.R. Wertheimer, L. Martinu, J. Vac. Sci. Technol. A 18 (2000) 882.
[57] A. Hallil, O. Zabeida, J.E. Klemberg-Sapieha, M.R. Wertheimer, L. Martinu, in: Proc. 42nd Annual Technical Conference, Society of Vacuum Coaters, Chicago, IL (1999) 311.
[58] R.A. Roy, D.S. Yee, in: J.J. Cuomo, S.M. Rossnagel, H.R. Kaufman (Eds.), Handbook of Ion Beam Processing Technology, Noyes, Park Ridge, NJ (1989) 194.
[59] B.A. Movchan, A.V. Demchishin, Fiz. Met. Metalloved. 28 (1969) 653.
[60] J.A. Thornton, J. Vac. Sci. Technol. 11 (1974) 666.
[61] R. Messier, A.P. Giri, R.A. Roy, J. Vac. Sci. Technol. A 2 (1984) 500.
[62] R. Messier, J. Vac. Sci. Technol. A 4 (1986) 490.
[63] P.J. Kelly, R.D. Arnell, J. Vac. Sci. Technol. A 16 (1998) 2858.
[64] J. Musil, in: Proceedings of 8th International Symposium on Elementary Processes and Chemical Reactions in Low Temperature Plasma, Casta, Slovakia (1992) 177.
[65] J.M.E. Harper, J.J. Cuomo, R.J. Gambino, H.R. Kaufman, in: O. Auciello, R. Kelly (Eds.), Ion Bombardment Modification of Surfaces, Elsevier, Amsterdam (1989) 127.
[66] J.E. Klemberg-Sapieha, J. Oberste-Berghaus, L. Martinu, R. Blacker, I. Stevenson, G. Sadkhin, Appl. Optics 43 (2004) 2670.
[67] A. Manenschijn, W.J. Goedheer, J. Appl. Phys. 69 (1991) 2923.
[68] A. Amassian, M. Svec, P. Desjardin, L. Martinu, J. Vac. Sci. Technol. A 24 (2006) 2061.
[69] A. Amassian, M. Svec, P. Desjardins, L. Martinu, J. Appl. Phys. 100 (2006) 063526.
[70] P. Jedrzejowski, A. Amassian, E. Bousser, J.E. Klemberg-Sapieha, L. Martinu, Appl. Phys. Lett. 88 (2006) 071915.
[71] M.R. Wertheimer, A.C. Fozza, A. Hollander, Nucl. Instrum. Methods Phys. Res. B 151 (1999) 65.
[72] A. Hollander, J.E. Klemberg-Sapieha, M.R. Wertheimer, J. Polym. Sci. A, Polym. Chem. 33 (1995) 2013.
[73] S.C. Gujrathi, in: E. Sacher, J.J. Pireaux, S.P. Kowalczyk (Eds.), Metallized Polymers, Vol. 440, ACS Symposium Series, ACS, Washington, DC (1990) 88.
[74] L.C. Feldman, J.W. Mayer, Fundamentals of Surface and Thin Film Analysis, North Holland, Elsevier Science, Amsterdam (1986).
[75] H. Bubert, H. Jenett (Eds.), Surface and Thin Film Analysis: A Compendium of Principles, Instrumentation, and Applications, Wiley-VCH, Weinheim (2002).
[76] M. Ohring, Materials Science of Thin Films, Academic Press, New York (1992).
[77] M. Born, E. Wolf, Principles of Optics, 6th ed., Pergamon, New York (1993).
[78] F. Urbach, Phys. Rev. 89 (1953) 1189.
[79] A.R. Forouhi, I. Bloomer, Phys. Rev. B 34 (1986) 7018.
[80] G.E. Jellison Jr., F.A. Modine, Appl. Phys. Lett. 69 (1996) 371 Erratum 69 (1996) 2137.
[81] D.A.G. Bruggeman, Ann. Phys. Leipzig 24 (1935) 636.
[82] D. Stroud, Phys. Rev. B 12 (1975) 3368.
[83] J.C. Garland, D.B. Tanner (Eds.), Electrical Transport and Optical Properties of Inhomogeneous Media, AIP Conf. Proc., Vol. 40, AIP, New York (1978).
[84] D.E. Aspnes, Chap. 5, in: E.D. Palik (Ed.), Handbook of Optical Constants of Solids, Academic, San Diego, CA (1985) 89.
[85] W.C. Oliver, G.M. Pharr, J. Mater. Res. 7 (1992) 1564.

[86] K. Holmberg, A. Matthews, Coatings Tribology; Properties, Techniques and Applications in Surface Engineering, Elsevier, New York (1998).
[87] L. Martinu, in: R. d'Agostino, P. Favia, F. Fracassi (Eds.), Plasma Treatments and Deposition of Polymers, Kluwer Academic Publishers, Dordrecht (1997) 247.
[88] P.J. Burnett, D.S. Rickerby, Thin Solid Films 154 (1987) 403.
[89] E. Stansbury, R. Buchanan, Fundamentals of Electrochemical Corrosion, ASM International (2000).
[90] M. Azzi, J.A. Szpunar, Biomol. Eng. 24 (2007) 443.
[91] L. Eckertova, Physics of Thin Films, Springer, New York (1986).
[92] W.M.M. Kessels, A.H.M. Smets, D.C. Marra, E.S. Aydil, D.C. Schram, M.C.M. van de Sanden, Thin Solid Films 383 (2001) 154.
[93] G. Lucovsky, M.J. Manitini, J.K. Srivastava, E.A. Irene, J. Vac. Sci. Technol. B 5 (1987) 530.
[94] R.A.B. Devine, M. Marchand, Appl. Phys. Lett. 63 (1993) 619.
[95] P.J. Martin, R.P. Netterfield, W.G. Sainty, J. Appl. Phys. 55 (1984) 235.
[96] A. Gupta, S. Toby, E.P. Gusev, H. Lu, Y. Li, M.L. Green, Prog. Surf. Sci. 59 (1998) 103.
[97] A. Ricard, J.E. Oseguera-Pena, L. Falk, H. Michel, M. Gantois, IEEE Trans. Plasma Sci. 18 (1996) 940.
[98] W. Hsieh, C.Y. Chang, S.C. Hsu, J. Appl. Phys. 74 (1993) 2638.
[99] S.M. Han, E.S. Aydil, J. Vac. Sci. Technol. A 14 (1996) 2062.
[100] N. Bertrand, B. Drevillon, P. Bulkin, J. Vac. Sci. Technol. A 16 (1998) 63.
[101] Y. Watanabe, M. Shiratani, Jpn. J. Appl. Phys. Part 1 32 (1993) 3074.
[102] A. Love, S. Middleman, A.K. Hochberg, J. Cryst. Growth 129 (1993) 119.
[103] D. Shamiryan, T. Abell, F. Iacopi, K. Maex, Mater. Today 7 (2004) 34.
[104] S.M. Han, E.S. Aydil, J. Appl. Phys. 83 (1998) 2172.
[105] C. Vallee, A. Goullet, F. Nicolazo, A. Granier, G. Turban, J. Non-Cryst. Solids 311 (1997) 212.
[106] J. Robertson, Philos. Mag. B 63 (1991) 47.
[107] D. Poitras, P. Leroux, J.E. Klemberg-Sapieha, S.C. Gujrathi, L. Martinu, Opt. Eng. 35 (1996) 2693.
[108] F. Fracassi, R. d'Agostino, G. Bruno, Plasmas Polymers 1 (1996) 3.
[109] R. Vernhes, O. Zabeida, A. Amassian, J.E. Klemberg-Sapieha, L. Martinu, Appl. Optics 43 (2004) 97.
[110] H.G. Tompkins, R.B. Gregory, P.W. Deal, S.M. Smith, J. Vac. Sci. Technol. A 17 (1999) 391.
[111] L. Martinu, in: S.I. Najafi, M.N. Armenise (Eds.), Functional Photonic and Fiber Devices, Vol. 2695, SPIE, Bellingham, WA (1994) 30.
[112] J.E. Klemberg-Sapieha, L. Martinu, M.R. Wertheimer, P. Günther, R. Schellin, C. Thielemann, G. Sessler, J. Vac. Sci. Technol. A 14 (1996) 2775.
[113] T. Hattori, S. Semura, N. Akasaka, Jpn. J. Appl. Phys. Part 1 38 (1999) 2775.
[114] W.-T. Tseng, Y.-T. Hsieh, C.-F. Lin, M.-S. Tsai, M.-S. Feng, J. Electrochem. Soc. 144 (1997) 1100.
[115] A. Badzian, T. Badzian, R. Roy, W. Drawl, Thin Solid Films 354 (1999) 148.
[116] Z. He, G. Carter, J.S. Colligon, Thin Solid Films 283 (1996) 90.
[117] A.M. Wrobel, A. Walkiewicz-Pietrzykowska, J.E. Klemberg-Sapieha, Y. Nakanishi, T. Aoki, Y. Hatanaka, Chem. Mater. 15 (2002) 1749.
[118] P. Jedrzejowski, J. Cizek, J.E. Klemberg-Sapieha, J. Vlcek, L. Martinu, Thin Solid Films 447–448 (2004) 201.
[119] R.F. Davis, Diamond Films and Coatings – Development, Properties and Applications, Noyes, Park Ridge, NJ (1993).
[120] J. Robertson, Mater. Sci. Eng. R37 (2002) 129.
[121] R. Clausing, L. Horton, J. Angus, P. Koidl (Eds.), Diamond and Diamond-Like Films and Coatings, Plenum, New York (1991).
[122] J. Pouch, S.A. Alterovitz (Eds.), Properties and Characterization of Amorphous Carbon Films, Materials, Science Forum, Vols. 52–53, Trans. -Tech., Aedermannsdorf, Switzerland (1990).
[123] A. Raveh, L. Martinu, S.C. Gujrathi, J.E. Klemberg-Sapieha, M.R. Wertheimer, Surf. Coat. Technol. 53 (1992) 275.
[124] J. Houska, J.E. Klemberg-Sapieha, L. Martinu, Surf. Coat. Technol. 203 (2009) 3770.

[125] N. Hellgren, M.P. Johansson, E. Broitman, L. Hultman, J.-E. Sundgren, Phys. Rev. B 59 (1999) 5162.
[126] R.E. Sah, B. Dischler, A. Bubenzer, P. Koidl, Appl. Phys. Lett. 46 (1985) 739.
[127] D. Lusk, M. Gore, W. Boardman, T. Casserly, K. Boinapally, M. Oppus, Diamond Relat. Mater. 17 (2008) 1613.
[128] L.S. Pan, D.R. Kania (Eds.), Diamond: Electronic Properties and Applications, Kluwer Academic, Dordrecht (1995).
[129] A. Feldman, Y. Tzeng, W.A. Yarbrough, M. Yoshikawa, M. Murakawa (Eds.), Applications of Diamond Films and Related Materials, Vol. 885, National Institute of Standards and Technology, Washington, DC (1995).
[130] C.F.M. Borges, M. Moisan, A. Gicquel, Diamond Relat. Mater. 4 (1995) 149.
[131] W.J. Zhang, Y.M. Chong, I. Bello, S.T. Lee, J. Phys. D: Appl. Phys. 40 (2007) 6159.
[132] C.Y. Chan, W.J. Zhang, S. Matsumoto, I. Bello, S.T. Lee, J. Crystal Growth 247 (2003) 438.
[133] H.Q. Li, K.M. Leung, K.L. Ma, Q. Ye, Y.M. Chong, Y.S. Zou, Appl. Phys. Lett. 91 (2007) 201918.
[134] H. Biederman, Plasma Polymer Films, Imperial College Press (2004).
[135] A. Alptekin, E. Sacher, G. Czeremuszkin, L. Martinu, M. DiRenzo, Electrochem. Soc. Proc. 97–8 (1998) 58.
[136] C.I. Butoi, N.M. Mackie, J.L. Barnd, E.R. Fisher, Chem. Mater. 11 (1999) 862.
[137] D. Zhang, M.J. Kushner, J. Vac. Sci. Technol. A 19 (2001) 524.
[138] E. Kay, J. Coburn, A. Dilks, Top. Curr. Chem. 94 (1980) 1.
[139] C.B. Labelle, K.K. Gleason, J. Vac. Sci. Technol. A 17 (1999) 445.
[140] A. Weber, R. Pochelmann, C.-P. Klages, J. Vac. Sci. Technol. A 16 (1998) 2120.
[141] U. Hetzler, E. Kay, J. Appl. Phys. 49 (1978) 5617.
[142] L. Martinu, H. Biederman, J. Nedbal, Thin Solid Films 136 (1986) 11.
[143] L. Martinu, J.E. Klemberg-Sapieha, in: N. Kaiser, H.K. Pulker (Eds.), Optical Interference Coatings, Springer (2003) 359.
[144] Y.H. Lee, K.K. Chan, M.J. Brady, J. Vac. Sci. Technol. A 13 (1995) 596.
[145] Y.H. Lee, Vacuum 51 (1998) 503.
[146] S. Larouche, H. Szymanowski, J.E. Klemberg-Sapieha, L. Martinu, S.C. Gujrathi, J. Vac. Sci. Technol. A 22 (2004) 1200.
[147] H. Szymanowski, O. Zabeida, J.E. Klemberg-Sapieha, L. Martinu, J. Vac. Sci. Technol. A 23 (2005) 241.
[148] J.-P. Masse, H. Szymanowski, O. Zabeida, A. Amassian, J.E. Klemberg-Sapieha, L. Martinu, Thin Solid Films 515 (2006) 1674.
[149] F. Arefi-Khonsari, F. Hellegouarc'h, J. Amouroux, J. Vac. Sci. Technol. A 16 (1998) 2240.
[150] J.H. Lee, D.S. Kim, Y.H. Lee, J. Electrochem. Soc. 143 (1996) 1443.
[151] K. Itoh, O. Matsumoto, Thin Solid Films 345 (1999) 29.
[152] T. Gato, W. Zhang, T. Hirai, Jpn. J. Appl. Phys. Part 1 38 (1999) 3668.
[153] J. Patscheider, S. Veprek, Plasma Chem. Plasma Process. 12 (1992) 129.
[154] C.E. Chryssou, C.W. Pitt, IEEE J. Quantum Electron. 34 (1998) 282.
[155] W.B. Henley, G.J. Sacks, J. Electrochem. Soc. 144 (1997) 1045.
[156] M. Seman, C.A. Wolden, J. Vac. Sci. Technol. A 21 (2003) 1927.
[157] C.G. Granqvist, Solar Energy Mater. Solar Cells 60 (2000) 201.
[158] M. Seman, C.A. Wolden, Solar Energy Mater. Solar Cells 82 (2004) 517.
[159] U. Kreibig, P. Zacharias, Z. Phys. 231 (1970) 128.
[160] D. Ricard, P. Roussignol, C. Flytzanis, Opt. Lett. 10 (1985) 511.
[161] F. Hache, D. Ricard, C. Flytzanis, U. Kreibig, Appl. Phys. A: Solids Surf. 47 (1988) 347.
[162] H.B. Liao, R.F. Xiao, J.S. Fu, H. Wang, K.S. Wong, G.K.L. Wong, Opt. Lett. 23 (1998) 388.
[163] J.-M. Lamarre, F. Billard, C. Harkati-Kerboua, M. Lequime, S. Roorda, L. Martinu, Opt. Commun. 281 (2008) 331.
[164] S. Veprek, J. Vac. Sci. Technol. A 17 (1999) 2401.
[165] A.A. Voevodin, J.P. O'Neill, J.S. Zabinski, Surf. Coat. Technol. 116–119 (1999) 36.
[166] J. Musil, Surf. Coat. Technol. 125 (2000) 322.

[167] P. Jedrzejowski, B. Baloukas, J.E. Klemberg-Sapieha, L. Martinu, J. Vac. Sci. Technol. A 22 (2004) 725.
[168] H. Holleck, in: A. Kumar, Y.W. Chung, J.J. Moore, J.E. Smugeresky (Eds.), Surface Engineering: Science and Technology I, Minerals, Metals and Materials Society (1999) 207.
[169] S. Veprek, A.S. Argon, Surf. Coat. Technol. 146–147 (2001) 175.
[170] J. Patscheider, T. Zehnder, M. Diserens, Surf. Coat. Technol. 146 (2001) 201.
[171] P. Jedrzejowski, J.E. Klemberg-Sapieha, L. Martinu, Thin Solid Films 426 (2003) 150.
[172] P. Jedrzejowski, J.E. Klemberg-Sapieha, L. Martinu, Thin Solid Films 466 (2004) 189.
[173] L. Hultman, J. Bareño, A. Flink, H. Söderberg, K. Larsson, V. Petrova, Phys. Rev. B 75 (2007) 155437.
[174] J. Houska, J.E. Klemberg-Sapieha, L. Martinu, Surf. Coat. Technol. 203 (2009) 3348.
[175] I. Zukerman, A. Raveh, Y. Landu, R. Weiss, R. Shneck, Y. Shneor et al., Surf. Coat. Technol. 201 (2007) 6171.
[176] T. Bell, H. Dong, Y. Sun, Tribol. Int. 31 (1998) 127.
[177] R. Snyders, E. Bousser, P. Amireault, J.E. Klemberg-Sapieha, E. Park, K. Taylor, Plasma Process. Polym. 4 (2007) S640.
[178] C. Campillo, S. Illias, C.F.M. Borges, M. Moisan, L. Martinu, New Diamond Front Carbon Technol. 11 (2001) 147.
[179] M. Azzi, M. Paquette, J.A. Szpunar, J.E. Klemberg-Sapieha, L. Martinu, Wear 267 (2009) 860.
[180] M.R. Wertheimer, L. Martinu, J.E. Klemberg-Sapieha, G. Czeremuszkin, in: K.L. Mittal, L. Pizzi (Eds.), Adhesion Promotion Techniques, Marcel Dekker, New York (1999) 139.
[181] J.E. Klemberg-Sapieha, D. Poitras, L. Martinu, N.L.S. Yamasaki, C.W. Lantman, J. Vac. Sci. Technol. A 15 (1997) 985.
[182] A.S. Da Silva-Sobrinho, M. Latrèche, G. Czeremuszkin, J.E. Klemberg-Sapieha, M.R. Wertheimer, J. Vac. Sci. Technol. A 16 (1998) 3190.
[183] J.E. Klemberg-Sapieha, L. Martinu, N.L.S. Yamasaki, C.W. Lantman, Thin Solid Films 476 (2005) 101.
[184] A. Bergeron, J.E. Klemberg-Sapieha, L. Martinu, J. Vac. Sci. Technol. A 16 (1998) 3227.
[185] A.S. Da Silva Sobrinho, N. Schühler, J.E. Klemberg-Sapieha, M.R. Wertheimer, M. Andrews, S.C. Gujrathi, J. Vac. Sci. Technol. A 16 (1998) 2021.
[186] A. Bergeron, D. Poitras, L. Martinu, Opt. Eng. 39 (2000) 825.
[187] S. Dahl, D. Rats, J. von Stebut, L. Martinu, J.E. Klemberg-Sapieha, Thin Solid Films 355–356 (1999) 290.
[188] K. Seshan (Ed.), Handbook of Thin-film Deposition Processes and Techniques: Principles, Methods, Equipment and Applications, William Andrew (2002).
[189] P.K. Chu, J.Y. Chen, L.P. Wang, N. Huang, Mater. Sci. Eng. R36 (2002) 143.
[190] H. Liang, B. Shi, A. Fairchild, T. Cale, Vacuum 73 (2004) 317.
[191] J.C. Sit, D. Vick, K. Robbie, M.J. Brett, J. Mater. Res. 14 (1999) 1197.
[192] R. Vernhes, O. Zabeida, J.E. Klemberg-Sapieha, L. Martinu, Appl. Opt. 43 (2004) 97.
[193] D. Bohling, M. Coda, R. Blacker, C. Burton, R. Gove, P. Murphy, in: Proc. 43rd Annu. Tech. Conf. of the SVC, Denver (2000) 222.
[194] R. Hora, C. Wohlrab, in: Proc. 36th Annu. Tech. Conf. of the SVC (1993) 51.
[195] R. Beckmann, K.D. Nauenberg, T. Naumann, U. Patz, G. Ieked, H. Hagedorn, in: Proc. 44th Annu. Tech. Conf. of the Society of Vacuum Coaters (SVC), Philadelphia (2001) 288.
[196] M.H. Blees, G.B. Winkelman, A.R. Balkenende, J.M.J. den Toonder, Thin Solid Films 359 (2000) 1.
[197] J.A. Dobrowolski, Chap. 42, in: M. Bass (Ed.), Optical Society of America's Handbook of Optics, McGraw–Hill, New York (1995).
[198] S. Pongratz, A. Zöller, J. Vac. Sci. Technol. A 10 (1992) 1897.
[199] U. Schulz, U.B. Schallenberg, N. Kaiser, Appl. Opt. 41 (2002) 3107.
[200] D. Poitras, L. Martinu, Appl. Opt. 39 (2000) 1168.
[201] J.E. Klemberg-Sapieha, L. Martinu, V. Fridman, D.E. Morton, in: Proc. of the 41st Annu. Tech. Conf. of Society of Vacuum Coaters (SVC), Chicago (1998) 138.
[202] A.C. Greenham, B.A. Nichols, R.M. Wood, N. Nourshargh, K.L. Lewis, Opt. Eng. 32 (1993) 1018.
[203] P.L. Swart, P.V. Bulkin, B.M. Lacquet, Opt. Eng. 36 (1997) 1215.

[204] R. Vernhes, A. Amassian, J.E. Klemberg-Sapieha, L. Martinu, J. Appl. Phys. 99 (2006) 114315.
[205] D. Poitras, S. Larouche, L. Martinu, Appl. Opt. 41 (2002) 5249.
[206] S. Larouche, L. Martinu, Appl. Opt. 47 (2008) 4321.
[207] D. Rats, D. Poitras, J.M. Soro, L. Martinu, J. von Stebut, Surf. Coat. Technol. 111 (1999) 220.
[208] D. Rats, J.M. Soro, L. Martinu, J. von Stebut, Surf. Coat. Technol. 123 (2000) 36.
[209] R. Vernhes, PhD Thesis, École Polytechnique de Montréal, Montréal, Québec, Canada, 2006.
[210] J.M. Mir, J.A. Agostinelli, J. Vac. Sci. Technol. A 12 (1994) 1439.
[211] K. Worhoff, P.V. Lambeck, A. Driessen, J. Lightwave Technol. 17 (1999) 1401.
[212] F. Bruno, M. del Guidice, R. Recca, F. Testa, Appl. Opt. 30 (1991) 4560.
[213] G. Giroult-Matlakowski, C. Charles, A. Durandet, R.W. Boswell, S. Armand, H.M. Persing et al., J. Vac. Sci. Technol. A 12 (1994) 2754.
[214] M. Hoffmann, P. Kopka, E. Voges, IEEE Photonics Technol. Lett. 9 (1997) 1238.
[215] W. Wirges, S. Bauer-Gogonea, S. Bauer, R. Gerhard-Multhaupt, L. Martinu, J.E. Klemberg-Sapieha, M.R. Wertheimer, in: Proc. SPIE 2213 (1994) 303.
[216] C. Wagner, J. Frankenberger, P.P. Deimel, IEEE Photonics Technol. Lett. 5 (1993) 1257.
[217] D.K.W. Lam, Appl. Opt. 23 (1984) 2744.
[218] S. Yokoyama, A.T. Nagata, Y. Kuroda, T. Doi, T. Namba, K. Miyake, J. Vac. Sci. Technol. A 13 (1995) 629.
[219] A. Malek-Tabrizi, S.I. Najafi, L. Martinu, in: S.I. Najafi, M.N. Armenise (Eds.), Functional Photonic and Fiber Devices, Vol. 2695, SPIE, Bellingham, WA (1996) 180.
[220] D.R. Beltrami, J.D. Love, A. Durandet, A. Samoc, C.J. Cogswell, Appl. Opt. 36 (1997) 7143.
[221] A.H. Mahan, Solar Energy Mater. Solar Cell 78 (2003) 299.
[222] S. Guha, J. Yang, J. Non-Cryst. Solids 352 (2006) 1917.
[223] A.V. Shah, J. Meier, E. Vallat-Sauvain, J. Wyrsch, U. Kroll, C. Droz, U. Graf, Solar Energy Mater. Solar Cells 78 (2003) 469.
[224] S. Guha, J. Yang, A. Banerjee, B. Yan, K. Lord, Solar Energy Mater. Solar Cells 78 (2003) 329.
[225] O. Vetterl, F. Finger, R. Carius, P. Hapke, L. Houben, O. Kluth, Solar Energy Mater. Solar Cells 62 (2000) 97.
[226] J. Yang, A. Banerjee, S. Guha, Solar Energy Mater. Solar Cells 78 (2003) 597.
[227] M. Zeuner, Private communication.
[228] H. Chatham, Surf. Coat. Technol. 78 (1996) 1.
[229] N. Schühler, A.S. da Silva Sobrinho, J.E. Klemberg-Sapieha, M. Andrews, M.R.S. Wertheimer, in: Proc. 39th Annu. Tech. Conf. of the Society of Vacuum Coaters (SVC), Philadelphia, PA (1996) 285.
[230] A.S. Da Silva Sobrinho, G. Czeremuszkin, M. Latrèche, M.R. Wertheimer, J. Vac. Sci. Technol. A 18 (2000) 149.
[231] J.D. Affinito, M.E. Gross, C.A. Coronado, G.L. Graff, E.N. Greenwell, P.M. Martin, in: Proc. 39th Annu. Tech. Conf. of the Society of Vacuum Coaters (SVC) (1996) 397.
[232] M.E. Gross, P.M. Martin, L.C. Olsen, G.L. Graff, P.E. Burrows, C.C. Bonham et al., in: Proc. 46th Annu. Tech. Conf. of the Society of Vacuum Coaters (SVC) (2003) 89.
[233] J. Madocks, J. Rewhinkle, L. Barton, Mater. Sci. Eng. B 119 (2005) 268–273.
[234] C.G. Granqvist, Solar Energy Mater. Solar Cells 92 (2008) 203.
[235] T. Ellison, B. Dotter, M. Izu, S. Ovshinsky, in: Proc. 40th Annu. Tech. Conf. of the Society of Vacuum Coaters (SVC) (1997) 309.
[236] D. Garg, P.B. Henderson, R.E. Hollingsworth, D.G. Jensen, Mater. Sci. Eng. B 119 (2005) 224.
[237] S. Guruvenket, D. Li, J.E. Klemberg-Sapieha, L. Martinu, J. Szpunar, Surf. Coat. Technol. 203 (2009) 2905.
[238] Y.T. Cheng, C.M. Cheng, Appl. Phys. Lett. 73 (1998) 614.
[239] A. Leyland, A. Matthews, Wear 246 (2000) 1.
[240] J. Musil, M. Jirout, Surf. Coat. Technol. 210 (2007) 5148.
[241] D. Galvan, Y.T. Pei, J.T.M. De Hosson, Surf. Coat. Technol. 200 (2006) 6718.
[242] S. Hassani, M. Bielawski, W. Beres, L. Martinu, M. Balazinski, J.E. Klemberg-Sapieha, Surf. Coat. Technol. 203 (2008) 204.
[243] J.E. Klemberg-Sapieha, L. Martinu et al., unpublished.

[244] S. Hassani, J.E. Klemberg-Sapieha, M. Bielawski, W. Beres, L. Martinu, M. Balazinski, Wear 265 (2008) 879.
[245] C. Donnet, A. Erdemir (Eds.), Tribology of Diamond-Like Carbon Films: Fundamentals and Applications, Springer, New York (2008).
[246] R. Butter, M. Allen, L. Chandra, A.H. Lettington, N. Rushton, Diamond Relat. Mater. 4 (1995) 857.
[247] P.E. Sinnet-Jones, J.A. Wharton, R.J.K. Wood, Wear 259 (2005) 898.
[248] A.S. Shanbhag, J.J. Jacobs, J. Black, J.O. Galante, T.T. Glant, J. Biomed. Mater. Res. 28 (1994) 81.
[249] H.F. Hildebrand, J.-C. Hornez, J.A.H. Helsen, Chap. 9, in: J. Breme (Ed.), Biological Response and Biocompatibility, John Wiley and Sons (1998).
[250] O. Zabeida, J.E. Klemeberg-Sapieha, L. Martinu, unpublished.
[251] S.D.A. Lawes, M.E. Fitzpatrick, S.V. Hainsworth, J. Phys. D.: Appl. Phys. 40 (2007) 5427.

CHAPTER 10

Unfiltered and Filtered Cathodic Arc Deposition

André Anders

> *All the colours make their first appearance about the edge of the circular spot. More explosions make them expand towards the extremity of the space first marked out; while others succeed in their places; till, after thirty or forty explosions, three distinct rings appear, each consisting of all colours.*
>
> (Joseph Priestley, describing interference colors of oxide coatings
> on glass by pulsed cathodic arcs, 1775)

10.1 Introduction

The deposition of films by cathodic arcs is very likely the oldest physical vapor deposition (PVD) technology. First coatings, observed by Joseph Priestley in the 1760s [1, 2], were of course unintentional. Yet, Priestley's description contains a number of surprising details given the hindsight of today's knowledge. Priestley used a bank of Leyden jars (early capacitors) to study the effects of electricity. At that time it was customary to use brass chains to conduct electricity, and as the current passed from link to link, short arcs in air occurred. Coincidentally, Priestley placed a glass plate below the chain, and each short arc left a coating on the glass surface (Figure 10.1). The main observations included well-adherent coatings, the formation of oxide films, and the peripheral deposition of fine black dust, which very likely were macroscopic quantities of nanoparticles formed in air.

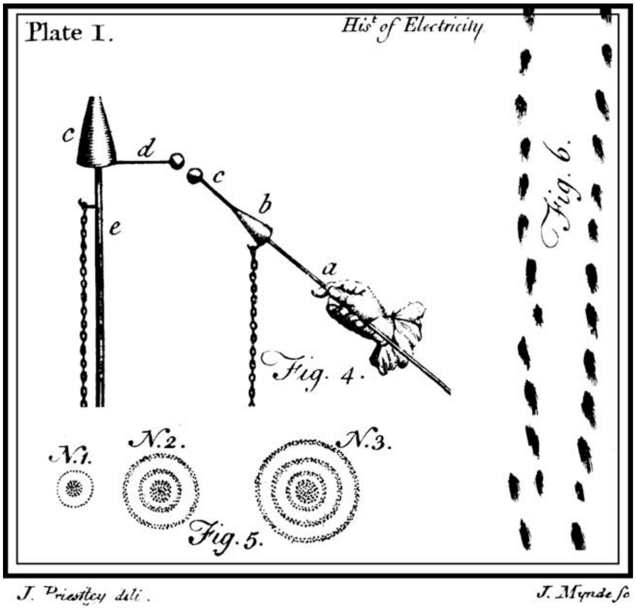

Figure 10.1: Deposition of metal and oxide with cathodic arcs in air by Joseph Priestley in the mid-1700s: metal chains were used as electrical conductors (left), and the short arcs between links produced coatings (the line of dots on the right). (Adapted from [2].)

We have come a long way in understanding cathode and deposition processes, as described in a recent book [3], and summarized in this chapter.

Cathodic arcs are of great interest to the coatings community for several reasons. Among them are: (1) the high deposition rates of metal and compound films; (2) generally good to very good adhesion of coatings; (3) the relative ease of forming hard and decorative coatings; and (4) the relatively wide range of useable partial pressure of reactive gas when forming stoichiometric films. On the negative side, the formation of macroparticles and their incorporation into the coating degrades the quality of the film. Deleterious effects in corrosion tests are obvious and post-deposition polishing and buffing is often necessary for decorative applications.

In this chapter, we follow the destiny of cathode atoms from the cathode surface, the birth place of cathode spots, phase transition to expanding plasma, travel of plasma ions through the interelectrode space, until they impact onto the substrate surface and become inserted below the substrate's surface (subplantation film growth).

Besides metal plasma generation and deposition, this chapter also addresses the macroparticle issue and practical measures, such as macroparticle filters, to mitigate their deleterious effects. Furthermore, examples are given for the construction of arc sources and other hardware. The chapter is concluded with a few important examples of cathodic arc plasma deposition, both unfiltered and filtered. Detailed accounts of film growth processes are not given in this chapter because they can be found elsewhere in this book.

10.2 Cathodic Arc Plasma Generation

10.2.1 Cathode Processes

10.2.1.1 Introduction

The generation of metal plasma at cathode spots is the central enabling process for coatings made by cathodic arc deposition technology. Although it is so important, the details of the cathode processes are not fully understood; however, great progress has been made in recent years in terms of modeling and plasma diagnostics.

The processes at the cathode appear strange even to the scientists and engineers who are generally familiar with discharge plasmas. The plasma root or attachment on the cathode is localized in bright, tiny spots that appear to move quickly, more or less randomly, on the cathode surface. In the presence of an external magnetic field, spot motion appears to be steered in a preferred direction, the $-\mathbf{j} \times \mathbf{B}$ or anti-Amperian direction. The cathode material transitions from a solid to dense plasma at these spots, and the dense cathode plasma in turn expands rapidly into the vacuum or low-pressure gas ambient.

The exact structure and dynamics of cathode spots are still the subject of research; however, there is now plenty of evidence that cathode processes are best described and understood with models that are based on stochastic and fluctuating properties. Consistently, this leads the concept of fractal cathode spots, which can accommodate the broad range of spatial patterns as well as the sets of characteristic times. In fact, the fractal model approach teaches to look for a relation between characteristic spatial patterns and time constants in the dynamic evolution on the one hand and the limits of spatial and temporal resolution on the other.

For example, over the years, there had been a debate on the true current density of cathode spots. Various techniques were employed delivering different answers. The current density plays a central role in cathode models because it is critically important for the power density distribution and energy balance which, in turn, govern all processes of electron emission, phase transitions, and plasma production. Once the current density has been determined, theoreticians can adjust their model accordingly and hope to reproduce other arc plasma features. The catch is that there is no single true value of a current density in light of a fractal model, even when considering one material under very specific conditions. Rather, the current density is a physical quantity showing self-similar properties in both time and space. This is nothing unusual for those dealing with fractals but may be difficult to comprehend in the field of plasmas and thin film growth. Therefore, a section will be devoted to summarizing the fractal approach to arc phenomena.

10.2.1.2 Arc Modes

The *cathode* processes determine the type of discharge. Arc discharges are characterized by a collective emission of electrons, as opposed to individual events of electron emission. For example, impact of an individual ion on a glow discharge cathode releases one secondary electron with a certain probability (yield), which is less than unity. A collective mechanism, in contrast, produces conditions where many electrons are released. For example, by heating the cathode, a significant number of electrons are in the high-energy tail of the Fermi energy distribution function, and those electrons can overcome the potential barrier and escape from the solid. This example is called thermionic emission, and the associated discharge is called a *thermionic arc*.

There are two main classes or modes of arc discharges [4]. One is the just-mentioned thermionic arc, and the other is the *cathodic arc*. The cathode processes of the cathodic arc mode are much more complicated and require a discussion of much greater detail than the thermionic arc because both high-temperature and high-electric field strength on the cathode surface are involved. In addition, cathodic arc processes are time dependent and fluctuating and include phase transitions and the destruction of the cathode.

There are three simple tests or criteria which allow us to distinguish thermionic from cathodic arcs. In the first test, we look at the cathode and evaluate the size or type of the emitting area.

The thermionic arc appears either spotless or with a large (e.g. mm size), more-or-less stationary spot. The cathodic arc, in contrast, is characterized by tiny spots, often many of them, that appear to move quickly on the cathode surface. The second test is to measure the arc voltage, i.e. the potential difference between cathode and anode, in a time-resolved manner, e.g. using an oscilloscope. The thermionic arc shows a well-defined, low-noise voltage level, whereas the cathodic arc shows a strongly fluctuating voltage. There are other tests such as locking at the fluctuations of the emitted light or of the composition of the plasma, but those tests are usually more involved. Finally, a third, simple test is to detect radio noise, for example using a simple radio receiver [5].

At this point, it is stressed that *two* fundamental arc modes exist, and that this chapter deals with cathodic arcs because only that mode delivers copious quantities of plasma of the cathode material.

To round up this introduction, *anodic arcs* need to be mentioned, too. This term is used to emphasize the origin of the (partially) ionized material between arc electrodes. In contrast to cathodic arcs, where the plasma species are ‘born’ at the cathode, the ionized vapor of anodic arcs comes from the anode [6]. This requires the anode to be at very high temperature so that evaporation can occur. The anode is generally not cooled but thermally isolated to reach very high temperature. It could be the anode base material that is evaporating, but more often the anode is designed as a crucible containing the material to be evaporated. The anodic arc could be designed to operate with a thermionic or cathodic arc cathode. In the former, the cathode is the source of electrons which heat the anode and (partially) ionize the vapor. In the latter, the cathode is the source of electrons and cathode material. This configuration is utilized in the *hot refractory anode vacuum arc* [7] where the cathode material is transported to the anode and re-evaporated. This is one possible approach to ion plating where the coating is produced with no or minimal macroparticle content yet the benefit of self-ion assistance is available.

10.2.1.3 Physics of Electron Emission

We may start considering electron emission with questions like: Why is the cathode active but the anode passive? What is so special about the cathode that the cathode determines the type of discharge, and not the anode?

The answer can be found when looking at the motion of electrons in metals, in plasmas, and at the interface between metal and plasma. Free electrons in the conduction band or in the plasma can carry the current freely (apart from interaction with other electrons and lattice atoms (in the solid) or ions (in the plasma)). However, there is a potential barrier on the surface between the Fermi level inside the metal and the potential in vacuum (or plasma). This potential barrier keeps electrons from spilling out. The height of the barrier is known as the *work function*. In order for electrons to move from the cathode’s Fermi level to the plasma level, they need to overcome the barrier by some mechanism, and this mechanism requires energy. In contrast,

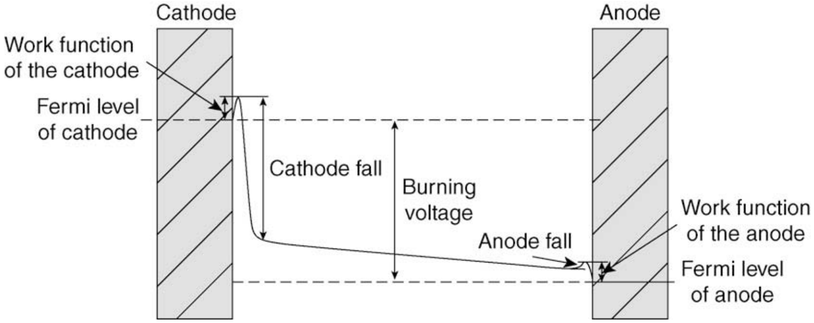

Figure 10.2: Potential distribution between anode and cathode of a cathodic arc. In this presentation, the common convention is adopted that the potential is plotted as negative potential to account for the negative charge of the electron. For details see text.

electrons from the plasma arriving at the anode simply fall into the Fermi level of the anode and the excess energy will become available (this explains why anodes tend to get hot without intentional heating).

Figure 10.2 illustrates the situation using the common convention that a negative potential is plotted to account for the negative charge of the electron. In doing so, a barrier for the electron motion appears as a hill, and an electron-accelerating potential gradient goes downhill. Consistently, the Fermi level of the anode is displayed lower than the Fermi level of the cathode. Figure 10.2 shows the work functions of the two electrodes (a bit pushed out of the metal for better visibility), the cathode fall (which in this negative potential presentation is really a fall), a relatively flat potential in the interelectrode gap, and an anode fall. The anode fall serves to balance the flow of plasma electrons to the anode in such a way that current is equal to the current determined by the electrical circuit. The sign of the anode fall can be either way. As shown, the anode 'fall' is actually a small barrier which will appear if the anode is very large and there is an oversupply of electrons.

Let us return to the question of what mechanism allows electrons to overcome the cathode work function. Electrons in a metal have a Fermi energy distribution function

$$f_{\mathrm{F}} = (E, T) = \frac{1}{1 + \exp\left(\frac{E - E_{\mathrm{F}}}{\mathrm{k}T}\right)} \tag{10.1}$$

which describes the probability that a state of energy E will be occupied in thermal equilibrium at a temperature T. The Fermi energy, E_{F}, can be defined as the highest energy of occupied states at temperature $T = 0$; it depends only on the density:

$$E_{\mathrm{F}} = \left(\frac{\hbar^2}{2m_{\mathrm{e}}}\right)\left(3\pi^2 n\right)^{2/3} \tag{10.2}$$

where $\hbar = h/2\pi$, h is Planck's constant, k is Boltzmann's constant, m_e is the electron mass, and n is the electron density. The Fermi distribution implies that only a small fraction of electrons can acquire energy of order kT above the Fermi energy. However, if the temperature is sufficiently high, some electrons can overcome the barrier in a classical way, namely when

$$E_z \geq \phi \tag{10.3}$$

where $E_z = m_e v_z^2/2$ is the kinetic energy of an electron in the z-direction, the direction perpendicular to the surface, and ϕ is the work function of the cathode material. The emission current density is then

$$j_{\text{thermionic}} = en\,(E)\,v_z \tag{10.4}$$

where $n(E)$ is the density of electrons satisfying Condition (10.3). For $T = 0$ obviously no electrons satisfy (10.3). One can calculate $n(E)$ by integrating the distribution function from $-\infty$ to $+\infty$ in the x and y directions and from ϕ to ∞ in the z-direction. At elevated temperature, the high-energy tail of the Fermi distribution (10.1) is dominated by the exponential term, where $(E - E_F) > \mathrm{k}T$ and the quantum-statistical Fermi distribution can be approximated by the classic Boltzmann distribution,

$$f_B = (E, T) = \exp\left(-\frac{E - E_F}{\mathrm{k}T}\right) \tag{10.5}$$

The result of the integration, using the Boltzmann distribution, is

$$j_{\text{thermionic}} = AT^2 \exp\left(-\frac{\phi}{\mathrm{k}T}\right) \tag{10.6}$$

where

$$\mathrm{A} = \frac{4\pi e m_e \mathrm{k}^2}{h^3} = 1.202 \times 10^6\ \mathrm{A/m^2K^2} \tag{10.7}$$

Equation (10.6) is the well-known Richardson–Dushman equation for *thermionic emission*, and A is called the universal Richardson constant. This is the mechanism for thermionic arcs, which can be stationary: note that time does not appear in those equations.

For cathodic arcs we have to go further and consider the electric field that exists near the cathode surface, $E_c = -dV/dz$, which can be very strong even though the cathode fall is only ~20 V because the cathode fall thickness can be extremely small. The electric potential distribution associated with a strong field narrows the work function barrier, as already indicated in Figure 10.2. Therefore, electrons have a chance not only to go classically *over* the barrier but also to tunnel quantum-mechanically *through* the barrier. The latter is called *field* *emission*. The derivation of the field emission current density and resulting Fowler–Nordheim formula is rather complicated and the interested reader is referred to the specialized literature [3, 8–10].

In a real cathodic arc situation, both high local temperature and high electric field strength are present. This leads to a non-linear amplification of the emission process, which is called *thermo-field emission* [11, 12]. The full equations are indeed lengthy so that researchers have developed approximate expressions. For example, Hantzsche's [9] formula for a typical material with a work function $\phi = 4.5\,\mathrm{eV}$ is based on a number of additive and harmonic combinations of thermionic and field emission,

$$j_{\mathrm{TF}}\left(T, \mathcal{E}\right) \approx k\left(AT^{2} + B\mathcal{E}^{9/8}\right)\exp\left[-\left(\frac{T^{2}}{C} + \frac{\mathcal{E}^{2}}{D}\right)^{-1/2}\right] \tag{10.8}$$

where $A = 120$, $B = 406$, $C = 2.727 \times 10^{9}$, $D = 4.252 \times 10^{17}$; the units for Eq. (10.8) are j_{TF} in A/cm^{2}, temperature T in K, electric field $\mathcal{E}$ in V/cm; the symbol $\mathcal{E}$ is used here to not confuse it with the symbol for energy, E.

Up to now, time has not appeared in any of those emission mechanisms and related equations. This changes completely when we consider the energy balance of an electron-emitting site. Two main processes lead to temperature enhancement: ion bombardment from the plasma, and Joule (resistive) heating of the cathode by the emission current (for a more detailed discussion, including the Nottingham effect, see [3]). Cooling of a site is mainly by heat conduction, electron emission, and radiation. Heating and cooling generally do not balance and therefore the temperature becomes a time-dependent variable. In particular, a positive feedback can evolve if the field is very strong and emission has already reached a high level: the Joule heating of the emitting location leads to higher temperature, which further enhances the emission, which in turn leads to greater Joule heating and yet higher temperature. Locations where this occurs can evaporate in an explosive manner, leading to a new form of electron emission called *explosive electron emission* [13].

Explosive electron emission is inherently non-stationary and always associated with the formation of plasma of the emitting material. Therefore, it is not just electron emission but emission of electrons and ions, and we simply refer to the process as *explosive emission*.

Mesyats and others [13–15] extensively studied explosive emission and concluded that a minimum amount of energy needs to be invested to explode (ignite) an emission center. From the theory of wire explosions [16] they adopted that the current density, j, and explosion delay time, t_{d}, satisfy

$$\int_{0}^{t_{\mathrm{d}}} j^{2}\mathrm{d}t \geq \bar{h} \tag{10.9}$$

Table 10.1: Specific action, $\bar{h}$, for selected materials (from [13, 17])

Material	$\bar{h}$ ($A^2 s/m^4$)
C	1.8
Al	18
Fe	14
Ni	19
Cu	41
Ag	28
Au	18

where $\bar{h}$ is called the specific action whose value depends on the cathode material but is approximately independent on current density, wire cross-section, or other discharge quantities (Table 10.1).

The minimum action can be considered the quantum of the explosive process, and therefore they introduced the term *ecton* (derived from *e*xplosion *c*enter, with the ending -ton in analogy with other particles or quasi-particles like photon, proton, exciton, etc.). To illustrate the concept: under certain conditions, each ecton is associated with the emission of about 10^{11} electrons within a time span of about 10 ns. The explosive or ecton phase is generally much shorter than the overall cycle or lifetime of an emission center.

The existence of a minimum action for spot operation can also be put in relation to the long-known fact that the arc current cannot be arbitrarily small. Depending on the cathode material and surface conditions, and the kind of background gas, if any, the arc discharge tends to chop and extinguish spontaneously. The minimum current where this occurs is called the chopping current [18, 19]. One wants the chopping current to be small (e.g. a few amperes) because the abrupt termination can generate high voltages by induction, which in fact may exceed the safe operational specifications and can cause harm to the operator or equipment.

10.2.1.4 Stages of an Emission Center

At this point it is clear that electron emission in cathodic arcs is a non-stationary process. The terms emission center and cathode spot were introduced, although their relationship requires clarification, which will be given when discussing the fractal properties of cathode spot.

One may think of an emission center as a location on the cathode surface where one can describe the evolution of electron and plasma generation. The evolution may be divided into four stages: (1) the pre-explosion stage; (2) the explosive emission stage; (3) the immediate postexplosion stage, where cool-down has started but electron emission and evaporation are still large; and (4) the final cool-down stage. Each of the four stages is highly dynamic. The ignition of an emission center is a very important element to understanding cathodic arcs. In this context, ‘ignition’ is not the initial triggering of the arc discharge, but the arc’s perpetual and repetitive mechanism to ‘stay alive.’

(1) The pre-explosion stage

Each location on the surface might be a candidate for the ignition of an emission center but in reality each location has its own history and properties such as the local work function, geometric features, surface coverage by oxide or water, etc. Some locations can be presumed to be more favorable to experience the ignition of an emission center. The conditions will be such that the local energy input will be higher than at neighboring locations owing to the specific local properties and their relation to the plasma and sheath conditions produced by predecessor emission sites. The conditions are favorable if the local work function is low and the field is enhanced owing to the presence of dielectric contamination and/or the presence of microprotrusions or nanoprotrusions. If such favorable conditions are coupled to a very high electric field strength (i.e. thin sheath due to high plasma density), and a high intensity of ion bombardment, the local energy input can lead to electron emission with thermal runaway, bringing the location to stage (2).

(2) The explosive emission stage

This stage is at the heart of the ecton model developed by Mesyats and co-workers [13, 20] mentioned above; the key feature is the thermal runaway in which electron emission and Joule heating close an amplifying feedback loop. The microexplosion causes destruction (erosion) of a microvolume, which is later evident as a microscopic crater on the cathode surface.

High-resolution, fast optical diagnostics indicate that the sequence of explosive events is rapid. For example, very fast optical imaging of very low current arcs, with 3–12 A, shows bursts of light every 50–70 ns, with the most intense phases having a duration of 10–20 ns [21].

(3) The immediate postexplosion stage

As long as the freshly formed crater is very hot, most likely still having a surface layer of molten cathode material, and the nearby plasma is very dense, electron emission remains strong by field-enhanced thermionic emission. The latter is thermionic emission in which the work function barrier ϕ is reduced (Schottky reduction) but does not reach the level of non-linear combination of thermionic emission and field emission (thermo-field emission). Besides electron emission, evaporation occurs from the pool of liquid material [22]. The neutral vapor represents a medium of low conductivity choking the flow of current. This blockage or choking greatly contributes to the apparent spot motion, as explained later.

Yet another effect is the plasma pressure acting on the liquid, which yields and thereby gives rise to the generation of microscopic droplets, generally known as macroparticles.

(4) The final cool-down stage

In the final stage, thermal conduction increases the hot area but the temperature decreases, and with it the electron emission ceases exponentially; see the temperature dependence of the Richardson equation (10.6). The explosively formed plasma has expanded, its density is lowered, therefore the cathode sheath thickness has increased, and the electric surface field is also reduced. Yet, this stage can be important to the overall cathode erosion since the hot surface may still deliver metal vapor, especially when the cathode material is of high vapor pressure.

This qualitative description of the stages of an emission center does not really address why the intense emission of this site cannot be maintained. We need to consider: What are the driving forces for the inevitable dynamics of the emitting system?

There are several factors, as follows. First, and this is perhaps most easily to understand, heat conduction leads to an increase in the area of the emission site, and this means that the dissipated power is spread over a larger area, hence the areal power density decreases with time.

Second, owing to the increase in resistance with temperature for all metals, $d\rho/dT > 0$, the region of the cathode bulk directly under the cathode spot is more resistive than all other areas or parts of the cathode. Hence, if there was an alternative, less resistive way for the current to flow, the current would switch to the new path.

Third, and most importantly, and somewhat ironically, the emission center itself builds a highly resistive barrier against current flow. In the explosive stage, the cathode matter transitions from the solid to the plasma phase, and it may initially bypass the gas phase by circumnavigating the critical point in the phase diagram [23]. At this stage, the most resistive zone for the current path is the non-ideal plasma phase. However, as time passes (and here we consider some tens of nanoseconds!), the reduced areal power density leads to a change of the path in the phase diagram: the material has now the time to transition through all conventional phases: solid–liquid–gas–plasma. From those four phases, the gas phase is by far the most resistive phase. Solid and liquid metal, and metal plasma are good conductors, but metal gas (vapor) is not! *The metal vapor chokes the flow of electricity*. As the growth of the emission area continues, the power density and related local surface temperature are reduced, electron emission decreases rapidly, though there may be still significant evaporation from the hot crater left by the explosion. At this point, the composition of the gas or plasma in front of the site becomes increasingly influenced by neutral vapor, and indeed the current transfer capability suffers greatly.

Fourth, in this situation, competition kicks in! The dense plasma near the emission site may have started a microexplosion at a new site. Now, the new site and the older, much larger site are electrically in parallel, and the path of lower resistance (i.e. where less metal vapor is hindering) takes over the current, which accelerates the death of the original emission site because less power is dissipated there. The low-conducting vapor mechanism took its toll.

Macroscopically, we see sequences of ignition, evolution, and death of emission sites, and we interpret this as cathode spot motion: it is a virtual motion based on the life cycle of emission sites.

10.2.1.5 Random Motion

In the absence of an external magnetic field, the probability of ignition of a new emission site is isotropically distributed, i.e. a new emission site could ignite with equal probability in any direction from the existing emission center. This makes the apparent motion of spots random, and indeed a good approximation of the actual motion is given by the random walk model [24, 25].

In this model, one assumes that each displacement is a small elementary step of step length s, which takes an average elementary time τ. Considering a *two*-dimensional random walk (i.e. a walk on a surface), the probability $P(R)$ for a total displacement to be in the interval $(R, R + dR)$, with $R = |\mathbf{R}|$, as measured from the starting point, is given by [26]

$$P(R)\,dR = \frac{R}{2Dt}\exp\left(-\frac{R^2}{4Dt}\right)dR \text{ for } t >> \tau \tag{10.10}$$

The function $P(R)$ is known as the Raleigh distribution. The diffusion constant, D, contains the parameters of the elementary step:

$$D = \frac{1}{4}\frac{s^2}{\tau} \tag{10.11}$$

The diffusion constant is material dependent; for example Jüttner measured $D = (2.3 \pm 0.6) \times 10^{-3}\ \text{m}^2/\text{s}$ for copper [27] and $D \approx 10^{-3}\ \text{m}^2/\text{s}$ for molybdenum [28], and Beilis et al. [29] determined $(1 \pm 0.3) \times 10^{-3}\ \text{m}^2/\text{s}$ for copper and $(4 \pm 1) \times 10^{-4}\ \text{m}^2/\text{s}$ for CuCr contact material.

The mean value for displacement is

$$\langle R \rangle = \int_0^\infty R\,P(R)\,dR = (\pi D t)^{1/2} = \frac{s}{2}\sqrt{\pi\frac{t}{\tau}} \tag{10.12}$$

and the observable, apparent spot velocity follows as

$$v_{\text{spot}} = \frac{d\langle R \rangle}{dt} = \frac{1}{2}\sqrt{\frac{\pi D}{t}} = \frac{s}{4}\sqrt{\frac{\pi}{t\tau}} \tag{10.13}$$

According to (10.13), and in contrast to steered motion which is dealt with in the next section, the apparent velocity of random motion decreases as the observation time increases.

This approach can be refined by modifying the probability distribution. For example, one may assume that the walker (i.e. the emission center) avoids locations for some time where ‘he’ has been before, and/or previously visited places may become preferred places after some time. Both features have been observed experimentally and can be explained by the time dependence of surface conditions and emission properties [30].

The close relation of random walk and Brownian motion is one of the many arguments why cathode spots have fractal properties [31]. The well-known Brownian motion is the scaling limit of random walk. Random walk is a discrete fractal exhibiting stochastic self-similarity on large scales, but self-similarity is cut off as scales approach the elementary step width s. Brownian motion in two dimensions is a true fractal showing self-similarity on all scales [32]. Brownian motion has the fractal (Hausdorff) dimension 2.

10.2.1.6 Steered Motion

Anything that breaks the symmetry will lead to deviations from the random walk. For example, the cathode could have a scratch, or an area of surface contamination, or an interface to a different material, or an external magnetic field could be present. In all of these cases, spot ignition may be preferred at certain locations, generally where the electric surface field is enhanced. Of special interest is the use of an external magnetic field because plasma production is not influence by any foreign material yet the most likely direction of the apparent spot motion can be predicted and influenced. The mechanism of how the symmetry is broken has stirred a lot of thinking and speculation, leading to a great proliferation of ideas and models [3].

The most convincing approach to date is the Jüttner–Kleberg model [30, 33] which is based on high-resolution observations of the emission of the microscopic plasma jets from active emission sites. The plasma density is higher in the direction of such jets, and therefore the sheath thickness is thinner, which leads to a higher electric surface field and enhances the probability of high electron emission and thermal runaway, i.e. the ignition of a new emission site (Figure 10.3).

The ejection of macroscopic plasma jets is not isotropic when a transverse (parallel to the cathode surface) magnetic component is present. This leads to a preferred direction in which new emission sites are ignited. The spot appears to be magnetically steered. The plasma column is bent in the Amperian $\mathbf{j} \times \mathbf{B}$ direction, though the virtual motion is to the opposite (the anti-Amperian or retrograde) direction.

As experimentally shown, the emission of the microscopic plasma jets is not exactly in the retrograde direction but rather it is statistically distributed with a high likelihood to be $\pm 45^\circ$

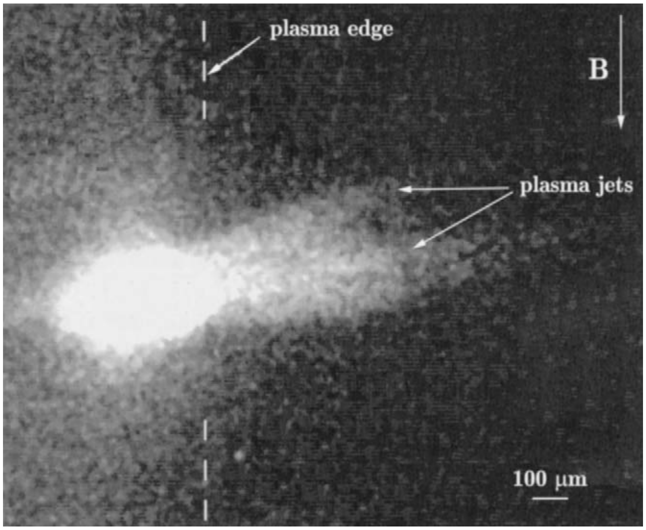

Figure 10.3: Ejection of two jets into approximate retrograde direction. The intensity of light emission of the plasma jets is weaker than the emission from the spot itself, and therefore the exposure was selected such as to make the jets visible, while the cathode spot is overexposed. (Adapted from [33].)

with respect to the retrograde direction. Therefore, the retrograde motion is actually composed of little microscopic zig-zag ignitions of new emission sites.

The average velocity of the steered motion increases with magnetic field in a roughly proportional manner,

$$v_{\mathrm{steered}} = cB_{\mathrm{t}} \tag{10.14}$$

where c is a material constant that also depends on the surface conditions, and B_{t} is the field parallel to the cathode surface. The value of c can vary greatly; for conditions where type 1 spots are observed (surfaces with non-metallic layers, non-conditioned surfaces), c can reach 1000 m/(s T) [34], whereas c-values of about 60 m/(s T) and 200 m/(s T) were determined for type 2 (clean) copper and CuCr cathodes, respectively [35]. The value can be even smaller when the cathode is very hot [36].

When the magnetic field vector has a transverse and normal component, i.e. it is tilted with respect to the surface normal, the direction of the virtual motion is also tilted to the retrograde direction (Figure 10.4). The angle between retrograde direction and actual direction of apparent motion is often called the Robson angle [35, 37, 38].

Steered spot motion is often used to control arc cathode erosion in practical arc plasma sources. It will be further discussed in Section 10.3.

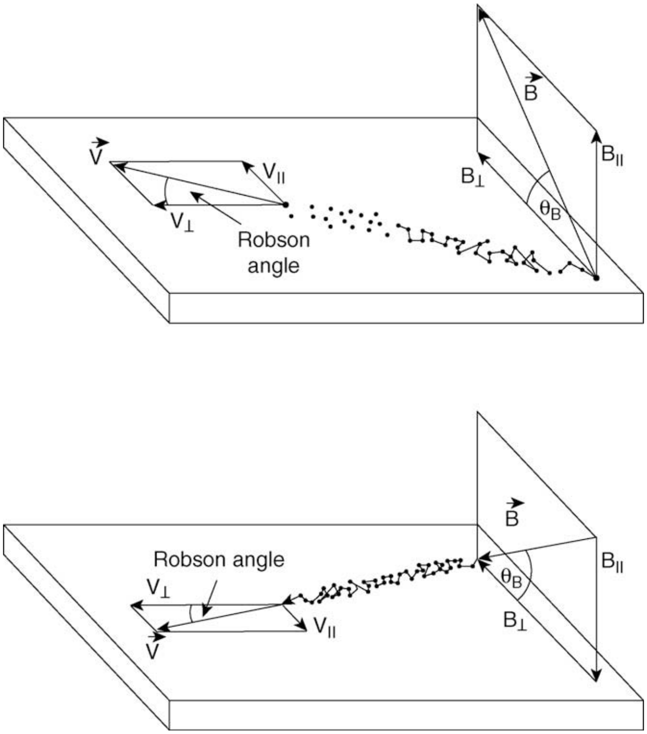

Figure 10.4: Illustration of the direction of the apparent motion when the magnetic field vector is tilted relatively to the cathode normal.

10.2.1.7 Fractal Nature of Cathode Processes

Fractals are mathematical, or physical/chemical/biological objects of the real world that show self-similarity [39]. That means they are invariant to scaling, i.e. to *multiplicative* changes of scale. Self-similarity may be discrete or continuous, deterministic or probabilistic.
Power laws

$$f(x) = cx^{\alpha} \tag{10.15}$$

are an abundant source of self-similarity [32], where c and α are constants, because multiplication with a constant preserves that $f(x)$ is proportional to x^{α}. Therefore, one fruitful approach to fractal modeling is to look for *power laws* describing the physical phenomena. There are several phenomena in cathodic arcs showing fractal properties, among them the random walk of emission centers [24, 25], the $1/f$ noise of ion current [40] and arc voltage [41], the fractal dimensions of about 2 for arc traces left by the spot's random walk [42], and the self-similarity in the patterns of emitted light [43, 44].

The fractal approach to cathodic modeling implies that a number of conventional assumptions are not applicable at all times; this includes a simplified layer structure of the cathode zone (it may well be used for the postexplosion stage), the assumption of a typical current density, size of the spot, etc. Instead, those properties are self-similar down to a physical cutoff size or time. One may consider the parameters associated with ectons as the lower physical cutoff limits. However, until now, no convincing lower limit has been demonstrated: ever smaller and faster properties have been detected as the spatial and temporal resolution of the instrumentation improved.

The simple question 'What is a cathode spot?' does not have a simple answer, but the definition 'A cathode spot is an assembly of emission centers showing fractal properties in spatial and temporal dimensions' captures the essential elements [3].

10.2.2 Properties of Cathodic Plasmas

10.2.2.1 Plasma Density

In this section we look at the expanding, interelectrode plasma, which is much more accessible than the plasma-producing cathode processes. The plasma properties are largely determined by the cathode processes, and therefore plasma diagnostics far from the spots helps to uncover the mysteries of the cathode spots [45].

As the generation of plasma is governed by the perpetual ignition, development and death of emission centers, plasma generation occurs in bursts; and the local plasma density is therefore strongly fluctuating or noisy. It is also clear that not all ions have the same velocity; rather, there is a broad velocity distribution which itself is noisy. As the plasma expands and flows away from the emission center, the fast ions from one plasma-generating burst will overtake the slow ions of the previous burst, and therefore density and ion velocity distribution are interrelated. In light of this, density values published in the literature have a meaning only in the time-averaged sense.

Electrons emitted from the cathode have to find the anode to close the electric circuit. Through electron–ion interaction (sometimes called electron–ion friction), the plasma tends to drift to the anode. The plasma expansion can generally be approximated by a cosine distribution

$$n \sim \cos^{\alpha} \vartheta \tag{10.16}$$

where ϑ is the angle to the surface normal. The exponent α describes how much the plasma plumes along the surface normal. In one extreme case, the anode may be large (i.e. whole chamber) and symmetric with respect to the cathode location, and no external field is present [46]. Then $\alpha \to 0$ and one gets a nearly spherical distribution. In many cases, a dedicated anode is used, and the expansion shows pluming with $\alpha > 1$.

An alternative approximate description is the exponential function [47]

$$n \sim F_{\max} \exp(-\omega^2/k^2) \tag{10.17}$$

where $F_{\max}$ is the maximum value (about 2.5%/sr for copper arcs of 100 A), ω is the solid angle, and k is the shape factor (about 4.6 sr for the example of an annular anode with 11 mm diameter and copper arc of 100 A [47]).

As the plasma expands its density drops according to the point source law

$$n = C\frac{I_{\text{arc}}}{r^2} \tag{10.18}$$

along the surface normal, where C is a constant related to the ion erosion rate specific to the cathode material, I_{arc} is the arc current, and r is the distance from the spot. For copper, $C \approx 10^{13}\ \text{A}^{-1}\ \text{m}^{-1}$[48]; the constants for other cathode materials can be estimated from ion erosion data relative to copper [47, 49–52]. Taking both the angular and distance dependence into account, a more general expression can be written as

$$n = C\frac{I_{\text{arc}}}{r^2}\cos^{\alpha}\vartheta \tag{10.19}$$

The plasma density distribution is greatly altered in the presence of an external magnetic field. The field is usually strong enough to magnetize electrons but not ions. With magnetization we mean a situation in which the electrons can complete many gyration rotations before a collisions occurs; this implies that the electron gyration radius

$$r_{\text{e}} = \frac{v_{\perp} m_{\text{e}}}{eB} \tag{10.20}$$

is much smaller than the typical size of the system (e.g. the cathode–anode distance), where B is the scalar value of the magnetic induction, m_{e} is the electron mass, and $v_{\perp}$ is the velocity component perpendicular to the magnetic field vector; for estimates one can use the thermal velocity. The magnetic induction is usually not strong enough to also magnetize ions, i.e. the ion gyration radius is usually not much smaller than the system size. Even though only the electrons are magnetized, the plasma as a whole tends to be guided by the magnetic field lines owing to the interaction of electrons with ions. This becomes very important when considering macroparticle filters (Section 10.4).

10.2.2.2 Ion Charge State Distributions

The comment on the fluctuating properties of the plasma density is also applicable to all other parameters, including the ion charge state distributions (CSDs). At a given location, fast fluctuations occur, reflecting the fractal properties of ion generation at and near the emission centers. Therefore, published ion CSDs always refer to time-averaged values. CSDs and the derived average, or most likely, velocities have been extensively studied [51, 53–62]. Multiply charged ions are of interest because, in contrast to most other low-temperature laboratory plasmas, they are produced in copious amounts by the cathodic arc processes. This suggests utilizing those ions as ion feedstock for metal ion sources, which indeed has been done in several embodiments [61, 63, 64].

Charge states are very important to most applications, especially because they directly influence the energy delivered to a surface in the energetic condensation process (Section 10.5). Table 10.2 provides CSDs as measured for vacuum arcs averaged over many individual measurements.

While the data of Table 10.2 give a good indication what to expect from the various cathode materials, one needs to realize that those data, especially the ion charge states, are the result of complicated ionization and recombination processes, and therefore variations can occur, especially when an external magnetic field is present, and when the expansion is impeded by background or process gas.

In the case of an external magnetic field, the average motion of electrons perpendicular to the magnetic field lines is greatly reduced, and the plasma is expanding at a reduced rate, which leads to less cooling compared to the freely expanding plasma. As a result, the ionization–recombination balance is shifted to greater ionization; higher charge states are obtained, and the average charge states are clearly shifted [51, 59, 60, 68–71].

Collisions of metal ions with background or processing gas atoms or molecules reduce the charge states of the metal ions [72–81], but they also contribute to activation of the collision partner. Activation includes electronic excitation, ionization, or, if the collision partner is a molecule, dissociation or excitation of vibrational or rotational modes. The reduction of metal ion charge state occurs most effectively through charge exchange collisions [82, 83] of the type

$$\mathrm{Me}^{Q+} + \mathrm{Me} \Rightarrow \mathrm{Me}^{(Q-1)+} + \mathrm{Me}^{+}, \ Q = 1, 2, 3, \ldots \tag{10.21}$$

where Me^{Q+} stands for the Q-fold charged metal ion. Charge exchange reactions with multiply charged ions will lead to ionization of the atom and to a reduction of the population of highly charged ions. Therefore, even though the total charge is conserved in each collision of the type (10.21), the average charge state number is not conserved because previously neutral particles are now included in the averaging of *ion* charge states. Neutral particles are conventionally not included in the averaging procedure mainly for reasons of practicality, i.e. because the concentration of neutrals is not known.

10.2.2.3 Plasma Velocity

The random component of the electron velocity is much greater than the plasma velocity in a laboratory frame of reference. Therefore, the electrons may be approximated with a

Table 10.2: Average ion velocity [51], burning voltage [65], cohesive energy [66], average charge state numbers [51,61], and electron temperature [67] for most conducting elements of the Periodic Table measured for arc currents 100–300 A at pressure 10^{-4} Pa

Symbol	Atomic no.	Arc burning voltage (V)	Average ion velocity (m/s)	Kinetic ion energy (eV)	Ion momentum (10^{-22} kg m/s)	Cohesive energy (eV/ atom)	Average ion charge state no.	Temperature of electrons (eV)	Approx. ion Mach no.
Li	3	23.5	23, 100	19.3	2.67	1.63	1.0	2.0	3.1
C	6	31	17, 300	18.7	3.45	7.37	1.0	2.0	3.0
Mg	12	18.6	19, 800	49.4	7.98	1.51	1.5	2.1	4.8
Al	13	22.6	15, 400	33.1	6.89	3.39	1.7	3.1	3.3
Si	14	21.0	15, 400	34.5	7.18	4.63	1.4	2.0	4.1
Ca	20	20.5	13, 900	39.9	10.2	1.84	1.9	2.2	4.2
Sc	21	21.6	14, 600	49.6	10.9	3.90	1.8	2.4	4.5
Ti	22	22.1	15, 400	58.9	12.2	4.85	2.1	3.2	4.3
V	23	22.7	16, 300	70.2	13.8	5.51	2.1	3.4	4.5
Cr	24	22.7	16, 300	71.6	14.1	4.10	2.1	3.4	4.6
Fe	26	21.7	12, 600	45.9	11.7	4.28	1.8	3.4	3.7
Co	27	21.8	12, 100	44.4	11.8	4.39	1.7	3.0	3.8
Ni	28	21.7	11, 500	40.6	11.2	4.44	1.8	3.0	3.6
Cu	29	22.7	13, 200	57.4	13.9	3.49	2.0	3.5	4.0
Zn	30	17.1	10, 300	35.7	11.1	1.35	1.4	2.0	4.2
Ge	32	20.0	11, 100	46.2	13.4	3.85	2.0	2.0	4.8
Sr	38	18.5	11, 500	60.5	16.8	1.72	2.0	2.5	4.9
Y	39	19.9	13, 200	80.3	19.5	4.37	2.3	2.4	5.8
Zr	40	22.7	15, 400	112	23.3	6.25	2.6	3.7	5.5
Nb	41	27.9	16, 300	128	25.1	7.57	3.0	4.0	5.6
Mo	42	29.5	17, 300	149	27.6	6.82	3.1	4.5	5.8
Ru	44	23.8	13, 900	139	23.3	6.74	2.9	4.5	4.8
Rh	45	23.8	14, 600	142	24.9	5.75	3.0	4.5	5.1

(Continued)

Table 10.2: (*Continued*)

Symbol	Atomic no.	Arc burning voltage (V)	Average ion velocity (m/s)	Kinetic ion energy (eV)	Ion momentum (10^{-22} kg m/s)	Cohesive energy (eV/ atom)	Average ion charge state no.	Temperature of electrons (eV)	Approx. ion Mach no.
Pd	46	23.5	12, 100	80.1	21.4	3.89	1.9	2.0	6.3
Ag	47	22.8	11, 100	68.7	19.9	2.95	2.1	4.0	4.1
Cd	48	14.7	6, 800	26.6	12.6	1.16	1.3	2.1	3.6
In	49	16.0	6, 000	21.6	11.5	2.52	1.4	2.1	3.2
Sn	50	17.4	7, 000	29.5	13.6	3.13	1.5	2.1	3.7
Ba	56	16.5	7, 900	44.6	18.0	1.90	2.0	2.3	4.4
La	57	18.7	6, 900	34.6	16.0	4.47	2.2	1.4	4.9
Ce	58	17.6	7, 900	45.5	18.4	4.32	2.1	1.7	5.1
Pr	59	20.5	8, 400	51.5	19.6	3.70	2.2	2.5	4.5
Nd	60	19.2	8, 100	49.7	19.5	3.40	2.2	1.6	5.6
Sm	62	18.8	8, 100	51.8	20.3	2.14	2.1	2.2	4.9
Gd	64	20.4	8, 100	54.1	21.3	4.14	2.2	1.7	5.6
Tb	65	19.6	8, 400	58.1	22.1	4.05	2.2	2.1	5.3
Dy	66	19.8	8, 400	59.4	22.6	3.04	2.3	2.4	5.0
Ho	67	20.0	8, 600	64.1	23.7	3.14	2.3	2.4	5.2
Er	68	19.2	8, 900	69.3	24.8	3.29	2.4	2.0	5.9
Hf	72	23.3	10, 300	97.5	30.4	6.44	2.9	3.6	5.2
Ta	73	28.6	12, 000	136	36.2	8.10	2.9	3.7	6.0
W	74	28.7	11, 100	117	33.6	8.90	3.1	4.3	5.2
Ir	77	25.5	10, 700	113	34.1	6.94	2.7	4.2	5.2
Pt	78	23.7	8, 100	67.2	26.4	5.84	2.1	4.0	4.1
Au	79	19.7	6, 900	49.0	22.6	3.81	2.0	4.0	3.5
Pb	82	17.3	5, 800	35.8	19.8	2.03	1.6	2.0	4.2
Bi	83	14.4	4, 700	23.9	16.3	2.18	1.2	1.8	3.6

The results do not noticeably depend on arc current and are valid for pressures up to about 10^{-2} Pa. No external magnetic field was applied. Most data were taken for $t > 150$ μs after arc initiation.

Maxwellian distribution and we can focus on the velocity distribution functions of ions. First, we will consider the situation without an external magnetic field and later move on to consider the influence of such an external field.

The description of ion motion can be thought of as being composed of a thermal motion and a drift, as seen in a laboratory frame of reference. If measured in one direction, usually with the detector facing the incoming plasma flow, the ion distribution function is a shifted Maxwellian distribution which can be expressed as [77, 81, 84, 85]

$$\phi_{\mathrm{i}}(E) = C_{\mathrm{s}} E \exp\left[\left(\sqrt{E} - \sqrt{E_{\mathrm{dir}}}\right)^2 / \mathrm{k}T_{\mathrm{i}}\right] \tag{10.22}$$

where C_{s} is a scaling constant, and E_{dir} is the kinetic energy of the directed motion. Distribution functions of kinetic energy, $\phi(E)$, and directed velocity, $f(v)$, are equivalent and can be converted [86]

$$\phi(E) = \frac{v(E)}{m} f\left[v(E)\right] \tag{10.23}$$

with $v(E) = (2E/m)^{1/2}$. The most likely velocity for a given cathode material, v_{i}^{*}, i.e. the peak value of the velocity distribution function, can readily be converted into the most likely ion energy according to $E_{\mathrm{kin}}^{*} = m_{\mathrm{i}}\left(v_{\mathrm{i}}^{*}\right)^2/2$. The most likely values of velocity and energy are not the average values because the distribution functions are not symmetric but have a long tail [87]. Time-of-flight (TOF) techniques give information on velocities [51, 88–92] and electrostatic field methods provide energy distributions [54, 55, 77, 85]. For the latter, one has to carefully take into account the acceleration or deceleration caused by the sheath at the detector entrance – doing so allows us to reconcile apparently differing results obtained by those methods.

Table 10.2 includes the most likely ion velocities (peak of the distribution) for a wide range of materials. If we look for example at the distribution functions measured by Byon and Anders [93], we find *one* distinct peak in the distribution functions, even though there was no resolution of charge states in those measurements (Figure 10.5). This shows that most ions drift with approximately the same velocity regardless of their charge state [91, 94].

For the case of expansion into vacuum and in the absence of significant magnetic fields, a two-fluid plasma model (ions, electrons) works fairly well to determine the average ion velocity. Assuming that all energy is deposited in a small volume at the cathode spot and

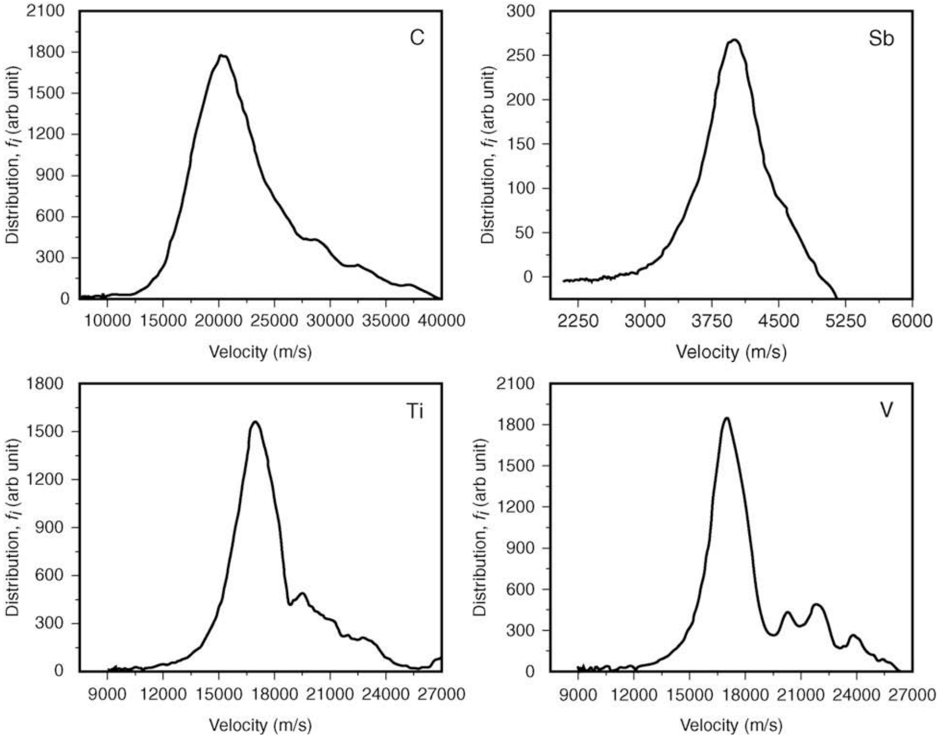

Figure 10.5: Examples of ion velocity distribution functions. The measuring principle implies greater errors at the high-energy end and those small peaks may be artifacts caused by density fluctuations. Note that each material has its own velocity scale. (Adapted from [93].)

considering adiabatic expansion, the expression

$$\bar{v}_{\mathrm{i}} \approx \frac{2}{\gamma - 1}\sqrt{\gamma \frac{\mathrm{k}T_{\mathrm{i}}^{*} + \bar{Q}\mathrm{k}T_{\mathrm{e}}^{*}}{m_{\mathrm{i}}}} \tag{10.24}$$

can be derived for the final ion velocity [10, 95], where $\gamma \approx 5/3$ is the adiabatic coefficient and the star superscript indicates the initial temperature in the vicinity of the cathode spot. Similarly, considering the equations of energy and motion for a multicomponent plasma, the relatively simple approximate expression

$$\bar{v}_{\mathrm{i}} \approx 3.5\sqrt{\bar{Q}\mathrm{k}T_{\mathrm{e}}^{*}/m_{\mathrm{i}}} \tag{10.25}$$

can be derived, where T_{e}^{*} denotes the electron temperature at the point where the ion velocity becomes supersonic [96–98]. To evaluate these expressions, one may use the temperature data [67] that have been derived from measured ion CSDs [61]. From the results (Figures 10.6 and 10.7), one can see that the correlation is surprisingly good.

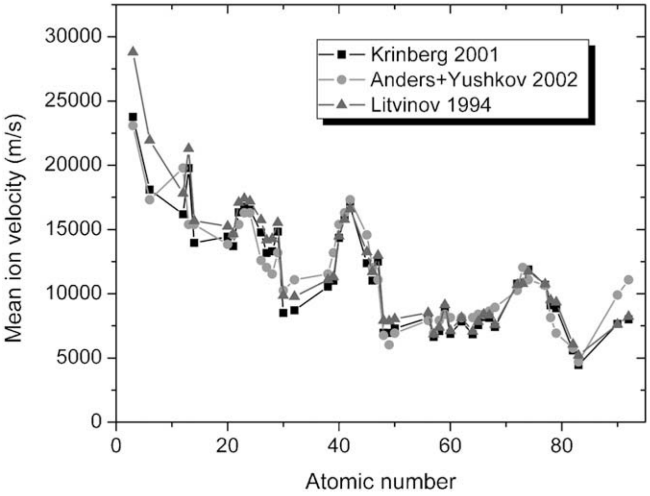

Figure 10.6: Mean ion velocity of vacuum arcs, as calculated by Litvinov [95] and Krinberg [98], compared to data from Anders and Yushkov [51].

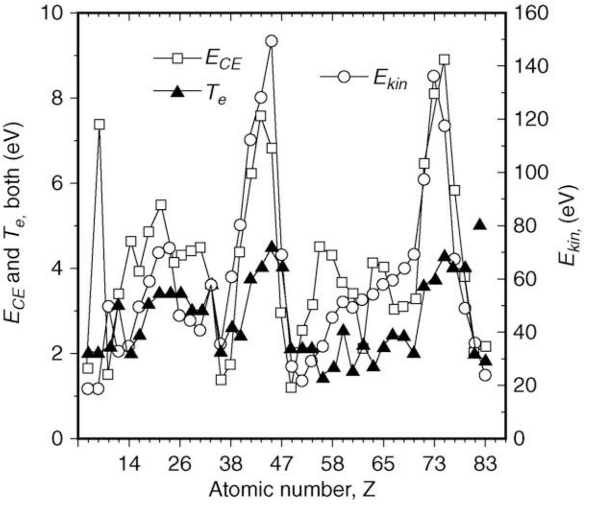

Figure 10.7: Most likely ion velocities for vacuum arc plasmas, converted to ion energies, the electron temperature near the cathode spot, and the cohesive energy of the cathode material. (Adapted from [51].)

10.3 Arc Plasma Sources

10.3.1 DC Sources

Practically all commercial cathodic arc systems operate with continuous direct current (DC) arcs to make use of the high deposition rate and reasonably low equipment cost. The typical arc current is between 40 and 100 A. The lower limit is determined by arc chopping (i.e. the spontaneous extinguishing of the cathodic arc discharge), whereas the upper limit is determined by cathode cooling considerations.

Arc sources for industrial coatings were originally designed in the late 1960s and early 1970s, for example by Sablev [99] and Snaper [100]. Their patents have expired and so the design features are freely utilized in various modern designs.

Snaper's arc patent contains many elements of typical arc sources. Figure 10.8 shows a version with a magnetically actuated mechanical trigger. The field coil has the dual function of

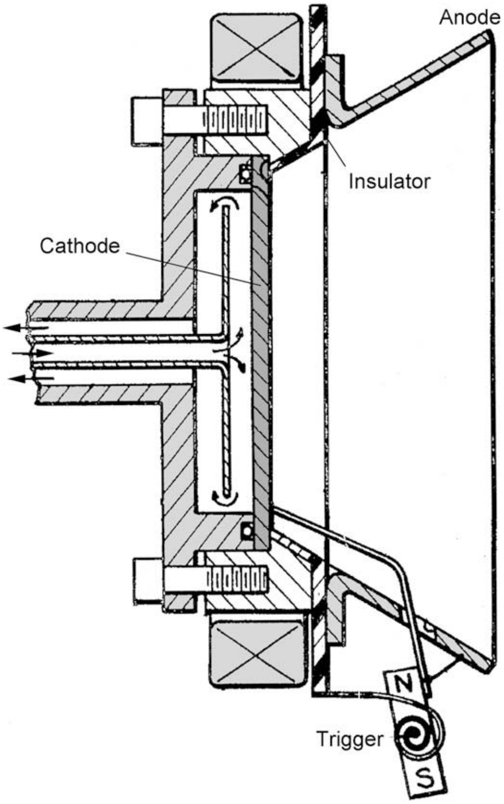

Figure 10.8: Arc source with magnetically actuated mechanical trigger. (Adapted from [101].)

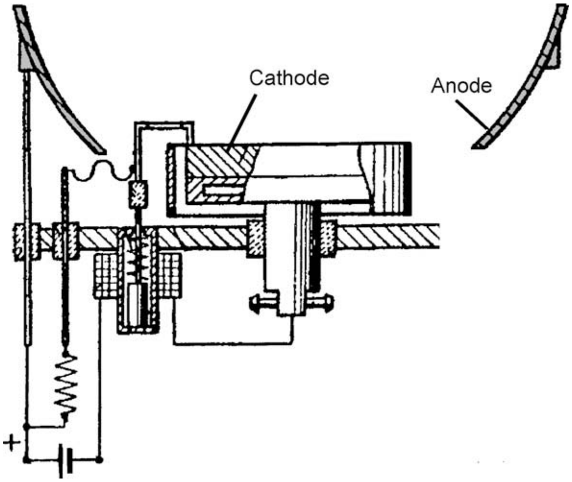

Figure 10.9: Random arc source by Sablev et al. featuring a mechanical trigger and dedicated anode. (Adapted from [103].)

removing the trigger from the cathode and increasing the directivity of the ionized beam. The cathode is held by a ceramic insulator, which limits the area on which arc spots can occur. Boron nitride has been identified as a preferred insulator material because it does not shatter when the arc spot burns at the cathode–ceramic interface. Snaper's source belongs in the category of random arc sources, because the apparent spot motion is not controlled by a magnetic field or other means (for spot steering, see Section 10.2.1).

Possible plasma contamination with ceramic material can be avoided when using a gap design, i.e. when the active part of the cathode is defined by an enclosing floating shield that defines a narrow gap to the cathode. Should an arc spot ignite inside the gap, the impedance is high and the arc either extinguishes or another spot on the designated 'correct' surface area takes over electron emission and plasma production. Sablev's original design [99] became the prototype for many source versions (Figure 10.9), and other improvements were made, like the labyrinth gap by Hovsepian [102].

In special cases, namely when the cathode material is of low cohesive energy (like Mg), it can be clamped with a part made from much higher cohesive energy (like Ta, Mo, W) without covering (hiding) it because arc spots are unlikely to ignite on those clamp materials.

Yet another way of controlling the location of spot operation is through magnetic steering (Section 10.2.1), and we speak of 'steered arc sources'. Steered arc sources can be compact, with cathodes typically ~ 5–10 cm in diameter, or they may have a very large and elongated cathode, perhaps as long as 1–2 m. Two rules govern the apparent spot motion: (1) the retrograde motion rule; and (2) the acute angle rule, which can be explained as follows.

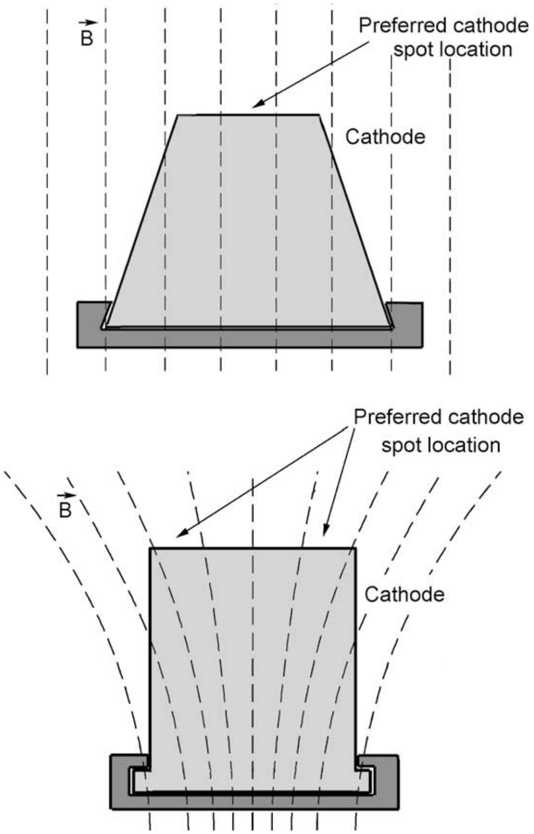

Figure 10.10: Through-field geometries used for spot steering.

According to the retrograde motion rule, the spot tends to move in the direction of $-\mathbf{j}\times\mathbf{B}$, where $\mathbf{j}$ is the vector of current density, which, per engineering definition, points from plus to minus, i.e. into the cathode. $\mathbf{B}$ is the vector of the magnetic induction at the location of interest on the cathode surface.

According to the acute angle rule, which applies in addition to the retrograde motion rule, the spot tends to move toward the direction given by the acute angle between the magnetic vector $\mathbf{B}$ and the normal of the cathode surface [104].

One may distinguish two basic magnetic field configurations [105]: (1) the through-field configuration, where magnetic field lines are essentially normal to the cathode surface (Figure 10.10); and (2) the arched field configuration, where field lines arch over the cathode, forming a magnetic tunnel, very much like in sputtering magnetrons (Figure 10.11).

As indicated in Figures 10.10 and 10.11, spot steering leads to preferred regions of arc spot operation and thus cathode erosion. In both cases, through-field and arched field, the spots

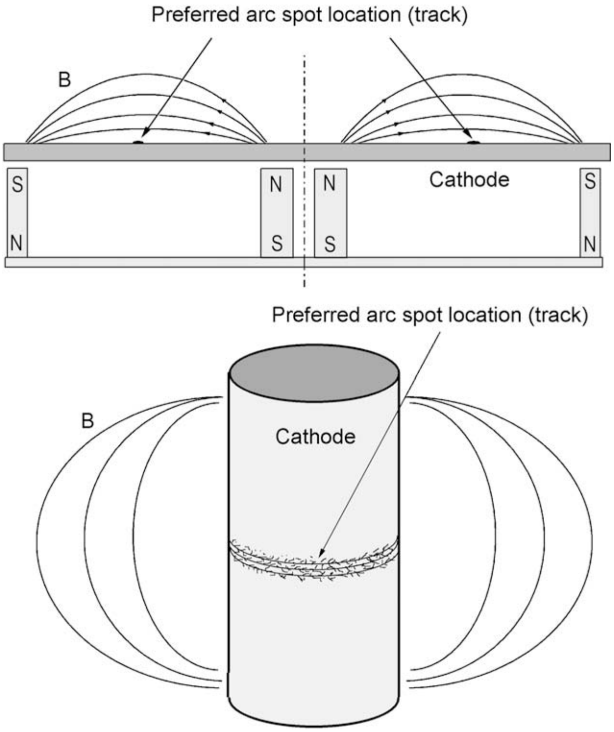

Figure 10.11: Arched or tunnel field geometries used for spot steering.

follow the retrograde motion rule when they have reached the optimum position according to the acute angle rule. For example, in the arched geometry, the spots tend to follow the tunnel formed by the arched field. Most steered arc sources use the through-field configuration because this type of field promotes the transport of plasma to the substrate. The arched field, in contrast, can trap plasma near the cathode. The through-field is especially desirable when the DC arc source is coupled to the field of a macroparticle filter.

Not all arc sources use magnetic spot steering. Some DC systems operate in a so-called switched mode where subtle *electric* effects are used to control the direction of spot ignition. The most prominent examples are systems developed by Vergason Technology, Inc. [106] and by Vapor Technologies, Inc. [107]. In Vergason's designs, the cathode is a long rod with spot sensors at both ends. The sensor picks up information based on the proximity of the spot, e.g. its magnetic field or light emission. The spot appears to travel to the side where the cable is connected, minimizing the loss in the cathode. When it arrives near the cable connector, the sensor provides information and a switch box connects the power contact to the other end of the cathode, thereby reversing the spot's travel direction. By adding a magnetic field [108], the arc spot appears to travel in a helix around and along the cathode rod.

10.3.2 Pulsed Sources

Pulsed arc sources are rare in the coating industry but are often used in laboratory research. They offer miniaturization, allowing us to use them in small chambers, typical for university-style research, with minimal requirements on average power consumption and cooling. New process parameters appear such as pulse length and duty cycle. At low duty cycle, temperature-sensitive substrates can be coated such as plastic sheets. One difficulty appears with pulsed operation: the need for frequent and often rapid arc triggering. This requires trigger concepts other than the mechanical trigger typically used for DC arc sources.

In the case of high current operation, generally exceeding 1 kA with high duty cycle ($\sim 10\%$), pulsed sources can reach the deposition rates of DC sources. The average plasma production scales with the average power, and one can readily derive requirements in terms of arc current and duty cycle when comparing DC and pulsed arc operation.

Multiple cathode spots form when the arc is operated at high arc current. Taking into account the self-magnetic field produced by the current, simultaneously existing cathode spots tend to repel each other, which can be understood when considering the motion of one spot in the magnetic field of the other. Therefore, pulsed high current arcs can be considered as a special case of magnetically steered arc. This kind of mutual spot influence can be utilized by implementing a trigger in the center of the cathode [109–112]. The spots repel each other, and the arc pulse is preferably terminated when the spots reach the outer rim or edge of the cathode, leading to optimum utilization of the cathode material.

10.4 Macroparticles and Macroparticle Control

10.4.1 Macroparticle Generation

Macroparticles are liquid or solid debris particles that are produced at cathode spots. Their presence is the most severe limitation to cathodic arc deposition technology. First, we will have a closer look what those particles are and how they are produced. Later in this chapter, mitigation measures such as macroparticle filters will be discussed.

Macroparticles have the term 'macro' in the name because they are indeed massive compared to ions, atoms, and electrons. Sometimes they are called droplets or microparticles and nanoparticles. They have a wide size distribution $f(d_{\mathrm{MP}})$ that can be best described by a power law:

$$f(d_{\mathrm{MP}}) = A d_{\mathrm{MP}}^{-\alpha} \tag{10.26}$$

where d_{MP} is the diameter or similar characteristic size of the macroparticle, and the parameters A and α are material dependent. The upper end of the distribution, i.e. the largest particle, is typically in the 10 μm range or even a bit larger for materials of low melting temperature. The lower limit of the distribution is not well known. Many quote about 0.1 μm, but this is more related to the limitations of the measuring equipment used, such as a scanning electron microscope (SEM).

When the emission site goes through the stages of life as described in Section 10.2, a highly localized zone forms between the relatively cold cathode and the hot plasma above it where the cathode material is in the liquid phase. This liquid is subject to the transient pressure exerted by the plasma and it responds by yielding. As a result, microscopic droplets or macroparticles as well as an erosion crater form. The macroparticles preferentially splash to the side, i.e. under a relatively shallow angle with respect to the cathode surface [50, 113], although some are formed as the plasma pressure reduces, and so a number are ejected in the direction normal to the surface.

Macroparticles are generally liquid when they form, and they tend to cool down as they travel away from the cathode. For refractory metals and graphite, they can be easily seen in flight owing to their incandescent nature, while macroparticles of low melting-point materials are not as hot and therefore more difficult to discern visually or photographically. Macroparticle size distributions and macroparticle interaction with the arc plasma have been studied over the years by many researchers [50, 54, 113–127] and a detailed review can be found elsewhere [3].

Once they arrive on a surface, such as a substrate to be coated, they may stick and be incorporated into the growing film (Figure 10.12). This, however, is not always the case. In particular, those macroparticles that have become solid before impact have a high likelihood of

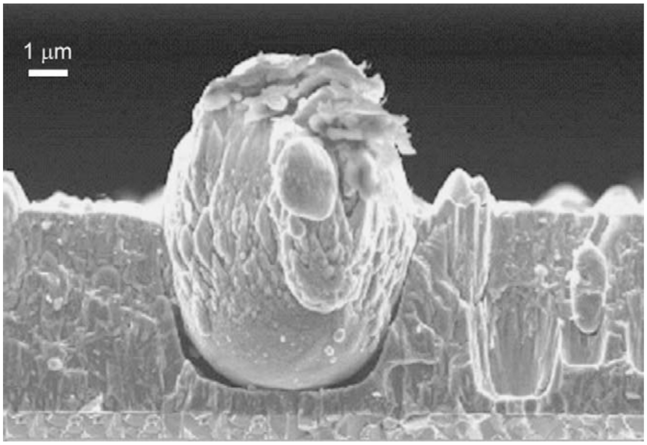

Figure 10.12: Incorporation of a large titanium macroparticle in a titanium nitride film: the oval shape of the large macroparticle is due to the deposition of nitride on top of the approximately spherical macroparticle; one can also see defects (holes) caused by loss of macroparticles in the sample fracture process. (Photograph courtesy of Andreas Schütze, Liechtenstein.)

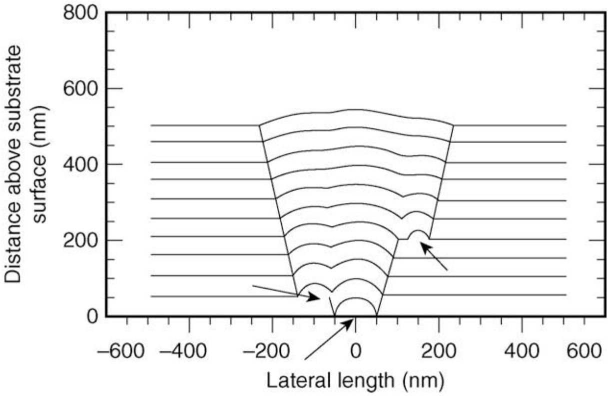

Figure 10.13: Computer simulation of film growth with incorporation of three macroparticles as indicated by the arrows. (Adapted from [128].)

bouncing back. Macroparticle reflection can still cause a defect in the growing film, and reflection is a major issue for macroparticle filters (see later in this chapter).

The incorporation of a macroparticle into the film is likely to cause a defect that is even larger than the macroparticle because the macroparticle will affect the growth of the film after its arrival: the resulting defect shape is conical (Figure 10.13)

10.4.2 Macroparticle Reduction

As already indicated, macroparticles are highly undesirable, and much effort has been invested to find methods to reduce, or even to eliminate, the macroparticle content in coatings. There are two main approaches: (1) reduce the macroparticle production in the first place; and (2), separate the plasma flow from the flux of macroparticles. In the following, those approaches will be examined more closely.

Macroparticle generation is related to the formation of a pool of liquid material, as mentioned before. Therefore, one idea is to reduce the time for which an emission site is active, thereby reducing the size of the liquid pool and the amount of material that can be ejected. This can be done in several ways.

As we know, ignition of a new emission site is promoted in the presence of a dielectric layer, leading to spots of type 1. Typically, several emission sites are simultaneously active, electrically in parallel, and the competition for carrying current extinguishes the more resistive sites, i.e. those that have already formed neutral vapor (choking effect; see Section 10.2). Therefore, reactive cathodic arc deposition has generally a much smaller macroparticle issue than the deposition of pure metals, a fortunate side-effect that is used heavily in the coating

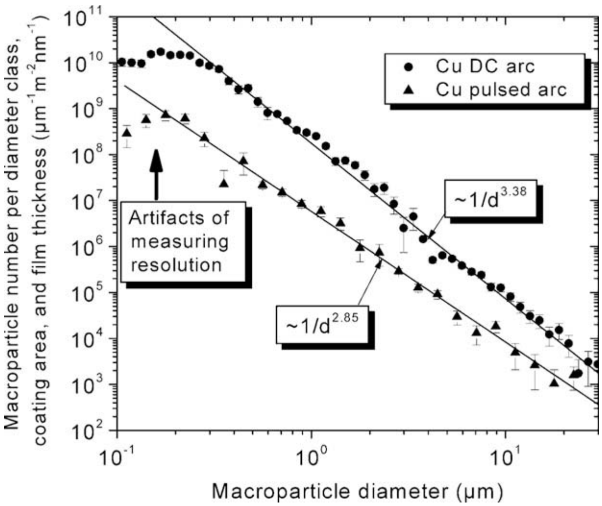

Figure 10.14: Comparison of copper macroparticle distribution functions for DC arcs and pulsed high-current arcs. The number of macroparticles is normalized to size class, deposition area, and film thickness. (Data courtesy of Peter Siemroth and co-workers, Dresden, Germany.)

industry. In fact, the industry may not exist but for that effect: unfiltered cathodic arc deposition is acceptable for many applications because the size of the macroparticle is relatively small and not detrimental to the application.

Another way to reduce the size of macroparticle is through enhancing the apparent spot velocity, which is just a different way of saying that the average time for which an emission site is active is reduced. As mentioned before, spot steering can be done magnetically or through electrical means. Figure 10.14 shows examples of macroparticle size distribution functions illustrating the spot steering effect, here via using a high current pulsed arc. In all cases, the power law character of the distribution is maintained, supporting the fractal approach to process understanding and modeling.

10.4.3 Macroparticle Filtering

Now let us consider the second approach of dealing with macroparticles, the separation of macroparticles from the plasma, known as macroparticle filtering. The concept is based on the possibility of guiding a plasma flow along magnetic field lines, toward a substrate, while macroparticles, even if charged, are too massive to be affected by magnetic or electric fields.

To understand the transport mechanism, we need to recall that charged particles, such as electrons, can be ‘magnetized’. By this we mean that (1) the gyration radius (Eq. 10.20) is smaller than a characteristic size like the radius of a filter duct, and (2) the electron can execute many gyrations before colliding with another particle. Averaging over the gyration motion one can state that the electrons move along magnetic field lines while their mobility perpendicular to the field line is greatly impeded. Cross-field motion is only enabled by collisions and collective plasma effects (which are beyond the scope of this chapter).

Plasma is a quasi-neutral ensemble of electrons and ions, and so one also needs to consider what ions do. If we plug the *ion* mass and a reasonable ion velocity and magnetic field strength in the equation for the gyration radius (Eq. 10.20), we can quickly see that the ion gyration radius is large, and therefore ions are generally not magnetized. Yet, when electrons are guided by the field, very small deviation from the quasi-neutral charge balance sets up very large electric fields, **E**, as can be calculated by the Poisson equation

$$\varepsilon_0 \nabla \cdot \mathbf{E} = \rho \tag{10.27}$$

where $\rho = n_\mathrm{i} - n_\mathrm{e}$ is the local net charge and $\varepsilon_0 \approx 8.854 \times 10^{-12}$ F/m is the permittivity of free space. The electric field keeps the plasma very close to being quasi-neutral and facilitates the flow of electrons *and* ions toward the substrate. Therefore, the transport of plasma in magnetic macroparticle filters is achieved with a combined magnetic and electric mechanism. Detailed descriptions can be made on the basis of hydrodynamic codes or by particle-on-cell simulations, which have been reviewed recently [3].

There are many different shapes, geometries, and sizes of macroparticle filters; the review [3] listed more than 20. Here, we will consider only the most important, illustrating the concept. That can be best done by first looking at the classic macroparticle filter developed in the 1970s in Kharkov, Ukraine (then the USSR). Taking a quarter torus device, originally conceived for studying hydrogen plasma transport for Tokomak-related nuclear fusion [129], Aksenov et al. [130, 131] injected cathodic arc plasma to produce high-quality films of diamond-like carbon (DLC), metals, and nitrides (Figure 10.15). In their apparatus, the filter duct is part of the vacuum chamber, and the guiding field coils are outside the vacuum and therefore can easily be cooled. Aksenov et al. isolated the duct wall so it could be positively biased to reduce plasma transport losses, which was later investigated and utilized by others, too [132, 133].

This classic design of a filter has been used and modified many times, for example, the bending angle could be less or greater than 90° [134, 135], and the bending could be out of plane [136, 137] in order to further reduce the likelihood that macroparticles are transported through the filter (Figures 10.16 and 10.17).

There are two main mechanisms of macroparticle transport. The most important issue is macroparticle bouncing from the inner wall of the filter; and such reflections can occur several times. Therefore, some macroparticles can reach the substrate even if there is no line of sight between cathode and substrate. The second mechanism could be loosely described as plasma

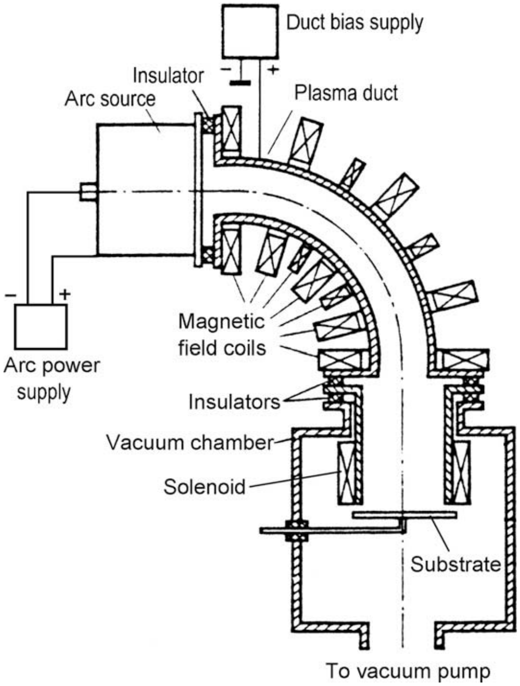

Figure 10.15: Classic 90°-duct filter by Aksenov et al. (Adapted from [131].)

wind, i.e. the action of the fast plasma flow on macroparticles. Momentum transfer from ions could carry small macroparticles with the plasma flow, as wind can transport dust particles.

One can state that filtering is not perfect and what really matters is the ratio of macroparticle reduction to plasma losses: the quality of a filter must be judged not only by how well macroparticles are removed but also by how much plasma is lost. To quantify plasma transport, one could consider the transport efficiency, defined as the ratio of the number of ions leaving the filter to the number of ions entering it. Filters are considered efficient when that ratio exceeds about 25%. While the ion current at the exit can be relatively easily measured, it is often difficult to determine the ion current at the filter entrance. Therefore, it is more common to use the ratio of ion current of the filtered plasma to the arc discharge current:

$$\eta_{\mathrm{system}} = I_{\mathrm{i,filtered}} / I_{\mathrm{arc}} \tag{10.28}$$

This ratio can be called the system coefficient and is typically in the range 1–4%. The system coefficient should not be called an 'efficiency' because it can never reach 100%. The arc current is mostly carried by electrons and merely serves as a suitable normalization, which works well because the amount of plasma scales approximately with the arc current.

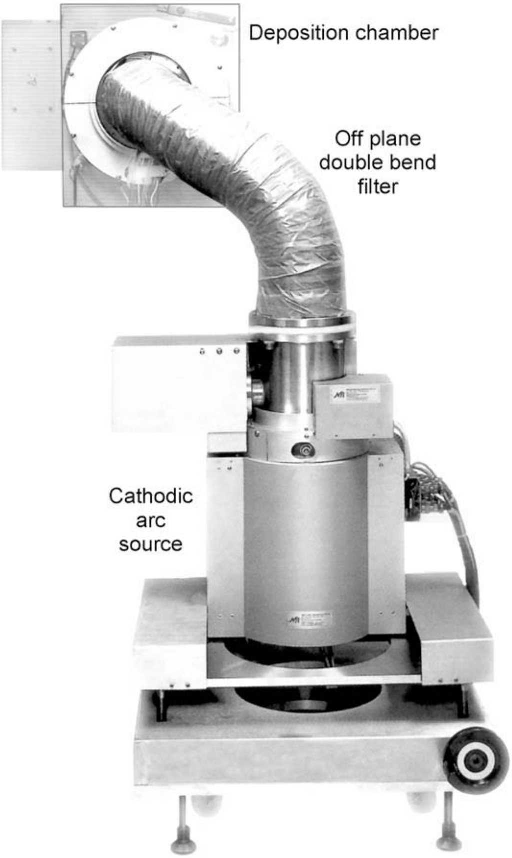

Figure 10.16: Off-plane double-bend (OPDB) filter system, originally developed at Nanyang Technical University, Singapore, and commercialized by NanoFilm Ltd, Singapore. (Courtesy of NanoFilm Ltd.)

One way of addressing the bouncing issue is to switch from a closed to an open filter architecture [137, 138]. By *closed* we mean a filter design where plasma and particle flow are enclosed, such as by the duct tube that is the part of the vacuum system. In contrast, an *open* filter has openings that allow macroparticles to escape from the filter volume. In the simplest case, a curved open coil as shown in Figure 10.18 could be used. An important element of the open filter design is the installation of a macroparticle blockage, a macroparticle firewall which prevents macroparticles from entering the clean substrate region. In effect, the macroparticle firewall separates a plasma source region, where macroparticles are allowed to fly until they usually come to rest somewhere on the bottom of the chamber, and the clean substrate region into which plasma is allowed to enter through a designated hole in the firewall.

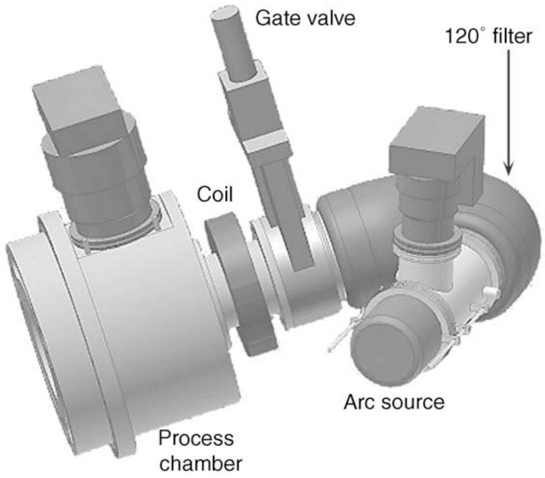

Figure 10.17: 120°-filter designed for pulsed high-current arc deposition, commercialized by Arc Precision GmbH, Wildau, Germany. (Courtesy of P. Siemroth.)

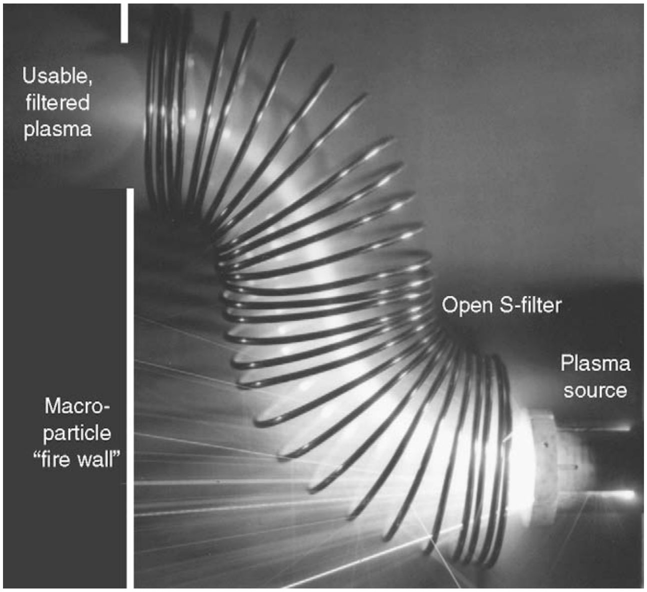

Figure 10.18: Open S-filter illustrating the concept of open-architecture filtering: the macroparticles can leave the filter volume; the macroparticle firewall separates the source region (right) from the substrate region (left).

As with closed filters, open filters can have a variety of shapes and sizes. Each of the filters has advantages and disadvantages, as discussed in greater detail in dedicated reviews ([138] and Chapter 7 of [3]), where other geometries such as the Venetian blind filter or large area filters for elongated cathodes are also considered.

10.5 Energetic Deposition

10.5.1 Energy Considerations

Film growth mechanisms are dealt with in Chapter 2 of this handbook and many other publications [139–141]. Therefore, it is sufficient here to point out some special effects and properties associated with the high degree of ionization and relatively high energy of the species in the condensing plasma.

Energetic deposition may be defined as a process in which most film-forming ions or atoms exceed the displacement energy [142], E_d, allowing them to penetrate the surface and come to rest under the surface. Film growth can therefore occur *under* the surface rather than *on* the surface. Such a process can be considered as ultra-shallow implantation or *subplantation* [143–145]. As a result, films are often highly defective and hard, and show high intrinsic stress. Yet, owing to film–substrate intermixing and with the formation of chemical bonds, the films can be well adherent unless the intrinsic stress is excessive, which leads to catastrophic failure by delamination. Therefore, special attention must be given to stress control, as discussed below.

At the low-energy end of energetic deposition, when the kinetic energy of condensing particles is in the range 5–25 eV and therefore not quite enough for subplantation, defects are greatly reduced and growth occurs on the surface with high adatom mobility, leading to dense, often well-textured films. The kinetic and potential energies of the condensing particles assist in the growth process and, to some limited degree, those particle energies are equivalent to substrate heating. This allows us to obtain films structures and properties at relatively low substrate temperature otherwise associated with higher temperatures. This is very important especially when a substrate is used that cannot tolerate higher temperature because it would anneal, decompose or otherwise be damaged.

Let us have a closer look at the energy contributions brought to the surface by the particles. First, there is the kinetic energy associated with the flow velocity. Cathodic arc ions have a considerable natural kinetic energy gained at the cathode spot, as mentioned in Section 10.2.2,

$$E_{i0} = m_i v_{i0}^2/2 \tag{10.29}$$

where v_{i0} can be approximately determined by the expression (10.25). The surface of a substrate is rarely exactly at the plasma potential, and therefore a sheath will form at the surface accommodating the potential difference ΔV_s. In most cases, the surface will be negative with respect to the plasma potential, and the ions gain kinetic energy according to

$$\Delta E_{\mathrm{i,kin}} = Qe\Delta V_{\mathrm{s}} \tag{10.30}$$

where Q is the charge state number (see Table 10.2). This point is very important because biasing of the substrate can be utilized to control the kinetic energy of arriving ions.

In one extreme case, when the negative bias is high, perhaps reaching the kV level, ions can be used to sputter the substrate and to produce buried layers and mixed interfaces. These effects are considered in the field of plasma immersion ion implantation and deposition [146].

In another extreme case, when positive bias is applied to the substrate, large electron currents are taken from the plasma, which leads to heating of the surface. This can be intentionally utilized or may be considered detrimental in cases where the objective was only to decelerate ions.

When ions arrive at the surface, they carry not only kinetic energy but also potential energy. The latter is usually neglected in the treatment of conventional PVD or CVD methods because the condensing species are not ionized. In cathodic arc deposition, however, the fraction of ions is very large, and so is the effect of potential energy. The largest contribution to potential energy is the ionization energy, E_{ion}. Strictly speaking, since we generally deal with multiply charged ions, it is the *cumulative* ionization energy,

$$E_{\mathrm{ion}} = E_{Q+}^{\mathrm{sum}} = \sum_{Q'=0}^{Q-1} E_{Q'} \tag{10.31}$$

where the ionization energy E_Q is defined as the energy needed to remove a bound electron from an ion of charge state Q, forming an ion of charge state $Q+1$ [147, 148]. Therefore, the greatest effect is from the more highly charged ions. The ionization energy should be reduced by the work function times the charge state number to account for the uptake of electrons from the solid.

There are other forms of potential energy, too. For example, the arriving ion may have a bound electron in an excited state, or if molecules are present, rotational and vibrational energy could be considered. Furthermore, as the condensing particle becomes bonded to the substrate, the cohesive energy is released. Therefore, the total energy brought to the surface by an ion may be written as

$$E_{\mathrm{total}}(Q) = E_{\mathrm{kin,0}} + Qe\Delta V_{\mathrm{sheath}} + E_{\mathrm{ion}} - Qe\phi + E_c + E_{\mathrm{else}} \tag{10.32}$$

where E_{else} summarizes all other small contributions including the energy gained by image charge acceleration.

A numerical evaluation of (10.32) shows that the kinetic energy readily exceeds the displacement energy in most cases, and that the contribution of potential energy is substantial, too, especially for multiply charged ions. Such large energy input could be described as atomic scale heating (ASH) [149, 150]. Considering film growth based on the arrival of large fluxes of condensable (film-forming) ions, each atom of the film was subject to ASH several times, namely, once when it arrived, and again when neighboring atoms arrived. Therefore, ASH is equivalent – to some degree – to conventional heating, resulting in dense films via enhanced surface mobility at generally low bulk temperature [149]. ASH eventually gives rise to temperature elevation of the substrate and the growing film as a whole [141].

10.5.2 Stress Generation and Relief

The effect of the high-energy input is significant for the properties of the resulting films. At high kinetic energy, facilitated by high negative bias, many processes occur, including the sputtering of surface atoms (ion etching), formation of short collision cascades as they are usually known from ion implantation [146, 151], and related rearranging of atoms and their bonds. Depending on the energy level and other factors, this allows us to influence the stress of the material, and in particular to produce thicker coatings at relatively low stress.

Following Bilek and co-workers [152–154], let us consider subsurface processes at high and moderate energies (those terms should always be seen in relation to the material's displacement energy, which lies generally between 20 and 40 eV). As the energy of arriving ions exceeds the displacement energy, they are inserted into the subsurface region where they cause densification and compressive stress. If the material is a metal it will yield to high stress by plastic deformation. However, if the material is covalently bonded it will longer resist plastic deformation. The material is metastable and tends to prefer a high coordination of bonds if more than one phase exists. For example, carbon will preferentially establish sp^3 bonds, diamond bonds, as opposed to the sp^2 bonds of the less dense graphitic material.

The evolution of stress can be understood by a competition of stress generation by subplantation (insertion) and atomic-scale annealing in a thermal spike volume [155]. For a thin film the stress σ is related to the strain ε by [156]

$$\sigma = \frac{Y}{1-\nu}\varepsilon \tag{10.33}$$

where Y and ν are the elastic (Young's) modulus and Poisson's ratio of the coating material. According to Davis [155],

$$\sigma(E_\mathrm{i}) \propto = \frac{Y}{1-\nu}\frac{E_\mathrm{i}^{1/2}}{\left(J/j + \kappa E_\mathrm{i}^{5/3}\right)} \tag{10.34}$$

where E_i is the energy of arriving ions, J is the net condensing flux, j is the ion bombarding flux, and κ is a material-dependent parameter. The more recent model by Bilek and McKenzie [152, 153] gives an improved fit to experimental data. Stress is determined by whether or not atoms have time to rearrange their bonding structure within the thermal spike volume. At low energy (e.g. $\sim 100\,\text{eV}$), the energy is removed quickly from the spike volume, i.e. the quench time is very short and the material densified, hence the compressive stress increases. At higher energies (e.g. $\sim 1\,\text{keV}$ or greater), the atoms in the heated volume can rearrange, the volume expands toward the surface, and hence stress is relieved.

This concept can be quantified, and because of its practical importance to cathodic arc deposition, it is briefly summarized here. One assumes that the region of the thermal spike is spherical, with radius R_{th}. Then the quench time is proportional to the square of the thermal spike radius or to the 2/3-power of the ion energy E_i [157],

$$t_{\text{quench}} \propto R_{\text{th}}^2 \propto E_i^{2/3} \tag{10.35}$$

For $E_i \sim 100\,\text{eV}$, the quench time is less than one picosecond, which is too short for significant rearrangement of atoms. The atoms will use a high bond coordination with the available neighbors to *minimize the total system energy under constraints*. The volume of the thermal spike is proportional to $\kappa\,(E_i - E_B) = (2/3)\,\pi R_{\text{th}}^3$, where E_B is the energy barrier for the ion to be inserted into the surface. The volume of the light gray region (Figure 10.19) can

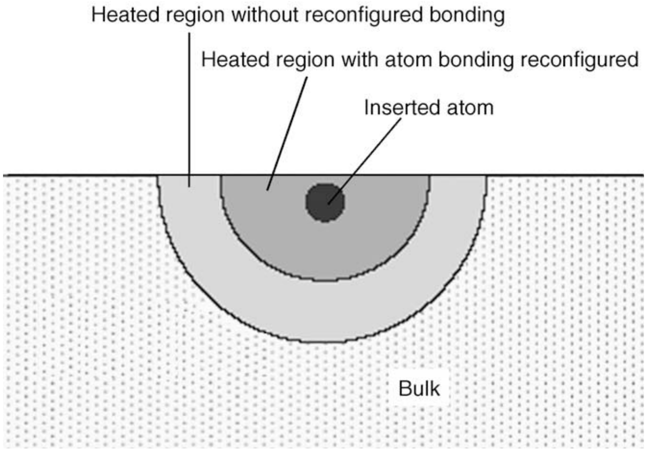

Figure 10.19: Geometry for a model of stress generation and relaxation: the thermal spike volume is assumed to be spherical with the inserted atom in the center. The stress is accumulated in the light gray region, the size of which is proportional to $E_i^{2/3}$. (Adapted from [152].)

be calculated as

$$V_{\text{stressed}} = 2\pi R_{\text{th}}^2 d\tau = 2\pi \left(\frac{\kappa}{2\pi}\right)^{2/3} E_{\text{i}}^{2/3} d\tau \tag{10.36}$$

where $d\tau$ is the thickness of the region where atom movement is restrained by bonds to unaffected atoms in the bulk. The thickness $d\tau$ is about one bond length regardless of the thermal spike volume or ion energy. The number of stressed sites is proportional to the volume V_{stressed} and

$$\sigma = C(E_{\text{i}} - E_{\text{B}})^{2/3} \tag{10.37}$$

where C and E_{B} are material constants.

When the kinetic ion energy clearly exceeds 100 eV, the effect on stress is quite different because the impacting ion creates a much larger volume of a thermal spike. The dark gray zone of Figure 10.19 is a transient melt where atoms are able to access many possible bonding configurations. Those atoms remain in a thermodynamically preferred configuration, i.e. one that minimizes bond and strain energy. The thermal spike volume can expand and raise the level of the free surface. The possibility of raising the surface, thereby minimizing the strain energy without constraint, is the basis for ion-induced stress relief by energetic ion bombardment.

Experimentally it has been observed that only a small fraction of high energy ions is needed to relieve stress, and that saturation of such stress relief occurs when the percentage of the energetic ions is still small. Saturation of stress relief occurs when the volume regions of unconstrained rearrangement start to overlap. The volume V still untreated by a thermal spike is reduced exponentially [152] as the surface is bombarded with sufficiently energetic ions,

$$\frac{V}{V_0} = \exp\left(-\frac{V_{\text{spike}} N}{V_0}\right) \tag{10.38}$$

where V_0 is the volume of a film slab under consideration, $V_{\text{spike}} = E_{\text{i}}/(E_{\text{A}} n_{\text{a}})$ is the volume of each thermal spike, E_{A} is the average energy given to atoms of the thermal spike volume, $N = n_{\text{a}} V \delta$ is the number of high-energy impacts before the slab is covered by more condensing atoms, n_{a} is the atom density of the slab, $\delta = wf$ is the duty cycle of high-energy ions, produced by pulsed biasing, for example, with w being the pulse width of the bias and f the bias pulse repetition frequency. Alternatively, δ could be the fraction of energetic ions produced by other means such as an external ion source. While these considerations were developed with the plasma immersion technique [146] in mind, the underlying physics and derivations are rather general. Using the above expressions, Eq. (10.38) becomes

$$\frac{V}{V_0} = \exp\left(-\frac{E_{\text{i}} f w}{E_{\text{A}}}\right) \tag{10.39}$$

The stress can be assumed to vary with the volume fraction treated by high-energy ions, from the as-deposited value, σ_0, to the relaxed, residual value after ion treatment, σ_{res}, leading to

$$\sigma = \sigma_0 \frac{V}{V_0} + \sigma_{\text{res}} \tag{10.40}$$

Using (10.39) gives

$$\sigma = \sigma_0 \exp\left(-\frac{E_{\text{i}} f w}{E_{\text{A}}}\right) + \sigma_{\text{res}} \tag{10.41}$$

We can use Eq. (10.37) to express the stress generated by ions with energy E_{G}, inserted into or just below the surface, and replace the stress-relieving ion with energy $E_{\text{i}} = E_{\text{R}}$, one obtains

$$\sigma = C(E_{\text{G}} - E_{\text{B}})^{\chi} \exp\left(-\frac{E_{\text{R}}\delta}{E_{\text{A}}}\right) + \sigma_{\text{res}} \tag{10.42}$$

where the exponent χ could be 2/3, as suggested by (10.37), but other exponents such as $\chi = 1$ or $\chi = 1/2$ also give a good fit [152] to experimental data for a number of materials such as TiN [158], AlN [155], BN [159], a-SiH [160], SiBCN [161], and hard amorphous carbon [162]. The different exponents can be interpreted to deviations from the idealized spherical shape of the thermal spike; for example, one could consider a cylindrical geometry of the thermal spike volume [163].

10.5.3 Preferred Orientation and Adhesion

The energy flux brought by the condensing ions can have a profound effect on nucleation, growth, and the resulting film microstructure. In 1983, Krohn et al. [164] found epitaxial relations of ultrathin gold islands deposited by pulsed cathodic arc on NaCl at 150 °C, namely (001)Au||(001) NaCl and [100]Au||[100]NaCl. The islands were smaller than those obtained by evaporation and coalescence occurred at smaller nominal film thickness.

In situ conductivity measurements of cathodic arc silver films showed that the contribution of kinetic energy promotes the formation of smaller, more frequent islands, as compared to sputtering [165]. Also here, the coalescence occurred at smaller nominal film thickness, which can be readily detected by a sharp increase in electrical conductivity. Investigating ultrathin titanium films made by a pulsed cathodic arc using in situ ellipsometry, Oates et al. [166] determined the percolation threshold for titanium on silicon to be 2.7–3.1 (± 0.1 nm) using a method by Arwin and Aspnes [167] which is based on finding the moment when the real part of the dielectric function becomes negative.

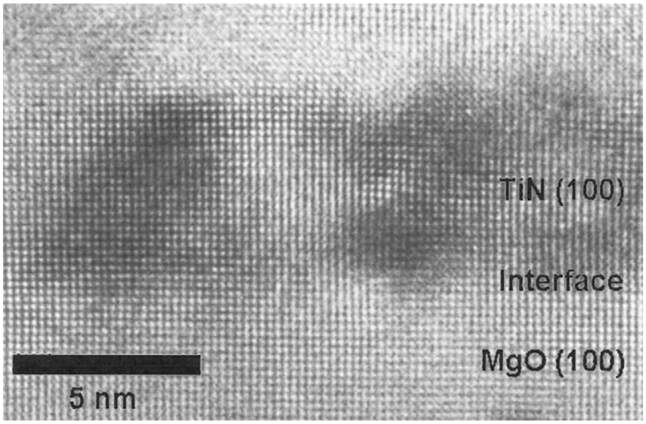

Figure 10.20: High-resolution TEM image showing the epitaxial growth of TiN on MgO(100); the titanium arc was operated in nitrogen at 7×10^{-2} Pa with the substrate at room temperature. (Courtesy of J. Gerlach (experiment) and T. Höche (TEM), both IOM Leipzig.)

Films made by energetic deposition tend to grow with a preferred orientation, where the specifics depend on the material and ion bombardment parameters; the film tends to prefer an orientation that is thermodynamically stable at low levels of biaxial stress [153]. The microstructure is directly linked to the ion-generated stress, which is a thermodynamic driving force toward a preferred orientation thereby minimizing the system's energy [158]. In some cases, the preferred orientation matches the substrate's crystal orientation and one obtains epitaxial growth (Figure 10.20).

The adhesion of a coating is greatly affected by the chemistry of the film and substrate, as well as by stress. A critical factor is whether or not the film material forms chemical bonds with the substrate material. For example, an amorphous carbon film made by a cathodic arc tends to adhere well to carbide-forming substrates such as silicon or titanium. The other important factor is stress. The related strain energy limits the thickness of the coating because it may be greater than the interface energy: the film cracks and delaminates. The energy related to strain grows as the film grows in thickness, which explains why in some cases one is able to grow a thin film (e.g. tens of nm) but completely fails to make thick films (e.g. ~ 1 μm or thicker).

10.5.4 Metal Ion Etching

A special case of processing occurs when a high negative bias is applied in either DC or pulsed mode with a high duty cycle because the result can be a net removal of material. Sometimes this is called metal ion etching – a sputtering process caused by the impact of energetic metal ions. This can indeed be an important first process step in the formation of a well-adherent coating. Since metal ions are deposited on or under the surface, we deal with a combined deposition and etching situation where the etching rate exceeds the deposition rate, hence the net removal by sputtering. For the process to work, the energy of ions needs to be about 1 keV or larger in order to obtain a sputtering yield that exceeds unity. Energy-dependent sputtering yields can be readily calculated for arbitrary material combinations using a Monte Carlo code such as TRIM or SRIM [168].

Metal ion etching by sputtering with typical voltages of $-1000\,\mathrm{V}$ or slightly greater can be beneficial compared to sputter etching with argon ions because some argon will remain below the surface and cause a defective, weak interface to the coating that is subsequently deposited. In contrast, the interface can be beneficially engineered when metal ions remain in the thus-sputtered cleaned surface. For example, cleaning of stainless steel with chromium ions results in a surface layer with enhanced chromium content. Chromium can become part of the substrate because, according to the equilibrium phase diagram [169], it has unlimited solubility in Fe below 512 °C. Towards the coating, chromium can readily form bonds to other metals or to nitrogen or oxygen.

In the 1970s, Aksenov et al. [170] used this cleaning effect obtained by metal ion etching. The cleaning of parts via energetic metal ions was used in the early 1980s, for example Bergman applied Ti ions etching with a bias of $-1000\,\mathrm{V}$ prior to the cathodic arc deposition of TiN [171]. One should keep in mind that a bias of $-1000\,\mathrm{V}$ translates into energies of at least 1 keV, 2 keV, and 3 keV, as the ions have a CSD including $Q = 1$, 2 and 3 (see Eq. 10.30).

The idea of replacing argon etching by metal ion etching prior to sputter deposition was later utilized in a patented process called arc bond sputtering (ABS), by Münz et al. [172]. This process was optimized using steered arcs for etching and unbalanced magnetrons for sputter deposition of coatings with very high critical loads [173–175].

10.6 Deposition of Coatings Using Unfiltered Cathodic Arc Plasma

10.6.1 Hard Coatings

10.6.1.1 Binary Coatings

Perhaps the most important coating made by (unfiltered) cathodic arcs is TiN because it combines decorative gold color with excellent wear and corrosion properties. The original widespread use of arc-deposited TiN coatings was in the former USSR and later, since the 1980s, also in Western Europe and the USA [171, 176–180]. Large batch coaters were developed to mainly deposit TiN at elevated temperatures (typically 450 °C) on cutting tools (drills, cutting inserts, etc.).

Other binary nitrides such as CrN, ZrN, and HfN [181, 182] have advantages over TiN in some applications. For example, CrN exhibits a lower coefficient of friction than TiN [181], and ZrN is superior to TiN for cutting of titanium alloys [183].

For high-speed cutting, where the coating of the cutting edge is subject to very high temperature (~ 1000 °C) in an oxidizing environment, TiN fails owing to oxidation. There was (and still is) a need for more advanced materials.

10.6.1.2 Ternary Coatings

By the late 1980s, $Ti_{1-x}Al_xN$, sometimes labeled (TiAl)N, and often simply abbreviated as TiAlN, emerged as a superior tool coating because it has a better oxidation resistance and hardness at high temperature compared to TiN [184]. Even though its wear properties at high temperature are superior, TiAlN has not completely replaced TiN because of its grayish color: the decorative character of the coating remains important, especially in the marketing phase of a product.

As with other ternary compounds, the ratio of the constituents can be tuned to affect the desired microstructure and properties. In the case of TiAlN, Ti and Al can be obtained from one TiAl alloy cathode, which is convenient and usually done. However, one may opt to utilize two separate cathodes to fine-tune the Ti–Al ratio in the film. In case of the alloy cathode, little can be done to adjust the Ti–Al ratio in the film, which is usually not exactly the same as the cathode owing to preferential sputtering from the substrate in the energetic deposition process. The substrates are slightly biased in the film growth phase, and especially the multiply charged ions have enough energy to cause sputtering of the growing film. The yields of sputtering Al and Ti are not exactly equal, and hence this preferential sputtering shifts the composition of the film [185].

The as-deposited films show a dense and columnar microstructure for various $Ti_{1-x}Al_x$ cathodes. When the aluminum content is $x \leq 0.66$ one finds a metastable cubic phase but for higher Al content, $x = 0.74$, a second hexagonal phase appears [186]. Higher Al content promoted the (200) orientation and had a large influence on the hardness of the as-deposited coatings with up to 32 GPa. The TiAlN films were stable with respect to phase composition and grain size when annealed at 900 °C; however, when the temperature was increased to 1100 °C, films deposited from the 67 at.% Al cathodes showed phase separation forming c-TiN and h-AlN via spinodal decomposition [187] to c-TiN and c-AlN [186, 188]. The formation of two or more phases increases the strength of the material by impeding the motion of dislocations (spinodal hardening). Therefore, the nanostructure that forms at high temperature increases the hardness of the coating and contributes to the superior performance of such a coating under load [189]. Hörling et al. [186] argued that softening by residual stress relaxation through lattice defect annihilation is approximately balanced by hardening by the formation of a coherent nanocomposite structure of c-TiN and c-AlN domains by spinodal decomposition, and therefore the hardness is approximately constant upon annealing.

The above conclusion was realized using a systematic set of single cathodes containing different ratios of the two metals. More flexibility in terms of research and development is given by systems with different cathodes such as Ti, Al, and Cr cathodes, leading to coatings in the Ti–Al–N, Ti–Cr–N, and Cr–Al–N range, and eventually even in the quaternary system where all three metals are used in the compound [190]. The Ti–Cr–N system showed only one phase, c-(TiCr)N, as long as the Cr content was low (10 at.%) [191]. Two phases, cubic (TiCr)N and hexagonal β-$(CrTi)_2N$, appeared with higher Cr content (17–58 at.%). The Cr content can be adjusted not only by the Cr arc current but also by biasing: the Cr content decreased with increasing substrate bias due to preferential sputtering of Cr. The two-phase coatings were nanocrystalline and showed high hardness with a maximum in the range 3700–3900 Vickers at a chromium contents of about 25–30 at.% and a load of 0.5 N [191].

Other examples of arc-deposited ternary nitrides are $Ti_{0.94}Hf_{0.06}N$ and $Ti_{0.92}Nb_{0.08}N$, which have been deposited on cemented carbide inserts using random and steered arc sources [192]. These coatings showed less flank and crater wear than conventional TiN and CVD-deposited TiC–TiN coatings.

Ternary compounds do not necessarily need two metals; rather, the process gas can be the source of two components, and the cathode delivers only one. Carbo-nitrides are prominent examples where changes in the gas composition between N_2 and CH_4 can be used to obtain TiC_xN_{1-x}, for example, with x ranging from zero (TiN) to unity (TiC) [193, 194]. The composition is determined not only by the gas supply variations but also by substrate bias. One should keep in mind that bias is also a means of supplying energy, and hence the substrate temperature increases. In this example, bias of -400 V led to a temperature of 550 °C of the cemented carbide inserts (WC-6 wt.% Co). The resulting films were dense and single-phased with a NaCl-type structure, highly stressed (up to -5.9 GPa) and superhard (up to 45 GPa).

10.6.1.3 Quaternary Coatings

The idea of using the gas as a source of two components can readily be applied to ternary coating systems, like TiCrN, to obtain quaternary compounds like TiCr(C,N). It should be emphasized that those multielement coatings tend to decompose into different phases, and in some cases one should speak of nanocomposites. The Ti–Cr–C–N system produces a nanocomposite of nanocrystalline TiCr(C,N) in an amorphous carbon (a-C) matrix when the carbon content is in the range 9–27 at.% [195]. This is not surprising because the carbon concentration exceeds the solubility of carbon in TiCrN. The nanocomposite exhibits higher hardness (about 30 GPa) compared to monolithic TiCrN (about 26 GPa).

Quaternary coatings can also be obtained from several cathodes or corresponding alloy cathodes. For example, the Ti–Al–N system can be expanded by adding Cr with the idea that protective chromium oxide might form on the surface (similar to stainless steel). As a side-effect, it was found that cathodes with several elements tend to produce fewer macroparticles [196]. The orientation of films of $(Ti_xCr_yAl_z)N$, with $x{:}y \approx 1{:}2$, $z = 0.63$–0.73, $x + y + z = 1$, changed from hexagonal to cubic when the negative substrate bias was increased beyond 50 V; the hardness increased up to 35 GPa. The coatings started to oxidize when the temperature exceeded 1000 °C, which is slightly better than TiAlN.

The trend of adding more components, going even beyond quaternary compounds, has become popular in recent years because coatings can be tailored to the applications. In general, combinations of the materials Ti–Al–Cr–Si–C–B–N are investigated, and other transition metals are also considered, such as Nb, V, Mo, Ta, and Hf.

10.6.1.4 Multilayers and Nanolaminates

A relatively straightforward approach to a (nano)structured coating is to use the multilayer deposition approach. Multilayer structures often outperform monolithic layers for a variety of reasons such as impeding dislocation movement and crack propagation. The total thickness of multilayers is often greater than 1 μm, while individual layers are just a few nanometers or tens of nanometers. When the individual layers of a multilayer system have ~ 10 nm or less thickness, one speaks of nanolayers. There are many papers devoted to the subject, and only some brief comments and literature references can be given here [197–210].

In most cases, the individual layers have a distinct composition and microstructure and an interface or buffer layer can be used to improve adhesion to the substrate. It is also possible to produce multilayers from only *one* element by periodically changing the microstructure via the deposition conditions. One example of the latter is a carbon–carbon structure where the layers have different sp^3 to sp^2 ratios [211, 212] (more about amorphous carbon near the end of this chapter).

One reason for using multilayers is that one can influence hardness and stress in a relatively decoupled way. For example, an optimized nanolayered WC–CrAlN heterostructure on silicon and S45C steel with a bilayer period of 2–10 nm exhibited a residual stress of less than 2 GPa, while the microhardness was very high, in the range 30–43 GPa [213].

When considering a nanostructure it is clear that the presence of macroparticles is detrimental because macroparticles are usually larger than the thickness of the individual layer or characteristic size of the grain, and sometimes they even exceed the thickness of the whole coating. To make matters worse, as mentioned before, the defects introduced by a macroparticles are larger than the macroparticles themselves. Therefore, it is highly desirable to improve the coating by eliminating macroparticles, which is done by switching to *filtered* arc deposition (accepting the loss of high rates; Section 10.7) or to a different technique altogether (losing some advantages of the self-ion-assisted process).

10.6.2 Decorative Coatings

Most coatings are actually multifunctional coatings. For example, the much-discussed TiN is used for its hardness, wear- and corrosion-resistant properties, as well as for its golden color.

The appearance of a coating is the result of extrinsic and intrinsic optical properties, where *extrinsic* refers to alteration of the light direction, resulting in matt or glossy surfaces, and *intrinsic* refers to wavelength-dependent (spectrally selective) reflection and absorption of the incident light.

The color of the coating results from the reflected light and therefore we need to consider interference of multiply reflected waves (in the case of transparent or slightly absorbing film materials), and the absorbing properties for spectrally absorbing coatings. The classic examples of decorative coatings, TiN and ZrN, fall in the latter category and deserve closer examination. Spectrally selective reflection is closely related to the incident light being spectrally selectively absorbed.

The most important process for arc-deposited decorative coatings like TiN is free electron absorption or intraband transition of electrons from partially filled valence bands to unfilled states just above the Fermi level. The electrons can absorb a broad range of photon energies, including photons in the visible part of the spectrum. The quantum-mechanical selection rules for electron transitions can force electrons to return to lower levels via different levels than their excitation paths, and the color of emitted light may not correspond to the absorbed light, contributing to color appearance.

While intraband transitions apply to conducting materials, the color of semiconducting or dielectric materials is mostly based on interband transitions. They occur when there is a filled valence band and an empty conduction band, separated by an energy gap. Photons with energy greater than the gap will cause electron transitions from the valence band into the conduction band, and the color results from the remaining, not absorbed, visible light. Materials whose bandgap is wider than the ultraviolet limit of the visible spectrum, $E_g > 3.5\,\mathrm{eV}$, are transparent to the eye but color can appear by interference of reflected light. Narrow bandgap materials, whose bandgap is smaller than the infrared limit of the visible spectrum, $E_g < 1.7\,\mathrm{eV}$, appear black since all of the visible light photons are sufficiently energetic to excite electrons into the conduction band. Material in the intermediate region, with a bandgap of $1.7\,\mathrm{eV} < E_g < 3.5\,\mathrm{eV}$, can show a characteristic color.

Color can also be caused by defects, e.g. in form of impurities that occupy an energetic state in the energy gap. Valence electrons can be excited into these states, giving rise to spectrally selective absorption, or color. Examples of this mechanism are the coloration of corundum (Al_2O_3) and diamond (C) by doping.

The most relevant arc-deposited decorative coating is TiN, and so let us have a closer look at the deposition–property relationship for this material. The golden color is mainly due to intraband transitions of the free electrons [214, 215].

In a simplified picture, the stoichiometry of the nitride determines the electrical and optical properties: the greater the nitrogen content, the lower the density of free electrons. Similar to having a plasma frequency defined for electrons in the plasma, one may consider electrons in the conduction band as free (Drude model) and assign them a plasma frequency, too,

$$\omega_{\mathrm{pl}} = \left(\frac{n_{\mathrm{e}} e^2}{\varepsilon_0 m_{\mathrm{e}}} \right)^{1/2} \tag{10.43}$$

where m_{e} stands for the effective electron mass, which is not exactly the same as the free electron mass we use in the plasma because here the electron–lattice interaction is taken into account in this way. The complex refractive index

$$N = n + ik = 1 - \frac{\omega_{\mathrm{pl}}^2}{\omega^2} \tag{10.44}$$

is zero at the plasma frequency, where k is the extinction coefficient and n is the real part of the refractive index. The plasma frequency separates the frequency domains that are either reflecting and absorbing ($\omega << \omega_{\mathrm{pl}}$) or transparent ($\omega >> \omega_{\mathrm{pl}}$) for electromagnetic waves of frequency ω. The region around the plasma frequency is also called the plasma edge.

Because the free carrier density of solids like TiN is rather high, typically about 10^{28} m^{-3}, the corresponding plasma frequency is about 5×10^{15} s^{-1}, which corresponds to waves in the ultraviolet (UV) region. Therefore, metals are reflecting and absorbing for all wavelengths longer than the UV spectral region, including the visible. For the conducting nitrides, the plasma frequency is reduced as the nitrogen content is increased. This leads to a more yellow appearance with an overall reduced reflectivity [215].

The same trends also hold for ZrN. As the nitrogen content increases, the plasma edge and related reflectivity minimum in the UV shift to longer wavelengths. The color of ZrN is more sensitive to changes in the composition than TiN. For the latter, changing the N/Ti ratio from under-stoichiometric 0.92 to over-stoichiometric 1.14 is hardly noticeable to the eye.

While TiN (gold) and TiC (dark gray) have a limited range of color, addition of another metal can have a dramatic effect, such as producing dark blue (Ti,Al)N. To obtain gray to black one may consider TiAlN with high Al content, while low Al content leads to a violet–bronze appearance. ZrCN exhibits a wide range of colors from stainless steel and nickel to brass, gold, and black [216]. The colors of TiCN coatings range from copper–reddish (bronze) to blue–gray. Ternary nitrides such (Ti,V)N, (Zr,V)N, (Zr,Al)N, and (Zr,Cr)N have an even greater range of possible colors [217].

10.7 Deposition of Coatings Using Filtered Cathodic Arc Plasmas

10.7.1 Tetrahedral Amorphous Carbon

Cathodic arc deposition is a technique that can produce diamond-like amorphous carbon films with very high sp^3 content, such that they are sometimes called amorphous diamond films [218–220]. For most applications of such films, the incorporation of macroparticles is not acceptable and therefore the case of a-C and ta-C films is considered here, under the heading *filtered* arc deposition. The now common term ta-C stands for tetrahedral amorphous carbon, indicating the dominance of tetrahedral or sp^3 hybridized carbon atoms. In contrast to many other deposition techniques, filtered cathodic arcs can operate in a vacuum, using a graphite cathode; the resulting films are hydrogen free apart from a small contamination due to the residual water in the vacuum chamber. Other elements, including hydrogen [221] or nitrogen [222–226], can be added when operating in a background gas containing hydrocarbons or ammonia, for example, or one can use metal organics or metal plasma from another discharge [227, 228].

Much has been published since the massive research efforts of the 1990s, and so it must suffice to summarize a few selected results and to point to some excellent reviews (e.g. [229–231]).

The earliest ta-C films were deposited in the late 1970s, and in fact ta-C films drove the development of the early macroparticle filters [232–234]. Much research followed in the 1990s when the extraordinary mechanical, chemical, optical, and electronic properties of a-C and ta-C were fully recognized [225, 235–240] and applications in the information storage [241–244], automotive/tooling [203, 245–247], and biomedical [248–250] industries were evident.

Using graphite as the feedstock material (cathode), carbon plasma is produced that contains mostly singly charged ions with a most likely kinetic energy of about 20 eV (see Table 10.2). The properties of the diamond-like material depend largely on the acceleration that carbon ions experience in the sheath to the substrate, which can be controlled via substrate bias [239] or plasma bias [251]. Deposition is generally done at room temperature because high temperature degrades the diamond-like properties of the material by reducing the density of metastable sp^3 bonds [252–254]. While the sp^3 hybrids determine the diamond-like properties such as high hardness, high Young's modulus, chemical inertness, and a wide optical band gap [255], the sp^2 hybrids are largely responsible for the electronic and optical properties because the π states lie closest to the Fermi level [256].

For applications in the magnetic storage industry, ultrathin a-C films are wanted because they combine corrosion protection with advantageous mechanical properties, and not least, because they allow wetting with a lubricant. In order to bring the read–write head as close as possible to the magnetic layer containing the magnetically stored information, the films on the medium (like a hard disk) and read–write head must be thin as possible, but continuous. The industry has succeeded in producing films as thin as 2 nm yet meeting the tough quality requirements, and efforts are underway to reduce the thickness even further. It is clear that we quickly run into the fundamental limits of the possible.

At the other extreme, where thick (> 1 μm) a-C or ta-C films are wanted, e.g. for microelectromechanical systems (MEMS) fabrication, the reduction of residual stress is paramount to prevent catastrophic failure by delamination. Repeated rapid thermal annealing up to 600 °C can be used to remove most of the compressive stress from ta-C films [252]. Another approach is the previously described bombardment with energetic ions (Section 10.5.2) [257, 258].

10.7.2 High-Quality Metal Films

As the expectations and requirements on coatings increase and other techniques deliver very good coatings, cathodic arc deposition needs to improve too, and that means addressing the macroparticle issue. The most complete and successful approach to date is the incorporation of a macroparticle filter, as mentioned in Section 10.4.3. This, however, means accepting plasma losses and associated reductions in the deposition rate, which is a major reason why filtered arc deposition is not widely implemented. Filtered arc deposition is used when dealing with high value added components.

An example of advanced filtered arc coatings is the precision metallization of semiconductors and MEMS structures. Using optimized pulsed bias, angle-dependent self-sputtering can be utilized to deal with even very small three-dimensional structures [259–261]. One of the impressive images is the near-conformal coating of a 1 μm trench structure with tantalum using a high-current pulsed filtered arc (Figure 10.21). More recently, even smaller structures have been successfully filled with copper using a filtered arc [262].

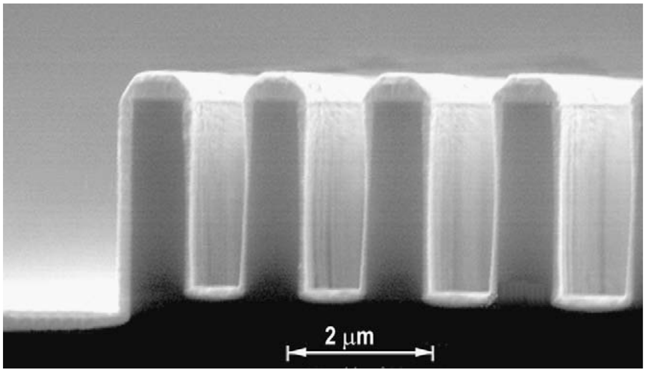

Figure 10.21: Conformal barrier coating of tantalum on a lithographically etched structure. (Photograph courtesy of P. Siemroth, Germany.)

10.7.3 Optical Films

Macroparticle contamination is especially undesirable for optical coatings and coatings related to optoelectronic devices because they deteriorate the appearance, or worse, may make the device dysfunctional. While such films can be made with other deposition techniques such as reactive magnetron sputtering or chemical vapor deposition (CVD), the self-ion-assistance of cathodic arc deposition gives the opportunity to produce superior coatings. For example, the refractive indices of optically transparent oxides are higher than those of their sputtered counterparts owing to the reduction or elimination of intercolumnar voids [263–265], and thereby they are also less prone to changes that occur owing to the uptake of moisture.

Oxide coatings can be readily obtained with the filtered cathodic arc operating in a low-pressure background of oxygen. The oxygen partial pressure is typically in the range of several Pa and must be adjusted depending on the arrival rate of metal on the substrate surface. Pulsed systems with lower average deposition rates can produce stoichiometric oxide films at even lower pressure.

The arc deposition process is relatively forgiving to variations in the oxygen partial pressure: the arc will operate in a stable manner and the films tend to be fully stoichiometric. In contrast to magnetron sputtering, the promotion of arcing by cathode poisoning is not an issue because, after all, we want to use the arc process in the cathodic arc anyway. Examples of high-quality optical films include Al_2O_3, TiO_2, VO_2, Nb_2O_5, and ZrO_2, with typical deposition rates of 25–50 nm/minute [266]. Despite ion assistance in the growth, the substrate temperature remains an important parameter that affects phase and texture of the coating.

Of special interest and importance is TiO_2 because it can have different phases: amorphous, brookite, anatase, and rutile. Cathodic arc deposition offers the possibility of synthesizing the rutile phase at room temperature provided the ions are accelerated by biasing to about 100 eV or greater [263, 267]. Lower bias favors the anatase phase, which is very important for photocatalytic applications.

Another material of interest is MgO, which is used as a transparent protective layer in alternating current plasma displays because it is highly transparent and has a high packing density and surface binding energy leading to good sputter resistance [268]. Cathodic-arc-deposited MgO films grew preferably with (200) and (220) orientation on glass and silicon when the partial pressures was increased from 1 to 4 Pa [269]. With increasing oxygen flow, the grain size increased from typically about 10 to about 25 nm, and the slight absorption seen in the blue and green disappeared: the transmittance exceeded 95% throughout the visible spectrum for the 1.0–1.3 μm thick films [269].

Yet another oxide synthesized by filtered cathodic arcs is aluminum oxide, which is interesting because it combines low absorption with high Young's modulus and hardness [270, 271]. The refractive index increased markedly when the substrate temperature was varied from 200 °C to 300 °C, indicating that ion assistance does not fully replace substrate heating, i.e. the substrate temperature remains an important parameter in energetic deposition.

The transparent optical materials are not limited to oxides; there are a number of wide bandgap nitrides such as AlN. Mändl et al. [272] produced AlN at substrate temperatures from about room temperature to 370 °C using continuous arc operation with a high deposition rate of 85–115 nm/minute. While thin films of 30 nm were amorphous, much thicker films, 1–3 μm, showed the NaCl structure with a microhardness of 18–20 GPa. As with most optical materials, AlN films are highly insulating with a resistivity of $1\text{–}2 \times 10^9\ \Omega\text{m}$. Besides being an interesting optical material, AlN films of thickness 1–3 μm are also good oxidation protection coatings up to 1100 °C [273].

10.7.4 Transparent Conducting Oxides

A special class of transparent oxide films comprises those that are electrically conducting. While most oxides are good insulators, some are wide bandgap semiconductors, usually of n-type, which have gained enormous economic importance in recent years owing to their use in numerous devices such as flat panel displays, solar cells, and touch screens. Indium–tin oxide (ITO) is the most common transparent conducting oxide (TCO) because it combines very high transmittance (> 80%) with very low electrical resistivity ($\sim 10^4\ \Omega\text{cm} = 1\ \mu\Omega\text{m}$). While ITO can be deposited by cathodic arc deposition [274], much research aims to find alternative, well-performing yet lower cost materials because the price of indium has become very high. Cathodic arc deposition plays an important role in this effort; in many cases, doped SnO_2 and ZnO films are being investigated [275]. Besides this cost-driven effort, research is also underway to find well-performing p-type TCOs [276, 277].

Pioneering work was done by Boxman and Goldsmith's group at Tel Aviv University [278]. Using a 90° filtered arc system they deposited SnO_2 on various substrates using a tin (Sn) cathode operating in an oxygen background. An optimum window of pressure was identified, with the best material made at 6 mtorr (0.8 Pa). The lower limit of the process window (3 mtorr or 0.4 Pa) was determined by the lack of oxygen to obtain the stoichiometric SnO_2, and the upper limit (12 mtorr or 1.6 Pa) was given by a drastically reduced deposition rate. The as-deposited films usually appear brownish or yellowish. Rapid thermal annealing at 300 °C in air reduces the resistivity by about one order of magnitude and the films become clear with a transmittance of about 85% in the visible.

Many more research projects have followed [275, 276, 279–289] as reviewed by Tay [288] and in a recent book [3].

10.7.5 Nitride Multilayers, Nanocomposites, and MAX Phases

Large area coatings with good uniformity are a challenge for filtered cathodic arcs. Those issues can be solved, as was demonstrated by Gorokhovsky et al., who developed their dual-arc large-area filtered arc deposition (LAFAD) facility [290], a commercial-size batch coater for high value added products. They deposited TiN/Ti multilayers and TiCrN/TiCr superlattice multilayer coatings on periodontal instruments [200].

As mentioned in Section 10.6.1, multilayers and nanostructures are of increasing relevance to modern applications. It is common to require that advanced structures do not suffer from macroparticle- or macroparticle-induced defects; hence, filtered arc deposition is considered here. This is especially true for an emerging class of materials called MAX phases [291], which consist of an early transition metal M, an element from the A groups of the Periodic Table, usually IIIA and IVA, and a third element, X, which is either nitrogen or carbon. The composition is $M_{n+1}AX_n$, where $n = 1$, 2 or 3. MAX phases form three groups, based on the number of atoms of the M, A, and X elements in each unit cell; these groups are known as 211, 312, and 413 materials. Examples for the first group are M_2AlC, with M = Sc, Y, La, Ti, Zr, Hf, V, Nb, Ta, Cr, Mo, W. More than 50 MAX phases are known today and more can be expected since this is a field of intense research. MAX phase materials have amazing properties because they combine the high temperature stability of ceramics with properties of metals such as good thermal and electrical conductivity. They are machinable, in contrast to conventional ceramics.

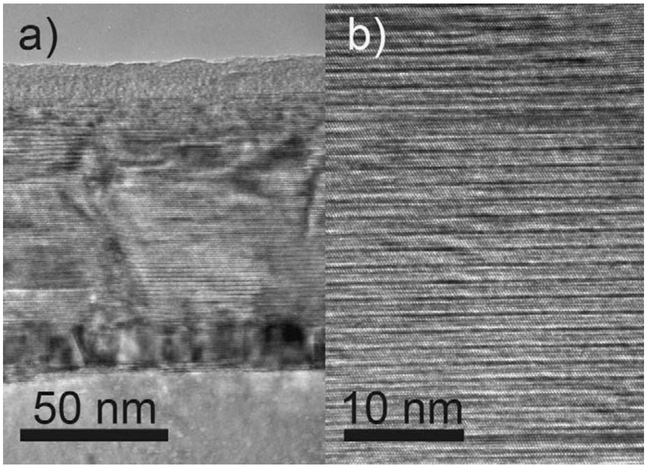

Figure 10.22: Cross-sectional TEM image of a Ti_2AlC MAX-phase coating synthesized by filtered three-cathode pulsed arc deposition at 900 °C: (a) low-resolution image, with the α–Al_2O_3(0001) substrate at the bottom, coating in center, and the amorphous-looking TEM-glue layer on top; (b) high-resolution image clearly showing the nanolaminate structure. (Image courtesy of J. Rosén (deposition) and P. Persson (TEM), work done at Sydney University.)

The synthesis of the Ti_2AlC MAX phase was successfully demonstrated using filtered cathodic arc deposition with a triple-cathode pulsed arc system [292]. The Ti:Al:C pulse ratios were fine-tuned to obtain the necessary stoichiometric relation in the coating, which was deposited on $\alpha-Al_2O_3(0001)$ substrates at 900 °C. Transmission electron microscopy (TEM) revealed epitaxial growth and the nanolaminated hexagonal structure with some rare cubic precipitates (Figure 10.22).

There are many more applications of unfiltered and filtered cathodic arc deposition, and the reader is referred to a recent, more comprehensive overview [3].

References

[1] J. Priestley, Experiments in which rings, consisting of all the prismatic colours, were made by electrical explosions on the surface of metals, in: The History and Present State of Electricity, Vol. II, London (1775) 329–335.
[2] J. Priestley, The History and Present State of Electricity, 3rd ed, London (1775).
[3] A. Anders, Cathodic Arcs: From Fractal Spots to Energetic Condensation, Springer, New York (2008).
[4] S. Anders, A. Anders, On modes of arc cathode operation, IEEE Trans. Plasma Sci. 19 (1991) 20–24.
[5] A. Anders, B. Jüttner, Cathode mode transition in high-pressure discharge lamps at start-up, Lighting Res. Technol. (GB) 22 (1990) 111–115.
[6] H. Ehrich, B. Hasse, M. Mausbach, K.G. Müller, The anodic vacuum arc and its application to coatings, J. Vac. Sci. Technol. A 8 (1990) 2160–2164.
[7] I.I. Beilis, R.L. Boxman, S. Goldsmith, V.L. Paperny, Radially expanding plasma parameters in a hot refractory anode vacuum arc, J. Appl. Phys. 88 (2000) 6224–6231.
[8] R.H. Fowler, L. Nordheim, Electron emission in intense electric fields, Proc. R. Soc. (London) A119 (1928) 173–181.
[9] E. Hantzsche, The thermo-field emission of electrons in arc discharges, Beitr. Plasmaphys. 22 (1982) 325–346.
[10] G.A. Mesyats, D.I. Proskurovsky, Pulsed Electrical Discharge in Vacuum, Springer, Berlin (1989).
[11] W.W. Dolan, W.P. Dyke, Temperature and field emission of electrons from metals, Phys. Rev. 35 (1954) 327.
[12] E.L. Murphy, R.H. Good Jr., Thermionic emission, field emission, and the transition region, Phys. Rev. 102 (1956) 1446.
[13] G.A. Mesyats, Explosive Electron Emission, URO Press, Ekaterinburg (1998).
[14] S.P. Bugaev, E.A. Litvinov, G.A. Mesyats, D.I. Proskurovskii, Explosive emission of electrons, Sov. Phys. Usp. 18 (1975) 51–61.
[15] E.A. Litvinov, G.A. Mesyats, D.I. Proskurovskii, Field emission and explosive emission processes in vacuum discharges, Sov. Phys. Usp. 26 (1983) 138.
[16] W.G. Chace, H.K. More, Exploding Wires, Plenum Press, New York (1962).
[17] Y.A. Kotov, V.S. Sedoi, L.I. Chemezova, The integral of action and the energy for electrically exploded wires, Institute of High Current Electronics, Tomsk (1986).
[18] R.P.P. Smeets, The origin of current chopping in vacuum arcs, IEEE Trans. Plasma Sci. 17 (1989) 303–310.
[19] A. Anders, Chopping effect observed at cathodic arc initiation, IEEE Trans. Plasma Sci. 28 (2000) 1303–1304.
[20] G.A. Mesyats, Cathode Phenomena in a Vacuum Discharge: The Breakdown, the Spark and the Arc, Nauka, Moscow (2000).
[21] M.B. Bochkarev, Ecton processes of low current vacuum arc imaged with streak technique, in: XXIth Int. Symp. Discharges and Electrical Insulation in Vacuum, Yalta, Ukraine (2004) 241–244.

[22] J. Prock, Solidification of hot craters on the cathode of vacuum arcs, J. Phys. D: Appl. Phys. 19 (1986) 1917–1924.

[23] A. Anders, S. Anders, A. Förster, I.G. Brown, Pressure ionization: its role in metal vapor vacuum arc plasmas and ion sources, Plasma Sources Sci. Technol. 1 (1992) 263–270.

[24] J.E. Daalder, Random walk of cathode arc spots in vacuum, J. Phys. D: Appl. Phys. 16 (1983) 17–27.

[25] E. Hantzsche, B. Jüttner, H. Pursch, On the random walk of arc cathode spots in vacuum, J. Phys. D: Appl. Phys. 16 (1983) L173–L179.

[26] B. Jüttner, V.F. Puchkarev, E. Hantzsche, I. Beilis, Cathode spots, in: R.L. Boxman, D.M. Sanders, P.J. Martin (Eds.), Handbook of Vacuum Arc Science and Technology, Noyes, Park Ridge, New Jersey (1995) 73–281.

[27] B. Jüttner, The dynamics of arc cathode spots in vacuum: new measurements, J. Phys. D: Appl. Phys. 30 (1997) 221–229.

[28] B. Jüttner, H. Pursch, V.A. Shilov, The influence of surface roughness and surface temperature on arc spot movement in vacuum, J. Phys. D: Appl. Phys. 17 (1984) L31–L34.

[29] I. Beilis, B.E. Djakov, B. Jüttner, H. Pursch, Structure and dynamics of high-current arc cathode spots in vacuum, J. Phys. D: Appl Phys 30 (1997) 119–130.

[30] B. Jüttner, I. Kleberg, The retrograde motion of arc cathode spots in vacuum, J. Phys. D: Appl. Phys. 33 (2000) 2025–2036.

[31] A. Anders, The fractal nature of cathode spots, IEEE Trans. Plasma Sci. 33 (2005) 1456–1464.

[32] M. Schroeder, M. Fractals, M. Chaos, Power Laws: Minutes from an Infinite Paradise, 8th ed., W.H. Freeman and Co, New York (2000).

[33] I. Kleberg, Dynamics of cathode spots in external magnetic field, Humboldt University, Berlin (2001) (in German).

[34] A.P. Ehiasarian, P.E. Hovsepian, R. New, J. Valter, Influence of steering magnetic field on the time-resolved plasma chemistry in cathodic arc discharges, J. Phys. D: Appl. Phys. 37 (2004) 2101–2106.

[35] K.K. Zabello, Y.A. Barinov, A.M. Chaly, A.A. Logatchev, S.M. Shkol'nik, Experimental study of cathode spot motion and burning voltage of low-current vacuum arc in magnetic field, IEEE Trans. Plasma Sci. 33 (2005) 1553–1559.

[36] D.Y. Fang, Temperature dependence of retrograde velocity of vacuum arcs in magnetic fields, IEEE Trans. Plasma Sci. 11 (1983) 110–114.

[37] A.E. Robson, A. von Engel, Origin of retrograde motion of arc cathode spots, Phys. Rev. 93 (1954) 1121–1122.

[38] K.K. Zabello, Y.A. Barinov, A.A. Logatchev, S.M. Shkol'nik, Cathode spot motion and burning voltage of low-current vacuum arc with electrodes of copper–chromium composition in magnetic field, in: Proc. of XXIth Int. Symp. Discharges and Electrical Insulation in Vacuum, Yalta, Ukraine (2004) 280–281.

[39] B.B. Mandelbrot, The Fractal Geometry of Nature, W.H. Freeman and Co., New York (1983).

[40] R.P.P. Smeets, F.J.H. Schulpen, Fluctuations of charged particle and light emission in vacuum arcs, J. Phys. D: Appl. Phys. 21 (1988) 301–310.

[41] A. Anders, E.M.Yu. Oks, G. Yushkov, Cathodic arcs: fractal voltage and cohesive energy rule, Appl. Phys. Lett. 86 (2005) 211503–1–3.

[42] S. Anders, B. Jüttner, Influence of residual gases on cathode spot behavior, IEEE Trans. Plasma Sci. 19 (1991) 705–712.

[43] T. Schülke, P. Siemroth, Vacuum arcs cathode spots as a self-similarity phenomenon, IEEE Trans. Plasma Sci. 24 (1996) 63–64.

[44] P. Siemroth, T. Schülke, T. Witke, Investigations of cathode spots and plasma formation of vacuum arcs by high speed microscopy and spectrography, IEEE Trans. Plasma Sci. 25 (1997) 571–579.

[45] E. Hantzsche, Mysteries of the arc cathode spot: a retrospective glance, IEEE Trans. Plasma Sci. 31 (2003) 799–808.

[46] A. Anders, G.Y. Yushkov, Angularly resolved measurements of the ion energy of vacuum arc plasmas, Appl. Phys. Lett. 80 (2002) 2457–2459.

[47] J. Kutzner, H.C. Miller, In flux from the cathode region of a vacuum arc, IEEE Trans. Plasma Sci. 17 (1989) 688–694.
[48] V.A. Ivanov, B. Jüttner, H. Pursch, Time-resolved measurements of the parameters of arc cathode plasmas in vacuum, IEEE Trans. Plasma Sci. 13 (1985) 334–336.
[49] C.W. Kimblin, Cathode spot erosion and ionization phenomena in the transition region from vacuum to atmospheric pressure arcs, J. Appl. Phys. 45 (1974) 5235–5244.
[50] J.E. Daalder, Components of cathode erosion in vacuum arcs, J. Phys. D: Appl. Phys. 9 (1976) 2379–2395.
[51] A. Anders, G.Y. Yushkov, Ion flux from vacuum arc cathode spots in the absence and presence of magnetic fields, J. Appl. Phys. 91 (2002) 4824–4832.
[52] A. Anders, E.M. Oks, G.Y. Yushkov, K.P. Savkin, Y. Brown, A.G. Nikolaev, Determination of the specific ion erosion of the vacuum arc cathode by measuring the total ion current from the discharge plasma, Tech. Phys. 51 (2006) 1311–1315.
[53] V.M. Lunev, V.G. Padalka, V.M. Khoroshikh, Plasma properties of a metal vacuum arc. II, Sov. Phys. Tech. Phys. 22 (1977) 858–861.
[54] W.D. Davis, H.C. Miller, Analysis of the electrode products emitted by dc arcs in a vacuum ambient, J. Appl. Phys. 40 (1969) 2212–2221.
[55] A.A. Plyutto, V.N. Ryzhkov, A.T. Kapin, High speed plasma streams in vacuum arcs, Sov. Phys. JETP 20 (1965) 328–337.
[56] I.G. Brown, B. Feinberg, J.E. Galvin, Multiply stripped ion generation in the metal vapor vacuum arc, J. Appl. Phys. 63 (1988) 4889–4898.
[57] I.G. Brown, X. Godechot, Vacuum arc ion charge-state distributions, IEEE Trans. Plasma Sci. 19 (1991) 713–717.
[58] A. Anders, S. Anders, B. Jüttner, I.G. Brown, Time dependence of vacuum arc parameters, IEEE Trans. Plasma Sci. PS-21 (1993) 305–311.
[59] E. Oks, I.G. Brown, M.R. Dickinson, R.A. MacGill, P. Spädtke, H. Emig, B.H. Wolf, Elevated ion charge states in vacuum arc plasmas in a magnetic field, Appl. Phys. Lett. 67 (1995) 200–202.
[60] F.J. Paoloni, I.G. Brown, Some observations of the effect of magnetic field and arc current on the vacuum arc charge state distribution, Rev. Sci. Instrum. 66 (1995) 3855–3858.
[61] I.G. Brown, Vacuum arc ion sources, Rev. Sci. Instrum. 65 (1994) 3061–3081.
[62] A.N. Pustovit, V.I. Zhila, G.G. Sikharulidze, Mass spectral diagnostics of plasma formed at cathode tip explosion, Sov. Phys. Tech. Phys. 31 (1986) 496–497.
[63] I.G. Brown (Ed.), The Physics and Technology of Ion Sources, Wiley-VCH, Weinheim (2004).
[64] A.I. Ryabchikov, I.B. Stepanov, S.V. Dektjarev, E.I. Lukonin, I.A. Shulepov, Very broad vacuum arc ion and plasma sources with extended large area cathodes, Rev. Sci. Instrum. 71 (2000) 704–706.
[65] A. Anders, B. Yotsombat, R. Binder, Correlation between cathode properties, burning voltage, and plasma parameters of vacuum arcs, J. Appl. Phys. 89 (2001) 7764–7771.
[66] C. Kittel, Introduction to Solid State Physics, John Wiley & Sons, New York (1986).
[67] A. Anders, Ion charge state distributions of vacuum arc plasmas: The origin of species, Phys. Rev. E 55 (1997) 969–981.
[68] A. Anders, G. Yushkov, E. Oks, A. Nikolaev, I. Brown, Ion charge state distributions of pulsed vacuum arc plasmas in strong magnetic fields, Rev. Sci. Instrum. 69 (1998) 1332–1335.
[69] I.A. Krinberg, On the mechanism of the external magnetic field action on the electron temperature and ion charge state distribution in a vacuum arc plasma, Techn. Phys. Lett. 29 (2003) 504–506.
[70] E.M. Oks, A. Anders, I.G. Brown, M.R. Dickinson, R.A. MacGill, Ion charge state distributions in high current vacuum arc plasma in a magnetic field, IEEE Trans. Plasma Sci. 24 (1996) 1174–1183.
[71] I.A. Krinberg, The ion charge–current strength relationship in stationary and pulsed vacuum discharges, Tech. Phys. Lett. 27 (2001) 45–48.
[72] C.W. Kimblin, A review of arcing phenomena in vacuum and in the transition to atmospheric pressure arcs, IEEE Trans. Plasma Sci. 10 (1971) 322–330.

[73] I.I. Demidenko, N.S. Lomino, V.D. Ovcharenko, V.G. Padalka, G.N. Polyakova, Ionization mechanism for nitrogen in a vacuum arc discharge, Sov. Phys Tech. Phys. 29 (1984) 895–897.

[74] P.J. Martin, D.R. McKenzie, R.P. Netterfield, P. Swift, S.W. Filipczuk, K.-H. Müller et al., Characteristics of titanium arc evaporation processes, Thin Solid Films 153 (1987) 91–102.

[75] M. Sakaki, T. Sakakibara, Excitation, ionization, and reaction mechanism of a reactive cathodic arc deposition of TiN, IEEE Trans. Plasma Sci. 22 (1994) 1049–1054.

[76] E. Oks, G. Yushkov, Some features of vacuum arc plasmas with increasing gas pressure in the discharge gap, in: XVIIth Int. Symp., Discharges and Electrical Insulation in Vacuum, Berkeley, CA (1996) 584–588.

[77] M.M.M. Bilek, P.J. Martin, D.R. McKenzie, Influence of gas pressure and cathode composition on ion energy distributions in filtered cathodic vacuum arcs, J. Appl. Phys. 83 (1998) 2965–2970.

[78] J.M. Schneider, A. Anders, I.G. Brown, B. Hjörvarsson, L. Hultman, Temporal development of the plasma composition of a pulsed aluminum plasma stream in the presence of oxygen, Appl. Phys. Lett. 75 (1999) 612–614.

[79] J. Rosén, A. Anders, L. Hultman, J.M. Schneider, Temporal development of the composition of Zr and Cr cathodic arc plasma streams in a N_2 environment, J. Appl. Phys. 94 (2003) 1414–1419.

[80] J. Rosén, A. Anders, L. Hultman, J.M. Schneider, Charge state and time resolved plasma composition of a pulsed zirconium arc in a nitrogen environment, J. Appl. Phys. 96 (2004) 4793–4799.

[81] J. Rosén, A. Anders, S. Mráz, A. Atiser, J.M. Schneider, Influence of argon and oxygen on charge-state-resolved ion energy distributions of filtered aluminum arc, J. Appl. Phys. 99 (2006) 123303-1–5.

[82] B.M. Smirnov, Atomic structure and the resonant charge exchange process, Uspekhi Fizicheskikh Nauk. 171 (2001) 233–266.

[83] R.K. Janev, J.W. Gallagher, Evaluated theoretical cross-section data for charge exchange of multiply charged ions with atoms. III. Nonhydrogenic target atoms, J. Phys. Chem. Reference Data 13 (1984) 1199–1249.

[84] J. Kutzner, H.C. Miller, Integrated ion flux emitted from the cathode spot region of a diffuse vacuum arc, J. Phys. D: Appl. Phys. 25 (1992) 686–693.

[85] J. Rosén, A. Anders, S. Mráz, J.M. Schneider, Charge-state-resolved ion energy distributions of aluminum vacuum arcs in the absence and presence of a magnetic field, J. Appl. Phys. 97 (2005) 103306-1–6.

[86] M.A. Lieberman, A.J. Lichtenberg, Principles of Plasma Discharges and Materials Processing, John Wiley & Sons, New York (1994).

[87] J. Rosén, J.M. Schneider, A. Anders, Charge state dependence of cathodic vacuum arc ion energy and velocity distributions, Appl. Phys. Lett. 89 (2006) 141502-1–3.

[88] K. Tsuruta, K. Skiya, G. Watanabe, Velocities of copper and silver ions generated from an impulse vacuum arc, IEEE Trans. Plasma Sci. 25 (1997) 603–608.

[89] A.S. Bugaev, V.I. Gushenets, A.G. Nikolaev, E.M. Oks, G.Y. Yushkov, Influence of a current jump on vacuum arc parameters, IEEE Trans. Plasma Sci. 27 (1999) 882–887.

[90] A.S. Bugaev, E.M. Oks, G.Y. Yushkov, A. Anders, I.G. Brown, Enhanced ion charge states in vacuum arc plasmas using a 'current spike' method, Rev. Sci. Instrum. 71 (2000) 701–703.

[91] G.Y. Yushkov, A. Anders, E.M. Oks, I.G. Brown, Ion velocities in vacuum arc plasmas, J. Appl. Phys. 88 (2000) 5618–5622.

[92] A. Anders, E. Oks, Charge-state-resolved ion energy distribution functions of cathodic vacuum arcs: A study involving the plasma potential and biased plasmas, J. Appl. Phys. 101 (2007) 043304-1–6.

[93] E. Byon, A. Anders, Ion energy distribution functions of vacuum arc plasmas, J. Appl. Phys. 93 (2003) 1899–1906.

[94] G. Yushkov, Measurements of directed ion velocity in vacuum arc plasmas by arc current perturbation methods, in: Proc. of XXth Int. Symp. on Discharges and Electrical Insulation in Vacuum, Xi'an, P.R. China (2000) 260–263.

[95] E.A. Litvinov, Kinetic of cathode jet at explosive emission of electrons, in: G.A. Mesyats (Ed.), High Current Nanosecond Pulsed Sources of Accelerated Electrons, Nauka, Novosibirsk (1974) (in Russian).

[96] I.A. Krinberg, M.P. Lukovnikova, Application of a vacuum arc model to the determination of cathodic microjet parameters, J. Phys. D: Appl. Phys. 29 (1996) 2901–2906.

[97] G.Y. Yushkov, A.S. Bugaev, I.A. Krinberg, E.M. Oks, On a mechanism of ion acceleration in vacuum arc-discharge plasma, Doklady Phys. 46 (2001) 307–309.

[98] I.A. Krinberg, Acceleration of multicomponent plasma in the cathode region of vacuum arc, Techn. Phys. 46 (2001) 1371–1378.

[99] L.P. Sablev, J.I. Dolotov, L.I. Getman, V.N. Gorbunov, E.G. Goldiner, K.T. Kirshfeld, V.V. Usov, Apparatus for vacuum evaporation of metals under the action of an electric arc, Patent US 3,783,231 (1974).

[100] A.A. Snaper, Arc deposition process and apparatus, Patent US 3,836,451 (1974).

[101] A.A. Snaper, Arc deposition process and apparatus, Patent US 3,625,848 (1971).

[102] P. Hovsepian, Lichtbogen-Verdampfungsvorrichtung, Patent DE 4220588 (1994).

[103] L.P. Sablev, N.P. Atamansky, V.N. Gorbunov, J.I. Dolotov, V.N. Lutseenko, V.M. Lunev, V.V. Usov, Apparatus for metal evaporation coating, Patent US 3,793,179 (1974).

[104] I.I. Aksenov, A.A. Andreev, Motion of the cathode spot of a vacuum arc in an inhomogeneous magnetic field, Sov. Tech. Phys. Lett. 3 (1977) 525–526.

[105] D.A. Karpov, Cathodic arc sources and macroparticle filtering, Surf. Coat. Technol. 96 (1997) 22–33.

[106] G.E. Vergason, Electric arc vapor deposition device, Patent US 5,037,522 (1991).

[107] K. Brondum, G. Larson, Low-temperature arc vapor deposition as a hexavalent chrome electroplating alternative, Vapor Technologies Inc., Longmont, CO (May 13, 2005).

[108] R.P. Welty, Apparatus and method for coating a substrate using vacuum arc evaporation, Patent US 5,269,898 (1993).

[109] P. Siemroth, T. Schülke, T. Witke, High-current arc – a new source for high-rate deposition, Surf. Coat. Technol. 68 (1994) 314–319.

[110] T. Witke, P. Siemroth, Deposition of droplet-free films by vacuum arc evaporation – results and applications, IEEE Trans. Plasma Sci. 27 (1999) 1039–1044.

[111] M. Büschel, W. Grimm, Influence of the pulsing of the current of a vacuum arc on rate and droplets, Surf. Coat. Technol. 142-144 (2001) 665–668.

[112] T.W.H. Oates, J. Pigott, D.R. McKenzie, M.M.M. Bilek, A high-current pulsed cathodic vacuum arc plasma source, Rev. Sci. Instrum. 74 (2003) 4750–4754.

[113] J.E. Daalder, Cathode spots and vacuum arcs, Physica C 104C (1981) 91–106.

[114] Y.Y. Udris, Investigation in the field of electric discharges in gases, Trudy VEI (All-Union Order of Lenin Institute of Electric Engineering), Vol.63, Gosenergoizdat, Moscow (1958) (in Russian).

[115] T. Utsumi, J.H. English, Study of electrode products emitted by vacuum arcs in form of molten metal particles, J. Appl. Phys. 46 (1975) 126–131.

[116] D.T. Tuma, C.L. Chen, D.K. Davis, Erosion products from the cathode spot region of a copper vacuum arc, J. Appl. Phys. 49 (1978) 3821–3831.

[117] B. Gellert, E. Schade, E. Dullni, IEEE Trans. Plasma Sci. PS-15 (1987) 545–551.

[118] G. Disatnik, R.L. Boxman, S. Goldsmith, Characteristics of macroparticle emission from a high-current-density multi-cathode spot vacuum arc, IEEE Trans. Plasma Sci. PS-15 (1987) 520–523.

[119] S. Shalev, S. Goldsmith, R.L. Boxman, S. Einav, J.M. Avidor, Laser Doppler anemometry: a tool for studying macroparticle dynamics in a vacuum arc, J. Phys. E: Sci. Instrum. 17 (1984) 56–61.

[120] S. Shalev, R.L. Boxmann, S.J. Goldsmith, Velocities and emission rates of cathode-produced molybdenum macroparticles in a vacuum arc, J. Appl. Phys. 58 (1985) 2503–2507.

[121] S. Shalev, R.L. Boxman, S. Goldsmith, IEEE Trans. Plasma Sci. PS-14 (1986) 59–62.

[122] B. Gellert, E. Schade, Optical investigation of droplet emission in vacuum interrupters to improve contact materials, in: XIVth Int. Symp. on Discharges and Electrical Insulation in Vacuum, Santa Fe (1990) 450–454.

[123] R.L. Boxman, S. Goldsmith, Macroparticle contamination in cathodic arc coatings: Generation, transport and control, Surf. Coat. Technol. 52 (1992) 39–50.

[124] M. Kandah, J.-L. Meunier, Study of microdroplet generation from vacuum arcs on graphite cathodes, J. Vac. Sci. Technol. A 13 (1995) 2444–2450.

[125] M. Kandah, J.-L. Meunier, Erosion study on graphite cathodes using pulsed vacuum arcs, IEEE Trans. Plasma Sci. 24 (1996) 523–527.

[126] S. Anders, A. Anders, K.M. Yu, X.Y. Yao, I.G. Brown, On the macroparticle flux from vacuum arc cathode spots, IEEE Trans. Plasma Sci. 21 (1993) 440–446.
[127] T. Schülke, A. Anders, Velocity distribution of carbon macroparticles generated by pulsed vacuum arcs, Plasma Sources Sci. Technol. 8 (1999) 567–571.
[128] D. Drescher, J. Koskinen, H.-J. Scheibe, A. Mensch, A model for particle growth in arc deposited amorphous carbon films, Diamond Rel. Mater. 7 (1998) 1375–1380.
[129] V.S. Voitsenya, A.G. Gorbanyuk, I.N. Onishchenko, B.G. Safronov, N.A. Khizhniyak, V.V. Shkoda, Motion of a plasmoid in a curvilinear magnetic field, Sov. Phys. Tech. Phys. 12 (1967) 185–192.
[130] I.I. Aksenov, V.A. Belous, V.G. Padalka, V.M. Khoroshikh, Transport of plasma streams in a curvilinear plasma-optics system, Sov. J. Plasma Phys. 4 (1978) 425–428.
[131] I.I. Aksenov, V.A. Belous, V.G. Padalka, V.M. Khoroshikh, Apparatus to rid the plasma of a vacuum arc of macroparticles, Instrum. Exp. Tech. 21 (1978) 1416–1418.
[132] A. Anders, S. Anders, I.G. Brown, Effect of duct bias on transport of vacuum arc plasmas through curved magnetic filters, J. Appl. Phys. 75 (1994) 4900–4905.
[133] M.M.M. Bilek, D.R. McKenzie, Y. Yin, M.U. Chhowalla, W.I. Milne, Interactions of the directed plasma from a cathodic arc with electrodes and magnetic field, IEEE Trans. Plasma Sci. 24 (1996) 1291–1298.
[134] S. Anders, A. Anders, M.R. Dickinson, R.A. MacGill, I.G. Brown, S-shaped magnetic macroparticle filter for cathodic arc deposition, IEEE Trans. Plasma Sci. 25 (1997) 670–674.
[135] T. Witke, T. Schuelke, B. Schultrich, P. Siemroth, J. Vetter, Comparison of filtered high current pulsed arc deposition (f-HCA) with conventional vacuum arc methods, Surf. Coat. Technol. 126 (2000) 81–88.
[136] X. Shi, B.K. Tay, H.S. Tan, E. Liu, J. Shi, L.K. Cheah, X. Jin, Transport of vacuum arc plasma through an off-plane double bend filtering duct, Thin Solid Films 345 (1999) 1–6.
[137] A. Anders, R.A. MacGill, Twist filter for the removal of macroparticles from cathodic arc plasmas, Surf. Coat. Technol. 133–134 (2000) 96–100.
[138] A. Anders, Approaches to rid cathodic arc plasma of macro- and nanoparticles: a review, Surf. Coat. Technol. 120–121 (1999) 319–330.
[139] J.S. Colligon, Energetic condensation: processes, properties, and products, J. Vac. Sci. Technol. A 13 (1995) 1649–1657.
[140] I.G. Brown, Cathodic arc deposition of films, Annu. Rev. Mater. Sci. 28 (1998) 243–269.
[141] O.R. Monteiro, Thin film synthesis by energetic condensation, Annu. Rev. Mater. Sci. 31 (2001) 111–137.
[142] M. Nastasi, J.W. Mayer, J.K. Hirvonen, Ion–Solid Interactions, Cambridge University Press, Cambridge (1996).
[143] S. Uhlmann, T. Fraunheim, Y. Lifshitz, Molecular-dynamics study of the fundamental processes involved in subplantation of diamondlike carbon, Phys. Rev. Lett. 81 (1998) 641–644.
[144] Y. Lifshitz, S.R. Kasai, J.W. Rabalais, W. Eckstein, Subplantation model for film growth from hyperthermal species, Phys. Rev. B 41 (1990) 10468–10480.
[145] C. Ronning, Ion-beam synthesis and growth mechanism of diamond-like materials, Appl. Phys. A 77 (2003) 39–50.
[146] A. Anders (Ed.), Handbook of Plasma Immersion Ion Implantation and Deposition, John Wiley & Sons, New York (2000).
[147] T.A. Carlson, C.W. Nestor, N. Wasserman, J.D. McDowell, Calculated ionization potentials for multiply charges ions, Atomic Data 2 (1970) 63–99.
[148] D.R. Lide (Ed.), Handbook of Chemistry and Physics, 81st ed., CRC Press, Boca Raton, New York (2000).
[149] J. Musil, Hard and superhard nanocomposite coatings, Surf. Coat. Technol. 125 (2000) 322–330.
[150] A. Anders, Atomic scale heating in cathodic arc plasma deposition, Appl. Phys. Lett. 80 (2002) 1100–1102.
[151] M. Nastasi, J.M. Mayer, Ion Implantation and Synthesis of Materials, Springer, Berlin (2006).
[152] M.M.M. Bilek, D.R. McKenzie, A comprehensive model of stress generation and relief processes in thin films deposited with energetic ions, Surf. Coat. Technol. 200 (2006) 4345–4354.
[153] M.M.M. Bilek, R.N. Tarrant, D.R. McKenzie, S.H.N. Lim, D.G. McCulloch, Control of stress and microstructure in cathodic arc deposited films, IEEE Trans. Plasma Sci. 31 (2003) 939–944.

[154] S.H.N. Lim, D.G. McCulloch, M.M.M. Bilek, D.R. McKenzie, Minimisation of intrinsic stress in titanium nitride using a cathodic arc with plasma immersion ion implantation, Surf. Coat. Technol. 174–175 (2003) 76–80.
[155] C.A. Davis, A simple model for the formation of compressive stress in thin films by ion bombardment, Thin Solid Films 226 (1993) 30–34.
[156] H. Windischmann, An intrinsic stress scaling law for polycrystalline thin films prepared by ion beam sputtering, J. Appl. Phys 62 (1987) 1800–1807.
[157] N.A. Marks, Evidence for subpicosecond thermal spikes in the formation of tetrahedral amorphous carbon, Phys. Rev. B 56 (1997) 2441.
[158] M.M.M. Bilek, D.R. McKenzie, W. Moeller, Use of low energy and high frequency PBII during thin film deposition to achieve relief of intrinsic stress and microstructural changes, Surf. Coat. Technol. 186 (2004) 21–28.
[159] B. Abendroth, R. Gago, A. Kolitsch, W. Moller, Stress measurement and stress relaxation during magnetron sputter deposition of cubic boron nitride thin films, Thin Solid Films 447–448 (2004) 131–135.
[160] Y. Yin, D. McKenzie, M. Bilek, Intrinsic stress induced by substrate bias in amorphous hydrogenated silicon thin films, Surf. Coat. Technol. 198 (2005) 156–160.
[161] J. Houska, J. Capek, J. Vlcek, M.M.M. Bilek, D.R. McKenzie, Bonding statistics and electronic structure of novel Si–B–C–N materials: ab initio calculations and experimental verification, J. Vac. Sci. Technol. A 25 (2007) 1411–1416.
[162] M.M.M. Bilek, M. Verdon, L. Ryves, T.W.H. Oates, C.T. Ha, D.R. McKenzie, A model for stress generation and stress relief mechanisms applied to as-deposited filtered cathodic vacuum arc amorphous carbon films, Thin Solid Films 482 (2005) 69–73.
[163] H. Hofsäss, H. Feldermann, R. Merk, M. Sebastian, C. Ronning, Cylindrical spike model for the formation of diamondlike thin films by ion deposition, Appl. Phys. A: Mater. Sci. Process. 66 (1998) 153–181.
[164] M. Krohn, K.-P. Meyer, H. Bethge, Epitaxy by vacuum arc evaporation, J. Crystal Growth 64 (1983) 326–332.
[165] E. Byon, T.H. Oates, A. Anders, Coalescence of nanometer silver islands on oxides grown by filtered cathodic arc deposition, Appl. Phys. Lett. 82 (2003) 1634–1636.
[166] T. Oates, D. McKenzie, M. Bilek, Percolation threshold in ultrathin titanium films determined by in-situ spectroscopic ellipsometry, Phys. Rev. B 70 (2004) 195406.
[167] H. Arwin, D.E. Aspnes, Unambiguous determination of thickness and dielectric function of thin films by spectroscopic ellipsometry, Thin Solid Films 113 (1984) 101–113.
[168] J.F. Ziegler, J. Biersack, Monte Carlo code SRIM2006.02, downloadable from: <http://srim.org/> (2006).
[169] J.-O. Andersson, B. Sundman, Thermodynamic properties of the Cr–Fe system, Calphad 11 (1987) 83–92.
[170] I.I. Aksenov, V.A. Belous, V.G. Padalka, V.M. Khoroshikh, Producing coatings with aluminium oxide base from separated flow of vacuum arc plasma, Fizika i Khimiya Obrabotki Materialov (1977) 89–93.
[171] C. Bergman, Arc plasma physical vapor deposition, in: 28th Annual SVC Technical Conference, Philadelphia, PA (1985) 175–191.
[172] W.-D. Münz, D. Schulze, F.J.M. Hauzer, A new method for hard coatings – ABS (arc bond sputtering), Surf. Coat. Technol. 50 (1992) 169–178.
[173] C. Schönjahn, A.P. Ehiasarian, D.B. Lewis, R. New, W.-D. Münz, R.D. Twesten, I. Petrov, Optimization of in-situ substrate treatment in a cathodic arc plasma: A study by TEM and plasma diagnostics, J. Vac. Sci. Technol. A 19 (2001) 1415–1420.
[174] A.P. Ehiasarian, P.E. Hovsepian, L. Hultman, U. Helmersson, Comparison of microstructure and mechanical properties of chromium nitride-based coatings deposited by high power impulse magnetron sputtering and by the combined steered cathodic arc/unbalanced magnetron technique, Thin Solid Films 457 (2004) 270–277.
[175] D.B. Lewis, D. Reitz, C. Wüstefeld, R. Ohser-Wiedemann, H. Oettel, A.P. Ehiasarian, P.E. Hovsepian, Chromium nitride/niobium nitride nano-scale multilayer coatings deposited at low temperature by the combined cathodic arc/unbalanced magnetron technique, Thin Solid Films 503 (2006) 133–142.

[176] I.I. Aksenov, A.A. Andreev, Vacuum arc coating technologies at NSC KIPT, Problems Atomic Sci. Technol., Series: Plasma Physics 3 (1999) 242.

[177] P.C. Johnson, Cathodic arc plasma deposition processes and their applications, in: 30th Annual SVC Technical Conference (1987) 317–324.

[178] B. Rother, J. Vetter, Plasmabeschichtungsverfahren und Hartstoffschichten, Deutscher Verlag für Grundstoffindustrie, Leipzig (1992).

[179] K.W. Mertz, H.A. Jehn (Eds.), Praxishandbuch moderne Beschichtungen, Carl Hanser Verlag, München (2001).

[180] A. Anders, A brief modern history of cathodic arc coating, in: D.M. Mattox, V. Harwood Mattox (Eds.), 50 Years of Vacuum coating and the Growth of the Society of Vacuum Coaters, Society of Vacuum Coaters, Albuquerque, NM (2007) 120–131.

[181] J. Vetter, R. Knaup, H. Dwuletzki, E. Schneider, S. Vogler, Hard coatings for lubrication reduction in metal forming, Surf. Coat. Technol. 86–87 (1996) 739–746.

[182] O.A. Johansen, J.H. Dontje, R.L.D. Zenner, Reactive arc vapor ion deposition of TiN, ZrN and HfN, Thin Solid Films 153 (1987) 75–82.

[183] P.C. Johnson, H. Randhawa, Zirconium nitride films prepared by cathodic arc plasma deposition process, Surf. Coat. Technol. 33 (1987) 53–62.

[184] J. Vetter, $(Al_x:Ti_y)N$ coatings deposited by cathodic vacuum arc evaporation, J. Adv. Mater. 31 (1999) 41–47.

[185] H. Freller, H. Haessler, $Ti_xAl_{1-x}N$ films deposited by ion plating with an arc evaporator, Thin Solid Films 153 (1987) 67–74.

[186] A. Hörling, L. Hultman, M. Odén, J. Sjölén, L. Karlsson, Mechanical properties and machining performance of $Ti_{1-x}Al_xN$-coated cutting tools, Surf. Coat. Technol. 191 (2005) 384–392.

[187] J.I. Gersten, F.W. Smith, The Physics and Chemistry of Materials, John Wiley & Sons, New York (2001).

[188] A. Hörling, L. Hultman, M. Odén, J. Sjolén, L. Karlsson, Thermal stability of arc evaporated high aluminum-content $Ti_{1-x}Al_xN$ thin films, J. Vac. Sci. Technol. A 20 (2002) 1815–1823.

[189] P.H. Mayrhofer, A. Hörling, L. Karlsson, J. Sjolen, T. Larsson, C. Mitterer, L. Hultman, Self-organized nanostructures in the Ti–Al–N system, Appl. Phys. Lett. 83 (2003) 2049–2051.

[190] O. Knotek, F. Loffler, H.J. Scholl, C. Barimani, The multisource arc process for depositing ternary Cr- and Ti-based coatings, Surf. Coat. Technol. 68–69 (1994) 309–313.

[191] J. Vetter, H.J. Scholl, O. Knotek, (TiCr)N coatings deposited by cathodic vacuum arc evaporation, Surf. Coat. Technol. 74–75 (1995) 286–291.

[192] S. Boelens, H. Veltrop, Hard coatings of TiN (TiHf)N and (TiNb)N deposited by random and steered arc evaporation, Surf. Coat. Technol. 33 (1987) 63–71.

[193] L. Karlsson, L. Hultman, M.P. Johansson, J.E. Sundgren, H. Ljungcrantz, Growth, microstructure and mechanical properties of arc evaporated TiC_xN_{1-x} $(0<=x:<=1)$ films, Surf. Coat. Technol. 126 (2000) 1–14.

[194] L. Karlsson, L. Hultman, J.E. Sundgren, Influence of residual stresses on the mechanical properties of TiC_xN_{1-x} $(x=0, 0.15, 0.45)$ thin films deposited by arc evaporation, Thin Solid Films 371 (2000) 167–177.

[195] Y.-Y. Chang, S.-J. Yang, D.-Y. Wang, Characterization of TiCr(C,N)/amorphous carbon coatings synthesized by a cathodic arc deposition process, Thin Solid Films 515 (2007) 4722–4726.

[196] K. Yamamoto, T. Sato, K. Takahara, K. Hanaguri, Properties of (Ti,Cr,AI)N coatings with high Al content deposited by new plasma enhanced arc-cathode, Surf. Coat. Technol. 174–175 (2003) 620–626.

[197] C.-L. Chang, W.-C. Chen, P.-C. Tsai, W.-Y. Ho, D.-Y. Wang, Characteristics and performance of TiSiN/TiAlN multilayers coating synthesized by cathodic arc plasma evaporation, Surf. Coat. Technol. 202 (2007) 987–992.

[198] S.-Y. Chun, A. Chayahara, Pulsed vacuum arc deposition of multilayers in the nanometer range, Surf. Coat. Technol. 132 (2000) 217–221.

[199] G.S. Fox-Rabinovich, K. Yamamoto, S.C. Veldhuis, A.I. Kovalev, L.S. Shuster, L. Ning, Self-adaptive wear behavior of nano-multilayered TiAlCrN/WN coatings under severe machining conditions, Surf. Coat. Technol. 201 (2006) 1852–1860.

[200] V. Gorokhovsky, B. Heckerman, P. Watson, N. Bekesch, The effect of multilayer filtered arc coatings on mechanical properties, corrosion resistance and performance of periodontal dental instruments, Surf. Coat. Technol. 200 (2006) 5614–5630.

[201] P.E. Hovsepian, D.B. Lewis, Q. Luo, W.-D. Munz, P.H. Mayrhofer, C. Mitterer et al., TiAlN based nanoscale multilayer coatings designed to adapt their tribological properties at elevated temperatures, Thin Solid Films 485 (2005) 160–168.

[202] O. Knotek, E. Lugscheider, F. Löffler, W. Beele, C. Barimani, Arc evaporation of multicomponent MCrAlY cathodes, Surf. Coat. Technol. 74/75 (1995) 118–122.

[203] D.R. McKenzie, R.N. Tarrant, M.M.M. Bilek et al., Multilayered carbon films for tribological applications, Diamond Rel. Mater. 12 (2003) 178–184.

[204] L. Ryves, M.M.M. Bilek, T.W.H. Oates, R.N. Tarrant, D.R. McKenzie, F.A. Burgmann, D.G. McCulloch, Synthesis and in-situ ellipsometric monitoring of Ti/C nanostructured multilayers using a high-current, dual source pulsed cathodic arc, Thin Solid Films 482 (2005) 133–137.

[205] S.B. Sant, K.S. Gill, Growth and characterization of cathodic arc evaporated CrN (TiAl)N and (TiZr)N films, Surf. Coat. Technol. 68–69 (1994) 152–156.

[206] H.J. Scheibe, W. Pompe, P. Siemroth, B. Buecken, D. Schulze, R. Wilberg, Preparation of multilayers films structures by laser arcs, Surf. Coat. Technol. 193–194 (1990) 788–798.

[207] J. Vetter, W. Burgmer, H.G. Dederichs, A.J. Perry, The architecture and performance of multilayer and compositionally gradient coatings made by cathodic arc evaporation, Surf. Coat. Technol. 61 (1993) 209–214.

[208] J. Vetter, T. Krug, V. von der Heide, AlTiCrNO coatings for dry cutting deposited by reactive cathodic vacuum arc evaporation, Surf. Coat. Technol. 174 (2003) 615–619.

[209] F.R. Weber, F. Fontaine, M. Scheib, W. Bock, Cathodic arc evaporation of (Ti, Al)N coatings and (Ti,Al)N/TiN multilayer-coatings – correlation between lifetime of coated cutting tools, structural and mechanical film properties, Surf. Coat. Technol. 177–178 (2004) 227–232.

[210] H. Ziegele, C. Rebholz, H.J. Scheibe, B. Schultrich, A. Matthews, Mechanical and tribological properties of hard aluminium–carbon multilayer films prepared by the laser-arc technique, Surf. Coat. Technol. 107 (1998) 159–167.

[211] S. Anders, D.L. Callahan, G.M. Pharr, T.Y. Tsui, C.S. Bhatia, Multilayers of amorphous carbon prepared by cathodic arc deposition, Surf. Coat. Technol. 94/95 (1997) 189–194.

[212] D.G. McCulloch, X.L. Xiao, J.L. Peng, P.C.T. Ha, D.R. McKenzie, M.M.M. Bilek et al., The structure and annealing properties of multilayer carbon films, Surf. Coat. Technol. 198 (2005) 217–222.

[213] H.Y. Lee, J.G. Han, S.H. Baeg, S.H. Yang, Characterization of WC-CrAlN heterostructures obtained using a cathodic arc ion plating process, Surf. Coat. Technol. 174–175 (2003) 303–309.

[214] A. Schlegel, P. Wachter, J.J. Nickl, H. Lingg, Optical properties of TiN and ZrN, J. Phys. C: Solid State Phys. (1977) 4889–4896.

[215] S. Niyomsoan, W. Grant, D.L. Olson, B. Mishra, Variation of color in titanium and zirconium nitride decorative thin films, Thin Solid Films 415 (2002) 187–194.

[216] M. Eerden, W. van Ijzendoorn, R. Tietema, G.J. van der Kolk, A systematic study of the properties of the Zr–C–N ternary system, deposited by reactive arc evaporation, in: 46th Annual Technical Conference, Society of Vacuum Coaters, San Francisco, CA (2003) 56–60.

[217] U. Beck, G. Reiners, U. Kopacz, H.A. Jehn, Decorative hard coatings: interdependence of optical, stoichiometric and structural properties, Surf. Coat. Technol. 60 (1993) 389–395.

[218] R. Lossy, D.L. Pappas, R.A. Roy, J.J. Cuomo, V.H. Sura, Filtered arc deposition of amorphous diamond, Appl. Phys. Lett. 61 (1992) 171–173.

[219] S. Falabella, D.B. Boercker, D.M. Sanders, Fabrication of amorphous diamond films, Thin Solid Films 236 (1993) 82–86.

[220] X. Wang, J.P. Zhao, Z.Y. Chen, S.Q. Yang, T.S. Shi, X.H. Liu, Field emission from amorphous diamond films prepared by filtered arc deposition, Thin Solid Films 317 (1998) 356–358.

[221] C.A. Davis, V.S. Veerasamy, G.A.J. Amaratunga, W.I. Milne, D.R. McKenzie, Properties of tetrahedral amorphous carbon films deposited in a filtered cathodic arc in the presence of hydrogen, Phil. Mag. B 69 (1994) 1121–1131.

[222] A. Stanishevsky, L. Khriachtchev, I. Akula, Deposition of carbon films containing nitrogen by filtered pulsed cathodic arc discharge method, Diamond Rel. Mater. 7 (1998) 1190–1195.

[223] B. Druz, Y. Yevtukhov, V. Novotny, I. Zaritsky, V. Kanarov, V. Polyakov, A. Rukavishnikov, Nitrogenated carbon films deposited using filtered cathodic arc, Diamond Rel. Mater. 9 (2000) 668–674.

[224] M. Kühn, C. Spaeth, R. Pintaske, S. Peter, F. Richter, A. Anders, The effect of additional ion/plasma assistance in CNx-film deposition based on a filtered cathodic arc, Thin Solid Films 311 (1997) 151–156.

[225] E. Liu, X. Shi, H.S. Tan, L.K. Cheah, Z. Sun, B.K. Tay, J.R. Shi, The effect of nitrogen on the mechanical properties of tetrahedral amorphous carbon films deposited with a filtered cathodic vacuum arc, Surf. Coat. Technol. 120–121 (1999) 601–606.

[226] J.P. Zhao, X. Wang, Z.Y. Chen, S.Q. Yang, T.S. Shi, X.H. Liu, Amorphous carbon and carbon nitride films prepared by filtered arc deposition and ion assisted arc deposition, Mater. Lett. 33 (1997) 41–45.

[227] P. Zhang, B.K. Tay, G.Q. Yu, S.P. Lau, Y.Q. Fu, Surface energy of metal containing amorphous carbon films deposited by filtered cathodic vacuum arc, Diamond Rel. Mater. 13 (2004) 459–464.

[228] A. Anders, N. Pasaja, S. Sansongsiri, Filtered cathodic arc deposition with ion-species-selective bias, Rev. Sci. Instrum. 78 (2007) 063901-1–5.

[229] D.R. McKenzie, Tetrahedral bonding in amorphous carbon, Rep. Prog. Phys. 59 (1996) 1611–1664.

[230] A. Erdemir, C. Donnet, Tribology of diamondlike carbon films: recent progress and future prospects, J. Phys. D: Appl. Phys. 39 (2006) R1–R17.

[231] J. Robertson, Diamond-like amorphous carbon, Mater. Sci. Eng. R 37 (2002) 129–281.

[232] V.E. Strel'nitskii, I.I. Aksenov, S.I. Vakula, V.G. Padalka, V.A. Belous, Properties of diamond-like carbon coating produced by plasma condensation, Sov. Techn. Phys. Lett. 4 (1978) 546–547.

[233] S.I. Vakula, V.G. Padalka, V.E. Strel'nitskii, A.I. Usoskin, Optical properties of diamond-like carbon films, Sov. Techn. Phys. Lett. 5 (1979) 573–574.

[234] I.I. Aksenov, S.I. Vakula, V.G. Padalka, V.E. Strel'nitskii, V.M. Khoroshikh, High-efficiency source of pure carbon plasma, Sov. Phys. Techn. Phys. 25 (1980) 1164–1166.

[235] J.J. Cuomo, D.L. Pappas, J. Bruley, J.P. Doyle, K.K. Saenger, Vapor deposition process for amorphous carbon films with sp^3 fractions approaching diamond, J. Appl. Phys. 70 (1991) 1706–1711.

[236] V.S. Veerasamy, G.A.J. Amaratunga, C.A. Davis, W.I. Milne, P. Hewitt, M. Weiler, Electronic density of states in highly tetrahedral amorphous carbon, Solid State Electron. 37 (1994) 319–326.

[237] M. Chhowalla, J. Robertson, C.W. Chen, S.R.P. Silva, C.A. Davis, G.A.J. Amaratunga, W.I. Milne, Influence of ion energies and substrate temperature on the optical and electronic properties of tetrahedral amorphous carbon (ta-C) films, J. Appl. Phys. 81 (1997) 139–145.

[238] L.K. Cheah, X. Shi, E. Liu, B.K. Tay, J.R. Shi, Z. Sun, Influence of hydrogen on the structure and properties of tetrahedral amorphous carbon films obtained by the filtered cathodic vacuum arc technique, Phil. Mag. B 79 (1999) 1647–1658.

[239] G.M. Pharr, D.L. Callahan, D. McAdams et al., Hardness, elastic modulus, and structure of very hard carbon films produced by cathodic-arc deposition with substrate bias, Appl. Phys. Lett. 68 (1996) 779–781.

[240] J.Y. Sze, B.K. Tay, D. Sheeja, S.P. Lau, Y.Q. Fu, D.H.C. Chua, W.I. Milne, Optical and electrical properties of amorphous carbon films deposited using filtered cathodic vacuum arc with pulse biasing, Thin Solid Films 447 (2004) 148–152.

[241] B. Bhushan, B.K. Gupta, R. Sundaram, S. Dey, S. Anders, A. Anders et al., Development of hard carbon coatings for thin-film tape heads, IEEE Trans. Magnet. 31 (1995) 2976–2978.

[242] J. Robertson, Ultrathin carbon coatings for magnetic storage technology, Thin Solid Films 383 (2001) 81–88.

[243] A. Anders, F.R. Ryan, Ultrathin ta-C films on heads deposited by twist-filtered cathodic arc carbon deposition (invited), Symposium on Interface Tribology Towards 100 Gbit/in^2 and Beyond, Seattle, WA (2000) 43–50.

[244] B. Druz, Y. Yevtukhov, I. Zaritskiy, Diamond-like carbon overcoat for TFMH using filtered cathodic arc system with Ar-assisted arc discharge, Diamond Rel. Materials 14 (2005) 1508–1516.

[245] H.J. Scheibe, B. Schultrich, R. Wilberg, M. Falz, Laser-arc technology for industrial hard coating deposition, Surf. Coat. Technol. 97 (1997) 410–413.

[246] M. Ikeyama, S. Nakao, Y. Miyagawa, S. Miyagawa, Effects of Si content in DLC films on their friction and wear properties, Surf. Coat. Technol. 191 (2005) 38–42.

[247] B.K. Tay, D. Sheeja, L.J. Yu, On stress reduction of tetrahedral amorphous carbon films for moving mechanical assemblies, Diamond Rel. Mater. 12 (2003) 185–194.

[248] D. Sheeja, B.K. Tay, S.P. Lau, L.N. Nung, Tribological characterisation of diamond-like carbon coatings on Co–Cr–Mo alloy for orthopaedic applications, Surf. Coat. Technol. 146–147 (2001) 410–416.

[249] R. Hauert, A review of modified DLC coatings for biological applications, Diamond Rel. Mater. 12 (2003) 583–589.

[250] S.C.H. Kwok, W. Zhang, G.J. Wan, D.R. McKenzie, M.M.M. Bilek, P.K. Chu, Hemocompatibility and anti-bacterial properties of silver doped diamond-like carbon prepared by pulsed filtered cathodic vacuum arc deposition, Diamond Rel. Mater. 16 (2007) 1353–1360.

[251] A. Anders, N. Pasaja, S.H.N. Lim, T.C. Petersen, V.J. Keast, Plasma biasing to control the growth conditions of diamond-like carbon, Surf. Coat. Technol. 201 (2007) 4628–4632.

[252] T.A. Friedmann, J.P. Sullivan, J.A. Knapp, D.R. Tallant, D.M. Follstaedt, D.L. Medlin, P.B. Mirkarimi, Thick stress-free amorphous-tetrahedral carbon films with hardness near that of diamond, Appl. Phys. Lett. 71 (1997) 3820–3822.

[253] O.R. Monteiro, J.W. Ager III, D.H. Lee, R.Y. Lo, K.C. Walter, M. Nastasi, Annealing of nonhydrogenated amophous carbon films prepared by filtered cathodic arc, J. Appl. Phys. 88 (2000) 2395–2399.

[254] Z. Tang, Z.J. Zhang, K. Narumi, Y. Xu, H. Naramoto, S. Nagai, K. Miyashita, Effect of mass-selected ion species on structure and properties of diamond-like carbon films, J. Appl. Phys. 89 (2001) 1959–1964.

[255] J. Robertson, Mechanical properties and coordinations of amorphous carbons, Phys. Rev. Lett 68 (1992) 220.

[256] R. Gago, M. Vinnichenko, H.U. Jager, A.Y. Belov, I. Jimenez, N. Huang et al., Evolution of sp^2 networks with substrate temperature in amorphous carbon films: experiment and theory, Phys. Rev. B 72 (2005) 014120–14129.

[257] R.N. Tarrant, C.S. Montross, D.R. McKenzie, Combined deposition and implantation in the cathodic arc for thick film preparation, Surf. Coat. Technol. 136 (2001) 188–191.

[258] R.N. Tarrant, N. Fujisawa, M.V. Swain, N.L. James, D.R. McKenzie, J.C. Woodard, PBII deposition of thick carbon coatings from a cathodic arc plasma, Surf. Coat. Technol. 156 (2002) 143–148.

[259] P. Siemroth, C. Wenzel, W. Kliomes, B. Schultrich, T. Schülke, Metallization of sub-micron trenches and vias with high aspect ratio, Thin Solid Films 308 (1997) 455–459.

[260] P. Siemroth, T. Schülke, Copper metallization in microelectronics using filtered vacuum arc deposition – principles and technological development, Surf. Coat. Technol. 133–134 (2000) 106–113.

[261] O.R. Monteiro, Novel metallization technique for filling 100-nm-wide trenches and vias with very high aspect ratio, J. Vac. Sci. Technol. B 17 (1999) 1094–1097.

[262] U.-S. Chen, H.C. Shih, Characterization of copper metallization for interconnect by 90[deg]-bend electromagnetic filtered vacuum arc, Nucl. Instrum. Meth. Phys. Res. B 237 (2005) 477–483.

[263] A. Bendavid, P.J. Martin, A. Jamting, H. Takikawa, Structural and optical properties of titanium oxide thin films deposited by filtered arc deposition, Thin Solid Films 356 (1999) 6–11.

[264] P.J. Martin, R.P. Netterfield, T.J. Kinder, Ion-beam-deposited films produced by filtered arc evaporation, Thin Solid Films 193 (1990) 77–83.

[265] P.J. Martin, R.P. Netterfield, T.J. Kinder, L. Descotes, Deposition of TiN, TiC, and TiO_2 films by filtered arc evaporation, Surf. Coat. Technol. 49 (1991) 239–243.

[266] P.J. Martin, A. Bendavid, R.P. Netterfield, T.J. Kinder, F. Jahan, G. Smith, Plasma deposition of tribological and optical thin film materials with a filtered cathodic arc source, Surf. Coat. Technol. 112 (1999) 257–260.

[267] A. Bendavid, P.J. Martin, H. Takikawa, Deposition and modification of titanium dioxide thin films by filtered arc deposition, Thin Solid Films 360 (2000) 241–249.

[268] J.K. Kim, E.S. Lee, D.H. Kim, D.G. Kim, Ion beam-induced erosion and humidity effect of MgO protective layer prepared by vacuum arc deposition, Thin Solid Films 447 (2004) 95–99.

[269] C. Zheng, D. Zhu, D. Chen, Z. He, L. Wen, W.Y. Cheung, S.P. Wong, Influence of O_2 flow rate on structure and properties of MgO_x films prepared by cathodic-vacuum-arc ion deposition system, IEEE Trans. Plasma Sci. 34 (2006) 1099–1104.

[270] B.K. Tay, Z.W. Zhao, C.Q. Sun, Effects of substrate bias and growth temperature on properties of aluminium oxide thin films by using filtered cathodic vacuum arc, Surf. Coat. Technol. 198 (2005) 94–97.

[271] J. Rosén, S. Mräz, U. Kreissig, D. Music, J.M. Schneider, Effect of ion energy on structure and composition of cathodic arc deposited alumina thin films, Plasma Chem. Plasma Process. 25 (2005) 303–317.

[272] S. Mändl, D. Manova, B. Rauschenbach, Transparent AlN layers formed by metal plasma immersion ion implantation and deposition, Surf. Coat. Technol. 186 (2004) 82–87.

[273] V.N. Inkin, G.G. Kirpilenko, A.J. Kolpakov, Properties of aluminium nitride coating obtained by vacuum arc discharge method with plasma flow separation, Diamond Rel. Mater. 10 (2001) 1314–1316.

[274] A.J.-C. Wen, K.-L. Chen, M.-H. Yang, W.-T. Hsiao, L.-G. Chao, M.-S. Leu, Effect of substrate angle on properties of ITO films deposited by cathodic arc ion plating with In–Sn alloy target, Surf. Coat. Technol. 198 (2005) 362–366.

[275] T. Minami, S. Ida, T. Miyata, High rate deposition of transparent conducting oxide thin films by vacuum arc plasma evaporation, Thin Solid Films 416 (2002) 92–96.

[276] T. David, S. Goldsmith, R.L. Boxman, p-type Sb-doped ZnO thin films prepared with filtered vacuum arc deposition, in: 47th Annual Technical Conference Proceedings of the Society of Vacuum Coaters, Dallas, TX (2004) 122–126.

[277] D.C. Look, B. Claflin, Y.I. Alivov, S.J. Park, The future of ZnO light emitters, Phys. Stat. Sol. (A) 201 (2004) 2203–2212.

[278] A. Ben-Shalom, L. Kaplan, R.L. Boxman, S. Goldsmith, M. Nathan, SnO_2 transparent conductor films produced by filtered vacuum arc deposition, Thin Solid Films 236 (1993) 20–26.

[279] R.L. Boxman, V. Zhitomirsky, S. Goldsmith, T. David, V. Dikhtyar, Deposition of SnO_2 coatings using a rectangular filtered vacuum arc source, in: 46th Annual Technical Meeting of the Society of Vacuum Coaters, San Francisco, CA (2003) 234–239.

[280] L. Kaplan, A. Benshalom, R.L. Boxman, S. Goldsmith, U. Rosenberg, M. Nathan, Annealing and Sb-doping of Sn–O films produced by filtered vacuum arc deposition – structure and electro-optical properties, Thin Solid Films 253 (1994) 1–8.

[281] L. Kaplan, V.N. Zhitomirsky, S. Goldsmith, R.L. Boxman, I. Rusman, Arc behaviour during filtered vacuum arc deposition of Sn–O thin films, Surf. Coat. Technol. 76 (1995) 181–189.

[282] L. Kaplan, I. Rusman, R.L. Boxman, S. Goldsmith, M. Nathan, E. BenJacob, STM and XPS study of filtered vacuum arc deposited Sn–O films, Thin Solid Films 291 (1996) 355–361.

[283] V.N. Zhitomirsky, R.L. Boxman, S. Goldsmith, Plasma distribution and SnO_2 coating deposition using a rectangular filtered vacuum arc plasma source, Surf. Coat. Technol. 185 (2004) 1–11.

[284] V.N. Zhitomirsky, T. David, R.L. Boxman, S. Goldsmith, A. Verdyan, Y.M. Soifer, L. Rapoport, Properties of SnO_2 coatings fabricated on polymer substrates using filtered vacuum arc deposition, Thin Solid Films 492 (2005) 187–194.

[285] S. Goldsmith, Filtered vacuum arc deposition of undoped and doped ZnO thin films: Electrical, optical, and structural properties, Surf. Coat. Technol. 201 (2006) 3993–3999.

[286] X.L. Xu, S.P. Lau, J.S. Chen, G.Y. Chen, B.K. Tay, Polycrystalline ZnO thin films on Si (100) deposited by filtered cathodic vacuum arc, J. Crystal Growth 223 (2001) 201–205.

[287] X.L. Xu, S.P. Lau, B.K. Tay, Structural and optical properties of ZnO thin films produced by filtered cathodic vacuum arc, Thin Solid Films 398-399 (2001) 244–249.

[288] B.K. Tay, Z.W. Zhao, D.H.C. Chua, Review of metal oxide films deposited by filtered cathodic vacuum arc technique, Mater. Sci. Eng. R: Reports 52 (2006) 1–48.

[289] H.W. Lee, S.P. Lau, Y.G. Wang, B.K. Tay, H.H. Hng, Internal stress and surface morphology of zinc oxide thin films deposited by filtered cathodic vacuum arc technique, Thin Solid Films 458 (2004) 15–19.

[290] V.I. Gorokhovsky, D.G. Bhat, R. Shivpuri, K. Kulkarni, R. Bhattacharya, A.K. Rai, Characterization of large area filtered arc deposition technology: Part II – Coating properties and application, Surf. Coat. Technol. 140 (2001) 215–224.

[291] M.W. Barsoum, T. El-Raghy, Synthesis and characterization of a remarkable ceramic: Ti_3SiC_2, J. Am. Ceram. Soc. 79 (1996) 1953–1956.

[292] J. Rosén, L. Ryves, P.O.Å. Persson, M.M.M. Bilek, Deposition of epitaxial Ti_2AlC thin films by pulsed cathodic arc, J. Appl. Phys. 101 (2007) 056101–56102.

CHAPTER 11

Vacuum Polymer Deposition

Mark E. Gross and Peter M. Martin

11.1 Introduction

Because of their unique physical, optical, and mechanical properties, thin film polymers have numerous technological and consumer product applications. They offer several advantages over inorganic thin film materials, including low cost, high deposition rates, low optical absorption, high smoothness, wide variety of compositions, formation of composites, high breakdown voltage, and high ductility. Disadvantages, however, are low mechanical strength and wear resistance, low chemical resistance in some cases, high gas permeability, low melting temperature, small range of refractive indices, and numerous optical absorption bands between near-infrared and infrared wavelengths. Thus, applications are restricted by many of the above properties, but are also expanded in many areas. Recent applications include ultralow-permeability gas and water barrier coatings for organic electronics, thin film solar cells, thin film batteries, multilayer optical coatings, thin film capacitors, nanocomposites and nanolaminates on plastic. Among the numerous methods used to deposit organic materials and polymers, vacuum polymer deposition (VPD), also known as the polymer multilayer (PML) process, produces ultrasmooth, nonconformal, and pinhole-free films at very high deposition rates over large areas.

Unlike any other vacuum deposition process, VPD films actually smooth the surface of the substrate [1]. All other vacuum deposition techniques essentially bombard the substrate with species from a source that can bond immediately to the surface (low energy), bond after moving some distance on the surface, or reflect off the surface. These traditional processes ‘grow’ the coating atom by atom or molecule by molecule from the substrate surface outward, and produce films that tend to reproduce the substrate surface on the length scale of the bombarding species. As a result, substrate surface roughness, from atomic scale upward, is replicated by the growing film. Furthermore, this adatom growth can increase surface roughness through mechanisms such as shadowing, dislocations, and grain boundary growth (see Chapters 2, 4, 5, and 12). These growth mechanisms usually increase the roughness as the film grows thicker. A VPD layer, in contrast, does not grow atom by atom upward from the substrate; a gas of monomer vapor condenses on the substrate as a full-thickness liquid film that covers the entire substrate surface and its features. The liquid film is then cross-linked into a solid layer by ultraviolet (UV) or electron beam (e-beam) radiation. The resulting surface is glassy with virtually no defects or pinholes. The VPD layer can be combined with conventional physical or chemical vapor deposition layers (PVD, CVD, PECVD, etc.) to form low-defect, ultrasmooth thin film structures.

VPD technology permits ultrafast deposition of polymer films in the same vacuum environment as conventional physical vapor deposition (sputtered or evaporated) thin films. With this technology, polymer films can be deposited on moving substrates at speeds up to 1000 feet/min (~ 300 m/min) and thicknesses ranging from a few angstroms to 1.3 mm with excellent adhesion to substrates and thickness uniformity of $\pm 2\%$. The VPD process has two forms, evaporative and non-evaporative. Each begins by degassing the working monomer, which is a reactive organic liquid. In the evaporative process, the monomer is metered through an ultrasonic atomizer into a hot tube where it flash evaporates and exits through a nozzle as a monomer gas. The monomer gas then condenses on the substrate as a liquid film that is subsequently cross-linked to form a solid polymer by exposure to UV radiation or an electron beam. In the non-evaporative process the degassed liquid monomer is extruded through a slotted die orifice onto the substrate. It is then cross-linked in the same fashion as in the evaporative process. Salts, graphite, or oxide powders, and other non-volatile materials can be deposited in a homogeneous mixture with the monomer. Such mixtures cannot be flash evaporated, but are required for electrolyte, anode, cathode, and capacitor film layers. The evaporative process can produce thicknesses up to approximately 10 μm at speeds as great as 1000 feet/min (~ 300 m/min). The non-evaporative process can deposit thicknesses from 10 μm to about 1.3 mm at substrate speeds approaching several hundred feet per minute.

The VPD process has several distinct advantages over conventional organic and organic/inorganic deposition processes:

- Polymer thin films are more cost-effective since polymer layers can be deposited 10–100 times more quickly.
- VPD technology permits polymer, polymer electrolyte, metal, and even oxide and nitride films to be deposited in a single pass through a vacuum coater, as a monolithic structure, in an integrated manufacturing process.
- The VPD process eliminates all of the unnecessary handling and laminations involved in conventional processes, and it also results in better adhesion between layers and defect-free interfaces.
- It is amenable to virtually all types of deposition processes, including roll-to-roll, in-line, and batch planetary substrate rotation
- Capital equipment and raw material costs are comparable to or less than those of conventional processes.

Another advantage of conventional VPD is that it has been found to be quite efficient at smoothing rough substrates. Surfaces with a roughness less than 10 Å RMS (Roughness Measurement System) are routinely obtained with UV-cured PML/oxide/PML barrier films deposited on both 150 Å RMS polyethylene terephthalate (PET) substrates and 5 μm RMS metal plates. With e-beam cure the roughness on PET is 180 Å RMS, higher than the initial substrate surface roughness. The increased surface roughness with e-beam curing is due to the electrostatic repulsion of the curing electrons trapped in the liquid setting up a standing wave pattern prior to full solidification.

11.2 Polymer Deposition Process

11.2.1 Vacuum Polymer Deposition

The VPD process involves vacuum flash evaporation of a monomer liquid which is subsequently condensed as a liquid film onto a substrate and then radiation cross-linked to form a solid film. The VPD process can be implemented in either batch or roll-to-roll web mode. Additionally, VPD can be combined with PVD processes to form novel hybrid deposition processes. This process works best for monomers with evaporation points less than $\sim 500\,^{\circ}$C. The process used to flash evaporate the monomer is as follows.

- Liquid monomer is first degassed and stirred while atmospheric gasses are pumped away to a suitable base pressure.

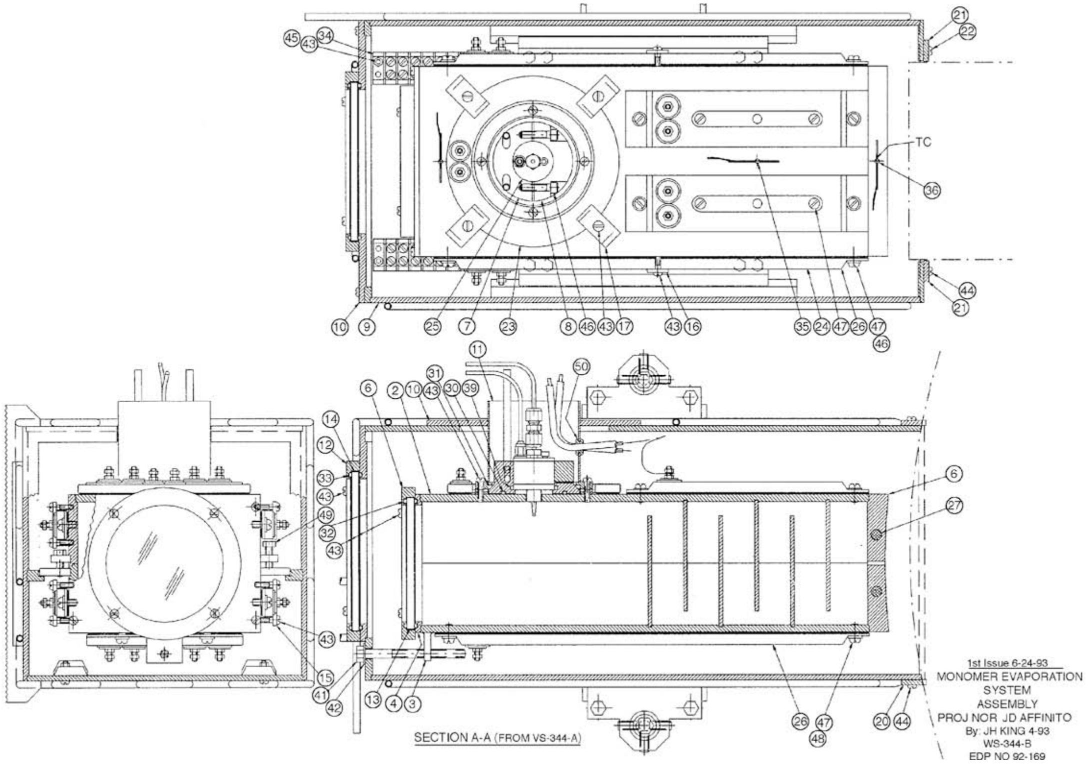

Figure 11.1: Schematic diagram of monomer evaporator [2].

- The heart of this process is the monomer flash evaporator shown schematically in Figure 11.1 [2]. The degassed monomer is then sprayed into the interior of a very hot enclosure that has a heated pressure baffling expansion nozzle on one end (Figure 11.1). By ‘very hot’, it is meant that the enclosure walls are hot enough to instantly vaporize the monomer spray, without a pool of liquid forming, yet not hot enough to pyrolize and/or polymerize the monomer on contact (between 100 °C and 500 °C, depending on the monomer used). Under these conditions the monomer evaporates as quickly as it is introduced into the enclosure. Thus, the mass flow of monomer gas exiting the nozzle is directly calculable from the monomer fluid feed rate. Baffles in the enclosure/nozzle system serve to build up pressure (of the molecular gas of monomer molecules) in the nozzle expansion chamber and to homogenize the monomer gas. Building the pressure serves to make the molecular gas stream exiting the slit in the nozzle more uniform across the length of the nozzle slit.
- The flow of monomer into the hot enclosure is controlled with a precision metering pump. Liquid monomer is fed through a capillary tube into an atomizer that distributes a mist of microdroplets into a heated enclosure. The monomer spray can be created by

a variety of techniques, including an ultrasonic atomizer, fuel injector, or by dripping onto a high-speed rotating disk. Dispersion with an ultrasonic atomizer gives the best thickness uniformity

- In a web coating process the monomer gas exits the evaporator through a narrow slit as a uniform line source, condenses as a liquid film on a cooled substrate that is moving past the slit, and the liquid film is subsequently polymerized when the substrate passes a UV or e-beam radiation source. The substrate must be at a lower temperature than the monomer gas for condensation to occur. Since the evaporator/slit can be constructed to emit a uniformly dense line of gas then, as long as the total fluid input is constant, the thickness of the polymer coating on web will be uniform in thickness along both its length and width. The monomer fluid is atomized to a fine mist and sprayed over as large an area as possible on the interior of a very hot enclosure to reduce cooling effects of the liquid on the hot interior surface of the evaporator. If the rate of monomer mass impingement per unit area is too high, the surface cools too rapidly and monomer liquid may build up on the interior surfaces of the evaporator. If such liquid build-up occurs, and the monomer resides on the surface for too long, the monomer will polymerize inside the evaporator. When the monomer polymerizes inside the evaporator the resultant polymer film interferes with heat transfer between the surface and the subsequently atomized liquid. Gradually more and more polymerization occurs, causing heat transfer to continuously degrade, and the rate of monomer retention within the evaporator continuously increases over the duration of the run. The VPD process has produced 1 μm thick films at line speeds of 600 m/min. The film thickness range known to be obtainable with the VPD process extends from a few tens of angstroms up to tens of micrometers, with the upper thickness limit largely imposed by the penetration depth of the cross-linking radiation employed.

11.2.2 Monomer Degassing

The degassing step is necessary to properly introduce the liquid monomer into the vacuum environment, and is necessary to maintain the vacuum integrity of the chamber, although it is always good practice to minimize the amount of the atmospheric gasses in order to minimize contamination of concurrent processes. If the liquid monomer is not degassed prior to injection into the vacuum, violent expansion occurs as the gas containing liquid enters the vacuum. The violent expansion causes pulsing and spitting at the injection port, which leads to large, erratic pulses in the flow of liquid into the evaporator. This subsequently leads to variations of the film thickness along the length of the linearly translating substrate. Several experiments have been performed to verify that no monomer components are removed during the vacuum degassing process.

11.2.3 Atomization

A number of atomizers can be used with the VPD process. For some low flow-rate VPD methods the liquid monomer will be passed through an ultrasonic atomizing nozzle. The amount of liquid monomer atomized by the nozzle is controlled by the liquid delivery system used with a nozzle. There are several liquid delivery systems suitable for this application, including gear pump, syringe pump, pressurized reservoir, peristaltic pump, and gravity feed. The flow rate range can be as low as a few microliters per second to up to several gallons per hour. Ultrasonic atomization produces a low-velocity controlled spray pattern attaining a narrow distribution of droplet size, normally in the micrometer range.

Factors to consider when selecting an ultrasonic atomizing system for each application are listed below:

- spray pattern desired – frequency of nozzle (25–120 kHz)
- characteristics of the liquid monomer, viscosity
- flow rate desired – bore of nozzle
- frequency generation – most companies that provide ultrasonic atomization equipment use a broadband frequency generator enabling the use of several different nozzles with one supply.

Ensuring an uninterrupted flow of liquid monomer and tuning the correct power setting for the ultrasonic nozzle to produce a uniform spray are critical to achieving a uniform polymer deposition. A monomer flow that is erratic and does not keep the nozzle bore full will result in pulsed deposition and resulting non-uniform polymer films, and the deposition will pulse. Tuning the power for the ultrasonic nozzle has an effect on the spray pattern and monomer droplet size. For process development purposes, it is important to be able to see the atomization process while adjusting the nozzle power, typically from 2 to 10 W. A power setting too low will result in monomer dripping off the nozzle, a power setting too high may produce the incorrect spray pattern and damage heat-sensitive monomers.

11.2.4 Cryocondensation Efficiency

The extremely high polymer deposition rate is not due solely to the rate at which the monomer is metered into the VPD flash evaporator, but also depends on condensation efficiency, substrate temperature, evaporation temperature, and other process conditions, as described below. High molecular weight monomers have dew points well above ambient temperatures so that monomer gas readily cryocondenses at ambient and higher temperatures. Thus, when the stream of monomer gas exiting the flash evaporator strikes the cooled substrate, a very high percentage of the gas immediately condenses as a liquid film. Condensation efficiencies as high as 95% have been demonstrated for hexane diol diacrylate monomer (or HDODA), MW = 214, evaporated at 230 °C and condensing on a substrate held at 5 °C. However, when the substrate temperature is raised to 25 °C, condensation efficiency for HDODA drops below 60%. When the substrate temperature is raised to 66 °C virtually no HDODA condenses. However, tripropyleneglycol (400) diacrylate monomer, MW = 508, condenses on a 66 °C substrate at 36% efficiency when evaporated at 290 °C. Therefore, the VPD rate is a very strong function of both the evaporation and condensation temperatures, monomer species, line speed, and monomer feed rate.

11.2.5 Monomer Cure

Once condensed onto the substrate, the liquid monomer must be cross-linked to form a polymer. Liquid monomer is cured, or cross-linked, using either high-intensity UV light radiation or an electron beam. Because temperature-sensitive substrate materials are generally used, and because it is too slow, thermal curing is not used in this process. However, as film thicknesses exceed 2–3 μm, only UV cure must be employed owing to the low energy distribution of the VPD e-beam source. The e-beam source is typically a diode sputter cathode enclosed in a grounded enclosure that has a slit in the wall facing the sputter glow discharge, and operated at about 15 kV. Low-energy electrons emitted from the plasma impinge upon the open slit, exit the box and initiate polymerization of the liquid monomer film. These electrons have energies ~ 15 keV and below, and cannot penetrate more than 2–3 μm into the liquid monomer.

UV wavelengths most suitable for photoinitiators used to cure acrylate monomers range between 200 and 400 nm. Several types of lamp are suitable for generating these wavelengths, including high-pressure mercury arc, and electrodeless and medium-pressure mercury arc lamps. A typical UV source is a fusion variable power supply lamp system. This system can vary 600 W/in (240 W/cm) power from 25% to 100%, and is designed to generate intense UV radiation in the 200–400 nm range. The wavelength can be tuned to optimize absorption by the photoinitiator used by selecting the correct bulb; type V 400–500 nm, type D 350–400 nm, type H 240–320 nm, and type H+ 210–320 nm. Output power can also be tuned for the cure desired. High-intensity UV light initiates a chemical reaction that cures the ink or the coating almost instantaneously.

11.2.6 Adhesion: Plasma Treatment

Polymer/metal or polymer/oxide multilayer stack structures have a wide range of optical, packaging, semiconductor, and display applications. A primary concern in the deposition of such stacks is adhesion at polymer–substrate, polymer–metal and metal–polymer interfaces. This is particularly critical for noble metals such as silver (Ag) because of the low chemical reactivity and absence of physical interlocking effects due to smooth substrate surfaces created by VPD coatings. The substrate surface must be sufficiently activated to promote an interaction with the depositing metal atoms. By removing surface contaminants, incorporating new and more reactive functional groups, and cross-linking weak subsurface layers, low-temperature plasma has proven to be very efficient for such applications. In addition, the plasma process is fully compatible with all other vacuum technologies, allowing in-line and high-speed processing of polymer/metal multilayer structures. The interaction of a plasma with the substrate surface results from the synergetic actions of energetic electrons, ions, atoms, molecules, and UV photons. Depending on the gas used, the interaction of plasma species with a polymer surface can lead to etching, surface activation, and deposition of thin films. Surface activation is generally accomplished with O_2, N_2, or Ar gases, and is strongly dependent on the chemical structure of the substrate surface. Table 11.1 summarizes adhesion studies using these gases and e-beam bombardment. In situ X-ray photoelectron spectroscopy (XPS) measurements indicate that plasma exposure causes destruction of initial C–O and O=C–O groups in the film and substrate. Other functional groups such as amide (NH–C=O) structures are also created, but at a much slower rate [3]. As a result, activation treatment conditions differ and must be optimized for each substrate surface. Plasma treatment can also influence the surface roughness of the substrate material, also shown in Table 11.1 [3]. This topic is addressed in Section 11.4.

Table 11.1: Summary of plasma adhesion enhancement [3]

Sample	Gas/EB	Treatment (J/cm^2)	O/C[a]	RMS surface roughness (nm)
PET			0.67	13.2
PET	Ar	8	0.85	7.9
PET	Ar	34	2.04	5.2
PET	EB	10	0.67	6.8
PET	EB	40	2.05	4.7
PET	N_2	8	0.40	2.5
PET	N_2	34	1.81	9.6
PET	O_2	8	0.93	10.6
PET	O_2	34	1	20.2
VPD			0.43	0.1
VPD	Ar	34	0.41	0.1
VPD	EB	34	0.39	0.1
VPD	O_2	34	0.69	0.1
VPD	O_2	34	0.42	0.2

[a] *Ratio determined by X-ray photoelectron spectroscopy. High O/C indicates increased plasma damage compared to native PET (C/O = 1.5).*

Adhesion of metal layers to VPD thin films can be enhanced by plasma pretreatment of the cross-linked polymer, and depends on the chemistry of the plasma [3]. For example, adhesion of silver to a VPD acrylate film was excellent when it was pretreated with a nitrogen (N_2) plasma, while poor when exposed to an argon (Ar) plasma. Similar findings were reported for several other polymeric systems [4]. Thus, both the incorporated nitrogen and plasma enhanced surface energy due to plasma bombardment contribute to the improved Ag/polymer adhesion.

11.2.7 Polymer Thickness Dependence

Polymer thickness depends on two factors: substrate temperature and monomer pressure at the substrate surface. Increasing the substrate temperature decreases the deposited thickness, while increasing monomer pressure at the substrate surface increases the deposited thickness. Thickness is directly proportional to cryocondensation efficiency, as presented earlier, and decreases rapidly with increased substrate temperature. An increased number of monomer molecules directly results in increased monomer pressure and higher deposition rate.

During the VPD process, substrate temperature can be monitored by several methods, the most widely used of which is an infrared sensor located in the vacuum system. Film thickness is a strong function of substrate temperature, particularly at lower temperatures. The components of the monomer blend used can also shift this thickness versus temperature plot.

Monomer pressure is normally measured in the evaporation chamber with a heated capacitance manometer. Pressure in the evaporation source is directly proportional to the flow of monomer into the source.

11.3 Plasma Vacuum Polymer Deposition and Liquid Multilayer Processes

11.3.1 Plasma Polymer Multilayer Process

The plasma polymer multilayer process (PPML) is a hybrid deposition process that combines key features of three existing vacuum deposition methods: the VPD process, plasma polymerization and plasma-enhanced chemical vapor deposition (PECVD). PPML is a high deposition rate process for solid films used for high molecular weight/low vapor pressure liquid, or even liquid/solid suspension, monomer precursors. The gas resulting from flash evaporation of a liquid monomer mixture, or from a suspension of insoluble solid particles in liquid monomer, is used as the support medium for a glow discharge in a PECVD-like process. Owing to the high molecular weight/low vapor pressure nature of the precursors, the plasma of the flash-evaporated gas cryocondenses at an extremely high rate on substrates at ambient and lower substrate temperatures. Upon condensation, the liquefied plasma immediately begins to polymerize to form a solid film owing to the high concentration of radicals and ions contained in the liquid film.

This process has been successfully implemented in a vacuum roll coating system using a roll-to-roll deposition process. Polymer films, molecularly doped polymer (MDP) composite films of polymers containing light emitting organic molecules, and MDP composite films of polymer containing organic dye molecules have been deposited at thicknesses ranging from 0.1 to 24 μm at web speeds as high as 96 linear meters per minute (lin. m/min). Figure 11.2 depicts a modified monomer exit slit that was installed in place of the conventional monomer exit slit of the standard VPD evaporator shown in Figure 11.1. This modified monomer exit slit creates a cavity between the monomer exit slit and the drum/substrate. Within this cavity is a high-voltage electrode, circumferential to the slit, lying between the drum/substrate and the monomer exit slit. Monomer gas exiting the evaporator becomes the support media for a glow discharge that is formed by biasing the high-voltage electrode. At a given bias voltage, the glow discharge current is a function of the monomer gas pressure in the electrode cavity between the drum/substrate and the monomer exit slit. The monomer pressure, in turn, is a function of the gap between the drum/substrate and the open face of the cavity, the flow rate of liquid monomer into the flash evaporator, and the flow of ballast gas (inert Ar or a reactive mixture) into the flash evaporator. A ballast gas is used when:

- the gap and liquid monomer flow rate are not sufficient to provide enough gas pressure to sustain a steady-state glow discharge, or

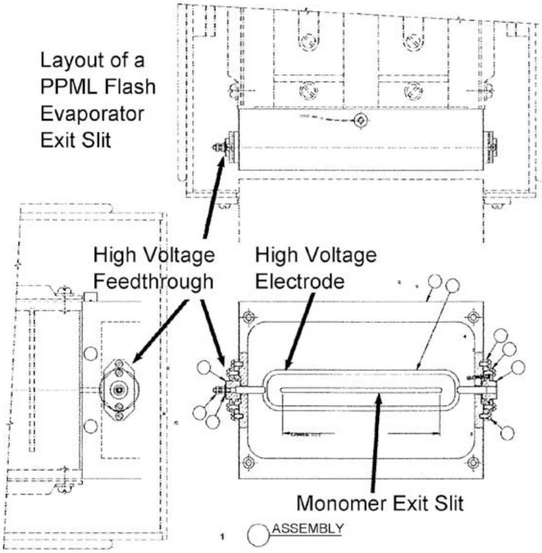

Figure 11.2: Modified monomer exit slit that was installed in place of the conventional monomer exit slit of the standard VPD evaporator.

- a specific physical, or chemical, reaction of the ballast gas with the monomer gas is desired.

PPML deposition, in systems similar to Figure 11.2, can be accomplished with a variety of bias voltage frequencies (direct current, mid-frequency, and radio frequency).

The following experiments were performed in a vacuum web coater to test the PPML process, and compare the results with conventional VPD. For a series of monomer flow rates between 0.125 and 0.625 ml/s the web was run for intervals at a series of line speeds between 0.5 and 96 m/min. Conductance calculations give estimates of the pressure in the electrode cavity shown in Figure 11.2 as ~ 0.02 torr for monomer flows of 0.125 ml/s and 0.1 torr for monomer flows of 0.625 ml/s. Each of the constant monomer flow/constant web speed intervals was further divided into three segments in which different cure mechanisms were used to polymerize the condensed monomer: UV cure, e-beam cure, and plasma cure. For these experiments, TRPGDA monomer was diluted with 5% Ezacure TZT photoinitiator (2,4,6-trimethylbenzophenone 4-methylbenzophenone). In experiments performed without photoinitiator added to the monomer and without UV cure segments, PPML films had the same physical properties as PPML films produced with photoinitiator in the monomer. During PPML cure segments, the glow discharge voltage was varied between 1 and 3 kV. The appearance of the deposited films was recorded as deposition proceeded.

Film thickness was measured after the deposition experiments. As a rough measure of the degree of polymerization, infrared spectral measurements were also made to determine whether residual acrylate C=C double bonds were detectable.

During the deposition experiments with TRPGDA monomers, UV- and e-beam-cured VPD layers appeared perfectly clear and transparent. At low plasma cure powers (normalized to unit flow rate of monomer), generally below about 600 W/ml/min of monomer, the PPML films also appeared clear during the deposition. At higher power levels, generally above 600 W/ml/min of monomer, however, PPML films appeared hazy during deposition. Preliminary optical microscope observations indicated that significant polymerization occurred in the gas phase at higher plasma powers, and that the resultant polymer ‘snows’ out along with the cryocondensed plasma.

11.3.1.1 Important PPML Points

The PPML process can thus be summarized as follows:

- The gas resulting from the flash evaporation of a relatively high molecular weight/low vapor pressure liquid monomer mixture or from suspensions of insoluble particles in liquid monomer can be used as the support medium for a glow discharge in a PECVD-like vacuum deposition process. Deposition rates are orders of magnitude higher than in conventional plasma polymerization or PECVD processes. This high deposition rate is due to cryocondensation of the monomer plasma onto the substrate as a liquid film that is already charged with radicals as the dominant condensation mechanism. This condensation process is found to proceed at ambient and higher substrate temperatures. Upon condensation, the liquefied plasma immediately begins to polymerize to form a solid film owing to the high concentration of radicals and ions contained in the liquid film.

- The PPML process does not appear to have any depth of cure limitations as with conventional e-beam-cured VPD films thicker than 2–3 μm or conventional UV-cured VPD films with highly UV absorbing monomers.
- The process has been successfully implemented in a roll-to-roll deposition process in a vacuum roll coating system. Polymer films, and molecularly doped polymer composite films of polymer and light-emitting organic molecules, have been deposited at thicknesses ranging from about 0.1 to 24 μm at web speeds between 96 and 0.5 lin. m/min.
- Since any molecule can form radicals in a plasma, the PPML process is adaptable to more applications than the acrylate/methacrylate dominated chemistry of the standard UV- or e-beam-cured VPD processes, but plasma power levels must be closely monitored.

11.3.2 Extrusion Process Liquid Multilayer Process

It is often necessary to molecularly dope a polymer film with an insoluble solid to increase its functionality [5, 6]. The liquid multilayer (LML) process starts with a degassed polymer slurry containing micrometer and nano-size particles of the solid and extrudes this slurry onto a substrate [2, 5, 6]. This slurry is subsequently cross-linked as discussed above to form a molecularly doped polymer. With the LML method the particle sizes of the insoluble material in the final polymer film layer are the same as those of the initial particles that were slurried with the liquid. The lower limit on LML layer thickness is on the order of 5–15 μm, and is highly dependent on viscosity, while VPD layer thickness can be less than 100 Å. Both VPD and LML processes are compatible with simultaneous, in-line, deposition by conventional vacuum coating processes described previously, such as sputtering, evaporation, or PECVD. The vacuum roll coater depicted in Figure 11.3 routinely integrates both VPD and LML processes with these conventional coatings.

Examples of molecular dopants that promote hole transport includes metal (8-quinolinolato) chelates, quinacridone derivatives, and triaryl amine derivatives. Metal (8-quinolinolato) chelates are used to dope electron transport layers in molecular electronic devices [2]. Typical monomers include simple acrylate molecules such as polymethylmethacrylate,

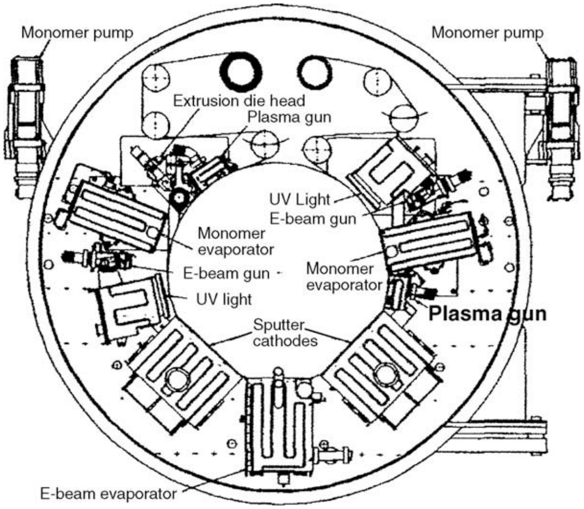

Figure 11.3: Vacuum roll coater with VPD and PVD stations, showing placement of monomer evaporator, plasma treatment, sputtering cathodes, and electron beam evaporator around the central drum of a web coater.

hexanedioldiacrylate, and tetraethyleneglycoldiacrylate; styrene and methyl styrene, and combinations of these precursors. The molecular weight of monomers is generally less than 1000, while for fluorinated monomers it is generally less than 2000. Monomers may be combined to form oligomers and resins for the polymer matrix, but these materials do not combine to form other monomers.

11.4 Surface Morphology

Virtually every PVD- or CVD-related process replicates the surface morphology of the substrate. Polymer films deposited by the VPD process actually smooth the substrate, as shown in Figure 11.4 [1]. This is demonstrated by the scanning electron micrograph (SEM) photographs that show the surface of virgin polyester, and the same surface with a 250 Å-thick sputtered Ta coating and a 1 μm thick VPD layer. VPD coatings routinely exhibit RMS surface roughness <0.1 nm (see Table 11.1).

As presented earlier, a web substrate can be subjected to plasma pretreatment before polymer deposition to activate the surface and improve adhesion, or to improve adhesion of subsequent layers [2]. Figure 11.5 shows RMS surface roughness of PET surfaces subjected to Ar, N_2, and O_2 plasmas, and the last column in Table 11.1 shows RMS surface roughness resulting from plasma and e-beam treatment. PET is a linear chain polymer, whereas VPD films are cross-linked. Referring to Table 11.1, surface treatments of the linear-chain polymer PET cause much stronger effects on its surface topography and composition than treatment of the

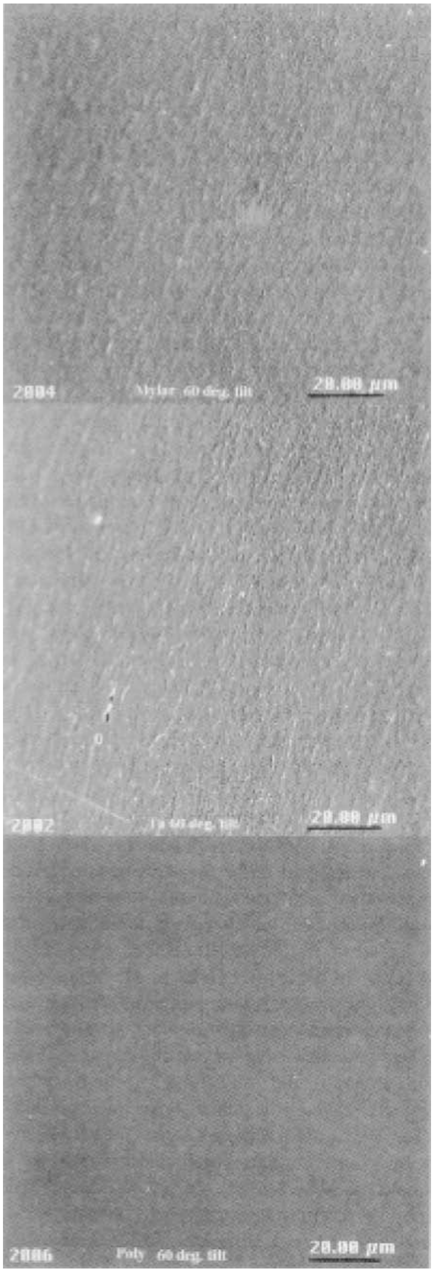

Figure 11.4: SEM picture of virgin, Ta- and VPD-coated polyester [1].

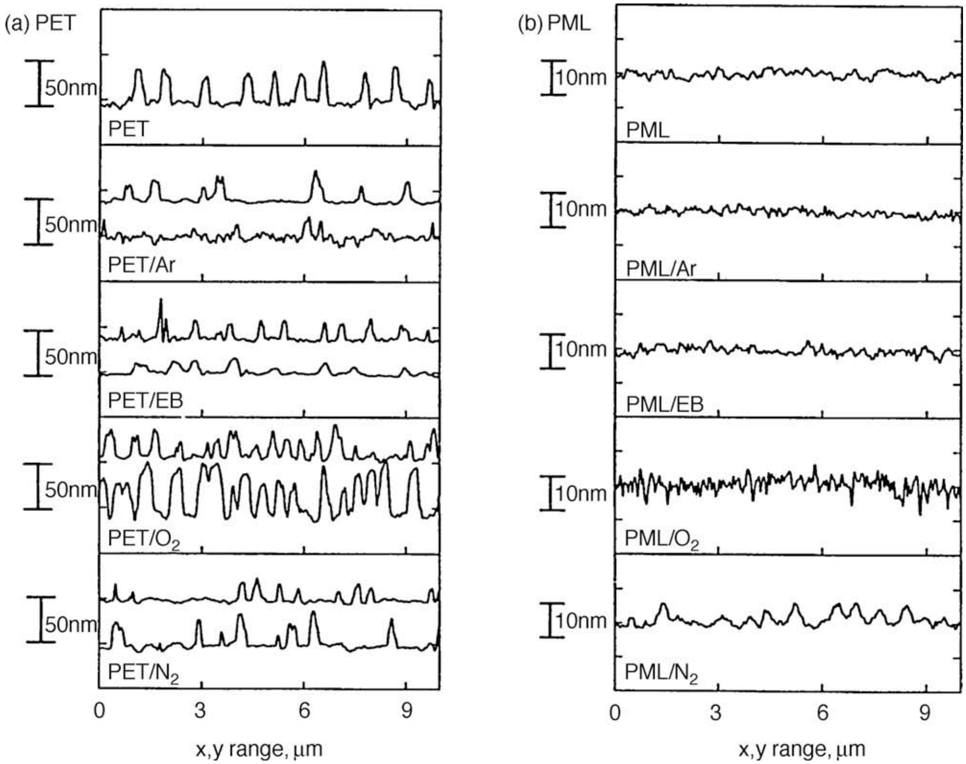

Figure 11.5: RMS surface roughness of PET surfaces subjected to Ar, N_2, and O_2 plasmas [2].

highly cross-linked VPD surface. Reactive gases like O_2 and N_2 were found to have a substantially higher impact on the surface topography and roughness of both PET and VPD when compared to treatments using inert gases such as Ar. Oxygen plasma, however, also noticeably changes the elemental composition of the VPD surface (see third column), and is preferred for adhesion improvement. It was also found that high-intensity e-beam corona treatments could interfere with adhesion of metals, metal-oxides, and polar polymers.

11.5 Multilayer Coatings

The versatility of the VPD process is demonstrated by the fact that virtually any PVD or vacuum deposition process can be used in conjunction with it to produce multilayer coatings, including magnetron sputtering, and electron and thermal evaporation. Applications for the VPD process include:

- ultrabarrier materials [1, 7]
- thin film Li-polymer batteries [8]

- thin film photovoltaics [8]
- light-emitting polymers [2]
- multilayer optical coatings on flexible substrates [9]
- wear- and abrasion-resistant coatings [10]
- nanolaminate structures [11]
- thin film solar cells [12]
- thin film capacitors [1]
- electroluminescent devices [2]
- radiation detectors
- contaminant resistance for fibers/fabrics [13]
- corrosion protection [13]
- antibacterial coatings [13].

For deposition of multilayer polymer/inorganic coatings, Figure 11.3 shows placement of the monomer evaporator, plasma treatment, sputtering cathodes, and e-beam evaporator around the central drum of a web coater. PECVD can also be integrated into this configuration. An in-line coater with the same features is shown in Figure 11.6. Since VPD processes require a higher chamber pressure, differential vacuum enclosures are required for PVD processes that operate at lower pressures. Enclosures operate at pressures required for magnetron sputtering (2–5 mtorr) or evaporation (e-beam and thermal). Although it would be beneficial to have enclosures to help certain polymer, the interior of some in-line machines is at the same

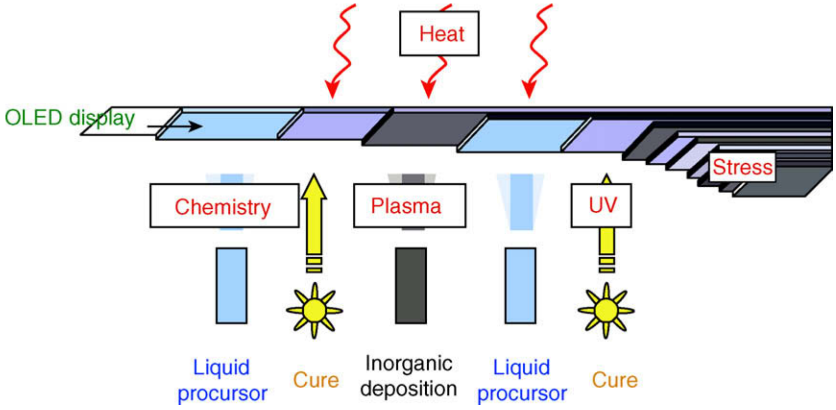

Figure 11.6: In-line VPD process (courtesy of Vitex Systems).

pressure with no enclosures required. Reactive gases can also be introduced into the enclosure for reactive sputtering. This process is used in roll-to-roll, in-line, or batch planetary substrate configurations.

This process is not limited to conventional single or multilayer structures. The polymer can be molecularly doped to increase its functionality [2]. Insoluble solids can be suspended in acrylate polymers. Active, luminescent QuinAcridone (QA) MDP can be produced which allows fabrication of light-emitting electrochemical cells, light-emitting polymers, and light-emitting organic diodes.

The general deposition sequence, which can be repeated sequentially, for a multilayer coating is as follows (around central drum in Figure 11.4):

- Plasma surface activation;
- Flash evaporate monomer;
- UV cure (smoothing layer);
- Deposit inorganic (oxide, nitride, metal) layer;
- Flash evaporate monomer;
- UV cure;
- Deposit inorganic layer.

This process is repeated until the requisite number of layers is deposited. Magnetron sputtering is generally preferred for deposition of the inorganic layer because films are denser than evaporated materials. However, if a very high rate is required, evaporation and PECVD may be the only options.

11.5.1 Ultrabarrier Coating

One of the most successful applications for this hybrid process is development and marketing of transparent ultrabarrier coatings for protection of atmospheric sensitive devices and materials. In addition, this work has spawned an entire new field of thin film materials [1, 8–13]. Transparent ultrabarrier coatings are needed to protect molecular electronics (e.g. organic light-emitting diodes (OLEDs)), thin film solar cells and thin film batteries from degradation due to water vapor and oxygen permeation. The basic structure of these coatings consists of alternating layers of polymer/oxide, polymer/metal or polymer/nitride, shown in Figure 11.7. The coatings are also deposited onto PET, other flexible polymers and plastics to reduce the water vapor transmission rate (WVTR) and oxygen transmission rate (OTR) by as much as six orders of magnitude. PET coated with the ultrabarrier coating is known as Flexible Glass$^{\text{TM}}$. The polymer layer creates an ultrasmooth, defect-free surface for deposition

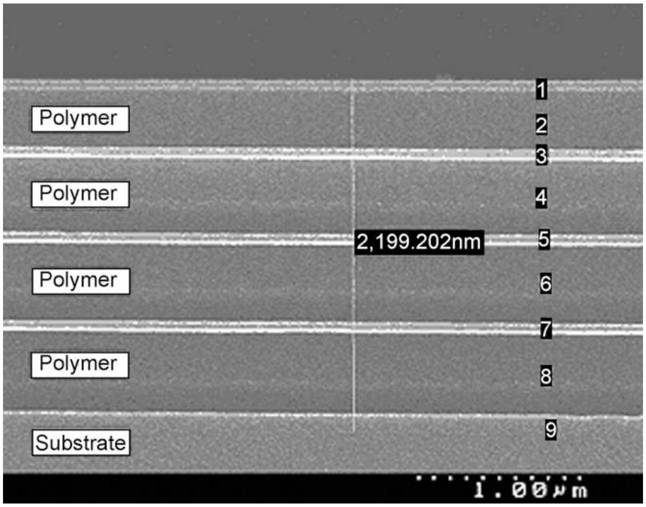

Figure 11.7: Layer structure of ultrabarrier coating.

of the low-permeation oxide, nitride, or metal layer. A UV cure is generally preferred for smoothing since an e-beam cure can increase surface roughness (see Table 11.1).

Figure 11.8 shows how the ultrabarrier coating is used to encapsulate an OLED [14]. OLEDs require a barrier protection ~ 10^{-6} g/m^2/d for water. If the OLED is on a flexible PET substrate, both sides of the OLED must be protected, which requires application of the ultrabarrier coating on the PET as well as over the OLED. Test results show that a 6-layer acrylate/Al_2O_3 ultrabarrier coating extends the performance of an OLED by at least 10,000 h [14].

Figure 11.8 shows two methods for encapsulation of a thin film solar cell, depending on which side is exposed to light or for an OLED must emit visible radiation [14]. The ultrabarrier

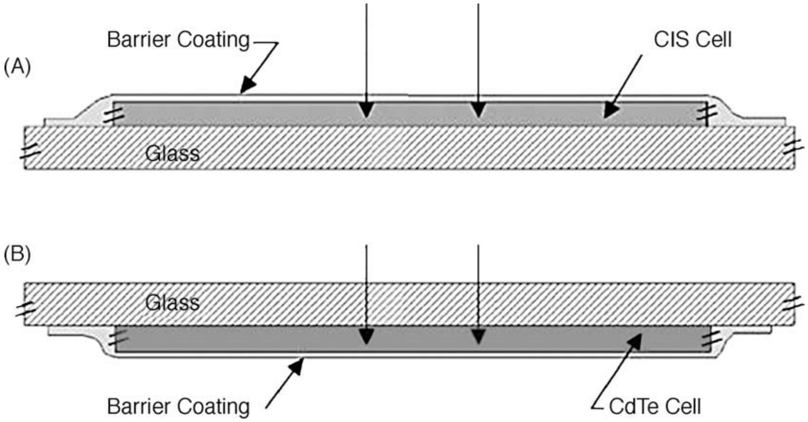

Figure 11.8: Ultrabarrier coating encapsulation of an OLED [14].

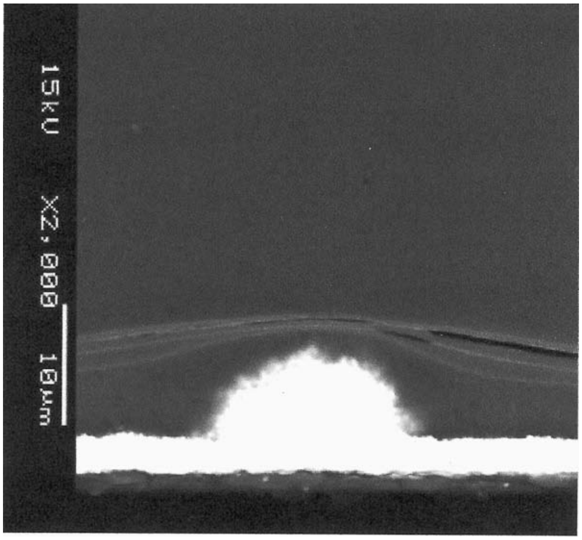

Figure 11.9: Encapsulation of solar cell nodule with ultrabarrier coating [12].

coating can encapsulate a structure significantly higher than the coating is thick, as apparent in Figure 11.9. Here a 0.5 μm thick VPD coating planarizes a 12 μm nodule of a thin film solar cell.

Figure 11.10 shows significant improvement in CdTe solar cell lifetime with application of the ultrabarrier coating [12]. Figure 11.10(A) shows the performance of a native (unprotected) cell, while Figure 11.10(B) shows the performance of a protected cell. After a short burn-in period, the efficiency of the protected cell does not degrade after 1000 h of testing. Ultrabarrier coatings have excellent optical (and very poor O_2 and H_2O) transmission, as demonstrated in

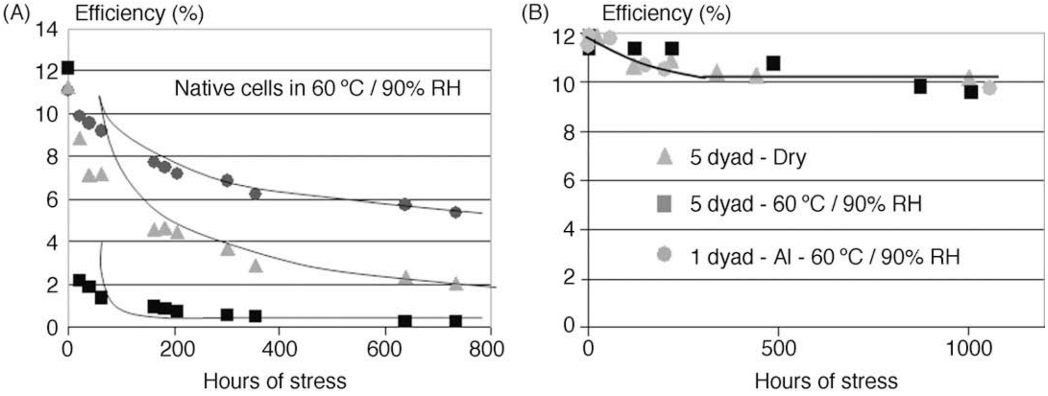

Figure 11.10: Efficiency vs hours of stress for native and protected CdTe solar cells [12].

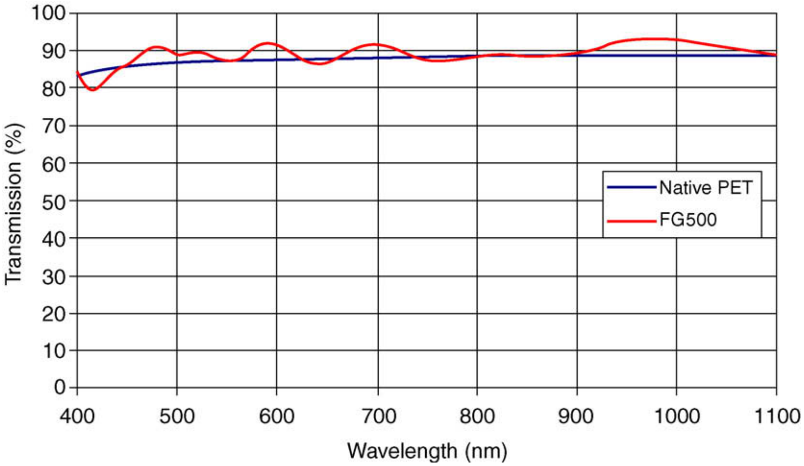

Figure 11.11: Transmission spectrum of ultrabarrier coating [10].

Figure 11.11 for the Barix™ coating marketed by Vitex Systems [14]. Without the ITO conductive electrode, transmission on PET is ~90%.

11.5.2 Nanolaminate Coatings

This hybrid deposition process is also used to deposit polymer/oxide and polymer/metal nanolaminate coatings, which are free-standing structures consisting of hundreds to thousands of alternating polymer/inorganic layers [15]. The nanolaminate can be transparent, used for lightweight windows, or opaque, used for capacitors. In addition to increased functionality, a major advantage of these coatings is their very low surface roughness and low optical scattering. The multilayer plastic substrate can include additional layers, including scratch-resistant layers, antireflective coatings, antifingerprint coatings, antistatic coatings, conductive coatings, transparent conductive coatings, and barrier coatings, to provide functionality to the substrate.

11.5.3 Advanced Applications

Advanced applications for multilayer VPD coatings include contaminant-resistant coatings for flat panel displays, fabrics, fibers, and yarns; corrosion-resistant coatings to replace the toxic heavy metals presently used (e.g. chromium); reduction of VOC release; and antibacterial coatings [13]. Contaminant-resistant coatings are based on acrylate formulations containing between 49% and 65% fluorine, which significantly decreases surface energies and increases hydrophobicity. These coatings are being developed for antismudge flat panel displays and windows, increasing chemical resistance for yarns and fabrics. A picture of a coated fiber is shown in Figure 11.12 [13].

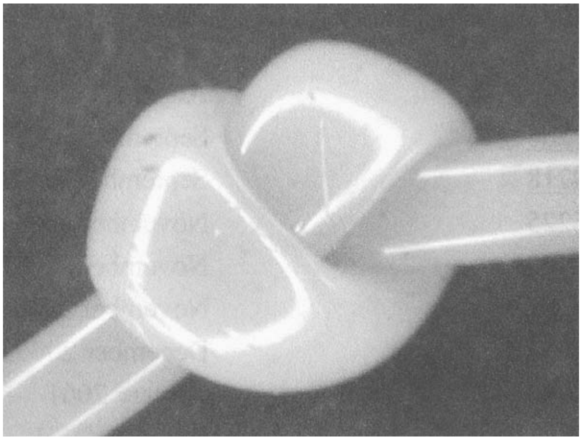

Figure 11.12: Microscope picture of fiber with corrosion-resistant coating [13].

Heavy metals, particularly chromium (Cr^{VI}) and mercury, have known toxicity. In addition, volatile organic compounds (VOCs) and chlorofluorocarbons (CFCs) can be released into the atmosphere during deposition of polymer coatings. Because PVD coatings are cross-linked using UV radiation, virtually no VOCs or CFCs are released during the deposition process. Corrosion inhibitors, such as benzotriazole and imidazole, can be added to the monomer mix. These technologies exploit enhanced barrier properties for corrosion control to reduce the need for effective corrosion inhibitors. It is postulated that an optimum balance exists between those properties that enhance inhibitor effectiveness and those that enhance physical barrier. These organic compounds bond with the metal surface and form a barrier that prevents or retards oxidation. On the other hand, the rosin-based coatings adhere to the metal substrate but do not chemically bond to it. Efficient, non-toxic, corrosion-resistant coatings will reduce environmental impact during manufacture and use, decrease costs, and extend the service life of the equipment.

Antibacterial coatings are being developed that incorporate biocide additives, such as silver, into the hydrophobic/oleophobic contaminant-resistant materials discussed previously. The modified coatings combine abrasion resistance, stain resistance, and antibacterial properties in a single polymer coating, with excellent potential for applications in the carpet and textile industries.

References

[1] J.D. Affinito et al., in: Society of Vacuum Coaters 39th Annual Technical Conference Proceedings (1996) 392.
[2] J.D. Affinito et al., in: Society of Vacuum Coaters 41st Annual Technical Conference Proceedings (1998) 220.
[3] J.D. Affinito et al., in: Society of Vacuum Coaters 40th Annual Technical Conference Proceedings (1997) 210.
[4] N. Inagaki, Plasma Surface Modification and Plasma Polymerization, Technomic, Basel, Switzerland (1996).

[5] J.D. Affinito et al., Method of making molecularly doped composite polymer material, US Patent 6,909,230.
[6] J.D. Affinito et al., Method of making molecularly doped composite polymer material, US Patent 6,613,395.
[7] A. Yializis, G.L. Powers, D.G. Shaw, IEEE Trans. Components Hybrids Manuf. Technol. 13 (1990) 66.
[8] M.E. Gross et al., in: Society of Vacuum Coaters 46th Annual Technical Conference Proceedings (2003) 89.
[9] P.M. Martin et al., in: Society of Vacuum Coaters 39th Annual Technical Conference Proceedings (1996) 187.
[10] M.G. Mikhael, A. Yialszis, in: Society of Vacuum Coaters 48th Annual Technical Conference Proceedings (2006) 663.
[11] P.M. Martin, W.D. Bennett, C.H. Henager, in: Society of Vacuum Coaters 50th Annual Technical Conference Proceedings (2007) 643.
[12] M.E. Gross et al., in: Society of Vacuum Coaters 49th Annual Technical Conference Proceedings (2006) 139.
[13] A. Yializis et al., in: Society of Vacuum Coaters 41st Annual Technical Conference Proceedings (1998) 477.
[14] G.L. Graff et al., in: Society of Vacuum Coaters 43rd Annual Technical Conference Proceedings (2000) 397.
[15] P.M. Martin et al., Multilayer plastic substrates, US Patent 6,962,671.

CHAPTER 12

Thin Film Nucleation, Growth, and Microstructural Evolution: An Atomic Scale View

J.E. Greene
Materials Science and Physics Departments and the Frederick Seitz Materials Research Laboratory, University of Illinois, Urbana, Illinois 61801, USA

12.1 Introduction

Understanding nucleation and growth at the atomic scale is fundamental to both the science and the technology of thin films. The increasingly stringent requirements of sophisticated thin film applications, processing technologies, and devices provide a strong impetus for obtaining ever better control over the dynamics of processes which govern the nanoscale chemistry and structure of as-deposited layers. The primary deposition variables determining nucleation and growth kinetics, microstructural evolution, and, hence, the physical properties of films are: the film material, the flux J and kinetic energy E of species incident at the growing surface, the growth temperature T_s, the flux of contaminants, and the substrate material, surface cleanliness, crystallinity, and orientation.

The kinetic energy of the incident flux during film growth by thermal evaporation, for which $E \sim 100$–200 meV, is determined by the temperature of the evaporant source. In contrast, typical average sputtered atom ejection energies range from 5 to 10 eV, which is of the order of, or higher than, bond energies in solids. In addition, energetic ions and fast atoms neutralized and reflected from the target during plasma or ion-beam sputter deposition have been shown to be useful in controllably altering the composition, chemistry, and structure of as-deposited layers through trapping, preferential sputtering, enhancing adatom mobilities, and dynamic collisional mixing [1–13].

This chapter is organized in the following manner. Section 12.2 deals with nucleation and the early stages of film growth. Thermodynamic and kinetic models are developed in Sections 12.2.1 and 12.2.2, respectively, and compared with experimental results. Three-dimensional (3D), two-dimensional (2D), and Stranski–Krastanow (S-K) ‘quantum dot’ growth modes are discussed sequentially in Sections 12.2.3, 12.2.4, and 12.2.5. Microstructure development is reviewed in Section 12.6, beginning with elemental films and their classification by structure zone diagrams (Section 12.6.1), then moving to multicomponent and multiphase film growth (Section 12.6.2). The chapter ends with a discussion of the role of low-energy ion irradiation (Section 12.6.3) for manipulating the dynamics of structural (and physical property) development including defect formation/annihilation, surface roughening/smoothening mechanisms, the evolution of preferred orientation, and synthesis of self-organized 3D nanostructures with unique properties.

12.2 Nucleation and the Early Stages of Film Growth

Nucleation on a substrate surface corresponds to a phase transition in which vapor or liquid phase atoms are deposited to coverages θ yielding sufficiently high 2D spreading pressures that local density fluctuations in the 2D gas give rise to the formation of stable clusters (nuclei). ‘Stable’ in this sense refers to clusters which have a higher probability to grow than to dissociate. There are three primary modes of film growth on substrates [14, 15], as illustrated schematically in Figure 12.1. During 3D, or Volmer–Weber, island growth, stable clusters develop into 3D islands which in turn coalesce to form a continuous film. This type of growth occurs when the adatoms are much more strongly bound to each other than to the substrate as is often the case for metal films on insulators or contaminated substrates (weakly interacting film/substrate interfaces with high interfacial energy densities). 2D layer-by-layer, or Frank–van der Merwe, growth corresponds to the case in which adatom–adatom binding energies are equal to, or less than, those between the adatoms and the substrate. In addition to the obvious case of homoepitaxy on a clean substrate, there are numerous examples of 2D

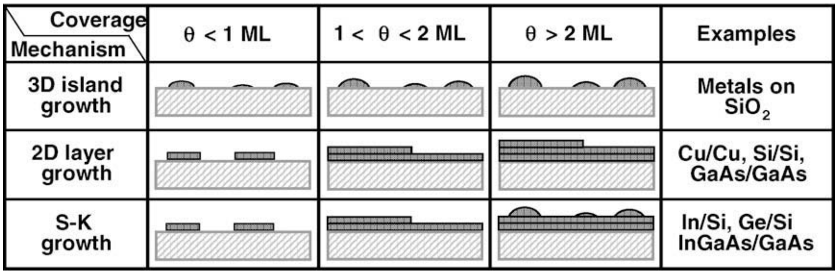

Coverage / Mechanism	θ < 1 ML	1 < θ < 2 ML	θ > 2 ML	Examples
3D island growth				Metals on SiO$_2$
2D layer growth				Cu/Cu, Si/Si, GaAs/GaAs
S-K growth				In/Si, Ge/Si InGaAs/GaAs

Figure 12.1: Schematic representations of three solid-film growth modes on substrates. θ is the overlayer coverage in monolayers.

heteroepitaxy in metal/metal (e.g. Cd on W), metal/semiconductor (Fe on GaAs), and semiconductor/semiconductor ($Si_{1-x}Ge_x$ on Si) systems. However, for heteroepitaxial growth, the continuously increasing thickness-dependent strain energy will eventually lead to the initiation of one or more relaxation mechanisms (e.g. misfit dislocation formation and/or surface roughening) at 'critical' layer thicknesses.

The third growth mode, predicted by Stranski and Krastanow (S-K) in 1938 [16], is a combination of the first two. In this case, after initially forming one or more 2D monolayers of a heterostructure, further layer growth becomes energetically unfavorable and 3D islands form. Other commonly used terms for this growth mode are islanding and strain-induced roughening. The transition from 2D to 3D growth is driven by the elastic strain energy $E_{\mathrm{elas}} \propto \varepsilon^2 h$, where $\varepsilon = (a_f - a_s)/a_s$ is the lattice parameter mismatch between the film (a_f) and the substrate (a_s) and h is the film thickness [17]. The transition occurs when the increase in the total film strain energy due to the growth of an additional layer is larger than the increase in surface energy required to form 3D islands which can partially relax via dilation as illustrated in Figure 12.2. Thus, the growth transition is driven by a decrease in total system energy [18, 19].

An example of an S-K system is In/Si(001)2×1 in which three In layers deposited at $T_s = 70\,°\mathrm{C}$ ($T_s/T_m = 0.8$; T_m is the In melting point in K) by molecular beam epitaxy (MBE) grow two-dimensionally and the next layer forms 3D islands which continue to evolve [20]. The archetype S-K model system is Ge/Si(001) owing to the interest in $Si_{1-x}Ge_x$/Ge(001) quantum dot electronics. For this case, the transition is also said to occur after approximately three monolayers (MLs) of growth, but detailed in situ scanning tunneling microscopy (STM) studies show that lines of Ge dimer vacancies begin to form at Ge coverages $\theta_{\mathrm{Ge}} < 1$ ML and orthogonal cross-hatch dimer vacancy rows start to form at ~2 ML [21, 22]; both are strain–relaxation mechanisms driven by the fact that the lattice constant of Ge is 4.2% larger than that of Si, giving rise to the formation of a large compressive stress σ_c.

The left side of Figure 12.3 schematically illustrates the essential features leading to nucleation on a substrate. An incident flux of film species must first become thermally

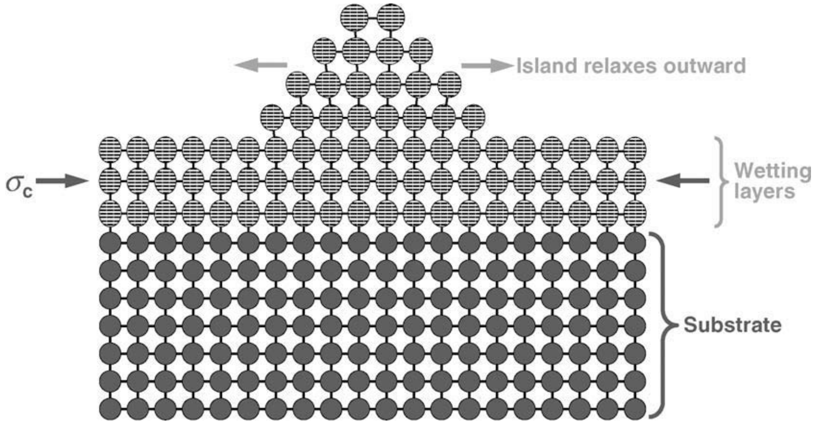

Figure 12.2: Schematic representation of strain-driven Stranski–Krastanow 'quantum dot' formation above an initial wetting layer. Here, the film lattice constant is larger than that of the substrate (i.e. $a_f > a_s$) and the layer is under compressive stress σ_c.

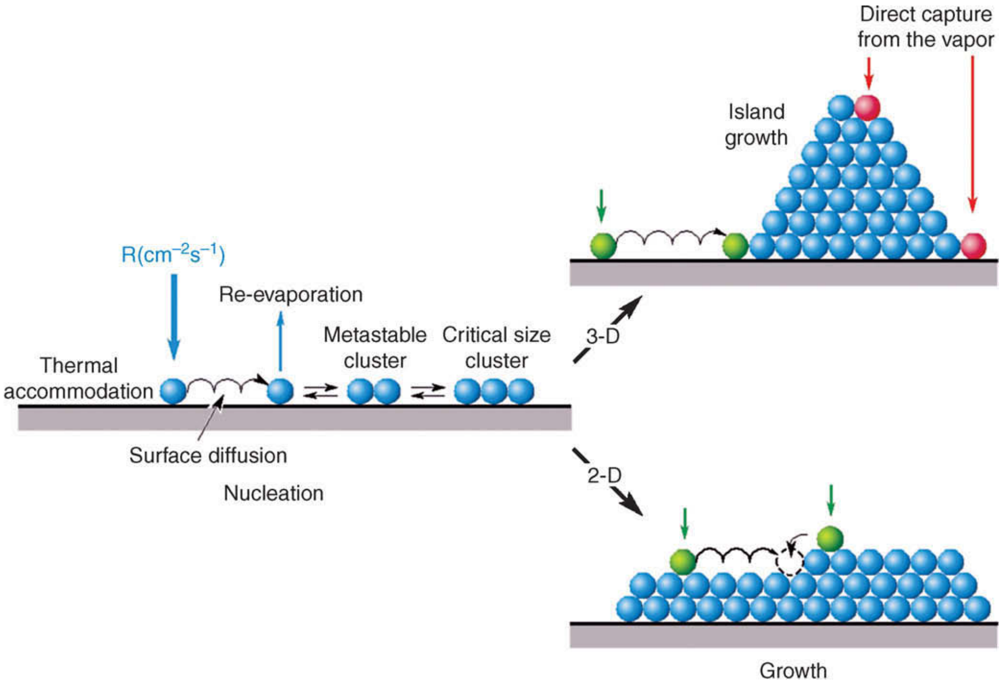

Figure 12.3: Schematic representation of processes leading to nucleation and 3D (upper right) and 2D (lower right) film growth.

accommodated with the substrate. For a given adatom, this typically occurs within a few vibrational periods (even for sputtered atoms incident with several eV). The adatoms then diffuse on the surface to interact with other adatoms or desorb (depending on film/substrate materials and T_s). At sufficiently low temperatures, a fraction of the clusters which are formed continue to grow in size (the rest dissolve back into the 2D gas) and become islands which eventually impinge on, and coalesce with, their neighbors to form a continuous film. Note that at high deposition rates R (in units of atoms/s) or low deposition temperatures such that $R >> N_s D_s$, where N_s is the substrate surface site number density (of the order of 10^{15} cm^{-2} for metals and semiconductors, depending on material and orientation) and D_s is the adatom surface diffusivity, the film is amorphous. This occurs since the adatoms do not have sufficient time to diffuse to low-energy sites before they are buried by subsequently deposited adatoms. Covalently and ionically bonded materials have low packing densities with strong bond directionality and are thus easily deposited in the amorphous state. Metals, however, exhibit much higher surface diffusivities and are considerably more difficult to obtain in the amorphous state. However, metallic glasses can be formed from deep eutectic alloys using special techniques to provide extremely fast cooling rates, $\geq 10^6$ K/s [23, 24].

12.2.1 Thermodynamic Descriptions of Experimental Results

Based on Figure 12.3, the minimum thermodynamic requirements to obtain net deposition would appear to be that the condensate pressure P in the gas phase is at least equal to its equilibrium vapor pressure P_{vp} over the solid. Actually, however, the supersaturation ratio $\zeta = P/P_{vp}$ must be much larger than one since small clusters have much higher vapor pressures than the corresponding bulk material due to their high surface-to-volume ratios. In analyzing film growth experiments, it is more convenient to use $\zeta = J/J_{vp}$ where the particle flux J is related to P via the kinetic definition of pressure:

$$J(\text{cm}^{-2}\,\text{s}^{-1}) = 3.513 \times 10^{22} P/(mT)^{1/2} \tag{12.1}$$

in which m is the molecular weight in amu, T is the gas temperature in K, and P is in torr.

A large surface-to-volume ratio also leads directly to the requirement that clusters must be greater than a minimum critical size in order for growth to occur. This is easy to understand in the simple case of homogeneous nucleation such as the formation of an embryonic ice particle in water cooled below the liquid freezing point $T_m = 0\,°\text{C}$. At temperatures less than T_m, solidification lowers the Gibbs free energy per unit volume ΔG_V. However, the formation of a solid cluster increases the system free energy ΔG by introducing an interfacial surface area between the ice cluster and the surrounding liquid. Surfaces and interfaces are 2D defects in infinite 3D crystals and their production requires the expenditure of energy. The difference between the decrease in ΔG_V, which varies as r^3 (r is the cluster radius) and the increase in interfacial energy, which varies as r^2, results in a free energy activation barrier for nucleation.

That is, the incipient clusters must reach a critical size before the volume term overcomes the surface term and stable nuclei are formed.

The net free energy associated with the formation of a solid spherical cluster in an otherwise homogeneous fluid is

$$\Delta G = 4\pi r^2\gamma + 4\pi r^3 \Delta G_V/3 \tag{12.2}$$

where γ is the interfacial energy per unit area. An expression for the critical cluster size r^* is obtained by setting the derivative $d(\Delta G)/dr = 0$ and solving to yield

$$r^* = -2\gamma/\Delta G_V \tag{12.3}$$

In modern literature, the critical size is generally represented as i^* in units of atoms; thus, the smallest *stable* nucleus is of size $(i^* + 1)$ atoms. Substituting Eq. (12.3) into (12.2) yields the nucleation activation barrier:

$$\Delta G^* = 16\gamma\pi^3/3(\Delta G_V)^2 \tag{12.4}$$

The factors 2 and $16\pi^3/3$ in Eqs (12.3) and (12.4) derive from geometry, i.e. the assumption here of spherical nuclei. The important results are that $r^* \propto \gamma/\Delta G_V$ and $\Delta G^* \propto \gamma^3/(\Delta G)^2$. Thus, as illustrated in Figure 12.4, nucleation is a simple stability problem

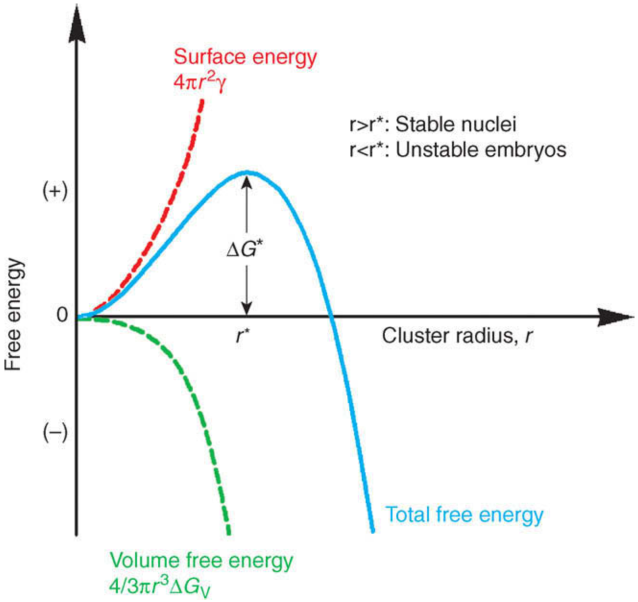

Figure 12.4: Schematic diagram showing total system free energy vs the radius *r* of a spherical nucleus in a homogeneous fluid. γ is the solid/liquid interfacial energy per unit area and ΔG is the Gibbs free energy per unit volume of the liquid-to-solid phase transition.

(r^2 in the energy cost term vs r^3 in the energy gain term) and an elementary self-assembly process.

To take this example a step further in order to estimate r^*, consider evaporating Au onto a NaCl(001) substrate at room temperature. Using Eq. (12.3) for r^*, the strategy is to derive an expression for ΔG_V beginning with the combined first and second laws of thermodynamics,

$$d(\Delta G) = VdP - SdT \tag{12.5}$$

where V and S are the system volume and entropy, respectively. Since thin films are generally deposited at constant $T = T_s$, the last term in (12.5) is ignored. For film growth in vacuum, the ideal gas law, $PV = NkT$, is a reasonable approximation. N/V is the number density of Au atoms in the incident flux and k is Boltzmann's constant. Substituting $V = NkT/P$ into (12.5) yields:

$$d(\Delta G)_T = NkT(dP/P) \tag{12.6}$$

Consider the addition of one more adatom to a cluster on a substrate which is maintained at T_s. Since ΔG_V is just $\Delta G/\Omega$, where Ω is the adatom volume, $d(\Delta G_V)_T = [kT_s/\Omega](dP/P)$, or

$$\Delta G_v = [kT_s/\Omega]\ell n(P/P_{vp}) = [kT_s/\Omega]\ell n(J/J_{vp}) = [kT_s/\Omega]\ell n(\zeta) \tag{12.7}$$

$\zeta = J/J_{vp}$ is the Au atom supersaturation. Substituting Eq. (12.7) into (12.3) yields

$$r^* = 2\Omega\gamma/kT_s\ell n(\zeta) \tag{12.8}$$

A reasonable value for J_{Au} during in situ transmission electron microscopy (TEM) studies of Au evaporation on NaCl(001) is 1×10^{13} cm^{-2} s^{-1} (~ 0.01 ML/s) [25]. This corresponds, from Eq. (12.1) with $m_{Au} = 196.97$ amu and $T_s = 300$ K, to a deposition pressure $P_{Au} \sim 7 \times 10^{-8}$ torr. The extrapolated vapor pressure P_{vp} of Au at 300 K is $\sim 10^{-30}$ torr [26]. Thus, ζ in this hypothetical experiment is $\sim 7 \times 10^{22}$. Substituting this, together with $\Omega_{Au} = 12.51$ Å^3 and the energy cost for covering the low surface tension NaCl substrate ($\gamma_{NaCl} = 0.014$ eV/Å^2) with Au ($\gamma_{Au} = 0.088$ eV/Å^2) [27] into Eq. (12.8) yields $r^* = 1.37$ Å which corresponds approximately to $i^* = 1$. Thus, the smallest stable Au cluster under these deposition conditions is $(i^* + 1) = 2$ atoms, consistent with experimental results.

The good agreement in the above example, however, is mostly fortuitous, as easily shown by simply changing T_s, which also changes ζ through the term P_{vp}. At 400 K, Eq. (12.8) yields $r^* = 1.83$ Å, which is larger than r^* at $T_s = 300$ K, but much less than the experimental result $(i^* + 1) = 4$ atoms. Nevertheless, Eq. (12.8) *does* show the correct trends: $r^*(T_s)$ increases with T_s since the cohesive energy of clusters decreases as $1/r$ [28]; thus, larger clusters are required to avoid thermal dissociation at higher deposition temperatures. In addition, based purely on kinetic arguments, adatom mobilities are higher at elevated T_s leading to longer surface mean free paths and, therefore, a smaller density of larger clusters (longer nucleation

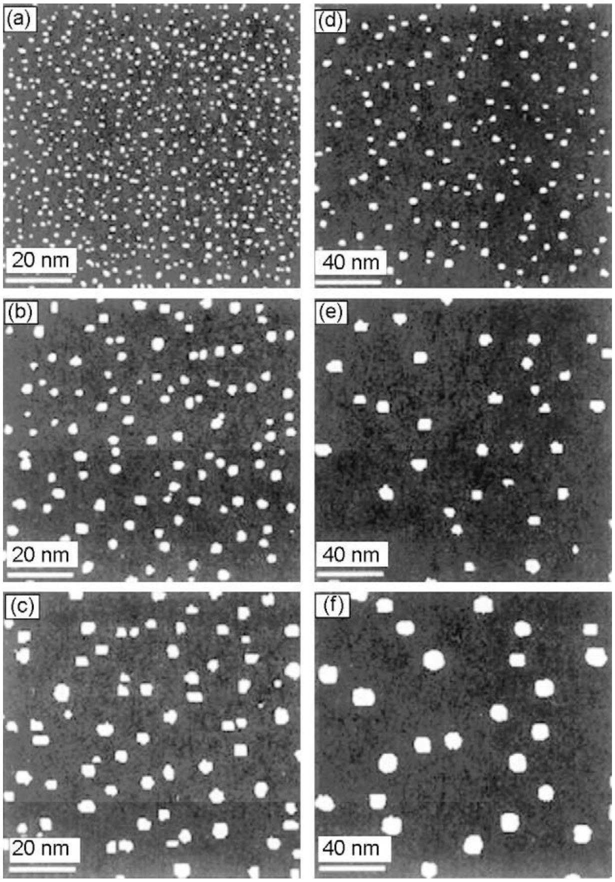

Figure 12.5: In situ STM images of Fe islands deposited on Fe(001) by MBE with a flux $J_{Au} = 1 \times 10^{13}$ cm^{-2} s^{1} to a coverage $\theta_{Fe} = 0.07$ ML at temperatures T_s = (a) 20, (b) 108, (c) 163, (d) 256, (e) 301, and (f) 356 °C. (From [29].)

lengths L_n) at the same coverage θ. An example is shown in Figure 12.5 for the 2D nucleation and growth of Fe on Fe(001). In these experiments, Fe was deposited at a flux $J = 1.4 \times 10^{13}$ cm^{-2} s^{-1} in ultrahigh vacuum (UHV) by MBE to a coverage $\theta_{Fe} = 0.07$ ML at temperatures T_s = (a) 20, (b) 108, (c) 163, (d) 256, (e) 301, and (f) 356 °C [29]. The images were obtained by in situ STM. Similarly, r^* also increases with decreasing flux J, i.e. decreasing ζ at constant T_s.

In the above discussion, homogeneous nucleation theory was employed, for illustration purposes, to describe the heterogeneous nucleation of Au/NaCl(001). This corresponds to the unrealistic case of nucleating a spherical particle with a contact angle of 180° on a solid surface (i.e. zero film/substrate interaction). The actual situation is, of course, much more complex. Nevertheless, most thermodynamic descriptions of heterogeneous 3D nucleation

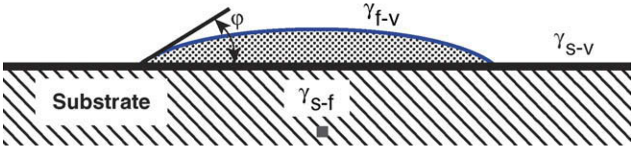

Figure 12.6: Schematic representation of a hemispherical cap-shaped island on a solid substrate. The γ terms are interfacial energies per unit area and the subscripts s, f, and v symbolize the substrate, film, and vapor phases. The wetting angle φ is related to the interfacial energies through Young's equation: $\gamma_{s-v} = \gamma_{f-s} + \gamma_{f-v}\cos\varphi$.

from the vapor phase are extensions of homogeneous nucleation theory using the capillarity, or droplet, model [30–32]. More sophisticated treatments are also available [15, 33, 34], but all thermodynamic models suffer from several shortcomings. The most important one is that values for surface energies, interface energies, formation energies, etc., which must be entered into the final equations are usually unknown for small clusters and, hence, bulk values, which can be very different, are used. Strongly size-dependent properties (e.g. reduced cohesive energies and melting points, increased vapor pressures, and the collapse of continuous densities of electronic states into discrete atom-like levels) are precisely the reason that nanostructures are so interesting. Thermodynamic models also generally employ convenient, but often unrealistic, geometries to represent nuclei that, on crystalline substrates which provide a template for preferential adatom diffusion directions, have shapes reflecting the underlying crystallography. Examples are one-dimensional Si and Ge clusters on Si(001)2×1 [35]. Nevertheless, as noted above, the capillarity model has the advantage that it captures much of the essential physics of the nucleation process.

To proceed, assume that a hemispherical 3D cluster of mean dimension r and contact angle φ forms on a solid surface as in Figure 12.6. The cluster has surface area a_1r^2 exposed to the vapor phase, a contact area a_2r^2 with the substrate, and a volume a_3r^2 where the a_i terms are functions of geometry. The total free energy of the cluster with respect to dissociation is

$$\Delta G = a_1r^2\gamma_{f-v} + a_2r^2\gamma_{s-f} - a_2r^2\gamma_{s-v} + a_3r^3\Delta G_V \tag{12.9}$$

γ_{f-v} is the positive free energy per unit area associated with the formation of a new surface between the film material f and the vapor phase v; γ_{s-f} is the substrate/film interfacial energy per unit area; and the term $a_2r^2\gamma_{s-v}$ accounts for the disappearance of free substrate surface due to cluster formation. Note that Eq. (12.9), like Eq. (12.2), corresponds to a stability problem characterized by r^2 vs r^3. Thus, we again take the derivative with respect to r and set it equal to zero to obtain r^*,

$$r^* = -2(a_1\gamma_{f-v} + a_2\gamma_{s-f} - a_2\gamma_{s-v})/3a_3\Delta G_V \tag{12.10}$$

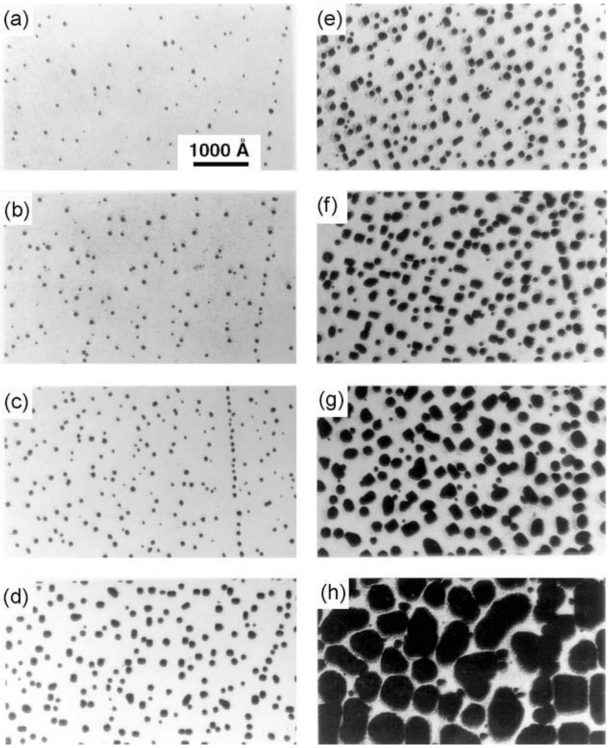

Figure 12.7: Replication transmission electron micrographs of Au islands deposited on NaCl(001) substrates cleaved in situ in UHV as a function of evaporation time: (a) 0.5, (b) 1.5, (c) 4, (d) 8, (e) 10, (f) 15, (g) 30, and (h) 85 minutes. The deposition rate *R* and growth temperature T_s were 1×10^{13} cm^{-2} s^{-1} and 250 °C, respectively. (Adapted from [25].) The non-random island arrays, along nearly straight lines, in frames (a)–(e) arise owing to preferential nucleation at low-angle grain boundaries created during substrate preparation by in situ substrate cleavage via a guillotine.

and substitute r^* into Eq. (12.9) to yield

$$\Delta G^* = 4(a_1\gamma_{\text{f-v}} + a_2\gamma_{\text{s-f}} - a_2\gamma_{\text{s-v}})^3/27a_3^2\Delta G_{\text{V}}^2 \tag{12.11}$$

While the equations for r^* and ΔG^* are more complex than (12.3) and (12.4), averaging the surface energy density (surface tension) terms still yields $r^* \propto \gamma/\Delta G_{\text{V}}$ and $\Delta G^* \propto \gamma^3/(\Delta G)^2$.

Figure 12.7 is a series of TEM images of Au clusters obtained during in situ UHV experiments in which an evaporated Au flux $J_{\text{Au}} = 1 \times 10^{13}$ cm^{-2} s^{-1} is incident on cleaved NaCl(001) substrates, maintained at 250 °C, for times ranging up to 85 minutes [25]. During the early stages – frame (a) corresponding to $t = 0.5$ minute – deposition kinetics are primarily controlled by nucleation. Coalescence dominates in frames (g) and (h), $t = 30$ and 85 minutes,

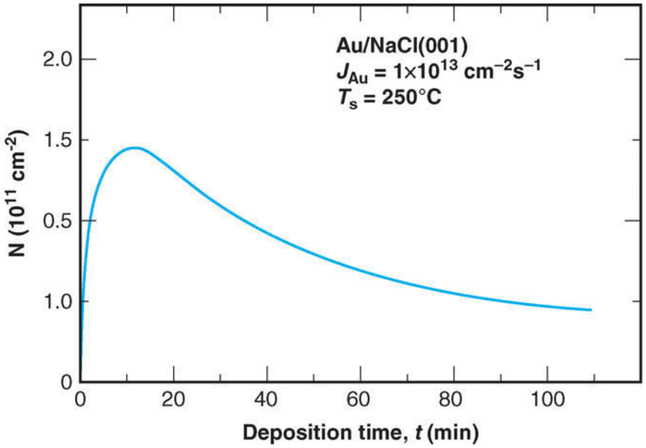

Figure 12.8: Au island number density on NaCl(001) as a function of deposition time. The MBE deposition flux J_{Au} and growth temperature T_s were 1×10^{13} cm^{-2} s^{-1} and 250 °C, respectively. (Adapted from [25].)

although some 'secondary' nucleation is clearly visible. At intermediate deposition times, nucleation, cluster growth, and coalescence are competing for adatoms. This is summarized in Figure 12.8, a plot of 3D cluster density N vs t [25]. The positive slope dN/dt of the N vs t curve (the nucleation rate) at $t \rightarrow 0$ begins to bend over as the average island separation becomes of the order of the adatom mean free path and adatom capture by established clusters (cluster growth) starts to overcome adatom loss by additional nucleation. At the maximum island density, $dN/dt = 0$, the rate at which existing clusters are lost by coalescence becomes equal to the time-dependent (i.e. coverage dependent) nucleation rate. On the far side of the curve at long times, the slope is negative and coalescence dominates.

Since the invention of the STM in 1983 [36], and the continuous development of UHV high-resolution in situ TEM over the past decades, it has been only natural that thin film scientists have studied nucleation on highly perfect single-crystal surfaces in pristine environments. Clusters as small as single adatoms and dimers can be imaged with STM under favorable conditions allowing the possibility of obtaining complete statistical cluster size distributions as a function of deposition conditions and layer coverage. Figure 12.9 shows STM results for 2D Fe cluster size distributions, in which j is the number of atoms per cluster, on Fe(001) as a function of the growth temperature $T_s = 20$–$356\,^\circ$C [29]. Deposition was carried out by MBE using $J_{Fe} = 1.4 \times 10^{13}$ cm^{-2} s^{-1}, as for Figure 12.5, to provide constant total coverages $\theta_{Fe} = 0.07$ ML. Nucleation and growth are competing processes and at a given coverage, cluster growth kinetics are favored over nucleation with increasing T_s due to longer adatom mean free paths leading to a tendency toward larger average island sizes with lower maximum island densities. Thus, cluster size distributions vary dramatically with T_s in Figure 12.9.

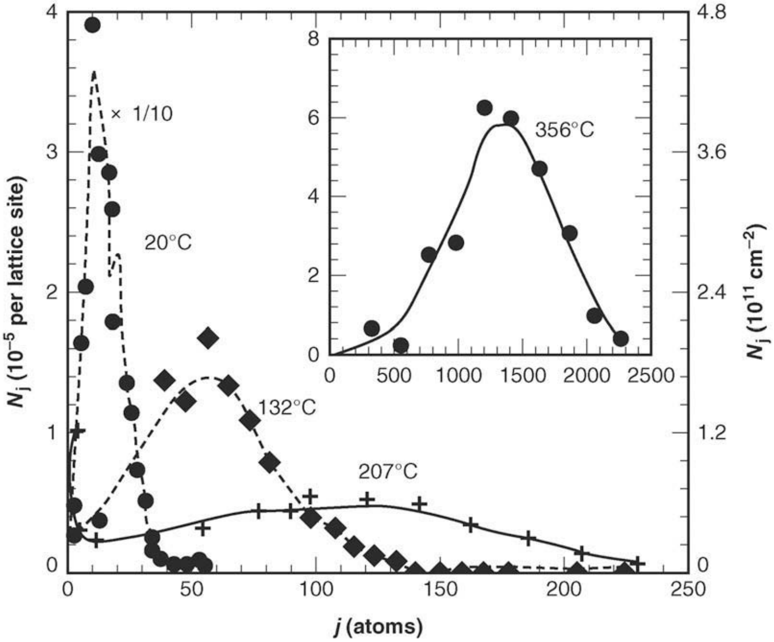

Figure 12.9: STM results for 2D Fe cluster size distributions, in which *j* is the number of atoms per cluster and N_j is the number of clusters of size *j*, on Fe(001) as a function of the growth temperature $T_s = 20$–$356\,°C$. Deposition was carried out by MBE using $J_{Fe} = 1.4 \times 10^{13}\ cm^{-2}\ s^{-1}$, as for Figure 12.5, with deposition times adjusted to provide constant total coverages $\theta_{Fe} = 0.07$ ML. (Adapted from [29].)

12.2.2 Kinetic Descriptions of Experimental Results

Owing to the limitations of the thermodynamic models discussed above, STM and TEM data are usually fitted using mean-field rate theory models, of the type originally developed by Zinmeister [37–41], to obtain critical cluster sizes i^*, surface diffusion energies E_s, jump attempt frequencies ν_s, and pairwise cluster-atom binding energies E_b. Reviews and more detailed discussions of the development of this approach may be found in [15] and [42].

The essence of atomistic kinetics approaches is to simultaneously solve parallel rate equations for the change in number density N_j of clusters of size j. Neglecting coalescence for the moment, one can write a series of ordinary differential equations to describe the time rate of change in the concentration of monomers, dimers, trimers, and higher order clusters on a substrate surface in response to an incident flux J of atoms. For monomers N_1,

$$\frac{dN_1}{dt} = J - \frac{N_1}{\tau_d} - K_1 N_1^2 - N_1 \sum_{j=2}^{n} (K_j N_j) \tag{12.12}$$

where n is the largest cluster size in the experiment being analyzed. The first term on the right side of Eq. (12.12) is the impingement rate, the second is the desorption rate, the third is the dimer formation rate in which K_1 is the rate constant, and the last term is the rate of monomer loss to higher order clusters. The adatom desorption lifetime $\tau_d = (1/\nu_d)\exp(E_d/kT_s)$, in which ν_d is the desorption attempt frequency and E_d is the desorption energy. For deposition at low temperatures (the complete condensation regime), the adatom desorption rate is insignificant and the second term can be ignored. At higher temperatures, τ_d can often be calculated since ν_d and E_d are known for many materials systems, especially for relatively high vapor pressure metal condensates such as P on Si(001), from thermally programmed desorption (TPD) experiments [43]. The rate constant K_1 corresponds to bimolecular recombination and is directly related to the adatom diffusivity; $K_1 = \sigma_1 D_s = \sigma_1 D_o \exp(E_s/kT_s)$, where σ_1 is the adatom capture probability. Cluster loss terms due to coalescence can also be added to Eq. (12.12) [42].

For clusters of size $j > 1$, parallel equations are written in the general form,

$$\frac{dN_j}{dt} = K_{j-1}N_1N_{j-1} - K_jN_1N_j. \tag{12.13}$$

The first term on the right side of Eq. (12.13) is the formation rate of clusters of size j by attachment of monomers to clusters of size $(j-1)$. The second term is the loss rate due to clusters of size j forming larger clusters of size $(j+1)$. In the simplest expression of this model, it is assumed that clusters of size $j > 1$ do not desorb or diffuse. In addition, under conditions of local equilibrium,

$$\frac{N_j}{N_{j-1}} = N_1C_j\exp\left(\frac{\Delta E_b}{kT_s}\right) \tag{12.14}$$

ΔE_b in Eq. (12.14), the pairwise binding energy difference between clusters of size j and $(j-1)$, is obtained either by fitting data as a function of T_s (see below) or by calculation using density functional theory. C_j is a statistical weighting factor which is a constant for a particular cluster size and configuration [44].

Consider a simple 2D nucleation example in which deposition occurs at sufficiently low temperature such that the desorption term in Eq. (12.12) can be neglected, stable clusters are immobile, the 2D sticking probability of adatoms to clusters of size $j \geq i^*$ is unity, and the coverage is small enough that coalescence is insignificant. In this case, the equation set reduces to:

$$\frac{dN_1}{dt} = J - D_sN_1N_j \tag{12.15}$$

$$\frac{dN_j}{dt} = D_sN_1N_{i^*} \tag{12.16}$$

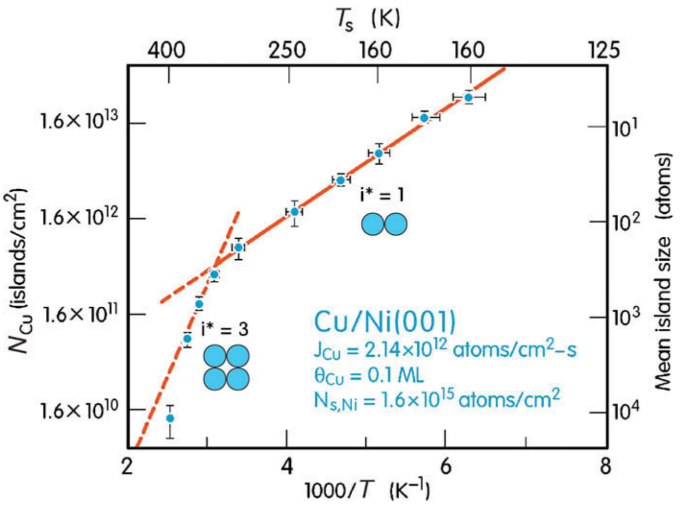

Figure 12.10: STM data from nucleation and growth experiments in which Cu is deposited onto Ni(001) surfaces to coverages $\theta_{Cu} = 0.1$ ML at temperatures ranging from 160 to 400 K (−113 to 127 °C) using MBE with $J_{Cu} = 2.14 \times 10^{12}$ cm^{-2} s^{-1}. Island density N_{Cu} and mean island size are plotted vs T_s. $N_{s,\,Ni}$ is the Ni(001) surface site density. (Adapted from [48].)

in which $j \geq i^*$. Initially, the cluster creation rate in Eq. (12.15) is $\sim D_s N_1 N_{i^*}$. However, as an appreciable cluster density is developed such that $\Sigma N_j \gg N_1$, adatom attachment to existing stable clusters becomes the dominant adatom loss term ($\sim D_s N_1 N_{j > i^*}$) and the total island density N reaches saturation $N_{sat}(\theta)$ until the island coalescence rate becomes significant and N decreases. The steady state solution to Eqs (12.15) and (12.16) yields a power-law scaling relationship $N \propto (J/D_s)^p$ where for 2D nucleation $p = (i^* + 1)/(i^* + 3)$ when $N_1 \sim N$ and $p = i^*/(i^* + 2)$ when $N = N_{sat} \gg N_1$ [45–47]. The surface diffusivity $D_s = \{1/4\}(\nu_s/N_s)$ $\exp(-E_s/kT_s)$.

Figure 12.10 shows STM data from nucleation and growth experiments in which Cu is deposited onto Ni(001) surfaces to coverages $\theta_{Cu} = 0.1$ ML at temperatures ranging from 160 K (−113 °C) to 400 K (127 °C) using MBE with $J_{Cu} = 2.14 \times 10^{12}$ cm^{-2} s^{-1} [48]. γ_{Cu}, the surface tension of (bulk) Cu, is approximately 10% lower than that of Ni [27]; thus, Cu spreads easily leading, initially, to 2D growth. The first thing to note in the experimental results is that over this relatively limited T_s range, the number density N_{Cu} of Cu islands decreases by $> 10^3$. The authors report that there was no evidence for the migration of small islands during these experiments.

The critical cluster size i^* in the low (160–320 K) and high (320–400 K) T_s ranges were obtained by noting from the above discussion that the deposition rate dependence of $N_{sat}(T_s)$ for 2D nucleation and growth at constant T_s (i.e. constant D_s) in the saturation island density

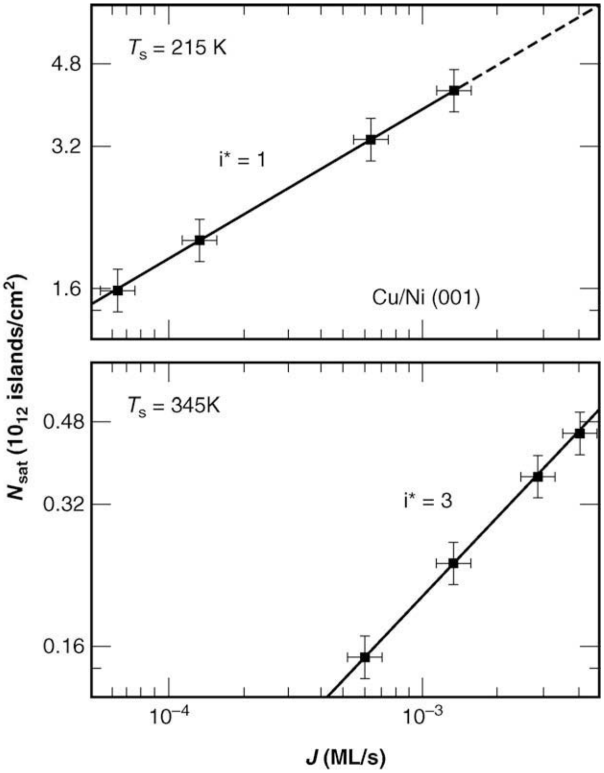

Figure 12.11: Saturation island densities N_{sat}, measured by in situ STM, on Ni(001) vs incident MBE Cu flux J_{Cu} at T_s = 215 and 345 K (−58 and 72 °C). i^* is the critical island size in units of atoms. (Adapted from [48].)

limit ($N >> N_1$) follows the power law relationship $N_{sat} \propto J^p$ with $p = i^*/(1^* + 2)$. Figure 12.11 shows measured $N_{sat}(J)$ values for temperatures $T_s = 215$ K (−58 °C) and 345 K (72 °C), near the middle of the two nucleation regions in Figure 12.10. At 215 K, the exponent $p = 0.32 \pm 0.01$ indicating that $i^* = 1$ and the smallest stable cluster is a Cu dimer. At 345 K, $p = 0.58 \pm 0.02$ yielding $i^* = 3$ and the Cu tetramer is now the smallest stable cluster. A similar scaling law approach was used by Zuo et al. [47] to determine minimum stable cluster sizes for Cu/Cu(001) as a function of deposition conditions.

$(i^* + 1) = 2$ and 4 are 'magic' cluster sizes for a square surface lattice. $(i^* + 1) = 3$ is not observed on a square net since the rate-limiting step for dissolution back into the 2D gas would be only one broken bond, just as the case for $(i^* + 1) = 2$. However, dissolving a stable cluster of size 4 atoms requires two broken bonds. Above $(i^* + 1) = 4$, there is no well-defined behavior on square lattices since all clusters are characterized by single or double bond breaking. Magic cluster sizes for a hexagonal surface net are 2, 3, and 7 atoms.

More general atomistic nucleation kinetics solutions are also available [42]. For example, in the complete condensation regime (no significant adatom loss by desorption), the cascade of Eqs (12.12)–(12.14) can be solved (with each term for $j < i^*$ being zero) to yield power law expressions for the saturation island density N_{sat} of the form:

$$N_{\text{sat}} \propto (J/\nu_s)^p \exp(E_p/kT_s) \tag{12.17}$$

where p and E_p depend on the experimental conditions. For 3D nucleation, $p = i^*/(i^* + 2.5)$ and $E_p = (E_{i^*} + E_s)$, while for 2D nucleation $p = i^*/(i^* + 2)$ with $E_P = (E_{i^*} + i^* E_s)/(i^* + 2)$. E_{i^*} is the binding energy of the critical nucleus; that is, $E_0 = E_1 = 0$, $E_2 = E_b$, and $E_3 \sim 2E_b$. The latter value is based on a bond-counting argument in which E_{i^*} is given by the number of nearest neighbor adatom bonds in the critical nucleus i^* times the pairwise bonding energy per bond E_b.

Consistent with the discussion on the thermodynamics of nucleation earlier in Section 12.2.1, the results in Figure 12.10 show that i^* increases with T_s and that at higher temperatures, the island density decreases while the average size increases. Equation (12.17) for 2D nucleation was used to fit the data and obtain the energetics. From the slope of the $i^* = 1$ region, the surface diffusion energy for Cu on Ni(001) was determined to be 0.35 eV, very close to the previously reported value for Cu/Cu(001), $E_s = 0.36$ eV [49], and the intercept of the $i^* = 1$ region provides an adatom jump attempt frequency $\nu = 4 \times 10^{11}$ Hz. Knowing E_s, the cluster binding energy $E_b = 0.46$ eV was obtained from the slope of the $i^* = 3$ region.

12.3 Three-Dimensional Nucleation and Growth

It is clear from Eq. (12.6) that 3D film growth (see schematic diagram in the upper right of Figure 12.3) is favored when $a_2 r^2 \gamma_{s-v} < a_1 r^2 \gamma_{f-v} + a_2 r^2 \gamma_{s-f}$; that is, the net surface free energy associated with the formation of a cluster is positive. Classic examples are depositing metals on gas–metal compounds such as SiO_2, NaCl, and TiO_2. All gas–metal compounds have relatively low surface energies, with saturated surface bonds, while metal surface energies are much higher. (Among metals, those with higher melting points have higher γ values; T_m is a measure of the cohesive energy and, hence, the bond strength). The relative inertness of gas–metal compound surfaces also means that, in addition to $\gamma_{f-v} > \gamma_{s-v}$ for metal deposits, the interfacial energy per unit area γ_{s-f} is large (a 'weakly interacting' interface), resulting in a high contact angle as observed in catalytic systems such as $Pd/TiO_2(011)$ [50].

12.3.1 Nucleation and Early Growth

During the early stages of 3D growth, adatom supply to the islands is primarily by deposition onto open substrate area followed by surface diffusion, as illustrated in the upper diagram of Figure 12.12. Direct deposition onto the islands is minimal owing to small average island

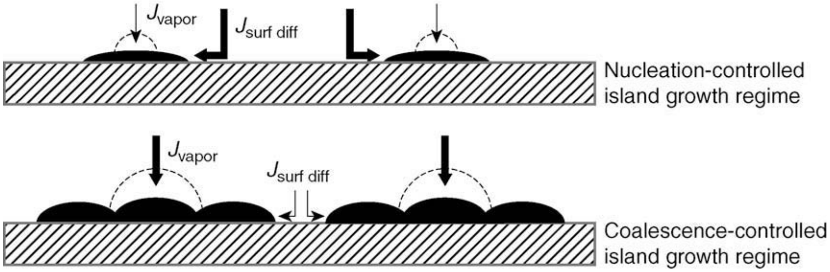

Figure 12.12: Schematic illustration of island growth in the nucleation-controlled (rate determined primarily by deposition onto the open terrace followed by surface diffusion) and coalescence-controlled (rate determined primarily by direct deposition) regimes. The dashed lines indicate equilibrium island shapes with a larger wetting angle φ. The widths of the arrows symbolize the magnitude of adatom supply. (Adapted from [51].)

sizes. Thus, because of the *kinetics* of adatom supply, the islands at this stage grow primarily laterally even if the *equilibrium* film/substrate contact angle is much larger, as illustrated schematically by the dashed lines. The contact angle can be obtained experimentally via annealing experiments. After significant island coalescence, however, adatom supply is primarily through direct deposition (lower diagram in Figure 12.12). At this stage, only a small amount of material is deposited into the relatively narrow trenches between islands.

Figure 12.13 provides a summary overview of a detailed STM study of the 3D growth of Ag islands during UHV evaporation, with a deposition rate $R = 0.08$ Å/s, on smooth (rms roughness ~2 Å) amorphous Si (a-Si) substrates at room temperature ($T_s/T_m = 0.24$) [51]. Each panel shows a representative image and line scan corresponding to a different deposition thickness. At $h = 3$ Å (Figure 12.13a), essentially all islands are 3D single crystals. The first stage of island coalescence is clearly visible by $h = 10$ Å (Figure 12.13b) leading primarily to larger compact single crystal islands (a few islands have grain boundaries) separated by trenches. Figure 12.13(c), $h = 54$ Å, shows that in the second stage of island coalescence (incomplete coalescence), polycrystalline islands exhibit irregular in-plane shapes separated by deep trenches; several 111 facets are visible in the region outlined by a rectangle, 111 and 001 facets in the circle. The continuous film regime, with few or no trenches and large 111 faceted grains, is reached by $h = 300$ Å (Figure 12.13d).

12.3.2 Three-Dimensional Island Coalescence

A series of TEM micrographs from a video file (Figure 12.14) illustrate the nature of morphological changes which occur during coalescence of 3D Au islands on hexagonal $MoS_2(0002)$ at 400 °C [52, 53]. In the 0.06 s between images (a) and (b), two pseudomorphic hexagonal Au islands have coalesced and are connected by a neck approximately 500 Å wide.

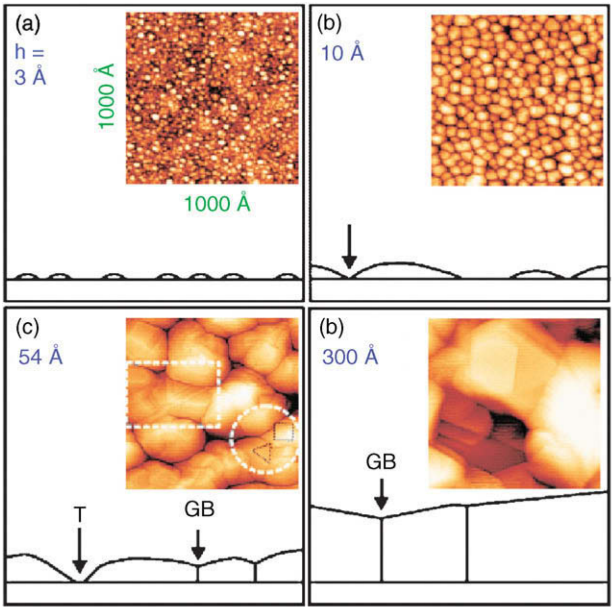

Figure 12.13: STM images (1000 × 1000 Å^2) of Ag layers deposited by MBE on a-Si substrates to thicknesses of (a) 3, (b) 10, (c) 54, and (d) 300 Å. The deposition rate was $R = 0.08$ Å/s. Schematic cross-sectional representations are also shown in which T and GB symbolize trenches and grain boundaries, respectively. (Adapted from [51].)

The initial contact point is at corner facets of the two islands. The driving force for coalescence is a reduction in surface energy by curvature-driven diffusion causing the islands to become taller and more compact. (A simple geometric calculation of the change in total surface area due to the coalescence of two half-sphere-shaped islands into one larger

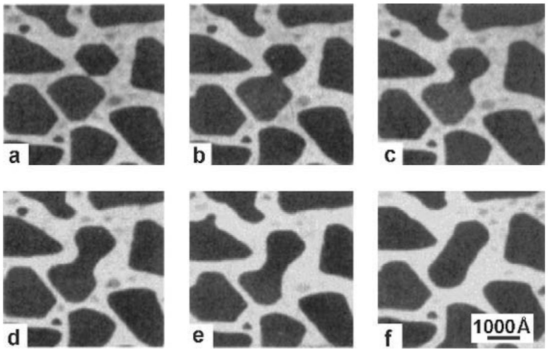

Figure 12.14: A series of TEM images from a movie file showing coalescence of two Au islands on $MoS_2(0002)$ during in situ evaporative deposition at 400 °C: (a) arbitrary $t = 0$, (b) $t = 0.06$ s, (c) 0.19 s, (d) 0.5 s, (e) 1.06 s, and (f) 6.19 s. (Adapted from [52, 53].)

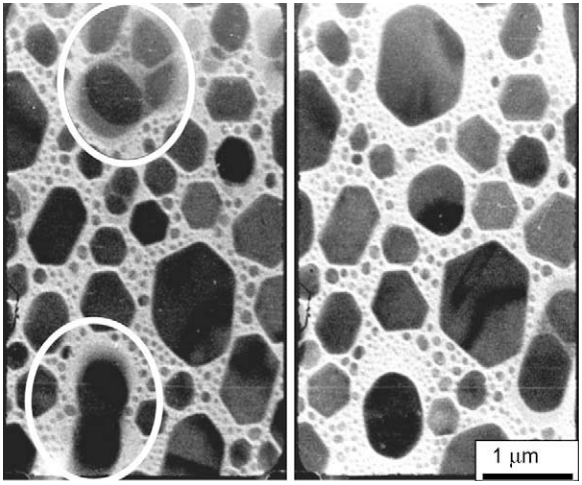

Figure 12.15: In situ plan-view TEM micrographs obtained during the growth and coalescence of In islands deposited at 5 Å/s on amorphous C substrates at T_s = 540 °C. The time lapse between obtaining the left and right images is 0.3 s. Note the denuded zones surrounding the coalesced islands. (From [54].)

half-sphere islands, ignoring the difference in interface area, yields a decrease in surface energy of ~26%). Over the next ~6 s from image (b) to image (f), the coalesced island relaxes back toward a hexagonal shape. During this process, the total projected area on the substrate decreases leading to the formation of a cluster denuded zone around the coalesced island, favoring additional secondary nucleation.

Plan-view TEM images showing denuded areas surrounding coalesced islands [54] are reproduced in Figure 12.15. The images, separated by 0.3 s, were obtained in situ during evaporation of In on an amorphous C substrate at $T_s = 40\,°\mathrm{C}$. The deposition rate was 5 Å/s.

Coalescence is often described as occurring in a liquid-like manner, although electron diffraction results show that it is generally a solid-state reaction. Liquid coalescence has, however, been reported for films grown at high T_s/T_m ratios [55] due to freezing point depression associated with small clusters [56]. Section 12.4.2 contains a more detailed discussion of coalescence kinetics using an analytical model to describe in situ STM results during the simpler case of 2D homoepitaxial growth, in this case for TiN(001) and TiN(111) layers grown by reactive magnetron sputter deposition in a UHV system.

In the early stages of deposition, when the fractional surface coverage is still relatively low, composite islands can relax to a pseudomorphic crystallographic shape following coalescence, as illustrated in Figure 12.15, and the islands are still single crystals. This process, termed complete coalescence as mutual island misorientation is eliminated via recrystallization (grain boundary diffusion), ultimately leads to an as-deposited average grain size which is much larger than average island sizes prior to the onset of coalescence. The driving force is the resulting decrease in the total grain boundary interfacial length. For metals, grain boundary tensions are of the order of one-third of the corresponding surface tensions [57]. However, as continued coalescence of larger islands occurs, recrystallization kinetics become too slow at lower growth temperatures and the composite islands are polycrystalline with trapped large-angle grain boundaries. In the final stages of coalescence, holes and channels are left in an otherwise continuous film. These voids are eventually filled by secondary nucleation, island growth, and further coalescence.

The average thickness at which three-dimensionally nucleated films become continuous depends on the choice of film and substrate materials, supersaturation, contamination, and T_s. This is clear from the combination of Eqs (12.7) and (12.10). Films which display a dense population of small islands during the initial stages of deposition will become continuous at a relatively low average film thickness, typically a few tens to a few hundreds of Å. However, films consisting of a low areal density of large islands during the early stages of deposition will exhibit an island structure which persists up to relatively large average film thicknesses.

In addition to large-angle grain boundaries, polycrystalline films grown at low T_s/T_m often exhibit a high density of other mechanical defects such as dislocations, dislocation loops, twins, stacking faults, and low-angle boundaries. Dislocations are generated to partially relax stresses produced in continuous films due to film/substrate lattice parameter and thermal expansion mismatch. Contamination can also play an important role by preferential adsorption on different surface facets and step edges and by inhibiting island reorientation and recrystallization during coalescence [8].

12.4 Two-Dimensional Nucleation and Growth

Referring again to Eq. (12.6), 2D Frank–van der Mewre growth is energetically favorable when $a_2r^2\gamma_{s-v} \geq a_1r^2\gamma_{f-v} + a_2r^2\gamma_{s-f}$ (see schematic diagram in the lower right of Figure 12.3). The simplest case, corresponding to the equality sign, is homoepitaxial growth in the absence of contamination. However, deposition of, for example, a low-melting-point (hence low γ) metal such as Cd on the higher melting-point (higher γ) metal W also fulfills the condition since γ_{s-f} in this case is relatively small. Wagner and Vooerhoeve [58] used a combination of TPD measurements as a function of T_s and overlayer coverage θ_{Cd} with replication TEM to study nucleation and the initial stages of metal MBE in UHV. They found that the desorption energy E_d of Cd on W is greater than that for Cd on Cd. On clean polycrystalline W substrates, E_d decreases from an initial value of 2.2 eV (averaged over all W grain orientations) at low coverages to a value approximately equal to the heat of sublimation of bulk Cd, 1.2 eV, at $\theta_{Cd} \sim 4$ ML. Thus, the Cd–W binding energy is much larger than that of Cd–Cd. It is therefore not surprising that TEM results show Cd exhibits *local* epitaxy and

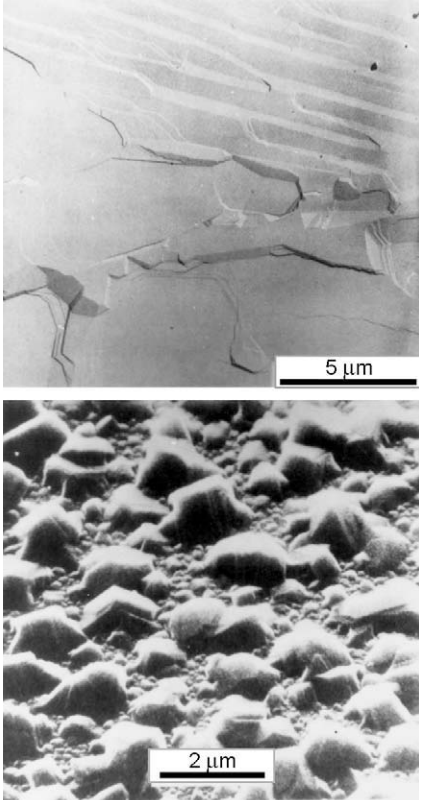

Figure 12.16: Electron microscopic images of Cd layers, $\theta_{Cd} \sim 500$ ML, grown at $T_s = 100\,°C$ on clean (upper) and O_2-contaminated (lower) polycrystalline W substrates. (From [58, 59].)

replicates each W grain. However, the introduction of a small amount of oxygen (less than a monolayer) dramatically alters the nucleation mode to 3D (the surface tension of gas–metal compounds is much less than that of metals [27], as briefly discussed in Section 12.3), and inhibits epitaxial growth [59]. The images in Figure 12.16 very graphically illustrate the effect of oxygen contamination for layers grown at $T_s = 100\,°C$.

12.4.1 Nucleation and Early Growth

Representative STM images showing 2D clusters of Fe deposited by MBE on Fe(001) with $J_{Fe} = 1.4 \times 10^{13}\ cm^{-2}\ s^{-1}$ to constant coverages $\theta_{Fe} = 0.07$ ML as a function of T_s between 20 and 356 °C were shown in Figure 12.5. Saturation cluster densities N_{sat} at $T_s = 20$–$250\,°C$, for which $i^* = 1$, are plotted in Figure 12.17 [60]. The results were fitted using the scaling relationship $N_{sat} \propto (J/D_s)^{1/3} \propto (1/D_s)^{1/3}$ (see discussion in Section 12.2.2) to obtain $E_s = 450 \pm 80$ meV with $D_o = 7.2 \times 10^{-4}\ cm^2\ s^{-1}$. The resulting Fe adatom surface diffusion

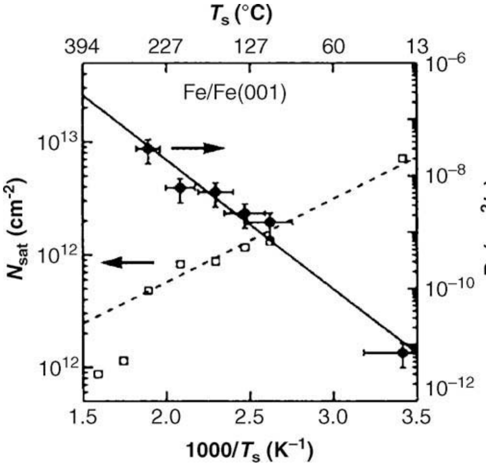

Figure 12.17: Temperature dependence of saturation Fe island densities N_{sat} (open squares) on Fe(001), obtained from direct STM measurements, and Fe adatom diffusion constants D_s (solid squares) obtained from rate equation analyses of N_{sat} vs T_s. The solid lines are least squares fits to the data at $T_s \leq 250\,°C$. (Adapted from [60].)

constants $D_s(T_s)$ are also plotted in Figure 12.17. Note that the open data points at $T_s > 250\,°C$ are well below the dashed line, corresponding to expected values for $N_{sat}(T_s)$, owing to the onset of significant island loss by coarsening (Ostwald ripening) [61].

Figure 12.18 shows representative in situ STM images of 2D single-atom-high islands of a two-component system, TiN, grown on TiN(001) substrates with atomically flat average terrace widths $L \sim 600$ Å, by reactive magnetron sputtering from a Ti target in purified N_2 at $P = 3$ mtorr [62]. The experiments were carried out in a multichamber UHV system at temperatures T_s of (a) 510, (b) 600, and (c) 800 °C using a Ti flux $J_{Ti} = 1.6 \times 10^{14}$ cm^{-2} s^{-1}. The TiN islands, corresponding to coverages $\theta_{TiN} = 0.5 \pm 0.06$ ML, are dendritic since at these relatively low temperatures ($T_s/T_m = 0.22$, 0.25, and 0.30), adatom kinetic energies are too low to overcome the binding energy at island steps and edge diffusion is small compared to terrace diffusion. Nevertheless, the islands, which are in the saturation coverage regime, still exhibit the local four-fold symmetry expected for NaCl cubic structures. Increasing T_s to 890 °C results in the formation of square 2D TiN(001) islands, bounded by side and corner facets, as shown in Figure 12.19 [63].

The number densities of the TiN(001) islands shown in Figure 12.18 are described as a function of deposition conditions by Eq. (12.17),

$$\begin{aligned} N_{sat} &= 0.2[4JN_s/\nu_s]^{i^*/(i^*+2)}\exp[(E_b + i^*E_s)/(i^*+2)kT_s] \text{ or} \\ L_n &\propto (\nu_s/J)^{i^*/(2i^*+4)}\exp[-(E_b + i^*E_s)/(2i^*+4)kT_s] \end{aligned} \qquad (12.18)$$

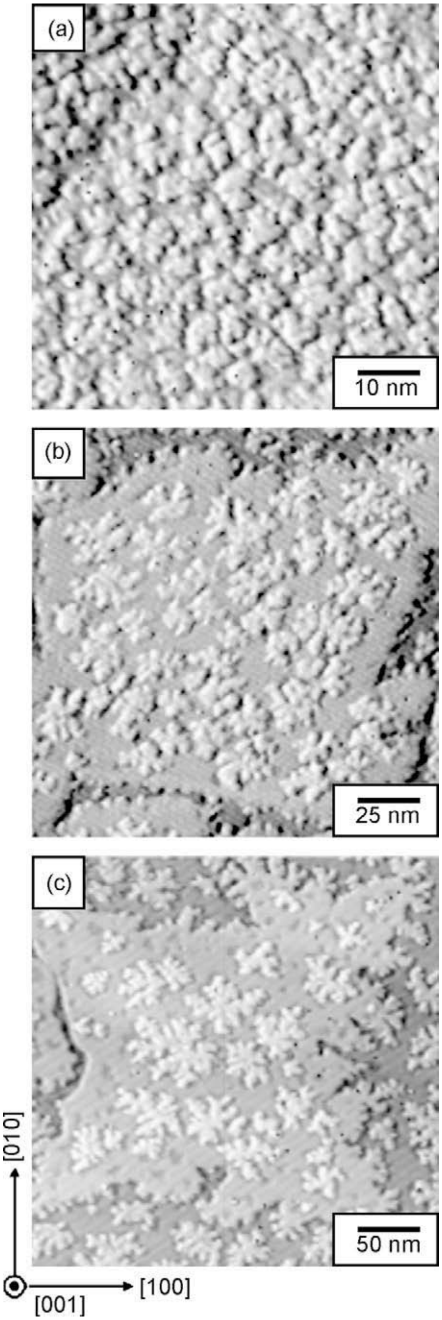

Figure 12.18: In situ STM image of 0.50 ± 0.06 ML TiN layers deposited at temperatures T_s with $J_{Ti} = 1.6 \times 10^{14}\ cm^{-2}\ s^{-1}$ on atomically flat TiN(001) terraces. T_s and image sizes are: (a) 510 °C and 700 × 700 Å^2, (b) 600 °C and 1700 × 1700 Å^2, and (c) 800 °C and 2000 × 2000 Å^2. (From [62].)

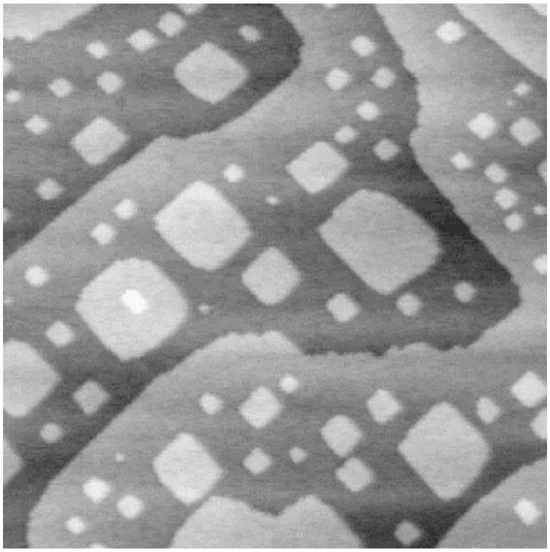

Figure 12.19: STM images of a 0.15 ML TiN layer deposited at $T_s = 850\,°C$ on atomically flat TiN(001) terraces. Image size: 1200 × 1450 Å^2. (From [63].)

where L_n is the nucleation length. L_n values were determined experimentally by in situ high-temperature STM and the results are plotted vs T_s in Figure 12.20. The total areas over which L_n was measured include > 150 islands at each temperature; the upper limit for T_s is 800 °C in order to avoid L_n approaching the average terrace width. Over this temperature range, $i^* = 1$ and Eq. (12.18) becomes

$$L_n \propto [(\nu_s/J)\exp(-E_s/kT_s)]^{1/6} \tag{12.19}$$

From the T_s-dependent L_n data shown in Figure 12.20, a least squares fit using Eq. (12.19) yields a surface diffusion activation energy $E_s = 1.4 \pm 0.1$ eV with a prefactor $\nu_s = 10^{13\pm1}\ s^{-1}$.

As a parallel approach to extracting the characteristic length for homoepitaxial nucleation on TiN(001), the characteristic island size R_c necessary to nucleate a second layer was also measured as a function of T_s. Karr et al. [64] and Kodambaka et al. [63, 65] have shown that TiN(001) has a relatively small Ehrlich barrier for adspecies diffusing over step edges. In this case, R_c can be extracted from measurements of the fraction f of islands of size R which exhibit second layer nucleation using an analytical relationship developed by Tersoff et al. [66], in which

$$f = \{1 - \exp[-(R/R_c)^8]\} \tag{12.20}$$

R_c is primarily dependent on the smallest island dimension since adatom diffusion is isotropic on a square lattice. Figure 12.21 shows a second layer island with an inscribed ellipse

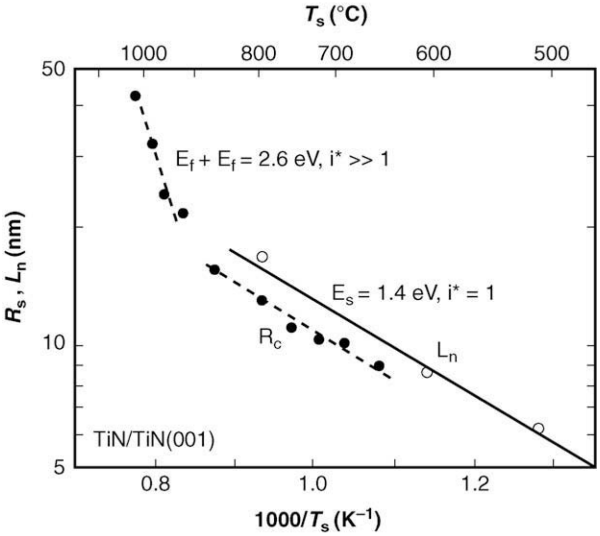

Figure 12.20: The solid data points (dashed lines) correspond to the characteristic TiN(001) island sizes R_c required for nucleation of an upper layer and the open data points (solid line) are the measured nucleation lengths L_n on large open terraces as a function of the deposition temperature T_s. (From [62].)

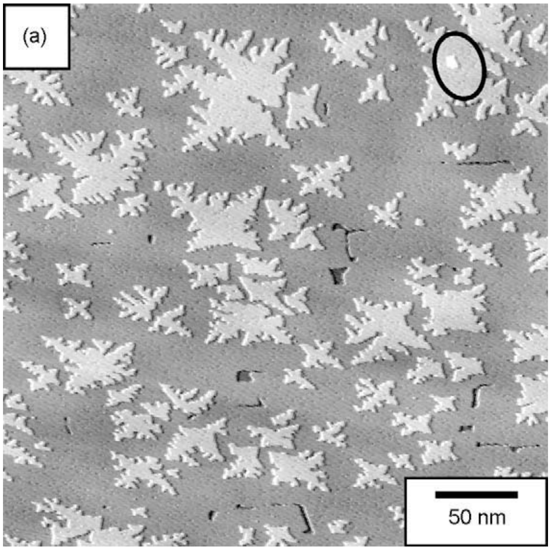

Figure 12.21: STM image of an 80 Å thick TiN/TiN(001) layer grown at $T_s = 920\,°C$ with $J_{Ti} = 1.6 \times 10^{14}\ cm^{-2}\ s^{-1}$. A second layer island is inscribed with an ellipse. Image size: $3400 \times 3400\ Å^2$. (From [62].)

representing island size R defined as one-half the minor axis of the largest ellipse which fits though the rough edges of the first layer island. Both R and $f(R)$ were measured for >100 islands at each growth temperature and R_c determined from Eq. (12.20). R_c results are plotted in Figure 12.20 as a function of T_s over the range from 650 to 1010 °C. The increase in the slope at $T_s > 865$ °C is due to an increase in the size of the smallest stable cluster, as discussed below.

In the low temperature regime for which $i^* = 1$, the characteristic island size R_c is given by [62]

$$R_c = \left(\frac{192}{\pi}\right)^{1/6} \left[\frac{\nu}{JN_s} \exp\left(\frac{-E_s}{kT_s}\right)\right]^{1/6} \tag{12.21}$$

A least squares fit of the $R_c(T_s)$ data in Figure 12.20 between 650 and 865 °C yields $E_s = 1.4 \pm 0.1$ eV with $\nu_s = 10^{13\pm1}$ s^{-1} for nucleation on growing islands, in agreement with the above results for nucleation on open terraces.

Identifying the diffusing species is fundamental to understanding atomic processes occurring during nucleation. For TiN(001), there are several possible candidates including Ti, N, and TiN_x ($x = 1, 2, 3, \ldots$) admolecules. Using *ab initio* density functional theory (DFT), the calculated Ti surface diffusion activation energy on TiN(001), 0.35 eV, is found to be a factor of four smaller than the E_s value measured by experiment [62]. Petrov et al. [67] showed that there is a significant flux of atomic N (including N_2^+ ions which dissociate upon collision) incident at the growing film surface during reactive magnetron sputter deposition of Ti in pure N_2. DFT results reveal that as N atoms diffuse and encounter each other on TiN(001), N_2 forms with a binding energy of 2.1 eV, but with an adsorption energy of only 0.2 eV with respect to gas-phase N_2. Thus, N_2 desorbs at near kinetic rates. Moreover, the calculated N diffusion barrier is 0.95 eV, significantly smaller than the $E_s = 1.4$ eV value obtained experimentally. The authors therefore conclude, consistent with additional DFT calculations, that TiN_x ($x = 1, 2, 3$) admolecules are the primary diffusing species rather than Ti or N adatoms. TiN_4 is unstable and dissociates to TiN_2 admolecules and N_2. Under high N supply rate conditions, as in these experiments, TiN_2 and/or TiN_3 are expected to be the primary diffusing species, while a reduction in the N supply increases the coverage of Ti and TiN adspecies at the expense of TiN_2 and TiN_3 leading to a change in nucleation kinetics, as demonstrated below, by decreasing the N_2 partial pressure in an Ar/N_2 mixture.

The results in Figure 12.20 reveal a dramatic increase in the rate of change in R_c vs T_s at $T_s > 865$ °C. This could be due to either a change in the nature of the primary diffusing species or a change in the critical cluster size. Assuming that i^* remains constant, the E_s value extracted from Figure 12.20 in the high T_s regime is 8.4 eV, larger than all TiN_x admolecule adsorption energies and therefore not physically reasonable. Thus, i^* must increase over the T_s range between 865 and 945 °C. For $T_s > 945\,°\mathrm{C}$, the linear relationship between $\ln(R_c)$ and $1/T_s$ is well fitted with $i^* \gg 1$ for which R_c is given by

$$R_c = 2\left[\frac{v}{JN_s}\left(\frac{-(E_s + E_c)}{kT_s}\right)\right]^{1/2} \tag{12.22}$$

where the cluster formation energy $E_c = E_b/i^*$. A least squares fit to the $945 \leq T_s \leq 1010\,°\mathrm{C}$ data in Figure 12.20 results in $(E_s + E_c) = 2.6 \pm 0.2$ eV with $\nu = 10^{13\pm1}$ s^{-1}. Assuming that the primary diffusing species remains constant over the temperature range of these experiments (i.e. $E_s = 1.4$ eV), $E_c = 1.2$ eV.

Wall et al. [68] tested the above conclusions concerning the rate controlling diffusing species during nucleation and early film growth of homoepitaxial TiN(001) by reducing the N_2 fraction in N_2/Ar mixtures while maintaining the total pressure and the total Ti flux constant at $P = 3$ mtorr and $J_{Ti} = 1.6 \times 10^{14}$ cm^{-2} s^{-1}, respectively. Typical R_c vs T_s results, fitted using Eq. (12.21), are shown in Figure 12.22. The smallest stable cluster size remains a dimer, but E_s decreases substantially from 1.4 eV with $f_{N2} = 1$ to 1.1 eV with $f_{N2} = 0.1$. The frequency prefactor ν is $10^{13\pm1}$ s^{-1} in both cases. Decreasing f_{N2} results in a factor of two increase in R_c due to lower steady-state N coverages favoring TiN_x adspecies with lower x values and, hence, higher surface diffusivities for the same TiN coverages θ_{TiN}.

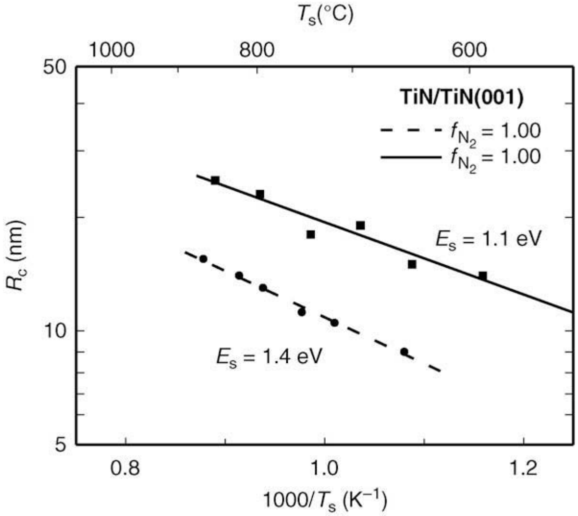

Figure 12.22: The characteristic TiN island size R_c required for nucleation of an upper layer during TiN(001) homoepitaxial growth ($J_{Ti} = 1.6 \times 10^{14}$ cm^{-2} s^{-1}) on TiN(001) as a function of the deposition temperature T_s in mixed Ar/N_2 atmospheres with N_2 gas fractions $f_{N2} = 0.10$ (■) and 1.00 (●). E_s is the surface diffusion barrier extracted from Eq. (12.21). (Adapted from [68].)

12.4.2 Two-Dimensional Island Coalescence

Continuing with the TiN results discussed above: at higher partial monolayer coverages, significant island coalescence is observed on TiN(001) as well as TiN(111) surfaces. Figure 12.23 shows typical in situ high-temperature STM images, from one of a large number of video files (200–400 images per movie acquired at a constant rate of 44 s/frame), of equilibrium-shaped TiN island coalescence and relaxation on both orientations [69]. In these experiments, the layers were grown by reactive evaporation in UHV. The upper panels correspond to TiN(001) island coalescence during annealing under N_2 overpressure at $T_a = 850\,°C$, while the lower panels correspond to truncated hexagonal TiN(111) islands at $T_a = 873\,°C$.

The square TiN(001) islands initiate coalescence at polar <100> corner facets which, from quantitative island coarsening and shape fluctuation analyses as a function of step orientation, are known to have high step energies and low stiffnesses [61, 63, 65]. The edge energy released upon contact results in rapid edge diffusion, driven by the system attempting to minimize total edge length, leading to the formation of a figure-eight-shaped island which relaxes to its equilibrium shape in ~ 840 s. The TiN(111) islands in the lower panel are truncated hexagons owing to the anisotropy in alternating <110> 2D island facets in which S_1 steps form <110>/{100} nanofacets with the TiN(111) substrate while S_2 steps form

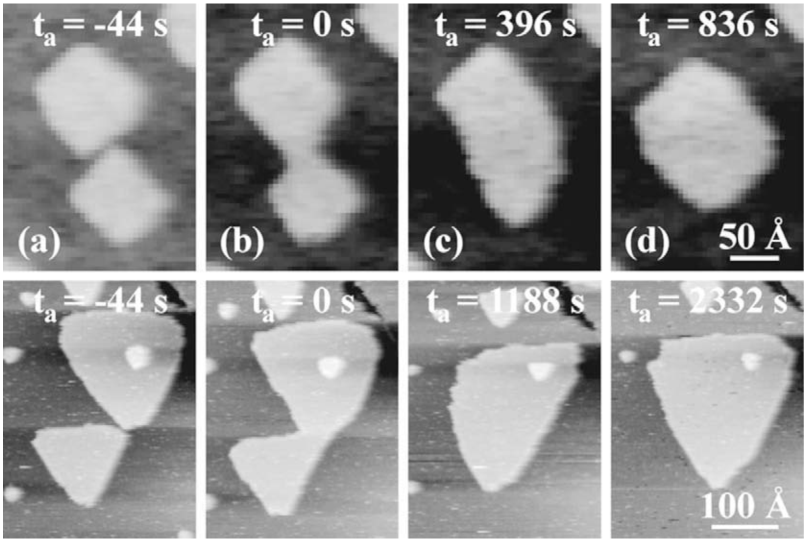

Figure 12.23: (a)–(d): Representative STM images, acquired at 44 s/frame, showing coalescence and subsequent reshaping of 2D TiN adatom islands during annealing in N_2. Upper panel: TiN(001), $T_a = 850\,°C$, scan size = 220 × 320 Å^2; lower panel: TiN(111), $T_a = 873\,°C$, scan size = 290 × 330 Å^2. (From [69].)

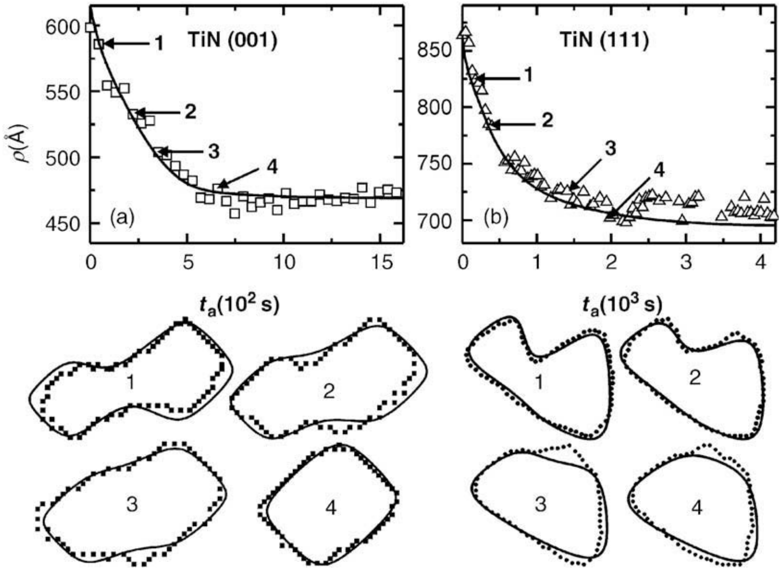

Figure 12.24: Upper panels: island perimeter ρ plotted as a function of annealing time t_a for the (a) TiN(001) and (b) TiN(111) adatom islands shown in Figure 12.23. Lower panels: time-dependent shapes of the islands labeled 1, 2, 3, and 4 in the upper panels. Symbols are experimental data while solid lines are calculated curves obtained using Eq. (12.23). (From [69].)

<110>/{110} nanofacets; the ratio of step energy densities (line tensions) is $\beta_2/\beta_1 = 1.40$ [70–72]. The TiN(111) islands initiate coalescence at corner <110> steps resulting in a sawtooth-shape island which relaxes to its equilibrium shape in ~2330 s.

Experimentally determined values for the total island perimeters $\rho(t_a)$ are plotted in Figure 12.24(a, b) as a function of time ($t_a = 0$ is defined as the time at which the islands make contact) during relaxation of the TiN(001) and TiN(111) coalesced islands in Figure 12.23. In both cases, ρ decreases monotonically to a saturated value ρ_{eq} corresponding to the equilibrium island shape. Previous island coarsening and decay measurements showed that TiN islands on both 001 and 111 surfaces maintain their equilibrium shapes, with thermal fluctuations, at these temperatures [61, 63, 65, 70–72], indicating that adatom edge mobilities are higher than surface mobilities and attachment/detachment rates at island edges, as shown quantitatively below.

In a continuum model for 2D island shape evolution, the normal component v_n of the step edge velocity is related to the step chemical potential μ as [69]

$$v_n(\varphi, t) = \left(\frac{\Omega\sigma_{\text{edge}}}{kT}\right) \nabla_s^2 \mu(\varphi, t) \tag{12.23}$$

φ in Eq. (12.23) is the local step orientation, i.e. the angle of the local step normal, $\nabla_s = (x_s^2 + y_s^2)^{-1/2}\partial/\partial s$ in which x_s and y_s represent first spatial derivatives of island boundary coordinates $x(s, t)$ and $y(s, t)$ with respect to arc length element s along the island boundary, Ω is the unit TiN molecular area, and σ_{edge} is the edge-atom mobility. μ can be expressed in terms of the step curvature $\kappa(s, t)$ and the local-orientation-dependent step stiffness $\tilde{\beta}(\varphi)$ as

$$\mu(\varphi, t) = \tilde{\beta}(\varphi)\kappa(s, t)\Omega \tag{12.24}$$

Using measured $\tilde{\beta}(\varphi)$ values from [63] and [65] (TiN(001)) and [70] and [71] (TiN(111)), calculated shapes for the islands in Figure 12.23 are shown in the lower panels of Figure 12.24 superimposed on the STM images. Calculated and measured total TiN(001) and TiN(111) island perimeters ρ, plotted in the upper panels of Figure 12.24, are in good agreement. From these results, extracted edge mobilities are $\sigma_{edge}^{001} = 22 \pm 3.6$ Å/s at 850 °C and $\sigma_{edge}^{111} = 36 \pm 7.6$ Å/s at 873 °C. The corresponding rates for diffusion- and detachment-limited island decay on 001 and 111 terraces are $\sigma_{diff}^{001} \sim 4.9\times10^{-2}$ Å/s and $\sigma_{det}^{111} \sim 7.8\times10^{-2}$ Å/s, respectively, at the same temperatures, significantly lower than the σ_{edge} values. Thus, edge diffusion is the energetically favored mechanism for mass transport on both TiN(001) and TiN(111) surfaces under these conditions.

12.5 Stranski–Krastanow Nucleation and Growth

As noted in Section 12.2, the elastic strain energy during heteroepitaxial growth varies as $E_{elas} \propto \varepsilon^2 h$, with $\varepsilon = (a_f - a_s)/a_s$. Thus, for a given film/substrate system (i.e. a given lattice parameter misfit ε), E_{elas} increases linearly with film thickness h. It has been known for more than a half century that highly strained films can partially relax via the punch-through of misfit dislocations. Matthews and Blakeslee [73] predicted in the early 1970s, based on thermodynamic arguments, that the critical film thickness h_d for obtaining dislocations in heteroepitaxial systems is:

$$h_d = \frac{\bar{b}(1 - \nu_f\cos^2\beta)\ell n(4h_d/\bar{b})}{8\pi\varepsilon(1 + \nu_f)\cos\lambda} \tag{12.25}$$

where $\bar{b}$ is the dislocation Burgers' vector, ν_f is the Poisson ratio of the film, β is the angle between $\bar{b}$ and the dislocation line vector, and λ is the angle between the slip direction and the line in the film/substrate interfacial plane which is normal to the line of intersection between the slip plane and the interface. For growth on 001-oriented diamond and zincblende structure semiconductors, the primary slip planes are {111} with the dislocation line and Burgers' vectors along <110> such that $\beta = \lambda = 60°$ and $\cos\beta = \cos\lambda = 0.5$. The agreement between the predictions of Eq. (12.25) and measurements from well-annealed films is quite good; however, as-deposited layers often have critical thicknesses much higher than the thermodynamic predictions of the Matthews–Blakeslee model, depending on the growth temperature and deposition rate, due to kinetic constraints. That is, there is a relatively high activation energy for nucleating misfit dislocations [74].

A competing relaxation mechanism to dislocation formation, multiplication, and glide is strain-induced roughening or S-K growth. In Section 12.4, it was shown, based on a consideration of surface energy terms in Eq. (12.9), that 2D growth is energetically favorable when $a_2 r^2 \gamma_{\mathrm{s-v}} \geq a_1 r^2 \gamma_{\mathrm{f-v}} + a_2 r^2 \gamma_{\mathrm{s-f}}$. This is a trivial thermodynamic statement for homoepitaxy in a clean environment. For heteroepitaxial growth, the equation predicts that lower surface tension films will grow in a 2D mode with smooth surfaces on higher surface tension substrates, assuming relatively low interfacial energies (e.g. Ge/Si(001), InSb/GaAs(001), Ag/Mo(001), $YBa_2Cu_3O_{7-\delta}$/$SrTiO_3$(001), etc.). However, such an analysis neglects another important thermodynamic factor, the elastic energy E_{elas}. Including this term, the equation becomes $a_2 r^2 \gamma_{\mathrm{s-v}} \geq a_1 r^2 \gamma_{\mathrm{f-v}} + a_2 r^2 \gamma_{\mathrm{s-f}} + \mathrm{E}_{\mathrm{elas}}$. Thus, for a given normalized lattice parameter mismatch between the film and substrate, even if the difference in surface tensions favors 2D growth, the strain energy cost begins to dominate above a critical film thickness $h_{\mathrm{S-K}}$ leading to a transition from initially 2D to 3D growth as originally predicted by Stranski and Krastanow [16]. That is, the decrease in system strain energy associated with island dilatational relaxation becomes larger than the energy cost to produce new surface area (see Figure 12.2).

Strain-induced roughening is favored over dislocation formation by higher film/substrate lattice-parameter mismatch and higher growth temperatures [75, 76]. The requirement for relatively high T_s/T_m values to activate strain-induced roughening derives from kinetic limitations to uphill diffusion (i.e. overcoming the step edge and formation energies) as discussed in the following sections. Tersoff and LeGoues [74] showed that the activation energy for strain-induced roughening decreases rapidly with increasing misfit strain ε, varying as ε^{-4}. In contrast, the activation energy for dislocation nucleation and multiplication varies much more slowly with layer strain, yielding an ε^{-1} dependence.

12.5.1 S-K Mechanism and Examples

A simple elastic stability analysis illustrates the basic physics, as well as the mechanism, of the S-K 2D to 3D transition. The results show that a flat surface under stress is unstable with respect to the development of surface roughening with wavelengths λ greater than a critical value λ_c [18, 19].

Consider the growth of an additional monolayer of material B on one or more pseudomorphic monolayers of B deposited on substrate material A, where $a_B > a_A$. Two limiting cases are

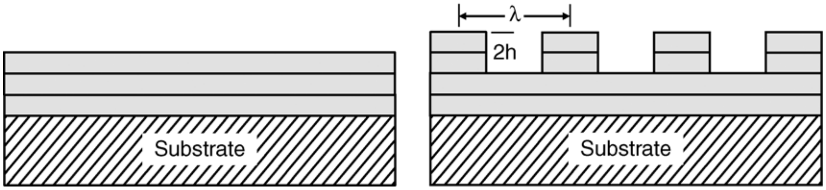

Figure 12.25: Schematic illustrations of two limiting cases in the deposition of an additional B layer on a stack of pseudomorphic B layers on substrate A for which $a_B > a_A$. Left figure: the upper B layer grows pseudomorphically. Right figure: the upper B layer forms an islanded square-wave of amplitude 2*h* and wavelength λ.

illustrated schematically in Figure 12.25. In the first case, the film continues to grow coherently at the expense of an increase in the system elastic energy per unit volume $E_{\text{elas, V}}$. In the second case, the film breaks up into islands separated by λ at the expense of increasing the total surface energy per unit area γ_B. To further simplify the problem, the surface morphology of the rough 'one-dimensional' (actually, 1 + 1 D) film is a square wave of peak-to-peak amplitude $2h$ and it is assumed that the roughening transition completely relaxes the strain associated with deposition of the upper layer (in reality, strain-induced roughening generally relaxes only a fraction of the strain).

The difference in total strain energy over one wavelength λ in the two limiting cases is

$$\Delta E = -E_{\text{elas},V} h\lambda + 2_{\gamma \text{B}}(2h) \tag{12.26}$$

The elastic energy per unit volume in (1 + 1) dimensions is given by $E_{\text{elas, V}} = Y_B \varepsilon^2/2$, in which Y_B is the Young's modulus of material B. Substituting $E_{\text{elas, V}}$ into Eq. (12.26) and setting $\Delta E = 0$ yields a critical roughening wavelength $\lambda_c = 8\gamma_B/Y_B\varepsilon^2$. Thus, the system will spontaneously roughen (island) in the presence of surface morphological perturbations with wavelengths greater than

$$\lambda_c > 8\gamma_B/Y_B\varepsilon^2 \tag{12.27}$$

As λ becomes larger than λ_c, the cost in additional system surface energy, $4\gamma_B h$ (which is not a function of λ), to form 3D islands is less than the increase in elastic strain energy, $E_{\text{elas,V}} h\lambda$, associated with the growth of an additional 2D commensurate layer. Conversely, if $\lambda < \lambda_c$, the increase in surface energy is much larger than the small decrease in elastic strain energy (λ is too small) and the surface roughening perturbation dissolves.

Note that in three dimensions, the S-K transition is just another stability problem, similar to the thermodynamic formulation of cluster nucleation in Section 12.2. The energy cost to form an S-K island is proportional to its surface area (i.e. $\propto r^2$), while the energy cost to deposit an additional coherent 2D layer is proportional to its volume (i.e. $\propto r^3$). Thus, there is a critical S-K island size r^* and a corresponding activation barrier ΔG^*. Strain relaxation due to S-K island formation must overcome the increase in surface energy to allow continued island growth.

An example of a system exhibiting S-K behavior is the growth of the tetragonal-structure low-melting point ($T_m = 156.6\,°C$) metal In on Si(001)2×1 [20, 77]. This material system has a very large lattice parameter misfit, -40% tensile ($a_{In} = 3.2523$ Å with $c_{In}/a_{In} = 1.52$, and $a_{Si} = 4.5309$ Å). The surface phase diagram for In/Si(001)2×1 is shown in Figure 12.26(a). For $T_s < 150\,°C$, In is a 2D gas (i.e. no significant adatom–adatom interactions) on Si(001) at coverages θ_{In} up to 0.1 ML, above which 2D In(2×2) islands nucleate and grow. The (2×2) phase is complete at $\theta_{In} = 0.5$ ML and further MBE In deposition leads to the layer-by-layer growth of a psuedomorphic epitaxial In(2×1) phase. At In coverages slightly larger than 3 ML (some supersaturation is required), 3D faceted polyhedral In islands nucleate and grow along <011> directions orthogonal to the underlying two-domain (2×1) dimer rows.

The in situ Auger electron spectroscopy (AES) results in Figure 12.26(b) exemplify the characteristic signature of a 2D to 3D S-K transition. For In deposition at $T_s = 70\,°C$, the intensity I_{Si} of the Si 92 eV $LM_{2,3}M_{2,3}$ peak decreases linearly with θ_{In} in successive straight line segments of length 1 ML, in agreement with theoretical predictions for 2D layer-by-layer growth, up to $\theta_{In} \sim 3$ ML, above which I_{Si} remains approximately constant as In evolves to a 3D island growth mode which attenuates the Si AES signal very slowly with increasing In

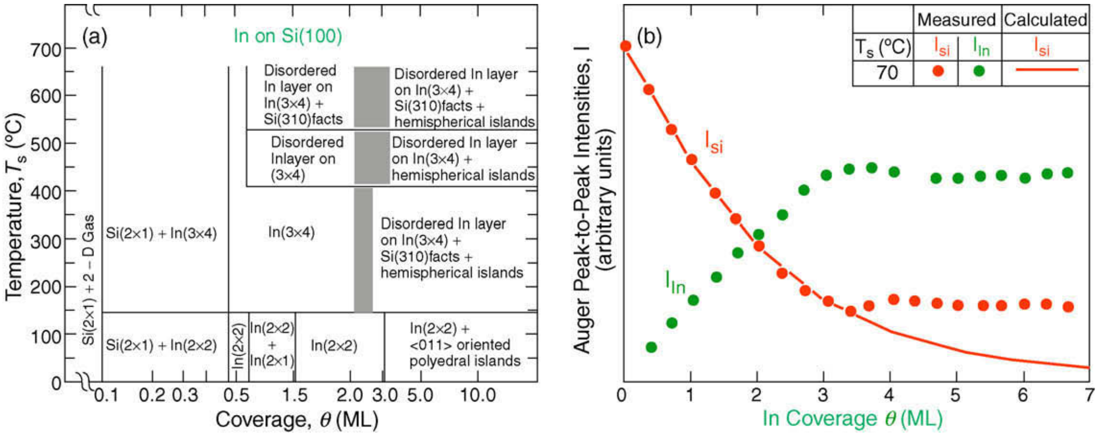

Figure 12.26: (a) Surface phase diagram for In on Si(001)2×1; (b) peak-to-peak intensities *I* of differentiated Si 92 eV $LM_{2,3}M_{2,3}$ and In 404 eV $MN_{4,5}N_{4,5}$ Auger lines as a function of In coverage θ_{In} on Si(001) at 70 °C. A calculated I_{Si} curve, assuming 2D In growth, is also shown. (Adapted from [20].)

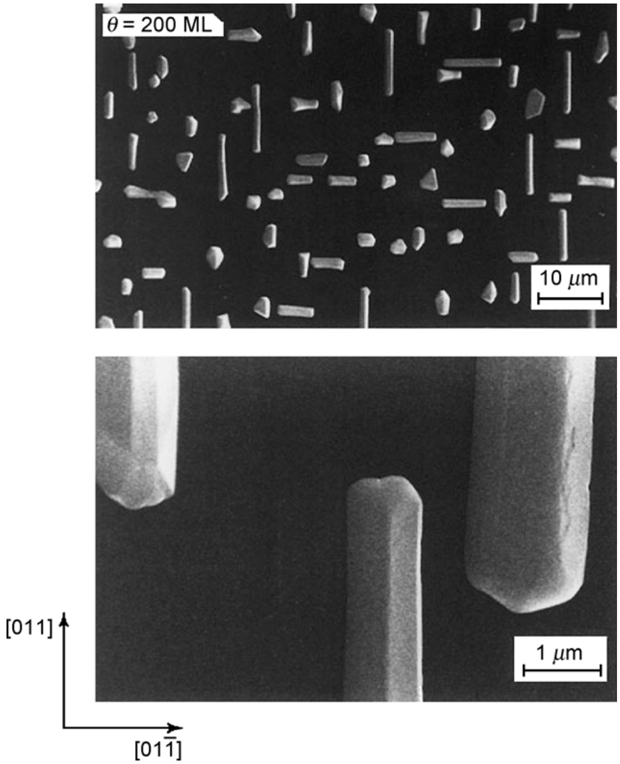

Figure 12.27: Scanning electron micrographs of polyhedral In islands on Si(001)2×1-In. The In layer was deposited by MBE with $J_{\mathrm{In}} = 1.1 \times 10^{13}\ \mathrm{cm}^{-2}\ \mathrm{s}^{-1}$ (0.016 ML/s) at $T_s = 70\,^{\circ}\mathrm{C}$ to a coverage $\theta_{\mathrm{In}} = 200$ ML. The In islands are elongated along [011] and [01$\underline{1}$] directions and the black background is the In wetting layer. (Adapted from [20].)

coverages. TPD measurements show that the In desorption energy E_d decreases from 2.8 eV in the 2D gas phase to 2.45 eV, approximately equal to the bulk In heat of vaporization, from 3D In islands [77]. AES results also reveal that the S-K transition occurs at much lower coverages, ~ 0.5 ML, at $T_s = 300\,^{\circ}\mathrm{C}$. A decrease in the transition layer thickness with increasing T_s is typical of S-K systems.

Figure 12.27 shows scanning electron micrographs of In/Si(001) after deposition of an equivalent thickness corresponding to 200 ML [20]. The black region is the pseudomorphic, ~ 3 ML thick, In wetting layer which has the Si substrate in-plane lattice parameter as demonstrated by a combination of low-energy electron diffraction (LEED) and AES measurements. The elongated In islands above the wetting layer are of the order 8–10 μm long by 1–1.5 μm wide and cover only $\sim 7\%$ of the substrate area. Thus, they are extremely tall, indicating a very large difference in surface tension between bulk In and the pseudomorphic

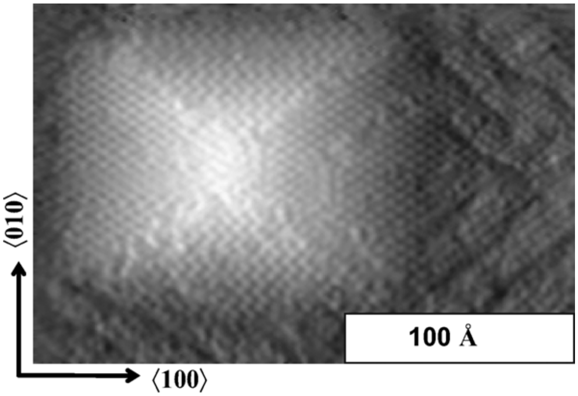

Figure 12.28: In situ STM image of a Ge {105}-faceted 'hut' pyramid, bounded by <100> edges, grown by GS-MBE from Ge_2H_6 on Si(001)2×1 at $T_s = 650\,°C$ with $R = 0.03$ ML/s to a coverage $\theta_{Ge} = 4$ ML. (From [22].)

In(2×1) wetting layer. Mapping the orthogonal <011> directions of the 3D In islands provides the layout of the underlying Si(001)2×1 terraces.

The archetypal system for S-K research, owing to the potential importance of quantum dot (QD) electronics, is Ge/Si(001). A crude estimate of λ_c for Ge on Si can be obtained by substituting bulk properties into Eq. (12.27) ($\gamma_{Ge} = 0.085$ eV-Å^2, $Y_{Ge} = 0.644$ eV-Å^3 [103 GPa], and $\varepsilon = 0.042$). This yields $\lambda_c \geq 660$ Å which, based on atomic force microscopy (AFM) and STM results, is of the correct order of magnitude [76, 78].

Comprehensive in situ STM investigations of Ge/Si(001) (with a lattice parameter mismatch of 4.2% compressive, $a_{Si} = 5.4309$ Å and $a_{Ge} = 5.6575$ Å) over more than 10 years have shown that while the simple model presented above captures much of the physics driving the S-K transition, the details are far richer and more complex. The wetting layer thickness in this system, as for In/Si(001), is ~3 ML. Figure 12.28 is an in situ image of a Ge QD grown on Si(001) at $T_s = 650\,°C$ to $\theta_{Ge} = 4$ ML by gas-source MBE (GS-MBE) using Ge_2H_6 with R = 0.03 ML/s. The Ge QD is pyramidal in shape, with <100> edges, faces composed of {105} facets, and a height-to-width aspect ratio $h/d = 0.1$. This highly perfect QD image raises some interesting questions. Why is the pyramid bounded by shallow {105} facets, 11.3° to the (001) substrate surface? The {105} facets are not low-energy planes in the diamond structure. Moreover, in the absence of other constraints, maximum strain relaxation would favor much steeper inclinations to allow more dilation and, hence, increased strain relaxation. Thus, there must be an opposing reaction to result in such a shallow angle. Another question is: how does the pyramid grow with a constant shape?

The underlying reason for the shallow {105} facets, and the explanation for why the pyramid aspect ratio remains constant during growth, was first provided by Jesson et al. [79]. The facet

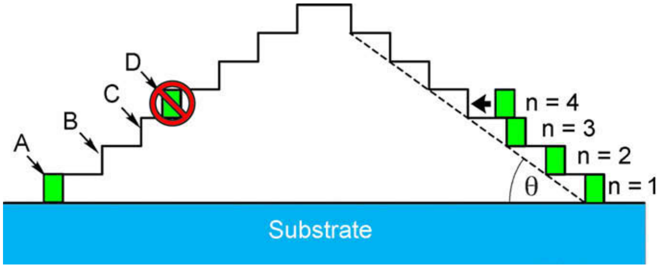

Figure 12.29: A schematic cross-sectional illustration of the growth of {105} faceted Ge pyramids on Si(001)2×1. (Adapted from [79].)

angle is limited to 11.3° owing to repulsive step–step interactions arising primarily from elastic monopole and electronic dipole interactions associated with step edge relaxation (the 1D equivalent of 2D surface relaxation) [80, 81]. The Ge {105} facet plane corresponds to steps that are 1.4 Å high and 7 Å wide. Increasing the facet angle reduces the step width and is therefore energetically unfavorable. Layer growth on {105} facets is illustrated in Figure 12.29 [79]. An atom stochastically deposited on step D, for example, decreases the step width and, thus, increases the system energy due to step–step repulsion, thereby causing the adatom to move downward in a cascade process to step A. This then allows the addition of another atom on step B. Continuing in this fashion results in *directed* self-organized facet-by-facet pyramid growth with a constant aspect ratio.

The size distribution of $Si_{1-x}Ge_x$ QDs on Si(001) depends on layer composition x through the lattice parameter misfit strain ε and the deposition conditions (T_s, R, and θ_{SiGe}). However, the distribution is far smaller than would be expected purely on the basis of random nucleation and growth of islands. This is due to the presence of a self-limiting mechanism associated with the formation of {105} faceted $Si_{1-x}Ge_x$ pyramids which causes the growth rate of larger pyramids to be less than that of smaller ones and, hence, decreases the pyramid size distribution. Thus, pyramids nucleated earlier are not necessarily larger than those nucleated later, as demonstrated in Figure 12.30 showing frames from an STM video file obtained during solid-source MBE Ge deposition on Si(001) at 300 °C with $R = 0.001$ ML/s [82]. The same pyramids in subsequent frames are labeled with the same number. Note that the Ge coverages listed here correspond to the excess Ge deposited *above* the nominal 3 ML thick wetting layer. With increasing size, the pyramid growth rate slows. However, since the Ge flux remains constant, the 'excess' Ge adatoms give rise to higher terrace supersaturations and, hence, additional pyramid nucleation. The latter effect offsets some of the decrease in size distribution due to size-dependent self-limited growth.

The change in system free energy ΔG due to pyramid formation on a wetting layer is:

$$\Delta G \propto C_f(\gamma_f - \gamma_w)A_f - C_{elas}\varepsilon^2 V \tag{12.28}$$

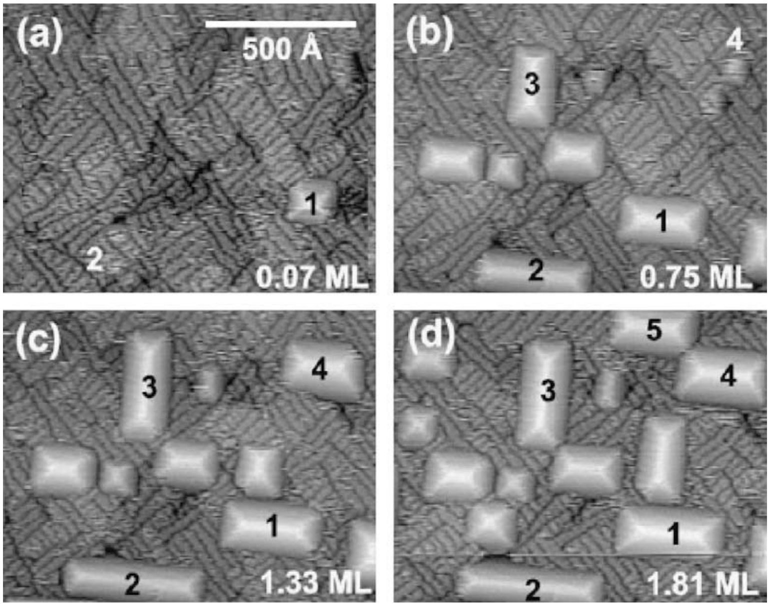

Figure 12.30: In situ STM images of MBE-grown Ge pyramids as a function of coverage (above the wetting layer) on Si(001)2×1. Image size = 1000 × 1000 Å^2, T_s = 300 °C, and R = 0.001 ML/s). (From [82].)

C_f and C_{elas} contain geometric factors and elastic constants, respectively; γ_f and γ_w are the Ge facet and wetting layer surface energies per unit area; and A_f and V are the facet area and pyramid volume. The first term in the above equation is the additional surface energy required to form a {105} facet, while the second term corresponds to the elastic strain energy released.

It is extremely rare to observe a partially filled {105} facet. This suggests that the completion of a new facet involves kinetically-activated nucleation followed by rapid growth of a critically sized nucleus. As noted above, the arbitrary inclusion of an adatom on an upper pyramid step is energetically very costly owing to step–step repulsion. It is much more favorable to grow the facet from the pyramid base upwards. (In addition, for small pyramids, most Ge adatoms approach from the surrounding wetting layer rather than directly from the vapor). This is equivalent to the nucleation and growth of a 2D island (here a {105} facet) as illustrated below.

Consider a rectangular island of height h on a {105} facet of base length s consisting of n steps (Figure 12.31). Initially, the energy cost to grow the island increases owing to a stress concentration at the base of the island. However, for sufficiently large facet coverage (i.e. above a critical nucleus size h*), the elastic energy released by pyramid dilation dominates and

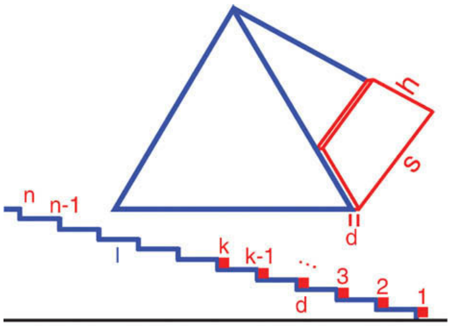

Figure 12.31: Upper figure: schematic illustration of the nucleation of a new {105} facet with length *s* and height *h* on a Ge pyramid grown on Si(001). Lower figure: schematic cross-section of a facet consisting of individual steps. A partly covered facet is completed up to the *k*th step. (Adapted from [79].)

the facet will be completed very rapidly (note also that the step length $s(k)$ decreases with k). Thus, there is a large activation barrier ΔG^*. Estimates of ΔG^* as a function of s and ε have been carried out using kinetic calculations incorporating step formation energy, facet surface energy, and elastic and dipole step–step interaction energies [83].

The strain energy per unit interface area associated with the deposition of one monolayer of Ge on Si(001) can be estimated using the classical equation $E_{\mathrm{elas}} = 2\,\mu_{\mathrm{f}}(1+\nu_{\mathrm{f}})\varepsilon^2 h_{\mathrm{f}}/(1-\nu_{\mathrm{f}})$ which assumes growth of a cubic structure material in the [001] direction and that the strain ε is within the Hooke's law limit [17]. The terms μ_{f} and ν_{f} are the shear modulus and Poisson ratio of the film. Inserting (bulk) Ge values for μ_{f} and ν_{f}, $E_{\mathrm{elas}} \sim 0.021$ eV/atom $= 1.4 \times 10^{13}$ eV-cm^{-2} $= 0.16$ GPa. Thus, it should not be surprising that relaxation of the large interfacial strain associated with the growth of Ge/Si(001)2×1 manifests itself long before the observation of QD formation above the 3 ML-thick wetting layer.

At Ge coverages $\theta_{\mathrm{Ge}} < 1$ ML, the surface (2×1) reconstruction evolves to (2×N) via the formation of dimer vacancy lines (DVLs) orthogonal to the 2×1 dimer rows, in which N is the average number of dimers separating DVLs. In situ STM measurements of MBE Ge layers grown at 300 °C with $R = 0.05$ ML/s show that the (2×N) periodicity decreases from $N \sim 17$ at $\theta_{\mathrm{Ge}} = 0.8$ ML toward $N = 8$, limited by trench–trench repulsion, at 2 ML [21]. The strain is reduced, at the cost of the trench formation energy, as Ge atoms adjacent to the trenches relax outwards into the trench. At θ_{Ge} greater than ~2 ML, dimer row vacancies (DRVs) form along the rows to further decrease the strain and the (2×N) reconstruction becomes (M×N) in an orthogonal quasi-periodic grid pattern. M is the DRV width, the number of vacant dimer rows. A few representative DVLs and DRVs are labeled in Figure 12.32, an in situ STM image of a 2.8 ML thick Ge/Si(001)2×1 film deposited by GS-MBE from Ge_2H_2 at $T_{\mathrm{s}} = 650$ °C (well above the H_2 desorption temperature) with $R = 0.03$ ML/s [22]. DVLs and DRVs are also visible in the wetting layer in Figures 12.28 and 12.30.

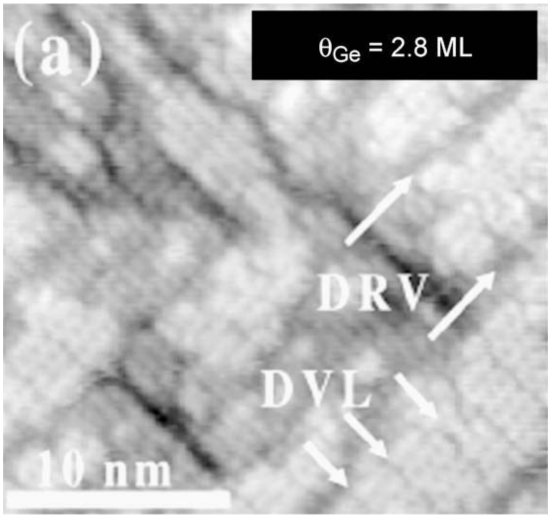

Figure 12.32: In situ STM image of a Ge(001)M×N layer grown on Si(001)2×1 by GS-MBE from Ge_2H_6 at $T_s = 650\,°C$ with $R = 0.03$ ML/s to a coverage $\theta_{Ge} = 2.8$ ML. A few representative dimer vacancy lines (DVLs) and dimer row vacancies (DRVs) are highlighted by arrows. (Adapted from [22].)

12.6 Structural Evolution of Polycrystalline Films at the Nanoscale and Microscale

Polycrystalline thin films have found diverse applications ranging from metallization and dielectric layers to optical, magnetic, and tribological coatings, to diffusion and thermal barriers, to catalytic and bioactive layers. The films exhibit a wide variety of microstructures characterized in terms of grain size and crystallographic orientation, lattice defects, phase composition, and surface morphology.

Atomic scale control of thin film microstructure during kinetically-limited low-temperature deposition, crucial for a broad range of industrial applications, has been a leading goal of materials science during the past few decades. Industrial demands for ever lower processing temperatures in device and product manufacturing mean that films are often deposited at $T_s/T_m \leq 0.2$–0.3. Thus, film synthesis takes place far from thermodynamic equilibrium. As a consequence, grain shape and orientation often evolve in a competitive fashion and the kinetic limitations induced by low-temperature growth allow for the controlled synthesis of metastable phases and artificial structures such as multilayers and self-organized nanocomposites.

Among the determinant atomic processes controlling structure evolution during film growth are surface and bulk diffusion. In addition to T_s, energetic particle bombardment can be used to enhance adatom mobilities and manipulate nucleation rates. The presence of alloying or impurity elements and their segregation to surfaces and grain boundaries also strongly influences the final result.

Extensive studies of the correlation between polycrystalline film structure and deposition parameters have been carried out over the past five decades. From an understanding of film formation follows the possibility for structural engineering at the microscale and nanoscale in order to design materials for specific technological applications. This spawned the development and refinement of structure zone models (SZMs) which systematically categorize self-organized structural evolution during film growth as a function of film growth parameters [84–90]. The history of SZMs has been reviewed by Thornton [91], Barna and Adamik [92], and Mahieu et al. [93]. In 1969, Movchan and Demchishin [84] observed that the microstructural evolution of evaporated Ti, Ni, W, ZrO_2, and Al_2O_3 coatings can be systematically represented by a single SZM diagram plotted as a function of film thickness h and the homologous growth temperature T_s/T_m.

The first SZMs were based on relatively low-resolution optical and scanning electron microscopy observations. Later, cross-sectional transmission electron microscopy (XTEM), STM, and AFM were employed to provide more detailed structural characterization, and in situ analyses began to reveal the rich dynamics of film growth. This, together with computational materials science, has provided atomistic insights into microstructural evolution during polycrystalline film growth. The use of amorphous substrates is beneficial for isolating the effects of individual deposition variables on texture development. Polycrystalline substrates bias texture through local pseudomorphic epitaxy. Nevertheless, the overall microstructure will still evolve toward a final state driven by the extant deposition conditions. It is important to note, however, that if surface diffusion rates are significant, once the substrate is covered, film growth will still proceed via local epitaxy on individual grains, even with amorphous substrates.

12.6.1 Elemental Polycrystalline Films and Structure-Zone Models

The nucleation barrier for low-temperature deposition on amorphous substrates is generally quite small, leading to randomly oriented islands [94, 95]. This has been demonstrated in a wide variety of materials. Early in situ TEM investigations included Au/SiO_2 [96, 97] and In/a-C [55, 98]. During island coalescence, there is a strong driving force for coarsening through surface atom diffusion and grain boundary motion. Islands with lower energy per atom E_b consume their neighbor(s) during coalescence and this process can result in large single-crystal islands as the system attempts to minimize the overall surface and interface energy. Thus, coarsening during coalescence is the first and most active phenomenon leading to selection of preferred orientation [99–101]. Absenting other kinetic constraints (see following sections), islands with the densest atomic planes are typically selected: (111) for fcc, (0002) for hcp, and (110) for bcc.

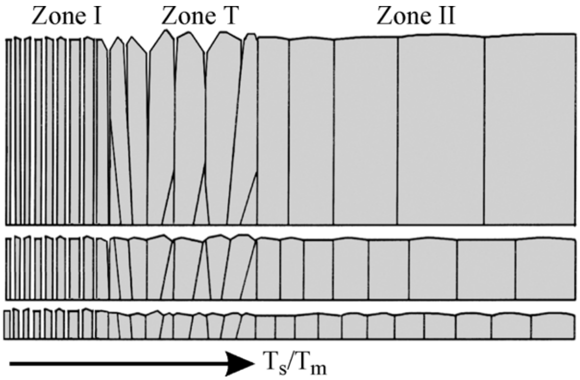

Figure 12.33: SZM schematically representing microstructural evolution of pure elemental films as a function of the reduced temperature T_s/T_m, where T_s is the deposition temperature and T_m is the melting point of the material, both expressed in K. (From [8].)

Depending on T_s/T_m and island size (due to melting point depression for nanoscale clusters) [56], coarsening can be very fast, often termed liquid-like coalescence, occurring either by rapid surface diffusion or by melting upon contact followed by crystallization. The driving force is the release of edge and surface energy. Rapid coalescence also results in new open substrate area for secondary nucleation, as shown in the in situ TEM image sequence (Figure 12.15) obtained during coalescence of In/a-C. At lower temperatures or larger island sizes, coarsening is slower and proceeds through grain boundary migration. Grain coarsening during coalescence of the contacting crystals is repeated until the local grain size becomes sufficiently large that grain boundary mobility is low on the timescale of coalescence.

The SZM in Figure 12.33, characterizing microstructure evolution in pure elemental films, consists of three regions [8]: zone I corresponds to very low deposition temperatures for which adatom diffusion is negligible; surface diffusion becomes significant in the transition zone T; and zone II represents film growth at deposition temperatures for which both surface and bulk diffusion are operative. The boundaries between zones are diffuse and transitions occur gradually over wide ranges in T_s/T_m.

During film growth in the low-T_s zone I regime (Figure 12.33), an underdense structure with a fine fiber texture is formed. Initial in-plane grain sizes are set by the saturation nucleation density N_{sat}. Adatom mobilities are low and columns preserve the random orientation of the nuclei as predicted by ballistic deposition models [102, 103]. The columns are generally not single grains, but composed of smaller more equiaxed grains, or completely amorphous. Surface roughness, which develops owing to atomic shadowing and limited surface diffusion, leads to extensive porosity. The wide angular distribution of the incident flux during sputter deposition, especially at pressures corresponding to non-ballistic transport, exacerbates these effects.

At higher film growth temperatures (zone *T*), grain coarsening occurs during coalescence of small islands with large surface to volume ratios, while grain boundaries are immobile in continuous films. Orientation selection during coarsening is incomplete, thus crystallites are nearly random or only weakly textured, and there is a wide distribution of initial grain sizes. The orientation and size of individual crystallites determine their behavior during subsequent growth processes characterized by competition among neighboring grains. In this T_s/T_m range, adatom surface diffusion is significant, resulting in local epitaxial growth taking place on individual grains. Pronounced columnar structure develops in which the columns are actually elongated grains.

The primary features of zone *T* competitive grain growth are illustrated by the kinetic Monte Carlo simulations of Gilmer et al. [104, 105] for sputter-deposited Al growth as shown in Figure 12.34(a). While there are initially equal distributions of 111 and 001 islands, the latter orientation eventually dominates, even though 111 is the low-energy surface, owing to anisotropies in surface diffusivities and adatom potential energies. That is, the average adatom residence time is significantly higher at lattice sites on low diffusivity (low potential energy) 001 surfaces versus high diffusivity (high potential energy) 111 surfaces. Therefore, during the

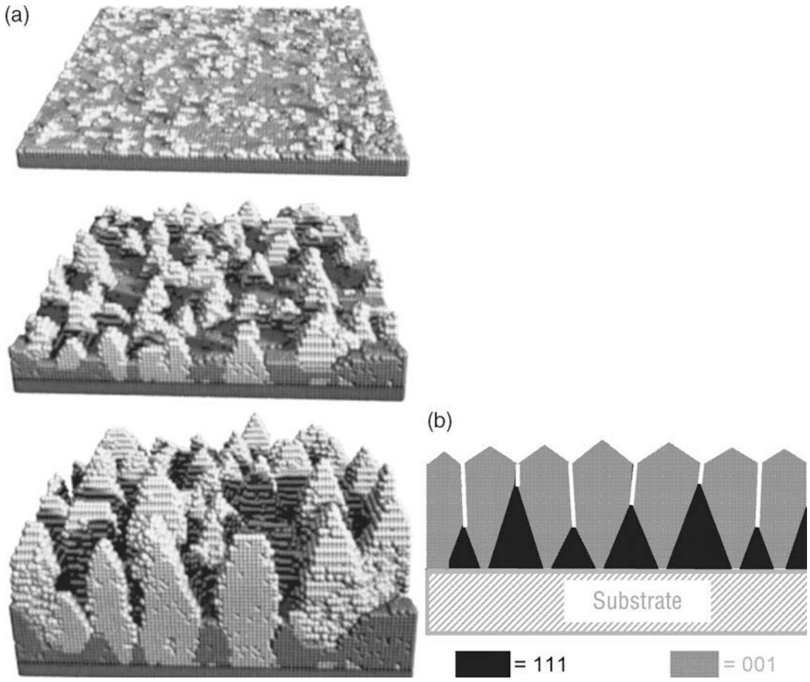

Figure 12.34: (a) Kinetic Monte Carlo simulation of competitive texture evolution during low-temperature sputter deposition of an Al film. Islands (and later columns) with lighter contrast are 001 oriented, while darker islands/columns are 111 oriented (from [104, 105]). (b) Schematic cross-section.

early stages, 111 islands tend to expand more two-dimensionally and thus fill more surface area (see upper panel in Figure 12.34a), while 001 grains favor more 3D growth. Following coalescence, however, adatoms which are stochastically deposited near grain boundaries and, through surface diffusion, can sample sites on both sides of the boundary, have a higher probability of becoming incorporated at the low-diffusivity surface which provides more stable, lower potential energy sites. Conversely, adatoms on high diffusivity planes have longer mean free paths with correspondingly higher probabilities to move off the plane and become trapped on adjacent grains. Thus, 001 grains become favored. Atomic shadowing enhances the difference, as protruding surfaces capture more off-normal flux. Thus, the low-diffusivity 001 grains slowly expand, overgrow the high-diffusivity grains, and become bounded by 111 facets. This leads to considerable surface roughness which scales with the average in-plane grain size.

The consequence of competitive growth is a continuous change in morphology, texture, and surface topography (hence, film properties) as a function of film thickness. Near the substrate, the microstructure consists of randomly oriented small grains, out of which V-shaped columns (Figure 12.34b) with favored orientations slowly emerge and overgrow kinetically disadvantaged columns. This gives rise to preferred orientation. The faceted column tops result, as noted above, in surface roughness which increases with thickness resulting in open column boundaries due to atomic shadowing.

At still higher T_s/T_m (zone II), bulk diffusion becomes significant. Grain boundary migration takes place not only during coalescence, but throughout the film growth process. Orientation selection during the coalescence stage is more pronounced and is driven by a decrease in the total grain boundary area as well as minimization of interface and surface energy [99]. Large grains with low surface and interface energy grow at the expense of smaller or unfavorably oriented grains. Normal grain growth is impeded if the grains have a strong texture, i.e. if the orientation selection was completed during coalescence, or the mean in-plane grain diameter reaches several times the film thickness [106]. Secondary recrystallization, also called abnormal grain growth, may follow in which the grain size distribution is transformed from monomodal, through bimodal, to a new monomodal distribution (unless grain growth is halted due to solute drag and/or grain boundary grooving) [106, 107] with much larger in-plane grain size. During secondary recrystallization, the degree of texture is further enhanced.

An example of grain boundary migration is shown in Figure 12.35, a series of STM topographs from a 300 Å thick polycrystalline Au film deposited by MBE on $SiO_2(0001)$ at room temperature with $R = 0.0028$ Å/s and then annealed using a very slow linear temperature ramp $dT_a/dt_a = 20\,^\circ\mathrm{C/h}$ [107]. X-ray diffraction (XRD) measurements of as-deposited samples reveal a 111 texture: approximately 84% of the grains are 111, ~16% 001, with no detectable 011 grains. The degree of 111 preferred orientation increases rapidly with annealing temperature.

The as-deposited polycrystalline Au film in the upper panel in Figure 12.35 has a highly irregular surface in which the roughness is controlled by grains with high-energy boundaries.

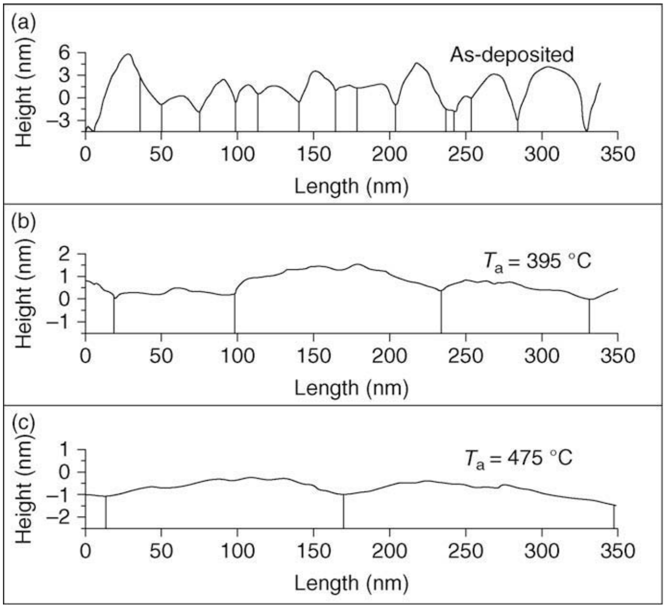

Figure 12.35: Typical STM topographical profiles from a 300 Å thick Au film deposited by MBE with $R = 0.0028$ Å/s on $SiO_2(0001)$ and subsequently annealed at 20 °C/h: (a) immediately after deposition, (b) at $T_a = 395$ °C, and (c) at $T_a = 475$ °C. Each dome is an individual grain. Vertical lines indicate the grain boundary locations. Note the different height scales. Individual steps and terraces are visible in panels (b) and (c). The topographs are from a video file obtained during annealing. (Adapted from [107].)

The grain boundary line tension γ_{gb} is related to the surface tension γ_s through the relationship

$$\gamma_{gb} = 2\gamma_s \cos(\varphi/2) \tag{12.29}$$

where φ is the dihedral angle as defined in Figure 12.36. Grains with high-energy boundaries have small dihedral angles, resulting in tall islands, and thus a rough surface. However, the

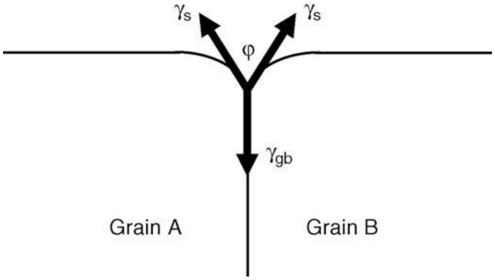

Figure 12.36: Schematic illustration of grain boundary grooving which occurs in order to minimize the total system energy. γ_{gb} is the grain boundary line tension, γ_s is the surface tension, and φ is the dihedral angle.

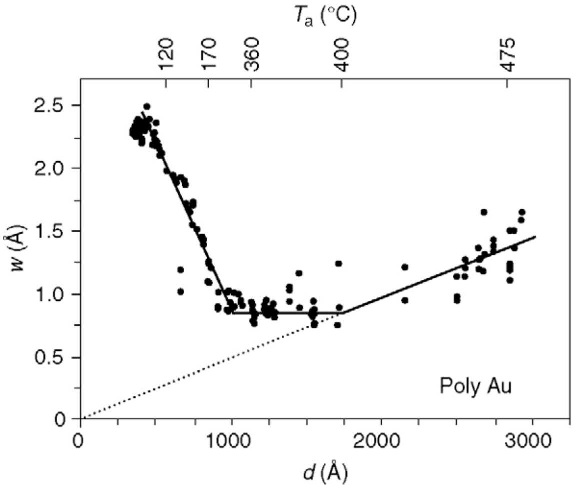

Figure 12.37: Surface roughness *w* of the polycrystalline Au film, corresponding to Figure 12.35, as a function of the average grain size *d* during annealing from room temperature to 475 °C at 20 °C/h. (Adapted from [107].)

high-energy grain boundaries tend to anneal out as T_a is increased and the remaining lower energy boundaries have larger φ values, yielding a smoother surface. This is illustrated in the in situ STM topographs Figures 12.36(b) ($T_a = 395$ °C) and 12.36(c) ($T_a = 475$ °C). Over the entire range of temperatures, surface adatom diffusion is sufficiently fast to maintain the surface shape at (or very close to) equilibrium with the evolving grain boundary configuration, as demonstrated by the fact that only very small shape changes are observed if the thermal ramp is halted and T_a maintained constant.

Figure 12.37 shows that the surface roughness *w* decreases by a factor of ~3× over the temperature range from 20 °C to ~325 °C, remains approximately constant with T_a until ~400 °C, and then increases again at higher T_a. Over the full annealing range, 20–475 °C, the average grain size d increases by an order of magnitude and XRD results show that the film texture transforms to essentially complete 111. In the first region, over which *w* decreases rapidly and *d* increases, the high-energy grain boundaries become mobile as T_a is increased and quickly reorient themselves in lower energy configurations (corresponding to cusps in the orientation vs grain boundary energy diagram). Thus, the average grain boundary energy decreases giving rise to an increase in the average dihedral angle φ (Eq. 12.29), and therefore a corresponding decrease in *w* from ~23 Å to 8 Å while *d* increases from ~300 Å to 1000 Å.

As T_a is raised further, the lower-energy grain boundaries also become mobile resulting in a continued gradual coarsening of the grain boundary network. This mechanism, by itself, has no significant effect on the average dihedral angle φ since the average grain boundary energy γ_{gb} remains constant. However, as a given grain diameter increases, the height variation across the grain also increases due to a self-similar scaling behavior. Over the intermediate regime in

Figure 12.37, as d increases from ~ 1000 Å to 1750 Å, the surface roughness w remains essentially constant owing to the competition between grain boundary reorientation (and texture development) which decreases w, and the growth of grains with low-angle boundaries which increases w. The third regime ($T_a \sim 400$–$475\,^\circ$C) is dominated by the continued growth of highly textured grains with low-energy boundaries as d increases from ~ 1750 Å to 3000 Å causing the average surface roughness w to increase from ~ 8 Å to 15 Å. The maximum grain size at the highest temperature, $T_a = 475\,^\circ$C, is ~ 3000 Å, a factor of 10× larger than the Au film thickness. Prolonged annealing at 475 °C had no further significant effect on d.

The grain growth history just described occurred through a combination of 'normal' and 'abnormal' mechanisms. During primary or normal grain growth, the grain size distribution remains monomodal as individual grain boundaries move toward their centers of curvature in order to reduce boundary curvature, total boundary length, and, thus, the total grain boundary energy. That is, grains larger than the average size grow, while smaller grains shrink. In columnar grain systems, grains with five or fewer sides tend to shrink, while those with seven or more sides grow [108]. Secondary (or abnormal) grain growth results initially in a bimodal grain size distribution which, if allowed to proceed to completion, leads again to a monomodal distribution, but with a lower density of larger grains. Driving forces for abnormal grain growth include local epitaxy [109], anisotropic surface and/or interfacial energies [110], anisotropic strain [111], and/or kinetic competition [112–114]. For example, since surface energy is strongly dependent on crystallographic orientation, those grains with orientations that lead to low surface energies have an energetic advantage during growth. In the polycrystalline Au film experiments, the entire grain distribution moved toward a complete 111 texture.

12.6.2 Multicomponent and Multiphase Film Growth

Polycrystalline thin films synthesized by reactive deposition provide additional pathways for microstructure control while yielding enhanced thermal and process stability. Here, the term reactive deposition encompasses the purposeful incorporation of dopants as well as unintentional atmospheric contaminants such as water vapor, oxygen, and hydrocarbons since even low concentrations of reactive elements (sometimes below the detection limits of modern analytical techniques) can have strong effects on microstructural development [92, 115, 116].

Consider the case of O-containing polycrystalline Al films deposited at room temperature, $T_s/T_m = 0.32$, corresponding to zone II in the pure Al SZM [117]. Changes in film structure and orientation as a function of increasing oxygen concentration, observed via in situ TEM investigations, are summarized in Figure 12.38 [8, 92]. Oxygen has low solubility in Al and segregates to surfaces and grain boundaries where it forms 2D oxide layers (oxide tissue phases) which greatly reduce Al adatom surface and grain-boundary mobilities. These layers modify all film formation processes, limiting grain coarsening during coalescence and film growth. They also periodically interrupt the local epitaxial growth of individual crystallites and

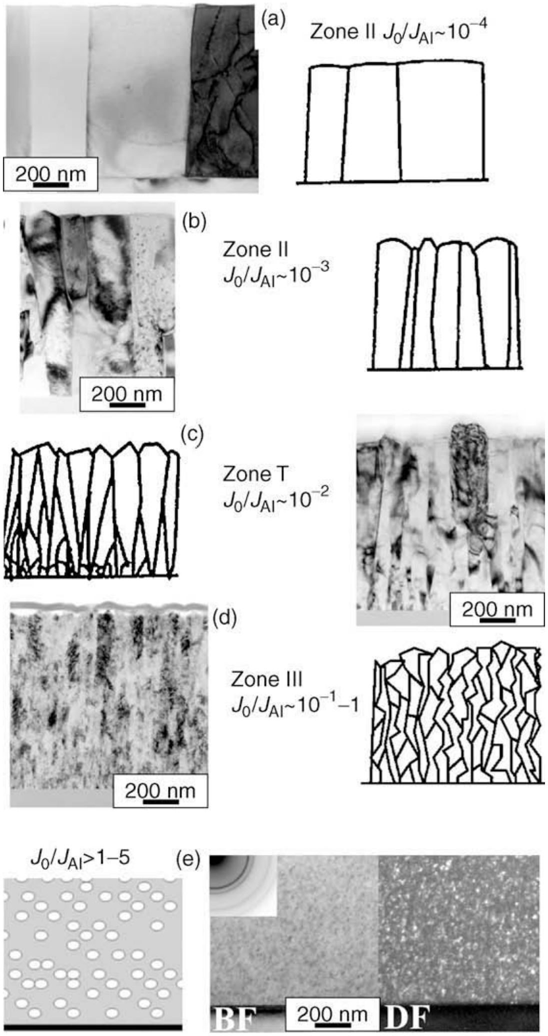

Figure 12.38: XTEM images, with corresponding schematic diagrams, showing the microstructure of Al films deposited by thermal evaporation on amorphous SiO_2 at room temperature as a function of the incident O to Al flux ratio J_O/J_{Al}. (From [8, 92].)

cause renucleation [55, 98]. By exploiting such phenomena, new microstructures and nanostructures can be controllably synthesized.

At low O/Al arrival rate ratios, $J_O/J_{Al} \sim 10^{-3}$, oxygen is incorporated into the grain boundaries and further accumulates during boundary migration, eventually inhibiting grain coarsening though solute drag. The resulting texture remains zone II with columns extending through the film, but with a lesser degree of preferred orientation and a smaller grain size, as shown in Figure 12.38(b).

With slightly higher oxygen concentration levels ($J_O/J_{Al} \sim 10^{-2}$), coarsening during coalescence is severely suppressed, resulting in grains with random orientation. The competitive growth which follows is governed by anisotropic crystallographic effects [118]: O segregates fastest at 111 surfaces. Oxygen is incorporated into the lattice of 001 and 110 crystal faces, while an oxide layer is formed on the 111 faces [119]. Oxygen tends to accumulate at step edges on 111 surfaces, blocking step motion and leading to step bunching. These pinning sites serve to nucleate the oxide phase. Neighboring 111 grains have rounded edges due to oxygen segregation while 111-oriented grains in contact with 001-facets remain sharp, as oxygen is incorporated in the latter. The 111 grains eventually develop rounded surfaces, indicating that local epitaxial Al growth has been interrupted by an oxide layer, above which renucleation of metal islands takes place. Crystal growth on 001-oriented grains is unimpeded by oxygen; these grains protrude above the average film surface and eventually win in competitive growth. They develop the shape of truncated octahedrons bounded by a 001 top face and 111 side faces. The degree of 001 preferred orientation increases with film thickness and is accompanied by greater surface roughness with increasing oxygen concentrations (Figure 12.38c).

At still higher oxygen concentrations ($J_O/J_{Al} \sim 0.1$–1), the oxide layer completely covers islands of all orientations at an early stage and coarsening during coalescence is blocked. Thus, film growth proceeds by repeated renucleation. The film is composed of 3D equiaxed (globular) grains with random orientation and a zone III structure (Figure 12.38d). With increasing oxygen concentration, the grain size decreases and can reach the nanometer range. An important byproduct of repeated nucleation and nanograin film formation is that surface faceting on individual columns, and the related shadowing effects, are eliminated. Thus, nanophase films are inherently much smoother and, as a result, denser. The presence of oxide phases also inhibits grain boundary migration in the bulk of the film, preventing grain coarsening and imparting higher thermal stability. This approach has been systematically exploited in order to synthesize superhard nanocomposite films based on transition metal (TM) nitrides and carbides, e.g. nc-TMN/a-Si_3N_4 [120, 121], nc-TMC/a-C [122], TiN_xB_y [123, 124], TiC_xB_y [125], and TMN/Cu [126], as well as supertough Y_2O_3-stabilized ZrO_2/Au layers [127].

As the oxygen concentration is further increased, ($J_O/J_{Al} \sim 2$–5), the role of the oxide and metal phases are reversed: the oxide phase nucleates first, while Al segregates to the surface and forms 3D islands [117, 128]. Resulting films are composed of metallic grains dispersed in an oxide matrix (Figure 12.38e) [129]. Such composite films, consisting of a low-diffusivity matrix with higher diffusivity metallic inclusions, are the basis of a class of ceramic–metallic coatings with diverse applications: resistors [130, 131], sensors [132], solar cell elements [133], low-friction hard coatings (e.g. TM/a-C) [134], and smart tribological coatings that adapt to the environment [135, 136].

At very high oxygen fluxes ($J_O/J_{Al} \gg 1$), the films consist entirely of aluminum oxide, which for room temperature growth is amorphous. T_s values exceeding 800 °C are required for the synthesis of the chemically and mechanically stable κ and α crystalline phases of alumina. There has, however, been a concerted effort to achieve hard crystalline alumina using ion-irradiation during growth at temperatures below 500 °C [137].

The addition of metallic elements, rather than gas-phase species, for multicomponent microstructural modification has been shown to both increase and decrease the average grain size depending on the choice of materials. For example, adding a few at.% Pt [138] or Cu [139] to Al leads, in contrast to tissue phase formation, to the nucleation of 3D islands of the minority phase(s) on the surface of the majority phase. Here, all adspecies have high surface mobilities. For the case of 350 Å thick Al + 4 at.%Pt layers co-evaporated onto a-C substrates at $T_s = 350$ °C, TEM imaging and diffraction analyses show that the minority phases are Al_5Pt and Al_6Pt. Equiaxed grains of the minority phase decorate grain boundaries and triple points, thus significantly decreasing grain boundary migration and grain coarsening [140].

The addition of Sn to Al has quite the opposite effect; rather than decreasing the grain size as with O and Pt, it acts to enhance grain growth. In a combinatorial materials science experiment, Barna and Adamik [92] deposited a 1000 Å thick Al(Sn) film on a-C at room temperature by co-evaporation using a geometry and relative deposition rates such that the Sn concentration in the film varied from near zero at the left edge of the field of view of a plan-view TEM image to 10 at.% at the right edge. At low Sn concentrations, the film is continuous with an average grain size of 30–50 Å, while at higher concentrations the film is still in the island growth stage with the grain size enhanced by a factor greater than 5×. Sn appears to be acting as a surfactant in increasing Al adatom surface mobility [141].

12.6.3 Ion Irradiation Effects

Films deposited at low temperatures with little or no ion irradiation tend, as noted in Section 12.6.1, to be columnar and underdense. Figure 12.39 is a typical XTEM image of such a structure; in this case, a TiN film grown by reactive magnetron sputtering in pure N_2, with $P_{N2} = 20$ mtorr, at $T_s = 350$ °C ($T_s/T_m = 0.17$) and $R = 0.75$ μm/h (2.1 Å/s) on amorphous SiO_2 with no applied substrate bias [142]. The film lattice constant was found by XRD to be equal to that of unstrained bulk TiN. Figure 12.39 shows that the film grain size, initially small, increases continuously with film thickness while the column boundaries become increasingly more open. The self-organized zone T (see Figure 12.33) columnar microstructure forms through random nucleation, limited coarsening during coalescence, and competitive column growth resulting in a microstructure consistent with that predicted by the kinetic Monte Carlo simulations and schematic diagram in Figure 12.34. The column tops are faceted owing to kinetic roughening, which, in combination with atomic shadowing, results in deep cusps

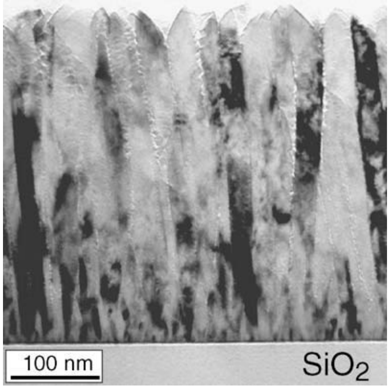

Figure 12.39: A bright-field XTEM micrograph of a TiN film deposited by magnetron sputtering in a pure N_2 atmosphere (20 mtorr) on amorphous SiO_2 at 350 °C. The ion-to-Ti flux ratio J_i/J_{Ti} incident at the growing film was < 1 with an ion energy $E_i = 20$ eV. (From [142].)

between columns and open column boundaries. The individual columns, however, are dense, indicating sufficient adatom surface mobility to sustain local crystal growth.

Many of the early applications of ion irradiation during film growth were designed to address issues arising from low-temperature deposition such as those apparent in Figure 12.39. The motivation was generally to increase film density and modify grain morphology (e.g. columnar to equiaxed) as well as to manipulate film texture. The experiments were carried out using plasma-based sputtering techniques by applying a negative bias to the substrate and later by using ion beam assisted deposition (IBAD) in which a secondary ion source is aimed at the substrate and growing film deposited by primary ion beam sputtering or evaporation. However, essentially all experiments employed what is today considered to be high-energy ion bombardment ($E_i > 100$ eV); that is, well above the bulk lattice atom displacement threshold, giving rise to significant residual ion-induced lattice damage. It was not until the development, in the late 1980s and early 1990s, of gridless Hall-current ion sources [143] for IBAD applications and tunable magnetically unbalanced magnetron sources [144] for plasma deposition, that the ability to independently vary ion currents (or, more importantly, ion/deposited-atom ratios J_i/J_{Me}) at the growing film over large values while using low-energy ions (typically ≤ 20 eV), that it became possible to control density, grain morphology, preferred orientation, surface smoothness, and film stress without the collateral introduction of detectable residual defects.

12.6.3.1 High Energy, Low Ion Flux

Mattox and Kominiak [145] were among the first to quantitatively demonstrate that the density of films grown under conditions leading to porous microstructures (e.g. low T_s and/or high pressures such as are typical of DC sputtering) can be increased by ion bombardment during

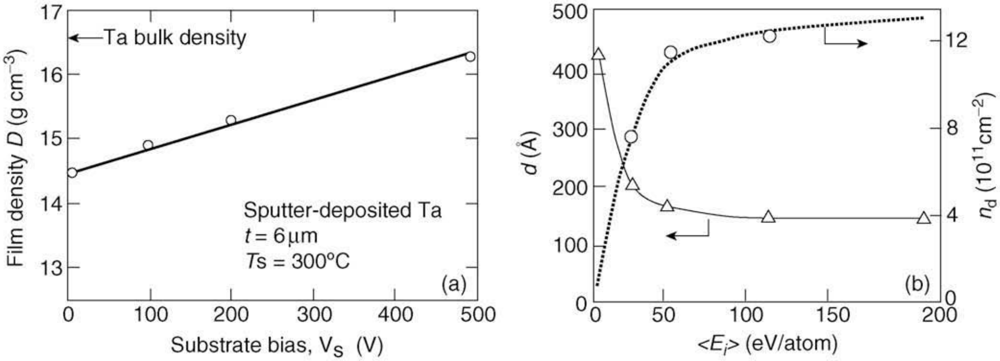

Figure 12.40: (a) Density, as a function of the negative substrate bias V_s, of 6-µm-thick Ta films deposited by dc sputtering in Ar (adapted from [145]). (b) Average grain size *d* and dislocation density n_d in Ag films deposited at room temperature as a function of the average normalized ion energy $<E_i>$ per deposited Ag atom. (Plotted from tabulated data in [146].)

deposition. The density of 6-µm-thick polycrystalline Ta films deposited at 300 °C ($T_s/T_m = 0.175$) by dc sputtering in Ar increased continuously with the applied negative substrate bias V_s from ~ 14.5 g cm^{-3} with $V_s = 0$ to 16.3 g cm^{-3} (bulk density = 16.6 g cm^{-3}) with $V_s = -500$ V, as shown in Figure 12.40(a).

Huang et al. [146] investigated the effect of Ar$^+$ bombardment during the growth of Ag films at room temperature using a UHV dual ion-beam apparatus. They observed that the void density decreased with increasing ion energy, consistent with the Ta dc sputtering result. However, they also found that the average grain size *d* decreased, from 420 to 145 Å, while the dislocation number density n_d increased from 7×10^{10} to 1.3×10^{12} cm^{-2}, as a function of the normalized ion irradiation energy $<E_i>$, defined as the total Ar$^+$ ion energy delivered to the film per deposited Ag atom. $<E_i>$ was varied from thermal (obtained by evaporation with no ion bombardment) to 190 eV/atom (see Figure 12.40b). In addition, the degree of 111 preferred orientation, determined by XRD, decreased and the plane stress reversed from 0.06 GPa tensile for underdense evaporated films to −0.45 GPa compressive with $<E_i> > 42$ eV/atom.

Densification via high-energy ion irradiation at the cost of residual defect production is clearly illustrated by the plan-view TEM micrographs in Figure 12.41 of polycrystalline $Ti_{0.5}Al_{0.5}N$ films deposited by reactive magnetron sputtering in mixed Ar/N$_2$ discharges with $P_{tot} = 8.2$ mtorr ($P_{N2} = 2.9$ mtorr) on stainless-steel substrates at ~ 450 °C ($T_s/T_m \sim 0.20$) with $J_i/J_{Me} \sim 0.9$ and $R = 0.2$ µm/minute (33.3 Å/s) [147]. The applied negative substrate bias V_s ranged from 0 to 250 V (corresponding to ion energies of ~ 6.5 to 255 eV when the plasma potential is included). XTEM images (not shown) reveal that films grown with $V_s = 0$ have a columnar microstructure with intercolumnar void networks similar to those in Figure 12.39. Film porosity decreases sharply with $V_s > 100$ eV until, with $V_s > 120$ V, no voids are observed

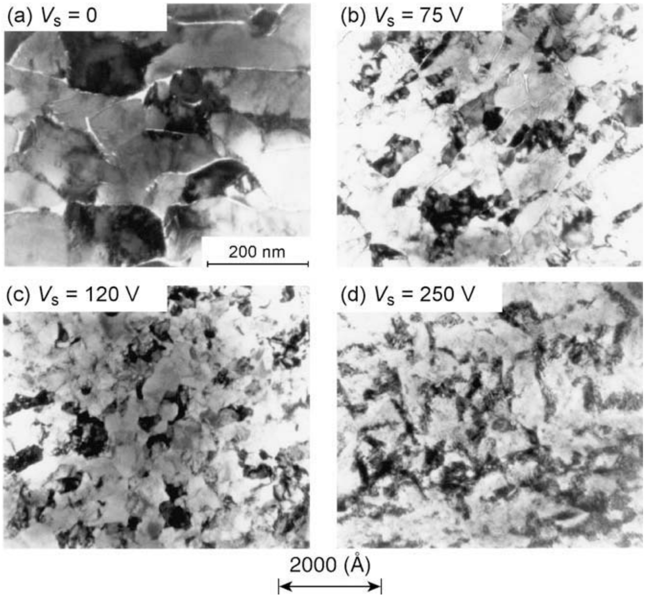

Figure 12.41: Transmission electron micrographs of polycrystalline $Ti_{0.5}Al_{0.5}N$ films deposited by reactive magnetron sputter deposition on stainless-steel substrates at $T_s \sim 450\,°C$ as a function of the applied negative substrate bias V_s with $J_i/J_{Me} \sim 0.9$. (a) $V_s = 0$; (b) 75 eV, (c) 120 eV, and (d) 250 eV. (From [147].)

using underfocus and overfocus contrast. However, the film compressive stress (owing to a combination of ion trapping and recoil implantation) increases and high dislocation loop densities are observed within individual grains in panels (b)–(d). In fact, the defect densities are large enough to disrupt column growth and force renucleation, as evidenced by the presence of Moiré fringes, leading to smaller grain sizes.

X-ray and electron diffraction patterns also reveal a very slow change in TiN preferred orientation from 111 to 002 with increasing E_i. However, the ion energy required to complete the transition is > 800 eV, for which the films have unacceptably high stress levels [148]. Thus, the use of high-energy, low-flux ion irradiation is not a practical approach for controlling film texture. The formation of 002 texture under such conditions is directly related to collision cascade effects [149]. Grains with open channel directions, such as 002, have higher survival probabilities due to the anisotropy in collision cascades; that is, the ion energy is distributed over larger depths in open channels leading to lower sputtering yields and less lattice distortion.

In summary, densification obtained in the high-energy ion irradiation regime ($E_i > 100$ eV) comes at a steep price, leading to high defect densities [150], high compressive stresses [151–153], and inert gas incorporation [148]. Ar concentrations C_{Ar} in TiN layers deposited on amorphous SiO_2 at 350 °C as a function of E_i, with $J_i/J_{Ti} \leq 1$, are below 0.5 at.% with

$E_i < 100$ eV, while at higher ion energies, C_{Ar} increases approximately linearly from 1 at.% at 200 eV to > 3 at.% at 800 eV.

12.6.3.2 Low Energy, High Ion Flux

Magnetron sputtering is a primary technique for the growth of polycrystalline thin films. It provides high deposition rates due to the Lorentz force, arising from the cross-product of the applied electric field used to accelerate the ions to the target and the permanent magnetic field, which traps the plasma immediately adjacent to the target and efficiently utilizes secondary electrons in the discharge to produce new ions. However, this very advantage becomes a disadvantage when attempting to use ion bombardment at the substrate for microstructural and compositional modification during film growth. The strong electromagnetic trap near the target means that the substrate and growing film are essentially outside the plasma; thus, a high substrate potential is required to obtain significant ion bombardment and, even then, the ion flux at the substrate is small. For typical magnetron discharges, depending on the target material, gas, pressure, and system geometry, ion/deposited-atom ratios at the substrate with $V_s = -100$ V are of the order $J_i/J_{Me} \sim 0.1$–0.5. This dramatically changed with the development of the tunable unbalanced magnetron which incorporates a Helmholtz coil external to the permanent magnets of the magnetron to unbalance the magnetic circuit and controllably open a leak in the plasma [144]. High ion/deposited-atom ratios, $J_i/J_{Me} > 50$, can be achieved using very low ion energies ($E_i < 10$–20 eV) with no significant change in film deposition rates. Moreover, the ion energy and ion flux incident at the substrate are independently controlled by V_s and the external magnetic field B_{ext}, respectively.

$E_i \leq 20$ eV is below the threshold for bulk lattice atom displacement in NaCl-structure TM nitrides. The residual stresses remain low in as-deposited films, yet the effects on texture and microstructure are dramatic. In some of the earliest experiments using unbalanced magnetrons [144, 154, 155], it was clearly demonstrated that the average ion bombardment energy per deposited atom $<E_i>$ is not a universal parameter for microstructural and texture modification as had been proposed by many authors. Figure 12.41 conclusively shows, for example, that changes in the stress state, stoichiometry, and texture of NaCl-structure polycrystalline $Ti_{0.5}Al_{0.5}N$ films deposited on a-SiO_2 follow completely different reaction paths depending on whether $<E_i>$ is varied by changing E_i (with a constant value of J_i/J_{Me}) or varying J_i/J_{Me} (with constant E_i) [154, 155]. Similar results have been reported for TiN [142], TaN [113], ScN [156], and many other materials.

The polycrystalline 1-μm-thick NaCl-structure $Ti_{0.5}Al_{0.5}N$ films used to obtain the experimental results summarized in Figure 12.42 were deposited by reactive magnetron sputtering from a TiAl alloy target on a-SiO_2 at 250 °C in pure N_2 discharges at 20 mtorr [155]. The relatively high pressures were chosen in order to thermalize the sputtered metal atoms and neutralized ions reflected from the target such that the only energetic species incident at the growing film were accelerated nitrogen ions (~96.5% N_2^+ and 3.5% N^+) [67]

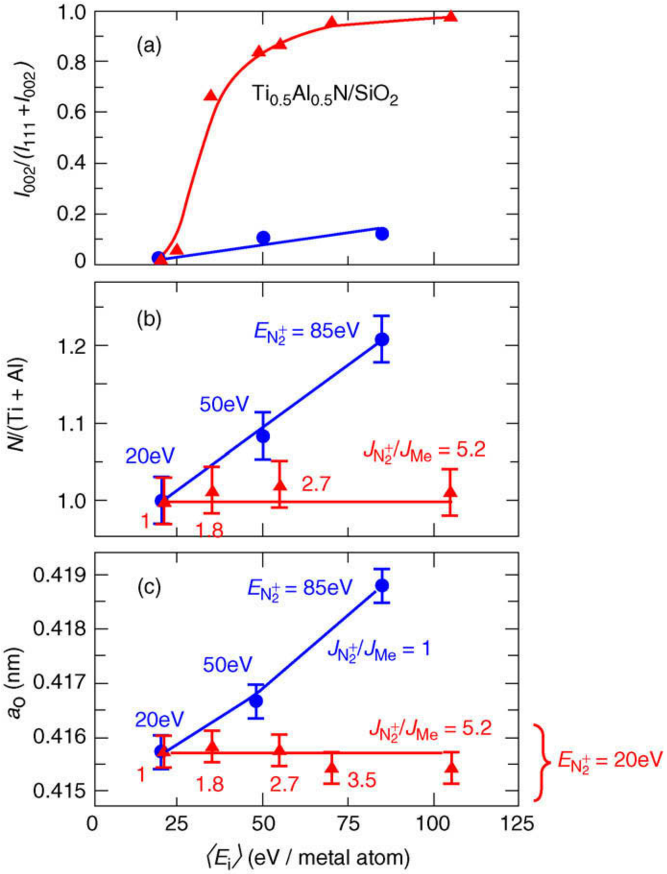

Figure 12.42: (a) Normalized X-ray diffraction peak intensities *I*; (b) composition ratios N/(Ti + Al); and (c) out-of-plane lattice parameters a_o from $Ti_{0.5}Al_{0.5}N$ alloys deposited on amorphous SiO_2 at 250 °C under N_2^+ ion irradiation as a function of the normalized energy $<E_i>$ per deposited metal atom varied through changes in either the ion energy E_i or the ion/metal flux ratio J_i/J_{Me}. (Adapted from [155].)

whose flux was controlled by varying B_{ext}. The results in Figure 12.42 show that raising $<E_i>$ through increases in E_i, with J_i/J_{Me} maintained constant at 1, increases the out-of-plane lattice constant a_o (panel c) and leads to trapping of excess N in the film (panel b). Both of these effects are signatures of a rapidly increasing compressive stress. TEM and XTEM analyses show that films grown with $E_i = 20$ eV (~ 10 eV per N following collisionally induced dissociation) and $J_i/J_{Me} = 1$ are underdense with both intercolumnar and intracolumnar porosity and an average column size $d = 300 \pm 150$ Å. Increasing E_i leads to densification and a reduction in column size to ~ 250 Å at 85 eV with a small increase in the volume fraction of 002 grains to ~ 15%. However, at $E_i = 100$ eV, the films are no longer single phase and instead consist of a TiN-rich columnar structure, with $d \sim 150$ Å, and wurtzite-structure AlN-rich precipitates of diameter ~ 30 Å. Thus, increasing the ion energy in order to achieve densification in low-temperature $Ti_{0.5}Al_{0.5}N$ films results in residual lattice defects which create compressive stress and, at $E_i > 85$ eV, phase separation.

In sharp contrast, maintaining E_i constant at 20 eV and increasing $<E_i>$ through increases in J_i/J_{Me} still leads to densification, but with no significant ion-induced stress, and the layers remain stoichiometric and singe phase. The column size distribution becomes more uniform with no measurable change in column size. An additional major benefit of this approach to coupling kinetic energy to the growing film during low-temperature deposition is shown in the upper panel of Figure 12.42. That is, the use of low-energy, variable ion flux irradiation allows film preferred orientation to be set at any value between 111 and essentially complete 002. This is important in many applications due to the anisotropic properties of TM nitrides. The mechanism for the change in texture, which involves a combination of ion-irradiation-induced surface chemistry, anisotropic adatom diffusion dynamics, and momentum transfer, is discussed in the following sub-section.

Ion-irradiation-induced surface smoothening

There are many polycrystalline thin film applications in which surface and interface smoothness is crucial to device operation. Examples include metal multilayer X-ray mirrors for semiconductor device lithography and giant magnetoresistance (GMR) devices such as non-volatile magnetic access memory and read head sensors in hard disk drives. The GMR effect derives from changes in electron-spin-dependent resistance across multilayer stacks, consisting of high-conductivity films sandwiched between ferromagnetic layers, owing to orientation switching of an external magnetic field. If the ferromagnetic layers have a roughness comparable in amplitude and wavelength to the spacer layer thickness, typically ~ 10–20 Å, it is difficult to reverse the magnetic field of the ferromagnetic layers because of Néel coupling. In addition, layer intermixing increases spin-independent scattering and loss of local magnetic alignment.

GMR multilayers are generally composed of material pairs with large miscibility gaps, and deposition is carried out at low temperatures, in order to minimize intermixing by thermal diffusion during deposition. The best GMR layers are synthesized using low-energy ion irradiation for reasons illustrated in Figure 12.43 showing molecular dynamics simulations, using embedded atom potentials, of two three-layer Cu/Co/Cu stacks. The experiments were designed to probe kinetic effects during the asymmetric growth of Cu/Co versus Co/Cu interfaces [157]. Both trilayer stacks were grown with thermal atoms (evaporation), but $E_i = 6$ eV Ar^+ ion irradiation with $J_i/J_{Me} = 5$ was added in panel (b). (Note that E_i is of the same order as the average energy of ballistic sputtered atoms, 5–10 eV, incident at the film growth surface during magnetron sputter deposition at low pressures, ~ 1 mtorr, with a target-to-substrate separation of a few cm.) The bottom Cu layer consists of eight planes of

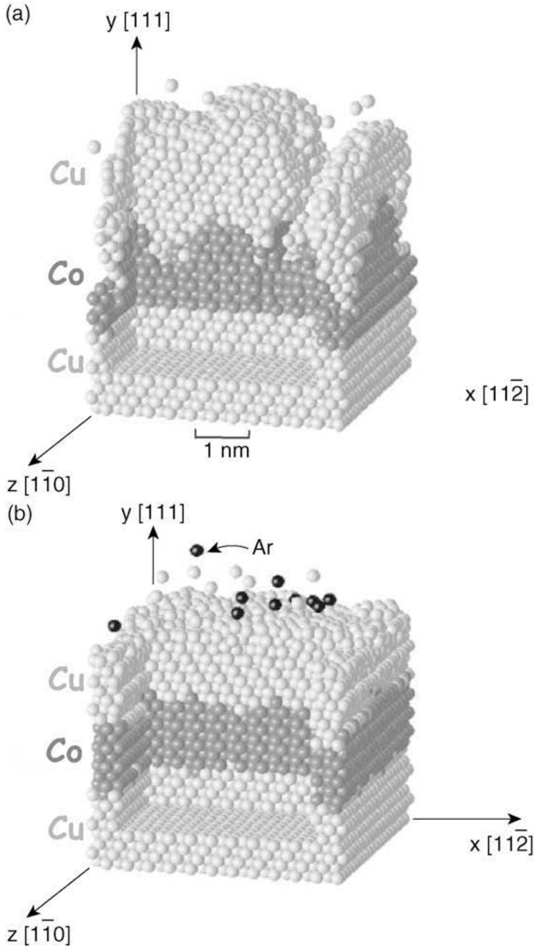

Figure 12.43: Molecular dynamics simulations of the growth of Cu/Co/Cu trilayers by sequential deposition of Co and Cu overlayers at room temperature on a Cu(111) substrate consisting of eight layers. The metal beam fluxes are thermal in both (a) and (b), but $E_i = 6$ eV Ar^+ ion irradiation, with $J_i/J_{Me} = 5$, is added in (b). (Adapted from [157].)

Cu(111); the Co and Cu overlayers were deposited at room temperature. In the thermal deposition case, panel (a), the Co diffusivity is low leading to a rough Co surface and Co/Cu interface. Thus, as the upper Cu layer buries the irregular Co surface, an even rougher upper surface is formed.

Panel (b) corresponds to the growth of the same trilayer system, but this time with very low energy ion irradiation simulating ion-assisted evaporation. The experiment is also a crude simulation of ballistic sputter deposition since ~83% of the arriving particles are energetic and the mass mismatch among Ar, Cu, and Co is not large. Ion-irradiation-enhanced adatom

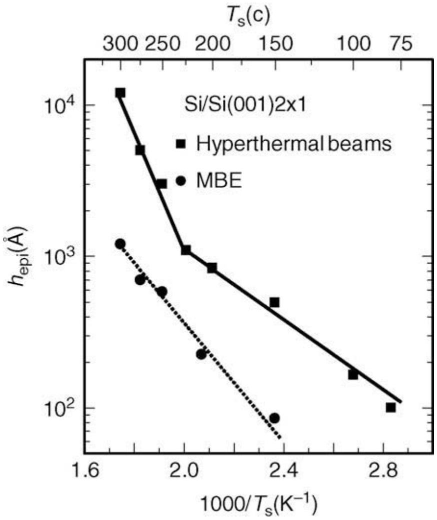

Figure 12.44: Epitaxial thickness h_{epi} of Si/Si(001) layers grown with hyperthermal E_{Si} = 11 eV beams (■) and with MBE (●) at $R \sim 1$ Å/s as a function of T_s. (Hyperthermal beams from [160]; MBE from [161].)

mobilities greatly decreases the roughness of both interfaces, and the surface, without adding to interfacial mixing. Clearly, the driving effect here is momentum transfer from the fast incident particles to surface atoms. Thus, the ion mass, ion energy, ion-to-thermal flux ratio, and ion angle of incidence can all be tuned to affect adatom mobilities and interfacial mixing in slightly different ways [10, 158, 159].

Experimentally, Lee et al. [160] have shown (Figure 12.44) that the epitaxial thickness h_{epi} of low-temperature ($T_s = 80$–$300\,°C$, $T_s/T_m = 0.21$–0.34) homoepitaxial Si/Si(001) layers grown from hyperthermal Si beams is increased by up to an order of magnitude above that recorded for MBE Si(001) epitaxy [161] at approximately the same deposition rate, $R \sim 1$ Å/s (Figure 12.44). The hyperthermal Si atoms were incident at the growing film with an orthogonal energy component of $E_{Si} = 11$ eV. In both cases, continued growth at film thicknesses $h > h_{epi}$ leads to increased kinetic surface roughening, growth front breakdown, and loss of epitaxy with a non-reversible transition to amorphous layer deposition. h_{epi} ranges from ~ 100 Å at $T_s = 100\,°C$, to 500 Å at 150 °C, to > 1 μm at 300 °C for Si(001) layers grown from hyperthermal species. For comparison, h_{epi} for MBE Si(001) varies from 70 Å at $T_s = 150\,°C$ to 1200 Å at $T_s = 300\,°C$ for MBE Si(001).

The slope change in the h_{epi} versus T_s curve for hyperthermal species in Figure 12.44 is explained as follows. While the energy of the hyperthermal growth species is too low to give rise to detectable residual bulk defect densities, they collisionally dissociate surface dimers and small clusters, thus resulting in higher adatom densities on all exposed surface levels. At sufficiently low growth temperatures (< 225 °C for this set of deposition conditions), this leads, on a given level, to an increased 2D gas supersaturation which in turn results in higher island nucleation rates with smaller average cluster sizes and, therefore, enhanced interlayer mass transport rates and epitaxial thicknesses. This effect is less important at higher growth temperatures as thermal diffusivities overcome the excess supersaturation due to collisionally formed adatoms.

Further increases in h_{epi} in the very low temperature regime, $< 225\,^{\circ}\mathrm{C}$, can be obtained by manipulating island nucleation kinetics in another manner, through changes in R. Initial decreases in R from 1.0 to 0.6 Å/s result in h_{epi} increasing from 500 to 800 Å at $T_{\mathrm{s}} = 150\,^{\circ}\mathrm{C}$ owing to increased adatom diffusion lengths at lower R values giving rise to higher step crossing probabilities and decreased surface roughness. However, there is a competing reaction. Increasing adatom diffusion distances by decreasing R at constant T_{s} also leads to increased island sizes and a reduction in the effects of energetic condensation on nucleation kinetics, both of which tend to increase surface roughness. Thus, for a given T_{s}, there is a maximum in h_{epi} vs R and the epitaxial thickness decreases again at even lower deposition rates.

Ion-irradiation-induced preferred orientation

As shown in Figure 12.42, the texture of polycrystalline $Ti_{0.5}Al_{0.5}N$ films (as well as other NaCl-structure TM nitrides) can be controlled from nearly complete 111 to 002 by varying $J_{\mathrm{i}}/J_{\mathrm{Me}}$, while maintaining $E_{\mathrm{i}} \leq 20\,\mathrm{eV}$, during low-temperature film growth. 002 is the low-energy surface for NaCl-structure TM nitrides [114, 162] and the films are not under significant strain. Thus, the 111 preferred orientation observed with low $J_{\mathrm{i}}/J_{\mathrm{Me}}$ ratios is kinetically limited. While 111 and 002 grains, approximately 50% each by area, coexist during the early stages of film growth, the 111 grains gradually overgrow the 002 oriented grains until at thicknesses > 1500 Å, the film has a nearly complete 111 texture [155] similar to the kinetic Monte Carlo simulation in Figure 12.34 (with, in the present case, the darker contrast regions representing 002 grains and the lighter regions 111 grains) and the XTEM micrograph in Figure 12.39. (See [113, 142] for similar results during TiN and TaN growth as a function of $J_{\mathrm{i}}/J_{\mathrm{Me}}$.) This is due to a combination of ion-induced surface chemistry, anisotropies in surface diffusivities, and differences in adatom potential energies.

For the growth of TM nitrides by reactive sputter deposition, the interplay and competition among several interrelated surface reaction and diffusional processes determine film growth kinetics, surface morphology, film microstructure, and texture [114]. The rate-limiting step for TM nitride film growth is cation incorporation which, in these experiments, proceeds at a rate of several ML/s. The N_2 supply rate is much larger, $> 10^3$ ML/s. If N_2 molecules reach Ti adatoms not yet incorporated in the lattice, they undergo dissociative chemisorption. However, all other incident N_2 molecules are only physisorbed and desorb at kinetic rates with estimated lifetimes of $\leq 10^{-9}$ s. This results in (002) surfaces which exhibit an essentially bulk-terminated structure with equal cation and anion number densities while polar (111) surfaces are fully N-terminated [114]. Ti adatoms form one N backbond on (002) and three N backbonds on (111) surfaces. Thus, cation diffusivities and potential energies are higher on 001-oriented grains than on 111 grains and, following the arguments in Section 12.6.1 for competitive grain growth, Ti adatoms have a larger chance of becoming trapped at 111 sites. Consequently, 111 grains slowly and inexorably expand at the expense of the 002 grains under low-T_s, low-ion-flux growth conditions.

ω-2θ and glancing-angle XRD scans from 1 μm thick low-temperature TiN ($T_s = 350\,°C$, $T_s/T_m \sim 0.17$) and $Ti_{0.5}Al_{0.5}N$ ($T_s = 250\,°C$, $T_s/T_m \sim 0.15$) layers grown in pure N_2 at 20 mtorr on a-SiO_2 with $E_i = 20$ eV and J_i/J_{Me} values ranging from ~ 1 to 15 contain (111) and/or (002) reflections (no other orientations were detected). (See [113] for similar results for TaN.) Normalized 111 and 002 peak intensities are plotted as a function of J_i/J_{Me} in Figure 12.45. Films grown with high flux ratios ($J_i/J_{Me} \geq 5$) exhibit an 002 texture, while those grown with low J_i/J_{Me} have a 111 preferred orientation. XRD pole figures reveal, in addition, that all diffraction peak maxima are aligned along the growth direction and that peak intensities are azimuthally symmetric. Measured residual stresses are low at all J_i/J_{Me} values.

XRD analyses as a function of film thickness h and J_i/J_{Me}, as well as cross-sectional selected-area electron diffraction results from thick films, reveal competitive grain growth up to $h \sim 1500$ Å, with both 111 and 002 grains present for $J_i/J_{Me} \leq 10$. At $J_i/J_{Me} = 1$, the films are porous and evolve to pure 111, while at $J_i/J_{Me} \sim 5$–10 the films are fully dense and it is the 002 columns which evolve by overgrowing the 111 columns. In addition, the 002 layers exhibit much smoother surfaces than the faceted 111 layers.

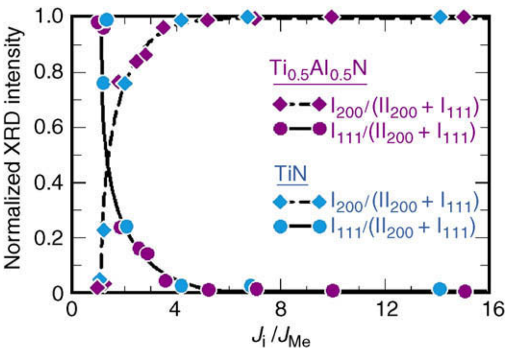

Figure 12.45: Normalized 111 and 002 peak intensities *I* from 1-μm-thick TiN [142] and $Ti_{0.5}Al_{0.5}N$ [155] layers deposited by reactive magnetron sputtering in pure N_2 (20 mtorr) on amorphous SiO_2 substrates at $T_s = 350\,°C$ (TiN) and 250 °C ($Ti_{0.5}Al_{0.5}N$) with $E_i = 20$ eV as a function of J_i/J_{Me}.

The above behavior can be understood based on the arguments, presented in Section 12.6.1, regarding competitive growth between grains exposing low- versus high-diffusivity planes to the growth front with low-energy high-flux N_2^+ ion irradiation switching the balance between 111 and 002 orientations. Incident collisionally dissociated 20 eV N_2^+ ions provide a continuous source of atomic N which can chemisorb on 001 grains ([001] is a non-polar direction in the NaCl-structure), but not on N-terminated 111 grains. This is in contrast to incident thermal N_2 species which, as discussed above, have very short lifetimes on both surfaces in the absence of a local population of free cations. Thus, increasing J_i/J_{Me} corresponds to raising the steady-state N coverage θ_N on 001 grains while θ_N remains at a constant N-terminated value on 111 grains. This has the important consequence of decreasing cation mean free paths on (002) surfaces due to capture of N adatoms to form TiN_i ($i = 1–3$) admolecules, in the case of TiN, which have much lower surface diffusivities than Ti adatoms as quantitatively demonstrated by TiN(001) nucleation results in Section 12.4.1 [62, 68] and *ab initio* density functional calculations [114]. That is, in the presence of an atomic N source, the 002 chemical potential decreases below that of 111. Consequently, the net flux of cations from 002 to 111 oriented grains is reversed under low-energy, high-flux N_2^+ irradiation conditions, resulting in the development of 002 texture.

In addition to controllably switching the texture from 111 to 002 with increasing ion flux, there is a corresponding increase in layer density and a decrease in surface roughness from underdense layers, with intercolumnar voids and self-organized growth mounds separated by deep surface trenches, to fully dense layers with smoother surfaces. The densification arises from less pronounced kinetic roughing due to ion-irradiation enhanced adatom surface mobilities resulting in smoother surfaces with less atomic shadowing.

The above results demonstrated that increasing J_i/J_{Me} with $E_i = 20\,\text{eV}$ during growth of NaCl-structure TM nitride films results in a transition from underdense 111 to a dense 002 preferred orientation. With the introduction of texture inheritance, however, it becomes possible to select the preferred orientation during the nucleation stage. This concept has been used to achieve dense, highly 111-oriented TiN films [163]. (Similar results were obtained with TaN [164].) Ti underlayers, 250 Å thick, are first deposited on amorphous substrates at 80 °C ($T_s/T_m = 0.18$) with $J_i/J_{Me} = 2$ and $E_i = 11$ eV. The Ti layers are fully dense with a zone II structure and very strong 0002 orientation. The TiN overlayers are then deposited with high J_i/J_{Me} values (> 10) and $E_i \sim 20$ eV, which on bare amorphous substrates results in dense 002 layers. In this case, however, local epitaxy on 0002 Ti grains yields fully dense TiN layers with a strong 111 texture; competitive grain growth is completely eliminated. Texture inheritance selects the preferred orientation while low-energy ion irradiation provides densification.

In addition to out-of-plane texture, *in-plane* preferred orientation can also be controlled using ion irradiation by taking advantage of anisotropic collisional cascade effects [165]. However, experiments to date have primarily been carried out with high-energy ions in an IBAD configuration. Selectively oriented layers of refractory metals [166], oxides [167, 168], and nitrides [169] have been obtained and used as templates to provide pseudomorphic texture inheritance to low-temperature overlayers. An example is the growth of highly 002 textured polycrystalline MgO films for seed layers on which to deposit oriented oxide superconductors. The strategy is to align an ion beam such that it is orthogonal to a high-symmetry, low-density plane in a growing MgO crystallite oriented with the (002) plane parallel to the substrate surface. Ion energy in open channel directions is distributed over larger depths yielding less lattice distortion and lower sputter yields. Therefore planes perpendicular to an open channel direction have higher survival probability. Since MgO has the NaCl structure, the beam is aligned orthogonal to the (101) plane at 45° to the [001] direction corresponding to the selection of in-plane preferred orientation along [100] [168].

Three-dimensional nanostructures

Three-dimensional nanostructures have recently become of interest owing to the possibility of achieving superhard layers with high wear resistance [121, 170], layers which actually increase in hardness with increasing temperature [124] (important for high-speed machining, turbine blade coatings, etc.), and supertough layers [171]. A general strategy is evolving which combines segregation of incommensurate phases to force periodic renucleation, during low-temperature deposition, with low-energy ion irradiation to control both phase distribution and preferred orientation [123, 124, 170, 171].

Relatively simple examples are the self-organized $Ti_{0.8}Ce_{0.2}N$ nanostructures shown in Figure 12.46 [171]. They are grown on amorphous SiO_2 ($R = 0.63$ Å/s) by reactive magnetron sputtering in pure N_2 at 5 mtorr with $T_s = 350\,^\circ C$. The constituent TM and rare-earth nitrides TiN ($a_{TiN} = 4.240$ Å) and CeN ($a_{CeN} = 5.021$ Å) exhibit a deep miscibility gap with a large lattice parameter mismatch. Z-contrast scanning XTEM, nanodiffraction, and electron energy loss spectroscopy analyses, combined with the high-resolution TEM and XTEM lattice images in Figure 12.46, show that the nanostructures are fully dense with a nearly complete 002 texture. The upper nanocomposite consists of ~20 Å diameter nanospheres encapsulated in a fully percolated disordered CeN-rich tissue phase. Continuous CeN surface segregation during growth of TiN-rich nanocrystallites leads to renucleation. TiN then segregates out of the growing CeN phase until it reaches a critical supersaturation to nucleate a new nanocrystallite. Increasing the ion irradiation intensity during TiCeN deposition results in the formation of quasi-periodic, 20 Å wide, CeN-encapsulated TiN-rich nanocolumns (lower image in Figure 12.46). Ion-irradiation enhanced surface mobilities combined with a large strain energy driving force gives rise to a surface-initiated spinodal decomposition process allowing the continued formation of adjacent CeN-rich and TiN-rich nanocolumns. The in-plane periodicity can be tuned by changing the overall Ce/Ti ratio, the ion irradiation conditions, T_s, and (to a lesser extent) R.

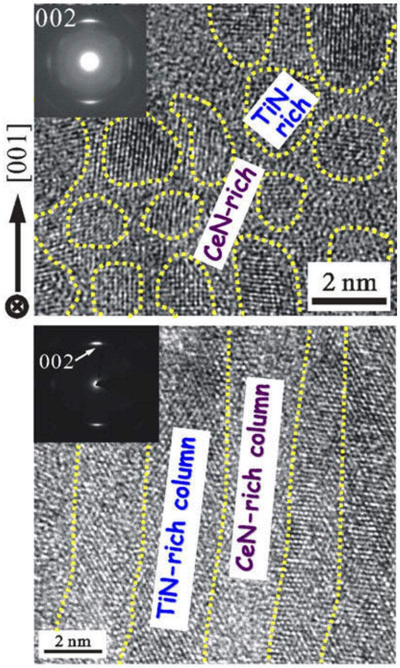

Figure 12.46: High-resolution XTEM micrographs, with corresponding selected-area diffraction patterns, from 3D $Ti_{1-x}Ce_xN$ nanostructures, of average composition $x = 0.20$, grown by reactive magnetron sputtering in pure N_2 (5 mtorr) on amorphous SiO_2 at $T_s = 350$ °C under different ion irradiation conditions. The nanocomposites consist of approximately spherical TiN-rich nanocrystallites (upper image) and nanocolumns (lower image), both ~ 20 Å in size, encapsulated in a disordered CeN-rich phase. (Adapted from [171].) The dotted lines and labels are to guide the eye.

A related example with a more complex nanostructure has the overall composition $TiB_{2.4}$ [123]. Since hexagonal-structure TiB_2 is a line compound, the excess B does not remain in solution. The nanocomposite is self-organized at two length scales and consists of quaisperiodic 200-Å-wide stoichiometric TiB_2 columns separated by 1–2 ML of B. The 200 Å nanocolumns are, in turn, composed of even smaller 50-Å-wide nanocolumns, also separated by a B tissue phase. The structures have a very high hardness since the narrow columns inhibit the nucleation and glide of dislocations while the strong covalent bonding of the B tissue phase prevents grain boundary sliding. Going a step further to synthesize Ti–B–N with overall compositions, such as $TiB_{0.80}N_{0.83}$ (38 at.% Ti, 30.5 at.% B, 31.5 at.% N), within a deep miscibility gap in the $TiN–TiB_2–BN$ ternary phase field, results in self-organized nanostructures which are not only hard, but whose hardness increases with temperature owing to increased ordering in the covalent tissue phase [124].

12.7 Conclusions

Atomic scale understanding of microstructural evolution, necessary for the controlled manipulation of the properties of thin film systems, is increasing rapidly. However, we are still far from having accurate quantitative descriptions. The field is presently driven both by scientific curiosity arising from the richness of surface and bulk phenomena involved and, more and more, by technological demands to provide materials with properties that do not exist at present. Rapid progress is now possible owing to the availability of at least first-order atomic-scale design rules. Overall, the field of thin films continues to be vital, intellectually challenging, and a long way from mature as it moves toward the ultimate goal of being able to develop designer materials, at the atomic scale, possessing any desired set of properties.

Acknowledgements

The author gratefully acknowledges the financial support of the Department of Energy, Division of Materials Science. He has also benefited from many years of close collaboration and friendship with Ivan Petrov (University of Illinois) as well as continuous discussions and scientific interactions with Lars Hultman (Linköping University) and Peter Barna (Hungarian Academy of Science).

References

[1] J.M.E. Harper, J.J. Cuomo, H.R. Kaufman, Modification of thin film properties by ion bombardment during deposition, in: A. Auciello, R. Kelly (Eds.), Ion Bombardment Modification of Surfaces, Elsevier, New York (1984).
[2] J.E. Greene, Thin film crystal growth by sputtering, in: S. Keller (Ed.), Handbook of Semiconductors, Vol. III, North Holland Publishing Co, Amsterdam (1980).
[3] J.E. Greene, epitaxial crystal growth by sputter deposition: applications to semiconductors. Part 2, CRC Crit. Rev. Solid State Mater. Sci. 11 (1984) 189.
[4] J.E. Greene, S.A. Barnett, J.-E. Sundgren, A. Rockett, Ion/surface interactions during film growth from the vapor phase, in: T. Itoh (Ed.), Ion Beam Assisted Film Growth, Elsevier, Amsterdam (1989) 101, Chap. 5.
[5] J.E. Greene, S.A. Barnett, J.-E. Sundgren, A. Rockett, Low-energy ion/surface interactions during film growth from the vapor phase: effects on nucleation and growth kinetics, defect structure and elemental incorporation probabilities, in: O. Auciello, A. Gras-Marti, D.L. Flamm (Eds.), Plasma–Surface Interactions and Processing of Materials, NATO Advanced Study Institute, Series E: Applied Sciences, Vol. 176, Kluwer Academic Publishers, Boston (1990).
[6] J.E. Greene, The role of low-energy ion/surface interaction effects during crystal growth from the vapor phase: nucleation and growth, microstructure evolution and defect formation and annihilation, in: D.T.J. Hurle (Ed.), Handbook of Crystal Growth, Vol. 1, Fundamentals, Elsevier, Amsterdam (1993) 639.
[7] J.A. Thornton, J.E. Greene, Sputter deposition processes, in: R.F. Bunshah (Ed.), Deposition Technologies for Films and Coatings, Noyes Publications, Park Ridge, NJ (1994) 249.
[8] I. Petrov, P.B. Barna, L. Hultman, J.E. Greene, J. Vac. Sci. Technol. 21 (2003) S117.
[9] D. Adamovic, E.P. Münger, V. Chirita, L. Hultman, J.E. Greene, Appl. Phys. Lett. 86 (2005) 211915.
[10] J.J. Quan, X.W. Zhou, H.N.G. Wadley, Surf. Sci. 600 (2006) 4357.

[11] D. Adamovic, V. Chirita, E.P. Munger, L. Hultman, J.E. Greene, Thin Solid Films 515 (2006) 2235.
[12] J.J. Quan, X.W. Zhou, H.N.G. Wadley, J. Cryst. Growth 300 (2007) 431.
[13] D. Adamović, V. Chirita, E.P. Münger, L. Hultman, J.E. Greene, Phys. Rev. B 76 (2007) 115418.
[14] E. Bauer, Z. Kristallogr. 110 (1958) 372.
[15] J.A. Venables, G.D.T. Spiller, M. Hanbücken, Rept. Prog. Phys. 47(399) (1984).
[16] I.N. Stranski, L. Krastanow, Sitzungsber. Wien. Akad. Wiss. Math.-Nat. Kl. IIB 146 (1938) 797.
[17] K.-N. Tu, J.W. Mayer, L.C. Feldman, Electronic Thin Film Science, Macmillan Publishing, New York (1992) 164.
[18] D.J. Sroloritz, Acta Metall. 37 (1989) 621.
[19] H. Gao, W.D. Nix, Annu. Rev. Mater. Sci. 29 (1999) 173.
[20] J. Knall, J.-E. Sundgren, G.V. Hansson, J.E. Greene, Surf. Sci. 166 (1986) 512.
[21] B. Voightländer, M. Kastner, Phys. Rev. B 60 (1999) R5121.
[22] A. Vailionis, B. Cho, P. Desjardins, D.G. Cahill, J.E. Greene, Phys. Rev. Lett. 85 (2000) 3672.
[23] V. Ponnambalam, S.J. Poon, G.J. Shiflet, J. Mater. Res. 19 (2004) 1320.
[24] D.C. Hofmann, J.-Y. Suh, A. Wiest, M.-L. Lind, M.D. Demetriou, W.L. Johnson, Proc. Nat. Acad. Science, in press (doi: 10.1073).
[25] A.H. Donohoe, J.L. Robins, J. Cryst. Growth 17 (1972) 70.
[26] R.E. Honig, RCA Rev. 23 (1962) 567.
[27] G.A. Somorjai, Chemistry in Two-Dimensions, Cornell Press, Ithaca, New York (1981).
[28] E. Rodunner, Chem. Soc. Rev. 35 (2006) 583.
[29] J.A. Stroscio, D.T. Pierce, Phys. Rev. B 49 (1994) 8522.
[30] J.P. Hirth, K.L. Moazed, in: G. Hass, R.E. Thun (Eds.), Thin Film Physics 4, Academic Press, New York (1967).
[31] C.A. Neugebauer, in: L.I. Maissel, R. Glang (Eds.), Handbook of Thin Film Physics, McGraw Hill, New York (1970) Chap. 8.
[32] R.S. Wagner, R.J.H. Voorhoeve, J. Appl. Phys. 43 (1971) 3948.
[33] B. Lewis, J.C. Anderson, Nucleation and Growth of Thin Films, Academic Press, New York (1978).
[34] S. Stoyanov, D. Kaschiev, in: E. Kaldis (Ed.), Current Topics in Materials Science, Vol. 7, North Holland, Amsterdam (1981).
[35] Z. Zhang, F. Wu, M.G. Lagally, Annu. Rev. Mater. Sci. 27 (1997) 525.
[36] G. Bining, H. Rohrer, C. Gerber, E. Weibel, Surf. Sci. Lett. 131 (1983) L379.
[37] G. Zinmeister, Vacuum 16 (1966) 529.
[38] G. Zinmeister, Thin Solid Films 2 (1968) 497.
[39] G. Zinmeister, Thin Solid Films 4 (1969) 363.
[40] G. Zinmeister, Kristall Technik 5 (1970) 207.
[41] G. Zinmeister, Thin Solid Films 7 (1971) 51.
[42] J.A. Venables, Introduction to Surface and Thin Film Processes, Cambridge University Press, Cambridge (2000).
[43] B. Cho, J. Bareno, Y.L. Foo, S. Hong, T. Spila, I. Petrov, J.E. Greene, J. Appl. Phys. 103 (2008) 123530.
[44] J.A. Venables, Phil. Mag. 27 (1973) 697 Appendix A.
[45] A. Zangwill, Evolution of Surface and Thin Film Microstructure, in: H.A. Atwater, E. Chason, M. Grabow, M. Lagally (Eds.), MRS Proceedings, Vol. 280, MRS, Pittsburgh (1993).
[46] A. Zangwill, J. Cryst. Growth 163 (1996) 8.
[47] J.K. Zuo, J.F. Wendelken, H. Durr, C.-L. Liu, Phys. Rev. Lett. 72 (1994) 3064.
[48] B. Müller, L. Nedelmann, B. Fisher, H. Brune, K. Kern, Phys. Rev. B 54 (1996) 17858.
[49] H. Durr, J.F. Wendelken, J.K. Zuo, Surf. Sci. 328 (1995) L527.
[50] M.J.J. Jak, C. Konstapel, A. van Kreuningen, J. Voerhoeven, J.W.M. Frenken, Surf. Sci. 457 (2000) 295.
[51] C. Polop, C. Rosiepen, S. Bleikamp, R. Drese, J. Mayer, A. Dimyati, T. Michely, N. J. Phys. 9 (2007) 74.
[52] D.W. Pashley, M.J. Stowell, J. Vac. Sci. Technol. 3 (1966) 156.
[53] D.W. Pashley, M.J. Stowell, M.H. Jacobs, J.T. Law, Phil. Mag. 10 (1964) 127.

[54] J.F. Pozca, in: E. Hahn (Ed.), Proc. 2nd Colloquium Thin Films, Hungarian Academy of Sciences, Budapest (1967) 93.
[55] J.F. Pocza, A. Barna, P.B. Barna, J. Vac. Sci. Technol. 6 (1969) 172.
[56] M. Zhang, M.Yu. Efremov, F. Schiettekatte, E.A. Olson, A.T. Kwan, S.L. Lai, T. Wisleder, J.E. Greene, L.H. Allen, Phys. Rev. B. 62 (2000) 10458.
[57] L.E. Murr, Interfacial Phenomena in Metals and Alloys, Addison-Wesley, Reading, MA (1975).
[58] R.S. Wagner, R.H.J. Voorhoeve, J. Appl. Phys. 42 (1971) 3948.
[59] R.H.J. Voorhoeve, R.S. Wagner, Met. Trans. 2 (1971) 3421.
[60] J.A. Stroscio, D.T. Pierce, R.A. Dragoset, Phys. Rev. Lett. 70 (1993) 3615.
[61] S. Kodambaka, S.V. Khare, I. Petrov, J.E. Greene, Surf. Sci. Rep. 60 (2006) 55.
[62] M.A. Wall, D.G. Cahill, I. Petrov, D. Gall, J.E. Greene, Phys. Rev. B 70 (2004) 035413.
[63] S. Kodambaka, V. Petrova, A. Vailionis, I. Petrov, J.E. Greene, Surf. Sci. 526 (2003) 85.
[64] B.W. Karr, D.G. Cahill, I. Petrov, J.E. Greene, Phys. Rev. B 61 (2000) 16137.
[65] S. Kodambaka, S.V. Khare, V. Petrova, A. Valionis, I. Petrov, J.E. Greene, Surf. Sci. 513 (2002) 468.
[66] J. Tersoff, A.W. Denier van der Gon, R.M. Tromp, Phys. Rev. Lett. 72 (1994) 266.
[67] I. Petrov, A. Myers, J.E. Greene, J.R. Abelson, J. Vac. Sci. Technol. A 12 (1994) 2846.
[68] M.A. Wall, D.G. Cahill, I. Petrov, D. Gall, J.E. Greene, Surf. Sci. 581 (2005) L122.
[69] S. Kodambaka, D.L. Chopp, I. Petrov, J.E. Greene, Surf. Sci. 540 (2003) L611.
[70] S. Kodambaka, V. Petrova, S.V. Khare, D.D. Johnson, I. Petrov, J.E. Greene, Phys. Rev. Lett. 88 (2002) 146101.
[71] S. Kodambaka, S.V. Khare, V. Petrova, D.D. Johnson, I. Petrov, J.E. Greene, Phys. Rev. B 67 (2003) 035409.
[72] J. Bareño, S. Kodambakab, S.V. Kharec, W. Swiecha, V. Petrova, I. Petrov, J.E. Greene, in: O. Miranda, M. Carbajal, L.M. Montano, O. Rosas-Ortiz, S.A.T. Velazquez (Eds.), TiN Surface Dynamics: Role of Surface and Bulk Mass Transport Processes, Advanced Summer School in Physics, American Institute of Physics, Melville, NY (2007).
[73] J.W. Matthews, A.E. Blakeslee, J. Cryst. Growth 27 (1974) 118.
[74] J. Tersoff, F.K. LeGoues, Phys. Rev. Lett. 72 (1994) 3570.
[75] N.-E. Lee, M. Matsuoka, M.R. Sardela, F. Tian, J.E. Greene, J. Appl. Phys. 80 (1996) 812.
[76] N.E. Lee, D.G. Cahill, J.E. Greene, J. Appl. Phys. 80 (1996) 2199.
[77] J. Knall, S.A. Barnett, J.-E. Sundgren, J.E. Greene, Surf. Sci. 209 (1989) 314.
[78] B. Voigtländer, Surf. Sci. Rep. 43 (2001) 127.
[79] D.E. Jesson, K.M. Chen, S.J. Pennycook, MRS Bull. 21 (1996) 31.
[80] H. Ibach, Surf. Sci. Rep. 29 (1997) 193.
[81] M. Geisen, Prog. Surf. Sci. 68 (2001) 1.
[82] M. Kastner, B. Voigtländer, Phys. Rev. Lett. 82 (2000) 2745.
[83] D.E. Jessen, G. Chen, K.M. Chen, S.J. Pennycook, Phys. Rev. Lett. 80 (1998) 5156.
[84] B.A. Movchan, A.V. Demchishin, Fiz. Met. Metalloved 28 (1969) 83.
[85] J.V. Sanders, in: J.R. Anderson (Ed.), Chemisorption and Reactions on Metallic Films, Academic Press, London (1971) 1.
[86] J.A. Thornton, Annu. Rev. Mater. Sci. 7 (1977) 239.
[87] R. Messier, A.P. Giri, A.R. Roy, J. Vac. Sci. Technol. A 2 (1984) 500.
[88] C.R.M. Grovenor, H.T.G. Hentzell, D.A. Smith, Acta Metall. 32 (1984) 773.
[89] D.A. Smith, A. Ibrahim, Mater. Res. Soc. Proc. 317 (1994) 401.
[90] R.A. Roy, R. Messier, Mater. Res. Soc. Symp. Proc. 38 (1985) 363.
[91] J.A. Thornton, J. Vac. Sci. Technol. A 4 (1986) 3059.
[92] P.B. Barna, M. Adamik, Thin Solid Films 317 (1998) 27.
[93] S. Mahieu, P. Ghekiere, D. Depla, Thin Solid Films 515 (2006) 1229.
[94] D.A. Smith, in: D. Wolf, S. Yip (Eds.), Materials Interfaces, Atomic Level Structure, and Properties, Chapman and Hall, London (1992) Chap. 6.
[95] C.V. Thompson, R. Carel, Mater. Sci. Eng. B 32 (1995) 211.

[96] D.W. Paschley, Phil. Mag. 15 (1966) 173.
[97] H. Lewis, Thin Solid Films 7 (1971) 179.
[98] J.F. Pocza, A. Barna, P.B. Barna, I. Pozsgai, G. Radnoczi, Jpn. J. Appl. Phys. 2 (1974) 525.
[99] D.W. Pashley, in: J.W. Matthews (Ed.), Epitaxial Growth, Part B, Academic Press, New York (1975) 1.
[100] J.F. Pocza, A. Barna, P.B. Barna, Kristall Technik 5 (1970) 315.
[101] G. Honjo, K. Yagi, in: E. Kaldis (Ed.), Current Topics in Materials Science, Vol. 6, North Holland, Amsterdam (1975) 195.
[102] A.G. Dirks, H.J. Leamy, Thin Solid Films 47 (1977) 219.
[103] D. Henderson, M.H. Brodsky, P. Chaudhari, Appl. Phys. Lett. 25 (1974) 64.
[104] F.H. Baumann, D.L. Chopp, T. Díaz de la Rubia, G.H. Gilmer, J.E. Greene, H. Huang et al., MRS Bull. 26 (2001) 182.
[105] G.H. Gilmer, H. Huang, T. Diaz de la Rubia, J.D. Torre, F. Baumann, Thin Solid Films 365 (2000) 189.
[106] C.V. Thompson, Annu. Rev. Mater. Sci. 20 (1990) 245.
[107] M.J. Rost, D.A. Quist, J.W.M. Frenken, Phys. Rev. Lett. 91 (2003) 026101.
[108] C.V. Thompson, Annu. Rev. Mater. Sci. 30 (2000) 159.
[109] C.V. Thompson, J. Floro, H.I. Smith, J. Appl. Phys. 67 (1990) 4099.
[110] C.C. Wong, H.I. Smith, C.V. Thompson, Appl. Phys. Lett. 48 (1986) 335.
[111] E.M. Zielinski, R.P. Vinci, J.C. Bravman, J. Appl. Phys. 76 (1994) 4516.
[112] J.E. Greene, J.-E. Sundgren, L. Hultman, I. Petrov, D.B. Bergstrom, Appl. Phys. Lett. 67 (1995) 2549.
[113] C.-S. Shin, D. Gall, Y.-W. Kim, N. Hellgren, I. Petrov, J.E. Greene, J. Appl. Phys. 92 (2002) 5084.
[114] D. Gall, S. Kodambaka, M.A. Wall, I. Petrov, J.E. Greene, J. Appl. Phys. 93 (2003) 9086.
[115] P.B. Barna, in: Proc. 9th Int. Vac. Congr., Madrid (1983) 382, and references therein.
[116] J.M. Schneider, K. Larsson, J. Lu, E. Olsson, B. Hjörvarsson, Appl. Phys. Lett. 80 (2002) 1144.
[117] A. Csanady, Y. Pitton, H.J. Mathieu, K. Kessler, R. Fuchs, M. Textor, Surf. Interface Anal. 21 (1994) 546.
[118] R. Michel, J. Castaldi, C. Allasia, C. Jourdan, J. Derrien, Surf. Sci. 95 (1980) 309, and references therein.
[119] P.B. Barna, M. Adamik, G. Safran, B. Pecz, A. Bergauer, H. Bangert, Phys. Stat. Sol. A 146 (1994) 31, and references therein.
[120] S. Veprek, J. Vac. Sci. Technol. A 17 (1999) 2401.
[121] S. Veprek, M.G.J. Veprek-Heijman, P. Karvankova, J. Prochazka, Thin Solid Films 476 (2005) 1.
[122] T. Zehnder, J. Patscheider, Surf. Coat. Technol. 133–134 (2000) 138.
[123] P. Mayrhofer, C. Mitterer, J.G. Wen, J.E. Greene, I. Petrov, Appl. Phys. Lett. 86 (2005) 13199.
[124] P.H. Mayrhofer, C. Mitterer, J.G. Wen, I. Petrov, J.E. Greene, J. Appl. Phys. 100 (2006) 044301.
[125] P.H. Mayrhofer, C. Mitterer, Surf. Coat. Technol. 133–134 (2000) 131.
[126] J. Musil, H. Hrubý, P. Zeman, H. Zeman, R. Čerstvý, P.H. Mayrhofer, C. Mitterer, Surf. Coat. Technol. 142–144 (2001) 603.
[127] A.A. Voevodin, J.J. Hu, T.A. Fitz, J.S. Zabinski, Surf. Coat. Technol. 146–147 (2001) 351.
[128] P.B. Barna, M. Adamik, U. Kaiser, S. Laux, H. Bangert, M. Pulliainen, K.A. Pishow, Surf. Coat. Technol. 100–101 (1998) 72.
[129] P.B. Barna, M. Adamik, L. Labar, L. Kover, J. Toth, A. Devenyi, R. Manaila, Surf. Coat. Technol. 125 (2000) 147.
[130] C.A. Neugebauer, Thin Solid Films 6 (1970) 443.
[131] A.F. Jankowski, Thin Solid Films 332 (1998) 272.
[132] J.E. Sundgren, R.C. Buchanan, Sens. Actuators A 90 (2001) 118.
[133] Q.-C. Zhang, Sol. Energy Mater. Sol. Cells 62 (2000) 63.
[134] K. Bewilogua, C.V. Cooper, C. Specht, J. Schröder, R. Wittorf, M. Grischke, Surf. Coat. Technol. 132 (2000) 275.
[135] J.S. Zabinski, M.S. Donley, V.J. Dyhouse, N.T. McDevit, Thin Solid Films 214 (1992) 156.
[136] A.A. Voevodin, J.S. Zabinski, Thin Solid Films 370 (2000) 223.
[137] J.M. Schneider, W.D. Sproul, A. Matthews, Surf. Coat. Technol. 98 (1998) 1473.
[138] A. Kovacs, P.B. Barna, J.L. Labar, Thin Solid Films 433 (2003) 78.

[139] J.M.E. Harper, K.P. Rodbell, J. Vac. Sci. Technol. B 15 (1997) 763.
[140] A. Barna, P.B. Barna, G. Radnoczi, F.M. Reicha, L. Toth, Phys. Stat. Sol. A 55 (1979) 427.
[141] C. Eisenmenger-Sittner, H. Bangert, H. Stori, J. Brenner, P.B. Barna, Surf. Sci. 489 (2001) 161.
[142] L. Hultman, J.-E. Sundgren, J.E. Greene, D.B. Bergstrom, I. Petrov, J. Appl. Phys. 78 (1995) 5395.
[143] H. Kaufman, R.S. Robinson, R.I. Seddon, J. Vac. Sci. Technol. A 5 (1987) 2081.
[144] I. Petrov, F. Adibi, J.E. Greene, W.D. Sproul, W.-D. Munz, J. Vac. Sci. Technol. A 10 (1992) 3283.
[145] D. Mattox, G. Kominiak, J. Vac. Sci. Technol. 9 (1972) 528.
[146] T.C. Huang, G. Lim, F. Parmiagiani, E. Kay, J. Vac. Sci. Technol. A 3 (1985) 2161.
[147] G. Hakansson, J.-E. Sundgren, D. McIntryre, J.E. Greene, D.-W. Munz, Thin Solid Films 153 (1987) 55.
[148] I. Petrov, L. Hultman, J.-E. Sundgren, J.E. Greene, J. Vac Sci. Technol. A 10 (1992) 265.
[149] D. Dobrev, Thin Solid Films 92 (1982) 41.
[150] I. Petrov, L. Hultman, U. Helmersson, J.-E. Sundgren, J.E. Greene, Thin Solid Films 169 (1989) 299.
[151] H. Windishman, J. Appl. Phys. 62 (1987) 1800.
[152] J.A. Thornton, D.W. Hoffman, Thin Solid Films 171 (1989) 5.
[153] C.A. Davis, Thin Solid Films 226 (1993) 30.
[154] I. Petrov, F. Adibi, J.E. Greene, L. Hultman, J.-E. Sundgren, Appl. Phys. Lett. 63 (1993) 36.
[155] F. Adibi, I. Petrov, J.E. Greene, L. Hultman, J.-E. Sundgren, J. Appl. Phys. 73 (1993) 8580.
[156] D. Gall, I. Petrov, N. Hellgren, L. Hultman, J.-E. Sundgren, J.E. Greene, J. Appl. Phys. 84 (1998) 6034.
[157] J.J. Quan, X.W. Zhou, H.N.G. Wadley, Surf. Sci. 600 (2006) 2275.
[158] X.W. Zhou, H.N.G. Wadley, R.A. Johnson, D.J. Larson, N. Tabat, A. Cerezo, A.K. Petford-Long, G.D.W. Smith, P.H. Clifton, R.L. Martens, T.F. Kelly, Acta. Mater. 49 (2001) 4005.
[159] X.W. Zhou, H.N.G. Wadley, Surf. Sci. 487 (2001) 159.
[160] N.-E. Lee, G.A. Tomasch, J.E. Greene, Appl. Phys. Lett. 65 (1994) 3236.
[161] D.J. Eaglesham, H.-J. Gossmann, M. Cerullo, Phys. Rev. Lett. 65 (1990) 1227.
[162] L. Hultman, S.A. Barnett, J.-E. Sundgren, J.E. Greene, J. Cryst. Growth 92 (1988) 639.
[163] J.-S. Chun, I. Petrov, J.E. Greene, J. Appl. Phys. 86 (1999) 3633.
[164] C.-S. Shin, I. Petrov, J.E. Greene, unpublished.
[165] R.M. Bradley, J.M.E. Harper, D.A. Smith, J. Appl. Phys. 60 (1986) 4160.
[166] L.S. Yu, J.M.E. Harper, J.J. Cuomo, D.A. Smith, J. Vac. Sci. Technol. A 4 (1986) 443.
[167] J.M.E. Harper, K.P. Rodbell, J. Vac. Sci. Technol. B 15 (1997) 763.
[168] C.P. Wang, K.B. Do, M.R. Beasley, T.H. Geballa, R.H. Hammond, Appl. Phys. Lett. 71 (1997) 2955.
[169] C.-H. Ma, PhD Thesis, Materials Science Department, University of Illinois.
[170] L. Hultman, J. Bareño, A. Flink, H. Söderberg, V. Petrova, M. Odén, J.E. Green, I. Petrov, Phys. Rev. B 75 (2007) 155437.
[171] T.-Y. Lee, S. Kodambaka, J.G. Wen, R. Twesten, J.E. Greene, I. Petrov, Appl. Phys. Lett. 84 (2004) 2796.

CHAPTER 13

Glancing Angle Deposition

Michael T. Taschuk, Matthew M. Hawkeye and Michael J. Brett

13.1 Introduction

Oblique angle deposition has been of interest to the thin film community for more than 100 years owing to enhancement of properties such as dichroism, birefringence, and anisotropic resistivity [1–4]. The film microstructure which produces these novel properties and

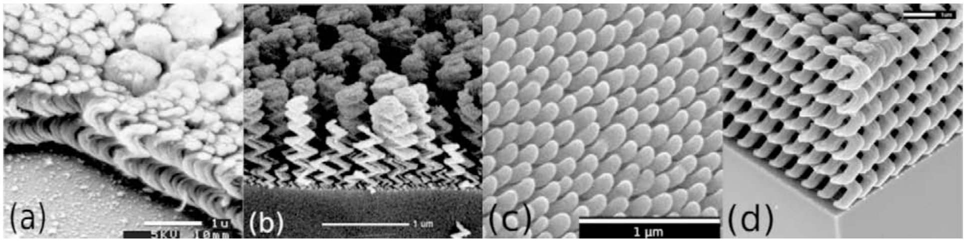

Figure 13.1: SEM images showing increasing control offered by the GLAD technique over the past 15 years: (a) early spirals, (b) early chevrons, (c) top–down view of Alq_3 spirals, and (d) Si square spiral. (a) and (b) are from 1994, (c) and (d) are from 2007. All scale bars are 1 μm.

capabilities depends on ballistic shadowing and formation of columnar microstructures during deposition.

Glancing angle deposition (GLAD) is an extension to oblique angle deposition where the substrate position is manipulated during film deposition. Although some early experiments used mobile substrates [5], oblique depositions are typically performed with a fixed substrate. GLAD developed as researchers realized they could manipulate the columnar structure by actively managing substrate position during deposition. Structures produced by GLAD have steadily improved in sophistication and quality as seen in Figure 13.1; modern GLAD implementations require real-time feedback and computer control of substrate position. Applications already demonstrated and those under investigation include:

- active and passive optical devices using numerous materials, providing design flexibility and creating characteristics useful in retarding elements, circular polarizers and polarized light emitters, among others;
- sensor devices (pressure sensors, optical resonators, humidity sensors, nanomotors);
- energy devices (electrochemical supercapacitors, microbattery charge storage, fuel cells, solar energy conversion).

Although GLAD has seen some impressive developments over the past 15 years, there is an extremely large parameter space available and the true complexity is not yet well understood. Empirical studies are far ahead of theoretical ones, because the key advantage of GLAD films – simultaneous control of multiple size scales – makes theoretical studies of GLAD films a challenge. Today, the dominant applications reflect large-scale effects; for example, optical properties are well understood. Even mid-range effects, such as surface area and mechanical properties, can be addressed experimentally and rest on reasonably developed theoretical models. Nanoscale applications, on the other hand, have been constrained by current limits on simulation size; as a better understanding of GLAD's nanoscale physics develops, exciting new applications of GLAD films are anticipated.

Readers interested in the technique's historical development are referred to the patents [6–8], reviews [9–12], and a book [13] which cover GLAD. This chapter focuses on experimental aspects of the GLAD technique – its methods and possibilities. Section 13.2 introduces the basic theory, and describes the canonical microstructures and apparatus required to produce GLAD films; Section 13.3 describes advanced GLAD techniques, covering procedures which occur before, during, and after a GLAD process; Section 13.4 discusses the properties of GLAD films at several length scales: single column properties, the properties of an ensemble of columns, and the 'bulk' properties of a GLAD film; and Section 13.5 reviews applications and devices made with GLAD films.

13.2 Theory, Structures and Apparatus

This section defines important terms that are used in the GLAD field to describe substrate position, geometric aspects of GLAD apparatus, film properties, and characteristic column morphologies. The first use and definition of such terms are indicated in *italic*. We note that some of the symbols used to represent the terms defined here are not used universally in the GLAD field, so some care must be exercised when examining the literature.

13.2.1 GLAD Theory

13.2.1.1 Incident Vapor Collimation

Ballistic shadowing is the foundation of GLAD-based thin film engineering. Such shadowing is only possible if the incoming vapor flux is well collimated. If there is a large angular spread in incoming vapor flux, shadows will be poorly defined. Two main approaches achieve collimated vapor flux: large distance between vapor source and substrate, and physical obstacles which select a subset of an uncollimated vapor plume. For a fixed substrate size, as distance from the source increases, incident vapor collimation improves. However, the number of collisions also increases the farther the vapor flux travels before reaching the substrate. To fabricate high-quality structures, the vapor mean free path should be larger than the source–substrate distance. This is easily achieved with electron-beam evaporation systems, widely used for GLAD depositions.

However, some materials are not suited to electron-beam or other evaporation methods. Techniques such as sputtering may be used, but at the cost of a wider angular distribution due to large target size and scattering from the working gas. In such cases, a physical screen which selects a subset of incident flux can restore collimation [14]. If even higher pressures must be used, alternative deposition techniques can maintain GLAD conditions. Sun et al. demonstrated reactive-pulsed-laser deposition of GLAD ZnO films at 0.1 torr, approximately three orders of magnitude above typical electron beam pressures [15, 16]. GLAD was still possible at such high pressures owing to an extremely oblique vapor flux, and a laser focal spot of $\sim 3\,\text{mm}^2$ which produces a very small angular distribution.

13.2.1.2 Film Nucleation and Column Growth

The previous chapter detailed film nucleation, growth, and microstructure evolution. Here we discuss only aspects of film nucleation that are important for producing GLAD thin films. During oblique deposition at an angle α, defined in Figure 13.2(a), any surface topology is amplified by ballistic shadowing. A nominally planar substrate will roughen through Volmer–Weber mode growth; any defects in the substrate will accelerate roughening [17]. This initial stage of GLAD film growth is given schematically in Figure 13.2(a).

The arrival of vapor flux and formation of film nuclei is a random process. The nuclei grow into columns, seen in Figure 13.2(b), and develop shadows. The columns and shadows they cast will have a size distribution. As a result, some nuclei will screen neighboring nuclei from incoming vapor flux, suppressing their growth (Figure 13.2c). Given sufficient time, smaller nuclei and columns can become completely shadowed and stop growing. This process, referred to as *column extinction* and seen schematically in Figure 13.2(d), continues throughout the growth of a GLAD film.

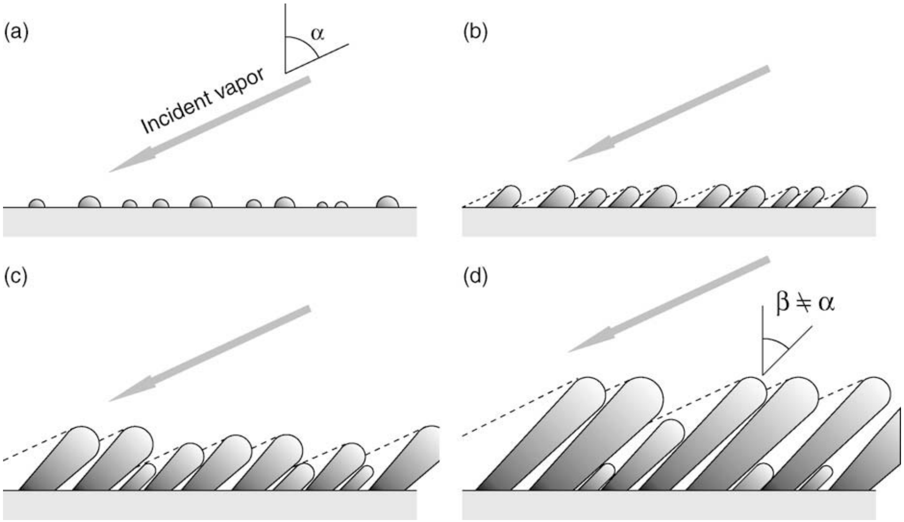

Figure 13.2: Schematic view of GLAD growth: (a) initial arrival of vapor flux at an angle α, producing a random distribution of nuclei on substrate surface; (b) nuclei grow, casting shadows across substrate; (c) columns develop, partially shadowing smaller neighbors and suppressing their growth; (d) columns grow at an inclined angle. Some columns have become extinct, fully shadowed by larger neighbors. Further growth is restricted to the top of columns.

As the nuclei grow, more incoming vapor flux will deposit on them. This self-reinforcing behavior develops isolated columns, provided that adatom surface mobility is low. Thus, GLAD principally occurs in zone I of Movchan and Demchishin's structure zone model [18], where $\mathrm{T}_{\mathrm{substrate}} \sim \leq 0.3T_{\mathrm{melting}}$ limits surface diffusion, leading to the formation of columnar grains. Eventually, only the top of nuclei are able to grow, developing into columns tilted towards the vapor source. *Column tilt angle* is described by a single angle, β, shown in Figure 13.2(d). When a column is parallel with the substrate normal, $\beta = 0°$, and would be $= 90°$ for a column parallel with the substrate surface. For some of the GLAD structures described in Section 13.2.2, it is possible to exhibit multiple values for β. Section 13.2.1.3 gives a detailed discussion of the variables affecting column tilt angle.

13.2.1.3 Column Tilt Angle

It has long been known that column tilt angle in oblique depositions does not fully follow the incidence angle of vapor flux. Various rules have been proposed to describe this behavior, but the experimental data reveal a dependence that cannot be described by a single relationship. The growth of GLAD columns depends on shadowing between columns, deposition temperature, deposition rate, deposition pressure, vacuum composition, substrate type, substrate preparation, and preferred crystallinity of the deposited material. Under these conditions, the general relationships known as the tangent rule and Tait's rule must be understood as guidelines only. For applications in which precise column tilt angle is important, these rules should be verified for any material system that has not been studied in the literature.

The tangent rule was one of the early attempts to describe the experimental data by Nieuwenhuizen and Haanstra [19], who proposed the relationship

$$\tan\alpha = 2\tan\beta \tag{13.1}$$

Hodgkinson et al. generalized the tangent rule, adding a fitting parameter that could be used to describe differences in material tilt angles [20]. However, as the deposition angle becomes increasingly oblique, the tangent rule fails to describe experimental data. Using a ballistic model for columnar growth, Tait et al. derived the following relationship [21]:

$$\beta = \alpha - \arcsin\left(\frac{1-\cos\alpha}{2}\right) \tag{13.2}$$

Although these rules can successfully provide a first order approximation of the expected behavior of β, the actual behavior of GLAD films can be perturbed from these relationships by several factors. Increased temperature has been shown to reduce β [22, 23], although non-monotonic behavior has also been observed [24]. Increased deposition rate has been shown to increase β for Fe thin films [25, 26], as has decreasing chamber pressure [25, 27]. Data from Lintymer et al. suggest that the effect of chamber pressure is more pronounced at higher α [27]. Differences between materials are observed [20], and different crystalline phases of a single material can have a significant effect [26]. The interaction between substrate and deposited film can also have an impact, and must be determined on a case-by-case basis [24]. Finally, some advanced GLAD substrate motion control techniques can decrease β in a controlled manner (see Section 13.3.2.1) and limited increases can be achieved through techniques such as ion-assisted GLAD (see Section 13.3.2.4).

13.2.1.4 Film Density

As part of Tait's geometric model for column growth, an expression for GLAD film density was derived [21]. Density is expressed in terms of ρ_0, the density of a film deposited at $\alpha = 0°$, and may be written as

$$\rho = \rho_0 \frac{2\cos\alpha}{1 + \cos\alpha} \tag{13.3}$$

Once again, this relationship can successfully provide a first order approximation of ρ, but the same caveats expressed in Section 13.2.1.3 about the tangent and Tait's rule also apply here. Exceptions to this relationship are known to exist, and for applications sensitive to small variations in density this equation must be verified.

13.2.2 Basic GLAD Structures

Substrate orientation is described in terms of two angles, defined in Figure 13.3. The deposition angle, α, defines the incidence angle of vapor flux: an α of 0° occurs when the substrate normal is pointed directly at the source; an α of 90° occurs when the substrate normal is perpendicular to a line between the center of the substrate and the center of the vapor source. The substrate rotation angle, ϕ, defines the azimuthal substrate position relative to an arbitrary starting position. While ϕ is periodic, in practice tracking the absolute angular displacement of

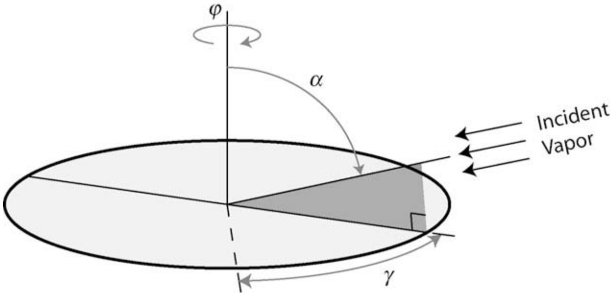

Figure 13.3: Schematic of the substrate coordinate system, showing the angle α, ϕ, and γ. The incident vapor vector and substrate normal define the deposition plane.

a substrate is useful. In this chapter, substrate positions will be described using an ordered pair notation: (α, ϕ). For some advanced techniques, it is useful to define an *offset angle*, γ, describing a temporary deviation from ϕ. This angle will be recorded separately: $(\alpha, \phi+\gamma)$.

Analogous to optics, we define *deposition plane*, defined by the substrate normal and a line connecting the center of the substrate with the center of the vapor source. Shadowing occurs only in the direction parallel to the incident vapor flux. As a result, there is no mechanism for limiting column growth in the transverse direction, leading to column broadening. The columns can continue broadening until they merge with adjacent columns [28]. Some methods discussed in Section 13.3 are designed to minimize the effects of column extinction and broadening.

The basic GLAD structures are shown in Figure 13.4, categorized by the variation of α and ϕ during deposition. The behavior of both α and ϕ is broken into three categories: constant, discrete and continuous. A constant designation means that the substrate remains stationary at a given angle during a deposition. A discrete designation means that the substrate undergoes periodic changes in a given angle, but remains stationary otherwise. A continuous designation means the substrate is in motion continuously during a deposition for the specified angle. While most examples of discrete and continuously varying substrate positions are periodic, there is no requirement that periodicity be retained. There are nine possible combinations of α and β motions, but only six are in common use. The six basic GLAD structures offer a wide selection of film morphologies, each of which is described below. Substrate angular velocities are described in terms of deposited film thickness (measured along substrate normal), and are denoted α' or ϕ'.

Slanted posts occur when a substrate is held stationary ((α, ϕ), $\alpha'=\phi'=0$) during a deposition. For isolated posts, α is typically above $\approx 70°$. *Chevrons* are produced by depositing a series of slanted posts. The substrate is held at (α, ϕ) for one arm of the chevron, followed by deposition of an additional arm with the substrate held at $(\alpha, \phi+\pi)$. This sequence has been repeated twice for the film shown in Figure 13.4(b). *Square spirals* fall into the same category as chevrons, but with a $\pi/2$ rotation at discrete intervals.

Vertical posts are produced by rotating the substrate at a constant rate during deposition ($(\alpha, \phi(t))$, $\alpha'=0$, $\phi'=k$). As seen in Figure 13.4(c), vertical posts can experience broadening during growth. The rate of rotation is an important parameter in controlling vertical post morphology [30]. *Helical* thin films can be produced using slower rotation rates.

A *slanted post stack* is produced with discrete changes in both α and ϕ during deposition, such that the substrate adopts the orientations: (α_1, ϕ_1), (α_2, ϕ_2), etc. For the case pictured in Figure 13.4(d), $\phi = n\pi$, where n is layer number.

High–low stacks are produced with a continuous rotation in ϕ, and discrete changes in α. Such films are well suited for optical applications: the film in Figure 13.4(e) is a Bragg stack. To

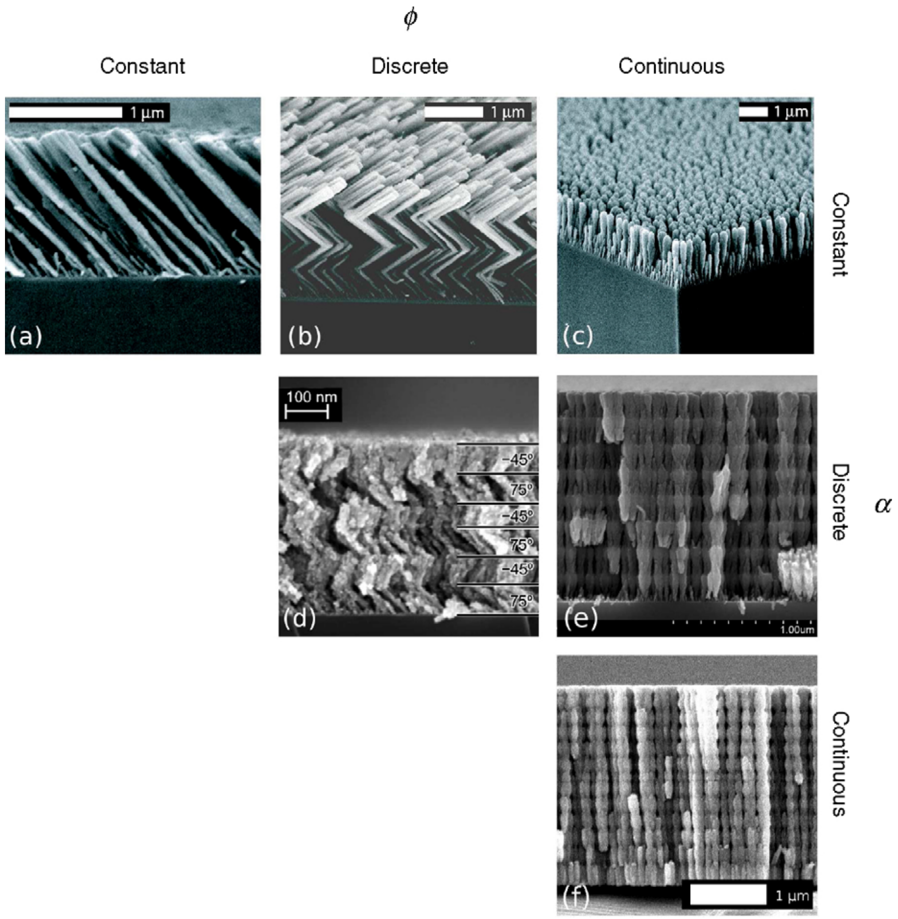

Figure 13.4: The basic GLAD structures: (a) slanted post; (b) chevron; (c) vertical post; (d) slanted post stack; (e) high–low stack and (f) rugate. These structures are fabricated using constant, discrete and continuous motion in α and β. ((a–c) Reproduced with permission from [29], (d) reprinted with permission from [108], © 2007 American Institute of Physics.)

produce a Bragg stack, the optical thickness of each layer should be λ/4. Substrate motion is defined by a repeating sequence: $(\alpha_1, \phi(t))$, $\phi' = k$; $(\alpha_2, \phi(t))$, $\phi' = k$.

Rugate filters are produced with a continuous rotation in both α and ϕ. Substrate motion can be described approximately as $(\alpha(t), \phi(t))$, $\alpha \approx a\sin(t) + \alpha_0$, $\phi' = k$. The exact functional form of α must be chosen to produce a sinuisodal index profile. The required α profile depends on the optical properties of GLAD films, discussed in Section 13.4.3.1. Capping layers and graded density films are also members of this category.

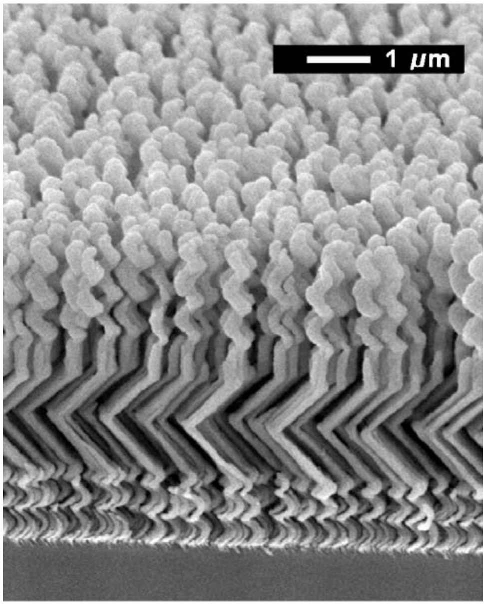

Figure 13.5: Combination of several structures from Figure 13.4. From bottom to top, this structure is composed of a helix, a one-period chevron, a short vertical post, and finished with another helix. (Reproduced with permission from [31].)

The six basic structures shown in Figure 13.4 can be combined to make very sophisticated structures, as seen in Figure 13.5. From bottom to top, this film was produced by combining a helix, chevron, vertical post, and another helix. Additional modifications to the basic structures described here are the subject of Section 13.3.

13.2.3 GLAD Apparatus

A schematic of a GLAD-capable physical vapor deposition (PVD) system is shown in Figure 13.6(a). The deposition angle α is defined as the angle subtended between the substrate normal and the incident vapor. Azimuthal rotation about the substrate normal is measured by the angle ϕ. In general, a line connecting the centers of the substrate and vapor source goes through the maximum of vapor flux plume.

Substrate rotation alters the location of the vapor source from the perspective of the growing columns. This changes the shadowing dynamics and the column growth will follow the source location. The manipulation of substrate orientation can therefore sculpt column growth, leading to the term sculptured thin film (STF), often used in the literature.

The requirements of a GLAD system vary with the required structures, since the necessary motions vary. A thorough description of a very capable system is given by Robbie et al. [11].

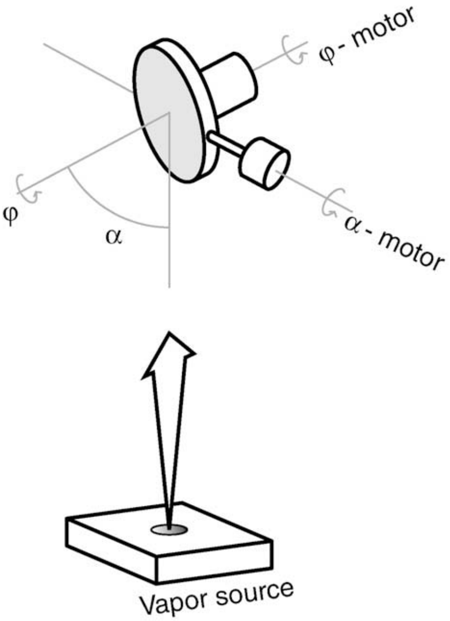

Figure 13.6: Schematic of GLAD apparatus and characteristic angles.

This section gives an overview of the requirements for a fully functional GLAD system capable of manufacturing the structures shown in Figure 13.4, and combinations thereof. In addition, system operating procedures specific to GLAD are discussed. It is worth noting that limited retrofits to existing deposition systems can make them GLAD capable.

13.2.3.1 Pressure Requirements

As discussed in Section 13.2.1.1, ballistic shadowing of incoming vapor flux is critical for GLAD. As a result, a flexible GLAD system should have a mean free path longer than the chamber dimensions. For typical systems with a source–substrate distance of ≈ 45 cm, an operating pressure of $\approx \leq 10^{-3}$ torr is required. While these constraints vary with source type used, in general a lower operating pressure is preferred for production of high-quality structures.

13.2.3.2 Vapor Sources

Many vapor sources have been used for GLAD, including electron-beam evaporation, thermal evaporation, sputtering, several co-sputtering techniques, and pulsed-laser deposition. Table 13.1 summarizes materials and vapor sources used in GLAD.

13.2.3.3 Substrate Motion

To produce the structures shown in Figure 13.4, it is necessary for the substrate to be able to assume any orientation between (0, 0) and $(\pi/2, \approx \infty)$. This may be accomplished using two

Table 13.1: Materials successfully deposited using GLAD

Material	Deposition method	Refs	Material	Deposition method	Refs
Elements			Nb_2O_5	e-beam	[34]
Aluminum	Thermal, e-beam	[30, 35, 36]	SiO	e-beam	[37, 38]
Carbon	IBS, PLD	[39–41]	SiO_2	e-beam	[32, 42]
Chromium	Thermal, sputter	[38, 43]	Ta_2O_5	e-beam	[44, 45]
Cobalt	e-beam, thermal	[46–49]	TiO_2	e-beam	[50, 51]
Copper	Sputter	[47, 52]	TiZrV	Sputter	[53]
Germanium	e-beam	[54, 55]	WO_3	Sputter, thermal	[56–58]
Iron	Thermal	[25, 26, 59]	Y_2O_3:Eu	e-beam	[60, 61]
Magnesium	e-beam	[62, 63]	YSZ	DVD, e-beam	[64–66]
Nickel	e-beam	[67]	ZnS	e-beam	[68]
Palladium	Effusion	[69]	$Zr_{65}Al_{7.5}Cu_{27.5}$	e-beam	[70, 71]
Platinum	Sputter	[72–74]	ZrO_2	e-beam	[75]
Ruthenium	Sputter	[74, 76]			
Selenium	Thermal	[77]	**Organic**		
Silicon	e-beam	[41, 47]	Alq_3	Thermal	[78, 79]
Silver	e-beam	[80–82]	C_{60}	Thermal	[83]
Tantalum	e-beam, sputter	[84, 85]	CuPc	Thermal	[86]
Tellurium	Thermal	[77]	Parylene C	Nozzle	[87]
Titanium	e-beam	[88, 89]	Pentacene	Thermal	[83]
Tungsten	Sputter	[47, 90]	PPX	Nozzle	[91]
			Znq_2	Thermal	[92]
Inorganic					
Al_2O_3	e-beam	[93, 94]	**Via templating**		
As_2S_3	Thermal	[95]	Acrylates	Spin-coating	[96]
CaF_2	Thermal	[97, 98]	Copper	Electroplating	[99]
CeO_2	e-beam	[100]	Gold	Electroplating	[101]
CrN	Sputter	[102]	HPR504	Spin-coating	[103]
GeSbSn	Thermal	[104]	LC	Spin-coating	[105]
HfO_2	e-beam	[106]	Nickel	Electroplating	[99, 101]
InN	RIP	[107]	Polystyrene	Melt infiltration	[101]
ITO	e-beam	[32, 108, 109]	Silicon	LPCVD	[110]
MgF_2	e-beam	[42, 97]	SOG	Spin-coating	[103]

DVD: directed-vapor deposition; e-beam: electron beam; IBS: ion-beam sputtering; LC: liquid crystal; PLD: pulsed-laser deposition, RIP: radio-frequency ion-plating, SOG: spin-on glass.

motors, as seen in Figure 13.6. We note that the ability to orient the substrate such that $\alpha > \pi/2$ is useful for shielding substrates from vapor flux during source conditioning, and that, in practice, ϕ should be unbounded. It is also useful to be able to monitor the absolute angular displacement of a substrate.

13.2.3.4 Monitoring Requirements

Production of high-quality GLAD structures depends on in situ, real-time measurement of the vapor flux plume to monitor deposition rate. For GLAD, *deposition rate* is defined as the increase in film thickness per unit time at the center of a substrate with an orientation of (0, 0). Monitoring deposition rate is typically accomplished with a crystal thickness monitor, and must be used to modify substrate motion to better satisfy the substrate motion algorithm. Optical in situ thickness monitoring methods are difficult in GLAD due to substrate motion, and have not yet been demonstrated.

13.2.3.5 Substrate Motion Algorithm

To take full advantage of deposition rate monitoring, substrate motion for a particular structure is defined as a series of ordered triplets. Each triplet defines a thickness (h_n) above the substrate, and a substrate orientation (α, ϕ) that should be satisfied when h_n is reached. Linear interpolation may be used between defined positions in the algorithm by the computer controlling substrate motion. Table 13.2 gives sample algorithms. By defining a target height h_n, rather than deposition time, substrate motion can be corrected to respond to changes in deposition rate, better matching the target structure.

The deposition rate is monitored by a crystal thickness monitor, and corrected for tooling to report deposition rate at the center of a substrate oriented at (0, 0). However, this rate does not correctly describe the vapor flux rate for an oblique substrate. The deposition rate must be corrected to the substrate frame of reference to satisfy the substrate motion algorithm. The *deposition ratio* is a function of α, defined as the ratio of thicknesses between a film deposited

Table 13.2: Examples of substrate motion algorithms

<table>
<tr><th colspan="2">Slanted post</th><th colspan="2">Chevron</th><th colspan="2">Slanted post stack</th><th colspan="2">Bragg stack</th></tr>
<tr><th>Height (nm)</th><th>(α, ϕ) (°)</th><th>Height (nm)</th><th>(α, ϕ) (°)</th><th>Height (nm)</th><th>(α, ϕ) (°)</th><th>Height (nm)</th><th>(α, ϕ) (°)</th></tr>
<tr><td>0</td><td>(80, 0)</td><td>0</td><td>(80, 0)</td><td>0</td><td>(85, 0)</td><td>0</td><td>(80, 0)</td></tr>
<tr><td>1000</td><td>(80, 0)</td><td>250</td><td>(80, 0)</td><td>200</td><td>(85, 0)</td><td>250</td><td>(80, 3600)</td></tr>
<tr><td></td><td></td><td>252</td><td>(80, 180)</td><td>202</td><td>(80, 180)</td><td>252</td><td>(60, 3600)</td></tr>
<tr><th colspan="2">Vertical post</th><td>500</td><td>(80, 180)</td><td>300</td><td>(80, 180)</td><td>500</td><td>(60, 7200)</td></tr>
<tr><th rowspan="2">Height (nm)</th><th rowspan="2">(α, ϕ) (°)</th><td>502</td><td>(80, 0)</td><td>302</td><td>(75, 0)</td><td>502</td><td>(80, 7200)</td></tr>
<tr><td>750</td><td>(80, 0)</td><td>700</td><td>(75, 0)</td><td>750</td><td>(80, 10800)</td></tr>
<tr><td>0</td><td>(80, 0)</td><td>752</td><td>(80, 180)</td><td>702</td><td>(65, 180)</td><td>752</td><td>(60, 10800)</td></tr>
<tr><td>1000</td><td>(80, 36000)</td><td>1000</td><td>(80, 180)</td><td>1000</td><td>(65, 180)</td><td>1000</td><td>(80, 14400)</td></tr>
</table>

The algorithms listed here will produce a film 1 μm thick, and assume a deposition rate compatible with a substrate reorientation within 2 nm of growth.

at an orientation of (α, 0) and a film deposited at (0, 0), assuming the same deposition rate and deposition time. Using the deposition ratio, it is possible to convert from the vapor deposition rate measured by the crystal thickness monitor to film height, as required.

As pointed out by Robbie et al., deposition ratios are not simply the expected cos α geometric scaling from rotating the substrate [11]. As the substrate is tilted at more oblique angles, the deposition ratio remains above the cos α dependence. This effect reflects the impact of shadowing combined with limited surface diffusion. To produce high-quality GLAD structures, a good understanding of a system's deposition rate for a given material is required. Calibration of deposition ratio can be performed by a series of depositions at different angles. The resulting data can be fitted parametrically, or by equations such as those described by Poxson et al. [32]. Substrate temperature can also affect deposition ratio through surface diffusion rates. As a result, different deposition ratios may be observed for different layers of multilayered structures as the temperature rises during deposition. Finally, column tilt angle can vary in multilayered structures, as observed by Harris et al. [33]. Such changes produce a change in deposition ratio, which must be corrected for high-quality structures.

13.2.4 Demonstrated Materials

Table 13.1 gives a selection of the materials that have been successfully deposited by GLAD. Neither the list of materials nor references are exhaustive, serving only as a starting point for the reader.

13.3 Advanced GLAD Processes

This section describes perturbations to the basic GLAD process described in Section 13.2. This section is broken up into three subsections, describing advanced techniques that are applied before, during, and after GLAD depositions. As we have seen in Section 13.2.2, complex structures can be assembled using the basic canonical structures. Similarly, many of the following techniques can be used in parallel, as they offer orthogonal improvements to the basic GLAD process.

13.3.1 Predeposition Treatment: Substrate Seeding

The ballistic shadowing process responsible for producing GLAD structures begins with the initial nucleation of deposited material. However, the nucleation process is random, and leads to a distribution in column size and random locations on the substrate surface [111, 112]. To produce a film ordered in the substrate plane, it is necessary to circumvent the randomness of nucleation. This may be achieved by introducing topography on the substrate surface, which act as 'forced' nucleation sites. While such topography need not be periodic, some of the most

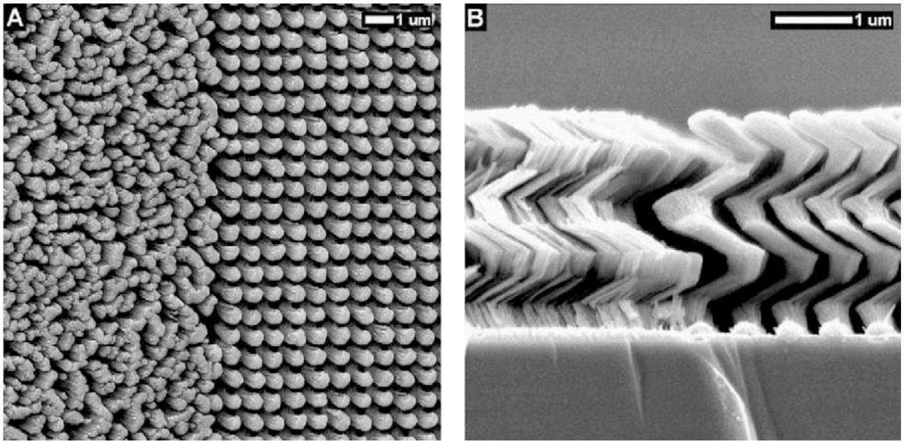

Figure 13.7: (a) Top–down and (b) cross-section SEM images of a GLAD film deposited on a substrate with an untreated (left side of both images) and seeded (right side of both images) regions. With careful design of the seeds, forced nucleation can produce GLAD films that exhibit ordering in the substrate plane. The individual GLAD columns are more uniform in the seeded region due to reduction of competitive growth. (Reproduced with permission from [113], © 2005 IEEE.)

successful examples have been produced with periodic arrays. These features act as the initial nucleation seeds for column growth.

With correct design of the shape, size, and spacing of these seeds, a single GLAD column will grow at each lattice point. Consequently, column uniformity can be greatly improved by reducing competitive growth. Figure 13.7 illustrates the difference between columns deposited on a bare substrate and on an appropriate seed layer.

The first report of GLAD onto forced nucleation sites was by Malac et al., who used electron-beam lithography to write features in PMMA resist [114]. Since then, many other researchers have used several techniques to achieve forced nucleation, including electron-beam lithography [85, 115–119], embossing [67], optical lithography [120–122], laser-direct write lithography [113, 123], monolayers of colloidal crystals [124–137], and block co-polymers [138]. While not yet demonstrated, the use of metal dot arrays fabricated using a diffraction mask and laser ablation have also been proposed as seeds for GLAD deposition [139]. In the following subsections, three rules of thumb for seed design are given, followed by a description of a more rigorous simulation method for seed design. Finally, advantages of the different seeding techniques used to date are discussed.

13.3.1.1 Seeding Theory

The first objective of forcing nucleation is to control the location of GLAD columns. This requires that growth from forced nucleation sites dominates growth elsewhere. Thus, it is desirable to maximize the incident vapor flux that deposits on the seeds, rather than allowing flux to freely impinge on the substrate and nucleate at random. This consideration produces the first rule of thumb for designing seeds. To prevent condensation between seeds for a given deposition angle α, the following condition should be satisfied,

$$\Delta \lesssim h \tan\alpha + d \tag{13.4}$$

where Δ is the center-to-center seed spacing, h is seed height, α is the deposition angle, and d is seed width [113]. When this condition is exactly satisfied, a shadow cast from one seed will just touch the base of a nearest neighboring seed. When the deposition plane is not aligned with the seed array, shadowing will not be complete. In general, deposition on the sides of seeds is not desirable, so Δ should be slightly less than the right side of Eq. (13.4).

The second objective of forced nucleation is to minimize the extinction processes that arise from competitive growth. The dependence of density on α in a GLAD film was discussed in Section 13.2.1.4. Neglecting column broadening, the in-plane density will determine the bulk density. The bulk density is determined by the macroscopic geometry of the deposition, and a GLAD film can only be perturbed from this value for short periods. For circular seeds,

$$\frac{\pi d^2}{4\Delta^2} \approx \frac{2\cos\alpha}{1+\cos\alpha} \tag{13.5}$$

where Δ, d and α are as defined in Eq. (13.4). The left-hand side of Eq. (13.5) is the fractional area covered by the seeds, and the right side is Eq. (13.3), Tait's equation for GLAD thin film density. If the fractional area covered by the seeds does not approximately match the density determined by the deposition angle α, the order initially imposed by forced nucleation will be lost as the GLAD film returns to its equilibrium density.

However, it is insufficient to simply match the expected density of the GLAD film with the fill fraction of the seeds. Equations (13.4) and (13.5) can be satisfied for any size of seed (d, h), simply by adjusting the interseed spacing Δ. In the limit, small seeds are equivalent to substrate surface roughness and large seeds are equivalent to a smooth substrate. These effects give rise to the third rule of thumb for seed design: seeds must be approximately equal in size to the expected size of a single GLAD column. An example where this rule was violated is given in Figure 13.8, where the seed size is larger than a single GLAD column, resulting in the growth of multiple columns from each seed.

If requirements for column spacing and uniformity are severe, then the simple design rules outlined above may be insufficient. In such cases, Summers has shown that a more rigorous simulation can guide seed design and deposition conditions for demanding applications [110]. In this work, seed profiles were simulated using parametric equations which captured some

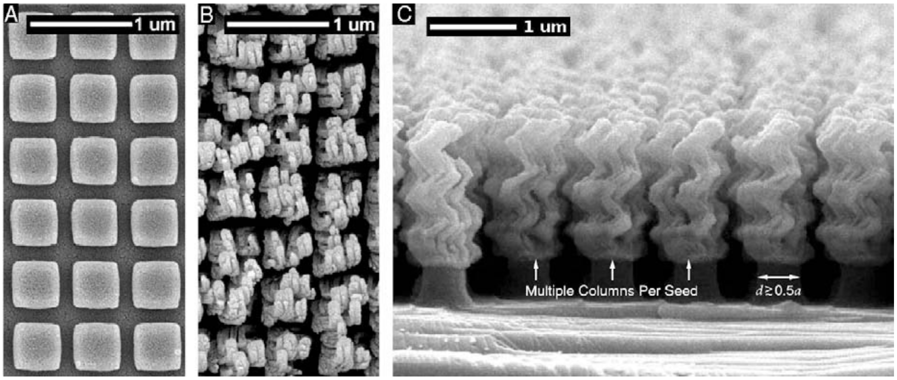

Figure 13.8: Illustration of importance of matching seed size to GLAD column diameter. Here the seeds (a) are much larger than the GLAD column diameter. Top (b) and side (c) views of multiple columns per seed. Similar effects are noted for different materials (b) is Si, while (c) is SiO_2. ((a, b) Reproduced with permission from [113], © 2005 IEEE, (c) reproduced with permission from [110].)

typical profiles found in electron-beam lithography. Seed diameter is given by

$$D(s) = D_0\left(\cos\frac{\pi s}{2}\right)^{\kappa} \tag{13.6}$$

where D is seed diameter, s is a height parameter which varies between 0 and 1, D_0 is the seed diameter at the substrate, and κ is an exponent which controls seed curvature. By projecting the shadow of such a seed, it is possible to calculate the area exposed to incoming vapor flux, known as interstitial deposition. Summers and Brett have shown that the column broadening of seeded GLAD structures improves as interstitial deposition is decreased [140]. As a result, simulation of this quantity can be used as a proxy for GLAD column quality.

Summers simulated the interstitial deposition fraction as a function of offset angle, γ, for several seed profiles, geometries, and deposition conditions [110]. This work was performed to optimize an advanced deposition method, called PhiSweep, for deposition of square spiral structures. Further details of the PhiSweep and related methods are given in Section 13.3.2.1. Some results for a square lattice of seeds, with seed parameters determined empirically from the work reported in [140], are presented in Figure 13.9. The expected decrease in interstitial deposition with increasing deposition angle and increasing fractional area coverage is observed. Moreover, the optimum offset angle is revealed by these simulations, and matches the experimental result determined by Summers and Brett [140]. Such modeling efforts can be extended to any seed profile or geometry, and used to determine the optimum deposition conditions.

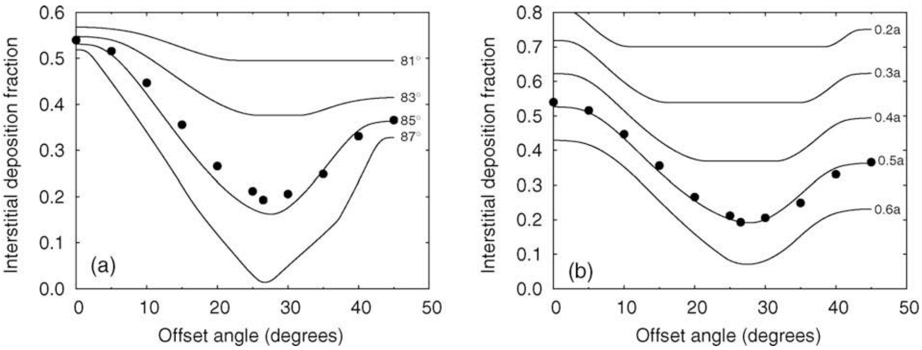

Figure 13.9: Interstitial deposition fraction as a function of (a) deposition angle and offset angle ($d = 0.49a$, $h = 0.166a$, $\kappa = 0.6$), and (b) seed diameter and offset angle ($\alpha = 85°$, $h = 0.166a$, $\kappa = 0.6$). The solid dots are experimental values from [140], and seed parameters were estimated empirically from the same source. (Adapted from [110].)

13.3.1.2 *Seeding Methods*

One additional constraint on seed design is production method. Examples from the literature are given in Figure 13.10. The previous design discussion has implicitly assumed that full control of seeds is possible. In principle, this is true of the electron-beam lithography [85, 115–119], laser direct-write lithography [113, 123], and optical lithography methods [120–122], within the resolution limits of the respective techniques. The drawback to these approaches is the long time required to produce a patterned substrate. While extremely flexible, scaling to large substrate areas may not be possible. One method that may scale to large substrate areas is embossing [67]. While embossing requires the use of a master, it retains most of the flexibility of the lithography techniques, but should be much faster since patterned substrate copies can be rapidly produced.

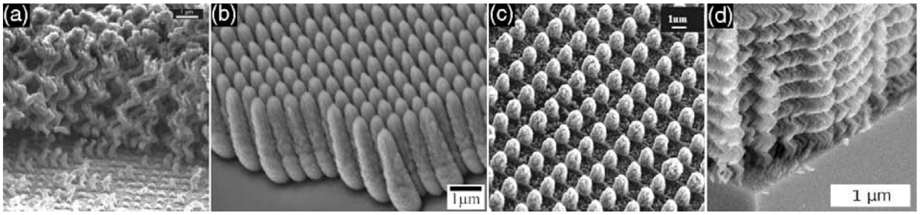

Figure 13.10: The first examples of the methods used to force nucleation in GLAD films: (a) electron beam [114]; (b) colloidal crystals [127]; (c) embossing [67]; and (d) block co-polymers [138]. ((a) Reprinted with permission from [114], © 1999 American Institute of Physics, (b) reproduced from [127] with permission from Elsevier, (c) reprinted with permission from [67], © 2001 American Chemical Society, (d) reproduced from [138].)

The other methods for seeding substrates for GLAD growth use self-assembly, and trade flexibility for speed. These include the use of colloidal crystals [124–131, 134, 135] and block co-polymers [138]. Such techniques can produce very large areas, but are typically confined to hexagonal geometries. Self-assembly techniques are also subject to crystal defects [130, 138, 141], which will adversely affect GLAD film column separation and broadening. An additional limitation of the self-assembly methods is the fixed seed spacing. As seen from the rules of thumb above, this is equivalent to reducing available deposition angles.

In practice, development of a seeding strategy might require several of these techniques in series: electron-beam lithography to explore the parameter space, and embossing or nanoprint lithography once the optimal conditions are understood. Forcing the nucleation of GLAD thin films can be a powerful technique for controlling resulting film properties. However, it is best used in combination with the advanced motion control techniques discussed in the next section.

13.3.2 Advanced Deposition Methods

In this section, we discuss modifications to the GLAD process during deposition, including advanced motion control methods, GLAD co-deposition, and substrate temperature control.

13.3.2.1 Substrate Motion Control

Columns in GLAD films tend to broaden into fan-like shapes during deposition, which can detrimentally affect film properties. To improve individual column structure, two techniques based on dynamic shadowing have been developed. As discussed in Section 13.2.1, shadowing is anisotropic, acting parallel to the deposition plane. Shadowing anisotropy may be reduced by rotating the substrate, and thus the column shadow, during deposition. Active control of the shadow forms the conceptual basis of the PhiSweep and substrate swing rotation techniques.

PhiSweep was introduced by Jensen and Brett [142]. The substrate motion in the PhiSweep method is defined by a sweep angle γ and a sweep pitch, along with the standard α and ϕ angles. The PhiSweep method, given schematically in Figure 13.11, deposits a thickness defined by the sweep pitch at a substrate orientation of $(\alpha, \phi + \gamma/2)$. The substrate is then rotated to an orientation of $(\alpha, \phi - \gamma/2)$ for a second segment, also equal to the sweep pitch. Once deposition is complete, the substrate returns to the original position for another cycle. These cycles are continued until the desired column length is obtained. Because of the symmetry of the substrate sweep, the column's net growth follows the central axis lying between the two segments along an orientation defined by (α, ϕ).

Jensen and Brett have shown that the morphology of Si columns is very sensitive to the values chosen for the PhiSweep method [142]. With a sweep pitch approximately equal to the column diameter, the PhiSweep technique produces a film composed of densely packed individual fibers 20–30 nm in width. It is thought that each change in substrate position acts as a new

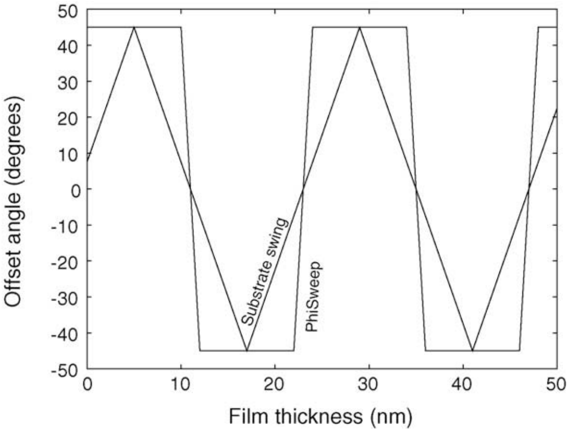

Figure 13.11: Offset angle as a function of thickness for the PhiSweep and substrate swing motion algorithms. The step function is the PhiSweep motion, the sawtooth is the substrate swing motion. Both algorithms will produce net column growth with an offset angle of 0°.

GLAD column, effectively suppressing the effects of competitive growth and column broadening.

One effect of the PhiSweep technique is a change in the effective deposition angle. Gish et al. have studied the β for PhiSweep columns deposited onto patterned substrates [143]. They have shown that the tilt angle of the PhiSweep fibers PS is related to the tilt angle of the traditional GLAD columns TG by

$$\tan \beta_{\mathrm{PS}} = \tan \beta_{\mathrm{TG}} \cos \gamma \tag{13.7}$$

Ye et al. introduced substrate swing rotation to eliminate anisotropic broadening in GLAD structures [122]. Unlike the PhiSweep method, the substrate is periodically rotated through a given angle (defined as swing angle ϕ). The motion of a substrate under this algorithm is also shown in Figure 13.11. The effects of the substrate swing method on column morphology is similar to that seen with the PhiSweep method. Column broadening is reduced, and column chaining is prevented. As seen in Figure 13.12, better defined columns are achieved, with approximately circular cross-sections in the plane of the substrate. As in the PhiSweep method, periodic rotation of the substrate changes effective deposition angle, α', given by

$$\tan \alpha' = \frac{2 \tan \alpha \sin \frac{\phi}{2}}{\phi} \tag{13.8}$$

For both the PhiSweep and substrate swing methods, the column tilt angle β will deviate from the expressions given in Section 13.2.1. The degree of deviation can be controlled using the

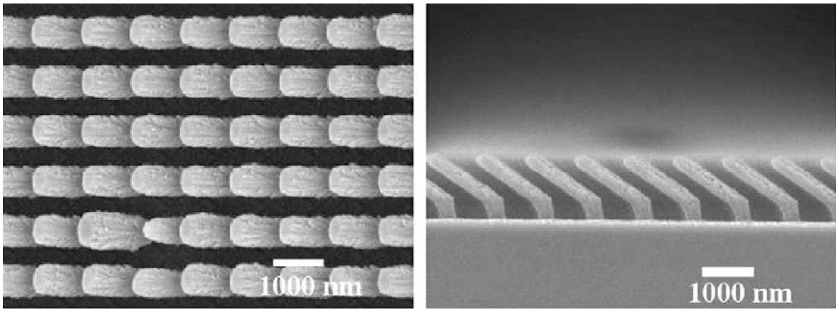

Figure 13.12: Structures produced by the substrate swing method. Excellent column uniformity is observed, and no broadening is observed. (Reproduced with permission from [122].)

analytic results of Eqs. (13.7) and (13.8). Both techniques offer an additional avenue for controlling tilt angle, partially decoupling β from α. Another method for decoupling β from α is the spin–pause method, developed by Robbie et al. [144]. In the spin–pause method, GLAD structures are fabricated by combining the growth of vertical posts (spin) and slanted posts (pause) in small segments. Although a constant α is maintained, varying the ratio of the spin mode growth and pause mode growth produces a reduced β.

The PhiSweep and substrate swing methods were introduced to minimize anisotropy in the planar cross-section of the columns. However, many physical properties of GLAD films are a product of structural anisotropy in the substrate plane. Thus, it can be desirable to maximize column broadening and enhance these properties. This has been achieved by Hodgkinson et al., who developed serial bideposition (SBD) [145]. In SBD, deposition occurs at oblique angles of incidence with rapid 180° rotations of the substrate every few nanometers of growth. In a plot like Figure 13.11, SBD would look like the PhiSweep method with an amplitude of $\pm 90^\circ$ and a period of a few nanometers. The time-averaged source direction is normal to the substrate and the net growth of the structures will be in the vertical direction. The shadowing mechanism is preserved, producing a highly pronounced structural anisotropy due to lateral broadening perpendicular to the deposition plane. This has been exploited to produce films with very high birefringence (see Section 13.5.1.1, Engineered birefringence). In a slanted column, the planar cross-section is elliptical due to competition between two effects. The first, broadening, orients the semi-major axis perpendicular to the deposition plane. The second, column tilting, orients the semi-major axis parallel to the deposition plane.

The advanced substrate motion techniques described here have the effect of modifying the available β for GLAD films. The trend for an unperturbed GLAD deposition is given by Tait's rule (Eq. 13.2). Column tilt angles below those predicted by Tait's rule can be accessed through the PhiSweep, substrate swing, SBD, and spin–pause methods. Column tilt angles above those predicted by Tait's rule are more difficult to obtain. The only method yet demonstrated in the literature is ion-assisted deposition, discussed below in Section 13.3.2.4. Using ion-assisted depositions, a small increase in β at high α can be achieved.

13.3.2.2 GLAD Co-deposition

Co-deposition techniques have long been used for GLAD films, [146–149], and have recently been the subject of intensive development [63, 71, 127, 135, 150–155]. Configurations that have been demonstrated include a single material deposited from two directions [126, 146], two materials deposited from similar directions [63, 154, 155], and two materials deposited from different directions [135, 148].

Su et al. and He et al. have studied the optical properties of oxide films with embedded Au [154] and Ag [63] nanoparticles, respectively. Such films exhibit interesting polarization properties. He et al. have produced Ti-doped Mg structures, which may have application as hydrogen storage structures [155]. Films composed of both anatase TiO_2 and monoclinic WO_3 were produced by Tesfamichael et al. for gas sensing applications [152].

Kesapragada and Gall have used GLAD co-deposition to modify the normal growth of a GLAD column [127]. First, single crystal 1.5 μm Cu columns were deposited using conventional GLAD. Then two sources located at ($\alpha = 84°$, $\phi = 0°$) and ($\alpha = 84°$, $\phi = 180°$) are used simultaneously to form Y-shaped structures, with each branch oriented toward their respective sputter source. Zhou and Gall have recently extended this work to produce columns composed of Si and Ta, shown in Figure 13.13 [135]. The columns are split longitudinally along the axis of the column, a morphology that may have piezo-activated or energy-scavenging applications.

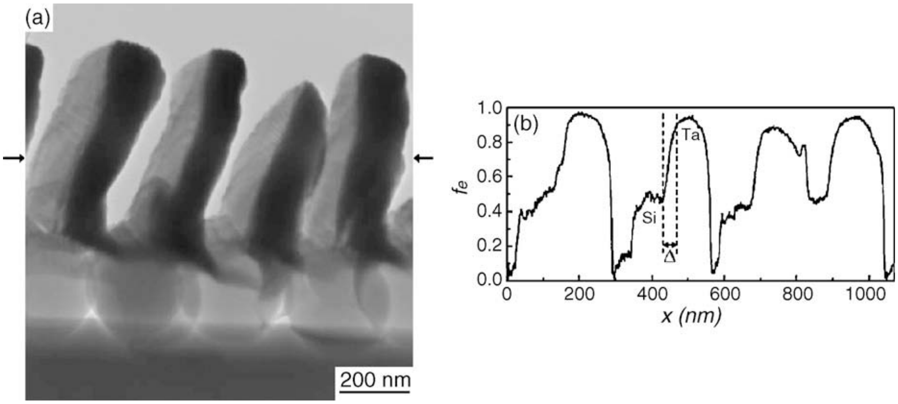

Figure 13.13: Co-deposition of Si and Ta to produce GLAD columns composed of two different materials, split along the longitudinal axis. (Reproduced with permission from [135], © Wiley-VCH.)

The use of co-deposition techniques in a GLAD system may require modification to the GLAD apparatus described in Section 13.2.3. For co-deposition methods, non-stoichiometric evaporation or sputtering will require careful calibration. In the case of sequential depositions with two different sources, a single vapor flux monitor is sufficient to control the GLAD process. For high-quality structures produced using two or more sources, independent, simultaneous measurements of each source will be required. In this case, individual vapor flux monitors must be shielded such that only one source contributes to each monitor.

13.3.2.3 Substrate Temperature Control

One of the key conditions of the GLAD deposition process is that surface diffusion is insufficient to allow adatoms to fill in ballistic shadows. During deposition, the substrate will heat through two mechanisms: direct radiative heating from the vapor source, and heating from vapor condensation on the substrate. Adatom diffusion length increases with temperature, so the effectiveness of ballistic shadowing decreases with temperature as adatoms diffuse further. Direct control of substrate temperature for GLAD has been studied by several groups [49, 69, 156–158]. GLAD depositions of Pd [69], Co [49], and TiO_2 [157] at cryogenic substrate temperatures have been reported.

A general degradation of GLAD helical structure quality has been reported by Schubert et al., who deposited Si spirals at substrate temperatures up to 475 °C [156]. Work by the same group, reported by Patzig and Rauschenbach [158], has shown that a single GLAD column can evolve through several of the classic GLAD structures: spirals, screws, and vertical posts, with carefully selected deposition conditions. Similar observations were reported by Robbie et al. for an S:O column [159].

The combination of material, deposition rate, substrate rotation rate (or algorithm), and substrate temperature together define a morphological phase space which will control the precise column morphologies produced during a GLAD deposition. The experiments reported by Robbie et al. [159] and Patzig and Rauschenbach [158] can be thought of as tracing a route through this space. There is a vast parameter space available for GLAD depositions, and only in isolated cases is the dependence of column structure on deposition parameters well understood. The careful experiments needed to understand these effects have begun, but much work remains. Another aspect of these issues, column crystallinity, is discussed in Section 13.4.1.1.

13.3.2.4 Other Advanced Methods

Ion-assisted GLAD

Ion-assisted GLAD has been studied by a few groups [50, 160–162]. The use of low-energy ion bombardment during GLAD deposition has been shown to increase β in slanted posts when the incident angle of the ion beam is less than the vapor flux deposition angle α

[50, 161]. This is likely due to resputtering of column top surfaces, leading to redeposition on the bottom surface of adjacent columns. Hodgkinson and Wu [50] and Fleischauer et al. [161] studied this effect for optical applications. Kitagawa et al. have optimized deposition angle for a scalable ion-assisted GLAD process to produce smooth diamond-like coatings [160]. Taschuk et al. have used ion-assisted GLAD to modify the density of vertical post films in an effort to improve the responsivity of relative humidity sensors [162].

External shadowing

Krause and Brett developed a modification to the GLAD technique, imposing an additional, macroscopic shadowing element which modifies GLAD depositions [163]. Their set-up and images of the resulting films are given in Figure 13.14. The addition of a cylinder at the center of a deposition chuck produces a region shadowed from incoming vapor flux. As a substrate rotates through this region, it experiences a periodic, momentary reduction in vapor flux which modifies GLAD structures. The response of helical thin films to such shadowing is seen in Figure 13.14(c–e).

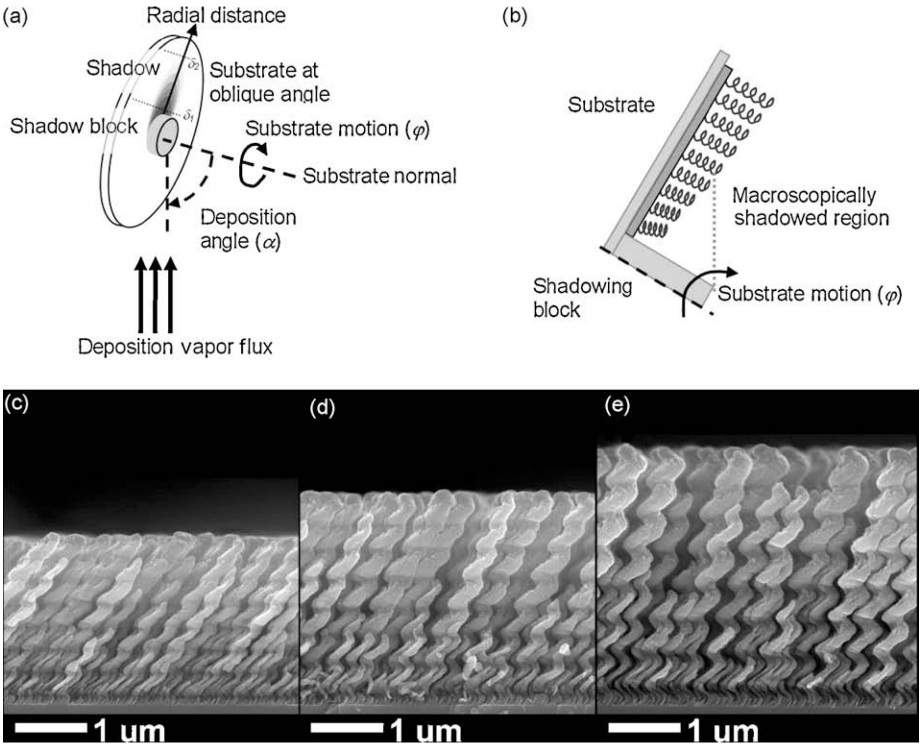

Figure 13.14: Shadowed GLAD method: (a) A shadow block placed in the center of the obliquely inclined substrate casts a shadow, resulting in (b) a graded thin film with structure defined by substrate motion. SEM images of $\alpha = 85°$ helices located (c) 1 mm, (d) 13 mm, and (e) 56 mm from shadow block edge. (Reproduced with permission from [163], © Wiley-VCH.)

Sequential GLAD

A simple way to combine the properties of different materials within a single GLAD film is to deposit different materials sequentially; a few recent examples are discussed here. A GLAD structure is grown with one material, followed by an additional deposition with a different material [153, 164–166]. This method is distinct from co-deposition, where two vapor sources are used simultaneously. Alouach et al. have deposited a GLAD Cu layer as seeds for Permalloy ($Ni_{80}Fe_{20}$) nanowire arrays [165]. Anisotropic Ag nanoparticles have been deposited on SBD SiO_2 posts for surface-enhanced Raman applications [166]. Photocatalytic properties of TiO_2 have been enhanced using WO_3 support structures [153].

13.3.3 Postdeposition Treatments

The structures available to GLAD are robust enough to survive several treatments, including annealing, etching, oxidization, chemical functionalization, and templating processes. In this section, postdeposition processing of GLAD thin films is discussed.

13.3.3.1 Annealing

Postdeposition annealing of GLAD structures is one method for achieving a crystalline, nanostructured thin film. The impact of annealing of GLAD thin films has been studied by many groups [15, 57, 60, 61, 69, 156, 157, 167–173]. Film morphologies have been widely observed to survive the annealing process [57, 156, 167, 171], although a reduction in surface area [69, 157] and thickness [61, 170] has been reported for some materials. One common application of annealing has been to activate photoluminescent materials such as Y_2O_3:Eu [60, 61, 169], ZnO [15], and Si through production of Si nanocrystals [174, 175]. Such annealing processes correct stoichiometric or crystallinity deficiencies in the as-deposited material, greatly improving the photoluminescent efficiency.

Another application of postdeposition annealing has been the blueshift of the wavelength of a circular Bragg peak [170]. In that work, Pursel et al. cite a combination of competing effects: a blueshift due to column thinning and a small reduction in circular pitch, and a redshift from TiO_2 transition (amorphous to anatase). Such competing effects complicate the use of annealing processes for GLAD films, but ellipsometric measurements can address the relative magnitude of these effects, allowing good design choices.

13.3.3.2 Density Modification: Etching and Oxidization

Although GLAD structures can take many forms, film density can be constrained. In such cases, it is possible to modify density postdeposition through etching processes which remove material [133, 176, 177], or oxidization processes which add material [178, 179]. Etching processes for GLAD thin films were first investigated in detail by Lakhtakia and Horn for tuning of optical filters [176]. Subsequent work by the same group demonstrated this effect experimentally with TiO_2 spectral hole filters [177]. In this work, Pursel et al. demonstrated a 25 nm blueshift in the wavelength of a spectral hole filter for an 80 minute etch. The leisurely rate of change suggests that precise adjustments to optical properties can be made.

Another method to modify GLAD film density while retaining the columnar structure is to oxidize the film. This approach has been explored for optical applications by Robbie et al. [178] and Summers and Brett [179]. Robbie et al. oxidized Si rugate optical filters, converting them to silica. This procedure enhances the filter's visible band transmission and reduces its average optical index. Summers and Brett oxidized Si square spirals in an effort to increase the structure's fill factor for photonic crystal applications [179]. This approach combines the high-quality structure produced by GLAD with a higher density than is usually attainable by direct deposition. Using these density modification techniques, a desired β can be achieved, without necessarily accepting the density produced by GLAD.

13.3.3.3 Chemical Functionalization

Owing to the wide selection of materials available to GLAD, it is possible to produce films that are amenable to chemical functionalization [82, 134, 180–184]. Tsoi et al. have demonstrated that GLAD structures can survive functionalization processes, and that the entire film is likely affected [180, 182]. In this work, siloxane-based functionalization was chosen for flexibility and durability of the resulting coatings [180]. Such work expands the available surface chemistry for GLAD films, which has applications in sensors and other devices. It is also possible to adjust the hydrophilicity of TiO_2 through ultraviolet irradiation. Taschuk et al. have exploited this effect, along with the photocatalytic nature of TiO_2, to develop an anti-aging procedure for relative humidity sensors [185]. The easily accessible, high surface area films produced by GLAD make excellent platforms for chemical functionalization treatments. Some applications for such treatments are discussed in Section 13.5.2.

13.3.3.4 GLAD Templating

Some materials, such as low-melting-point metals or complex organics, are difficult or impossible to deposit directly in a GLAD film. In cases where the properties of such materials must be combined with the geometric properties of a GLAD film, templating methods can be used [96, 99, 101, 103, 186]. Harris et al. developed the templating method [103] shown in Figure 13.15.

The template process begins with a GLAD film (Figure 13.15a), which is filled with an intermediate material such as photoresist (Figure 13.15b). The choice of intermediate material is important, since it must be orthogonally etchable with the template material. The intermediate material is etched to expose the top of the original GLAD film (Figure 13.15c), which is subsequently etched to produce a perforated thin film composed of the intermediate material (Figure 13.15d). Au, Ni, and polystyrene perforated thin films were produced by Elias et al. using a similar method [101].

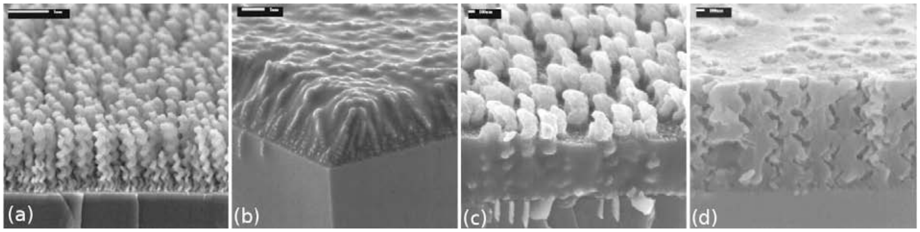

Figure 13.15: GLAD templating begins with (a) a standard GLAD film, which is (b) filled with an intermediate material such as photoresist. The photoresist is (c) etched to expose the tops of the original GLAD film, which is (d) then etched to produce a perforated thin film retaining the GLAD geometry. (Reproduced with permission from [103], © 2001, The Electrochemical Society.)

Harris et al. produced Cu and Ni GLAD copies of a SiO_2 GLAD film through a double-templating process [99]. A template is first produced using the above process, followed by electrodeposition through the perforated thin film to achieve a copy. This work was extended to organic materials by Elias et al., although vacuum filling was necessary to infiltrate the various acrylates into the perforated thin film template [96].

Summers has developed a low-pressure chemical vapor deposition (LPCVD) process for production of inverse square spirals [110], a photonic crystal structure discussed further in Section 13.5.1.1 (Photonic crystals).

13.4 Properties of GLAD Thin Films

This section discusses the properties of GLAD thin films at several different length scales. Below $\approx$100 nm, properties related to a single column dominate. Such properties include crystallinity, width and magnetic anisotropies. Between $\approx$ 100 nm and $\approx$ 1 μm, an ensemble of columns control properties such as surface area and electrical conductivity. Above 1 μm, the 'bulk' properties of the overall film control thermal and optical properties. GLAD's ability to partially decouple the different length scales in thin film fabrication makes it possible to produce materials with interesting and useful properties.

13.4.1 Column Properties

13.4.1.1 Crystallinity

Since GLAD is a low-temperature process ($T_{\text{substrate}} \sim \leq 0.3\ T_{\text{melting}}$), one does not expect a thin film with long range crystalline order to be produced during deposition. However, owing to the small size of individual GLAD columns, adatom mobility can be sufficient to produce single-crystal columns during deposition. Such columns have been produced for a wide range of materials: Al [30], Co [115], CrN [187], Cu [125, 126], Ge [54, 55], Mg [62], Sn [188], Ti-doped Mg [63], Ru [76], β-phase W [90, 189], and ZnO [190]. Crystalline organic GLAD

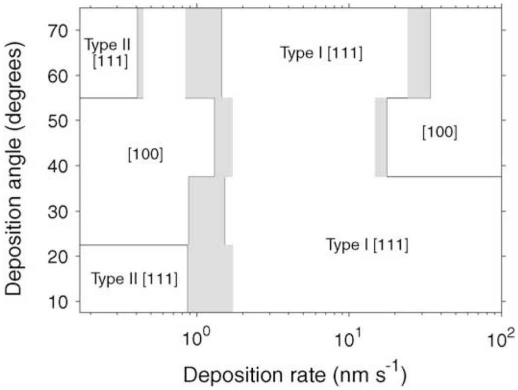

Figure 13.16: Okamoto et al. phase diagram for Fe thin film texture as a function of deposition rate and angle. Shaded regions are mixtures of phases in the horizontal direction. (Adapted from [26].)

films have also been produced for C_{60} and pentacene [83]; partially crystalline films composed of PPX derivatives have recently been reported [91]. No catalyst was required to achieve single-crystal nanorods, unlike conventional vapor–liquid–solid techniques.

Van der Drift identifies three principal factors which may introduce texture in a thin film: preferentially oriented nucleation, evolutionary or competitive selection of initially random nucleation, and postdeposition crystallization [191]. Annealing of GLAD films is discussed in Section 13.3.3; here we discuss texture formation during GLAD processes. Since different crystal faces grow at different rates, the vertical growth rate of a crystal is sensitive to its orientation. Assuming randomly oriented crystallites at the substrate, the orientation with the greatest vertical growth rate will be the most likely to survive and emerge as the dominant texture in the film. Because of its competitive nature, this principle is reminiscent of the competitive growth process found in GLAD.

Conditions under which GLAD columns become textured have been reported by many groups [25, 26, 49, 54, 55, 59, 90]. Okamoto et al. have been studying oblique deposition of Fe thin films for many years [25, 26, 59], culminating in a detailed mapping of Fe crystallinity as a function of deposition angle and deposition rate, as shown in Figure 13.16. Similar studies for Co [49] and Ge [54, 55] have been performed.

Karabacak et al. have studied single-crystal β-W formation [90]. A schematic for Karabacak's model is given in Figure 13.17. During initial growth, a mixture of α-W and β-W islands form on the substrate. However, the β-W islands are favored in GLAD growth since they have lower adatom mobilities and act as diffusion sinks for deposited adatoms. Once the β-W islands start collecting more adatoms, they will grow faster and thus tend to capture more incoming vapor flux, reinforcing the faster growth.

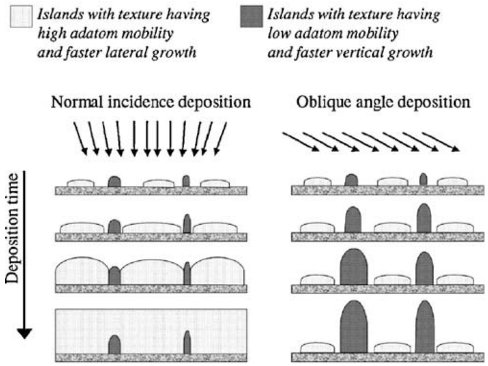

Figure 13.17: Karabacak's model for texture formation in β-W GLAD thin films. During initial nucleation, a mixture of phases is produced. Differential adatom mobility causes the β-W regions (dark gray) to act as diffusion sinks for adatoms. At oblique deposition angles, the enhanced growth rate of β-W regions is enhanced by geometric shadowing. (Reprinted with permission from [90], © 2003 American Institute of Physics.)

The relationship between column growth direction and crystallinity has been studied for several materials [24, 76, 192–197]. A preferential crystalline orientation is observed in many cases, but no general trend exists. Hagemeyer et al. have studied the deposition of Co–Cr magnetic thin films for a variety of substrates and deposition conditions for a fixed α of 45° [24]. Hagemeyer et al. note that the c axes of their films were always oriented along the column growth direction. However, Moon and Shin report that the $\langle 111 \rangle$ axes of Co-Pt films were not aligned with column growth direction [192]. The situation becomes more complicated for the case of rotating substrates [76, 193, 194]. Yamaguchi et al. observed an optimum rotation rate for producing crystalline YSZ layers by GLAD [193]. Alouach and Mankey have found a dependence of Cu crystal orientation on α and substrate rotation rate [194]. Similar results were obtained for Ru columns by Morrow et al. [76]. One final avenue of control is the expected dependence of film crystallinity on substrate material and crystallinity [24, 195].

Grain boundaries can influence column morphology during growth. Wang et al. have demonstrated that stacking faults can cause bifurcation in Cu vertical post films [125]. Through a combination of molecular dynamics simulations and experimental investigations, they were able to attribute the formation of Y-shaped columns to the interaction of stacking faults and a large diffusion barrier between different facets of the Cu crystal. By manipulating the deposition conditions, it may be possible to control this branching and use it to fabricate more complicated nanostructures.

Nanocrystallites have been observed within and on GLAD columns [119, 154, 171, 174, 175]. Indutnyy et al. have produced Si nanocrystals within SiO_2 columns by annealing SiO_2 films at

700 °C and 950 °C, followed by radio-frequency (RF) plasma passivation in a mixed H_2/N_2 atmosphere [174]. Photoluminescence from the Si nanocrystals was observed in the original report, and studied further as a function of several chemical treatments [175]. Summers et al. [119] and Schubert et al. [156] have observed the presence of similar nanocrystals, though photoluminescence was not investigated. Using a co-sputtering GLAD technique, amorphous SiO_2 columns with Au nanocrystals have been produced by Su et al. [154].

The empirical studies discussed here are ahead of theoretical or modeling efforts in this area. While some molecular dynamics work, such as that performed by Wang et al., is offering useful insights into the underlying physics governing GLAD columns, in general the size of physically interesting domains renders molecular dynamics simulations intractable. One avenue for development of this area is to make further use of the literature on magnetic materials deposited by oblique angle sputtering techniques. While the magnetic work is typically confined to $\alpha \leq 60^\circ$ and stationary substrates, it does offer some useful insight into GLAD processes.

In general, the impact of crystallinity on a particular material in a GLAD film must be evaluated on a case by case basis. While it may not be possible to control crystallinity or texture in all cases, the dependence of crystallinity on deposition angle reported by Alouach et al. and Morrow et al. suggests that the GLAD technique might offer an opportunity to control thin film crystallinity in an interesting manner. One of the common characteristics of the work presented in this section is the relatively high rotation rates: 30 rpm or higher. This may have the effect of isolating adatoms on the surface, such that crystal–adatom interactions would dominate column growth. While much work remains to be done in this area, the wide range of behaviors observed to date indicates that this is a promising area.

13.4.1.2 Column Width

Vertical post films are deposited at oblique incidence with a constant substrate rotation. Column diameter of vertical post films has been studied as a function of deposition angle and film height by many groups [91, 112, 198–202]. Column diameter is described using a power law:

$$w\,(t, \alpha) \propto t^{p(\alpha)} \tag{13.9}$$

where w is column width, t is film thickness, and p is a characteristic growth coefficient which depends on deposition angle α. Literature results for several materials are given in Figure 13.18. This work started with Karabacak et al., who derived theoretical limits for p based on interface growth models [198]. Such models exhibit two characteristic growth coefficients, describing growth parallel and perpendicular to the substrate plane projection of the incoming vapor flux. Karabacak et al. extended results applicable to the case of stationary substrates to the GLAD case by taking a geometric average of the growth coefficients. A limited range for p

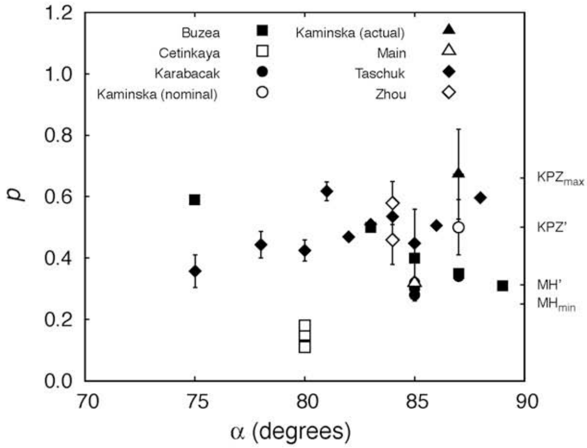

Group	Material	Reference
Buzea	Si	[200]
Cetinkaya	PPX-COCF$_3$ PPX-Cl PPX-Br	[91]
Karabacak	Co, Si, W	[198]
Kaminska	Si	[112]
Main	Si	[199]
Taschuk	TiO$_2$	[202]
Zhou	Al, Ta	[201]

Figure 13.18: Literature values for *p* from the column growth model described in the text. The theoretical limits for *p* for shadowing dominated (KPZ limit, 0.5) and diffusion dominated growth (MH limit, 0.3) are given on the right side of the plot. Both limits are violated by experimental data points. Experimental data are described in the table. Several data points and error bars are not visible due to overlap with other results.

was obtained:

$$\frac{5}{16} \leq p \leq \frac{1}{2} \tag{13.10}$$

The upper limit corresponds to shadowing dominated growth, imposed by the Kardar–Parisi–Zhang (KPZ) model. The lower limit corresponds to growth with shadowing and diffusion, imposed by the Mullins–Herring (MH) model. The interface models are well described by Barabási and Stanley [203]. Experimental values for p are given in Figure 13.18. The limits derived by Karabacak et al. are shown on the right side of the plot, denoted by KPZ$'$ and MH$'$. The minimum and maximum values for the stationary cases (MH$_{\text{min}}$ and KPZ$_{\text{max}}$) are also given.

The data in Figure 13.18 show that no consensus has yet emerged for literature values. The data given here are for many materials, listed in the table inset in Figure 13.18. While the data from Karabacak et al. and Cetinkaya et al. suggests that p varies with material, it is clear from the Buzea and Taschuk data that significant scatter exists even for a single material. This scatter is also observed between different groups, as seen by the scatter for Si columns at an α of 85°. As a result, the variation in p as a function of material reported by Karabacak and Cetinkaya may not be statistically significant.

More serious is the violation of the theoretical limits proposed by Karabacak et al. While most data are within the range given by Eq. (13.10), data from multiple groups are outside.

Interestingly, some of the values are beyond the minimum and maximum values for the stationary interface models, though this is less conclusive for the KPZ_{max} limit. Further experimental and theoretical work will be required to quantify this property of GLAD films. Given the incomplete understanding of the issues controlling the scaling of column width in GLAD films, an empirical approach for each deposited material will be necessary.

13.4.1.3 Magnetic Anisotropy

On a sufficiently small scale, surface effects and boundary conditions strongly influence the magnetic properties of structured material. Much research has examined magnetic properties of such materials and how they can be controlled by GLAD. Early studies in oblique deposition of magnetic materials observed pronounced anisotropy, where the material possesses a hard and an easy magnetization axis [28, 59, 204–209]. This anisotropy is created by the columnar structure of the deposited film and is not a product of crystallinity or strain.

Magnetic properties of slanted post films can be explained using two anisotropy fields, H_1 and H_2 [59]. Field orientation is determined by the columnar structure: H_1 is parallel to the column axis and H_2 lies in the substrate plane, orthogonal to H_1. The film planar anisotropy is the difference between H_2 and the planar projection of H_1. By varying film structure, it is possible to control the magnetic anisotropy magnitude. The magnetic anisotropy can further be tailored by simultaneously depositing two different materials from opposite directions [147, 210–213]. This produces compositionally graded columns with complicated ferromagnetic and non-ferromagnetic domain structures.

Recent research continues to examine the magnetic properties of GLAD films, with new approaches including magnetic force microscopy [46, 214], optical techniques [46, 215], and scanning tunneling microscopy [216]. These studies provide more information about anisotropy, coercivity, and domain formation in these structures.

13.4.1.4 Organic Materials

Direct organic material deposition with GLAD has been studied by several groups [78, 79, 83, 87, 91, 92]. Pursel et al. used a nozzle to direct vaporized parylene C onto a substrate at an oblique angle [87]. The parylene C subsequently polymerizes, but retains GLAD film structures. One of the more remarkable results in this area has been the Alq_3 structures produced by Hrudey et al. [78]. Scanning electron microscope (SEM) images of characteristic Alq_3 helical GLAD thin films are shown in Figure 13.19. These films are extremely smooth, exhibit excellent uniformity, and self-organize over short distances into hexagonal-close packed ordering. The deposition of organic materials with GLAD is a rapidly developing field, and interesting results are expected as these new materials are investigated.

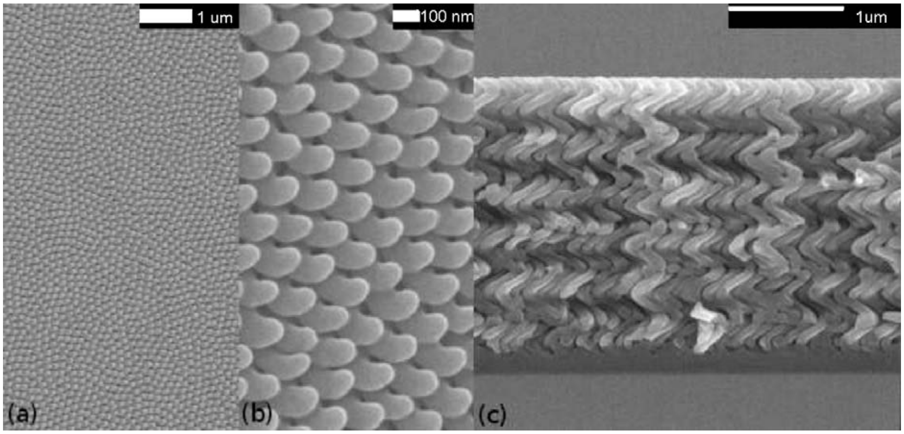

Figure 13.19: Alq_3 columns fabricated using the GLAD technique self-assemble in an ordered manner. The columns themselves maintain their shape, the number of columns and an increase in their spacing throughout the thickness of the film and exhibit a much greater uniformity from column to column. (Reproduced with permission from [169], © Wiley-VCH.)

13.4.2 Column Ensemble Properties

13.4.2.1 Interface Width

Interface width is defined by the statistical distribution of column heights. Similar to column width, it has been found to follow a power law with film thickness:

$$T_{\text{interface}}(t, \alpha) \propto t^{\beta(\alpha)} \tag{13.11}$$

where $T_{\text{interface}}$ is the interface thickness, t is film thickness, α is deposition angle, and β is a characteristic growth coefficient which depends on deposition angle α. Note that the use of β here does not represent column tilt angle. Surface roughness of GLAD films has been studied by several groups [68, 71, 73, 84, 102, 217, 218]. A summary of results for β from the literature is given in Figure 13.20. A strong dependence on deposition angle is observed, rising to a nearly linear scaling of surface roughness with film thickness for highly oblique depositions. Although only a limited data set is available from the literature, the report of Vick et al. [218] and the strong trend observed here suggests that this parameter depends less on material than the column width parameter discussed in Section 13.4.1.2.

Another measure of GLAD surface roughness can be made by treating it as a self-affine surface; this measure depends only weakly on deposition angle [73, 84]. A final point is that surface roughness depends on rotation rate [70], which may offer an additional degree of control over this property.

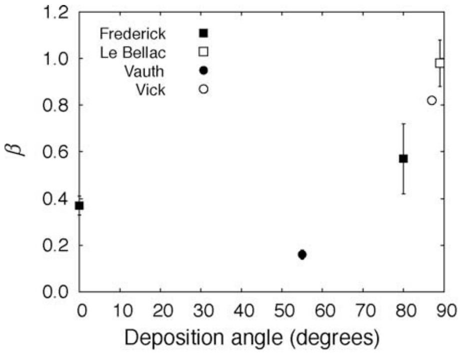

Group	Material	Reference
Frederick	CrN	[102]
Le Bellac	Cr	[217]
Vauth	$Zr_{65}Al_{7.5}Cu_{27.5}$	[71]
Vick	SiO_2, Ti	[218]

Figure 13.20: Literature values for the interface growth coefficient β. A value of $\beta = 1$ indicates that surface roughness scales linearly with film thickness. Experimental data are described in the table.

13.4.2.2 Areal Column Density

Areal column density has not been studied as much as other properties, although a few reports of specific materials have been made [38, 91, 130, 158, 219, 220]. Typical values in the range of $\approx$ 20 columns per square micrometer are observed for films at least a few hundred nanometers thick. For specific materials, a few general trends do exist. As a result of column competition, areal column density decreases with film thickness [91, 219, 220]. Similarly, increasing substrate temperature has been shown to decrease column number density [130, 158].

Column number density is closely related to column width, which is not yet well understood (see Section 13.4.1.2). In general, understanding GLAD column areal density scaling will require an improved understanding of column width scaling, which remains an open research question. Column density varies with film thickness, deposition angle, and material, and must be evaluated for any given application. In some cases, it should be possible to exert some influence over column density through the advanced substrate motion control techniques discussed in Section 13.3.2.1.

13.4.2.3 Surface Area

The columnar microstructure of GLAD films can result in large surface areas. The surface area of GLAD films has been studied in several reports, including experimental measurements [53, 69, 157, 221–226], simulations [227], and geometric estimates [142]. Figure 13.21 summarizes the experimental literature values as a function of α and material.

Surface area increases with deposition angle up to $\approx 70°$, and then decreases slightly; peak location varies with material. The surface area magnitude also depends on material, with oxides tending to exhibit higher surface areas than pure elements. The data reported by Kim et al. for Pd are an exception to this general trend, deposited at an extremely low temperature of 22 K [69]. It is clear that deposition temperature does play a significant role from the TiO_2

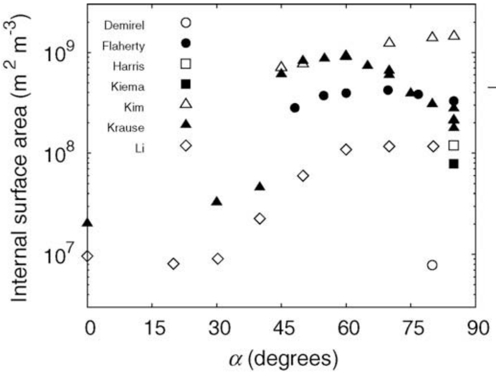

Group	Material	Reference
Demirel	PPX	[225]
Flaherty	TiO_2	[157]
Harris	SiO_2	[221]
Kiema	C	[223]
Kim	Pd	[69]
Krause	TiO_2	[226]
Li	Ti	[53, 224]

Figure 13.21: Literature values for surface area of GLAD thin films as a function of deposition angle and material. A strong dependence on material is observed. The Flaherty data and Krause data are for TiO_2. The discrepancy is attributed to different substrate temperatures during deposition: Flaherty deposited at 100 K, while Krause left substrate temperature uncontrolled. Experimental data are described in the table. Several data points are not visible due to overlap with other results.

data from Flaherty et al. and Krause et al., who deposited at 100 K and above room temperature, respectively [157, 226]. However, further work will be required to evaluate the impact of deposition temperature on GLAD surface area.

13.4.2.4 Mechanical Properties

Because GLAD films are composed of separated columns rather than a continuous solid film, interesting mechanical properties are observed. GLAD films can act as stress relief layers, and stiffness can be adjusted through film microstructure. In general, these properties are the product of an ensemble of columns, but some work has successfully isolated the mechanical properties of single GLAD columns. Some studies have also been made of the mechanical response of GLAD films to droplets encompassing an ensemble of columns.

Hardness

Hardness of GLAD films has been studied by several groups [27, 43, 95, 160, 228]. Researchers have found that hardness decreases with α, and a summary of literature results is found in Figure 13.22. Lintymer et al. have studied hardness for Cr films composed of slanted posts [27] and chevrons [43]. The data suggest that structure type and period number of a GLAD film have an effect on hardness. However, the data are noisy, and further work will be required to ascertain the magnitude of such effects.

Young's modulus

Helical columns fabricated using GLAD closely resemble springs, and many reports have been made on the Young's modulus of such structures [27, 37, 38, 43, 44, 186, 229–233]. For many

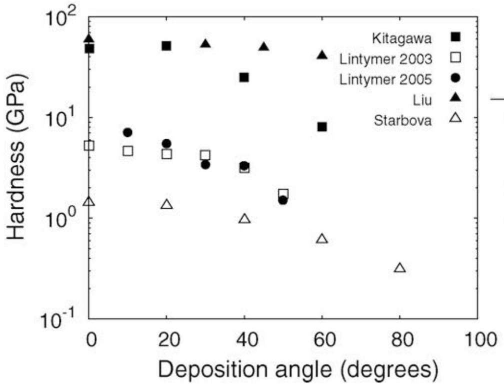

Group	Material	Reference
Kitagawa	DLC	[160]
Lintymer (2003)	Cr	[27]
Lintymer (2005)	Cr	[43]
Liu	DLC	[228]
Starbova	As_2S_3	[95]

Figure 13.22: Literature values for GLAD thin film hardness. Hardness decreases with increasing deposition angle. The Lintymer data are for Cr slanted posts (2003) and Cr chevrons (2005). Although noisy, the Lintymer data suggest that the structure type and period number of a GLAD film can affect hardness. Experimental data are described in the table. DLC: diamond-like carbon.

measurements, indentor size is large enough that an array of springs is probed in parallel, although atomic force microscopy (AFM) measurements have been made of isolated columns [229–231]. Limited measurements of shear resistance have been reported, but the result for Ta_2O_5 indicates, as expected, that GLAD films are more resistant to normally oriented stress than shear stress. The Young's modulus values exhibited by GLAD films depend on material and deposition angle. Table 13.3 summarizes literature results.

Stress

Stress in GLAD films tends to be much reduced from that found in films deposited at $\alpha = 0°$, assuming equivalent thickness. Since a GLAD film is made up of isolated columns, it is free to

Table 13.3: Young's and shear moduli of GLAD thin films

Material	Young's (GPa)	Shear (GPa)	Structure	Deflection (nm)	Ref.
Alq_3	0.93	–	Helix	3.2	[233]
Cr	140	–	Helix	60–70	[38]
	80–170[a]	–	Slanted post	–	[27]
	100–250[a]	–	Chevron	–	[43]
Ni	154	–	Inverse helix	25	[186]
Si	94 ± 10	–	Slanted post	–	[231]
SiO	92	–	Helix	60–70	[38]
Ta_2O_5	0.375	0.06	Helix	–	[44]
Ti	110	–	Helix	60–70	[38]

[a] *Non-monotonic dependence on α, measured for 0–50°.*

undergo movement that is uncoupled over short length scales, which reduces stress. Stress in GLAD films has been the subject of, or noted in, many reports [39, 159, 234–237]. Using GLAD films as stress-reduction layers has been studied by Karabacak et al. [235] for W slanted post films and Sumigawa et al. [236] for Ta_2O_5 helical films. Initial work by Robbie et al. reported a 0.01 GPa residual stress in MgF_2 thin films deposited at $\alpha = 85°$ [159, 234]. Similar results were reported by Jaing et al., who studied residual stress in MgF_2 films as a function of deposition angle [237]. Jaing's data indicate that stress depends non-linearly on α, but remains below 0.3 GPa in magnitude for $0° < \alpha < 70°$. Cuomo et al. report that stress decreases in diamond-like carbon films as deposition angle increases [39].

Nanocarpet effect

The mechanical response of an ensemble of columns to a droplet introduced to the film has been the subject of a few reports [238–240]. Such studies are important because they speak to the robustness of GLAD devices outside a controlled laboratory environment. Fan et al. studied the damage which occurs when a droplet strikes a vertical post GLAD film [238]. The authors identify a central damage region due to droplet impact, a surrounding region of columns which are tilted toward the center of the droplet as it spreads, and a final randomized region as the droplet edge percolates through the film. This work has been followed up by theoretical studies [239], and a study of droplet-induced damage as a function of GLAD structure [240]. Slanted posts were found to be the most resistant to droplet-induced damage; vertical posts the most susceptible.

13.4.2.5 Electrical Properties

Electrical properties of GLAD films have been studied by several groups [26, 27, 39, 241–243]. The development of columns can strongly affect the electrical properties of a GLAD thin film, and a few trends are observed in literature reports. First, increasing α increases in-plane resistivity as film density decreases, reducing the number of electrical pathways available [27, 243]. For thin diamond-like carbon films, resistivity decreases as incidence angle increases, probably due to an increasing number of sp^2 bonds [39]. Second, the development of columnar microstructure breaks the electrical symmetry of a GLAD thin film, exhibited as different electrical resistivities in directions parallel and perpendicular to the GLAD nanocolumns. This anisotropy also increases with α [26, 241, 243], although a maximum has been observed in Fe–Si multilayered structures [242]. GLAD film conductivity is important in sensor and solar applications.

13.4.3 Bulk Properties

13.4.3.1 Optical Properties

The microstructural and nanostructural control provided by GLAD makes it ideally suited to fabricating engineered optical materials, where optical properties are determined by the structure. In thin films produced by PVD, the link between columnar structure and the film's optical properties is well known [244, 245]. The traditional focus of PVD optical coatings is to produce homogeneous, robust, dense films. GLAD is a departure from this goal, aiming to create unique properties in thin film materials. The optics of GLAD thin films has been studied in great detail, so a very good understanding exists in the literature. Correspondingly, the dominant application of GLAD thin films has been optical.

In the earliest works on oblique deposition, researchers observed polarization-sensitive properties in obliquely deposited films [246]. Metallic films deposited at oblique incidence were found to preferentially absorb one polarization state over the other, a property known as dichroism. Similarly, transparent materials display birefringence [247]. The anisotropy observed in obliquely deposited films is not generated by crystal structure or stress, rather it is created by film structure.

In a stationary oblique deposition corresponding to a slanted post structure, the resulting film will be optically biaxial [248]. To describe such a material, three refractive indices and their respective orientations are required. These orientations are determined by the structure of the slanted post and are (i) along the column axis, (ii) lying in the plane and parallel to the broadening direction, and (iii) mutually orthogonal to the other two. A vertical post film is also anisotropic. However, because the structure is symmetric in the substrate plane only two refractive indices are required, one lying in and one perpendicular to the substrate plane [249]. The film is no longer biaxial, but instead the anisotropy is uniaxial.

Because of the structural control provided by the GLAD technique, optically isotropic materials can be engineered into anisotropic forms. Furthermore, the anisotropic magnitude and orientation can be varied throughout the thickness of the film via deposition angle adjustment. These two properties of the GLAD technique are used to fabricate polarization discriminating optics, discussed in Section 13.5.1.1.

Effective medium theories

GLAD thin films exhibit a distribution in column size, shape, and separation. Therefore, predicting film optical properties from first principles is very difficult. However, in any practical measurement, the beam spot is macroscopic in size and therefore averages over a number of columns. This immediately suggests theoretically approaching GLAD films with some sort of averaging method: exactly the basis of effective medium (EM) theory, which attempts to replace a heterogeneous structured system with a homogeneous uniform approximation that is much more amenable to further calculations [250, 251]. In general, the refractive index of a two-component mixture will depend on many parameters. We therefore define an effective refractive index n_{e},

$$n_{\mathrm{e}} = f\,(n_1, n_2, \rho_1, \lambda, \text{geometry}) \tag{13.12}$$

where n_1 and n_2 are the indices of the two components, ρ_1 is the fraction of total volume occupied by component 1 ($\rho_1 + \rho_2 = 1$), and λ is the wavelength of light (which is most often ignored based on a quasistatic approximation). n_e is also influenced by system geometry, which dictates the particular EM theory used. For example, the Maxwell–Garnett and Bruggeman EM equations can be respectively derived from a separated-grain structure and an aggregate structure [252]. The accuracy of a given EM theory depends on how well it represents the underlying microstructure of the real sample, in addition to knowing precise values for n_1, n_2, and ρ_2. That said, EM approaches have been successfully used by many researchers to approximate the properties of GLAD thin films [42, 253–256]. The anisotropy seen in GLAD films can be quantitatively understood using generalized versions of the classic Maxwell–Garnett and Bruggeman theories [257–260]. The Maxwell–Garnett equation is

$$\frac{n_e^2 - n_2^2}{n_2^2 + q_2\left(n_e^2 - n_2^2\right)} + \frac{n_2^2 - n_1^2}{n_2^2 + q_1\left(n_1^2 - n_2^2\right)}\rho_1 = 0 \tag{13.13}$$

and the Bruggeman equation is

$$\frac{n_1^2 - n_e^2}{n_e^2 + q_1\left(n_1^2 - n_e^2\right)}\rho_1 + \frac{n_2^2 - n_e^2}{n_e^2 + q_2\left(n_2^2 - n_e^2\right)}\rho_2 = 0 \tag{13.14}$$

In these theories, the constituent phases can adopt ellipsoidal shapes, providing a rough approximation of columnar structure, through the depolarization tensors q_1 and q_2. (In application, the approximation $q_1 = q_2$ is often used.) For an ellipsoid with axes a, b, c, the principal axes of the depolarization tensor are aligned with the ellipsoid and are given by

$$q_i = \frac{xyz}{2}\int_0^\infty \frac{ds}{\left(s + i^2\right)\sqrt{\left(s + a^2\right)\left(s + b^2\right)\left(s + c^2\right)}}, \quad i = a,\ b,\ c \tag{13.15}$$

Tabulation of this integral for different ratios of the axes can be found in the literature [261]. In practice, however, the depolarization values q_a, q_b, and q_c are used as fitting parameters in numerical optimization, with the added constraint that $q_a + q_b + q_c = 1$.

Optical indices

The deposited film's planar density is determined by shadow length and can, therefore, be controlled with deposition angle. Varying the amount of bulk material in the film provides a means of tuning the film's refractive index. This has been demonstrated by many researchers investigating various important optical materials. Optical constants have been reported for many materials including dielectrics (TiO_2 [256, 262, 263], Ta_2O_5 [247, 256], WO_3 [247], Nb_2O_5 [34], ZrO_2 [256, 264], HfO_2 [106], SiO_2 [42], MgF_2 [42], ZnS [68]), semiconductors

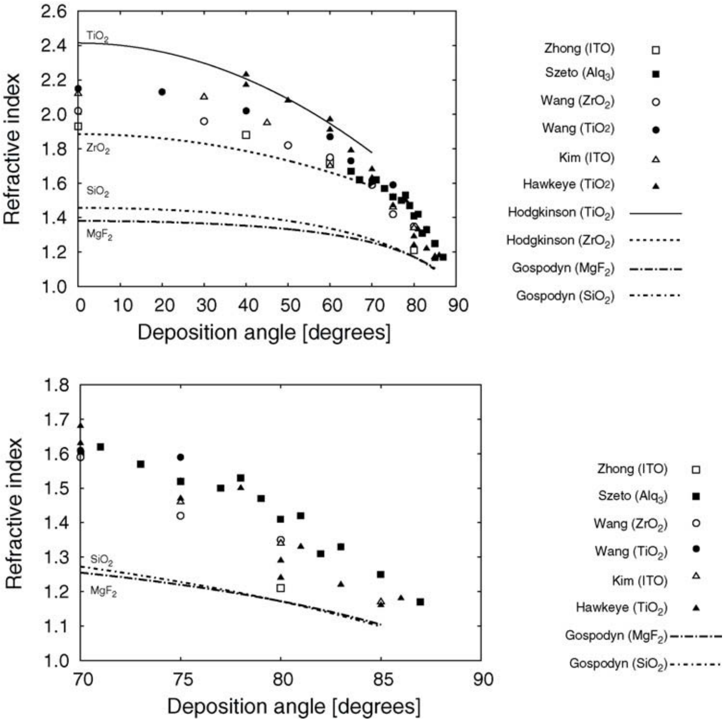

Figure 13.23: Optical index as a function of α for several optical materials. The top figure shows the full range, while the bottom figure focuses on highly oblique angles. Literature references for these and other materials may be found in the text.

(Si [249]), chalcogenides (a-As_2S_3 [95, 265], a-As_2Se_3 [265], a-$GeSe_2$ [266], GeSbSe [104]), transparent conductors (ITO [267, 268]), and organics (Alq_3 [269]).

Figure 13.23 shows several data sets taken from the literature. The general relationship between n and α is continuous and monotonic; increasing α lowers the film's planar density and reduces n. At low α, the deposited film is dense, with only a small fraction of void region, and n approaches bulk thin film values. At high α, the film is highly porous and n asymptotically approaches unity. This can be seen in Figure 13.23, where as α nears 90°, the data sets converge toward $n = 1$, regardless of material.

Of particular note in Figure 13.23 are the data sets of the same material from different publications. Wang et al., Hawkeye and Brett, and Hodgkinson et al. all studied TiO_2 structures. Wang et al. [262] and Hodgkinson et al. [256] studied slanted post structures and Hawkeye and Brett [263] examined vertical post structures. Additionally, these investigations used different measurement techniques, with Wang et al. using Swaneopel's method, Hawkeye and Brett fitting reflectance data, and Hodgkinson et al. using an ellipsometric technique. What can be seen in the data sets is good but not perfect agreement, which is quite reasonable given the sensitivity of TiO_2 films to preparation conditions [270]. A similar conclusion can be reached in the reported optical constants of ITO from Zhong et al. [268] and Kim et al. [267], and of ZrO_2 from Wang et al. [264] and Hodgkinson et al. [256]. The agreement between these data sets highlights the applicability and reproducibility of the GLAD technique in controlling refractive index. While sensitivity to preparation conditions is an issue, it is a concern in any thin film manufacturing and process variables must always be optimized.

13.4.4 GLAD Properties Summary

One of the challenges for GLAD is rooted in the very aspect that makes GLAD films of such interest: the combination of different length scales together with the corresponding physics, into a single material. As we have seen in this section, understanding the behavior of GLAD columns requires well-developed nanoscale physics. In many cases, this understanding has not yet developed. While ballistic and Monte Carlo simulation methods are well developed, they are limited by our knowledge of the physics. Molecular dynamics simulations are one way to discover new phenomena from the bottom up, and current practical simulation sizes are nearly at a useful scale for GLAD films. While increasing computer speed and improved molecular dynamics simulation techniques will ease this burden, an increased theoretical effort will be required.

As the length scale increases, the physical understanding improves. The mid-range effects, such as surface area and mechanical properties, are more easily addressed experimentally, and have a better developed set of models on which to draw. The large-scale effects, such as optical properties, are well understood, and here the design of GLAD films for particular applications becomes much more straightforward. As we will see in the next section, the dominant applications of GLAD reflect this superior understanding of the long length scale effects. However, as a better understanding of the nanoscale physics present in GLAD develops, exciting new applications of GLAD films are anticipated.

13.5 GLAD Applications

GLAD thin films have found application in many fields, exploiting the properties discussed in the previous section. The dominant application of GLAD thin films is optical, reflecting in part the well-developed theoretical support, combined with the ease with which GLAD can control structure on a scale relevant to optical applications. Many applications, including sensor, catalysis, and energy applications, rely on the extremely large surface areas of GLAD thin films. In this section, we review a selection of the diverse applications to which GLAD films have been applied. The focus is on optical and sensor applications, with brief discussions of mechanical devices, catalysis applications, magnetic data storage, energy applications, and manufacturability of GLAD thin films.

13.5.1 Optical

13.5.1.1 Passive Optical Applications

Engineered birefringence

As discussed in Section 13.4.3.1, slanted post films are inherently birefringent leading to proposed application as optical waveplates and retarding elements. Motohiro and Taga investigated various metal oxide films and developed a Ta_2O_5 quarter waveplate based on a chevronic columnar structure [247]. Harris et al. fabricated various anisotropic layers from ITO, making birefringent transparent conducting films, for flat panel display applications [109]. Hodgkinson et al. developed the SBD technique to maximize film birefringence [145, 271]. Van Popta et al. combined SBD with annealing treatments, producing TiO_2 thin films with a birefringence of $\Delta n = 0.22$, the highest reported value in SBD films [272].

Chiral filters

The ability to control the optical anisotropy orientation has led to one of the most novel applications of the GLAD technique. In a helical columnar film, the optical anisotropy twists following the helical structure. This produces a periodic rotation of the planar anisotropy which is different for circular polarization states of left-and right-handedness. Light of the same handedness as the structure undergoes a Bragg reflection whereas light of the other handedness is transmitted. This leads to an optical filter distinguishing between circular polarization states of opposite handedness, reproducing the properties of cholesteric liquid crystals in an inorganic medium [273]. The optics of such media are complicated and theoretical investigations require either 4×4 matrix techniques [255, 274, 275] or dyadic approaches [276] to deal with the varying anisotropy. The reflectance band spectral location is determined by the helix pitch (vertical period) and the film's average refractive index. Controlling the helical pitch is straightforward as it is determined by the substrate rotation speed relative to the deposition rate, allowing production of circular polarization filters for different wavelength regions [277]. By increasing the birefringence of the structure and/or the number of helical periods in the film, very strong optical effects can be achieved [278, 279]. More recent work has focused on increasingly sophisticated structures, such as helices with engineered defects [280], perturbed structures [281], polygonal helices [51], and apodized structures [282].

Optical coatings

Many researchers have fabricated GLAD optical coatings based on controlling refractive index. The refractive index can be controlled along the film thickness by changing α during deposition. Because various materials can be deposited and many refractive index profiles can be realized, the GLAD process provides significant design flexibility. Kennedy and Brett fabricated SiO_2 graded index antireflection coatings which strongly increase transmittance over a wide wavelength range [283]. The transmittance data for Kennedy's film are given in Figure 13.24 for both transverse electric (TE) and transverse magnetic (TM) polarizations and incidence angles up to 30°.

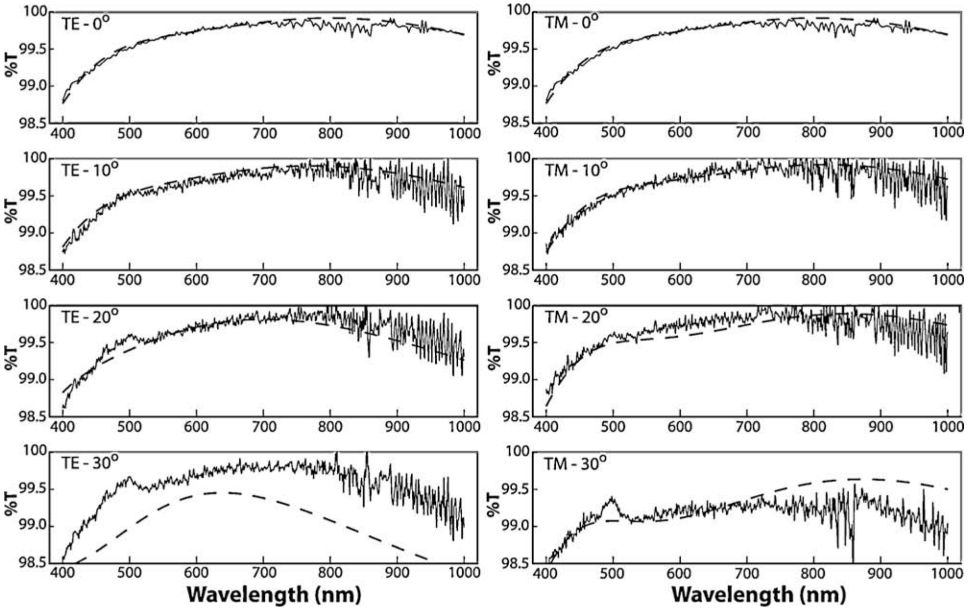

Figure 13.24: GLAD fabricated graded-index antireflection coatings demonstrate excellent performance, with a maximum of 99.9% transmittance at normal incidence. Over 99% of incident light (both TE and TM polarizations) is transmitted through the sample over a broad wavelength range 450–1000 nm even at angles up to 30°. (Reproduced with permission from [283], © 2003 Optical Society of America.)

This work has been continued and extended in SiO_2/TiO_2 [284, 285] and ITO [267] (see Figure 13.25). Multiple groups have reported fabrication of optical rugate filters, which are characterized by a sinusoidal refractive index profile. These filters have been deposited using MgF_2 [234], Si [249], SiO_2 [178], and TiO_2 [286, 287]. Bragg multilayers have also been fabricated using Si [288], TiO_2 [289], ITO [108], and Eu-doped Y_2O_3 [61]. Rugate and Bragg

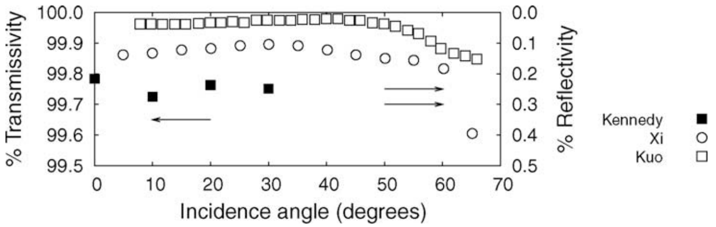

Figure 13.25: Reflectivity (TE) at 632 nm as a function of incidence angle. Closed squares are from Kennedy et al. [283] and are direct measurements of transmission. Open symbols are from Xi et al. [284] and Kuo et al. [285], and are reflectivity measurements. Vertical scales have been aligned assuming no scattering; reflectivity measurements thus represent an upper bound.

optical filter structures produce reflectance bands due to interference of light propagating through the film. Incorporating defects into the periodic index profile produces narrow peaks within the reflectance band of the film.

Photonic crystals

Another interesting application of GLAD is in the fabrication of three-dimensional (3D) photonic crystals (PCs). In a PC, the material is precisely structured to form a 3D dielectric crystal lattice. The combined effects of interference and scattering form photonic stopbands, analogous to the electronic stopbands in semiconductor crystals. The square spiral PC proposed by Toader and John, based on connecting nearest neighbors of the diamond lattice with dielectric cylinders, is amenable to fabrication with the GLAD technique [290]. SEMs of square spiral structures are shown in Figure 13.26(a, b). Inverse square spirals have also been predicted to exhibit good photonic band gap properties. Through an LPCVD process,

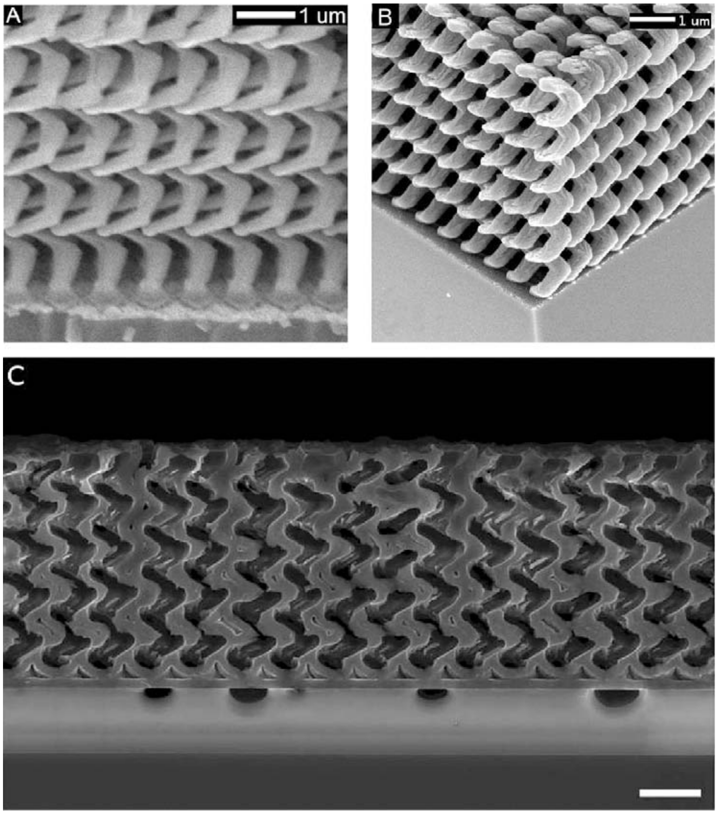

Figure 13.26: Square spiral structures, when arranged in a tetragonal lattice, are 3D photonic crystals. Direct square spirals are shown in (a) and (b), an inverse is shown in (c). ((a) Reproduced with permission from [291], © 2005 Optical Society of America, (c) reproduced with permission from [110].)

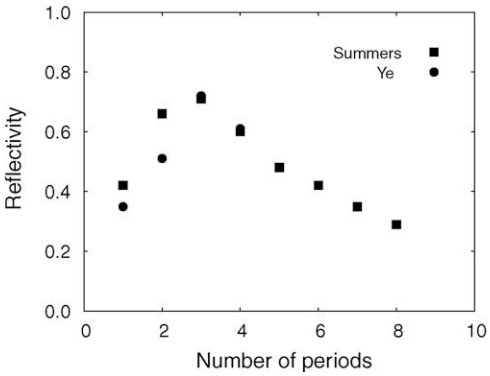

Figure 13.27: Peak band gap reflectivity from Si square spirals as a function of period number. Although an initial increase in band gap reflectivity is observed, after three periods the reflectivity decreases. Data from Summers et al. and Ye et al. (Adapted from [110].)

Summers has produced a Si inverse structure, using a square spiral as a template [110]. A cross-sectional SEM is shown in Figure 13.26(c).

Achieving the planar ordering of square spiral columns requires deposition onto lithographically patterned substrates, which was first demonstrated by Kennedy et al. [292, 293]. Through simple modification of the underlying seed template, different defects can be engineered into the PC, a prerequisite for ultracompact integrated optic device proposals [123]. Much work has been devoted to optimizing the square spiral structure, eliminating problems such as broadening and bifurcation [140, 294]. The PhiSweep and substrate swing techniques have been used to maximize the optical properties of the square spiral PC, with recent results reporting forbidden bands with bandwidths of 16.1% [140] and 14.7% [294], respectively. In the results reported by both Ye et al. [294] and Summers and Brett [140], the stopband reflectivity increases with the number of PC periods up to three periods (Figure 13.27). At this point, structural degradation becomes problematic and the reflectivity decreases.

13.5.1.2 Active Optical Applications

Liquid crystal devices

Because the GLAD films are porous, it is possible to infiltrate the film with optically interesting materials such as nematic liquid crystals (LCs) [295, 296]. Nematic LCs are electrically controllable and have been used to create a switchable GLAD device [297]. In this device, helical columns were deposited onto an electrode layer. Another electrode layer was placed on top and the resulting cell was vacuum-filled with the LCs. In the unaddressed state (zero voltage) the LCs align with the helical structure and increase the polarization selectivity of the filter. Addressing the device aligns the LC and reduces selectivity. The device can therefore be electrically switched between states. Other recent work on GLAD/LC hybrids has examined the alignment of LC molecules in the GLAD structures [298, 299].

Luminescent devices

The GLAD technique can directly fabricate structures out of luminescent materials, producing polarized light emitters. Hrudey et al. fabricated slanted and helical columnar films from Y_2O_3:Eu [60, 169]. Depending on the particular structure, these films were found to preferentially emit one polarization state over the other. The slanted posts preferentially emitted linearly polarized light, with electric field vector aligned with the column tilt, and the helical columns emitted circularly polarized light of handedness opposite to the helical structure. The polarization selectivity of these films was relatively low, owing to a degradation of the structure in thicker films. This problem was overcome by Hrudey et al. by depositing helices made of Alq_3 [78, 79]. These helices maintained their structure over many periods and displayed much improved photoluminescence properties.

13.5.2 Sensors

The high porosity, large surface area, controlled morphology, and ability to use any PVD-compatible source material make GLAD films strong candidates for sensing applications. Properties such as response time, response shape and magnitude depend on the underlying film morphology. Given the very small pore size in GLAD films, Knudsen diffusivity can be applied to vapor movement through GLAD films. Assuming a pore with 10 nm radius, and an average thermal velocity of $\sim 600\,\mathrm{m\,s^{-1}}$, a diffusivity of $\approx 4 \times 10^{-6}\,\mathrm{m^2\,s^{-1}}$ is expected. Applying Fickian diffusion yields an expected diffusion length scaling of $\sqrt{4Dt}$. Diffusion time through a 1.5 µm film should take $\approx$140 ns, orders of magnitude faster than the experimental results, which suggests that adsorption is the limiting factor in GLAD sensors, rather than diffusion. This is opposite from the behavior of typical bulk sensors, and represents an interesting opportunity for GLAD-based sensor technology.

13.5.2.1 Optical Sensors

GLAD films are inherently sensitive to the ambient environment since any fluids moving into the porous film will change the material's optical properties. This environmental sensitivity is advantageous for optical sensing applications. Lakhtakia et al. fabricated helical columns and monitored changes to the optical spectrum as liquids penetrated the film [280]. One of the weaknesses of GLAD sensors is specificity – the film will react to any gas which enters the film. Sensor specificity has been addressed in one case through chemical functionalization by van Popta et al., who reduced the hydrophilicity of a TiO_2 GLAD film [181]. Chemical functionalization was also used by Fu et al., who demonstrated fluorescence detection of *Salmonella* on Si–Au GLAD films [184].

Surface-enhanced Raman sensors

Another sensing approach which has received significant research attention is surface-enhanced Raman spectroscopy (SERS) [82, 166, 183, 219, 300, 301]. The interaction of light with metal structures is highly sensitive to the surrounding medium's dielectric constant. When molecules adsorb to the metal, they can be detected through shifts in the optical absorption peak. GLAD SERS substrates have exhibited enhancement factors as high as 5×10^8 [183], and are able to discriminate between different bacteria strains [302] and even between distinct RNA strands [301].

Reflection/transmission monitors

GLAD films have also been used in transmission or reflection modes for sensing applications [181, 303, 304]. Using a spectral hole filter, van Popta et al. [181] and Chang et al. [304] have produced sensors in which a transmission peak changes in response to changes in relative humidity. Such sensors could be fiber coupled to perform remote measurements. Zhang et al. have used a grating coated with GLAD nanorods in reflection, monitoring the adsorption of proteins on the surface through a change in the peak wavelength of a reflection peak [303].

13.5.2.2 Electrical Sensors

Electrically based sensors using GLAD films as sensing layers have been studied using many combinations of material and probe methods [94, 162, 185, 305–307]. GLAD humidity sensors typically exhibit a three order of magnitude change in capacitance combined with response times well below 100 ms. This application area is another example of the empirical development of GLAD exceeding the theoretical work. Initial attempts at modeling the electrical and temporal response of these sensors are underway [94, 202], but much work remains. An interesting use of the GLAD technique in this area was by Kanamori et al., who produced a porous electrode, allowing high-speed access to a fluorinated polyimide sensing layer [308].

13.5.2.3 Mechanical Sensors

Kesapragada and Gall created a pressure sensor from sputter-deposited Cr chevronic columns [126]. When a compressive load is applied to the film, each column elastically deforms and can contact neighboring columns. This changes the conduction path through the film, altering the film's electrical resistance. The authors loaded the film with a pressure of 0.8 MPa (an estimated force of 0.1 nN per column) while monitoring resistance with a two-point probe measurement. The resistance reversibly changed by 50% during loading–unloading cycles. Larger pressures (> 1 MPa) resulted in plastic deformation of the structure and a degradation in sensor performance.

13.5.2.4 Sensor Aging

The advantages that render GLAD a promising platform for sensor technology are also a vulnerability, since the sensing medium is open to the environment and susceptible to damage. Relative humidity sensor response has been observed to degrade significantly over a period of several days [185]. The aging process for GLAD RH sensors is not well understood, and presents an obstacle for application of such systems outside a laboratory setting. However, in the case of TiO_2 GLAD films, photocatalytic treatments have been shown to address the aging process, and it may be possible to extend such techniques to other material systems.

13.5.3 Mechanical Devices

Various devices have been developed based on the mechanical properties of GLAD microstructures, including electrically actuated devices [230, 233] and sensors [141] (see Section 13.5.2.3). Such technology could find application as standalone resonant devices or when integrated into microelectromechanical platforms. Electrically controlled actuation has been demonstrated with two approaches. Singh et al. deposited Si helical columns and coated them with a thin layer of Co (deposited by chemical vapor deposition) [230]. When a current is passed through the Co layer, a magnetic field is induced which creates an attractive force between the coils of the helix. The current is applied by an atomic force microscope. The compression of the helix can be tuned by varying the current passing through the coils, with a maximum displacement of 6 nm at a 20 mA current demonstrated by the authors. Another electrically based approach was taken by Dice et al., who fabricated Alq_3 helices between Al electrical contacts [233]. This parallel-plate capacitor arrangement creates an electrostatic force when the contacts are charged. At an applied voltage of 6 V, a 1.2 nm compression is observed.

Another approach to producing motion of GLAD structures is found in the work of He et al. [151]. Using GLAD, the authors fabricated chevronic Si columns with tips partially coated with Pt. After fabrication, the columns were ultrasonically removed from the substrate and dispersed in water. Upon adding H_2O_2, the structures rotated and moved in the solution. The structures are propelled by the decomposition of H_2O_2 into H_2O and O_2, a reaction catalyzed by the Pt layer. In addition to the chevronic structure, square spiral structures were also fabricated and catalytically propelled in a complicated 3D rolling motion. Through careful design and fabrication, it may be possible to create nanomotors based on this work.

13.5.4 Applications in Catalysis

Structured materials with high surface area are of great interest in catalysis where either the catalytic material itself is structured, or it is supported on a high surface area scaffold. Because GLAD is able to sculpt many materials into a high surface area form, there have been interesting examples of GLAD-fabricated catalysts.

Platinum is a widely used catalyst and structured GLAD Pt films have been investigated for various applications. Harris et al. fabricated Pt helices and used them to catalyze the breakdown of typical automotive exhaust compounds [72]. Bonakdarpour et al. used GLAD-fabricated titanium vertical columns as supports for Pt nanoparticles [89]. These supported catalysts had an order of magnitude greater surface area than smooth Pt films, and were used as oxygen reduction electrocatalysts for fuel cell applications.

Titanium dioxide is a photocatalytic material compatible with the GLAD process. Several groups have studied the photocatalytic properties of TiO_2 thin films [153, 173, 309], or induced changes in the surface chemistry to adjust film properties [185]. Suzuki et al. studied the photocatalytic activity of GLAD films as a function of structure and deposition angle [309], with a maximum occurring at $\approx 70^\circ$. This corresponds roughly to the maximum internal surface area for TiO_2 films, discussed in Section 13.4.2.3. Improved photocatalytic activity has been demonstrated with annealing of the TiO_2 structure [173], and fabrication of a WO_3/TiO_2 structure that enhances charge transfer [153].

13.5.5 Magnetic Tape Data Storage

Magnetic GLAD films possess anisotropic magnetic properties. Such films have high coercivities, a measure of the field required to change the film magnetization, a characteristic which is useful for information storage technologies. In particular, oblique deposition formed the basis of commercially manufactured video tape [310]. In this roll-to-roll coating process, spools of polymer tape substrate are unwound and exposed to the Co or Ni evaporation source. The source is partially shuttered and the tape receives flux from a range of oblique angles as it is pulled through the system. The fabrication of this product provides an interesting example of oblique deposition being scaled to industrial production.

Magnetic tape continues to be a mature, high-performance technology for data storage and oblique deposition is still a prominent manufacturing technique [311]. In order to achieve higher storage densities, the obliquely deposited layers must become thinner. Towards this goal, thinner films and smaller grain sizes can be achieved through the use of underlayers which serve to promote magnetic anisotropy in the subsequently deposited columnar structures [312, 313].

13.5.6 Energy Applications

There is increasing scientific, commercial, and social interest in developing clean and affordable energy technologies. In this research, nanofabrication techniques feature prominently and there are multiple examples using GLAD. Applications in this field focus on three main advantages of the GLAD technique: increased surface area, microstructural and nanostructural control, and material flexibility. Furthermore, the proven scalability and reliability of thin film production suggest reduced costs in manufacturing. The current state of research is preliminary, with basic proof-of-principle objectives being studied. More studies focusing on parameter optimization and device integration are required.

13.5.6.1 Charge Storage

Developing new and efficient charge storage devices is an important topic of energy research. Electrochemical capacitors have attracted attention because of their high energy densities, which make them suitable for applications such as battery miniaturization and hybrid vehicles [314]. Because electrochemical capacitors benefit from high surface areas, Broughton and Brett examined GLAD Mn films for application as electrochemical capacitors [222]. They report a measured specific capacitance of 256 F/g, which is only a moderate value. However, they emphasize the suitability of the process for high-throughput fabrication.

Another charge storage application of GLAD is in microbattery fabrication. Microbattery devices are being developed to improve the performance of modern electronics and microdevices such as microelectromechanical systems (MEMS). GLAD has been used to produce high surface area, structured electrodes for Li-ion rechargeable batteries. Figueroa et al. [56] deposited WO_3 vertical and helical columns and Fleischauer et al. [315] fabricated Si vertical post structures. Both studies examined the charge storage characteristics of the structured materials.

13.5.6.2 Fuel Cells

Fuel cells are a promising future source of clean energy, but significant work is required on many aspects of these devices. In order to overcome issues with efficiency, hydrogen storage, and cost many nanofabrication techniques, including GLAD, are being applied to various aspects of fuel cell technology [66, 66, 89]. Saraf et al. have studied the use of GLAD to create higher efficiency electrolytes for solid oxide fuel cells [66]. They infiltrated GLAD-fabricated yttria stabilized zirconia (YSZ) columns with a CeO_2 sol-gel solution for use as intermediate temperature electrolytes. The authors suggest that the increased CeO_2/YSZ interface area will improve the ion conduction properties of the electrolyte and lead to more efficient fuel cell performance. Bonakdarpour et al. have produced columnar Ti supports for Pt catalysts [89]. Oxygen reduction and H_2O_2 release were characterized, and a 10–15 times enhancement in electrochemical surface area over a conventional smooth Pt surface was observed. Another group is studying the properties of GLAD-fabricated structures for hydrogen storage applications. He and Zhao have fabricated Mg columns using GLAD and coated them with a V catalysis layer in a second deposition process [316]. The combination of high-surface Mg and the presence of V as catalyst improved the hydrogen storage properties of the material.

13.5.6.3 Solar Cells

Solar cells are another intensely studied clean energy source. A common approach in solar cell research is to use high surface area electrodes to improve collection efficiency. Using GLAD, Kiema et al. fabricated and tested a dye-sensitized solar cell based on annealed TiO_2 columns [168]. Xie et al. also fabricated TiO_2 columns using GLAD for use in solar cells [317]. The ability to precisely control the column structure with GLAD provides an advantage over other approaches, such as using colloidal TiO_2. GLAD has also been used in preliminary studies of organic and hybrid solar cells. Gerein et al. spin cast an organic hole transport material into the void regions of a GLAD TiO_2 columnar film creating a very high interface area between the two materials [318]. With the GLAD process, van Dijken et al. fabricated high surface area copper phthalocyanine films for use in bulk heterojunction organic solar cells [86].

13.5.7 Microfluidics

Microfluidic applications of GLAD films have been studied for a number of years [319–321]. Seto et al. produced a combination of porous vertical posts and solid walls suitable for microfluidic applications with an engineered substrate [319]. Kiema et al. employed electron-beam lithography to produce an array of ordered columns, surrounded by unseeded areas [320]. The contrast in pore size distribution between the seeded area and unseeded area allows microfluidic flow to be confined to the patterned areas. Recently, Bezuidenhout and Brett demonstrated nanostructured ultrathin layer chromatography plates with 5 μm thick SiO_2 GLAD films [321]. These devices exploit GLAD's capability to engineer structural anisotropy, and decoupled analyte movement from the solvent flow. With further development, two-dimensional chromatographic devices may be possible.

13.5.8 Manufacturability of GLAD Thin Films

The uniformity of GLAD thin films varies with structure and deposition angle, and is well discussed by Buzea et al. [322]. Film thickness for a slanted post film deposited at 70° is given in Figure 13.28. As expected, there is a significant variation with increasing distance between the vapor source and substrate position, and minimal dependence in the transverse direction.

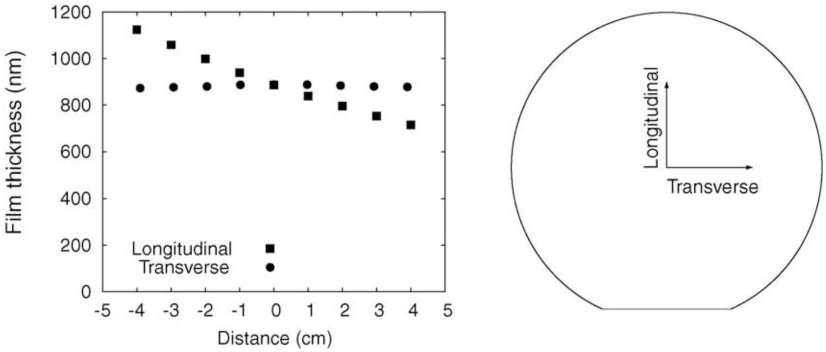

Figure 13.28: Thickness of a TiO_2 slanted post GLAD film as a function of substrate position. Since no substrate motion was used to produce the slanted posts, this represents a worst case for GLAD thin film uniformity. Directions are as defined in the schematic on the right, with the base of the arrows corresponding to (0,0). Vapor flux incident upon wafer from bottom of page with a 43 cm throw distance. A deposition angle of 70° was used. (Data courtesy of N.G. Wakefield and J.C. Sit.)

An increase in α will lead to larger variations in the longitudinal direction, but have minimal effect in the transverse direction. Since there is no substrate motion, no averaging of film flux can take place; slanted posts represent a worst case. For different structures, such as vertical posts or helices, a significant reduction in variation is observed.

13.6 Summary

GLAD is a highly flexible nanofabrication technique combining oblique angle deposition and precise manipulation of substrate position during deposition. By depositing at oblique angles, columnar structures arise owing to a combination of ballistic shadowing and limited surface diffusion. The resulting columns are tilted toward the incident flux direction, and can be sculpted into various morphologies: slanted and vertical posts, helices, chevrons, square spirals, and combinations thereof. GLAD can partially decouple the different length scales involved in thin film production, yielding novel materials with interesting properties. GLAD is compatible with a large number of materials, further increasing the combinatorial power of the GLAD technique.

Advanced GLAD techniques may offer additional control or modification of the canonical GLAD structures. Such techniques include forced nucleation through seeding and advanced substrate motion control to combat film broadening. GLAD films are robust, such that several postdeposition techniques such as annealing, etching, and oxidization can be used to further modify the structures. Many of these techniques may be applied in parallel, producing high-quality structures that may be tuned to match application needs.

GLAD can produce single-crystal columns without catalysts or postdeposition annealing. GLAD films have extremely large surface areas, and values as high as 10^9 m^2 m^{-3} have been observed. Stress in GLAD films is extremely low, because the porous structure is free to move. The refractive index of GLAD films can be tuned from a material's bulk value down to ≈ 1. The flexibility of the GLAD process has produced a variety of interesting properties, and rapid progress in the near future is expected.

While GLAD has been used for many applications, the dominant use to date is in optics. GLAD offers the unique ability to produce an engineered index gradient with a single material in a one-step deposition process, and has been used to produce high-quality optical filters. Control over 3D structure on the same length scale as optical band wavelengths has led to photonic crystal applications. Developing applications include sensors and energy applications, which depend on the large surface area of GLAD films. However, such applications are not as well developed, limited in part by insufficient understanding of the nanoscale physics accessible by GLAD thin films.

Although GLAD has seen impressive developments over the past 15 years, empirical studies are far ahead of theoretical ones. The factors controlling the fine details of column growth are not yet well understood. However, it is clear from the literature that GLAD has access to an extremely large parameter space, and with further work the full power of GLAD will become available. As physical understanding and experimental techniques improve, exciting new applications for GLAD are expected.

References

[1] A. Kundt, Annalen der Physik 27 (1886) 59.
[2] F. Kaempf, Annalen der Physik 26 (1905) 308.
[3] C. Maurin, Comptes Rendus Hebdomaires des Seances de l'Academie des Sciences 142 (1906) 870.
[4] C. Bergholm, Annalen der Physik 43 (1914) 1.
[5] N.O. Young, J. Kowal, Nature 183 (1959) 104.
[6] K. Robbie, M. Brett, Method of depositing shadow sculpted thin films, US Patent 5,866,204 (1999).
[7] K. Robbie, M. Brett, Glancing angle deposition of thin films, US Patent 6,206,065 (2001).
[8] K. Robbie, M. Brett, Shadow sculpted thin films, US Patent 6,248,422 (2001).
[9] D. Vick, J. Sit, M. Brett, Glancing angle deposition of thin films, in: Recent Developments in Vacuum Science and Technology, Research Signpost, Kerala, India (2003) 67–94.
[10] B. Dick, M. Brett, Nanofabrication by Glancing Angle Deposition, Encyclopaedia of Nanoscience and Nanotechnology 6 (2004) 703.
[11] K. Robbie, G. Beydaghyan, T. Brown et al., Rev. Sci. Instr. 75 (2004) 1089.
[12] M. Hawkeye, M. Brett, J. Vac. Sci. Technol. A 25 (2007) 1317.
[13] A. Lakhtakia, R. Messier, Sculptured Thin Films, SPIE: The International Society for Optical Engineering, Bellingham, Washington (2005).
[14] B. Dick, M. Brett, T. Smy et al., J. Vac. Sci. Technol. B 19 (2001) 1813.
[15] Y. Sun, J. Gospodyn, P. Kursa et al., Appl. Surf. Sci. 248 (2005) 392.
[16] M. Taschuk, Y. Sun, Y. Tsui, Appl. Phys. A 90 (2008) 141.
[17] C. Ratsch, J.A. Venables, J. Vac. Sci. Technol. A 21 (2003) S96.
[18] B.A. Movchan, A.V. Demchishin, Fiz. Metal. Metalloved. 28 (1969) 653.
[19] J.M. Nieuwenhuizen, H.B. Haanstra, Philips Tech. Rev. 27 (1966) 87.
[20] I. Hodgkinson, Q.H. Wu, J. Hazel, Appl. Opt. 37 (1998) 2653.
[21] R.N. Tait, T. Smy, M.J. Brett, Thin Solid Films 226 (1993) 196.
[22] N.G. Nakhodkin, A.I. Shaldervan, Thin Solid Films 10 (1972) 109.
[23] T. Hashimoto, K. Okamoto, K. Hara et al., Thin Solid Films 91 (1982) 145.
[24] A. Hagemeyer, H. Richter, H. Hibst et al., Thin Solid Films 230 (1993) 199.
[25] K. Okamoto, T. Hashimoto, K. Hara et al., Thin Solid Films 147 (1987) 299.
[26] K. Okamoto, K. Itoh, Jpn. J. Appl. Phys. 44 (2005) 1382.
[27] J. Lintymer, J. Gavoille, N. Martin et al., Surf. Coat. Technol. 174–175 (2003) 316.
[28] D.O. Smith, M.S. Cohen, G.P. Weiss, J. Appl. Phys. 31 (1960) 1755.
[29] J. Steele, M. Brett, J. Mater. Sci. Mater. Electron. 18 (2007) 367.
[30] B. Dick, M. Brett, T. Smy, J. Vac. Sci. Technol. B 21 (2003) 2569.
[31] A. van Popta, J. Sit, M. Brett, Proc. SPIE 5464 (2004) 198.
[32] D. Poxson, F. Mont, M. Schubert et al., Appl. Phys. Lett. 93 (2008) 101914.
[33] K. Harris, D. Vick, T. Smy et al., J. Vac. Sci. Technol. A 20 (2002) 2062.
[34] X. Xiao, G. Dong, C. Xu et al., Appl. Surf. Sci. 255 (2008) 2192.
[35] R. Ditchburn, G. Smith, J. Appl. Phys. 69 (1991) 3769.
[36] Y. Jen, C. Yu, Appl. Phys. Lett. 91 (2007) 021109.
[37] M.W. Seto, K. Robbie, D. Vick et al., J. Vac. Sci. Technol. B 17 (1999) 2172.
[38] M.W. Seto, B. Dick, M.J. Brett, J. Micromech. Microeng. 11 (2001) 582.

[39] J. Cuomo, D. Pappas, R. Lossy et al., J. Vac. Sci. Technol. A 10 (1992) 3414.
[40] D. Vick, Y.Y. Tsui, M.J. Brett et al., Thin Solid Films 350 (1999) 49.
[41] M. Colgan, M. Brett, Thin Solid Films 389 (2001) 1.
[42] J. Gospodyn, J.C. Sit, Opt. Mater. 29 (2006) 318.
[43] J. Lintymer, N. Martin, J. Chappé et al., Surf. Coat. Technol. 200 (2005) 269.
[44] H. Kirakata, S. Matsumoto, M. Takemura et al., Int. J. Sol. Struct. 44 (2007) 4030.
[45] J. Sanchez-Valencia, A. Borras, A. Barranco et al., Langmuir 24 (2008) 9460.
[46] F. Tang, D.-L. Liu, D.-X. Ye et al., J. Appl. Phys. 93 (2003) 4194.
[47] T. Karabacak, G.-C. Wang, T.-M. Lu, J. Vac. Sci. Technol. A 22 (2004) 1778.
[48] M.T. Umlor, Appl. Phys. Lett. 87 (2005) 082505.
[49] K. Itoh, F. Ichikawa, Y. Takahashi et al., Jpn. J. Appl. Phys. 45 (2006) 2534.
[50] I. Hodgkinson, Q. Wu, Mod. Phys. Lett. B 15 (2001) 1328.
[51] A.C. van Popta, M.J. Brett, J.C. Sit, J. Appl. Phys. 98 (2005) 083517.
[52] T. Karabacak, J. DeLuca, P. Wang et al., J. Appl. Phys. 99 (2006) 064304.
[53] C. Li, J. Huang, R. Lin et al., J. Mater. Res. 23 (2008) 579.
[54] W. Choi, L. Li, H. Chew et al., Nanotechnology 18 (2007) 385302.
[55] L. Li, X. Fang, H. Chew et al., Adv. Funct. Mater. 18 (2008) 1080.
[56] R. Figueroa, T. Cruz, A. Gorenstein, J. Power Sources 172 (2007) 422.
[57] W. Smith, Z. Zhang, Y. Zhao, J. Vac. Sci. Technol. B 25 (2007) 1875.
[58] G. Beydaghyan, J. Renaud, G. Bader et al., J. Mater. Res. 23 (2008) 274.
[59] K. Okamoto, T. Hashimoto, K. Hara et al., J. Phys. Soc. Jpn. 31 (1971) 1374.
[60] P.C.P. Hrudey, M. Taschuk, Y.Y. Tsui et al., J. Vac. Sci. Technol. A 23 (2005) 856.
[61] J. Gospodyn, M. Taschuk, P. Hrudey et al., Appl. Opt. 47 (2008) 2798.
[62] F. Tang, T. Parker, H. Li et al., J. Nanosci. Nanotech. 7 (2007) 3239.
[63] Y. He, Y. Zhao, J. Wu, Appl. Phys. Lett. 92 (2008) 063107.
[64] D. Hass, A. Slifka, H. Wadley, Acta Mater. 49 (2001) 973.
[65] K. Harris, D. Vick, E. Gonzalez et al., Surf. Coat. Technol. 138 (2001) 185.
[66] L. Saraf, D.W. Matson, V. Shutthanandan et al., Electrochem. Solid State Lett. 8 (2005) A525.
[67] B. Dick, J.C. Sit, M.J. Brett et al., Nano Lett. 1 (2001) 71.
[68] S. Wang, X. Fu, G. Xia et al., Appl. Surf. Sci. 252 (2006) 8734.
[69] J. Kim, Z. Dohnálek, B. Kay, Surf. Sci. 586 (2005) 137.
[70] S. Mayr, K. Samwer, J. Appl. Phys. 91 (2002) 2779.
[71] S. Vauth, C. Streng, S. Mayr et al., Phys. Rev. B 68 (2003) 205425.
[72] K.D. Harris, J.R. McBride, K.E. Nietering et al., Sens. Mater. 13 (2001) 225.
[73] A. Dolatshahi-Pirouz, M. Hovgaard, K. Rechendorff et al., Phys. Rev. B 77 (2008) 115427.
[74] D. Ye, T. Lu, T. Karabacak, Phys. Rev. Lett. 100 (2008) 256102.
[75] M. Levichkova, V. Mankov, N. Starbov et al., Surf. Coat. Technol. 141 (2001) 70.
[76] P. Morrow, F. Tang, T. Karabacak et al., J. Vac. Sci. Technol. A. 24 (2006) 235.
[77] M. Peterson, F. Cocks, Sol. Ener. 24 (1980) 249.
[78] P.C.P. Hrudey, K.L. Westra, M.J. Brett, Adv. Mater. 18 (2006) 224.
[79] P.C.P. Hrudey, B. Szeto, M.J. Brett, Appl. Phys. Lett. 88 (2006) 251106.
[80] S. Chaney, S. Shanmukh, R. Dluhy et al., Appl. Phys. Lett. 87 (2005) 031908.
[81] Y. Zhao, S. Chaney, Z. Zhang, J. Appl. Phys. 100 (2006) 063527.
[82] D. Gish, F. Nsiah, M. McDermott et al., Anal. Chem. 79 (2007) 4228.
[83] J. Zhang, I. Salzmann, S. Rogachewski et al., Appl. Phys. Lett. 90 (2007) 193117.
[84] K. Rechendorff, M. Hovgaard, J. Chevallier et al., Appl. Phys. Lett. 87 (2005) 073105.
[85] S. Kesapragada, P. Sotherland, D. Gall, J. Vac. Sci. Technol. B 26 (2008) 678.
[86] J. van Dijken, M.D. Fleischauer, M.J. Brett, Proc. 33rd IEEE PVSC (2009).
[87] S. Pursel, M.W. Horn, M.C. Demirel et al., Polymer 46 (2005) 9544.

[88] J.C. Sit, D. Vick, K. Robbie et al., J. Mater. Res. 14 (1999) 1197.
[89] A. Bonakdarpour, M. Fleischauer, M. Brett et al., Appl. Catal. A 349 (2008) 110.
[90] T. Karabacak, A. Mallikarjunan, J. Singh et al., Appl. Phys. Lett. 83 (2003) 3096.
[91] M. Cetinkaya, N. Malvadkar, M. Demirel, J. Poly. Sci. B: Poly. Phys. 46 (2008) 640.
[92] G. Dice, M. Brett, in: MNE 2008, Athens, Greece (2008).
[93] J.J. Steele, J.P. Gospodyn, J.C. Sit et al., IEEE Sen. J. 6 (2006) 24.
[94] J. Steele, M. Taschuk, M. Brett, IEEE Sen. J. 6 (2009) 1422.
[95] K. Starbova, J. Dikova, N. Starbov, J. NonCryst. Sol. 210 (1997) 261.
[96] A.L. Elias, K.D. Harris, C.W.M. Bastiaansen et al., J. Micromech. Micromach. 15 (2005) 49.
[97] K. Robbie, M.J. Brett, A. Lakhtakia, J. Vac. Sci. Technol. A 13 (1995) 2991.
[98] H. Li, T. Parker, F. Tang et al., J. Cryst. Growth 310 (2008) 3610.
[99] K.D. Harris, J.C. Sit, M.J. Brett, IEEE Trans. Nanotech. 1 (2002) 122.
[100] I. Hodgkinson, S. Cloughley, Q. Wu et al., Appl. Opt. 35 (1996) 5563.
[101] A. Elias, K. Harris, M. Brett, J. Microelectromech. Sys. 13 (2004) 808.
[102] J. Frederick, J. D'Arcy-Gall, D. Gall, Thin Solid Films 494 (2006) 330.
[103] K. Harris, K. Westra, M. Brett, M. Electrochem, Solid State Lett. 4 (2001) C39.
[104] R. Martin-Palma, J. Ryan, C. Pantano, J. Vac. Sci. Technol. A 25 (2007) 587.
[105] A. Elias, M. Brett, K. Harris et al., Mol. Cryst. Liq. Cryst. 477 (2007) 137/[631].
[106] N. Jie, Z. Yu, Z. Qin et al., J. Am. Ceram. Soc. 91 (2008) 3458.
[107] Y. Inoue, A. Yamaguchi, T. Fujihara et al., J. Electrochem. Soc. 154 (2007) J212.
[108] M. Schubert, J. Xi, J. Kim et al., Appl. Phys. Lett. 90 (2007) 141115.
[109] K. Harris, A. van Popta, J. Sit et al., Adv. Funct. Mater. 18 (2008) 2147.
[110] M. Summers, Periodic thin films by glancing angle deposition, PhD thesis, University of Alberta, Edmonton, Alberta, Canada (2009).
[111] T. Karabacak, G.-C. Wang, T.-M. Lu, J. Appl. Phys. 94 (2003) 7723.
[112] K. Kaminska, A. Amassian, L. Martinu et al., J. Appl. Phys. 97 (2005) 013511.
[113] M.O. Jensen, M.J. Brett, IEEE Trans. Nanotech. 4 (2005) 269.
[114] M. Malac, R.F. Egerton, M.J. Brett et al., J. Vac. Sci. Technol. B 17 (1999) 2671.
[115] B. Dick, M.J. Brett, T.J. Smy et al., J. Vac. Sci. Technol. A 18 (2000) 1838.
[116] M. Malac, R.F. Egerton, J. Vac. Sci. Technol. 19 (2001) 158.
[117] M. Malac, R.F. Egerton, Nanotechnology 12 (2001) 11.
[118] M.W. Horn, M.D. Pickett, R. Messier et al., J. Vac. Sci. Technol. B 22 (2004) 3426.
[119] M. Summers, B. Djurfors, M. Brett, J. Microlith. Microfab. Microsyst. 4 (2005) 033012.
[120] D.-X. Ye, T. Karabacak, B.K. Lim et al., Nanotechnology 15 (2004) 817.
[121] M.W. Horn, M.D. Pickett, R. Messier et al., Nanotechnology 15 (2004) 303.
[122] D.-X. Ye, T. Karabacak, R.C. Picu et al., Nanotechnology 16 (2005) 1717.
[123] M.O. Jensen, M.J. Brett, J. Nanosci. Nanotech. 5 (2005) 723.
[124] A. Kosiorek, W. Kandulski, P. Chudzinski et al., Nano Lett. 4 (2004) 1359.
[125] J. Wang, H. Huang, S.V. Kesapragada et al., Nano Lett. 5 (2005) 2505.
[126] S.V. Kesapragada, D. Gall, Appl. Phys. Lett. 89 (2006) 203121.
[127] S. Kesapragada, D. Gall, Thin Solid Films 494 (2006) 234.
[128] C.M. Zhou, D. Gall, Thin Solid Films 515 (2006) 1223.
[129] C. Zhou, D. Gall, Appl. Phys. Lett. 88 (2006) 203117.
[130] C. Zhou, D. Gall, J. Vac. Sci. Technol. A 25 (2007) 312.
[131] C. Zhou, D. Gall, Appl. Phys. Lett. 90 (2007) 093103.
[132] C. Zhou, D. Gall, Thin Solid Films 516 (2007) 433.
[133] X. Zhou, S. Virasawmy, W. Knoll et al., Plasmonics 2 (2007) 217.
[134] A. Pawar, I. Kretzschmar, Langmuir 24 (2008) 355.
[135] C. Zhou, D. Gall, Small 4 (2008) 1351.

[136] C. Patzig, B. Rauschenbach, B. Fuhrmann et al., J. Appl. Phys. 103 (2008) 024313.
[137] C. Patzig, T. Karabacak, B. Fuhrmann et al., J. Appl. Phys. 104 (2008) 094318.
[138] M. Taschuk, J. Chai, J. Buriak et al., Physica Stat. Sol. C 6 (2009) 127.
[139] M. Möche, J.W. Gerlach, R. Bäder, T. Höhme, K. Zimmer, B. Rauschenbach, Phys. Stat. Sol. RRL 2 (2008) 34.
[140] M. Summers, M. Brett, Nanotechnology 19 (2008) 415203.
[141] S.V. Kesapragada, O.N.P. Victor, D. Gall, Nano Lett. 6 (2006) 854.
[142] M.O. Jensen, M.J. Brett, Appl. Phys. A 80 (2005) 763.
[143] D.A. Gish, M.A. Summers, M.J. Brett, Photon. Nanostruct. Fund. Appl. 4 (2006) 23.
[144] K. Robbie, J. Sit, M. Brett, J. Vac. Sci. Technol. B 16 (1998) 1115.
[145] I.J. Hodgkinson, Q.H. Wu, M.J. Brett et al., Vacuum deposition of biaxial films with surface-aligned principal axes and large birefringence Δn, Vol. 9 of OSA Technical Digest Series, Optical Society of America, Washington, DC (1998) 104–106.
[146] S. Keitoku, K. Nishioka, Jpn. J. Phys. 20 (1981) 1249.
[147] H. van Kranenburg, C. Lodder, Mater. Sci. Eng. R11 (1994) 295.
[148] Y. Watanabe, S. Hyodo, T. Motohiro et al., Thin Solid Films 256 (1995) 68.
[149] Y. Takeda, T. Motohiro, T. Hioki et al., J. Vac. Sci. Technol. B 16 (1998) 7.
[150] Y. He, J. Fu, Y. Zhang et al., Small 3 (2007) 153.
[151] Y. He, J. Wu, Y. Zhao, Nano Lett. 7 (2007) 1369.
[152] T. Tesfamichael, N. Motta, T. Bostrom et al., Appl. Surf. Sci. 253 (2007) 4853.
[153] W. Smith, Y. Zhao, J. Phys. Chem. C 112 (2008) 19635.
[154] X. Su, M. Li, Z. Zhou et al., J. Lumin. 128 (2008) 642.
[155] Y. He, Z. Zhang, C. Hoffman et al., Adv. Funct. Mater. 18 (2008) 1676.
[156] E. Schubert, J. Fahlteich, Th. Höche, G. Wagner, B. Rauschenbach, Nuc. Instr. Meth. Phys. Res. B 244 (2006) 40.
[157] D. Flaherty, Z. Dohnálek, A. Dohnálková et al., J. Phys. Chem. C 111 (2007) 4765.
[158] C. Patzig, B. Rauschenbach, J. Vac. Sci. Technol. A 26 (2008) 881.
[159] K. Robbie, C. Shafai, M. Brett, J. Mater. Res. 14 (1999) 3158.
[160] T. Kitagawa, K. Miyauchi, N. Toyoda et al., Jpn. J. Appl. Phys. 43 (2004) 3955.
[161] M. Fleischauer, J. Sorge, R. Joseph et al., Mater. Res. Soc. Symp. Proc. 960 (2007) 0960.
[162] M. Taschuk, J. Sorge, J. Steele et al., IEEE Sen. J. 8 (2008) 1521.
[163] K. Krause, M. Brett, Adv. Funct. Mater. 18 (2008) 3111.
[164] K. Harris. Fabrication and application of highly porous thin films, PhD thesis, University of Alberta, Edmonton, Alberta, Canada (2003).
[165] H. Alouach, H. Fujiwara, G. Mankey, J. Vac. Sci. Tecnol. A 23 (2005) 1046.
[166] M. Suzuki, W. Maekita, Y. Wada et al., Nanotechnology 19 (2008) 265304.
[167] M. Colgan, B. Djurfors, D. Ivey et al., Thin Solid Films 466 (2004) 92.
[168] G.K. Kiema, M.J. Colgan, M.J. Brett, Sol. Ener. Mater. Sol. Cells 85 (2005) 321.
[169] P. Hrudey, M. Taschuk, Y. Tsui et al., J. Nanosci. Nanotech. 5 (2005) 229.
[170] S. Pursel, M. Horn, A. Lakhtakia, Opt. Expr. 14 (2006) 8001.
[171] E. Schubert, J. Fahlteich, B. Rauschenbach et al., J. Appl. Phys. 100 (2006) 016107.
[172] X. Xiao, G. Dong, H. Qi et al., Chin. Phys. Lett. 25 (2008) 2181.
[173] Y. He, Z. Zhang, Y. Zhao, J. Vac. Sci. Technol. B 26 (2008) 1350.
[174] I. Indutnyy, I. Maidanchuk, V. Min'ko et al., J. Optoelectron. Adv. Mater. 7 (2005) 1231.
[175] I. Indutnyy, V.M.I.Yu. Maidanchuk, P. Shepelyavyi et al., Semiconductors 41 (2007) 1248.
[176] A. Lakhtakia, M. Horn, Optik 12 (2003) 556.
[177] S. Pursel, M. Horn, A. Lakhtakia, Opt. Eng. 46 (2007) 040507.
[178] K. Robbie, Y. Cui, C. Elliott et al., Appl. Opt. 45 (2006) 8298.
[179] M. Summers, M. Brett, Microelectron. Eng. 85 (2008) 1222.
[180] S. Tsoi, E. Fok, J.C. Sit et al., Langmuir 20 (2004) 10771.

[181] A.C. van Popta, J.J. Steele, S. Tsoi et al., Adv. Funct. Mater. 16 (2006) 1331.
[182] S. Tsoi, E. Fok, J.C. Sit et al., Chem. Mater. 18 (2006) 5260.
[183] J. Driskell, S. Shanmukh, Y. Liu et al., J. Phys. Chem. C 112 (2008) 895.
[184] J. Fu, B. Park, G. Siragusa et al., Nanotechnology (2008) 155502.
[185] M. Taschuk, J. Steele, A. van Popta et al., Sens. Actuat. B 134 (2008) 666.
[186] S.P. Fernando, A.L. Elias, M.J. Brett, J. Mater. Res. 21 (2006) 1101.
[187] J. Frederick, D. Gall, Appl. Phys. Lett. 87 (2005) 053107.
[188] H. Wang, Y. Shi, W. Chu et al., Chin. Phys. Lett. 25 (2008) 234.
[189] J. Singh, F. Tang, T. Karabacak et al., J. Vac. Sci. Technol. B 22 (2004) 1048.
[190] R. Teki, T. Parker, H. Li et al., Thin Solid Films 516 (2008) 4993.
[191] A. van der Drift, Philips Res. Rep. 22 (1967) 267.
[192] K. Moon, S. Shin, J. Appl. Phys. 79 (1996) 4991.
[193] N. Yamaguchi, K. Wada, K. Kimura et al., J. Ceram. Soc. Jpn 111 (2003) 883.
[194] H. Alouach, G. Mankey, J. Vac. Sci. Technol. A 22 (2004) 1379.
[195] H. Alouach, G. Mankey, Appl. Phys. Lett. 86 (2005) 1223114.
[196] F. Tang, T. Karabacak, P. Morrow et al., Phys. Rev. B 72 (2005) 165402.
[197] K. Wada, M. Yoshiya, N. Yamaguchi et al., Surf. Coat. Technol. 200 (2006) 2725.
[198] T. Karabacak, J.P. Singh, Y.-P. Zhao et al., Phys. Rev. B 68 (2003) 125408.
[199] E. Main, T. Karabacak, T.-M. Lu, J. Appl. Phys. 95 (2004) 4346.
[200] C. Buzea, G. Beydaghyan, C. Elliott et al., Nanotechnology 16 (2005) 1986.
[201] C. Zhou, D. Gall, J. Appl. Phys. 103 (2008) 014307.
[202] M. Taschuk, J. Steele, M. Brett, AVS 55th International Symposium and Exhibition, Boston, MA, USA, (2008).
[203] A.-L. Barabási, H.E. Stanley, Fractal Concepts in Surface Growth, Cambridge University Press, Cambridge (1995).
[204] T.G. Knorr, R.W. Hoffman, Phys. Rev. 113 (1959) 1039.
[205] D.O. Smith, J. Appl. Phys. 30 (1959) 264S.
[206] E.W. Pugh, E.L. Boyd, J.F. Fredman, IBM J. Res. Dev. 4 (1960) 163.
[207] V. Kambersky, Z. Malek, Z. Frait et al., Czech. J. Phys. B 11 (1961) 171.
[208] M.S. Cohen, J. Appl. Phys. 32 (1961) 87S.
[209] W.J. Schuele, J. Appl. Phys. 35 (1964) 2558.
[210] F.A. Pronk, J.C. Lodder, IEEE Trans. Mag. 24 (1988) 1744.
[211] H. van Kranenburg, J.C. Lodder, Y. Maeda et al., IEEE Trans. Mag. 26 (1990) 1620.
[212] H. van Kranenburg, C. Lodder, T.J.A. Popma, J. Magnet. Magnet. Mater. 120 (1993) 225.
[213] H. van Kranenburg, C. Lodder, T.J.A. Popma, J. Magnet. Magnet. Mater. 120 (1993) 353.
[214] A. Lisfi, J.C. Lodder, Phys. Rev. B 63 (2001) 174441.
[215] F. Tang, D.-L. Liu, D.-X. Ye et al., J. Magnet. Magnet. Mater. 283 (2004) 65.
[216] P. Morrow, X.T. Tang, T.C. Parker et al., Nanotechnology 19 (2008) 065712.
[217] D.L. Bellac, G.A. Niklasson, C.G. Granqvist, Europhys. Lett. 32 (1995) 155.
[218] D. Vick, T. Smy, M.J. Brett, J. Mater. Res. 17 (2002) 2904.
[219] X. Tang, G. Zhang, Y. Zhao, Nanotechnology 17 (2006) 4439.
[220] F. Tang, T. Karabacak, L. Li et al., J. Vac. Sci. Technol. A 25 (2007) 160.
[221] K.D. Harris, M.J. Brett, T.J. Smy et al., J. Electrochem. Soc. 147 (2000) 2002.
[222] J.N. Broughton, M.J. Brett, M.J. Electrochem, Solid State Lett. 5 (2002) A279.
[223] G.K. Kiema, M.J. Brett, J. Electrochem. Soc. 150 (2003) E342.
[224] C.-C. Li, J.-L. Huang, R.-J. Lin et al., J. Vac. Sci. Technol. A 25 (2007) 1373.
[225] M.C. Demirel, Colloids Surf. A: Physicochem. Eng. Aspects 321 (2008) 121.
[226] K. Krause, M. Taschuk, M. Thommes et al., Fall Materials Research Symposium, Boston, MA, USA (2008).
[227] M. Suzuki, Y. Taga, J. Appl. Phys. 90 (2001) 5599.

[228] F. Liu, K. Yao, Z. Liu, Surf. Coat. Technol. 201 (2007) 7235.
[229] D. Liu, D. Ye, F. Khan et al., J. Nanosci. Nanotech. 3 (2003) 492.
[230] J.P. Singh, D.-L. Liu, D.-X. Ye et al., Appl. Phys. Lett. 84 (2004) 3657.
[231] C. Gaire, D. Ye, F. Tang et al., J. Nanosci. Nanotech. 5 (2005) 1893.
[232] J. Singh, T. Karabacak, D. Ye et al., J. Vac. Sci. Technol. B 23 (2005) 2114.
[233] G. Dice, M. Brett, D. Wang et al., Appl. Phys. Lett. 90 (2007) 253101.
[234] K. Robbie, A.J.P. Hnatiw, M.J. Brett et al., Electronics Lett. 33 (1997) 1213.
[235] T. Karabacak, C. Picu, J. Senkevich et al., J. Appl. Phys. 96 (2004) 5740.
[236] T. Sumigawa, H. Hirakata, M. Takemura et al., Eng. Fract. Mech. 75 (2008) 3073.
[237] C. Jaing, M. Liu, C. Lee et al., Appl. Opt. 47 (2008) C266.
[238] J. Fan, D. Dyer, G. Zhang et al., Nano Lett. 4 (2004) 2133.
[239] Y. Zhao, J. Fan, Appl. Phys. Lett. 88 (2006) 103123.
[240] J. Fan, J. Fu, A. Collins et al., Nanotechnology 19 (2008) 045716.
[241] K. Kuwahara, S. Shinzato, Thin Solid Films 164 (1988) 165.
[242] A. Yamada, W. Takakura, S. Ikeda et al., Phys. Stat. Sol. A 189 (2002) 753.
[243] D. Vick, M. Brett, J. Vac. Sci. Technol. A 24 (2006) 156.
[244] M. Harris, H.A. MacLeod, S. Ogura et al., Thin Solid Films 57 (1979) 173.
[245] M. Harris, M. Bowden, H.A. MacLeod, Opt. Comm. 51 (1984) 29.
[246] L. Holland, J. Opt. Soc. Am. 43 (1953) 376.
[247] T. Motohiro, Y. Taga, Appl. Opt. 28 (1989) 2466.
[248] I. Hodgkinson, F. Horowitz, H.A. Macleod et al., J. Opt. Soc. Am. A 2 (1985) 1693.
[249] K. Kaminska, T. Brown, G. Beydaghyan et al., Appl. Opt. 42 (2003) 4212.
[250] R. Landauer, AIP Conf. Proc. 40 (1978) 2.
[251] D.E. Aspnes, Thin Solid Films 89 (1982) 249.
[252] G.A. Niklasson, C.G. Granqvist, O. Hunderi, Appl. Opt. 20 (1981) 26.
[253] G.B. Smith, Opt. Comm. 71 (1989) 279.
[254] G. Mbise, G.A. Niklasson, G.C. Granqvist et al., J. Appl. Phys. 80 (1996) 5361.
[255] G.W. Mbise, D.L. Bellac, G.A. Niklasson et al., J. Phys. D 30 (1997) 2103.
[256] I. Hodgkinson, Q.H. Wu, S. Collett, Appl. Opt. 40 (2001) 452.
[257] R.R. Bilboul, J. Phys. D 2 (1969) 921.
[258] R.W. Cohen, G.D. Cody, M.D. Coutts et al., Phys. Rev. B 8 (1973) 3689.
[259] C.G. Granqvist, O. Hunderi, Phys. Rev. B 16 (1977) 3513.
[260] S. Berthier, J. Physiq. I 4 (1994) 303.
[261] J.A. Osborn, Phys. Rev. 67 (1945) 351.
[262] S. Wang, G. Xia, H. He et al., J. All. Comp. 431 (2007) 287.
[263] M.M. Hawkeye, M.J. Brett, Phys. Stat. Sol. A 206 (2009) 940.
[264] S. Wang, G. Xia, X. Fu et al., Thin Solid Films 515 (2007) 3352.
[265] P. Bhardwaj, P.K. Shishodia, R.M. Mehra, J. Mater. Sci. 38 (2003) 937.
[266] P. Bhardwaj, P.K. Shishodia, R.M. Mehra, J. Mater. Sci. 42 (2007) 1196.
[267] J.K. Kim, S. Chhajed, M.F. Schubert et al., J. Appl. Phys. 102 (2007) 013517.
[268] Y. Zhong, Y.C. Shin, C.M. Kim et al., J. Mater. Res. 23 (2008) 2500.
[269] B. Szeto, P.C.P. Hrudey, J. Gospodyn et al., J. Opt. A 9 (2007) 457.
[270] J.M.B.E. Pelletier, G. Albrand, J.P. Borgogno et al., Appl. Opt. 28 (1989) 3303.
[271] I. Hodgkinson, Q.H. Wu, Appl. Opt. 38 (1999) 3621.
[272] A.C. van Popta, J. Cheng, J.C. Sit et al., J. Appl. Phys. 102 (2007) 013517.
[273] D.W. Berreman, T.J. Scheffer, Phys. Rev. Lett. 25 (1970) 577.
[274] J.W. Berreman, J. Opt. Soc. Am. 62 (1972) 502.
[275] P. Yeh, J. Opt. Soc. Am. A 69 (1979) 742.
[276] A. Lakhtakia, W.S. Weiglhofer, Proc. Math. Phys. Sci. 448 (1995) 419.

[277] A.C. van Popta, J.C. Sit, M.J. Brett, Appl. Opt. 43 (2004) 3632.
[278] I. Hodgkinson, Q.H. Wu, B. Knight et al., Appl. Opt. 39 (2000) 642.
[279] I. Hodgkinson, Q.H. Wu, Adv. Mater. 13 (2001) 889.
[280] A. Lakhtakia, M.W. McCall, J.A. Sherwin et al., Opt. Comm. 194 (2001) 33.
[281] I. Hodgkinson, Q.H. Wu, L.D. Silva et al., Optics Lett. 30 (2005) 2629.
[282] A.C. van Popta, K.R. van Popta, J.C. Sit et al., J. Opt. Soc. Am. A 24 (2007) 3140.
[283] S.R. Kennedy, M.J. Brett, Appl. Opt. 42 (2003) 4573.
[284] J. Xi, M. Schubert, J. Kim et al., Nature Photonics 1 (2007) 176.
[285] M. Kuo, D. Poxson, Y. Kim et al., Optics Lett. 33 (2008) 2527.
[286] A.C. van Popta, M.M. Hawkeye, J.C. Sit et al., Optics Lett. 29 (2004) 2545.
[287] M.M. Hawkeye, M.J. Brett, J. Appl. Phys. 100 (2006) 044322.
[288] K. Kaminska, K. Robbie, Appl. Opt. 43 (2004) 1570.
[289] M.M. Hawkeye, M.J. Brett, Proc. SPIE 6832 (2008) 683204.
[290] O. Toader, S. John, Science 292 (2001) 1133.
[291] M.O. Jensen, M.J. Brett, Opt. Expr. 13 (2005) 3348.
[292] S.R. Kennedy, M.J. Brett, O. Toader et al., Nano Lett. 2 (2002) 59.
[293] S.R. Kennedy, M.J. Brett, H. Miguez et al., Photon. Nanostruct. Fund. Appl. 1 (2003) 37.
[294] D.X. Ye, Z.P. Yang, A.S.P. Chang et al., J. Phys. D 40 (2007) 2624.
[295] K. Robbie, D.J. Broer, M.J. Brett, Nature 399 (1999) 764.
[296] S.R. Kennedy, J.C. Sit, D.J. Broer et al., Liq. Cryst. 28 (2001) 1799.
[297] J.C. Sit, D.J. Broer, M.J. Brett, Liq. Cryst. 27 (2000) 387.
[298] A.L. Elias, M.J. Brett, M.E. Sousa et al., J. Appl. Phys. 99 (2006) 116105.
[299] N.G. Wakefield, A.L. Elias, M.J. Brett et al., Molec. Cryst. Liq. Cryst. 475 (2007) 85.
[300] H. Chu, Y. Liu, Y. Huang et al., Opt. Expr. 15 (2007) 12230.
[301] J. Driskell, A. Seto, L. Jones et al., Biosens. Bioelectron. 24 (2008) 917.
[302] H. Chu, Y. Huang, Y. Zhao, Appl. Spect. 62 (2008) 922.
[303] W. Zhang, N. Ganesh, I. Block et al., Sens. Actuat. B 131 (2008) 279.
[304] D. Chang, Y. Park, C. Hwangbo, J. Kor. Phys. Soc. 53 (2008) 2700.
[305] A. Wu, M. Seto, M. Brett, Sens. Mater. 8 (1999) 493.
[306] K.D. Harris, A. Huzinga, M.J. Brett, M.J. Electrochem, Solid State Lett. 5 (2002) H27.
[307] J.J. Steele, A.C. van Popta, M.M. Hawkeye et al., Sens. Actuat. B 120 (2006) 213.
[308] Y. Kanamori, E. Itoh, K. Miyairi, Mol. Cryst. Liq. Cryst. 472 (2007) 327/[717].
[309] M. Suzuki, T. Ito, Y. Taga, Appl. Phys. Lett. 78 (2001) 3968.
[310] K. Chiba, K. Sato, Y. Ebine et al., IEEE Trans. Cons. Electron. 35 (1989) 421.
[311] R.H. Dee, Proc. IEEE 96 (2008) 1775.
[312] T. Ishida, K. Tohma, H. Yoshida et al., IEEE Trans. Mag. 36 (2000) 183.
[313] L.T. Nguyen, F.D. Tichelaar, J.C. Lodder, J. Magnet. Magnet. Mater. 290-291 (2005) 1294.
[314] R. Kötz, M. Carlen, Electrochim. Acta 45 (2000) 2483.
[315] M.D. Fleischauer, J. Li, M.J. Brett, J. Electrochem. Soc. 156 (2009) A33.
[316] Y. He, Y. Zhao, Phys. Chem. Chem. Phys. 11 (2009) 255.
[317] Z. Xie, B. Henry, K. Kirov et al., Thin Solid Films 511-512 (2006) 523.
[318] N.J. Gerein, M.D. Fleischauer, M.J. Brett, Proc. 33rd IEEE PVSC (2009).
[319] M. Seto, K. Westra, M. Brett, J. Mater. Chem. 12 (2002) 2348.
[320] G. Kiema, M. Jensen, M. Brett, Chem. Mater. 17 (2005) 4046.
[321] L. Bezuidenhout, M. Brett, J. Chromat. A 1183 (2008) 179.
[322] C. Buzea, K. Kaminska, G. Beydaghyan et al., J. Vac. Sci. Technol. B 23 (2005) 2545.

CHAPTER 14

Nanocomposite Coatings for Severe Applications*

Ali Erdemir[1] **and Andrey A. Voevodin**[2]
[1]*Argonne National Laboratory, Energy Systems Division, Argonne, IL 60439, USA*
[2]*Air Force Research Laboratory, Materials and Manufacturing Directorate,*
Wright-Patterson Air Force Base, OH 45433-7750, USA

14.1 Introduction

Bulk nanomaterials and thick nanocomposite coatings (i.e. thicker than 50 μm) have been available for a long time and are currently used in the fabrication of some critical components in microelectronics, tooling, biomaterials, catalysis, and a wide range of energy-related fields (fuel cells, batteries, etc.) [1–3]. However, during the last two decades, multifunctional nanostructured and nanocomposite coatings have become increasingly more popular, mainly because of their impressive property and performance characteristics as well as lower cost.

---

* The submitted manuscript has been created by the University of Chicago as Operator of Argonne National Laboratory (‘Argonne’) under Contract No. DE-AC02-06CH11357 with the US Department of Energy. The US Government retains for itself, and others acting on its behalf, a paid-up, nonexclusive, irrevocable worldwide license in said article to reproduce, prepare derivative works, distribute copies to the public, and perform publicly and display publicly, by or on behalf of the Government.

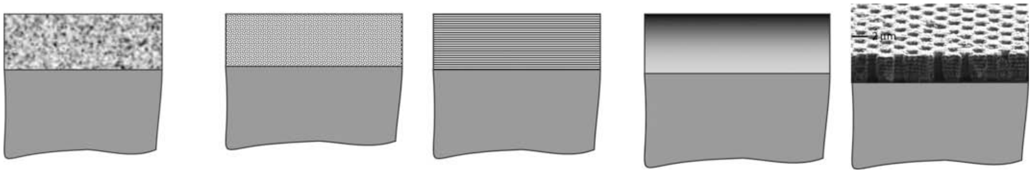

Figure 14.1: Schematic representation of various design architectures for nanostructured and composite coatings [4].

Figure 14.1 schematically illustrates some of the design architectures that are typically used for nanostructured and composite films at the moment [4]. These coatings certainly represent a new class within the very broad field of surface engineering and are the result of breakthrough developments in physical and chemical vapor deposition (PVD and CVD) technologies in recent years. Regardless of the coating type and architecture, they are able to reduce friction and wear; improve thermal and electrical properties; and increase resistance to corrosion, erosion, and fatigue-related degradations even under very harsh operating conditions. Most of the mechanical tools and components that used to be coated with conventional or single-component coatings (like TiN) are nowadays coated with a nanostructured or nanocomposite film, mainly because of its longer durability and much better performance characteristics. Some of the key advantages of nanostructured and composite coatings over traditional coatings are their superior mechanical hardness, resilience, and toughness; high resistance to wear, scuffing, fatigue, oxidation, and corrosion; lower friction; and ability to produce low shear tribofilms on dry or marginally lubricated sliding surfaces with self-adaptive behavior in variable environments and temperatures [4–15].

Nanostructured and composite coatings are primarily produced by advanced PVD and CVD techniques. Among others, deposition systems based on ion plating, multicathode arc-PVD, and magnetron sputtering have dominated the coating industry in recent years. Most of these techniques rely on the generation of energetic plasma streams and control of the energy, density, and chemistry of highly ionized deposited atomic and molecular fluxes to generate complex compositions, nanostructures, and architectures optimized for a coating application. As an additional benefit, highly energetic deposition fluxes permit production of desired coating structures at low processing temperatures, broadening the application to temperature-sensitive substrates. The use of multiple targets or evaporation sources and, most recently, a combination of different types of plasma sources in these methods provides the flexibility and convenience that are needed for achieving a truly nanocomposite structure. Compared to bulk nanocomposites, these coatings are much cheaper to produce and more flexible to apply on all kinds of substrate materials. It takes little material to produce such coatings on substrates at a desired thickness; hence, the cost due to raw materials is minimal. The bonding between the latest generation nanocomposite coatings and their substrates is very strong, thanks to the recent advances in interface engineering and novel technologies like arc-bond coating and high-power impulse magnetron sputtering (HIPIMS), as well as the use of special bond or transition layers that effectively reduce internal stress build-up at the interface and hence the possibility of coating delamination.

Owing to their very small grain sizes (ranging from a few nanometers to 100 nm), the surface finish of nanocomposite or nanostructured coatings is much smoother than that of conventional coatings. Unlike their monolithic counterparts with large columnar grains and typically highly textured crystalline orientation, nanocomposite or nanostructured coatings do not contain crystalline facets or uneven growth patterns that can cause roughening of the coating surface. Nanocomposite and nanostructured coatings maintain their properties uniformly when applied to complex geometry substrates (drills, mills, turbine blades, gear teeth, biomedical implants, etc.), since there is no preferential growth directions in their nanocrystalline constituents and, thus, no associated anisotropy of the coating properties. Furthermore, they are free of large pits, pinholes, protrusions, and other surface and structural defects. Because of their nanostructured and composite nature, these coatings can be produced with a wide range of physical, chemical, thermal, mechanical, and tribological properties; hence, when used in industrial applications, they can provide multiple functionalities. For example, they can dramatically increase hardness and hence reduce wear of underlying substrates under harsh sliding or machining conditions while at the same time providing low friction and excellent protection against corrosion or chemical degradations. They can also provide superior thermal, optical, magnetic, biomedical, electronic, catalytic, and surface acoustic properties [7, 10, 11, 16–18].

Because of their unique properties and increasing popularity, nanostructured and composite coatings have been the subject of numerous books, journal articles, reports, research papers, etc. This chapter is intended to provide an overview of recent developments in these coatings. They are already used in large volumes for machining and manufacturing applications, and new applications are emerging in the aerospace, transportation, and biomedical fields. The main emphasis of the chapter will be on the fundamental tribological mechanisms that control their superior friction and wear properties at severe operation conditions (high surface loads and temperatures, lack of lubricants, and aggressive oxidizing environments). It is obvious that future tribosystems will be subjected to much more stringent operation conditions than before, mainly because of the increased power density dissipated (e.g. cutting tools) or transmitted (e.g. gears and bearings) at mechanical interfaces, and because of the trend toward reduced size and much higher mechanical and thermal loadings at the contact area. To overcome these challenges, new coatings are urgently needed with a capacity to further improve durability and performance and to adapt to the much harsher and rapidly changing operation conditions of future mechanical systems. Accordingly, in the following sections, we provide an overview of recent developments in the design and deposition of nanostructured and composite coatings. We also review the structural and mechanical properties of such coatings that are important for their performance in various applications.

14.2 Advances in Deposition Processes for Nanocomposite Coatings

Over the years, PVD and CVD processes, such as sputtering, ion plating, cathodic arc, pulsed laser deposition (PLD), ion-beam assisted deposition (IBAD), and plasma-enhanced chemical vapor deposition (PECVD), have undergone significant modifications in their size, configuration, and power source requirements to become very robust and reliable and to allow large throughput. As a result, the cost of making nanostructured and composite coatings with such processes has decreased substantially and made them more affordable. With recent modifications in their internal design and configuration (such as sample holders, multiple modes of rotation, strategically positioned cathodes or sputtering targets, and additional ionization and/or evaporation sources), it has become much easier to achieve high deposition rates and more uniform and complete coverage on uneven or odd-shaped workpieces. The use of multiple targets or evaporation sources has enabled the production of novel nanocomposite coatings with complex microstructures and chemical compositions that provide superhardness and other impressive mechanical properties [4, 6, 7, 19, 20]. At present, reactive magnetron sputtering with pulse-direct current (DC) and HIPIMS capabilities and standard and/or filtered cathodic-arc PVD techniques are used extensively by industry for the deposition of conventional and nanocomposite coatings [9, 21–24]. Other methods, such as PLD and IBAD, are also used but at much smaller scales for the production of nanocomposite coatings. With the introduction of femtosecond laser sources, the PLD method has gained new interest mainly because of the better control of the ablation processes, resulting in fewer droplets and other irregularities on the coating surface [25]. Figure 14.2 shows schematics for the three advanced methods currently used to produce most of the nanostructured or composite films.

14.2.1 Hybrid Deposition Processes for Nanocomposite Coatings

For the production of nanostructured or composite coatings, it may be necessary to combine two or more of the deposition methods mentioned earlier in one system. Furthermore, the use of high-ionization power sources like HIPIMS and cathodic arc deposition is important for producing coatings with strong bonding, dense structure, and superior mechanical properties. For example, in such systems, one can do sputtering and cathodic arc PVD individually, sequentially, or both together. One can also switch between the standard and HIPIMS modes to achieve unique structural features. With the use of HIPIMS or cathodic arc methods, one can also achieve robust interface mixing and, hence, strong film-to-substrate bonding, which is extremely important for load-carrying capacity and durability. Subsequently, the sputtering mode may be used to achieve a dense and uniform coating morphology with smooth surface finish. The use of filtered cathodic arc or HIPIMS sources may further help in achieving a smooth surface finish on the coated parts. Alternatively, one can use both sputtering and arc-PVD at the same time to take advantage of both methods in not only achieving a strong

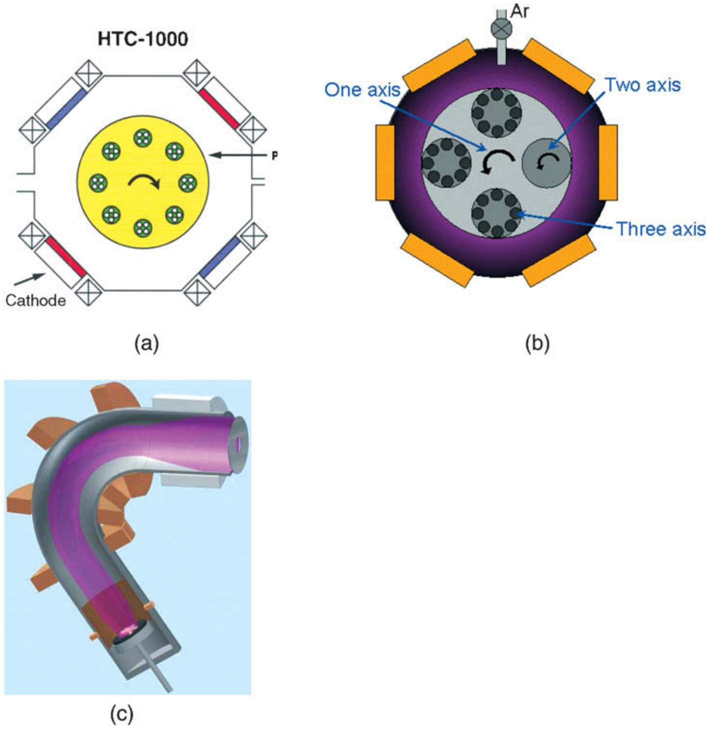

Figure 14.2: Schematic representation of (a) hybrid magnetron sputtering and cathodic arc PVD system (courtesy of R. Dielis, Hauzer Techno Coating), (b) closed-field magnetron sputter ion plating system (courtesy of D. Teer, Teer Coatings, Ltd), and (c) filtered cathodic arc PVD system (courtesy of P. Siemroth, Arc Precision GmbH).

bonding but also the rapid deposition of a dense and uniform coating. These methods are commonly referred to as 'hybrid' deposition processes, and they are ideal for the production of nanocomposite and nanolayered coatings with duplex, multiplex, or superlattice structures. Again, in these more advanced processes, the physical size or interior architecture of the deposition systems is slightly altered to accommodate additional targets and appropriate power sources (cathodic arc, pulse-DC, HIPIMS, etc.) in order to permit the flexibility of producing coatings by one of the methods alone, two or three of them in sequence, or all of them together.

Most nanocomposite or nanolayered coatings that are in use today are produced by sputtering and arc-PVD techniques, with a smaller fraction being produced by electron beam or pulsed laser evaporation. As mentioned above, either of these techniques may be used alone or simultaneously to achieve a graded, multilayered, or nanocomposite coating architecture. For example, W/C or Ti/C multilayer coatings are produced by sputtering or evaporation of W and C or Ti and C targets in sequence at short durations during deposition (Figure 14.3a) [26, 27]. For the deposition of nanocomposite W–C or Ti–C films, the sputtering or evaporation rates of

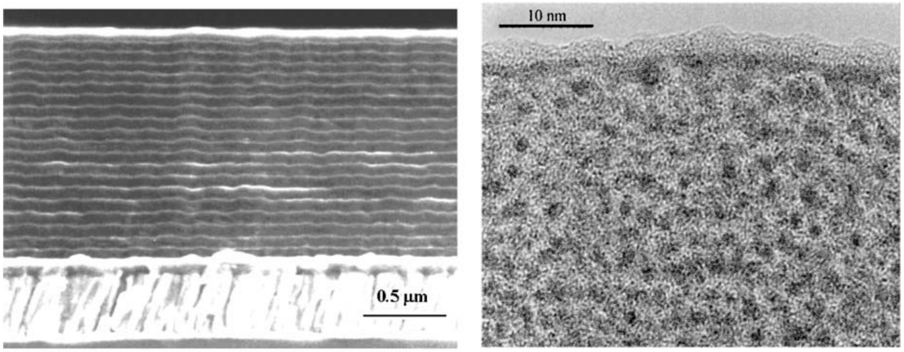

(a) (b)

Figure 14.3: TEM images of (a) nanolayered Ti/C [27] and (b) nanocomposite W/C:H films (courtesy of Hauzer Techno Coating).

targets are adjusted to result in a discrete phase of each ingredient or their reaction products (i.e. WC or TiC phases) embedded in a matrix of diamond-like carbon, as shown in the transmission electron microscopy (TEM) image in Figure 14.3b. Hybrid methods have opened interesting possibilities to embed temperature-sensitive materials inside coatings, which before had required high growth temperatures. One example is a uniform dispersion of MoS_2 nanograins in an alumina oxide layer [28].

The successful design, synthesis, and production of nanocomposite films for large-scale applications require proper selection and control of several deposition parameters [20, 29, 30]. Such a practice is essential for maintaining the chemical, structural, and mechanical integrity of the workpieces that are being coated. One of the major issues in most modern deposition technologies is the unintentional heating of substrate materials. This may cause degradation of the mechanical properties of such materials, especially upon exposure to temperatures that are much higher than the tempering temperatures [31]. In the case of arc-PVD and HIPIMS, overheating is always a possibility, mainly because of the high energy and high power density of these processes, but this problem can be effectively controlled by adjustments to process parameters (e.g. use of pulse regimes, independently of the substrate heating and cooling arrangements). For some tools and bearing steels like AISI 52100 and 440C, the tempering temperatures are less than 200 °C. If these materials are heated above this temperature during coating, their hardness values decrease considerably, and they may not be able to support the hard coating on their surfaces and fail quickly during actual use. In the past, low deposition temperatures had a large negative effect on the adhesion and microstructural density of the deposited coatings. Poor adhesion to the substrate, poorly connected columnar structures perpendicular to the substrate, grain-boundary voids, and defect networks were typical of the coatings produced at low deposition temperatures by conventional PVD deposition. Such coatings were not able to withstand the high cyclic loads of many manufacturing or transportation applications. As mentioned earlier, with the recent use of highly energetic plasma technologies like HIPIMS and cathodic arc deposition, such adhesive and cohesive problems have been effectively overcome, and the current coatings possess strong adhesion to substrate materials as well as strong cohesion between grains.

In the case of CVD processes, because the temperatures are typically much higher, CVD may not be a good choice for heat-sensitive substrates. If a low temperature CVD is used, a postdeposition hardening heat treatment is often a must, but depending on the coating type, major problems may occur on the hard coating itself. Chief among them is severe oxidation or partial delamination of coatings from the substrate surface due to chemical reactions and thermal distortions. High-speed steels, certain intermetallics, and cemented carbides can safely be exposed to deposition temperatures as high as 450 °C without major structural, chemical, or mechanical degradations. In contrast, for the deposition of nanocomposite coatings on titanium-, aluminum-, and magnesium-based engineering materials, one has to use relatively low temperatures; otherwise, major degradations or distortions may take place in such substrates. Because of their light weights, these materials are much desired for structural components in all kinds of transportation applications. There is also interest in using these materials in tribological and mechanical applications for aerospace and biomedical needs. However, mainly because of their high sensitivity to heat, extra precautions must be taken to avoid degradation in mechanical properties or loss of structural integrity of light alloy substrates.

As already mentioned, recent advances in power supplies have led to much higher ionization efficiencies and plasma current densities in PVD systems. Cathodic arc PVD, closed-field unbalanced magnetron sputter ion plating, asymmetric polarity pulsed-DC sputtering, and HIPIMS processes are good examples of techniques yielding high ionization efficiencies and plasma densities. With these advances, it is now possible to maintain substrate temperatures at acceptable levels and yet attain dense microstructures and strong adhesion in between many coatings and their substrates. Among others, HIPIMS and droplet-emission-restricted cathodic arc technologies represent a most recent trend and are gaining increased acceptance and applications in many fields. All in all, the high ionization efficiency of these novel methods provides high mobility and, hence, surface and bulk diffusivity of impinging ions and/or atoms. These conditions can positively influence nucleation and growth processes to produce strong film-to-substrate adhesion, dense film morphology, smooth surface finish, and nearly perfect chemical stoichiometry, even at relatively low deposition temperatures.

14.2.2 Modern Coating Practices for the Synthesis of Nanocomposite Coatings

In today’s world, PVD and CVD methods are used extensively for a variety of industrial applications and in large volumes to improve the performance and durability of machine tools and other critical components [32–34]. In particular, most tools and dies used in manufacturing applications now have a high-performance coating. As already highlighted above, modern coating techniques provide the means for producing high-performance nanocomposite and nanostructured coatings with excellent adhesion and surface finish at reasonable cost and at reduced substrate temperatures. At the moment, several coatings methods are available for the deposition of thin hard coatings as mentioned briefly earlier and covered in other chapters in this handbook. Some of these are well established and used routinely by industry, while others are still being developed, especially the ones involving the use of HIPIMS. The most popular traditional coating methods include cathodic arc evaporation, magnetron sputtering, CVD, and PLD. The modern magnetron sputtering systems can be configured to have pulsed DC or HIPIMS power sources. These methods are described in detail in some of the other chapters in this handbook, but a brief description is provided here for a few of the most popular methods.

Magnetron sputtering is perhaps the oldest and most widely used technique. It can produce very thin or thick composite coatings consisting of nanoscale to microscale hard and/or soft layers and phases. The ingredients that make up each phase are sputtered from a metallic, ceramic, or composite target in sequence or all together to build the nanolayered or nanocomposite films by means of Ar ion sputtering. Argon is introduced into a PVD sputtering chamber and ionized by collisions with electrons trapped by a magnetic field in the vicinity of targets. These ions are then accelerated toward target surfaces by strong electrical fields, for which high-voltage/low-current DC power supplies are used with a negative polarity on the targets. In pulsed DC sputtering, reverse polarity is used to enable sputtering of insulating materials. Sputtering occurs during negative voltage pulses of high amplitude (order of 400–600 V), which are intercepted with low-voltage positive pulses to attract electrons to the target surface and remove any accumulated positive charge. A recent practice of pulsed DC sputtering is to use asymmetric positive and negative voltage pulses of various lengths with an order of 100 kHz repetition rate. The relative duration of the negative and positive pulses defines a duty cycle, which is often adjusted to achieve an optimum sputtering efficiency [35, 36].

In the case of cathodic arc PVD, high-current/low-voltage power sources are used. The range of currents may vary from as low as 30 A to as high as 1000 A. The voltage range is from 20 to 100 V. During deposition, high electrical current is localized in arc spots rapidly moving on the surface of the targets in intersected electrical and magnetic fields. This condition leads to extreme heating followed by the evaporation of atoms and/or clusters from these spots in the form of highly ionized species with typical ion energies of 20 to 150 eV. Occasionally, larger nanoscale to microscale particles or droplets are also detached from the surface of the target material, and some of these may also reach the substrate and become incorporated into the growing films. The droplets are often in the range of 0.01–20 μm, and as a rough generalization, materials with higher melting points generate smaller and fewer droplets than those with lower melting points. The droplets are generated from a portion of the target material that is heated sufficiently to melt but not evaporate. Reduction of droplets is possible with the increase of the velocity of arc spot travel on an evaporated cathode surface under the guidance of an external magnetic field. Removal of droplets from the deposition fluxes is achieved with ‘droplet filters’ that typically guide the plasma stream away from the path of the droplet emission trajectories and allow placement of an evaporated cathode out of sight from the substrate, as illustrated in Figure 14.2(c). Filtered cathodic arc evaporation techniques provide droplet-free and nearly 100%-ionized fluxes of the evaporated materials arriving at the substrates. This condition gives additional flexibility for deposition control by substrate biasing and ionized flux steering [37–40]. All filtering techniques undergo a loss of the evaporated target material, and many industrial coaters select to use not-filtered cathodic arc evaporation methods. At the same time, large-area plasma filtering was reported for industrial scale-up use [41], which may be the next trend in cathodic vacuum arc deposition.

Both magnetron sputtering and arc-PVD methods have advantages and disadvantages. In the case of magnetron sputtering, the current densities are not high enough to cause sufficient mixing at the film–substrate interface and to refine the grain morphology to provide a dense structure. Relatively poor adhesion and columnar morphology may have adverse effects on coating durability in demanding machining applications, where strong film-to-substrate adhesion as well as high structural density is needed. In the case of the cathodic arc PVD technique, the coating microstructure is much denser, and the bonding between coating and substrate material is stronger owing to intense metal ion bombardment in the beginning as well as later during the film growth. However, microdroplets coming from the cathode surface increase the roughness of the resultant films. Increased roughness, especially in hard coating surfaces, is unacceptable for most applications where the primary objective is friction reduction and wear resistance of the complete system. Droplet filtration is an acceptable remedy but comes with a price of inefficient cathode-material utilization. Nevertheless, these techniques allow for high process throughput at reasonable costs and are being used by most industrial coaters.

The recently introduced HIPIMS method seems to overcome the deficiencies of magnetron sputtering and arc-PVD in such a way that it can enable strong film-to-substrate bonding as well as avoid any droplet formation on the surface of growing films. This method can have a huge positive impact on many tribological applications. HIPIMS is an ionized PVD method based on conventional direct-current magnetron sputtering (DC-MS). In DC-MS very little of the sputtered material is ionized since the plasma power density is not high enough. Increasing the power density will increase the plasma density and ionize more of the sputtered material, but it will eventually melt the target and lead to arcing, which of course is not a desirable situation. Instead, by applying high power in repeated short pulses, the average power is kept low enough for the cooling system to maintain the target temperature below the melting point.

The power supplies used in HIPIMS are usually based on an artificial pulse-forming network and operate in a repetitive manner. They became available only recently as a result of

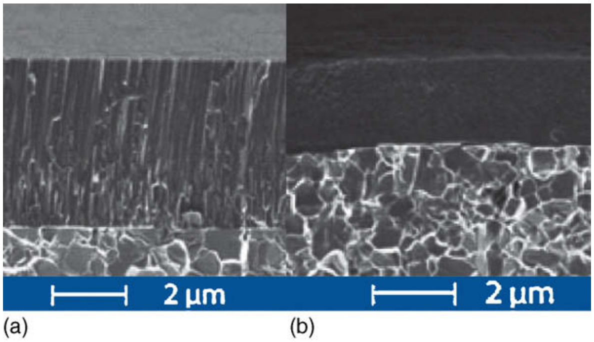

Figure 14.4: Structural morphology of (Cr,Al)N films deposited by (a) conventional magnetron sputtering and (b) HIPIMS techniques [45].

breakthroughs in high-power electronic circuits that handle short but high-current and high-voltage pulses with good reliability and at reasonable equipment costs. A HIPIMS power source can be attached to an existing magnetron sputtering system. In principle, all that needs to change is the power supply. In recent years, the HIPIMS method has yielded high plasma densities (of the order of $10^{19}\,\mathrm{m}^{-3}$) consisting of both metallic and gaseous ions. The many advantages inherent to this method have been discussed in the previous literature [22, 42–44]. The fraction of ionized species may vary between 30 and 90%, depending on the material type. As a result, the coating becomes very dense. Figure 14.4 shows the structural morphology of two films: one deposited by magnetron sputtering, the other by HIPIMS [45]. Such a structural change in film morphology leads to much better mechanical properties such as higher hardness, greater toughness, and better structural cohesion. In summary, HIPIMS combines many of the advantages of cathodic arc and magnetron sputtering in one technique and holds great promise for a variety of demanding industrial applications.

In addition to the modern PVD techniques mentioned above, CVD techniques are available for the deposition of nanocomposite or nanostructured coatings for use in various engineering applications. Among others, plasma-activated or -enhanced CVD processes have become popular in recent years and are used to deposit nanocomposite diamond-like carbon (DLC) films. Other CVD methods (such as hot-filament or microwave CVD processes) are also available for the deposition of microcrystalline and nanocrystalline diamond films. Compared to DLC, diamond coatings require high deposition temperatures (as high as 1000 °C). Microwave CVD, which uses a hydrogen–methane plasma, is used for the synthesis of diamond films at very high temperatures. The same method is also used to produce nanocrystalline diamond films with grain sizes in the range of 2–6 nm; in this case, hydrogen is replaced with argon in the plasma [46]. In the case of nanocomposite DLC films, small nanocrystalline phases of transition metal carbides are usually dispersed within an amorphous matrix [26, 47]. Such films can also be prepared in a nanolayered fashion, consisting of a few nanometers of a metallic or compound phase followed by amorphous carbon.

The modern PVD and CVD methods mentioned above are capable of industrial-scale production of nanocomposite coatings and hence are used extensively by industry in the manufacturing and transportation sectors. The deposition rates of these methods have been adjusted to reduce the production cycles and improve the reproducibility of coating quality and reliability from one run to another. In particular, with recent advances in hybrid deposition processes, much greater flexibility has been achieved in the design and production of novel nanocomposite coatings in large scale. Some of these systems are based on cathodic arc and HIPIMS techniques, which are used not only to effectively clean substrate surfaces but also to form a graded interface that can lead to strong bonding [21]. These systems consist of multiple targets that are strategically located within the deposition systems so that the production of nanolayered or multilayered coatings is much easier and effective. These designer coatings with far superior structural, mechanical, and tribological properties are able to provide longer durability when used in machining or metal-forming applications [11, 13, 45, 48].

14.3 Mechanical and Tribological Properties of Nanocomposite Coatings

Demands for greater power density, reliability, productivity, and energy efficiency in advanced mechanical systems require new materials and coatings with far superior property and performance characteristics. The modern deposition techniques mentioned above are capable of producing the kinds of nanostructured and composite coatings that are needed for such demanding applications. In fact, most of the current coatings used in high-speed machining and other demanding applications are nanostructured or made of nanolayers or nanophases. Some of these coating architectures are illustrated in Figure 14.1. Nanolayered coatings consist of discrete layers of two or more metals and/or ceramics in an alternating fashion, and the thickness of each layer may vary from a few atoms to several angstroms and/or nanometers [7, 27, 48–50]. The ones that are in the range of a few atomic layers are often referred to as superlattice coatings [20, 51]. From a mechanical and tribological properties point of view, this class of layered coatings may achieve superhardness and toughness as well as superior thermal and tribological properties [52]. By varying the thickness of alternating layers, one can achieve nanoscale to microscale grading between the layers and thus better control the physical, mechanical, and tribological properties. Achieving a high-precision layer build-up (especially at subnanometer scales) is not an easy task. It often requires the strategic selection and close control of several deposition parameters, including temperature, deposition rate, speed of rotation, target masking, bias voltage, ionization efficiency, and the average energy of the ionized and neutral species [20]. All of these parameters have a strong effect on surface and bulk diffusion of impinging atoms and on adatom mobility, nucleation, and growth processes, and hence, layer uniformity or coverage of substrate materials.

Most of the nanostructured and composite coatings used by industry are currently produced by hybrid PVD or CVD systems. They can be produced in numerous forms. In a typical nanocomposite coating architecture, one can have a smaller nanocrystalline phase embedded in a larger amorphous matrix or a minor amorphous phase surrounded by a predominantly crystalline phase [5, 7, 53, 54]. With the uses of multiple targets, one can also produce composite coatings consisting of more than two or three phases. Strong bonding is important between the phases so that they do not create debonding or interface cracking under mechanical and/or tribological loadings.

The mechanical properties of nanolayered or composited coatings are much better than those measured in single-phase films or their bulk composites consisting of the same metals, alloys, or ceramic phases. Several factors can influence the mechanical and tribological properties of nanocomposite coatings. Among others, the size, shape, and orientation of nanograins that make up the composite film are most influential. Furthermore, several factors (the surface area and thickness of the grain-boundary phases, the extent of residual stresses, and the presence or absence of voids, pinholes, cracks or discontinuities within or across the films) may also have a dramatic effect on their mechanical and tribological properties. Veprek et al. [55] showed on an example of superhard TiN/Si_3N_4 coatings, that even the smallest impurities of oxygen in one monolayer of amorphous Si_3N_4 tissue separating TiN nanocrystalline grains dramatically affect the mechanical properties of such materials, removing any superhardness. The literature typically reports a broad range of mechanical properties of the produced nanocomposite and nanostructured coatings, depending not only on the coating architecture, but also on the deposition methods and the quality of the process control.

For the far superior mechanical properties of nanostructured and nanocomposite coatings, several theoretical models have been proposed by researchers. In one of these theories, Koehler [56] has proposed that the superior mechanical hardness of nanostructured coatings stems from the fact that dislocations (even if they are generated within the grains) are effectively stopped or blocked by grain boundaries, and gross plastic deformation becomes very difficult. In another theory, the Hall–Petch relationship of grain size versus hardness was thought to account for the superhard nature of nanocomposite coatings [57]. In the Hall–Petch model, the yield strength or hardness $H(d)$ of a polycrystalline solid is related to its average grain diameter d as in $H(d) = H_0 + Kd^{-1/2}$ (H_0 and K are material-specific constants). According to this equation, a composite material with smaller grains would have much higher hardness. In bulk materials or composites, this relationship holds quite well up to a grain size of 0.01 μm. Below this size, the hardness often decreases mainly because of the increased effect of grain-boundary sliding [58].

Table 14.1: Examples of superhard coatings and their grain size and mechanical properties

Coating	Average grain size (nm)	% Cu (at.)	Hardness, H (GPa)	E^* $(E/(1-v^2))$ (GPa)	Refs
Zr–Cu–N	38	1–2	55	395	[59–61]
Zr–Ni–N	6	4.1 (Ni)	57	430	[62]
CrCu–N	70–90	1	35		[63]
Al–Cu–N	9, 5	8, 1	47	313	[61]
Zr–Cu–N	10–15	23	23	250	[59–61]
ZrN	–	0	16		[60]
nc-TiN/a-Si_3N_4			40–60	> 500	[6, 64]
nc-TiN/a-Si_4N_4/a-$TiSi_2$			> 80		[30]

Considering both models, with the selection of the right kinds of grain and grain-boundary phases, one can produce hard and tough nanocomposite coatings. For example, if the grain boundaries in a coating are made of a strong phase, then the dislocation motion will become very restricted, or the dislocations will be effectively confined to the grains themselves; hence, the coating will endure high loads before there is a major deformation or fracture. Using such an approach, many research groups have recently developed nanocomposite coatings and demonstrated their superhard nature. Table 14.1 presents some of these coatings and their compositions. Those coatings with hardness values of 40 GPa or more are considered superhard. Their grains are in nano domains (3–5 nm), and the grain boundaries are decorated by very thin (one atomic layer) and immiscible grain-boundary phases [7]. Again, the selection of the phases that make up the grain boundaries is important. The phases must be immiscible yet strongly bonded at the grain boundaries so that they do not easily yield to dislocation motions from one grain to the next.

The mechanical hardness of nanocomposite coatings is among the highest, and many of them are designated as superhard. A simple rule of mixtures cannot be used to estimate their hardness. Typical hardness values for nanocomposite coatings vary between 40 and over 90 GPa. For example, TiN/Si_3N_4, Ni/ZrN, and Cu/MoN exhibit hardness values greater than 40 GPa [4, 5, 7, 29, 53]. If a rule of mixture had been used to estimate their hardness, their composite hardness values should have been much lower. In reality, they exhibit hardness values two to three times higher than the phases they are composed of. At higher concentrations or volumes of metallic phases (over 50%), nanocomposite coatings may exhibit hardness values less than 10 GPa, while at very low concentrations (1–4%), the hardness goes up, and values greater than 50 GPa are feasible. In short, the hardness of nanocomposite coatings can be tuned by varying the concentration of individual phases that make up the bulk coating. It is important to note that the hardness of all coatings may be influenced by the levels of internal stresses within these coatings. Therefore, one has to determine the extent of internal stresses in relation to the hardness of a given coating. A high level of internal stress may be beneficial to the hardness of a coating, but it is also detrimental to the fatigue and wear resistance of such coatings.

Another impressive property that makes nanocomposite coatings unique is their superior fracture toughness, which is important for durability of hard coatings in most mechanical applications where cyclic shear and normal forces are applied [65]. Hardness is important for load-bearing capacity of a coating, but fracture toughness is equally important for resisting crack initiation and growth. Recent experimental studies have confirmed that most nanostructured and composite coatings possess relatively high fracture toughness [53, 66]. The high fracture toughness of nanocomposite coatings has been attributed largely to their nano-sized grain morphology. Specifically, nano-sized grains with a large-grain boundary network are believed to provide an ideal condition for resisting crack initiation in superhard coatings [55]. Even if a crack initiates within a grain, strong and thin (order of one monolayer) grain boundaries can deflect and branch them, reducing the stress concentration factor and arresting further crack growth. Grain-boundary sliding was also suggested as a mechanism for crack energy dissipation at highly localized strains in nanocomposite tribological coatings [14]. Overall, compared to most traditional hard coatings, nanocomposite coatings are ideal for demanding mechanical applications, such as high-speed cutting tools or load-bearing aerospace materials.

While high hardness and toughness are critical for the proper functioning of a coating in intended applications, for such coatings to last long, they must also have strong adhesion or bonding to the substrate materials. In most tribological applications, adhesion determines a film's endurance life, load-bearing capacity, and effectiveness in such applications. In fact, strong adhesion between a coating and its substrate is perhaps the most important prerequisite for most mechanical and tribological applications [67, 68]. Even if the coating is superhard and tough, with poor adhesion, it fails quickly under the influence of high normal and shear forces in most mechanical applications. As mentioned earlier, high levels of internal stresses may cause adhesive as well as cohesive delamination in a coating. The effect of internal stresses is the greatest at the film–substrate interface. If the adhesion of the coating to the substrate is poor, then the coating delaminates from the surface. High levels of physical intermixing and chemical reactions between the constituents of coating and substrate materials can significantly improve the adhesion of coatings. Also, poor mechanical interlocking at the coating–substrate interface may increase the likelihood for delamination.

With the use of modern deposition processes, achieving strong bonding between hard coatings and their substrates is easy. Most of the advanced techniques such as arc-PVD and HIPIMS are able to promote high levels of interdiffusion or mixing between coating and substrate atoms at the interface and thus very strong bonding.

14.4 Nanostructured and Composite Coatings for Tribological Applications

During the 1980s, transition metal carbides, nitrides, borides, and oxides attracted the greatest attention for tribological applications. However, during the last decade or so, attention has shifted to multifunctional nanocomposite coatings with gradient, duplex, multilayered, and nanocomposite architectures, mainly because of their superior tribological properties and diverse application possibilities in transportation, aerospace, and manufacturing fields [8, 15, 32]. Owing to their nanocomposite nature, these coatings can provide high fracture toughness in addition to high mechanical hardness and resilience under severe loading conditions for many tribological applications. If the phases are selected strategically, they can achieve self-lubricating capacity and provide low-friction and low-wear coefficients over a broad range of test conditions, temperatures, and environments. Some of the nanocomposite coatings may also enable machining or manufacturing under dry or marginally lubricated conditions [5, 7]. This is a much desired goal in many engineering applications but not easy to realize. In such coating architectures, the ingredients of each layer are strategically selected so that they may become lubricious through tribochemical interactions with the chemical species in operating environments under the influence of ambient or frictional heating, thus enabling tools to operate even in the absence of additional liquid or other lubricants [69].

In most tribological applications, nanostructured and composite coatings are expected to provide superior friction and wear. Some of the other important requirements are strong adhesion to the substrate material, high mechanical hardness and toughness, high thermal/chemical stability, uniform and adequate thickness, dense morphology, smooth surface finish, and self-lubrication. Recent experimental work which was referenced in the above paragraph has shown that when all of these requirements are met, the tribological coatings can improve the performance and durability of tools and components. For example, in metal-forming and metal-cutting operations, where the wear mechanism is dominated by microfracture or plastic deformation, nanostructured and composite coatings can resist crack initiation because of their high fracture toughness. Because of their hardness, under heavy loading in vertical directions, they can resist deformation on the surface as well and thus increase the load-bearing capacity of base materials.

Besides the manufacturing and machining applications, nanocomposite coatings are attractive for use in transportation, biomedical, and aerospace fields [70, 71]. In the field of transportation, the use of liquid or grease lubricants (engine oils, greases, etc.) with all kinds of chemical additives is essential for the functionality and durability of most sliding, rolling, or rotating components. One of the key additives is zinc dialkyl dithiophosphate (ZDDP), which is used in almost all types of engine and other industrial lubricants owing to its ability to withstand extreme pressures and its anti-friction, anti-wear, and anti-oxidation characteristics, especially under severe contact conditions. Without it, most current lubricants become essentially useless. Another important additive is molybdenum dialkyl dithiocarbamate (MoDTC), which is used primarily to control friction between sliding surfaces. Both of these key anti-friction and anti-wear additives were recently found to be environmentally unsafe and/or potential carcinogens. In particular, ZDDP has been determined to adversely impact the emission control and after-treatment devices of modern engines by poisoning their catalyst systems (especially the NO_x catalyst in diesels). Both ZDDP and MoDTC contain heavy elements besides sulfur and phosphorus, and hence, they contribute to the particulate emissions. Furthermore, the sulfur in these additives reacts with moisture in the combustion chamber and forms acids, which can trigger corrosion and additional wear problems on sliding surfaces.

At the moment, the uses of these lubricants in transportation and other industrial sectors are being curtailed mainly because of their harmful effects on the environment. The most desirable scenario will be to engineer both the coatings and future lubricants in such a way that they become compatible or complementary to one another's performance characteristics, and as a whole, they represent a better lubrication possibility than what can be provided by either of them. For example, in a specially designed nanocomposite coating, while one phase provides extreme resistance to wear and deformation, a second or third phase may preferentially react with the additives in oils to provide high lubricity and protection against wear. It is also possible to design new nanocomposite coatings around the existing liquid lubricants or additives to achieve further improvements in lubrication performance [8, 72]. These coatings can be regarded as smart or adaptive tribological coatings because of their excellent compatibility with, and favorable response to, the lubricants and test environments.

In addition to the lubricated contacts, nanostructured and composite coatings can be useful in other tribological applications involving dry sliding at elevated temperatures or high vacuum and corrosive environments. Despite being chemically stable, under very aggressive or oxidative conditions, these coatings may undergo minor oxidation. In most tribological applications, in addition to the temperature of the operating environment, significant frictional heating may also exist and trigger chemical and/or oxidative interactions with the solid, liquid, or gaseous media in the test environments. Some of the reaction products are self-lubricating, while others might be hard and abrasive; hence, they are detrimental to the lifetime of the coated component. At present, high-speed machining or sliding is greatly desired in numerous industrial applications, which call for much higher chemical and thermal stability for the nanocomposite coatings. In addition to the traditional oxidation-retarding elements, such as Cr, Ti, and Al, more exotic elements like Y and Ce are being incorporated in many composite coatings to further enhance their resistance to oxidation [73]. Some of the tools and dies used in many manufacturing operations are routinely coated by such means to achieve superior resistance to oxidation as well as wear and scuffing.

Conventional PVD coatings can be anisotropic, and most are made of a columnar microstructure. Under heavy loading, deformation or fracture can occur through the column boundaries. However, in the case of nanostructured and composite coatings, the grains are extremely small, and the morphology is not necessarily columnar; hence, they cannot be easily deformed or fractured under loading. The average grain size of nanocomposite film is in a range that is not well suited for crack initiation and propagation. In another words, Griffith's criteria for crack growth are difficult to meet in nanostructured and composite coatings [74]. Therefore, one of the main reasons why nanostructured coatings exhibit superior wear properties is that they are better able to prevent crack initiation and growth.

Another unique feature of the nanostructured and composite coatings is that, mainly because of their superhardness and stiffness, the real contact areas are very small during a tribological sliding situation. When combined with high chemical inertness or stability, smaller contact areas on a sliding surface may often lead to lower friction (especially if one of the constituent phases is self-lubricating). For most tribological applications, low friction in addition to low wear and high resistance to galling or scuffing are major requirements. Nanocomposite coatings can be designed to include a self-lubricating phase, such as MoS_2, to provide low friction, while the hard phase can provide low wear. In lubricated sliding applications, one of the phases may be selected from those metals that can easily form self-lubricating secondary films on the sliding surfaces and thus provide much lower friction. Figure 14.5 shows the frictional behavior of a nanocomposite MoN–Sn film under boundary-lubricated sliding

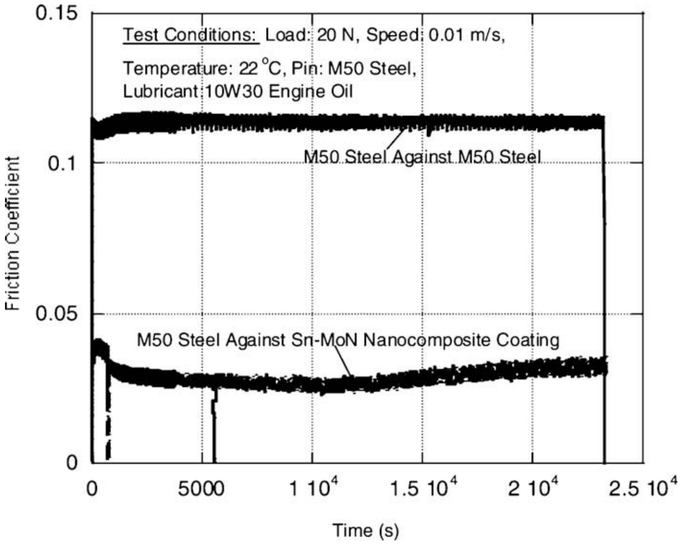

Figure 14.5: Friction coefficients of steel sliding against steel and steel sliding against Sn–MoN nanocomposite film under boundary-lubricated sliding conditions [72] (Courtesy of CRC Publications).

conditions. When compared with an uncoated steel surface, the Sn–MoN coating provided a much lower friction coefficient. It is possible that such a reduction in friction is due to the low-shear-strength Sn phase in the nanocomposite structure. Tin may have also reacted with additives in oil to produce a low-shear boundary film on the sliding surface.

During the last two decades the cost of PVD and CVD coatings has decreased significantly. As a result, these coatings are now used for a wide range of mainstream applications. In particular, in the field of machining and transportation, vacuum-based hard coatings are replacing or supplementing the traditional surface treatments, such as carburizing and nitriding. Obviously, different applications require different coatings with different thickness, hardness, and chemical composition. For example, the requirements for coatings in cutting and forming operations are different from those in engine applications. High-temperature oxidation stability, adhesion, thermal conductivity, affinity of the coating material for the counterface material, and hardness are the most important factors in cutting and forming operations; surface roughness, fatigue resistance, better cohesion and adhesion, wear resistance, low frictional behavior, and responsiveness to additives in engine oils are the most important requirements from coatings in transportation applications. In addition, some other issues need close attention. For cutting and forming tools, highly alloyed and expensive steel substrates (such as high speed steel and M2 tool steel) are often used, and they can endure deposition temperatures of up to 450–500 °C without significantly compromising their high hardness; however, low alloyed and cheap steel substrates are more common in engine components because they keep the cost down, and usually maximum deposition temperatures cannot exceed 150–200 °C.

The remainder of this section individually treats the different types of coatings developed for tribological applications.

14.4.1 Self-Lubricating Nanocomposite Coatings

For many years, researchers and practitioners have prepared and used many types of composite materials to combat friction and wear in mechanical applications [75, 76]. At present, several kinds of metal-, ceramic-, and polymer-matrix composites are impregnated with graphite, molybdenum disulfide, polytetrafluoroethylene (PTFE), and hexagonal boron nitride, which can provide low friction in sliding bearing applications. These and a few other composite materials, which are available as fairly thick (0.1–0.2 mm) coatings, are used for combating friction and wear, especially at elevated temperatures [77].

Most self-lubricating composite materials can also be applied on a surface by plasma spraying or electroplating methods [78]. Electroless nickel, chromium, and nickel–phosphorus coatings that contain small amounts of nanoscale graphite, MoS_2, PTFE, and diamond particles can be produced and used to achieve relatively thick metal-matrix films with self-lubricating properties [79]. In addition to these traditional practices, the modern PVD methods mentioned above can be used to deposit self-lubricating materials as thin (a few micrometers) nanocomposite coatings. Conceptually, the approach is similar to the conventional methods used in the production of the bulk self-lubricating composite materials and/or coatings mentioned above. However, structurally, the individual grains that make up such coatings are on the nanoscale or mixed homogeneously within the produced layers. For example, self-lubricating MoS_2 films have been used extensively by the aerospace industry to achieve and maintain low friction for many years. However, as a monolithic film, MoS_2 may not provide very long wear life. Extensive research into alloying MoS_2 and WS_2 with certain elements or compounds, such as Ni, Pb, Ag, Au, C, Ti, Sb_2O_3, TiN, and PbO, resulted in much improved wear life and reduced environmental sensitivity [80–83]. During deposition of alloyed MoS_2 or WS_2 films, deposition temperatures and other parameters can be controlled to achieve dense structure or morphology, and the texture or orientation of the films can be manipulated to achieve additional life extension and superior frictional behavior. Under certain deposition conditions, the nanocomposite or alloyed films become amorphous, but during tribological testing, they revert to a crystalline structure, which is essential for low friction [80, 84].

As in bulk self-lubricating composite materials, the soft solid lubricant phases in self-lubricating nanocomposite films are often selected from graphite, hexagonal boron nitride, and transition metal dichalcogenides such as molybdenum, tungsten, and niobium disulfide or diselenide. Their self-lubricating characteristic is related to a layered crystal structure. Specifically, the crystal structures of these solids are made of atomic layers in a stack. The atoms lying in the same layer are closely packed and strongly bonded to each other, while the layers are relatively far apart, and they are held together by weak van der Waals' forces. When present between sliding surfaces, these layers can align themselves parallel to the direction of relative motion and slide over one another with relative ease to provide low friction. Among the many types of nanocomposite coatings, the ones that contain WS_2 and MoS_2 have become very popular owing to their very low friction and wear coefficients. They are well-suited for many types of aerospace applications [71, 83]. Typical friction coefficients available through the use of such nanocomposite coatings are in the range of 0.01–0.05 in vacuum or inert test environments.

With the addition of certain metals (like Ti, Cr, and Ni), relatively hard versions of MoS_2 and other films have been produced, and as a result much longer wear life has been achieved in these coatings. The friction coefficients of such coatings were also shown to be much lower in humid air compared to those of the monolithic MoS_2 films. For example, the friction coefficient of a MoS_2–Ti film against steel or ceramic balls is below 0.1 in humid air and less than 0.05 in dry N_2; when compared with conventional MoS_2 films, its Vickers hardness is much higher and hence it lasts longer in tribological applications [85]. Furthermore, the frictional properties of this coating are not greatly affected by moisture in the test environment, and it is proposed for use in various dry-sliding and machining applications (e.g. milling, drilling, tapping, cold-forming dies and punches, stamping, bearings, and gears for aerospace and vacuum applications) [85, 86].

Various research groups have attempted to co-sputter MoS_2 with hard nitrides, borides, and oxides to achieve much longer durability in sliding bearing applications. As an example, this method can be used with either TiN or TiB_2 targets or a single target that consists of both TiN and MoS_2. As a result, the coatings are made of distinct nanolayers or phases of hard ceramic and soft MoS_2 phases. Depending on the amount of the hard phase, the hardness of the composite coating can be as high as 20 GPa, while their friction coefficients are in the range of 0.1–0.3, even in humid environments. These coatings can also perform well in machining [87]. When softer metallic or ceramic phases are used, the resultant nanocomposite films are also soft. For example, sputter deposition of multiple layers of MoS_2 and Pb results in a relatively soft film, but the wear life is much longer than that of either the MoS_2 or Pb films [88].

Using sputtering, pulsed laser, or arc-PVD methods, more complex multicomponent TiC/DLC, MoS_2/TiC/DLC, or WS_2/WC/DLC coatings have also been introduced, and as a result much improved tribological properties have been achieved over broad ranges of temperature and environmental humidity [15, 89]. These are also called adaptive or chameleon coatings owing to their reversible tribological properties, permitting stable operation and endurance in the cycled humidity and space-ambient environments needed for aerospace applications. Figure 14.6(a) shows a schematic of such a coating architecture, while Figure 14.6(b) shows how an actual nanocomposite coating produced according to such architecture behaves during testing in humid and dry environments [15]. The hard TiC and DLC phases in these coatings provide high strength and resistance to wear, while the solid lubricants DLC and MoS_2 ensure low friction in humid and dry environments, respectively.

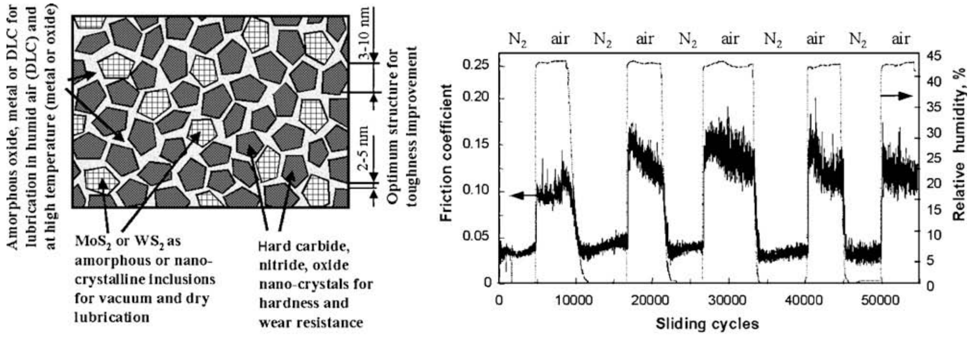

(a) (b)

Figure 14.6: (a) Schematic illustration of a nanocomposite coating with chameleon-like surface adaptive behavior and (b) frictional behavior; a YSZ/Au/MoS_2/DLC coating during a test with dry nitrogen and humid air environments. Note that frictional response is reversible and dominated by lubrication provided by MoS_2 in dry nitrogen and by DLC in humid air [15].

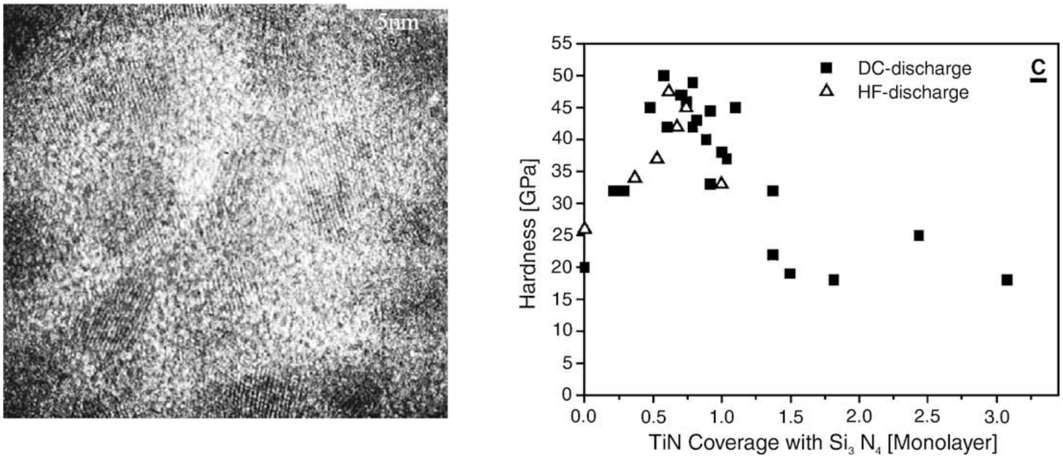

Figure 14.7: (a) High-resolution TEM image of TiN/Si_3N_4 nanocomposite coating, and (b) dependence of hardness on the thickness of the grain-boundary Si_3N_4 phase [90].

14.4.2 Superhard Nanocomposite Films

Nanocomposite coatings are made of either alternating layers of two or more chemically distinct phases or one of the phases dispersed or embedded into another phase. In the case of layered nanocomposite coatings, layers can be made of metallic and/or ceramic-based materials, and the thickness of each layer can be controlled down to 1 nm or less or up to several tens of nanometers. Mixed nanocomposite coatings can have a minor and a major phase; often, the minor phase is in the crystalline form while the matrix or major phase is crystalline or amorphous. Figure 14.7 shows a high-resolution TEM image of the TiN/Si_3N_4 system, together with its hardness profile with respect to the thickness of the grain-boundary Si_3N_4 phase [90]. The TiN/Si_xN_y system is one of the most studied, mainly because of its reported superhardness. While TiN represents the major or crystalline phase, Si_xN_y makes up the grain-boundary phase and is reported to be amorphous. The other major phases that have been used in the synthesis of similar superhard coatings include VN, NbN, ZrN, and (TiAl)N, again, embedded in an amorphous Si_3N_4 matrix [7, 30, 74, 91, 92].

Owing to their superhardness, these coatings are resistant to wear, abrasion, and erosion. Their thermal stability has also been reported to be excellent; hence, they are well suited for high-speed machining or high-temperature metal-forming operations. Their sliding friction coefficients are not very low under dry-sliding conditions. A liquid and/or solid lubricant must be used to achieve reasonably low friction coefficients in sliding contacts. The superhardness and high thermal stability of these coatings are thought to be the main reasons for their protection against wear. Under lubricated sliding conditions, they can also provide low friction, which is important for saving energy in many sliding contacts. Besides the system

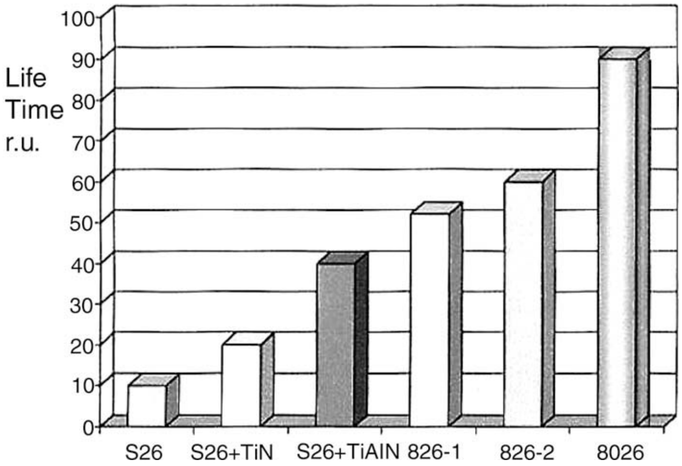

Figure 14.8: Cutting performance of various hard coatings while milling a CK45 steel. (Cutting conditions: feed rate, 0.23 mm/tooth; depth of cut, 2 mm; cutting speed, 179 m/minute). S26: indexable uncoated insert; S26 + TiN: TiN-coated; S26 + TiAlN: (TiAl)N-coated; 826-1 and -2: same inserts coated with $(Ti_{1-x}Al_x)N/a\text{-}Si_3N_4$ nanocomposite coatings; 8026: nc-$(Ti_{1-x}Al_x)N/a\text{-}Si_3N_4$ multilayer nanocomposite coating [91] (Courtesy of Pure and Applied Chemistry).

mentioned, numerous other multilayer superhard coatings have been developed in recent years and studied extensively under various machining and sliding conditions. For example, a series of composite systems consisting of CrN/NbN and TiAlN/VN has been developed and studied extensively for their friction- and wear-reducing abilities [29, 73, 93].

The nanocomposite coatings mentioned above have been fully developed and offered for industrial uses in recent years. Compared to their single-component predecessors, such as TiN, TiC and (TiAl)N, they work extremely well. For example, in a series of machining trials, nanocomposite TiN/Si_3N_4 coatings exhibited significantly higher durability, as shown in Figure 14.8 [91]. As can be imagined, during such cutting operations, the cutting edges of tools become very hot. Therefore, the nanocomposite coatings must have the ability to resist oxidation and maintain their superhardness and structural integrity; otherwise, they lose their nanocomposite natures and then their superhardness, which is essential for their impressive performance in such severe applications [94].

14.4.3 High-Temperature Adaptive Nanocomposite Coatings

High-temperature friction and wear reduction in oxidizing environments is one of the most difficult challenges for which nanocomposite coating architectures provide a considerable breakthrough, offering surface adaptation capability in various temperature regimes, resisting oxidation, and sustaining high contact loads. Oxides are most typically used. Many oxides demonstrate adequate stability up to 1000 °C, and above, but are characterized by strong covalent bonding, which suggests that the surfaces would be difficult to shear. In fact, ceramic materials typically yield high friction coefficients (0.8 to 1.0) that generate high tensile stresses and produce surface cracks and debris particles [95]. However, substoichiometric oxides of several transition metals, known as Magneli phases, form a homologous series of compounds with the formula Me_nO_{2n-1}, Me_nO_{3n-1}, or Me_nO_{3n-2} with planar lattice faults that result in crystallographic shear planes with reduced binding strength [96]. In general, the friction coefficients for single transition metal oxides forming Magneli phases range from 0.2 to 0.5 at homologous temperatures above 0.7 [97].

Several transition metal oxides (MO_x, WO_x, VO_x, etc.) and double oxides, such as molybdates and tungstates, deform by plastic flow at high temperature rather than brittle fracture at elevated temperatures. For example, MoO_3 has a friction coefficient of 0.2 at 700 °C [98]. One possible mechanism for such shear at elevated temperatures was linked to formation of an oxygen vacancy, as it was explored on rutile [99]. Erdemir [100] also suggested that the ionic potential of metal oxides and, for double oxides, the difference in relative ionic potentials of the oxides is related to the reduced shear strength required for friction reduction. Oxidation of some metals results in a reduction of the melting point, thereby forming a lubricious glaze with low shear strength at high homologous surface temperatures. Alkaline halides, such as CaF, can provide low-shear surface glazes at high temperatures (500–900 °C), close to their melting points, with friction coefficients around 0.2 [101]. At temperatures <500 °C, coatings of CaF and CeF improve wear resistance with friction coefficients <0.3 [102, 103], but have been reported to become brittle at low temperatures after one thermal cycle in air [104].

In general, the brittleness of oxides significantly limits their tribological applicability as monolithic coatings, especially when applied to less rigid substrates, such as steels and superalloys. Therefore, recent efforts with nanocomposite coating architectures have focused on a realization of thin oxide layers at the coating surface for friction and oxidation control, while the bulk of the coating remains in a non-oxidized state to ensure load support and fracture toughness. Both multilayer and nanocomposite concepts are being explored for this purpose, with surface adaptation by high temperature tribo-oxidation being one of the most common. For example, TiAlN and many other cutting tool coatings are based on hard phases with metal additions that form thermally stable protective oxide layers [105] that can be somewhat lubricous, with friction coefficients of 0.3–0.6 and low wear rates. Self-hardening and microstructure evolution in TiAlN, TiCrN, and TiBN coatings can occur over extended periods at high temperature to further increase wear resistance [9, 20, 106, 107]. The properties of these thin film compounds are sometimes modified further with one or more elements, such as vanadium [69], known to form Magneli phases at very high temperatures (>600 °C). Recent studies have included exploration of Mo–N and W–N based coatings, designed to oxidize in dry machining operations where high contact temperatures are common, and to create wear-resistant and somewhat lubricious oxide phases upon heating [108, 109].

Explorations of more complex nanocomposite architectures, such as yttria-stabilized zirconia (YSZ)–Ag–MoS_2, have shown that the chemistry of the oxide layer formation can be controlled catalytically to guide formation of different lubricious oxides over a broad temperature range. For example, the addition of MoS_2 was found effective as both lubricant and catalyst of silver molybdate formation, as the friction coefficient dropped to below 0.2 over the temperature range 25–700 °C for a series of coatings with different compositions. The low friction coefficients were attributed to the presence of MoS_2 and silver at <300 °C, silver molybdate compounds at 300–600 °C, and MoO_3 at higher temperatures [110]. Similar examples provide coatings consisting of a Mo_2N matrix with nanoscopic MoS_2 and Ag lubricant phases [111].

An alternative mechanism to oxide lubrication at moderate temperatures (300–600 °C) is the use of noble metals in the hard nanocomposite coating. This approach relies on the activation of metal diffusion from coating bulk to the surface to provide lubrication in contact areas at elevated temperatures. For example, inclusions of nanoscopic grains of gold in YSZ matrices were used to provide a temperature-actuated metal lubrication with friction coefficients to about 0.2 [112]. Other examples include TiC/Ag [113], YSZ–Ag [114], and CrN–Ag [115, 116] nanocomposite coatings. Typically up to 20 at.% of noble metal can be dispersed in ceramic matrices before significant softening occurs [117]. Such coatings are produced in a metastable condition by PVD methods, using forced co-deposition of metal and nanocrystalline ceramics at substrate temperatures of 150–200 °C. Heating during coating use activates metal diffusion and segregation at the contact surface, providing a low shear strength interface with typical lubrication up to 500 °C. Possible shortcomings include excessive contact deformations at elevated temperatures, reduction in mechanical stability of coating matrix, and non-reversibility of the diffusion process important for temperature cycling.

Ongoing research shows promise in combining oxide chemistry adaptation and controlled metal diffusion for lubrication during temperature cycles [118–120]. Insertion of diffusion control layers into a nanocomposite coating provides the means to restrict oxygen diffusion into the coating bulk as well as restrain noble metal diffusion to the surface. The coating immediately below the next intact diffusion barrier layer would essentially be in the as-deposited condition and ready to adapt to any ambient temperature upon exposure by the wear process. A three-layer coating made of the two adaptive YSZ–Ag–Mo lubricant layers with a TiN diffusion barrier between them is shown in Figure 14.9 after being thermally ‘actuated’ by postdeposition heating to 500 °C. While the top layer has the composition modification due to the silver diffusion to the surface, the adaptive layer below TiN was intact and ready to go for the next temperature cycle as soon as the wear process breached it. A similar coating with four adaptive layers provided stable friction coefficients over several temperature cycles, as illustrated in Figure 14.10.

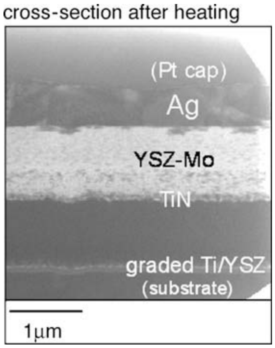

Figure 14.9: Cross-section TEM image of a multilayer coating made of two adaptive YSZ–Mo–Ag nanocomposite layers separated with a TiN diffusion barrier and applied to an Inconel 718 superalloy substrate with a Ti/YSZ bonding layer. Image was taken after coating heating to 500 °C and subsequent cooling in air, demonstrating Ag diffusion to the coating surface and preservation of the coating uniformity under the TiN barrier layer. Top Pt layer was added during TEM cross-section preparation [120].

These multilayer coatings lend themselves to incorporation of sensor layers to allow in situ measurement of the extent of wear, and can be designed to provide a warning prior to failure, since diffusion barrier materials doped with rare earth elements that fluoresce with characteristic spectra can be placed at known thicknesses. If the area being worn is illuminated, the spectrum of scattered light gives off distinctive and intense spectra, allowing an easy reporting of the in situ wear state condition, which is critical for some aerospace and transportation applications [121].

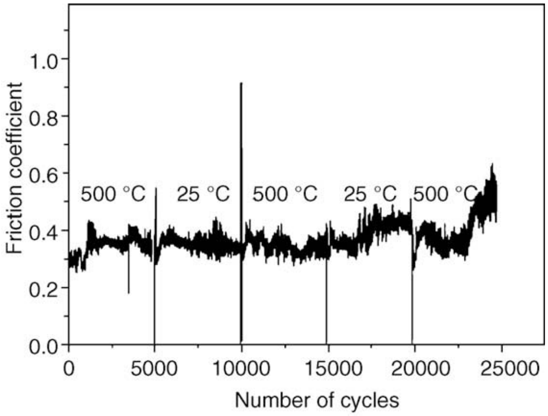

Figure 14.10: Friction coefficients measured during pin-on-disk sliding experiments with repeated heating and cooling of a multilayered coating with four YSZ–Ag–Mo adaptive nanocomposite layers separated by TiN diffusion barrier layers and applied to an Inconel 718 superalloy substrate. Data were obtained in laboratory air with a Si_3N_4 ball as a sliding counterpart [119].

14.4.4 Nanostructured Diamond and Diamond-Like Carbon Films

Diamond and DLC films have attracted tremendous interest during the past three decades mainly because of their unusual mechanical, tribological, thermal, optical, and electrical properties. Both coatings are effective in reducing sliding friction and wear of machine elements and, hence, are used as solid lubricants in many industrial applications. Diamond is crystalline and represents the hardest known material, while DLC is amorphous but combines some of the many attractive properties of diamond. Besides diamond and DLC, there exist several other kinds of carbon-based materials (graphite, graphite fluoride, glassy carbon, and carbon–carbon or carbon–graphite composites) that also provide very impressive tribological properties in a wide range of applications, including seal materials for the rotating-equipment industry. The high-friction carbon–carbon composites are used in the making of high-performance brakes for racing cars and various aircraft.

14.4.4.1 Nanocrystalline Diamond Films

Diamond is the hardest natural material known and hence offers huge possibilities for combating friction and wear under some of the harshest application conditions. Reported friction coefficients for diamond are generally below 0.1, and its wear resistance against many engineering materials is superb. At elevated temperature, it may oxidize and undergo oxidative wear, especially during sliding against ferrous-based materials. The high chemical inertness of diamond ensures extreme resistance to corrosive attacks in highly acidic media. Because bulk diamond is very expensive, it cannot be used as a tribomaterial in many engineering applications. However, for the past 30 years, synthetic diamond films have been produced on appropriate tribological surfaces by CVD methods [122, 123]. These films are highly crystalline and possess many of the attractive properties of natural diamond. One major drawback in applications involving tribology has been their relatively rough surface finish, which can cause high friction and wear. During the last two decades, great strides have been made in controlling surface roughness of diamond films by effective polishing or by reducing the grain size to the nanoscale. Polishing of superhard diamond has proved to be difficult and expensive, while producing diamond films with nanoscale grains is much easier and is now a common practice for applications involving friction and wear. In one of the methods, appropriate mixtures of Ar–C_{60} and Ar–CH_4 were used as the main precursors in a microwave CVD process, and high-quality nanocrystalline diamond films with a smooth surface finish were produced by Gruen [46]. The grain size of these films is in the range of 2–5 nm (Figure 14.11), and their surface finish is 10–20 nm (Roughness Measurement System (RMS)). The friction coefficients of such films are in the range of 0.02–0.05 in open air, mainly because of their smooth surface finish. A rough or microcrystalline diamond film would have provided friction coefficients of more than 0.2 under the same test conditions [124–126]. Nanocrystalline diamond films are currently used in machining, sliding or rotating-bearing applications (such as mechanical seals), microelectromechanical systems, atomic force microscopy tips, and other engineering applications.

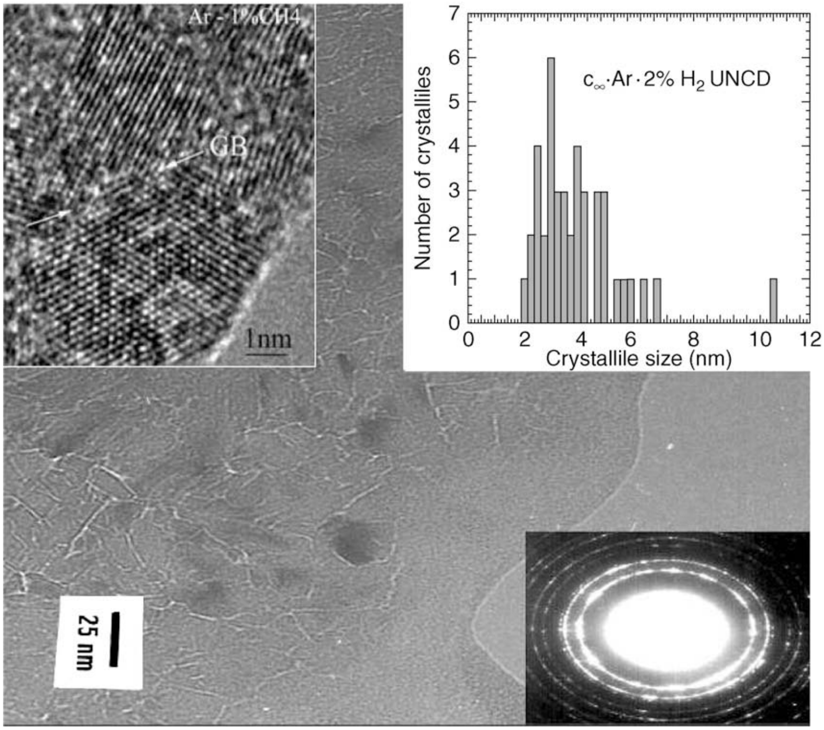

Figure 14.11: TEM image of nanocrystalline diamond film (left inset shows details of nanograins and grain boundaries; right inset shows grain size distribution) [72] (Courtesy of CRC Publications).

14.4.4.2 Nanostructured Carbide-Derived Carbon Coatings

Another interesting carbon film that emerged in recent years is carbide-derived carbon (CDC). It is produced at atmospheric pressures in a tube furnace by simply passing chlorine or a mixture of chlorine plus hydrogen gases over the carbide-based materials at elevated temperatures (600–1100 °C). Chlorine leaches out the metallic part and leaves the carbon behind as a coating. For example, in the case of SiC, Si reacts with chlorine and leaves the reaction chamber as $SiCl_4$ gas, and the carbon left behind consolidates and becomes a solid film [127–130]. For the production of CDC, one does not need a high vacuum or plasma deposition system. As shown in Figure 14.12, the CDC film is truly nanostructured and composed of nanocrystalline diamond and graphite phases, carbon nano-onions, and amorphous carbon [127, 128].

Like diamond and DLC, CDC is an excellent tribological material. It provides low friction and wear coefficients under a wide range of sliding conditions. Figure 14.13 compares the friction coefficient of CDC with that of SiC. As evident, CDC provides three to four times lower

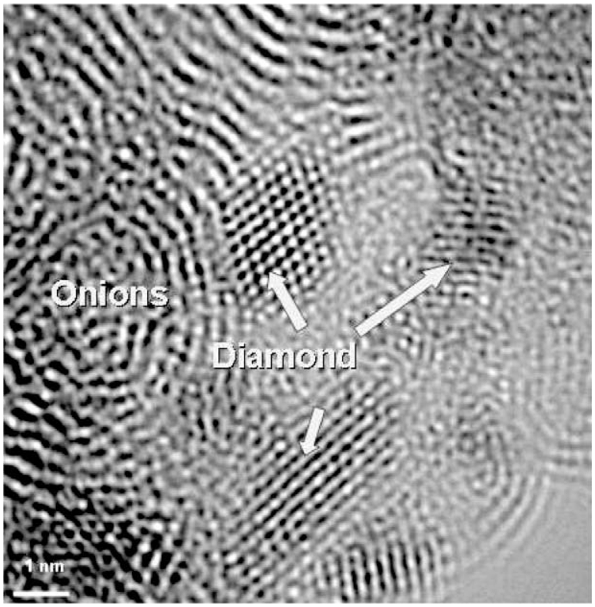

Figure 14.12: High-resolution TEM photomicrograph of nanostructured CDC film on SiC substrate. The sample was treated for 24 hours at 1000 °C in Ar/3.5% Cl_2 [127] (Courtesy of Nature).

friction coefficient than SiC. By subjecting CDC to hydrogen plasma treatment, much lower friction coefficients (in the range of 0.02–0.05) have been achieved, and such dramatic reductions in friction have been attributed to the hydrogen termination of the dangling σ-bonds of surface carbon atoms.

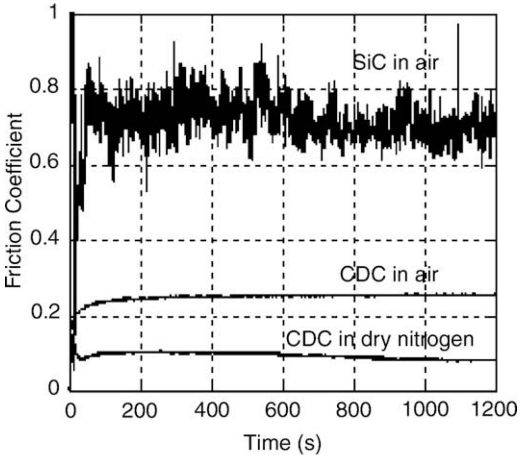

Figure 14.13: Friction performance of CDC against Si_3N_4 ball in humid air and dry nitrogen. For comparison, the friction coefficient of SiC is also provided [72] (Courtesy of CRC Publications).

14.4.4.3 Nanocomposite DLC Films

Structurally, DLC films are amorphous and made of sp^2- and sp^3-hybridized carbon atoms. They can be alloyed with additional elements without changing their amorphous structures. For example, hydrogen and nitrogen atoms can be introduced in large quantities without causing any structural transformations. Those with large amounts of hydrogen are called 'hydrogenated' DLCs, while those containing nitrogen are known as carbon nitride films. The DLC films with a high proportion of sp^3-bonding are superhard and hence resistant to wear. In contrast, DLC films with high amounts of sp^2-bonded carbon are soft and hence may have relatively poor frictional behavior. Almost all of the DLC films available today provide very low friction and wear coefficients in open air. Test environments and conditions can have significant effects on the friction and wear of DLC films. Some DLC films work best in inert or vacuum-like environments, while others operate best in the presence of humidity or other gaseous species. To further improve the tribological functionality, researchers have been introducing additional crystalline phases into these films. Such nanocomposite films are thought to provide even lower friction and wear and significantly higher load-carrying capacity. These DLC films are used in tribological applications that range from magnetic hard disks to various automotive parts and components.

Multilayer DLC coatings have been studied extensively by several investigators for their mechanical and tribological properties. In particular, films of C/W and C/Cr multilayers have attracted the most attention [50, 66, 131]. These coatings have been produced on steel substrates and evaluated for their tribological properties under dry- and lubricated–sliding conditions [26, 132, 133]. The results indicated that these coatings indeed possess superior load-carrying capacity and wear resistance not only in laboratory tests but also in actual applications.

Some of the nanostructured carbon films consisted of nanoscale carbide and other crystalline phases that are evenly dispersed or embedded into the amorphous carbon matrix. Figure 14.3 shows nanolayered and nanocomposite carbon films that are currently used for tribological applications. As another example, a nanocomposite TiC/DLC system is shown in Figure 14.14(a) [14]. Owing to a large network of grain boundaries between the nanocrystalline TiC phase and the amorphous DLC matrix, such a film is able to effectively limit crack initiation. Even if a crack is present or has initiated, grain boundaries effectively deflect or terminate further crack growth and film delamination. Figure 14.14(b) shows how such a composite film behaves under severe deformation conditions. Apparently, encapsulation of 3–10 nm sized grains of hard crystalline TiC within the amorphous DLC matrix restricts dislocation activity, diverts and arrests macrocrack development, and maintains a high level of hardness (32 GPa) similar to that of other superhard coatings. Overall, the combination of the nanocrystalline TiC and amorphous DLC phases with a functionally graded interface provides excellent toughness and high resistance to adhesive failure under severe tribological situations. There are numerous

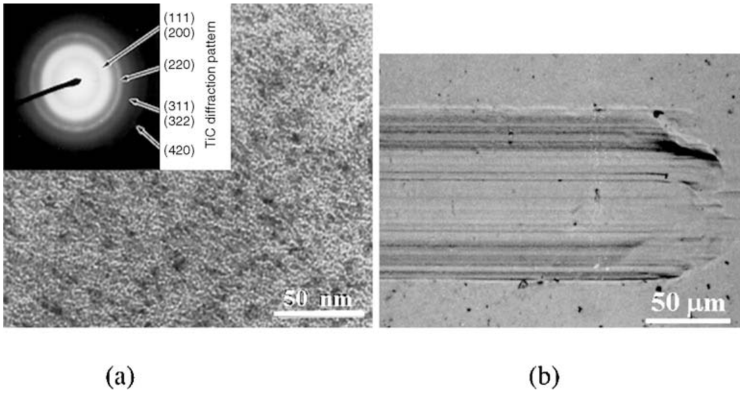

Figure 14.14: (a) TEM image and electron diffraction of TiC/DLC nanocomposite coating, and (b) TEM image of plastic deformation obtained by scratching a diamond needle of 0.2 mm radius under 50 N. Note that the coating remains intact on the surface and does not show any evidence of delamination [14].

other tribological coatings with nanolayered or composite architectures. Tribological test results from them further confirm that these films are better able to resist wear and provide much lower friction coefficients in dry, humid, and vacuum environments, as well as in oils, compared with the monolithic or single-phase DLC coatings.

14.5 Summary

In this chapter, we attempted to summarize key recent developments in the production and use of nanostructured and composite coatings and their tribological properties. Structurally, these coatings are unique and may consist of two or more phases in a nanolayered or evenly distributed nanocomposite fashion. At present, several PVD and CVD techniques are available for the deposition of nanocomposite coatings on all kinds of substrates. In particular, with the cathodic arc and HIPIMS methods, formation of multiphase and hence multifunctional coatings has become much easier. Reported laboratory and field test results show that unlike conventional coatings, nanostructured and composite coatings provide far superior friction and wear properties even under very harsh tribological conditions, including high contact loads and elevated temperatures in oxidizing environments. Some of the nanocomposite coatings are superhard and able to extend the wear life of metal-cutting and metal-forming tools significantly. The selection of grain-boundary phases and their thickness seems to control the hardness, toughness, and other mechanical properties of these films. In the case of multilayer coatings, the thickness of the layers and their chemical compositions seems to play important roles in their mechanical and tribological properties. These coatings can be designed to provide self-lubricating properties regardless of the test environments and conditions with a surface self-adaptation capability to cope with high mechanical loads and contact speeds, as well as variable humidity and elevated temperatures in oxidizing environments. With the selection of optimal coating ingredients and/or phases, the effects of test environments and/or conditions on friction and wear may be reduced. Nanocrystalline diamond and nanocomposite CDC and DLC films are some of the prime examples that can provide self-lubricating capability with friction coefficients below 0.1, even under very harsh sliding conditions. Overall, nanostructured and nanocomposite coatings hold great promise for applications involving severe operating conditions. In particular, these coatings can be ideal for transportation, aerospace, and manufacturing applications. Because of their superior mechanical properties and high chemical and structural stability, nanocomposite coatings can significantly lower friction and wear losses under rolling, rotating, sliding, cutting, grinding, chopping, drilling, milling, and forming operations that exist in numerous industrial sectors. They can also provide significant energy, environmental, and economic benefits in such operations.

Acknowledgments

This work was supported by the US Department of Energy, Office of Energy Efficiency and Renewable Energy, Freedom Car and Vehicle Technologies Program, under Contract No. DE-AC02-06CH11357. Additional support is provided in part by the Air Force Office of Scientific Research (Grant No. FA9550-08-1-0010).

References

[1] P.M. Ajayan, L.S. Schadler, P.V. Braun, Nanocomposite Science and Technology, Wiley-VCH, Weinheim (2003).
[2] H.S. Nalwa, Handbook of Organic–Inorganic Hybrid Materials and Nanocomposites, Vols. 1–2, American Scientific Publication (2003).
[3] D. Vollath, D.V. Szabo, Synthesis and properties of nanocomposites, Adv. Eng. Mater. 6 (2004) 117–127.
[4] C. Donnet, A. Erdemir, Historical developments and new trends in tribological and solid lubricant coatings, Surf. Coat. Technol. 180–181 (2004) 76–84.
[5] J. Musil, Physical and mechanical properties of hard nanocomposite films prepared by magnetron sputtering, in: Nanostructured Hard Coatings, Kluwer Academic, New York (2005) 1–46.
[6] S. Veprek, Ultra hard nanocomposite coatings with hardness of 80 to 105 GPa, Societe Francaise du Vide (2000) 185–192.
[7] S. Veprek, Superhard nanocomposites: design concept, properties, present and future industrial applications, Eur. Phys. J., Appl. Phys. 28 (2004) 313–317.
[8] A. Erdemir, Review of engineered tribological interfaces for improved boundary lubrication, Tribol. Int. 38 (2005) 249–256.
[9] C. Mitterer, P.H. Mayrhofer, Design of nanostructured hard coatings for optimum performance, Key Eng. Mater. 264–268 (2004) 453–458.
[10] H. Holleck, H. Leiste, A. Stuber, S. Ulrich, Nanoscale protective coatings for highly stressed tools and components, Z. Metallk. 94 (2003) 621–627.
[11] E. Lugscheider, K. Bobzin, C. Pinero, F. Klocke, T. Massmann, Development of a superlattice (Ti, Hf, Cr) N coating for cold metal forming applications, Surf. Coat. Technol. 177 (2004) 616–622.

[12] Y.-W. Chung, W.D. Sproul, Superhard coating materials, MRS Bull. 28 (2003) 164–168.

[13] W.D. Münz, Super lattice-structured hard coatings, in: Trends and Applications of Thin Films, Vides, Nancy (2000) 12–16.

[14] A.A. Voevodin, J.S. Zabinski, Supertough wear resistant coatings with ‘chameleon’ surface adaptation, Thin Solid Films 370 (2000) 223–231.

[15] A.A. Voevodin, J.S. Zabinski, Nanocomposite and nanostructured tribological materials for space applications, Composite Sci. Technol. 65 (2005) 741–748.

[16] D.V. Shtansky, N.A. Gloushankova, I.A. Bashkova, M.I. Petrzhik, A.N. Sheveiko, F.V. Kiryukhantsev-Korneev et al., Multifunctional biocompatible nanostructured coatings for load-bearing implants, Surf. Coat. Technol. 201 (2006) 4111–4118.

[17] D.V. Shtansky, Ph.V. Kiryukhantsev-Korneev, A.N. Sheveiko, A.E. Kutyrev, E.A. Levashov, Hard tribological Ti–Cr–B–N coatings with enhanced thermal stability, corrosion- and oxidation-resistance, Surf. Coat. Technol. 202 (2007) 861–865.

[18] V.I. Gorokhovsky, C. Bowman, P. Gannon, D. VanVorous, A.A. Voevodin, C. Muratore et al., Deposition and characterization of hybrid filtered arc/magnetron multilayer nanocomposite cermet coatings for advanced tribological applications, Wear 265 (2008) 741–745.

[19] E. Bergmann, G.I. van der Kolk, B. Buil, T. Hurkmans, The next generation of deposition equipment for wear protection coatings, Surf. Coat. Technol. 114 (1999) 101–107.

[20] P.H. Mayrhofer, C. Mitterer, L. Hultman, H. Clemens, Microstructural design of hard coatings, Prog. Mater. Sci. 51(8) (2006) 1032–1114.

[21] A.P. Ehiasarian, W.D. Münz, L. Hultman, U. Helmersson, I. Petrov, High-power pulsed-magnetron-sputtered CrN_x films, Surf. Coat. Technol. 163 (2003) 267–272.

[22] A.P. Ehiasarian, P.Eh. Hovsepian, L. Hultman, U. Helmersson, Comparison of microstructure and mechanical properties of chromium nitride-based coatings deposited by high power impulse magnetron sputtering and by the combined steered cathodic arc/unbalanced magnetron technique, Thin Solid Films 457 (2004) 270–277.

[23] P. Karvankova, M.G.J. Veprek-Heijman, O. Zindulka, A. Bergmaier, S. Veprek, Superhard nc-TiN/a-BN and nc-TiN/a-TiB_x/a-BN coatings prepared by plasma CVD and PVD: a comparative study of their properties, Surf. Coat. Technol. 163–164 (2003) 149–156.

[24] V.I. Gorokhovsky, C. Bowman, P. Gannon, D. VanVorous, A.A. Voevodin, A. Rutkowski et al., Tribological performance of hybrid filtered arc-magnetron coatings. Part I: Coating deposition process and basic coating properties characterization, Surf. Coat. Technol. 201 (2006) 3732–3747.

[25] A.S. Loir, F. Garrelie, F. Donnet, Toward the deposition of tetrahedral diamondlike carbon films on hip joints by femtosecond pulsed laser ablation, Surf. Coat. Technol. 188–89 (2004) 728–734.

[26] A.A. Voevodin, S.V. Prasad, J.S. Zabinski, Nanocrystalline carbide amorphous carbon composites, J. Appl. Phys. 82 (1997) 855–858.

[27] A.A. Voevodin, S.D. Walck, J.S. Zabinski, Architecture of multilayer nanocomposite coatings with super-hard diamond-like carbon layers for wear protection at high contact loads, Wear 203–204 (1997) 516–527.

[28] A.A. Voevodin, J.S. Zabinski, Hybrid plasma deposition methods for synthesis of nanostructured materials, in: A.A. Voevodin, D.V. Shtansky, E.A. Levashov, J.J. Moore (Eds.), Nanostructured Thin Films and Nanodispersion Strengthened Coatings, Kluwer Academic, Dordrecht (2004) 103–111.

[29] M. Jilek, T. Cselle, P. Holubar, M. Morstein, M.G.J. Veprek-Heijman, S. Veprek, Development of novel coating technology by vacuum arc with rotating cathodes for industrial production of nc-$(Al_{1-x}Ti_x)$ N/a–Si_3N_4 superhard nanocomposite coatings for dry, hard machining, Plasma Chem. Plasma Process. 24 (2004) 493–510.

[30] S. Veprek, A. Niederhofer, K. Moto, T. Bolom, H.D. Mannling, P. Nesladek et al., Composition, nanostructure, and origin of the ultrahardness in nc-TiN/a-Si_3N_4/a- and nc-$TiSi_2$ nanocomposites with H-v = 80 to < = 105 GPa, Surf. Coat. Technol. 133 (2000) 152–159.

[31] A.J. Perry, D.G. Teer, Surface technology for temperature-sensitive materials, Surf. Coat. Technol. 97(1–3) (1997) 244–249.

[32] S. Veprek, M.J.G. Veprek-Heijman, Industrial applications of superhard nanocomposite coatings, Surf. Coat. Technol. 202 (2008) 5063–5073.

[33] D.T. Quinto, Technology perspective on CVD and PVD coated metal-cutting tools, Int. J. Refract. Metals Hard Mater. 14(1–3) (1996) 7–20.

[34] A. Erdemir, Solid lubricants and self-lubricating films, in: Handbook of Modern Tribology, CRC Press, Boca Raton, FL (2001) 787–818.

[35] S. Schiller, K. Goedicke, J. Reschke, V. Kirchhoff, S. Schneider, F. Milde, Pulsed magnetron sputter technology, Surf. Coat. Technol. 61 (1993) 331–337.

[36] P.J. Kelly, R.D. Arnell, Magnetron sputtering: a review of recent developments and applications, Vacuum 56 (2000) 159–172.

[37] I.I. Aksenov, V.A. Belous, V.G. Padalka, V.M. Khoroshikh, Apparatus to rid the plasma of a vacuum arc of macroparticles, Instrum. Exp. Techn. 21 (1978) 1416–1418.

[38] R.L. Boxman, V. Zhitomirsky, B. Alterkop, E. Gidalevich, I.I. Beilis, M. Keidar, S. Goldsmith, Recent progress in filtered vacuum arc deposition, Surf. Coat. Technol. 86–87 (1996) 243–253.

[39] A. Anders, Approaches to rid cathodic arc plasmas of macro- and nanoparticles: a review, Surf. Coat. Technol. 120–121 (1999) 319–330.

[40] P.J. Martin, A. Bendavid, Review of the filtered vacuum arc process and materials deposition, Thin Solid Films 394 (2001) 1–15.

[41] V.I. Gorokhovsky, R. Bhattacharya, D.G. Bhat, Characterization of large area filtered arc deposition technology: Part I – Plasma processing parameters, Surf. Coat. Technol. 140 (2001) 82–92.

[42] U. Helmersson, M. Lattemann, J. Bohlmark, A.P. Ehiasarian, J.T. Gudmundsson, Ionized physical vapor deposition (IPVD): a review of technology and applications, Thin Solid Films 513 (2006) 1–24.

[43] V. Kouznetsov, K. Macák, J.M. Schneider, U. Helmersson, I. Petrov, A novel pulsed magnetron sputter technique utilizing very high target power densities, Surf. Coat. Technol. 122 (1999) 290–293.

[44] A.P. Ehiasarian, R. New, W.-D. Munz, L. Hultman, U. Helmersson, V. Kouznetsov, Influence of high power densities on the composition of pulsed magnetron plasmas, Vacuum 65 (2002) 147–154.

[45] S. Bolz, K. Bobzin, N. Bagcivan, P. Immich, J. Alami, R. Cremer, T. Leyendecker, Properties of (Cr, Al) N and (Cr, Al, Si) N coatings for cutting tools deposited by HPPMS, Thin Solid Films 517 (2008) 1251–1256.

[46] D.M. Gruen, Nanocrystalline diamond films, Annu. Rev. Mater. Sci. 29 (1999) 211–259.

[47] W.J. Meng, T.J. Curtis, L.E. Rehn, P.M. Baldo, Plasma-assisted deposition and characterization of Ti-containing diamondlike carbon coatings, J. Appl. Phys. 83(11) (1998) 6076–6081.

[48] S.H. Yao, W.H. Kao, Y.L. Su, T.H. Liu, On the tribology and micro-drilling performance of TiN/AlN nanolayer coatings, Mater. Sci. Eng. A Struct. Mater. Prop. Microstruct. Process. 386(1–2) (2004) 149–155.

[49] Z. Zhou, W.M. Rainforth, B. Rother, A.P. Ehiasarian, P.Eh. Hovsepian, W.D. Münz, Elemental distributions and substrate rotation in industrial TiAlN/VN superlattice hard PVD coatings, Surf. Coat. Technol. 183(2–3) (2004) 275–282.

[50] P.Eh. Hovsepian, Y.N. Kok, A.P. Ehiasarian, A. Erdemir, J.G. Wen, I. Petrov, Structure and tribological behaviour of nanoscale multilayer C/Cr coatings deposited by the combined steered cathodic arc/unbalanced magnetron sputtering technique, Thin Solid Films 447–448 (2004) 7–13.

[51] S.A. Barnett, A. Madan, Hardness and stability of metal–nitride nanoscale multilayers, Scripta Mater. 50(6) (2004) 739–744.

[52] L. Hultman, C. Engström, M. Odén, Mechanical and thermal stability of TiN/NbN superlattice thin films, Surf. Coat. Technol. 133–134 (2000) 227–233.

[53] S. Zhang, D. Sun, Y. Fu, H. Du, Recent advances of superhard nanocomposite coatings: a review, Surf. Coat. Technol. 167 (2003) 113–119.

[54] C. Mitterer, P.H. Mayrhofer, Some materials science aspects of PVD hard coatings, Adv. Solid State Phys. 41 (2001) 263–274.

[55] S. Veprek, P. Karvankova, M.G.J. Veprek-Heijman, Possible role of oxygen impurities in degradation of nc-TiN/a-Si_3N_4 nanocomposites, J. Vac. Sci. Technol. B 23 (2005) L17–L21.

[56] J.S. Koehler, Attempt to design a strong solid, Phys. Rev. B 2 (1970) 547–551.

[57] D.R. Askeland, P.P. Phule, The Science and Engineering of Materials, 4th ed., Thomson Learning (2003) 153–154.

[58] J. Schiotz, F.D. Di Tolla, K.W. Jacobsen, Softening of nanocrystalline metals at very small grains, Nature 391 (1998) 561–563.

[59] J. Musil, P. Zeman, H. Hruby, P.H. Mayrhofer, ZrN/Cu nanocomposite film – a novel superhard material, Surf. Coat. Technol. 120–121 (1999) 179–183.

[60] P. Zeman, R. Cerstvy, P.H. Mayrhofer, C. Mitterer, J. Musil, Structure and properties of hard and superhard Zr–Cu–N nanocomposite coatings, Mater. Sci. Eng. A 289 (2000) 189–197.

[61] J. Musil, H. Hruby, P. Zeman, H. Zeman, R. Cerstvy, P.H. Mayrhofer, C. Mitterer, Hard and superhard nanocomposite Al–Cu–N films prepared by magnetron sputtering, Surf. Coat. Technol. 142–144 (2001) 603–609.

[62] J. Musil, J. Vlcek, Magnetron sputtering of hard nanocomposite coatings and their properties, Surf. Coat. Technol. 142–144 (2001) 557–566.

[63] J. Musil, I. Leipner, M. Kolega, Nanocrystalline and nanocomposite CrCu and CrCu–N films prepared by magnetron sputtering, Surf. Coat. Technol. 115 (1999) 32–37.

[64] S. Veprek, S. Reiprich, A concept for the design of novel superhard coatings, Surf. Coat. Technol. 268 (1995) 64–71.

[65] A. Leyland, A. Matthews, On the significance of the H/E ratio in wear control: a nanocomposite coating approach to optimised tribological behaviour, Wear 246 (2000) 1–11.

[66] A. Czyzniewski, Deposition and some properties of nanocrystalline WC and nanocomposite WC/a-C:H coatings, Thin Solid Films 433(1–2) (2003) 180–185.

[67] K. Holmberg, A. Matthews, H. Ronkainen, Coatings tribology-contact mechanisms and surface design, Tribol. Int. 31(1–3) (1998) 107–120.

[68] K. Holmberg, H. Ronkainen, A. Laukkanen, K. Wallin, A. Erdemir, O. Eryilmaz, Tribological analysis of TiN and DLC coated contacts by 3D FEM modelling and stress simulation, Wear 264 (2008) 877–884.

[69] P.H. Mayrhofer, P.E. Hovsepian, C. Mitterer, W.D. Münz, Calorimetric evidence for frictional self-adaptation of TiAlN/VN superlattice coatings, Surf. Coat. Technol. 177 (2004) 341–347.

[70] C. Donnet, A. Erdemir, Solid lubricant coatings: recent developments and future trends, Tribol. Lett. 17 (2004) 389–397.

[71] A.A. Voevodin, J.P. O'Neill, J.S. Zabinski, Nanocomposite tribological coatings for aerospace applications, Surf. Coat. Technol. 119 (1999) 36–45.

[72] A. Erdemir, O.L. Eryilmaz, M. Urgen, K. Kazmanli, N. Mehta, B. Prorok, Tribology of nanostructured materials and coatings, in: Y. Gogotsi (Ed.), Handbook of Nanomaterials, CRC Publication (2005) 685–711.

[73] W.D. Münz, D.B. Lewis, P.E. Hovsepian, C. Schonjahn, A. Ehiasarian, I.J. Smith, Industrial-scale manufactured superlattice hard PVD coatings, Surf. Eng. 17(1) (2001) 15–27.

[74] S. Veprek, P. Nesládek, A. Niederhofer, F. Glatz, M. Jílek, M. Síma, Recent progress in the superhard nanocrystalline composites: towards their industrialization and understanding of the origin of the superhardness, Surf. Coat. Technol. 108–109(1–3) (1998) 138–147.

[75] P.K. Rohatgi, S. Ray, Y. Liu, Tribological properties of metal matrix graphite particle composites, Int. Mater. Rev. 37 (1992) 129–149.

[76] S.E. Mcelwain, T.A. Blanchet, L.S. Schadler, W.G. Sawyer, Effect of particle size on the wear resistance of alumina-filled PTFE micro- and nanocomposites, Tribol. Trans. 51 (2008) 247–253.

[77] C. DellaCorte, H. E. Sliney, Tribological properties of PM 212: a high-temperature self-lubricating powder metallurgy composite, NASA TM-102355 (1990).

[78] F. Zimmerman, D.G. Clark, K.T. Aust, U. Erb, Pulse electrodeposition of Ni–SiC nanocomposite, Mater. Lett. 52(1–2) (2002) 85–90.

[79] M. Ghorbani, M. Mazaheri, K. Khangholi, Y. Kharazi, Electro deposition of graphite–brass composite coatings and characterization of their tribological properties, Surf. Coat. Technol. 148(1) (2001) 1–76.

[80] J.S. Zabinski, M.S. Donley, V.J. Dyhouse, N.T. McDevitt, Chemical and tribological characterization of PbO–MoS_2 films grown by pulsed laser deposition, Thin Solid Films 214 (1992) 156–163.

[81] J.S. Zabinski, M.S. Donley, S.D. Walck, T.R. Schneider, N.T. McDevitt, Effects of dopants on the chemistry and tribology of sputter-deposited MoS_2 films, Tribol. Trans. 38 (1995) 894–904.

[82] M.R. Hilton, R. Bauer, S.V. Didziulis, M.T. Dugger, J. Keem, J. Scholhamer, Structural and tribological studies of MoS_2 solid lubricant films having tailored metal-multilayer nanostructures, Surf. Coat. Technol. 53 (1992) 13–23.

[83] J.R. Lince, Tribology of co-sputtered nanocomposite Au/MoS_2 solid lubricant films over a wide contact stress range, Tribol. Lett. 17(3) (2004) 419–428.

[84] K.J. Wahl, L.E. Seitzman, R.N. Bolster, I.L. Singer, Low-friction, high-endurance, ion-beam-deposited Pb–Mo–S coatings, Surf. Coat. Technol. 73 (1995) 152–159.

[85] D.G. Teer, J. Hampshire, V. Fox, V. Bellido-Gonzalez, The tribological properties of MoS_2/metal composite coatings deposited by closed-field magnetron sputtering, Surf. Coat. Technol. 94–95 (1997) 572–578.

[86] D.G. Teer, New solid lubricant coatings, Wear 251 (2001) 1068–1074.

[87] R. Gilmore, M.A. Baker, P.N. Gibson, W. Gissler, Preparation and characterization of low-friction TiB_2-based coatings by incorporation of C or MoS_2, Surf. Coat. Technol. 105 (1998) 45–50.

[88] M.C. Simmonds, A. Savan, H. Van Swygenhoven, E. Pfluger, S. Mikhailov, Structural, morphological, chemical and tribological investigations of sputter-deposited MoS_x/metal multilayer coatings, Surf. Coat. Technol. 108–109 (1998) 340–344.

[89] A.A. Voevodin, J. Bultman, J.S. Zabinski, Investigation into three-dimensional laser processing of tribological coatings, Surf. Coat. Technol. 107 (1998) 12–19.

[90] S. Veprek, M.G.J. Veprek-Heijman, P. Karvankova, J. Prochazka, Different approaches to superhard coatings and nanocomposites, Thin Solid Films 476(1) (2005) 1–29.

[91] S. Veprek, M. Jilek, Superhard nanocomposite coatings. From basic science toward industrialization, Pure Appl. Chem. 74(3) (2002) 475–481.

[92] S. Veprek, A.S. Argon, Towards the understanding of mechanical properties of super- and ultrahard nanocomposites, J. Vac. Sci. Technol. B 20 (2002) 650–664.

[93] W.D. Münz, D.B. Lewis, P.E. Hovsepian, C. Schönjahn, A. Ehiasarian, I.J. Smith, Industrial-scale manufactured superlattice hard PVD coatings, J. Vac. Sci. Technol. A 18(4) (2000) 1681–1689.

[94] M. Jilek, P. Holubar, M. Veprek-Heijman, S. Veprek, Toward the industrialization of superhard nanocrystalline composites for high speed and dry machining, MRS Symp. Proc. 750 (2003) 393.

[95] F.P. Bowden, D. Tabor, The Friction and Lubrication of Solids, Oxford University Press, New York (1986).

[96] A. Magneli, Structures of the ReO_x-type with recurrent dislocations of homologous series of molybdenum and tungsten oxides, Acta Crystallogr. 6 (1953) 495–500.

[97] M.B. Peterson, S.Z. Li, S.F. Murray, Wear-resisting oxide films for 900 °C, Report No. 20082401, Argonne National Laboratory, 1994, pp. 1–53.

[98] M.B. Peterson, S.F. Murray, J.J. Florek, Consideration of lubricants for temperatures above 1000 °F, ASLE Trans. 2 (1959) 225–234.

[99] M.N. Gardos, H. Hong, W.O. Winer, The effect of anion vacancies on the tribological properties of rutile (TiO_{2x}), Part II: Experimental evidence, Tribol. Trans. 36 (1990) 209–220.

[100] A. Erdemir, A crystal-chemical approach to lubrication by solid oxides, Tribol. Lett. 8 (2000) 97–102.

[101] H.E. Sliney, T.N. Strom, G.P. Allen, Fluoride solid lubricants for extreme temperatures and corrosive environments, ASLE Trans. 8 (1963) 307–322.

[102] S.F. Murray, S.J. Calabrese, Effect of solid lubricants on low speed sliding behavior of silicon nitride at temperatures to 800 °C, Lubric. Eng. 49 (1993) 955–964.

[103] H.E. Sliney, Solid lubricant materials for high temperatures – a review, Tribol. Int. (October 1982) 303–314.

[104] P.J. John, S.V. Prasad, A.A. Voevodin, J.S. Zabinski, Calcium sulfate as a high temperature solid lubricant, Wear 219 (1998) 155–161.

[105] O. Knotek, M. Bohmer, T. Leyendecker, On structure and properties of sputtered Ti and Al based hard compound films, J. Vac. Sci. Technol. A 4 (1986) 2695–2700.

[106] P.H. Mayrhofer, A. Hörling, L. Karlsson, J. Sjölén, T. Larsson, C. Mitterer, L. Hultman, Self-organized nanostructures in the Ti–Al–N system, Appl. Phys. Lett. 83 (2003) 2049–2051.

[107] P.H. Mayrhofer, M. Stoiber, C. Mitterer, Age hardening of PACVD TiBN thin films, Scripta Mater. 53 (2005) 241–245.

[108] G. Gassner, P.H. Mayrhofer, K. Kutschej, C. Mitterer, M. Kathrein, A new low friction concept for high temperatures: lubricious oxide formation on sputtered VN coatings, Tribol. Lett. 17(4) (2004) 751–756.

[109] G. Gassner, P.H. Mayrhofer, K. Kutschej, C. Mitterer, M. Kathrein, Magneli phase formation of PVD Mo–N and W–N coatings, Surf. Coat. Technol. 201 (2006) 3335–3341.

[110] C. Muratore, A.A. Voevodin, Molybdenum disuflide as a lubricant and catalyst in adaptive nanocomposite coatings, Surf. Coat. Technol. 201 (2006) 4125–4130.

[111] S.M. Aouadi, Y. Paudel, B. Luster, S. Stadler, C. Muratore, C. Hager, A.A. Voevodin, Adaptive $Mo_2N/MoS_2/Ag$ nanocomposite coatings for aerospace applications, Tribol. Lett. 29 (2008) 95–103.

[112] A.A. Voevodin, J.J. Hu, T.A. Fitz, J.S. Zabinski, Nanocomposite tribological coatings with chameleon friction surface adaptation, J. Vac. Sci. Technol. A 20 (2002) 1434–1444.

[113] J.L. Endrino, J.J. Nainaparampil, J.E. Krzanowski, Microstructure and vacuum tribology studies of TiC–Ag composite coatings deposited by pulsed laser deposition, Surf. Coat. Technol. 157 (2002) 95–102.

[114] C. Muratore, A.A. Voevodin, J.J. Hu, J.S. Zabinski, Tribology of adaptive nanocomposite yttria-stabilized zirconia coatings containing silver and molybdenum, Wear 261 (2006) 797–805.

[115] K. Kutschej, C. Mitterer, C.P. Mulligan, D. Gall, High temperature tribological behavior of CrN–Ag self-lubricating coatings, Adv. Eng. Mater. 8 (2006) 1125–1129.

[116] C.P. Mulligan, D. Gall, CrN–Ag self-lubricating hard coatings, Surf. Coat. Technol. 200 (2005) 1495–1500.

[117] A. Voevodin, J.G. Jones, J.J. Hu, T.A. Fitz, J.S. Zabinski, Growth and structural characterization of yttria stabilized zirconia–gold nanocomposite films with improved toughness, Thin Solid Films 401 (2001) 187–195.

[118] C. Muratore, A.A. Voevodin, J.J. Hu, J.S. Zabinski, Multilayered YSZ–Ag–Mo/TiN adaptive tribological nanocomposite coatings, Tribol. Lett. 24 (2006) 201–206.

[119] C. Muratore, J.J. Hu, A.A. Voevodin, Tribological coatings for lubrication over multiple thermal cycles, Surf. Coat. Technol. 203 (2009) 957–962.

[120] J.J. Hu, C. Muratore, A.A. Voevodin, Silver diffusion and high-temperature lubrication mechnisms of YSZ–Ag–Mo based nanocomposite coatings, Composite Sci. Technol. 67 (2007) 336–347.

[121] C. Muratore, D.R. Clarke, J.G. Jones, A.A. Voevodin, Smart tribological coatings with wear sensing capability, Wear 265 (2008) 913–920.

[122] A. Erdemir, Friction and wear of diamond and diamond-like carbon films, Proc. Inst. Mech. Eng. J: J. Eng. Tribol. 216(J6) (2002) 387–400.

[123] A. Erdemir, C. Donnet, Tribology of diamond, diamondlike carbon and related films, in: B. Bhushan (Ed.), Modern Tribology Handbook, CRC Press, Boca Raton, FL (2000) 871–899.

[124] A. Erdemir, C. Bindal, G.R. Fenske, C. Zuiker, R. Csencsits, A.R. Krauss, D.M. Gruen, Tribological characterization of smooth diamond films grown in Ar–C-60 and Ar–CH_4 plasmas, Diamond Films Technol. 6(1) (1996) 31–47.

[125] A. Erdemir, C. Bindal, G.R. Fenske, C. Zuiker, A.R. Krauss, D.M. Gruen, Friction and wear properties of smooth diamond films grown in fullerene plus argon plasmas, Diamond Relat. Mater. 5(9) (1996) 923–931.

[126] A. Erdemir, G.R. Fenske, A.R. Krauss, D.M. Gruen, T. McCauley, R.T. Csencsits, Tribological properties of nanocrystalline diamond films, Surf. Coat. Technol. 121 (1999) 565–572.

[127] Y. Gogotsi, S. Welz, D.A. Ersoy, M.J. McNallan, Conversion of silicon carbide to crystalline diamond-structured carbon at ambient pressure, Nature 411 (2001) 283–287.

[128] D.A. Ersoy, M.J. McNallan, Y. Gogotsi, A. Erdemir, Tribological properties of carbon coatings produced by high-temperature chlorination of silicon carbide, Tribol. Trans. 43(4) (2000) 809–815.

[129] D.A. Ersoy, M.J. McNallan, Y. Gogotsi, Carbon coatings produced by high-temperature chlorination of silicon carbide ceramics, Mater. Res. Innovat. 5(2) (2001) 55–62.

[130] S. Welz, Y. Gogotsi, M.J. McNallan, Nucleation, growth, and graphitization of diamond nanocrystals during chlorination of carbides, J. Appl. Phys. 93(7) (2003) 4207–4214.

[131] P.E. Hovsepian, D.B. Lewis, C. Constable, Q. Luo, Y.N. Kok, W.D. Münz, Combined steered cathodic arc/unbalanced magnetron grown C/Cr nanoscale multilayer coatings for tribological applications, Surf. Coat. Technol. 174 (2003) 762–769.
[132] B. Podgornik, J. Viintin, S. Jacobson, S. Hogmark, Tribological behaviour of WC/C coatings operating under different lubrication regimes, Surf. Coat. Technol. 177–178 (2004) 558–565.
[133] O. Wänstrand, M. Larsson, P. Hedenqvist, Mechanical and tribological evaluation of PVD WC/C coatings, Surf. Coat. Technol. 111(2–3) (1999) 247–254.

CHAPTER 15

Non-Elemental Characterization of Films and Coatings

Donald M. Mattox

15.1 Introduction

A *coating* may be defined as a near-surface region having properties differing from the bulk of the material which is prepared by adding a material to the surface (*overlay coating*).
A *modified surface* is a near-surface region whose properties differ from the bulk of the material and which is formed from the bulk material by changing the composition, phase, or properties; the substrate material is detectable in this region. Generally a modified surface is also referred to as a coating.

These definitions imply no thickness limitation but usually involve a functional or property difference between the coating and substrate. Thus a coating allows the dissociation of the surface properties from the bulk properties and allows engineering, fabrication, and design flexibility which can be obtained by separating the surface properties from the structural requirements.

Disadvantages of coatings are associated with:

1. Presence of an interface and the need for adhesion;
2. A sharp discontinuity in material properties at the interface;
3. Need for fabrication methods, some of which are expensive;
4. Need for process control for a reproducible product;
5. Properties of the coating material may differ significantly from the material in bulk form and the properties may be very process dependent.

Films are thin coatings, and in some instances the film properties are influenced by the substrate properties. In this chapter, a film is defined as a coating with a thickness less than 1 micron (10^3 nanometers or 40 micro-inches).

Films and coatings may be fabricated in a variety of compositional, morphological, and microstructural configurations. These include:

1. Monolithic – one composition throughout;
2. Alloyed or mixed and not reacted;
3. Compound;
4. Graded composition;
5. Layered structures – few to many, alternating;
6. Composite (dispersed phases);
7. Dispersed impurities – possibly to greater than solubility limits;
8. Special configuration, e.g. fine line metallization;
9. On surfaces with properties that influence the film properties, e.g. roughness, hardness.

Films, coatings, and modified surfaces are often unique materials with properties that differ from those normally encountered in the same materials prepared in other ways, and these unique characteristics should be considered when making property, stability/degradation or compositional measurements. In many instances, these unique properties are derived from the fabrication techniques and parameters as well as the limited size and thicknesses that are encountered in film structures. Unique conditions, characteristics, and properties of films and coatings include:

1. Substrate influence on properties;
2. Presence of the interface and interfacial *(interphase)* material;
3. Graded composition and properties with thickness;
4. Dispersed impurities;
5. Non-stoichiometric compositions;
6. Unique microstructures (bulk, surface), e.g. columnar morphology;
7. High surface/volume ratio;
8. Local property variations, e.g. pinholes, nodules;
9. Non-equilibrium conditions (defects, stress, crystallographic phase, structures, composition, impurities, etc.).

15.2 Characterization

There are many reasons to characterize a film or coating. These include:

1. In development: determining the effect of processing variables on properties of the material (process sensitivity). Determining degradation modes;
2. Determining functionality and establishing performance limits for a specific application;
3. Establishing product acceptance specifications (functionality, stability);
4. Establishing a baseline for satisfactory composition, structure, or performance so that subsequent materials may be compared to this 'standard';
5. Monitoring reproducibility of processing;
6. Determining the stability of the material under service and degradation conditions;
7. Assisting in failure analysis;
8. Avoiding surprises.

Note: characterization is essentially meaningless unless the formation conditions are reproducible. This means that the process must be reproducible and this is generally ensured by using process controls and specifications.

In many cases, property measurements are used to establish processing reproducibility. For instance, in the deposition of a metallization film, one might make:

1. A thickness measurement to insure that the right amount of material has been deposited and that the deposition conditions (contamination in a plasma when sputtering, for instance) have not changed when using the specified deposition parameters;
2. An adhesion measurement to insure that the surface preparation was adequate and that the surface was not recontaminated during processing;
3. An electrical resistivity (or resistance) measurement to insure functionality of the material;
4. Environmental aging to insure stability of adhesion and electrical resistivity during subsequent processing, storage, and service;
5. Pinhole density measurements to ensure that the likelihood of developing 'opens' in patterned metallization is small.

Characterization may be categorized as: *(i)* absolute; *(ii)* relative; *(iii)* functional; *(iv)* behavioral; and *(v)* stability.

Absolute characterization means obtaining a specific value such *as: (i)* specific elemental composition (weight percent); *(ii)* resistivity (ohm-centimeters); *(iii)* geometrical thickness (microns, angstroms); *(iv)* density (grams/cm^3), etc. In order to get absolute values it is often necessary to use accurate measuring techniques and to compare the measured values to standards for the parameter of interest.

Relative characterization means a comparison to an acceptable value (or known variation thereto) such as: an Auger peak height, x-ray fluorescence intensity, color, relative hardness, etc. Often precise, but not necessarily accurate, measurement techniques are used. Relative evaluations are generally more easily obtained and are less costly than are absolute values.

Functional characterization relates to the final use of the material and include such properties as: adhesion, electrical resistivity, hardness, wear behavior, optical absorption, etc.

Behavioral properties are not directly related to functionality but are a function of processing. These properties may be important in use or to indicate possible changes in film properties. An example is adsorption of gases or contaminants.

Stability properties refer to the property changes in the product during subsequent processing, handling/storage, and service. Stability measurements are usually done as a function of environment (temperature, chemical species, fatigue, etc.). These environments must be carefully defined and specified.

Properties may be general, such as film thickness, or may vary locally such as the presence of pinholes, nodules in the film, or small areas of high film stress. The general properties may not be uniform over a large surface area or may not be constant from one area to another on the deposition fixtures (position equivalency). Often variations may be due to substrate conditions, deposition parameters, etc. This means that some care must be taken in selecting the samples (or areas) to be characterized and the sampling statistics must take into consideration the possibility of such variations.

The importance of the property also determines the type of statistics used in property measurements. For example, one may measure the mean-time-to-failure of a conductor due to electromigration, but since one failure can cause failure of a circuit, it may be more important to know the time-to-first-failure for reliability calculations. It is often helpful (or necessary) to interact with a statistician in order to develop a meaningful statistical evaluation program.

In some cases, special substrates *(witness plates* or *monitor plates)* may be used to give properties or conditions that are not generally available on the product to be used. Examples are: (*i*) the use of thin substrates that can be deformed by film stress, and *(ii)* smooth surfaces that may be masked to give 'steps' for stylus or interferometric thickness measurements. In some measurements such as those used for adhesion tests or stress measurements, it is very important that the witness plates be of the same material as the substrates and processed in the same manner. In cases where different materials, surface conditions (e.g. smooth vs. rough) or different processing (e.g. cleaning) is used for the witness plates, the effects of these differences on the measured parameters must be known.

Some film properties may be measured during the deposition process (in situ) and may be used to control the deposition process. This may be called *in situ characterization* and includes such measurements as:

1. Mass deposited (using deposition rate monitors, weight gain measurements);
2. Optical transmission, reflectance, and extinction (used with optical coating processes);
3. Film resistivity (using masks and conductor patterns).

Upon opening a deposition system, some characteristics may be determined before the parts are removed from their fixtures. These characteristics may be called the *first check characterization* and include:

1. Uniformity of appearance and color over the deposition fixture, i.e. from sample-to-sample or over a large area;
2. Color (e.g. TiN [1]) and reflectivity – is it like other deposition runs?
3. Optical texturing – when viewed from different angles does the reflectance look different from different areas? This is an indication of morphological variation.

If there are a number of samples in the run, or if the area is large, one should determine if all the positions in the deposition system are equivalent (i.e. *position equivalency*). It may be helpful to identify each sample and its position in the fixture for future reference – variations in properties may be position dependent for reasons such as: angle-of-incidence of the depositing flux, plasma density variations, heating variations, presence of nearby virtual leaks, etc.

After the samples have been removed from the fixturing they may be subjected to further testing. Simple and easy tests may be used to determine functionality and relative comparison. These simple tests include: *(i)* adhesion; *(ii)* residual stress; *(iii)* reflectivity; *(iv)* electrical resistivity; *(v)* thickness; *(vi)* optical transmission of films on optically transparent substrates for thickness or pinholes; *(vii)* some types of elemental composition; *(viii)* chemical etch rate; and *(ix)* oblique lighting to see bumps on smooth surfaces. Often these simple tests can give the first indication of problems in processing or functionality. In many cases one characterization technique will give results that depend on several properties of the material. For example: a chemical etch rate test will depend on film density, pinholes, surface area, thickness, and chemical composition.

After the films have been exposed to the ambient, do they change with time? Changes may be evident in color, adhesion, chemical composition of the surface, wetting angle, or bondability.

After the simple and easy tests, the films may be subjected to more complex and comprehensive tests which generally take a much longer time and require special techniques and configurations.

In many cases, the functionality of the system must be determined in context of the intended use of the film. The best test is the *operational life-test* where the film is used as it would be in service and samples are tested periodically to determine any degradation. Since this means a long test period, it is often desirable to used *accelerated life-tests* where the degradation mechanisms are accelerated by increasing the temperature (corrosion, diffusion processes), chemical concentration (corrosion), cyclic rate (fatigue failures), etc. A comparison between the accelerated tests and the operational tests gives an *acceleration factor*. A major concern in accelerated life tests is to be sure the right degradation mechanisms are being accelerated. Most often, both types of tests (operational and accelerated) are run, and in addition, *control samples* (archival or shelf samples) are kept in pristine condition so that operational or accelerated aged samples can be compared to the original materials. All of this assumes that the samples were reproducible when fabricated.

Many characterization techniques require destruction of the sample. Examples are: many adhesion tests, some compositional profiling techniques, mechanical properties testing. In some cases, evaluations may be made by non-destructive evaluation (NDE) tests and the tested sample can be used for further processing. Examples are: electrical resistivity (four-point probe resistivity), adhesion (tensile pull to value, ‘Mattox bad breath test’), and composition (x-ray fluorescence).

Characterization may be at all levels of sophistication and expense. In this chapter, we discuss some of the most common characterization techniques, but before a characterization strategy is developed, the following questions should be asked.

- Most important – is the processing and product reproducible?
- How will the information be used?
- How varible is the product from lot-to-lot, and from various positions in the deposition system?
- Are the statistics correct? Should a statistician be consulted?
- In development work: are the experiments properly designed to give the information needed to establish limits on the processing variables and the product properties?
- What is important? Who determines what is important and the acceptable limits?
- How quickly is the information (feedback) needed?
- Who will do the characterization? Are the right questions asked, and is the necessary background information provided?
- Does the testing program include subsequent processing, operational, and environmental considerations?
- Is needless characterization being done, or can simpler and less expensive characterization methods be used?
- Can the characterization be done effectively in the necessary environment (development, production, quality assurance) and by the required workers (Ph.D.'s, hourly workers)?
- How will the specifications for the characterization methods be written?

Specifications must be written for characterizations that must be done repeatability. Methods of characterizing the sample should be carefully specified. Often professional organizations have specifications and standards for determining specific properties, tests, procedures, or processing [2]. These specifications and standards may be classed *as: (i)* industrial; *(ii)* military; and *(iii)* international.

Some of the organizations that have specifications and standards are:

Mil. Specs – Military Specifications

ISO – International Standards Organization

ASTM – American Society for Testing and Materials

ANSI – American National Standards Institute

API – American Petroleum Institute

ASME – American Society of Mechanical Engineers

ASQC – American Society for Quality Control

AWS – American Welding Society

AVS – American Vacuum Society (recommended practices)

EIA – Electronic Industries Association

IEEE – Institute of Electrical and Electronic Engineers

IES – Illuminating Engineering Society

ISA – Instrument Society of America

NEMA – National Electrical Manufacturers Association

SAE – Society of Automotive Engineers

UL – Underwriters Laboratories

NBS – National Bureau of Standards

IPC – Institute for Interconnecting and Packaging Electronic Circuits

Others

There are several ways of retrieving the standards and specifications. One is the VSMF microfilm system with a subject index and microfilmed standards and specifications. ASTM (American Society for Testing and Materials) has a series of publications of their standards.

In many cases, published standards and specifications have to be modified for a specific application.

15.3 Film Formation

In order to understand how some of the unique film properties come about, we need to understand how the film fabrication is performed. Other chapters in this volume treat the subject of film fabrication methods. In addition, we need to understand how a film or coating is formed with a specific fabrication process. For example: let us summarize how atomistically deposited films are formed.

The stages of atomistically deposited film formation are [3]: *(i)* surface preparation; *(ii)* condensation and nucleation of the adatoms; *(iii)* interface formation; *(iv)* film growth and; in some cases *(v)* post-deposition treatments. The characteristics of these stages may be very dependent on processing parameters. For example: *(i)* substrate heating is normally a very important process variable; *(ii)* angle-of-incidence of the depositing material flux may be important in developing the film morphology; and *(iii)* concurrent energetic particle bombardment during deposition may be used to modify all stages of film growth [4, 5].

Surface preparation may be defined as the treatment of a surface in order to obtain satisfactory processing, function, or stability [6]. Surface preparation may be in the form of: *(i)* cleaning; *(ii)* modification of surface chemistry; *(iii)* modification of the physical or morphological properties of the surface; *(iv)* formation of nucleation sites or addition of nucleating agents (sensitization); and *(v) activation* of the surface to make it more chemically reactive.

When adatoms impinge on a surface they may have a degree of mobility on the surface before they nucleate and condense [5, 7, 8]. The nucleation density of adatoms on a substrate surface (and mode of growth) determines the interfacial contact area and the development of interfacial voids – generally a high nucleation density is desirable for good film adhesion. The nucleation density depends on the kinetic energy and surface mobility of the adatoms, chemical reaction, and diffusion of the adatoms with the surface, adsorbed surface species [9], and the nucleation sites available [10].

The nucleation stage of film formation may be studied by: *(i)* Transmission Electron Microscopy (TEM); *(ii)* Scanning Tunneling Microscopy (STM) [11]; *(iii)* electrical conductivity and temperature coefficient of electrical conductivity (conductors on insulating substrates); *(iv)* optical transmission as a function of mass deposited (film on transparent substrate); *(v)* extinction of the XPS (x-ray photoelectron spectroscopy) signal from the substrate as a function of deposited mass; or *(vi)* changes in the work function with deposited mass.

Interface formation will begin during nucleation of the adatoms on the surface and may proceed throughout the deposition process and even during post-deposition processing, subsequent processing, and in-service usage, depending on conditions.

The interfacial types may be categorized as [3]: *(i)* abrupt; *(ii)* mechanical; *(iii)* diffusion; *(iv)* compound; and *(v) pseudodiffusion*. The abrupt interface is formed when there is no diffusion and thus the interface is a sharp transition from one material to another in the space of a lattice parameter (e.g. Au on NaCl). In this case the gradient of materials properties is large. Due to the lack of reaction and the method of film growth, interfacial voids may be formed at the abrupt interface giving poor adhesion. The mechanical interface is an abrupt interface with mechanical interlocking. This type of interface may provide good adhesion if the surface roughness is ‘filled-in’ and interfacial voids are avoided.

The diffusion type interface is formed when there is interdiffusion of the film and substrate materials. A problem with this type of interface may be the development of voids in the interfacial (*interphase*) material if the diffusion rates of the materials are different (Kirkendall voids) [12]. In the compound interface, diffusion is accompanied by reaction to form a compound material. The interphase material formed may be brittle, have Kirkendall voids, and develop microcracks due to the stresses developed in forming the compound material [13] – all of which reduce the fracture strength of the interface region and hence lower the film adhesion [14]. The pseudodiffusion type of interface may be formed under low-temperature deposition conditions or when the materials are insoluble, by physically mixing the depositing materials during multilayer film deposition, or by implantation or recoil implantation of atoms into the substrate surface. Figure 15.1 schematically depicts the types of interfaces and problems that can be associated with each type of interface.

Heating during deposition may enhance diffusion of chemical reactions of the depositing atoms with the surface. Energetic particle bombardment may alter the interface formation by affecting the nucleation processes (cleaning, changes in surface chemistry, nucleation sites), by increasing the contact area, decreasing the interfacial voids, generating surface defects, enhancing chemical reaction, and by providing a high thermal input into the surface region.

Generally interfaces and interphase materials are difficult to characterize because of their small extent and the dependence of the materials properties on interfacial flaws and the

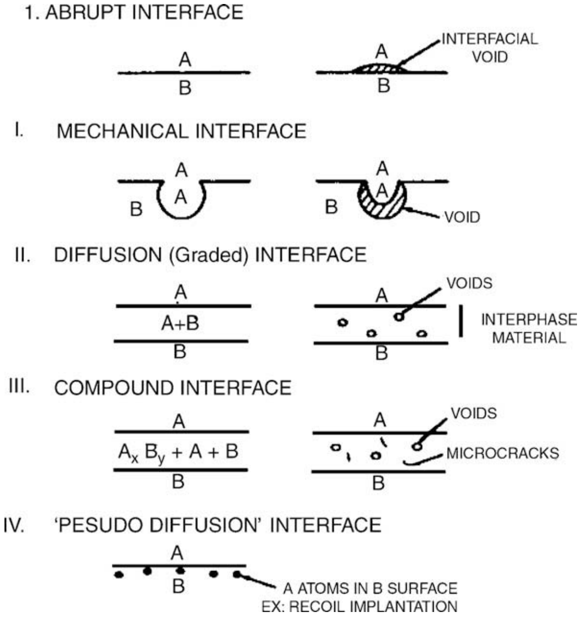

Figure 15.1: Types of interfaces and problems that can be associated with each type of interface.

properties of the surrounding materials. Interfaces may be studied by TEM techniques. Fracture-related studies may also be informative.

Film growth occurs by nucleation on a ‘like-material’ and the same considerations as for nucleation on a foreign surface apply. In addition, larger-scale effects must be considered. In particular, at low deposition temperatures, geometrical effects may lead to the development of a columnar growth morphology [15] that often leads to undesirable film properties such as microporosity, low film density, high chemical etch rates, contamination retention and others. The addition of energetic particle bombardment during deposition can change the growth morphology giving a more dense film [16–20].

For reactive film deposition processes, two general cases exist. In the first case, there is a condensible species and a gaseous reactive species (e.g. Ti + N). In the second case, both species are condensible and reactive under the proper conditions but may only form a mixture under other conditions (e.g. Ti + C). In reactive film deposition processes, the rate and degree of reaction is dependent on the chemical reactivity of the reactive species, the temperature, the extent of the reaction, and the availability of the reactive species to the depositing species which, in turn, may be very dependent on system geometry and relative surface areas [21].

When a reactive species is present, concurrent energetic particle bombardment enhances chemical reactions. The nature of this enhancement is poorly understood since heating, physical collisions, molecular fragmentation, intermediate species, and the presence of energetic electrons (secondary electrons) may each play a role in the chemistry of the reaction. The existence of bombardment-enhanced chemical reactions is well established in etching studies where the reaction products are volatile [22, 23] and bombardment effects are found in reactive film deposition processes where the reaction products are non-volatile (reactive deposition) [24].

In the condensation of atoms, a residual lattice strain developed which is usually evident as a residual tensile stress in the film. Where there is concurrent bombardment during deposition, this strain may be compressive in nature due to the *atomic peening* (stuffing) of atoms into the lattice by recoil implantation. These growth stresses are very important to some film properties such as adhesion and stability [14, 25, 26].

It should be realized that very few surfaces are chemically and physically homogeneous. Inhomogeneity in the substrate surface leads to variations in film nucleation, growth, and properties. Processing which leads to greater surface and growth homogeneity will lead to greater film homogeneity.

Substrate morphology, surface chemistry, and physical properties may have a important affect on film growth and thus on the subsequent film properties. Substrate specification and characterization are important parts of process development and production reproducibility.

Specifications for the in-coming substrate material and the surface preparation must be included as part of the process development.

Post-deposition processing may be used to change the film or interface properties. Such processing includes: *(i)* burnishing or shot peening (soft metal films); *(ii)* rapid thermal processing [27]; *(iii)* annealing; *(iv)* ion beam mixing [28].

15.4 Elemental and Structural Analysis

Some elemental and structural analysis techniques are covered in other chapters of this book (others are not, see Ref. [29]) but since they are closely tied to the non-elemental characterization techniques that are covered in this chapter, a few points about this type of characterization from that point of view are included here.

Elemental and structural analysis is typically done by someone separate from the processing activity. Often the analysts are very parochial, so careful consideration is required to determine which analytical technique is best suited to the question/problem at hand. At the least, several people and techniques and several sources of information may be required to make a decision. It may be necessary to work with the analyst to develop a program which will answer the questions that need to be addressed.

Each analytical person/technique must be given the background necessary obtain the needed information. If the person using the scanning electron microscope looks for unusual features and takes pictures of strange things on the surface, a very distorted view of the product will emerge. If an Auger analysis of a sample that was carried in a week ago doesn't have carbon on the surface, then the Auger system is not working right. If hydrogen in the film is a concern, then Auger analysis is not appropriate; Nuclear Reaction Analysis is needed. Many analytical techniques are very dependent on the sample preparation. Generally, one must determine if the findings of elemental and structural analysis are important or not. The product or process engineer must work with the analyst to obtain meaningful results.

In compositional analysis there is a big difference in time and effort between detection with relative values and absolute numbers. Usually, to get absolute values, it is necessary to obtain or make standards for comparison and this may be very difficult. Often it is just as informative to get relative values. It is also very important to have archival samples with which to compare the analytical results.

Surface analysts take great pride in getting the highest resolution possible, but often variations (e.g. pinholes) in a large area and high resolution of a small area (such as a SEM analysis) is not appropriate, and other characterization techniques should be used.

Elemental and structural analysis is a great way to run up characterization costs. Typically the turn-around time and feedback times are long. Pretty pictures of microstructures and absolute numbers from compositional analysis may not be necessary but they might look good in a report or paper.

15.5 Some Property Measurements

Many different property measurements may be made on a film or coating. In many cases, the property measurements are highly specific. This part of the chapter will concentrate on a few of the most common property measurements.

15.5.1 Adhesion

Good adhesion, as defined by the fabrication, testing, and service conditions, is a fundamental requirement of any film-substrate system. Good adhesion is determined by a large number of factors, many of which are difficult to control without careful processing. Process development is often done in an empirical manner, aided by some basic considerations of the factors most likely to give good adhesion and properties which are detrimental to good adhesion. From these considerations one can decide what must be done to obtain good adhesion and the proper procedures for testing the adhesion

The American Society for Testing and Materials defines adhesion as the ‘condition in which two surfaces are held together either by valence forces or by mechanical anchoring or by both together,’ (ASTM Definition D 907-70) [30]. In engineering applications, adhesion is the physical strength of an interface between regions of a material system. Such interfaces are found in grain boundaries, solids in contact (friction, wear), and in film-substrate systems. Adhesion failure is the separation of the materials at or near the interface over a large area, usually under stress. Adhesion failure is the end result of fracture and/or deformation of material and may depend on the properties of the substrate material near the interface *(nearby material)*, the interphase material or the film material.

Adhesion strength is an irreversible macroscopic property of the system and is amenable to specification and testing. ‘Good adhesion’ is when the interfacial region (or nearby material) does not fail under service conditions nor at unacceptably low stress levels under fabrication and test conditions [3].

The mechanical properties of the interfacial (interphase) material are crucial to good adhesion. This interfacial material may have a composition, microstructure, and properties which differ from either of the bulk materials. An interface may be sharp or diffuse, rough or smooth.

The formation or presence of the interfacial region may affect the composition, stress, or microstructure of the nearby material (film or substrate) which may be weakened by a number of processes such as diffusion or flaw formation.

The stresses which may cause adhesion failure include: mechanical (tensile, shear, compressive, shock, fatigue), chemical (corrosion, solution) and thermal/time (diffusion, reaction). Internal (residual) film stresses may contribute to the failure [3].

The principal methods of attaining adhesion are by: surface energy reduction [31–33], high fracture energy of the interfacial region [3, 14], or the use of bonding agents to provide a ‘new’ surface.

The deposition process and process variables may have an important bearing on the resultant adhesion by changing the nucleation, growth and properties of the deposit. Energetic processes, such as high temperature or high particle kinetic energy processes [34], promote the formation of diffusion, compound, or pseudodiffusion type interfaces. High temperature processing imposes constraints such as matching the coefficient of expansion of the deposited material to the substrate materials so that thermally-induced residual stresses are not produced during cool-down.

Post-deposition treatments may be used to increase adhesion. These treatments include: heating, *ion mixing* (e.g. see Refs. [28, 36]) and the diffusion of reactive species to the interface [36, 37]. Heating of the film-substrate couple allows stress relief in some systems [38, 39]. Even time alone under ambient conditions can give changes in the adhesion. This may occur by allowing stress relief (grain growth) and diffusion of species to the interface. For example, plasma cleaning of glass surfaces prior to silver deposition has been shown to give a time-dependent improvement in the adhesion of the silver films after deposition [40]. Of course some post-deposition treatments, such as may occur during subsequent processing, can cause loss of adhesion.

The loss of adhesion under mechanical stress (tensile, compressive, shear) occurs by deformation and fracture of material at or near the interface. The fracture mode (brittle or ductile) depends on the properties of the material and the presence of flaws which may create easy fracture paths and can act as stress concentrators to initiate and propagate the fracture. Another important factor in fracture propagation is the presence of stress and stress gradients in the material. These stresses may enhance fracture propagation (tensile stress) or retard fracture propagation (compressive stress), to some degree. The stress may be intrinsic to the system – arising from the deposition process, or may be extrinsic – arising from applied stresses. In either case, the nature of the stresses which appear at the interface depend on the properties of the materials involved.

Localized regions of high intrinsic stress may be found in films due to growth discontinuities or defects such as pinholes [41] or nodules, or near features such as edges. These stressed areas may lead to localized adhesion failure under applied stress.

The fracture path is determined by the properties of the film and substrate materials, the presence and distribution of flaws, stress distribution, and the presence of features which may blunt or change the fracture propagation direction. Conceptually, the energy needed to propagate the fracture and create the new surfaces can be measured and this fracture energy would be a good measure of the adhesion of the system [42, 43]. Energy may be absorbed by: *(i)* plastic deformation (slip, atom motion); *(ii)* elastic deformation (heat); *(iii)* generation of free surfaces.

The fracture of a brittle material is often accompanied by acoustic emission which results from the release of energy. This acoustic emission has both an energy and a frequency spectrum [45]. In one method of the detection of adhesion failure by acoustic emission, the coated surface is scratched by a rounded diamond point and the load on the point is increased while monitoring the acoustic emission using a piezoelectric accelerometer. This mode of detection is often more sensitive than the normally-used optical detection techniques

The fracture of an insulator interface is often accompanied by the emission of electrons, photons and/or ions (fractoemission). This fractoemission is probably due to microdischarges resulting from charge separation during fracture [45].

Adhesion is determined by the nature of the stresses that appear at the interface and the fracture energy needed to propagate a fracture. Good adhesion is promoted by: high fracture toughness of the materials, low concentration of flaws, non-planar defects, presence of fracture blunting features, interfacial roughness that necessitates the change of direction of a propagating fracture, low stresses and stress gradients, and the absence of operational degradation mechanisms.

Poor adhesion may be attributable to: low degree of chemical bonding (as evidenced by a low nucleation density), poor interfacial contact, low fracture toughness (brittle materials, flaws, stresses), high residual film stresses, and operational degradation mechanisms. Poor adhesion may be localized, giving local failure on stress (pinholes, nodules, spallation).

Loss of adhesion may also occur due to non-mechanical stresses such as: corrosion or solution of interfacial material, generation of flaws, diffusion to or away from the interface of species which can influence adhesion, precipitation of diffusing species (e.g. H, He) at the interface, or static fatigue processes that propagate existing flaws in brittle materials. These degradation processes are often time, temperature, and environment dependent.

An example of the loss of adhesion due to corrosion effects is the degradation of some Ti-Au metallizations in an HCl environment [46]. This electrochemical degradation may be eliminated by the addition of a thin intermediate layer of palladium between the titanium and the gold.

An example of the loss of adhesion due to diffusion is the diffusion of chromium from the interface of an oxide-Cr-Au metallization through the gold to the surface on heating to >200 °C in air. At the surface, the chromium oxidizes and creates a non-bondable surface and the loss of chromium at the interface results in loss of adhesion. This out-diffusion of the interfacial material is dependent on the composition of the gaseous ambient, and a non-oxidizing ambient reduces the diffusion [47]. The addition of a small amount of oxygen in the chromium and/or the gold during deposition reduces the chromium diffusion rate and gives a more thermally stable metallization [48]. The adhesion of the Ti-Au metallization can be degraded by the diffusion of Ti to the surface and by chlorine impurities in the film material (chemically-induced segregation) [49].

The diffusion of hydrogen through a film to an interface where it precipitates has been used by the electroplating community as an adhesion test [50]. Gases incorporated into a surface or film during surface preparation or film deposition may diffuse to the interface on heating, giving a loss of adhesion.

Diffusion of water vapor through a polymer film to the interface can lead to the degradation of metal-polymer adhesion [52]. Interfacial mixing can improve the moisture degradation properties of polymer-metal film systems [52].

Film properties may influence the apparent adhesion of a film-substrate couple. The deformation, microstructural, and morphological properties of the film material determine the ability of the material to transmit mechanical stress and to sustain residual stresses.

The objective of adhesion testing is to duplicate the stresses to which the interface will be subjected in subsequent processing, testing, and service. Adhesion testing is used to monitor process and product reproducibility. A part of the adhesion testing program should include possible time, environment, or stress dependent degradation mechanisms. Generally adhesion tests subject rather large areas to stresses and often do not detect localized areas of poor adhesion. The use of acoustic emission with some adhesion tests may give an indication of the onset of failure. Adhesion tests are generally very difficult to analyze and are most often used as comparative tests in product acceptance specifications. The best test of adhesion is functionality under service conditions!

Typically adhesion testing is done by lot sampling on product or witness samples that are characteristic of the product. It should be remembered that the properties of the substrate material and surface preparation procedures may have an important effect on the measured adhesion, so the witness sample material and its preparation should be carefully controlled.

Stressing a film to test for adhesion may result in other failure modes such as cracking of the film, even though the film does not separate from the surface [53].

Methods of accelerating the degradation modes for accelerated adhesion testing should reflect the same degradation modes as are to be found in service. Acceleration may be accomplished by increased temperature, mechanical fatigue, thermal fatigue, concentrated chemical environment, or by the introduction of interfacial flaws by some technique.

Non-destructive adhesion testing techniques would be highly desirable but are of limited availability at the present time. Possibly thermal-wave techniques, which have been used to monitor ion implantation damage [54], can be used to detect interfacial flaws.
Testing-to-a-limit may be used and some use of acoustic emission to detect onset of failure has been attempted.

Since adhesion is a macroscopic property of the system, the adhesion test methods generally involve testing over an appreciable area. In some cases, the testing may be over a much larger area than we are really interested in. Adhesion testing should test the coating under stresses similar to those encountered in production and service.

There are a large number of potential adhesion tests [55–59] and each investigator or technology community favors different tests. Adhesion tests may be categorized by the method that the stress is applied to the film/coating.

The following are some types of adhesion tests:

Functionality

Tensile (pull) tests:
  Wire bond
  Thermocompression (TC) bond
  Soldered bond
  Epoxy bonded stud
  Electroplated stud
  Rotor tests

Peel tests;
  ‘Tape test’

Topple tests

Shear tests:
  TC ball bond (push-off test)
  Ring shear

Lap shear tests

Deformation (of substrate) tests:
  Bend
  Pull

Indentation test

Scratch test (with acoustic emission)

Stress-wave test:
  Flyer plate/foil
  Laser pulse

Abrasion tests Thermal stressing

Diffusion test – diffusion of hydrogen to interface (electroplaters)

Weird tests:
  Mattox bad breath test (unpublished)

The best test of adhesion is 'does it work?' under subsequent processing, testing, and service. This may be called a functionality test.

The peel test is a common test for adhesive bonding [60, 61] and a variation of the peel test is the tape test, where an adhesive tape is stuck on the film surface, then a peel test is performed. This test is good for detecting poor adhesion (up to about 1000 psi) but is very sensitive to the method used – type of tape, method of application of the tape, pull angle, pull rate, etc. Often the film is scribed (cut, cross-hatched) beneath the tape to provide an edge on which the tape pulls. Measurement is in grams/mm.

The scratch test is an old adhesion test method [62] (more sophisticated than the scrape test) where a complex deformation is introduced into the surface and then the failure mode is observed and a *critical load* for failure is assigned [63]. This test has been the subject of numerous investigations. The stresses associated with a moving stylus have been analyzed [64]. The loaded stylus used for the scratch test may fracture a brittle substrate material giving erroneous results [65]. The use of an SEM with an in situ scratch testing capability allows the observation of the failure and material transfer without time or environmental effects [66]. The scratch test can be combined with acoustic emission to give an indication of the onset and magnitude of failure [62, 67]. The hardness of the substrate material may have a significant affect on the scratch resistance (cracking) of thin coatings [68]. A commercial unit is available to perform the scratch test along with acoustic emission.

The tensile test generally utilizes a wire or stud bonded to the surface and a tensile tester. Bonding of the wire is usually done by thermocompression bonding, ultrasonic bonding, or soldering. Bonding of a stud to the surface is usually done by thermosetting epoxy bonding. Tensile strengths to about 10,000 psi can be measured, but the analysis of the result can be difficult [69]. Care must be taken to avoid bonding stresses which will reduce the apparent adhesion. Commercial testers are available for the stud-bond test. One interesting variation of the tensile test is used to study the fracture energy of the interface. This test involves bonding a surface to the film, then performing a *notch* tensile test [42].

The shear tester [70] uses a bump bonded to the surface and a shearing (actually peeling) motion to determine the strength of the bond or of the adhesion of the film. Commercial units are available to perform this test.

In stress wave adhesion tests, a stress wave is propagated through the system and the reflection of the stress wave at the interface results in a tensile stress [71–73]. The stress can be injected into the solid from a flyer plate, a flyer foil or a pulse of radiation (laser). Conceptually, this technique could be used to initiate, then stop, an interfacial fracture so the fracture mode could be studied. The onset of the fracture could be detected by acoustic emission.

The most recent advance in adhesion tests is the monitoring of acoustic emission during adhesion testing. As fractures form and propagate, there is a release of acoustic energy which may be monitored. The onset of acoustic emission correlates with the onset of adhesion failure in deformation tests. Acoustic emission can be correlated to the fracture of the interface of films on plastic surfaces [74], plasma sprayed coatings [75], and hard coatings on tools [61, 67].

Thermal stress adhesion testing is used on coatings intended for high temperature applications and are often combined with mechanical stresses such as found in thermal barrier coatings [76] and coatings for fusion reactor applications [77].

The Mattox Bad Breath test consists of breathing on the film (best on a brittle substrate material) so that moisture condenses on the film. If the film has a high residual stress, the moisture will tend to accelerate fracture propagation, and blistering (compressive stress) or cracking (tensile stress) will be enhanced. This is an easy ‘first test’ and the test is non-destructive if the film adhesion and adhesion stability are good.

15.5.2 Film Thickness

A film or coating thickness may be defined in three ways: *(i)* geometrical thickness – separation between surfaces; *(ii)* mass thickness; and *(ii)* property thickness.

The geometrical thickness is the separation between surfaces and is measured in mils, microinches, nanometers, angstroms, or microns, and does not take into account the composition, density, microstructure, etc. A general problem with this measurement is the definition of the surfaces. Mass thickness is measured in micrograms/cm^2 which can be converted to a geometrical thickness if one knows (or assumes) the density of the material. Property thickness measures some property such as X-ray absorption, beta (electron) backscatter, ion backscattering, optical adsorption or electrical conductivity which may be sensitive to density, composition, microstructure, crystallographic orientation of the film, etc. Property thickness measuring techniques often require calibration standards. Different thickness measuring techniques may give differing values for the thickness.

Thickness measuring techniques may also be categorized as contacting and non-contacting. The following are some of the most commonly used.

Contacting techniques:

- Surface profilometer (stylus technique). Measures the height of a step from the substrate surface to the film surface. Step is formed by masking during deposition or by masking and etching. Stylus scans length of several centimeters with a resolution of <0.2 mictrons and measures height of greater than 100 Å [78]. Sensitivity is dependent on surface roughness, flatness, and abruptness of the step. Commercial units are available that scan over a surface and present the surface topography on a screen.

Non-contacting techniques:

- Michelson interferometry – Measures the height of a step using a split beam of light. The differing optical path lengths give constructive and destructive interference patterns. By knowing the wavelength of the light and the number of fringes, the step height can be calculated. Measures step heights of 300–20,000 Å ± 150–300 Å [79, 80].
- X-ray fluorescence (XRF) – Measures the mass per unit area of a material. By assuming the density (or calibrating the instrument) the measurement can be presented as a thickness. Measures thicknesses from 100 nm to 40 microns, depending on the material [81].
- X-ray absorption – Measured by X-ray attenuation. Thickness by knowing the absorption coefficient or by calibration. Measures thicknesses from 0.1 to >1000 µm ± 5%.
- Ellipsometry – Measures dielectric film thickness by the rotation of polarization axis as the beam passes through the film. Thickness is determined by knowing the index of refraction of the dielectric or calibration [82].
- Beta backscatter – Energetic electrons from a radioactive source are backscattered from the film and underliying substrate. Thickness is measured by calibration. Thickness range depends on the electron source and the scattering properties of the material. For example, using a C^{14} source, 1.25 to 1.9 microns of gold can be measured; using a Ru^{106} source, 15 to 38 microns gold can be measured ± 5% [82].
- Other techniques
  - Scanning Tunneling Microscopy (STM) (step height);
  - Atomic Force Microscopy (AFM) (step height);
  - Photon Tunneling Microscopy (PTM) (step height);

- Magnetic eddy current techniques;
- Multiple beam interferometry (step height, 10–10,000 Å).

The determination of which technique is best for a particular application depends on a number of factors [83–85].

15.5.3 Film Stress

Films and coatings on substrates may have a residual stress that is either compressive – as if the material were being compressed, or tensile – due to the differences of coefficient of expansion of the film and substrate (high temperature deposition), or from strains grown-in during the growth process. These stresses contribute to adhesion failure (immediate or long-term) or may affect mass transport properties such as void growth [86], low temperature recrystallization (crystalline materials) [87], or a low strain point temperature (glasses) [88].

Films under compression will try to expand and if the substrate is thin the film will bow the substrate with the film being on the convex side. If the film has a tensile stress, the film will try to contract, bowing the substrate so the film is on the concave side. Tensile stress may relieve itself by microcracking the film. Compressive stress may relieve itself by buckling, giving wrinkled spots (usually associated with contamination on the surface), or a wavy pattern (clean surface) if the stress is isotropic [9]. The residual stresses may be anisotropic with direction in the film [80]. A great deal can be learned about the film stress by observing the stress relief patterns [14].

The film stress may not be uniform through the film thickness, i.e. there may be a stress gradient in the deposit. (If the stress is not uniform, the film will curl up when separated from the substrate; if uniform, the separated film will lie flat.) The total film stress is a function of film thickness.

By knowing the mechanical properties of the substrate and film material, the film thickness and the substrate deflection the film stress can be calculated. There are a number of ways that the deflection of a beam can be measured and the stress calculated [90–96]. Figure 15.2 shows a commercially available attachment for use with a microscope to generate an interference pattern that can give the radius of curvature [80].

If the beam is long and narrow so that there is no 'angle-iron' stiffening effect, and the beam was clamped flat during the deposition, the film stress (σ_f) can be calculated from [97]:

$$\sigma_\mathrm{f} = \frac{t_\mathrm{f} E_\mathrm{s}}{(6\rho)} \left[\left(\frac{t_\mathrm{s}}{t_\mathrm{f}} \right)^2 - \frac{t_\mathrm{s}}{t_\mathrm{f}} + 6 \frac{E_\mathrm{f}}{t_\mathrm{s}} \frac{y_\mathrm{f}}{t_\mathrm{f}} \right] \tag{15.1}$$

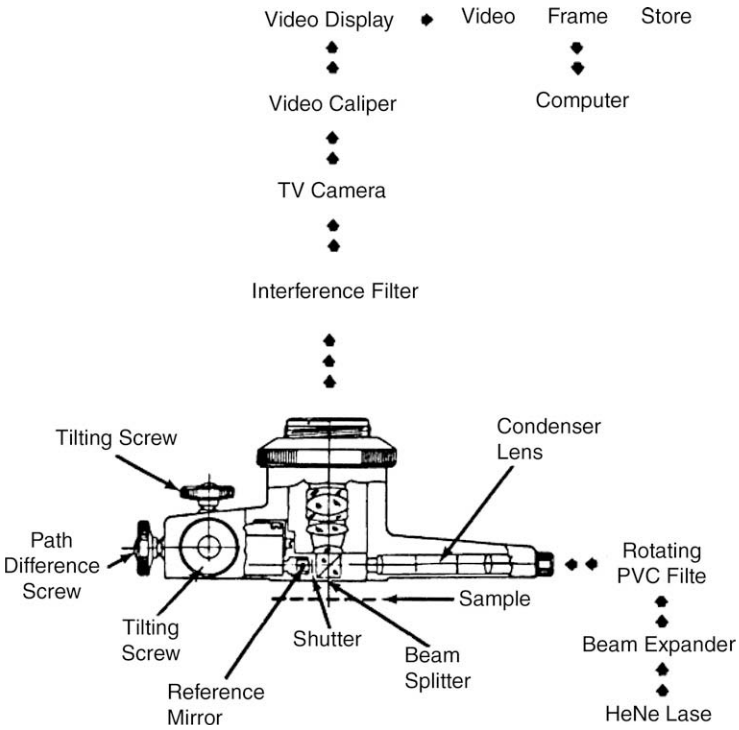

Figure 15.2: Michelson interferometer attachment for optical microscope.

where T_f and T_s are the thicknesses of the film and substrate, E_f and E_s are the elastic moduli of the film and substrate material, ρ is the radius of curvature and the term y_f/t_f is the relative position in the film for which the stress is calculated and is measured from the midplane of the film ($y_f = 0$) and is positive toward the film-substrate interface where the film stress is maximum.

Figure 15.3 shows a sample calculation.

A major uncertainty in measuring film stress is the elastic modulus (and Poisson's ratio) of the film material which has to be assumed in most cases. If the last term in Eq. (15.1) can be made small in comparison with the other terms, the stress determination can be made without knowing or assuming E_f. This can be done by making t_s/t_f very large, which also means measuring a small R_s. This can be done with a sensitive, large optics interferometer [97]. The system shown in Figure 15.4 is capable of detecting the radius of curvature of more than 1 km over an area 2.5 cm in diameter.

Film lattice strain (stress) may also be measured by X-ray diffraction and lattice parameter measurements [98]. However, this technique may not give the same value of stress as measured by the deflection techniques since it does not sum over all the stresses (those

Molybdenum film (6 μm) on microsheet glass (75 μm)

$E_{mo} = 47 \times 10^6$ psi

E_{0211} Microsheet glass = 10.7×10^6 psi (Corning glass)

ρ = Radius of curvature = 6.31 in

$$\sigma_f = \frac{t_f E_s}{6\rho}\left[\left(\frac{t_s}{t_f}\right)^2 + 6\,\frac{E_f}{E_s}\,\frac{Y_f}{t_f}\right] \quad \frac{-1}{2} \le \frac{Y_f}{t_f} \le \frac{1}{2}$$

SUBSTRATE:

$$\sigma_f = \frac{t_s E_s}{6\rho}\left[-1 + 6\,\frac{Y_s}{t_s}\right] \quad \frac{-1}{2} \le \frac{Y_s}{t_s} \le \frac{1}{2}$$

t_f = Film thickness

t_s = Substrate thickness

ρ = Radius of curvature

$Y_{s,f}$ = Distance from mid plane

E_s = Substrate Young's modulus

E_f = Film Young's modulus

Mean stress in film	σ_f = 9,900 psi ± 930 psi Tension
Max film stress at interface	σ_f = 10,830 psi -Tension
Max glass stress at interface	σ_c = −3,170 psi -Compression

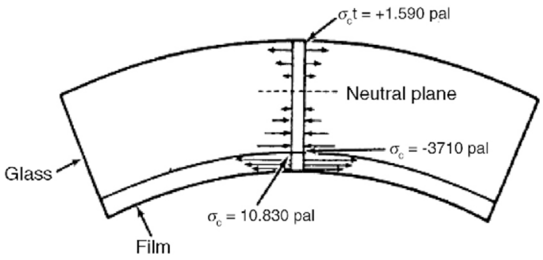

Figure 15.3: Sample stress calculation for a molybdenum film on a thin glass substrate.

associated with the grain boundaries for instance) and is influenced by other factors such as grain size and film morphology. Strain in the surface lattice (few atom layers) can be measured by LEED techniques [99].

15.5.4 Coefficient of Thermal Expansion

The coefficient of thermal expansion of residual growth-stress-free films (annealed) can be determined using the same techniques used for determining the stress in the films by making the measurements at various temperatures. Again, one must know (or assume) the properties of the film and substrate materials. One often finds low temperature mass transport in as-deposited films (driven by high residual stresses and high defect concentrations/mobilities) giving low temperature annealing (strain point for glasses) [88] and grain growth [87] during testing at elevated temperatures. These changing properties will affect the expansion measurements until the film is annealed.

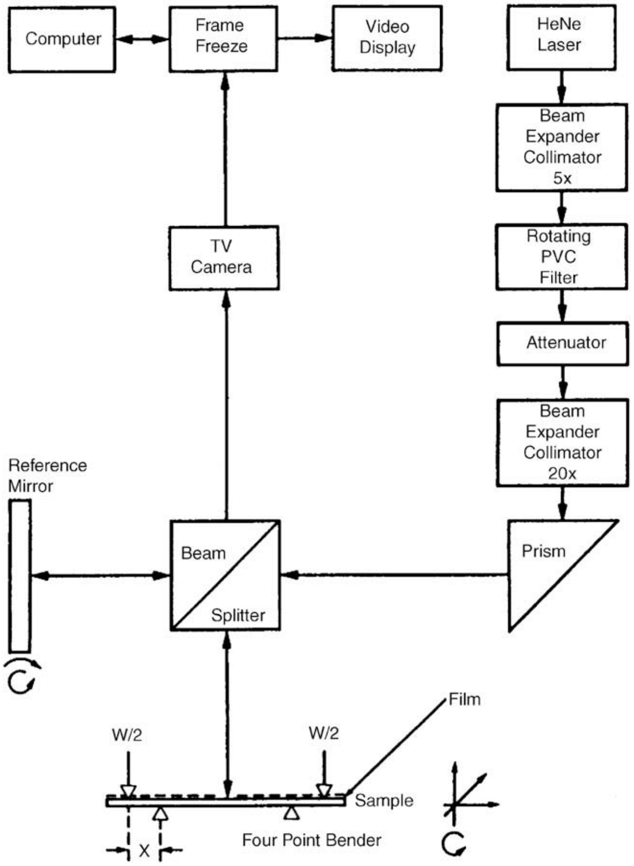

Figure 15.4: Large area Michelson interferometer with associated illumination and data treatment system [97]. The setup shown is for measuring the mechanical properties of a coated substrate by four-point loading of the sample.

15.5.5 Mechanical Properties

The hardness of a material is usually defined as the resistance to deformation and is usually measured as the permanent deformation of a surface by a specifically shaped indenter under a given load [100–101]. This does not give an indication of the plastic deformation associated with loading. The hardness of a material may be influenced by the grain size, dispersed phases, defect structure, microstructure, density, temperature, deformation rate, etc. For films and coatings, there may be substrate influences on the deformation which affect the measurements. As a rule, the coating thickness should be 10X the indentation depth to obtain meaningful results. Surface effects may also influence the indentation measurements for thin films, particularly those with oxide layers.

Techniques to measure the microhardness of films and modified surfaces (particularly ion implanted ones) usually use microindentation techniques [102–110]. In addition to hardness, the elastic properties of the material can be determined from the maximum penetration depth compared to the residual depth of the indentation after the indenter has been removed. The impact of microspheres with a surface may be used to measure microhardness and its variation over a surface [111].

An advanced microindentation hardness testing system is commercially available. It is a computer-controlled machine capable of performing indentation tests with load and depth resolutions of 2.5 millinewtons and 0.4 nanometers up to a maximum load of 10 grams. It detects penetration movement by changes in capacitance between stationary and moving plates.

15.5.6 Electrical Resistivity

The bulk resistivity of a material is given in micro-ohm cm and the resistance of a path is calculated from:

$$R = \rho L/A$$

where ρ is the resistivity, L the length, and A the area. For a thin film, the resistivity may be a strong function of the film properties such as morphology, composition, etc. [112].

The film resistivity is often given as the sheet resistivity (sheet ρ) in ohms per square since the resistance of any square is the same no matter what the size of the square, as long as the thickness is uniform and other properties are the same.

The sheet resistance is measured using a four-point probe technique where the current [1] is injected through two probes and the voltage drop (V) between two other probes is measured [113, 114]. This technique avoids contact resistance problems [115, 116].

For a linear probe arrangement, the resistivity is given by:

$$R_\mathrm{s} = 4.532\ V/I$$

Probe separation of commercial units may be as low as 0.025 inches.

For layered structures of materials having a nonuniform resistivity, the measurement is more complicated [117, 118]. Resistivity (conductivity) can also be measured by induction without contacting the surface of the film [119].

15.5.7 Temperature Coefficient of Resistivity (TCR)

The TCR of metals is positive, i.e. increasing resistance with increasing temperature while that of tunneling-type conductors (insulators) is negative, i.e. decreasing resistance with increasing temperature. To measure the TCR, one only needs to combine a resistance measuring device with a temperature-controlled environment. The measured TCR combines effects found in the film, i.e. metallic conduction in the grains (columns), with tunneling through oxides at columnar boundaries. Often the film TCR is much less than that of the bulk material and may be of an opposite sign altogether. TCR measurements can give an indication of the perfection of the film material.

15.5.8 Electromigration

Electromigration is the movement of film atoms in the *electron wind* when metallizations are used to carry high current densities (Al: 10^6 A/cm^2-steady, 10^7 A/cm^2-pulse). The origin of the electromigration effect is poorly understood but it is probably dependent on local temperature, film stress, and lattice defects in the film material. The electromigration may result in hillock formation or void formation. Electromigration is measured by subjecting the conductor to the high current density, detecting failure (often defined as 50% reduction in cross-section area) and evaluating many samples prepared in the same way. Elevated temperatures, and processing techniques that introduce lattice defects, broaden the statistical failure curve and bring the early failures to a shorter time.

Electromigration seems to be a statistical problem with some failures occurring far below the mean value. This can cause early failure of the electrical circuits if there is no circuit redundancy. Electromigration can be minimized and the statistical spread can be lessened by process control, *burn-in* of the circuits to eliminate the metallizations most prone to failure (*infant mortality*), addition of dispersed particles (1–4% Cu in Al), multilayering of the metallization (e.g. 3000 Å Al alternated with 50–100 Å Ti) or the use of *cap* (passivating) material [120]. Electromigration kinetics are dependent on the composition and structure of the film [121].

15.5.9 Density

The density of a material depends on: *(i)* composition; *(ii)* closed porosity (void) volume; and *(iii)* definition of the surfaces. Densities are given in g/cm^3.

A deposited material may easily have several atomic percent of foreign material incorporated into the lattice or may easily be off-stoichiometry by an appreciable amount, and this composition variation affects the density of the deposit. Voids affect the density in an obvious way.

Density may be measured by several general techniques: *(i)* geometry-property relationships; and *(ii)* displacement-flotation techniques.

In the geometry techniques, the size or thickness of the sample is determined as well as some property such as mass or x-ray absorption. For example, Rutherford backscattering may be used to give the areal atom density and a profilometer can be used to give the geometrical thickness [122].

Properties other than mass must be related to the mass by known properties or calibration. A principle difficulty with this technique is in defining the surface in order to make accurate thickness measurements.

The displacement techniques include: *(i)* micropycnometry; *(ii)* density gradient column; *(iii)* hydrostatic weighing; and *(iv)* volume displacement.

The most accurate techniques have been developed to study radiation-induced void formation in metals and utilizes hydrostatic weighing of small samples (30 mg) with an electrobalance to a precision of 0.04% [123]. Density gradient columns utilize a thermal gradient in liquids of varying density (liquid densities to 3.2 gr/cm^3). The sample will float at a level of the same density fluid (watch out for buoyant air bubbles attached to the sample). Calibration floats are used to determine the fluid density.

Pycnometry involves the displacement of a liquid or gas from a container of accurately known volume and the weight of the sample.

Density is often related to other film properties such as chemical etch rate, corrosion, compressive strength, index of refraction, etc.

15.5.10 Porosity

The porosity in a deposit may consist of: *(i)* open porosity where the pores are interconnected; *(ii)* closed porosity where the pores are isolated and not interconnected; and *(iii)* through-porosity where the pore extends through the deposit from the surface to the interface. Typically, a deposit will contain both open and closed porosity to some extent. A material with closed porosity will show a decrease in density while a material with open porosity will not (as measured by many of the techniques described under density measurements). *Voids* is another term used for isolated pores, while *micro voids* is the term used for very small voids down to clusters of lattice vacancies (few angstroms in diameter).

Voids in the bulk of the material form by the growth processes or by agglomeration of defects during or after deposition. Voids in the bulk affect density of the material, the deformation and fracture properties of the material, and the thermal and acoustic transmission of the material.

Closed voids in materials are typically measured and studied by: *(i)* density measurements; or *(ii)* transmission electron microscopy (TEM).

In TEM, the sample is thinned and the voids are observed directly by using the underfocus-overfocus technique. Voids as small as 7 Å in diameter may be resolved using this technique.

Open porosity may be of several forms. Uniformly distributed interconnected pores develop as the pore volume becomes large (greater than about 5%). Oriented porosity develops due to the growth mode of the deposited material such as forming a columnar morphology. Through-porosity often develops because a substrate-surface discontinuity gives geometrical shadowing of the depositing flux.

Open porosity can affect material properties in both desirable and undesirable ways. Generally undesirable effects include: *(i)* high surface areas; *(ii)* easy access to the interfacial region; and *(iii)* easily deformed material. A high surface area results in: *(i)* high chemical etch rates; *(ii)* high corrosion rates; *(iii)* easy contamination/difficult cleaning; and *(iv)* dependence of properties (e.g. resistivity) on surface effects (e.g. oxidation). Easy access to the interfacial region may result in; *(i)* interfacial corrosion (loss of adhesion); and *(ii)* rapid diffusion paths (surface diffusion).

Desirable effects of porosity include: *(i)* less residual film stress; *(ii)* low thermal conductivity (thermal barriers); *(iii)* higher resistance to thermal shock; and *(iv)* reduced mass transport effects such as grain growth. Open porosity in thick deposits may be measured by:

1. Mercury porosimetry;
2. Gas absorption/desorption (BET [Brunauer-Emmett-Teller] [124], Surface Acoustic Wave attenuation;
3. Dye penetrants-fluorescence, radioactive.

In mercury porosimetry the sample is immersed in mercury and pressure (0.5 to 30,000 psia) is used to force mercury into the pores (3.2 nm to 213 microns) (mercury intrusion) [125]. The smaller the pores, the greater the pressure that is needed to force the mercury into the pores. Force vs. volume-change is then a measure of the pore volume distribution. Because of the 'bottle-neck' effect, the measurement is often biased toward the small pore size. Calculations of pore size depend on the contact angle between mercury and the material being measured.

Through-porosity, or cracks through metal films, on metal substrates may be measured by electrographic printing [126] where a chemical solution in a paper or gel is placed in contact with the film and a copper electrode is placed behind the paper. The electrode is made the cathode and the substrate is made the anode and a current is passed through the system (typically 200 mA, 30 sec). The paper is then observed for spots which indicate that some of the dissolved substrate material has reacted with the chemical solution.

Some electrographic porosity tests are listed below:

Deposit	Reagent solution	(Indication)
Au on Cu	Potassium ferricyanide	(brown spots)
Ag on Cu	Potassium ferricyanide	(brown spots)
Sn on Fe	Potassium ferricyanide	(blue spots)
Au on Ni	Ammoniacal dimethylglyoxime and sodium chloride	(red spots)
Cr on Ni	Dimethylglyoxime	(pink spots)
Cu on Fe	Dimethylglyoxime	(deep cherry red spots)
Ni on steel	Sodium chloride + hydrogen peroxide	(rust spots)
Zn or Cd on steel	Sodium hydrosulfide	(black spots)

Porosity through thin dielectric films on metallic substrates may be measured by [127–130]:

1. Corrosion (liquid, gas);
2. Selective chemical dissolution (electrographic printing, solution analysis);
3. Electrochemical decoration;
4. Anodic current measurement;
5. Gas bubble generation (electrolytic);
6. Absorption (dyes, radioactive materials, liquids, gases).

Porosity through metal films on metallic substrates may be measured by:

1. Corrosion – selective of substrate materials;
2. Selective chemical dissolution;
3. Anodic currents (controlled potential) [131];
4. Corrosion potentials (anodic polarization).

Figure 15.5 shows the corrosion products that have built up in a pore in a gold film on a Kovar® surface.

A special case of porosity measurement is the use of a Surface Acoustic Wave (SAW) device where a film deposited on a piezoelectric crystal adsorbs gases, changes the mass, and thus the acoustic dampening [132]. From the adsorption/desorption curves, a pore size distribution can be calculated. The SAW configuration is capable of detecting mass changes of 100 picograms/cm^2.

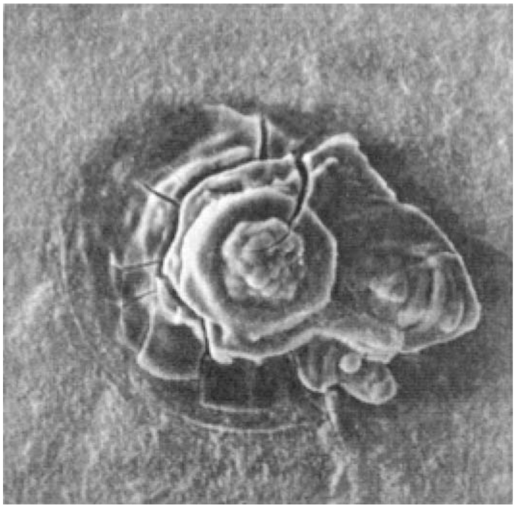

Figure 15.5: SEM photograph of corrosion products emerging from a pore in a gold coating on Kovar®. Corrosion was performed in a moist UV/O_3 atmosphere.

15.5.11 Chemical Etch Rate (Dissolution)

The chemical etch rate of a material depends on density, surface area, intrinsic stress, stoichiometry, solution strength, and dissolution rate of the bulk, fully-dense stoichiometric material. Chemical etch rates are primarily used as a comparative technique [133]. Reactive Plasma Etching (RPE) and Reactive Ion Etching (RIE) are versions of chemical etching which use a plasma to activate the reactive species, which react with the surface, giving a volatile reaction product. The film microstructure and phase distribution can have an important effect on the RIE etch rate and uniformity [134].

15.6 Summary

This discussion has given the reader an indication of the factors in film deposition technologies and film growth that affect the properties of the resulting material. Some simple characterization techniques have been discussed but there are many more to be found in the literature. The need for reproducible samples and characterization specifications has been strongly emphasized.

References

[1] A.J. Perry, Thin Solid Films 135 (1986) 73.
[2] S. Walters, Mechanical Engineering (April 1984) 38.
[3] D.M. Mattox, in: K.L. Mittal (Ed.), Adhesion Measurement of Thin Films, Thick Films and Bulk Coatings, American Society for Testing and Materials (1978) 54, ASTM STP 640.

[4] D.M. Mattox, in: E. Broszeit, W.D. Munz, H. Oechsner, K.-T. Rie, G.K. Wolf (Eds.), Plasma Surface Engineering, Informationsgesellschaft, Verlag 1 (1989) 15.
[5] J.E. Greene, *Proc. NATO Advanced Studies Institute on Plasmasurface Interactions and Processing of Materials*, Alicante, Spain NATO ASI Series, (Sept 4–16, 1988) (to be published).
[6] D.M. Mattox, 'Surface Preparation' Ch. 6, this volume.
[7] *Surface Mobilities on Solid Materials – Fundamental Concepts and Applications*, (V.T. Binh, ed.), NATO ASI Series, Series B, Physics Vol. 86, Plenum Press (1983).
[8] B. Lewis, J.C. Anderson, Nucleation and Growth of Thin Films, Academic Press (1978).
[9] D.M. Mattox, J. Appl. Phys. 37 (1966) 3613.
[10] R. Miranda, J.M. Rojo, Vacuum 34 (1984) 1069.
[11] C.E.D. Chidsey, D.N. Loiacono, T. Sleaton, S. Nakahara, Surf. Sci. 200 (1988) 45.
[12] K. Olumura, J. Electrochem. Soc. 128 (1981) 571.
[13] E. Philofsky, Solid State Electronics 13 (1970) 1391.
[14] D.M. Mattox, R.E. Cuthrell, in: D.M. Mattox, J.E.E. Baglin, R.E. Gottschall, C.D. Batich (Eds.), MRS Proc., Materials Research Society (1988) Vol. 119.
[15] B.A. Movchan, A.V. Demchishin, Fiz. Met. Metalloved 28 (1969) 653.
[16] D.M. Mattox, G.J. Kominiak, J. Vac. Sci. Technol. 9 (1972) 528.
[17] R.D. Bland, G.J. Kominiak, D.M. Mattox, J. Vac. Sci. Technol. 11 (1974) 671.
[18] J.A. Thornton, J. Vac. Sci. Technol. A4 (1986) 3059.
[19] R. Messier, A.P. Giri, R.A. Roy, J. Vac. Sci. Technol. A2 (1984) 500.
[20] R. Meissier, J.E. Yehoda, J. Appl. Phys. 58 (1985) 3739.
[21] S. Berg, H.-O. Blom, T. Larsson, C. Nender, J. Vac. Sci. Technol. A5 (1987) 202.
[22] M.W. Geis, G.A. Lincoln, N. Efremow, W.J. Piacentini, J. Vac. Sci. Technol. 19 (1981) 1390.
[23] H.F. Winters, J.W. Coburn, T.J. Chuang, J. Vac. Sci. Technol. B1 (1983) 469.
[24] J.M.E. Harper, J.J. Cuomo, H.T.G. Henzell, Appl. Phys. Lett. 36 (1980) 456 also *Appl. Phys. Lett.*, 37:540 (1980).
[25] R.W. Hoffman, Thin Solid Films 89 (1982) 155.
[26] H.K. Pulker, Thin Solid Films 89 (1982) 191.
[27] R. Singh, J. Appl. Phys. 63(8) (1988) R59.
[28] C.R. Wie, J.Y. Yang, T.A. Tombrell, R.W. Grant, R.M. Housley, Vacuum 38 (1988) 157.
[29] R. Wahn (Ed.), Metals Handbook, 9th. ed., Vol. 10, American Society for Metals, Metals Park, OH (1986) 44073.
[30] R.J. Good, J. Adhesion 8 (1976) 1.
[31] H.K. Pulker, A.J. Perry, R. Berger, Surf. Technol. 14 (1981) 25.
[32] A.J. Kinloch, [polymer] J. Mat. Sci. 15 (1980) 2141.
[33] K.L. Mittal (Ed.), Adhesion Aspects of Polymeric Coatings, Plenum (1981).
[34] D.M. Mattox, J. Vac. Sci. Technol. 10 (1973) 47.
[35] J.E.E. Baglin, in: P. Mazzolsdi, G. Arnold (Eds.), Ion Beam Modification of Insulators, Elsevier (1987) Ch. 15.
[36] P. Benjamin, C. Weaver, Proc. Royal Soc. 261A (1961) 516.
[37] M. Laugier, Thin Solid Films 75 (1981) L19.
[38] G.J. Kominiak, D.M. Mattox, J. Electrochem. Soc. 120 (1973) 1535.
[39] M. Hershkovitz, I.A. Blech, Y. Komem, Thin Solid Films 130 (1985) 87.
[40] A. Kikuchi, S. Baba, A. Kinbara, Thin Solid Films 124 (1985) 343.
[41] R.R. Zito, Thin Solid Films 87 (1982) 87.
[42] W.D. Bascom, P.F. Becher, J.L. Bitner, J.S. Murday, *Adhesion Measurement of Thin Film, Thick Film and Bulk Coatings*, (K.L. Mittal, ed.), ASTM STP 640 (1977) 63–82.
[43] T.S. Oh, R.M. Cannon, R.O. Richie, J. Am. Cer. Soc. 70 (1987) C352.
[44] H.E. Hintermann, J. Vac. Sci. Technol. B2 (1984) 816.
[45] L.A. K'Singam, J.T. Dickenson, L.C. Jensen, J. Am. Cer. Soc. 68 (1985) 510.

[46] J.D. Speight, M.J. Bill, Thin Solid Films 15 (1973) 325.
[47] S.K. Ray, R.K. Lewis, Thin Solid Films 131 (1985) 197.
[48] D.M. Mattox, unpublished results.
[49] S. Krzyzanowski, W.D. Sylwestrowicz, J. Mat. Sci. Lett. 1 (1982) 35.
[50] A.W. Hothersall, C.J. Leadbeater, J. Electrodepositers Tech. Soc. 14 (1938) 207.
[51] J.D. Venables, J. Mat. Sci. 19 (1984) 2431.
[52] H.K. Yasuda, A.K. Sharma, E.B. Hale, W.J. James, J. Adhesion 13 (1982) 269.
[53] J.C. Grosskreutz, M.B. McNeil, J. Appl. Phys. 40 (1969) 355.
[54] W.L. Smith, A. Rosecwaig, D.L. Willenborg, J. Opsal, M.W. Taylor, Solid State Technol. 29 (1986) 85.
[55] K.L. Mittal, J. Adhesion Sci. Technol. 1 (1987) 247.
[56] K.L. Mittal, Electrocomponent Sci. Technol. 3 (1976) 21.
[57] D. Davies, J.A. Whittaker, Metallurgical Rev. 12 (1967) 15 Metals and Materials, 1 (1967).
[58] J. Valli, U. Makela, A. Matthews, Surf. Eng. 2 (1986) 49.
[59] B.N. Chapman, J. Vac. Sci. Technol. 11 (1974) 106.
[60] D.J. Brown, A.H. Windle, D.G. Gilbert, P.W.R. Beaumont, J. Mat. Sci. 21 (1986) 314.
[61] Il-B. Yoon, Jpn. J. Appl. Phys. Suppl. 2 Pt 1 (1974) 849.
[62] A.J. Perry, Thin Solid Films 107 (1983) 167.
[63] A.J. Perry, Thin Solid Films 78 (1981) 77.
[64] M.T. Laugier, J. Vac. Sci. Technol. A5 (1987) 67.
[65] M.T. Laugier, J. Mat. Sci. Lett. 5 (1986) 253.
[66] S.V. Prasad, T.H. Kosel, J. Matl. Sci. Lett. 3 (1984) 133.
[67] H.E. Hintermann, J. Vac. Sci. Technol. B2 (1984) 816.
[68] J.H. Je, E. Gyarmati, A. Naoumidis, *Thin Solid Films* 135, 57, 86.
[69] A.F. Jankowski, J. Mat. Sci. 22 (1987) 346.
[70] J.L. Jellison, IEEE PHP 11 (1975) 206.
[71] N.C. Anderholm, A. Goodman, Patent # 3,605,486 (Sept 20, 1971).
[72] J.L. Vossen, in: K.L. Mittal (Ed.), Adhesion Measurements of Thin Films, Thick Films and Bulk Coatings, ASTM Publications (1978) 122–131, ASTM STP-640.
[73] J.W. Dini, H.R. Johnson, Rev. Sci. Instrum. 46 (1975) 1705.
[74] R.E. Van de Leest, Thin Solid Films 124 (1985) 335.
[75] S. Aithal, G. Rousset, L. Bertrand, P. Cielo, S. Dallaire, Thin Solid Films 119 (1984) 153.
[76] C.C. Berndt, R.A. Miller, Thin Solid Films 119 (1984) 173.
[77] D.M. Mattox, A.W. Mullendore, J.B. Whitley, H.O. Pierson, Thin Solid Films 73 (1980) 101.
[78] I. Sherrington, E.H. Smith, Wear 125 (1988) 241.
[79] I. Sherrington, E.H. Smith, Wear 125 (1988) 289.
[80] R.E. Cuthrell, D.M. Mattox, C.R. Peeples, P.L. Dreike, K.P. Lamppa, J. Vac. Sci. Technol. A6(5) (1988) 2914.
[81] F. Ferrandino, Metal Finish 84(5) (1986) 29.
[82] S. Yaghmour, W.E.J. Neal, Surf. Technol. 25 (1985) 297.
[83] O.S. Rajora, A.E. Curzon, Thin Solid Films 123 (1985) 235.
[84] A. Piegari, E. Masetti, Thin Solid Films 124 (1985) 249.
[85] W.A. Pliskin, S.J. Zanin, in: L.I. Maissel, R. Glang (Eds.), Handbook of Thin Film Technology, McGraw-Hill (1970) Ch. 11.
[86] C.Y. Li, R.D. Black, W.R. LaFontaine, Appl. Phys. Lett. 53 (1988) 31.
[87] J.W. Patten, E.D. McClanahan, J.W. Johnson, J. Appl. Phys. 42 (1971) 4371.
[88] G.J. Kominiak, D.M. Mattox, J. Electrochem. Soc. 120 (1973) 1535.
[89] K. Ogawa, T. Ohkoshi, T. Takeuchi, T. Mizoguchi, T. Matsumoto, Jpn. J. Appl. Phys. 25 (1986) 695.
[90] A. Brenner, S. Senderoff, *J. of Research of the National Bureau of Standards,* Research Paper RP1954, 42:105–123 (Feb 1949).
[91] C.N. Kouyumdjiev, Surf. Technol. 26 (1985) 35.

[92] C.N. Kouyumdjiev, Surf. Technol. 26 (1985) 45.
[93] C.N. Kouyumdjiev, Surf. Technol. 26 (1985) 57.
[94] G. Sotirova, S. Armyanov, Surf. Coat. Technol. 28 (1986) 33.
[95] C.N. Kouyumdjiev, Surf. Coat. Technol. 28 (1986) 39.
[96] H.K. Pulker, Thin Solid Films 89 (1982) 191.
[97] R.E. Cuthrell, F.P. Gerstile, D.M. Mattox, Rev. Sci. Instrum. 60(6) (1989) 1018.
[98] V.M. Hauk, E. Macherauch, Adv. X-ray Anal. 27 (1983) 81.
[99] E.G. McRae, R.A. Malic, Surf. Sci. 163 (1985) L702.
[100] H.T. Angus, Wear 54 (1979) 33.
[101] *Microindentation Techniques in Material Science*, (Blau and Lawn, eds.), ASTM Special Publication No. 889 (1986).
[102] P.J. Blau, Metallography 16 (1983) 1.
[103] A.G. Dirks, J.J. van den Broek, P.E. Wierenga, JAP 55 (1984) 4248.
[104] P.E. Wierenga, A.J.J. Franken, *JAP* 55, 4244, 84.
[105] B. Jonsson, S. Hogmark, Thin Solid Films 114 (1984) 257.
[106] W.C. Oliver, Mat. Res. Soc. Bull. 11(5) (1986) 15.
[107] M.F. Doerner, W.D. Nix, J. Mat. Res. 1 (1986) 601.
[108] R.J. Bourcier, C.M. Stone, F.G. Yost, Sandia Report SAND85-0486, (Sept 1985).
[109] R.J. Bourcier, G.C. Nelson, A.K. Hayes, A.D. Romig Jr., J. Vac. Sci. Technol. A4 (1986) 2943.
[110] D.T. Schmale, R.J. Bourcier, E. Martinez, Sandia Laboratory Report SAND86-0509 (April 1986), available from NTIS.
[111] S. Cook, R.V. Latham, Surf. Coat. Technol. 27 (1986) 379.
[112] M.A. Angadi, J. Mat. Sci. 20 (1985) 761.
[113] L.B. Valdes, Proc. IEEE (IRE) 42 (1954) 420.
[114] W.A. Keenan, W.H. Johnson, A.K. Smith, Solid State Technol. 28(6) (1985) 143.
[115] S.S. Cohen, Thin Solid Films 104 (1983) 361.
[116] S.S. Cohen, G. Gildenblat, M. Ghezzo, D.M. Brown, J. Electrochem. Soc. 129 (1982) 1335.
[117] J. Albers, H.L. Berkowitz, J. Electrochem. Soc. 132 (1985) 2453.
[118] J. Albers, H.L. Berkowitz, J. Electrochem. Soc. 131 (1984) 392.
[119] P. Esqueda, M. Octavio, R.C. Callarotti, Thin Solid Films 89 (1982) 33.
[120] V. Teal, S. Vaidya, D.B. Fraiser, Thin Solid Films 136 (1986) 21.
[121] L.E. Felton, J.A. Schwartz, R.W. Pasco, D.A. Norbury, J. Appl. Phys. 58 (1985) 723.
[122] A. Antilla, J. Koskinen, M. Bister, J. Hirvonen, Thin Solid Films 136 (1986) 29.
[123] N.A. Pratten, J. Mat. Sci. 16 (1981) 1737.
[124] D.M. Young, A.D. Cromwell, The Physical Absorption of Gases, Butterworth Pub. (1962).
[125] H.M. Rootare, in: J.S. Horschorn, K.H. Roll (Eds.), Advanced Experimental Techniques in Powder Metallurgy, 5, Plenum (1970) 225.
[126] A. Tvarusko, H.E. Hinterman, Surf. Technol. 9 (1979) 209.
[127] W. Kern, RCA Rev. 34 (1973) 655.
[128] W. Kern, R.B. Comizzoli, J. Vac. Sci. Technol. 14 (1977) 32.
[129] W. Kern, Solid State Technol. 17 (1974) 78.
[130] W. Kern, Solid State Technol. 17 (1974) 35.
[131] R.J. Morrissey, J. Electrochem. Soc. 119 (1972) 446.
[132] S.J. Martin, G.C. Frye, A.J. Ricco, T.E. Zipperian, Proc. IEEE, 1987, *Ultrasonics Symposium*, p. 563 (1987).
[133] W.A. Pliskin, in: E.M. Murt, W.G. Guldner (Eds.), Physical Measurement and Analysis of Thin Films, Plenum Press (1969) Ch. 8.
[134] S. Adachi, N. Susa, J. Electrochem. Soc. 132 (1985) 2980.

CHAPTER 16

Characterization of Thin Films and Coatings

D.R. Baer and S. Thevuthasan

16.1 Introduction

Just as the numbers and types of thin films have grown dramatically, so have the needs and approaches for their characterization also expanded significantly. Adequate characterization of a film or coating depends on the process to create the coating as well as the planned or potential application(s) and expected lifetime. Characterization of a coating or film necessarily requires application of methods that determine properties of the coating and not primarily the substrate.

This places some focus on methods that determine properties of layers and not 'bulk' material. However, the increasing importance of microstructures and nanostructures in coatings and films places an increased importance in methods with high spatial resolution. The growing use of organic films and coatings and the importance of molecular functionalization of inorganic surfaces increase the importance for different types of molecular characterization tools. In most circumstances appropriate characterization requires use of a combination of tools.

The purpose of this chapter is to provide an introduction to the basic methods and overview applications for some of the most important tools for characterization of films, coatings, and surfaces. The chapter will be organized in the following sections:

- Section 16.2: Techniques Overview – this section provides a high level summary of the types of information that can be obtained by different methods and includes information about their sensitivity and resolution.
- Section 16.3: Incident Photon Methods – techniques involving incident photons are described and some brief examples of application are shown. Methods included are: X-ray photoelectron spectroscopy (XPS), X-ray diffraction (XRD), X-ray reflectivity (XRR), Fourier transform infra-red spectroscopy (FTIR), laser Raman spectroscopy (RS), ellipsometry, and photoluminescence spectroscopy.
- Section 16.4: Incident Ion Methods – methods initiated by ion irradiation are summarized, including: Rutherford backscattering spectrometry (RBS), nuclear reaction analysis (NRA), ion channeling, elastic recoil detection analysis (ERDA), secondary ion mass spectrometry (SIMS), glow discharge mass spectrometry and uses of focused ion beams (FIBs) (often in combination with scanning electron microscopy).
- Section 16.5: Incident Electron Methods – methods involving incident electrons include: Auger electron spectroscopy (AES), scanning electron microscopy (SEM), energy dispersive X-ray spectroscopy (EDXS), transmission electron microscopy (TEM), and electron diffraction (low-energy electron diffraction (LEED) and reflection high-energy electron diffraction (RHEED)).
- Section 16.6: Other Methods – additional methods described include scanning probe microscopy (SPM) (including scanning tunneling microscopy (STM) and atomic force microscopy (AFM)) and atom probe microscopy.

16.2 Techniques Overview

The type or types of information required determines the characterization methods needed to investigate a coating or film. In this section several different approaches are used to summarize the range of information that can be provided by a selection of conventional and some newly developing characterization methods.

The growing need for film, coating, interface, and surface characterization has stimulated a growth of industry in the development of analysis tools, the creation of specialized organizations within companies to address specific measurements, and independent consultants that can expertly perform such measurements. By taking advantage of the assistance of experts at companies or user facilities, a researcher can use the sophistication of the instruments and capabilities without being a technique expert [1]. However, for those seeking information, it is highly useful to understand what types of information can be obtained by different methods and the likely sensitivity. Tables and figures in this section provide a highly simplified overview of the types of information that can be obtained by different analysis methods. They are intended to help guide a researcher or engineer toward what might be the most useful technique(s) for a specific need. It must be recognized that many materials are exceptional in different ways and issues related to damage, sensitivity, or single interface may alter the relative value and importance of different methods. Some advantages and limitations of the different methods are included in the descriptions of the specific methods.

Table 16.1 provides a list of the methods summarized in this chapter along with a brief indication of the information that can be obtained. The techniques are organized by the nature of the incident or probe beam used to initiate the information process. Because methods can be used in a variety of ways and combinations to produce specific types of information, Table 16.2 organizes the methods by types of information that may be obtained from a given sample. Although these tables are useful, it is not easily possible to create compact tables that provide all of the needed information in a useful form. Several approaches have been made by different organizations to summarize information from different techniques.

Two bubble charts created by Evans Analytical Group (EAG) [2] and National Physical Laboratory (NPL) [3] have proven to be highly useful. The NPL bubble chart on surface and nanoanalysis (Figure 16.1) summarizes the types of information that can be extracted from specific methods and the spatial resolution of the methods. The NPL chart nicely complements the analytical resolution versus detection limit information contained in the EAG chart (Figure 16.2). The real value of these bubble charts is that they identify important aspects of many different analysis methods in an understandable fashion. Such charts can be used to guide a potential user toward useful methods to obtain the information needed. However, it remains important to explore the most relevant methods in more detail to determine whether the desired information can actually be obtained.

In the technique descriptions that follow, several techniques are summarized. One objective in each area has been to provide a general overview of how the method works. For each method a short summary of strengths and limitations is provided. Because each method can be used in relatively simple or much more sophisticated ways, it is useful to explore methods of potential

Table 16.1: Film, coating, and surface characterization methods ordered by incident or probing beam

Probing beam	Technique	Types of information
Photons	X-ray photoelectron spectroscopy (XPS)	Surface composition (Li and heavier), surface chemical state
	X-ray diffraction (XRD)	Film crystal structure and phase
	X-ray reflectance (XRR)	Film thickness and interface roughness
	Laser Raman	Molecular structure
	Fourier transform infrared spectroscopy (FTIR)	Molecular structure
	Ellipsometry	Film thickness
	Photoluminescence spectroscopy	Luminescence properties
Ions	Rutherford backscattering spectrometry	Film composition, film thickness, elemental profiles, information about interface
	Nuclear reaction analysis	Specific isotope composition and distribution
	Ion channeling	Crystalline quality and defect (impurity) locations, information about interface
	Elastic recoil detection analysis	Light element concentration and depth distribution
	SIMS/Nano-SIMS/TOF-SIMS	Molecular and elemental species
	Low-energy ion scattering	Outer surface composition, surface structure
	Glow discharge mass spectrometry	Depth profile
	Focused ion beam	Ion-induced EDS, secondary ion microscopy, ion-induced secondary electron microscopy, nanolithography (site specific cross-sections), film surface cleaning
Electrons	Auger electron spectroscopy	Surface elemental (and chemical state) composition
	Scanning electron microscopy	Surface topography, film thickness?
	Transmission electron microscopy	Microstructure, chemical information, film thickness?
	Low-energy electron diffraction	Surface structure
	Energy-dispersive X-ray spectroscopy	Composition and composition distribution
Other Methods	Scanning probe methods (STM, AFM, etc.)	Topography, electronic structure, site-specific information
	Atom probe microscopy	Atom distributions

Table 16.2: Types of information needed and useful characterization methods

Information	Method	Comments or range of applicability
Composition		
Surface composition	XPS	Outer 10 nm
	AES	Outer 10 nm
	SIMS	Outer 1 nm
	LEIS	Outer < 1 nm
Depth distribution	Ion sputter profiles with XPS, AES, or SIMS	Less than a few µm
	RBS/NRA	Up to 2 µm
Film thickness	XRR	10 nm < thickness < 1 µm
	XPS	1 nm resolution, 10 nm depth
	TEM	Need cross-section
	RBS	Up to 2 µm
	Ellipsometry	
Structure	XRD	Phases and orientations
	RHEED	Structure during growth
	LEED	Surface structure
	TEM electron diffraction	Structure with spatial resolution
Film surface roughness	AFM	
	Profilometry	
Molecular structure	Raman/IR	Non-destructive
	TOF-SIMS	Destructive

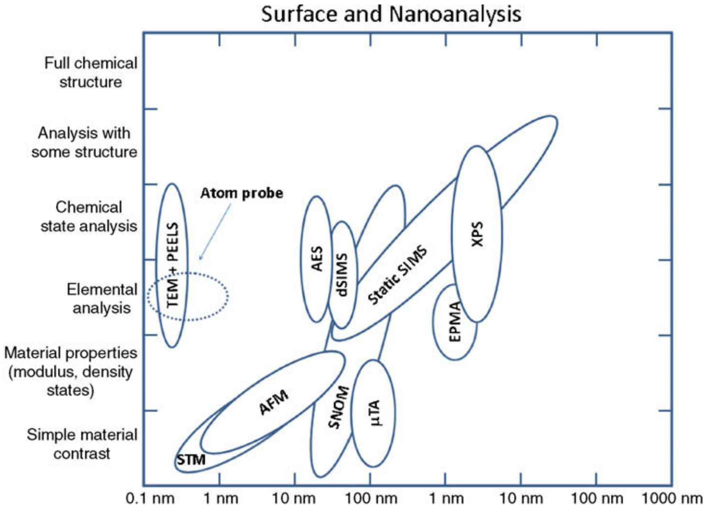

Figure 16.1: Diagram showing types of information that can be collected and spatial resolution of a variety of surface and materials analysis methods. Many of the methods are listed in Table 16.1. (Diagram prepared by the National Physical Laboratory [3], Teddington, UK; used with permission.)

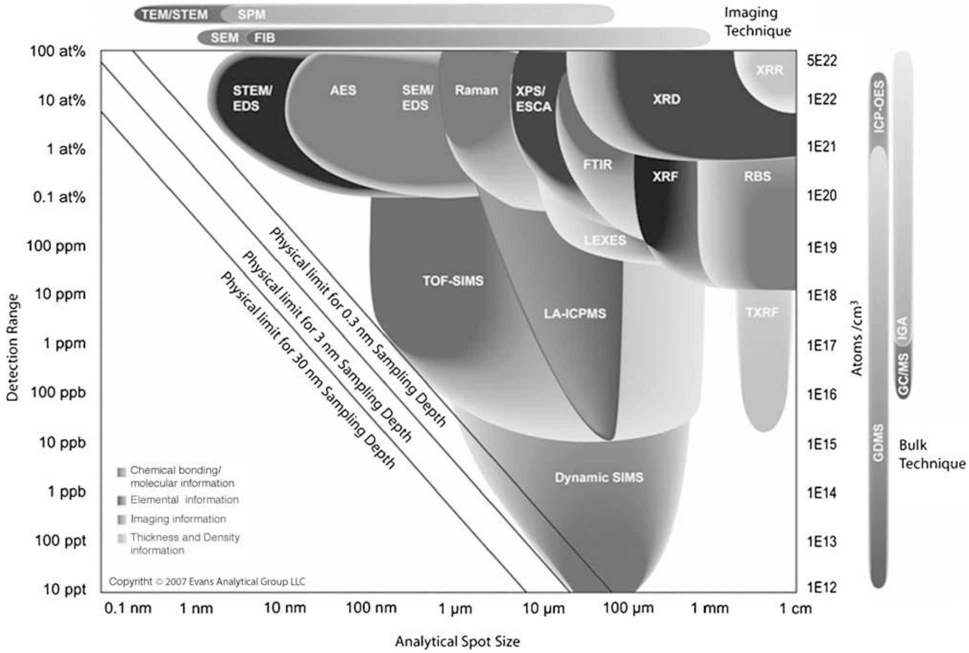

Figure 16.2: Diagram of analysis resolution versus detection limit for a variety of analytical methods. (Chart developed by Evans Analytical Group [2]; used with permission.)

interest in much more detail and appropriate references are provided. Increasingly useful information is available on the internet. Wikipedia references on some techniques are quite good and can provide a useful introduction. Many vendor sites also provide general information about methods in addition to specific details of the equipment they manufacture. A range of excellent new and older books have been published that cover such topics as 'Fundamentals of Surface and Thin Film Analysis' [4], 'Analytical Techniques for Thin Films' [5] and materials characterization [6].

16.3 Incident Photon Methods

Techniques involving incident photons are described and some brief examples of application are shown. Methods included are: X-ray photoelectron spectroscopy (XPS), X-ray diffraction (XRD), X-ray reflectivity (XRR), optical methods such as laser Raman spectroscopy (RS) and Fourier transform infrared spectroscopy (FTIR), ellipsometry, and photoluminescence spectroscopy. One advantage of the fully optical methods including FTIR, ellipsometry, and Raman is that they can be conducted in any environment for which the optical path can be established, including liquid and solid environments. Consequently, measurements may be conducted during growth or in reactive environments. In contrast, vacuum-based methods, such as XPS, have more restrictive operation requirements.

16.3.1 X-Ray Photoelectron Spectroscopy

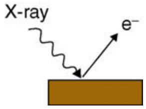

M.H. Engelhard

16.3.1.1 Introduction

XPS involves the detection of photoelectrons emitted from a sample as a result of irradiation of the sample by single-energy X-ray photons. XPS or electron spectroscopy for chemical analysis (ESCA) has become a relatively simple and increasingly routine technique for the compositional and chemical state analysis of surfaces. The basic principle of XPS is the photoelectric effect discovered by Hertz in 1887 [7, 8] and extended to surface analysis by K. Siegbahn and his research group at Uppsala University, Sweden, during the mid-1960s. Siegbahn won the Nobel Prize in Physics in 1981 for his work in XPS and coined the acronym ESCA [9]. Both XPS and ESCA are commonly used to describe this technique.

XPS is useful for quantitative analysis of surface composition and can detect all elements with the exception of hydrogen and helium through the detection of the binding energies of the photoelectrons. Small variations in binding energies of the photoelectron lines as well as Auger lines (see Section 16.5.1), satellite peaks, and multiple splitting can be used to identify chemical states. XPS is initiated by irradiating a sample with monoenergetic soft X-rays, most commonly Mg Kα (1253.6 eV with a line width $\approx$ 0.7 eV) or Al Kα (1486.6 eV with a line width $\approx$ 0.85 eV). In many modern instruments the Al Kα X-ray line is further narrowed (to $\approx$ 0.35 eV) using a monchrometer. Schematic representations of the photoemission and Auger processes are shown in Figures 16.3 and 16.4 [10].

16.3.1.2 Technique Overview

Although the incident X-ray photons penetrate many micrometers deep into the sample, XPS is surface sensitive owing to the short path length of photoelectrons. Photoelectrons with kinetic energies ranging from 300 to 1500 eV are most commonly used for XPS analysis. Because of the short range of these photoelectrons the sampling depth (related to the distance electrons can travel without inelastic scattering – the electron inelastic mean free path (IMFP)) is in the range of 0.5–3 nm [11, 12] (3–8 atom layers). The electron intensity decays for atoms

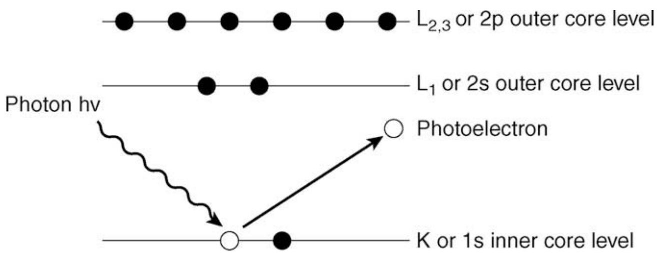

Figure 16.3: Schematic diagram of photoemission process used for XPS. X-rays excite and remove an electron from a core level. The kinetic energy of that electron is equal to the energy of the photon, minus the binding energy of the core electron and the work function of the spectrometer ($kE = hv - BE - \Phi s$) [10].

below the surface, making the practical limit ~8–10 nm for determining non-destructive composition as a function of depth analysis [13].

Electrons emitted from the sample without inelastic energy loss appear as spectral lines or photoelectron peaks as a function of binding energy. Electrons that have lost energy appear as spectral background. The energy of the photoelectrons emitted from the sample is characteristic of each element and the binding energy (BE) of the ejected electrons is determined from the measured kinetic energy (KE) by the following equation [7, 10, 14]:

$$BE = hv - KE - \Phi_s \tag{16.1}$$

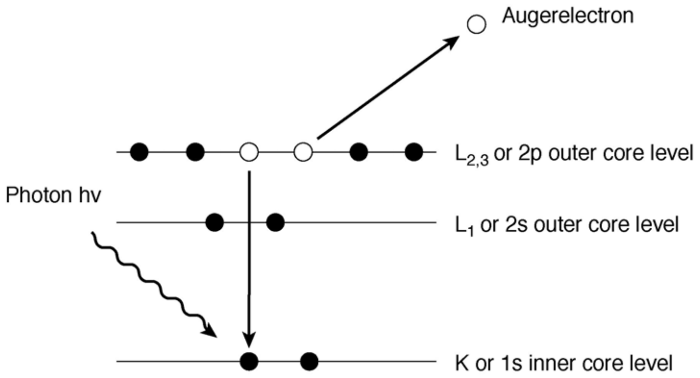

Figure 16.4: Schematic diagram of the Auger process. A core-level vacancy (such as created in Figure 16.3) is filled by an electron from a higher level shell and a third electron is emitted to conserve energy. The energy of the emitted Auger electron, $E_{KLL} \approx E_K - E_L - E_L$. Note that the energy of the Auger electron is independent of the energy of the photon creating the core-level vacancy [10].

where BE = binding energy of core level electron, $h\upsilon$ = characteristic energy of X-ray photon, KE = kinetic energy of ejected photoelectron, and Φ_s = spectrometer work function.

16.3.1.3 Data Collection

XPS data are collected in one of two different modes. Wide scans or survey spectra involve the collection of data over a wide energy range, typically 1000 eV, and are important to determine the true nature of the surface composition and can be used for quantification. An example of a survey scan of an iron oxide grown on a silicon wafer is shown in Figure 16.5. Note that in addition to the expected Fe and O photoelectron peaks the spectrum consists of some other peaks. Some of them correspond to Auger peaks for Fe and O, while others are due to contamination from C and F. Narrow scans collected at higher energy resolution and smaller energy windows are useful for examining the chemical state of specific elements. The Ce 3d photoelectron peaks from a ceria (CeO_2) film which contains mostly Ce^{4+} before and after a reduction process, which introduces a significant amount of Ce^{3+}, are shown in Figure 16.6.

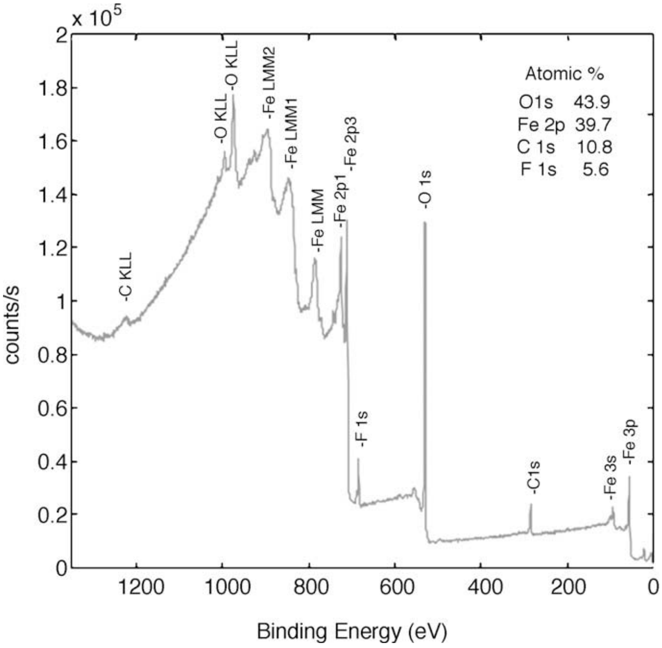

Figure 16.5: XPS survey scan of an iron oxide grown on a silicon wafer. In addition to Fe 2p and O 1s photoelectron peaks, O KLL and Fe LMM Auger peaks are observed. Also present are C and F peaks from surface contamination.

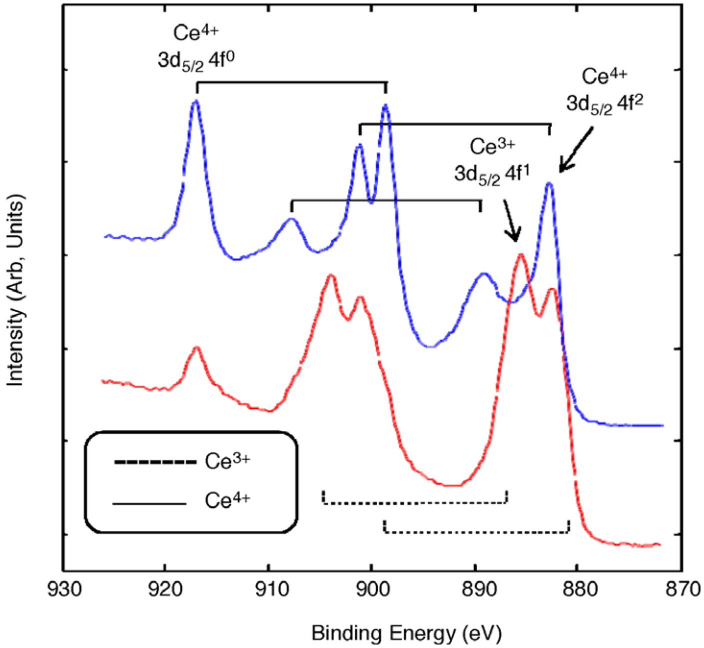

Figure 16.6: Narrow scans of Ce 3d photoelectron peaks from a ceria (CeO_2) film which contains mostly Ce^{4+} (top) and the film after a reduction process which introduces a significant amount of Ce^{3+} (bottom). High-resolution narrow scans for particular core levels provide useful information about the chemical state information.

Starting in the 1990s, some XPS instruments have been developed with increased ability to generate or collect photoelectrons from increasingly smaller regions of a specimen, taking XPS into the realm of X-ray microscopy. Some modern laboratory-based instruments can achieve spatial resolution approaching $\sim 1\ \mu m$ (higher resolution is possible using synchrotron-based X-ray sources). An example of the spatial mapping available from an instrument with $\approx 10\ \mu m$ spatial resolution is shown in Figure 16.7. This specific sample is a magnification standard for which the dots are indium oxide-doped tin oxide (ITO) and the surrounding coating consists of chromium oxide [15].

16.3.1.4 Depth Profiling

Depth profiling is now routinely possible with modern instruments equipped with ion guns and high spatial resolution spectrometers (see Section 16.4.5). Depth profiling using ions for etching (typically Ar and Xe) is routinely used to determine elemental or chemical profiles in a film. The use of C_{60} ions for sputtering of polymer films is becoming increasingly popular since the damage induced by C_{60} ions is less than that of inert gas ions.

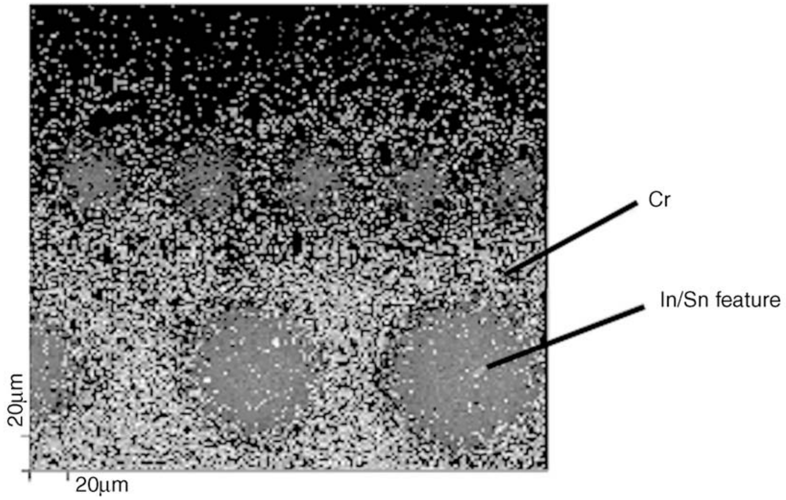

Figure 16.7: XPS surface elemental mapping of In/Sn circular features from a magnification standard (MRS-3 magnification reference standard [15], Geller Microanalytical Laboratory) using a Phi-Quantum Scanning XPS system (www.emsl.pnl.gov).

The use of any energetic ions for etching may be inappropriate for some sensitive materials since chemical degradation may occur. For these types of sensitive samples the use of angle resolved X-ray photoelectron spectroscopy (ARXPS) may be helpful in providing a non-destructive depth profile of the near surface layer. ARXPS is accomplished by tilting the sample to vary the angle between the axis of the photoelectron analyzer and the normal to the sample surface (the photoemission angle, θ). XPS data can be collected at a series of photoemission angles, θ, ranging from few degrees to 75°. These angle resolved data can be analyzed using a variety of available software tools that are commonly used to define the depth distribution of chemical species and surface layering [16, 17]. IMFP values used in layer thickness calculations can be obtained from the database of surface analysis by AES and XPS [18, 19] by the National Institute of Standards and Technology (NIST).

16.3.1.5 Quantification

The number of photoelectrons detected from an element is dependent upon the concentrations of that element in the sample. Electrons are detected, and data are digitized and analyzed by computer software programs to measure the peak height or peak area after removal of the spectral background [16, 20]. The use of a Shirley background subtraction [21] routine is one of the more common methods for background subtraction. For quantification and chemical state analysis, it is important to include or correct for X-ray satellites, chemically shifted spectral lines, shake-up peaks, and plasmon losses. Peak areas are used with empirically derived sensitivity factors or atomic sensitivity factors (ASFs) in calculating the relative concentrations [22, 23]. With the use of standards, an accuracy of 5% or better can be obtained with a reproducibility of better than 2%. A simplified form of the basic expression for quantitative XPS is given by the following equation [7, 10, 24]:

$$C_x = (I_x/S_x)/(\Sigma I_\mathrm{i}/S_\mathrm{i}) \tag{16.2}$$

where C_x = atomic concentration of element x, I_x = measured intensity of photoelectron peak, and S_x = sensitivity factor for element x.

16.3.1.6 Strengths and Limitations of Incident Photon Methods

Strengths:

- Measure surface elemental composition and chemical state information.
- Generally, little or no damage except for some organics and polymers [18, 25].
- Identification of all elements except for H and He.
- Applicable for a wide variety of materials, including insulating samples.
- Non-destructive depth information (up to 10 nm).
- Depth profiling with matrix-level concentrations.
- Thickness measurements.
- Spatial resolution (x–y) for laboratory-based system currently limited to ~ 1–10 μm.

Limitations:

- Require ultrahigh vacuum.
- Detection limits typically ~ 0.01–0.1 at.%.
- Smallest analytical area ~ 1–10 μm.
- Limited specific organic information.
- Preferential sputtering can be a challenge during quantitative analysis.

16.3.2 X-Ray Diffraction and Reflection

P. Nachimuthu

XRD is one of the most powerful non-destructive bulk techniques for analyzing a wide range of materials from research and development to production and engineering environments

[26, 27]. Because of the advancements in instrument engineering, technology, and computational aspects, XRD methods are being applied for a wide range of materials, enabling answers to many different types of diffraction challenges. Many of these methods apply to characterization of thin films. Applications include phase analysis, determination of crystalline structure and epitaxial orientation, measurement of thickness and interfacial roughness, determination of texture and residual stress in films, studies of nanomaterial development and measurements of their reactivity, and polymorph screening. Furthermore, XRD measurements can be made in non-ambient conditions allowing study of dynamic processes such as reactions involving the solid state, phase transitions, crystallite growth, and thermal expansion. Although the XRD can be applied in many frontiers of research and developments, the scope of this article is restricted to thin films.

XRD is especially valuable as a tool to understand the growth and characterization of epitaxial layers and other thin film materials. Using one of the state-of-the-art laboratory-based high-resolution X-ray diffraction (HRXRD) instruments available today, lattice parameters (both in-plane and out-of-plane) of an epitaxial layer can be determined with great precision. Another interesting use of HRXRD for thin films is the determination of the thermal expansion coefficient by plotting lattice parameters obtained (usually from non-ambient measurements) as a function of temperature. The orientation relationship between the epitaxial layer and the substrate can be analyzed by X-ray pole-figure measurements. Whether any polycrystalline materials are present in the epitaxial layer can be determined by glancing-incidence X-ray diffraction (GIXRD) measurements. The thickness of the thin film and the interface roughness between the thin film and the substrate can be determined by XRR measurements and modeling, not only for simple thin films but also for multilayered structures. All these parameters can be important for advanced materials used in high-tech devices in order to understand the device performance and failure. In the following sections, each technique is described and specific detailed examples are provided.

16.3.2.1 High-Resolution X-Ray Diffraction

HRXRD is useful for careful measurements of small changes in the lattice parameter which may result from strain, doping elements into the host lattice, or other effects. HRXRD can be obtained using a laboratory-based triple-axis (four-circle) diffractometer. It requires a sealed X-ray tube or rotating anode, a mirror with a four-bounce duMond–Hart–Bartels (dHB) design monochromator to isolate $K\alpha_1$ in the incident beam path, and a two- or three-bounce monochromator in front of the detector. Usually a Ge(220) crystal monochromator is used. A Ge(440) crystal monochromator can be used to further improve the resolution at the expense of intensity.

As one example of measured changes in lattice parameter, the HRXRD spectra collected from $6H$–SiC films at room temperature and after three different levels of H^+ irradiation ($610\,H^+/nm^2$ at 340 K, 880 and $1870\,H^+/nm^2$ at 210 K) for out-of-plane (00012) and in-plane

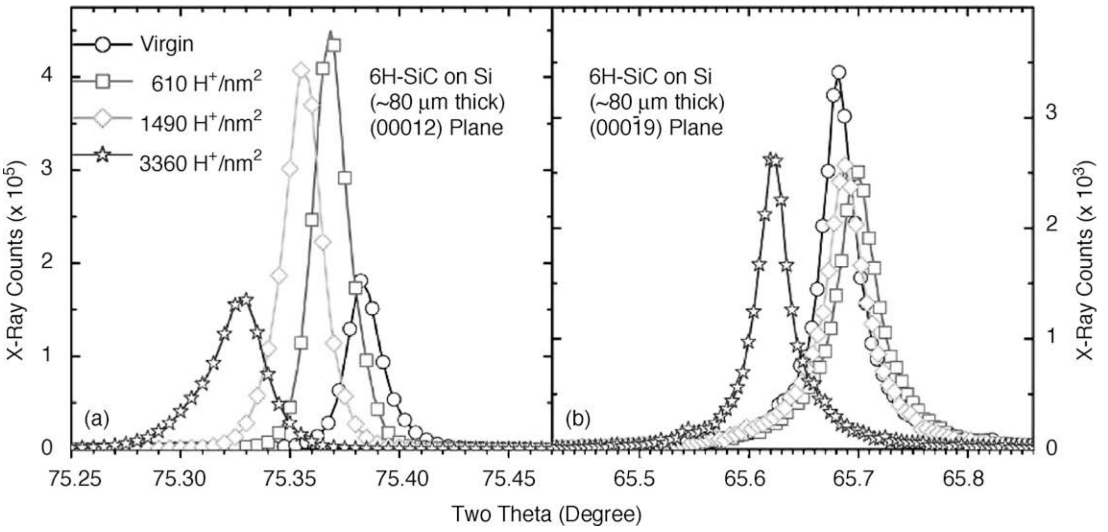

Figure 16.8: HRXRD 2θ–ω scans for (a) (0, 0, 0, 12) and (b) $(10\bar{1}9)$ planes in the 6*H*–SiC single crystal film before and after irradiation using 610 H^+/nm^2 at 340 K, followed by additional fluences of 880 and 1870 H^+/nm^2 at 210 K [28]. The different two theta angles for these peaks show differences in lattice parameter due to the hydrogen irradiation.

$(10\bar{1}9)$ reflections are reproduced in Figure 16.8[28]. A Philips X'Pert materials research diffractometer with a fixed Cu anode operating at 45 kV and 40 mA was used for the measurements. A hybrid monochromator, consisting of four-bounce Ge(220) crystals and a Cu X-ray mirror, was employed in the incident beam path to provide monochromatic X-rays from Cu $K\alpha_1$ ($\lambda = 0.154056$ nm and $\Delta\lambda/\lambda \sim 23$ ppm) with a beam divergence of 12 arc sec. An additional monochromator with a three-bounce Ge(220) channel-cut analyzer was placed in front of a proportional counter in the diffracted beam path with the same beam divergence. The diffractometer had the angular precision and reproducibility of 0.0001° and 0.0003°, respectively, for both polar (θ) and tilt angles (φ).

A manual procedure involving multiple scans of ω, 2θ–ω, and azimuthal angle φ was followed to achieve a similar condition for each of the HRXRD measurements. In order to determine the *c*-axis lattice parameter *c*, systematic scans of 2θ–ω were performed over $2\theta = 30$–$80°$ with a step of 0.005° per 4 s. Seven diffraction peaks from 6*H*–SiC (0006) to (0, 0, 0, 12) planes are detected without reflection contributions from the Si substrate (not shown). For better accuracy, only the (0, 0, 0, 12) peak at the highest angle was selected for lattice parameter calculation. Similarly, for determination of the *a*-axis lattice parameter *a*, 2θ–ω scans around the $(10\bar{1}9)$ plane were conducted from $2\theta = 63.7$–$67.7°$ at a step of 0.005° per 5 s. By taking one angular step (0.005°) as the peak position uncertainty, the experimental error for measuring parameters *c* and *a* in this study can be estimated to be $|\delta c| = 0.00017$ nm ($|\delta c/c| = 0.01\%$) and $|\delta a| = 0.00006$ nm ($|\delta a/a| = 0.02\%$), respectively.

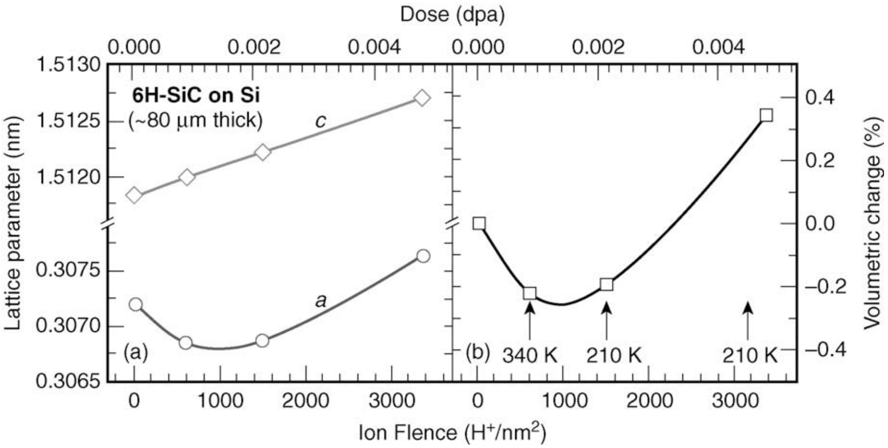

Figure 16.9: (a) Lattice parameters and (b) volumetric changes of the 6*H*–SiC single crystal film before and after irradiation to 610 H^+/nm^2 at 340 K, followed by additional fluences of 880 and 1870 H^+/nm^2 at 210 K. This information was extracted from the data collected in Figure 16.8. The dose in displacements/atom is estimated at a depth of 40 μm [28].

For out-of-plane and in-plane reflections, the diffraction peak positions shift as ion fluence increases. Although the magnitude of the shifts is small, it is well above the experimental error. The lattice parameters obtained from Figure 16.8 and corresponding volumetric changes of the 6*H*–SiC single crystal film prior to and following irradiation to 610 H^+/nm^2 at 340 K, followed by additional fluences of 880 and 1870 H^+/nm^2 at 210 K, are shown in Figure 16.9. The *c*-axis lattice parameter increases monotonically with the increasing dose, while *a*-axis lattice parameter decreases at extremely low doses. An initial volumetric contraction of the unit cell is observed. The decrease in the *a* parameter may originate from the irradiation-induced vacancies and the possible formation of antisite defects that cause the lattice structure on the basal plane to shrink [29].

16.3.2.2 Texture and Pole Figures

The texture of a material or film is the distribution of crystallographic orientations of grains in a sample. There are several different possible situations for a film grown on a single crystal substrate: (1) If the thin film is 'epitaxial', the single extended crystal has near-perfect registry with same orientation as the under layer which is also nearly perfect; (2) If the thin film is 'textured epitaxial', the layer orientation is close to registry with the underlayer, both normal and parallel to the surface plane, and the layer is composed of mosaic blocks; (3) When the film is 'textured polycrystalline', the crystallites are preferentially oriented normal to the surface and randomly oriented in plane and there will be a distribution of crystallite sizes. Texture is seen in almost all engineered materials, and it can have a great influence on material properties. Texture is often represented using a 'pole figure', in which a specified crystallographic axis (or pole) from each of a representative number of crystallites is plotted in

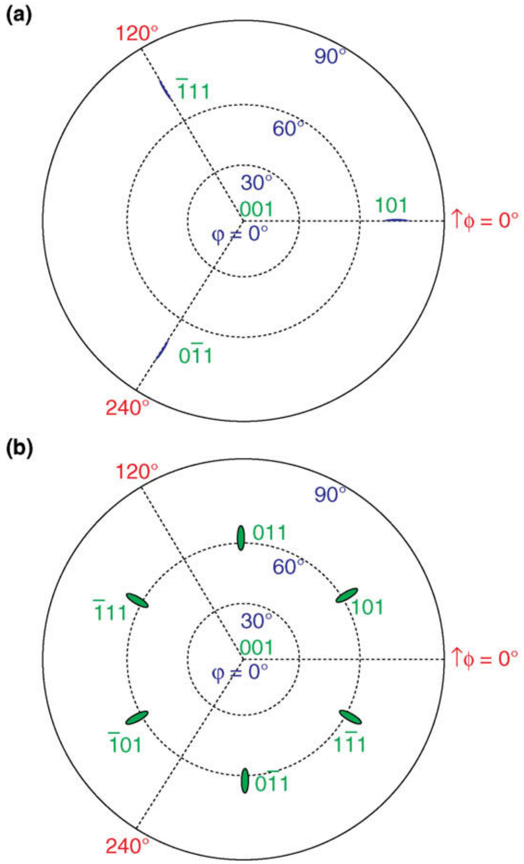

Figure 16.10: Pole figures from a ZnO film grown on an alumina substrate. The figures are for (a) the Al_2O_3 (202) X-ray reflections, and (b) ZnO (101) X-ray reflections. The ZnO film was grown in 10 mtorr H_2 on α-Al_2O_3 (001) at 500 °C. The pole elongation along the radial direction is an instrumental effect from the line-focused X-ray optics [30]. The single crystal nature and orientation of the substrate are demonstrated in (a) and the epitaxial orientation and domain structure of the ZnO films grown at 500 °C in (b).

a stereographic projection, along with directions relevant to the material's processing history. The pole-figure measurements provide information regarding preferred orientation, the epitaxial relationship between the thin film and the substrate, and single or multiple in-plane domains present in a thin film.

The pole figures for a ZnO film grown by pulsed laser deposition (PLD) on α-Al_2O_3(001) substrate in 10 mtorr of H_2 at 500 °C are shown in Figure 16.10(a, b) for Al_2O_3(202) reflections from the Al_2O_3 substrate and ZnO(101) reflections from the thin film, respectively [30]. The elongation of the poles along the radial direction is an instrumental effect from the line-focused

X-ray optics. The goniometer was set to ZnO(101) reflection for ZnO(001) oriented film on Al_2O_3(001) substrate and all the reflections that are parallel to the [101] direction were observed. Similarly, the goniometer was set to Al_2O_3(202) reflection for Al_2O_3 substrate and all the reflections parallel to the [202] direction were detected. By comparing the experimental data with the theoretical stereographic projections, the epitaxial relationship between the thin film and the substrate, and the number of in-plane domains in the thin film were determined. In the present example, ZnO films grown on α-Al_2O_3(001) at 500 °C show pole figures which are characteristic of epitaxial ZnO(001) with a single domain rotated 30° in-plane about [001].

16.3.2.3 Glancing-Incidence X-Ray Diffraction

The GIXRD technique has been developed for the analysis of polycrystalline thin films on single crystal substrates. In GIXRD, the X-ray beam is incident at a small angle ($\sim 5°$), and the detector is scanned over a 2θ range of interest and is an asymmetric scan. The X-ray incidence angle and the slit size can be determined for a given instrument configuration based on the sample dimension for complete X-ray coverage of the sample surface to improve the sensitivity. In GIXRD, diffraction will be detected only from polycrystalline materials, unlike epitaxial thin films and single crystal substrates, as the Bragg condition will not be satisfied under this configuration. This technique is used to verify the presence or absence of any polycrystalline material in epitaxial thin films on single crystal substrates. As a representative example, GIXRD pattern from $\sim$ 50 nm thick ZnO film grown on Al_2O_3(001) following annealing at 1000 °C for 3 hours is shown in Figure 16.11 [31]. The ZnO thin film is (001) oriented preferentially as confirmed by HRXRD, and the substrate is Al_2O_3(001) oriented single crystal. It can be seen from Figure 16.11 that the cubic $ZnAl_2O_4$ phase has been identified. The lattice parameter from GIXRD pattern is found to be 0.8106 nm. This value is comparable to the literature value of 0.80848 nm (PDF# 005-0669) [32]. High-temperature annealing results in diffusion of Al from the Al_2O_3 substrate to ZnO thin film. Though the thickness of the ZnO film is $\sim$ 50 nm, it becomes possible to identify the polycrystalline $ZnAl_2O_4$ phase because of the GIXRD principle.

16.3.2.4 X-Ray Reflectivity

In many advanced technologies, thin layered films become increasingly important. Single-layer or multilayer structures can be found in all kinds of research and development environments. Thus there is an increasing need to precisely characterize these thin layer structures. Measurements of layer thickness, interface roughness, and layer density are important to analyze and control development and production processes. XRR is a powerful non-destructive technique to characterize thin layers. Far below the critical angle of total external reflection, X-rays penetrate only a few nanometers (2–5 nm) onto thin film. Above the critical angle, the probing depth increases rapidly. XRR measurements allow the density, thickness, and roughness of external and internal interfaces of thin films to be determined. A minimum layer thickness of 1 nm and density changes of $\sim$ 1–2% can be measured under

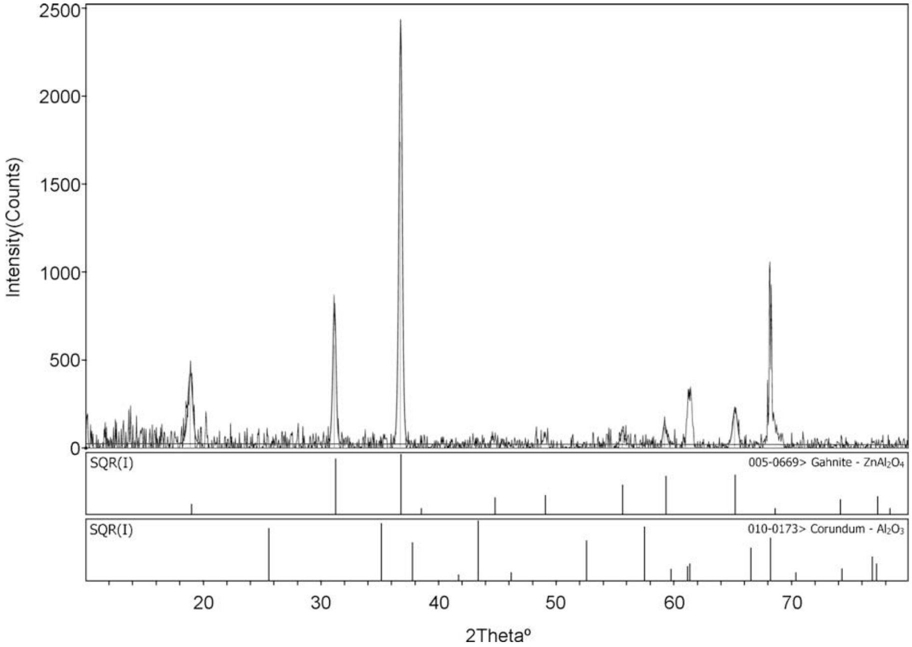

Figure 16.11: Glancing-incidence X-ray diffraction (GIXRD) pattern from ZnO film grown on α-Al_2O_3 (001) following annealing at 1000 °C for 3 hours [31]. These data confirm the highly oriented nature of the films and the presence of a $ZnAl_2O_4$ phase. The peaks around 61° and 69° represent the diffraction from the substrate.

optimum sample conditions. This method is sufficiently sensitive to provide precise information on the presence of interface layers in layered structures.

As a representative example, XRR specular curves for Fe/Al and Al/Fe films grown on Si are shown in Figure 16.12 together with theoretical simulation (solid lines) [33, 34]. The engineered thin film structures are not perfectly smooth and possess surface and/or interface roughness. While the presence of surface roughness decreases the specular intensity of the whole curve progressively, interface roughness gives rise to progressive damping of the Kiessig fringes. The interface roughness, σ, consists of topological roughness, σ_T, and chemical roughness, σ_C, via the relation $\sigma = \sqrt{\sigma_C + \sigma_T}$. Therefore, XRR diffuse scans are essential to separate the topological and chemical roughness for an interface. The film thickness measured from RBS and XRR, and the interface roughness from both specular and diffuse scans, are shown in Table 16.3 for the bilayer films of Fe/Al and Al/Fe.

Topological roughness affects the reflectivity by scattering X-rays into non-specular directions, whereas chemical roughness leads to more gradual changes in electron density at the interfaces, and thus reduces the reflectivity of X-rays at the interface. The sixth column in Table 16.3 shows the chemical roughness, σ_C, of each layer determined by fitting XRR diffuse

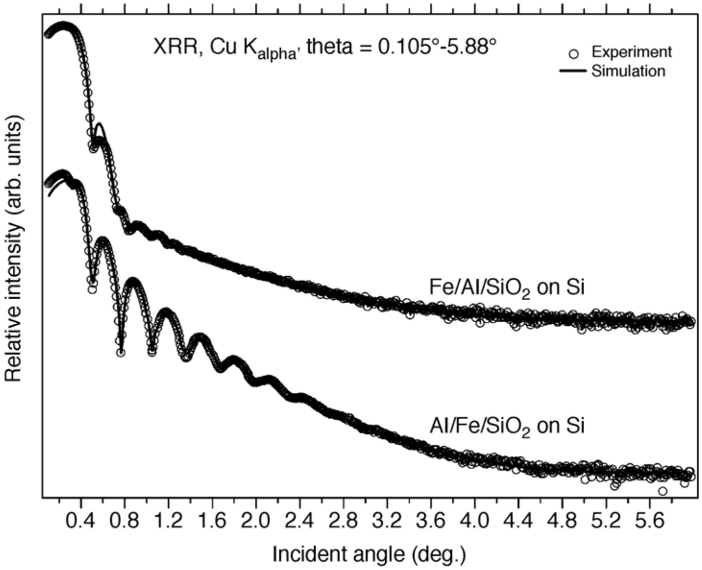

Figure 16.12: XRR specular scans (open circles) and BEDE simulations (solid lines) for bilayer films of Fe/Al (upper curve) and Al/Fe (lower curve) [33].

Table 16.3: Layer structure, thickness, and total roughness (chemical and topological) of individual layers determined by fitting RBS and XRR spectra for (a) Fe/Al/SiO_2 on Si and (b) Al/Fe/SiO_2 on Si

Layer No.	Layer	RBS, t (Å)	XRR, t (Å)	XRR, σ (Å)	XRR, σ_c (Å)
(a) Fe/Al/SiO_2 on Si					
1	Fe_2O_3	46	48.1	24.9	21.9
2	Fe	105	124.0	21.0	18.5
3	AlFe	25	41.1	19.4	17.8
4	Al	146	99.1	18.7	17.6
5	Al_4Si	–	5.3	3.1	2.9
6	SiO_2	2454	2487.3	2.4	2.1
(b) Al/Fe/SiO_2 on Si					
1	Al_2O_3	11.4	11.7	7.0	5.4
2	Al	140	140.9	2.8	2.6
3	AlFe	16	20.6	7.3	6.4
4	Fe	129	136.5	10.8	9.9
5	SiO_2	2362	2366.9	20.9	20.5

scans. Total thicknesses of the individual layers, as listed in the fourth column of Table 16.3, are determined by adding the contributions of the individual layer thickness and half of the chemical roughness on each side of the respected layer. The intermixing lengths for Fe–Al bilayers are 20.6 Å and 41.1 Å for Al/Fe and Fe/Al bilayer films, respectively. There is a considerable difference between Fe–Al intermixing lengths depending on whether Al is deposited on Fe or Fe is deposited on Al.

16.3.2.5 Strengths and Limitations of XRD and XRR

Strengths:

- Non-destructive bulk technique for thin films, solids and liquid media.
- Phase analysis, crystalline structure, epitaxial orientation, texture and residual stress analysis are possible.
- Reactions and polymorph screening.
- Crystallite growth and thermal expansion coefficient can be obtained.
- Film thickness and interface roughness can be measured.

Limitations:

- Provides bulk information and requires minimum of 1–5 wt% for phase identification.
- Thickness cannot be measured for thin film with roughness over 50 nm.
- XRR does not work if there is no difference in electron density between the layers or layer and substrate.

16.3.3 Raman and Infrared Spectroscopies

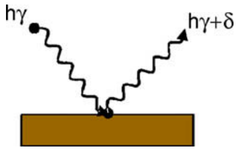

S. V. N. T. Kuchibhatla

Raman and infrared (IR) spectroscopies are optical methods used to study vibrational, rotational, and other low-frequency modes and vibrational energies of molecules. They enable information to be gathered about molecular bonds and their vibration modes. These two optical methods are powerful tools that can be used to provide information about the molecular structure and composition of surfaces, thin films, and coatings. The most important aspect of practical interest is the complementary nature of Raman and IR spectra. For example, while Raman is used for understanding spatial profiles of curing process in the paint industry, IR spectroscopy is used for understanding the kinetics of the curing process. Further, some weak or undetectable features in one technique exhibit strong characteristic features in the other.

16.3.3.1 Raman Spectroscopy (RS)

The Raman effect is a specific form of inelastic scattering of light that serves as the basis of RS and has its origin in the curiosity of Sir C.V. Raman about the ‘color of the sea’ [35]. RS, the analysis technique that uses Raman effect, was initially confined to the fundamental studies of the physicists owing to the feeble nature of the signal from various samples and the tedious data collection involved. However, with the availability of lasers as light sources, advanced optical components, and computers for data acquisition and analysis, RS has evolved into a powerful and routine analysis technique for multiple disciplines [36]. The uniqueness of the Raman effect lies in its very high sensitivity to the bonds and their variations. Because of its ability to provide molecular information in many different environments, it is widely used in research and industry. As one industrial example, the paint industry uses this technique to monitor the transformations in industrial coating in situ as part of their day-to-day operations.

This section is divided into two parts: the basic principle and several applications. The development of new instrumentation has widened the use of RS from liquid samples to crystalline/amorphous solids, thin films, coatings, especially in the corrosion (prevention) industry, along with significant use in fundamental research. Various useful applications of the instruments will be briefly discussed, along with some of the variations in sample geometry.

Basic principle

RS relies on inelastic scattering of monochromatic light, usually from a laser in the visible, near-IR, or near-ultraviolet (UV) range. The light interacts with phonons or other excitations in the system, resulting in the energy of some of the incident photons being shifted up or down. A Raman spectrum is a plot of the intensity of light as a function of frequency above and below the frequency of the incident light. Light is observed as frequencies including that of the incident photon (Rayleigh scattering) as well as frequencies reflecting the energy changes owing to the inelastic (Raman) scattering. The latter depend on the molecular/electronic structure of the molecules and the quantum mechanical selection rules for Raman scattering. The separation of Raman lines and the Rayleigh line in the spectrum is a direct indication of the vibrational frequencies of molecules or atoms in the crystal lattice. While the scattering from the Raman process is known as ‘Stokes scattering’, the reverse process which arises from previously existing excited vibrational states in the sample is known as ‘anti-Stokes scattering’. Accordingly, while the Raman lines appear at lower absolute frequencies than the Rayleigh line, the anti-Stokes lines appear at higher absolute frequencies in a spectrum. As the anti-Stokes scattering is highly dependent on the population of the excited vibrational states, it is only used in specialized cases of Raman analysis, as explained later in this section.

The intensity of Raman lines is 10^{-3} to 10^{-6} of the intensity of the Rayleigh lines, which usually have their intensities in the range of 10^{-3} to 10^{-5} of the intensity of the incident photon. This feeble nature of the intensity of Raman lines was a major issue for researchers until the mercury discharge lamps were replaced with continuous gas lasers. This intense monochromatic source, coupled with the double monochromator system, invented in 1965, to discriminate the stray light resulted in the modern RS systems. The amount of material analyzed is dependent on the optical density of the sample being measured. A schematic of RS and the scattering lines are presented in Figure 16.13(a). When the light used for excitation is focused on a small area, it is possible to conduct RS in a microscope mode with resolution at the micrometer level.

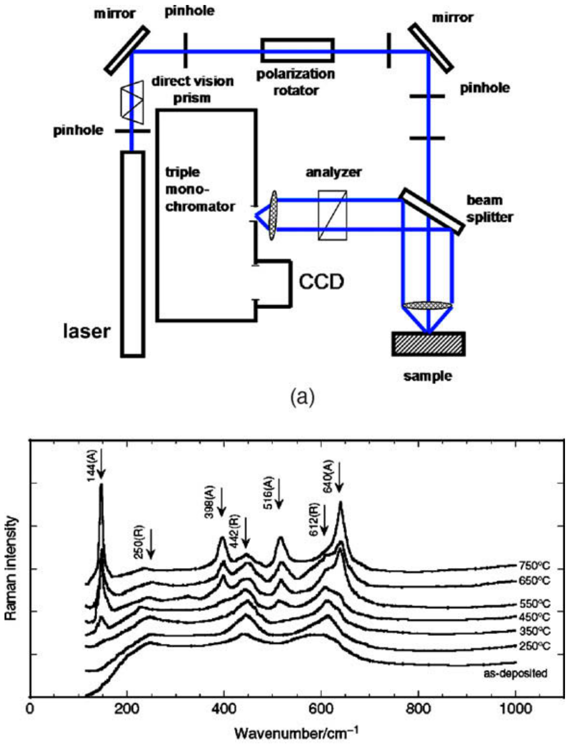

(a)

(b)

Figure 16.13: (a) Line diagram of a Raman microscope showing a light source, optical components to direct the light, the sample, a monochromator to separate parts of the optical spectrum, and a detector (CCD). (b) Effect of temperature on the phase transformation in titania (TiO_2) films deposited by RF magnetron sputtering. (Figure 16.13(b) is taken from [40].)

Exhaustive and quantitative description of the physics behind the Raman effect and the analysis techniques is outside the scope of this handbook, hence the interested reader is advised to follow the references and various information sites that result from a web search.

Applications

RS is primarily a non-destructive, structural characterization tool. The vibrational frequencies are sensitive to bond characteristics such as length, strength, and their arrangement. Mass, equilibrium spatial arrangement, relative displacement during vibration, and bond force constants of atoms in a molecule or crystal can influence the frequency of the Raman peak [37]. Therefore, RS can be wisely used for understanding defect structure and disorder in crystals coupled with the chemical information obtained from other techniques such as FTIR. Although the technique was initially developed for understanding the scattering of light in various liquids, currently minerals, powders, thin films, organic/inorganic coatings, and single and polycrystalline materials are all subjects of investigation. RS is used for fingerprinting, understanding vibrational motions of crystals with the help of selection rules, phase transformations, defect structure and disorder analysis, structure of amorphous gels and glasses. Raman microscopy is effectively used for studying the inclusions in grain boundaries, fracture analysis, precipitate and interfacial analysis. In the backscattering geometry and cross-sectional sample-view, coatings and multilayers can be analyzed by avoiding any scattering from the substrate [6]

Phase transformations in crystalline, inorganic thin films and coatings

Vacuum and ambient annealing treatments are carried out to understand the thermal stability of coating materials such as TiN, CrN, and TiAlN, and their multilayers [38, 39]. The variations in the spectral positions and the intensity of the optical phonon mode have been used to understand the phase transformations and the defect structure in the coatings. Barshilia and Rajam [38] used Raman analysis to precisely determine the oxidation onset in various materials and reported that the TiAlN/CrN multilayered coatings are stable until 900 °C. It was reported that the micro-Raman analysis could be used to detect the presence of minor phases such as anatase-TiO_2 which are difficult to trace by XRD. Micoprobe Raman analysis has been used to detect the presence and spatial distribution of the anatase and rutile TiO_2 phases and the stoichiometric changes in the TiO_2 was determined by studying the Raman active peak shifts due to oxygen deficiencies. Hong et al. [40] used RS to study the effect of annealing temperature on TiO_2 phase evolution. As shown in Figure 16.13(b), they observed a gradual transformation of as-deposited amorphous film to crystalline TiO_2 film with increasing anatase to rutile ratio with increasing temperature. Inorganic coatings (hydroxyapatite (HA), tricalcium phosphate (TCP)) on biomedical implants (Ti-based) have also been analyzed with the help of micro- and macro-Raman analyses. The key advantage of Raman analysis is its ability to distinguish HA and TCP more easily than XRD and FTIR [41].

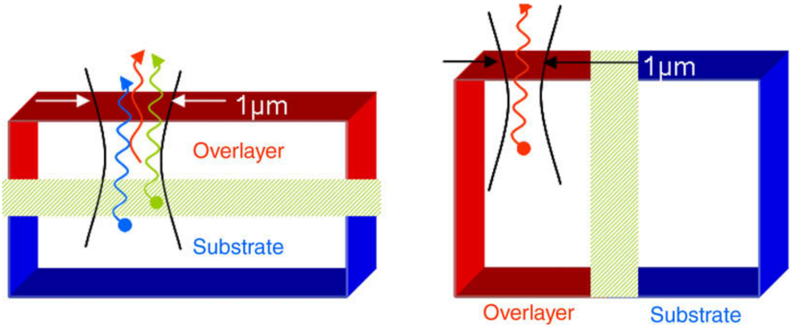

Figure 16.14: Depiction of the sample orientations in plane (left) and cross-section (right) geometries indicating the advantages of cross-section geometry in avoiding substrate signal. In the figure, while the region indicated by black arcs shows the interaction area different arrows indicate the depth from which the signal is obtained.

Depth profile and cross-sectional analysis using μ-Raman spectroscopy

Raman microscopy or μ-RS is not just confined to the surface but can be effectively used for studying the depth distribution. By changing the energy of the incident light the penetration depth can be varied and the desired depth resolution can be obtained. However, this technique suffers from an inherent difficulty if the penetration depth of the material (coating or film) is much higher than the thickness because the substrate peaks also contribute to the spectra, thereby spoiling the resolution. This problem becomes more severe when the analysis is desired on multilayered and transparent films. However, if the desired layers are the size of the optical beam or larger, samples can be analyzed in the cross-sectional geometry (Figure 16.14). As opposed to the plan-view geometry where all the participating layers contribute to the phonon characteristics, the cross-sectional geometry with linear scans at multiple positions can provide a detailed picture of the multilayered heterostructures. BN, SiC, carbon, diamond and diamond-like carbon (DLC) films on Si substrates were analyzed by Werninghaus with cross-sectional geometry [42].

Organic/polymer coatings and corrosion science

One of the most important applications of RS in coatings technology is the compositional mapping of coatings. Sequential acquisition of Raman spectra by incrementally rastering the laser beam across the sample can yield a compositional map. Based on the number of Raman bands to be tracked, the complexity and acquisition times will increase. Line scans are also possible with the help of a charge-coupled device (CCD) camera and a spectrograph. Use of a water-immersion objective for studying ligand distribution on chromatographic adsorbent particles was reported by Larsson et al. [43]. The ability of this technique to distinguish the core and coatings was used to identify the uniform distribution of allyl groups and surface layers of sulfopropyl groups. The surface morphology of rubber domains within the coated substrate contributes strongly to the material characteristics such as adhesion and impact resistance. While conventional imaging analyses were unsuccessful in studying the interfacial characteristics, the use of Raman imaging coupled with contrast enhancement functions resulted in a better understanding of near-surface composition of thermoplastic olefin (TPO) coated with chlorinated polyolefin [44]. Owing to the excellent spatial resolution available ($\sim 1\ \mu$m) from Raman imaging, it can be used for studying the crystallinity gradients of the polymer coatings on metal substrates and to evaluate the mechanical performance. The use of polarized confocal Raman microscopy to track the polymer molecular orientation has also been reported. The combination of confocal laser scanning microscopy and ATR-FTIR with confocal Raman microscopy was used to track the UV curing of polymer coatings [41].

Corrosion is a widely studied problem and Raman microscopy can uniquely contribute to this field by in situ monitoring of the degradation. The laser can be focused onto the metal surface through the surface coating and the spectra can be collected as a function of time. Multiple forms of iron oxides and hydroxides have been identified with the help of Raman analysis of coated steel coupons immersed in a corrosive environment. Redox states of the protective coating and the solution/coating interfacial product analysis are key advantages of RS in the field of corrosion science. Surface-enhanced Raman scattering (SERS) has been found to be very useful in analyzing the anticorrosion coatings on Cu surface [41]. In principle, the SERS technique uses a large increase in the electric field strength near a rough (noble) metal surface coupled with a chemical enhancement due to a charge-transfer between the coating (adsorbate) and the metal. This method requires careful attention to a number of parameters such as surface roughness, reactivity of metal and adsorbate under the laser beam, and further complications are also possible owing to complex spectra with numerous other features due to selective band enhancement and molecular orientation effects on the surface.

Recently, scientists from NIST [45] have reported the use of coherent anti-Stokes Raman scattering (CARS) as a possible alternative for SERS. The coherent nature of CARS helps improve the collection efficiency and sensitivity. This technique also eliminates the need for coinage metals (Ag, Au, and Cu), improves the signal-to-noise ratio, and provides the ability analyze the influence of interaction into the bulk of the substrate as well. This technique, when completely developed, is expected to be used for the characterization of advanced electronic applications such as organic light-emitting diodes and thin film transistors.

As evident from the various examples above, Raman microscopy is a very important tool for the characterization and property evaluation of thin films and coatings in a wide range of applications.

Strengths:

- High sensitivity to the chemical bonds and their variations.

- Offers suitable spatial resolution for compositional mapping of coatings and multilayer heterostructures (regions as small as ~ 1 μm in diameter).
- Provides the ability to study phase (material) transformations in situ for liquid, solid (organic and inorganic), thin films and coatings.
- Flexible sample handling.
- Signals can be enhanced using various methods, e.g. resonance Raman enhancement or SERS.

Limitations:

- Very low-intensity signal – partly solved by using high-intensity lasers and specialized equipment – however, some instruments and techniques impose various other restrictions.
- A common source of interference is fluorescence or other photoluminescence from the sample.
- Raman intensities and bandwidths are also dependent on crystallinity. Features from amorphous materials can be weak and broad.
- Absolute quantification may not be possible.
- Difficult to understand and track trace chemical impurities.

16.3.3.2 Infrared Spectroscopy

S. V.N.T. Kuchibhatla

IR spectroscopy is the subset of optical spectroscopy that uses the IR portion of the spectrum, the central part of which ranges from less than 2 μm to more than 30 μm in wavelength. For most of this frequency range the photon energies (0.6–0.04 eV) are not usually large enough to excite electronic levels, but may excite vibrational or rotational states of covalently bonded atoms or groups. Because molecules rotate or vibrate at specific frequencies it is possible to identify molecular groups and many of the types of molecular bonds present, provided they satisfy the dipole selection rule.

The Fourier transform (FT) of IR spectroscopy (making it FT-IR or FTIR) involves the use of a beam splitter, movable mirrors, a multiwavelength IR source and a Michelson interferometer, as shown in Figure 16.15. Because IR light is usually of low intensity, the use of FT spectroscopy [46] allows the collection of better data in a shorter time. The data collected are actually an interferogram that is the FT of the absorption (or reflection spectra).

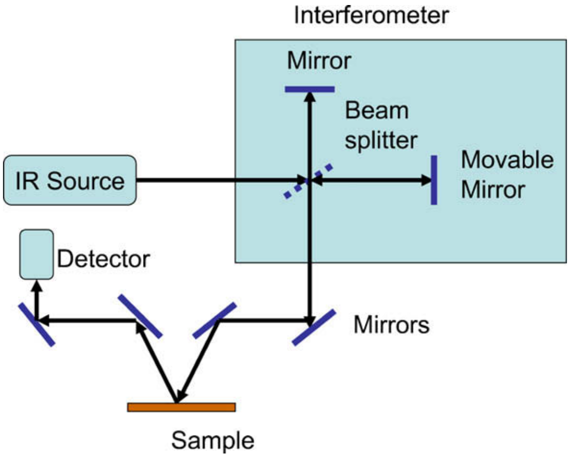

Figure 16.15: Schematic drawing of FTIR spectrometer set up for analysis of signal reflected from a sample.

FTIR can be used to identify the molecular structure of organic contaminants, to identify the presence of organic layers or particles, and with careful use the thickness can be determined [47]. Because FTIR can be done in air or other environments, it is possible to monitor sorption or decomposition processes as they occur. Spectra can be obtained in either transmission or reflectance modes. Signals from thin films can be compared and differences quantified. FTIR can be used to identify or verify film thickness and composition; it is also useful for examining surface residues and identifying contaminants.

Applications

FTIR has been useful for determining the thickness of epitaxially grown films of Si [48, 49] and other advanced thin film materials for which chemical bonding information, film thickness (including ultrathin oxides and photoresists), and dielectric function are important [50]. Also, FTIR is used to characterize polymer coating materials, for the identification of microscopic defects during weathering and curing processes. As mentioned before, FTIR is often used as a complementary technique along with RS. While Raman spectra are used to track C=C consumption and O–O production, FTIR is used to detect O–O–H production during the thermal/UV cure of polymer coatings. Agbenyega et al. [51] have listed the comparative strengths and weakness of signals from various bonds from Raman and FTIR spectra. FTIR in attenuated total reflection (ATR) geometry, known as ATR-FTIR, can offer a depth resolution up to 2 μm, making it a more surface-sensitive technique. Hence, ATR-FTIR is widely used to study surface degradation during weathering of polymer coatings. Ellis et al. [52] reported the use of ATR-FTIR and FT-RS for studying changes in polyurethane-acrylic paints (containing pigments with titanium and iron oxides) on phosphated-steel panels. It was shown that the

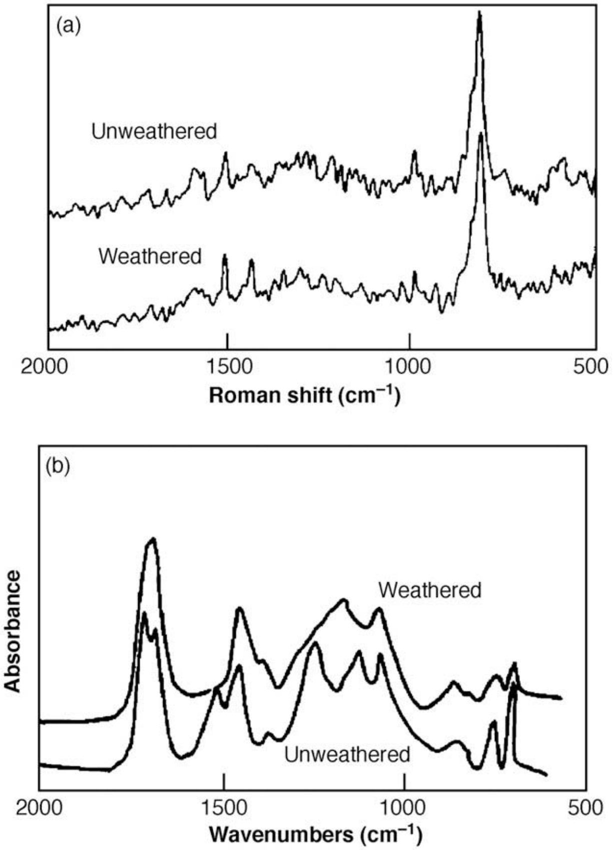

Figure 16.16: Red pigmented panels, fresh and weathered samples. (a) FT-Raman and (b) ATR-FTIR spectra [52].

ATR-FTIR is better suited for understanding transitions in the urethane bands. Also, in the case of panels with very high absorption such as red colored panels with pigments containing iron oxide, the FT-Raman signal is very weak. However, major changes have been observed in the urethane band (1525 nm^{-1}) region of ATR-FTIR spectra. FT-Raman and ATR-FTIR spectra corresponding to weathered and unweathered conditions are shown in Figure 16.16(a, b) [52].

Strengths:

- Identification of organic groups and compounds.
- Can operate in ambient or other environmental conditions.
- Can identify some inorganic compounds.
- Usually non-destructive.

Limitations:

- Limited sensitivity.
- Limited inorganic information.
- Quantitative with standards or in special cases.
- Minimum analysis area ~ 10 μm.

16.3.4 Ellipsometry

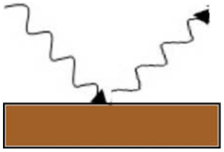

M.H. Engelhard

Ellipsometry is a century-old optical method which, with modern approaches of computer control and data processing, is becoming increasingly important for the analysis of many types of thin films [53, 54]. The technique is based on the analysis of polarized light reflected from the sample which probes the complex refractive index (or dielectric function tensor) which can be used to extract information about film thickness, roughness, crystal quality, chemical composition, or electrical conductivity. The material is probed to the optical depth of the sample. It is sensitive enough to measure properties of films as thin as a few tenths of nanometers, but, if the optical properties allow, it can be used to study layers as thick as several micrometers.

When light is incident on the surface, some of the light is reflected from the surface and some light enters the material, as shown in Figure 16.17. The portion of light entering the material does not continue at the sample angle, but is refracted according to Snell's law. As shown in Figure 16.17, the electromagnetic field of the incident light can be broken into two components, one in the plane of incidence to the sample (p) and the other perpendicular (s). Based on the properties of the material, the attenuation and phase shift of these electromagnetic components differ. Ellipsometry typically reports the differences in reflectivity using two parameters to record the differences in the amplitude and phase of the reflected waves using the equation:

$$\rho = R_P/R_s = \tan\psi \exp(i\Delta) \tag{16.3}$$

In this equation delta (Δ) indicates the difference between the phase angle of the parallel and perpendicular components of the incoming wave and outgoing wave, and psi (ψ) is the angle

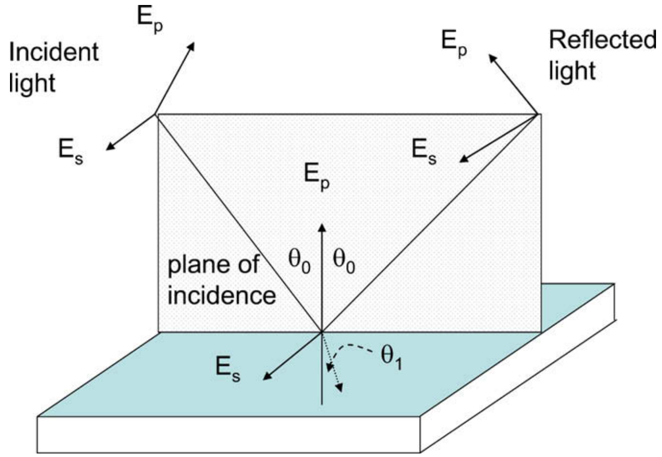

Figure 16.17: Schematic drawing of incident and reflected components of a monochromatic beam of light interacting with a surface. The electric vectors of the plane polarized light are labeled as p waves (in the place of incidence) and s waves (perpendicular to the plane of incidence). Note that a portion of the light enters the material.

whose tangent is the ratio of the magnitudes of the total reflection coefficients. These values are related to the ratio of the Fresnel amplitude reflection coefficients for the p- and s-polarized light.

Single wavelength measurements at one angle can be used to determine film and sample properties. However, additional information can be available if measurements are taken as a function of wavelength (or angle) which allows the complex refractive index of the sample to be obtained from which a number of fundamental physical properties can be extracted [55].

Information about the sample requires the use of models to fit the ellipsometric data. Typically this involves: (1) creating a model that represents the sample, including the number of layers present; (2) associating a dispersion relation of the optical properties of each layer; and (3) fitting the experimental data to the model. Many of the recent advances in ellipsometry involve the use of computers and relate experimental data to appropriate models [56].

Ellipsometry measurements are widely used to determine the thickness of surface coatings and thin films. As already noted, the absolute thickness depends on the model and parameters used in the model. As an example, the thickness of two NIST standard thin SiO_2 films on Si (#2531) was measured by ellipsometry and XRR and the results compared. The NIST reference values for Δ and ψ are $90.03 \pm 0.04°$ and $22.18 \pm 0.04°$ for one sample (sample L) and $89.79 \pm 0.04°$ and $22.32 \pm 0.04°$ for the other (sample R). These were obtained at a wavelength of 632.8 nm and at an angle of incidence ϕ of $71.330 \pm 0.004°$. Using a single-layer model this translates into an oxide layer thickness of 47.7 ± 0.5 nm for sample L and 48.0 ± 0.5 nm for sample R. We used a different type of ellipsometer that collected a range of wavelengths and obtained the thickness as 47.89 ± 0.5 nm for sample L and 48.15 ± 0.77 nm for sample R. These results are well within the stated uncertainty for these measurements. For comparison we also conducted XRR on these samples and obtained thickness values of 47.6 nm for sample L and 48.0 nm for sample R. These measurements clearly demonstrate that the thickness values measured by ellipsometry and XRR are within the expected uncertainty of the measurements.

In another example, ellipsometry was used to measure the variation of oxide thickness over the surface of an oxidized Si wafer. This wafer was planned to be used as a reference for determining ion sputter rates and ion sputter rate consistency. Although many wafers show excellent uniformity, the example shown in Figure 16.18 shows significant variation in oxide thickness with the difference between the minimum and maximum values of approximately 20 nm for an oxide of nominal thickness of 40 nm.

Strengths:

- Highly sensitive, rapid and reproducible, comparison measurement.

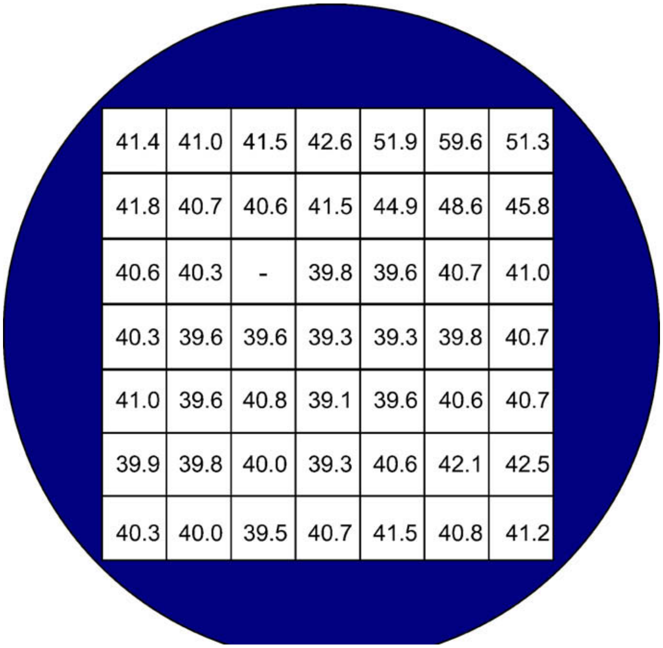

41.4	41.0	41.5	42.6	51.9	59.6	51.3
41.8	40.7	40.6	41.5	44.9	48.6	45.8
40.6	40.3	-	39.8	39.6	40.7	41.0
40.3	39.6	39.6	39.3	39.3	39.8	40.7
41.0	39.6	40.8	39.1	39.6	40.6	40.7
39.9	39.8	40.0	39.3	40.6	42.1	42.5
40.3	40.0	39.5	40.7	41.5	40.8	41.2

Figure 16.18: Drawing of oxidized Si wafer divided into 49 coupons to use as sputter profile reference materials. The thickness (in nm) of each coupon was measured by ellipsometry using the one-layer model, as marked on the drawing. For this particular wafer both ellipsometry and XRR indicate that there are significant variations in the oxide thickness depending on the location on the wafer.

- No reference measurement needed (but knowing some parameters helpful or necessary).
- Many important properties of materials can be inferred, including both real and imaginary parts of the dielectric function.
- Can be conducted during growth and processing if optical path available (no vacuum requirement).

Limitations:

- Model dependent for physical properties.
- Special approaches are needed for thick films and thick multilayers.

16.3.5 Photoluminescence Spectroscopy

Z. Wang

Photoluminescence is a process in which a substance absorbs photons and then re-emits photons (usually at somewhat lower energies with smaller number of photons). Photoluminescence spectroscopy analyzes the distribution of energies involved in the photoabsorption and photoemission processes, the efficiency of the photoemission as well as their temporal characteristics. Because of the non-destructive and contactless nature, photoluminescence spectroscopy applies to solids, solution, solid suspensions, and gaseous materials, making it a highly versatile and sensitive technique for molecular detection and structural analysis.

16.3.5.1 The Physical Principle of Photoluminescence Spectroscopy

The physical principle of photoluminescence spectroscopy is depicted by the Jablonski diagram [57] (Figure 16.19), named after the Polish physicist Aleksander Jabłoński. Absorption of photons promotes an electron from the electronic ground state (S_0) to certain vibrational levels ($v = 0, 1, 2, \ldots$), of the first (S_1) or higher electronic excited state ($S_{2,3} \ldots$). The excited electron quickly relaxes to the lowest vibrational level ($v = 0$) of that excited state (typically within 1×10^{-12} s) by vibrational relaxation (VR), then relaxes to S_1 through internal conversion (IC), which occurs when a vibrational state of an electronically excited state can couple to a vibrational state of a lower electronic state. The resulting electron can further deactivate either radiatively by emitting a photon (FL) or non-radiatively through one of three processes: (1) IC quenching to the ground state; (2) collisional quenching (CQ) to the ground state; or (3) intersystem crossing (ISC) to a triplet excited states (T_1) that usually lies at lower energy relative to S_1. From were, the electron can either emit a photon by phosphorescence or deactivate through IC to S_0.

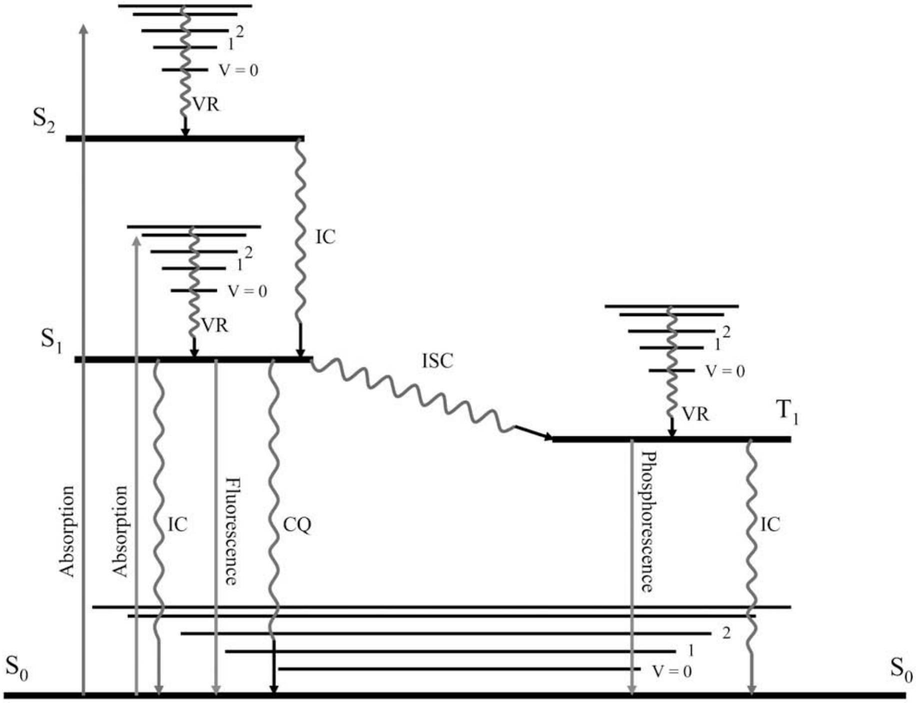

Figure 16.19: Jablonski diagram showing principles of photoluminescence spectroscopy. Absorption of a photon excites an electron to an excited state from which it decays by a variety of processes to lower energy states. Observation of the photons emitted provides fundamental information about the energy levels in the system. See text for more details [57].

For molecular materials, the intensity and profile of the photoluminescence spectra are direct measures of various important material properties such as the relative energies of the ground and excited states, electronic transitions and concentrations of the emitting species [58]. The temporal dependence of the photoluminescence reflects the relaxation characteristics of the excited state, molecular bonding environment, and identification and quantification of photoluminescence quenchers. The polarization change of photoluminescence reveals the electronic transitions involved and the direction of the transition moments. For lanthanides-based materials and some transition metals, the symmetry is related to band splitting pattern and for lanthanides, such as Eu(III) and Tb(III), the quenching behavior offers clues about the vibrational characteristic of its immediate surroundings, such as high-energy vibrators, O–H and N–H [59, 60]. Fluorescence energy transfer studies allow identification of other fluorophores in the vicinity of a molecule as well as the distance between them and the nature of their association.

For semiconductor materials, photoluminescence occurs in a similar mechanism. Photoexcitation of a semiconductor material promotes an electron from the valence band to the conduction band, leaving a 'hole' in the valence band. The excited electron in the conduction band relaxes quickly, typically within 15–25 ps [61], to the band edge via inter- or intra-sub-band scattering and then recombines with the hole either radiatively by emitting a photon or non-radiatively by passing the energy on to one or more phonons, to 'trapping' states that are created by impurities, dopants, or defects and lie in between the conduction band and the valence band (Shockley–Read–Hall recombination), or to another electron or hole (Auger recombination). For radiative recombination, the emitted photon usually has an energy equal to the band gap energy, $h\nu = E_g$, where h is Planck's constant, ν is the frequency of the emitted photon, and E_g is the bandgap energy. Therefore, photoluminescence spectra and decay behavior (or lifetime) provide direct measurement of the bandgap energy, which help identify and quantify the elemental composition of compound semiconductors, and determine the presence of impurities, dopant concentrations, and structural defects, and understand the electron–hole recombination mechanisms and evaluation and quality control of semiconductor materials.

16.3.5.2 Instrumentation

The complexity of photoluminescence instrumentation largely depends on the parameters of interests. Conventional photoluminescence (more commonly termed fluorescence) spectrometers typically use xenon lamps as the excitation source. Most xenon lamps are effective in a broad wavelength range from the UV to near-IR region. The excitation beam is dispersed through scanning monochromators for sample excitation at different wavelength (energies). The emitted fluorescence is collected at either a right angle (90° relative to the excitation beam) or front face (~ 30°) and dispersed through a second scanning monochromator and then detected by a photomultiplier tube. Multiple slit mechanisms are employed at both the excitation and emission sides to increase the monochromaticity of the excitation beam as well as the photoluminescence emission. Photoluminescence lifetime measurements are achieved by replacing the continuous wave xenon lamp with flash xenon or xenon–mercury lamps or pulsed lasers and recording the photoluminescence intensity change as a function of time after the pulsed excitation.

The availability of lasers and CCD detectors in the last couple of decades has significantly improved the photoluminescence technique [62]. Lasers provide high-power, coherent monochromatic light, greatly improving the spectral resolution and detection limit. Pulsed lasers with pulse width at nanoseconds to femtoseconds not only permit photoluminescence measurements with lifetimes in a broad range from milliseconds to subpicoseconds, and cover most photoluminescence materials, but also facilitate a new suite of photoluminescence measurements, called time-resolved photoluminescence spectroscopy [63]. Photoluminescence spectra recorded at different delay times after the laser pulse allow temporal resolution of the emitted fluorescence spectra and thus help with the identification of materials with photoluminescence centers in different chemical environments and the elucidation of the recombination mechanisms. The use of CCD detectors eliminates the scanning process of the emission monochromator and thus significantly improves the throughput of the measurements. This is particularly useful when using pulsed laser excitation sources. For these, the entire photoluminescence measurements can be recorded with a single laser pulse, thus avoiding measurement errors introduced by the instability and fluctuation of the excitation sources.

16.3.5.3 Photoluminescence Applications in Thin Film Materials and Future Directions

Because of its high sensitivity, providing rich information about the band structure, electron-hole recombination and relaxation processes, and relative ease of use, photoluminescence spectroscopy applies to the characterization, photophysical, photochemical, and mechanistic studies of a wide array of thin film materials including ZnO/II–VI semiconductors [64], III–V semiconductors [65], lanthanide-based optoelectronic materials [66, 67], inorganic and organic light-emitting diodes (LEDs and OLEDs) [68], thin film photovoltaic materials [69], and radiation detection devices [70]. Interested readers are referred to many of the previous review articles and book chapters cited here [63, 71, 72].

Zinc oxide is a wide-band (3.37 eV, 60 meV exciton binding energy) semiconductor with potential applications in photoelectronics, light-emitting devices, gas sensors, and solar cells. Studies have shown that many properties of ZnO films are strongly dependent on the crystal structure and orientation of ZnO, its crystalline quality and defect states, and thus vary as a function of film preparation method, selection of substrate, and growth conditions. As an example, for ZnO thick films (~ 200 nm thickness) deposited on indium tin oxide (ITO glass) by radio-frequency (RF) magnetron sputtering at a substrate temperature of 400 °C, the UV photoluminescence of the film initially increases as the oxygen partial pressure (PO_2) increases from 0% to 60%, but then decreases as PO_2 increases further (Figure 16.20) [73].

The initial increase probably resulted from the improved stoichiometry of the films, associated with the incorporation of oxygen at oxygen vacancies, while excessive PO_2 may worsen the stoichiometry of the films by introducing interstitial oxygen or zinc vacancies. Gaussian fitting of the UV-photoluminescence band gives three peaks situated at 380, 395, and 410 nm, corresponding to recombination of free excitons through an exciton–exciton collision process, emission from the ITO layer and O dangling bonds on the ITO surface layer of the interface between substrate and ITO, respectively. The relative intensity of the 410 nm peak increases with the excitation intensity.

The versatility of fluorescence detection also makes it possible to integrate photoluminescence instruments with other experimental techniques such as optical microscopes and scanning

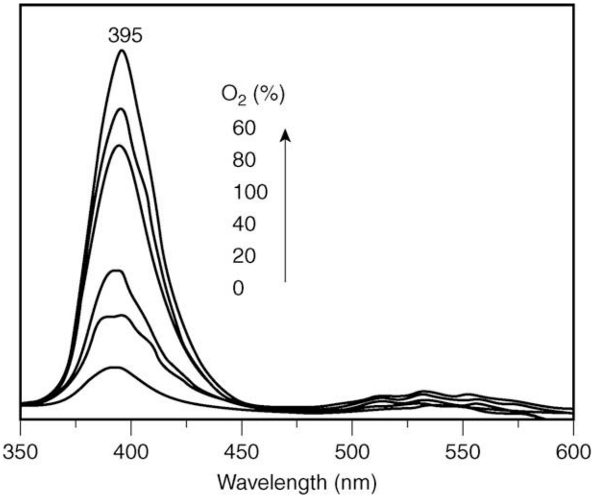

Figure 16.20: Photoluminescence (PL) spectra of ZnO thin films on ITO glass with increasing P(O_2) [73].

atomic force microscopes. In addition, the non-contact nature of the techniques allows the sample to be measured at different temperatures. The current trend in the application of photoluminescence for thin film studies is closely coupled with technical developments in laser fluorescence spectroscopy and scanning probe microscopy. Examples of such developments are near-field scanning optical microscopy (NSOM) and non-linear optical spectroscopy. NSOM is based on designs that limit the photoexcitation volume using a tapered, metal-coated optical fiber, or field-enhanced excitation by noble metal probes [74]. Using NSOM, spatial resolution much less than the diffraction limit can be achieved. Combining NSOM with photoluminescence spectroscopy allows study of the photoluminescence properties of thin film material with ultrahigh spatial resolution. Using this method, Crowell et al. [75] were able to image photoluminescence in an InGaN/GaN quantum well with a spatial resolution of approximately 100 nm for temperatures between 50 and 295 K, and directly correlated the spatial features of the thin film material with photoluminescence characteristics (Figure 16.21).

Time-resolved photoluminescence (TRPL) measures photoluminescence intensity as a function of time. With commercial high-speed detection devices such as time-correlated single-photon counting and streak camera with femtosecond lasers as excitation sources, luminescence measurement reaches a resolution of a few picoseconds. A new type of TRPL technique that is based on sum frequency generation (or frequency up-conversion) has been demonstrated [76]. This technique offers a time resolution on the order of the laser pulse width, as short as tens of femtoseconds. Rainó et al. [77] used this technique to measure the rise and decay dynamics of the ground and first excited states of InAs quantum dots (QDs) capped with an InGaAs quantum well and found that the higher energy states of the QDs do

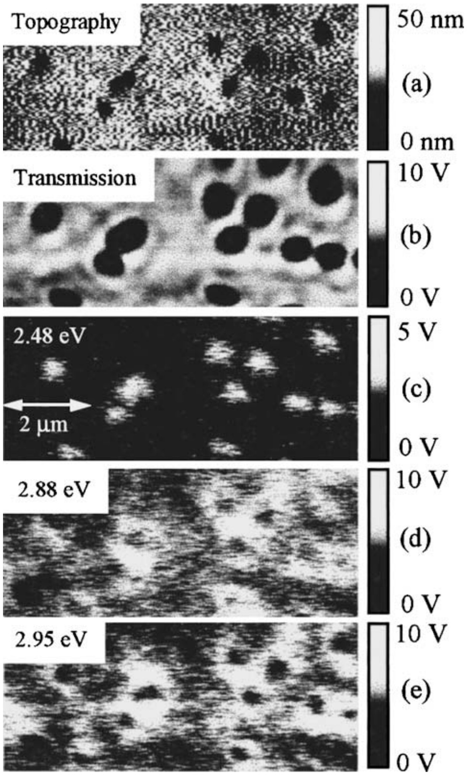

Figure 16.21: Images of a 2.5 × 8 μm region of the sample at $T = 295$ K obtained using the near-field technique: (a) topographic image of the InGaN/GaN sample measured using the shear-force feedback technique; (b) transmission image at the excitation energy of 3.16 eV; (c–e) photoluminescence images obtained at detection energies of 2.48, 2.88, and 2.95 eV, respectively. The grayscale for each image is indicated at the right [75].

not act as intermediate stages in the carrier relaxation, while the carriers can cool down to any lower energy states following relaxation through a continuum background.

Strengths:

- Non-contact, non-invasive/non-destructive.
- Requires minimum sample preparation.
- Sensitive to impurities and defects (low detection limits).
- Applies to broad temperature range.
- Ease of integration with other techniques.

- Offers direct observation of the electronic transition energies, including bandgap energy.
- The energetics and dynamics provide ideal tools in the study of recombination mechanisms.

Limitations:

- Only applies to materials that fluoresce.
- Only detects electronic states that relax radiatively.
- In some cases, unknown quenching mechanisms prevent quantitative measurement.

16.4 Incident Ion Methods

Ion beams are used in a variety of ways to characterize films and surfaces. Most of the techniques involve either analyzing ions scattered from a sample to extract information about the sample or using incident ions to remove material from the sample. Both methods are included in this section. The several techniques involving elastic and inelastic scattering have several common physical aspects and they are described as a unit, including: (1) low-energy ion scattering (LEIS); (2) medium-energy ion scattering (MEIS); and (3) high-energy ion scattering (HEIS) methods such as Rutherford backscattering spectrometry (RBS), nuclear reaction analysis (NRA), ion channeling, and elastic recoil detection analysis (ERDA). Other sputtering methods, such as sputter depth profiling, secondary ion mass spectrometry (SIMS), glow discharge mass spectrometry (GDMS) and some applications of focused ion beams (FIBs) use energetic ion beams. In addition, FIBs are often combined with electron microscopy as the ion beam can be useful in the collection of high-resolution images. The final section is on sputter depth profiling, which is useful for determining depth distributions and layer thickness. This final section also includes a table comparing a variety of approaches for determining film or layer thickness.

16.4.1 Ion Scattering Methods (LEIS, MEIS, HEIS, RBS, NRA, ERDA, Channeling)

V. Shutthanandan and Y. Zhang

Ion beams have been effectively used in material modification and material analysis for more than 40 years. Ions at different energies are used to alter surfaces (or films) or to collect different types of information about them. The picture in Figure 16.22 shows different capabilities associated with various ion energy ranges. A few hundred eV to a few keV inert gas ions, in particular argon ions, are extensively used in sputter cleaning of surfaces which are necessary for surface science studies. In addition, a few keV inert gas ions along with alkali ions are very useful in determining the structural and chemical properties of surface layers and adsorbate layers. This capability is called LEIS spectroscopy, which is very surface sensitive

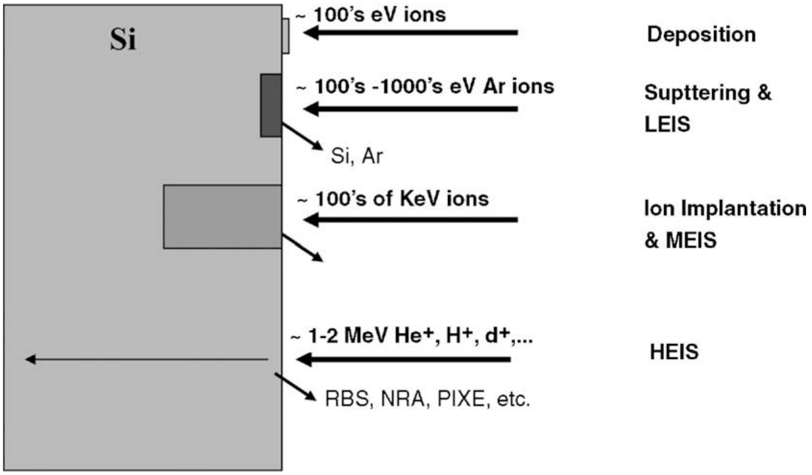

Figure 16.22: Schematic illustration of the uses of ion beams with various energies on Si substrate.

and it is described in detail in the following sections. MEIS spectrometry is a powerful capability to characterize thin films of a few nanometers thickness. In general, about 100 keV helium or hydrogen ions are used as an incident ion beam and electrostatic analyzers are used to characterize the backscattered ions at large scattering angles. High-energy ion beams are generally used for material characterization of both thin and thick films. Although several high-energy ion beam-based techniques are available for material characterization, RBS, NRA, proton-induced X-ray emission (PIXE), and ERDA are commonly used.

Although not the focus here, ion beams are also important for material deposition and substrate modification. Ions with energies between a few eV and a few tens of eV enable the 'soft' landing of larger molecules on the surfaces and the deposition of thin films using ion beam-assisted deposition. Material properties can be modified using ion implantation and it has been a very valuable tool in the semiconductor industry. The research community is investigating this capability for other applications including spintronics and photocatalysis. Ion implantation is often carried out using ion beams with energies in the range of a few tens of keV to a few hundreds of keV.

In general, the ion scattering spectroscopies are mass sensitive and mass selected information can be obtained from the data. As a result, backscattering and forward scattering capabilities along with nuclear reaction analysis capabilities are isotope specific. The experimental data can be simply simulated using classical mechanics principles as discussed in the following sections. The following elements are important to understanding and modeling ion scattering from surfaces:

- Energy transfer from a projectile to a target nucleus in an elastic two-body collision – This concept is related to kinematic factor which depends on the mass of the projectile, target atoms, and the scattering angle. The energy of the outgoing ions is related to the incoming ions through this factor.

- Likelihood of occurrence of such a two-body collision – This factor is defined as the scattering cross-section and the height of the experimental spectrum is determined by the scattering factor.
- Energy loss of a projectile moving through a dense medium – Since the ion beam loses energy when it travels through the material, the stopping cross-section which is related to the energy loss as a function of depth provides depth perception.
- Statistical fluctuations in the energy loss of a projectile moving through a dense medium – When the ion beams travel through the material, the energy spread will be increasing owing to the interaction with the material as a function of depth. This ‘energy straggling’ needs to be taken into account in interpreting the experimental data and determining various properties of the material.

Scattering kinematics

The simple solution to the equations associated with energy and momentum conservation leads to the following equation (Figure 16.23):

$$K = \frac{E_1}{E_0} = \frac{\frac{1}{2}M_1 V_1^2}{\frac{1}{2}M_1 V_0^2} = \left[\frac{\left(M_2^2 - M_1^2 \sin^2\theta\right)^{1/2} + M_1 \cos\theta}{M_1 + M_2}\right]^2 \tag{16.4}$$

K is called the kinematic factor and it represents the ratio of the incident energy of the projectile to the outgoing projectile energy. The masses of the projectile and target atom are M_1 and M_2, respectively, and the scattering angle is θ. The outgoing projectile energy, $E_1 = KE_o$, and by measuring the energy of the backscattered ions the composition of the material can be determined as a function of depth. The variation of *K* as a function of the mass

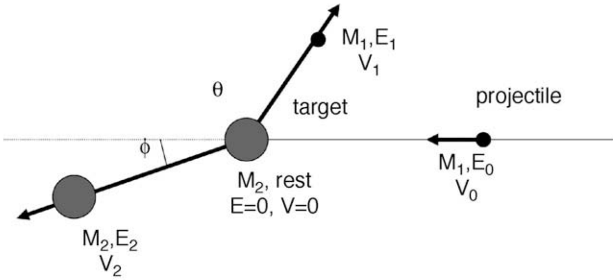

Figure 16.23: A cartoon picture depicting the elastic collision between the projectile with mass M₁ and target atom with mass M₂.

of the target atoms for light projectiles such as hydrogen and helium ions indicates that the differences in K for light target atoms are larger in comparison to the heavy target atoms. As such, for the helium ions which are commonly used for RBS, light target atoms can be easily separated while the separation between heavy target atoms is relatively difficult, in particular when the elements are close to each other. Heavy target atoms can be separated using heavy projectiles, but these may damage the sample.

Scattering cross-section

The scattering cross-section, σ, is defined by the following equation:

$$\begin{aligned}
\sigma(\theta) &= \left[\frac{Z_1 Z_2 e^2}{4E}\right]^2 \frac{4\left\{[1-((M_1/M_2)\sin\theta)^2]^{\frac{1}{2}}+\cos\theta\right\}^2}{\sin^4\left(\frac{\theta}{4}\right)[1-((M_1/M_2)\sin\theta)^2]^{\frac{1}{2}}} \\
K &= \frac{E_1}{E_0} = \frac{\frac{1}{2}M_1V_1^2}{\frac{1}{2}M_1V_0^2} = \left[\frac{\left(M_2^2-M_1^2\sin^2\theta\right)^{1/2}+M_1\cos\theta}{M_1+M_2}\right]^2
\end{aligned} \tag{16.5}$$

where Z_1 and Z_2 are the atomic number of the projectile and target atom, respectively, and E is the energy of the projectile. This equation clearly demonstrates that the energy and atomic number of the target atom depend on the scattering factor as follows:

$$\sigma(\theta) \sim Z_2^2$$

$$\sigma(\theta) \sim E^{-2}$$

Since the scattering cross-section relates to the signal amplitude of the backscattering spectrum, the backscattering signal would vary as a square of the atomic number of the target elements. As such, the backscattering signals from the material that consists of heavy elements will provide larger signals. On the other hand, the signals from the light elements are weak and the detection and quantification of light elements in a heavy element matrix will be difficult. As such, thin films that contain heavy elements on light element substrates can be successfully characterized using backscattering spectrometry. The energy dependence of the scattering cross-section exhibits the $1/E^2$ relationship and for $E > \{1/2\}$ MeV the scattering cross-section does not vary significantly as a function of energy. Less variation in scattering cross-section at higher energies makes the thin film analysis easier and 2 MeV helium ions are generally used for RBS.

Energy loss and energy straggling

When the energetic ions travel through the material they lose energy owing to nuclear and electronic interactions with the target atoms. In general, since the radius of the nucleus is small, nuclear stopping is small in comparison to the electronic stopping. Excitation and ionization during the inelastic collisions with the electrons in target atoms contribute to the electronic stopping.

The rate of energy loss is defined as dE/dx, the change in energy (dE) per unit distance (dx) the ion beams travel inside the material. The stopping cross-section (ε) is defined as the ratio between the rate of energy loss and the areal density of target atoms within the distance ($(1/N)(dE/dX) - N$ is the areal density of the atoms within the distance dx). Since the stopping cross-sections have been already established for many materials as a function of energy, the thickness of the materials can be determined.

Although energy spread (energy straggling) as a function of depth is important for bulk materials, for thin film measurements this can usually be neglected. As such, energy straggling is not discussed in detail in this chapter.

As discussed in the above sections, the analysis of ion scattering data is straightforward because the kinetics of energetic ion–atom collisions and scattering can be accurately described by simple classical mechanics concepts. During the collision, the ions lose some of their energies to target atoms. The backscattered ions have energies equivalent to the product of the incident energy and the kinematic factor while the target atoms recoil to the forward direction owing to the energy gained. As such, the final energies of the scattered ions and forward recoiled atoms can be determined in a particular direction using the mass of the projectile ion and target atoms. LEIS, MEIS, and HEIS capabilities are briefly described in the following sections.

16.4.1.1 Low-Energy Ion Scattering

Incident ions with energies ranging from 1 to 10 keV are used in LEIS investigations. Since the ions have low energies, the ions penetrating beyond the first one or two layers are neutralized and, as a result, not detected. As such, this capability is very surface sensitive. Some of the ions which interact with the surface layer are also neutralized. In addition to the scattered ions, the neutrals can be used to obtain information from surfaces. LEIS can be efficiently used to characterize surface composition and surface structure [78–84]. Ion neutralization can be used to probe the spatial distribution of surface electrons. Since the number of scattered ions is very small compared to the incident ions ($<5\%$) neutralization was initially perceived as a feature that complicates ion scattering analysis. Most of the conventional ion scattering systems were not equipped with instrumentation able to capture the neutrals and it was difficult to separate neutralization effects. To overcome the issues associated with neutralization, Niehus and co-workers [85, 86] developed the use of alkali ions instead of conventionally used inert gas ions. Alkali ions have low neutralization probabilities and, as a result, the scattered intensity of the ion is significantly higher than that of inert gas ions. However, surface contamination by alkali ions can be an issue. During the late 1980s and early 1990s time-of-flight (TOF) methods including mass spectroscopy of recoiled ions (MSRI) and direct recoiling spectroscopy (DRS) to analyze both scattered ions and recoiled neutrals were developed and

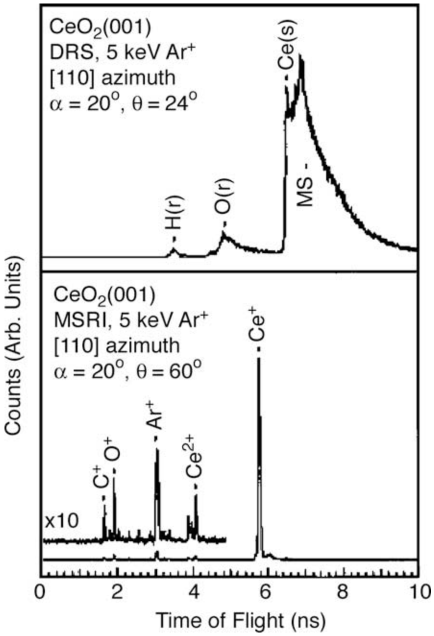

Figure 16.24: Direct recoil spectroscopy (upper panel) and mass spectroscopy of recoiled ions (lower panel) results from the CeO_2(001) surface after annealing to 925 K in an oxygen background of 1×10^{-7} torr, and cooling to 295 K before evacuating the oxygen [90].

these methods provided much more information about surface structure [87–89]. In MSRI capability, TOF methods and time-focusing electrostatic analyzers are used to separate the isotropically resolved mass spectrum. The high-mass resolution and the inherent surface sensitivity available with the MSRI technique provide a powerful capability for structure measurements.

As an example, Herman [90] used angle-resolved MSRI (AR-MSRI) to examine the surface structure of the CeO_2(100) surface. These measurements were made in a custom-built ultrahigh vacuum (UHV) chamber at the Environmental Molecular Sciences Laboratory (EMSL). A 5 keV pulsed Ar^+ ion beam was used at an incident angle of 20° with the sample surface. The AR-MSRI measurements were made in an electrostatic analyzer which was positioned at a 30° scattering angle (60° between the incident ions and the recoiling ions). Typical DRS and MSRI data from this surface are presented in Figure 16.24.

In DRS, the main signals obtained were hydrogen and oxygen recoils, argon single scattering from cerium, and multiple scattering events. In the MSRI spectrum the signal from Ce^+ dominates and the area under this peak can be collected as a function of azimuthal angle to obtain the structural information. Figure 16.25 shows the experimental AR-MSRI data for Ce along with the calculated values for three different models such as oxygen-terminated full one-layer (1 × 1) surface, cerium-terminated full one-layer (1 × 1) surface, and oxygen-terminated half-monolayer surface.

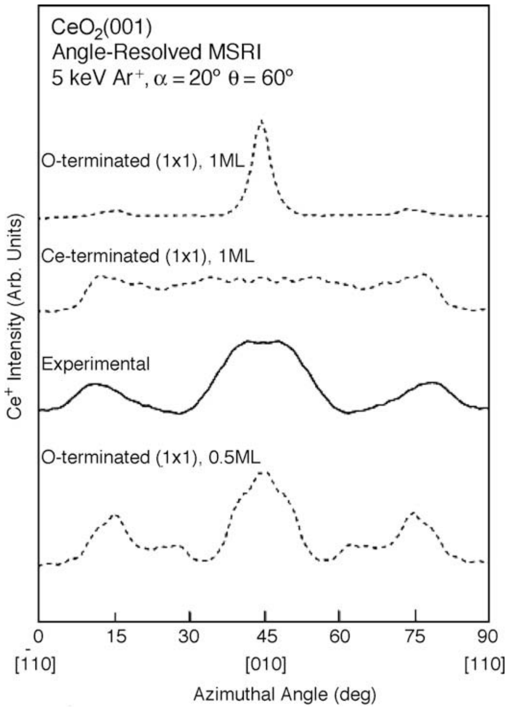

Figure 16.25: Angle-resolved mass spectroscopy of recoiled ions intensities for cerium with respect to azimuthal angle. The experimental data are shown as a solid line and calculated data are shown as dashed lines for the models discussed in the text [90].

As clearly seen in the figure, the best fit for the experimental data is obtained for an oxygen terminated surface that has 0.5 ML of oxygen removed. As discussed in this example, the MSRI technique has much higher mass resolution than either LEIS or DRS, and AR-MSRI can effectively determine the surface structure by comparing the experimental data with simulations.

Strengths:

- Determination of surface structure and terminations of single crystal surfaces.
- Surface composition with high sensitivity.
- Non-destructive analysis.

Limitations:

- Limited analysis depth (few monolayers).
- Neutralization issues with inert gas ions.

16.4.1.2 Medium-Energy Ion Scattering

Since MEIS typically utilizes 100 keV ions as incident particles and electrostatic analyzers to detect the scattered ions, it is a refinement of the more common technique of RBS, but with enhanced depth and angle resolution. In general, collimated light ions such as H^+ and He^+ are used in MEIS experiments. The incident ions are generally aligned with a particular known direction and the energy and angle of the scattered ions are analyzed simultaneously to measure atomic mass, depth, and surface structure. As explained in the subsections at the beginning of this ion scattering section, mass and depth are determined. MEIS can achieve a depth resolution of one atomic layer in many cases. To calculate the surface structure the scattered intensity measurements are performed as a function of azimuthal and polar angles when the incident ion beam is aligned with a crystallographic axis. When the ion beam is aligned with a crystallographic axis the surface atoms shadow deeper atoms from the ion beam. For a particular crystal, this alignment along certain incident directions can allow the ion beam to illuminate only the top one, two, or three layers, according to choice. Ions scattered from the second layer will have their outward paths blocked at certain angles by first layer atoms. The angular variation of scattered ions can be related to the geometrical arrangement of surface atoms. The experimental data should be compared with computer simulations to determine the complete surface structure.

Goncharova et al. [91] analyzed high-quality single crystal $SrTiO_3$ (STO) films grown by molecular beam epitaxy on Si substrates using MEIS. The investigators used a 98–130 keV H^+ beam aligned along one of the low index directions of the Si substrate and an electrostatic analyzer to collect the backscattered ions. In this type of experimental set-up, it is possible to obtain subnanometer depth resolution, which is significantly higher in MEIS experiments than in normal RBS using high-energy ion scattering. Figure 16.26 shows the energy distribution of the backscattered protons collected in this experiment.

The data shown in Figure 16.26(a, b) were collected from 3.5 nm and 7.8 nm thick STO films, respectively. The signals from Sr, Ti, and O sublattices in the films and Si from the substrate are well separated and the features grown at the STO/Si interface due to annealing are clearly visible.

Depth profiles of elements were obtained by performing computer simulations of the backscattered ion energy distributions [92, 93]. However, the depth resolution differs for different species and varies for deeper layers. Near the surface region, quantitative depth profiles for different species can be extracted with a resolution as high as 0.3 nm. Because of energy straggling, the depth resolution deteriorates in deeper layers. In general, the calculated resolution depends on the film material. For ZrO_2 thin films, the depth resolution at a depth of 3 nm is approximately 0.8 nm.

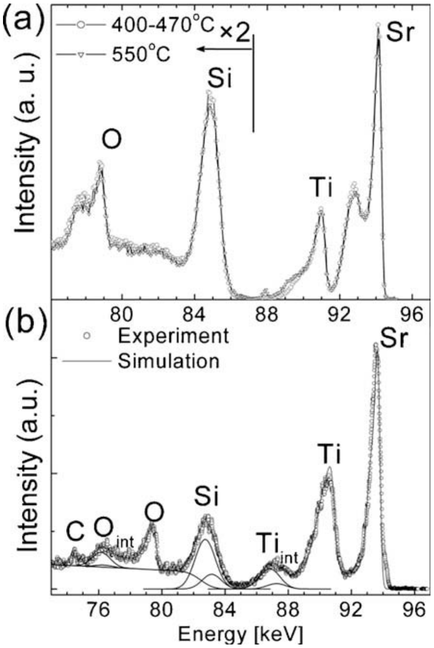

Figure 16.26: MEIS energy distributions for (a) 3.5 nm thick STO films on Si(001) recrystallized at 450 and 550 °C, and (b) a 7.8 nm thick STO film recrystallized at 550 °C. Interface peak deconvolution is demonstrated for 7.8 nm film [91].

Strengths:

- Absolute quantifications of film thickness and stoichiometry of heavy element films on light element substrates.
- Very high depth resolution.
- Crystalline quality measurements and lattice site locations of dopant in single crystals.
- Determination of surface structures.

Limitations:

- Limited analysis depth (~ 100 nm).
- Difficult for light element films on heavy element substrates.

16.4.1.3 High-Energy Ion Scattering Methods

RBS and channeling

Incident ions with energies ranging from 0.5 to 4 MeV are used in HEIS investigations. High-energy ion scattering (especially RBS and channeling techniques) have been extensively used to study the stoichiometry, structure, and thickness of thin films. In these experiments, a He^+ ion beam is incident on the sample (film on a substrate) with an energy that is typically between 0.5 and 2.0 MeV. In this regime, the Coulomb scattering can be treated classically (Rutherford scattering) and as a result, reasonably accurate numerical simulations of the ion scattering yield can be performed. As explained earlier, this technique is element specific since the recoil energy of the backscattered He^+ ion is mass dependent. Since the ion loses energy as it travels through the target material, an energy spectrum of the backscattered ions also yields information about the depth of the backscattering event. On the other hand, if the ion beam is well aligned with a major axial direction of a single crystal target, the ions channel into the crystal along the relatively open areas between the rows of atoms. Ions which backscatter from the first (surface) atom in each row give rise to the surface peak observed in the backscattered ion energy distribution curve, while the small-angle forward scattered ions form a shadow cone which extends into the solid. Subsequent atoms along the row and within the shadow cone do not lead to backscattering events, for a static model of an ideally terminated bulk lattice. By rotating the sample by a few degrees with respect to the angle of incidence away from the low index direction, the channeling mode becomes a random mode. In this mode, virtually all the atoms in the sample are exposed to the ion beam and as a result the highest backscattered ion yield can be obtained. The variation of integrated yield over a small region near the surface peak as a function of tilt or polar angle produces an angular yield curve or rocking curve.

As an example, RBS and channeling measurements performed along the <100> direction of 40 nm thick $SrTiO_3$ films that were grown on Si substrate is shown in Figure 16.27 [94]. Since Sr and Ti in the films are much heavier than the Si in the substrate, the backscattered He signals from Sr and Ti appear without any interference from the backscattered He signals from

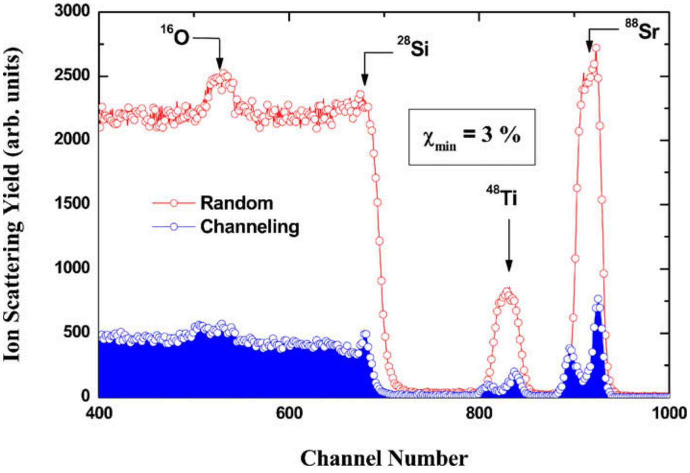

Figure 16.27: RBS spectra measured along channeling (blue) and random (red) direction of 400 Å thick $SrTiO_3$ on Si [94].

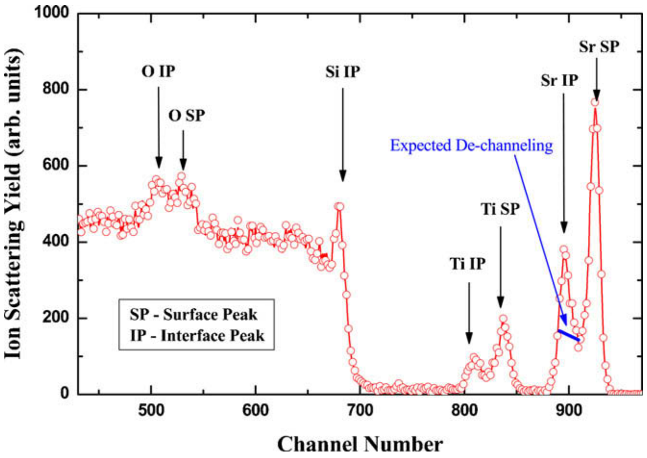

Figure 16.28: Channeling spectrum from 400 Å thick $SrTiO_3$ film on Si substrate. Individual peaks not apparent in the random direction appear, providing additional information about the film structure. Sr surface peak (SP), Sr interface peak (IP), Ti SP, Ti IP, Si IP, O SP and O IP are identified in the spectrum.

Si in the RBS spectrum. The stoichiometry of the film was determined to be Sr:Ti:O = 1:1:3 using SIMNRA simulations. The film thickness (39.6 nm) was also measured using the width of the Sr and Ti peaks assuming the bulk density of the $SrTiO_3$. The minimum yields (the ratios of the aligned yield to the random yield just below the surface peaks) for both Sr and Ti are approximately 3%; thus, the film appears to be well ordered and compares to high-quality bulk $SrTiO_3$ single crystals.

When the channeling spectra were carefully examined, seven distinct peaks were visible, as presented in Figure 16.28. The first peak on the high-energy side is the surface peak from Sr atoms at the top of the film (Sr-SP). The second peak is attributed to some Sr atoms visible to the ion beam at the $SrTiO_3$/Si interface (Sr-IP). Similarly, the next two peaks are surface (Ti-SP) and interface (Ti-IP) peaks related to Ti atoms. Some Si atoms at the interface are also visible to the ion beam and this is evident from the fifth peak in the spectrum (Si-IP). The sixth peak is related to the backscattered ion contribution due to the surface oxygen atoms (O-SP) from the film, and the last peak is due to the visibility of oxygen atoms to the ion beam at the interface (O-IP). Sr, Ti, and O interface peaks are composed of the normal dechanneling yield in these three sublattices plus the dechanneling from disordered atoms, which are not aligned with the ion beam in the interface region. Normal dechanneling yield in the film is expected to be significantly lower compared to the interface peak areas and, as such, these peaks are generated mostly due to backscattering yield from disordered atoms in the interface region. IP/SP ratios calculated using the atomic areal densities are approximately 0.65 for Sr and Ti, and 1.04 for O. The difference in IP/SP ratios between Sr, Ti, and O indicates that the degree of disordering associated with interfacial Sr and Ti is approximately the same, but significantly less than that of O. Additional interfacial oxygen disordering can be attributed to the oxygen atoms in the reported amorphous silica and silicate-like layers. However, the contribution from the silicate-like template layer cannot be separated from the amorphous silica layer by RBS owing to the lack of depth resolution (~ 20 nm). Nevertheless, such a silicate-like layer can be identified and separated from the amorphous silica in XPS spectra. The visibility of Si atoms in the interface region can be due to the Si atoms in the amorphous silica and silicate-like layers, and those not completely shadowed by the $SrTiO_3$ film.

Strengths:

- Absolute quantifications of film thickness and stoichiometry of heavy element films on light element substrates without the use of standards.
- Buried interface analysis up to 1000 nm.
- Crystalline quality measurements and lattice site locations of dopant in single crystals.

Limitations:

- Poor depth resolution.
- Difficult for light element films on heavy element substrates.

Nuclear reaction analysis

As mentioned earlier, RBS is ideal technique for depositing thin film of high Z materials on low Z substrates. For the other cases, such as low Z thin films on high Z matrix, quantification of light elements is difficult using RBS. However, other ion beam based techniques such as NRA and TOF heavy ion ERDA are available for light element detection. In NRA, an incoming energetic particle (usually a proton or deuteron) interacts quantum mechanically with light element atoms and produces some other particles (e.g. neutrons, protons, and alpha particles) and gamma rays. Most of the light elements and their isotopes can be detected and quantified using NRA. Some of the commonly used nuclear reactions are $H(^{19}F, \gamma)^{16}O$, $D(d, p)T$, $^{16}O(d, p)^{17}O$, $^{18}O(p, \alpha)^{15}N$, $^{12}C(d, p)^{13}C$, and $^{14}N(d, p)^{15}N$. As an example, a NRA spectrum obtained from the $SrTiO_3$ deposited on Si is shown in Figure 16.29. Since the nuclear reaction cross-sections can be measured experimentally, we can quantitatively measure the total amount of oxygen in the film by measuring the area under the proton peak. By combining RBS and NRA one can easily study the film stability under various annealing environments.

Strengths:

- Absolute quantifications of light elements and their isotopes.
- Quantitative hydrogen depth profiling.

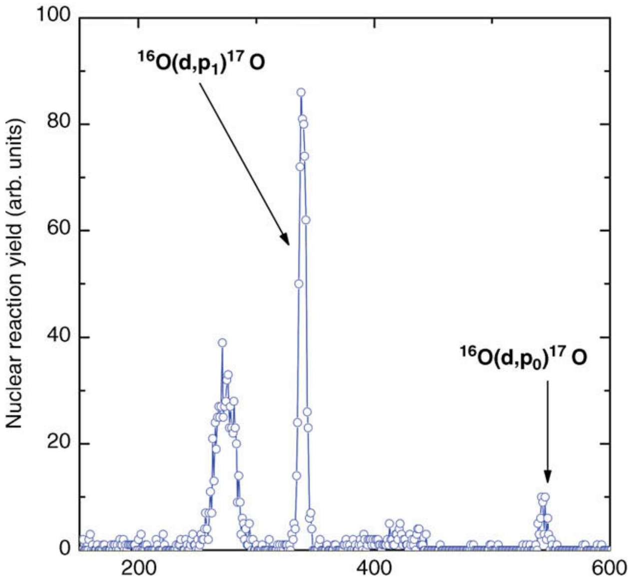

Figure 16.29: $^{16}O(d,p_1)^{17}O$ **nuclear reaction spectrum from 400 Å thick** $SrTiO_3$ **on Si.**

- Buried interface analysis.
- Lattice site locations of anion dopant(s) in epitaxial oxide films.

Limitations:

- Poor depth resolution.
- Large data collection time.
- More cross-section data needed.

Advanced elastic recoil detection analysis

When the incident particles hit the target at an off-normal angle with energy in the range 0.05–5 MeV per nucleon, target nuclei recoil elastically from the target surface. Detecting recoiling target nuclei to acquire information on the target composition is termed elastic recoil detection analysis (ERDA). Since the mid-1980s, ERDA has undergone rapid development by a number of groups.

ERDA is similar to RBS but has a number of important differences. For MeV helium ions, commonly used in RBS because of the elastic nature of the scattering process, the primary ions backscattered from the heaviest elements have the highest energy. Since these high-energy particles can be detected without background and the scattering cross-section increases with increasing target Z, this method of backscattering results in good sensitivity for the heavier elements in the sample surface region. The ratio of the cross-sections can be approximated by $d\sigma_{\text{light}}/d\sigma_{\text{heavy}} \approx (Z_{\text{light}}/Z_{\text{heavy}})^2$ for $M_1 \ll M_2$. This implies that it is very difficult to measure low-Z elements when the matrix consists of heavy elements since the signal will be very difficult to observe in the presence of the large signal from the heavy elements.

In a single collision, momentum considerations prevent scattering of projectile ions in backward directions when $M_1 > M_2$. Therefore RBS is completely insensitive to target elements that are lighter than the projectile ions. However, by using a detector in a forward scattering geometry, one can detect forward-scattered heavy projectiles and recoiling atoms from a single collision. The detection of elastically scattered recoils is the basis of ERDA. For the case of ERDA with heavy ions ($M_1 \gg M_2$), the cross-section for recoils is approximately proportional to Z_2/M_2 and therefore almost constant. This implies that the recoil cross-section does not decrease dramatically for light elements, which is the case for RBS, as discussed above. Furthermore, the use of a heavy-ion beam in ERDA makes it possible to reduce the scattering of the primary beam into the detector by placing the detector at an angle $\phi > \theta_{\text{max}}$, thereby enhancing the sensitivity. $\theta_{\text{max}} = \sin^{-1}(M_2/M_1)$ and is typically 20–40° for heavy projectiles such as ^{81}Br. The ability of ERDA to detect light and heavy elements makes it unique in its ability to quantitatively characterize surface film structures on a nanometer scale.

As one of the most promising ion beam analysis techniques, ERDA combined with a multidispersive detector telescope, such as a time-of-flight (TOF-E) detector telescope or thin Si detector (ΔE-E), provides simultaneous detection and absolute quantification of elemental depth profiles in complex matrices. Two powerful ERDA techniques are shown in Figure 16.30 and TOF-E ERDA is shown in Figure 16.31.

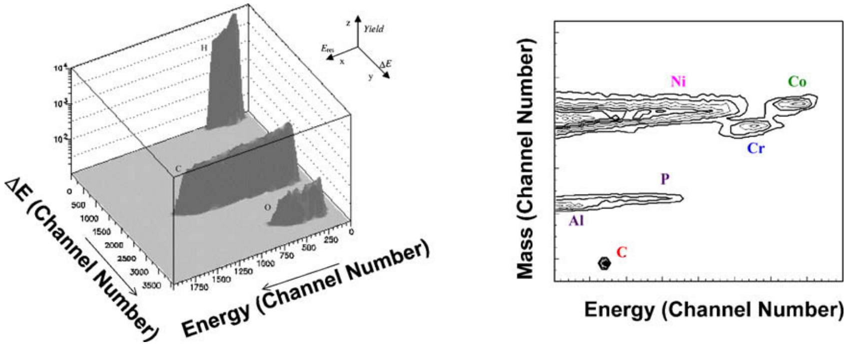

Figure 16.30: Two experiments of ERDA spectra. Left: 3D representation of a ΔE-E ERDA histogram of a sample containing H, C and O. Right: complex C/Co/Cr/Ni-P/Al multilayer structure with elements of close atomic mass obtained from TOF-E ERDA.

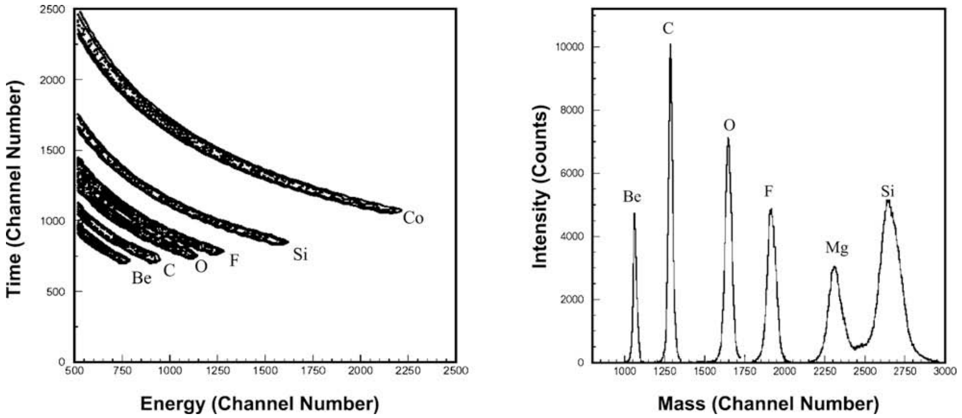

Figure 16.31: Two examples of TOF-E ERDA spectra. Left: simultaneous detection of elements: Be, C, O, F, Si, and Co using TOF-E ERDA. Right: good mass separation using TOF-E ERDA.

ERDA provides characterization of multielemental stoichiometry in multilayer thin films or complex matrices (Figures 16.30 and 16.31) from the surface to depths of about 1 μm with nanometer depth resolution. Since this is a powerful method to investigate elemental concentrations in the surface regions, this capability can be effectively applied in many different areas including characterization of oxide thin films for optical, magnetic and catalytic applications and characterization of environmental and biological samples. Both ΔE-E and TOF-E ERDA techniques can be applied to study hydrogen absorption, desorption, and diffusion, which are important in hydrogen storage, separations, and catalysis.

Strengths:

- Quantitative depth profiles of light elements including their isotopes.
- Good depth resolution.
- Good mass resolution for lighter atoms.

Limitations:

- Destructive analysis.
- Limited analysis depth (up to 1000 nm).
- Poor mass resolution for heavier atoms.

16.4.2 Secondary Ion Mass Spectrometry

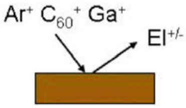

Z. Zhu

Secondary ion mass spectrometry (SIMS) is a very powerful surface analysis technique, which has been widely used in the semiconductor industry, materials research, environmental research, biological research, and catalysis research. Quite a few review papers and books addressing the details of this technique and its applications have been published [95, 96]. In general, secondary particles and clusters are generated as a result of the sputtering effect (Figure 16.32) when an energized primary ion beam (normally 10–30 keV) impacts a sample surface. Most of the secondary particles and clusters are neutral, but about 1–5% of them are charged ions. These secondary ions can be collected and analyzed so that a mass spectrum can be obtained.

The first generation of practical SIMS instruments was developed in the 1950s and 1960s. They used a continuous primary ion beam, with a magnetic sector as a mass analyzer. This kind of instrument was primarily used in depth profiling impurities in semiconductor materials, such as Si and GaAs wafers. The current of the primary ion beam is commonly in the nA to μA range, so that materials can be sputtered away quickly (0.01–1 nm/s). Such use is now known as ‘dynamic SIMS’, and currently it is the standard technique used to monitor impurities in semiconductor materials. Dynamic SIMS has extremely high detection limits, from parts per billion (ppb) to parts per million (ppm), depending on the specific element and sample.

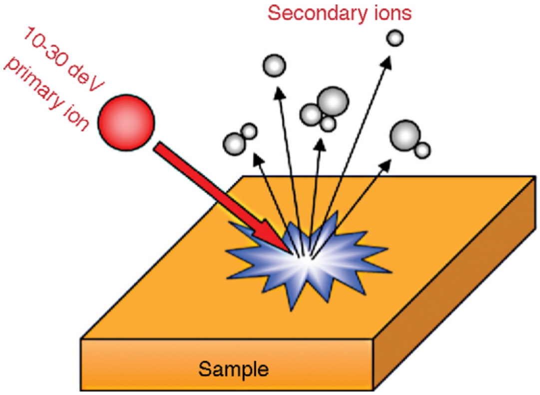

Figure 16.32: Schematic description of the SIMS principle.

Dynamic SIMS cannot be considered as a pure surface analysis technique since it removes materials from surface very quickly. However, it is a very useful method to obtain information about film and layer composition, diffusion and implant profiles, and the structure of interfaces.

In the 1970s, Benninghoven developed the ‘static SIMS’ technique. A very low current (picoampere level) pulsed primary beam was used to replace the continuous primary beam so that ion-induced damage was very limited and the surface could be considered to be in a ‘static state’. At the same time, Time-of-flight (TOF) mass analysis technique and single ion counting electronics were incorporated into the instrumentation. Thus, almost all secondary ions can be collected and detected. A useful mass spectrum can be easily obtained in a relatively short time before the total ion dose reaches the static limit, approximately 10^{12} ions/cm^2. TOF-SIMS has become the most commonly available SIMS technique in surface analysis laboratories.

The primary capability of TOF-SIMS is to provide surface mass spectra. A mass resolving power of 10,000 is not difficult, and such power is very useful for accurate mass peak assignment and enables the identification of molecular or atomic species of nominally the same mass. The top panel in Figure 16.33 shows a positive ion mass spectrum from an oxidized silicon wafer surface. We can see Si^+, SiO^+, Si_2^+, and Si_2O^+ peaks, indicating Si and O atoms as the major surface components. The bottom panel in Figure 16.33 shows a negative ion mass spectrum of a sucrose film on a silicon substrate. The molecular peak with isotope peaks strongly suggest that sucrose molecules stay on top of the surface.

One of TOF-SIMS’s unique capabilities is elemental/molecular mapping. Currently, most primary ion sources are liquid metal guns, and the primary ion beam can be focused into $\sim 100\,\text{nm}$ diameter so that high lateral spatial resolution image can be provided. Figure 16.34 shows a ZrO^+ ion image and Ni^+ ion image in a fuel-cell electrode, which is composed of micrometer-size yttria-stabilized zirconia (YSZ) grains and nickel oxide grains. From the image, it is easy to distinguish different grains and their relative positions.

TOF-SIMS can also perform depth profiling. However, since the primary ion beam current is very low, a second sputtering beam, which has adequately high current (10 nA to 1 μA), is introduced. This strategy is called dual-beam depth profiling. Compared with the magnetic mass analyzer in dynamic SIMS, dual-beam TOF-SIMS depth profiling has a relatively low sensitivity, normally one to two orders of magnitude lower than that of dynamic SIMS. Nevertheless, this sensitivity is adequate for most depth profiling requirements. At the same time, the function of dynamic SIMS instruments is so specific that only a few semiconductor companies and research institutes use them. Therefore, TOF-SIMS depth profiling is becoming more and more popular in many areas of scientific research.

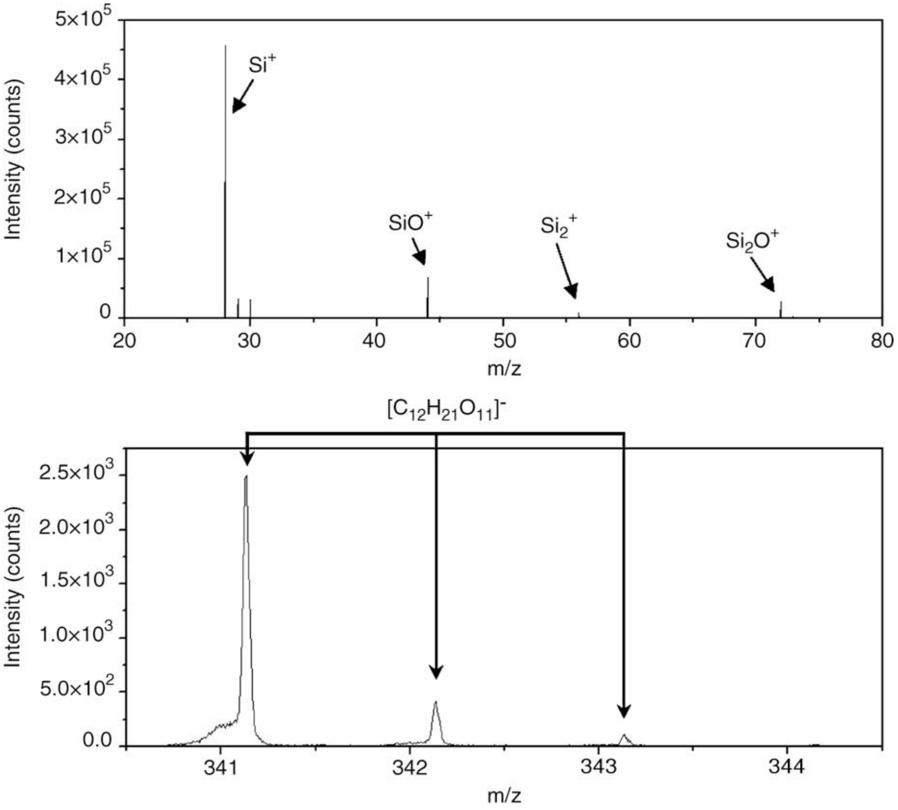

Figure 16.33: Top: positive ion spectrum of an oxidized silicon wafer surface. Bottom: negative ion spectrum of sucrose (cane sugar) film.

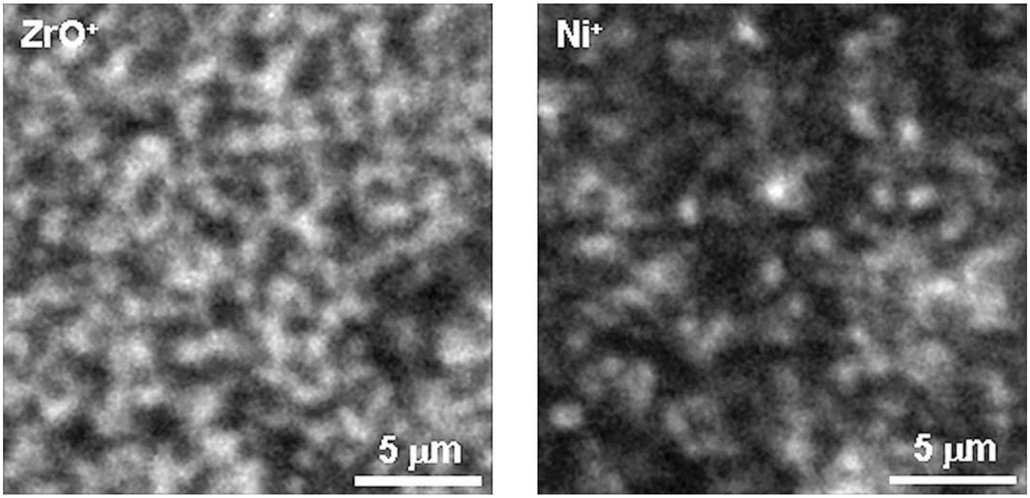

Figure 16.34: SIMS images of a fuel cell electrode which is composed of yttria-stabilized zirconia grains and nickel oxide grains.

Table 16.4: Brief comparison of XPS, Auger, and TOF-SIMS

	Elemental information	Elemental valence state	Molecular information	Elemental sensitivity	Lateral resolution	Quantitative analysis
TOF-SIMS	Yes	No	Yes	< 0.0001%	100 nm	Needs reference samples
XPS	Yes	Yes	No	~ 0.1%	10 μm	Directly
Auger	Yes	Yes	No	~ 1%	10 nm	Directly

XPS and Auger spectrometry are two of the most popular surface analysis techniques, so it is useful to compare TOF-SIMS with them. Table 16.4 shows the relative strengths of these three techniques. From this table, it is easily found that three major advantages of TOF-SIMS are isotope information capability, molecular information capability, and extra-high sensitivity. Two major disadvantages are lack of elemental valence information and inconvenience of quantitative analysis. Therefore, TOF-SIMS is normally used in the following situations:

- if isotope information is required;
- if molecular information is required;
- if element/molecular concentrations are lower then 0.1% or 1%;
- if reasonably high lateral resolution (down to 100 nm) elemental/molecule mapping is required.

In recent years, great developments have been made in biological applications of TOF-SIMS [97]. Cluster ion sources such as Au_n^+, Bi_n^+, and C_{60}^+ have been commercially available and they can enhance organic molecular ion signals by one to three orders of magnitude. In particular, a C_{60}^+ beam can sputter through quite a few organic, polymer, and biological materials without significant damage, so that molecular depth profiling is feasible. It is anticipated that TOF-SIMS applications in biological research will become more extensive during the next decade.

Strengths:

- High isotope sensitivity.
- Provides elemental information with high spatial resolution.
- Widely used technique for elemental mapping and depth profiling in the TOF mode.

Limitations:

- Damages the sample surface (partly avoided by using lower sputter beam currents).
- Lacks quantitative and chemical state information.

16.4.3 Glow Discharge Mass Spectrometry

GDMS involves the sputtering of a sample by ions accelerated from a low-pressure gas discharge (plasma) [98]. Similar to SIMS, the method detects species sputtered from the sample. The method has high sensitivity and dynamic range, but no spatial resolution. It can be considered as one of the most powerful methods for the determination of trace elements analysis and depth profiling in bulk materials or thin films.

Typically, Ar is used at pressures ranging from 10 to 100 Pa and Ar^+ ions are accelerated to the sample with energies of hundreds to thousands of eV. Neutral atoms sputtered from the sample, which serves as a cathode, are ionized by the plasma and the positively charged ions are extracted into a mass spectrometer [99, 100]. Because sputtering and ionization occur at different times and at different locations in the instrument, substrate effects on ion yield (such as occur for SIMS) are minimized, and calibration and quantification are significantly simplified. Consequently, GDMS is a useful tool for the measurement of trace composition and impurities in thin films as well as for obtaining sputter depth profiles. The method has excellent detection limits (from ppm to ppb) and high dynamic range (allowing bulk, trace element, and contamination analysis), and can be used for sputter profiling for flat relatively thick films ($\sim$0.5 to 50 μm).

The depth profile of an Li-doped ZrO_2 film grown on a Si substrate is shown in Figure 16.35 [100]. The main profiles highlight the major elements while an insert shows, in some detail,

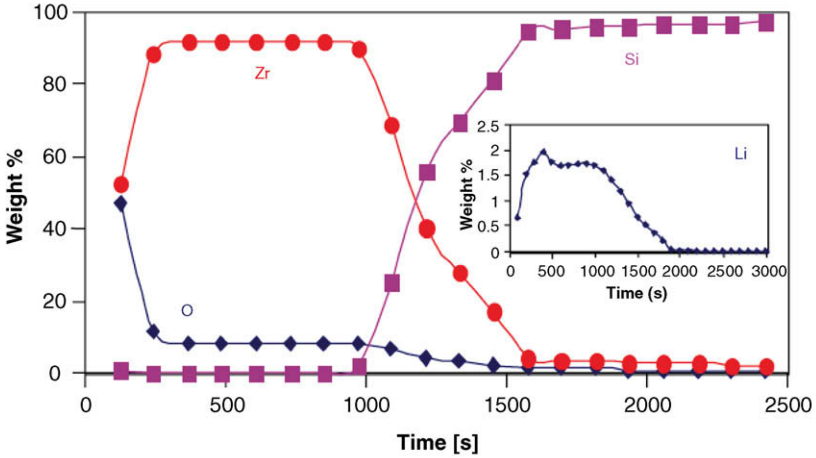

Figure 16.35: The main plot shows a GDMS depth profile for major elements in a thin layer of ZrO_2 deposited on Si and doped with Li. The inset highlights the profile of the Li dopant [100].

the concentration of the Li dopant. Betti and de las Heras conducted these measurements as a part of investigations utilizing GDMS to characterize materials used in nuclear research including B and Li-doped zircalloy cladding materials. The figure shows weight percentage profiles of Si, O, and Zr in the film, interface, and substrate Si.

The applications of SIMS and GDMS have been compared as applied for obtaining depth profiles of hard coatings [101]. The measurements suggest that the resolution for these depth profiles was as good as or better in GDMS as in SIMS.

Strengths:

- Trace element detection in most inorganic materials (all elements except H).
- Depth profiling for flat samples detecting major and trace elements.
- Sensitivity is mostly insensitive to matrix.
- Full element characterization from films, powders, and particulates.
- Equal value for conductors and insulators.

Limitations:

- Vacuum-compatible materials only.
- Not suitable for organics or polymers.
- Not sensitive to sample inhomogeneity.
- Limited depth resolution ($\sim 1\ \mu m$).

16.4.4 Dual-Beam FIB/SEM for Thin Film Analysis

L.V. Saraf

For 3D imaging of surfaces and films and to enable preparation of samples for special types of selected area analysis, it is very useful to combine a FIB (developed from the mid-1970s) [102–104] with an electron gun as part of a dual-beam FIB/SEM system. Such a dual-beam instrument typically contains a liquid metal gallium ion source (LMS) that operates at voltages from 0.5 to 30 kV with a beam size as small as 5 nm, and an electron beam operating at voltages between 0.35 and 30 kV with a beam diameter of nominally 1 nm. In one commercial system, as a specific example, these beam columns are angled at 52° to each other. The focused gallium ion beam provides opportunities for both sample imaging and modification. A dual-beam FIB/SEM has the ability to acquire high-resolution images while modifying a sample surface (often by sputtering) with the help of ions. Standalone FIBs and dual-beam systems have been used for highly efficient selected site TEM sample preparation and in the

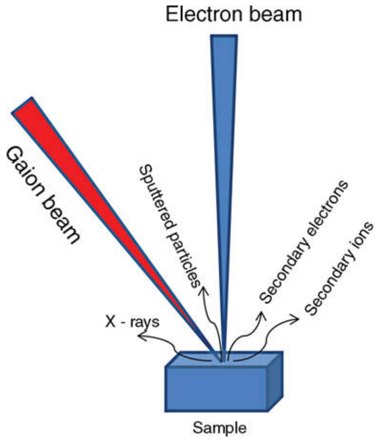

Figure 16.36: A schematic diagram of focused ion beam milling/imaging and scanning electron microscopy imaging process. The diagram shows the two incident beams and types of particles and photons emitted from a sample.

semiconductor industry to fix site-specific defects in integrated circuits [105]. As the field progressed further, additional analysis capabilities were added along with the basic dual beam to create many useful analysis and sample modification possibilities. Newer capabilities include sophisticated sample manipulation, gas-phase injection for material deposition, and analytical capabilities for crystallographic, chemical, and surface analysis. The distance from the end of the electron beam column to a spot where electron and gallium ion beams cross or can be focused together is typically noted by the term 'eccentric height'. Most of the fundamental physics concepts and fundamental understanding that exist for ion–solid interactions associated with medium-energy ion implantation, related cascade collisions [106], and damage created in solids also apply to the FIB/SEM case. The schematic presented in Figure 16.36 shows the layout of a typical FIB/SEM. Many systems have capabilities for electron- or ion-induced EDXS and these can be used for ion and electron beam lithography and ion- and electron beam-induced metal or carbon deposition. FIB/SEM can provide a powerful method for extraction specimen cross-sections for AES or TEM analysis from specific areas.

Two applications of the instruments are highlighted here, namely 3D microstructural analysis ion beam induced imaging.

16.4.4.1 3D Microstructural Analysis

FIB milling of the sample is inherently a damaging process. However, by combining the precise low-energy sample milling with high-resolution SEM image analysis, one can obtain a true shape, size distribution, and crystallography of the materials in three dimensions. In many circumstances analysis using 2D imaging suffers from a lack of important information which can be overcome by 3D analysis. Important information such as number of defects per unit volume, their connectivity, structural phase transformation, and true shape can only be obtained by adding analysis in a third dimension. The FIB/SEM, sometimes combined with electron backscattering diffraction (EBSD), energy-dispersive X-ray spectroscopy (EDXS), and SEM capabilities, can provide a variety of 3D information. Areas as large as 1 mm^3 can be precisely analyzed using this combination [107]. This type of imaging is generally called tomography, which means 'imaging by sectioning'. A high-energy Ga ion beam (30 kV) combined with a fine current (typically in ~ tens of pA) can be used to raster over the desired sample surface area, which results in controlled sample surface material removal due to sputtering. The sputtered depths can be controlled as low as 10–15 nm per slice, which is at least an order of magnitude lower than any mechanically available slicing technique. After every slice, any one of these capabilities (EBSD, EDXS, or SEM) can be utilized to obtain the information related to structural, chemical, and surface morphology. Processing several hundred, up to 1000, frames of data can provide a very accurate picture of the sample, its defects, porosity, and connectivity in the third dimension. The schematic drawing in Figure 16.37 indicates typical sample and beam layouts for a tomography experiment. As shown, the sample is typically tilted to 52°, making the sample surface perpendicular to Ga ion beam. A large area is removed around the region of interest by ion milling, leaving the desired area (as shown) intact. Since the ion beam will slice normal to sample surface, thin sections from the edge are typically sliced all the way to the trench bottom, followed by data collection and SEM imaging from the sliced side of the rectangle. In this way, SEM imaging is done at a

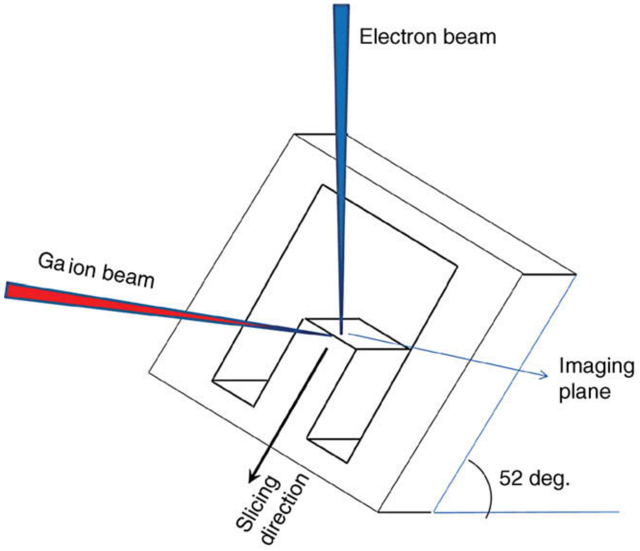

Figure 16.37: Typical sample layout for tomography experiments in FIB/SEM dual-beam system. See text for details.

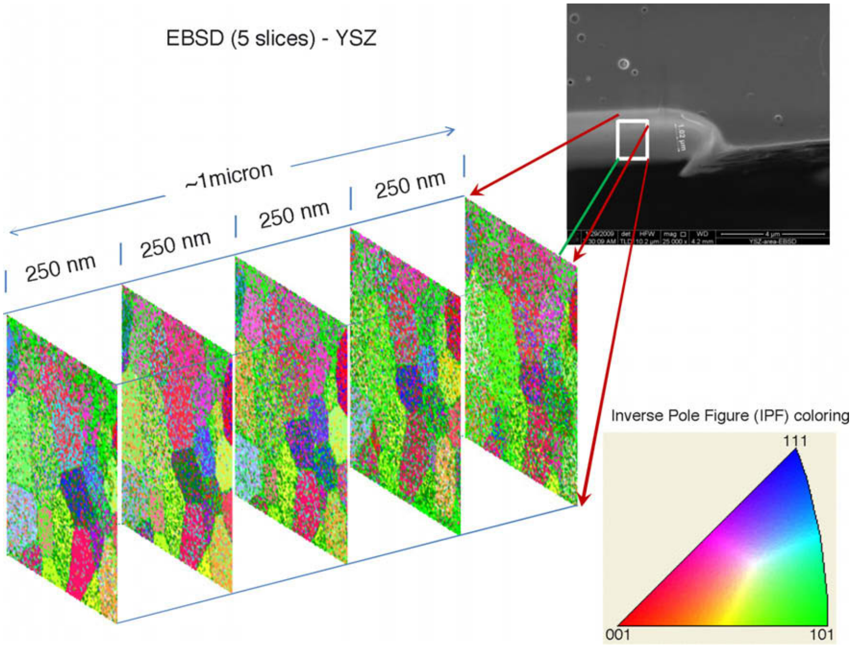

Figure 16.38: Electron backscattered diffraction (EBSD) maps produced after five slices in yttria-stabilized zirconia (YSZ). The slices in YSZ were made by using a focused ion beam (FIB) in a dual-beam FIB/SEM.

38° angle. Advanced image processing software programs typically have the ability to angle-correct image data. If the sample is kept at eccentric height, SEM will image the exact area sectioned by the ion beam. Using this approach for large area sectioning and imaging applications, the overall process gets simpler and faster in modern dual-beam systems [108]. Proper care should be taken while using ion beam-sensitive samples because ion beam-induced damage such as amorphous areas can affect EBSD and other analysis of the data.

An EBSD map produced after five slices in YSZ is shown in Figure 16.38. In this example, inverse pole-figure grain orientation map along the *x*-direction in the case of YSZ (a material frequently used in solid oxide fuel cells) is shown. In general, pole figures in EBSD indicate crystallographic directions in which grains in a polycrystalline material are distributed, whereas inverse pole figures show how grains in a selected direction in the polycrystalline sample are distributed as opposed to the reference frame of the crystal. Since fundamental grain orientation properties are very important in understanding ionic transport behavior in YSZ, an inverse pole-figure map can be important in analyzing transport properties of YSZ (in this case along the *x*-direction). If YSZ is stabilized in a cubic system, there will be 24 symmetric sections where the inverse pole-figure information is repeated. However, for interpretation purposes, information from any one of those 24 symmetric sections can be useful.

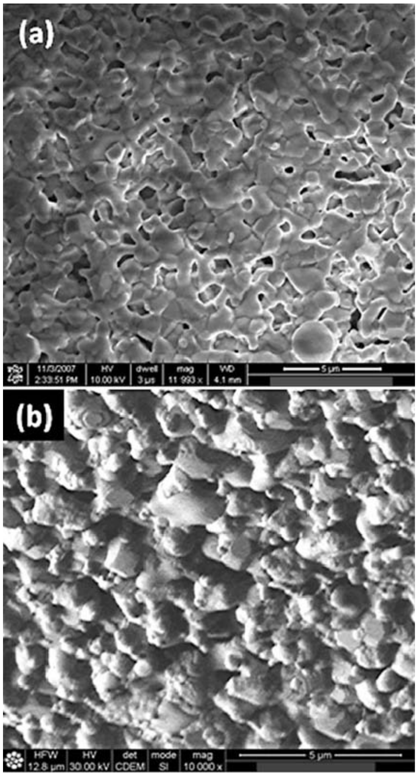

Figure 16.39: An example of Ni-YSZ (a) secondary electron image, and (b) secondary ion image. The secondary ion image provides better grain contrast and morphology.

16.4.4.2 Ion Beam Induced Imaging

Interaction of the gallium ion beam with the sample surface can generate secondary electrons which can be readily used to acquire high-resolution images of the sample. These electrons are generally referred as ion-induced secondary electrons (ISEs) and often provide different image contrasts in comparison to electron-induced images from an SEM. Figure 16.39 shows a comparison between SEM and secondary ion imaging of Ni–YSZ. The ISE process typically generates 1–10 electrons/ion from an ion beam with 5–30 keV energy [109]. These are primarily low-energy electrons which are usually collected from the first few monolayers of the sample. Therefore, the nature of the sample surface, its oxidation and gallium beam-induced surface modifications are heavily expected to affect the rate of electron emission. It is known that gallium ion beam generated from a liquid metal ion source (LMIS) can be focused at most to ~ 7 nm. Since electron beams can be focused well below 1 nm, spatial resolution obtained from focused electron beam source is much better than ion beam source. However, when it comes to imaging the sample surface, ion beams have a unique advantage, in that the contrast produced by changes in sample topography is much better in ion beams as a source than electron beams. This is due to the channeling effects produced by ion beams. Sample topography differences, and orientation of individual polycrystalline or nanocrystalline grains, are expected to strongly affect the imaging contrast. The crystalline surface which is aligned with the direction of ion beam is expected to be channeled by the ion beam and produce low backscattered electrons as opposed to other polycrystalline orientations. Therefore channeled crystal will appear much lighter than surrounding darker grains, if the surrounding grains are oriented in the off-normal axis with respect to the incoming ion beam channeling direction. By using ion beam-induced imaging in conjunction with conventional secondary electron imaging, one can make interpretations about the microstructure and grain-boundary formation mechanisms in any polycrystalline sample. This effect is even more magnified when elements with a high Z value are involved in the analysis.

Strengths:

- 3D analysis.
- High phase contrast ion imaging.
- Selected area sample preparation and extraction.

Limitations:

- Requires vacuum.
- Damages the sample.
- Ga deposition and induced damage.

16.4.5 Sputter Depth Profiles and Sample Thickness Measurements

M.H. Engelhard

In many circumstances, it is important to obtain information about the elemental or molecular distribution of components within a film. It can also be essential to know the thickness of a film or the layers within a film. Sputter depth profiling can be a useful way to address both these requirements. In this section, information is provided both about sputter depth profiling and some methods to determine film thickness. The depth profiling section provides some general background and information about some of the more recent advances and new directions in sputter profiling.

16.4.5.1 Composition Profiles

It is often important to understand the composition profiles of thin films or coatings as they are synthesized, as they age, or when failure occurs. Depending on the thickness and required resolution, a variety of destructive or non-destructive approaches can be used. Ion-induced sputter depth profiling has been found to be very useful for many different applications. Sputter depth profiling has been well reviewed, including several useful reviews by Hofmann

Table 16.5: Typical ions used in common sputter depth profiling methods, with suitable ion energy ranges

Method	Typical ions used	Typical ion energies(keV)	Comments
TOF-SIMS	Cs^+	0.2–10	Detect material removed
	O_2^+	0.2–10	
	C_{60}^+/C_{60}^{2+}	5–40	
Dynamic SIMS	Cs^+/O_2^+	0.5–20	Detect material removed
GDMS	Ar^+	0.3–5	Detect material removed
AES	Ar^+	0.5–5	Detect material remaining on surface
XPS	Ar^+	0.5–5	Detect material remaining on surface
	(some C_{60}^+)		

[110, 111] that examine both general considerations about general aspects of profiling and the methods for obtaining information about interfaces. Sputter profiling can be done by several different methods, including AES, SIMS, XPS, and GDMS. As shown in Table 16.5, there are both similarities and differences among these methods. As highlighted by Hofmann [111], some methods examine material removed from the samples (SIMS and GDMS) while other methods examine material remaining on the surface (AES and XPS). A few factors important to ion sputtering depth profiling are noted below:

- Beam energy, angle of incidence, flatness of the sample, sample rotation, and other conditions significantly impact the rate and overall quality of sputter depth profiles [112, 113]. An example of the impact of sample rotation on resolution of the depth profile of a multilayer NiCr sample is shown in Figure 16.40.
- Higher beam energies usually produce faster sputter rates, but have decreased interfacial resolution.
- AES and SIMS are known as the methods for which sputter profiling has been very common. The development of higher spatial resolution XPS capability has allowed increased use of XPS for sputter depth profiling.
- Many factors influence the interfacial resolution. These include all of the factors listed above for depth profile quality, plus (for XPS and AES) the kinetic energy of the electrons used for elemental analysis. Lower kinetic energy electrons have shorter IMFP and allow increased interfacial resolution [113].
- Among the recent developments in ion sputtering is the increased use of cluster ion beams (C_{60}^+, SF_5^+, etc.) [114, 115]. They are especially useful for depth profiling of organic materials, biological tissues, and polymer materials. As an example, the

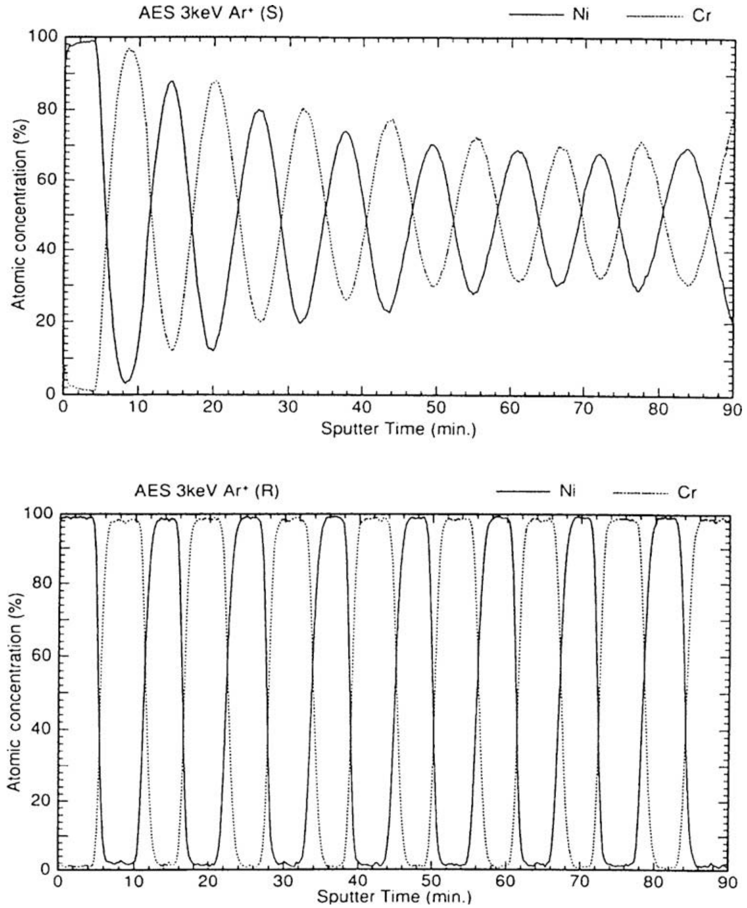

Figure 16.40: Auger electron spectroscopy sputter depth profiles of a NiCr multilayer film (30 nm layers) generated using 3 kV Ar^+ beam with and without sample rotation. The data show that rotation can significantly improve the depth resolution and allow high-quality data to be collected from the sample [113].

differences between Ar^+ and C_{60}^+ sputtering and XPS analysis of plasma-treated ethylene-tetrafluoroethylene-copolymer (ETFE) [116] are highlighted in Figure 16.41. There is little apparent damage with the C_{60}^+ sputtering and almost immediate damage with the Ar^+. In addition, TOF-SIMS experiments shows that molecular information can be preserved after C_{60}^+ sputtering in the ice matrix or trahelose matrix [117, 118]. It should be noted, however, that C_{60}^+ or any form of cluster sputtering does not work ideally in all circumstances and that the impact of sputtering by many types of cluster is subject to a good deal of current research [119]. Seah [120] has proposed a framework for understanding the yield dependence of cluster sputtering depending on the ion mass and atomic number. Mahoney and co-workers [121] have examined the

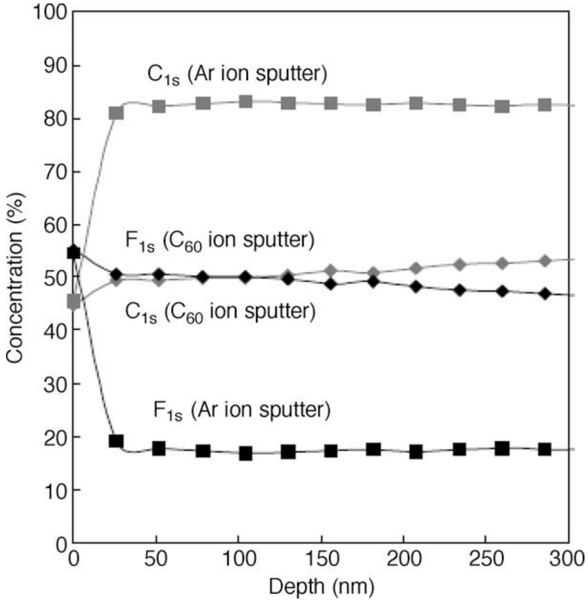

Figure 16.41: XPS sputter profiles generated using Ar^+ and C_{60} sputtering of plasma-treated ethylene-tetrafluoroethylene-copolymer (ETFE). Note that there is a rapid variation in the F and C signals for Ar^+, while the C_{60} ion sputtering is more consistent with expected composition of ETFE [116].

temperature dependence of damage, while Yu et al. [122] suggest that a combination of $C_{60}{}^+$ and Ar^+ sputtering can extend the useful range for sputter profiling organic films.

16.4.5.2 Film Thickness

Many different methods can be used to determine film thickness. The importance of the different methods will vary with the nature and thickness of the films and general comments may not apply in all circumstances. However, some of the common methods to determine thickness are listed in Table 16.6 along with the nominal thickness ranges where they most commonly apply. Some of the issues or concerns related to applying the methods are noted. It is important to realize that some methods require a vacuum and some are destructive.

Particularly for ultrathin films, which are of increasing importance for some electronic materials and other applications, there has been significant work conducted considering the advantages, limitations, and overall consistency of the various thickness measurement methods [123]. It seems particularly important to note that there are apparently some small but systematic offsets among the different measurement methods that fundamentally relate to what

Table 16.6: Nominal thickness ranges for different techniques

Technique	Nominal thickness range	Comments
Ion sputter profile – XPS	3 nm $< d <$ μm	Composition and thickness, destructive
Ion sputter profile – AES	3 nm $< d <$ μm	Composition and thickness, destructive
Ion sputter profile – static SIMS	3 nm $< d <$ μm	Composition, thickness, dopant profiles, destructive
Ion sputter profile – dynamic SIMS	3 nm $< d <$ μm	Composition, thickness, dopant profiles, destructive
Angle resolved XPS	$d <$ ∼10 nm	Composition, thickness, non-destructive, model dependent, requires flat samples
Peak to background XPS	$d <$ ∼10 nm	Composition, thickness, non-destructive, model dependent
TEM	1 nm $< d <$ ∼ μm	Based on cross-section
RBS	0.1 nm $< d <$ ∼ 1 μm	Best for heavy elements on light substrate
NRA – resonant	8 nm $< d <$ 3 μm	H-NRA
NRA – non-resonant	50 nm $< d <$ 3 μm	
ERDA	0.1 nm $< d <$ 500 nm	H ERDA and heavy ion ERDA
MEIS	0.1 nm $< d <$ 0.2 μm	
GDMS	0.5 μm $< t <$ 10 μm	Trace element sensitivity
XRR	5 nm $< t <$ ∼100 nm	Thickness and roughness information
Stylus profilometer	50 nm $< t <$ 500 μm	Measures height variations, needs appropriate edge to determine thickness; provide measure of roughness; stylus usually non-destructive, but varies with material
Optical profilometer	50 nm $< t <$ 500 μm	Opaque sample requirement, needs edge to determine thickness, Estimated roughness analysis, non-destructive

is being measured and how the measurement is understood [124]. Especially for very thin films, knowing about such differences can be important in obtaining a consistent understanding of films.

Strengths:

- Quantitative depth profiles.
- Accurate film thickness measurements.

Limitations:

- Requires vacuum.
- Extensive sample damage.

16.5 Incident Electron Methods

Methods involving incident electrons include Auger electron spectroscopy (AES), scanning electron microscopy (SEM), energy dispersive X-ray spectroscopy (EDXS), transmission electron microscopy (TEM), and electron diffraction (low-energy electron diffraction (LEED) and reflection high-energy electron diffraction (RHEED)).

16.5.1 Auger Electron Spectroscopy

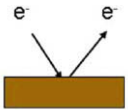

A.S. Lea

Because of its ability to focus an electron beam, AES has the highest spatial resolution of any conventional surface analysis tool. AES has been highly important for electronic materials, analysis of particles and grain boundaries, and for use in obtaining sputter profiles of many types of materials. AES relies on the Auger process to probe the elemental composition of the outermost layers of surfaces. First discovered by Auger and Meitner in the 1920s, the Auger process results from an energetic electron or photon, typically 2–20 keV, stimulating the atom by creating a hole in a core shell through ejection of an ionizing electron [125, 126]. The atom relaxes when an outer shell electron drops down to fill the core level hole and the excess energy is then released by one of two competing processes: through the release of a photon or the release of a third outer shell electron, the so-called Auger electron. Since electron shell energy levels are unique to each atom, the energy of this Auger electron is characteristic of the

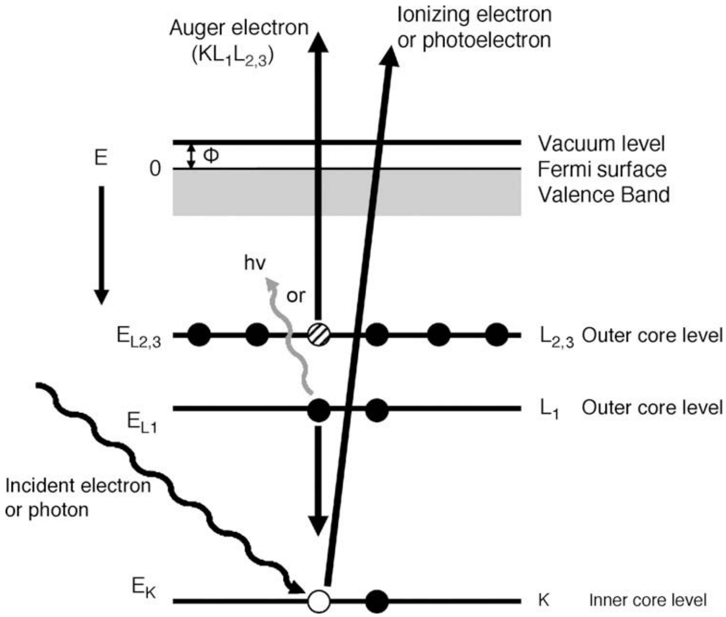

Figure 16.42: Schematic of the Auger process showing that a core shell vacancy in the K level is filled by an electron from a higher energy level and a third electron, the Auger electron, is emitted.

atom from which it originated and depends on the electronic transitions involved. For the process involving the energy levels depicted in Figure 16.42, the kinetic energy of the Auger electron is given by Eq. (16.6):

$$E_{KL_1L_{2,3}} = E_K - E_{L_1} - E_{L_{2,3}} - \phi \tag{16.6}$$

where E_K is the energy of the ionized core-level electron, E_{L_1} is the energy of the outer level electron that drops down to fill the hole, $E_{L_{2,3}}$ is the energy level of the Auger electron, and ϕ is the spectrometer work function, i.e., the energy necessary to promote an electron from the Fermi level to the vacuum level.

While it may appear that a plethora of transitions are possible yielding numerous Auger transitions in the energy spectrum, particularly for high Z elements, only a few occur with sufficient probability that they are visible in the Auger spectra. This minimizes the appearance of overlapping peaks and makes AES spectra relatively easy to interpret. This is due to both the electron-impact cross-section (how easily core holes are created) and the Auger and fluorescence yields. The energy level of the core hole often determines the transitions that will be favored. For a K shell hole, transitions can occur from the L levels, producing strong KLL peaks in the energy spectrum. Higher level transitions, such as those from M levels, may also

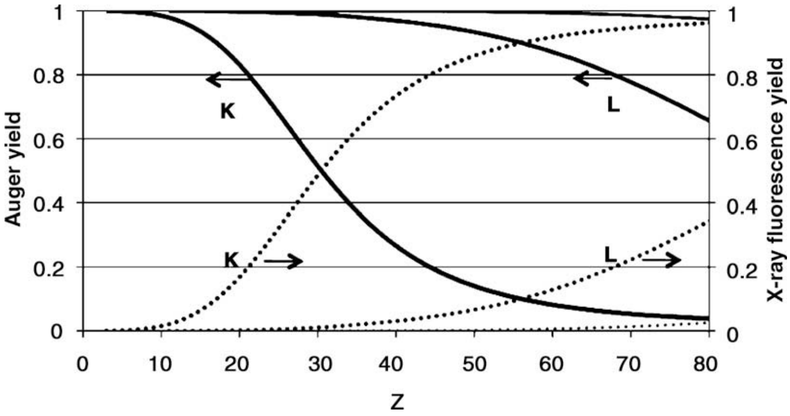

Figure 16.43: Plot of Auger electron emission (solid lines) and X-ray fluorescence (dashed lines) yields as a function of atomic number (Z) for each core shell vacancy using data from Hubbell et al. [127]. AES has good sensitivity for low Z elements.

occur, but are much less likely to do so. The strongest electron–electron interactions are between levels that are close in energy, and this gives rise to the characteristic KLL, LMM, MNN peaks seen in Auger spectra. The probabilities of Auger yield and fluorescence (X-ray) yield for the various transitions are shown in Figure 16.43 [127]. In the case of a K shell hole, the Auger yield is highest for low Z elements, whereas the fluorescence yield is greater for the high Z elements and so AES is much more sensitive to low Z elements than electron probe microanalysis.

The surface sensitivity of AES, as well as the other electron spectroscopies, is due to the low IMFP of electrons. Auger electrons, with kinetic energies ranging from about 30 to 2500 eV, have material-dependent IMFPs (λ) ranging from about 0.2–2 nm. The information depth for AES is $\sim 3\lambda$ and so the Auger peaks visible in the spectra originate from only 0.5–5 nm beneath the surface. While the energetic primary beam can penetrate micrometers below the surface, those Auger electrons that originate at depths below the information depth lose their characteristic energy owing to inelastic collisions and contribute to the background observed in AES spectra. The low IMFP also necessitates the use of ultrahigh vacuum conditions to minimize scattering off residual gas atoms and has the additional benefit of keeping the surface clean from adsorbates that may collect on the surface at higher pressures.

The highly energetic incident electron beam penetrates deep into the sample and initiates an electron cascade, whereby inelastic collision of the primary electrons with surrounding atoms causes these electrons to lose a portion of the primary energy. The energy transfer can also propagate additional electrons through ionization of atoms within the substrate. These mechanisms contribute to the broad featureless background observed in the Auger spectra.

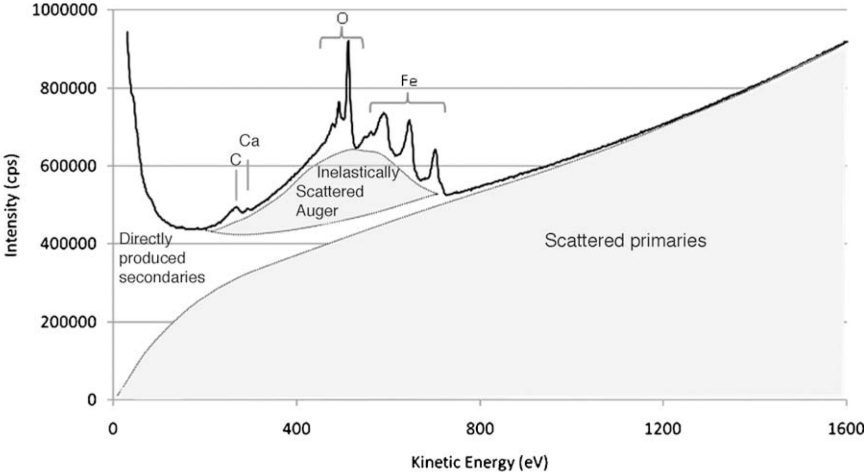

Figure 16.44: Raw Auger spectrum of a natural hematite sample. Shown in the figure are the Auger peaks on top of a large background that must be removed for accurate quantification.

Low-energy electrons emitted from the surface are designated as secondary electrons and are captured by the secondary electron detector, allowing one to obtain SEM images of the surface at high resolution during the AES analysis.

Figure 16.44 shows a plot of a typical Auger spectrum with the Auger peaks superimposed on top of a large background of backscattered primaries, inelastically scattered Auger electrons, and secondary electrons. This large background, while easily removed through differentiation, still limits the sensitivity that can be achieved with this technique.

As seen from Eq. (16.6), the kinetic energy of the Auger electron is independent of the energy of the incident radiation. It is only necessary to impart sufficient energy to the atom to generate an electron hole in a core-level shell. The probability with which this occurs is greatest when the energy of the incident radiation is two to three times the energy of the core shell and so the Auger process is most efficient when the incident radiation is 2–20 keV. Whereas it is possible to utilize either photons or electrons to initiate the process, electron beams are used in most instruments since they are more easily focused than X-rays and can provide higher spatial resolution [128]. While both LaB_6 filaments and field emitters are high-current sources utilized in Auger spectrometers, newer generation instrumentation are migrating towards field emission electron guns through which beam sizes below 20 nm are now achievable. This small beam size combined with the short IMFP provides AES with the smallest analytical volume of any standard surface analysis equipment.

The schematic of a typical Auger spectrometer is depicted in Figure 16.45. In this set-up, electron optics focus the electrons generated from either a field emission source or an LaB_6

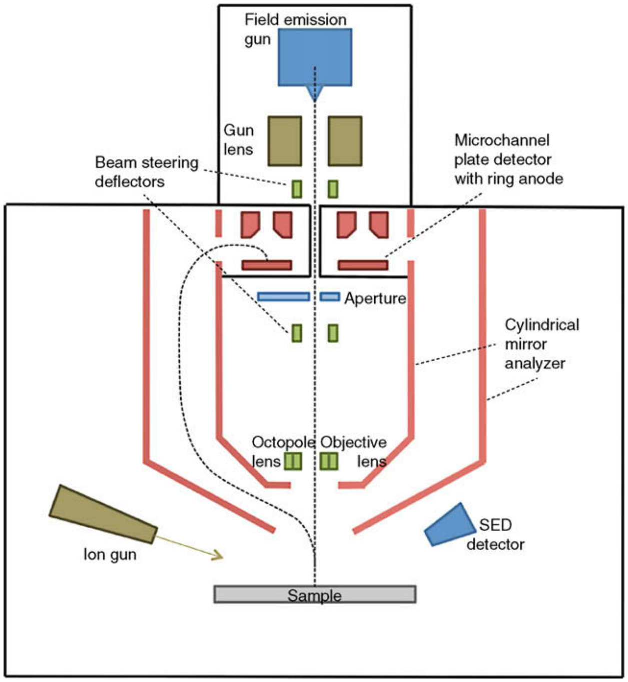

Figure 16.45: Schematic diagram of an Auger spectrometer including the electron gun, focusing lenses, sample, and cylindrical mirror electron analyzer.

filament onto the sample. Electrons produced from the sample enter the coaxial cylindrical mirror analyzer (CMA) and are focused into the electron multiplier and detector. The voltage on the outside plates of the CMA is swept such that at any given time, only electrons that fall within a narrow energy window are able to reach the detector. In this manner, the spectrometer can scan the energy spectrum and measure the intensity of incident electrons as a function of their kinetic energy. The spectrometer is often equipped with an ion source for depth profiling experiments, and in the case of newer generation instruments, charge neutralization. Most spectrometers are also equipped with a secondary electron detector which permits acquisition of high-resolution SEM images of the surface during AES analysis.

As alluded to earlier, the Auger peaks visible in an intensity versus energy [$N(E)$ vs E] spectrum sit on top of a large background of backscattered primary electrons, secondary electrons, and inelastically scattered Auger electrons, and are typically only a small percentage of the total electrons that reach the electron detector. In order to perform quantitative analysis, it is necessary to derivatize the spectrum [$d(N(E))/dE$ vs E] to remove the background and utilize the intensity of the derivatized Auger peaks in the quantification. The underlying equation for quantification is given by Eq. (16.7):

$$\text{Atomic concentration of element } i = (I_i/\text{RSF}_i)\times 100/(\Sigma_i I/\text{RSF}) \tag{16.7}$$

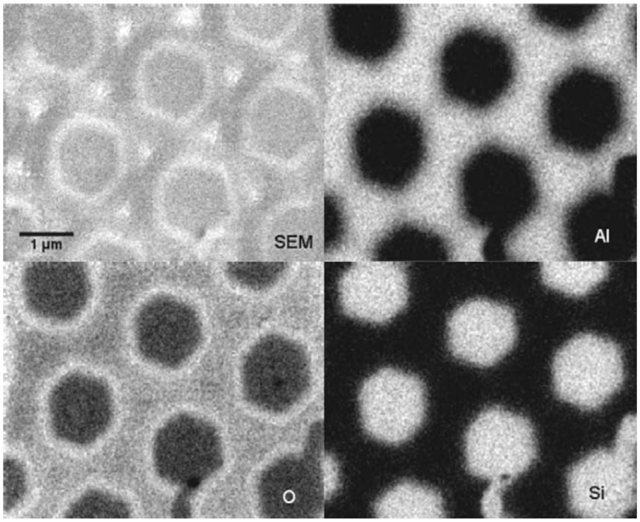

Figure 16.46: AES elemental map of Al patterned onto a Si substrate. This figure highlights the distribution and relative intensities of the elements one can obtain using this technique.

where I_i is the transition-specific peak-to-peak intensity of element i in the derivative spectrum, and RSF_i is the transition-specific relative sensitivity factor for element i. The relative sensitivity factors are either obtained from published data [129, 130] or experimentally determined by the operator using a well-defined set of standards. Equation (16.7) is a relatively simple version of a more complex equation that does not take into consideration the instrument transmission function (sensitivity dependence of the analyzer on the kinetic energy of the electron being detected). It provides an estimate of the actual concentration of the species in the sample. The reader is referred to previous work [131] that describes the methods needed to determine the instrument transmission function required for accurate quantification.

Similar to XPS, the sensitivity of AES is element specific; however, in general, AES has lower sensitivity than XPS. This lower sensitivity is due to the large background upon which the Auger peaks reside. In order to remove the background and provide quantitative information, the spectra are smoothed and differentiated, but this decreases the signal-to-noise ratio. The sensitivity one can obtain using AES ranges from about 0.1 to 5 at.% depending on element, data acquisition time, and the presence of interfering peaks.

Newer generation AES equipment has the capability to produce 2D maps of elemental distribution on the sample surface. By moving the tightly focused electron beam in a raster pattern across the surface and obtaining peak and background intensities for each element of interest, a high-resolution, location-specific distribution of the elements can be generated and correlated to an SEM image of the same location. Figure 16.46 shows one such elemental map for Al patterned onto a Si substrate. This capability is extremely valuable for identifying regions of enrichment or depletion or for samples with an inhomogeneous distribution of elements.

Instruments equipped with ion guns have the capacity to acquire depth-specific concentration profiles. To generate these depth profiles, high-energy ions (typically Ar or O_2) impinging on the sample remove material from the sample surface, producing a sputter crater. By alternating this ion sputtering with Auger electron analysis at the center of the sputter crater, one can obtain depth-specific information about the presence of elements and their abundance. It is necessary, however, to calibrate the rate of material removal in the sputtering process to get accurate depth calibration. This is typically done using standards of known thickness (such as thermally oxidized SiO_2 on a silicon wafer), although it should be pointed out that different materials have different, though not too dissimilar, sputter rates.

While AES provides quantitative information about the concentration and distribution of elements on the surface of the sample with high resolution and is useful for analysis of nanoscale materials with little sample preparation, there are some limitations to the technique that should be mentioned here. Foremost, since this technique utilizes highly energetic electrons as the primary beam and generates backscattered primary, secondary, and Auger electrons, any sample that is not conducting (or at least semi-conducting) is subject to charge accumulation. This accumulation of charge at or near the sample surface may either shift the characteristic energy of electrons leaving the surface (either slightly or dramatically) and/or change the energy and position of the incident electron beam, which in many cases does not allow one to obtain valuable Auger spectra [132]. Small insulating particles or films generally can be analyzed, but bulk, insulating materials with high resistivity can be problematic. There are procedures in place to lessen this charging effect (such as sample masking, sample tilting, changing primary beam energy, using low-energy ions) [133], but in some cases even these methods are inadequate and utilization of other surface analysis techniques is advised. In addition, electrons have a short IMFP and readily impart some of their energy to neighboring atoms as they propagate through the sample. This can result in damage to the sample, particularly for organic materials, through a number of mechanisms including bond scission, desorption, and sample heating [25]. This can become problematic if the sample changes its composition on the time-scale that is necessary to perform the analysis or if subsequent analyses using a different technique are to be performed.

Strengths:

- Highest spatial resolution surface analysis instrument.
- Quantitative elemental concentrations.
- All elements other than H and He can be detected.
- Surface sensitive.

- Elemental mapping.
- Depth profiles.

Limitations:

- Charging of bulk insulating materials can prevent EDS and EBSD analysis.
- Limited ability to obtain chemical information.
- Electron beam can damage sensitive materials.
- High background due to inelastic electron scattering.

16.5.2 Scanning Electron Microscopy

B.W. Arey

A scanning electron microscope images the topography and structure of a sample by collecting secondary or backscattered electrons created by scanning the sample with a focused electron beam, the energy ranges from 100 eV to 30 keV. The resulting images can be collected at very high magnification to provide a great deal of information about surface topography. The incident beam also excites characteristic X-rays which can be used to collect elemental information about the sample using energy or wavelength dispersive X-ray detectors.

When an electron strikes the surface some electrons are backscattered (and have energies similar to the incident beam), some lower energy secondary electrons are excited (< 50 eV), a few Auger electrons are produced (Section 16.5.1), and characteristic X-rays are excited (Figure 16.47). Using different types of detectors each of these types of electrons or photons can be used to create images or determine other information about samples. A simplified drawing showing components of a scanning electron microscope is shown in Figure 16.48.

Secondary electron imaging shows the topography of surface features a few nm across. Films and stains as thin as 2 nm produce images with adequate contrast. Materials are viewed at

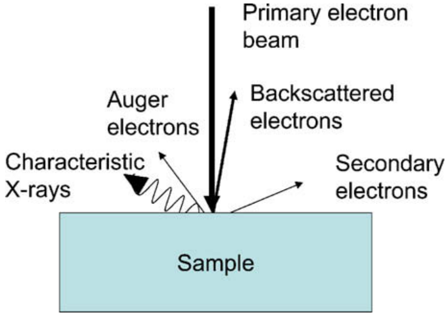

Figure 16.47: Schematic drawing showing types of electrons and photons produced when an electron beam interacts with a solid sample.

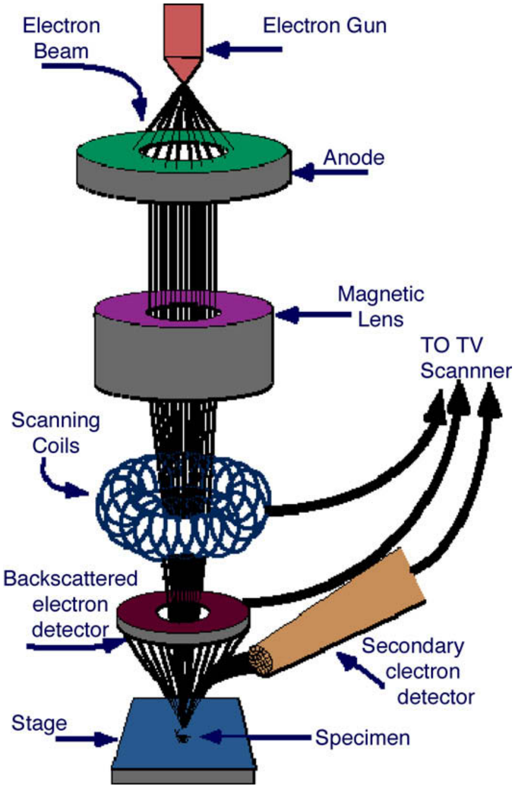

Figure 16.48: Schematic of SEM components. Note that there are detectors for secondary electrons (< 50 eV) and for elastically backscattered electrons which have energies approximately equal to the incident electrons. Other detectors can be added for X-rays or Auger electrons. (With permission from Prof. S. Chumbley, http://mse.iastate.edu\microscopy\path2.html.)

useful magnifications up to 800,000× without the need for extensive sample preparation and without damaging the sample. Thickness of thin films can be determined using SEM micrographs. As an example, we used SEM to determine the thickness of an ion beam sliced $SrTiO_3$ film. In this work we used 40 keV H^+ ions followed by subsequent annealing [134]. The SEM micrograph of this film is shown in Figure 16.49.

Backscattered electron imaging highlights the spatial distribution of elements or compounds with different atomic number within the top micrometer of the sample. Features as small as 10 nm are resolved and composition variations of as little as 0.2% can be measured.

EDXS can be used to identify the elemental composition of materials imaged in a scanning electron microscope for all elements with an atomic number greater than boron. Most elements are detected at concentrations on the order of 0.1%. As the electron beam of the SEM is scanned across the sample surface, it generates X-ray fluorescence from the atoms in its path.

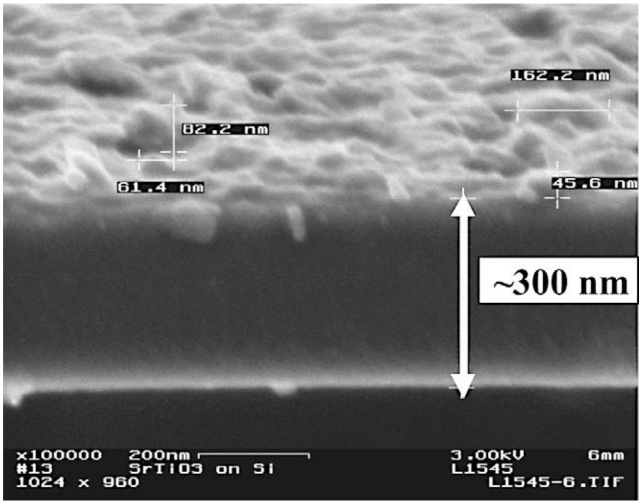

Figure 16.49: SEM micrograph of H^+ irradiated and 570 K annealed $SrTiO_3$ [134].

The energy of each X-ray photon is characteristic of the element that produced it. The EDXS microanalysis system collects the X-rays, sorts and plots them by energy, and automatically identifies and labels the elements responsible for the peaks in this energy distribution. The drawback of using EDXS on thin films is the interaction volume, the amount of material excited by the incident electrons, which extends from all of the volume of the film material and well into the substrate. Although the electron beam size may be as small as several nm, the diameter of material excited is proportional to the depth of the material excited, which can be a micrometer or so, depending on the energy. To reduce this, one can reduce the accelerating voltage or tilt the sample. There will be some interaction with bulk material but the effect can be minimized.

EBSD is a technique which allows crystallographic information to be obtained from samples in the scanning electron microscope. In EBSD a stationary electron beam strikes a tilted crystalline sample and the diffracted electrons form a pattern on a fluorescent screen. This pattern is characteristic of the crystal structure and orientation of the sample region from which it was generated. The diffraction pattern can be used to measure the crystal orientation, measure grain boundary misorientations, discriminate between different materials, and provide information about local crystalline perfection. When the beam is scanned in a grid across a polycrystalline sample and the crystal orientation measured at each point, the resulting map will reveal the constituent grain morphology, orientations, and boundaries. These data can also be used to show the preferred crystal orientations (texture) present in the material. A complete and quantitative representation of the sample microstructure can be established with EBSD. In the past 10 years EBSD has become a well-established technique for the scanning electron microscope, and obtaining crystallographic information from samples is now both routine and easy.

Strengths:

- Electron imaging of microstructures.
- Elemental analysis and mapping.
- Electron backscattering for heavy element analysis.

Limitations:

- Requires vacuum.
- Bulk sensitive.
- Electron beam can damage the sample.
- High background due to Bremsstrahlung irradiation.
- EDXS analysis is semi-quantitative.

16.5.3 Methods Related to Transmission Electron Microscopy (TEM, AEM, HRTEM, STEM, EELS)

C.M. Wang

Although TEM can be viewed as a high-resolution imaging tool that uses electrons as an illumination source [135–141], electron microscopes are multitechnique instruments that can provide a wide variety of information about thin films and many other types of specimens. The information may include sample morphology, structure, grain size, chemical composition, and composition distribution. Based on diffraction limit, the imaging resolution, as a rule of thumb, equals approximately half of the wavelength of the illumination light. Electron beam accelerated by 200 kV potential corresponds to a wavelength of ~0.0025 nm. Consequently, TEM will provide much higher imaging resolution than an optical microscope. It should be noted that image resolution is not at the theoretical limit because of lens aberrations, as illustrated below.

In a very simple terms, a transmission electron microscope is structured much like an optical microscope, consisting of four essential parts: (1) an electron gun, which generates and accelerates the electron beam (light source); (2) a condenser lens, which manipulates the electron beam from the electron gun; (3) an objective lens, which is the first lens to take over the information following the interaction of the electron beam with the thin section of the specimen; and (4) an image recording system, such as an image plate and CCD. Since the invention or demonstration of the first functioning transmission electron microscope by Ernst von Ruska and his colleagues in Berlin around 1934 [142], TEM has gone through a

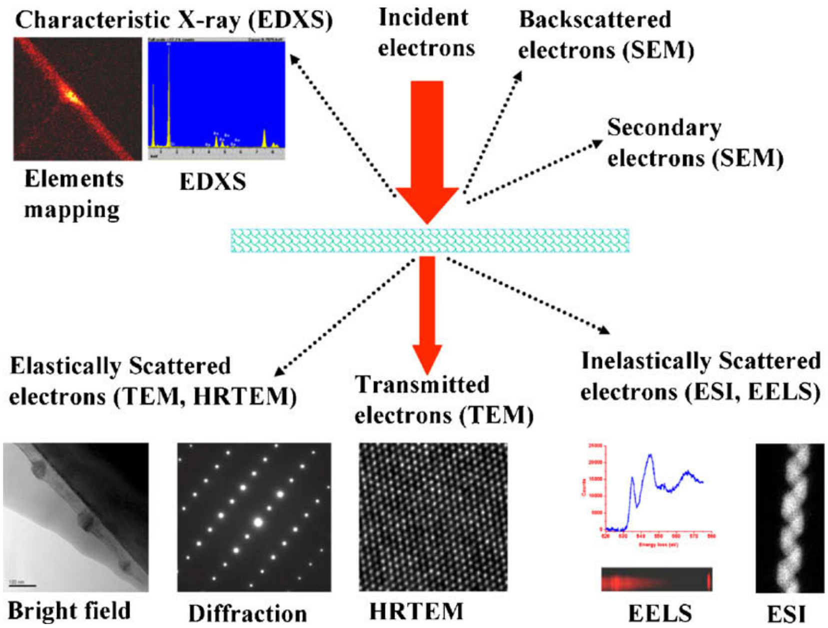

Figure 16.50: Schematic drawing showing the interaction of electrons with a thin section of specimen and the signals that are used either for formation of image or spectroscopy.

tremendous evolution in both the instrumentation and imaging modes based on the physics of the interaction of electrons with the specimen. At least in part, the different development paths account for the many terminologies that are applied to different aspects of TEM. For example, if the chemical composition analysis capability is emphasized, the technique is termed analytical electron microscopy (AEM). If the diffraction contrast and low magnification imaging capability are emphasized, it is normally termed conventional transmission electron microscopy (CTEM). If the phase contrast and lattice structural image are emphasized, it is normally termed high-resolution transmission electron microscopy (HRTEM). If a focused beam is scanned over the specimen, this is known as scanning transmission electron microscopy (STEM). If the signals related to inelastic electron scattering process are collected, this leads to the techniques of energy-dispersive X-ray spectroscopy (EDXS) and electron energy-loss spectroscopy (EELS). Generally speaking, the terminology is associated with how the electron source/beam is generated, how the electron beam is manipulated, and/or what kind of signal is collected following the interaction of the electron beam with the specimen. The interactions of the electron beam and the signals that relate to each of these terminologies are summarized in Figure 16.50.

Electron sources can be generally divided into three types: (1) the thermionic gun, which relies on heating up of a filament to reddish-hot to obtain electrons; therefore the electrons have a typical energy spread of ~ 1.5 eV; (2) the cold field emission gun, which is based on applying a strong electric field to a filament tip to extract electrons; this kind of source typically yields electrons with an energy spread of ~ 0.3 eV; and (3) the Schottky field emission gun, which is a thermally assisted field emission gun and yields electrons with energy spread of typically ~ 0.8 eV. Among these three types of electron guns, the Schottky field emission gun normally has the highest brightness and is widely used in modern TEM as well as SEM. The electrons from the electron gun are accelerated with a potential typically in the range of 80–300 kV (for some special microscopes it has an acceleration voltage of 400 kV and 1200 kV) in the lens columns.

The condenser lens in a microscope is normally composed of several electromagnetic lenses and the essential role of the condenser lenses is to allow the operator to control electron beam characteristics such as beam diameter/size, convergence angle of the beam, and current density of the electron beam. One of the important and challenging aspects associated with TEM is the specimen, which must be thin enough to allow the transmission of the electron beam with an acceleration voltage ranging from 80 to 400 kV. A typical thickness of a TEM specimen can range from several nanometers to ~ 1000 nm. Methods to make such thin material sections for TEM are a field of art, science, and technology which will be briefly described in the subsequent paragraphs.

With a stationary ray of electron beam impacting a thin section of specimen, a significant portion of the electron beam will transmit through the thin section of the specimen. When an objective lens focuses the electrons emerging from the bottom surface of the sample, the images can be magnified. This occurs for TEM, CTEM, and HRTEM imaging and is schematically illustrated in Figure 16.51. The figure illustrates the basic concepts, the physics, and the mathematical treatment on the formation of the image in HRTEM. As with any kind of imaging tool some type of contrast is needed to generate an image. In this imaging configuration there are three types of contrast mechanisms: (1) mass thickness contrast originates from the differences in the scattering of electrons by the nuclei of the elements. This contrast mechanism leads to a high Z element appear darker than a low Z element in the bright field (BF) image if they have the same sample thickness; (2) diffraction contrast is controlled by the crystal structure and orientation of the crystal with respect to the electron beam. This mechanism is conveniently controlled by the use of objective aperture at the back focal plane of the objective lens. If the transmitted beam is used to form the image, this is called the BF image. If only a diffraction beam is selected to form the image, it is called the dark field (DF) image; (3) phase contrast arises whenever more than two beams are used to form the image. An HRTEM image is a typical phase-contrast image.

During STEM imaging, a focused electron beam is scanned point by point over a thin section of the specimen and electrons transmitted through the specimen are collected. The basic concepts, physical principles, and mathematical treatments of the STEM imaging are shown in Figure 16.52. If the directly transmitted beam is collected, it is called a STEM-BF image. If electrons scattered to higher angles are collected, it is called a STEM-HAADF image (where

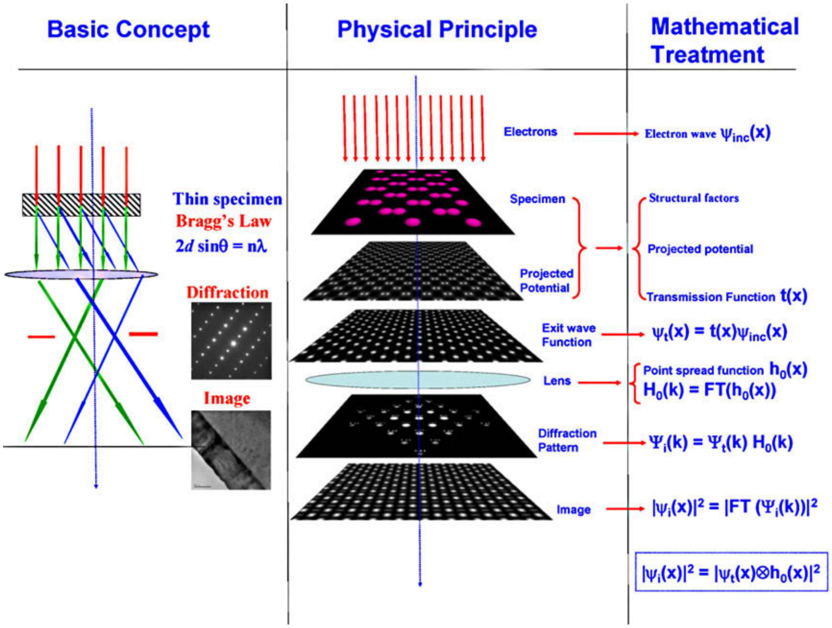

Figure 16.51: Schematic drawing showing the basic concept, physical principle, and the mathematical treatment of the formation of an HRTEM image. FT: Fourier transform.

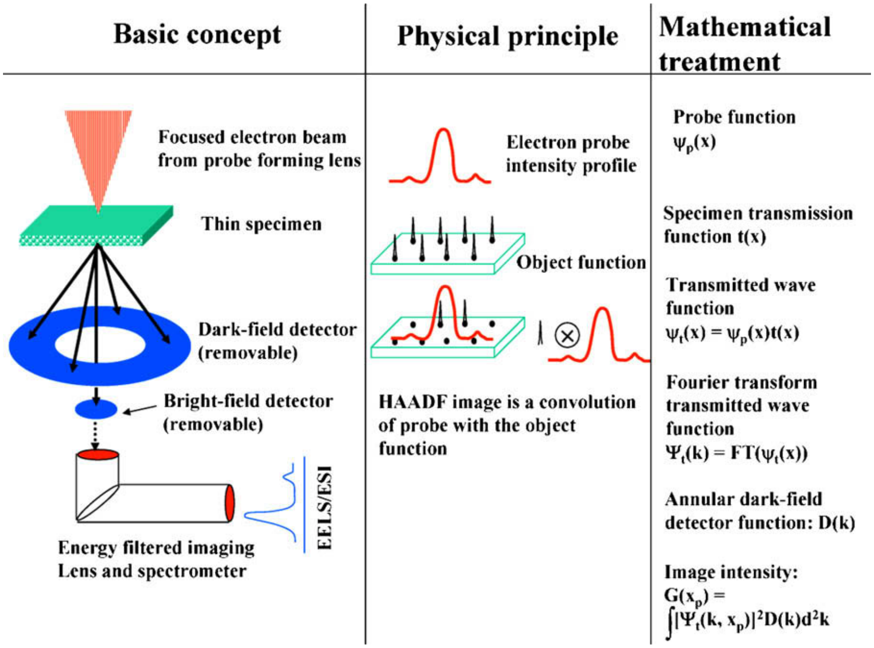

Figure 16.52: Schematic drawing showing the basic concept, physical principle, and the mathematical treatment for the formation of an STEM image. FT: Fourier transform.

HAADF means high-angle annular dark field) image. In STEM-HAADF imaging, the image intensity is approximately proportional to the square of the atomic number (termed Z-contrast imaging). Z-contrast imaging allows heavy atomic species to be visualized directly from the image contrast features [143].

High-energy electrons transmitted through a thin TEM specimen will be both elastically and inelastically scattered by the atoms in the material. Acquiring the chemical composition of the specimen based on the analysis of the signals related to the inelastic scattering of the electrons by the specimen is normally referred to as AEM (such as EDXS and EELS). Chemical composition analysis based on the measurement of characteristic X-rays from each element is called EDXS and is frequently used to detect the chemical composition of the specimen for elements heavier than boron.

Analyzing the energy lost by some of the electrons after the interaction with the specimen is known as EELS, as schematically illustrated in Figure 16.53. EELS is not only a tool for chemical composition analysis, but can yield chemical bonding information. In principle, one of the inelastic scattering processes is the excitation of the core electron to the unoccupied energy level, which is a process governed by the quantum dipole selection rule, $\Delta l = \pm 1$, with l being the angular momentum quantum number. Similarly to the X-ray absorption process, which can be divided into X-ray absorption near-edge structure (XANES) and extended X-ray absorption fine structure (EXAFS), EELS can also be divided into two sections: energy loss near-edge structure (ELNES) and extended electron energy loss fine structure (EXELFS). Therefore, the information obtainable with XANES can be similarly obtained using ELNES, and at the same time, ELNES has the advantage of high spatial resolution such as analysis of chemical composition from one atomic column to the next. The ELNES feature in essence maps out the unoccupied density of states with a specific angular momentum quantum number. For example, if a K-edge EELS spectrum is recorded, that will give the density of states

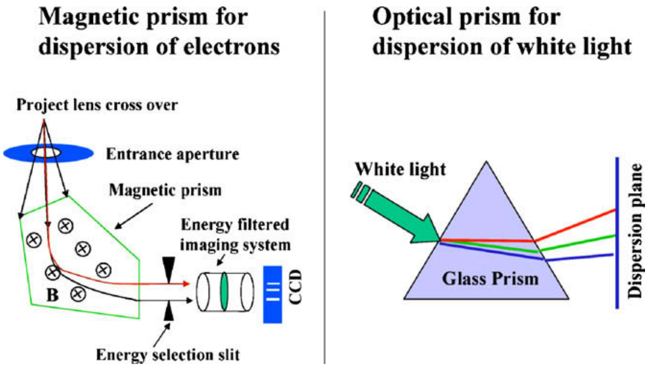

Figure 16.53: Schematic drawing showing the operating principle for the acquisition of electron energy-loss spectra with the spectrometer post-column attached to a TEM (left panel), which is analogized by the dispersion of a ray of white light by an optical prism (right panel).

related to unoccupied p-states. ELNES is an ideal tool for verification of first principle calculations of density of states. ELNES can be used to extract information related to the local bonding/coordination environment, and the valence state of the absorbing atoms with a spatial resolution of a single atomic column. EELS fine structure features are critically influenced by the energy resolution of the whole system. One way to increase the energy resolution of EELS is to reduce the energy spread of the primary electron beam. This can be accomplished using an electron monochromator.

An electromagnetic lens is not an ideal lens and is therefore subject to aberrations. It is the lens aberrations that limit the resolution of the HRTEM and STEM imaging as well as the capability for high spatial chemical composition analysis. Two types of aberration are of particular importance: spherical aberration and chromatic aberration [144–146]. It has been known for a long time that magnetic lens aberration can be corrected using a multipole magnetic lens. However, owing to difficulties related to the precise alignment of each part, a usable corrector was not built until 1998. The development of fast computing capabilities and computer-controlled alignment has led to dramatic developments over the past decade, enabling aberration correctors to be developed for TEM and STEM. All such correctors are based on assemblies of multipole magnetic lenses to compensate the phase shift of the electron waves. For TEM imaging, the aberration corrector corrects the objective lens aberration and thus makes the HRTEM image with sub-Ångstrom resolution. For STEM imaging, the aberration corrector corrects the electron probe forming lens aberration and thus makes the formation of electron probe with a size of sub-Ångstrom possible. Overall, a combination of lens aberration corrector and electron monochromator will lead to sub-Ångstrom spatial resolution for imaging and $\sim 0.2\,\text{eV}$ energy resolution for EELS [147].

With much improved high-spatial and high-energy resolution, tremendous progress has been made on the extension of aberration-corrected TEM and spectroscopy to the analysis of materials at or near realistic environmental conditions: the aberration-corrected environmental transmission electron microscope (ETEM). The ETEM offers the capability of studying the key issues of scientific/technological interest, including the real-time observation of catalytic processes, phase transformation, phase nucleation and growth, mass transport and coarsening processes across the domain of solid–gas, solid–solid, and solid–liquid, and oxidation and reduction processes at elevated temperature and pressure.

Thin sections for TEM can be prepared by a range of methods involving a variety of specialized tools. These methods include one or a combination of the following steps: microtoming, mechanical polishing, dimpling, electropolishing, tripod polishing, ion-beam thinning, and FIB cutting. FIB cutting is a relatively new and very well-controlled way for the preparation of TEM specimen, especially if one seeks a site-specific sample preparation. However, one of the drawbacks associated with the FIB-prepared TEM sample is the ion beam damage and the contamination of the specimen by both the Ga ion and the Pt coatings. For thin film analysis, the structure of the thin film as well as the interface structure between the film

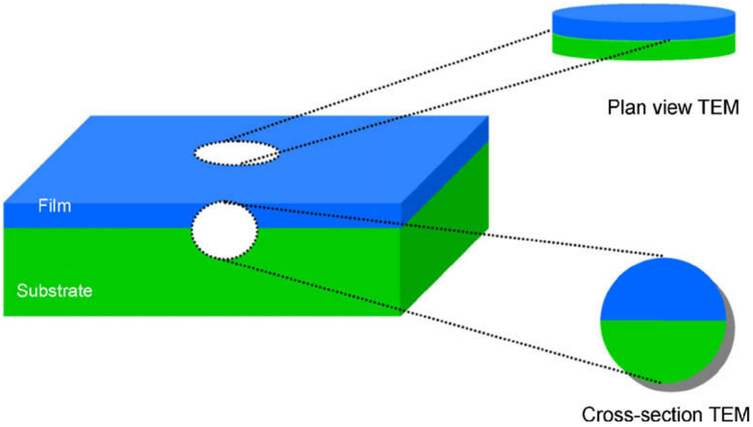

Figure 16.54: Schematic drawing showing preparation of thin section of TEM specimen from a sample with a thin film deposited on a substrate. The specimen can be prepared both either cross-sectional view or plan view. A cross-sectional specimen can be prepared from different directions to observe the specimen through different zone axes.

and the substrate can be analyzed either in plan view or in cross-sectional view as schematically illustrated in Figure 16.54. Two optical images showing two thin-section TEM samples are presented in Figure 16.55. One sample was prepared by dimpling of a thin section with a thickness of about 100 μm, followed by Ar ion beam thinning to obtain perforation at

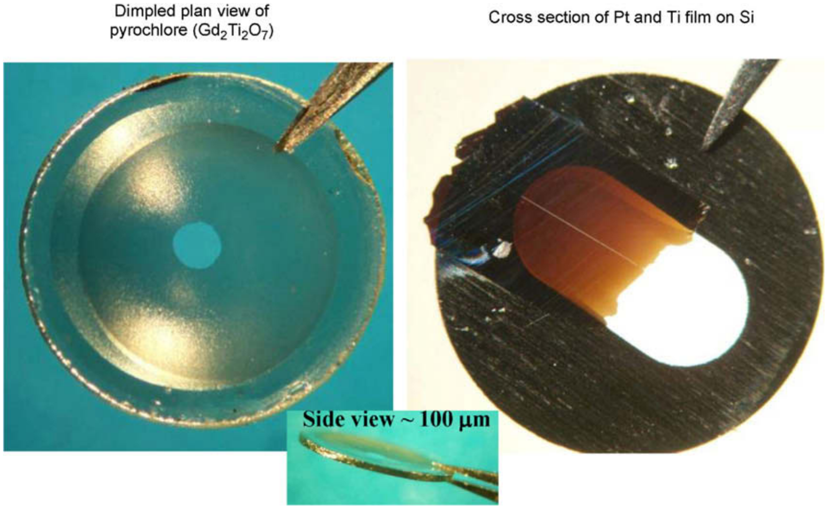

Figure 16.55: Optical images of two TEM specimens. Left: The sample is prepared by dimpling and followed by ion beam thinning to make the perforation at the center of the specimen. Note that the diameter of the specimen is 3 mm and the side view shows the thickness of the sample at the outer rim as ~100 μm. Right: The image shows a cross-sectional TEM sample mounted on a molybdenum ring. The sample was prepared by tripod polishing. The central bright line is due to the glue used in making the sample.

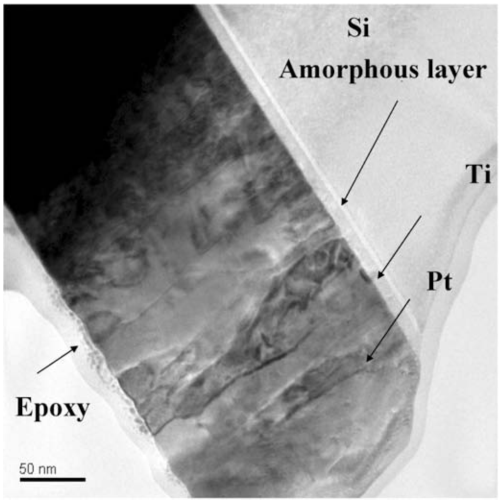

Figure 16.56: Cross-sectional TEM image of the Pt/Ti metal film coated on Si. Note the amorphous layer of silicon oxide sandwiched between the crystalline Si and the Ti film. This image shows that the mass-thickness contrast mechanism resulting in much darker contrast from Pt film. Note that the internal features within the Pt film are also revealed by the diffraction contrast mechanism.

the center of the disk. Another cross-sectional TEM specimen with Ti/Pt metal film deposited on Si was prepared by tripod wedge polishing followed by slight Ar ion polishing.

16.5.3.1 Examples

In this section, we provide specific examples that relate to thin film analysis. A bright field cross-sectional view of Pt and Ti metal films coated on a Si wafer is shown in Figure 16.56. In the image the Pt film appears darker than the Ti film, owing to the high Z of Pt relative to Ti (z contrast mechanism). Fine structural contrast features in the Pt film are related to diffraction contrast and show that the Pt film is not a single crystalline film.

A cross-sectional TEM image showing a thin film of TiO_2 anatase deposited on an LAO ($LaAlO_3$) substrate is shown in Figure 16.57 [148]. This bright-field TEM reveals the existence of TiO_2 rutile inclusions in the thin film and selected area electron diffraction (SAED) can be used to determine the relative orientation of these inclusions with respect to the film as well as the LAO substrate.

A combination of bright-field images, dark-field images, and SAED can also be used to illustrate fine structural features. This is vividly illustrated in Figure 16.58 for the case of multilayer alternating thin films of CeO_2 and ZrO_2 deposited on YSZ. The dark-field image reveals the defective structural nature of the film, while the diffraction pattern clearly demonstrates that all the film layers are in good epitaxial relationship. EDXS elemental

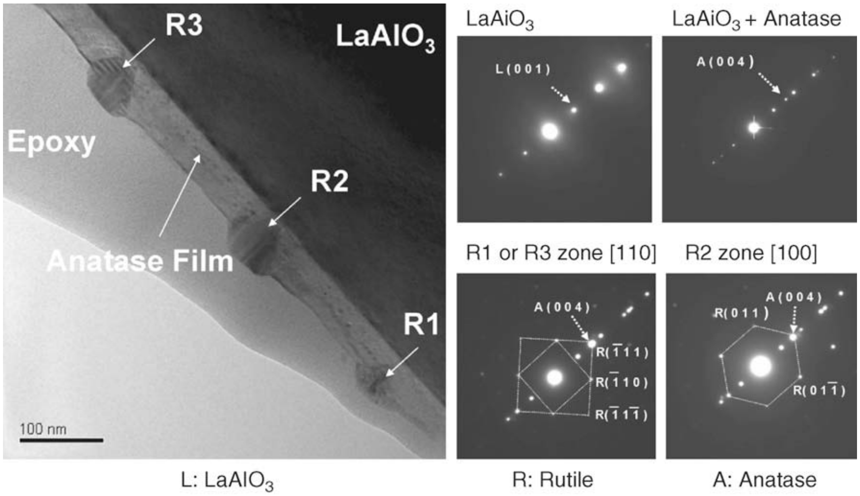

Figure 16.57: Cross-sectional TEM image of anatase film deposited on $LaAlO_3$ substrate. Note the formation of rutile inclusions in the anatase film. Electron diffraction was used to identify the relative orientation of the rutile inclusion with respect to the anatase film. R3 and R1 have the same orientation, while R2 possesses another orientation with respect to the anatase film [148].

mapping can also be used to map the distribution of the elements in the film and this is demonstrated in Figure 16.59 for the case of the multilayer films shown in Figure 16.58 [149].

For thin films deposited on a substrate, the TEM sample can be prepared both in a plan view and in a cross-sectional view. Figures 16.60 and 16.61 illustrate such an example for the case of Fe_2O_3 film deposited on Al_2O_3 substrate [150]. The interface structure is observed in the cross-sectional view using HRTEM imaging (Figure 16.60). Interface periodic mismatch dislocations can be clearly seen and the Burgers vector of the dislocation can be determined based on the HRTEM imaging. For the plan-view imaging, owing to the isostructural nature of both Fe_2O_3 and Al_2O_3 and lattice constant differences, the Moiré pattern dominates the image contrast (Figure 16.61). The distribution of the dark contrasted dots represents the distribution of the interface mismatch dislocations across the whole interface. The power of STEM-HAADF Z-contrast imaging on the direct revealing of the interface structure across a film and the interface is illustrated in Figure 16.62, for which TiO_2 was deposited on LAO. Because the STEM-HAADF image contrast is directly related to Z^2, the large Z element will appear as a bright dot. Therefore, the La column will be much brighter. This contrast provides a way to judge the interdiffusion of atomic species between the film and the substrate. Apparently, the interface is very sharply defined for the case of TiO_2 on LAO. The single atomic column imaging power of STEM-HAADF is also clearly demonstrated for the case of

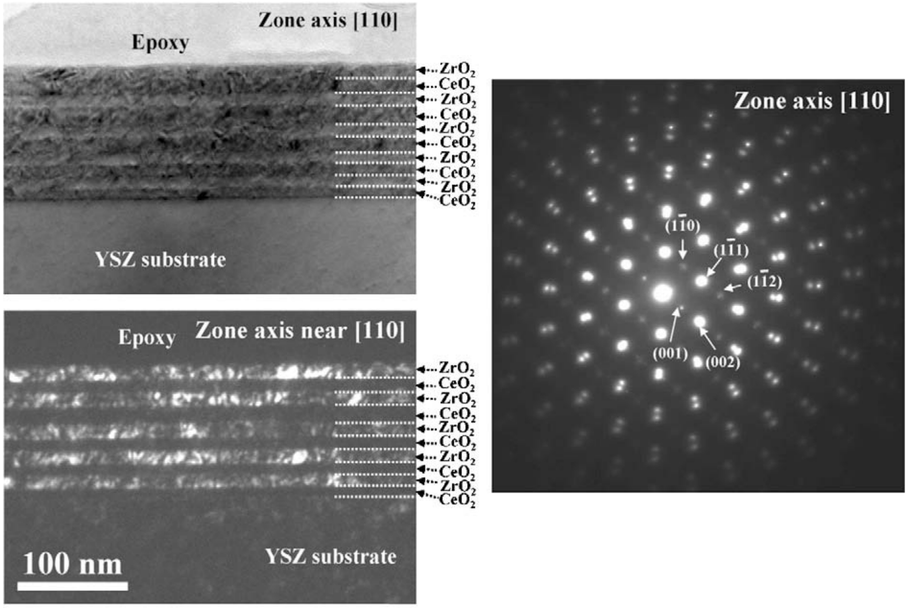

Figure 16.58: Cross-sectional TEM image of alternating ZrO$_2$/CeO$_2$ films deposited on YSZ substrate. The layered structured was revealed by both bright-field (left top) and dark-field (left bottom) images. The epitaxial orientation relationship is revealed by the selected area electron diffraction (right) [149].

Au implanted into MgO substrate, as shown in Figure 16.63, through vacancies produced by Au irradiation in MgO. HAADF-STEM imaging provides direct evidence on the clustering of vacancies in excess of Au atoms to form quantum antidots at the immediate neighborhood of the Au clusters, leading to a spatially associated Au nanocluster and the quantum antidots. The antidots show a terraced layer structure and are typically faceted along MgO(100). Figure 16.63 also directly reveals that Au atom substitutes for the Mg atom lattice position [151].

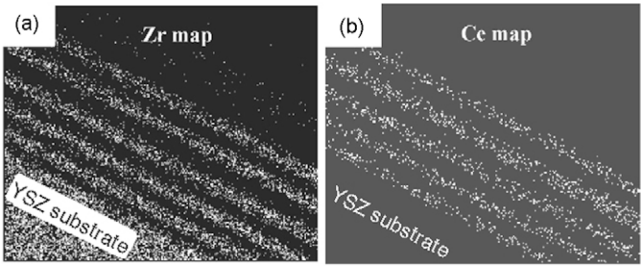

Figure 16.59: Cross-sectional TEM EDXS elemental mapping showing the Zr and Ce distribution in an alternating ZrO$_2$/CeO$_2$ films deposited on YSZ substrate [149].

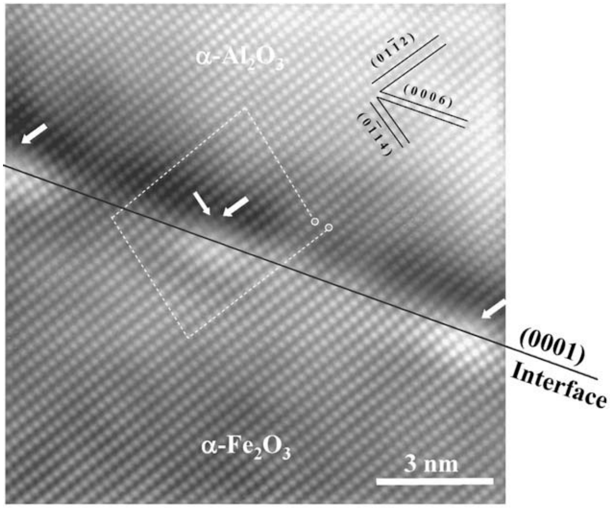

Figure 16.60: Cross-sectional HRTEM image revealing the structure of the misfit dislocations across Al_2O_3 and Fe_2O_3. A Burgers circuit was drawn around one of the dislocations and it gives a projected magnitude of the Burgers vector = $|\frac{1}{2}[\bar{1}010]| = 0.41$ nm. The image was taken from $[\bar{2}110]$ zone axis [150].

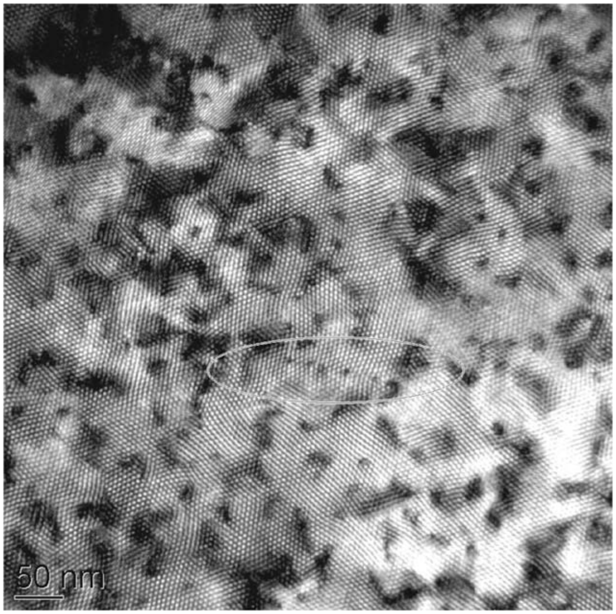

Figure 16.61: Plan-view TEM image revealing the distribution of the interface mismatch dislocations in two dimensions (typically the black dots) when Fe_2O_3 film was deposited on Al_2O_3 substrate. The regular 'lattice-like' pattern is a Moiré pattern due to the same structure of Al_2O_3 and Fe_2O_3, epitaxial growth, and slightly different lattice constant [150].

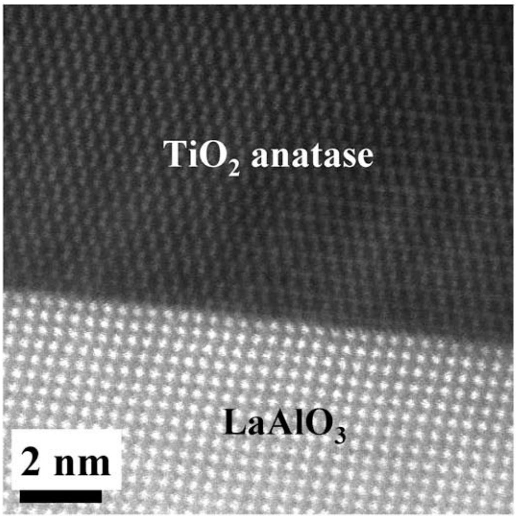

Figure 16.62: STEM-HAADF cross-sectional view, showing the interface between TiO_2 thin film and LAO substrate.

Strengths:

- High spatial resolution for structural information, crystallography, chemical composition, atomic charging and bonding information.
- Capable of analysis using a tiny amount of sample.
- At some degrees, a direct tool for visualization.
- Elemental analysis and mapping.
- Z-contrast STEM imaging to obtain atomic species distribution.
- Chemical state analysis by EELS.

Limitations:

- Requires vacuum.
- Sample preparation is tedious and artifacts are introduced during sample preparation.
- Electron beam modification of the specimen (beam damage).
- Strong dependence of image contrast on the imaging condition.

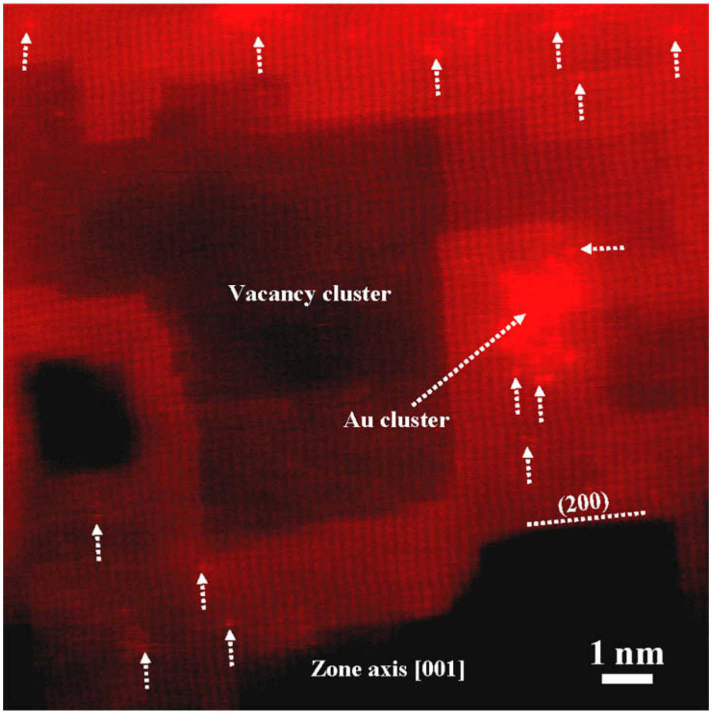

Figure 16.63: STEM-HAADF image of Au implanted in MgO, showing that the dark-contrasted regions are the vacancy clusters. Note the faceting of the vacancy cluster at the (001) planes as well as the thickness change along the electron beam direction [151]. The arrows identify the Au clusters.

16.5.4 Electron Diffraction (LEED and RHEED)

S. V. N. T. Kuchibhatla

For many decades, electron diffraction has been an indispensable technique for understanding the crystal structure of surfaces, overlayers, and thin films [136] and is widely used as a tool for monitoring the quality of epitaxial films during growth. Both low-energy electron diffraction (LEED) and reflection high-energy electron diffraction (RHEED) are conceptually similar to XRD for the bulk crystal structure determination. The fundamental difference between the electron diffraction (ED) techniques and XRD is in the much lower penetration depths in the former case. While the electron penetration depth is confined to the order of 2–4 monolayers (1–3 nm) the X-rays can penetrate through the bulk of a crystal (up to $\sim 10^5$ nm) [6]. LEED plays a crucial role in understanding the surface structure, in particular overlayer structure from adsorbates, surface relaxation, and reconstruction. Excellent surface sensitivity

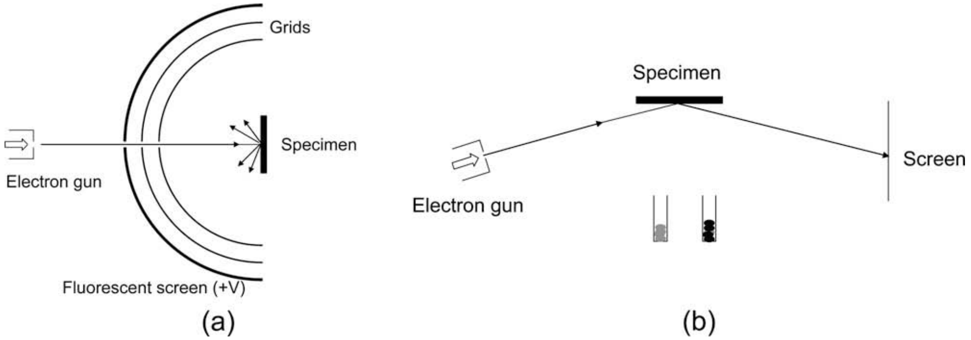

Figure 16.64: Typical instrument configuration for (a) LEED, and (b) RHEED.

and the ease with which the instrument can be used to monitor the in situ growth make RHEED important in thin film research.

The Techniques

Typical instrument configurations for LEED and RHEED are shown in Figure 16.64. The main differences between LEED and RHEED are beam energy and the scattered electron path. While the LEED uses perpendicular incidence and backscattered electrons, RHEED uses glancing incidence ($\leq 3^\circ$) and forward scattered electrons. Owing to the backscattered geometry, LEED instrumentation is generally difficult to incorporate for monitoring in situ growth. Hence, RHEED with no physical interference with the deposition process became a more popular technique during molecular beam epitaxy (MBE) growth of thin films.

16.5.4.1 Low-Energy Electron Diffraction

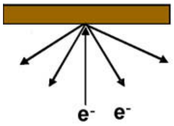

The position and intensity of diffraction peaks can be used to understand the structural characteristics of the surface or overlayer under investigation and LEED instrumentation can be used to obtain both these components as a function of electron energy. The basic LEED set-up consists of an electron source, usually producing an electron beam 1 mm in diameter and aligned perpendicular to the sample surface, a series of hemispherical grids oriented with their origin at the sample surface, and a phosphor screen held at high positive potential. The hemispherical grids are placed at different potentials to provide a field-free path to the diffracted electrons and to allow only the elastically scattered electrons. The screen is kept at high potential (several kilovolts) to show visible fluorescence when the electrons strike the screen. These fluorescent spots from various diffracted beams will result in a periodic diffraction pattern, which can be captured with the help of a CCD camera.

LEED is often used in two qualitatively different modes, one to determine or verify the symmetry of the surface and the second to determine the surface structure in some detail. The diffraction spots seen in a LEED pattern (Figure 16.65) provide information about the symmetry of the surface structure of the sample (they do not directly provide information about the actual atomic positions) [152]. LEED is frequently used in this qualitative mode to verify sample surface cleanliness, surface orientation, and the presence of ordered adsorbate layers. Photometric measurements on the phosphor screen or a Faraday cup (adjustable to follow changes in the diffracted beam position with changing primary electron energy) can be used to determine the intensity of the diffraction spots as a function of incident beam energy.

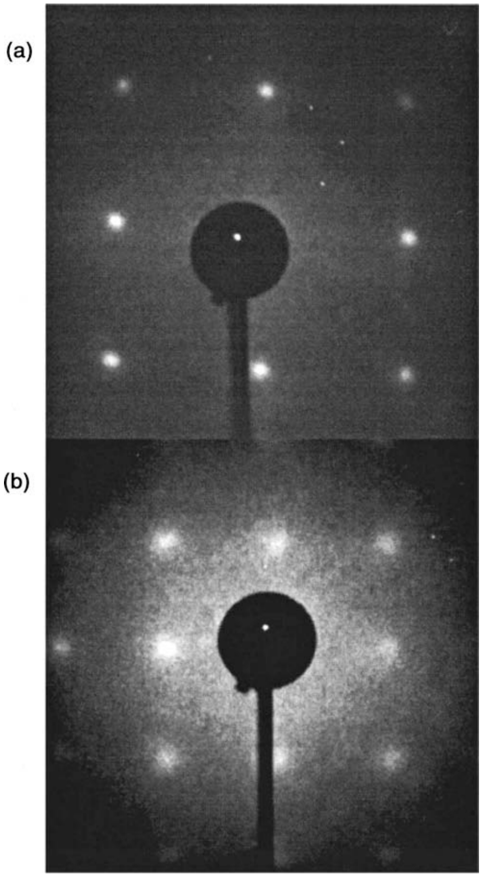

Figure 16.65: Typical LEED patterns of (a) STO (001) substrate (~98 eV incident beam), and (b) CeO_2(001) film deposited on STO at 650 °C (~165 eV incident beam) [152].

In order to obtain information about the actual atomic positions, intensity versus primary electron energy curves (i.e. *I–V* curves) can be collected and diligently analyzed using models of the surface structure along with the calculations involving multiple electron scattering.

Despite the complicated nature of multiple scattering at low energies, the use of *I–V* curves and theoretical modeling has continued to be useful for detailed analyses of surface structures and is a major tool for examining surface reconstructions. Most real surfaces are not 'ideal' because many surfaces relax from bulk positions in order to reduce the surface energy. This process is popularly known as reconstruction. Understanding surface reconstruction using LEED can not only reveal the symmetry of the final structure but also provide information regarding the interaction between the surface and overlayer [153].

16.5.4.2 Reflection High-Energy Electron Diffraction

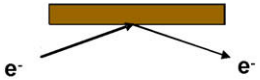

In addition to surface crystal structure, RHEED can be effectively used to understand the growth mode and deposition rate of films in situ. RHEED involves reflection of electrons incident at grazing angles onto the film/substrate surface. When the films grow layer by layer in a smooth fashion, the RHEED pattern appears as lines or streaks. On the other hand, if the growth is associated with 3D structures typical diffraction spots appear, indicating a rough surface. Therefore RHEED is useful to evaluate the quality of a growing film in situ (as shown in Figure 16.66a–c). Chambers presents a detailed overview and explanation of various RHEED patterns in a review article [154].

The semicircular zones of scattered beams in Figure 16.66(a–c) are a result of coherent diffraction over length scales comparable to the electron coherence length (~ 1000 Å for a well-collimated beam). These scattered beams consist of spots for a crystalline surface. These spots, as presented in Figure 16.66(a), are the diffracted beams within the zeroth order Laue zone of Al_2O_3(0001). The spacing between two spots or two streaks is inversely proportional to the in-plane lattice parameter perpendicular to the beam.

Under specific conditions, where the terrace widths are smaller than the electron coherence length, the spots in a RHEED pattern become streaks. This leads to a spread in the electron beam in the incident direction causing streaks to appear in the diffraction pattern. Further, when the dimensions of the clusters growing on a substrate can result in predominantly transmission of electrons (predominantly elastic scattering) rather than reflection, the diffraction pattern appears as spots, as shown in Figure 16.66(c).

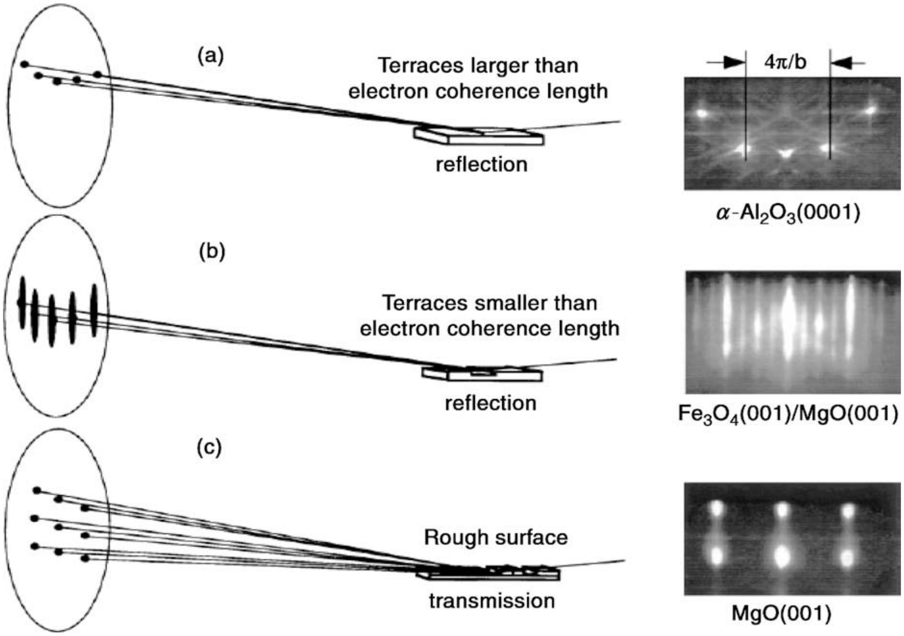

Figure 16.66: Representative RHEED images along with possible surface characteristics. Evidently, the RHEED pattern is dependent on the terrace widths on the film surface and the aspect ratio of the film [154]. In the top right panel, the interplanar spacing in the film is denoted as b.

Typical RHEED patterns observed for epitaxial CeO_2 film on $SrTiO_3(100)$ substrate are presented in Figure 16.67. These RHEED images are acquired during the deposition (in situ). Kim et al. [152] used RHEED analysis along with photoelectron diffraction to explain the growth of CeO_2 on $SrTiO_3(100)$. The effect of deposition temperature is evident from the RHEED patterns. While the 550 °C substrate temperature leads to island growth, 650 °C and 750 °C lead to epitaxial layered growth.

Strengths:

LEED

- Extremely surface sensitive.
- Overlayer structural symmetry can be determined.
- Surface reconstruction; impurity adsorptions can be identified.

RHEED

- Suitable for in situ analysis.

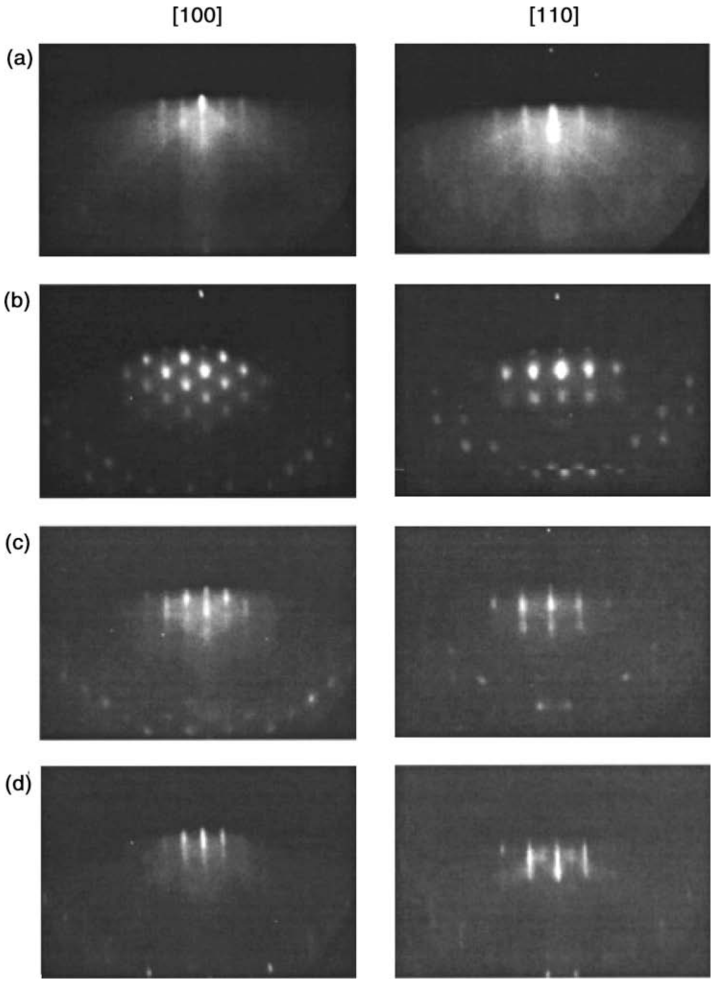

Figure 16.67: Typical RHEED (~ 15 keV incident beam) patterns obtained during the growth of CeO_2 film on (a) STO(001) substrate with the incident beam along (100) and (110) directions at substrate temperatures, (b) 550 °C, (c) 650 °C, and (d) 700 °C [152].

- Excellent technique for monitoring epitaxial growth mode (island, layer, etc.).
- Patterns are indicative of structural quality.

Limitations:

LEED

- Backscattered geometry limits its use for in situ analysis.
- Often, substrate diffraction pattern may also be present, thereby analysis becomes complicated.

RHEED

- Fixed position of the RHEED optics restricts the geometry of deposition instrumentation.
- May not be suitable for high-pressure deposition chambers.

16.5.4.3 Reciprocal Lattice and Surface Crystallography

In 2D space the lattice can be conveniently defined with the help of lattice vectors a, b. The comparison of 3D and 2D lattices and the corresponding Miller indices are presented in Figure 16.68.

The reciprocal lattice in the 2D system can further be described as dealt as in the 3D case explained later in this section. A detailed explanation of the relation between the surface and substrate lattices and aspects of surface crystallography are explained in detail in various dedicated surface science textbooks.

A fundamental understanding of electron and photon (e.g. X-ray) diffraction involves considering the wave nature of electrons. In addition, it is beneficial to use the concept of a reciprocal lattice. Since LEED deals with 2D surface structures the reciprocal lattice concepts associated with 2D structures are briefly described here. Electrons have wave-like properties which allow them to be scattered by a 2D array of atoms, providing the basis for ED. Despite the oversimplified nature of the following discussion, it is helpful for understanding the concepts important to ED [153]. If k_0 is the incident electron wave vector, its amplitude can be obtained by the deBroglie equation:

$$k_0 = \frac{2\pi}{\lambda} = 2\pi\left(\frac{2meV}{h^2}\right)^{1/2} = 2\pi\left(\frac{V}{150}\right)^{1/2} \tag{16.8}$$

where V is in volts, λ is wavelength of the incident beam (Å), and the unit for k_0 is $(\text{Å})^{-1}$.

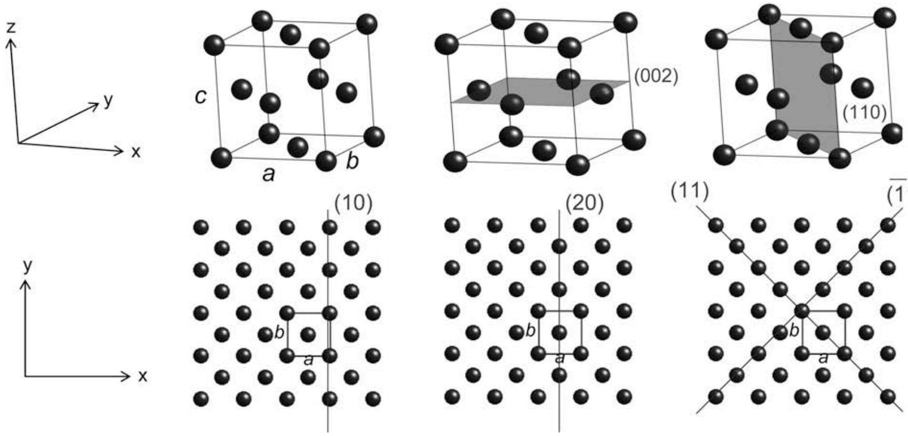

Figure 16.68: Miller indices description for (top) three dimensions, and (bottom) two dimensions.

The 2D arrays of atoms can be described with the help of two unit vectors a, b, similar to the 3D description with vectors a, b, c. As mentioned before, it is more convenient to use reciprocal lattice notation to understand the interaction between the electrons (in wave form) and the atomic rows. The reciprocal lattice coordinates can be deduced from the regular lattice coordinates. If a^*, b^*, and c^* are the lattice coordinates in the reciprocal space, then

$$\begin{aligned} a^* &= \frac{2\pi b\times c}{a(b\times c)} \\ b^* &= \frac{2\pi c\times a}{a(b\times c)} \\ c^* &= \frac{2\pi a\times b}{a(b\times c)} \end{aligned} \tag{16.9}$$

This implies that the reciprocal lattice can be constructed by translation of reciprocal lattice vectors, defined relative to the real-space vectors. Before going further, it will be useful to understand the concept of the Ewald sphere. The important feature of this sphere is that when the sphere cuts through the reciprocal lattice point the Bragg condition is satisfied and the diffraction maximum occurs. Further, the criterion for constructive interference (diffraction maximum) can only be observed when the change in the electron wave vector in the scattering event equals a reciprocal lattice vector.

$$(k' - k_0) = g = ha^* + kb^* + lc^* \tag{16.10}$$

The Ewald sphere is an empirical construction [136] with a radius $k_0 = 2\pi/\lambda$, with the vector k_0 extending from the center of the sphere terminating at a reciprocal lattice point. When the reciprocal lattice point lies on the Ewald sphere, the condition $(k' - k_0) = g$ will be met. The reciprocal lattice construction in the 2D case (e.g. a single atomic layer) involves allowing lattice vector c to approach infinity, thereby resulting in $c^* \to 0$. This makes the reciprocal lattice appear like a series of rods in a 2D array rather than a 3D array of spots. This implies that diffraction can be observed whenever a rod intersects the circle. Figure 16.69(a–c)

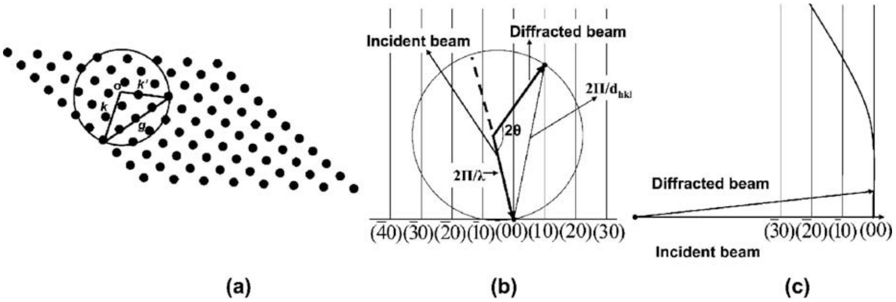

Figure 16.69: Ewald sphere construction for (a) the 3D case, (b) LEED configuration, (c) RHEED configuration [154].

depicts the Ewald sphere construction for the 3D case and for LEED and RHEED methods [6, 154].

16.6 Other Methods

Additional methods described include scanning probe microscopy (SPM) (including STM and AFM) and atom probe microscopy.

16.6.1 Scanning Probe Microscopy (STM, AFM)

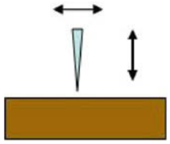

A.S. Lea

SPM is a branch of microscopy that has developed in a variety of useful ways to provide nanometer-resolution information about many properties of a sample, including topography, hardness, and conductivity. Images that are formed arise from the interaction of a proximal probe with a surface. The image is formed as the probe is scanned mechanically across the surface in a raster pattern while keeping track of the probe sample interaction as a function of tip position. Depending on the type of probe that is utilized, different scanning probe methods can be invoked. The two that are most commonly use in the analysis of surfaces and thin films are STM and AFM. AFM is often called scanning force microscopy (SFM) to be consistent with the nomenclature of the other types of scanning probe microscopies. While these two techniques will be highlighted in this section, it is pointed out that there are over 20 different SPM techniques in existence today. The spatial resolution of these techniques varies depending on the type of interaction utilized, but in some cases atomic resolution is achievable.

The origin of the scanning probe microscope came with the invention of the STM by Binnig and Rohrer in 1981 [155]. Though the electron tunneling process had been known since the 1950s, the ability to control the tunnel gap and scan an electrode across the surface facilitated the invention of the STM. This was largely due to the development of piezoelectric actuators that control motions in a highly precise and accurate manner. It could be argued that the invention of the STM led to the development of the field of nanotechnology, not to mention the other scanning probe techniques, and for this effort Binning and Rohrer were awarded the Nobel Prize in Physics in 1986, a mere five years after its invention.

16.6.1.1 Scanning Tunneling Microscopy

STM is a powerful technique that enables the imaging of conductive surfaces down to the atomic level. This technique is based on the quantum tunneling of electrons between two surfaces as they are brought sufficiently close together that their electron clouds begin to overlap. In STM, the tip of an atomically sharp electrode is positioned within a few nanometers of the surface and at low tip voltage bias probes the density of electronic states of the atoms comprising the surface by monitoring the tunneling current. Figure 16.70 depicts the tunneling processes for two surfaces that are within close proximity such that their electron clouds overlap. In the case of a negative tip bias, current is measured through tunneling of electrons from the occupied states in the tip into the unoccupied states in the sample [156]. For a positive tip bias, electrons tunnel from occupied states in the sample into unoccupied states in the tip. Depending on the applied bias voltage, one can therefore image either the occupied or unoccupied states in a sample. Figure 16.71(a) depicts the imaging of the occupied electronic states of the silicon carbide sample using a positive tip bias, and Figure 16.71(b) the unoccupied states of the SiC(0001) when a negative tip bias is utilized [157].

It is evident from Figure 16.71 that in some cases atomic resolution is achievable using STM. The basis of this high resolution is the distance dependence of the tunneling current. The basic equation for the tunneling current (or transmission probability) is:

$$I \, \alpha \, e^{-2\kappa z} \tag{16.11}$$

where z is the separation distance between the tip and sample, and parameter is defined by $\kappa^2 = 2m(V_B - E)/\hbar^2$. Here, m is the mass of an electron, V_B is the potential in the barrier, E is the energy of the electronic state, and $\hbar$ is Planck's constant [156]. In the simplest case, V_B is the vacuum level, so for states at the Fermi level, $(V_B - E)$ is just the work function (ϕ). The

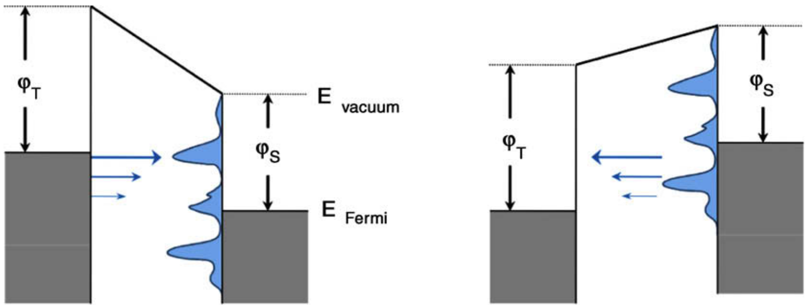

Figure 16.70: Energy level diagram of the tip and sample during STM in two different bias conditions: (a) with a negative tip potential in which electrons tunnel from the tip into unoccupied states in the sample, and (b) a positive tip in which electrons tunnel from occupied states in the sample into the tip.

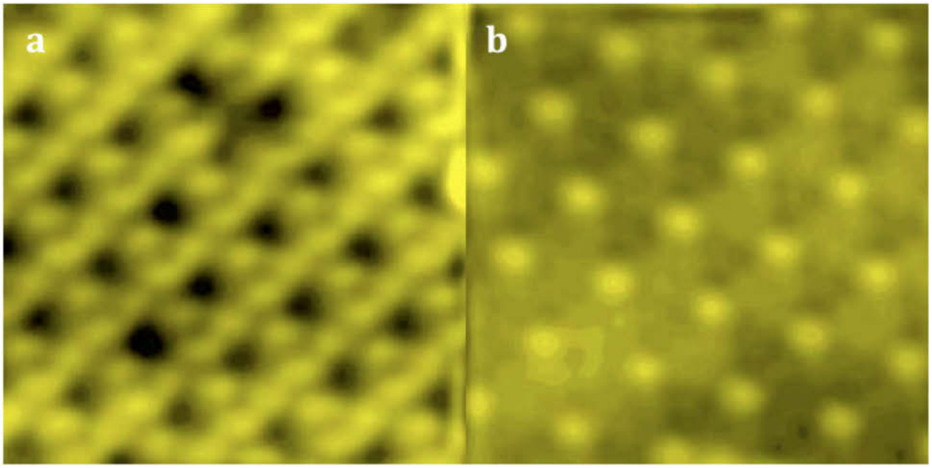

Figure 16.71: Imaging of a SiC(0001) 3 × 3 surface using (a) a positive tip potential in which the occupied states of the sample are shown and (b) a negative tip potential in which the unoccupied states of the sample are shown [157].

values of most work functions are around ~ 4–5 eV, meaning that κ is approximately 1 Å^{-1}. Using this value for κ in Eq. (16.11), one can see that the tunneling current drops by an order of magnitude for every Ångstrom of separation. It is not hard to see that most of the interaction between the tip and the sample comes from a single atomic asperity at the end of the STM tip, which enables one to measure tunneling currents on a sub-Ångstrom level and produce atomic scale images. The optimum spatial resolution for an STM is approximately <0.1 Å vertically and <1 Å laterally, but this depends on the tip sharpness, surface roughness, electronic noise, and level of vibration in the system.

The strong dependence of the tunneling current on the separation distance demands the ability to precisely control the tunneling junction. This precision is achieved through the use of piezoelectric actuators that can control movement of the STM tip in three dimensions on a sub-Ångstrom scale. A typical schematic of an STM instrument is depicted in Figure 16.72. The piezoelectric actuators are monoliths typically made from lead–zirconium–titanates (PZTs) and have a sensitivity on the order of 1–5 Å/V [158].

In order to maintain this precise level of control it is necessary to isolate the instrument from external vibrations, limiting these to magnitudes much less than 1 Å using vibration isolation equipment [159]. The principle behind the operation of an STM is quite simple. While a voltage bias is applied across the tunnel barrier, the tunneling current is measured and kept constant through computer-controlled feedback which controls the separation distance using the vertical piezoelectric actuator, as the tip is rastered across the sample surface using the horizontal actuators. This is the 'constant current' operation mode in which the sample topography is reflected through the path of the tip. Another, though less practical, mode is the

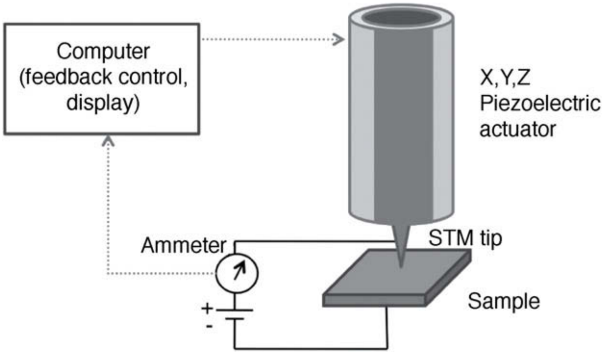

Figure 16.72: Simplified schematic of a typical STM instrument.

‘constant height’ mode, where the tip is maintained at a fixed height above the average surface and the topography is reflected in the variations in tunneling current. The constant current mode is in many cases the most practical imaging mode and is used to obtain topographic images of surfaces, down to the atomic scale in some cases.

Strictly speaking, STM measures not sample topography, but the local density of states of the sample. In the simplest case of an elemental sample, the local density of states is uniform and the variation in tunneling current is indeed directly related to topography. For multicomponent samples, this is not the case, as different atoms have different densities of electronic states. An excellent example of this is depicted in Figure 16.73, which shows a quantum corral comprised of Fe atoms arranged in a circular pattern on a Cu (111) [160] substrate. While there are no atoms on the surface lying in the corral, local maxima and minima, corresponding

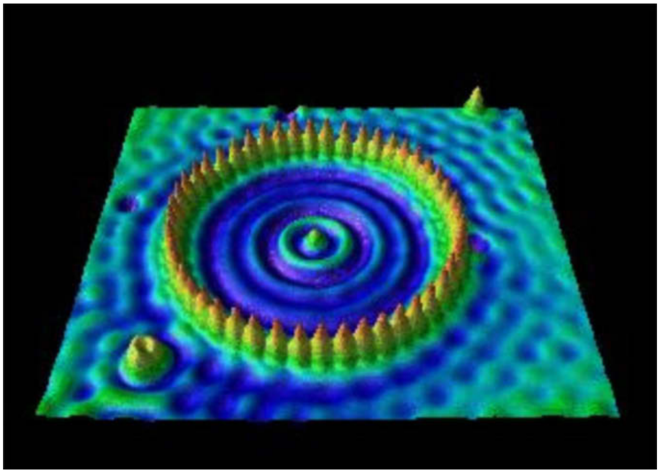

Figure 16.73: STM image of Fe atoms on Cu(111). Inside the quantum corral the STM measures the variations in local density of states due to electron standing waves [160].

to the standing electron waves generated by this construction, are visible. Adsorbates on a sample surface, which have different electronic density of states from that of a uniform substrate, and which alter the surface topography of the sample, will change the tunneling current passing through the tip as it passes over it. This provides contrast in an STM image, allowing this technique to probe the shape, conformation, and distribution of atoms or molecules residing on the surface of an atomically flat conducting substrate.

Scanning tunneling spectroscopy [161] is another valuable imaging mode, whereby the tunneling current is measured as a high-frequency voltage modulator is added to the tip bias. The usefulness of this method becomes apparent through the Wentzel–Kramers–Brillouin (WKB) approximation of the tunneling current shown in Eq. (16.12):

$$I = \int \rho_t(E)\, \rho_s(eV + E)\, T(E, eV) dE \tag{16.12}$$

where $\rho_t(E)$ is the density of electronic states in the tip at energy E, $\rho_s(eV+E)$ is the density of electronic states in the biased sample, and $T(E, eV)$ is the tunneling transmission probability. Assuming that the density of states in the tip is constant, then a measure of dI/dV produces a signal that is directly proportional to the local density of states in the sample. Another useful tunneling spectroscopy mode involves measuring the tunneling current as the tip height is modulated slightly above the surface [161]. In this mode, it is possible to obtain $d(\ln I)/dz$ which is directly proportional to the local work function (see Eq. 16.11) across the entire surface.

One of the strengths of STM is its ability to operate in different controlled environments, allowing it to be broadly applicable to many scientific disciplines. The STM can operate under vacuum, in ambient conditions, in aqueous (condensed phase) systems, and at hyperthermal or cryogenic temperatures. This versatility enables the instrument to collect data in kinetic systems in real time, allowing the researcher to collect dynamic information about the systems being investigated. This has become particularly useful in the investigation of fundamental chemical reactions that occur on model surfaces under controlled environments, enabling researchers to study the reaction pathways in catalytic systems. STM has been an invaluable tool in such diverse fields as materials synthesis and characterization, catalysis, microelectronics, electrochemistry, and biology.

A few limitations of the technique are mentioned here. First and foremost, since the interaction of the probe and sample involves tunneling current, it is necessary that the sample is sufficiently conducting to allow current to flow between the tip and sample. Insulating specimens are therefore very difficult to analyze using STM. Second, the precise control of the tunnel gap needed in a STM precludes the study of extremely rough samples. Roughness on the order of a few micrometers is generally considered too rough to make imaging practical. Third, one needs to be wary of possible tip-induced image artifacts due to poorly shaped tips, allowing for multiple tip–surface interactions.

Strengths:

- Subatomic vertical resolution.
- High lateral spatial resolution (atomic in some cases).
- Operates in ambient, vacuum or aqueous conditions.
- Little sample preparation necessary (except UHV STM).

Limitations:

- Samples limited to conductors or semiconductors.
- Tip artifacts are possible.
- Not amenable for samples with excessive roughness.

16.6.1.2 Atomic Force Microscopy (Scanning Force Microscopy)

AFM [162] is another scanning probe technique that permits imaging of surfaces down to the atomic level. But unlike STM, in which the tunneling current between an electrode and the sample is used to produce images, AFM monitors the force between a sharp tip and the sample and utilizes this force to produce images. In many other respects it is similar to an STM: there is a piezoelectric actuator to precisely control the sensor above the surface and to raster the tip across the sample, there is a control system to provide feedback to the piezoelectric actuators and display the images, and there is an isolation system to dampen ambient vibrations.

A schematic of the instrument is depicted in Figure 16.74. In this case, the probe is a microfabricated, cantilevered, force sensor that deflects as a result of the sample-induced forces placed on the sharp tip that is positioned on or above the sample surface. The cantilever

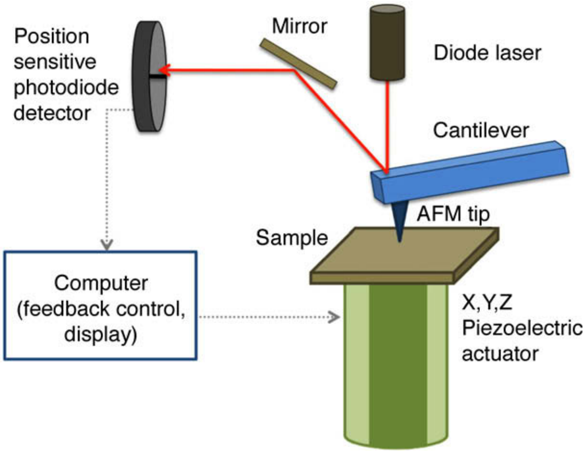

Figure 16.74: A simplified schematic of a typical AFM instrument.

deflects upward in the case of a net repulsive force, or downward in the case of a net attractive force. The extent of deflection is proportional to the force applied to the sensor and is generally described by Hooke's law [163].

$$F = kx \tag{16.13}$$

where F is the force exerted on the cantilever, k is the spring constant of the cantilever, and x is the distance of deflection. The deflection can be measured using an optical lever, in which a laser diode is focused on the end of the cantilever, which is typically angled downward from horizontal at $\sim 10^\circ$. The reflective coating on the back side of the cantilever permits reflection of the laser light to a position-sensitive photodiode detector located some distance away from the cantilever. A deflecting cantilever changes the position of the laser spot on the photodiode, which is monitored by the control system. In the case of an AFM, this deflection, usually associated with topography, is utilized to generate an image of the sample surface. One specific advantage AFM has over STM is its ability to image non-conducting samples.

An AFM tip that is positioned close to a surface is subject to a number of possible forces from the sample. These include electrostatic, magnetic, adhesive, van der Waals', hard-core overlap, hydrophobic, and specific interaction (e.g. antigen–antibody) forces. Most of these forces have long decay lengths and generally cannot provide the adequate sensitivity needed to produce atomic scale images [163, 164]. That is not to say that AFM cannot produce atomic scale images (Figure 16.75) [165], but rather a well-defined set of conditions must be met to obtain atomic scale images.

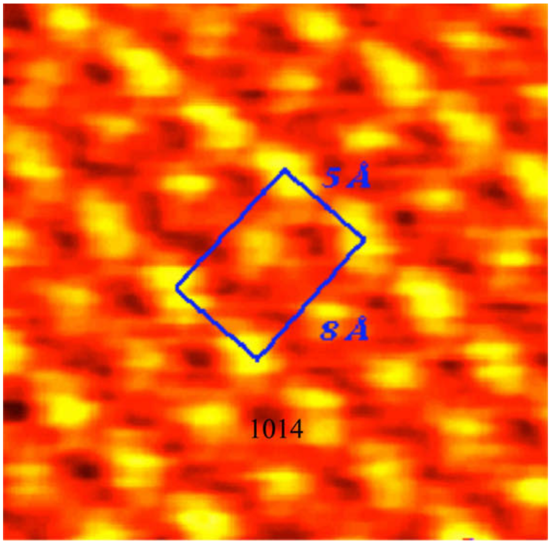

Figure 16.75: Atomic scale image of the (1014) surface of calcite in water. Superimposed on the image is the unit cell [165].

The atomic force microscope can operate in a number of imaging modes, including contact mode, (true) non-contact mode, and intermittent (or sometimes called tapping) mode. In contact mode, a relatively soft silicon nitride cantilever is typically used to probe the surface. Similarly to STM imaging modes, the contact mode AFM can operate in constant height mode, in which the tip is kept at a fixed height at or above the surface and the cantilever deflection is used to generate an image. Analogous to the constant current mode in STM, a constant force mode fixes the deflection of the cantilever and the position of the cantilever above the surface, as controlled by the piezoelectric actuators, is used to generate a topographic image. Contact mode imaging has been the easiest way to obtain atomic scale images, since it monitors the highly sensitive hard-core repulsive forces generated between the tip and the sample. One of the disadvantages of using contact mode imaging is its potential to produce scan-induced artifacts, such as manipulation of loosely bound adsorbates on the surface through shear forces [166]. Soft samples are also subject to the high compressive forces involved in contact imaging.

In non-contact imaging, the tip is oscillated at its resonant frequency at some small distance above the surface. Changes in the long-range attractive van der Waals' forces exerted on the tip due to topography cause the resonant frequency of the cantilever to shift [167]. The signal applied to the piezoelectric actuators needed to keep the resonant frequency constant is then used to generate a topographic image. Non-contact imaging is mostly used in vacuum systems, where instabilities due to surface adsorbates (i.e. water, contamination) are minimal.

In intermittent contact imaging, the cantilever is initially oscillated at its resonant frequency at amplitudes much greater than those utilized in non-contact imaging. As the tip is brought close to the sample surface, it comes in contact with the surface and its amplitude is reduced [168]. This reduced amplitude is then utilized to maintain a fixed separation distance between the tip and the sample through adjustment of the piezoactuators. Intermittent contact is the preferred method of imaging when atomic resolution is not needed, since smaller compressive and shear forces are applied to the sample compared to contact imaging.

The atomic force microscope can also be utilized in a force spectroscopy mode to measure the specific interaction forces between tip and sample or between structures immobilized onto the tip and sample [169]. In this mode, the tip is positioned in contact or within proximity of the sample surface and the cantilever is retracted. The force exerted on the cantilever as a function of the cantilever position is measured and force–distance plots can be obtained. Such experiments can extract information on the forces necessary to unravel macromolecules (e.g. DNA, proteins), specific interactions (e.g. antigen–antibody, actin–myosin), hydrophobic forces, and adhesive forces between surfaces.

Similarly to the scanning tunneling microscope, the atomic force microscope can be operated under a wide array of controlled operating environments, such as ambient, condensed phase (aqueous) and vacuum conditions, at elevated temperatures and pressures, and at cryogenic temperatures. This permits this instrument to be utilized in a large number of scientific disciplines, including biology, materials synthesis and characterization, geochemistry, and nanomechanics. Because of its unique ability to measure forces and image non-conducting materials, the atomic force microscope has become particularly important in the biological field for imaging of proteins, biological structures, and cells as well as for directly measuring interaction forces between complementary structures (e.g. DNA strands, antigen–antibody, actin–myosin). The ability to image surfaces under controlled environments in real time allows the researcher to observe the time-dependent changes in dynamic systems and obtain kinetic data for a wide variety of systems.

Because of the longer range interactions of many of the forces involved in AFM imaging [163] a much larger area of the AFM tip interacts with the surface compared to an STM tip. For this reason, tip shape has a larger influence on images than it does in STM. The image obtained with an AFM is approximately equivalent to the convolution of the tip with the actual surface topography. If the features one is trying to image are much larger than the tip radius, then the resultant image is a fairly accurate representation of the true topography. If, on the other hand, the tip radius is much larger than the features on the surface, the tip will impose its shape onto the observed topography and broaden the features in the images. It is therefore critical that one is aware of the tip broadening artifacts, the need to use sharp tips, and the deconvolution procedures needed to extract accurate dimensions in the images if artifacts are present [170]. The larger interaction area of the tip also means that spatial resolution for AFM images is generally not as high as that obtained using STM.

Strengths:

- Atomic scale vertical resolution.
- High lateral spatial resolution (atomic in some cases).
- Operates in ambient, vacuum, or aqueous conditions.
- Little sample preparation necessary (except UHV AFM).
- Can image insulating samples.
- Special approaches can be used to obtain magnetic, electrochemical, hardness, and other properties of a surface or film.

Limitations:

- Tip artifacts are possible.
- Soft samples can be subject to damage from shear or compressive forces.
- Not amenable for samples with excessive roughness.

16.6.2 Atom Probe Microscopy/Tomography

Atom-probe tomography (APT) [171] is an evolving technique, based on atomic resolution field ion microscopy [172], which can provide quantitative 3D compositional imaging and analysis of a volume that is approximately $100 \times 100 \times 500\,\text{nm}^3$ with a resolution of 0.2 nm [173]. In effect, APT provides the position and identity of atoms (isotopes) in that volume with analytical detection sensitivity in the 1 ppm range. Specimens to be examined using APT are formed into sharp tips, often using FIBs or electrochemical etching. Atoms on the specimen apex are then field evaporated as ions with the projected position and time of flight recorded using a microchannel plate and position-encoding anode (Figure 16.76). The path of the ions is determined by the position on the tip and the time of arrival (time of flight) is determined by the mass of the ion. The erosion of the specimen is highly controlled, with atoms evaporating one at a time from the apex. Therefore the detector hit data can be analyzed to provide the 3D position and mass-to-charge-state ratio for each atom which comprises the specimen. All elements and isotopes are detected and identified with equal efficiency. In effect, APT combines atomic resolution image information (like that of the TEM) with mass (compositional) information (like that of TOF-SIMS). The technique can be used to collect information that uniquely relates composition and structure at the atomic level.

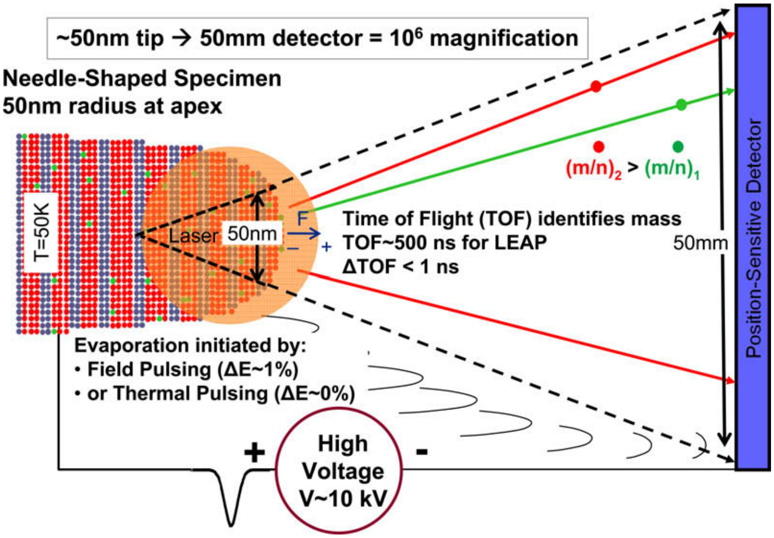

Figure 16.76: Schematic drawing of an atom probe microscope. The sample is a sharpened tip from which atoms are removed one layer at a time using either a voltage or thermal pulse. The mass of the atoms removed is measured by time-of-flight mass spectrometry [174]. (Reproduced with permission from IMAGO Scientific Instruments.)

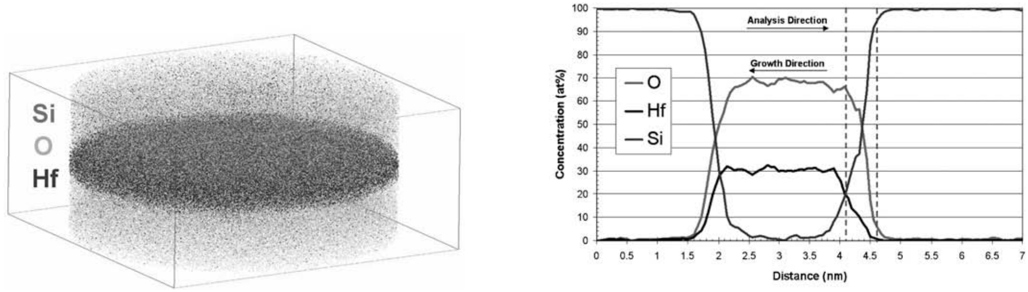

Figure 16.77: (a) A thin HfO_2 high-k layer analyzed by atom probe tomography (APT); (b) compositional profile through the high-*k* layer [174]. (Reproduced with permission from IMAGO Scientific Instruments.)

Atom-probe microscopy has traditionally been applied to metals using the field evaporation approach. The addition of the thermal pulse using laser technology has significantly expanded the range of materials to which the methods can be applied. The method can now be used on insulating materials and has been demonstrated for simple organic samples. The significant challenge of sample preparation for modern complex nanomaterials and thin films has been greatly facilitated by the application of FIB. Using the ion beam method, it is now possible to specifically select an area of a sample for analysis and to shape that area into the type of tip to which APT can be applied.

One example of a layer analysis obtained using APT is characterization of a high-*k* thin film of HfO_2. Using APT it is possible to obtain a 3D image of the interface between Si and the HfO_2 atom by atom (Figure 16.77a) and to construct a concentration profile (Figure 16.77b). The profile shows the high-*k* dielectric layer ~2.5 nm thick, and also indicates the formation of an SiO_2 layer [174].

APT is progressing toward being a routine atomic scale analytical microscopy tool that will be highly useful in many areas. However, it is still evolving and not many researchers or research groups have significant experience with the technique. It is a vacuum method for which analysis of phases, internal interfaces, and composition of solids can be accomplished. Through the use of cryotechnology and thermal pulsing the method is being extended to organic and biological materials. It provides information that complements information available by other methods and in some circumstances it will be the approach of choice. As this application becomes more routine, its use is likely to expand significantly. For current information about instrumentation readers can approach appropriate vendor websites [174, 175].

16.7 Summary

This chapter has provided an overview of several capabilities based on photon, electron, and ion methods that can be effectively used to understand the structural, chemical, and electronic characteristics of a wide range of materials including thin films and coatings. To obtain various details, it is often necessary to choose a combination of techniques (usually a subset which provide complementary information) based on properties of the materials under consideration, potential application, and with the resolution and sensitivity offered by the techniques. The information provided in this chapter is intended to be used as a guide to these methods and the readers are encouraged to explore the myriad of knowledge databases available through the World Wide Web, peer-reviewed journals, and handbooks. With the increasing emphasis on the use of nanostructured materials and materials designed for a wide variety of functional applications involving thin films and coatings, the surface-sensitive techniques discussed in this chapter are increasingly used to understand the physical, electronic, and chemical properties of the surfaces and films. Researchers and industries are working toward developing instruments with increased sensitivities and the ability to operate in realistic environments (in situ capabilities), and toward enabling multitechnique combinations in single instruments that address present-day and increasing research needs. A recent National Academy of Sciences report noted that many tools previously of interest primarily to experts are needed by researchers working on many types of thin films and coating research. These methods are available through user facilities (such as EMSL), technical experts at universities and within corporations, and specialized technical analysis companies. Such interdisciplinary collaborations are expected to make significant impacts in the characterization of materials and enable the continued dynamic advancements of technologies that rely on thin films and coatings technology.

Acknowledgments

This chapter has been prepared by staff of EMSL, a national scientific user facility sponsored by the Department of Energy’s Office of Biological and Environmental Research and located at Pacific Northwest National Laboratory, operated for DOE by Battelle Memorial Institute (www.emsl.pnl.gov). Portions of the work presented have been sponsored by the DOE Office of Basic Energy Science. Some of the examples offered show data collected as part of EMSL user activities. Although many different people contributed to the development of this document, we particularly wish to thank Dr T. Kelly for comments on the APT section and Dr C. Windisch Jr for comments on the optical sections. The authors acknowledge Kristin Lerch and Barbara Diehl for editorial help.

References

[1] G.E. Brown, S.R. Sutton, G. Calas, User facilities around the world, Elements 2 (2006) 9–14.
[2] Evans Analytical Group, EAG analytical techniques. <www.eaglabs.com/techniques/analytical_techniques/>
[3] <http://www.npl.co.uk/server.php?show=nav.526> (2009).
[4] L.C. Feldman, J.W. Mayer, Fundamentals of Surface and Thin Film Analysis, North-Holland, New York (1986).

[5] K.N. Tu, R. Rosenberg, Treatise on Materials Science and Technology, Analytical Techniques For Thin Films, Vol. 27, Academic Press, Boston, MA (1988).
[6] C.R. Brundle, C.A. Evans, S. Wilson, Encyclopedia of Materials Characterization: Surfaces, Interfaces, Thin Films, Butterworth-Heinemann, Boston, MA (1992).
[7] D. Briggs, M.P. Seah, Practical Surface Analysis, John Wiley, Chichester (1990).
[8] K. Siegbahn, Alpha- Beta- and Gamma-Ray Spectroscopy, North-Holland, Amsterdam (1965).
[9] K. Siegbahn, Electron-spectroscopy for atoms, molecules, and condensed matter, Science 217 (1982) 111–121.
[10] J.F. Moulder, J. Chastain, R.C. King, in: Handbook of X-Ray Photoelectron Spectroscopy: A Reference Book of Standard Spectra for Identification and Interpretation of XPS Data, Physical Electronics, Eden Prairie, MN (1995).
[11] M.P. Seah, W.D. Dench, Quantitative electron spectroscopy of surfaces: a standard data base for electron inelastic mean free paths in solids, Surf. Interface Anal. 1 (1979) 2–11.
[12] S. Tanuma, C.J. Powell, D.R. Penn, Proposed formula for electron inelastic mean free paths based on calculations for 31 materials, Surf. Sci. 192 (1987) L849–L857.
[13] S. Tanuma, C.J. Powell, D.R. Penn, Calculations of electron inelastic mean free paths for 31 materials, Surf. Interface Anal. 11 (1988) 577–589.
[14] E. Rutherford, The connexion between the beta and gamma ray spectra, Phil. Mag. 28 (1914) 305–319.
[15] J. Geller, NIST and NPL (NIST counterpart in the UK) traceable – Certified reference material. A magnification reference standard designed for microscopy by microscopists. <www.gellermicro.com> (2007).
[16] PHI MultiPak^{TM} Surface Analysis Software. <http://www.phi.com/>
[17] XPS and ARXPS website. <http://goliath.emt.inrs.ca/surfsci/arxps/index.html>
[18] G. Beamson, D. Briggs, High Resolution XPS of Organic Polymers: The Scienta ESCA300 Database, Wiley, Chichester (1992).
[19] NIST Electron Inelastic-Mean-Free-Path Database: Version 1.1. <http://www.nist.gov/srd/nist71.htm>
[20] CasaXPS: Processing software for the XPS, AES, SIMS and more. <www.casaxps.com>
[21] D.A. Shirley, High-resolution X-ray photoemission spectrum of valence bands of gold, Phys. Rev. B 5 (1972) 4709.
[22] S.D. Wagner, Quantitative surface analysis of materials, in: N.S. McIntyre (Ed.), Quantitative Surface Analysis of Materials: A Symposium, American Society for Testing and Materials, Philadelphia, PA (1978) 31.
[23] C.D. Wagner, Factors affecting quantitative-determinations by X-ray photoelectron-spectroscopy, Anal. Chem. 49 (1977) 1282–1290.
[24] D.J. O'Connor, B.A. Sexton, R.S.C. Smart, Surface Analysis Methods in Materials Science, Springer, Berlin (1992).
[25] D.R. Baer, M.H. Engelhard, D.J. Gaspar, A.S. Lea, Comparing beam damage rates using susceptibility tables, in: D. Briggs, J.T. Grant (Eds.), Surface Analysis by Auger and X-ray Photoelectron Spectroscopy, Appendix F, Surface Spectra, Manchester (2003).
[26] B.E. Warren, X-Ray Diffraction, Addison-Wesley, Reading, MA (1969).
[27] B.D. Cullity, Elements of X-Ray Diffraction, Addison-Wesley, Reading, MA (1978).
[28] W. Jiang, P. Nachimuthu, W.J. Weber, L. Ginzbursky, Variation in lattice parameters of 6H-SiC irradiated to extremely low doses, Appl. Phys. Lett. 91 (2007) 091918.
[29] G. Conibeer, M. Green, R. Corkish, Y. Cho, E.C. Cho, C.W. Jiang et al., Silicon nanostructures for third generation photovoltaic solar cells, Thin Solid Films 511 (2006) 654–662.
[30] Y.J. Li, T.C. Kaspar, T.C. Droubay, A.G. Joly, P. Nachimuthu, Z. Zhu et al., A study of H and D doped ZnO epitaxial films grown by pulsed laser deposition, J. Appl. Phys. 104 (2008) 053711.
[31] Y.J. Li, T.C. Kaspar, T.C. Droubay, Z. Zhu, V. Shutthanandan, P. Nachimuthu, S.A. Chambers, Electronic properties of H and D doped ZnO epitaxial films, Appl. Phys. Lett. 92 (2008) 152105.
[32] F. Swanson, National Bureau of Standards (US), Circulation 539(2) (1953) 38.

[33] W. Priyantha, R.J. Smith, H. Chen, M. Kopczyk, M. Lerch, C. Key, et al., Al–Fe interface intermixing and the role of Ti, V, and Zr as a stabilizing interlayer at the interface, J. Appl. Phys. 29 (2009) 053504.

[34] W. Priyantha, H. Chen, M. Kopczyk, R.J. Smith, A. Kayani, A. Comouth et al., Interface mixing of Al/Fe and Fe/Al bilayer systems and the role of Ti as a stabilizing interlayer using Rutherford backscattering spectrometry and X-ray reflectometry, J. Appl. Phys. 103 (2008) 014508.

[35] C.V. Raman, The Molecular Scattering of Light: Nobel Lecture, Calcutta University Press, Calcutta (1930).

[36] I.R. Lewis, H.G.M. Edwards, Handbook of Raman Spectroscopy: From the Research Laboratory to the Process Line, Marcel Dekker, New York (2001).

[37] N.J. Everall, Raman spectroscopy in coatings research and analysis: Part II. Practical applications, JCT Coat. Tech. 2 (2005) 46–52.

[38] H.C. Barshilia, K.S. Rajam, Raman spectroscopy studies on the thermal stability of TiN, CrN, TiAlN coatings and nanolayered TiN/CrN, TiAlN/CrN multilayer coatings, J. Mater. Res. 19 (2004) 3196–3205.

[39] M. Franck, J.P. Celis, J.R. Roos, Microprobe Raman-spectroscopy of tin coatings oxidized by solar beam heat-treatment, J. Mater. Res. 10 (1995) 119–125.

[40] L.V. Hong, N.T.H. Le, N.C. Thuan, N.D. Thanh, N.X. Nghia, N.X. Phuc, Observation of the phase formation in TiO_2 nano thin film by Raman scattering, J. Raman Spectrosc. 36 (2005) 946–949.

[41] N.J. Everall, Raman spectroscopy coatings research and analysis: Part I. Basic principles, JCT Coat. Tech. 2 (2005) 38–44.

[42] T. Werninghaus, Micro-Raman Spectroscopy Investigation of Hard Coatings, Shaker, Aachen (1997).

[43] M. Larsson, J. Lindgren, A. Ljunglof, K.G. Knuuttila, Ligand distributions in agarose particles as determined by confocal Raman spectroscopy and confocal scanning laser microscopy, Appl. Spectrosc. 57 (2003) 251–255.

[44] H.R. Morris, J.F. Turner, B. Munro, R.A. Ryntz, P.J. Treado, Chemical imaging of thermoplastic olefin (TPO) surface architecture, Langmuir 15 (1999) 2961–2972.

[45] Z.D. Schultz, M.C. Gurau, L.J. Richter, Broadband coherent anti-Stokes Raman spectroscopy characterization of polymer thin films, Appl. Spectrosc. 60 (2006) 1097–1102.

[46] R.J. Bell, Introductory Fourier Transform Spectroscopy, Academic Press, New York (1972).

[47] D. Wang, Y. Yang, J. Zou, New correction method for FTIR online film-thickness measurement, in: A.E. Mark (Ed.), Society of Photo-Optical Instrumentation Engineers (SPIE) Conference Series, SPIE (1996) 12–20.

[48] C.J. Wang, R. Wise, L. Shaohua, J. Haigis, S. Farquharson, B. Fowler, In-line FTIR for epitaxial silicon film thickness measurement on an applied materials centura cluster tool, in: Advanced Semiconductor Manufacturing Conference and Workshop, ASMC 94 Proceedings, IEEE/SEMI (1994) 229–231.

[49] S. Charpenay, P. Rosenthal, G. Kneissl, C.H. Gondran, H. Huff, Model-based analysis for precise and accurate epitaxial silicon measurements, Solid State Technol. 41 (1998) 161.

[50] P.A. Rosenthal, J. Xu, S. Charpenay, J.E. Cosgrove, N.M. Ravindra, Infared analysis of advanced thin film materials, JOM-e (2000) 52.

[51] J.K. Agbenyega, M. Claybourn, G. Ellis, A study of the autoxidation of some unsaturated fatty-acid methyl-esters using Fourier-transform Raman-spectroscopy, Spectrochim. Acta A Mol. Biomol. Spectrosc. 47 (1991) 1375–1388.

[52] G. Ellis, M. Claybourn, S.E. Richards, The application of Fourier-transform Raman-spectroscopy to the study of paint systems, Spectrochim. Acta A Mol. Biomol. Spectrosc. 46 (1990) 227–241.

[53] I. Ohlidal, D. Franta, Ellipsometry of thin film systems, Prog. Opt. 41 (2000) 183–284.

[54] J.B. Theeten, D.E. Aspnes, Ellipsometry in thin-film analysis, Annu. Rev. Mater. Sci. 11 (1981) 97–122.

[55] H.G. Tompkins, W.A. McGahan, Spectroscopic Ellipsometry and Reflectometry: A User's Guide, Wiley, New York (1999).

[56] E. Teboul, L. Yan, M. Gaillet, Characterization of TFT-LCD and OLEDs devices by phase modulated spectroscopic ellipsometry for display applications, in: F. So, G.B. Blanchet, Y. Ohmori (Eds.), Organic Electronics – Materials, Devices and Applications, MRS Fall Symposium, 0965-S03-07 (2006).

[57] A. Jablonski, About the mechanism of the photoluminescence (transl.), Z. Phys. 94 (1935) 38–46.

[58] J.R. Lakowicz, Topics in Fluorescence Spectroscopy, Vol.2, Plenum Press, New York (1991).

[59] F.S. Richardson, Terbium (III) and europium (III) ions as luminescence probes and stains for biomolecular systems, Chem. Rev. 82 (1982) 541–552.

[60] W.D. Horrocks Jr., M. Albin, Lanthanide ion luminescence in coordination chemistry and biochemistry, in: S.J. Lippard (Ed.), Progress in Inorganic Chemistry, Wiley & Sons, New York (1984) 1–104.

[61] D.J. Jang, J.T. Olesberg, M.E. Flatte, T.F. Boggess, T.C. Hasenberg, Hot Carrier dynamics in a (Gainsb/Inas)/Gainalassb superlattice multiple quantum well measured with mid-wave infrared, subpicosecond photoluminescence upconversion, Appl. Phys. Lett. 70 (1997) 1125–1127.

[62] O.H.Y. Zalloum, M. Flynn, T. Roschuk, J. Wojcik, E. Irving, P. Mascher, Laser photoluminescence spectrometer based on charge-coupled device detection for silicon-based photonics, Rev. Sci. Instrum. 77 (2006) 023907.

[63] A.K. Viswanath, Photoluminescence and ultrafast phenomena in III–V nitride quantum structures, in: A.A. Balandin, K.L. Wang (Eds.), Handbook of Semiconductor Nanostructures and Nanodevices 4, American Scientific Publishers, Stevenson Ranch, CA (2006) 45–118.

[64] H.C. Gardner, D.E. Gallardo, S. Dunn, N. Gaponik, A. Eychmuller, A photoluminescence study of film structure in Cdte nanoparticle thin films, J. Nanosci. Nanotechnol. 8 (2008) 2578–2581.

[65] M. Nakayama, H. Tanaka, M. Ando, T. Uemura, Photoluminescence and optical gain due to exciton-electron scattering in a high quality gan thin film, Appl. Phys. Lett. 89 (2006) 031909.

[66] S. Penna, A. Reale, R. Pizzoferrato, G.M.T. Beleffi, D. Musella, W.P. Gillin, Near-infrared photoluminescence of erbium tris (8-hydroxyquinoline) spin-coated thin films induced by low coherence light sources, Appl. Phys. Lett. 91 (2007) 021106.

[67] H. Fukada, S. Matsui, T. Miyata, T. Minami, Photoluminescence and electroluminescence from Eu-activated $CaAl_2O_4$-based multicomponent oxide thin-film phosphors, J. Vac. Sci. Technol. A 26 (2008) 944–948.

[68] H. Mu, D. Klotzkin, A. de Silva, H.P. Wagner, D. White, B. Sharpton, Temperature dependence of electron mobility, electroluminescence and photoluminescence of Alq_3 in OLED, J. Phys. D Appl. Phys. 41 (2008) 235109.

[69] K. Durose, S.E. Asher, W. Jaegermann, D. Levi, B.E. McCandless, W. Metzger et al., Physical characterization of thin-film solar cells, Prog. Photovoltaics 12 (2004) 177–217.

[70] Y.W. Zhang, M. Elfman, B.D. Milbrath, W.J. Weber, Evaluate scintillation response over a continuous energy region, IEEE Trans. Nucl. Sci. 55 (2008) 1097–1101.

[71] P.G. Coleman, Defect profiles in semiconductor structures, Phys. Status Solidi C 4 (2007) 3620–3626.

[72] I.T. Ferguson, A.G. Thompson, F.H. Barnet, F.H. Long, Z.C. Feng, Epitaxial film growth and characterization, in: M.H. Francombe, C.E.C. Wood, A.G.U. Perera, P. Broussard, J.D. Adam, D. Taylor (Eds.), Thin Films, Academic Press, New York (2001) 1–71.

[73] X.M. Teng, H.T. Fan, S.S. Pan, C. Ye, G.H. Li, Abnormal photoluminescence of ZnO thin film on ITO Glass, Mater. Lett. 61 (2007) 201–204.

[74] E.J. Sanchez, L. Novotny, X.S. Xie, Near-field fluorescence microscopy based on two-photon excitation with metal tips, Phys. Rev. Lett. 82 (1999) 4014–4017.

[75] P.A. Crowell, D.K. Young, S. Keller, D.D. E.L. Hu, Awschalom, near-field scanning optical spectroscopy of an ingan quantum well, Appl. Phys. Lett. 72 (1998) 927–929.

[76] J. Shah, Ultrafast luminescence spectroscopy using sum frequency generation, IEEE J. Quant. Electron. 24 (1988) 276–288.

[77] G. Rainó, G. Visimberga, A. Salhi, M. Todaro, M. De Vittorio, A. Passaseo et al., Picosecond timescale carrier dynamics of inas quantum dots: the role of a continuum background, Superlattices Microstruct. 43 (2008) 445–448.

[78] D.P. Smith, Scattering of low-energy noble gas ions from metal surfaces, J. Appl. Phys. 38 (1967) 340.

[79] W. Heiland, F. Iberl, E. Taglauer, D. Menzel, Oxygen adsorption on (110) silver, Surf. Sci. 53 (1975) 383–392.

[80] H.H. Brongersma, J.B. Theeten, Structure of oxygen adsorbed on Ni (001) as determined by ion scattering spectroscopy, Surf. Sci. 54 (1976) 519–524.

[81] E.P.T.M. Suurmeijer, A.L. Boers, Low-energy ion reflection from metal surfaces, Surf. Sci. 43 (1974) 309–352.
[82] A.G.J. Dewit, R.P.N. Bronckers, J.M. Fluit, Oxygen-adsorption on Cu (110) – determination of atom positions with low-energy ion scattering, Surf. Sci. 82 (1979) 177–194.
[83] M. Aono, Y. Hou, C. Oshima, Y. Ishizawa, Low-energy ion scattering from the Si (001) Surface, Phys. Rev. Lett. 49 (1982) 567.
[84] M. Aono, R. Souda, Quantitative surface atomic-structure analysis by low-energy ion-scattering spectroscopy (ISS), Jpn. J. Appl. Phys. Part 1 24 (1985) 1249–1262.
[85] H. Niehus, G. Comsa, Determination of surface reconstruction with impact-collision alkali ion-scattering, Surf. Sci. 140 (1984) 18–30.
[86] H. Niehus, Analysis of the PT (110) – (1X2) surface reconstruction, Surf. Sci. 145 (1984) 407–418.
[87] H. Niehus, W. Heiland, E. Taglauer, Low-energy ion-scattering at surfaces, Surf. Sci. Rep. 17 (1993) 213–303.
[88] J.W. Rabalais, Low-energy ion-scattering and recoiling, Surf. Sci. 299 (1994) 219–232.
[89] K. Eiperssmith, K. Waters, J.A. Schultz, Atomic-beam modifications of insulator surfaces, J. Am. Ceram. Soc. 76 (1993) 284–291.
[90] G.S. Herman, Surface structure determination of CeO_2 (001) By angle-resolved mass spectroscopy of recoiled ions, Phys. Rev. B 59 (1999) 14899.
[91] L.V. Goncharova, D.G. Starodub, E. Garfunkel, T. Gustafsson, V. Vaithyanathan, J. Lettieri, D.G. Schlom, Interface structure and thermal stability of epitaxial $SrTiO_3$ thin films on Si (001), J. Appl. Phys. 100 (2006) 044103.
[92] B.W. Busch, J. Kwo, M. Hong, J.P. Mannaerts, B.J. Sapjeta, W.H. Schulte et al., Interface reactions of high-kappa Y_2O_3 gate oxides with Si, Appl. Phys. Lett. 79 (2001) 2447–2449.
[93] E.P. Gusev, H.C. Lu, T. Gustafsson, E. Garfunkel, Growth-mechanism of thin silicon-oxide films on Si (100) studied by medium-energy ion-scattering, Phys. Rev. B 52 (1995) 1759–1775.
[94] V. Shutthanandan, S. Thevuthasan, Y. Liang, E.M. Adams, Z. Yu, R. Droopad, Direct observation of atomic disordering at the $SrTiO_3$/Si interface due to oxygen diffusion, Appl. Phys. Lett. 80 (2002) 1803–1805.
[95] J.C. Vickerman, D. Briggs, TOF-SIMS: Surface Analysis by Mass Spectrometry, SurfaceSpectra/IM, Manchester/Chichester (2001).
[96] J.C. Vickerman, A.A. Brown, N.M. Reed, Secondary Ion Mass Spectrometry: Principles and Applications, Oxford University Press, Oxford (1989).
[97] A. Brunelle, O. Laprevote, Recent advances in biological tissue imaging with time-of-flight secondary ion mass spectrometry: polyatomic ion sources, sample preparation, and applications, Curr. Pharm. Des. 13 (2007) 3335–3343.
[98] Glow discharge plasmas in analytical spectroscopy. <http://www.loc.gov/catdir/description/wiley034/2002072636.html> (2003).
[99] M. Betti, L.A. de las Heras, Glow discharge mass spectrometry in nuclear research, Spectrosc. Eur. 15 (2003) 15–24.
[100] M. Betti, L.A. de las Heras, Glow discharge spectrometry for the characterization of nuclear and radioactively contaminated environmental samples, Spectrochim. Acta B Atom. Spectrosc. 59 (2004) 1359–1376.
[101] P. Konarski, K. Kaczorek, M. Cwil, J. Marks, SIMS and GDMS depth profile analysis of hard coatings, Vacuum 82 (2008) 1133–1136.
[102] V.E. Krohn, G.R. Ringo, Ion-source of high brightness using liquid-metal, Appl. Phys. Lett. 27 (1975) 479–481.
[103] R.L. Seliger, J.W. Ward, V. Wang, R.L. Kubena, High-Intensity scanning ion probe with submicrometer spot size, Appl. Phys. Lett. 34 (1979) 310–312.
[104] L.W. Swanson, Liquid-metal ion sources – mechanism and applications, Nucl. Instrum. Meth. Phys. Res. 218 (1983) 347–353.

[105] L.A. Giannuzzi, F.A. Stevie, Introduction to Focused Ion Beams Instrumentation, Theory, Techniques, in: and Practice, Springer, New York (2005).

[106] P. Sigmund, Theory of sputtering. I. Sputtering yield of amorphous and polycrystalline targets, Phys. Rev. 184 (1969) 383.

[107] M.D. Uchic, L. Holzer, B.J. Inkson, E.L. Principe, P. Munroe, Three-dimensional microstructural characterization using focused ion beam tomography, MRS Bull. 32 (2007) 408–416.

[108] E.L. Principe, Focused Ion Beam Systems: Basics and Applications, Cambridge University Press, Cambridge (2007).

[109] C.A. Volkert, A.M. Minor, Focused ion beam microscopy and micromachining, MRS Bull. 32 (2007) 389–395.

[110] S. Hofmann, Sputter depth profile analysis of interfaces, Rep. Prog. Phys. 61 (1998) 827–888.

[111] S. Hofmann, Sputter-depth profiling for thin-film analysis, Phil. Trans. R. Soc. Lond. Ser. A 362 (2004) 55–75.

[112] B.R. Chakraborty, Sputter depth profiling of nanoscale interfaces by optimizing depth resolution in secondary ion mass spectrometry, in: 12th ISMAS Symposium cum Workshop on Mass Spectrometry, Indian Society for Mass Spectrometry, Dona Paula, Goa (2007).

[113] S. Hofmann, Characterization of nanolayers by sputter depth profiling, Appl. Surf. Sci. 241 (2005) 113–121.

[114] G. Gillen, A. Fahey, M. Wagner, C. Mahoney, 3D molecular imaging SIMS, Appl. Surf. Sci. 252 (2006) 6537–6541.

[115] N. Winograd, The magic of cluster SIMS, Anal. Chem. 77 (2005) 142A–149A.

[116] Y. Yamamoto, S.H. Kiyoshi Yamamoto, XPS-depth analysis using C_{60} ion sputtering of buried interface in plasma-treated ethylene-tetrafluoroethylene-copolymer (ETFE) film, Surf. Interface Anal. 40 (2008) 1631–1634.

[117] J. Cheng, N. Winograd, Depth profiling of peptide films with TOF-SIMS and a C-60 probe, Anal. Chem. 77 (2005) 3651–3659.

[118] A. Wucher, S.X. Sun, C. Szakal, N. Winograd, Molecular depth profiling of histamine in ice using a buckminsterfullerene probe, Anal. Chem. 76 (2004) 7234–7242.

[119] A.G. Shard, F.M. Green, I.S. Gilmore, C-60 ion sputtering of layered organic materials, Appl. Surf. Sci. 255 (2008) 962–965.

[120] M.P. Seah, Cluster ion sputtering: molecular ion yield relationships for different cluster primary ions in static SIMS of organic materials, Surf. Interface Anal. 39 (2007) 890–897.

[121] C.M. Mahoney, A.J. Fahey, G. Gillen, C. Xu, J.D. Batteas, Temperature-controlled depth profiling of poly (methyl methacrylate) using cluster secondary ion mass spectrometry. 2. Investigation of sputter-induced topography, chemical damage, and depolymerization effects, Anal. Chem. 79 (2007) 837–845.

[122] B.-Y. Yu, Y.-Y. Chen, W.-B. Wang, M.-F. Hsu, S.-P. Tsai, W.-C. Lin et al., Depth Profiling of organic films with X-ray photoelectron spectroscopy using C60+ and Ar+ co-sputtering, Anal. Chem. 80 (2008) 3412–3415.

[123] M.P. Seah, S.J. Spencer, F. Bensebaa, I. Vickridge, H. Danzebrink, M. Krumrey et al., Critical review of the current status of thickness measurements for ultrathin SiO_2 on Si. Part V. Results of a CCQM pilot study, Surf. Interface Anal. 36 (2004) 1269–1303.

[124] M.P. Seah, Intercomparison of silicon dioxide thickness measurements made by multiple techniques: the route to accuracy, J. Vac. Sci. Technol. A 22 (2004) 1564–1571.

[125] J.T. Grant, in: D. Briggs, J.T. Grant (Eds.), Surface Analysis by Auger and X-ray Photoelectron Spectroscopy, SurfaceSpectra/IM Publications, Manchester/Chichester (2003).

[126] D. Briggs, J.C. Riviere, in: D. Briggs, M.P. Seah (Eds.), Practical Surface Analysis: By Auger and X-ray Photo-Electron Spectroscopy, Wiley, Chichester (1983).

[127] J.H. Hubbell, P.N. Trehan, N. Singh, B. Chand, D. Mehta, M.L. Garg et al., A review, bibliography, and tabulation of K, L, and higher atomic shell X-ray-fluorescence yields, J. Phys. Chem. Ref. Data 23 (1994) 339–364.

[128] M. Kudo, in: D. Briggs, J.T. Grant (Eds.), Surface Analysis by Auger and X-ray Photoelectron Spectroscopy, IM, Chichester (2003).

[129] M.P. Seah, I.S. Gilmore, Quantitative AES. VIII: Analysis of Auger electron intensities from elemental data in a digital Auger database, Surf. Interface Anal. 26 (1998) 908–929.

[130] K.D. Childs, C.L. Hedberg, Handbook of Auger Electron Spectroscopy: A Book of Reference Data for Identification and Interpretation in Auger Electron Spectroscopy, Physical Electronics, Eden Prairie, MN (1995).

[131] M.P. Seah, A system for the intensity calibration of electron spectrometers, J. Electron Spectrosc. Relat. Phenom. 71 (1995) 191–204.

[132] J. Cazaux, Mechanisms of charging in electron spectroscopy, J. Electron Spectrosc. Relat. Phenom. 105 (1999) 155–185.

[133] D.R. Baer, A.S. Lea, J. Geller, J. Hammon, L. Kover, M.P. Seah, et al., Approaches to analyzing insulators with Auger electron spectroscopy: update and overview (2009) d.o.i.: 10.1016/j.elspec.2009.03.02.

[134] S. Thevuthasan, W. Jiang, W.J. Weber, Cleaving oxide films using hydrogen implantation, Mater. Lett. 49 (2001) 313–317.

[135] R.F. Egerton, Electron Energy-Loss Spectroscopy in the Electron Microscope, Plenum Press, New York (1996).

[136] D.B. Williams, C.B. Carter, Transmission Electron Microscopy: A Textbook for Materials Science, Plenum Press, New York (1996).

[137] E.J. Kirkland, Advanced Computing in Electron Microscopy, Plenum Press, New York (1998).

[138] M. De Graef, Introduction to Conventional Transmission Electron Microscopy, Cambridge University Press, Cambridge (2003).

[139] B. Fultz, J.M. Howe, Transmission Electron Microscopy and Diffractometry of Materials, Springer, Berlin (2002).

[140] J.C.H. Spence, High-Resolution Electron Microscopy, Oxford University Press, Oxford (2003).

[141] D.C. Joy, A.D. Romig, J. Goldstein, Principles of Analytical Electron Microscopy, Plenum Press, New York (1986).

[142] E. Ruska, Uber Fortschritte im Bau und in der Leistung des magnetischen Elektronenmikroskops, Z. Phys. A 87 (1934) 580–602.

[143] S.J. Pennycook, M. Varela, C.J.D. Hetherington, A.I. Kirkland, Materials advances through aberration-corrected electron microscopy, MRS Bull. 31 (2006) 36–43.

[144] M. Haider, S. Uhlemann, E. Schwan, H. Rose, B. Kabius, K. Urban, Electron microscopy image enhanced, Nature 392 (1998) 768–769.

[145] O. Scherzer, Spharische Und Chromatische Korrektur Von Elektronen-Linsen, Optik 2 (1947) 114–132.

[146] D.J. Smith, Development of aberration-corrected electron microscopy, Microsc. Microanal. 14 (2008) 2–15.

[147] D.A. Muller, L.F. Kourkoutis, M. Murfitt, J.H. Song, H.Y. Hwang, J. Silcox et al., Atomic-scale chemical imaging of composition and bonding by aberration-corrected microscopy, Science 319 (2008) 1073–1076.

[148] S.A. Chambers, C.M. Wang, S. Thevuthasan, T. Droubay, D.E. McCready, A.S. Lea et al., Epitaxial growth and properties of MBE-grown ferromagnetic Co-doped TiO_2 anatase films on $SrTiO_3$ (001) and $LaAlO_3$ (001), Thin Solid Films 418 (2002) 197–210.

[149] C.M. Wang, S. Azad, V. Shutthanandan, D.E. McCready, C.H.F. Peden, L. Saraf, S. Thevuthasan, Microstructure of ZrO_2–CeO_2 hetero-multi-layer films grown on YSZ substrate, Acta Mater. 53 (2005) 1921–1929.

[150] C.M. Wang, S. Thevuthasan, F. Gao, D.E. McCready, S.A. Chambers, The characteristics of interface misfit dislocations for epitaxial alpha-Fe_2O_3 on alpha-Al_2O_3 (0001), Thin Solid Films 414 (2002) 31–38.

[151] C.M. Wang, V. Shutthanandan, S. Thevuthasan, G. Duscher, Direct imaging of quantum antidots in MgO dispersed with Au nanoclusters, Appl. Phys. Lett. 87 (2005) 153115.

[152] Y.J. Kim, Y. Gao, G.S. Herman, S. Thevuthasan, W. Jiang, D.E. McCready, S.A. Chambers, Growth and structure of epitaxial CeO_2 by oxygen-plasma-assisted molecular beam epitaxy, J. Vac. Sci. Technol. A 17 (1999) 926–935.

[153] J.B. Hudson, Surface Science: An Introduction, John Wiley & Sons, New York (1998).

[154] S.A. Chambers, Epitaxial growth and properties of thin film oxides, Surf. Sci. Rep. 39 (2000) 105–180.

[155] G. Binnig, H. Rohrer, C. Gerber, E. Weibel, Surface studies by scanning tunneling microscopy, Phys. Rev. Lett. 49 (1982) 57.

[156] J. Tersoff, in: D.A. Bonnell (Ed.), Scanning Tunneling Microscopy and Spectroscopy: Theory, Techniques, and Applications, VCH, New York (1993).

[157] H.E. Hoster, M.A. Kulakov, B. Bullemer, Morphology and atomic structure of the SiC $(000\bar{1})$ 3×3 surface reconstruction, Surf. Sci. 382 (1997) L658–L665.

[158] H. Jaffe, Piezoelectric ceramics, J. Am. Ceram. Soc. 41 (1958) 494–498.

[159] D.A. Bonnell, in: D.A. Bonnell (Ed.), Scanning Tunneling Microscopy and Spectroscopy: Theory, Techniques, and Applications, VCH, New York (1993).

[160] M.F. Crommie, C.P. Lutz, D.M. Eigler, Confinement of electrons to quantum corrals on a metal-surface, Science 262 (1993) 218–220.

[161] R.J. Hamers, in: D.A. Bonnell (Ed.), Scanning Tunneling Microscopy and Spectroscopy: Theory, Techniques, and Applications, VCH, New York (1993).

[162] G. Binnig, C.F. Quate, C. Gerber, Atomic force microscope, Phys. Rev. Lett. 56 (1986) 930–933.

[163] E. Meyer, Atomic Force Microscopy, Progress in Surface Science 41 (1992) 3–49.

[164] N.A. Burnham, R.J. Colton, in: D.A. Bonnell (Ed.), Scanning Tunneling Microscopy and Spectroscopy: Theory, Techniques, and Applications, New York (1993).

[165] Y. Liang, A.S. Lea, D.R. Baer, M.H. Engelhard, Structure of the cleaved $CaCO_3$ $(10\bar{1}4)$ surface in an aqueous environment, Surf. Sci. 351 (1996) 172–182.

[166] A.S. Lea, A. Pungor, V. Hlady, J.D. Andrade, J.N. Herron, E.W. Voss, Manipulation of proteins on mica by atomic force microscopy, Langmuir 8 (1992) 68–73.

[167] F.J. Giessibl, Atomic-resolution of the silicon (111) – (7X7) surface by atomic-force microscopy, Science 267 (1995) 68–71.

[168] R. Garcia, A. San Paulo, Dynamics of a vibrating tip near or in intermittent contact with a surface, Phys. Rev. B 61 (2000) 13381–13384.

[169] T. Hugel, M. Seitz, The study of molecular interactions by AFM force spectroscopy, Macromol. Rapid Commun. 22 (2001) 989–1016.

[170] Guide to Scanner and Tip Related Artifacts in Scanning Tunneling Microscopy and Atomic Force Microscopy, E2380-04, ASTM International, West Conshohocken, PA (2004).

[171] T.F. Kelly, M.K. Miller, Invited Review Article: Atom probe tomography, Rev. Sci. Instrum. 78 (2007).

[172] E.W. Muller, J.A. Panitz, S.B. McLane, Atom-probe field ion microscope, Rev. Sci. Instrum. 39 (1968) 83.

[173] T.F. Kelly, K. Thompson, E.A. Marquis, D.J. Larson, Atom probe tomography defines mainstream microscopy at the atomic scale, Microsc. Today 14 (2006) 34–40.

[174] <http://www.imago.com/imago/techNote/viewAction.do?tnid=25>

[175] <http://www.cameca.fr/html/atom_probe_technique.html>

CHAPTER 17

Atmospheric Pressure Plasma Sources and Processing

Hana Baránková and Ladislav Bárdos
Uppsala University, Ångström Lab., Plasma Group, Box 534, SE-751 21 Uppsala, Sweden

17.1 Introduction

Plasma processing represents a very broad spectrum of methods and devices utilizing electrical discharges in selected gases or vapors for interactions with solids, liquids, or gases. In general, all these interactions are based on charged particles (electrons, ions) generated in the discharge and on their control by applied electric and magnetic fields. Although the designation *plasma* should be used only for those parts of the discharge where the number density of negative electrons (and negative ions in electronegative gases) is equivalent to the number density of positive ions, in practice the whole discharge is simply denoted as plasma. The densities and energies of charged particles depend on many factors, for example on the power generator (applied field, frequency, pulsing properties, etc.), on the type of gas (molecular, atomic, chemical composition, etc.), and very strongly also on the gas pressure. In the processing technology typical plasma systems usually work at reduced or low gas pressures, where rarefied gas brings about low collision frequency between particles. Under these conditions it is possible for electrons to attain very high energies but at the same time the gas particles can remain at low energy and temperature. Such plasmas are called *non-equilibrium* or *non-thermal*, or simply *cold plasmas*. When the gas pressure is higher the frequency of collisions increases and the particle energies become closer and closer to each other, to the state when all particle energies are practically equivalent (above approximately 100 torr). This is the case of *equilibrium* or *thermal plasma*, composed of high-temperature gas particles. High temperatures of over 10,000 K can be reached in thermal plasma.

It is important to note that in most cases only a certain portion of gas particles is in an ionized state. For example, the degree of ionization in low-pressure plasma processing devices such as magnetrons or arc evaporators is typically less than 1%. At pressures of about 10 mtorr (1.33 Pa) where the density of neutral gas particles is about 10^{14} cm^{-3}, the density of ions is typically less than 10^{12} cm^{-3} (typically 10^{9}–10^{10} cm^{-1} in magnetrons and 10^{10}–10^{12} cm^{-1} in arc evaporators).

Atmospheric pressure plasma systems, mainly those based on thermal equilibrium plasma, have been used for material processing for more than 100 years. An example of everyday technology based on thermal atmospheric plasma is electric welding. A high current arc is capable of melting metallic electrodes as well as conductive surfaces to be welded together. In most thermal plasma sources more than 80% of the applied power is transferred into heat. Simple arc sources forming jet plasmas are often used for thermal spraying of powders. Industrial torches operate at direct current (DC) powers roughly from 10 kW up to 1 MW and at gas flows of the order of 1000 slm. The gas close to the cathode tip can reach temperatures of about 10,000 °C. The temperature then decreases in both the radial and axial directions [1]. In ‘transferred arcs’ the plasma can be heated to temperatures as high as about 15,000 °C at absorbed power up to about 10 MW. The arc current can reach the order of 1 kA. Water-cooled electromagnetic coils can cause rotation of the arc to stabilize it and to decrease thermal load at the anode surface. Very hot equilibrium plasmas can be produced in inductive (electrodeless) plasma sources. One example is a plasma torch with radio-frequency (RF) inductive coil (frequency order from 1 to 10 MHz) powered up to about 100 kW. The plasma temperature of about 10,000 °C can be measured in the axis of the coil [2].

High gas temperatures in thermal plasmas are obviously not desirable in ‘softer’ surface treatments such as coating, cleaning, or dry etching. For this purpose a cold plasma is required, where the main energy carriers are electrons while heavier particles (ions, gas atoms, and molecules) remain cold. So far, large-scale industrial technology is based mostly on cold plasmas at reduced or low gas pressures where the neutral gas temperature is below 1000 °C and long mean free paths allow large volumes of the plasma. During recent decades the non-equilibrium (cold) plasmas at reduced gas pressure became a widespread standard industrial technology for coating and surface processing in microelectronics, machinery, optics, etc. However, from the end of the twentieth century there is rapidly growing interest in replacing low-pressure plasma systems with cold atmospheric plasma systems, where expensive vacuum equipment can be eliminated.

In many cases the low-temperature non-equilibrium atmospheric plasma devices have certain limitations and cannot compete with low-pressure plasma. At the same time they have a very promising unique potential for a number of new non-conventional applications, including new surface treatments and processing of materials. Typical features of the atmospheric plasma are reviewed below, mainly with respect to surface processing, to give a realistic picture about this emerging technology.

17.2 Generation of Non-Equilibrium Plasma at Low and High Gas Pressures

In 1970 Kekez et al. [3] studied gas breakdown processes in hydrogen and krypton in an adjustable gap (distance *d*) between two parallel planar electrodes ({3/4} inch in diameter) at different gas pressures *p* up to atmospheric pressure. They found that the time function of the current flowing in the gap after applying the pulsed voltage always has several characteristic phases. A model approach of their observations describing the individual phases is shown in Figure 17.1. Providing that the voltage in the pulse exceeds the breakdown value the current starts at a moderate level resembling a glow discharge where the ionization follows Townsend's mechanism with ionization avalanches, and the gas breakdown follows the well-known Paschen law. During later phases (roughly after 100 ns) there is a growing probability of forming large current filaments, or *streamers*, representing local arcs.

17.2.1 Electrical Breakdown of Gas at Reduced Pressures

Townsend avalanches proceed in a space-charge-free field to the point where a secondary emission from the cathode provides sufficient feedback of electrons to maintain the stable discharge. In a simplified description of the DC avalanche each electron emitted from the cathode moves in an electric field toward the anode at a distance *d* from the cathode and collides with the neutral gas particles forming exp (αd) new electrons and the same number of

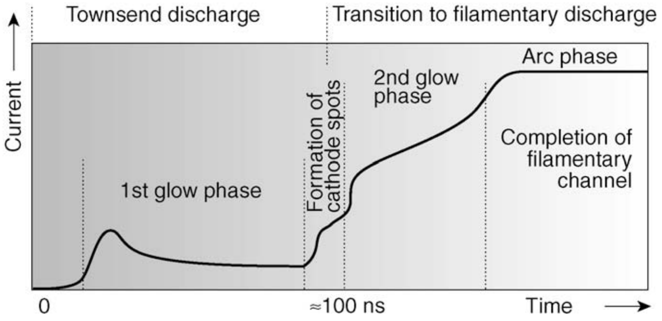

Figure 17.1: Model approach describing individual phases of gas breakdown in hydrogen and krypton in an adjustable gap (distance *d*) between two parallel planar electrodes {3/4} inch in diameter at different gas pressures *p* up to the atmospheric pressure. (According to [3].)

positive ions. The coefficient α is the so-called 1st Townsend coefficient. To fulfill the requirement of equal numbers of opposite charged particles in the plasma, one ion must remain in the space to compensate the initial electron. The rest of $[\exp(\alpha d) - 1]$ ions should return to the cathode where they can, with a probability of γ (3rd Townsend coefficient), form $\gamma\,[\exp(\alpha d) - 1]$ secondary electrons. When the number of secondary electrons can replace the initial electron, we may write a simple balance equation, which actually represents the Paschen breakdown condition, $1 = \gamma\,[\exp(\alpha d) - 1]$. By multiplying both sides by gas pressure p and after a simple mathematical operation the equation can be rewritten into the form:

$$pd = p/\alpha \ln(1 + 1/\gamma).$$

The DC breakdown always follows the well-known Paschen function $V_b = f(pd)$ [4]. The Paschen function (curve) has a concave shape with certain minimum breakdown voltage at a certain value of pd. For a fixed geometry (d = constant) the breakdown voltages V_b are higher at both low and high gas pressures. In a typical low-pressure plasma processing systems with gas pressures in the interval $0.1\ \mathrm{Pa} \le p \le 100\ \mathrm{Pa}$ and distances d between electrodes of a few centimeters the voltages required to start the plasma can be reasonably low ($V_b \le 1\ \mathrm{kV}$). It should be noted that similar principles to those in DC breakdown are also valid for RF breakdown. An example of an experimental Paschen curve for breakdown in a 3 mm diameter cylindrical hollow cathode in nitrogen at pressures between 20 and 500 Pa for two different frequencies is shown in Figure 17.2 [5]. It is seen that the average voltage for the breakdown can even be below 100 V.

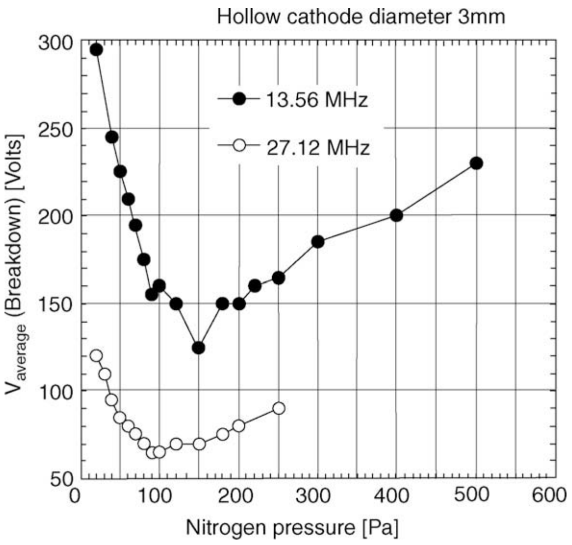

Figure 17.2: An experimental function of the discharge ignition voltage versus the nitrogen pressure in the radio frequency hollow cathode system at two different frequencies. (According to [5].)

17.2.2 Electrical Breakdown of Gas at High Pressures

In contrast to low-pressure breakdown, atmospheric and higher pressure breakdown in dry air requires more than 30 kV with a 1 cm gap between electrodes. Even when the distance is shortened to $d \approx 1$ mm it still requires about 3 kV at 1 atmosphere. The experimental DC values in a 1 mm gap reported in [6] are 3.2 kV in air, 1.5 kV in Ar, and 0.75 kV in He. Measurements of the RF breakdown at atmospheric pressure in fused hollow cathode (FHC) systems (see Section 17.3 and Figure 17.3e) with about a 1 mm gap between the cathode structure and a grounded counter-electrode show peak-to-peak voltages of 1.2 kV in air, 0.4 kV in Ar, and 0.18 kV in Ne [7]. The high voltages necessary to ignite atmospheric discharges often lead to formation of hot filamentary arcs (streamers), as can be seen in later phases of the

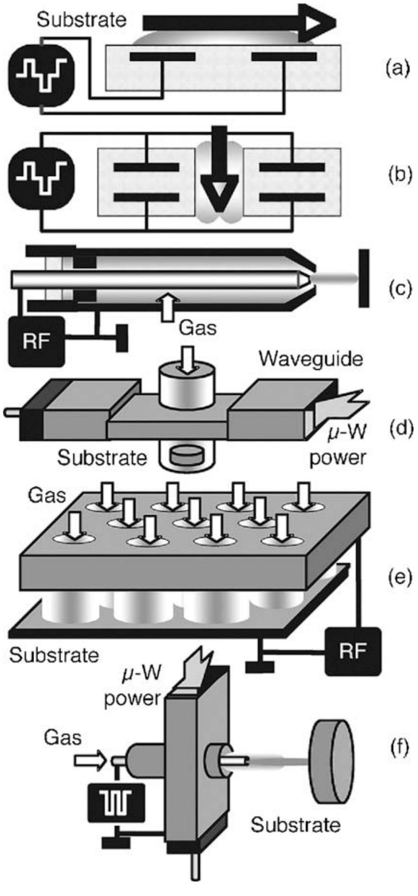

Figure 17.3: Examples of cold atmospheric plasma sources: (a) Dielectric barrier discharge (DBD) with electrodes inside a dielectric barrier; (b) DBD with parallel pairs of electrodes; (c) radio-frequency (RF) plasma jet; (d) microwave waveguide plasma source; (e) fused hollow cathode (FHC) plasma source; (f) hybrid hollow electrode activated discharge (H-HEAD) plasma source.

pulsed breakdown shown in Figure 17.1. This very common form of discharge appears more frequently in molecular gases than in atomic gases [6]. In a realistic model of DC atmospheric breakdown in CO_2 lasers by Palmer [8], the streamers appear mainly at large electrode distances d when the volume ionization by a single avalanche forms the space-charge field comparable to the total applied field. Then the secondary avalanches (caused e.g. by photoionization) converge toward the primary avalanche and form highly conducting filaments. This resembles a 'micro-thunderstorm' with a breakdown (lightning) between clouds. A typical streamer has a diameter of about 0.2–0.4 mm in pure N_2 and about 1 mm in air [9]. It can conduct up to several amperes of the DC current in air [13]. Both the streamer diameter and the current depend on the applied voltage. It might be interesting to note that the 30 kA currents in a typical lightning flash in real thunderstorms with current channel diameters of about 0.1 m (1–10 m is the light channel diameter) might be well compared with the micro-thunderstorm in air with 3 A streamers having diameter of 1 mm. The current density in both flashes is 1.2 kA/cm^2. Also, shapes of the streamers often exhibit branching, similarly to the lightning flashes, and they are quite noisy. Multiple plasma streamers are undesirable in applications because they can cause uneven treatment and local damage to thermally sensitive substrates, for example webs.

17.2.3 Suppression of Streamers in High-Pressure Plasmas

There are several options by which to suppress or even avoid arc streamers. For example, in a small gap, d, the probability of space charges formation is lower, as could be understood from Section 17.2.2, which limits the volume breakdown and formation of conductive channels with streamers. In many atmospheric plasma systems helium is used because of its small atoms (He has a diameter of ~ 0.28 nm, while the air molecule has a diameter of ~ 0.97 nm), high diffusion coefficient D and a long mean free path compared to other gases. Helium ions are very efficient in production of secondary electrons (high secondary electron emission coefficient γ), which enables lower breakdown voltages.

Another option is the utilization of high-frequency power. For example, microwave power (2.45 GHz) is often used because of its stabilizing effect in volume ionization without the necessity for electrode-based secondary electrons. This enables the electric field to be decreased. It has been shown experimentally that the breakdown voltage in He at about 80 kPa (600 torr) decreases with the frequency in an interval between 5 and 30 MHz [10].

In the electrode systems powered by alternating current generators different dielectric barriers covering the electrodes can be used to limit the current. In these dielectric barrier discharge (DBD) systems only displacement current can flow and formation of the arc-based streamers is naturally limited.

A further option is using special electrode shapes with sharp edges or cones forming high-intensity local electric fields [11, 12]. A short pulse power preventing the development of arcs is very efficient, too. Much effort has been put into designing special shapes of pulses, usually in combination with dielectric barriers, where the correct ratio between positive and negative parts of the pulse is important to neutralize the charge accumulated on the barrier surface and decrease the probability of forming streamers.

17.2.4 Space-Charge Sheaths at Low and High Gas Pressures

In all plasma devices the interface between the plasma and solid surfaces (electrode, substrate, reactor wall) – the space-charge sheath – plays an important role. At low gas pressures the sheath can be considered collisionless but it is obviously not so at high pressures. In a low-pressure approach the sheath thickness d_s depends on the gas pressure p roughly as $d_s \approx p^{-1/2}$. If d_s at 1 mbar is about 1 mm it should be $10^{-3/2}$ (≈ 0.032) times shorter at 1 bar, i.e. about 30 μm. Calculations of the sheath thickness at atmospheric pressure based on the conventional Child–Langmuir approach lead to values of about 10 μm at largest. However, experiments show about one order thicker sheaths, particularly in the atmospheric RF discharges [7, 14, 15]. This is important, for example, for RF hollow cathode devices, where the distance between the opposite walls must be sized to at least $2d_s$. A simple realistic model of the atmospheric pressure RF sheath taking into account secondary and fast electrons [16] confirms experimental d_s values of about 100 μm. Thus, the intense discharges in RF electrodes with rectangular openings or holes of 400 μm in size are certainly based on the hollow cathode effect, and explanations using conventional approaches may be rather confusing.

Recent model studies of electron kinetics in atmospheric RF microdischarges in helium confirm that the electron energy distribution function in atmospheric pressure microdischarges is far from the equilibrium, and simulation results from conventional fluid models should therefore be interpreted with particular caution [17]. For an RF-powered plasma at atmospheric pressure, the electron collision frequency is much higher than the RF driving frequency (usually 13.56 MHz). Consequently, the electron energy relaxation time ($\approx$ 5 ps to 10 ns) is much shorter than the RF period ($\approx$ 74 ns) and the electron energy distribution function is time modulated. It is therefore possible to consider the RF-coupled capacitive discharges at atmospheric pressure as a kind of succession of DC discharges sustained at different voltages [17]. However, similarly to RF plasmas at low pressures, the heavy ions cannot follow the instantaneous RF field.

17.3 Examples of Cold Atmospheric Plasma Sources

Several examples of plasma sources for generation of cold atmospheric plasma are shown in Figure 17.3. Probably the simplest and the most widespread cold atmospheric plasma sources shown in Figure 17.3(a, b) are based on the DBD (see reviews [18, 19]). A dielectric barrier at one or both electrodes efficiently prevents streamers. There are a great number of different constructions and shapes of electrodes and dielectric barriers in the DBD plasma sources for different applications. Typical treatments of moving planar substrates are indicated in Figure 17.3(a, b). Accumulated surface charges on dielectric barriers can be neutralized by a bipolar pulsed DC power. The DBD of this type can be used arbitrarily in all kinds of gases, in both static and flowing regimes.

Figure 17.3(c) shows a typical jet plasma source powered by an RF generator [20]. These sources can also be arranged with a dielectric barrier covering one or both electrode surfaces. The operating frequency of such coaxial sources can be easily extended up to the microwave range. Increasing the frequency of the power generator up to the microwave range usually reduces the problem with streamers substantially and enables generation of the glow plasma in virtually all molecular gases.

A simple microwave source of cold atmospheric plasma is shown in Figure 17.3(d) [21]. The source can be assembled from standard waveguide components with a tapered part to increase the electric field in the axis of dielectric reactor passing through this part. Different microwave systems and principles can be used for constructions of plasma applicators, including microwave resonators and radiating structures.

Many atmospheric plasma sources are based on microdischarges where small size atmospheric plasma units are multiplied to form arrays or integrated in-line or area-distributed systems. Very specific systems for generation of the large-area plasmas are based on multiple hollow cathodes integrated in an FHC. Figure 17.3(e) shows schematically an FHC reactor where multiple hollow cathodes, powered for example by an RF generator, are positioned close to each other so that individual plasmas interact with each other [22]. Such an arrangement enables very low RF powers for keeping the plasma over the whole electrode surface ($\geq 0.2\,\mathrm{W/cm^2}$ in neon) and low breakdown RF voltages. It is therefore possible to ignite the plasma without any additional tools. Figure 17.4 shows an example of a circular cartridge FHC system (diameter of 35 mm) with about 900 hollow cathodes producing argon plasma in open air at an RF power of 70 W [23].

The hybrid plasma source ‘hybrid hollow electrode activated discharge’ (H-HEAD) (Figure 17.3f) combines a microwave antenna with a hollow cathode powered by an RF or pulsed DC generator. The microwave plasma is produced by surface waves and the energy of particles can be controlled by the hollow cathode. Such a source is capable of producing very long plasma columns (up to 18 cm) at very low gas flows (≤ 250 sccm), and it works virtually with all types of gas [24, 25]. Recent results [26] proved that it is possible to operate the source in water vapor or even in water. A photograph of the plasma generated with the antenna immersed in water held in a simple container is shown in Figure 17.5.

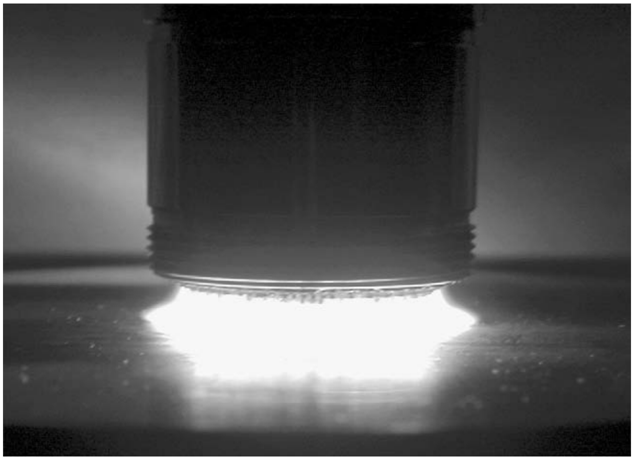

Figure 17.4: Fused hollow cathode (FHC) cold atmospheric discharge in Ar + air. Parameters: RF power = 70 W, 2 slm Ar, plasma diameter = 35 mm.

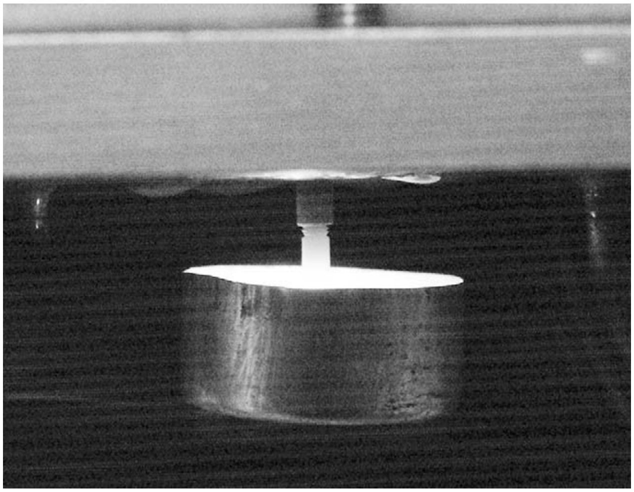

Figure 17.5: Water plasma generated by the H-HEAD source at 200 W with the microwave antenna immersed in the water container. Condensed water is seen at the bottom part of the source.

17.4 Characteristic Features and Typical Applications of Cold Atmospheric Plasma

Because of considerable differences between the low-pressure plasmas and atmospheric pressure plasmas it is not realistic to expect that the low-pressure plasma can be simply replaced by an atmospheric plasma and used for the same applications.

17.4.1 Typical Features and Application Abilities of Atmospheric Plasma

Important features and typical application abilities for cold atmospheric plasma are briefly listed and commented on below.

1. *Start-up (breakdown) regimes and tools are sometimes needed* as the breakdown voltages in atmospheric plasma systems are often considerably higher than the maintenance voltages. Similarly, the impedances with and without plasma can be very different. Figure 17.6 shows an example of ignition of a hybrid microwave plasma [24] by a high-voltage spark produced by a Tesla coil.
2. *Occasional arcing and non-uniform (filamentary) plasmas*, mainly in molecular gases, can be prevented by special designs of both the plasma source and the power generator (see e.g. [11, 12, 27]). Some of these options have been discussed in Section 17.2.3.
3. *Almost no use of magnetic fields can be expected*. The mean free path is usually very short in comparison with the Larmor radii of charged particles in 'normal' magnetic fields (induction $B \leq 0.1$ T). However, at a high current density of 1.2 kA/cm^2 in streamers it may be possible to affect their motions in non-equilibrium filamentary plasmas. Detailed

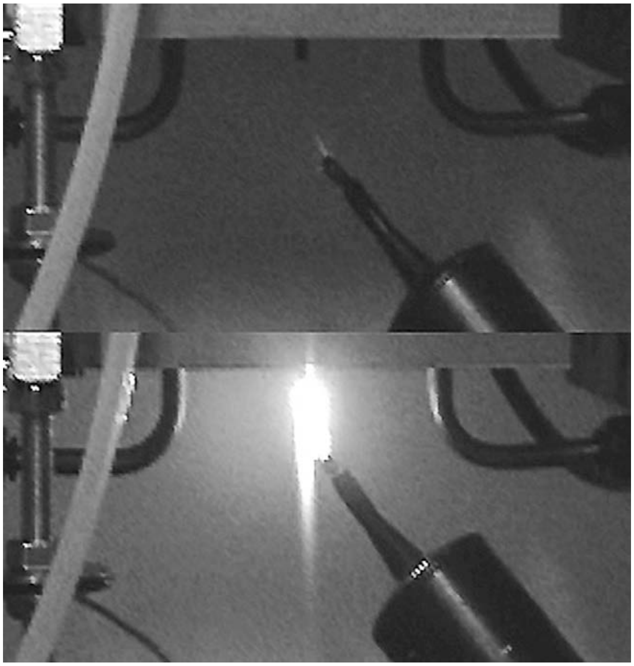

Figure 17.6: Spark ignition of the plasma plume in the hybrid plasma source (H-HEAD) by the Tesla coil. A spark ignited between the Tesla coil and the microwave antenna of the H-HEAD source (upper picture) causes instant formation of the plasma plume (lower picture).

experiments are needed to verify this. Pulsed magnetic fields have already been proven to affect atmospheric spark discharges [28].

4. *The plasma has restricted dimensions* due to the short mean free paths of particles. For example, the calculated mean free path at atmospheric pressure and a gas temperature of 100 °C is only 12 nm for air (molecular diameter of 0.97 nm) and 146 nm for helium (atomic diameter of 0.28 nm) [29]. Processing of 3D substrates often requires large gas throughputs (already of the order of 10 slm at a laboratory scale) and the use of helium as a carrier gas. An exception is the H-HEAD source [24, 25], where long plasma plumes can be generated at very low gas throughputs (about 0.1 slm). For large-area treatments multiple plasma structures similar to FHC systems should be applied (see e.g. [30]). Movements of the plasma source or substrate, or both, are often required.

5. *Low ion energies exclude sputtering*. Pumping the energy selectively into electrons in atmospheric plasmas and a high collision frequency naturally limit the energy of ions. This, in practice, excludes the ion-assisted processes well known in the physical vapor deposition (PVD) of films in low-pressure plasma systems. Note that theoretical threshold ion energies for sputtering by noble gas ions exceed 1 eV and experimental values usually exceed 10 eV [31].

6. *Production of dangerous by-products* can take place in open systems. Different nitrogen oxides, NO_x (N_2O, NO, NO_2), can be generated in high-voltage air-assisted plasmas. Quite low levels of nitrogen oxides (≥ 0.1 ppm) in the air can irritate human eyes, nose, throat, and lungs, and cause coughing, shortness of breath, tiredness, and nausea [32]. Another possible by-product is ozone, which can damage the human lung at levels of ≥ 130 ppb. Cyanogens (CN, HCN) and CO are particularly dangerous. For certain processes a hermetic chamber and proper ventilation are absolutely necessary.

7. *Atmospheric plasma can also be used in processes opposite to those discussed in (6) above, for removal of dangerous by-products and flue gas abatement* (NO_x, CO, SO_x, volatile organic compounds, etc.). Applications for abatement of hazardous components in the flue gas from power plants and for exhaust aftertreatment from diesel engines have been tested for more than 20 years (see e.g. [33, 34] and references therein).

8. *Atmospheric plasma can be used in particle and film treatment, recrystallization and sintering*. This point can be considered an emerging application despite the fact that sintering experiments in plasma began more than 20 years ago [35]. As the treatment may require elevated plasma temperatures, utilization of decaying parts of thermal plasmas can be more efficient than cold plasma.

9. *Short mean free paths in atmospheric plasma* are highly compatible with microscale or nanoscale processes leading to production of microparticles or nanoparticles and objects. One example is the use of microhollow cathodes for dry etching and diamond deposition

in reactors at slightly reduced pressures [36]. Another example is the production of nanocrystalline diamond on stainless steel by hybrid plasma at atmospheric pressure in air mixed with ethanol [37].

10. *Atmospheric plasma can serve as a source of ultraviolet (UV) and vacuum ultraviolet (VUV) radiation*. An example is VUV radiation with a wavelength of $\approx 130\,\text{nm}$ from atmospheric microhollow cathodes in argon [38].

11. *Atmospheric plasma can be used for disinfection, cleaning, deactivation, and decontamination of surfaces*. The plasma has ability to kill bacteria [39] at least due to an intense UV light [40]. There are many promising applications in chemical and possibly also nuclear decontamination.

12. *There are many potential medicinal applications of cold atmospheric plasma*. Besides disinfection and treatment of inorganic surfaces, new treatments and cures of human skin and different biological objects are being tested in numerous laboratories all over the world (see e.g. [41, 42]). Such treatments obviously cannot be carried out under vacuum by low-pressure plasma. This new field of research requires thorough, careful, and long-term multiple experiments.

13. *Reactive interactions of cold atmospheric plasma with (and inside) liquids* are tested to study processes inside liquid (submersible arrangements) (see e.g. [43]). Direct contact of the plasma with or inside liquid can be arranged without interference of the air. An example of this kind of arrangement has been discussed above (Section 17.3 and Figure 17.5). Experiments confirm, for instance, the applicability of underwater plasma arrangements for the treatment of cotton yarns [44]. New developments and processes using submerged plasmas can be expected in the near future.

14. *Diesel fuel reforming and related applications in plasma chemistry*. Plasma-based fuel converters enrich the fuel with hydrogen by boosting partial oxidation, which reforms hydrocarbon fuels into a hydrogen-rich gas for more powerful and efficient combustion with considerably fewer effluents and particles. Experiments began in the 1990s [45].

17.4.2 Applications of Atmospheric Plasma in Coating and Surface Processing

Cold atmospheric plasmas are often used for the efficient pretreatment and activation of surfaces, particularly webs. Such treatment is about ten times faster than in low-pressure plasmas. However, traces of streamers in the high-voltage filamentary discharges can damage the surfaces of plastic webs. The low-power FHC discharges can activate plastic webs without damage and without undesirable changes in polymer crystallinity [46]. Cold atmospheric plasma pretreatment of surfaces is already used as a standard commercial technology [47].

Film parameter control is limited in atmospheric plasma coating because of low ion energies and high collision frequency at atmospheric pressure. It is not realistic, for example, to expect efficient control of coating properties (texture, hardness) by bias-controlled ion bombardment. The films deposited in an atmospheric plasma are mostly amorphous [48], unless an elevated substrate temperature is used. Production of hard coatings without substantial heating of the substrate or additional post-treatment (e.g. annealing) is a problem.

Feasible coating regimes in cold atmospheric plasma are based on plasma-enhanced chemical vapor deposition (PECVD). All coating regimes reported so far in the literature are based on PECVD using precursors diluted mainly in He carrier. Large-area coating of 2 m wide webs using liquid precursors can be performed in commercial DBD arrangements with multiple flat electrodes [49]. The PECVD regimes are based on the formation of reactive radicals. Evaporation of material targets can be applied only in special arrangements. Note that high voltages and high collision frequency in the atmospheric plasma systems can produce intense UV radiation from the plasma, which may assist in surface activation, photo-assisted chemistry, enhanced gas activation, etc.

Atmospheric plasma coating systems in arrangements open to the ambient air are suitable for deposition of oxides and oxynitrides. Other film compositions require hermetic chambers protecting the plasma from the ambient atmosphere. Our experiments show that even when the plasma is generated in an inert gas the optical emission spectra confirm high emission intensities of the molecular nitrogen and oxygen band systems, excited oxygen atoms, etc. The active oxygen produced in the plasma can be used for surface oxidation. We have observed rapid surface oxidation of molybdenum substrates in H-HEAD air atmospheric plasma in the presence of ethanol vapor. Polycrystalline MoO_3 formations shown on the scanning electron microscope image in Figure 17.7 were observed after several tens of minutes of air plasma

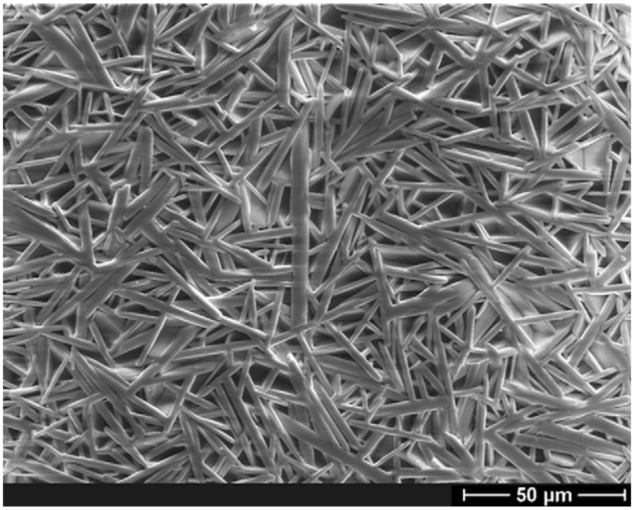

Figure 17.7: Typical formations of polycrystalline MoO_3 created on Mo surface by oxidation of Mo substrate in the hybrid atmospheric air plasma generated by the H-HEAD source. Microwave power 300 W, pulsed DC voltage 30 ns, 8 kV, 100 Hz.

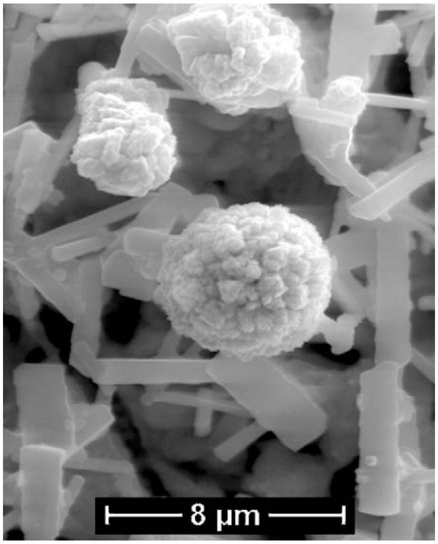

Figure 17.8: Multiple nucleation of diamond crystals on MoO_3 formations observed in air hybrid plasma interacting with an alcohol vapor. (See [37].)

treatment by a hybrid plasma source (shown in Figure 17.3f) at much larger areas than corresponding to the diameter of the interacting plasma on the Mo substrate, and even on the opposite side of the substrate. As shown in Figure 17.8, the MoO_3 surface can be used for nucleation of diamond crystals formed from an alcohol vapor in the air plasma generated by the hybrid source [37].

17.5 General Conclusions

Low-temperature, non-equilibrium atmospheric plasma shows very promising potential for a number of new, non-conventional applications, including new surface treatments and processing of materials. However, the principles, characteristic features, and feasible processes in cold plasma at atmospheric and higher pressures are often considerably different from those in low-pressure, low-temperature plasmas. It is therefore reasonable to conclude that cold atmospheric plasma extends the potential of plasma technology without considerable competing with conventional and well-established low-pressure plasma systems.

Acknowledgments

Financial support from the Foundation for Strategic Environmental Research (MISTRA) and Johan Gustaf Richerts Scientific Foundation in Sweden is gratefully acknowledged.

References

[1] M. Vardelle, A. Vardelle, P. Fauchais, M.I. Boulos, Am. Inst. Chem. Eng. J. 29 (1983) 236.
[2] J. Mostaghimi, P. Proulx, M.I. Boulos, Plasma Chem. Plasma Process. 4 (1984) 199.
[3] M.M. Kekez, M.R. Barrault, J.D. Craggs, J. Phys. D: Appl. Phys. 3 (1970) 1886.
[4] F. Paschen, Weid. Annalen der Physik 37 (1889) 69.
[5] L. Bárdos, in: Proc. XXI. Int. Conf. on Phenomena in Ionized Gases (ICPIG), Bochum, 1993 (Arbeitsgemeinschaft Plasmaphysik, Ruhr-Universität Bochum) Vol. III (1993) 98.
[6] R. Sankaranarayanan, B. Pashaie, S.K. Dhali, Appl. Phys. Lett. 74 (1999) 3119.
[7] H. Baránková, L. Bárdos, Surf. Coat. Technol. 163–164 (2003) 649.
[8] A.J. Palmer, Appl. Phys. Lett. 25 (1974) 138.
[9] R. Ono, T. Oda, J. Phys. D: Appl. Phys. 36 (2003) 1952.
[10] S. Kanazawa, M. Kogoma, T. Moriwaki, S. Okazaki, J. Phys. D: Appl. Phys. 21 (1988) 838.
[11] S. Okazaki, M. Kogoma, M. Uehara, Y. Kimura, J. Phys. D: Appl. Phys. 26 (1993) 889.
[12] A. Larsson, J. Phys. D: Appl. Phys. 31 (1998) 1100.
[13] J. Park, I. Henins, H.W. Hermann, G.S. Selwyn, J. Appl. Phys. 89 (2001) 15.
[14] J. Laimer, S. Haslinger, W. Meissl, J. Hell, H. Störi, Vacuum 79 (2005) 209.
[15] J.J. Shi, M.G. Kong, IEEE Trans. Plasma Sci. 33 (2005) 278.
[16] D. Söderström, H. Baránková, L. Bárdos, IEEE Trans. Plasma Sci. 35 (2007) 522.
[17] F. Iza, J.K. Lee, Proc. 18th Int. Symp. on Plasma Chemistry (ISPC-18), Kyoto University, August 26–31, 2007, Presentation 28A-p5, Abstract p. 218, Poster no. 28P-124, pdf file paper 00381. <http://plasma.kuee.kyoto-u.ac.jp/ispc18/>.
[18] U. Kogelschatz, Plasma Chem. Plasma Proc. 23 (2003) 1.
[19] R.R. Roth, J. Rahel, X. Dai, D.M. Sherman, J. Phys. D: Appl. Phys. 38 (2005) 555.
[20] L. Mollwo, Ann. Physik 7 (1958) 97.
[21] K.M. Green, M.C. Borras, P.P. Woskov, G.J. Flores III, K. Hadidi, P. Thomas, IEEE Trans. Plasma Sci. 29 (2001) 399.
[22] H. Baránková, L. Bárdos, Appl. Phys. Lett. 76 (2000) 285.
[23] H. Baránková, L. Bárdos, Surf. Coat. Technol. 174–175 (2003) 63.
[24] L. Bárdos, H. Baránková, J. Vac. Sci. Technol. A 23 (2005) 933.
[25] H. Baránková, L. Bárdos, D. Söderström, J. Vac. Sci. Technol. A 24 (2006) 1410.
[26] L. Bárdos, H. Baránková, unpublished results, Project sponsored by J. Gustaf Reachert Foundation in Sweden (2008).
[27] F. Massines, A. Rabehi, P. Decomps, R.B. Gadri, P. Segur, C. Mayoux, J. Appl. Phys. 83 (1998) 2950.
[28] V. Majidi, D.M. Coleman, Appl. Spectrosc. 41 (1987) 200.
[29] C.R. Nave, HyperPhysics 2006; Mean Free Path Calculation, Georgia State University, Atlanta, GA. <http://hyperphysics.phy-astr.gsu.edu/Hbase/kinetic/menfre.html>.
[30] O. Sakai, Y. Kishimoto, K. Tachibana, J. Phys. D: Appl. Phys. 38 (2005) 431.
[31] D.E. Harrison Jr, G.D. Magnuson, Phys. Rev. 122 (1961) 1421.
[32] For more information contact Agency for Toxic Substances and Disease Registry, Division of Toxicology, Atlanta, GA. <http://www.atsdr.cdc.gov/>.
[33] J.C. Hilliard, F.J. Weinberg, Nature 259 (1976) 556.
[34] S. Masuda, H. Nakao, IEEE Trans. Ind. Appl. 26 (1990) 374.
[35] D.L. Johnson, R.A. Rizzo, Am. Ceram. Soc. Bull. 59 (1980) 467.
[36] R.M. Sankaran, K.P. Giapis, J. Phys. D: Appl. Phys. 36 (2003) 2914.
[37] L. Bárdos, H. Baránková, Plasma Proc. Polym. 4 (2007) 511.
[38] K.H. Schoenbach, A. El-Habachi, W. Shi, M. Ciocca, Plasma Sources Sci. Technol. 6 (1997) 468.
[39] M. Laroussi, IEEE Trans. Plasma Sci. 30 (2002) 1409.
[40] M. Moisan, J. Barbeau, S. Moreau, J. Pelletier, M. Tabrizian, L'H. Yahia, Int. J. Pharmaceut. 226 (2001) 1.
[41] S. Tümmel, N. Martens, J. Wang, W. Viöl, Plasma Process. Polym. 4 (2007) 5465.

[42] G. Fridman, M. Peddinghaus, H. Ayan, A. Fridman, M. Balasubramanian, A. Gutsol et al., Plasma Chem. Plasma Proc. 26 (2006) 425.
[43] N. Parkansky, B. Alterkop, R.L. Boxman, S. Goldsmith, Z. Barkay, Y. Lereah, Powder Technol. 150 (2005) 36.
[44] A.Yu. Nikiforov, C. Leys, Plasma Chem. Plasma Proc. 26 (2006) 415.
[45] D.R. Cohn, A. Rabinovich, C.H. Titus, L. Bromberg, Int. J. Hydrogen Energy 22 (1997) 715.
[46] H. Baránková, L. Bárdos, Surf. Coat. Technol. 146–147 (2001) 486.
[47] Commercial info available at <http://www.plasmatreat.com/>.
[48] J.L. Hodkinson, D.W. Sheel, H.M. Yates, M.E. Pemble, Plasma Proc. Polym. 3 (2006) 597.
[49] L. O'Neill, S.P. Ryan, L.-A. O'Hare, S.R. Leadley, A.J. Goodwin, Proc. 48th Tech. Conf., Society of Vacuum Coaters, Denver, SVC, Albuquerque (2005). <http://www.svc.org/p. 219>.

CHAPTER 18

Jet Vapor Deposition

Paul Komarenko, Michael Drago, Michael Gorski, Takashi Tamagawa
and Bret Halpern
Jet Process Corporation, 57B Dodge Avenue, North Haven, CT 06473, USA

18.1 Introduction

Jet Vapor Deposition^{TM} (JVD^{TM}) uses high-speed inert gas jets to carry film components to substrates. This transport takes place in a fast flow system, mechanically pumped to pressures in the range of 1 torr. Developed by Jet Process Corporation (JPC) and now used commercially, JVD has been applied to a wide range of thin and thick film applications, demonstrating an adaptability to new problems, and a versatility for making complex materials quickly and economically.

Our work in the past shows that JVD is particularly well suited to solder deposition for *microelectronic packaging*, where there is a growing need to solder small electronic devices on ever smaller circuit features at higher density. Deposition of the required solder bumps, often of expensive alloys such as eutectic AuSn, taxes the capability of standard techniques to produce correct properties in an economical way. JVD is thus fast becoming a method of choice, and JPC has become an important supplier of solder layers and related adhesion, diffusion barrier, and protective cap layers.

JVD's signature innovation is a novel vapor source: a *sonic jet in low vacuum* which transports condensable atoms, molecules, or clusters, to a substrate and deposits them efficiently in a small area. Larger areas are coated by arranging for relative two-dimensional (2D) motion between substrate and one or more jet sources. The combination of jet sources and mechanisms for jet–substrate relative motion characterizes JVD.

The use of the jet in low vacuum for deposition, first investigated by Halpern [1] and later by Schmitt and Halpern [2, 3], has opened new pathways to both microscopic property control and manufacturing efficiency. JPC has developed several jet sources based on different principles, which are now basic components of a *multiple jet, moving substrate* process [4] for depositing metals, semiconductors, dielectrics, oxides, nitrides, and organics. These materials can be grown by JVD in many forms: multicomponent, alloy, multilayer, host–guest, and nanocluster films. The growth rates are high, approaching in some cases *micrometers per minute* over areas of several hundred cm^2. Deposition is carried out without toxic precursors or effluent, on substrates that remain cool, near room temperature. By straightforward control of jet source conditions, JVD can generate and deposit either atoms or nanoclusters, both at high rate. Atoms and clusters behave differently in deposition, particularly in penetration of photoresist mask windows needed for solder bump deposition. All these features of JVD are valuable for deposition of solder and related layers. JVD is deceptively simple, but it has a fortunate combination of useful characteristics, which will be discussed in the following sections:

Section 18.2: Principles of JVD sources and systems

Section 18.3: Relative motion between jet source and substrates

Section 18.4: Three JVD jet sources

Section 18.5: Generation and deposition of atoms and clusters

Section 18.6: Application of JVD to solder and related layers.

Apart from solder deposition, the previous edition of this Handbook described a variety of past applications showing the range of JVD. These applications and related references are briefly summarized in the Appendix.

18.2 Principles of JVD Sources and Systems

Jet sources can have different designs, but all are mounted on flanges aimed into a low-pressure deposition chamber. A fast flow of inert gas through each jet source is sustained by a mechanical pump and Roots blower [5, 6] with pumping speeds typically in the range of 5000–10,000 liters/minute, but sometimes higher or lower. These pumps comprise a reliable, inexpensive vacuum technology.

A typical jet source is a 3 inch (7.62 cm) diameter cylindrical nozzle, with an endplate having an exit orifice ~ 1 cm in diameter. Helium or argon, and occasionally nitrogen, is supplied to the nozzle and exits from it as a jet. Ordinarily the nozzle pressure P_n is several torr, and the

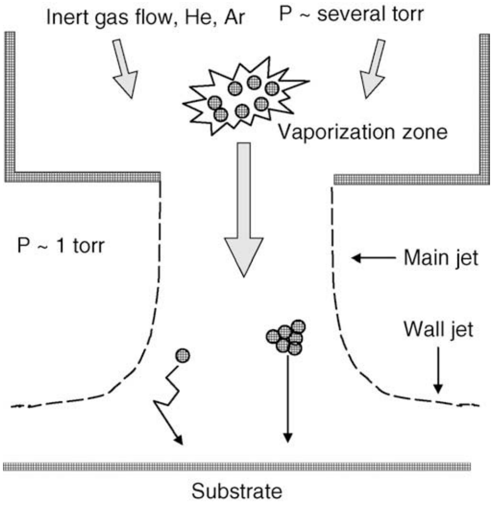

Figure 18.1: Generalized jet source, showing nozzle, main jet, and wall jet. The nozzle exit diameter is typically 1 cm. Metal atoms are vaporized near exit, deposit in localized area. Trajectories before impact: atom, diffusive; cluster, straight.

downstream pressure P_d is 1 torr or less, but the range may be wide: in different applications both pressures can be higher or lower. When the ratio $P_n/P_d > 2$, the flow is *critical*, and the jet emerges at the speed of sound; for He at 298 K, the exit velocity is $\sim 10^5$ cm/s. There is considerable latitude in the source shape, orifice size, and operating parameters of a jet source. Figure 18.1 shows a generalized jet source.

The jet can entrain any atomic, molecular, or cluster vapor, and convey it to a substrate for condensation. A vapor source is placed upstream of the nozzle exit, a region in which the carrier gas is accelerating toward the speed of sound. Depending on the material, vaporization can be effected by several techniques, such as thermal evaporation, glow discharge sputtering, and microwave plasma or direct current (DC) discharge reaction. Atoms of gold, for example, injected upstream into the He flow will be swiftly captured and transported downstream by the jet. On a flat substrate placed perpendicular to the jet, and several centimeters downstream, a bright gold deposit will quickly appear; virtually all the gold atoms deposit in a circular zone comparable to the nozzle exit area. The deposit is symmetric but non-uniform, being thicker toward the center. The capture efficiency for metal atoms is generally high, and for clusters even higher; Figure 18.1 indicates the trajectories of an atom and a cluster before impact on the substrate. We will discuss later the designs of three sources based on different vapor generation approaches.

The use of single or multiple jets in JVD synthesis follows from the structure of a single inert gas jet. The jet contour can be made visible by atomic emission from a plasma ignited in the jet, or by chemiluminescence, say from active N_2. The structure of free jets issuing from small-diameter nozzles at high pressure has been amply described [7], but particularly useful features arise under JVD conditions, where the nozzle exit diameters are relatively large, ~ 1 cm, and the nozzle pressures are usually between 1 and 10 torr.

On exiting the nozzle, the jet expands into a zone of reduced density in which nearly all atoms move in the same direction at the speed of sound. In JVD this zone is nearly collision free; it terminates at the Mach disk, located a distance $x \sim 0.67\, d_n(P_n/P_d)^{1/2}$ downstream of the nozzle of diameter d_n [7]. The pressure ratio usually lies in the range $2 < P_n/P_d < 10$, and the Mach disk is located several nozzle diameters, or several centimeters, downstream. Beyond the Mach disk the density rises sharply to the downstream background value, the jet speed drops to $\sim 3 \times 10^4$ cm/s, determined by the system pumping speed, and collisions again occur in the jet. Further downstream the jet diverges little, under typical JVD conditions, and remains fairly collimated over distances of tens of centimeters.

Jet collimation has important consequences. Because axial transport is much faster than radial diffusion, the jet remains a spatially distinct source independent of other nearby jets, so that several jets can be operated close to each other.

A heavy atom injected into the light carrier jet will travel with the jet, but will also execute a 'random walk'. For example, an atom of Au injected on the jet axis will diffuse a distance x away from the axis during the transit time to the substrate $\tau = L/v$ according to

$$x^2 \sim 2D\tau \sim 2DL/v \tag{18.1}$$

where D is the diffusion coefficient, L is the distance to the substrate, and v is the jet speed downstream of the Mach disk. For $L \sim 10$ cm, $v \sim 3\times10^4$ cm/s, and $D \sim 600$ cm^2/s (diffusion in He at 1 torr), the diffusion distance is ~ 4 mm. Therefore most Au atoms will have diffused only a few millimeters from the axis by the time they arrive at the substrate; they are effectively trapped within the jet, and cannot easily escape. This already suggests a high capture efficiency on the substrate, which is particularly important for expensive metals. In a real jet source, vaporization does not occur exactly on axis, but from an extended area such as a hot W coil, so that a fraction of Au atoms are nearer the jet boundary and can escape more readily. But the fraction lost turns out to be small.

On impact with the substrate the *free jet* flares radially into a *wall jet*. Visualization experiments show that the transition from free jet to wall jet is sharp; the thickness of the wall jet is only a few millimeters. When the Au atoms arrive near the substrate, the wall jet can be expected to carry some of them away, as well as broaden the deposit. But a thin wall jet favors deposition; metal atoms in the wall jet can still diffuse fast to the substrate. In the wall jet too, only a small fraction of gold atoms are transported far enough to be lost.

We confirmed the high capture efficiency of Au atoms by mass balance experiments; a known length of Au wire is vaporized in the nozzle, and the weight deposited downstream is measured with a microbalance. We found that 95% of the Au wire vaporized in the nozzle deposited on the substrate, with the remainder carried away in the wall jet. Jet collimation and localized deposition can be regarded as the JVD equivalent of *line of sight* deposition in high vacuum. The deposition efficiency is far higher in JVD, however: all vaporized material goes in one direction, is confined to the jet, and most of it deposits in the impact zone.

The large inertia of Au atoms entrained in the jet may also favor high capture efficiency. When the axial He jet transforms sharply into a radial wall jet, heavy Au atoms turn the corner only with difficulty, and tend to move straight toward the substrate [8]. We have not yet determined the relative importance of diffusion and inertia in the wall jet region under our operating conditions, but studies of deposition under conditions of much higher pressure ratio P_n/P_d and much smaller nozzle diameter than JVD do show inertial effects under restricted conditions [9]. In JVD cluster deposition, inertia plays an important role, to be discussed later.

Simultaneously flowing jets are not only spatially distinct, but the operation of one does not alter the upstream nozzle conditions of any other. As long as P_n/P_d exceeds ~ 2, the pressure P_n in the nozzle remains constant despite changes in downstream P_d resulting either from changes in pumping speed or from injection of gas downstream. If the pump can sustain critical flow, the jets all emerge at the speed of sound, and neither information nor mass can propagate upstream. Therefore the calibration of one jet source is unaffected by simultaneous operation of other jets. This makes it possible to run several jet sources together to make multicomponent films of accurate composition.

Another example of the benefits: we vaporize many metals in a hollow cathode sputter jet, or a wirefeed jet, and then oxidize the growing metal film with O_2 or O atoms injected downstream. Inside the nozzle, the metal sputtering target or any other metal vapor source is then shielded from the oxidants downstream by sonic flow out of the nozzle; a comparable protection in high-vacuum PVD is nearly impossible.

In sum, JVD's jets in low vacuum have a relatively simple behavior, despite variations in density and speed near the Mach disk. The main jet is fast, collimated, and well defined, and the wall jet is thin. Consequently, the jet delivers metal or other vapor efficiently; deposition is localized, film growth is fast, and radial wall jet flow does not greatly broaden the deposit. Multiple jets are basically independent.

18.3 Relative Motion between Jet Sources and Substrates

In order to deposit uniform films over larger areas, the jet source and substrate are moved relative to each other in two dimensions [4]. Solder must be deposited on a range of substrates

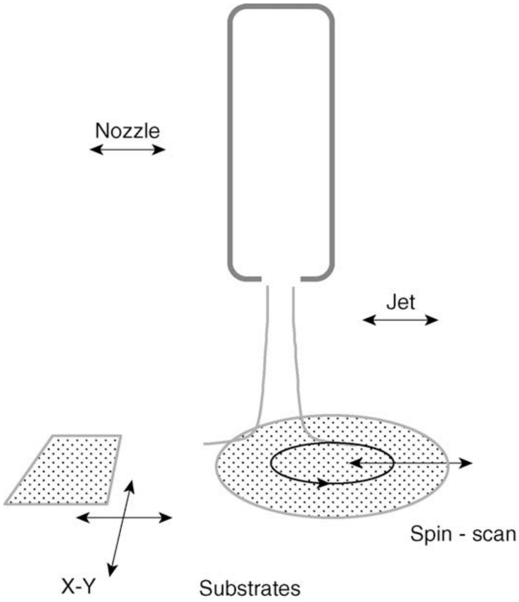

Figure 18.2: Schemes for 2D relative motion between substrate and jet sources. Different combinations of rotation and translation are possible.

including flat patterned silicon wafers of 2, 4, 6, and 8 inch diameter, rectangular substrates of similar area, and small components such as CuW heat sinks of irregular shape and millimeter dimensions. JVD systems must be versatile enough to coat single wafers or batches, by providing the 2D relative motion between jet and substrate. As shown in Figure 18.2, one can move the source or the substrate (or even the gas jet itself) with motion control electronics giving appropriate combinations of rotation and translation. Motion is transmitted mechanically through chamber walls via bellows assemblies and ferrofluidic seals, or by stepper motors within the chamber. Figure 18.2 also suggests the various combinations that have been implemented at JPC. For example, in Figure 18.3 substrates are mounted on a carousel which can both spin rapidly and translate slowly along its axis; the carousel motion is computer controlled, and various motions can be programmed. The jet is aimed radially at the carousel. If the carousel is only spinning, a band of deposition appears around it; if the carousel is also vertically *scanned* at constant speed, the band broadens to cover the entire carousel surface, and that of any substrate on it. The deposit thickness is uniform because all areas are exposed for equal times to a constant jet flux. This approach is ideal for batches of small or moderate sized substrates, where the *flatness* of the substrate does not depart much from the curvature of the carousel, so film thickness remains uniform. To keep the size of carousels and chambers manageable, this batch processing is limited to 4 inch diameter wafers or 4 × 4 inch squares.

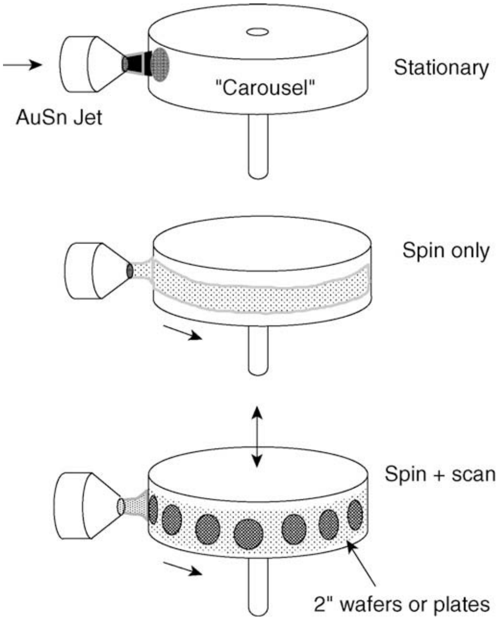

Figure 18.3: A spinning, oscillating carousel for batch deposition of uniform films on small wafers or small substrates of other shape.

Several jet sources can be aimed at the carousel. To make a *layered* compound, the jet sources are run in sequence, as in Figure 18.4, for different times determined by the required layer thickness. To deposit a *multicomponent* compound, several jets are run at the same time, while the substrate is sweeping through all the jets at high speed. Relative motion between substrate

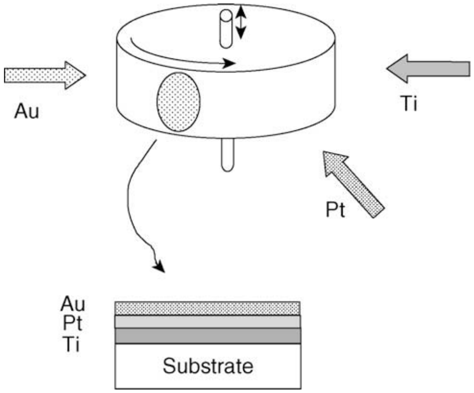

Figure 18.4: Sequential deposition of layers such as Ti, Pt, and Au, using multiple jet, moving substrate approach for substrates on a carousel.

and several jet sources can often be made so fast that micromixing occurs at submonolayer level. For example, lead zirconate titanate (PZT) can be made using three metal jets of Pb, Zr, and Ti, plus a plasma jet of oxygen, by choosing the carousel spin frequency so that less than one monolayer of any metal is deposited on any substrate during its time of passage through any of the jets. The three components are then well mixed and quickly converted to oxide by the oxygen plasma jet.

Larger substrates, such as 4, 6, or 8 inch wafers, or a limited number of small substrates, are better processed with a *single wafer, spin–scan* approach, as in the right side of Figure 18.2. The wafer is mounted on a fast spinning platter; the spin provides one degree of motion, and slow translation of the jet source or the platter provides the second degree. For example, the jet source can be mounted on a sliding vacuum flange, while the wafer spins around a fixed axis; the sliding jet source can then scan the wafer periodically across a diameter. The *scan* speed is slow at the wafer's edge and rapid through the wafer's center, to equalize residence times. The correct relation between scan speed and position must be found by experiment, but this approach gives uniform films and economical use of material for single wafer coating.

To coat a single wafer with a sequence of metal layers, we move the entire spinning platter past a sequence of jet sources. The simplest arrangement of sources is either a straight line or a circle. The spinning wafer visits each jet source in sequence, performing a slow scan back and forth in front of each source to give the desired multilayer sequence. For example, Figure 18.5 shows a compact *index arm* configuration in which several sources are arranged in a circle.

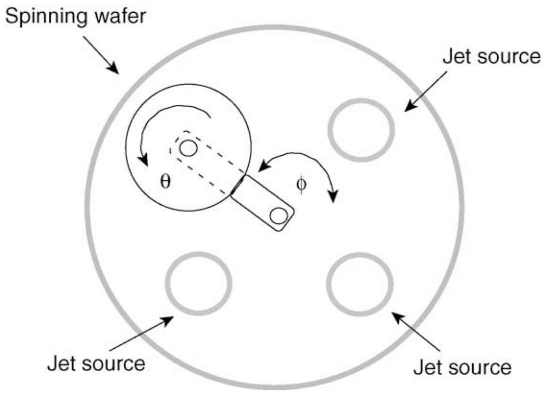

Figure 18.5: Index arm deposition system for depositing a sequence of layers on a single wafer. The wafer spins rapidly through an angle θ, while the index arm moves through angle ϕ, visiting each jet source in turn and executing a programmed periodic scan through an arc of angle ϕ in front of each source.

The index arm first positions one edge of the spinning wafer in front of the first source; the arm then executes a scan by sweeping the wafer back and forth through a short arc from one edge of the wafer through the opposite edge. The index arm then *indexes* to the next jet source, where the spin and scan motion is repeated. The same process can be done for a straight line of sources, but the index arm configuration allows a smaller, more compact chamber. At JPC, we use this index arm configuration for solder coating of a single wafer (4, 6, or 8 inch); a typical solder deposition might require a standard Ti + Pt + Au bond barrier, followed by a thick layer of AuSn or other solder, requiring four sources in the chamber. The ability to provide all solder-related layers for small numbers of substrates, without vacuum break, is important for customer research and development.

Spin–scan deposition on a single wafer results in a radially symmetric film, and this makes possible a direct measurement of film density. Symmetry results because the spin is very fast, around 800 rpm, and the scan is slow, several minutes for a 6 inch wafer. The film volume is found by taking profilometer height readings along a radius, and then doing a numerical integration. The mass of the film is measured with a microbalance; a 10 μm AuSn film on a 6 inch wafer weighs >2 g. We found that the density of AuSn deposited via JVD was $\sim 95\%$ of bulk, suggesting low porosity and low internal surface for adsorption of contaminants that impede wetting when the solder melts.

The high density result is also interesting in view of the extremely high local deposition rate and low substrate temperature in JVD, factors which should favor lower density. The average deposition rate is 10 μm over the 6 inch diameter area in ~ 40 minute, already substantial. But the local, instantaneous deposition rate is about 100 times as great, of the order of *micrometers per second*, since the entire flux of AuSn is delivered through a small jet area of $\sim 1\ \text{cm}^2$. It is also worth emphasizing that the substrate temperature always remains low in spin–scan operation, because no point on a substrate remains opposite a jet long enough to become hot, no matter how metal vaporization is accomplished inside the nozzle. In single wafer coating, the final wafer temperature never reaches 80 °C, so the process is relatively cool. Moreover, even when the wirefeed rate is increased by a factor of 4, with a corresponding increase in local deposition rate, the measured density remains high. We believe that this behavior is peculiar to low melting metals, such as the solder alloys, which have low Tammann temperatures [10], implying a surface atom mobility that favors dense films, even at the low substrate temperatures and high local rates of JVD. This is fortunate, since solder layers are generally thick, and must be deposited at a high rate if the process is to be economical, and on substrates that must remain cool if photoresist masks are to be undamaged.

In sum, the contributions of several jets can be integrated even at high overall growth rate. Jets operated singly in a prescribed time sequence yield multilayer structures; jets operated together give alloys or doped films, or, in a reactive mode, compounds such as oxides and nitrides. The multiple jet, moving substrate strategy has proven very successful at JPC, particularly for solder layer deposition, in both single wafer and batch modes.

18.4 Three JVD Jet Sources

Virtually all work in JVD is done with three jet source designs: (1) wirefeed to hot filament jet; (2) hollow cathode sputter jet; and (3) capillary feed wick jet.

18.4.1 Wirefeed to Hot Filament Source

Shown in Figure 18.6, this is the mainstay used at JPC for commercial production of solder coatings [6, 11]; AuSn can serve as an example. A fine wire of AuSn alloy is fed continuously

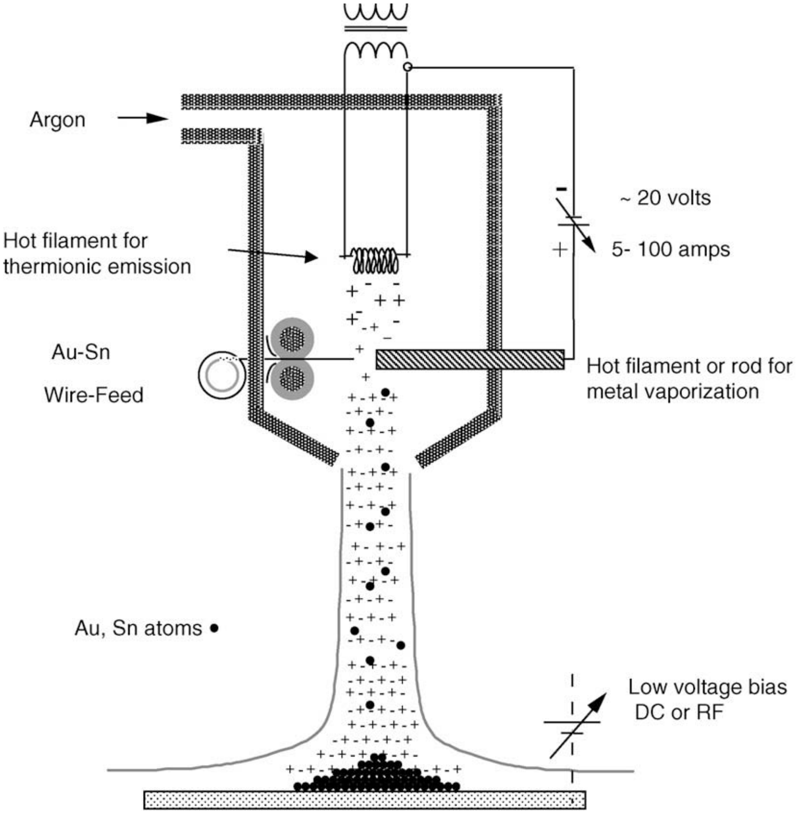

Figure 18.6: This deposition source combines the main features of the hot filament wirefeed and the e-jet plasma JVD sources. High argon ion density permits substrate cleaning, as well as ion bombardment of the growing film at low energy and high current.

against an electrically heated W coil structure located just upstream of the nozzle exit. On contact, the AuSn wire melts, wets, and vaporizes; individual Au and Sn atoms are swept downstream with the jet and deposit on the substrate, concentrated within a circle ~ 1 cm in diameter; radial diffusion of Au and Sn in the jet gives the AuSn deposit a Gaussian profile. At constant AuSn wirefeed rate the flux of Au and Sn atoms is constant, and the AuSn deposition rate is proportional to wirefeed rate, considerably simplifying thickness calibration. The Au to Sn ratio of the wire is preserved in the growing film.

Inclusion of a second hot filament as a source of thermionic electron emission enables electron avalanching and ignition of a low-voltage, high-current Argon plasma, which is then carried by the jet to the substrate. In addition to high-rate deposition, this *e-jet source* can supply Ar^+ ions at high density, $\sim 10^{15}$ ions/cm^3, for substrate precleaning or ion bombardment of the growing film [12–15]. The wirefeed to hot filament can be used for metals that do not alloy with and degrade the hot tungsten coil structure. This includes all metals commonly used for solder deposition, such as AuSn, InSn, and other alloys, etc., if they can be purchased as wire. Very high rates are possible with this wirefeed jet source; even a relatively slow wirefeed can give deposition rates approaching micrometers per minute over a 4 inch wafer. Most of JPC's commercial deposition of solders is carried out with the hot filament wirefeed and e-jet combination, in both atomistic and cluster modes.

18.4.2 Hollow Cathode Sputter Jet Source

This jet source is based on sputtering at high pressures of ~ 1 torr, and has been in use for many years at JPC. A hollow cathode provides a target for argon glow discharge sputtering of metal atoms, and also plays the role of a cylindrical nozzle. Argon is let in at one end, flows through the hollow cathode, and forms the sonic jet which sweeps sputtered atoms to the substrate. JVD sputter jet sources give much lower deposition rates than the wirefeed; they are limited by power dissipation, and the hollow cathode must be encased in a water-cooled copper block. However, they can generate a vapor of virtually any metal, and are appropriate for thin films in the several thousand Ångstrom range, as for example layers of Ti, Pt, and Au required as adhesion, diffusion barrier, and protective layers prior to solder bumping. The deposition rate can be calibrated against Ar^+ sputter current; when the gas flow conditions are fixed, this calibration is stable and accurate.

Clusters can also be generated in the sputter jet. Although the atom generation rates are much lower than the wirefeed, and therefore local gas phase metal atom concentrations are lower, nevertheless we have found conditions suitable for cluster initiation, growth, and deposition.

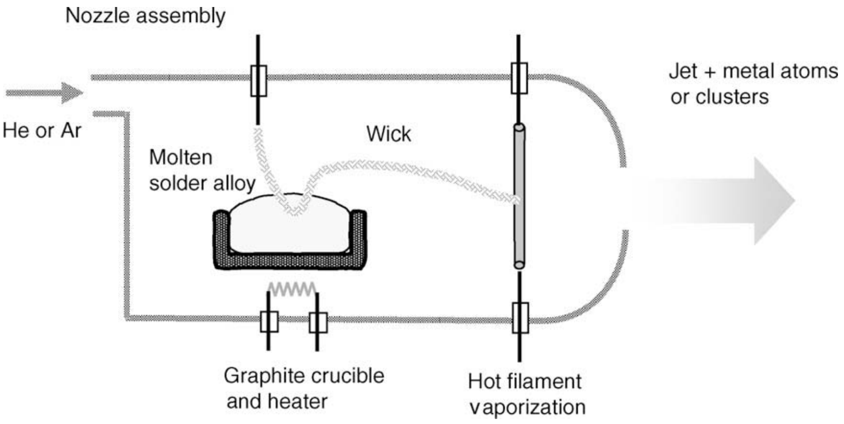

Figure 18.7: Wick jet source showing basic components: molten solder crucible, wire strand wick, and hot filament for vaporization.

18.4.3 Wick Jet Capillary Feed Source

The wick jet, shown in Figure 18.7, has three components connected in series inside the nozzle:

- a *reservoir* of molten solder, at a temperature somewhat above the melting point;
- a *wick fabricated* from tungsten wires, at temperature greater than that of the reservoir;
- a *hot zone vaporizer* consisting of a tungsten filament at very high temperature.

One end of the wick dips in the molten solder; the other is connected to the hot zone. The junction of the wick and hot zone is positioned upstream of the nozzle orifice. The wick and hot zone are Joule heated to their respective temperatures by a simple combination of alternating and direct electric currents (AC and DC).

The wick jet works by capillarity. As metal atoms vaporize from the hot zone, surface tension draws more liquid metal from the reservoir, through the wick, to the hot zone. In steady state the rates of vaporization and replenishment are equal.

The wick jet is universal for all solder metals, because all solder metals are compatible with hot tungsten. Wick transmission is sufficient to maintain an extremely high vaporization rate at the hot zone, and therefore a high deposition rate downstream. A major economic advantage of the wick jet is its use of bulk material as the supply for the reservoir; the material cost is thus as low as possible, with impurity level the only variable. Surface oxides float to the top of the reservoir, but are not drawn up the wick to be vaporized. Alloy compositions that do not lend themselves to wire drawing are easily handled as a melt, so there is no constraint on solder composition. Other advantages include the absence of moving parts, simple construction, and flexible form. The wick is particularly adaptable for nanocluster generation, and we first

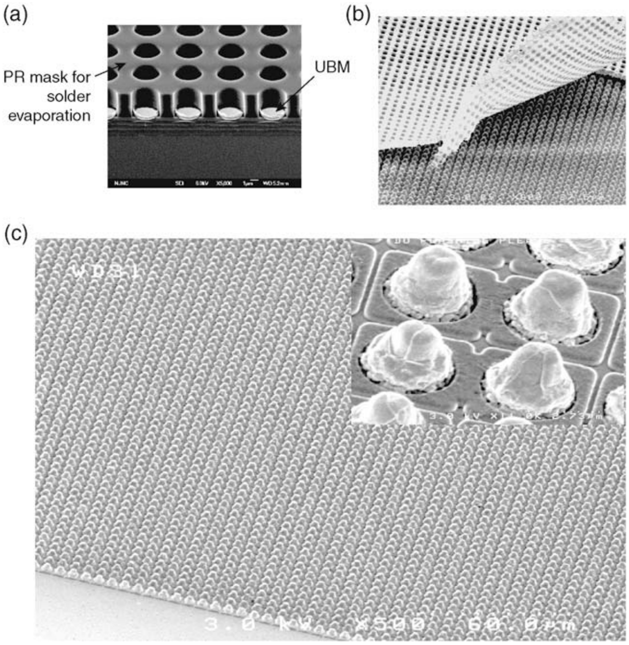

Figure 18.8: Indium solder bumps deposited by JVD, 3 μm on 5 μm pitch. (a) Photoresist mask; (b) lift-off; (c) as-deposited bumps. (Photograph courtesy of Alcatel-Lucent Bell Labs.)

observed cluster deposition using a wick jet. The solder bumps in Figure 18.8 were produced with an experimental wick jet design.

18.5 Generation and Deposition of Atoms and Clusters

With modest changes in pressure and flow, JVD jet sources give a choice of generating either metal atoms or metal nanoclusters. Cluster deposition is advantageous for solder layers, because atoms and heavier clusters will fill holes in photoresist masks in very different ways; cluster deposition is highly directional.

In the normal JVD range, at pressures ~ 1 torr and high jet speed, only single metal atoms deposit, but not clusters. Cluster formation must be initiated by first stabilizing a dimer. This requires a three-body collision of two metal atoms and one carrier gas atom, or else three metal atoms. While contributions of heterogeneous processes in the nozzle cannot be ruled out [16], three-body collisions are highly improbable in the jet: the metal atom and Ar or He concentrations are normally too low, and the transit times from nozzle to substrate are too short. The time for a metal atom to undergo a three-body collision, using a typical three-body recombination rate constant [17], is

$$\tau_{3B} \sim 10^{32}/(\mathrm{M})(\mathrm{Ar}) \sim 0.1/P_{\mathrm{m}} P_{\mathrm{Ar}} \tag{18.2}$$

where (M) and (Ar) are gas-phase concentrations (no./cm^3) of metal atoms and Ar atoms, and P_m, P_{Ar} are the pressures in torr of metal atoms and Ar atoms. For $P_m = 0.01$ torr and $P_{Ar} = 1$ torr, $\tau_{3B} \sim 10$ s. Since this far exceeds the normal transit time from nozzle to substrate, dimers cannot form.

Nevertheless, nanoclusters can be generated at high rate by moderate changes in several JVD conditions. From eq. (18.2), changes in carrier gas pressure, jet speed, source to substrate distance, identity of carrier gas (third body), and metal vaporization rate will all affect the dimer three-body nucleation rate. The time for subsequent cluster growth will be influenced by the distance from vaporization point to nozzle exit, and also exit to substrate distance. Moreover, all of these parameters can be conveniently altered to switch a jet source from atom generation to nanocluster generation. The transition is fairly sharp, but readily controllable. For example, at constant carrier gas flow rate, partially closing the pump valve will lower the jet speed, and increase the pressures of carrier gas and entrained metal atoms, which provides a simple way to initiate clustering.

Once dimers are formed, subsequent growth to trimers, tetramers, and nanoclusters is relatively fast. An energized trimer will be formed from a stabilized dimer by addition of a metal atom. This trimer has an excess energy of ~ 1 atom heat of vaporization, and a finite lifetime with respect to loss of that atom via unimolecular decomposition; if there are enough collisions with cold carrier gas atoms during that lifetime, enough excess energy will be removed to stabilize the trimer. Similar reasoning applies to a tetramer. As the number of atoms in the cluster increases, energy is more readily delocalized, and the unimolecular lifetime becomes longer. In JVD sources the carrier gas remains relatively cool, so that at accessible JVD pressures small clusters are quickly stabilized and growth is fast. The final cluster size then depends on the available concentration of metal atoms in the jet, which can be controlled by wirefeed rate or a sputter jet current. Cluster size can also be influenced by varying the distance to the substrate and the jet speed. In JVD wirefeed and wick jet sources the overall rate of cluster deposition is very high, at least equal to the rates of atom deposition, so that cluster deposition is fast and economical.

In sum, JVD sources can be adjusted in several ways to control cluster nucleation and growth rates. The freedom to choose between atom and cluster deposition has proven useful for solder layer applications.

18.6 Application of JVD to Solder and Related Layers

Electronic components must often be bonded to metal pads on an integrated circuit by solder [18]. One approach is to use a *preform* cut from solder foil to the correct dimensions and placed manually between the component and the pad. But as circuit dimensions diminish, placement of small preforms becomes difficult, and there is a limit to how thin a preform can be cut and handled. Under these conditions, it is better to deposit a photoresist mask that exposes only the solder pads, and then vapor deposit a solder layer over the entire patterned wafer. After photoresist lift-off, the contact pads remain coated with solder, ready for component placement.

Since the total contact pad area is only a small fraction of the wafer area, the lift-off approach may seem wasteful of expensive solders such AuSn. Some solders can be deposited electrochemically on just the contact pads, but it can be difficult to electrodeposit alloys with precise composition, where even small errors will affect the solder melting point, a critical property. JPC customers report incomplete satisfaction with electroplated AuSn, a frequent reason for turning to JVD.

In the past decade JPC has refined the JVD solder deposition technology [19], and is now able to supply all elemental and alloy solders, such as In, Sn, AuSn, InBi, InSn, SnAg, SnInAg, and SnCuAg. Solder bumping places severe requirements on process economics and material quality, and JVD addresses those requirements with several advantages:

- high deposition rates for atoms and clusters;
- accurate composition and thickness control;
- in situ ion etching to assure adhesion;
- alloy rather than component layer deposition;
- minimal material waste;
- adaptability to large and small substrates;
- compatibility with conventional photoresist and lift-off technology;
- single wafer or batch processing.

Prior to solder coating, wafers must be precleaned, particularly if they have patterned resist layers, where organic residue can compromise solder adhesion on pads. In JVD, the substrate can be cleaned with a high flux of low-energy argon ions generated by an e-jet source. Even without bias, the plasma sheath at the wafer surface provides a $\sim 8\text{–}10\,\mathrm{V}$ potential for bombarding ions, which is effective for removing a few monolayers of resist. An alternative is to use a JVD *microwave discharge jet* to generate high levels of atomic oxygen that removes organics by fast conversion to CO and CO_2 even at room temperature.

Almost all solders are currently deposited at JPC using the hot filament, wirefeed jet source, though indium must be done with the wick jet. All solder metals and alloys are compatible with the wirefeed source; none will alloy with or damage hot tungsten, so that the jet source lifetime is very long. Alloy wire of correct solder composition, for example eutectic AuSn

80/20, is vaporized into the jet as Au and Sn atoms; the right composition is reproduced in the depositing AuSn film. Precise composition, and therefore melting point, is a key requirement for a solder film, and customers take pains to verify it, by energy-dispersive X-ray spectroscopy measurements, melting/freezing point measurements, and finally by the performance of the solder in bonding. Solder layers can be from several to 20 μm thick, and both the wirefeed and wick jet sources can make such layers at high rate. For example, with 15 mm AuSn wire, fed at 2 inches per minute, a 6 inch diameter wafer will be uniformly coated in ~45 minutes. The wirefeed rate can be greatly increased, and the coating time reduced proportionately.

Solder bumps of micrometer dimension and area densities of millions/cm^2 can be made using conventional photoresist lithography [20, 21], but reliable manufacturing of such arrays is still a challenge. Moreover, as the circuit features become smaller, filling small holes in a photoresist mask adds to the challenge. Most patterned wafers received at JPC present large area pads several tens of micrometers wide. If the solder layer is to be several micrometers thick, then the resist walls must be about twice as high. For large area bond pads the aspect ratio (photoresist thickness/pad width) will be substantially less than 1. For these low aspect ratio cases, the wirefeed *atomistic* deposition of individual Au and Sn atoms is a reliable approach; on the pad the deposited solder has the correct thickness and a flat profile. However, small-area pads, with lateral dimensions ~ 10 μm or less, will still require several micrometers of solder. The photoresist will still be thick, and the windows in the photoresist will have a higher aspect ratio. We found that as the aspect ratio approached 1, small holes were difficult to fill, if we tried to fill them by depositing atoms.

The difficulty has the following origin. Although the jet is collimated and traveling line-of-sight normal to the substrate, the metal atoms inside it are not; they collide frequently with He or Ar atoms, their velocities are randomized, and they impact the film at angles that can be far from perpendicular. Some of these impacting metal atoms will not ‘see’ the bottom of a deep hole. For small windows with aspect ratio of order 1, resist walls cut off atoms coming from angles far from the normal, and shadowing is severe. In addition, ‘breadloafing’ from deposition on the sidewalls will further constrict the resist window as deposition continues. As a result, the solder bump is no longer flat, but dome shaped; moreover, it will be significantly thinner than needed. One can compensate by depositing excess metal, but this wastes material and time.

JVD provides an effective alternative: generate and deposit heavier *nanoclusters*. The nanoclusters grow inside the nozzle, are accelerated by the jet, and travel toward the substrate. A massive nanocluster will be hit many times by randomly directed carrier gas atoms, but its transverse velocity components remain extremely small. The trajectory of the nanocluster then remains parallel to the jet, and it impacts the growing film at a right angle. In consequence, there is little shadowing by resist walls, and since sidewall deposition is also reduced, there is reduced breadloafing [22]. The resist window is therefore filled by solder clusters *from the bottom up*, giving a flat-topped solder bump of undiminished thickness. The sequence of scanning electron micrographs in Figure 18.8 shows the photoresist mask, the lift-off process under way, and an array of indium (In) bumps made from In nanoclusters deposited by JVD [20]. The bump diameter is 3 μm, while the pitch is 5 μm. The flat top on the In bumps is noticeable. These are quite small-diameter bumps, and there has been some breadloafing, evident in the slightly conical shape. In other work, in which In was deposited in 4 × 4 and 6 × 6 μm windows, breadloafing had much less of an effect, and the bump sides were less sloped. It is worth emphasizing that this cluster filling process gave uniform deposition over 6 and 8 inch diameter wafers, and was carried out at economically high deposition rates, e.g. 5 μm of In over a 6 inch wafer in < 15 minute.

18.7 Summary

JVD's *jet in low vacuum* strategy is applicable to many kinds of thin film. In addition to simple metal films, these include multilayers, alloys, multicomponent oxides and nitrides, organic and host–guest films, cluster and cluster embedded films.

The jet in a low vacuum strategy is economical to implement. Even relatively small, inexpensive mechanical pumps will maintain critical flow conditions, providing high-speed collimated jets in a small-footprint, flexible apparatus. The carrier gas flows represent only a small material cost. The batch process turnaround time in a JVD chamber is a matter of minutes.

Mechanisms for relative motion between jet source and substrates, combined with the use of several jets simultaneously or in sequence, allow design of processes for substrates of many sizes and shapes, for production of many complex film materials. JVD metal sources are based on techniques such as glow discharge sputtering or direct vaporization, which can deposit nearly every metal in the Periodic Table, with no toxic metal precursors or harmful exhausts.

In JVD, rates of metal deposition are generally high because the jet entrains a large partial pressure of metal atoms, travels at the speed of sound, remains collimated, and deposits atoms with a high capture efficiency in a localized area. Even if metal atoms comprise less than 1% of the jet, the deposition rate will approach micrometers per minute over a 4 inch wafer. Rates of cluster deposition are equally high.

Solder layer deposition in particular is naturally suited to JVD, as a consequence of high deposition rates, short pump down times, efficient material use, and plasma precleaning.

Much of JVD's versatility arises from the use of independent jets and relative motion schemes to give multilayer structures. These capabilities have now been focused on the vapor deposition of solder metals and alloys, addressing a growing need in microelectronic packaging technology. JVD can provide not only the solder layers, but also the required adhesion, diffusion barrier, and protective cap layers. JVD employs several jet source designs that can run at high deposition rate, while ensuring the required solder properties: precise composition, melting point, purity, and adhesion, independent of substrate size and shape. Moreover, the ease of converting from atom to cluster deposition has important consequences for jet deposition of solder layers, significantly extending downward the size range of solder bumps that can be cleanly deposited. All of the common solder elements and alloys are compatible with JVD jet sources, and can be vaporized and deposited with accurate preservation of composition, in atomic or cluster form. Localized deposition and high capture efficiency make JVD intrinsically economical for costly materials such as AuSn.

Appendix Survey of Miscellaneous JVD Films and Applications

Here we briefly review some past work that illustrates the range of capabilities of JVD.

Cu + Au Multilayer Electrodes

We used Cu and Au jet sources in sequence, to make thin film electrodes in production runs for AT&T Bell Laboratories and a US Navy application. The substrates were 50 mm diameter piezoceramic wafers less than 1 mm thick; these required a 1.5 μm Cu electrode, flashed with 50 nm Au, on both sides of the wafer, with a 0.25 mm border free of metal and cleanly defined at the perimeter. Wafers were mounted on the carousel in accurately machined receptacles which supported the wafer, oriented it toward the jets, and defined the border.

Al, Al_2O_3 Microlaminates

Jet sources of Al and O_2 were used to deposit thick microlaminates consisting of 50 nm layers of Al alternating with 5 nm of Al oxide [23] at high rate. The microlaminates coating exhibited a hardness equal to that of microlaminates made by sputtering [24], a far slower ultrahigh vacuum process.

PZT: Ferroelectric FRAM Non-Volatile Memories

Four jet sources simultaneously supplied Pb, Ti, Zr, and O_2 to Pt-coated, heated Si wafers mounted on a spinning carousel. The Pt barrier layer was also deposited by JVD. The resulting 1 μm PZT film of PZT was deposited in less than 1 hour [25], and exhibited excellent values of remanent polarization, coercive field, switching endurance, and dielectric constant, equaling or exceeding those obtained with more conventional methods.

PZT: Pyroelectric Detectors

PZT was deposited on 18 substrates of 2 inch diameter mounted on a carousel, using three jet sources of Zr, Ti, and PbO, in a 0.5 torr downstream O_2 pressure [26, 27], with substrates at

550 °C to promote perovskite growth. The remanent polarization, coercive field, pyroelectric coefficient, and dissipation factor, compared favorably to bulk PZT.

Nickel Ferrite Ceramic Films

We deposited ceramic films of stoichiometric $NiFe_2O_4$ using a single wirefeed plus e-jet source; $NiFe_2$ alloy wire was vaporized thermally inside the nozzle. The source was run in plasma mode, so that a 1 inch square alumina substrate in front of the jet was heated to $T \sim 600\,^{\circ}C$, in part by ion–electron surface recombination. $NiFe_2O_4$ films of thickness $> 25\ \mu m$ were grown at rates $\sim 100\ \mu m/hour$. Films were nearly crystalline, with good magnetic and physical properties as characterized by magnetization, stress-induced anisotropy, and hysteresis loops [28].

Electronic-Grade Silicon Nitride

Silicon nitride films of remarkable electronic quality were grown on a room-temperature substrate using a microwave discharge jet source [29] that produces Si atoms, Si-bearing molecular fragments, and N atoms from SiH_4 and N_2. In a metal-nitride semiconductor (MNS) capacitor the electrical behavior was superior to that of any previously reported [29–33], as characterized by breakdown strength, radiation hardness, interface trap density, etch rate in buffered oxide etch, index of refraction, breakdown strength, density of interface states, reduced tunneling current, and low H content.

Fiber Coating

Despite the directionality of the JVD jet source, we showed that a thin fiber oriented perpendicular to the jet could be coated uniformly. This is possible because the collision mean free path in the jet at 1 torr is $\sim 100\ \mu m$; fibers of smaller diameter will be struck uniformly from all directions by metal atoms, as if in high vacuum. We have coated 12.5 µm alumina fibers with thousands of Ångstroms of Cu and Al, with uniformity verified by scanning electron microscopy.

Coating of Thermally Sensitive Membranes

The low substrate temperature capability of JVD is being exploited in the coating of Au and Pt as fine line electrodes on a 9 µm PVDF piezoelectric membrane through a foil mask. PVDF is thermally sensitive, and can be depoled at $T \sim 350\,^{\circ}C$, so the low-temperature capability of JVD is critical.

Ceramic Host–Organic Guest Films

Using multiple jets including a novel organic vapor jet [34], we trapped complex guest organic molecules such as rhodamine B and methyl red in a range of host ceramic films: SiO_2, SiN_x, Al_2O_3, and MgO, at high guest concentrations $\sim 1\%$. Using this approach we demonstrated deposition, patterning and photobleaching of Methyl Red/ceramic to make thin film wave guides. We made a thin film solid host dye laser by trapping rhodamine 6G, and also an acid–base indicator using trapped methyl red [35]. Ceramic host–organic guest films can be made by mechanical or sol gel methods [36], but these are multistep processes, limited to soluble species, often including time-consuming thermal treatment. In JVD the host–guest combination is generated in minutes, at room temperature, and by a vapor deposition technique compatible with existing semiconductor microelectronic processing.

Polymer Deposition: Parylene

We constructed a parylene–N vapor jet source [37] in which the cracking reactions of the Gorham process [38] were carried out inside a small nozzle structure, which then accelerates the active fragments to the substrate. In addition, we mixed into the main flow a stream of atomic hydrogen. The results were a greatly enhanced deposition rate, enhanced adhesion, increased hardness, and a reduction in dielectric constant from 1. 65 to ~ 1.47. X-ray diffraction showed an amorphous film, with no hint of crystallinity. There is a dramatic effect of H atoms on parylene–N deposition rate and properties.

Deposition on Liquid and Paper Surfaces

JVD's low vacuum conditions enable deposition on liquids of sufficiently low vapor pressure, and on surfaces not tolerated in a high vacuum system. Thus, we were able to deposit Au and other metal atoms on liquid water, glycerol, and epoxy surfaces, thereby generating Au colloids [1, 39]. We deposited 5 μm of Cu on a strip of paper 2 inches wide and 3 feet long, wrapped around a spinning carousel, using a wirefeed source. The adhesion was excellent, and the Cu coating carried ~ 10 A without any sign of paper carbonization or Cu delamination.

References

[1] B.L. Halpern, J. Colloid Interface Sci. 86 (1982) 337.
[2] J.J. Schmitt, B.L. Halpern, US Patent 4,788,082 (1988).
[3] J.J. Schmitt, B.L. Halpern, US Patent 5,725,672 (1998).
[4] B.L. Halpern, J.J. Schmitt, J. Vac. Sci. Technol. A 12(4) (1994) 111111623.
[5] B.L. Halpern, J.J. Schmitt, J.W. Golz, D.L. Johnson, D.T. McAvoy, J.Z. Zhang, Y. Di, in: Society of Vacuum Coaters, Proceedings of 35th Annual Technical Conference, Baltimore, MD (March 22–27, 1992).
[6] B.L. Halpern, J.J. Schmitt, Y. Di, J.W. Golz, D.L. Johnson, D.T. McAvoy et al., Metal Finishing (December 1992).

[7] J.B. Anderson, in: P.P. Wegener (Ed.), Molecular Beams and Low Density Gas Dynamics, Marcel Dekker, New York (1974) Chap. 1.
[8] J. Fernandez de la Mora, B.L. Halpern, J.A. Wilson, J. Fluid Mech. 149 (1984) 217.
[9] J. Fernandez de la Mora, J. Chem. Phys. 82 (1985) 3453.
[10] J. Sun, D. Ma, H. Zhang, X. Liu, X. Han, X. Bao et al., J. Am. Chem. Soc. 128 (2006) 15756.
[11] J.J. Schmitt, B.L. Halpern, US Patent 5,356,673 (1994).
[12] B.L. Halpern, US Patent 5,571,332 (1996).
[13] B.L. Halpern, J.W. Golz, J.-Z. Zhang, D.T. McAvoy, A.R. Srivastava, J.J. Schmitt, in: A.R. Srivastava, C.R. Clayton, J.K. Hirvonen (Eds.), Advances in Coatings Technologies for Corrosion and Wear Resistant Coatings, Minerals, Metals, and Materials Society (1995).
[14] J.W. Golz, J.-Z. Zhang, H. Han, B. Motherway, A.R. Srivastava, B.L. Halpern, J.J. Schmitt, in: A.R. Srivastava, C.R. Clayton, J.K. Hirvonen (Eds.), Advances in Coatings Technologies for Surface Engineering, Minerals, Metals, and Materials Society (1997).
[15] J.-Z. Zhang, J.W. Golz, M. Gorski, J.J. Schmitt, B.L. Halpern, IMAPS Proceedings, International Symposium on Microelectronics (1997) 144.
[16] W. Knauer, J. Appl. Phys. 62 (1987) 841.
[17] J.A. Kerr, S.J. Moss, CRC Handbook of Bimolecular and Termolecular Rate Constants, Vol. II, Table 197, CRC Press, Boca Raton, FL (1981).
[18] G. Riley, Tutorial 2. Solder Bump Flip Chip. <http://www.flipchips.com/tutorials.html>.
[19] M. Gorski, B.L. Halpern, Advanced Packaging 31 (February 2003).
[20] N. Basavanhally, D. Lopez, V. Aksyuk, D. Ramsey, E. Bower, R. Cirelli et al., IEEE Trans. Adv. Packag. 30 (2007) 622.
[21] P. Merken, J. John, L. Zimmermann, C. Van Hoof, IEEE Trans. Adv. Packag. 26 (2006) 60.
[22] K. Wegner, E. Barborini, P. Piseri, P. Milani, Kona 24 (2006) 54.
[23] L.M. Hsiung, J.-Z. Zhang, D.C. McIntyre, J.W. Golz, B.L. Halpern, J.J. Schmitt, H.N.G. Wadley, Scripta Metall. Mater. 29 (1993) 293.
[24] A.T. Alpas, J.D. Embury, D.A. Hardwick, R.W. Springer, J. Mater. Sci. 25 (1990) 1603.
[25] C.-L. Huang, B.A. Chen, T.P. Ma, J.W. Golz, Y. Di, B.L. Halpern, J.J. Schmitt, Ferroelectrics (March 1992).
[26] J. Golz, Y. Di, B. Halpern, J.J. Schmitt, P. Cirino, A. Bartlett, Mater. Res. Soc. Symp. Proc. 284 (1993) 541.
[27] K.K. Deb, T. Tamagawa, Y. Di, G. Cui, B.L. Halpern, J.J. Schmitt, J. Electron. Mater. 30(2) (2001) 89.
[28] G.F. Dionne, G.-J. Cui, T. McAvoy, B.L. Halpern, J.J. Schmitt, IEEE Trans. Magnet. 31(6) (1995).
[29] D. Wang, T.P. Ma, J.W. Golz, B.L. Halpern, J.J. Schmitt, IEEE Electron Device Lett. 13 (1992) 482.
[30] J.J. Schmitt, B.L. Halpern, US Patents 5,256,205 (1993); 5,356,672 (1994).
[31] X.-W. Wang, T.P. Ma, G.-J. Cui, T. Tamagawa, J.W. Golz, S. Karechi et al., Jpn. J. Appl. Phys. 34 (1994) 955.
[32] A. Mallik, X.W. Wang, T.P. Ma, G.J. Cui, T. Tamagawa, B.L. Halpern, J.J. Schmitt, J. Appl. Phys. 79 (1996) 8507.
[33] T.P. Ma, IEEE Trans. Electron. Devices 45 (1998) 1.
[34] B.L. Halpern, US Patent 5,650,197 (1997).
[35] J.-Z. Zhang, D.T. McAvoy, B.L. Halpern, J.J. Schmitt, R. Zanani, K. Schaschek, J. Electron. Mater. 23(11) (1994).
[36] D. Avnir, V.R. Kaufmann, R. Reisfeld, J. Non-Cryst. Solids 74 (1985) 395.
[37] B.L. Halpern, P. Komarenko, R.F. Graves, P.D. Fuqua, J.F. McDonald, G.-R. Yang et al., Mater. Res. Soc. Symp. Proc. Vol. 544, Materials Research Society (1999).
[38] W.F. Beach, C. Lee, D.R. Bassett, T.M. Austin, R. Olson, Encyclopedia of Polymer Science and Engineering, 2nd ed., Vol. 17, John Wiley & Sons, New York (1989) 990.
[39] D.L. Johnson, J.J. Schmitt, B.L. Halpern, Mater. Res. Soc. Symp. Proc. 206 (1991) 333.

Index